AAPG Memoir 42
SEG Investigations in Geophysics, No. 9

Interpretation of Three-Dimensional Seismic Data

Seventh Edition

By
Alistair R. Brown

Consulting Reservoir Geophysicist

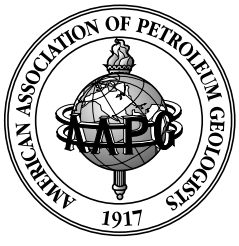

Published jointly by
The American Association of Petroleum Geologists
and the Society of Exploration Geophysicists

Tulsa, Oklahoma, U.S.A.

Downloaded 25 Jun 2012 to 95.28.162.50. Redistribution subject to SEG license or copyright; Terms of Use: http://segdl.org/

Seventh Edition
Copyright © 2011, 2004, 1999, 1996, 1991, 1988, 1986
The American Association of Petroleum Geologists and (2011 and 2004 and 1999 only)
the Society of Exploration Geophysicists
All Rights Reserved

ISBN13: 978-0-89181-374-3

AAPG and SEG grant permission for a single photocopy of an item from this publication for personal use. Authorization for additional copies of items from this publication in any form (hardcopy, digital/electronic scanning, or other digital transformation into computer-readable and/or transmittable form) for personal or corporate use is granted provided the appropriate fee is paid directly to the Copyright Clearance Center, 222 Rosewood Drive, Danvers, Massachusetts 01923, http://www.copyright.com. For circumstances occurring outside authorization of Copyright Clearance Center contact permissions@aapg.org.

AAPG Editor: Stephen E. Laubach
Geoscience Director: James B. Blankenship

SEG Editor: Vladimir Grechka
Director, Publications: Ted Bakamjian

This publication is available from:

The AAPG Bookstore
P.O. Box 979
Tulsa, OK, USA 74101-0979
Tel.: +1-800-364-AAPG (USA, Canada)
or +1-918-584-2555
Fax: +1-800-898-2274 (USA)
or +1-918-560-2652
http://bookstore.aapg.org
e-mail: bookstore@aapg.org

Society of Exploration Geophysicists
P.O. Box 702740
Tulsa, OK , USA 74170-2740
Tel +1-918-497-5546
Fax +1-918-497-5565
www.seg.org/bookmart/
e-mail: books@seg.org

Geological Society Publishing House
Unit 7, Brassmill Enterprise Centre
Brassmill Lane, Bath, BA1 3JN, U.K.
Tel: +44-1225-445046
Fax: +44-1225-442836
www.geolsoc.org.uk
http://bookshop.geolsoc.org.uk
e-mail: dawn.angel@geolsoc.org.uk

Canadian Society of Petroleum
Geologists
#160, 540 5th Avenue S.W.
Calgary, Alberta T2P 0M2, Canada
Tel: +1-403-264-5610
Fax: +1-403-264-5898
www.cspg.org
e-mail: jamie.croft@cspg.org

Affiliated East-West Press Private Ltd.
G-1/16 Ansari Road, Darya Ganj
New Delhi 110 002
India
Telephone: +91-11-23264180
Fax: +91-11-23260536
E-mail: affiliat@vsnl.com

The American Association of Petroleum Geologists (AAPG) does not endorse or recommend products or services that may be cited, used, or discussed in AAPG publications or in presentations at events associated with the AAPG.

Downloaded 25 Jun 2012 to 95.28.162.50. Redistribution subject to SEG license or copyright; Terms of Use: http://segdl.org/

Preface to the Seventh Edition

The original suggestion to prepare a book on Interpretation of Three-Dimensional Seismic Data occurred in 1979, only four years after the advent of commercial 3-D surveys. Who would then have thought that 3-D would become such an important part of our business? The first edition of this book was published 23 years ago. To date the book has been through six editions and more than 23,000 total copies have been sold, that is 1000 per year, or 3 per day. The subject continues to be important and there is still a lot to learn.

Extracting more geology from seismic data continues to be the prevailing theme. Understanding the data properly and using modern workstations in an appropriate manner are critical. I continue to emphasize the techniques which I consider important and useful. Too many interpreters today use techniques because they exist rather because there is some established or postulated purpose. Seismic data is composed of structural continuity, stratigraphic and reservoir variability, the seismic wavelet, and noise of various kinds. Seismic interpretation is the thoughtful procedure of separating them. The first two are desirable geologic information; the second two are to be recognized and excluded.

Several new sections, figures and text updates have been added to continue the value of this book into the future. But the major additions are chapters or subchapters on Inversion, Visualization, and Spectral Decomposition. Rebecca Latimer in *Inversion and Interpretation of Impedance Data* compares the different methods of inversion and tells us which to use in different situations. David Roberts in *Visualization and Visual Integration* demonstrates some amazing insights possible with modern methods. Greg Partyka helps the interpreter understand *Spectral Decomposition* and shows how to get additional interpretive leverage out of a narrow frequency band. I really appreciate the efforts of these authors and also many other people who have had an impact on the content of this book. I appreciate the discussions with my clients, with course participants and with industry friends. They have all helped my understanding of the subject which I now pass on to you, so that you get more geological information out of your seismic data.

We now include a digital version of the book on disk, and we hope that this innovation is useful. On the disk you will also find several movies and animations. These emphasize the value of motion for visualization, and also add support to other messages throughout the book.

Alistair R. Brown
Dallas, Texas
October 2010

Downloaded 25 Jun 2012 to 95.28.162.50. Redistribution subject to SEG license or copyright; Terms of Use: http://segdl.org/

Preface to the Sixth Edition

Where oil is first found is in the minds of men.

-— WALLACE PRATT

This quotation is familiar to all geoscientists, but it is just as pertinent today as it has ever been. Today's advanced geophysical workstations are truly magnificent tools, but we should remember that they are only tools. The skill remains the geological interpretation of geophysical data. I sometimes apologize to myself and others that this still needs to be said — but it surely does! I am indeed disappointed by the general standard of seismic interpretation in the world today.

Too many interpreters rely on the workstation to find the solution. All too often, I am in contact with seismic interpreters who have misidentified a horizon, failed to understand the phase and polarity of their data, distorted the result with a poor use of color, used an inappropriate attribute, failed to recognize a significant data defect, or are still frightened by machine autotracking. We cannot benefit from some of the more advanced techniques available today until these issues have been properly overcome. More education at a fairly fundamental level is still required.

For these reasons, I have resisted the temptation to expand the book into various recent and more advanced topics. The present book is large enough, anyway! So, I freely acknowledge the omission or incomplete treatment of inversion, amplitude variations with offset, geostatistics, visualization, and converted and shear wave interpretation.

The modifications for the Sixth Edition, then, are not extensive. There are several updates and corrections, and some new data examples. Those still grappling with the phase and polarity of their data may find assistance in Appendix C. Appendix D is a Summary of Recommendations to help today's interpreter get more out of 3-D seismic data within a reasonable period of time. These recommendations and much of the book are aimed at redressing the problems discussed above. Please consider basic interpretation issues in conjunction with modern workstation techniques. Let's get the balance between geology, geophysics, and computer science *right!*

Alistair R. Brown
Dallas, Texas
April 2003

Downloaded 25 Jun 2012 to 95.28.162.50. Redistribution subject to SEG license or copyright; Terms of Use: http://segdl.org/

Preface to the Fifth Edition

It is less than three years since I was writing the Preface to the Fourth Edition. This rapid turnaround demonstrates the popularity of 3-D technology and the buoyancy of book sales. I hope this book remains an important reference for 3-D interpreters for many more years. For this edition we have included SEG as co-publisher in order to reach even more readers.

The Fifth Edition contains three new chapters: **Depth Conversion and Depth Imaging** is the longest. Depth conversion is a time-honored subject that has been long neglected by this book; I appreciate the help of Agarwal and Denham in filling the gap. Depth imaging is a new and important subject, so the results-oriented contribution by Abriel and his Chevron colleagues is a significant addition. **Regional and Reconnaissance Use of 3-D Data** is a demonstration of how extensive the use of 3-D data has become. Huge surveys and several normal-sized surveys joined together are providing new views of large areas. **Four-D Reservoir Monitoring** addresses the subject of multiple 3-D surveys over the same field being used to monitor changing reservoir conditions. This chapter shows some interesting results for several fields.

I have added examples of hydrocarbon reservoir reflections to Chapter 5. There are still good opportunities for recognizing hydrocarbons directly in our normal seismic data if we use the best modern data, we display it in an optimal fashion, and we think about it correctly. Important as AVO (Amplitude Variations with Offset) is, stacked and migrated amplitudes are still pregnant with hydrocarbon and reservoir information. My understanding of frequency-derived attributes has developed recently and this subject provides a significant addition to Chapter 8.

The importance of zero phase has always been a keen subject of this book and today there is a widespread appreciation of this important subject. When we get our data close to zero phase, difficult as this is, we are left with the option, or ambiguity, of two polarities. There is no true standard of zero-phase processed polarity and therefore the simple word "normal" has no universal meaning. However, there are distinct regional preferences which constitute local norms. Thus I recommend the adoption of the terms **American Normal Polarity** and **European Normal Polarity,** which are the most popular in these regions but are, of course, opposite to each other. American Normal, undoubtedly the most widespread in North America, is where a positive amplitude (peak, or in common color usage, blue reflection) represents an increase in acoustic impedance, and a negative amplitude (trough, or in normal color usage, red reflection) represents a decrease in acoustic impedance. European Normal, undoubtedly the most widespread in Europe, is where a positive amplitude (blue) represents a decrease in impedance and a negative amplitude (red) represents an increase in impedance. Neither America nor Europe is completely homogeneous in its polarity usage. The international movement of companies and their staff works against homogeneity, as do ignorance and errors in acquisition and processing, and a different interpretation of recording standards. Australia follows European Normal Polarity and appears to be the most homogeneous region of the world.

Let the data speak to you. Listen to what they have to say and try to believe it. Too many interpreters today impose on their data a geologic model that becomes a barrier to understanding. The seismic response (wavelet, phase, polarity, bandwidth, etc.) is the critical link between the seismic data and the geology. Understanding this response is vital if we are to grasp the detailed geology behind the data. Let us all remember this as we advance our competencies of information extraction.

A new subject not fully covered by this edition is Volume Visualization. We have had the first stages of this subject for several years and various volumetric displays are already in this book. However, recently Virtual Reality has arrived and Immersive Visualization Systems permit us to "experience the data directly." We are beginning to see vision domes, visionariums, virtual workbenches, and virtual caves using such tools as active or passive stereo, 3-D wands, haptic gloves, and sonification. Here is a new world of opportunity for collaboration of teams of people inside the data. It will be some time, however, before these systems are broadly available, so they will be reported fully in a later edition. These and other new computer developments are very exciting, but it is important to remember that they are just tools; they are not *the* solution. There remains no substitute for cogent geophysical and geological thought!

Alistair R. Brown
Dallas, Texas
March 1999

Downloaded 25 Jun 2012 to 95.28.162.50. Redistribution subject to SEG license or copyright; Terms of Use: http://segdl.org/

Preface to the Fourth Edition

Consider everything to be geology until proved otherwise.

—— MILO BACKUS

This is being written shortly after the 20th anniversary of the first commercial 3-D survey. Few could then have imagined how important and widespread the technology would become. Mature petroleum areas are now totally covered with 3-D, surveys being contiguous, overlapping or on top of each other. Speculative 3-D surveys are commonplace and have made more 3-D data available to more interpreters. Many speculative surveys are very large; one in the Gulf of Mexico covers 700 blocks or more than 16,000 km^2. Surveys over producing fields are being repeated for seismic monitoring of production, generally known as 4-D.

There are now many published stories of exploration and exploitation successes attributed to 3-D seismic data. Three-D reduces finding costs, reduces risk, and improves success rates. Royal Dutch/Shell reports that its exploration success outside North America increased from 33% in 1990 to 45% in 1993 based largely on 3-D. Their seismic expenditures are now 90% on 3-D surveys. Exxon considers "3-D seismic to be the single most important technology to ensure the effective and cost-efficient exploration and development of our oil and gas fields." Exxon reports that their success in the Gulf of Mexico in the period 1987-92 was 43% based on 2-D data and 70% based on 3-D data; in the same period in The Netherlands the numbers were 47% (2-D) and 70% (3-D). Mobil reports that in the South Texas Lower Wilcox trend their success based on 2-D was 70% but this rose to 84% based on 3-D. Amoco have concluded that "the average exploitation 3-D survey detects six previously unknown, high quality drill locations," and "adds $9.8 million of value" to a producing property. Petrobras reports that in the Campos Basin offshore Brazil their success rate has increased from 30% based on 2-D data to over 60% based on 3-D.

With this tremendous level of activity and euphoria, and with exploration and development problems becoming more difficult, the issue of the moment is to apply the technology appropriately. There is still a great amount of data underutilization. In an attempt to correct this, let us not impose too rigorous a geologic model on our interpretations; let us seek a full understanding of the seismic character, and allow the data to speak to us. "Consider everything to be geology until proved otherwise."

On the other hand our data has its shortcomings and interpreters benefit greatly from an understanding of geophysical principles and of the processes that the data has been through before it reaches the interpretation workstation. Reductions in acquisition costs have sometimes been over-zealous resulting in significant data irregularities which can only be partly fixed in data processing. There is no substitute for good signal-to-noise ratio. We cannot expect "to make a silk purse out of a sow's ear" and 3-D is certainly not a universal panacea. Reservoir evaluation or characterization using 3-D data is popular today and so it should be, but data quality imposes limitations. I know several projects where the results have been disappointing because the data just wasn't good enough. We must have realistic expectations.

The largest single development in 3-D interpretation techniques since the publication of the last edition has been the generation, display and use of seismic attributes. This Fourth Edition has a whole new chapter on the subject. In addition there are many new data examples and procedural diagrams distributed throughout the book in an attempt to bring the treatment of every aspect of 3-D interpretation up-to-date.

Alistair R. Brown
Dallas, Texas
April 1996

Downloaded 25 Jun 2012 to 95.28.162.50. Redistribution subject to SEG license or copyright; Terms of Use: http://segdl.org/

Preface to the Third Edition

The 3-D seismic method is now mature. Few people would doubt this, and the huge number of geophysicists, geologists and engineers using it are testimony to the accepted power of 3-D seismic technology. Three-D seismic is used for exploration, for development and for production, and hardly a corner of the world is as yet untouched by the technology. Substantially more than 50% of all seismic activity in the Gulf of Mexico and the North Sea is now 3-D! The total land area of The Netherlands is now 30% covered by 3-D seismic data! Execution of 3-D surveys is a condition for the granting of some licenses. Some companies, or divisions of companies, have given up 2-D data collection altogether!

The new Foreword to this edition provides a striking accolade for 3-D seismic and its association with the interactive workstation. Workstations are today almost as numerous as 3-D surveys, and so they should be. But both of them are underutilized. The amount of information in modern 3-D seismic data is very great and the capability to extract it lies in the proper use of the computer-driven workstation. All too many of today's practitioners are applying traditional 2-D methods carried over from their experience of 2-D data. This is natural but inefficient, time-consuming and misdirected. The 3-D interpreter needs to understand and use the tools available to him in order to do justice to his investment in 3-D data. Oil company management needs to offer appropriate encouragement to geoscientists. The next phase of our technological evolution must be to make proper use of what we already have.

Another impediment to proper utilization of 3-D data is confused terminology. We find a plethora of terms referring to the same product. For example, a horizontal section or time slice is also referred to, unfortunately, as a Seiscrop, Seiscrop section, isotime (slice or section), horizontal time slice, time-slice map or seiscut. At one time companies saw a competitive advantage in special or trademarked names, but that time has passed. Everybody in the 3-D processing or display business can make a time slice. Interpreters of three-dimensional data need to make regular use of time slices as they are essential to a complete interpretation. Fancy names just encourage inexperienced 3-D interpreters to distance themselves from the product and develop the opinion that they are a phenomenon to be marvelled at rather than a section pregnant with geologic information. I believe that much of the confusing terminology has arisen because of a lack of distinction between the process and the product. We use the process of *amplitude extraction* to make the product of a **horizon slice;** we construct a section in the *trace* direction to make a **crossline;** we *reconstruct a cut* through the volume to make an **arbitrary line.** The interactive system vendors generate most of these capabilities for us and are concerned more about the procedure. Interpreters are concerned more about the utilization of the product. This book attempts to clarify these issues by using only the more accepted terms.

The Third Edition sees a further significant expansion in material with many new companies—oil companies, service companies, and interactive workstation vendors—contributing data examples. Examples from Europe play a more significant role than in previous editions and there are five new case histories.

Alistair R. Brown
Dallas, Texas
September 1991

Downloaded 25 Jun 2012 to 95.28.162.50. Redistribution subject to SEG license or copyright; Terms of Use: http://segdl.org/

Preface to the Second Edition

Since publication of the first edition, 3-D seismic technology has continued its trend toward universal acceptance and maturity. Much of this has resulted from the emphasis on development and production prompted by the recent depression in exploration.

I have found a great demand for short courses on interpretation of three-dimensional seismic data, for which this book has served as the text, and this has fueled the need to update the content for a Second Edition. The expansion in text and figures is about 30%, including more case history examples. During the expansion my objective has been to extend the application and appeal of the book by broadening the field of contributing companies, of types of display, interactive system and color usage, and of the range of subsurface problems addressed with 3-D seismic data. Emphasis continues on the synergistic benefits of amplitude, phase, interactive approaches and color.

Alistair R. Brown
Dallas, Texas
June 1988

Preface to the First Edition

The whole is more than the sum of the parts.

— ARISTOTLE

Three-dimensional seismic data have spawned unique interpretation methodologies. This book is concerned with these methodologies but is not restricted to them. The theme is two-fold:

—How to use 3-D data in an optimum fashion, and

—How to extract the maximum amount of subsurface information from seismic data today.

I have assumed a basic understanding of seismic interpretation which in turn leans on the principles of geology and geophysics. Most readers will be seismic interpreters who want to extend their knowledge, who are freshly confronted with 3-D data, or who want to focus their attention on finer subsurface detail or reservoir properties.

Color is becoming a vital part of seismic interpretation and this is stressed by the proportion of color illustrations herein.

Alistair R. Brown
Dallas, Texas
January 1986

Downloaded 25 Jun 2012 to 95.28.162.50. Redistribution subject to SEG license or copyright; Terms of Use: http://segdl.org/

Special Acknowledgment for the Seventh Edition

Now that this book has been in use, through various editions, for more than 22 years, I must reflect on the many contributions that have ensured its success. Most particularly I must thank Bill Abriel, Rebecca Latimer, David Roberts, Greg Partyka, Malcolm Lansley, Les Denham, and Dave Agarwal for writing sections for me. Many people, too numerous to name, have kindly released data examples and discussed their interpretations with me. AAPG and SEG have cooperated in the book's publication since the Fifth Edition. Anne Thomas has edited all editions. The high quality of the product depends significantly on her editorial expertise.

Acknowledgments for Subsequent Editions

I really appreciate the help that so many people have provided. Most particularly I must thank the principal authors of the contributed material. Also, many individuals provided me with one, two or three figures and secured for me their release; in some cases this involved considerable effort because several companies were involved in group surveys. My classes of short course students have provided critical comment and discussion and these have prompted me to sharpen up the subject matter and to generate several new explanatory diagrams. To all of these helpful people—a big Thank-you.

Acknowledgments for the First Edition

I have found the writing and organization of this book daunting, challenging and rewarding. But it certainly has not been accomplished without the help of many friends and colleagues. First, I would like to thank Geophysical Service Inc. (GSI) and especially Bob Graebner for encouraging the project. Bob Sheriff, University of Houston, has been my mentor in helping me to discover what writing a book entails. Bob McBeath has been a constant help and source of technical advice; he also read all the manuscript. I am indebted to many companies who released data for publication, and also to the many individuals within those companies who provided their data and discussed its interpretation with me. In particular, Roger Wright and Bill Abriel, Chevron U.S.A., New Orleans, were outstandingly helpful. Colleagues within GSI who provided significant help were Mike Curtis, Keith Burkart, Tony Gerhardstein, Chuck Brede, Bob Howard, and Jennifer Young. Last but not least, my wife, Mary, remained sane while typing and editing the manuscript on a cantankerous word processor.

Downloaded 25 Jun 2012 to 95.28.162.50. Redistribution subject to SEG license or copyright; Terms of Use: http://segdl.org/

Downloaded 25 Jun 2012 to 95.28.162.50. Redistribution subject to SEG license or copyright; Terms of Use: http://segdl.org/

About the Author

Alistair Ross Brown was born and raised in Carlisle in the northernmost part of England. The first and middle names demonstrate Scots ancestry. He graduated in Physics from Oxford University in 1963, having attended The Queen's College. Later the necessary geology component was obtained at the Australian National University in Canberra, Australia. He married Mary, another Oxford graduate, in 1963 and they have three children. Now there are also five grandchildren.

Alistair's professional career in geophysics began in Australia where for seven years he was employed by the Bureau of Mineral Resources, and there gained experience in seismic data collection, processing, and interpretation. The Brown family returned to England in 1972 where Alistair worked for Geophysical Service International (GSI). He soon specialized in experimental seismic interpretation and was asked to interpret the first commercial 3-D seismic survey in 1975. Early experimental 3-D interpretation and display soon brought him to Dallas, the worldwide headquarters of GSI, and the family relocated there in 1978.

As 3-D surveys became more and more numerous during the 1980s, Alistair continued to investigate the best ways to interpret them. Interactive workstations emerged in the early part of the decade and he started using an early version in late 1980. After presenting several papers on aspects of 3-D interpretation in the late 1970s and early 1980s, Alistair started teaching the subject to oil company personnel. This led to his independence in 1987.

He is now a Consulting Reservoir Geophysicist specializing in the interpretation of 3-D seismic data, the effective use of interactive workstations, and the understanding of seismic amplitude. His courses and consultation are acclaimed worldwide and his time is dedicated to helping interpreters get more out of their 3-D seismic data.

Alistair is an active member of SEG, AAPG and EAGE. He received SEG's Best Presentation Award in 1975; he was recognized by Texas Instruments as a Senior Member of Technical Staff in 1981; he has been a continuing education instructor for SEG and AAPG; he was an AAPG Distinguished Lecturer in 1988, an SEG Distinguished Lecturer in 1991, the Petroleum Exploration Society of Australia Distinguished Lecturer in 1994, and the first joint AAPG/SEG Distinguished Lecturer in 1999/2000. Also he was Chairman of *The Leading Edge* Editorial Board during 1986-88, and, in 1998, he received SEG's Special Commendation Award. Alistair is an Honorary Member of the Geophysical Society of Houston and of the Dallas Geophysical Society. In October 2006 he was awarded Honorary Membership in the Society of Exploration Geophysicists, and in June 2009 he was awarded the Distinguished Service Award of the American Association of Petroleum Geologists.

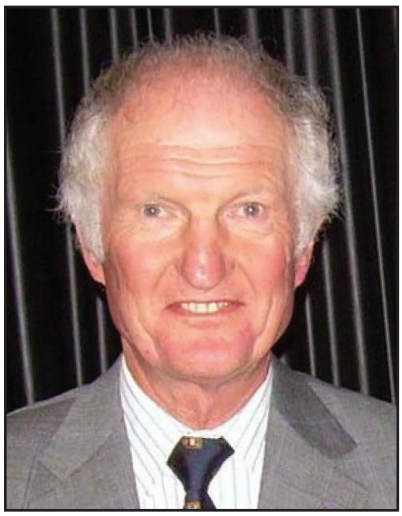

Downloaded 25 Jun 2012 to 95.28.162.50. Redistribution subject to SEG license or copyright; Terms of Use: http://segdl.org/

Contents

Prefaces ..... **iii**

Foreword **The Business Impact of 3-D Seismic** ..... **xv**
by W. K. Aylor, Jr.

Chapter 1 **Introduction** **1**
The Nature of Seismic Reflection • Philosophy of Seismic Interpretation • History of 3-D Seismic Methods • Resolution • Examples of 3-D Data Improvement • Survey Design • Volume Concept • Slicing the Data Volume • Workstations • Dynamic Range and Data Loading • Acquisition Footprint • References

Chapter 2 **Color, Character and Zero-Phaseness** **31**
Color Principles • Interpretive Value of Color • Assessment of Phase and Polarity • Psychological Impact of Color • References

Chapter 3 **Structural Interpretation** **61**
Direct Contouring and the Importance of the Strike Perspective • Fault Recognition and Mapping • Interpretation in the Vicinity of Salt • Composite Displays • Interpretation Procedures • Advantages and Disadvantages of Different Displays • Subtle Structural Features • Visualization and Autotracking • References

Chapter 4 **Stratigraphic Interpretation** **103**
Recognition of Characteristic Shape • Reconstituting a Depositional Surface • Methods of Making Horizon Slices • Horizon Slice Examples • Unconformity Horizon Slices • Windowed Amplitude • References

Chapter 5 **Reservoir Identification** **157**
Bright Spots as They Used to Be • The Character of Hydrocarbon Reflections • Examples of Bright Spots, Flat Spots, Dim Spots and Phase Changes • Polarity and Phase Problems, Multiple Contacts and Transmission Effects • Use of Frequency, Amplitude Variations with Offset and Shear Waves • Philosophy of Reflection Identification • Questions an Interpreter Should Ask in an Attempt to Validate the Presence of Hydrocarbons • The Occurrence of Hydrocarbon Indicators • References

Chapter 6 **Tuning Phenomena in Reservoirs** **203**
Effect of Tuning on Stratigraphic Interpretation • Deterministic Tuning Curves • Statistical Tuning Curves • Understanding the Magnitude of Tuning Effects • Well Tying and Tuning Effects • References

Chapter 7 **Reservoir Evaluation** **217**
Reservoir Properties Deducible from Seismic Data • Horizon Slices over Reservoir Interfaces • Composite Amplitude • Net Pay Thickness • Pore Volume • Well Calibration • Statistical Use of Tracked Horizon Data • Fault Slicing • References

Chapter 8 **Horizon and Formation Attributes** **247**
Classification of Attributes • Time-derived Horizon Attributes • Coherence • Post-stack Amplitude Attributes • Hybrid Attributes • Frequency-derived Attributes • Volumetric Attributes and Curvature • Amplitude Variation with Offset • Use of Multiple Attributes

Spectral Decomposition **295**
contributed by G. A. Partyka, M. D. Bush, P. G. A. Garossino, and P. R. Gutowski
Principles of Spectral Decomposition • Recommended Workflow • Significance of Spectral Balancing • Interpretation Recommendations • Resolution Benefits of Spectral Decomposition • Acknowledgments • References

Chapter 9 **Inversion and Interpretation of Impedance Data** **309**
contributed by R. B. Latimer
Introduction • The Nature of Impedance Data • Quality Control of Seismic-derived Inverted Data • Log Analysis, Editing, and Rock Properties • Band Limitation and Impedances • Scale Differences • Methods of Inverting Seismic Data — General Considerations • Inversion Methods — Post-stack • Inversion Methods — Based on 3-D Stratigraphic Models • Inversion Methods — Pre-stack or Angle-stack • Which Inversion Method Do I Use? • Quality Control of Input Data • Interpretation of Impedance Data — General Considerations • Impedance Interpretation When the Relationship Is Unclear • Key Messages • Acknowledgments • References • Additional Reading

Downloaded 25 Jun 2012 to 95.28.162.50. Redistribution subject to SEG license or copyright; Terms of Use: http://segdl.org/

Chapter 10 Depth Conversion and Depth Imaging 351
Introduction

Depth Conversion 353
contributed by L. R. Denham and D. K. Agarwal
Sources and Computation of Velocity • General Considerations in Depth Conversion • Depth Conversion Using a Single Velocity Function • Depth Conversion Using Mapped Velocity Function • Depth Conversion Using Layers • Map Migration • Dealing with Conversion Errors • Discussion • References

Three-Dimensional Depth Image Interpretation 367
contributed by W. L. Abriel, J. P. Stefani, R. D. Shank, and D. C. Bartel
Concept of 3-D Depth Imaging • Why Time Imaging Is Not Depth Imaging • Required Elements of 3-D Depth Imaging • Three-Dimensional Post-stack Depth vs. 3-D Post-stack Time Imaging • Noise Characteristics of Depth-Imaged Data • Pre-stack Depth Imaging • Example of Pre-stack vs. Post-stack 3-D Depth Imaging — Model Data • Example of Pre-stack vs. Post-stack 3-D Depth Imaging — Live Data • Discussion • Acknowledgments

Chapter 11 Regional and Reconnaissance Use of 3-D Data 395
References

Chapter 12 Visualization and Visual Integration 413
contributed by D. M. Roberts
Introduction • Computer Hardware • The Power of Visualization • Data Inspection • Opacity • Data Interpretation • Coloring Surfaces by Amplitude • Stratigraphic Interpretation • Coherence Data • Surface Illumination • Advanced Attribute Visualization • Interpretation Quality Control • Visual Integration • Concluding Comments • Acknowledgments

Chapter 13 Four-Dimensional Reservoir Monitoring 449
Summary of Principles • Four-Dimensional Survey Results • References

Chapter 14 Case Histories of 3-D Seismic Surveys 463
"Field Appraisal with 3-D Seismic Surveys Offshore Trinidad," by R. M. Galbraith and A. R. Brown 463
"Three-Dimensional Seismic Monitoring of an Enhanced Oil Recovery Process," by R. J. Greaves and T. J. Fulp 470
"Impact of 3-D Seismic on Structural Interpretation at Prospect Cougar," by C. J. McCarthy and P. W. Bilinski 484
"Three-Dimensional Seismic Interpretation of an Upper Permian Gas Field in Northwest Germany," by H. E. C. Swanenberg and F. X. Fuehrer 492
"Seismic Data Interpretation for Reservoir Boundaries, Parameters, and Characterization," by W. L. Abriel and R. M. Wright 500
"A 3-D Reflection Seismic Survey over the Dollarhide Field, Andrews County, Texas," by M. T. Reblin, G. G. Chapel, S. L. Roche, and C. Keller 509
"Shallow 3-D Seismic and a 3-D Borehole Profile at Ekofisk Field," by J. A. Dangerfield 517
"Extending Field Life in Offshore Gulf of Mexico Using a 3-D Seismic Survey," by T. P. Bulling and R. S. Olsen 526
"Lisburne Porosity — Thickness Determination and Reservoir Management from 3-D Seismic Data," by S. F. Stanulonis and H. V. Tran 537
"Value of Geophysics in the Production of Bay Marchand Field," by W. L. Abriel and W. Haworth 552

Appendix A Considerations for Optimum 3-D Survey Design, Acquisition and Processing 589
contributed by R. M. Lansley
General Issues • Marine Data Acquisition • Land Data Acquisition • Data Processing • References

Appendix B Interpretation Exercise 597
Background Information • Structural Component of Exercise • Stratigraphic Component of Exercise • Procedure • Solution

Appendix C Instructions for Assessing Phase and Polarity 610

Appendix D Summary of Recommendations to Help Today's Interpreter 615

Index 616

Downloaded 25 Jun 2012 to 95.28.162.50. Redistribution subject to SEG license or copyright; Terms of Use: http://segdl.org/

Downloaded 25 Jun 2012 to 95.28.162.50. Redistribution subject to SEG license or copyright; Terms of Use: http://segdl.org/

Foreword

The Business Impact of 3-D Seismic

William K. Aylor, Jr.
Coordinator, 3-D Seismic Network of Excellence, Amoco (Retired)

The oil and gas business has witnessed over the past decade a quantum leap in effectiveness of geophysics in E&P operations. Indeed the industry may never before have witnessed a technological advance as profound as or with the overwhelming business impact of 3-D seismic. Under refinement and development for almost three decades, the 1990s saw the coalescing of technical cross currents that have shaken the economic foundations of the oil and gas industry, and have fueled a world economic growth spurt. Today oil prices have been reported as being at the lowest level in 50 years, due in a major part to inordinately high supplies; that is, higher volumes found by 3-D seismic.

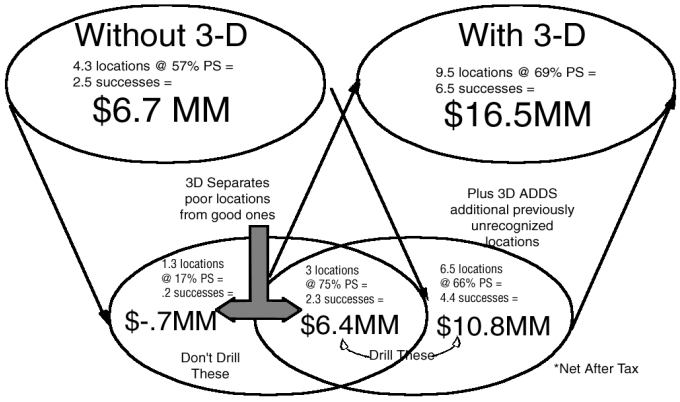

Fig. F-1. The average Amoco exploitation 3-D survey added $9.8 million of present value when applied to a typical international development opportunity.

From our current perspective at the end of the millenium, we can only marvel at what has occurred. The contributors to this achievement have been numerous, but certainly to be included in a tally of major contributors would be improvements in our understanding of scattered noise in acquisition design, recording electronics with routine availability of thousands of recorded channels, development of high bandwidth, high-density storage devices, availability of massively parallel as well as high-speed, low-cost computers, development of high-speed networks, development of depth imaging algorithms, advances in rock properties and direct hydrocarbon detection methods, and refinement and integration of seismic interpretation work stations with geological and engineering methods.

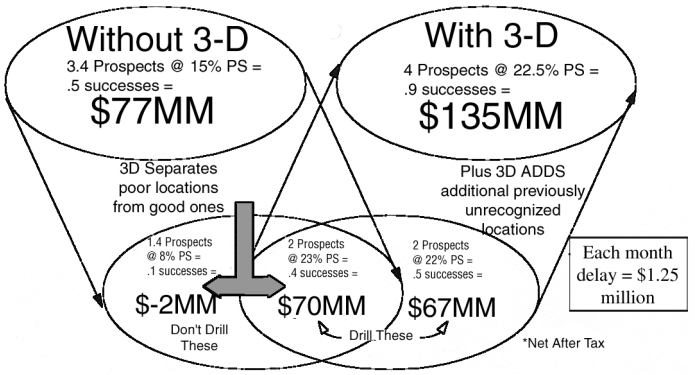

Fig. F-2. The average Amoco exploration 3-D survey added $58 million of present value when applied to a typical international exploration opportunity.

The impact of any new technology on an industry is dependent on two major factors, the effectiveness of the pre-existing technology (that used immediately prior to introduction of the new technology) and the effectiveness of the new technology itself. The greater the gap in capability between the two, the greater the impact of the new technology.

Having personally used the 2-D methods of the 1970s and '80s during my career, I can attest to the fact that, when these methods were employed, they seemed to be highly viable and capable. Indeed, adoption of digital recording over analog recording brought multiple fold, and much better images of apparent 2-D cross sections of the earth. This improvement helped

Downloaded 25 Jun 2012 to 95.28.162.50. Redistribution subject to SEG license or copyright; Terms of Use: http://segdl.org/

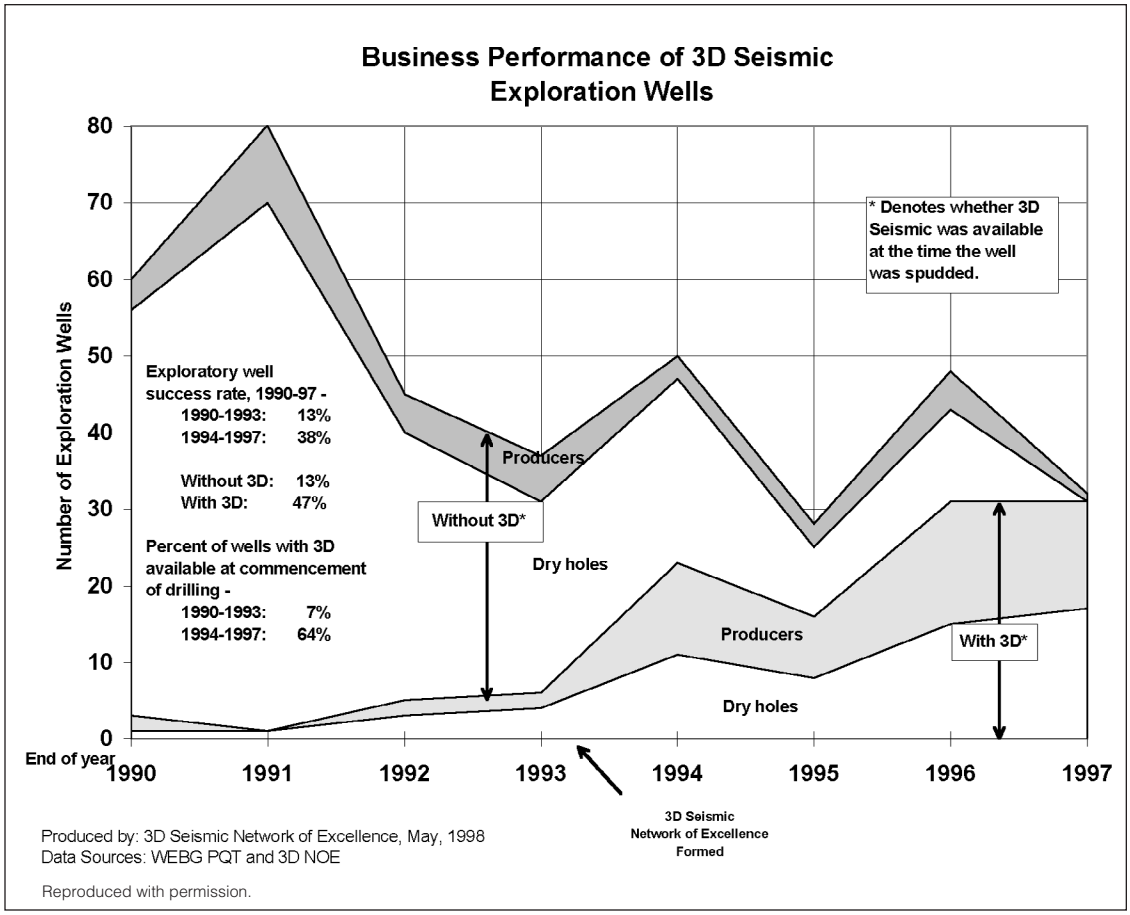

Reproduced with permission.

Fig. F-3. Since 1993, there has been a marked increase in the proportion of Amoco exploration wells drilled with 3-D coverage and a steady improvement in drilled success rate.

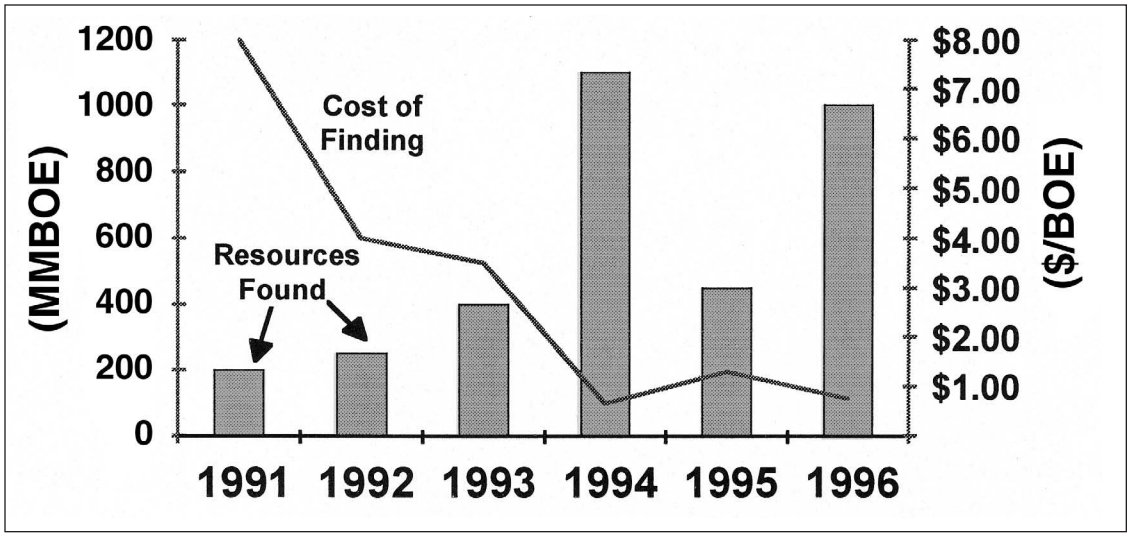

Fig. F-4. Exploration finding costs dropped and resources found increased during this period.

us chip away at a better understanding of the subsurface, even though the industry correctly re-adopted the time-honored slogan generally applicable to each generation of oilmen, "all the easy oil has already been found." Likewise, development of synthetic seismograms, wave equation 2-D time migration, true amplitude processing, and 2-D seismic modeling all had incremental impacts on the volumes and rates of finding and producing oil and gas.

But in my view, none of the above comes close to the impact that 3-D seismic has had on the oil industry. I have been very fortunate in the last few years to be in a position within my company to view firsthand the dramatic impact that 3-D has had on our E&P operations. Some companies were undoubtedly ahead of the pace of Amoco's 3-D activity, and many lagged our pace, so I like to think of the Amoco 3-D experience as a microcosm of the experience of the

Downloaded 25 Jun 2012 to 95.28.162.50. Redistribution subject to SEG license or copyright; Terms of Use: http://segdl.org/

industry in general. Whether this is the case could be debated, but if it is close to being true, then this technology's impact on the industry and the world economy has been profound.

In 1994, Amoco's upstream business units collected data to characterize to what degree 3-D was impacting E&P operations. Using pre-drill estimates of success, we characterized the number and quality of prospects prior to and subsequent to acquiring a 3-D survey. Both exploitation and exploration surveys were analyzed, and the results are summarized in Figures F-1 and F-2. Here we see that 3-D segregated poor, low-probability of success (PS) prospects from better, higher-PS prospects. Even more importantly, 3-D also found new high-PS prospects that had not been previously detected at all. When we applied suitable investment and revenue streams (using $15/barrel of oil equivalent), we found the value of these 3-D surveys was tens of millions of dollars. All of this analysis had been done looking at changes in PS in prospects prior to drilling; but would the value hold up when drilled wells were analyzed?

To understand the impact of 3-D on exploration drilling results, we began to monitor success rates of wells drilled with the benefit of 3-D prior to spudding versus the success rates of wells without 3-D. These data have been reported in several forums throughout the mid- to late 1990s, and are recapped in Figure F-3. This remarkable chart shows the transition from a 2-D seismic world to a 3-D one, and the impact amazes me even today. As can be seen, the

Table F-1. Impact of 3-D on Amoco major field revisions in 1997.

Degree of 3-D coverage	Number of fields	Total revisions*	Average revision*
Full coverage	17	444,108	26,124
None & Partial	21	-7,609	-362
Total	38	436,499	11,487

*thousands of BOE

Table F-2. Coverage of major Amoco fields by 3-D in 1997.

No. of fields fully covered by 3-D	42	55%
No. of fields not covered by 3-D	10	13%
No. of fields partially covered by 3-D	25	32%
Total no. of important fields	77	

company went from a 14% drilled success rate in 1990 to 47% in 1997, 5% of prospects covered by 3-D in 1990 to 97% in 1997, a drilled success for oil wells during 1990-1997 of 3% without 3-D vs. 37% with 3-D, and a drilled success for gas wells during 1990-1997 of 24% without 3-D vs. 54% with 3-D. Because of this success in this period, there have been major improvements in the cost of finding and in volumes found, as is shown in Figure F-4. Here we can see that the cost of finding has dropped from around $8 per barrel to under $1 per barrel, while volumes found in 1994 and 1996 were about 1 billion BOE per year. This in turn has very beneficially impacted Amoco's production replacement profile as is shown in Figure F-5.

Development effectiveness has also been dramatically improved by 3-D. Figure F-1 shows that looking at pre-drill numbers, we were seeing a dramatic segregation of low-PS development locations from high-PS ones, and we were defining new, high-PS locations not previously recognized. With 3-D and without 3-D drilling results were not available for development wells, so a different means of judging the effects of 3-D on development work had to be devised, which is shown in Table F-1. Here we have measured the impact of 3-D on field revisions for 1997. Field revisions are a useful way of summarizing changes in reserves for the major properties owned by the company, as well as the major changes in reserves for all the company's properties. Here we see that fields which had full 3-D coverage experienced much

Downloaded 25 Jun 2012 to 95.28.162.50. Redistribution subject to SEG license or copyright; Terms of Use: http://segdl.org/

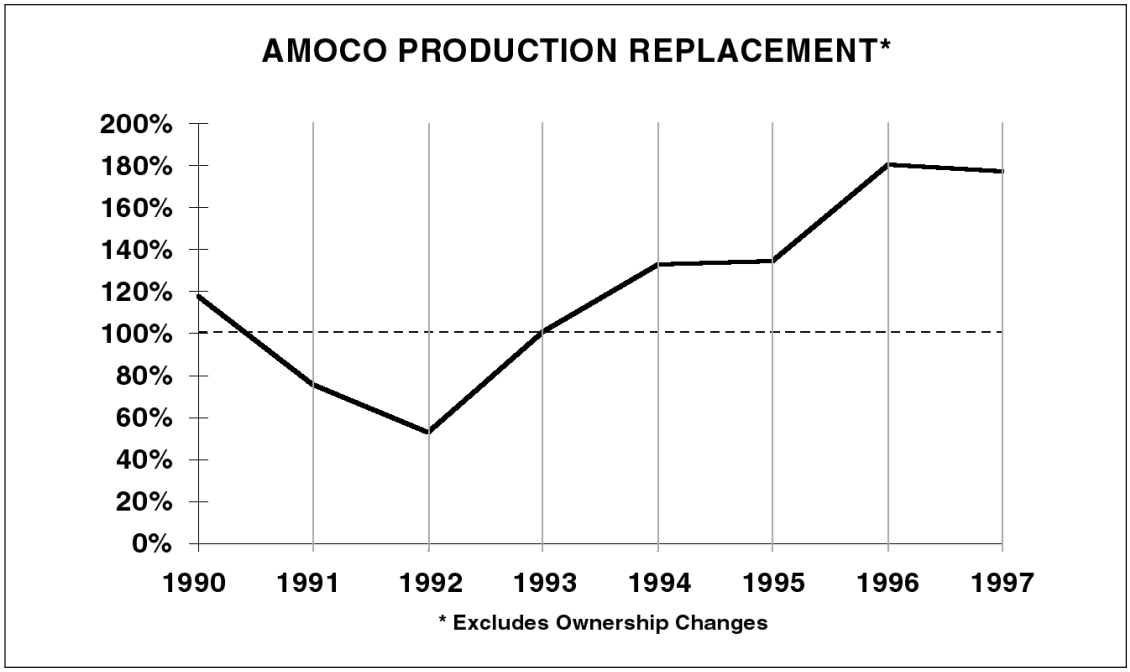

Fig. F-5. Since 1992 there has been a steady improvement in production replacement performance at Amoco.

higher positive reserve changes than fields that were partially or not at all covered. Table F-2 shows another interesting aspect of these data: in spite of the huge success of 3-D in both exploration and development work, at least within Amoco, 3-D was slow to be adopted for development work. Indeed, by 1997, only 55% of Amoco's fields were fully covered by 3-D, even at a time when 97% of its exploration wells were covered by 3-D.

Often in the practice of geophysics, our progress is so incremental that its business impact is difficult to notice and quantify. Once in a while we are privileged to witness a quantum leap in effectiveness and proficiency caused by our technology. Such has been our experience with 3-D seismic. Maybe in the future there will be technologies that rival 3-D's capabilities and proficiency at predicting economic accumulations of hydrocarbons. However, the huge impact on world hydrocarbon supplies and prices caused by the great leap forward from 2-D to 3-D seismic technology will be very difficult to match, because the bar has now been raised so high by this magnificent technology.

Downloaded 25 Jun 2012 to 95.28.162.50. Redistribution subject to SEG license or copyright; Terms of Use: http://segdl.org/

Introduction

The Nature of Seismic Reflection

Seismic reflections come from interfaces where the acoustic properties of the rocks change, and this fact is the basis of our understanding of the nature of seismic data. Acoustic impedance of a rock layer is the product of the density and the velocity of that layer, and strictly a reflection is generated by a contrast in acoustic impedance. In fact impedance and lithology normally follow each other, so that impedance boundaries and lithologic boundaries normally concur.

Consider a sand encased in shale, perhaps the most common situation forming a hydrocarbon reservoir. The shale-sand interface at the top generates a reflection, and the sand-shale interface at the base generates a reflection (Figure 1-1). Thus a sand has a reflection from the top and another from the base. These two reflections should be considered together in all studies of the reservoir sand.

At one location the sands normally have one impedance and the shales have another impedance. (Typically, sands have a lower impedance than shales in younger rocks and a higher impedance than shales in older rocks.) Thus the interfaces at top and base of a sand reservoir will almost always have impedance contrasts in the opposite sense. The sense of the impedance contrast determines the polarity of the seismic reflection, so that the top and base reflections for a sand reservoir encased in shale are opposite polarity from each other. This is a very significant piece of information used in the identification of reservoir reflections. Numerous figures in this book illustrate the pairing of top and base reflections — for example, Figure 1-20 and many figures in Chapters 2 and 5.

Tying of geologic data and seismic data together involves some knowledge of velocity, but the depth-to-time tie is not sufficient. We must identify seismic reflections on the basis of the character expected from the geologic interfaces and the fact that the layer of interest will normally have a top reflection and a base reflection. Consideration of the top and base reflections together involves the topics of natural pairing, choice of color schemes, data phase, data polarity, seismic resolution, and tuning, all of which are subjects of this book.

Philosophy of Seismic Interpretation

A proper understanding of seismic data is a necessary precursor to successful interpretation. Before horizon tracking commences the data must be qualified to understand what geologic information extraction is possible. The interpreter must consider data quality, frequency content, resolution, data phase, and data polarity, and must learn as much as possible about the data acquisition and processing (Appendix A). The interpreter must determine whether the data are fit-for-purpose, and not spend time conducting studies which have no chance of success. He must of course consider the background geology but should not be completely constrained by it. Modern 3-D

Downloaded 25 Jun 2012 to 95.28.162.50. Redistribution subject to SEG license or copyright. Terms of Use: http://segdl.org/

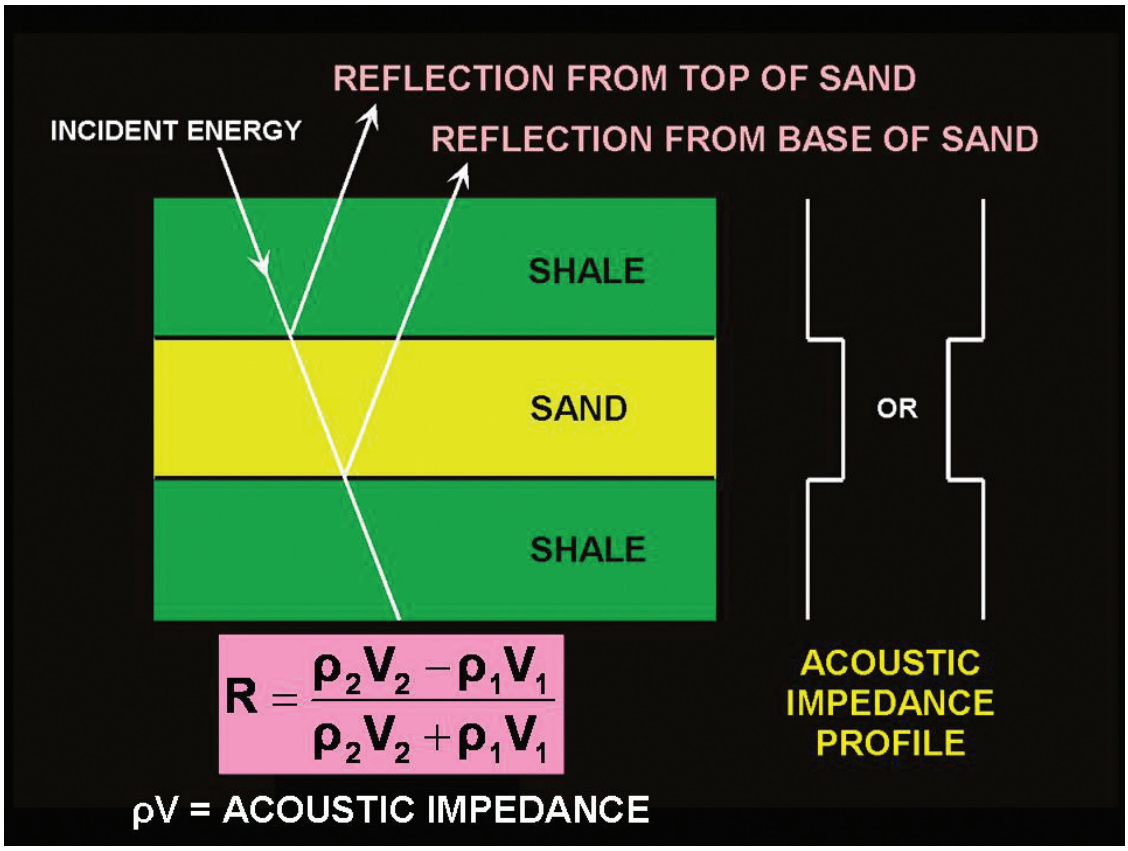

Fig. 1-1. Reflections come from interfaces, top and base of a sand reservoir.

seismic data can under some circumstances dictate a new geologic model.

Visualization is important today and always has been. Thinking in three dimensions is a critical ability of seismic interpreters. Three-dimensional seismic data match the dimensions of the data to the dimensions of the earth, and thus make visualization easier. But the greatest benefit of modern 3-D seismic data is their improved quality and resolution. There is typically an amazing amount of geologic detail in seismic data today, and the task of seismic interpretation is to extract it. Noise and spurious events are also present, so that the job of interpretation is to separate the desired geology from the unwanted noise. The better the data quality is understood, the better this separation can be accomplished.

Computer-driven workstations are the tools of seismic interpretation, and modern workstations contain an amazing array of capabilities. The challenge of the workstation user is thus to be aware of the possibilities and to select the tool appropriate to the objective. We do not use workstation capabilities only because they are fashionable. So the modern interpreter must integrate not only geology and geophysics but computer-intensive workstation technology as well. Technological synergism reigns but creative pragmatism retains its place.

History of 3-D Seismic Methods

The earth has always been three-dimensional, and the limitations of the old-fashioned 2-D seismic survey had long been recognized. The first 3-D seismic experiments were apparently conducted by Esso in the 1960s, and the first publication of their results was by Walton (1972). This early work lacked migration so the images were poor. Geophysical Service Inc. (GSI) was the first seismic service company to be involved, and they conducted a large-scale field experiment, with the support of six oil companies, in the state of New Mexico in 1972–74 (Schneider, 1998). Three-dimensional surveys were first performed on a contractual basis in 1975, and the following

Downloaded 25 Jun 2012 to 95.28.162.50. Redistribution subject to SEG license or copyright; Terms of Use: http://segdl.org/

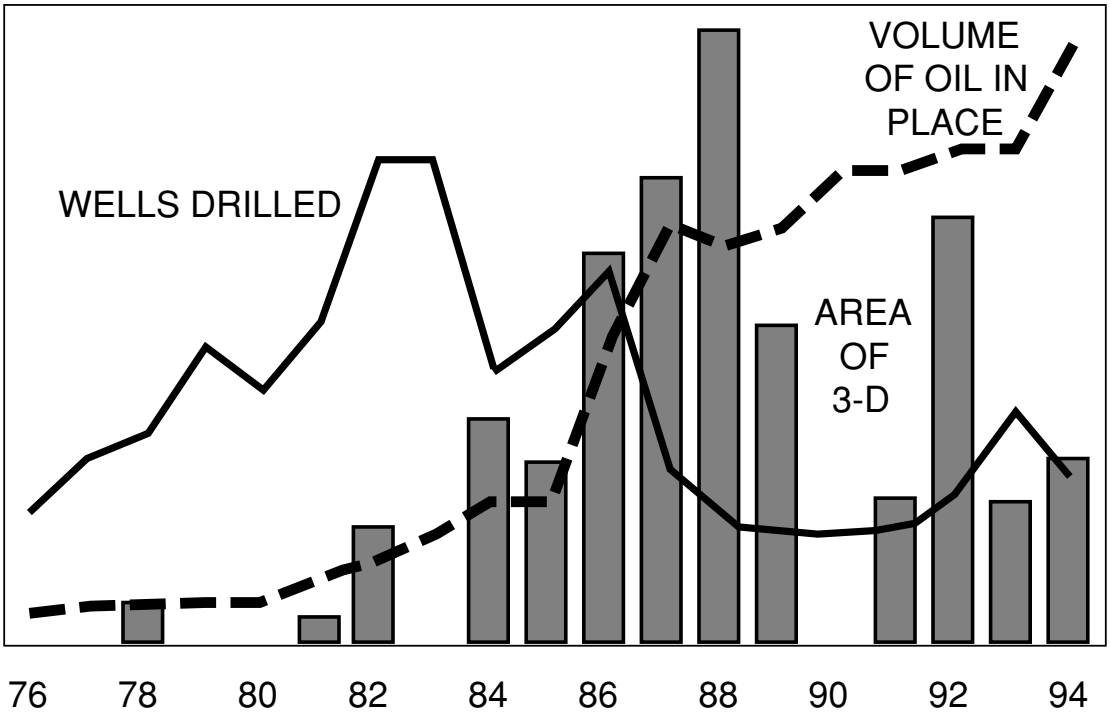

Fig. 1-2. Area covered by 3-D surveys, exploratory wells drilled and volume of oil in place for the period 1976 to 1994 in the Campos Basin offshore Brazil (from Martins et al., 1995). (Courtesy Petrobras.)

year Bone, Giles, and Tegland (1976) presented the technology to the world. The evolution and present state-of-the-art of the 3-D seismic method have been chronicled in a comprehensive reprint volume by Graebner, Hardage, and Schneider (2001).

The essence of the 3-D method is areal data collection followed by processing and interpretation of the closely spaced data volume. Initially 3-D was seen as expensive so its application was restricted to development applications (Tegland, 1977). In order to promote 3-D for exploration a widely spaced (and hence under-sampled) version was introduced, but this was not very successful. Today fully-sampled 3-D surveys are conducted on land, at sea, and in various transition zone environments.

The full economic benefit of 3-D seismic started to be appreciated in the late 1980s, as exemplified by this accolade:

> *"We acquired two offshore blocks which contained a total of seven competitor dry holes. Our exploration department drilled one more dry hole before making a discovery. At that point we conducted a 3-D survey while the platform was being prepared. When drilling commenced, guided by the 3-D data, we had 27 successful wells out of the next 28 drilled. In this erratic depositional environment, we believe such an accomplishment would not have been possible without the 3-D data."* (R. M. Wright, Chevron U.S.A. Inc, personal communication, 1988)

In the 1990s 3-D seismic surveys became mainstream, as Nestvold (1992) clearly demonstrates. Today mature petroleum areas are covered with 3-D data, often with many different vintages representing progressive improvements in technology. Martins et al. (1995), working in the Campos Basin offshore Brazil, have tracked the 3-D survey coverage in relation to the wells drilled and the oil reserves booked (Figure 1-2). This demonstrates very nicely that 3-D seismic can indeed replace the drilling of exploration wells. William Aylor, in the Foreword to this book, also demonstrates the business impact of 3-D seismic surveys.

Downloaded 25 Jun 2012 to 95.28.162.50. Redistribution subject to SEG license or copyright; Terms of Use: http://segdl.org/

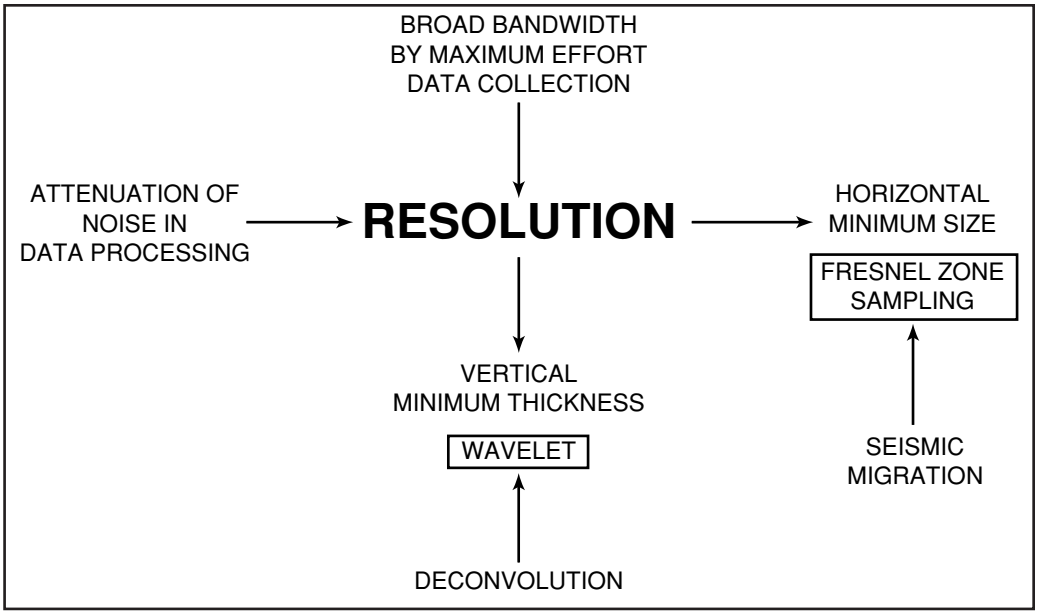

Fig. 1-3. Factors affecting horizontal and vertical seismic resolution.

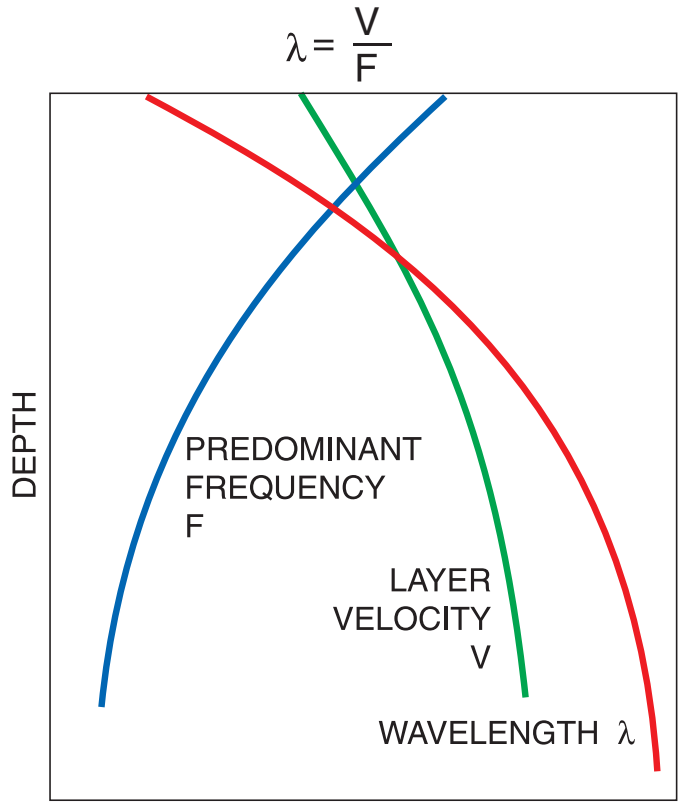

Fig. 1-4. Wavelength, the seismic measuring rod, increases significantly with depth making resolution poorer.

Resolution

The fundamental objective of a 3-D seismic survey is increased subsurface resolution. Resolution has both vertical and horizontal aspects and is significantly affected by the methods of data collection and processing (Figure 1-3). Sheriff (1985) discusses the subject qualitatively. The resolving power of seismic data is determined by the wavelength, which is defined as the distance in meters or feet from the crest of one reflection to the crest of the next one of the same color (polarity). The wavelength is calculated as the quotient of formation velocity and predominant frequency (Figure 1-4). Seismic velocity increases with depth because the rocks are older and more compacted. The predominant frequency decreases with depth because the higher frequencies in the seismic signal are more quickly attenuated. The result is that the size of the

Downloaded 25 Jun 2012 to 95.28.162.50. Redistribution subject to SEG license or copyright; Terms of Use: http://segdl.org/

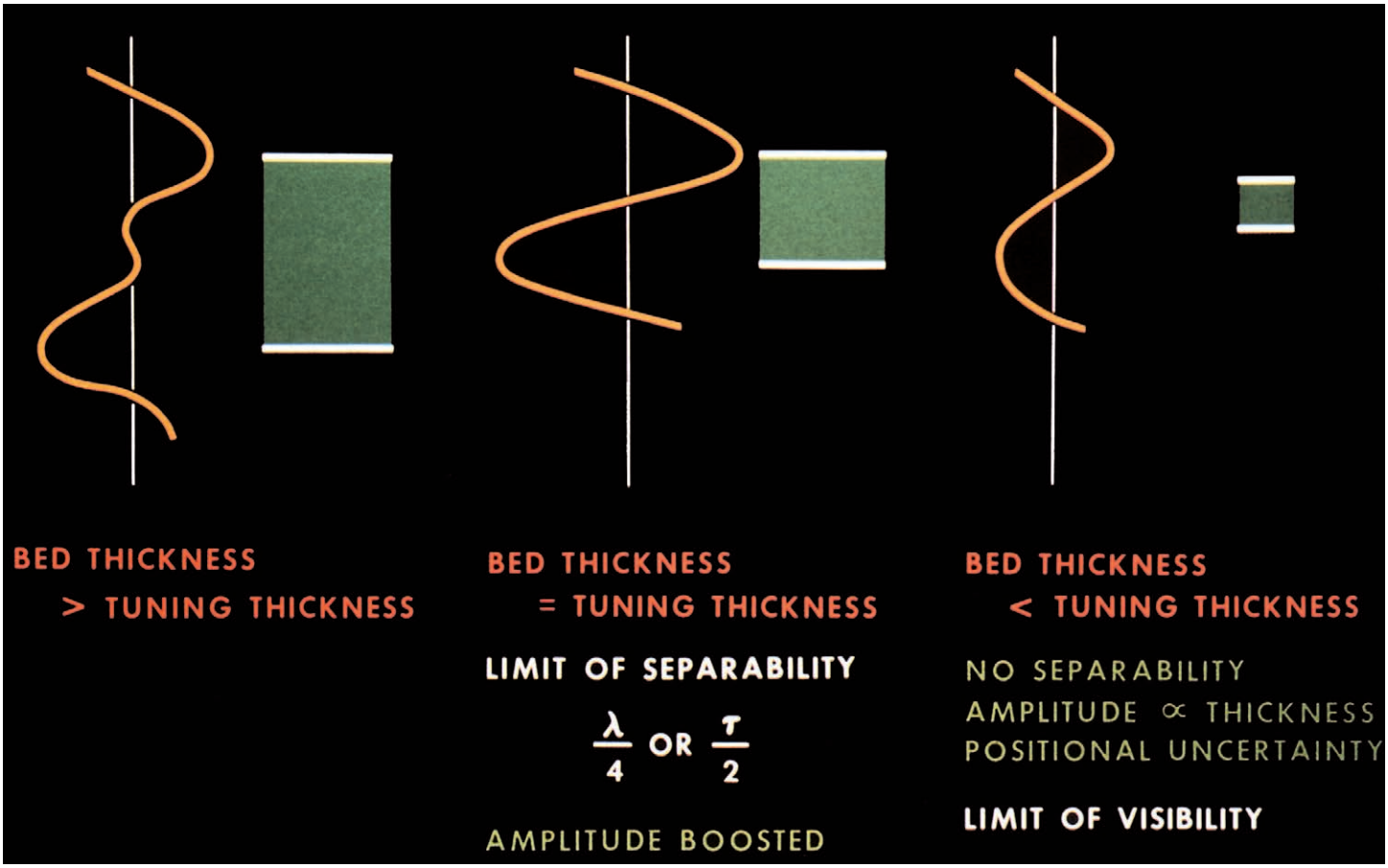

Fig. 1-5. Resolution of the reflections from the top and bottom of a bed is dependent on the interaction of closely spaced wavelets.

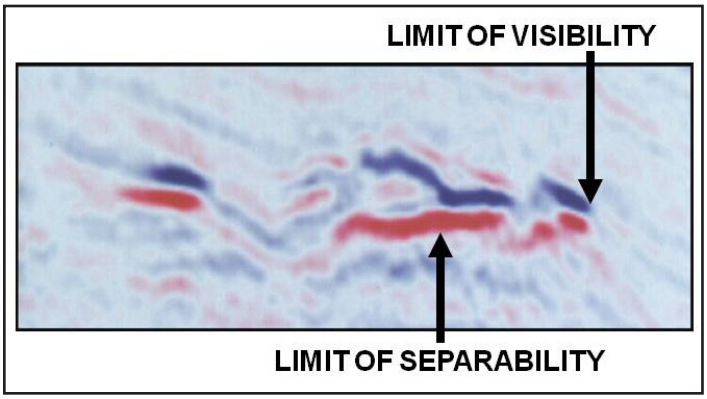

Fig. 1-6. Demonstration of Limit of separability and Limit of visibility.

wavelength increases significantly with depth, making resolution poorer.

Vertical resolution has two limits, both resulting from the interaction of the wavelets reflected from top and base of the bed under study. The **limit of separability** is equal to one-quarter of a wavelength (or half a period) and is simply the bed thickness corresponding to the closest separation of the two wavelets (Figure 1-5). For thinner beds than this, the top and base reflections are still visible but the amplitude is progressively attenuated until the **limit of visibility** is reached, when the reflected signal becomes obscured by the background noise. Figure 1-6 demonstrates clearly the concept of the two limits. The limit of visibility is a variable fraction of a wavelength and depends on the acoustic contrast of the layer of interest relative to the embedding material, the random and systematic noise in the data, and the phase of the seismic wavelet.

Downloaded 25 Jun 2012 to 95.28.162.50. Redistribution subject to SEG license or copyright; Terms of Use: http://segdl.org/

Table 1-1. Typical Limits of Visibility and Separability for a range of geologic situations.

			Age of rocks		VERY YOUNG	YOUNG	MEDIUM	OLD	VERY OLD
			Depth of target		VERY SHALLOW	SHALLOW	MEDIUM	DEEP	VERY DEEP
			Formation Velocity (m/s)		1600	2000	3500	5000	6000
			Predominant Frequency (Hz)		70	50	35	25	20
			Wavelength (m)	λ	23	40	100	200	300
			LIMIT OF SEPARABILITY	$\frac{\lambda}{4}$	**6**	**10**	**25**	**50**	**75**
LIMIT OF VISIBILITY		Poor S/N	e.g. Water sand poor data	$\sim\frac{\lambda}{8}$	**3**	**5**	**13**	**25**	**38**
		Moderate S/N	e.g. Water or oil sand fairly good data	$\sim\frac{\lambda}{12}$	**2**	**3**	**8**	**17**	**25**
		High S/N	e.g. Gas sand good data	$\sim\frac{\lambda}{20}$	**1**	**2**	**5**	**10**	**15**
		Outstanding S/N	e.g. Gas sand excellent data	$\sim\frac{\lambda}{30}$	**<1**	**1**	**3**	**7**	**10**

units are meters

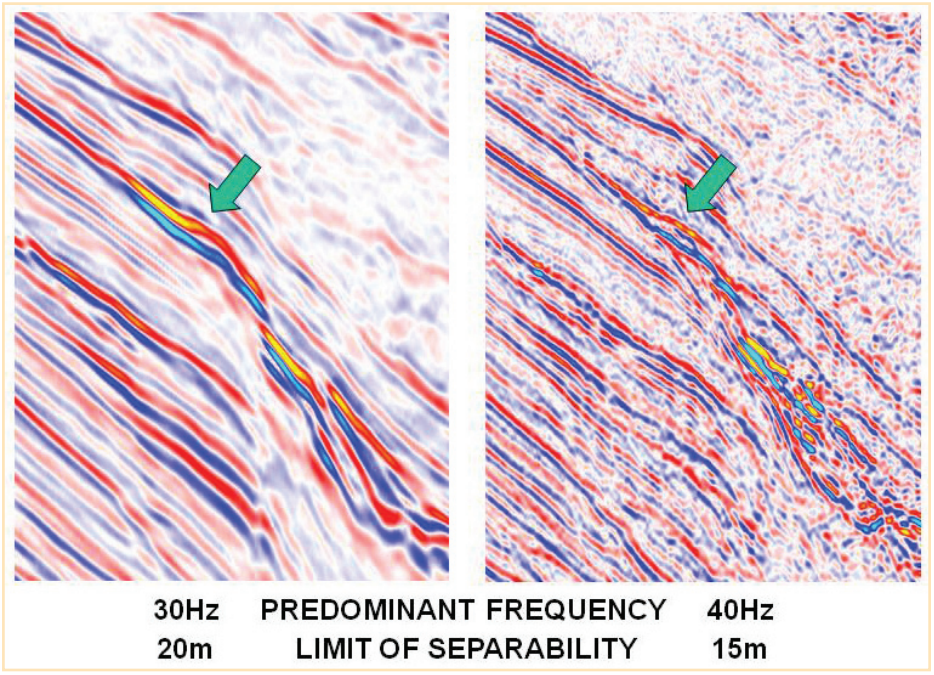

Fig. 1-7. The effect of frequency on the limit of separability. Note that top and base reflections (at green arrows) are well separated for the higher predominant frequency. (Courtesy Fugro GeoConsulting.)

Downloaded 25 Jun 2012 to 95.28.162.50. Redistribution subject to SEG license or copyright; Terms of Use: http://segdl.org/

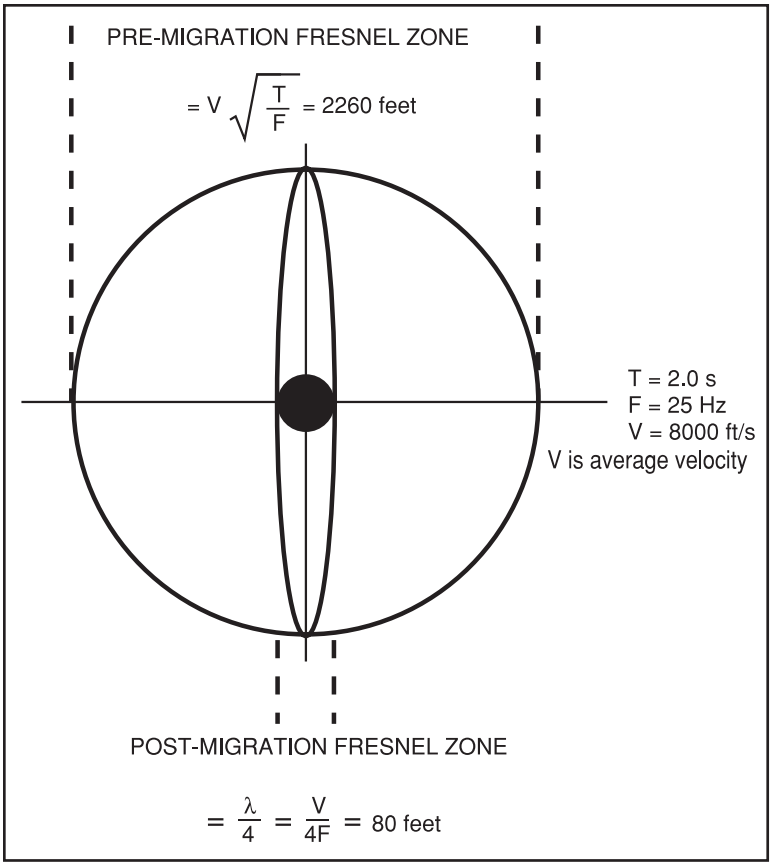
PRE-MIGRATION FRESNEL ZONE
$= V\sqrt{\frac{T}{F}}$ = 2260 feet
T = 2.0 s
F = 25 Hz
V = 8000 ft/s
V is average velocity
POST-MIGRATION FRESNEL ZONE
$= \frac{\lambda}{4} = \frac{V}{4F}$ = 80 feet

Fig. 1-8. Effect on Fresnel zone size and shape of 2-D and 3-D migration.

Table 1-2. Seismic visibility of a 5-meter sand.

Layer Velocity	Predominant Frequency	Wavelength	Sand 5 m
2000 m/s	40 Hz	50 m	λ/10
3000 m/s	30 Hz	100 m	λ/20
4000 m/s	20 Hz	200 m	λ/40

Table 1-1 illustrates five geologic situations of different rock ages and target depths. In order to calculate the resolution limits, one must think in terms of wavelength fractions and calculate the magnitude of the wavelength. The predominant frequency is determined by counting cycles in the data, and the layer velocity is estimated from a check-shot survey or a sonic log, or is guessed from knowledge of age, depth, and lithology. From predominant frequency and layer velocity, the wavelength and thus the limit of separability are directly calculated. Figure 1-7 shows two versions of the same data with very different predominant frequencies. Note the different amounts of separation between reflections, particularly at the position of the arrow.

For the limit of visibility, Table 1-1 offers four different wavelength fractions for different acoustic contrasts and signal-to-noise ratios. In this way the limit has been calculated for a matrix of twenty different situations, illustrating the enormous possible range in seismic visibility of thin beds. A rule-of-thumb based on the experience of the author is that the thinnest visible bed will be one-thirtieth of a wavelength, and this in the most favorable circumstances. If the reservoir of interest does not have a thickness above seismic visibility, then the study of reservoir porosity, net pay, lithology, etc. will not be possible. Table 1-2 converts 5 meters (postulated as the thickness of your reservoir) into wavelength fractions in three very different geologic situations. One-tenth of a wavelength should be visible in most circumstances, one-twentieth of a wavelength will be difficult to see seismically, and one-thirtieth probably will be invisible in all circumstances.

Migration is the principal technique for improving horizontal resolution, and in doing so it performs three distinct functions. The migration process (1) repositions reflections out-of-place because of dip, (2) focuses energy spread over a Fresnel zone, and (3) collapses diffraction patterns from points and edges. Seismic wavefronts travel in three dimensions and thus it is obvious that all the above are, in general, three-dimensional issues. If we treat them in two dimensions, we can only expect part of the

Downloaded 25 Jun 2012 to 95.28.162.50. Redistribution subject to SEG license or copyright; Terms of Use: http://segdl.org/

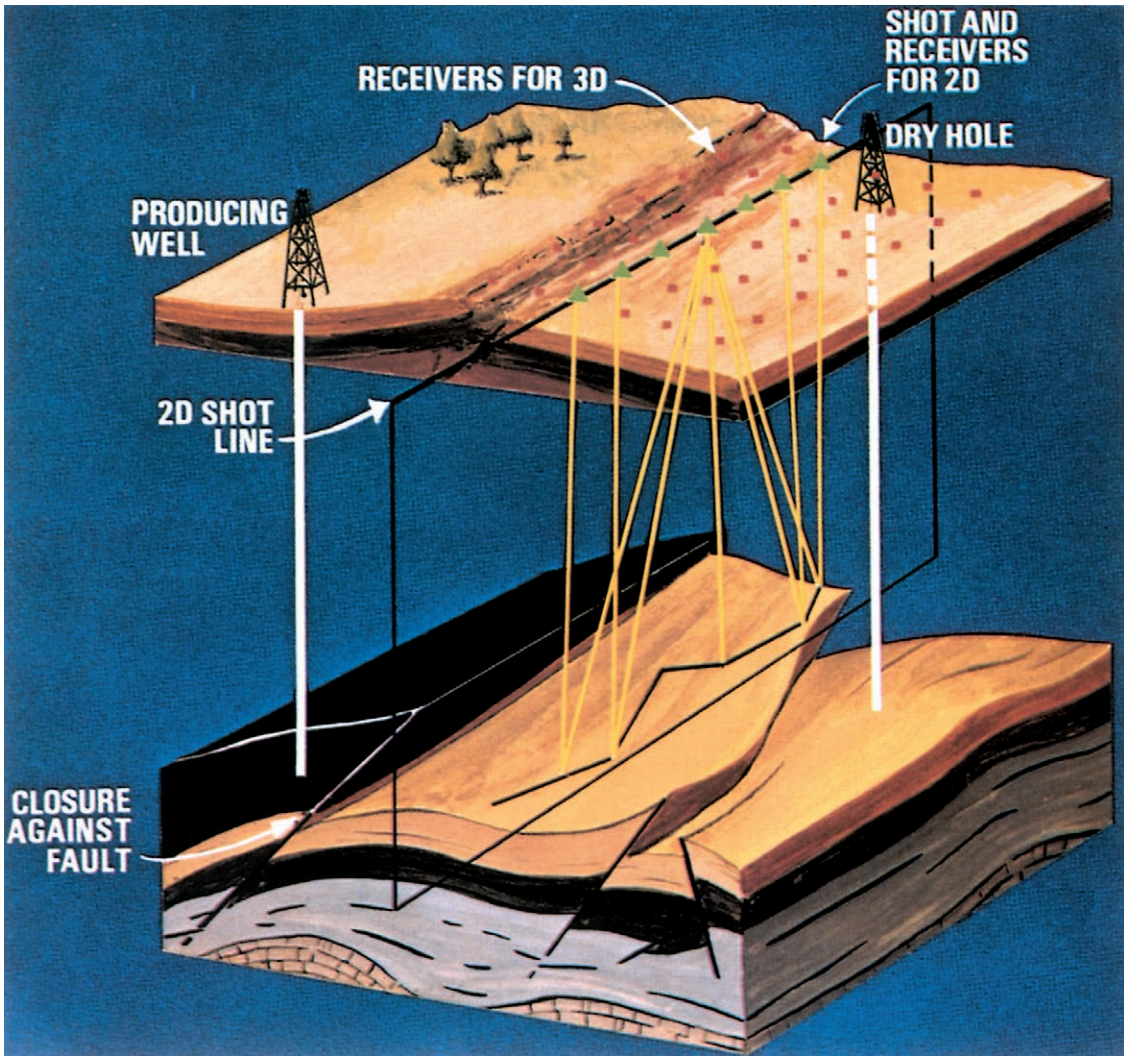

Fig. 1-9. Subsurface structure causes reflection points to lie outside the vertical plane through shots and receivers.

potential improvement. In practice, 2-D lines are often located with strike and dip of major features in mind so that the effect of the third dimension can be minimized, but never eliminated. Figure 1-8 shows the focusing effect of migration in two and three dimensions. The Fresnel zone will be reduced to an ellipse perpendicular to the line for 2-D migration (Lindsey, 1989) and to a small circle by 3-D migration. The diameter of one-quarter of a wavelength indicated in Figure 1-8 is for perfect migration. In practice, the residual Fresnel zone may be about twice this size.

The accuracy of 3-D migration depends on the velocity field, signal-to-noise ratio, migration aperture, and the approach used. Assuming the errors resulting from these factors are small, the data will be much more interpretable both structurally and stratigraphically. Intersecting events will be separated, the confusion of diffraction patterns will be gone, and dipping events will be moved to their correct subsurface positions. The collapsing of energy from diffractions and the focusing of energy spread over Fresnel zones will make amplitudes more accurate and more directly interpretable in terms of reservoir properties. In short the horizontal resolution of the data will be greatly improved.

Examples of 3-D Data Improvement

The interpreter of a 2-D vertical section normally assumes that the data were recorded in one vertical plane below the line traversed by the shots and receivers. The extent to which this is not so depends on the complexity of the structure perpendicular to the line. Figure 1-9 demonstrates that, in the presence of moderate structural

Downloaded 25 Jun 2012 to 95.28.162.50. Redistribution subject to SEG license or copyright; Terms of Use: http://segdl.org/

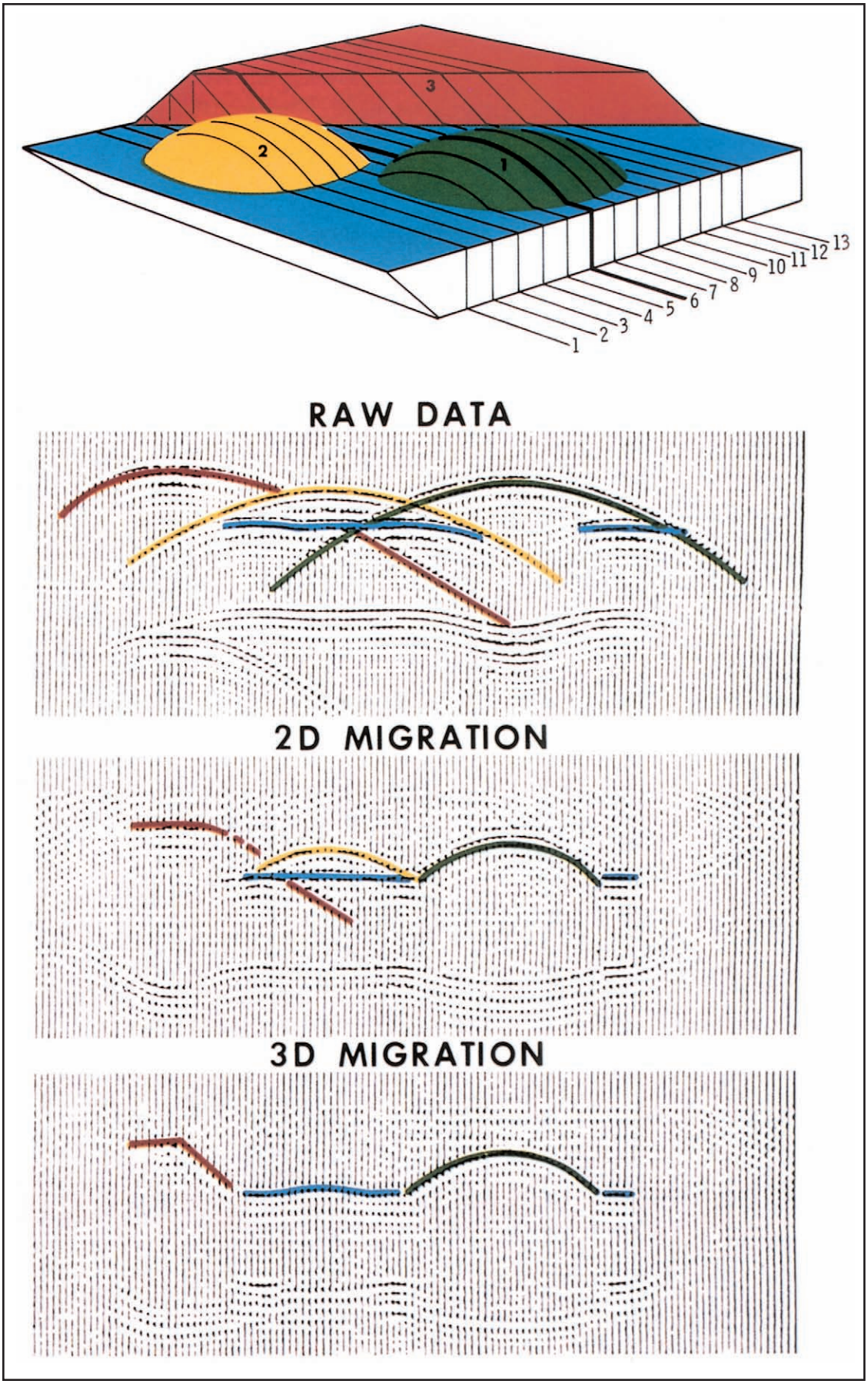

Fig. 1-10. Model of two anticlines and one fault with seismic data along Line 6 showing comparative effects of 2-D and 3-D migration (from French, 1974).

Downloaded 25 Jun 2012 to 95.28.162.50. Redistribution subject to SEG license or copyright; Terms of Use: http://segdl.org/

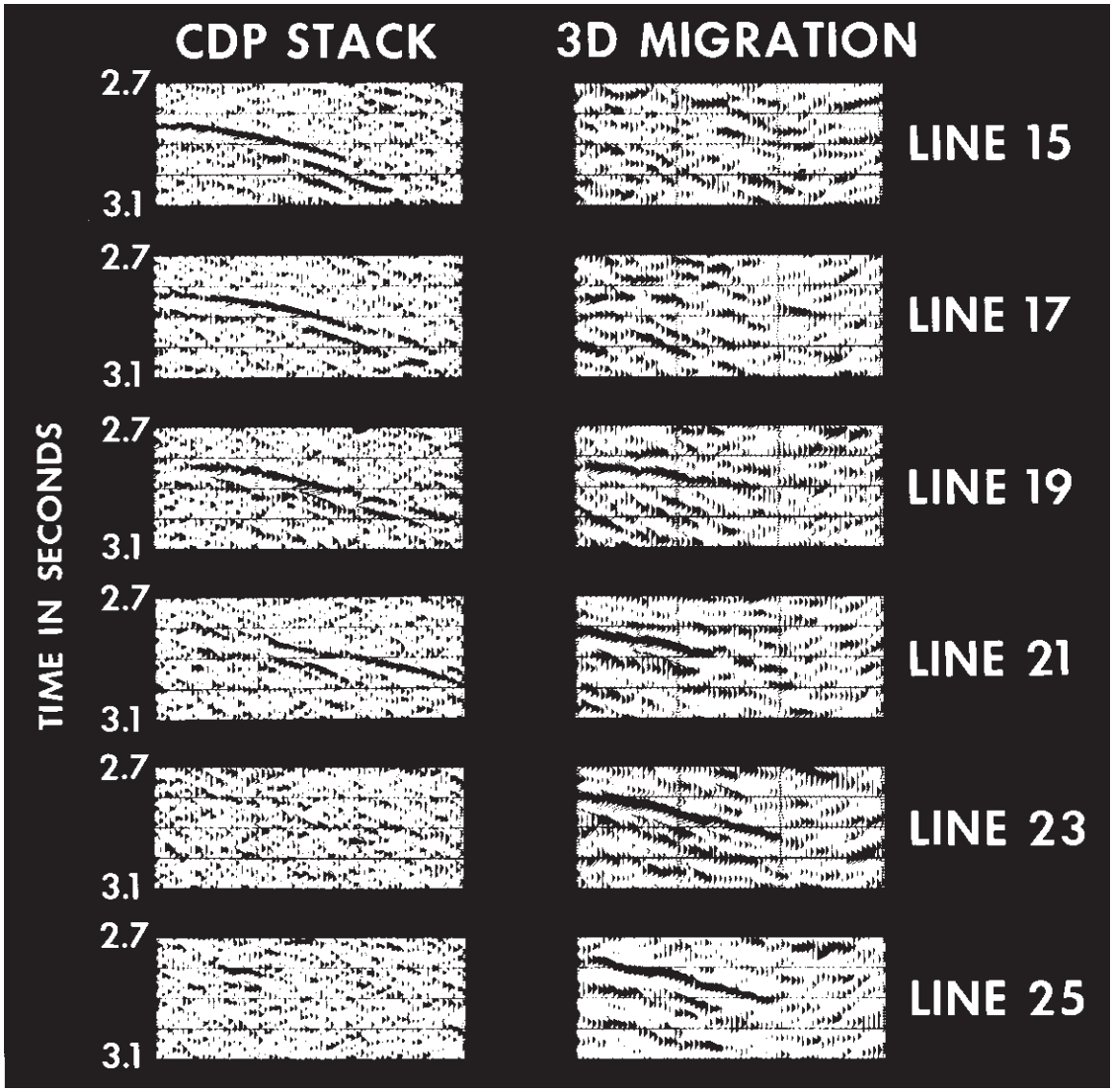

Fig. 1-11. Three-dimensional movement of a dipping reflection by 3-D migration. (Courtesy Geophysical Service Inc.)

complexity, the points at depth from which normal reflections are obtained may lie along an irregular zig-zag track. Only by migrating along *and* perpendicular to the line direction is it possible to resolve where these reflection points belong in the subsurface.

French (1974) demonstrated the value of 3-D migration very clearly in model experiments. He collected seismic data over a model containing two anticlines and a fault scarp (Figure 1-10). Thirteen lines of data were collected although only the results for Line 6 are shown. The raw data have diffraction patterns for both anticlines and the fault so the section appears very confused. The situation is greatly improved with 2-D migration and anticline number 1 (shown in green) is correctly imaged, as Line 6 passed over its crest. However, anticline number 2 (shown in yellow) should not occur on Line 6 and the fault scarp has the wrong slope. The 3-D migration has correctly imaged the fault scarp and moved the yellow anticline away from Line 6 to where it belongs.

Figure 1-11 demonstrates this three-dimensional event movement on real data. The same panel is presented before and after 3-D migration for six lines. Here we can observe the movement of a discrete patch of reflectivity to the left and in the direction of higher line numbers.

Figure 1-12 shows improved continuity of an unconformity reflection. The 2-D migration has collapsed most of the diffraction patterns but some confusion remains.

Downloaded 25 Jun 2012 to 95.28.162.50. Redistribution subject to SEG license or copyright; Terms of Use: http://segdl.org/

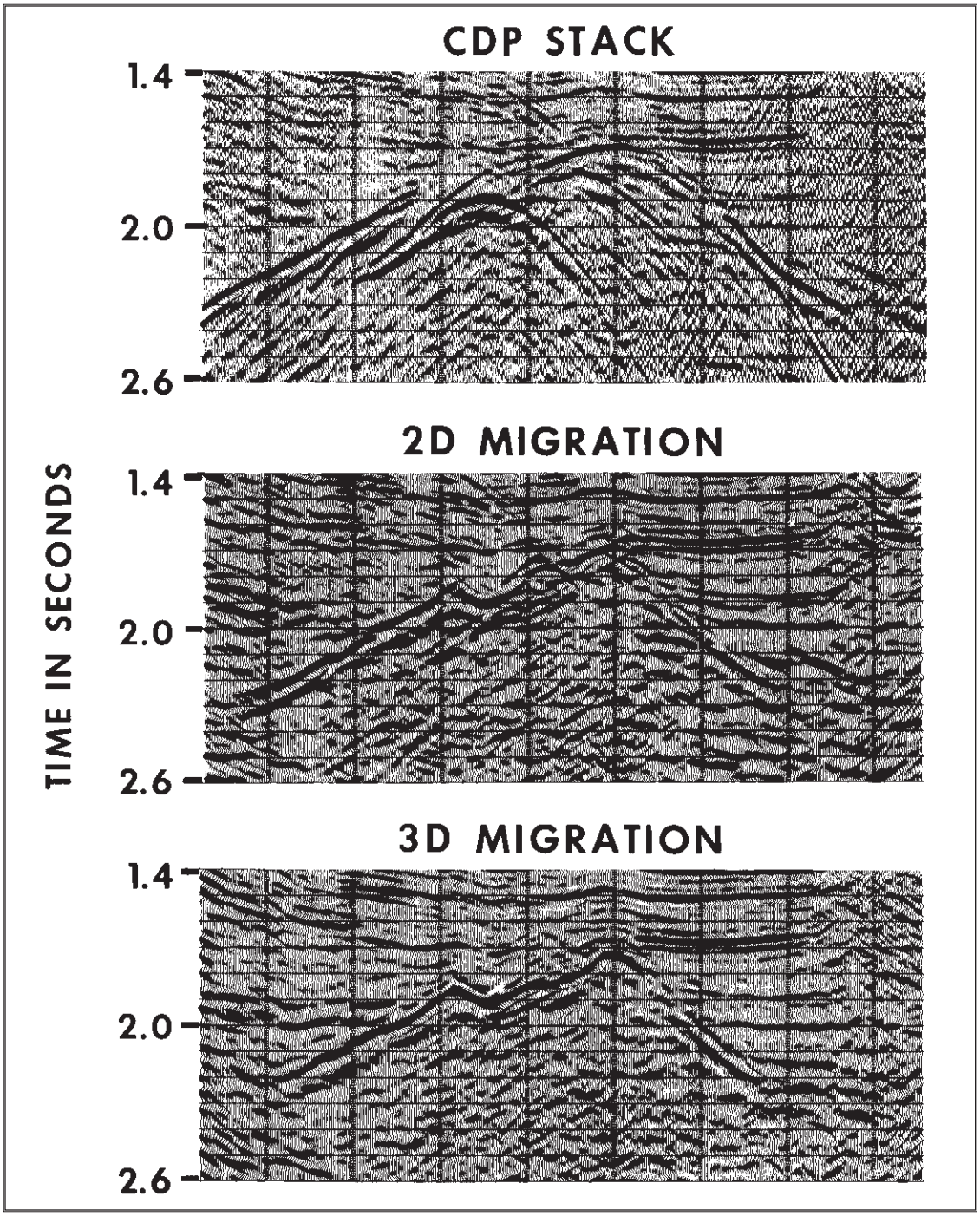

Fig. 1-12. Improved structural continuity of an unconformity reflection resulting from 2-D and 3-D migration.

The crossline component of the 3-D migration removes energy not in the plane of this section and clarifies the shape of the unconformity surface in significant detail.

Figure 1-13 shows the effect of 3-D migration in enhancing the visibility of a fluid contact reflection by removing energy not belonging in the plane of this section.

Figure 1-14 shows some major differences between the stacked and 3-D migrated versions of a line from Australia. It is easy to visualize the impact this change would have on an interpretation.

Figure 1-16 shows portions of three lines passing through and close to a salt diapir. Line 180 shows steeply dipping reflections at the edge of the salt mass, brought into place by the 3-D migration. Line 220 shows an apparent anticline which is caused by reflections dipping up steeply toward the salt face in a plane perpendicular to that of Figure 1-16. In this prospect, 3-D migration imaged reflections underneath a salt

Downloaded 25 Jun 2012 to 95.28.162.50. Redistribution subject to SEG license or copyright; Terms of Use: http://segdl.org/

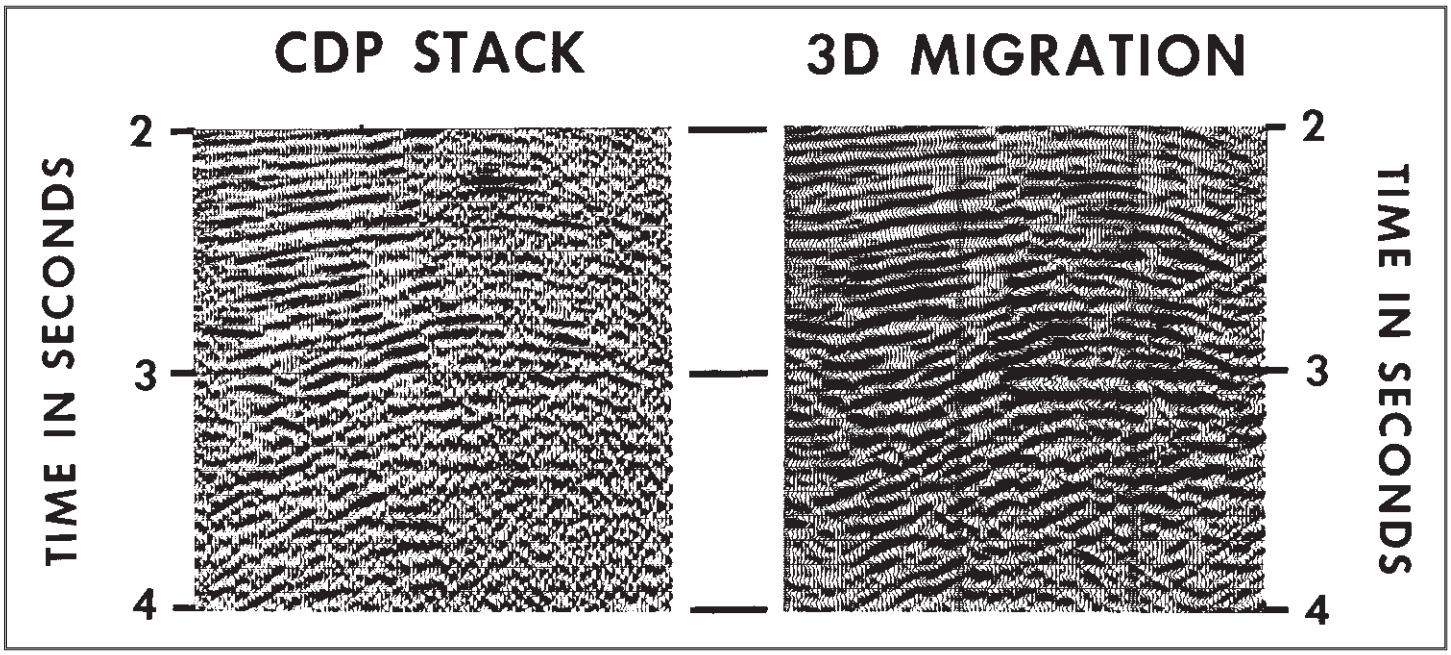

Fig. 1-13. Improved visibility of a flat spot reflection after removal of interfering events by 3-D migration.

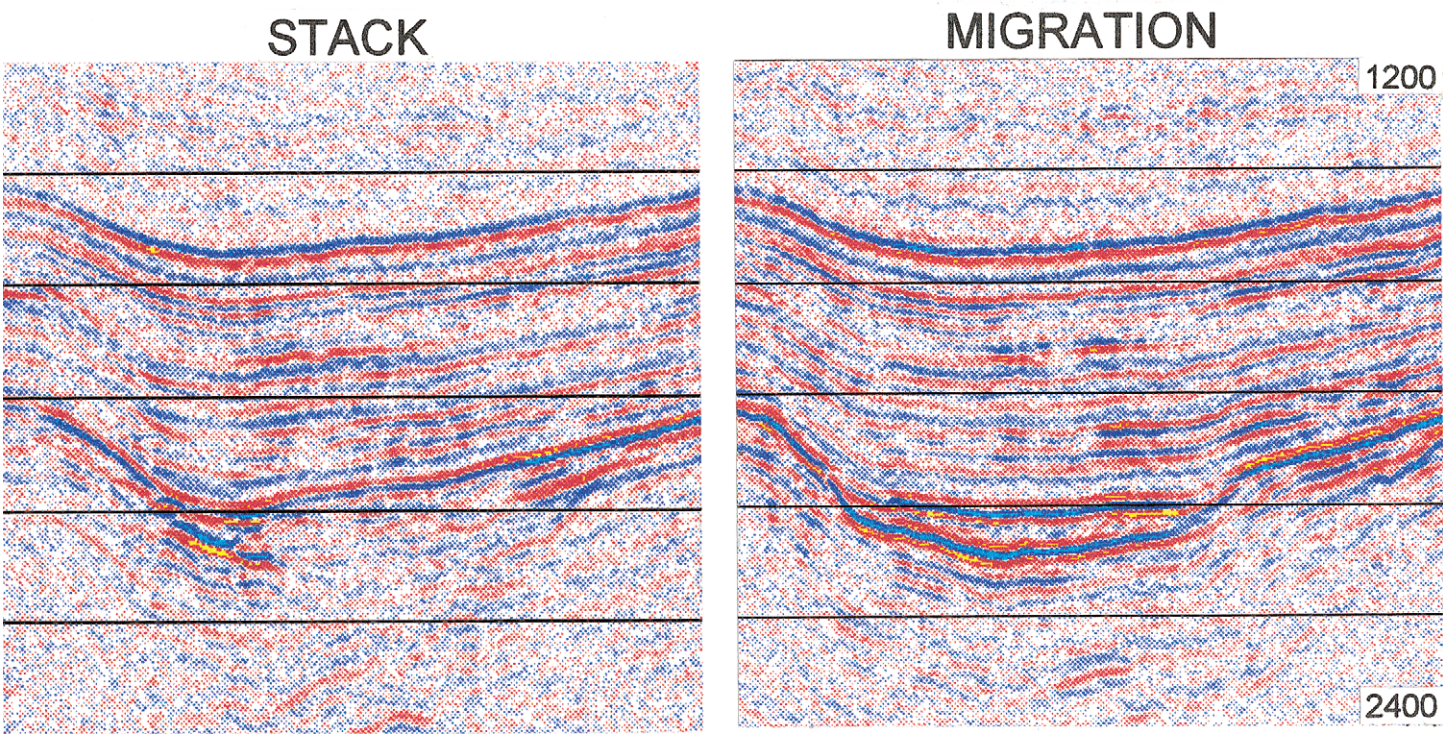

Fig. 1-14. Striking impact of 3-D migration on the attitude and continuity of reflections in South Australia. (Courtesy Santos Ltd.)

Downloaded 25 Jun 2012 to 95.28.162.50. Redistribution subject to SEG license or copyright; Terms of Use: http://segdl.org/

Table 1-3. Alias frequency (in hertz) as a function of subsurface spacing (in meters) and dip (in degrees) for an RMS velocity of 2500 m/s.

	SUBSURFACE SPACING				
DIP	12.5	25	50	75	100
5	574	287	143	96	72
10	288	144	72	48	36
15	193	96	48	32	24
20	146	73	37	24	18
25	118	59	30	20	15

Table 1-4. Basic formulas for the design of a 3-D survey.

Maximum subsurface spacing (2 samples per wavelength)	$= \frac{1}{2F_{max}\,DIP_{max}}$	where	T	is seismic two-way traveltime in seconds
Desirable subsurface spacing (3 samples per wavelength)	$= \frac{1}{3F_{max}\,DIP_{max}}$		DIP	is measured in seconds per unit distance
Migration distance (or half-aperture)	$= \frac{TV^2DIP}{4}$		F	is seismic frequency
Fresnel zone radius	$= \frac{V}{2}\sqrt{\frac{T}{F_{min}}}$		V	is seismic velocity

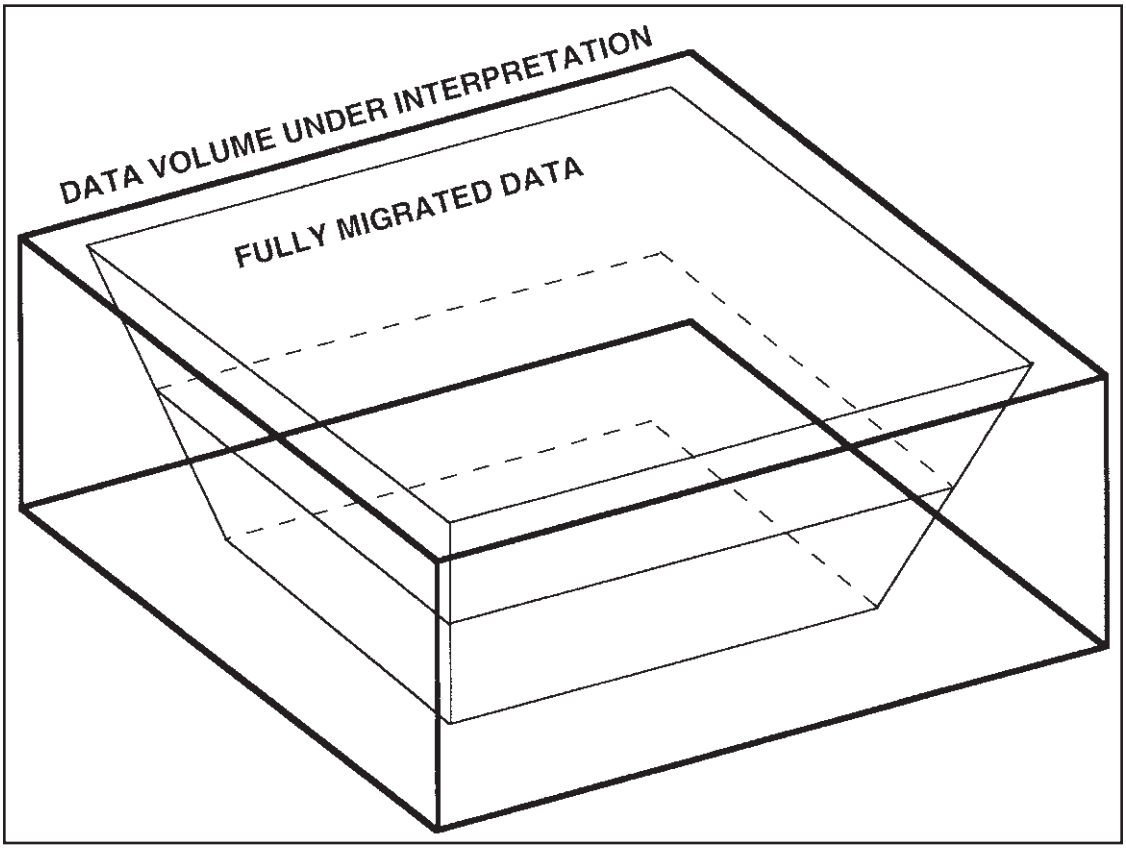

Fig. 1-15. Data around the edge of a 3-D survey are incompletely migrated because of migration distance and Fresnel zone radius. Interpreters should be extra cautious when working in this region.

overhang and provided valuable detail about traps located there against the salt face (Blake et al., 1982).

When comparing sections before and after 3-D migration to appraise its effectiveness, it is important to bear in mind the way in which reflections have moved around. In the presence of dip perpendicular to the section under scrutiny, the visible data before and after 3-D migration are different. It is unreasonable to compare detailed character and deduce what 3-D migration did. It is possible to compare a section before 3-D migration with the one from the same location after 3-D migration and find that a good quality reflection has disappeared. The migrated section is not consequently worse; the good reflection has simply moved to its correct location in the subsurface.

Figure 1-17 shows a horizontal section at a time of 224 ms from a very high resolution 3-D survey in Canada aimed at monitoring a steam injection process. The section on the left is from the 3-D volume before migration and the section on the right is from the volume after migration. The two black dots indicate wells. The striking visibility of a channel after migration results from the focusing of energy previously

Downloaded 25 Jun 2012 to 95.28.162.50. Redistribution subject to SEG license or copyright. Terms of Use: http://segdl.org/

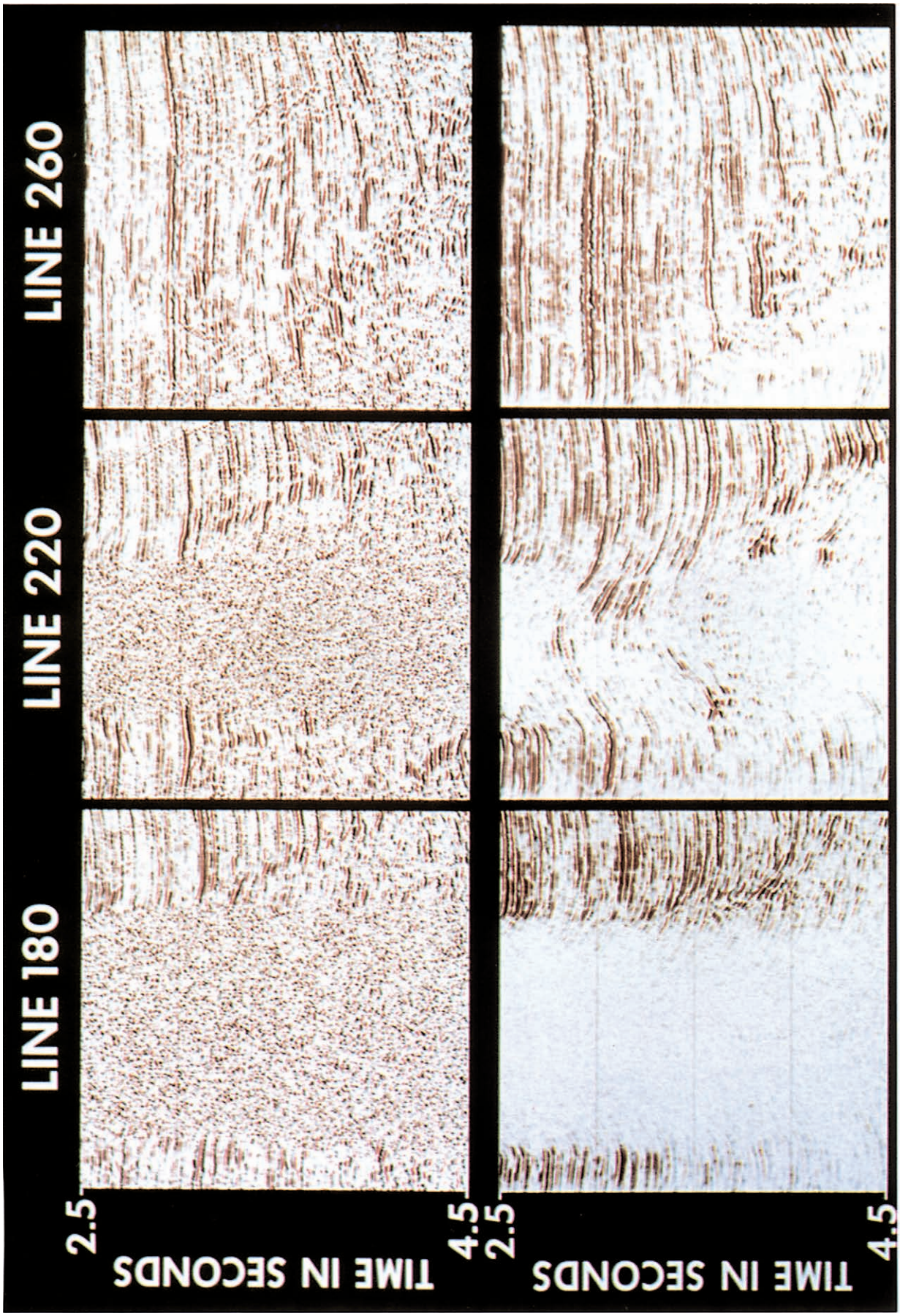

Fig. 1-16. Three vertical sections through or adjacent to a Gulf of Mexico salt dome before migration (top) and after migration (bottom), showing the repositioning of several reflections near the salt face. (Courtesy Hunt Oil Company.)

Downloaded 25 Jun 2012 to 95.28.162.50. Redistribution subject to SEG license or copyright; Terms of Use: http://segdl.org/

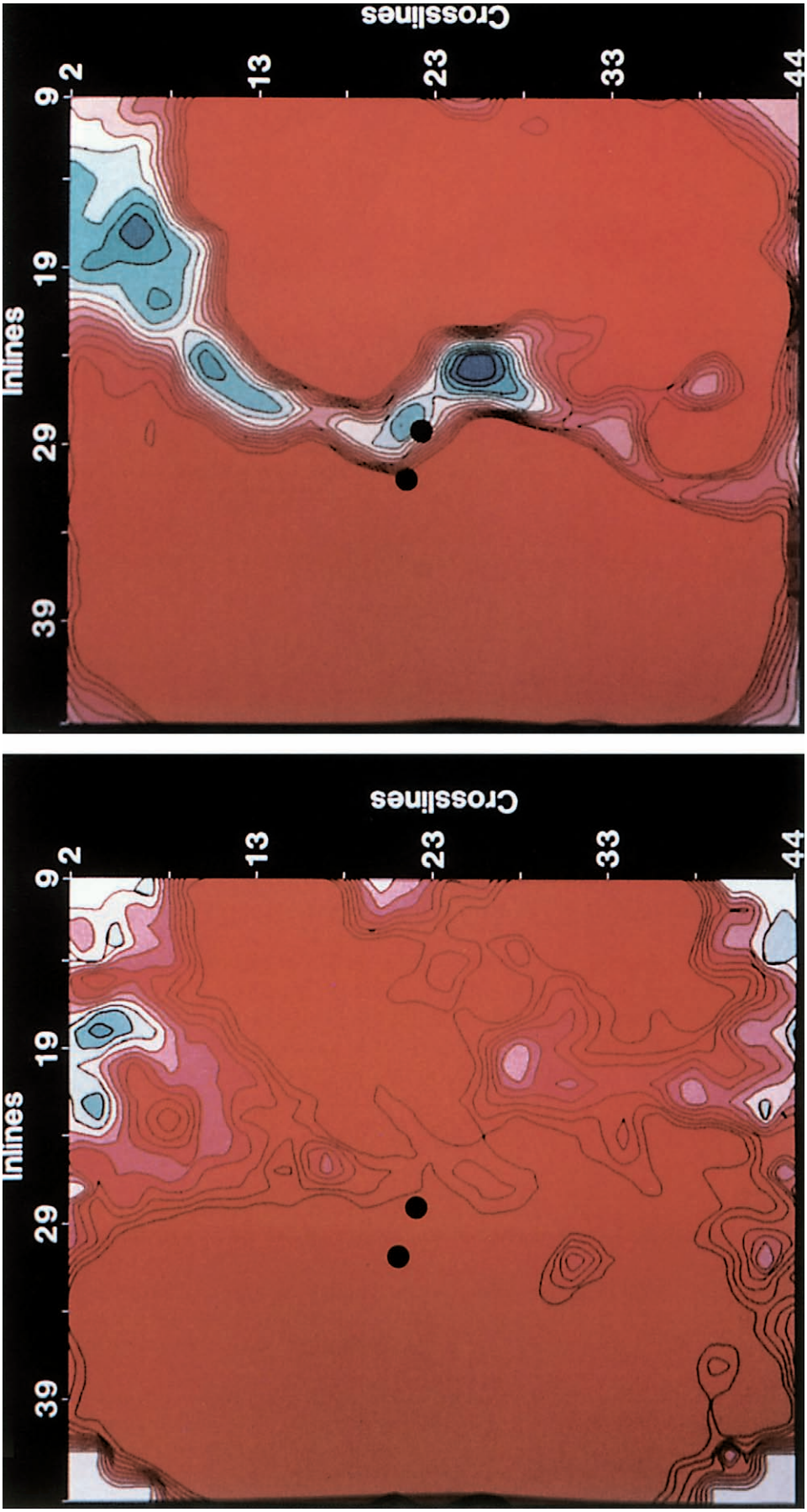

Fig. 1-17. Horizontal sections before migration (left) and after migration (right) showing the necessity of 3-D migration for the observation of shallow channels. (Courtesy Amoco Canada Petroleum Company Limited and N. E. Pullin.)

Downloaded 25 Jun 2012 to 95.28.162.50. Redistribution subject to SEG license or copyright; Terms of Use: http://segdl.org/

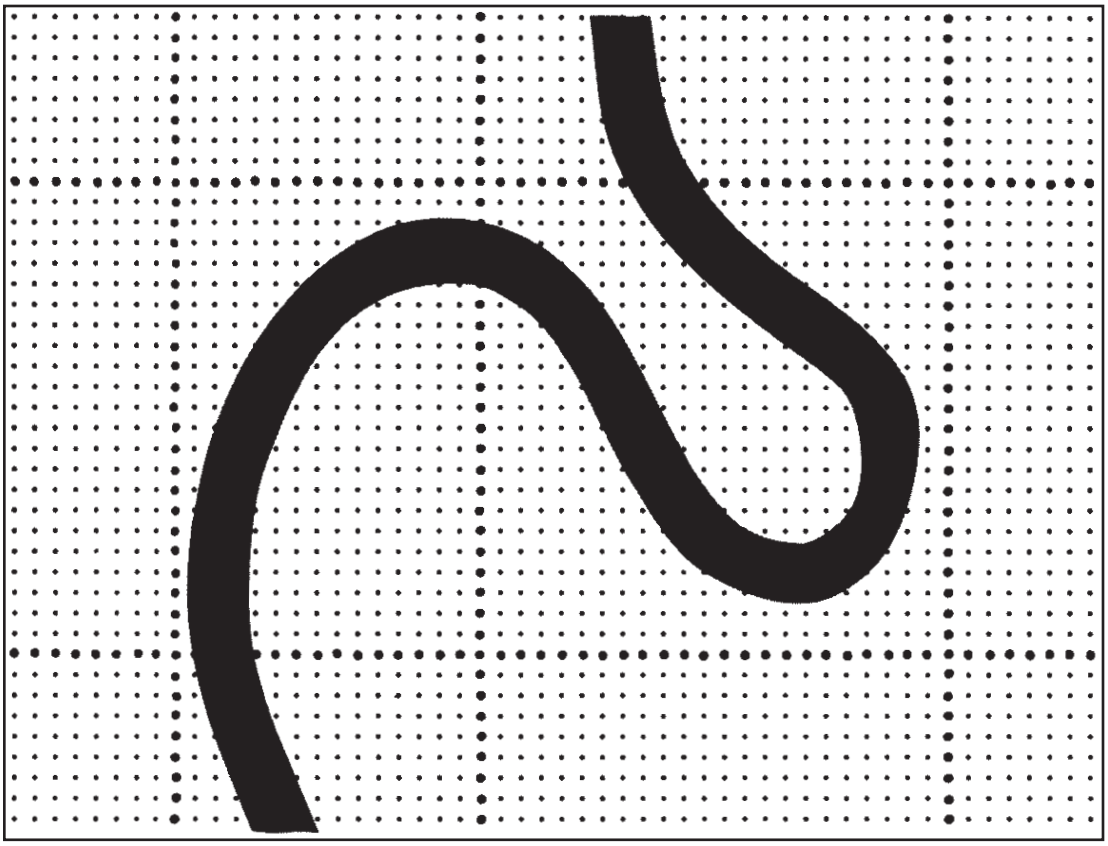

Fig. 1-18. Areal coverage of a 3-D survey compared to the coverage of a grid of five 2-D lines, and the ability of each to delineate a meandering channel.

spread over the Fresnel zone. The fact that one well penetrates the channel and the other does not is significant: they are only 10 m apart.

Survey Design

The sampling theorem requires that, for preservation of information, a waveform must be sampled such that there are at least two samples per cycle for the highest frequency. Since the beginning of the digital era, we have been used to sampling a seismic trace in time. For example, 4 ms sampling is theoretically adequate for frequencies up to 125 Hz. In practice we normally require at least three samples per cycle for the highest frequency. With this safety margin, 4 ms sampling is adequate for frequencies up to 83 Hz.

In space, the sampling theorem translates to the requirement of at least two, and preferably three, samples per shortest wavelength in every direction. In a normal 2-D survey layout this will be satisfied by the depth point spacing along lines but not by the spacing between lines. Hence the restriction that widely-spaced 2-D lines can be processed individually on a 2-D basis but not together as a 3-D volume.

If the sampling theorem is not satisfied the data are aliased. In the case of a dipping event, the spatial sampling of that event must be such that its principal alignment is obvious; if not, aliases occur and spurious dips result after multichannel processing. Table 1-3 shows the frequencies at which this aliasing occurs for various dips and subsurface spacings. Clearly, a 3-D survey must be designed such that aliasing during processing does not occur. Tables like the one presented can be used to establish the necessary spacing considering the dips and velocities present. In order to impose the safety margin of three samples, rather than two, per shortest wavelength, the frequency limit is normally considered to be around two-thirds of each number tabulated. The formulas in Table 1-4 provide a general method of establishing the spacings required. The first formula, based on two samples per shortest wavelength, gives the maximum

Downloaded 25 Jun 2012 to 95.28.162.50. Redistribution subject to SEG license or copyright; Terms of Use: http://segdl.org/

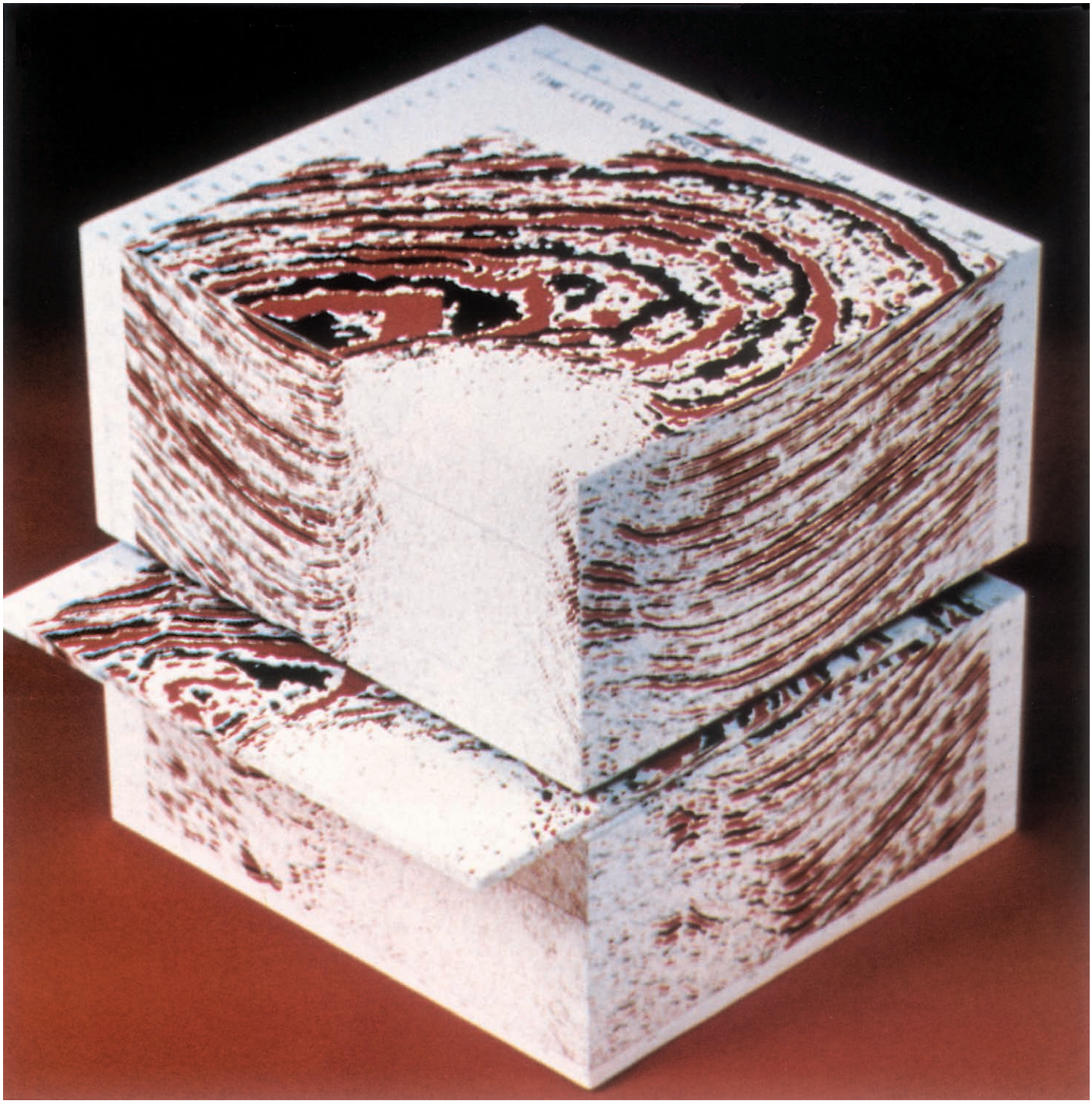

Fig. 1-19. 3-D data volume showing a Gulf of Mexico salt dome and associated rim syncline. (Courtesy Hunt Oil Company).

spacing that can be used to image the structure. Given our ignorance of the subsurface structure at the time the 3-D survey is being designed, we should allow a significant safety margin by collecting at least three samples per shortest spatial wavelength.

Table 1-4 also shows the two formulas needed to calculate the width of the extra strip around the periphery of the prospect over which data must be collected in order to ensure proper imaging in the area of interest. The calculation of migration distance, the extra fringe width needed for structure, should use the local value of dip measured perpendicular to the prospect boundary. The Fresnel zone radius, the extra fringe width needed for stratigraphy, needs to be considered for the proper focusing of amplitudes. The two strip, or fringe, widths thus calculated should be added

Downloaded 25 Jun 2012 to 95.28.162.50. Redistribution subject to SEG license or copyright; Terms of Use: http://segdl.org/

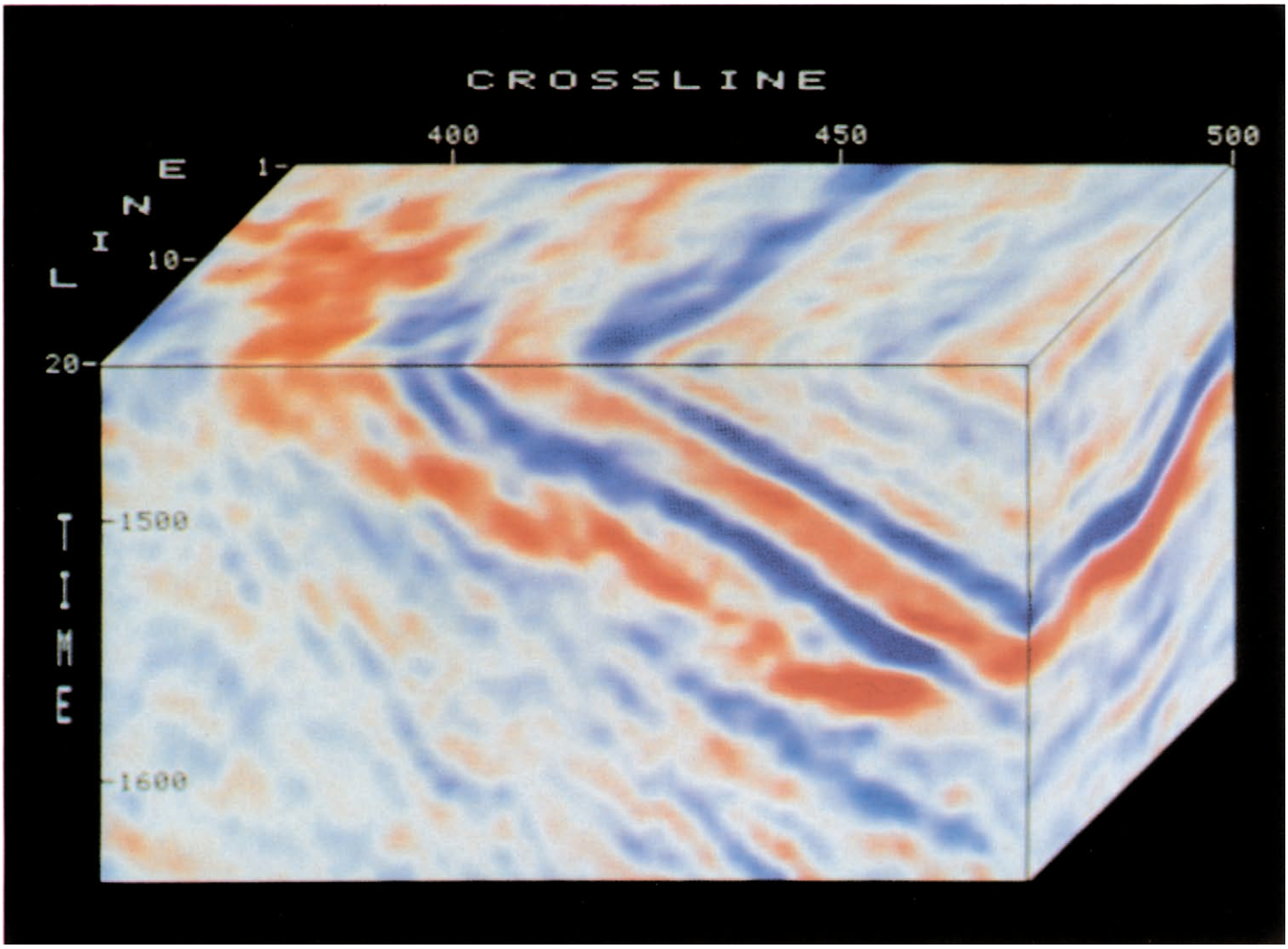

Fig. 1-20. 3-D data volume showing a bright spot from a Gulf of Mexico gas reservoir. (Courtesy Chevron U.S.A. Inc.)

together in defining the total survey area.

A typical 3-D seismic interpreter does not get involved in designing surveys but nevertheless needs to appreciate these issues. Figure 1-15 demonstrates that, of the data volume under interpretation, only the central portion is fully migrated and therefore fully reliable. The fringe between the inner and outer volumes is the migration distance and the Fresnel zone radius. If the interpreter is working in this fringe zone he needs to realize that the data are unreliable and the results are subject to greater risk.

Proper design of a 3-D survey is critical to its success, and sufficiently close spacing is vital. The formulas of Table 1-4 are addressing structural design issues. In areas of shallow dip where the survey objectives are stratigraphic, the selected spacing must be such that there are at least two samples within the lateral extent of any expected stratigraphic feature of interest, for example the width of a channel. Figure 1-18 demonstrates a typical comparison between the subsurface sampling of a 2-D and 3-D survey. The bold dots indicate the 2-D survey depth points which satisfy the sampling theorem along each line. The 3-D survey requires a similarly close spacing in both directions over the whole area. In addition to the opportunity for three-dimensional processing which the areal coverage provides, note the sampling and thus potential definition of a meandering stream channel. Sampling for stratigraphic features like this channel requires at least two but preferably three samples within the channel width. In practice, 3-D depth point spacing ranges between 6 and 50 m.

Downloaded 25 Jun 2012 to 95.28.162.50. Redistribution subject to SEG license or copyright; Terms of Use: http://segdl.org/

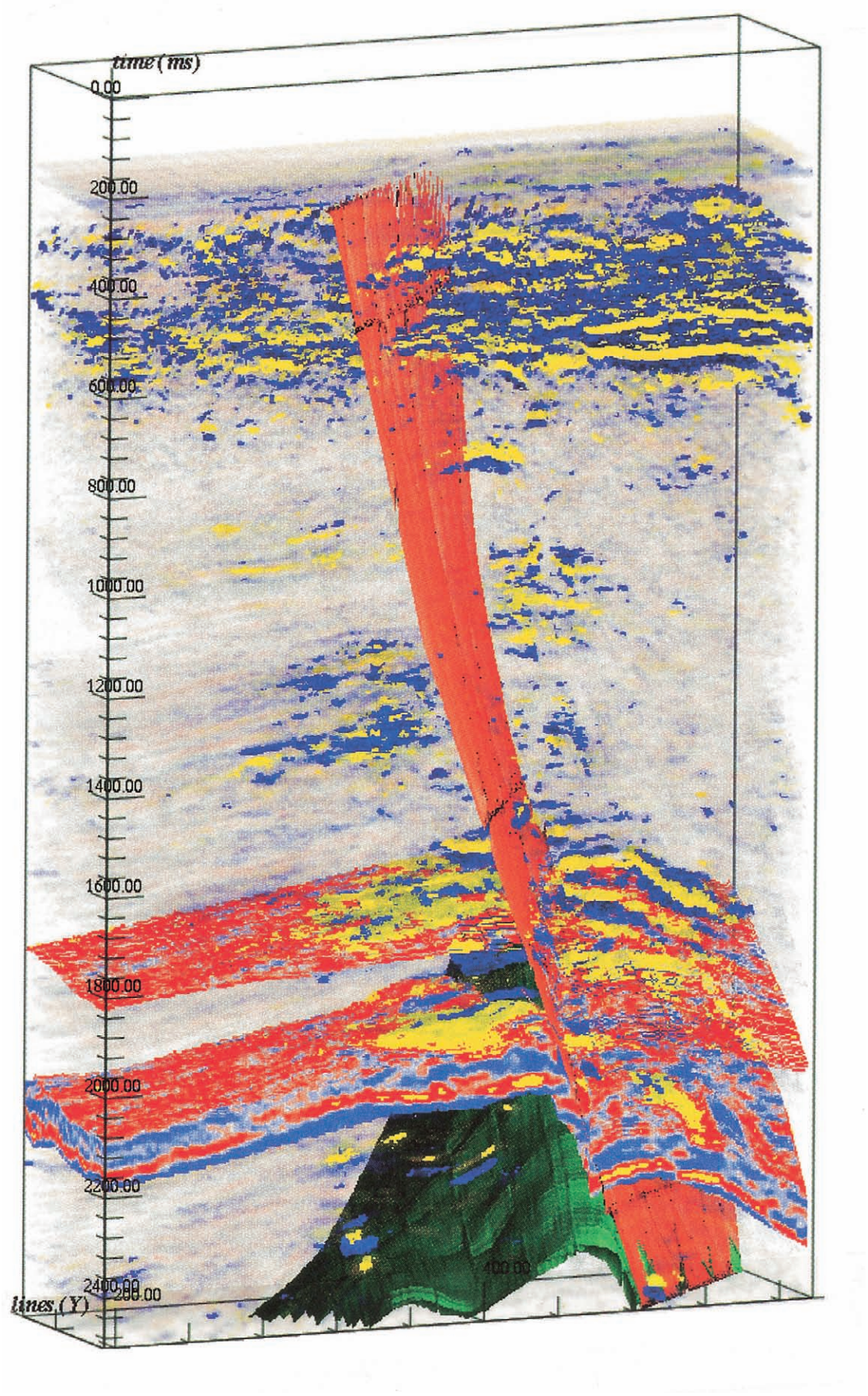

Fig. 1-21. Voxel-rendered view of data volume which, by making the voxels semi-transparent, permits the interpreter to look into the volume. (Courtesy CogniSeis Development.)

Downloaded 25 Jun 2012 to 95.28.162.50. Redistribution subject to SEG license or copyright; Terms of Use: http://segdl.org/

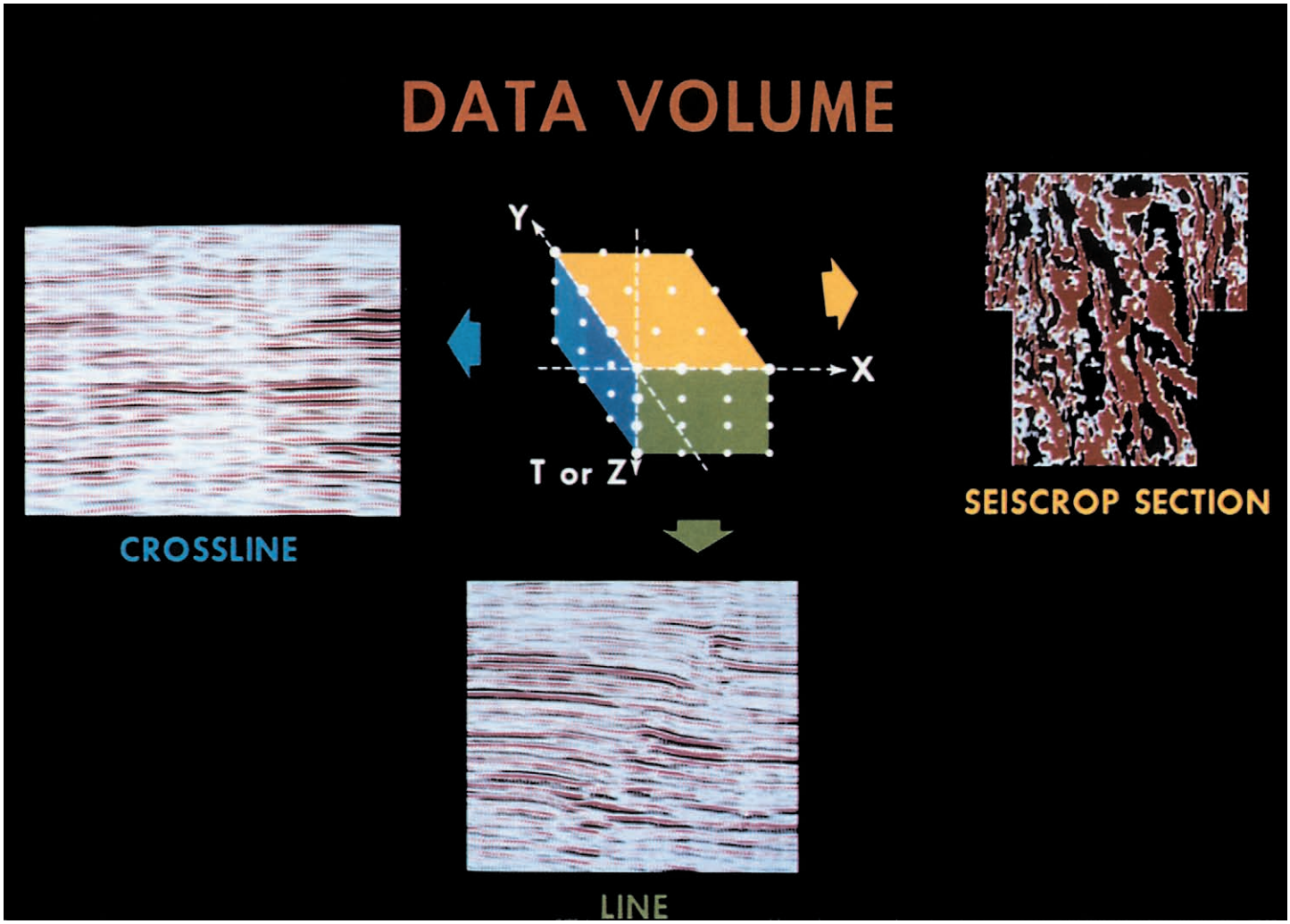

Fig. 1-22. Three sets of orthogonal slices through a data volume provide the basic equipment of the 3-D seismic interpreter.

Volume Concept

Collection of closely spaced seismic data over an area permits three-dimensional processing of the data as a volume. The volume concept is equally important to the seismic interpreter. With 3-D data, the interpreter is working directly with a volume rather than interpolating a volumetric interpretation from a widely-spaced grid of observations. The handling of this volume and what can be extracted from it are principal subjects of this book. One property of the volume pervades everything the 3-D interpreter does: The subsurface seismic wavefield is closely sampled in every direction, so that there is no grid loop around which the interpreter must tie, and no grid cell over which he must guess at the subsurface structure and stratigraphy. This is an opportunity which an interpreter must use to full advantage. Because the sampling requirements for interpretation are the same as for processing, all the processed data points contain unique information and thus should be used in the interpretation. Thus, the interpreter of a 3-D volume should not decimate the data available to him but, given that he has time constraints imposed on him, he should use innovative approaches with horizontal sections, specially selected slices, and automatic spatial tracking, in order to comprehend all the information in the data. In this way the 3-D

Downloaded 25 Jun 2012 to 95.28.162.50. Redistribution subject to SEG license or copyright; Terms of Use: http://segdl.org/

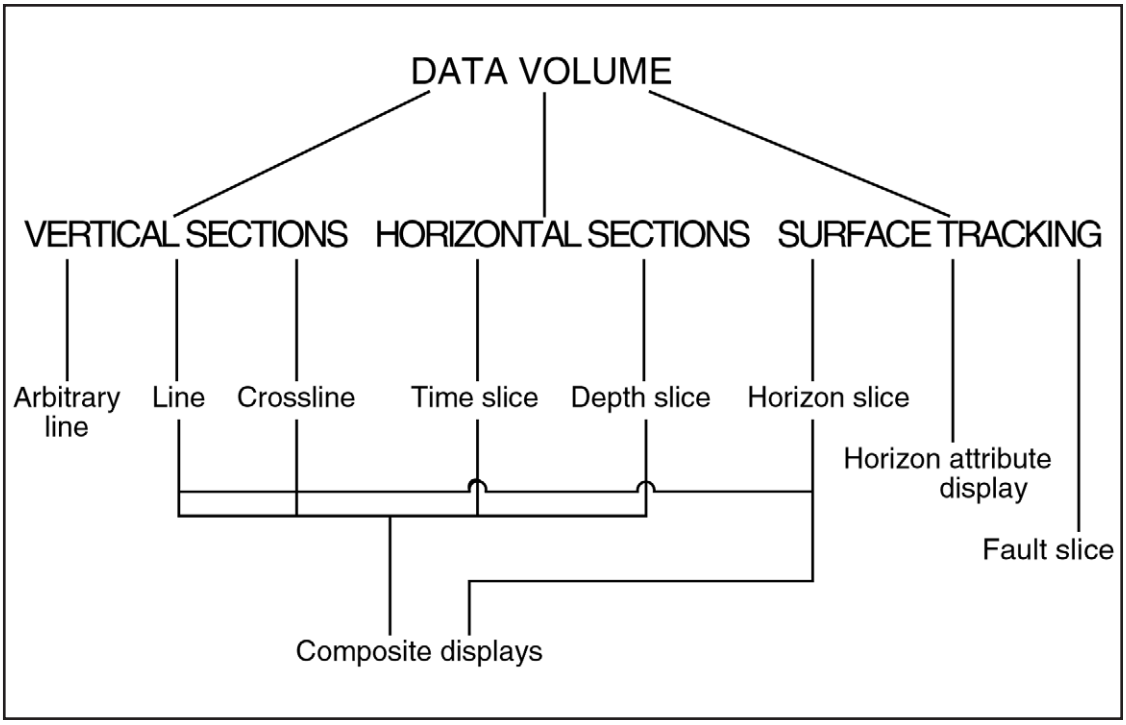

Fig. 1-23. Recognized and approved terms for display products from 3-D seismic data. All display seismic amplitude unless specified otherwise. Use of all other terms should be discouraged.

seismic interpreter will generate a more accurate and detailed map or other product than his 2-D predecessor in the same area.

Figure 1-19 shows a view of a 3-D data volume through a salt dome. It demonstrates the volume concept well and the interpreter can use a display of this kind to help in appreciation of subsurface three-dimensionality. Figure 1-20 shows another cube, in this case generated interactively, which helps in the three-dimensional appreciation of a much more detailed subsurface objective. Neither of these displays, however, permits the interpreter to look *into* the volume of data.

True 3-D display has recently become a reality on computer workstations and Figure 1-21 shows an example. The portion of the volume being displayed is composed of voxels, or volume elements, and these are rendered with differing degrees of transparency so that the interpreter can really see into the volume. In Figure 1-21 there are four interpreted surfaces as well as the semi-transparent data. As with any volumetric display the dynamic range is reduced because of the quantity of data viewed. These types of display are very useful for data visualization but they are not yet fully integrated into mainstream interpretation systems.

Slicing the Data Volume

The majority of 3-D interpretation is performed on slices through the data volume. There are no restrictions on the dynamic range for the display of any one slice, and therefore all the benefits of color, can be exploited (see Chapter 2). The 3-D volume contains a regularly-spaced orthogonal array of data points defined by the acquisition geometry, and maybe adjusted during processing. The three principal directions of the array define three sets of orthogonal slices or sections through the data, as shown in Figure 1-22.

The vertical section in the direction of boat movement or cable lay-out is called a **line** (sometimes an **inline**). The vertical section perpendicular to this is called a **crossline**. The horizontal slice is called a **horizontal section, time slice, or depth slice**. The terminology used for slices through 3-D data volumes has become somewhat confused. One of the objectives of this chapter is to clarify terms in common use today.

Three sets of orthogonal slices through the data volume (as defined above) are regarded as the basic equipment of the 3-D interpreter. A complete interpretation will

Downloaded 25 Jun 2012 to 95.28.162.50. Redistribution subject to SEG license or copyright; Terms of Use: http://segdl.org/

Fig. 1-24. An early optical workstation.

make use of some of each of them. However, many other slices through the volume are possible. A **diagonal line** may be extracted to tie two locations of interest, such as wells. A zig-zag sequence of diagonal line segments may be necessary to tie together several wells in a prospect. In the planning stages for a production platform, a diagonal line may be extracted through the platform location along the intended azimuth of a deviated well. All these are vertical sections and are referred to as **arbitrary lines**.

More complicated slices are possible for special applications. A slice along or parallel to a structurally interpreted horizon, and hence along one bedding plane, is a **horizon slice.** Slices of this kind have particular application for stratigraphic interpretation, which is explored in Chapter 4. **Fault slices** generated parallel to a fault face have various applications in structural and reservoir interpretation and will be discussed in Chapter 7. **Horizon attribute displays** are the subject of Chapter 8.

Figure 1-23 shows a hierarchy of approved terms for display products from 3-D seismic data. It shows, for example, the equivalence of horizontal and vertical sections, and the equivalence of time slices with lines and crosslines. In order to aid worldwide communication, use of other terms is discouraged.

Workstations

In the early days of 3-D interpretation a sequence of horizontal sections was displayed on film-strip and shown as a motion picture (Bone, Giles, and Tegland, 1983).

Downloaded 25 Jun 2012 to 95.28.162.50. Redistribution subject to SEG license or copyright; Terms of Use: http://segdl.org/

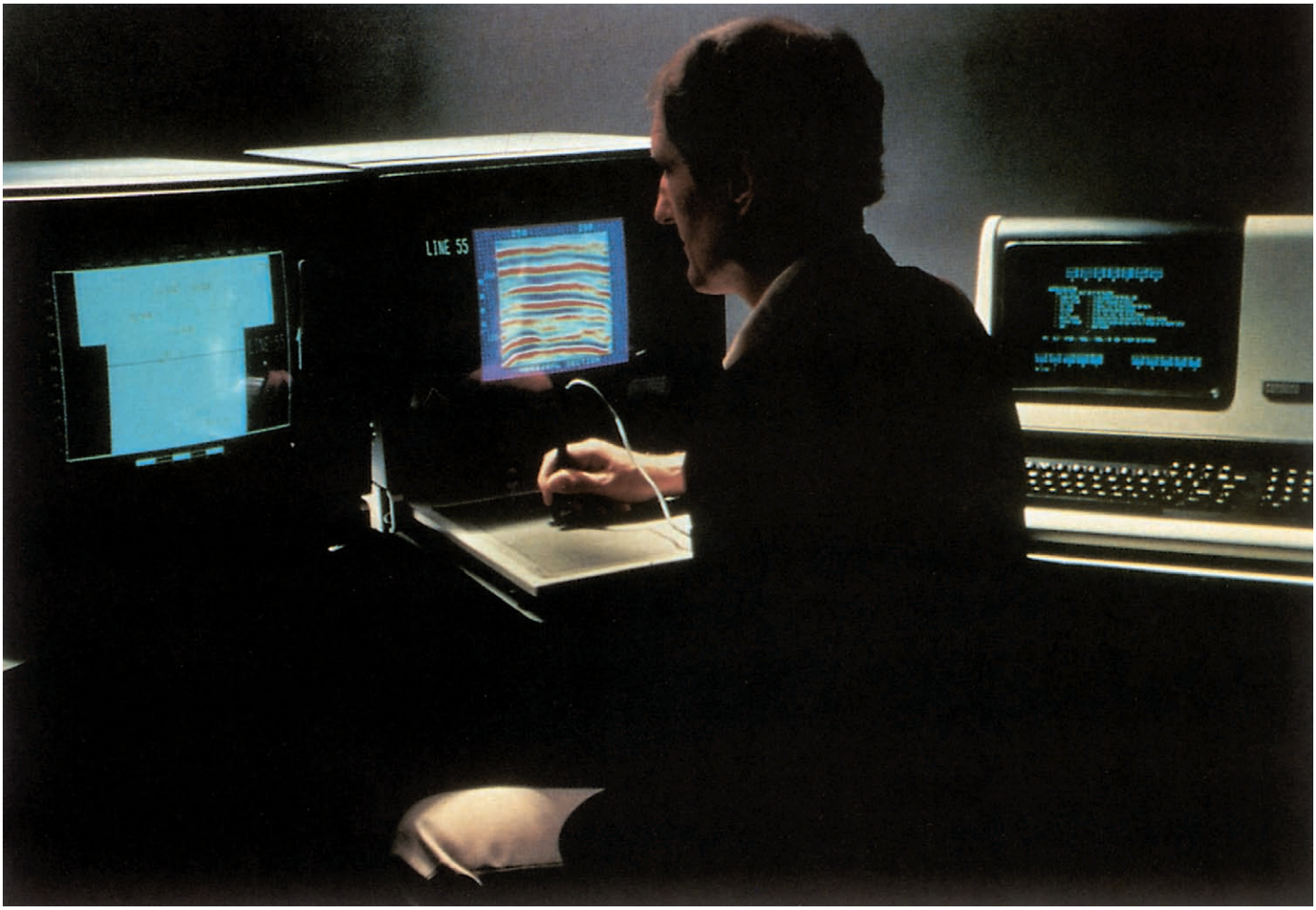

Fig. 1-25. An early interactive workstation.

From this developed the Seiscrop Interpretation Table — initially a commercially-available piece of equipment incorporating a 16mm analytical movie projector. This machine was originally developed for coaches wanting to examine closely the actions of professional athletes.

The Seiscrop Interpretation Table then evolved into a custom-built device (Figure 1-24). The data, either horizontal or vertical sections, were projected from 35mm film-strip onto a large screen. The interpreter fixed a sheet of transparent paper over the screen for mapping and then adjusted the size of the data image, focus, frame advance, or movie speed by simple controls.

Today 3-D interpretation is performed interactively and there has been an explosion in workstation usage in recent years. The interpreter calls the data from disk and views them on the screen of a color monitor (Figure 1-25). The large amount of regularly-organized data in a 3-D volume gives the interactive approach enormous benefits. In fact, many interactive interpretation systems addressed 3-D data first as the easier problem, and then developed 2-D interpretation capabilities later.

Most of the interpretation discussed in this book resulted from use of an interactive workstation, and many of the data illustrations are actual screen photographs. Furthermore, the facilities of the system contributed in several significant ways to the success of many of the projects reported here. Hence it is appropriate to review the interpretive benefits of an interactive interpretation system.

(1) **Data management** — The interpreter needs little or no paper; the selected seismic data display is presented on the screen of a color monitor and the progressive results of interpretation are returned to the digital database.

Downloaded 25 Jun 2012 to 95.28.162.50. Redistribution subject to SEG license or copyright; Terms of Use: http://segdl.org/

(2) **Color** — Flexible color display provides the interpreter with maximum optical dynamic range adapted to the particular problem under study.

(3) **Image composition** — Data images can be composed on the screen so that the interpreter views what is needed, no more and no less, for the study of one particular issue. Slices through the data volume are designed by the user in order to customize the perspective to the problem.

(4) **Idea flow** — The rapid response of the system makes it easy to try new ideas. The interpreter can rapidly generate innovative map or section products in pursuit of a better interpretation.

(5) **Interpretation consistency** — The capability to review large quantities of data in different forms means that the resulting interpretation should be more consistent with all available evidence. This is normally considered the best measure of interpretation quality.

(6) **More information** — Traditional interpretive tasks performed interactively will save time; however, the extraction of more detailed subsurface information is more persuasive and far-reaching.

Dynamic Range and Data Loading

Interactive interpretation must commence with data loading and this is a critical first step. Data processing has always been performed using 32 bits to describe each amplitude value. This large word size ensures that significance is retained during all computations. The first interactive systems in the early 1980s were 32-bit machines but soon a demand for speed dictated that data be loaded using 8 bits only. The small word reduces response time and minimizes storage space for the survey data. Today interactive systems offer a choice of 8-bit, 16-bit, or 32-bit dynamic range, although color monitors normally display 8 bits only.

Figure 1-26 shows a typical statistical distribution of amplitudes in a data volume. There are a large number of very low amplitudes, a fairly large number of moderate amplitudes but a very small number of high amplitudes. Mainstream structural interpretation tends to work on moderate amplitude horizons. The high amplitude tails of the distribution are localized anomalies which, in tertiary clastic basins, are often the hydrocarbon bright spots. The interpreter avoids the low amplitudes as much as possible because they are the most subject to noise. Thus most interpretive time is devoted to the amplitudes lying in the stippled areas of Figure 1-26.

If interpretation is to be conducted using 8 bits only, scaling 32-bit amplitude numbers to 8-bit amplitude numbers must be done during data loading. If the maximum amplitude in the volume is set to ± 128, relative amplitudes are preserved within the precision of the 8 bits. However, this often severely limits the dynamic range available in the stippled, or heavily used, amplitude regions. Clipping of the highest amplitudes is a common reaction to this problem so that a smaller value is set to ±128. More dynamic range is then available for the mainstream structural interpretation but the highest amplitudes are destroyed and hence unavailable for stratigraphic or reservoir analysis. This can be very damaging particularly in areas like the Gulf of Mexico. Some interactive workstations load 8-bit data with a floating point scalar defined individually for each trace and stored in the trace header. This lessens but does not remove the dynamic range problem discussed above.

A common and generally desirable solution today is to load the data using 16 bits for each amplitude value. In this way clipping is irrelevant and unnecessary. There is plenty of dynamic range for structural interpretation *and* bright spot studies, because amplitude values available with 16 bits cover the range ± 32,768.

An interesting comparison of 8-bit and 16-bit interpretation was conducted by Roberts and Hughes (1995). They concluded that there are always differences between interpretation products from 8-bit and 16-bit volumes but they are generally less than 5%. These may or may not be tolerable, and they stressed the need for *sensible clipping*. Figure 1-27 is a test for and demonstration of data clipping. Contrasting colors have been placed in the extremities of the otherwise-gradational color scheme. The large

Downloaded 25 Jun 2012 to 95.28.162.50. Redistribution subject to SEG license or copyright; Terms of Use: http://segdl.org/

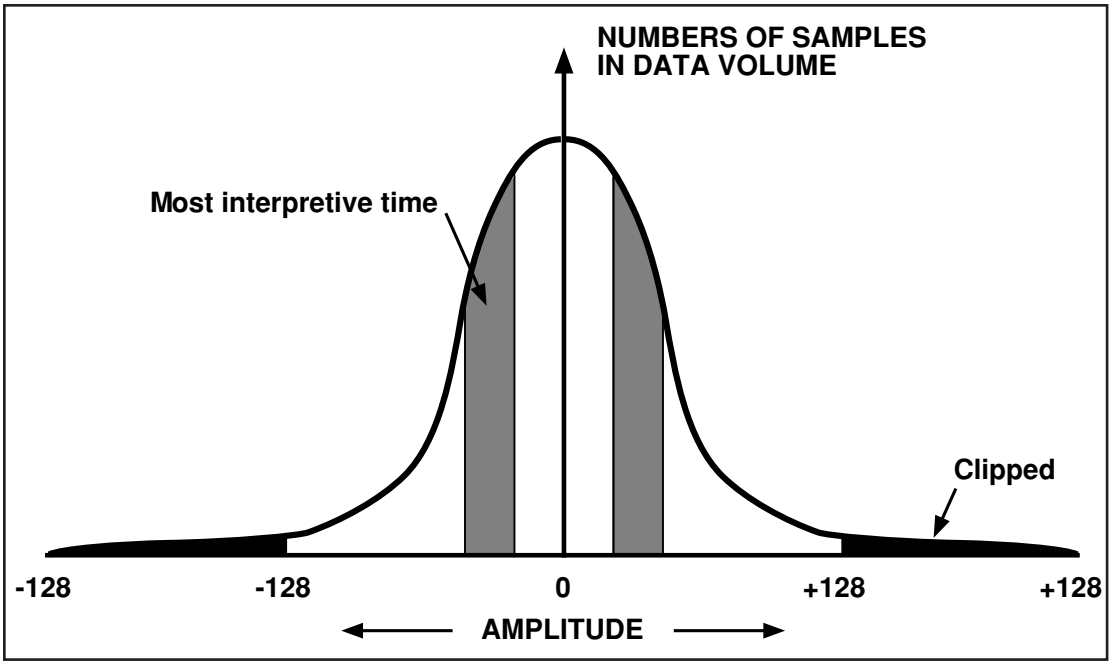

Fig. 1-26. Typical statistical distribution of amplitudes in a 3-D data volume. Plus or minus 128, the largest number which can be described by 8 bits, may be set to the largest amplitude, or alternatively to some smaller amplitude, thus causing data clipping.

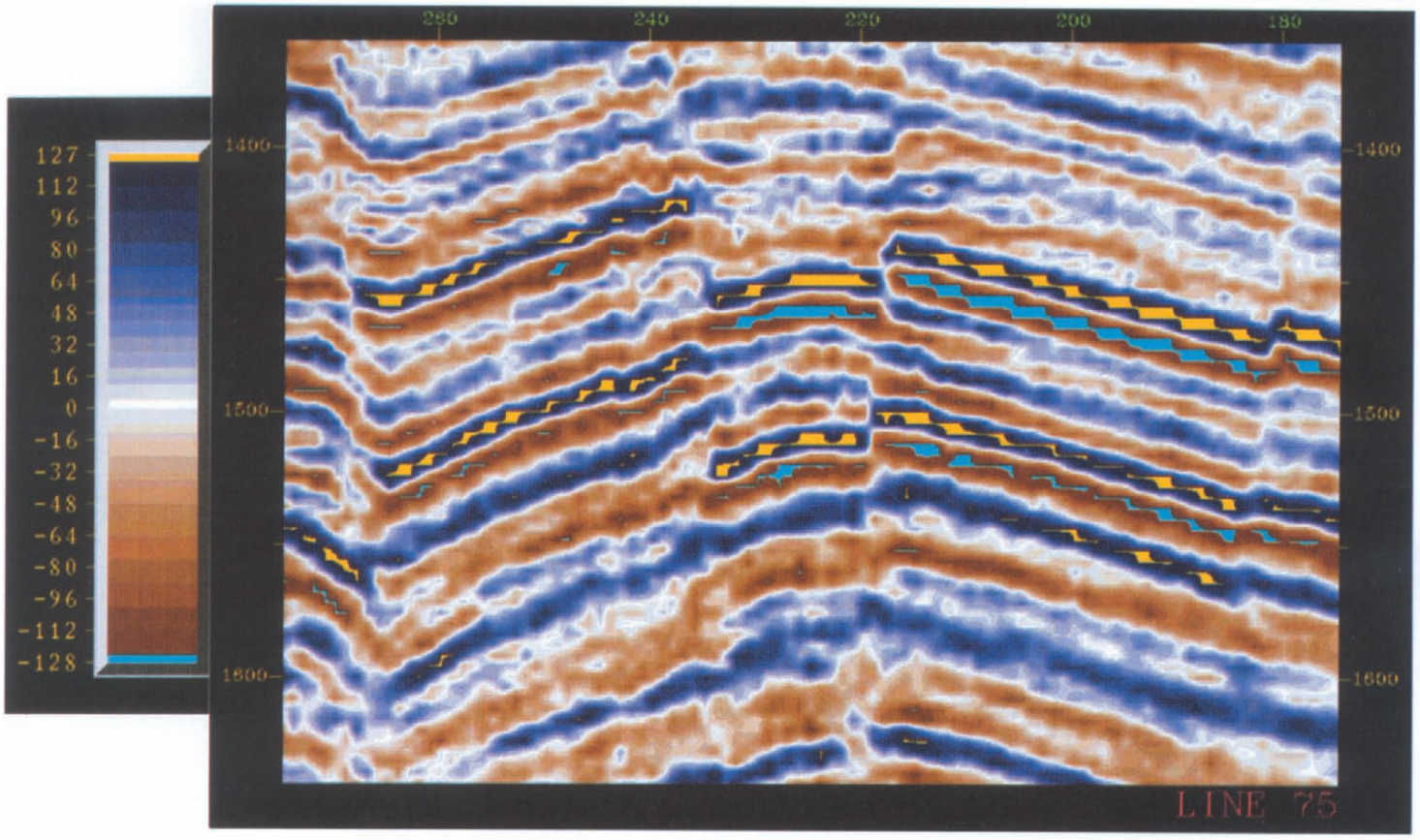

Fig. 1-27. Test for and demonstration of data clipping.

Downloaded 25 Jun 2012 to 95.28.162.50. Redistribution subject to SEG license or copyright; Terms of Use: http://segdl.org/

amounts of yellow and cyan demonstrate an anomalously high occupancy of those highest amplitudes, that is the data has been heavily clipped.

The author is opposed to data clipping as it places restrictions on interpretation activities. Generally the best solution is to use 16 bits and sometimes 32 bits. The total interpretation project today often involves a significant amount of post-interpretation computation. The larger number of bits helps ensure that numeric significance is maintained during these operations. Fortunately faster and cheaper hardware is now available which makes the use of 16 or 32 bits much less of a burden than it was in the past.

Acquisition Footprint

Seismic data acquisition and processing should be conducted in a very regular manner. We want to interpret visible irregularities in the data in terms of geology; we do not want spatial irregularities in the data to indicate the variations in the acquisition or processing operation. Ideally, we would like every bin to be filled with the same number of recorded traces with the same offset distribution and with the same azimuth distribution. However, this is impossible to achieve within a reasonable budget. If any or all of the recording parameters vary in some spatially systematic way, then the data acquisition geometry is commonly visible in the data as a footprint. Cordsen, Galbraith, and Peirce (2000) discuss various acquisition geometries and the many causes of footprint.

Figure 1-28 shows a severe footprint on a horizon slice extracted from land data. Shot lines and receiver lines are typically laid out perpendicular to each other on land (left), causing the gridlike pattern in amplitude (right). Marine data typically have a linear footprint aligned in the direction of boat movement. Figure 1-29 shows a mild marine footprint and a channel system. Footprint is difficult to predict, is more apparent at shallow depths, is generally expensive to eliminate in the field, and is complicated to remove in data processing. Interpreters need to be alert to footprint so that they do not confuse it with stratigraphic patterns. The horizon slice, the most important display for stratigraphic interpretation (Chapter 4), is particularly sensitive to footprint. Often an interpreter observes footprint in his data when he sees the first horizon slice, and this is the very time he wishes he didn't have the problem.

Difficulties of survey access caused by obstacles or no-permit zones lead to gaps in surface coverage and thus to an irregular footprint effect. Interruptions in surface coverage can cause amplitude terminations at depth which can be confused with stratigraphic boundaries. Figure 1-30 shows a red-over-blue amplitude objective high on structure which at first sight looks prospective. However, the severe lack of surface coverage on the right reduces amplitude for all reflections and thus reduces confidence that the amplitude objective has a geologic cause. Figure 1-31 is similar. The very strong hydrocarbon amplitude on the right at depth is greatly attenuated on the left because of surface effects.

Downloaded 25 Jun 2012 to 95.28.162.50. Redistribution subject to SEG license or copyright; Terms of Use: http://segdl.org/

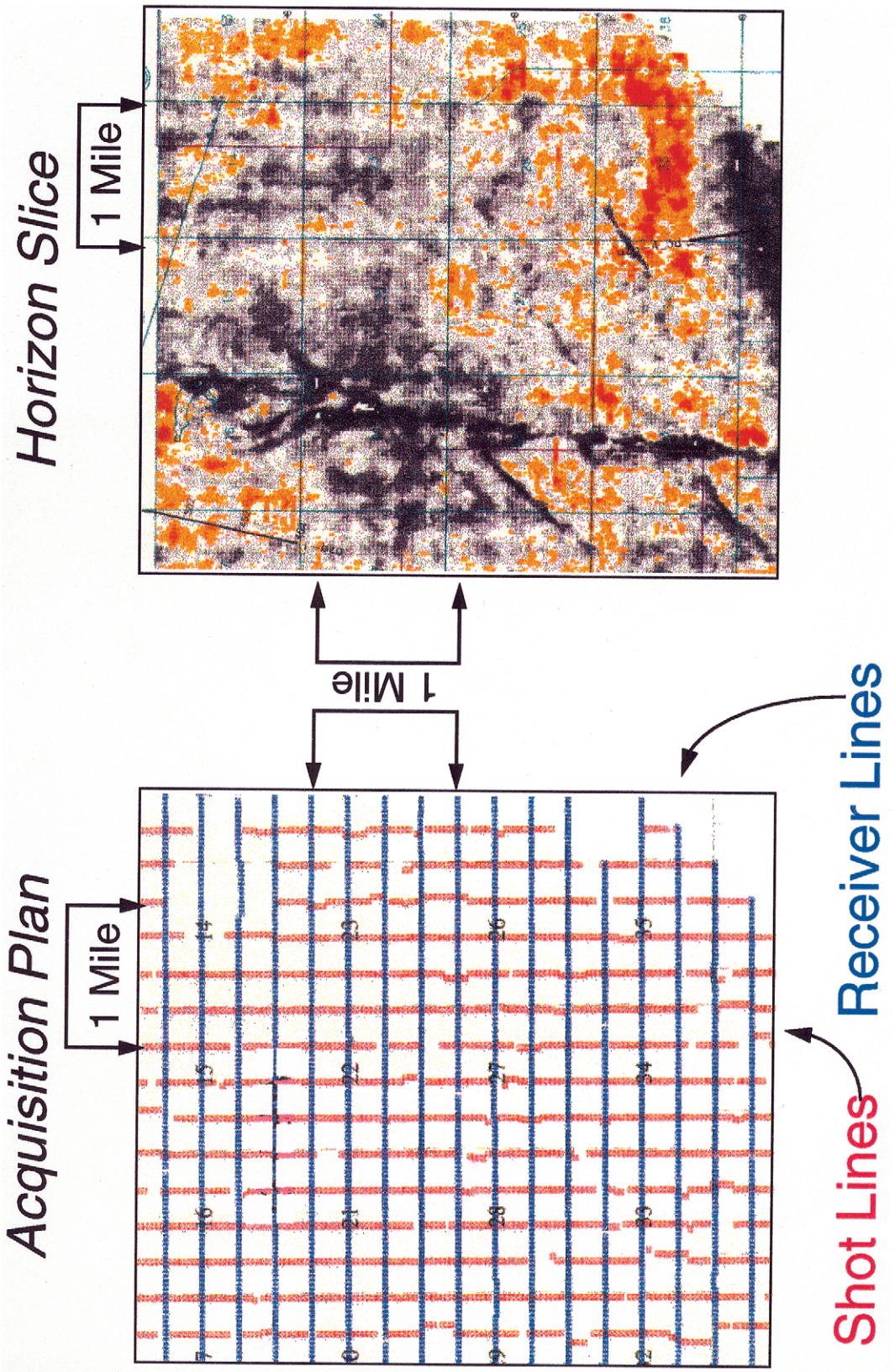

Fig. 1-28. Acquisition footprint is the imprint of the data acquisition geometry on horizon slices and similar areal displays. Example of a severe footprint for a land survey. (Courtesy Amoco Production Company.)

Downloaded 25 Jun 2012 to 95.28.162.50. Redistribution subject to SEG license or copyright; Terms of Use: http://segdl.org/

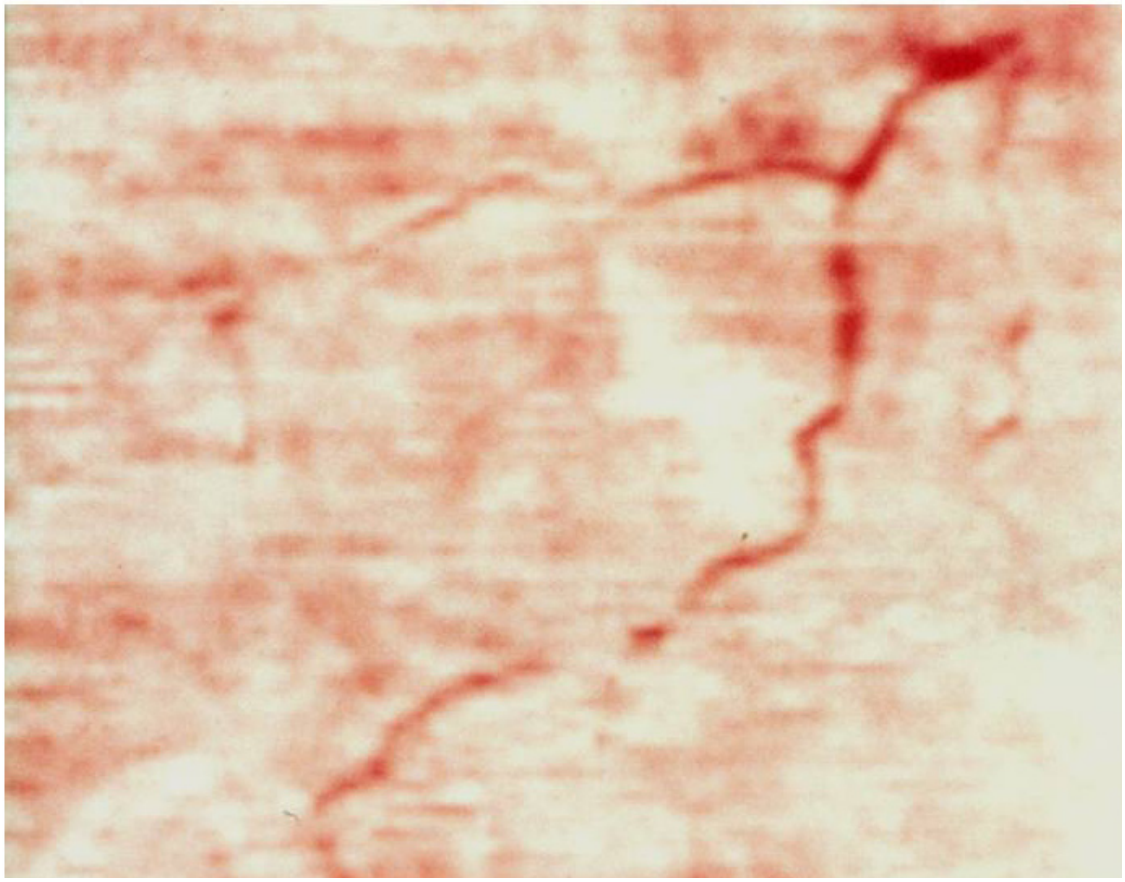

Fig. 1-29. Footprint in marine data. Note mild lineations running left to right.

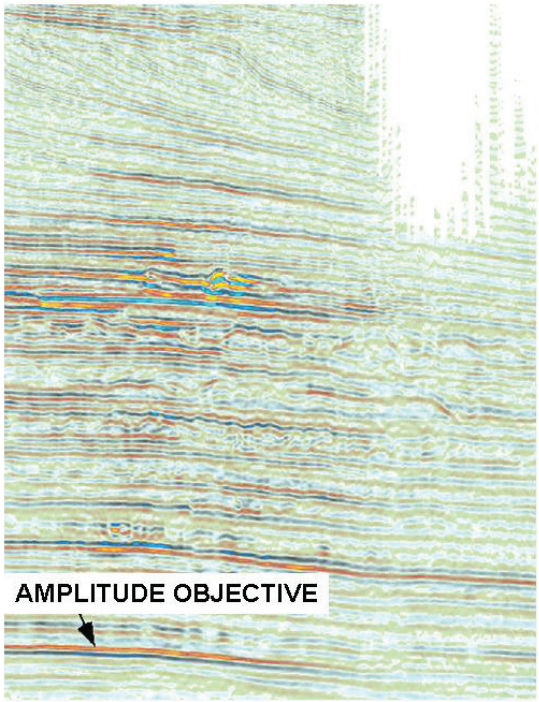

Fig. 1-30. Amplitude objective appears less prospective because all amplitudes on right are reduced by low surface coverage (after Sheriff et al., 2010; used by permission of the Society of Exploration Geophysicists). (Courtesy Pemex.)

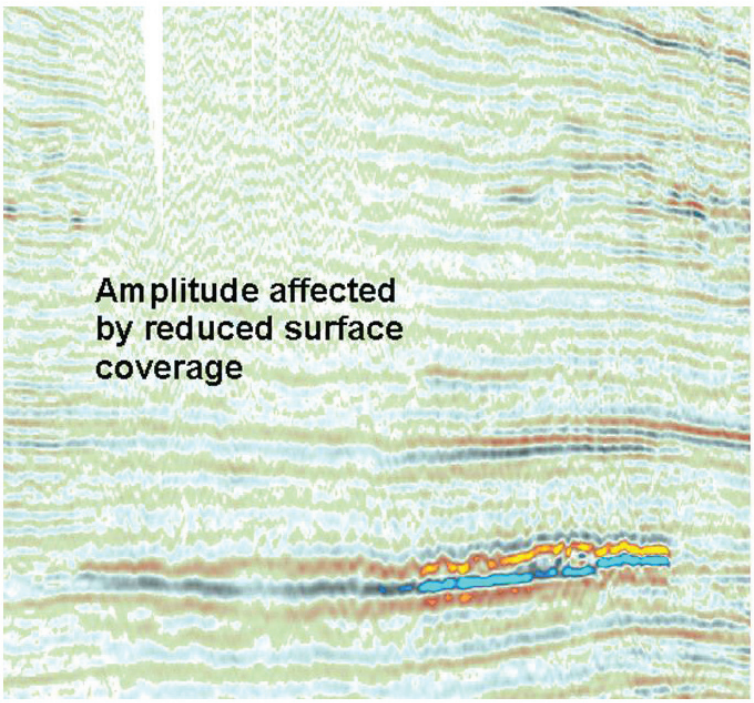

Fig. 1-31. Known hydrocarbon amplitude severely affected on left by reduced surface coverage. (Courtesy Pemex.)

Downloaded 25 Jun 2012 to 95.28.162.50. Redistribution subject to SEG license or copyright; Terms of Use: http://segdl.org/

References

Blake, B. A., J. B. Jennings, M. P. Curtis, and R. M. Phillipson, 1982, Three-dimensional seismic data reveals the finer structural details of a piercement salt dome: Offshore Technology Conference paper 4258, p. 403–406.

Bone, M. R., B. F. Giles, and E. R. Tegland, 1976, 3-D high resolution data collection, processing and display: Houston, Texas, presented at 46th Annual SEG Meeting.

Bone, M. R., B. F. Giles, and E. R. Tegland, 1983, Analysis of seismic data using horizontal cross-sections: Geophysics, v. 48, p. 1172–1178.

Cordsen, A., M. Galbraith, and J. Peirce, 2000, Planning land 3-D seismic surveys: SEG Geophysical Developments, no. 9, 204 p.

French, W. S., 1974, Two-dimensional and three-dimensional migration of model-experiment reflection profiles: Geophysics, v. 39, p. 265–277.

Graebner, R. J., B. A. Hardage, and W. A. Schneider, 2001, 3-D seismic exploration: SEG Geophysics Reprint Series, no. 22, 857 p.

Lindsey, J. P., 1989, The Fresnel zone and its interpretive significance: The Leading Edge, v. 8, no. 10, p. 33–39.

Martins, C. C., C. A. da Costa, C. E Theodoro, L. R. Guardado, and V. F. Andrade, 1995, 3-D Seismic: A successful strategy in the Campos Basin: The Leading Edge, v. 14, p. 701–704.

Nestvold, E. O., 1992, 3-D seismic: Is the promise fulfilled?: The Leading Edge, v. 11, no. 6, p. 12–19.

Roberts, G. A., and M. J. Hughes, 1995, Workstation interpretation — a comparison of data stored at 8 and 16 bits: Poster paper and EAGE Annual Convention, Glasgow.

Schneider, W. A., 1998, 3-D seismic: A historical note: The Leading Edge, v. 17, p. 375–380.

Sheriff, R. E., 1985, Aspects of seismic resolution, *in* O. R. Berg and D. Woolverton, eds., Seismic stratigraphy II: An integrated approach to hydrocarbon exploration: AAPG Memoir 39, p. 1–10.

Sheriff, R. E., A. R. Brown, and R. M. Lansley, 2010, Fundamentals of reservoir geophysics, *in* D. H. Johnston, eds., Methods and applications in reservoir geophsics, Chapter 2: The supporting technologies: SEG Investigations in Geophysics Series No. 15, p. 101–122.

Tegland, E. R., 1977, 3-D seismic techniques boost field development: Oil and Gas Journal, v. 75, no. 37, p. 79–82.

Walton, G. G., 1972, Three-dimensional seismic method: Geophysics, v. 37, p. 417–430.

Downloaded 25 Jun 2012 to 95.28.162.50. Redistribution subject to SEG license or copyright; Terms of Use: http://segdl.org/

Downloaded 25 Jun 2012 to 95.28.162.50. Redistribution subject to SEG license or copyright; Terms of Use: http://segdl.org/

Color, Character and Zero-Phaseness

Color Principles

"The total quantity of information recorded on a typical seismic line is enormous. It is virtually impossible to present all this information to the user in a comprehensible form." This quotation from Balch (1971) is even more true today than it was in 1971 and color has become an important contributor to the problem's solution. The human eye is very sensitive to color and the seismic interpreter can make use of this sensitivity in several ways. Taner and Sheriff (1977) and Lindseth (1979) were among the first to present color sections which demonstrated the additional information color can convey. Of equal importance is the increased optical dynamic range of a color section compared to its black and white variable area/wiggle trace equivalent. Both these properties are of great importance in stratigraphic interpretation.

Some understanding of color principles will help an interpreter maximize the use of color. It is helpful to visualize colors as a three-dimensional solid but there are three relevant sets of coordinates in terms of which the color solid can be expressed:

(1) the three additive primary colors — red, green, blue;
(2) the three subtractive primary colors — magenta, yellow, cyan; and,
(3) hue, saturation, density.

Figure 2-1 is a diagrammatic representation of a color cube showing the interrelationship of the above sets of coordinates. Figure 2-2 is a photograph of an actual color cube oriented to correspond to the diagram of Figure 2-1. Figure 2-3 is a photograph of the same cube from the opposite direction.

This cube was made using a color plotter, but the principles under discussion are independent of the display device. Any system which combines pigments employs the **subtractive primary colors** — magenta, yellow and cyan. Figure 2-2 and 2-3 show the *absence* of any color, which is *white*, at the top and progressively increasing quantities of magenta, yellow and cyan down the upper edges of the cube. These primaries, paired in equal quantities, give the **additive primary colors** — red, green and blue — at the three lower corners. All three subtractive primaries combined in equal quantities give black, seen at the bottom apex of the cube.

Any display system which combines light, such as a color monitor, follows the cube of Figures 2-2 and 2-3 from *bottom to top*. The *absence* of color is then *black*. Light of the three additive primary colors, red, green and blue, combine in pairs to make magenta, yellow and cyan and altogether to make white.

The cube photographs display only those colors on the surface of the cube. In fact, a much larger number of colors is inside. Down the vertical axis from white to black is the gray scale for which the **density** increases progressively (Figure 2-1).

Downloaded 25 Jun 2012 to 95.28.162.50. Redistribution subject to SEG license or copyright; Terms of Use: http://segdl.org/

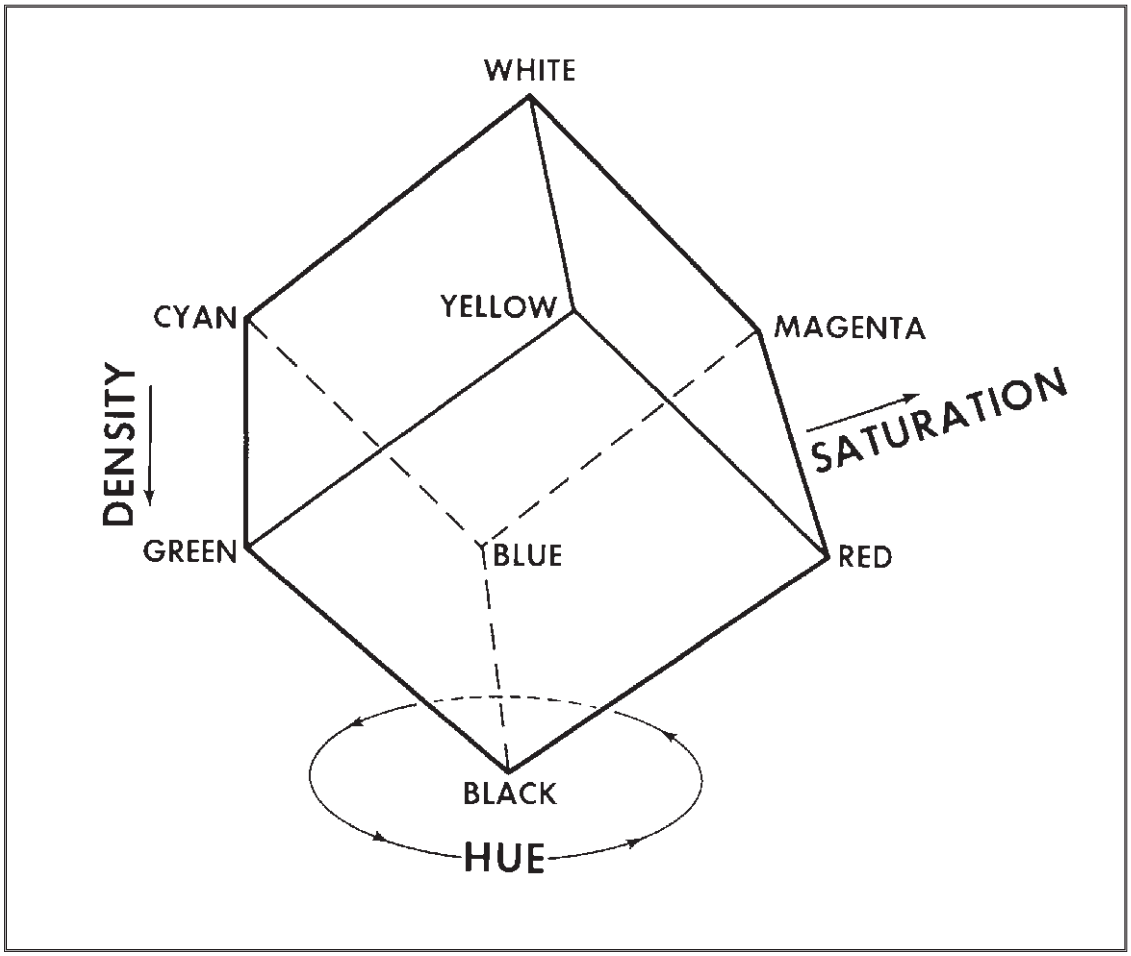

Fig. 2-1. Diagram of a color cube showing the relationship of the subtractive primary colors (magenta, yellow and cyan) to the additive primary colors (red, green and blue) to the color parameters (hue, saturation and density).

The **saturation** measures the distance from this central axis, ranging from zero on the axis to 100% on the surface of the cube. The **hue** is the rotational parameter measuring the spectral content of a color.

For the color cube illustrated in Figures 2-2 and 2-3 there are 17 levels (0-16) of each of the subtractive primaries — magenta, yellow and cyan. The total number of colors in the cube is thus $17 \times 17 \times 17$ or 4,913, of which 1,538 are fully saturated colors on the surface. One way of studying the colors available inside the cube is to slice it along a chosen density level. Figure 2-4 shows density level 16, which has maximum strength magenta, yellow and cyan at the corners and gray of density 33% at the center. This display clearly demonstrates the significance of hue as the rotational parameter and saturation as the radial distance from the gray axis. The additive primaries, red, green and blue, lie on density level 32 with gray of density 67% at the center.

Figure 2-5 is a color chart used in an interactive interpretation system (Gerhardstein and Brown, 1984). It is based on the mixing of light and hence involves the additive primaries — red, green and blue. All the colors displayed in Figure 2-5 are fully saturated; that is, they lie only on the surface of the color cube. The right half of the chart is a projection of a color cube similar to that of Figures 2-2 and 2-3 when viewed from the top. The left half of the chart is a view of the same color cube from the bottom. Interactive workstations make the selection and building of logical, efficient and intuitive color schemes easier if the selection chart is founded directly on the color cube, as in Figure 2-5.

Interpretive Value of Color

Today's interpreter uses color in two fundamentally different ways: with a *contrasting* or with a *gradational* color scheme. A map or a section displayed in *contrasting*

Downloaded 25 Jun 2012 to 95.28.162.50. Redistribution subject to SEG license or copyright; Terms of Use: http://segdl.org/

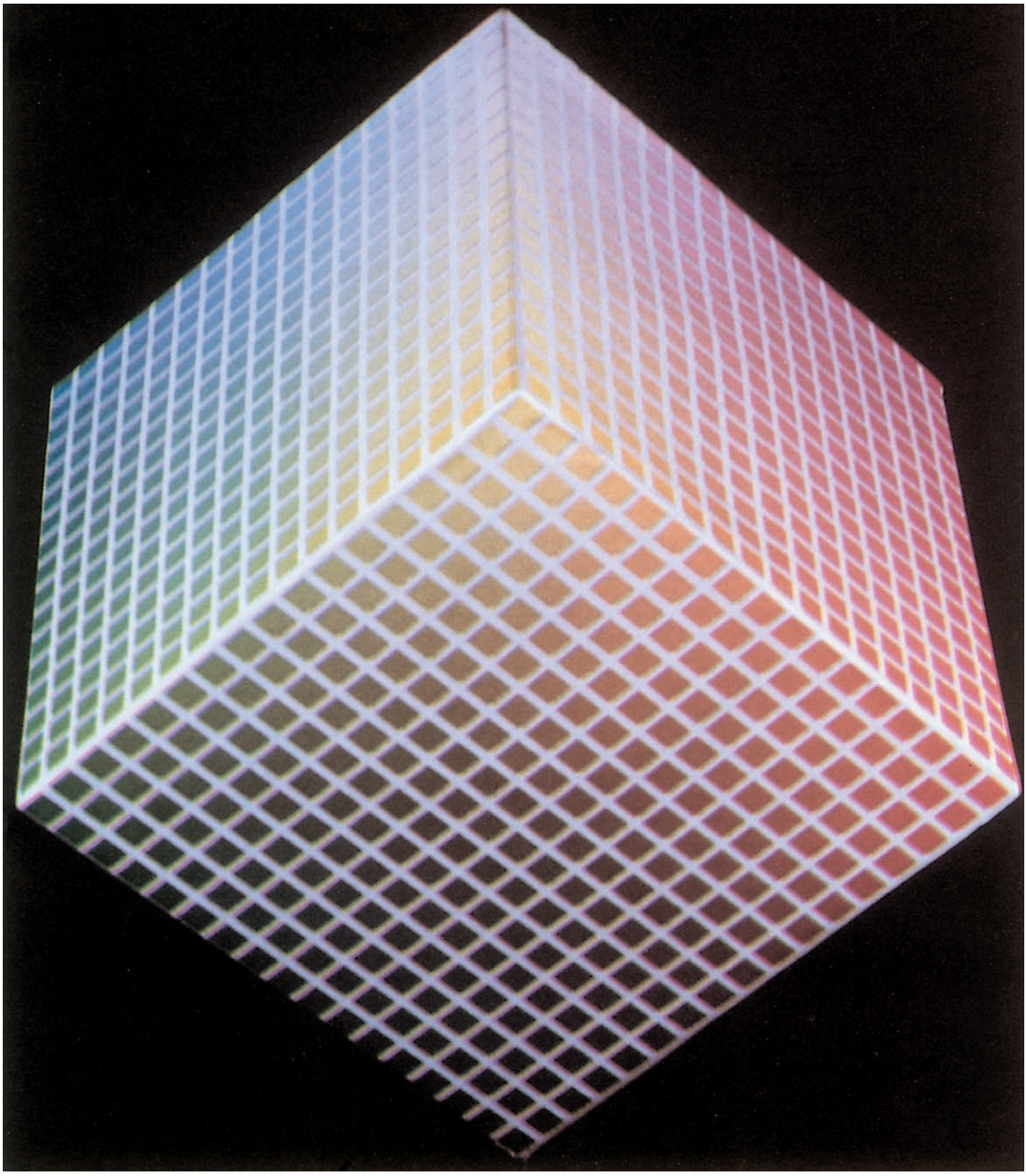

Fig. 2-2. Photograph of a color cube oriented the same as the diagram in Figure 2-1.

colors is normally accompanied by a legend, so the reader can identify the value of the displayed attribute at any point by reading the range of values associated with each color. Figure 2-6 is a structural contour map with a contour interval of 20 ms.

For an effective color display it is important that the range of values associated with each color, the number of colors used and their sequence, the contrast between adjacent colors, and the display scales are all carefully chosen. A color display must convey useful information and at the same time be aesthetically pleasing. For a map such as Figure 2-6 it is desirable to perceive equal visual contrast between adjacent colors, so that no one color boundary is more outstanding than another. A spectral sequence of colors was selected.

Figure 2-7 is a nomogram used for assessing visual color contrast. Visual contrast between two colors is, of course, somewhat subjective. Numerical color contrast is the sum of the absolute values of the differences in the amounts of the three primary colors. Zero density is white, maximum density (100%) is black, and density can have

Downloaded 25 Jun 2012 to 95.28.162.50. Redistribution subject to SEG license or copyright; Terms of Use: http://segdl.org/

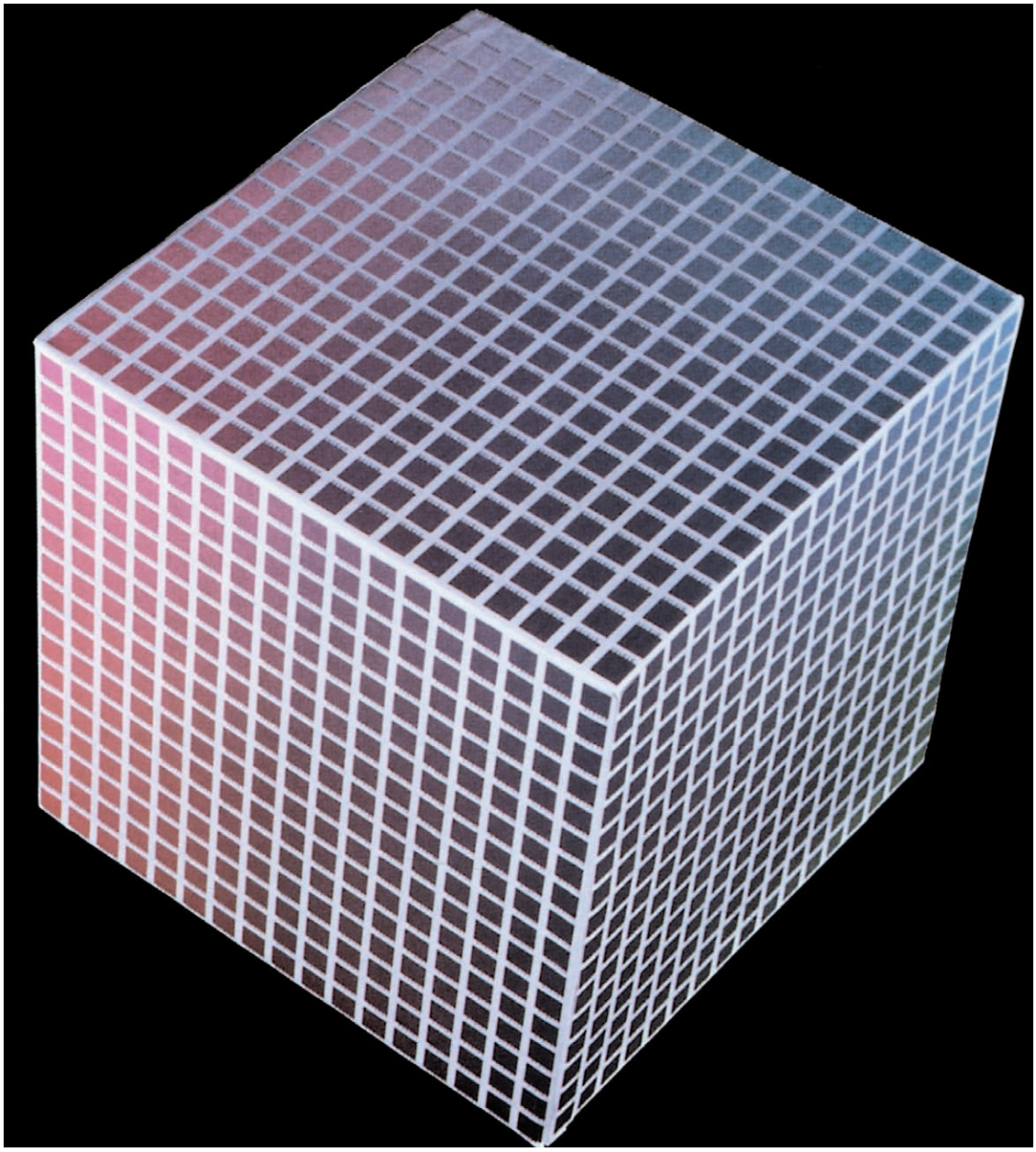

Fig. 2-3. Photograph of the same color cube as in Figure 2-2 from the back.

either arbitrary or percentage units between these extremes. Figure 2-7 shows that, for a particular visual color contrast, numerical contrast should be approximately proportional to average density. In other words, a larger numerical contrast is needed between darker colors.

A *gradational* color scheme is used when the interpreter is looking for trends, shapes, patterns and continuity. Figure 2-8 includes a vertical section displayed with gradational blue for positive amplitudes (peaks) and gradational red for negative amplitudes (troughs). Absolute amplitude levels are unimportant but relative levels are very important. Much stratigraphic information is implied by the lateral variations in amplitude along each reflection. The blue and red give equal visual weight to peaks and troughs. If the display gain is properly set, only a few of the highest amplitudes reach the fully saturated color and the full range of gradational shades expresses the varying amplitudes in the data. This increased dynamic range gives the interpreter the best opportunity to judge the extent and the character of amplitude anomalies of interest.

Figure 2-8 also provides a comparison of gradational color and variable area/wiggle

Downloaded 25 Jun 2012 to 95.28.162.50. Redistribution subject to SEG license or copyright; Terms of Use: http://segdl.org/

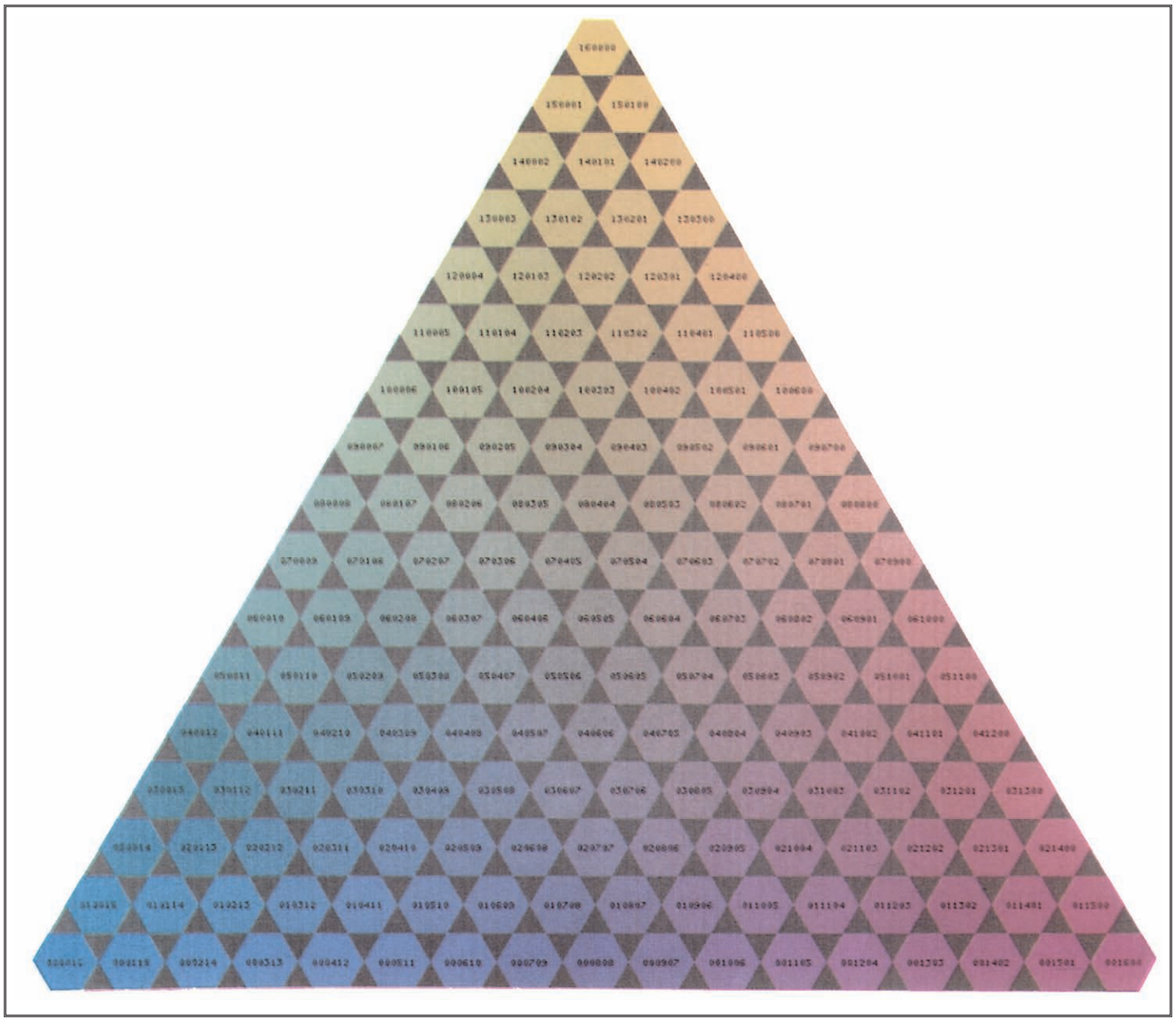

Fig. 2-4. Horizontal slice through the color cube at density level 33%, showing magenta, yellow and cyan at the corners and gray at the center.

trace for the same piece of data. The shortcomings in the variable area/wiggle trace display relative to the color section are: (1) the visual weights of peaks and troughs are very different, which makes comparison difficult and biases the interpreter's eye towards the peaks; (2) some of the peaks are saturated or clipped; and (3) the troughs, where they have significant amplitudes, are not visible beneath the depth points where they belong. The red flat spot reflection is clearly visible on the color section as are the relative amplitudes of peaks and troughs. At the extreme right of the section, coincident amplitude maxima in the peak and the trough indicate a tuning phenomenon (see Chapter 6).

Figure 2-9 provides a similar comparison between gradational color and variable area/wiggle trace. In addition, three different horizontal scales are used from which a further shortcoming of variable area/wiggle trace is apparent — that the dynamic range is limited and dependent on horizontal scale.

The color schemes of Figures 2-8 and 2-9 are more explicitly called double-gradational schemes with symmetry of blue and red about zero amplitude. The need for equal visibility of peaks and troughs has long been recognized. Backus and Chen

Downloaded 25 Jun 2012 to 95.28.162.50. Redistribution subject to SEG license or copyright; Terms of Use: http://segdl.org/

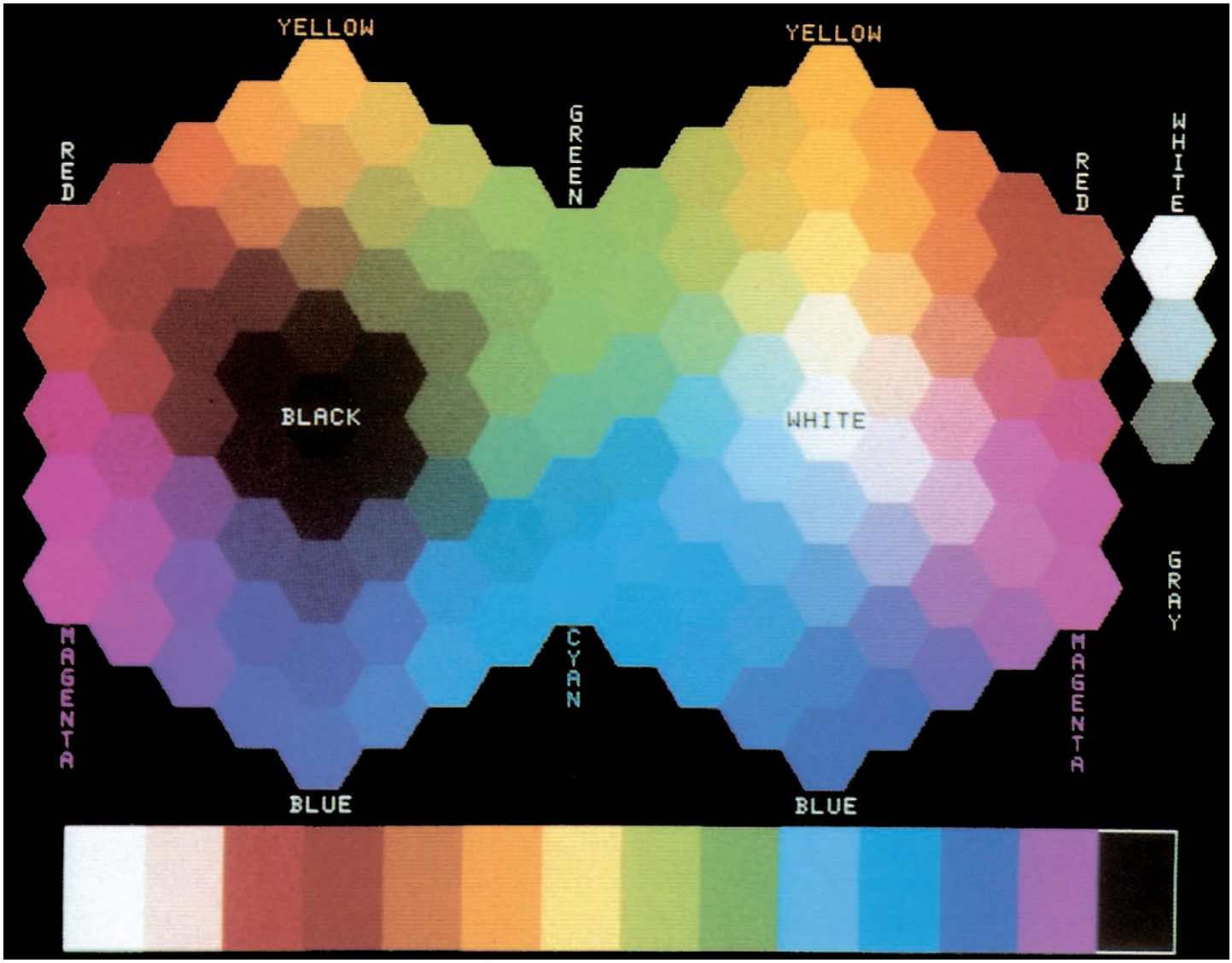

Fig. 2-5. Color selection chart from an interactive interpretation system. Note how its organization is based on the color cube.

(1975) generated dual-polarity variable-area sections with the peaks in black and the troughs in red. Figure 2-10 is an example of this display from Galbraith and Brown (1982). These were early attempts to generate symmetry or balance between positive amplitudes (peaks) and negative amplitudes (troughs).

Before continuing the discussion on different color schemes, it is important to understand why balance between positives and negatives is important. Consider a sand reservoir encased in shale. There is a reflection from the shale/sand interface at the top and a reflection from the sand/shale interface at the base. These are the two reflections from this reservoir, and both of them contain information about the reservoir. If some reservoir property (fluid, porosity, etc.) changes, then both reflections are equally affected. Thus the amplitudes of top and base reflections vary in unison, and the observation of this is called *natural pairing*. Observation of natural pairing requires a balanced double-gradational color scheme and is an important aspect of reservoir reflection identification (see Chapter 5).

The double-gradational blue-white-red color schemes of Figure 2-8 and 2-9 are balanced; pure primary blue is at one extremity and pure primary red is at the other extremity. This is the most universally applicable color scheme for interpreting seismic data. Figure 2-11 shows an extension of this with an additional gradation of cyan for the higher positive amplitudes and an additional gradation of yellow for the higher negative amplitudes. This has enhanced dynamic range compared with the blue-

Downloaded 25 Jun 2012 to 95.28.162.50. Redistribution subject to SEG license or copyright; Terms of Use: http://segdl.org/

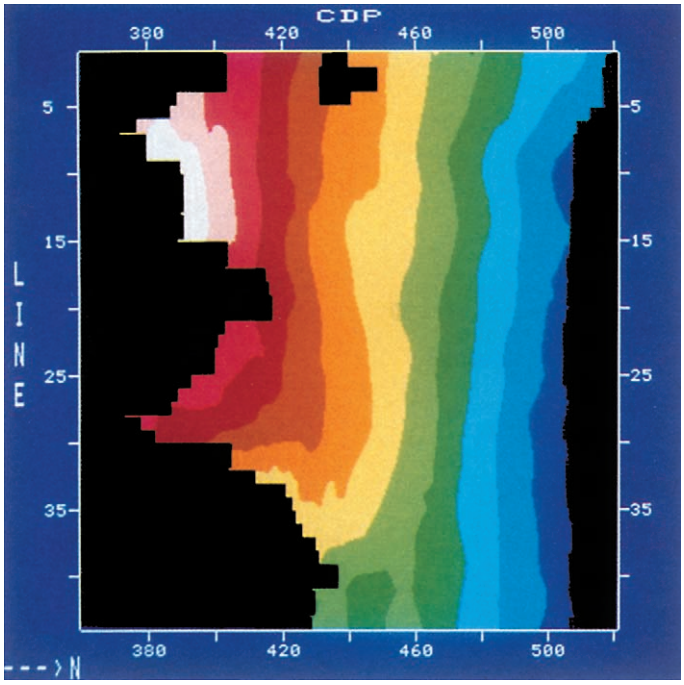

Fig. 2-6. Time-structure map displayed in a contrasting spectral color scheme.

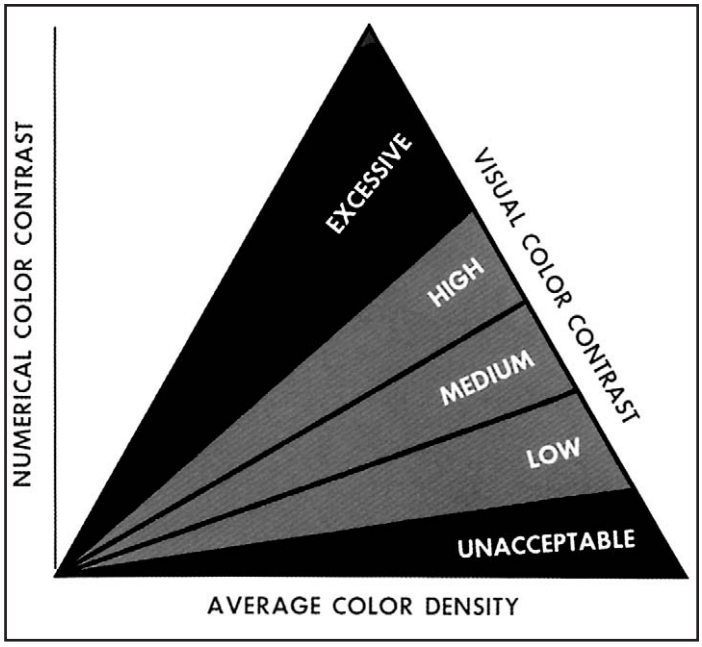

Fig. 2-7. Contrast-density nomogram used for establishing a color scheme with acceptable visual contrast between adjacent colors.

white-red but still has perfect balance on the color cube. Blue and red are both additive primaries, and cyan and yellow are both subtractive primaries. These balanced double-gradational color schemes are particularly important for reservoir reflection identification and recognition of hydrocarbon fluid effects.

Figure 2-12 shows a single-gradational gray scale with black at maximum positive and white at maximum negative. A single-gradational color scheme enhances low-amplitude events and thus is useful for general structural interpretation and recognition of subtle faults.

Figure 2-13 shows the same piece of data with four color schemes. The lower left is the standard blue-white-red. In the upper left, some contrasting colors have been added to highlight the highest amplitudes. This is usually not a good idea. Contrasts attract the eye to that particular amplitude level, whereas interpretation of amplitude actually entails the study of amplitude trends, patterns, and relativities. A much better way to add dynamic range to a double-gradational color scheme was illustrated with the additional gradations of cyan and yellow in Figure 2-11. The upper right panel of Figure 2-13 has too few gradations. The excessive contrasts of the lower right panel demonstrate how contrasting color schemes are inappropriate for seismic data.

The multiple color bars of Figure 2-14 show examples of what to do and what not to do. A is the quasi-standard blue-white-red, properly balanced with primary blue at one end and primary red at the other. F is a common variant using a non-primary blue and reddish brown; this is marginally inferior. G uses black and red, which is inferior because these colors are not balanced on the color cube. B is the enhanced dynamic range double-gradational color scheme with added cyan and yellow. Depending on the amplitude statistics of the data, this scheme may need to be adjusted, as shown in C. This kind of compression or expansion of the color scheme is important to maintain visibility of amplitude variations. Too much color scheme compression, however, such as in K, can obliterate amplitude variations and give the same impression as data clipping. H has the cyan and yellow but with contrasting

Downloaded 25 Jun 2012 to 95.28.162.50. Redistribution subject to SEG license or copyright; Terms of Use: http://segdl.org/

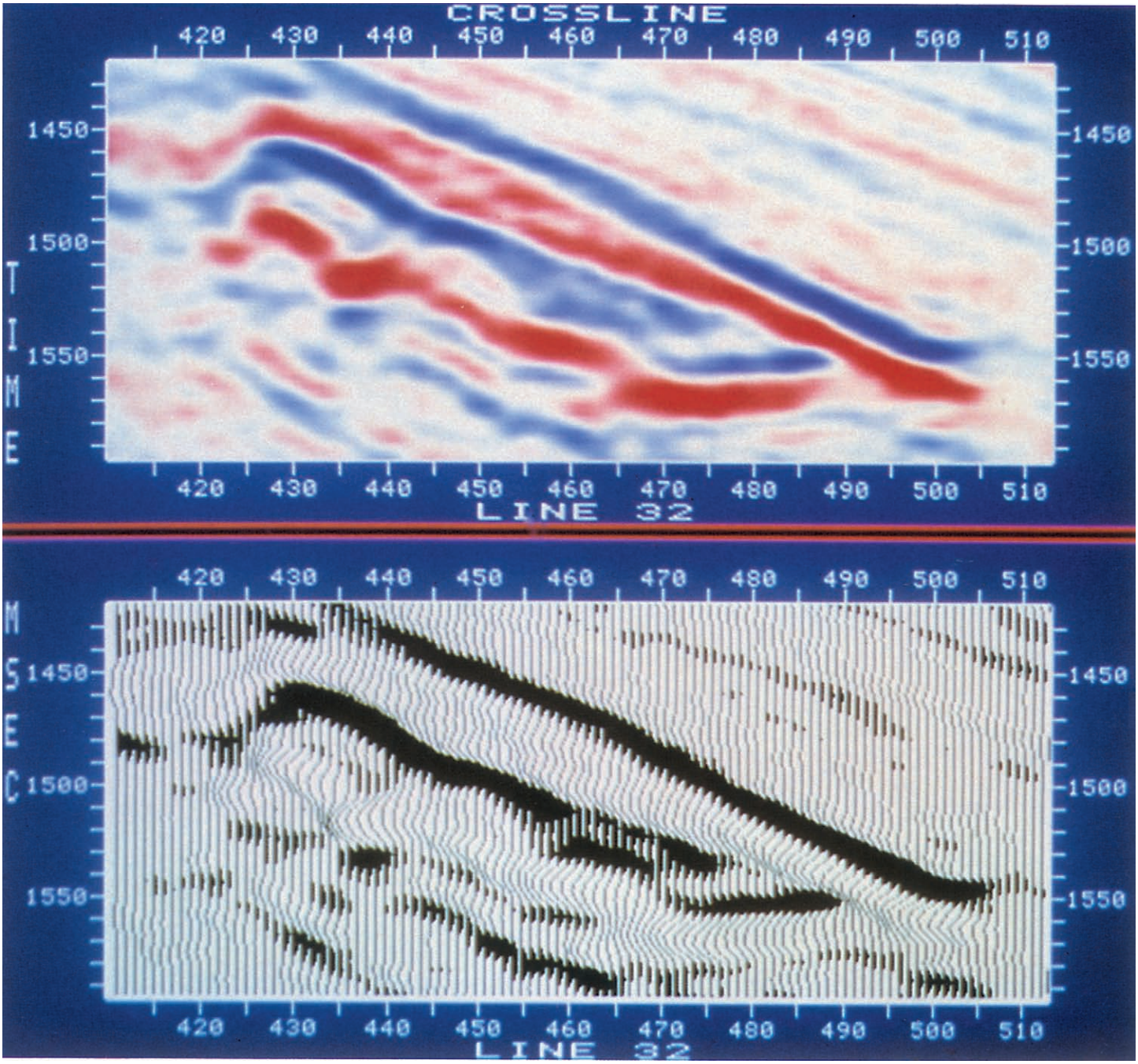

Fig. 2-8. Vertical seismic section displayed with gradational blue for peaks and gradational red for troughs compared to same section displayed in variable-area/wiggle trace. (Courtesy Chevron U.S.A. Inc.)

color boundaries, so this is not recommended for normal use. J is unbalanced about zero and is thus a most confusing color scheme. D and E are both single-gradational color schemes useful for structural interpretation and fault recognition.

The recognition of channels, bars and other depositional features on horizontal sections and horizon slices is important for the stratigraphic interpreter. Here again the proper use of gradational color coded to amplitude helps the detectability of these features because of the eye's ability to integrate a wide range of densities. Figures 2-15 and 2-16 illustrate an inferred channel on a horizon slice (see Chapter 4) and the use and abuse of color for its detection. A well at about Line 55, Crossline 250, indicates that at least the lower part of the areal bright spot (Figure 2-15) is a sand-filled channel. How extensive is this channel? It seems probable that it extends to include the central zone between Lines 70 and 80 and between Crosslines 180 and 270. However, after crossing two faults, a curvilinear feature can be seen continuing

Downloaded 25 Jun 2012 to 95.28.162.50. Redistribution subject to SEG license or copyright; Terms of Use: http://segdl.org/

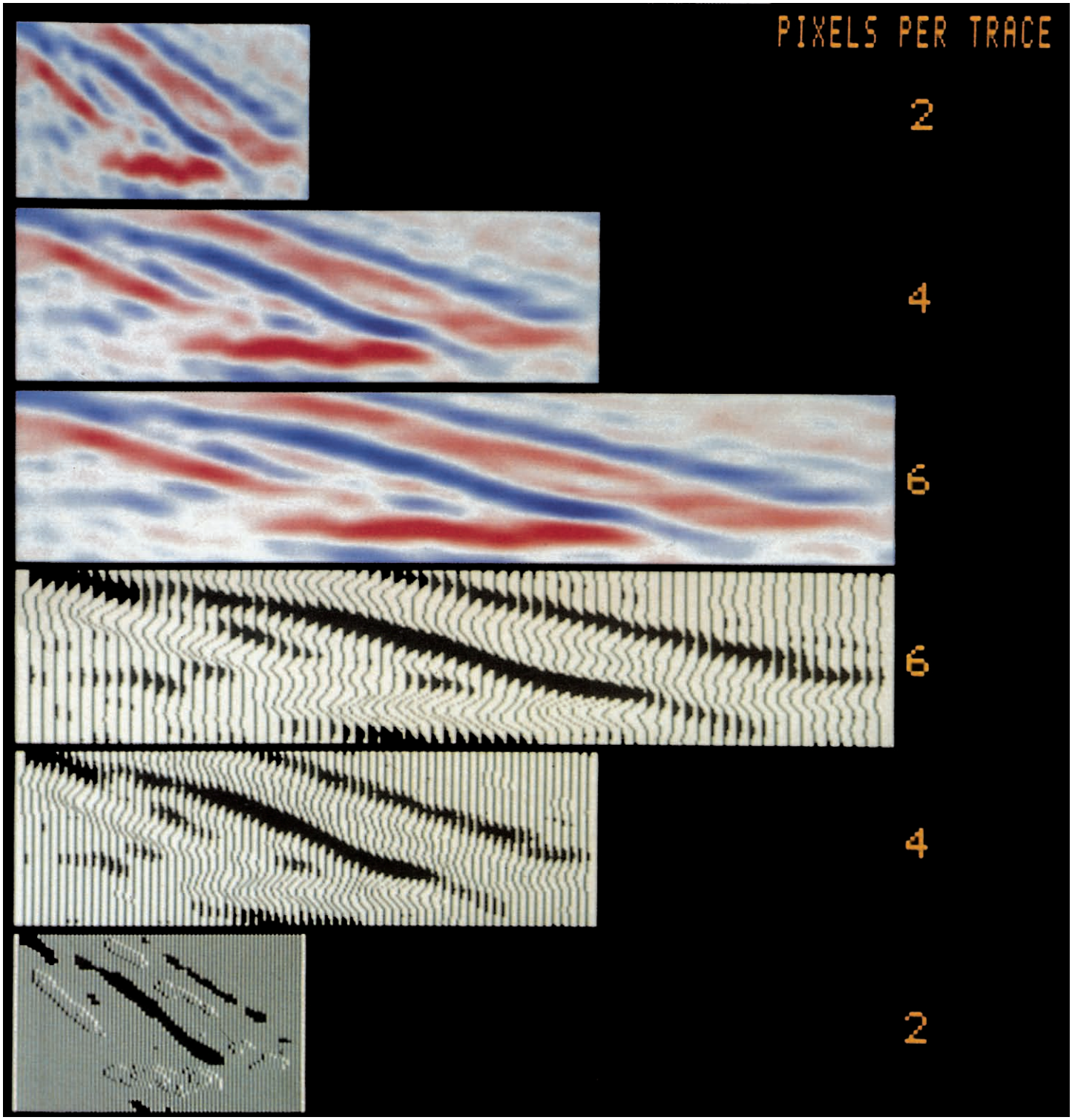

Fig. 2-9. Comparison of double-gradational blue and red with variable-area/wiggle trace display illustrating respectively independence and dependence of dynamic range on horizontal scale.

Downloaded 25 Jun 2012 to 95.28.162.50. Redistribution subject to SEG license or copyright; Terms of Use: http://segdl.org/

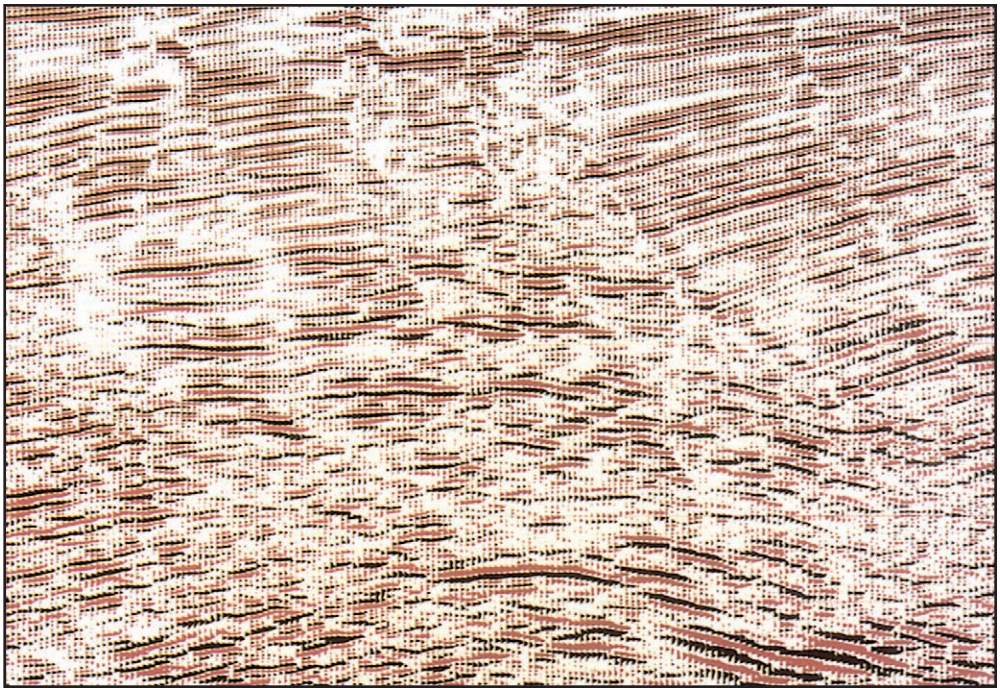

Fig. 2-10. Vertical section displayed in dual-polarity variable-area, showing fault definition. (Courtesy Texaco Trinidad Inc.)

Fig. 2-11. Enhanced dynamic range double-gradational color scheme where cyan has been added for the highest positive amplitudes and yellow has been added for the highest negative amplitudes. (Courtesy Chevron U.S.A. Inc.)

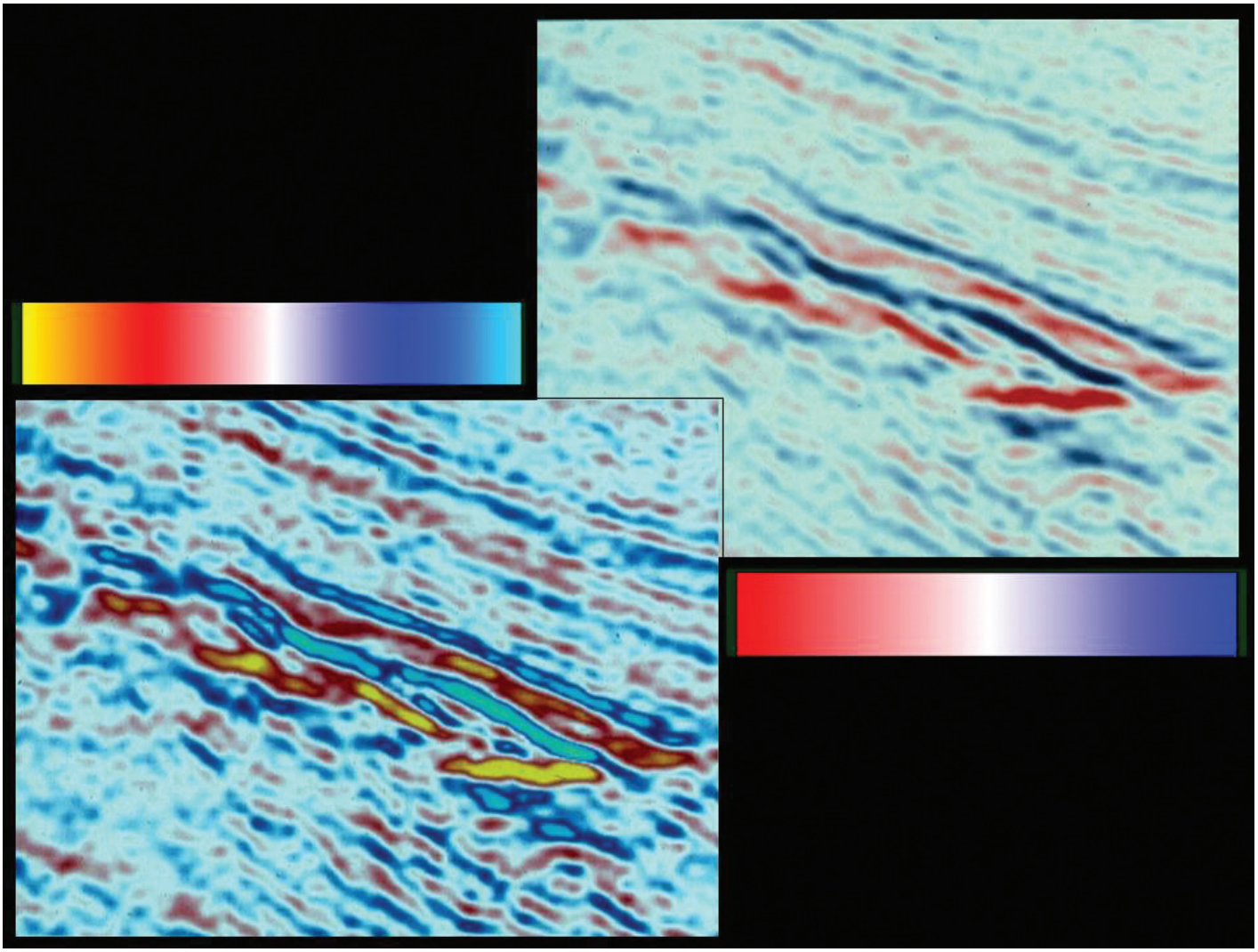

Downloaded 25 Jun 2012 to 95.28.162.50. Redistribution subject to SEG license or copyright; Terms of Use: http://segdl.org/

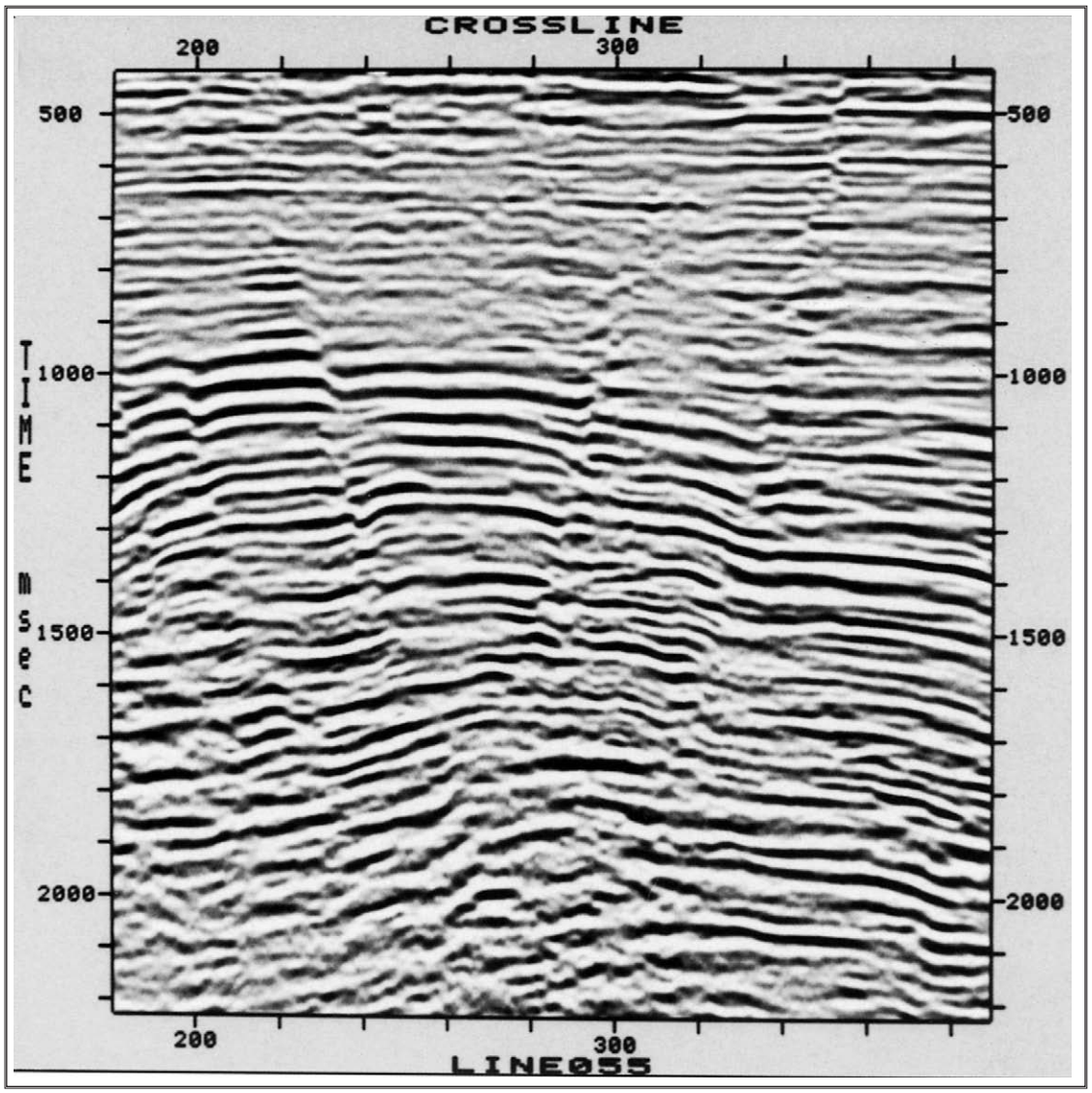

Fig. 2-12. Vertical section displayed with single-gradational gray scale in order to enhance low amplitude events. (Courtesy Texas Pacific Oil Company Inc.)

to the upper right to Line 122, Crossline 330. Is this a continuation of the channel system even though the amplitude is much reduced? We do not know the answer to this question, but we have been able to observe the continuity of this extensive curvilinear feature because of the use of gradational color.

Figure 2-16 shows the same section in contrasting colors and the detectability of the inferred channel is much reduced. In fact the eye tends to be drawn to the red and pink circular maxima at Crossline 250 between Lines 45 and 60 rather than the longer arcuate high amplitude trends. When applying a gradational color scheme to a horizon slice showing the spatial amplitude distribution of one trough, as in Figure 2-15, a gradational color scheme should be used to match the one-sided range of amplitudes. For the horizon slice for a peak (for example Figure 4-28) the same principle applies but the color scheme should be inverted. In order to aid the understanding of amplitudes, horizon slice colors should be matched to vertical section colors!

Downloaded 25 Jun 2012 to 95.28.162.50. Redistribution subject to SEG license or copyright; Terms of Use: http://segdl.org/

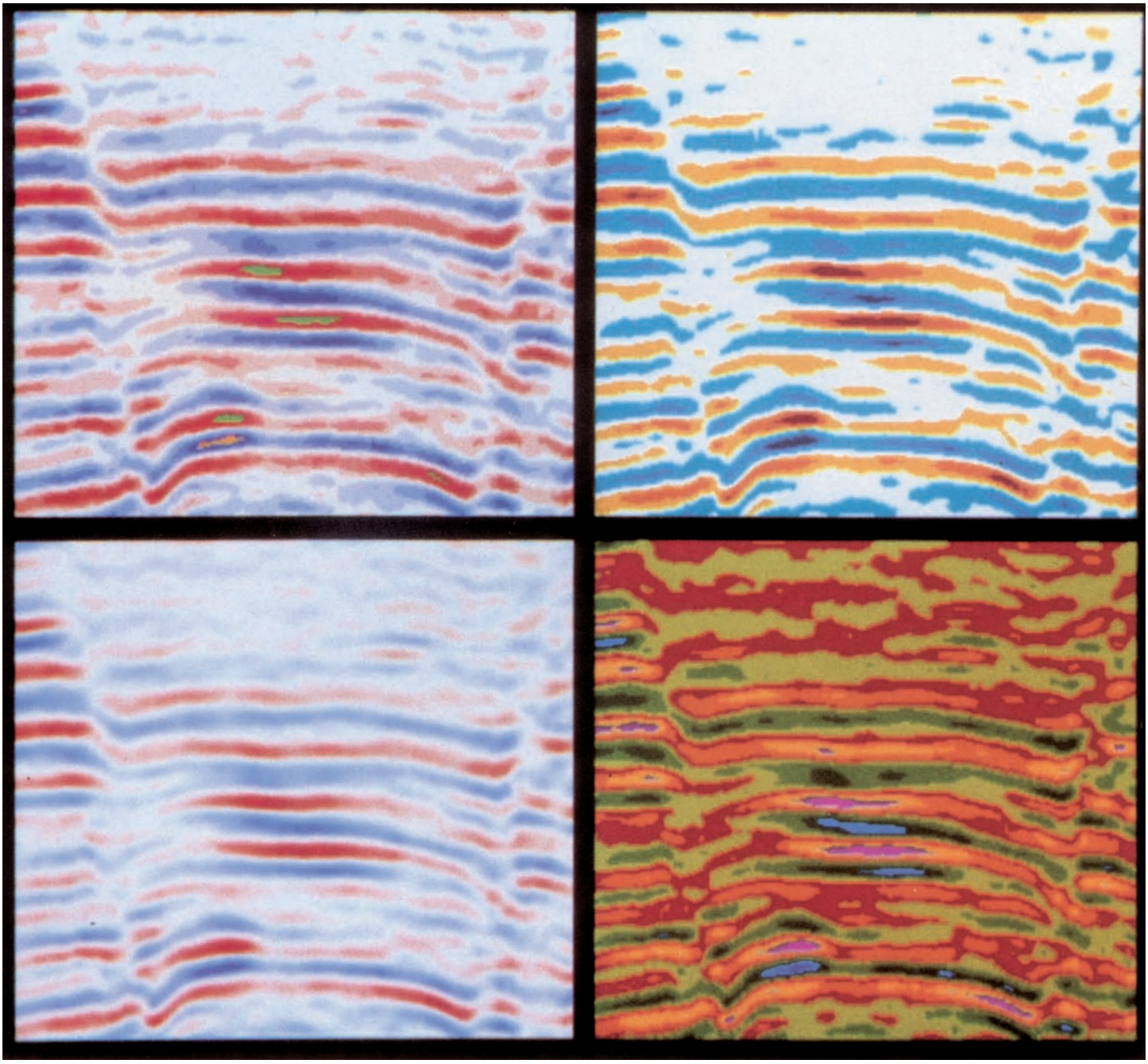

Fig. 2-13. Four different color schemes applied to the same vertical section segment. (Courtesy Texas Pacific Oil Company Inc.)

Downloaded 25 Jun 2012 to 95.28.162.50. Redistribution subject to SEG license or copyright; Terms of Use: http://segdl.org/

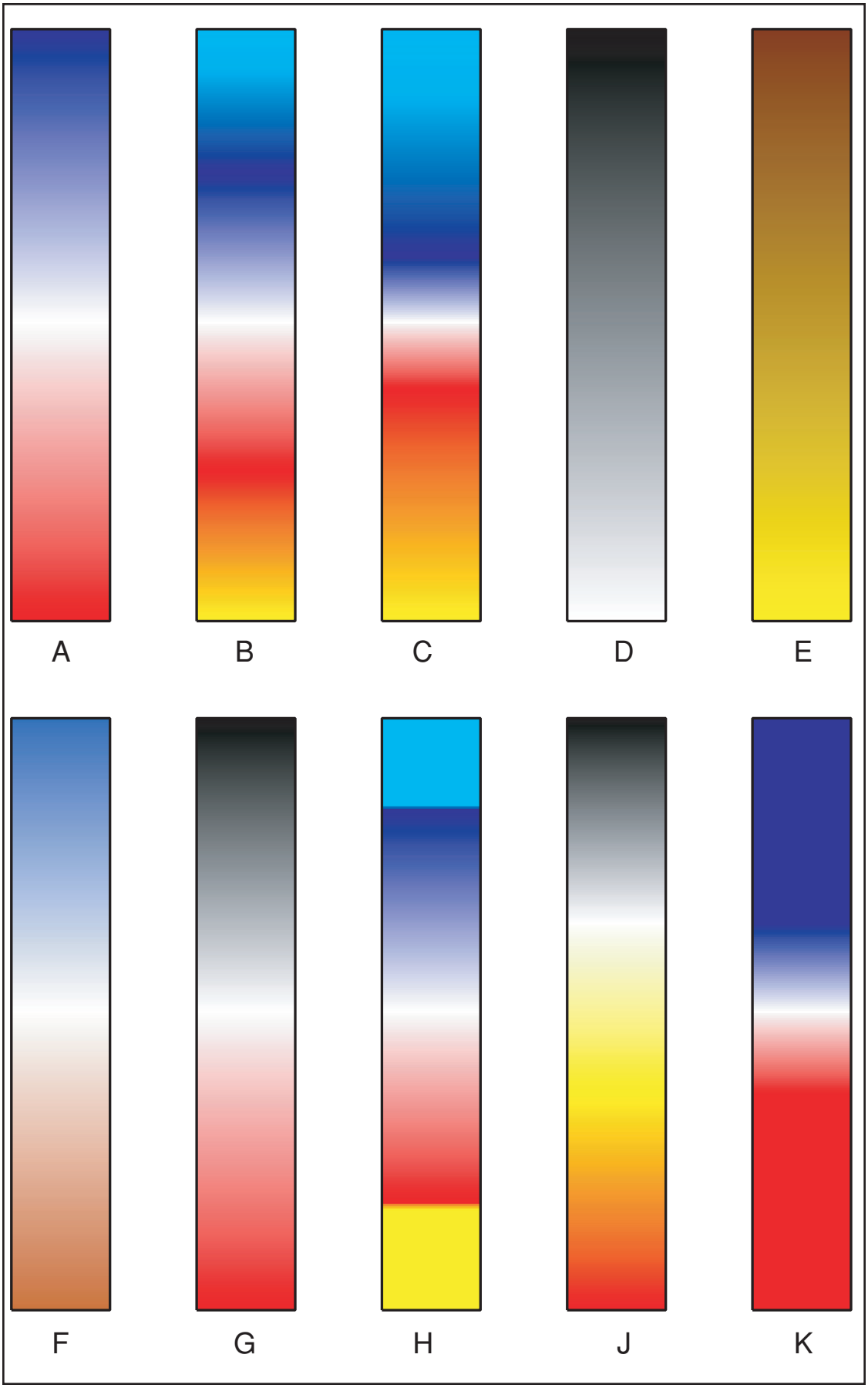

Fig. 2-14. Multiple color schemes, some good and some bad, for seismic data.

Downloaded 25 Jun 2012 to 95.28.162.50. Redistribution subject to SEG license or copyright; Terms of Use: http://segdl.org/

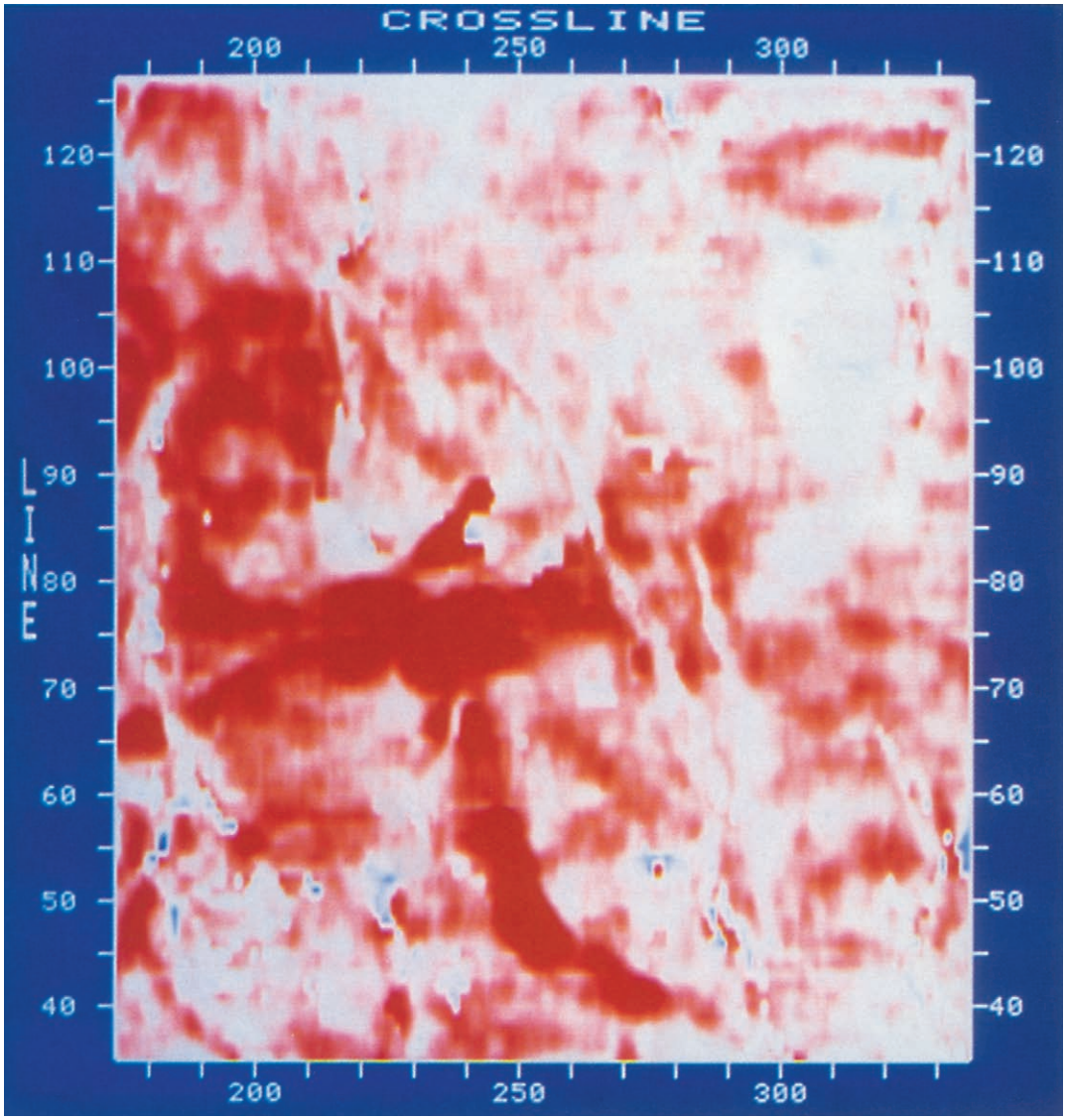

Fig. 2-15. Horizon slice showing an inferred channel system displayed with a gradational color scheme. (Courtesy Texas Pacific Oil Company Inc.)

Assessment of Phase and Polarity

Most interpreters today prefer zero-phase data. The reasons they give to support this preference include the following:

(1) the wavelet is symmetrical with the majority of the energy being concentrated in the central lobe;

(2) this wavelet shape minimizes ambiguity in associating observed waveforms with subsurface interfaces;

(3) a horizon track drawn at the center of the wavelet coincides in time with the travel time to the subsurface interface causing the reflection;

(4) the maximum amplitude occurs at the center of the waveform and thus coincides with the time horizon; and,

(5) the resolution is better than for other wavelets with the same frequency content.

Much data processing research has been devoted to wavelet processing, which can be defined as the replacement of the source wavelet, the receiver response, and the filtering effects of the earth by a wavelet of known and desirable characteristics. Wood (1982) outlined the principles of wavelet processing and the properties of zero-phase wavelets, and Kallweit and Wood (1982) addressed the issues of resolution. Some relevant processing issues are discussed in Appendix A. Today's interpreter, particularly one who has a stratigraphic objective, wants to be able to assess whether the data provided have been properly deconvolved to a zero-phase condition. This can be done in many ways. Cross-correlation of a synthetic seismogram with the seismic trace at

Downloaded 25 Jun 2012 to 95.28.162.50. Redistribution subject to SEG license or copyright; Terms of Use: http://segdl.org/

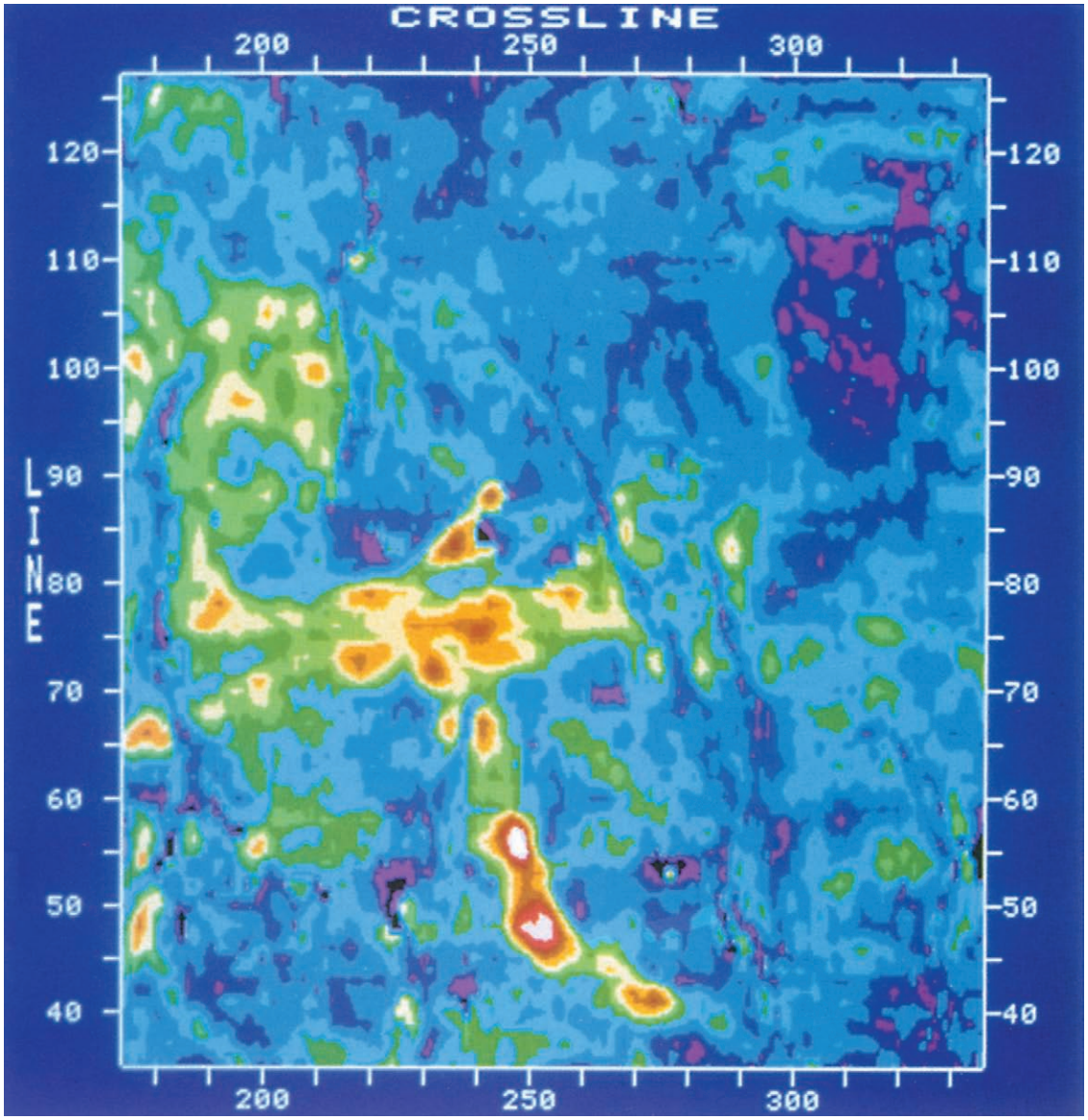

Fig. 2-16. Same horizon slice as in Figure 2-15 displayed with a contrasting color scheme, which reduces visibility of the channel system. (Courtesy Texas Pacific Oil Company Inc.)

the well location is an analytical technique. So is the extraction of a wavelet from the data and the study of its shape. But whatever is done, today's interpreter needs an increased awareness of zero-phaseness and the ability to recognize it, or other phases, in his or her data.

Understanding wavelet phase gives increased importance to the understanding of polarity. For processed seismic data, polarity convention is confused, and in addition color display introduces the need for conventions in color usage. In presenting an interpretation using colored sections, the critical issue is to communicate the polarity and color usage for that data. It is less important what conventions are used because peaks and troughs are equally visible in color display. The author has developed a subjective appraisal of the polarity and color conventions in use today and these are diagrammed in Figure 2-17. American polarity is preferred in the Americas but is by no means universal in this region. European polarity is preferred in Europe and the rest of the world but again is by no means universal there. If we are diligent in always using blue for positive amplitude and red for negative amplitude, then only two choices remain. Are the data American or European polarity? This becomes a very important, and hopefully straightforward, determination for today's interpreter.

Downloaded 25 Jun 2012 to 95.28.162.50. Redistribution subject to SEG license or copyright; Terms of Use: http://segdl.org/

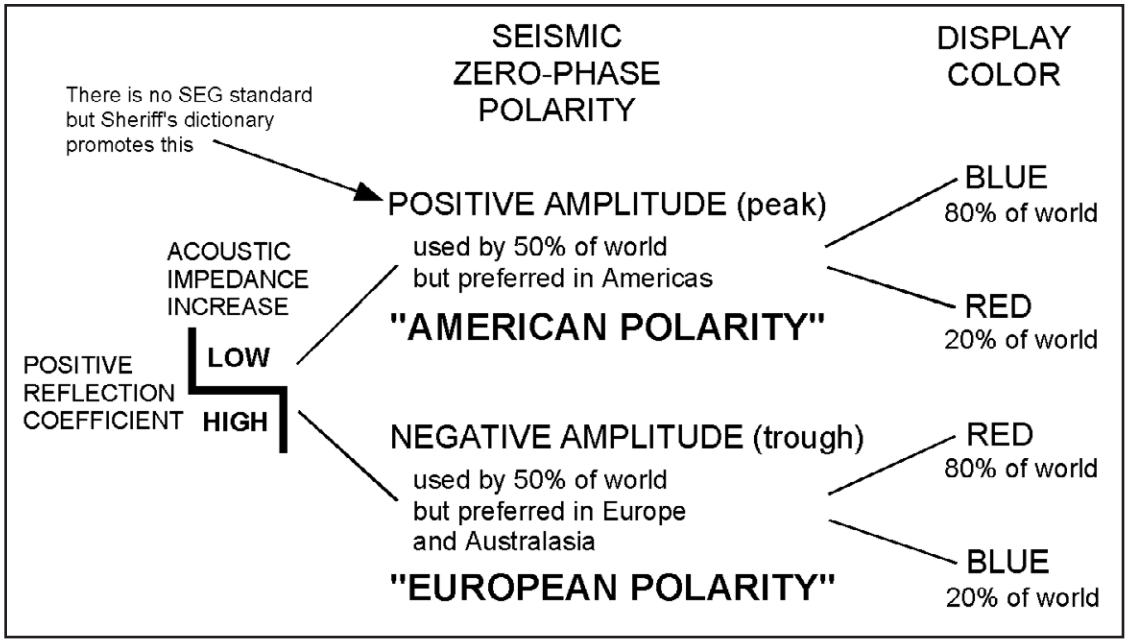

Fig. 2-17. Polarity and color conventions, and definition of American and European polarity.

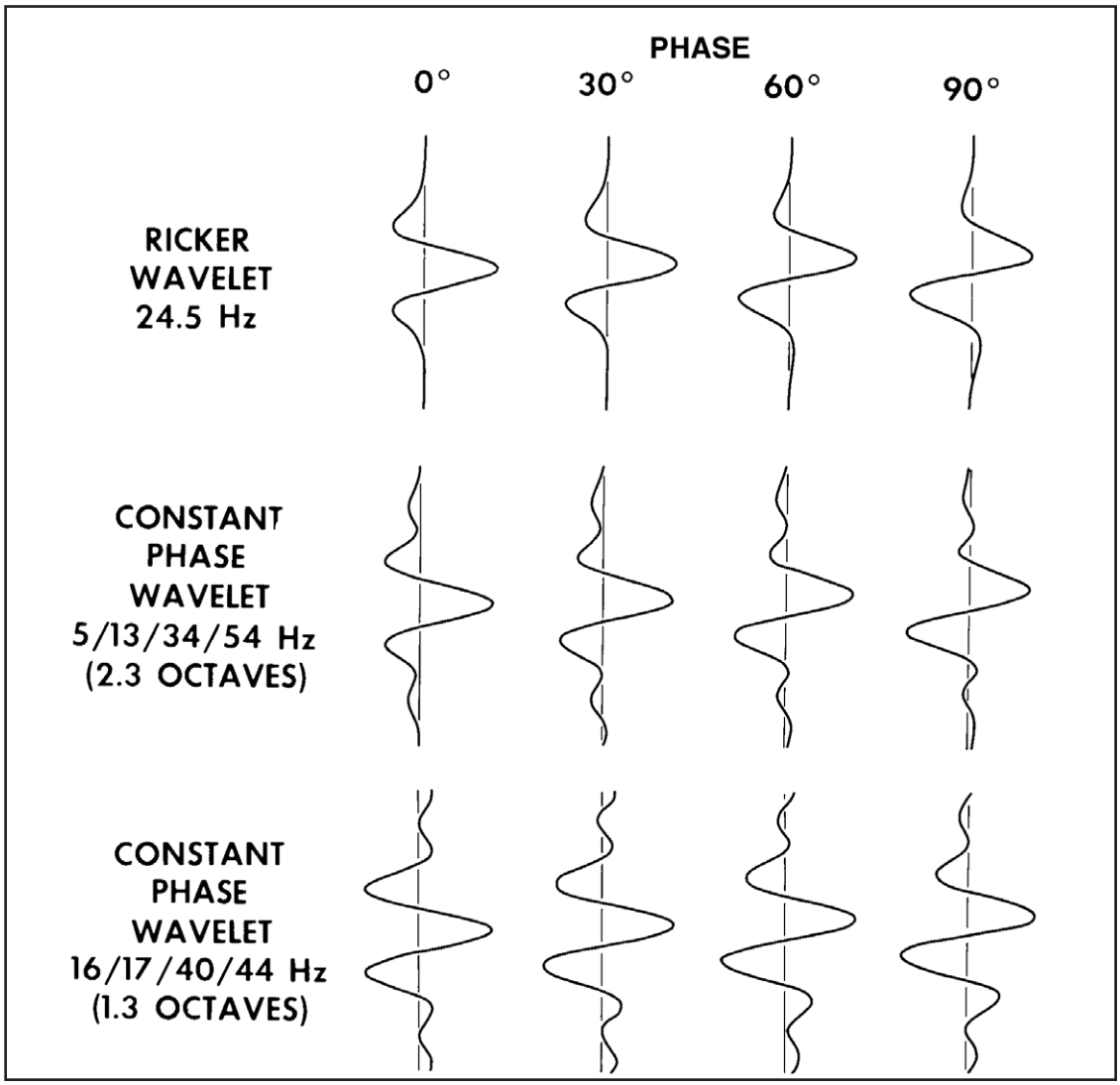

Fig. 2-18. Effect of phase shifting constant-phase wavelets.

Downloaded 25 Jun 2012 to 95.28.162.50. Redistribution subject to SEG license or copyright; Terms of Use: http://segdl.org/

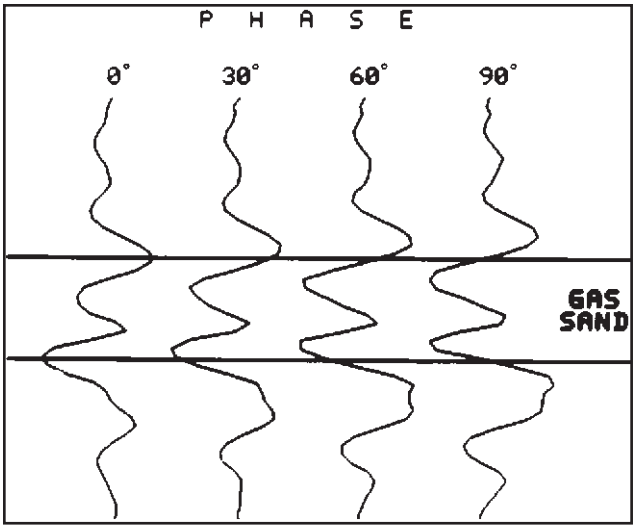

Fig. 2-19. Effect of phase shifting a real data trace showing reflections from the top and base of a gas sand. (Courtesy Chevron U.S.A. Inc.)

Fig. 2-20. Bright reflections from the top and base of a gas sand with constant phase shifts applied. (Courtesy Chevron U.S.A. Inc.)

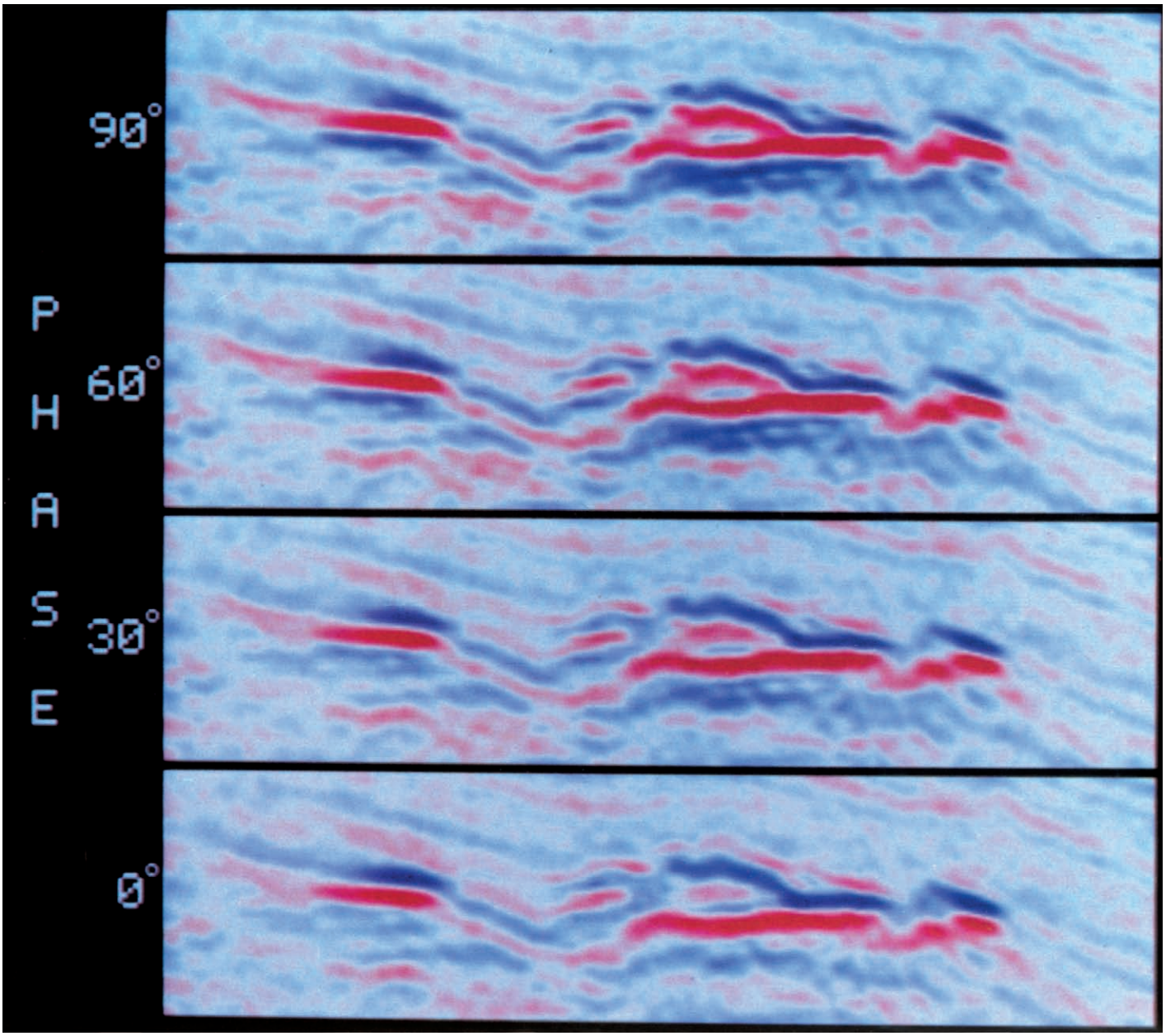

Downloaded 25 Jun 2012 to 95.28.162.50. Redistribution subject to SEG license or copyright; Terms of Use: http://segdl.org/

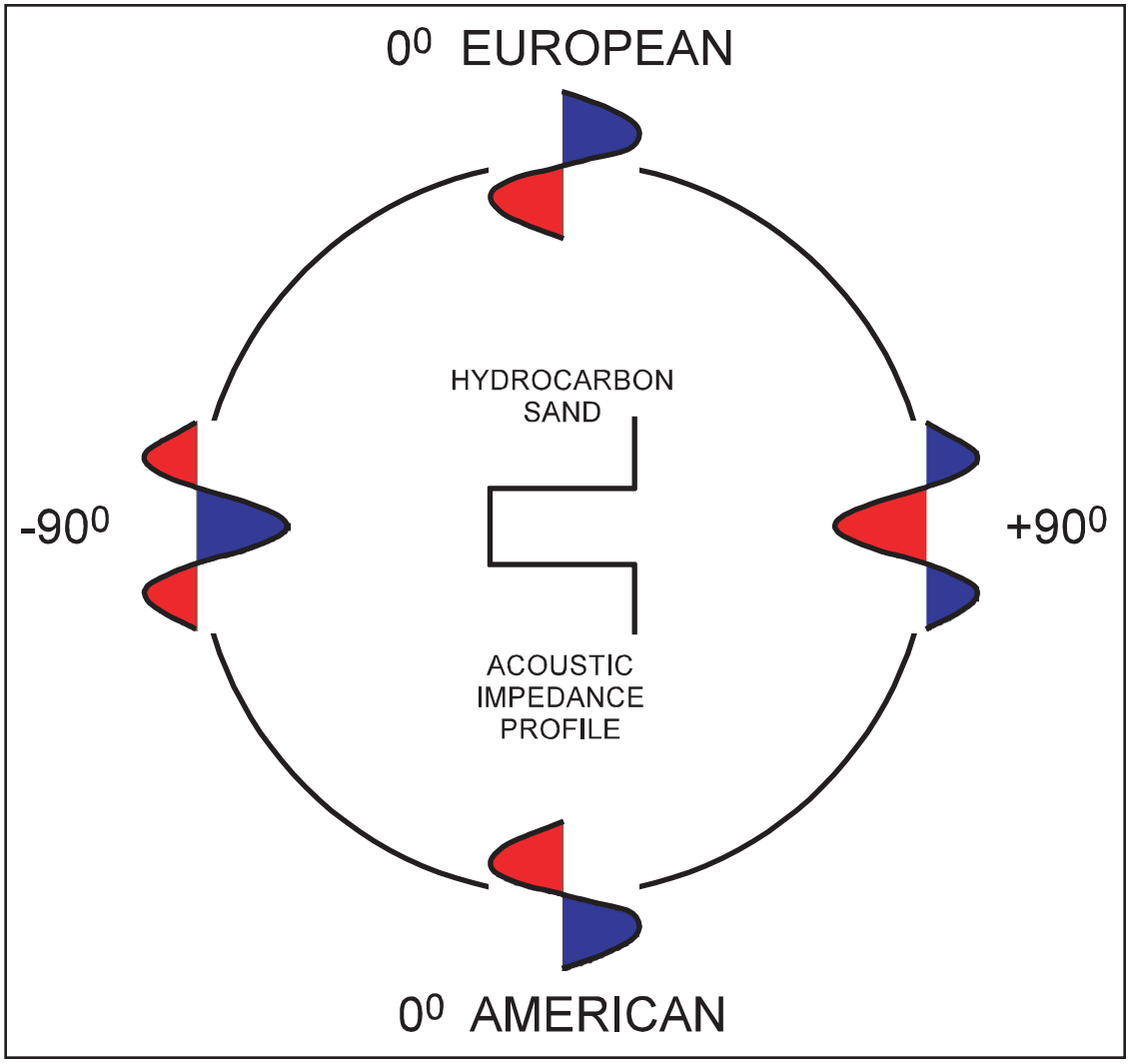

Fig. 2-21. The principal phase and polarity conditions that we should look for in our data. The responses illustrated are for a low-impedance interval with significant contrasts at top and base, such as a hydrocarbon sand.

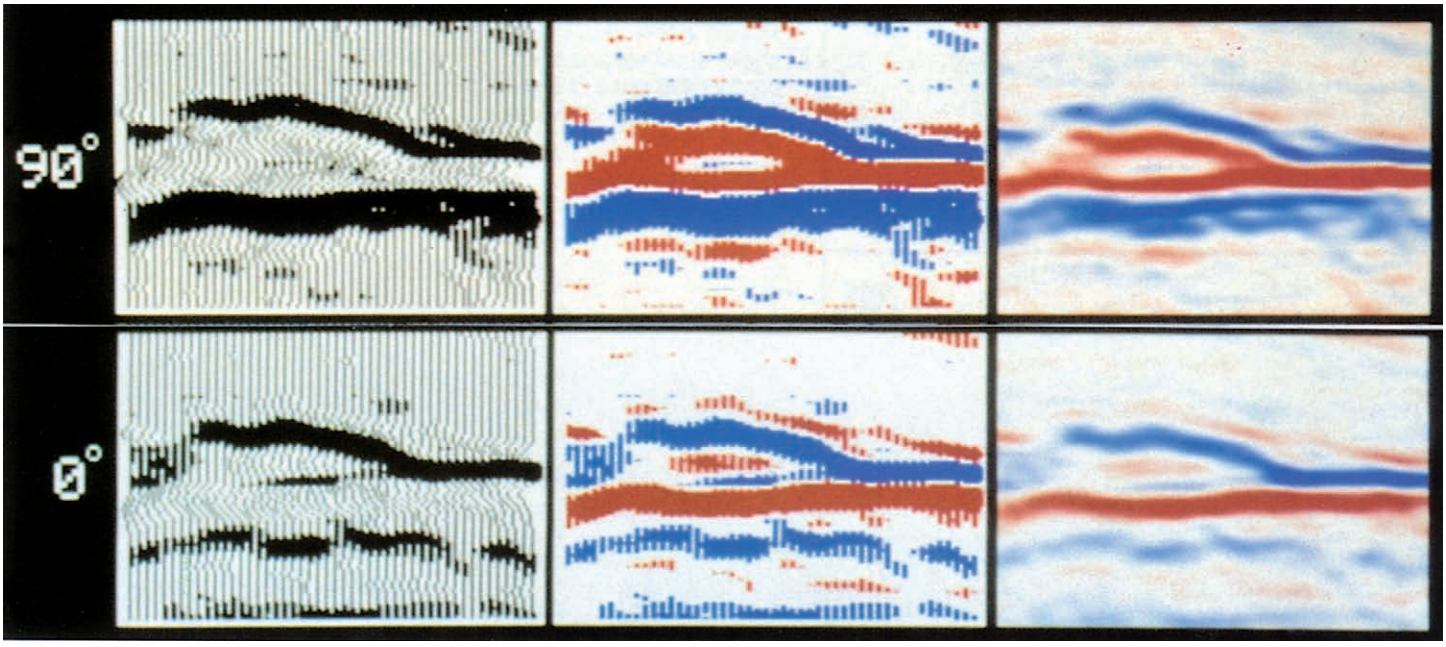

Fig. 2-22. Comparison between variable-area/ wiggle trace, dual-polarity variable area, and gradational color for the interpretive assessment of data phase. (Courtesy Chevron U.S.A. Inc.)

Downloaded 25 Jun 2012 to 95.28.162.50. Redistribution subject to SEG license or copyright; Terms of Use: http://segdl.org/

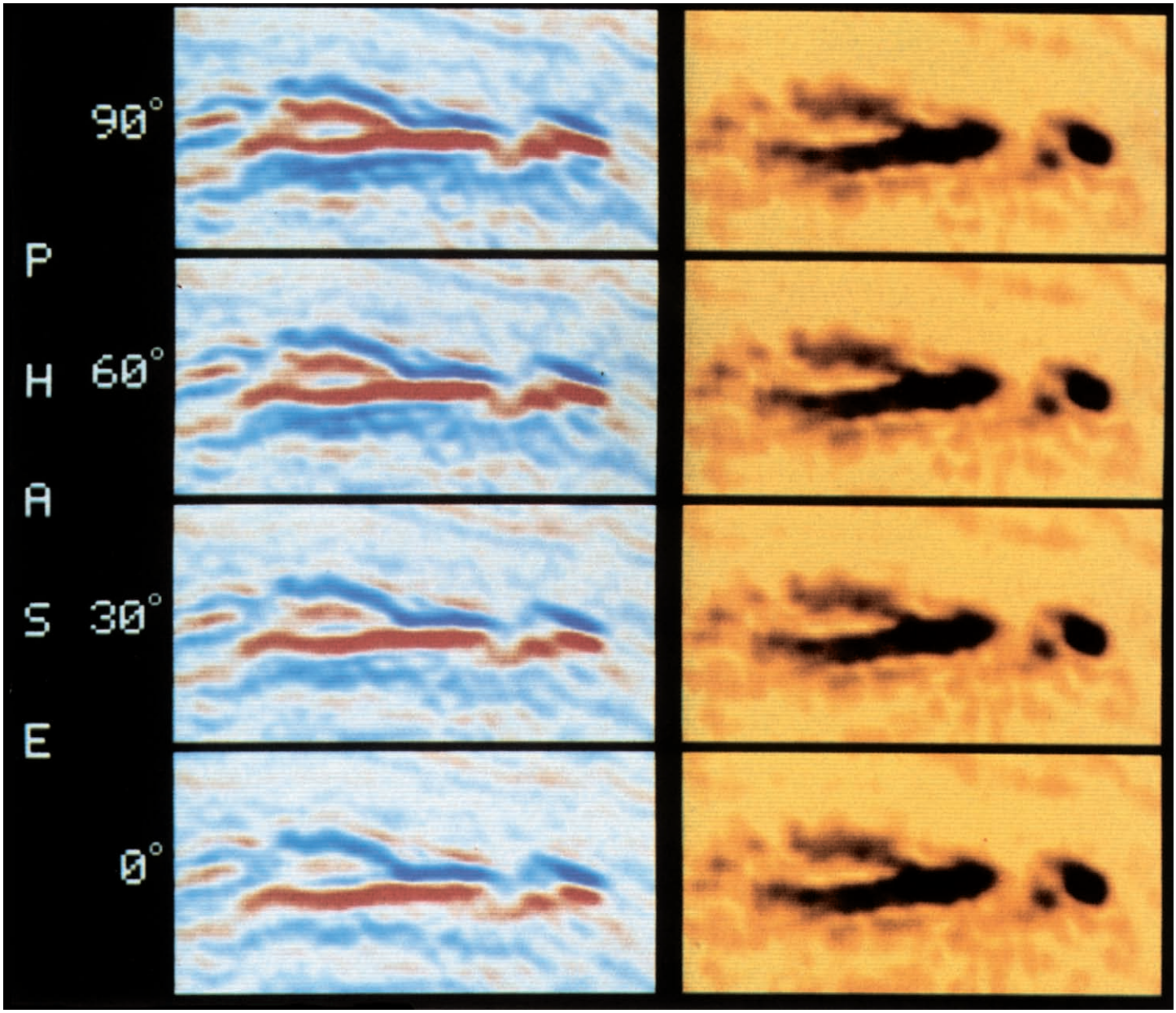

Fig. 2-23. Use of reflection strength or envelope amplitude to obscure the effects of phase distortion. (Courtesy Chevron U.S.A. Inc.)

The interpretive assessment of zero-phaseness requires high signal-to-noise ratio reflections and maximum dynamic range color display. But first zero-phaseness will be considered on model data. Figure 2-18 shows three zero-phase wavelets and their equivalents shifted by 30, 60, and 90 degrees. The first is a Ricker wavelet, the second is derived from a bandpass filter of 2.3 octaves with gentle slopes, and the third is derived from a bandpass filter of 1.3 octaves with steep slopes. The common property of these three wavelets is that the separation of central peak and first side lobe is the same for each — 16 ms. The Ricker wavelet has no side lobes beyond the first. The 2.3 octave wavelet is a good wavelet extracted from actual processed data and has low side lobes. The 1.3 octave wavelet is a poor wavelet with relatively high side lobes.

The visual assessment of zero-phaseness amounts to a visual assessment of wavelet symmetry. In these model examples 30° of distortion is visible for all the wavelets but the higher side lobe levels of the narrower band wavelet make the distortion less pronounced. For the larger distortions, for example at 60°, the central peak and the larger side lobe are more easily confused for the narrower band wavelet, so in practice it may be difficult to decide whether the peak or the trough is the principal extremum.

Downloaded 25 Jun 2012 to 95.28.162.50. Redistribution subject to SEG license or copyright; Terms of Use: http://segdl.org/

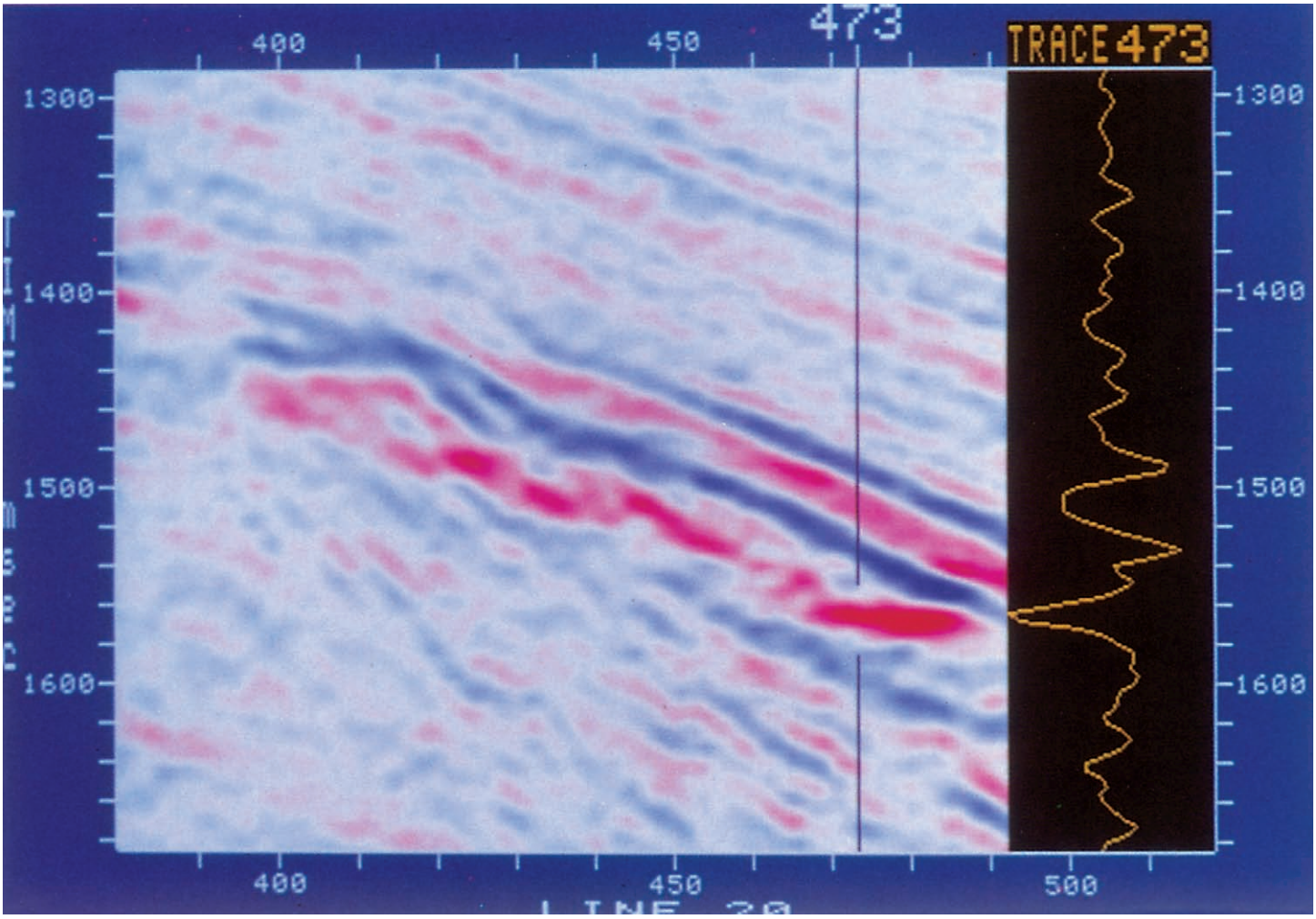

Fig. 2-24. Flat-spot reflection displaying zero-phaseness, visible in gradational red for many traces and in wiggle format for one trace. (Courtesy Chevron U.S.A. Inc.)

At a distortion of 90° the time horizon lies at the zero crossing between the largest amplitude peak and trough, and these are of equal size.

Figure 2-19 is a single trace example from real data where there was a known low-impedance gas sand. The top of the low-impedance zone is a peak and the base a trough (European polarity). The trace labelled 0° shows peak and trough each symmetrically placed over their corresponding interfaces. The phase distortions are again evident when presented in this way.

In practice, interpreters must assess zero-phaseness on a section containing many traces in case one trace is unrepresentative. We select a high amplitude reflection, which, on the basis of a simple model, can be related to a single interface. The interpreter can then assume that the interference of events from adjacent parallel interfaces, multiples or noise is small. Figure 2-20 illustrates a bright spot from a gas reservoir where it is assumed that the above conditions hold except that there are two interfaces at the top and at the base of the reservoir. In the panel labelled 0° there is one blue event from the top of the reservoir and one red event from its base, and they have approximately the same amplitude. Side lobes are low and symmetrical as far as can be determined. This is the signature expected for the zero-phase response of a gas sand.

For the 90° case in Figure 2-20 the top of the gas sand has a signature of blue-over-red and the base one of red-over-blue. This confirms the modeling illustrated in Figure 2-18 and certainly shows a more complex character than the zero-phase section. The intermediate levels of phase distortion show the progression from the 0° to 90° condition. Observation of these more complicated phase characteristics can be followed by experimental phase rotation of the data.

Downloaded 25 Jun 2012 to 95.28.162.50. Redistribution subject to SEG license or copyright; Terms of Use: http://segdl.org/

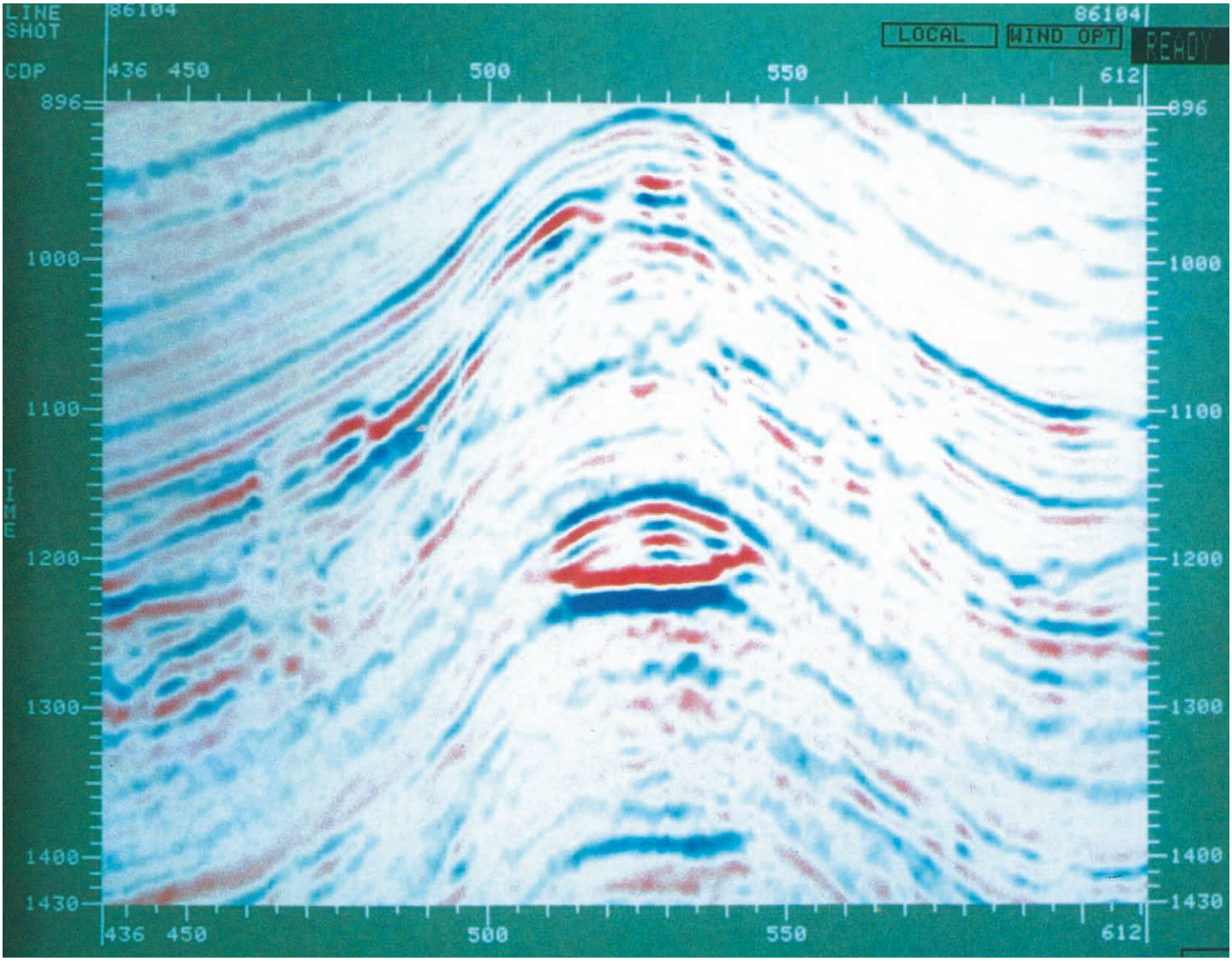

Fig. 2-25. Gulf of Mexico flat spot displaying a phase of approximately 90°. (Courtesy Geophysical Service Inc.)

The most common phase distortion confronting an interpreter is 90°, but it is also common to find the polarity opposite to what is normal for the region (European polarity data in America, for example). Figure 2-21 shows the four principal phase and polarity conditions to which the interpreter should be alert. They are illustrated for a low-impedance interval, such as a gas sand, and thus they correspond to the real data of Figure 2-20. All of these four conditions exist in all regions of the world. More detailed instructions for the interpretive assessment of phase and polarity appear in Appendix C.

The interpreter's ability to make this kind of assessment of phase and polarity depends critically on the display used. Figure 2-22 presents the same data panel in the same phase conditions for three different modes of display. Variable area/wiggle trace demonstrates how the visual imbalance between peaks and troughs makes the assessment of relative amplitudes impossible. Dual polarity variable area has corrected the visual imbalance but demonstrates the limited dynamic range of variable area. Gradational color demonstrates the visual balance between peaks and troughs and also the improved dynamic range. Relative amplitudes of peaks, troughs and side lobes can now be assessed with maximum available clarity for fairly high trace density. One disadvantage, however, of gradational color display is the stringency imposed on the reproduction process. The illustration that you, the reader, are studying is of reduced

Downloaded 25 Jun 2012 to 95.28.162.50. Redistribution subject to SEG license or copyright; Terms of Use: http://segdl.org/

Fig. 2-27. Gulf of Mexico shallow gas reflections showing a phase of approximately 90°. (Courtesy Mobil Exploration & Producing U.S. Inc.)

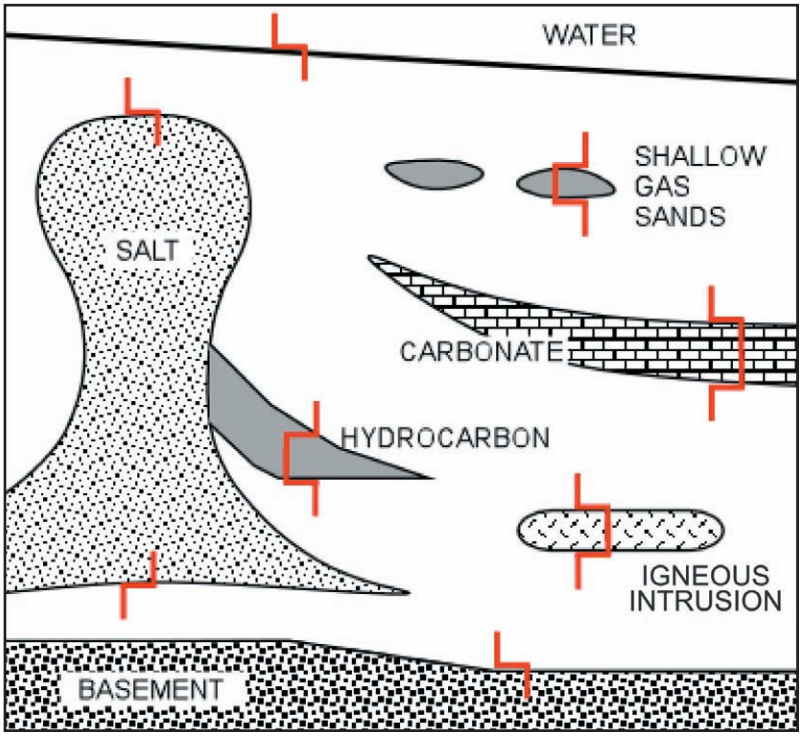

Fig. 2-26. Subsurface features which can generate sufficiently high-amplitude reflections to be useful for interpretive assessment of phase and polarity. Probable impedance profiles are drawn.

Downloaded 25 Jun 2012 to 95.28.162.50. Redistribution subject to SEG license or copyright; Terms of Use: http://segdl.org/

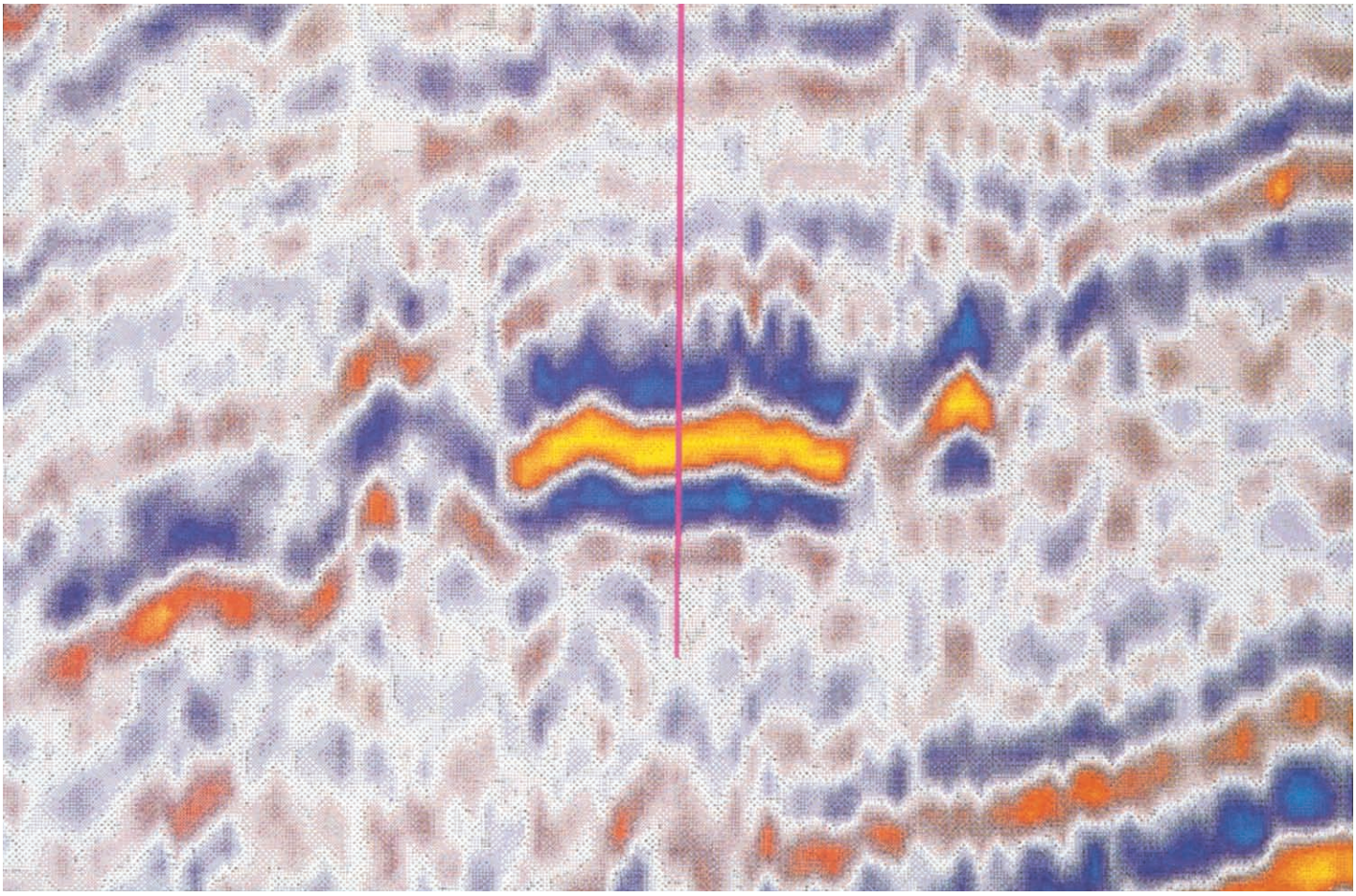

Fig. 2-28. Gulf of Mexico Miocene gas reservoir reflections showing a phase of approximately 90°. (Courtesy Conoco Inc. and Digicon Geophysical Corp.)

quality compared to the screen image of the color monitor on which the original assessment was made.

If the phase of the data is unknown and cannot be assessed, reflection strength (also known as envelope amplitude; Taner and Sheriff, 1977) provides a display in which amplitude can be studied independent of phase. Figure 2-23 shows identical reflection strength sections corresponding to the four regular amplitude sections with different phases.

Any high-amplitude reflection which can be assumed to originate from a single interface is usable for assessing zero-phaseness when displayed in color. A fluid contact reflection, or flat spot, is normally an excellent candidate. If the structural horizons have moderate dip and the reservoir is fairly thick, the flat spot reflection will be well resolved and structurally unconformable. (The characteristics of fluid contact and other reservoir reflections are discussed more extensively in Chapter 5.) The flat spot in Figure 2-24 shows clearly one high-amplitude symmetrical red trough, indicating that the data are zero phase. A fluid contact is always an increase in impedance, so the observation that this flat spot is red indicates that the data are European polarity. The flat spot in Figure 2-25 shows a high-amplitude red-over-blue character, indicating an approximately 90° phase condition.

Figure 2-26 illustrates diagrammatically the sources of seismic reflections that often have a sufficient signal-to-noise ratio to be useful for interpretive phase assessment. Top of salt is good but may not be smooth enough and may be a gradational contact. The water bottom should be observed but it is often quite unreliable, presumably because it is not a single interface. Hydrocarbon reservoirs, shallow gas, and igneous intrusions are all excellent. Reflection terminations and unconformability are always helpful in isolating the character from the geologic feature under study.

Downloaded 25 Jun 2012 to 95.28.162.50. Redistribution subject to SEG license or copyright; Terms of Use: http://segdl.org/

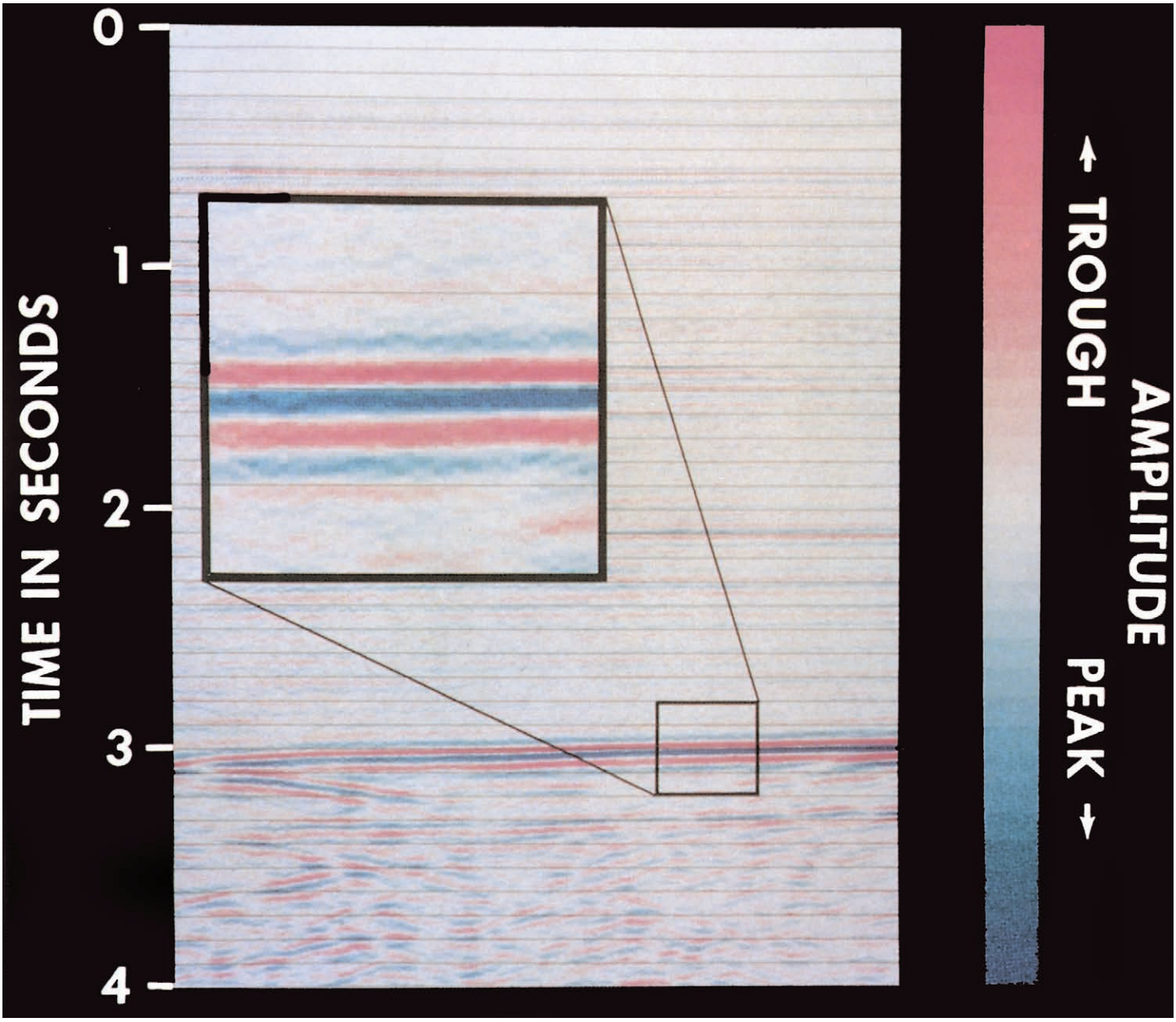

Fig. 2-29. Basement reflection displaying zero-phaseness. The central lobe is blue and the basement is hard; thus the data are American polarity. (Courtesy Geophysical Service Inc.)

Downloaded 25 Jun 2012 to 95.28.162.50. Redistribution subject to SEG license or copyright; Terms of Use: http://segdl.org/

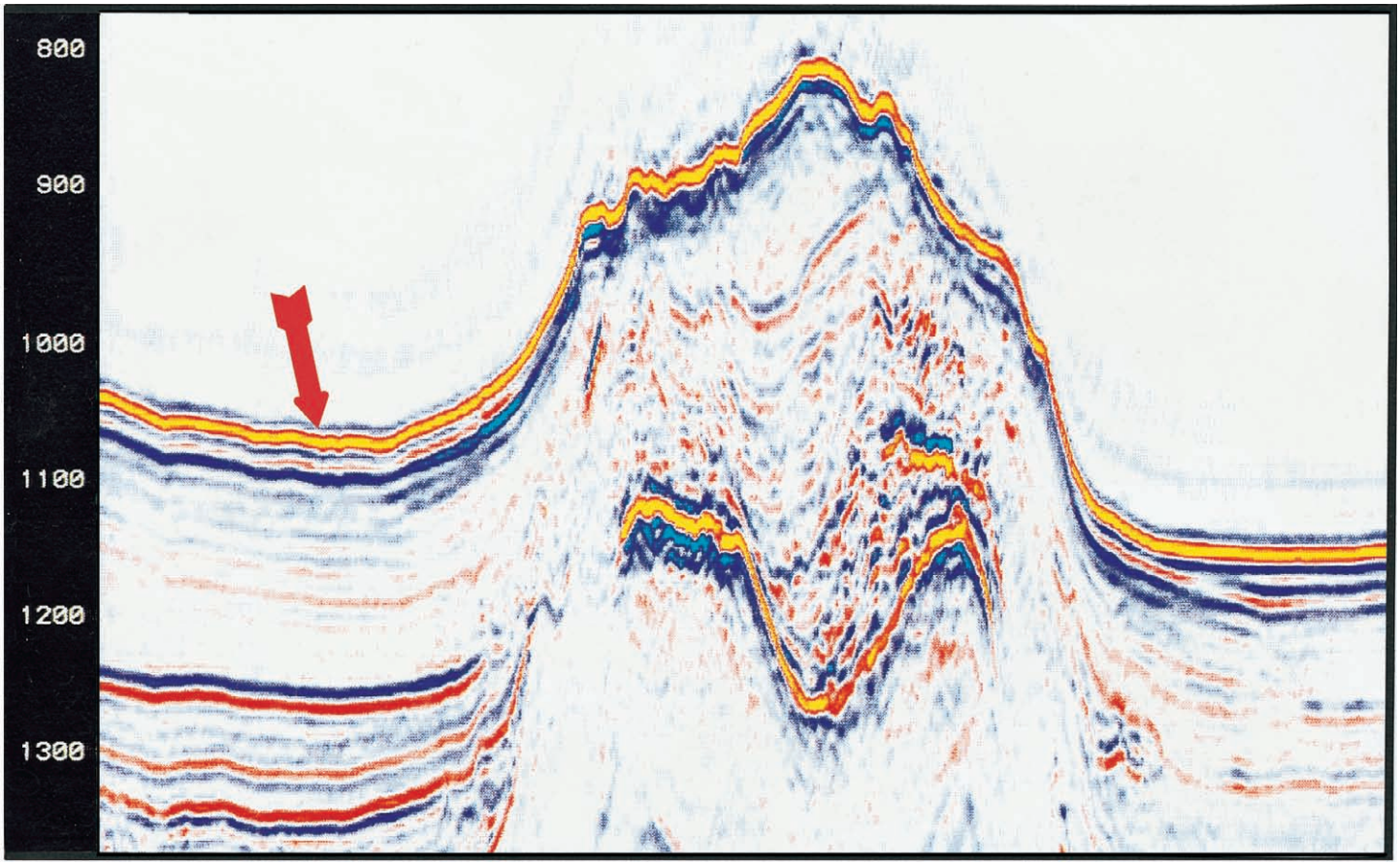

Fig. 2-30. Water-bottom reflection in deep water displaying zero-phaseness and European polarity. (Courtesy Conoco Inc.)

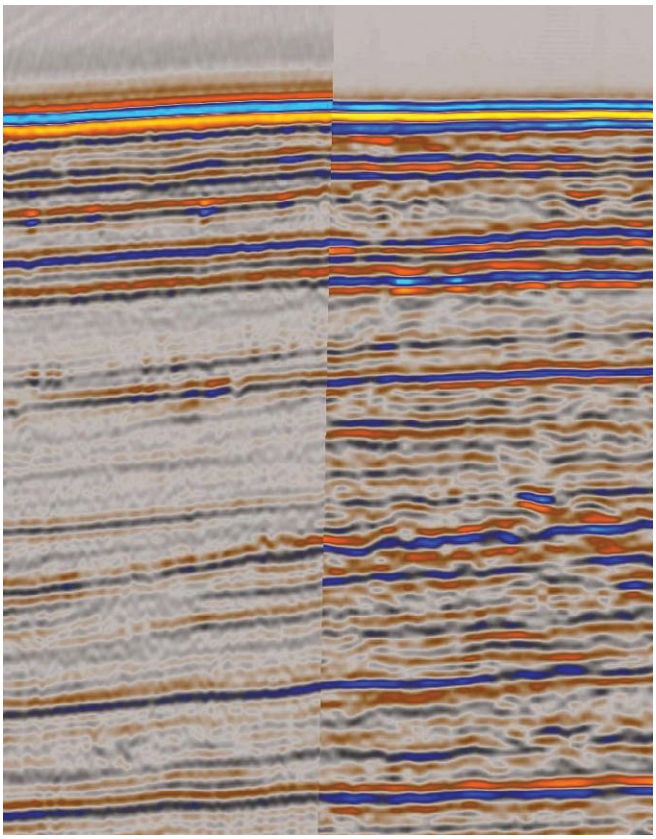

Fig. 2-31. Two data sets tie fairly well and are thus the same phase and polarity. But note that the apparent water-bottom reflections are very different. (Courtesy StatoilHydro and Landmark.)

Downloaded 25 Jun 2012 to 95.28.162.50. Redistribution subject to SEG license or copyright; Terms of Use: http://segdl.org/

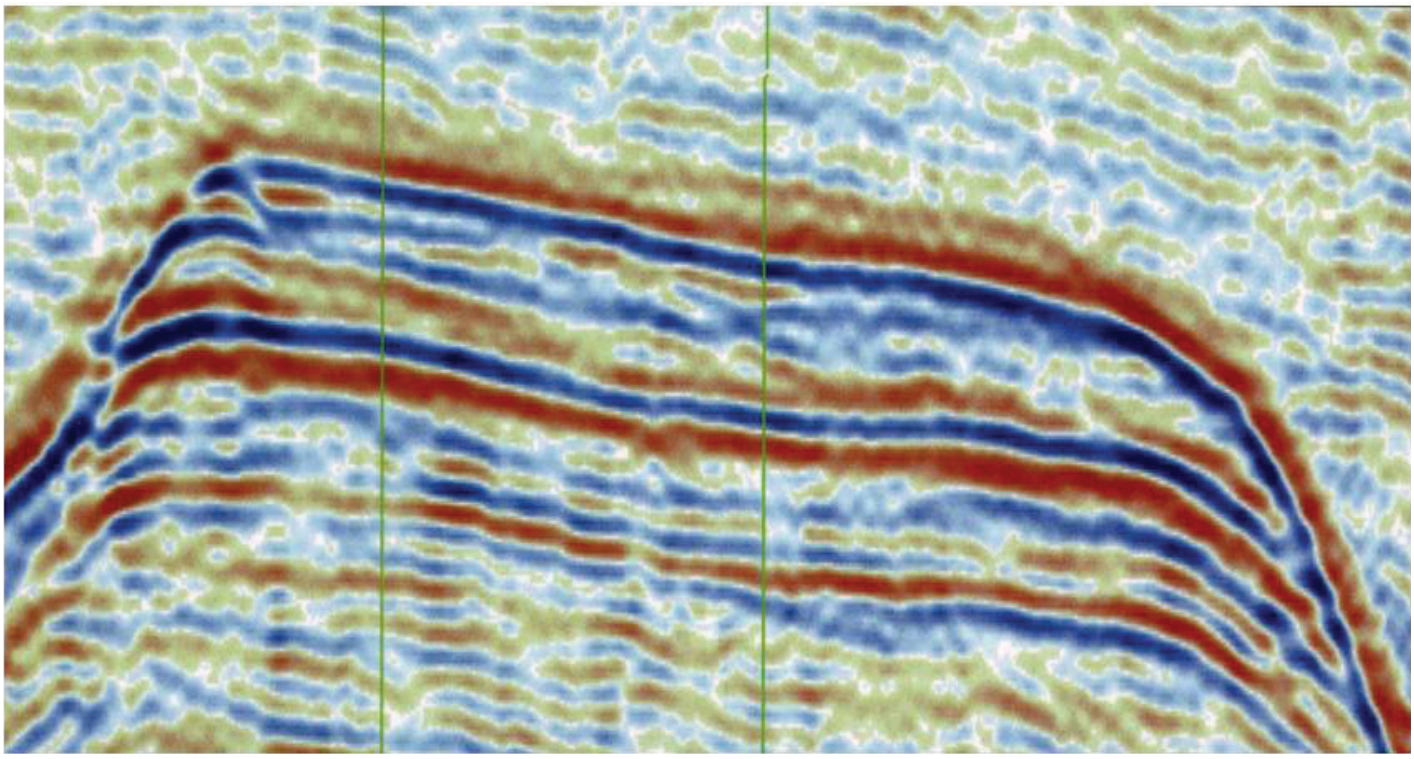

Fig. 2-32. Carbonate buildup from Malaysia. Top reflection indicates the character of 90° phase. Note that the character remains the same on the unconformable flank (from Masaferro et al., 2004).

Figure 2-27 shows reflections from the top and base of shallow gas. Both are double events indicating a phase of 90°. Figure 2-28 shows strong reflections from a Miocene gas reservoir. Here the reservoir is thin so that the reflection from the top and the reflection from the bottom overlap each other, thus giving reinforcement to the red/yellow in the center. This again is an indication of 90° phase data, a remarkably common phenomenon.

Figure 2-29 shows an outstanding basement reflection which is probably from a single subsurface interface. The waveform of the reflection is clear, almost symmetrical, and spatially consistent. This indicates that the data are close to zero phase, at least around the time of 3 seconds (s).

Figure 2-30 shows a strong water-bottom reflection in deep water in the Gulf of Mexico. At the position of the red arrow the character is symmetrical, indicating zero phase. However, on top of the seamount the assessment is ambiguous because a blue reflection appears to be part of the water-bottom reflection. As the sediments thicken off the seamount, it becomes clear that the blue reflection is in fact not associated with the water bottom but just happened to be within a quarter-wavelength of it on top of the seamount. Experience shows that water-bottom reflections are particularly unreliable in assessing phase and polarity because of the difficulty in isolating the exact seismic character of the water bottom. This unreliability is well illustrated in Figure 2-31. Two data sets offshore Norway intersect and tie fairly well, indicating that they have the same phase and polarity. However, the apparent water-bottom reflections are very different (for unknown reasons) and thus appear to be indicating different phases. Probable shallow gas on both sections suggests that both data sets are zero-phase American polarity.

Figure 2-32 shows a Malaysian carbonate buildup with a strong reflection at the clastic-carbonate interface. The character of this reflection is double-lobed red-blue, indicating that the data are 90° phase. Note that on the flank of the structure, where there is marked unconformability, the character remains the same. This observation adds extra weight to the phase assessment. Figure 2-33 shows an igneous intrusion in Gulf of Mexico sediments. The display on the left gives a view of the whole body, which helps to confirm that it is a localized intrusive rock. The character seen on the

Downloaded 25 Jun 2012 to 95.28.162.50. Redistribution subject to SEG license or copyright; Terms of Use: http://segdl.org/

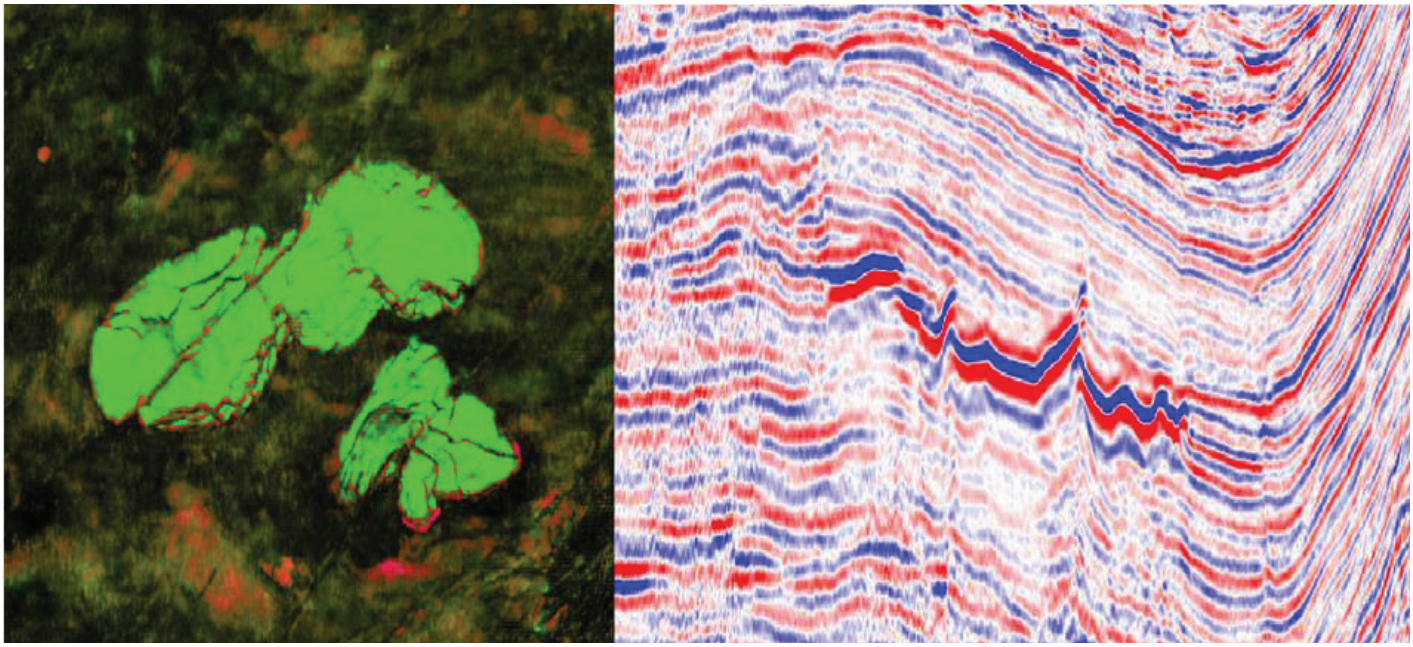

Fig. 2-33. Igneous intrusion from Gulf of Mexico. Voxel view on left helps confirm identity of body. Section on right indicates data to be zero-phase American polarity. (Courtesy Pemex.)

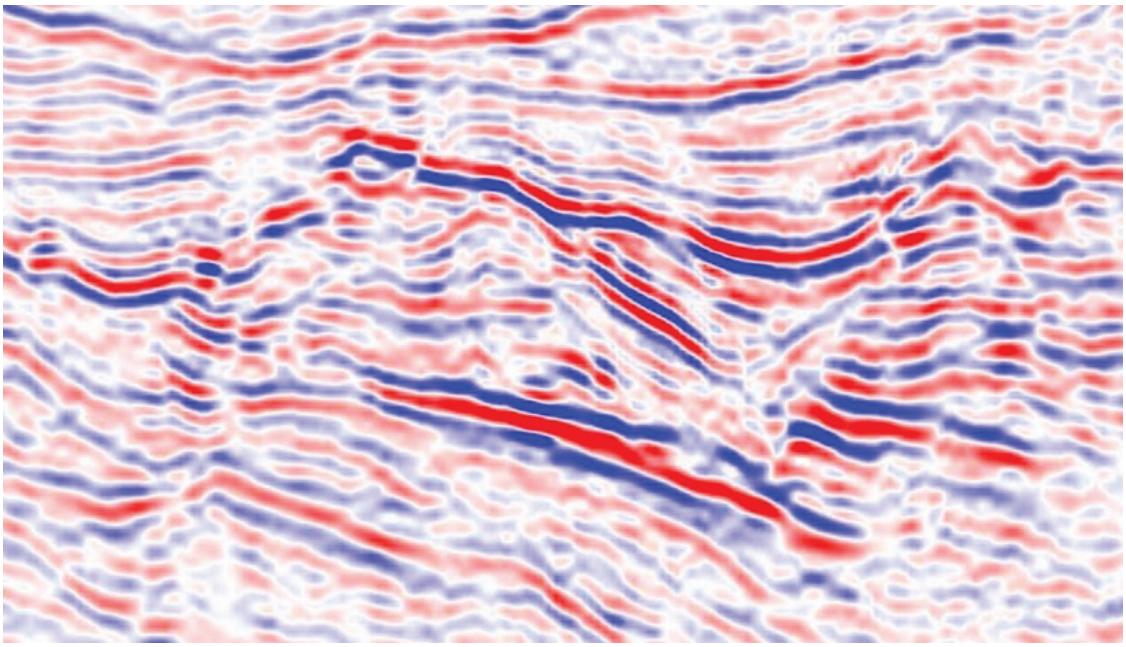

Fig. 2-34. Reflection triplets and triplets splitting into opposing pairs indicate 90° data, even though we know nothing about the local geology.

right shows a high-amplitude blue-over-red character, in some places parallel to bedding and in some places across bedding. An intrusion must be hard and have a top and a base reflection, so the data are zero-phase American polarity.

A bottom simulating reflection (BSR) should also be a good phase and polarity indicator. A BSR is the reflection from the base of the gas hydrate stability zone and should be a single impedance decrease. If the BSR is locally unconformable with the sedimentary reflections, then the character for this single interface should be clear.

A triplet of high-amplitude reflections often indicates top and base reflections of a bed in 90° phase. Figure 2-28 is a good illustration of this. Figure 2-34 shows many triplets and also places where triplets split into two pairs. All this is strongly indicative of 90° phase, even though we know nothing about the geology of this area.

The most commonly occurring phase and polarity conditions are then zero-phase American polarity, zero-phase European polarity, +90° phase, and –90° phase. To a

Downloaded 25 Jun 2012 to 95.28.162.50. Redistribution subject to SEG license or copyright; Terms of Use: http://segdl.org/

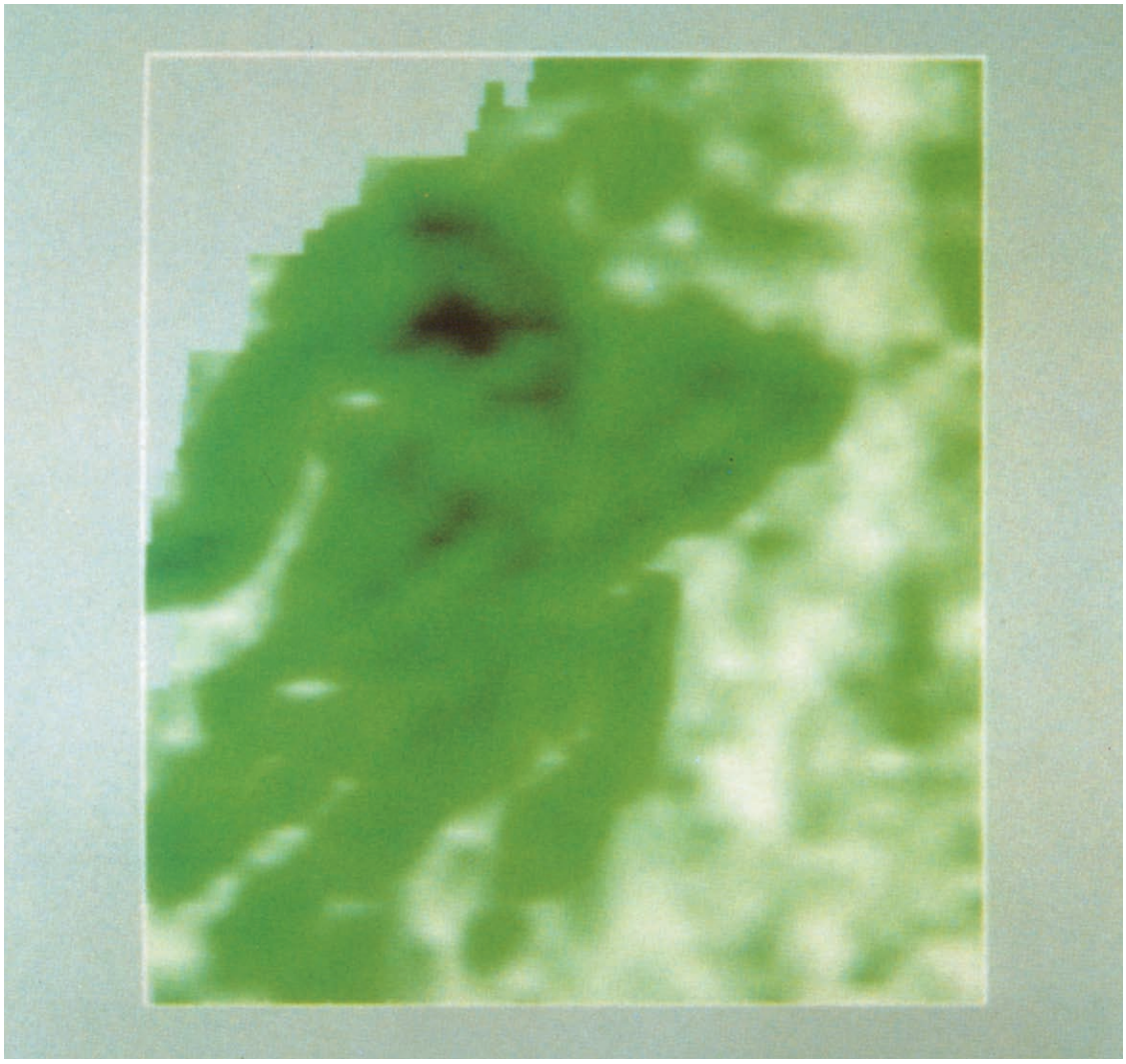

Fig. 2-35. Horizon slice displaying amplitude in gradational green to accentuate lineations due to faulting. (Courtesy Chevron U. S. A. Inc.)

first approximation and to simplify the subject, interpreters need to consider only these four possibilities. The two versions of zero phase are equally desirable, each having all the beneficial properties of zero-phase wavelets. The two versions of 90° are equally undesirable, so corrective action should be taken and the data volume phase rotated. Please refer to Appendix C for several phase circles diagramming the character for the four principal phase conditions for different acoustic contrasts. Intermediate phase conditions (e.g., 30° and 60°) appear to be rare. Time-variant phase, although possible, also appears to be rare. A further and more analytical discussion on phase and polarity and their impact on the interpreter is provided by Simm and White (2002).

Psychological Impact of Color

Studies on the psychological impact of color have shown that hues of yellow, orange and red are advancing and attracting, while hues of green and blue are cooler and receding. The interpreter can take advantage of this in communicating his results. It would seem logical to display the structural highs, the isopach thicks and the amplitude highs in advancing colors in order to promote their prospectivity. Figure 2-6 is a structure map which demonstrates this point.

Figures 2-35, 2-36 and 2-37 are the same horizon slice displaying reflection amplitude

Downloaded 25 Jun 2012 to 95.28.162.50. Redistribution subject to SEG license or copyright; Terms of Use: http://segdl.org/

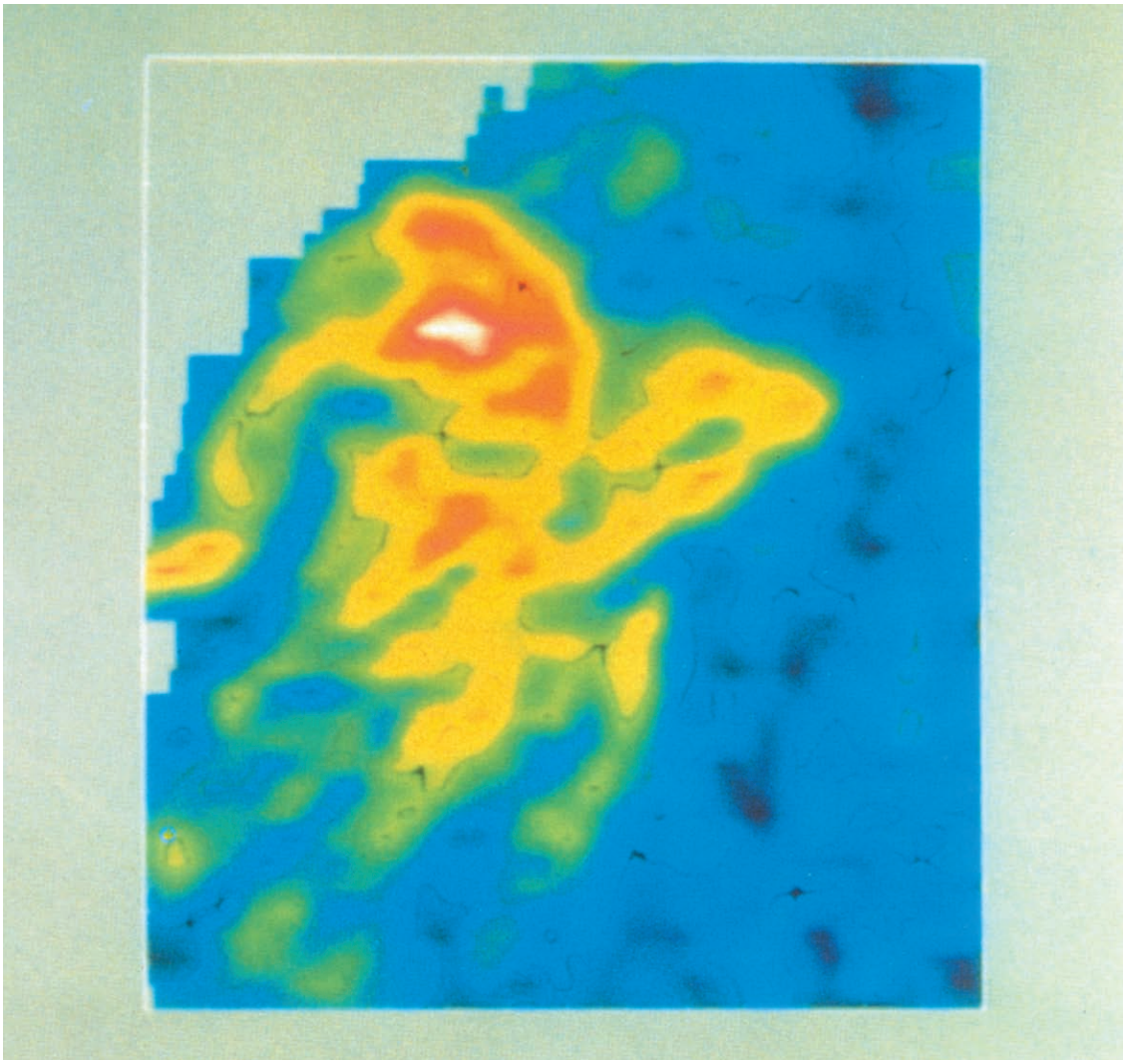

Fig. 2-36. Same horizon slice as in Figure 2-35 displayed in a wider range of hues to draw attention to the high amplitudes using advancing colors. (Courtesy Chevron U.S.A. Inc.)

over a Gulf of Mexico reservoir, but presented with three different color schemes. In Figure 2-35 these data are represented in a green gradational scheme to accentuate the lineations due to faulting. The gradational colors accentuate these lineations by using the full dynamic range of color density and allow the eye to integrate all of the data quickly.

Figure 2-36 shows the same data displayed with a gradational color scheme using a wider range of hues. Now the relative strength of the amplitudes has much more impact on the eye; the advancing reds and yellows appear much more interesting than the cooler greens and blues. By using this scheme, the large anomaly near the top of the display draws considerable attention. A successful well was targeted and drilled, based on this display.

Yet another display of the same data (Figure 2-37) shows that a large area of high amplitude may be considered prospective. Here the low amplitude zones have been colored with fairly neutral grays. Further drilling potential can be considered on the basis of this display if amplitude strength is the key to developing this reservoir.

Thus one horizon slice was used for three different purposes by employing three different color schemes. The first drew attention to the faulting, the second to a particular anomaly, and the third to total drilling potential. Separate features of the data were enhanced differently by the different uses of color.

Downloaded 25 Jun 2012 to 95.28.162.50. Redistribution subject to SEG license or copyright; Terms of Use: http://segdl.org/

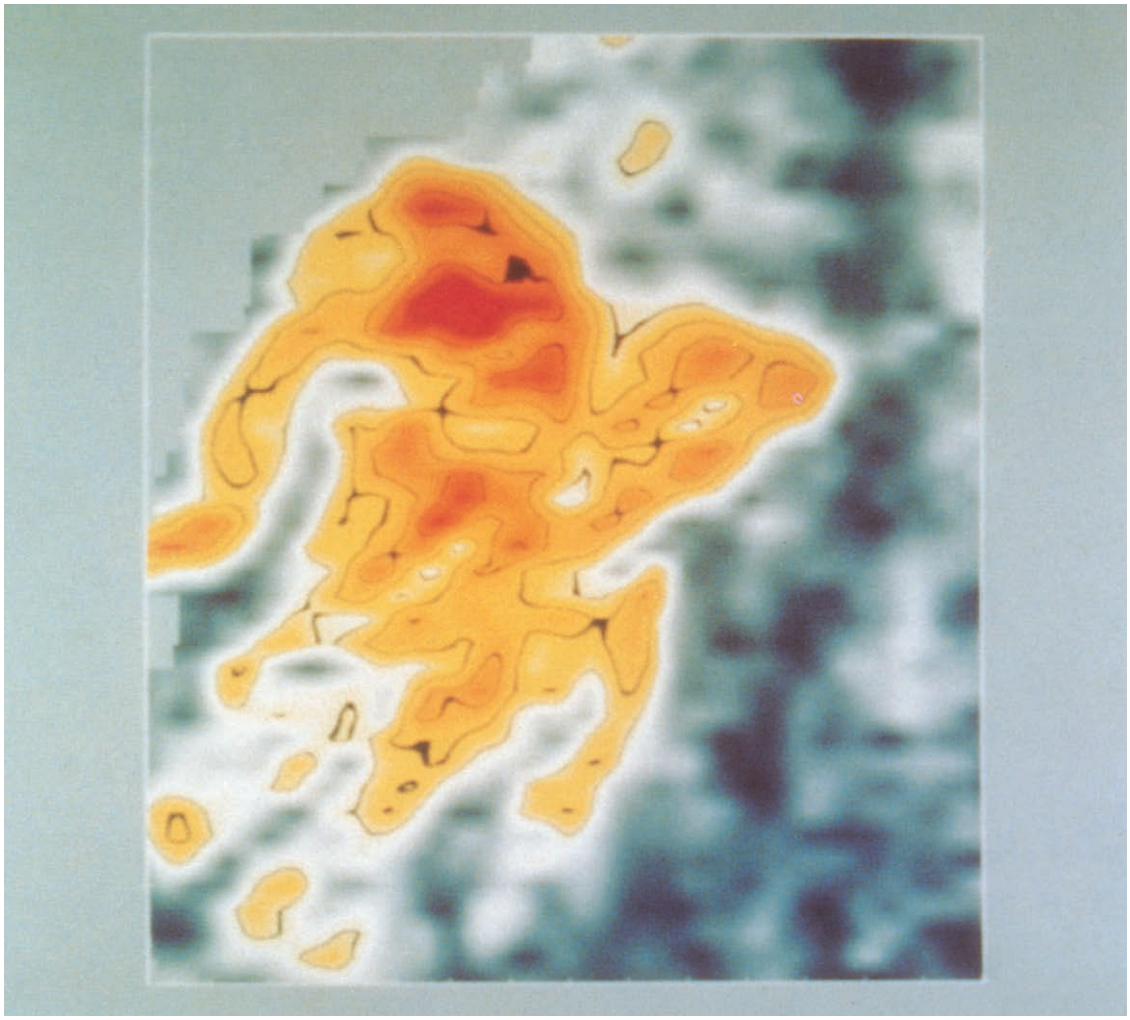

Fig. 2-37. Same horizon slice as in Figure 2-35 displayed in reds, yellows and grays to accentuate total drilling potential. (Courtesy Chevron U.S.A. Inc.)

References

Backus, M. M., and R. L. Chen, 1975, Flat spot exploration: Geophysical Prospecting, v. 23, p. 533–577.

Balch, A. H., 1971, Color sonograms; a new dimension in seismic data interpretation: Geophysics, v. 36, p. 1074–1098.

Galbraith, R. M., and A. R. Brown, 1982, Field appraisal with three-dimensional seismic surveys offshore Trinidad: Geophysics, v. 47, p. 177–195.

Gerhardstein, A. C., and A. R. Brown, 1984, Interactive interpretation of seismic data: Geophysics, v. 49, p. 353–363.

Kallweit, R. S., and L. C. Wood, 1982, The limits of resolution of zero-phase wavelets: Geophysics, v. 47, p. 1035–1046.

Lindseth, R. O., 1979, Synthetic sonic logs — a process for stratigraphic interpretation: Geophysics, v. 44, p. 3–26.

Masaferro, J. L., R. Bourne, and J. C. Jauffred, 2004, Three-dimensional seismic visualization of carbonate reservoirs and structures, *in* G. P. Eberli, J. L. Masaferro, and J. F. Sarg, eds., Seismic imaging of carbonate reservoirs and systems: AAPG Memoir 81, p. 11–41.

Simm, R. W., and R. E. White, 2002, Phase, polarity and the interpreter's wavelet: First Break, v. 20, p. 277–281.

Taner, M. T., and R. E. Sheriff, 1977, Application of amplitude, frequency and other attributes to stratigraphic and hydrocarbon determination, *in* C. E. Payton, ed., Seismic stratigraphy — applications to hydrocarbon exploration: AAPG Memoir 26, p. 301–327.

Wood, L. C., 1982, Imaging the subsurface, *in* K. C. Jain, and R. J. P. deFigueiredo, eds., Concepts and techniques in oil and gas exploration: Society of Exploration Geophysicists Special Publication, p. 45–90.

Downloaded 25 Jan 2012 to 95.28.162.50. Redistribution subject to SEG license or copyright; Terms of Use: http://segdl.org/

Structural Interpretation

Direct Contouring and the Importance of the Strike Perspective

The 3-D seismic interpreter works with a volume of data. Normally this is done by studying some of each of the three orthogonal slices through the volume. This chapter explores the unique contribution of the horizontal section to structural interpretation. The interpreter of structure needs to be able to judge when to use horizontal sections and when to use vertical ones in the course of an overall interpretive project.

Figure 3-1 demonstrates the conceptual relationship between a volume of subsurface rock and a volume of seismic data. Consider the diagram first to represent subsurface rocks and the gray surface to be a bedding plane. The two visible vertical faces of the rectangular solid show the two dip components of the plane; the horizontal face shows the strike of the plane. Now consider the rectangular solid of Figure 3-1 to be the equivalent volume of seismic data. The gray plane is now a dipping reflection and its intersections with the three orthogonal faces of the solid show the two components of dip and the strike as before. Hence the attitude of a reflection on a horizontal section indicates directly the strike of the reflecting surface. This is the fundamental property of the horizontal section from which all its unique interpretive value derives.

Contours follow strike and indicate a particular level in time or depth. When an interpreter picks a reflection on a horizontal section, it is directly a contour on some horizon at the time (or depth) at which the horizontal section was sliced through the data volume.

Figure 3-2 shows three horizontal sections, four milliseconds apart. By following the semicircular black event (peak) from level to level and drawing contours at an appropriate interval, the structural contour map at the bottom of Figure 3-2 was generated. Note the similarity in shape between the sections and the map for the anticlinal structure and the strike east of the faults. In the central panel the peaks from 1352 ms are printed in black and the peaks from 1360 ms in blue/green. This clearly demonstrates the way in which the events have moved with depth.

Figures 3-3 and 3-5 provide one vertical section and several horizontal sections from which the relationship between the two perspectives can be appreciated. Line P (Figure 3-3) runs north-south through the middle of the prospect with south at the right. The time interval 2632-2656 ms shows some continuous reflections. Proceeding from south to north (right to left, Figure 3-3; bottom to top, Figure 3-5) the structure is first a broad closed anticline, then a shoulder, then a smaller anticline.

Figure 3-5 demonstrates a simple exercise in direct contouring from a suite of horizontal sections. The red event (trough) expanding in size from left to right has been progressively circumscribed in the lower part of the figure. The last frame is a raw contour map of this horizon. This first structural representation has been made quickly

Downloaded 25 Jun 2012 to 95.28.162.50. Redistribution subject to SEG license or copyright; Terms of Use: http://segdl.org/

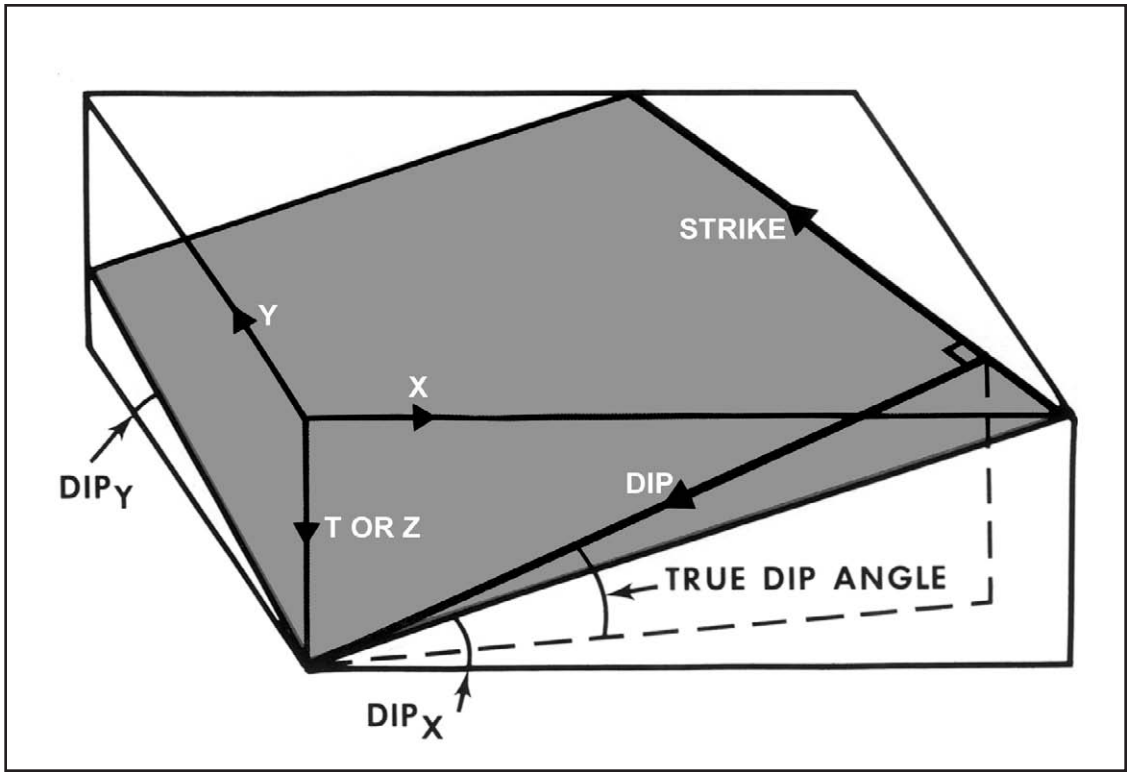

Fig. 3-1. Relation between dip and strike of a seismic reflector within a data volume.

and efficiently without the traditional intermediate tasks of timing, posting and contouring. When drawing structural contours from horizontal sections in this way, it is wise to visualize the three-dimensionality of the structure and to appreciate where on the seismic waveform the contour is being drawn (Figure 3-4). The latter problem applies particularly to the use of variable area displays as used, for example, in Figure 3-5. The contour is here drawn all the way around the red event only because the dip is down all the way around the structure; this is a consistent point on the seismic waveform, namely its upper edge (Figure 3-4).

Figure 3-6 shows 24 horizontal sections covering an area of about 5 sq mi (13 sq km). These can be used as a structural interpretation exercise. Obtain a small piece of transparent paper and register it over the rectangular area. Begin with the upper left frame and find the red event in its lower right corner. Mark this event by following its maximum amplitude and then mark its changed position from frame to frame until you reach 2160 ms. Your resultant contour map should show that the dip is generally northwest and that the strike swings about 40° toward the north over the structural range of the map. You will probably detect a fault toward the west of the area as well. If you study the arcuate events west of the fault, you will recognize a small anticline closing against the fault and a small syncline south of it. There is no way to establish the correlation across the fault.

An event on a horizontal section is generally broader than on a vertical section as dips are usually less than 45°. Figure 3-7 shows the effect of dip and frequency on the width of an event on a horizontal section. A gently dipping event is very broad and a steeply dipping event is much narrower. Increasing dip and increasing frequency both make horizontal section events narrower. The width of an event on a horizontal section is strictly half the spatial wavelength.

Because typical dips are much less than 45°, fewer horizontal sections than vertical ones are needed to study the full extent of a reflection within a given data volume. This gives horizontal sections greater efficiency than vertical sections in structural mapping. Combining this benefit with the fact that horizon tracks (picks) are directly contours, then the value of horizontal sections to structural interpretation is substantial.

Text continues on page 73.

Downloaded 25 Jun 2012 to 95.28.162.50. Redistribution subject to SEG license or copyright; Terms of Use: http://segdl.org/

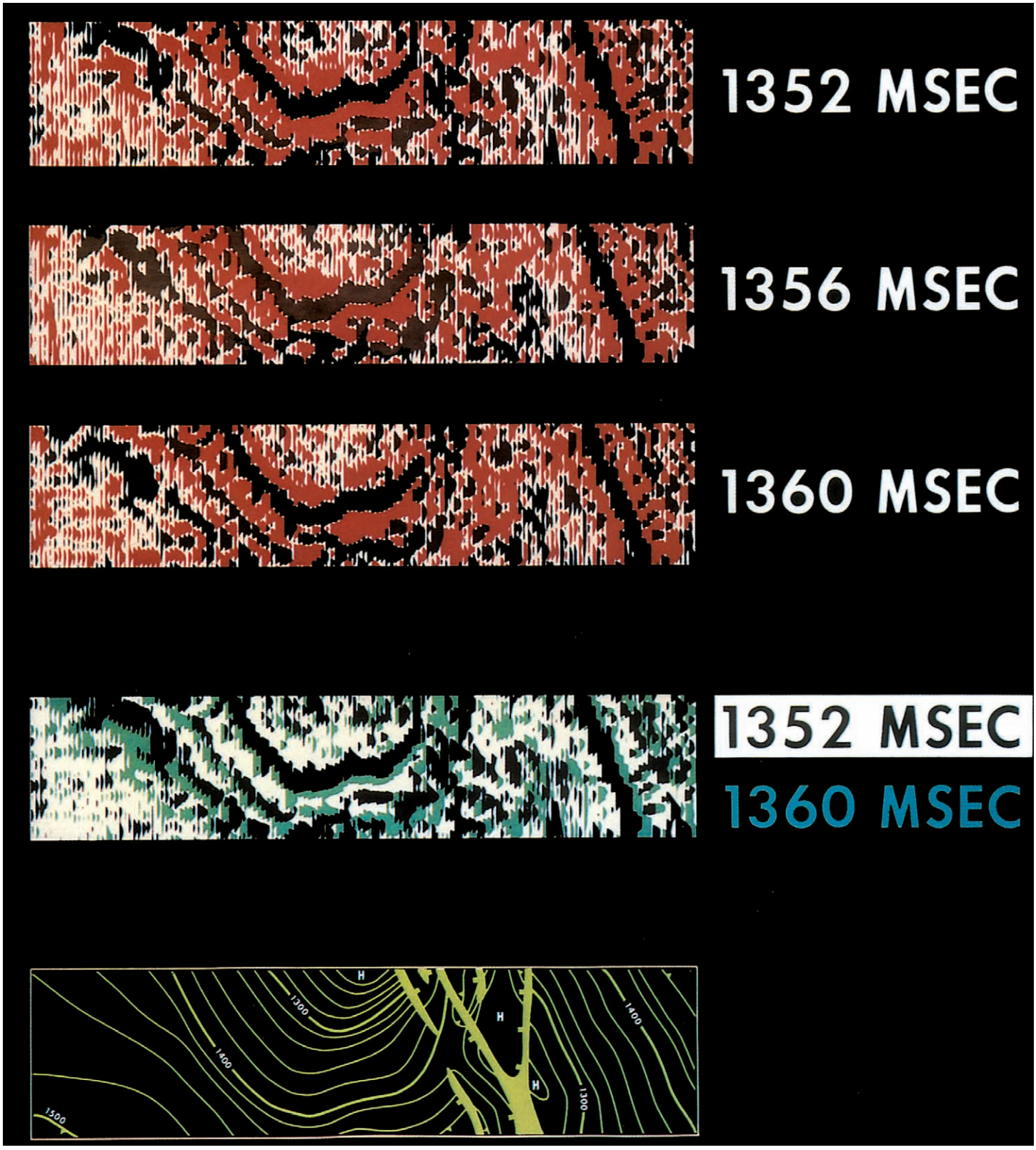

Fig. 3-2. Dual polarity horizontal sections from offshore Holland; two-level single polarity horizontal section, showing movement of events from 1352 ms to 1360 ms; interpreted contour map on horizon seen as strongest event on horizontal sections.

Downloaded 25 Jun 2012 to 95.28.162.50. Redistribution subject to SEG license or copyright; Terms of Use: http://segdl.org/

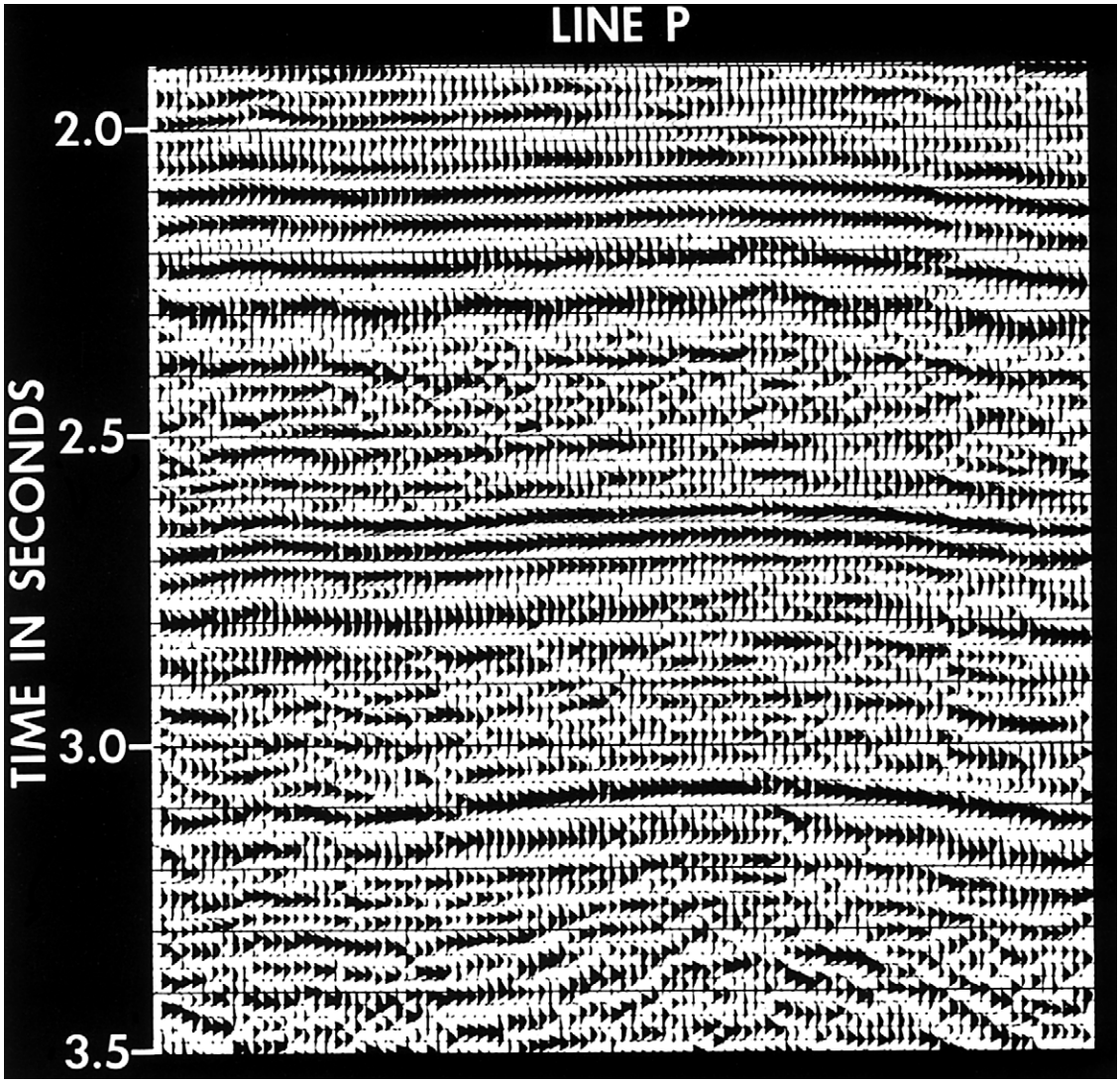

Fig. 3-3. North-south vertical section from Peru through same data volume sliced in Figure 3-4. (Courtesy Occidental Exploration and Production Company.)

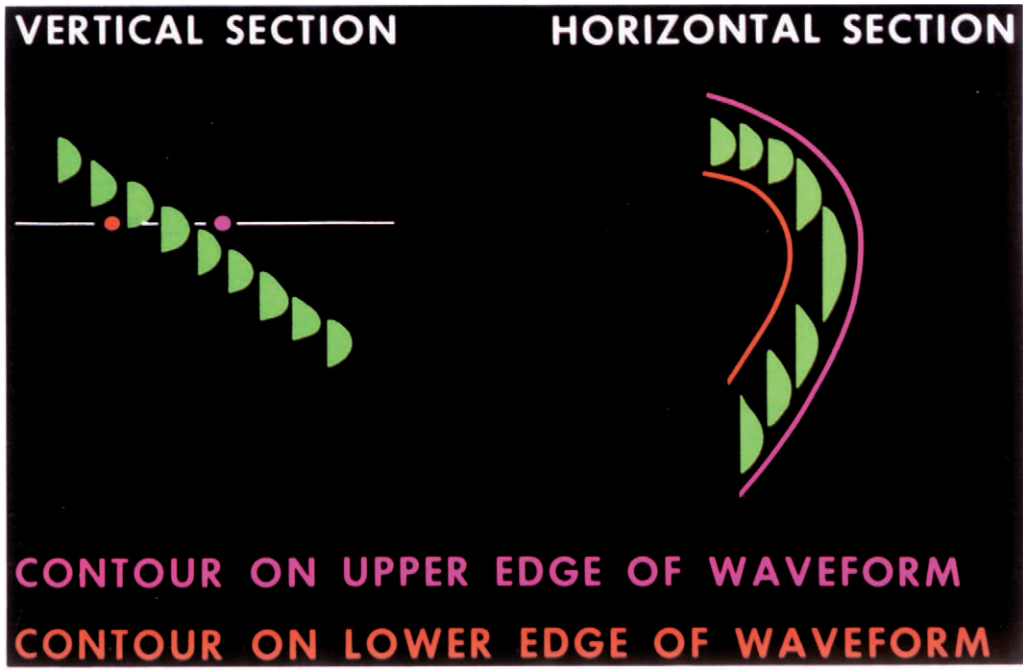

Fig. 3-4. Where on the waveform should one place the contour when working with variable area display?

Downloaded 25 Jun 2012 to 95.28.162.50. Redistribution subject to SEG license or copyright; Terms of Use: http://segdl.org/

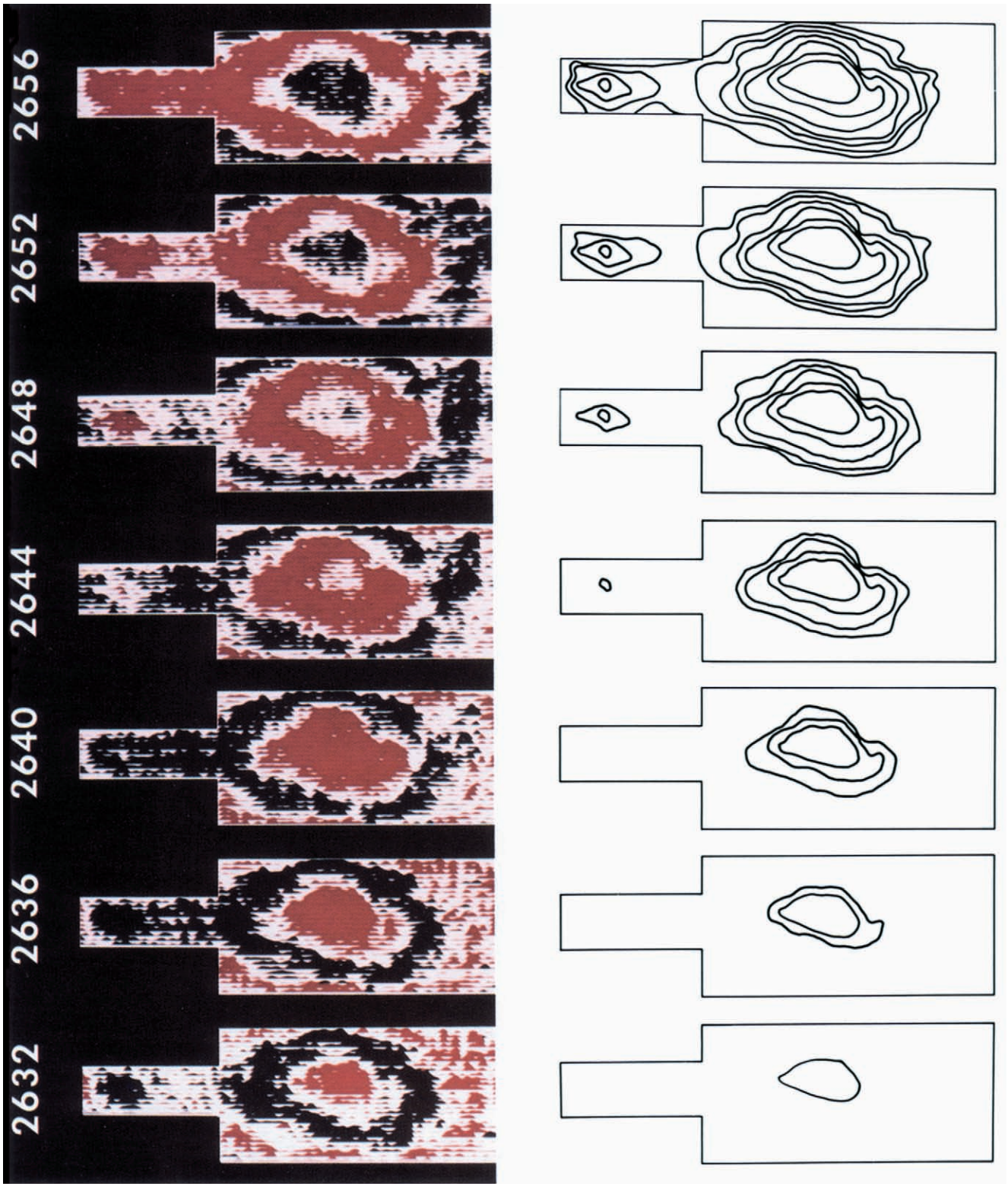

Fig. 3-5. Horizontal sections, 4 ms apart, from Peru (courtesy Occidental Exploration and Production Company) and raw interpreted contour map made by successively circumscribing the red event on each section.

Downloaded 25 Jun 2012 to 95.28.162.50. Redistribution subject to SEG license or copyright; Terms of Use: http://segdl.org/

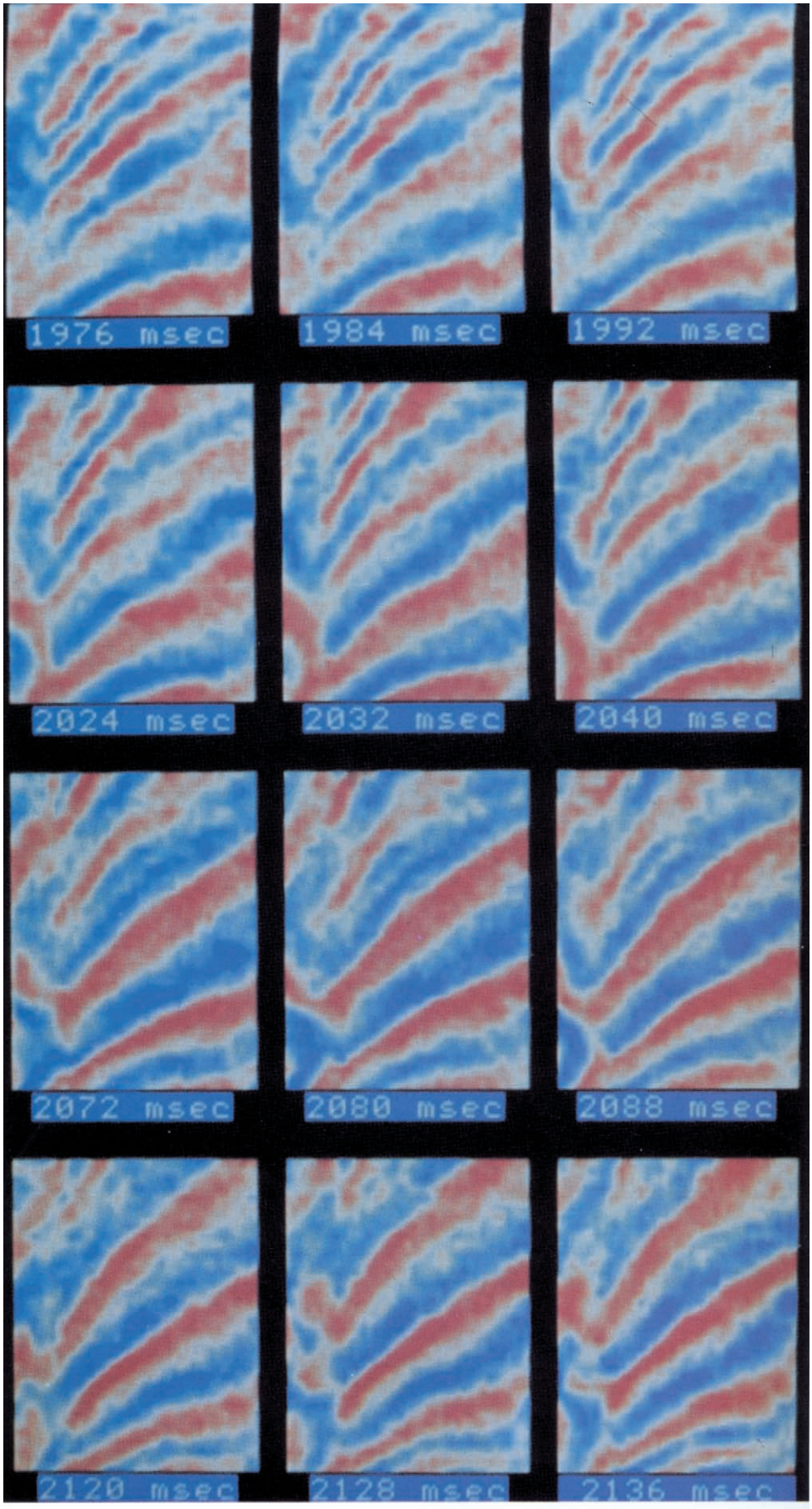

Fig. 3-6. Horizontal sections, 8 ms apart, from offshore Trinidad. (Courtesy Texaco Trinidad Inc.)

Downloaded 25 Jun 2012 to 95.28.162.50. Redistribution subject to SEG license or copyright; Terms of Use: http://segdl.org/

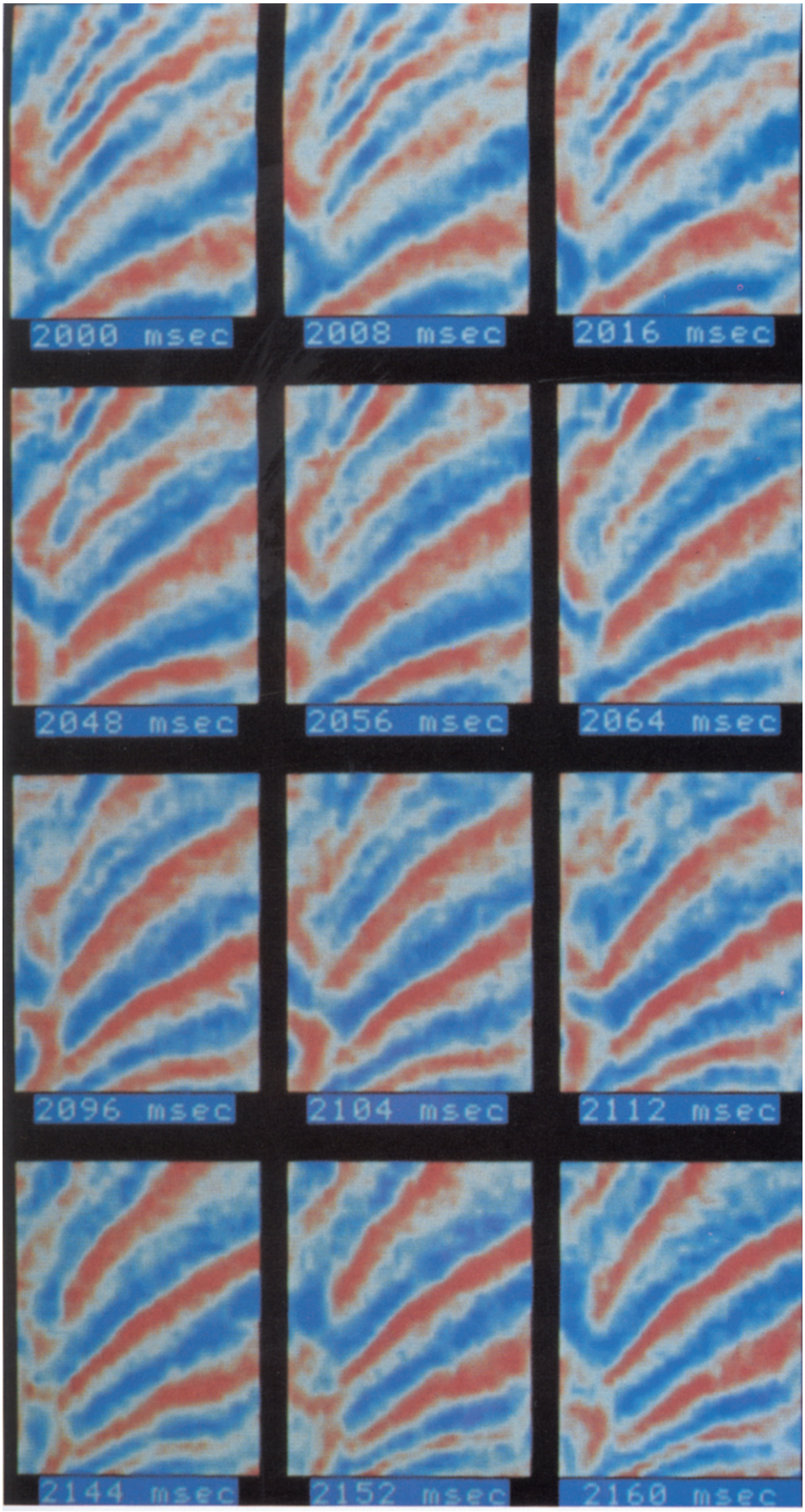

Downloaded 25 Jun 2012 to 95.28.162.50. Redistribution subject to SEG license or copyright; Terms of Use: http://segdl.org/

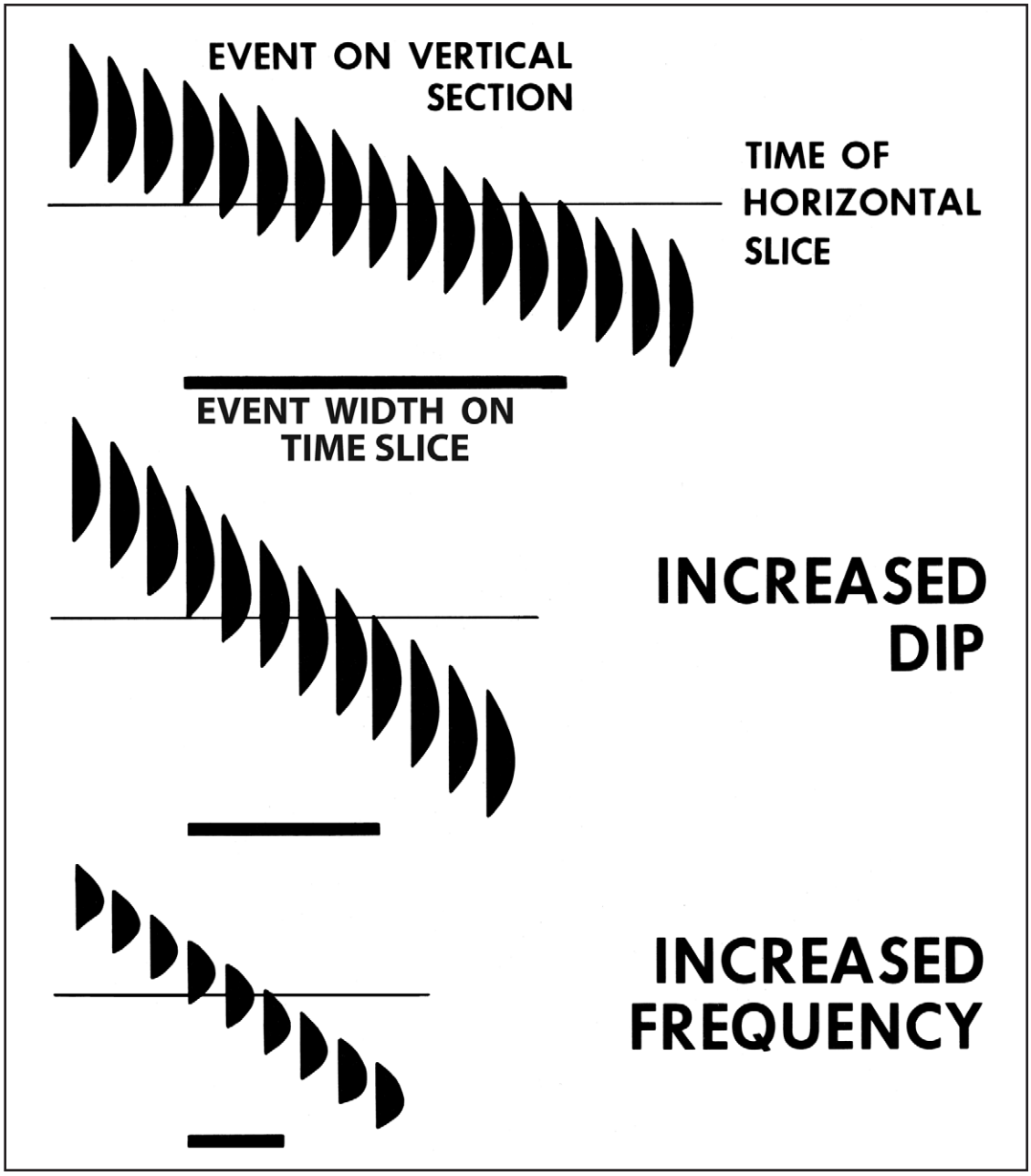

Fig. 3-7. The width of an event on a horizontal section decreases with increased dip and also with increased frequency.

Downloaded 25 Jun 2012 to 95.28.162.50. Redistribution subject to SEG license or copyright; Terms of Use: http://segdl.org/

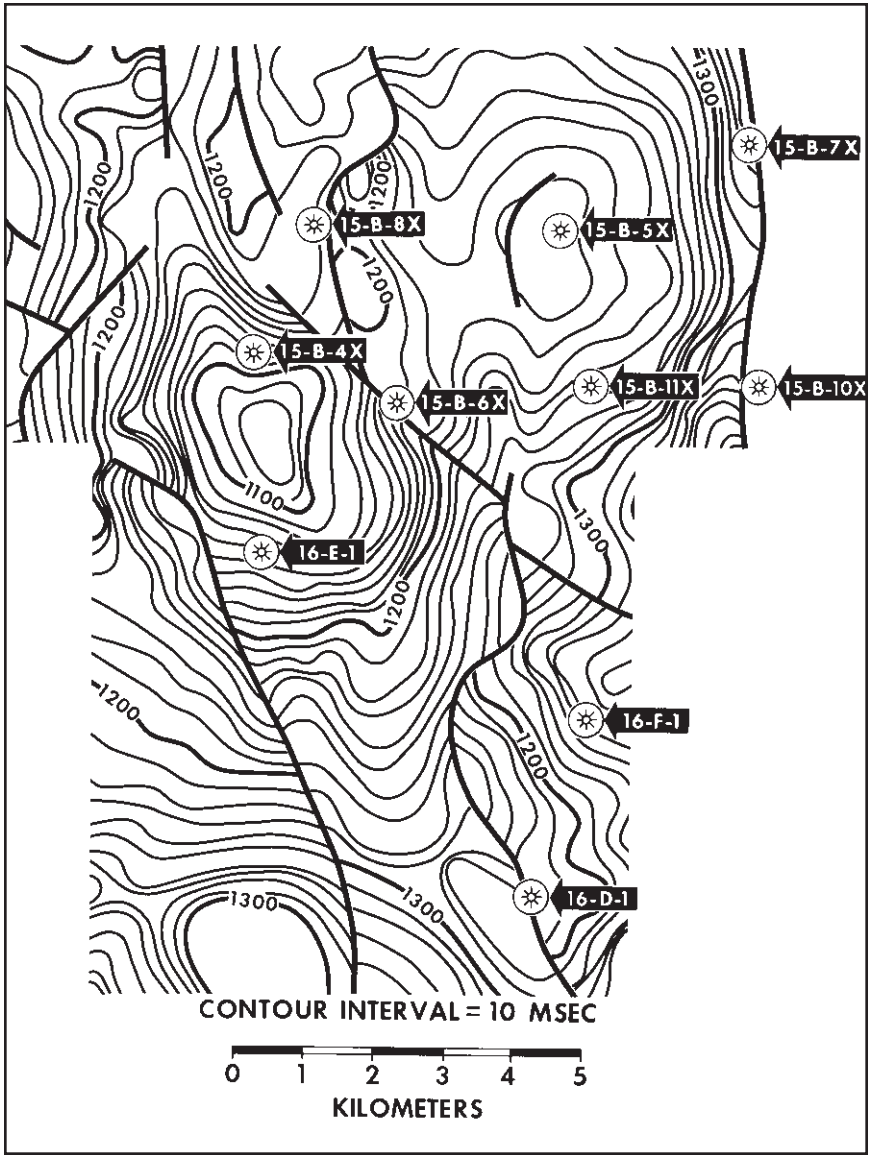

Fig. 3-8. Structural contour map derived from 2-D data from the Gulf of Thailand. (Courtesy Texas Pacific Oil Company Inc.)

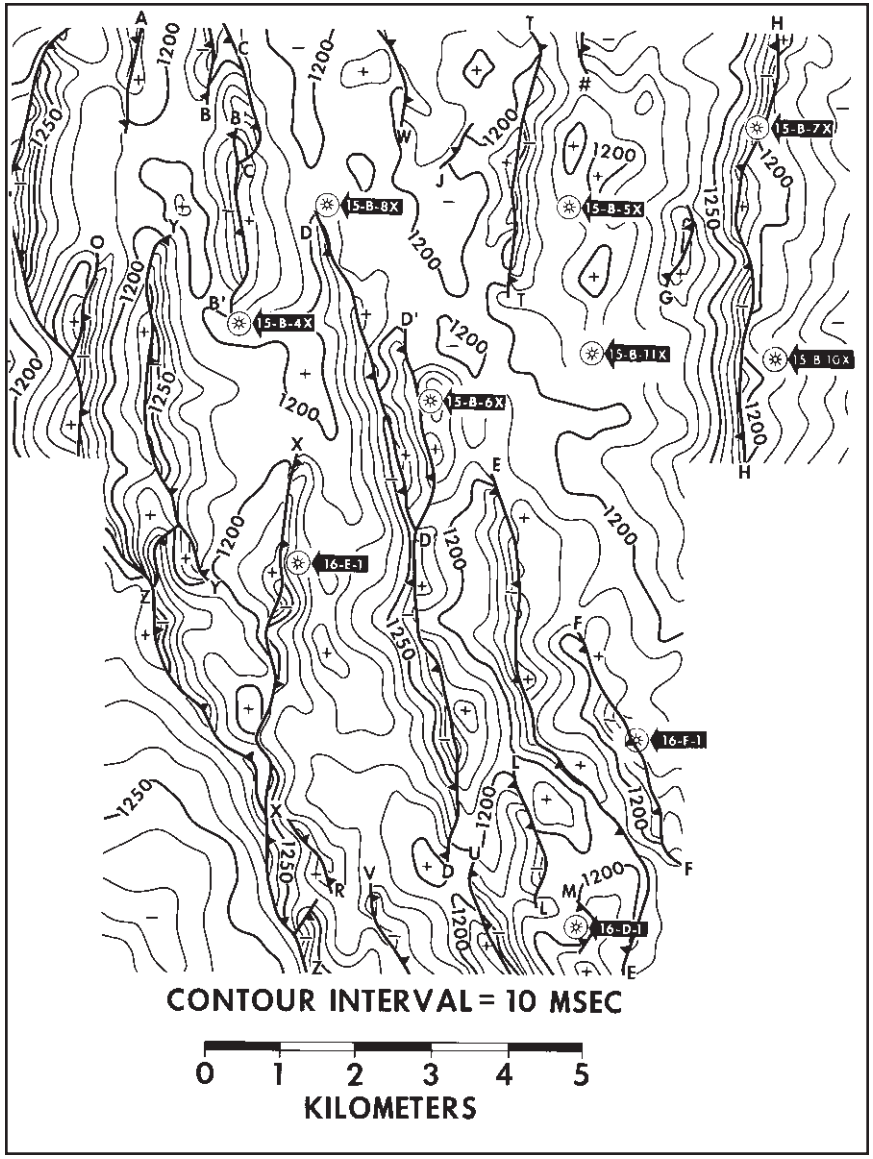

Fig. 3-9. Structural contour map derived from 3-D data from the Gulf of Thailand for the same horizon mapped in Figure 3-8. (Courtesy Texas Pacific Oil Company Inc.)

Downloaded 25 Jun 2012 to 95.28.162.50. Redistribution subject to SEG license or copyright; Terms of Use: http://segdl.org/

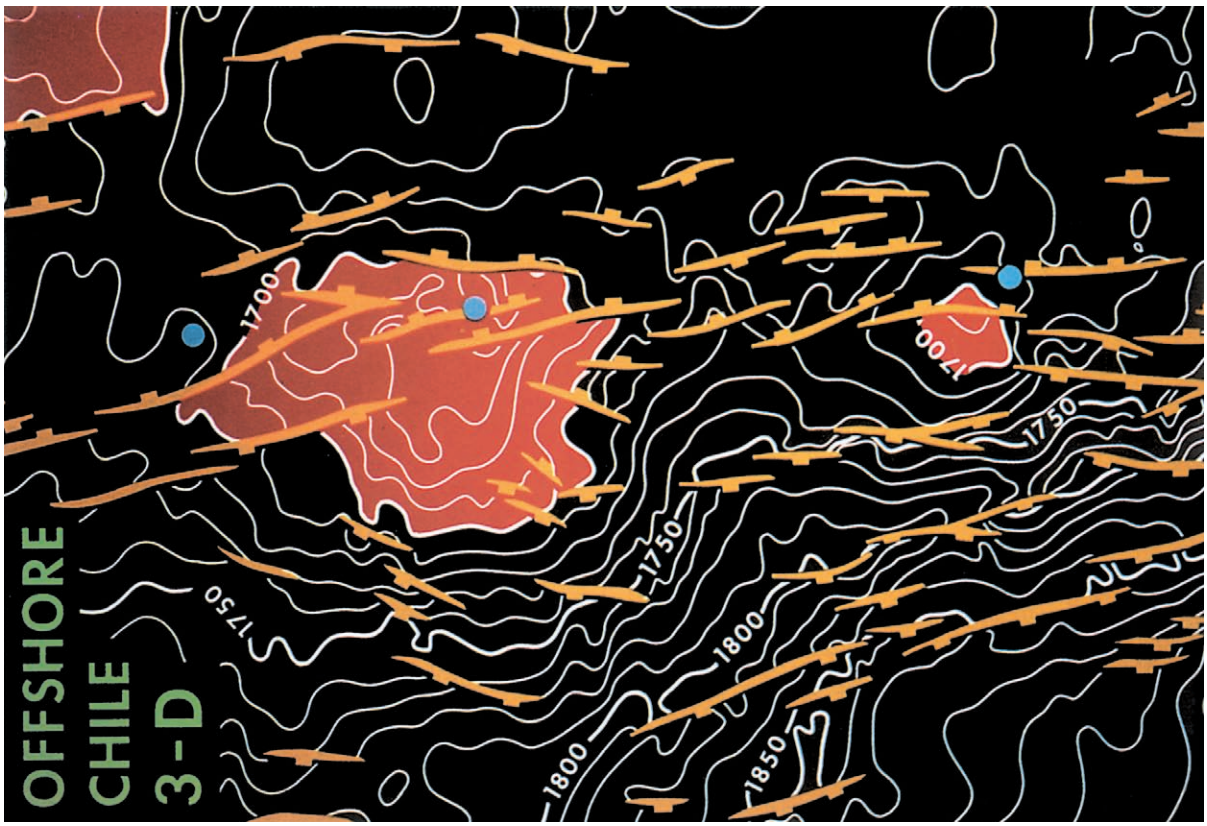

Fig. 3-11. Structural contour map derived from 3-D data from offshore Chile for the same horizon mapped in Figure 3-10. (Courtesy ENAP).

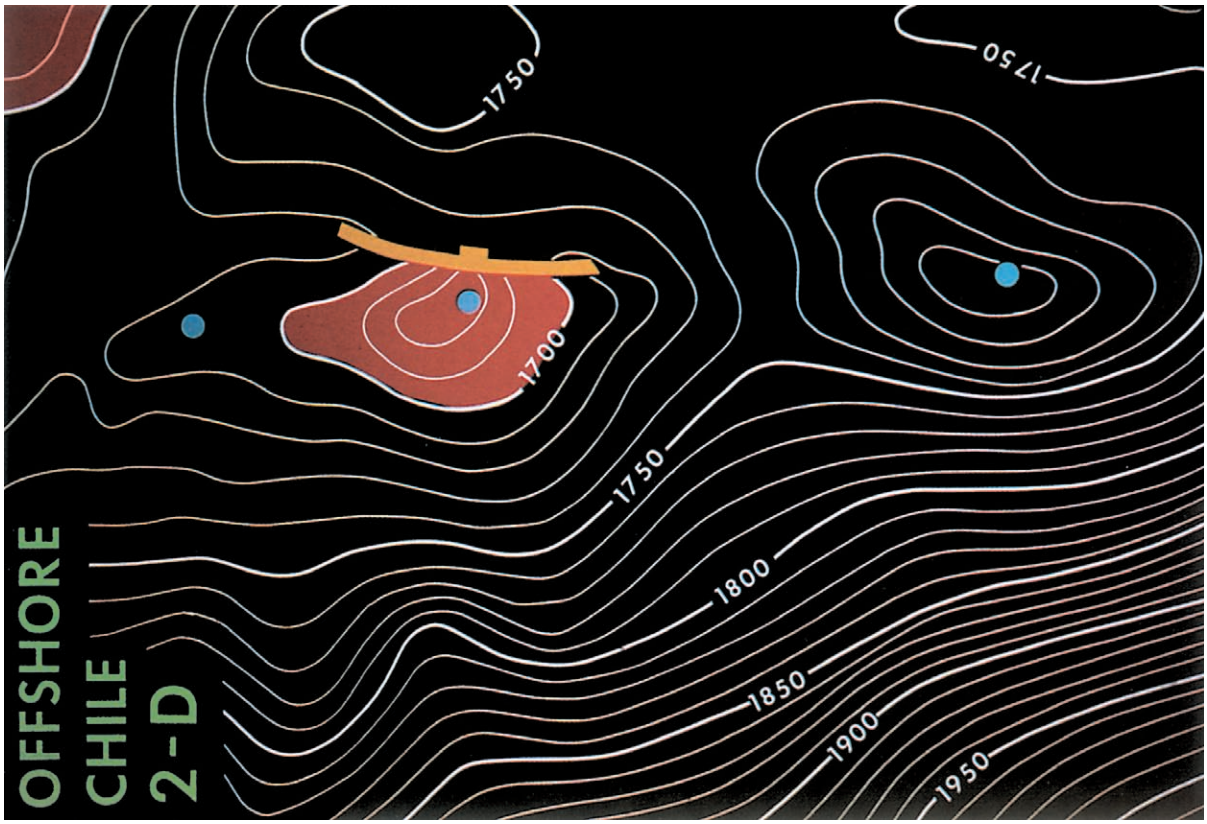

Fig. 3-10. Structural contour map derived from 2-D data from offshore Chile. (Courtesy ENAP).

Downloaded 25 Jun 2012 to 95.28.162.50. Redistribution subject to SEG license or copyright; Terms of Use: http://segdl.org/

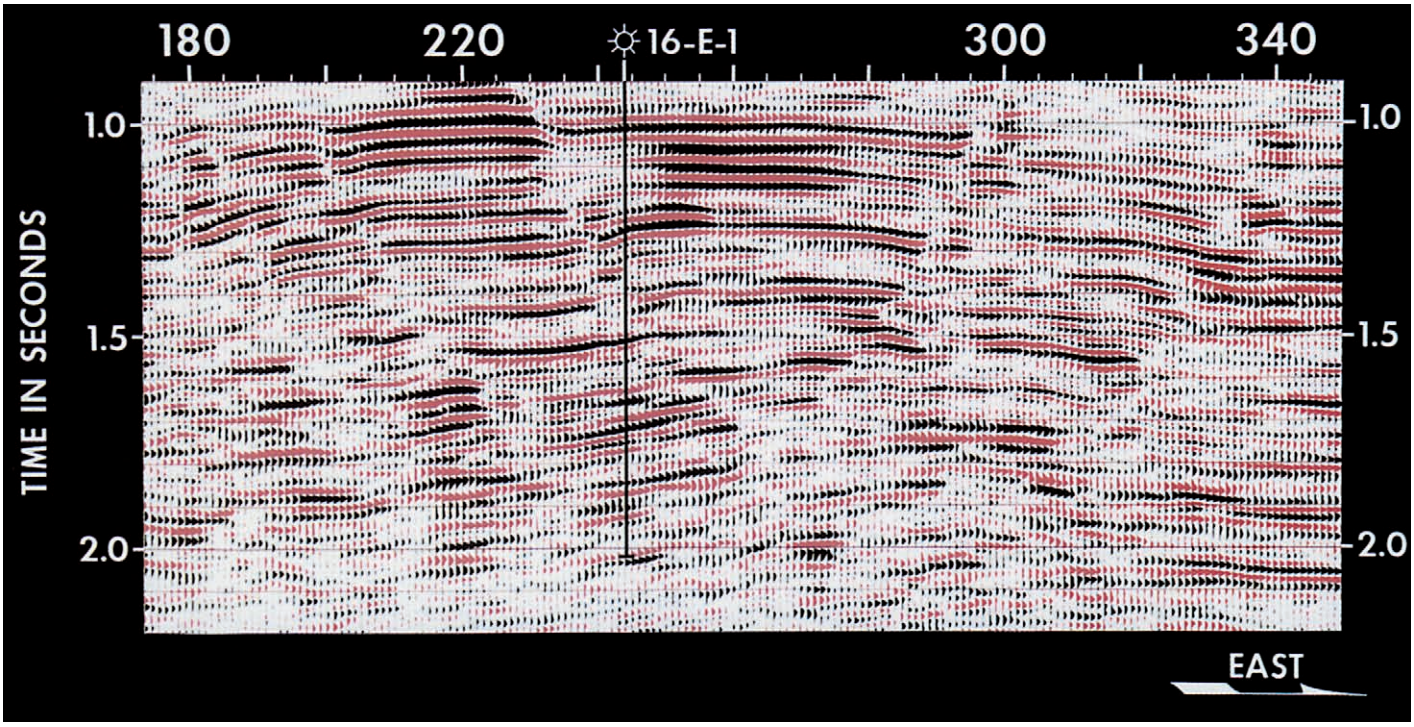

Fig. 3-12. Line 55 from Gulf of Thailand 3-D data. (Courtesy Texas Pacific Oil Company Inc.)

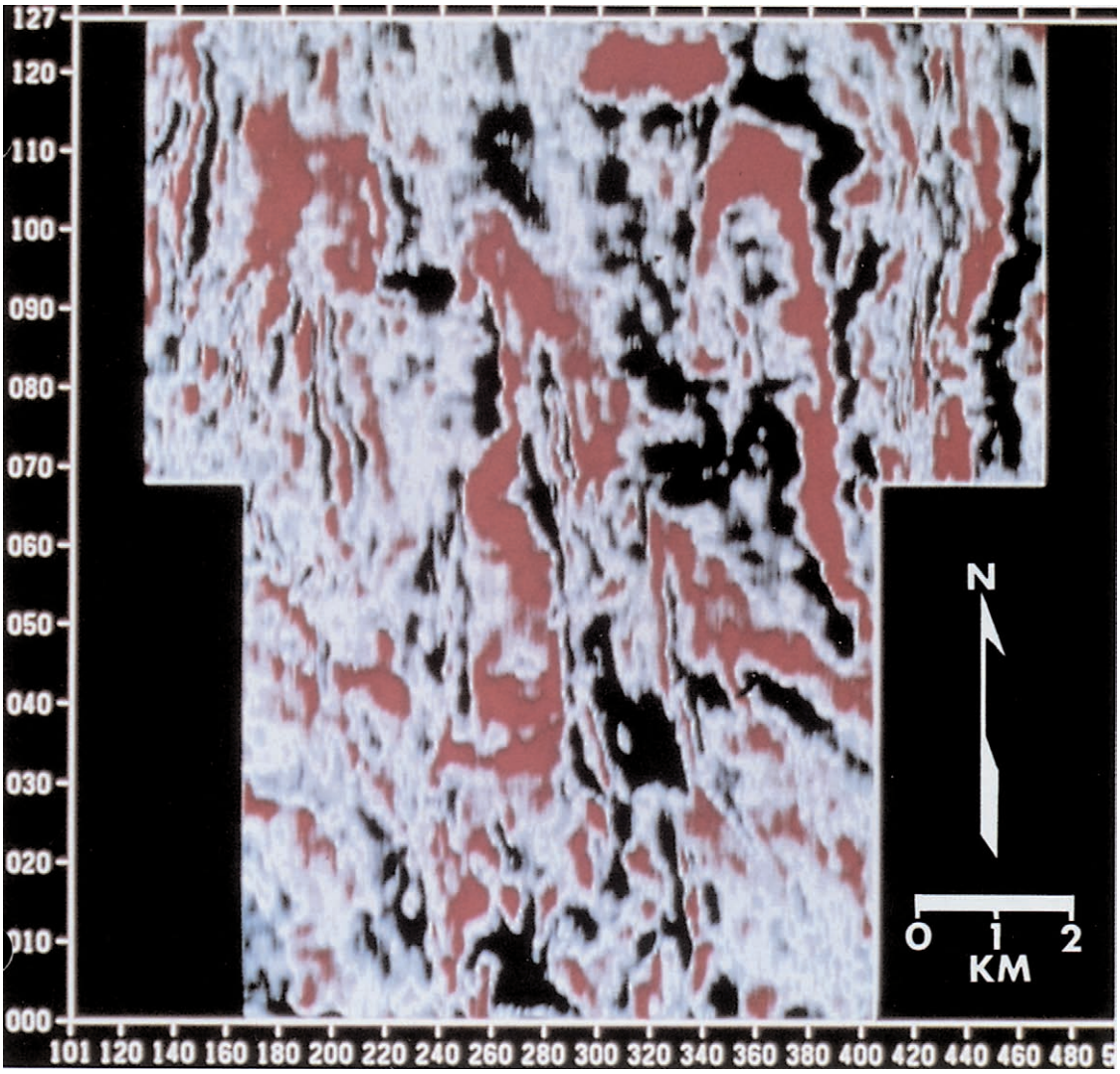

Fig. 3-13. Horizontal section at 1388 ms, from Gulf of Thailand. (Courtesy Texas Pacific Oil Company.)

Downloaded 25 Jun 2012 to 95.28.162.50. Redistribution subject to SEG license or copyright; Terms of Use: http://segdl.org/

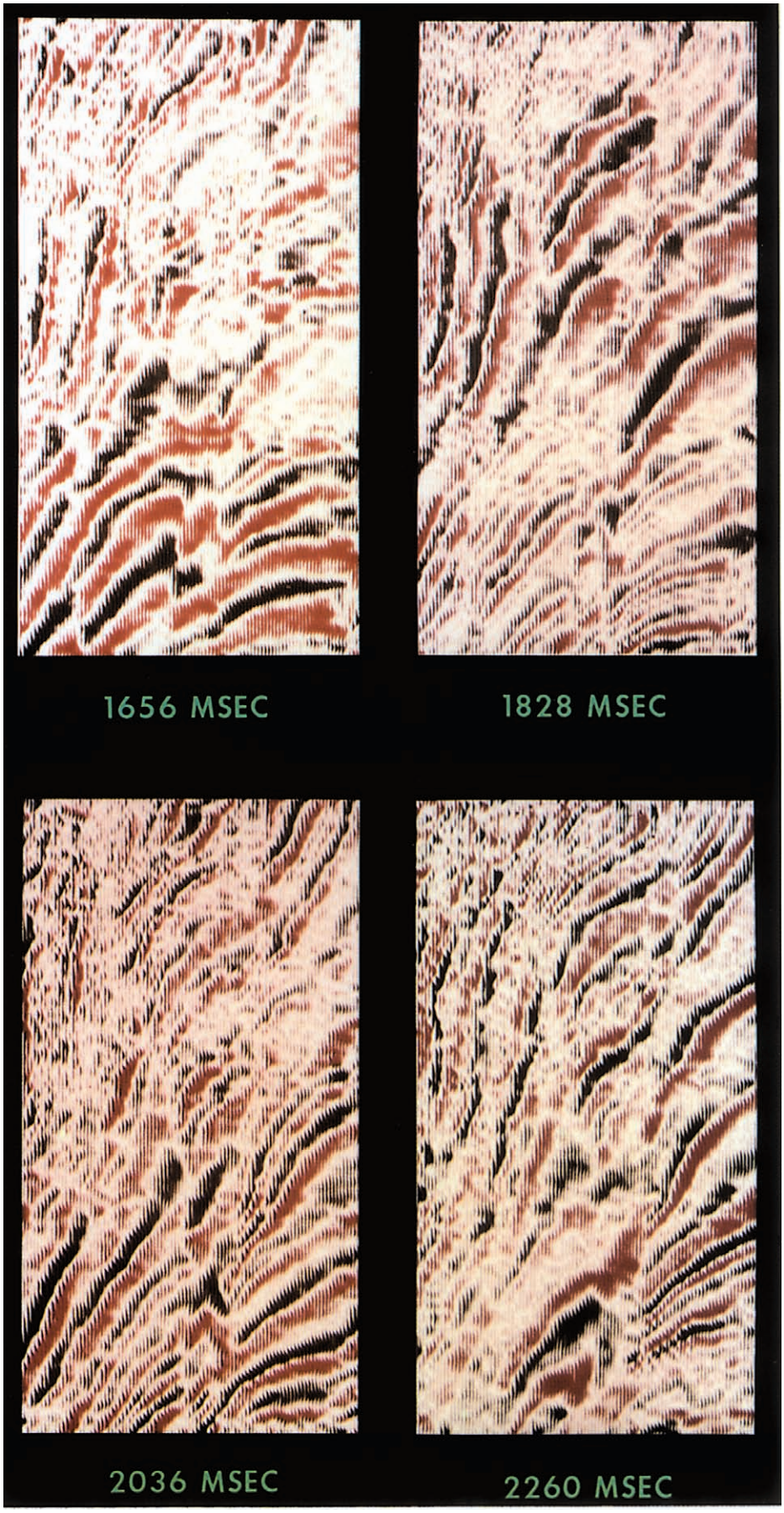

Fig. 3-14. Horizontal sections from offshore Trinidad. Event terminations indicate faulting. (Courtesy Texaco Trinidad Inc.)

Downloaded 25 Jun 2012 to 95.28.162.50. Redistribution subject to SEG license or copyright; Terms of Use: http://segdl.org/

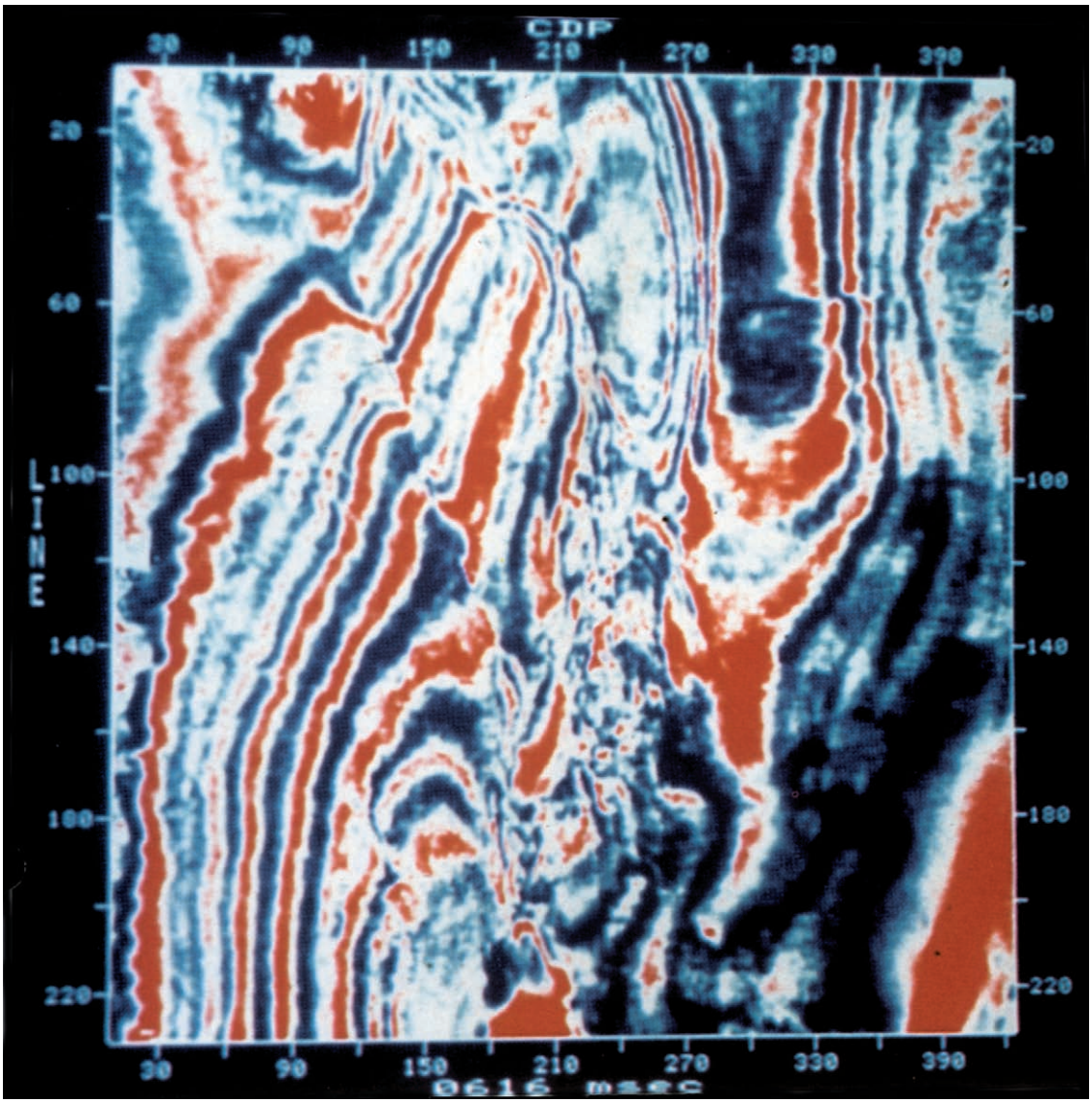

Fig. 3-15. Horizontal section from onshore Europe. Event terminations indicate faulting.

Fault Recognition and Mapping

When an interpreter works with 3-D data after having previously mapped from 2-D data over the same prospect, the most striking difference between maps is commonly the increased fault detail in the 3-D map. Figures 3-8 and 3-9 provide a typical comparison and also demonstrate increased detail in the shape of the structural contours. Comparison of Figures 3-10 and 3-11 also shows a considerable increase in the number of faults and in the structural detail. The three well locations indicated in blue appear structurally quite different on the 2-D and 3-D maps.

We expect to detect faults from alignments of event terminations. Figure 3-12 shows a vertical section from the 3-D data which provided the map of Figure 3-9. The event terminations clearly show several faults. The horizontal section of Figure 3-13 is from the same data volume and, in contrast, does not show clear event terminations. Figure 3-14 shows four horizontal sections from a different prospect but one in a similar tertiary clastic environment. Here event terminations clearly indicate the positions of three major faults on each of the four sections.

Why are event terminations visible at the faults in Figure 3-14 but not in Figure 3-13? The answer lies simply in the relationship between structural strike and fault strike. Any horizontal section alignment indicates the strike of the feature. If there is a significant angle between structural strike and fault strike, the events will terminate.

Downloaded 25 Jun 2012 to 95.28.162.50. Redistribution subject to SEG license or copyright; Terms of Use: http://segdl.org/

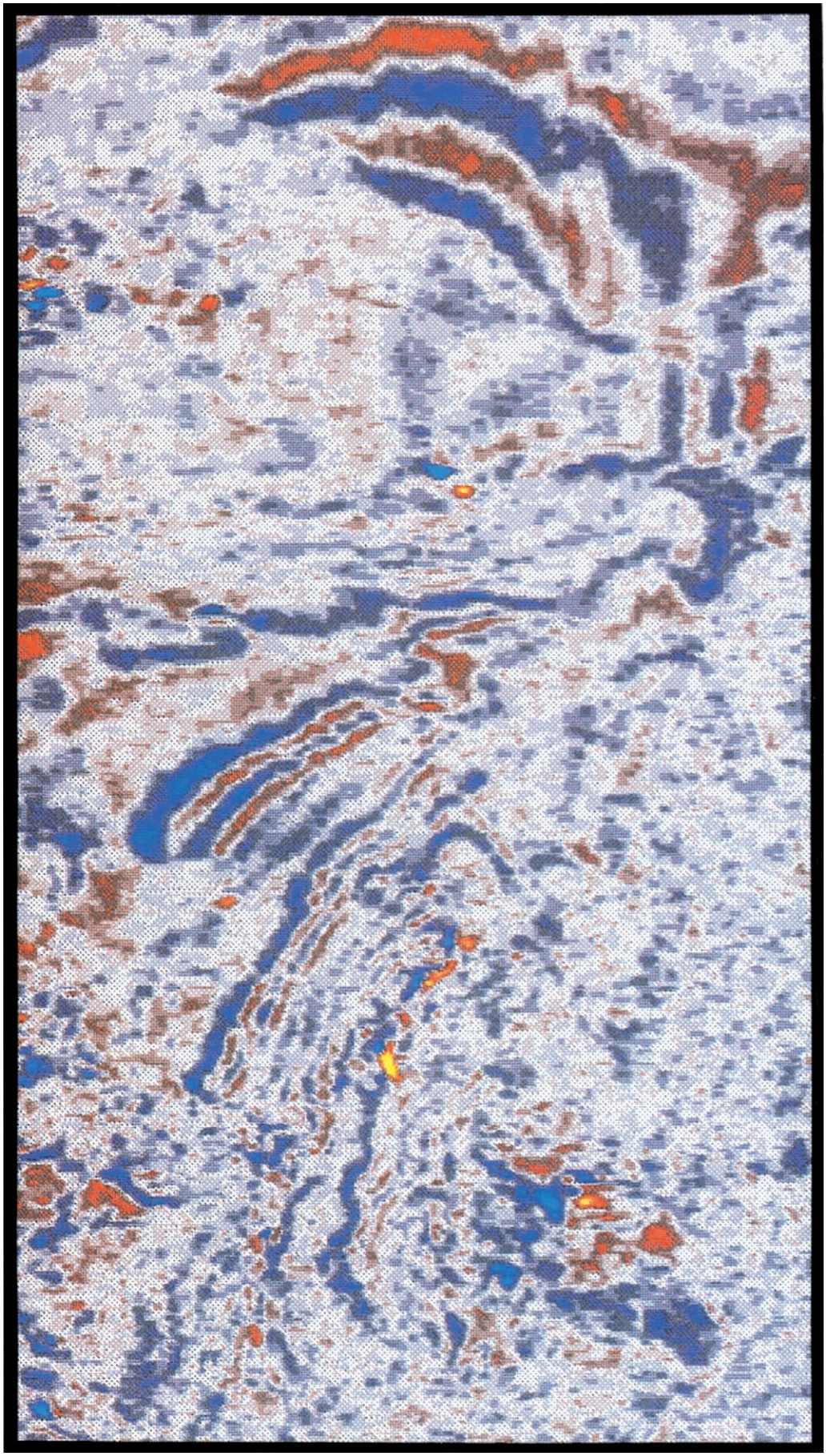

Fig. 3-16. Horizontal section at 1500 ms, from Gulf of Mexico, showing many clearly visible faults. At least 10 are identifiable. (Courtesy Conoco Inc. and Texaco U.S.A. Inc.)

Downloaded 25 Jun 2012 to 95.28.162.50. Redistribution subject to SEG license or copyright; Terms of Use: http://segdl.org/

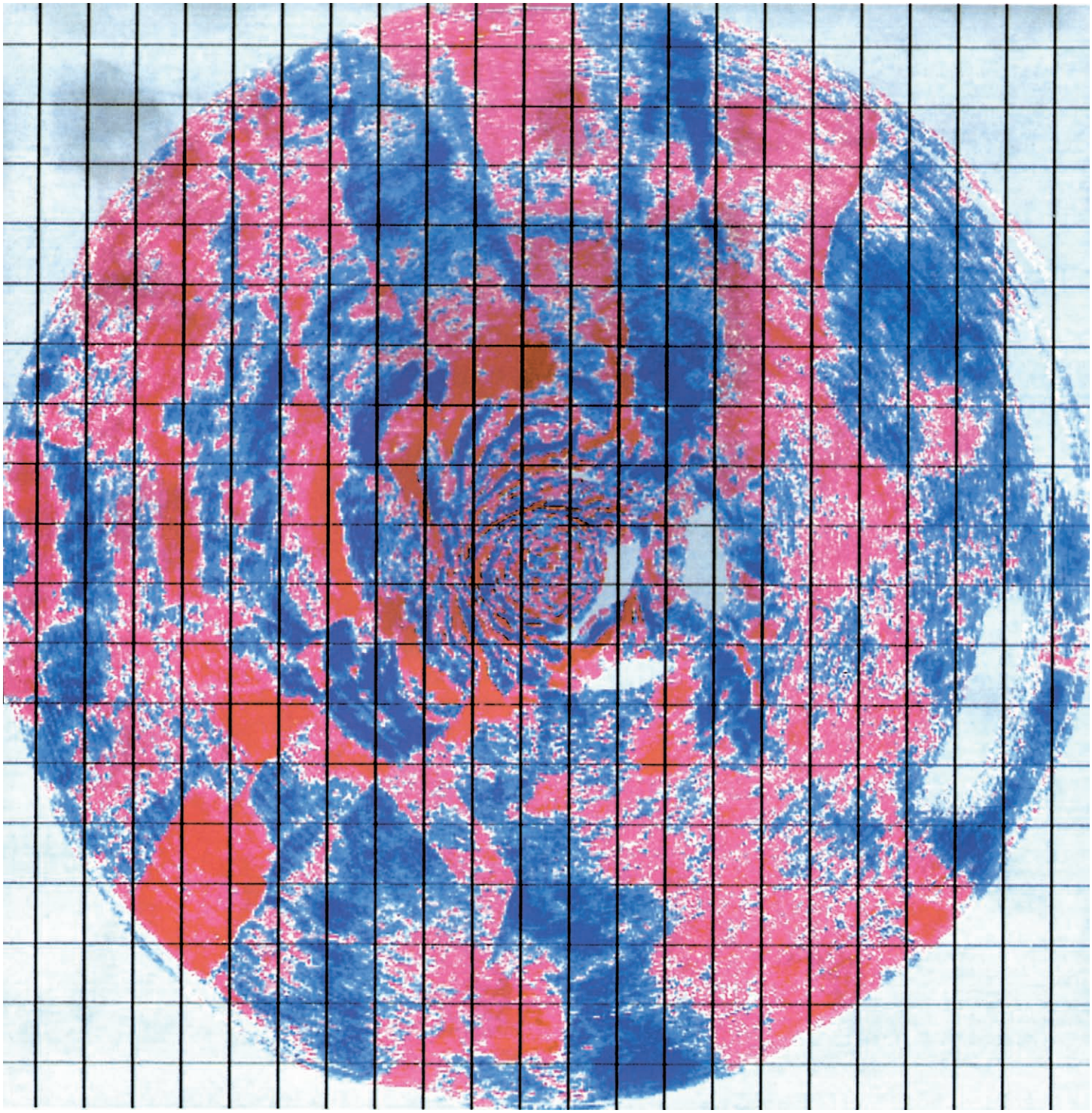

If structural strike and fault strike are parallel, or almost so, the events will not terminate but will parallel the faults. Comparison of Figures 3-13 and 3-9 demonstrates that situation. The difficulty of seeing faults on a time slice when they parallel structural strike is overcome by using the attribute coherence (see Chapter 8).

Because an alignment of event terminations on a horizontal section indicates the strike of a fault, the picking of a fault on a horizontal section provides a contour on the fault plane. Thus picking a fault on a succession of suitably spaced horizontal sections constitutes an easy approach to fault plane mapping. The faults evident in Figure 3-14 have been mapped in this way.

Fig. 3-17. Horizontal section at 1000 ms, from Gulf of Mexico Concentric Circle Shoot, showing many radial faults surrounding a salt dome. (Courtesy Tensor Geophysical Service Corporation.)

Downloaded 25 Jun 2012 to 95.28.162.50. Redistribution subject to SEG license or copyright; Terms of Use: http://segdl.org/

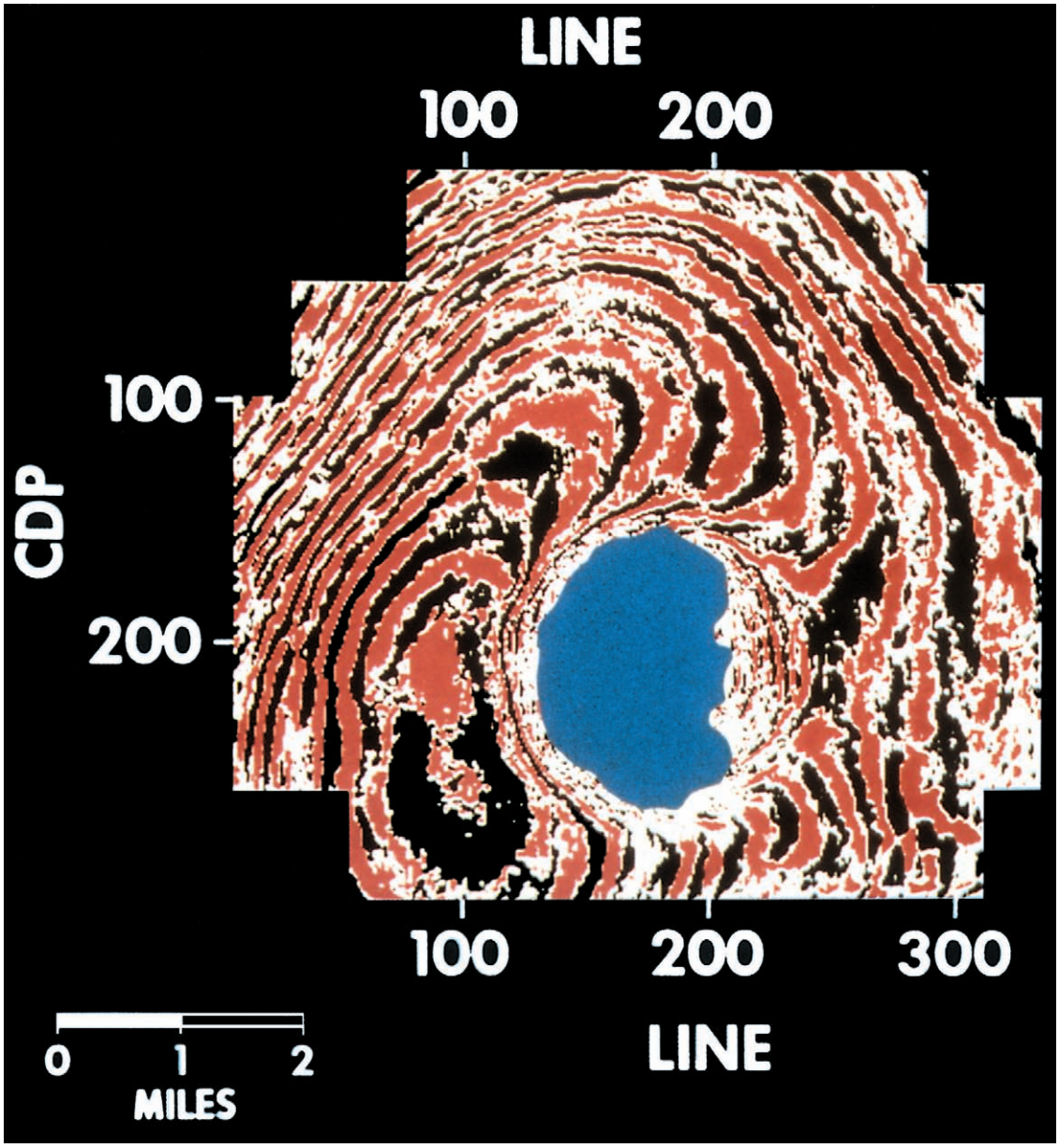

Fig. 3-18. Horizontal section at 3252 ms from Eugene Island area of Gulf of Mexico showing interpreted shape of salt plug. (Courtesy Hunt Oil Company.)

In the lower right corner of the horizontal section at 2260 ms (Figure 3-14) two fault blocks show events of quite different widths. This is the effect of dip which was explained by Figure 3-7. We also see a similar effect of dip in Figure 3-13 where the faults are mostly traced by narrow sinuous events striking approximately north-south.

Figure 3-15 shows a variety of structural features: prominent faults, more subtle faults, culminations, and various character changes. It is very important that horizontal sections play their proper role in fault interpretation. In the early stages of structural interpretation of a prospect, the major faults will be identified on some widely-spaced vertical sections. The way in which these faults join up into a fault framework should then be established from horizontal sections. This is part of the overall recommended procedure of Figure 3-32. Lineations of event terminations will normally link the faults already recognized vertically. Figures 3-16 and 3-17 show clearly visible faulting that evidently could be used in this way.

Today's interactive workstations help in the coordinated use of vertical and horizontal sections by providing the capability of cross-posting. When a fault is picked on a vertical section, its intersection will appear on an intersecting horizontal section.

Downloaded 25 Jun 2012 to 95.28.162.50. Redistribution subject to SEG license or copyright; Terms of Use: http://segdl.org/

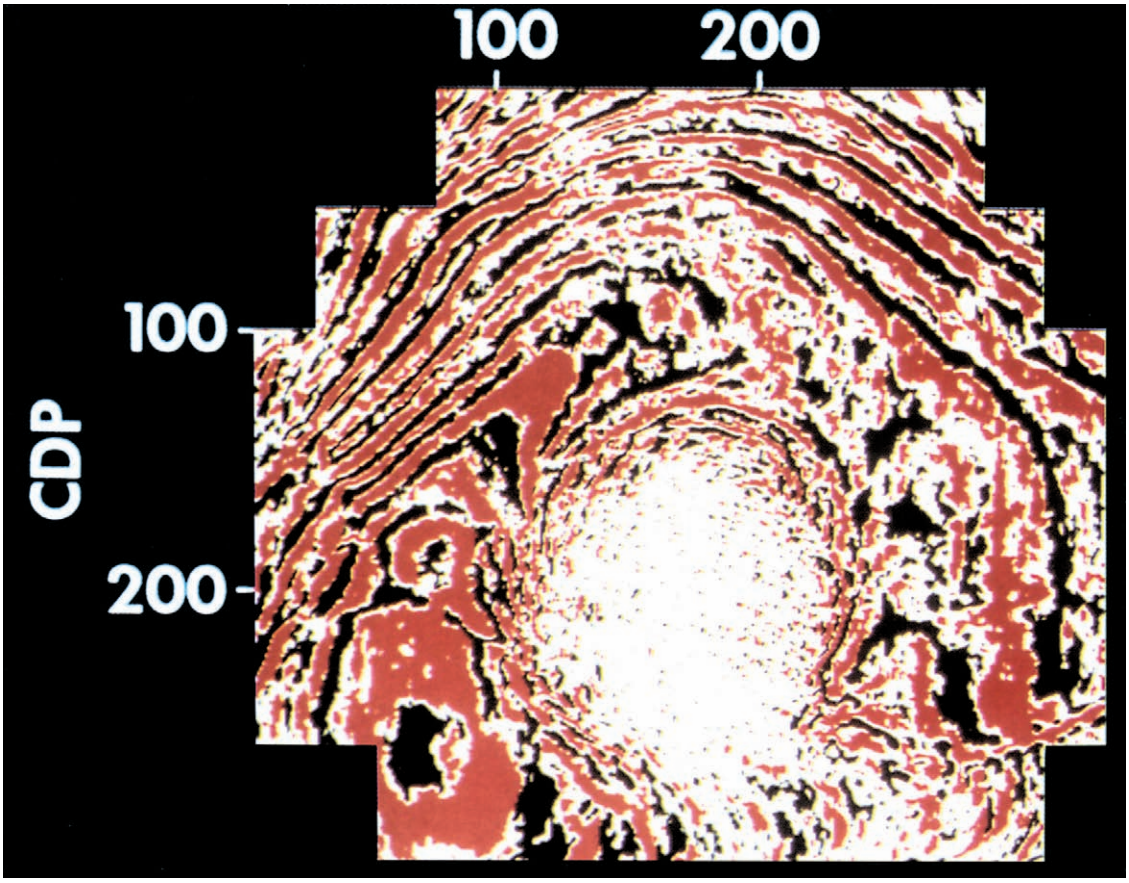

Fig. 3-19. Horizontal section at 3760 ms from Eugene Island area of Gulf of Mexico. (Courtesy Hunt Oil Company.)

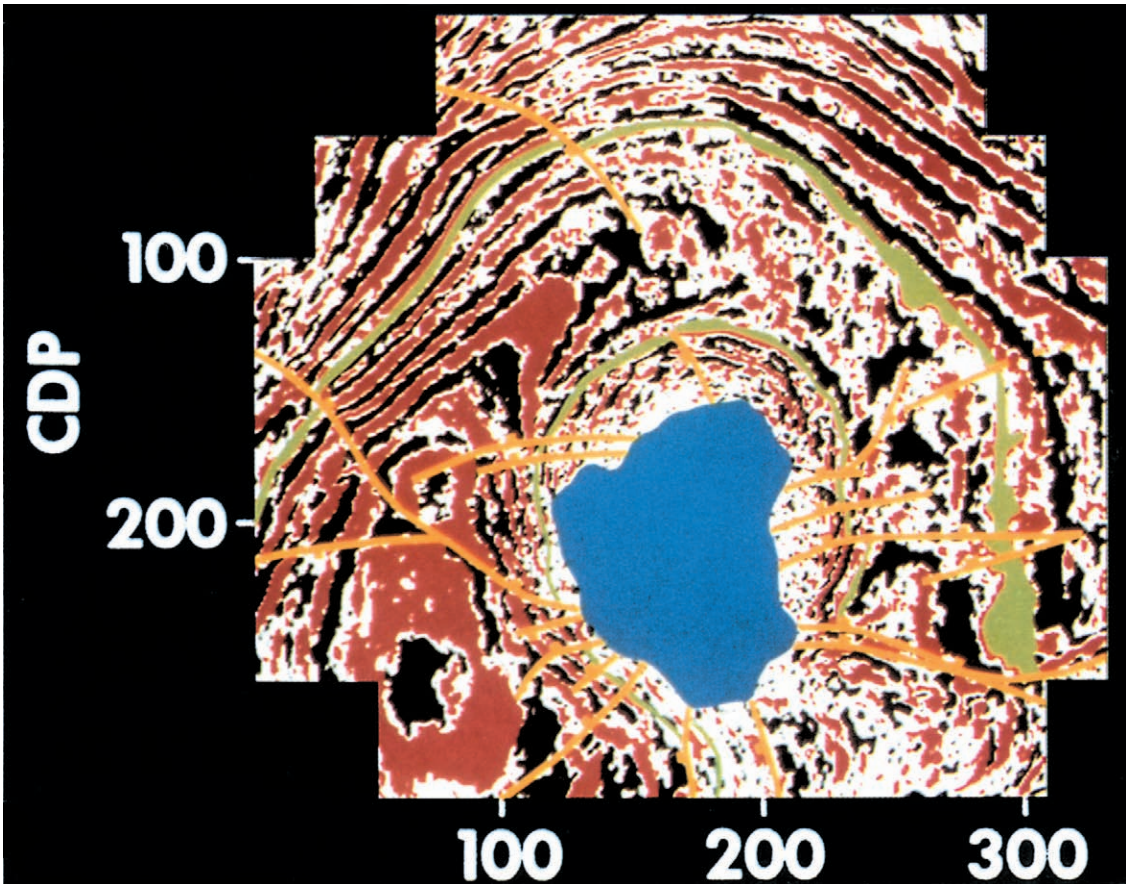

Fig. 3-20. Same horizontal section as Figure 3-19 with interpretation of faults and the green horizon. (Courtesy Hunt Oil Company.)

Downloaded 25 Jun 2012 to 95.28.162.50. Redistribution subject to SEG license or copyright; Terms of Use: http://segdl.org/

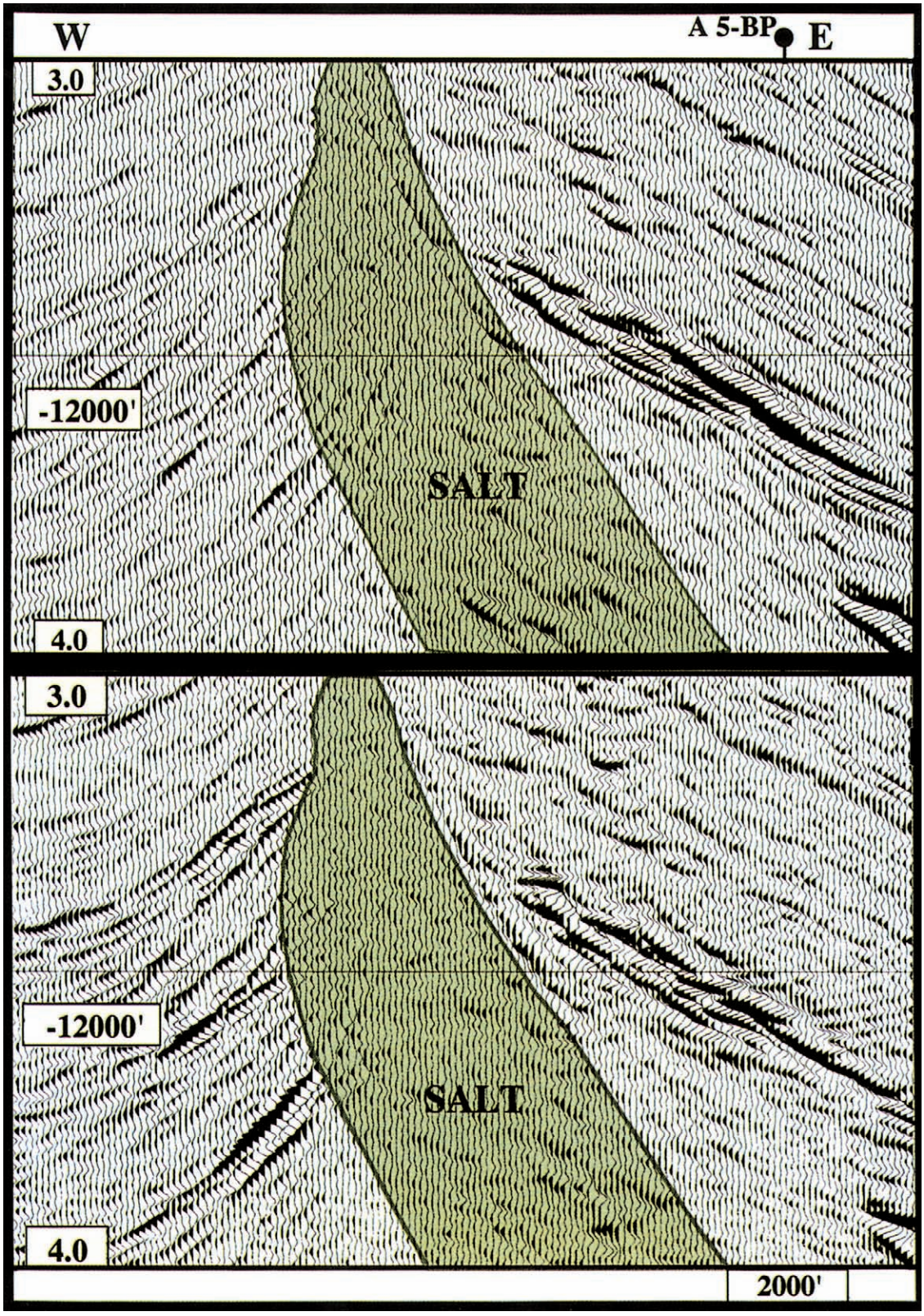

Fig. 3-21. Line 556 from the E-W survey at Bullwinkle (upper section). This line is extracted along the inline direction of this survey, hence the shooting direction is dip to the salt/sediment contact. Line 556 from the N-S survey at Bullwinkle (lower section). This line is extracted from the crossline direction of this survey. The shooting direction is perpendicular to the plane of the section and therefore strike to the salt/sediment contact. Note the improved sediment image along the western side of the overhung salt. This is attributed to less salt-related ray path distortion. (Courtesy Shell Oil Company.)

Downloaded 25 Jun 2012 to 95.28.162.50. Redistribution subject to SEG license or copyright; Terms of Use: http://segdl.org/

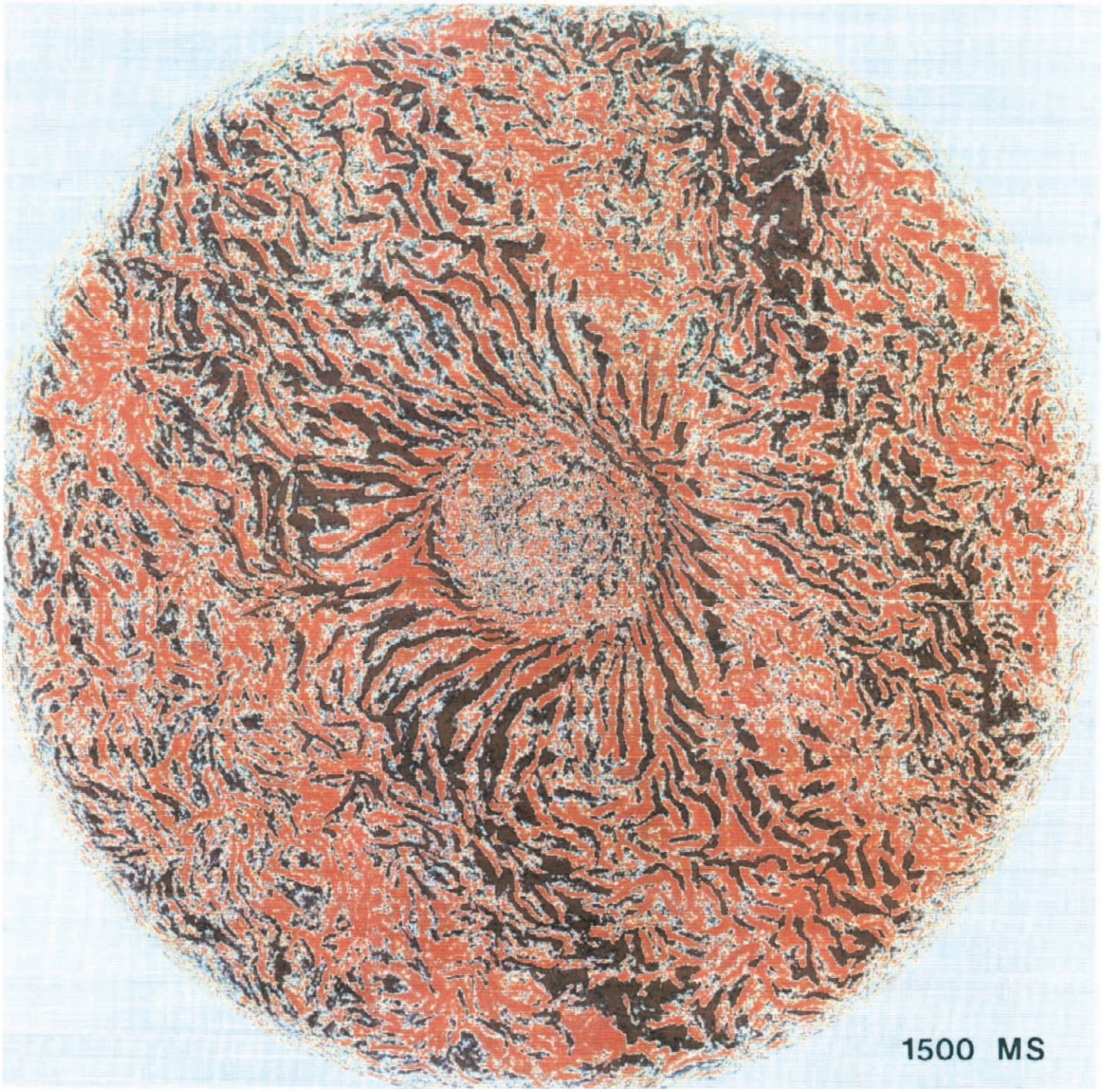

Fig. 3-22. Time slice 1500 ms, from a circular 3-D survey in the North Sea. The shattered appearance results from the shattering of a thin limestone. (Courtesy Mobil North Sea Limited.)

Downloaded 25 Jun 2012 to 95.28.162.50. Redistribution subject to SEG license or copyright; Terms of Use: http://segdl.org/

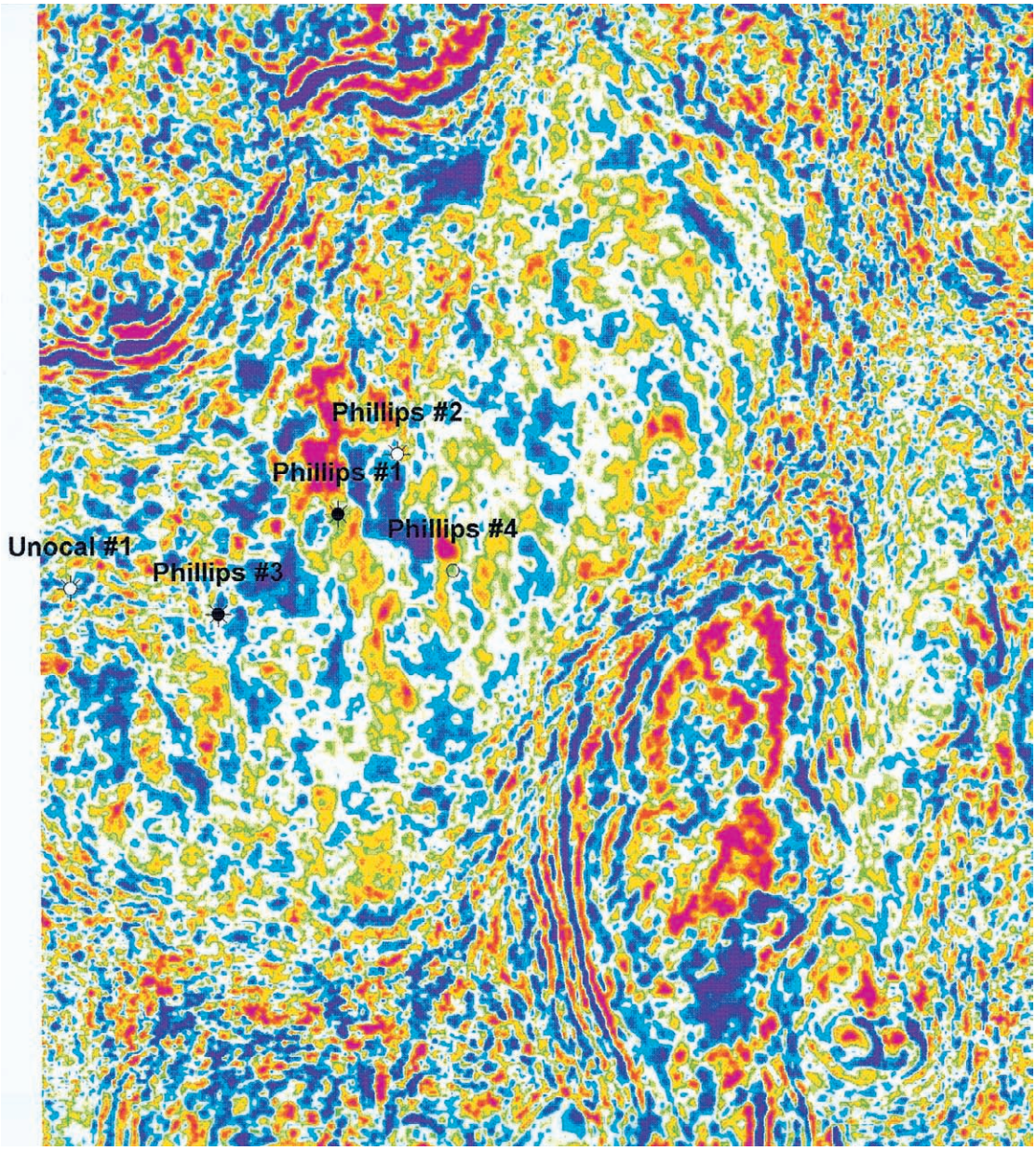

Fig. 3-23. Depth slice 4530 meters, from 3-D pre-stack depth migrated data volume covering the Gulf of Mexico Mahogany prospect. (Courtesy Diamond Geophysical Service Corporation.)

When faults have been picked on several vertical and horizontal sections, the faults can be displayed as surfaces to check their geological validity.

Interpretation in the Vicinity of Salt

The horizontal section of Figure 3-18 shows a rim syncline surrounding a salt diapir. The narrow events around the salt indicate the steep dips near the intrusion. Figures 3-19 and 3-20 show a deeper horizontal section from the same volume without and with interpretation. The horizon of interest, marked in green on Figure 3-20, is intersected twice, once on either side of the rim syncline. The faulting at this level, marked in yellow, is complex but can be seen fairly well on this one horizontal section. From pre-existing 2-D data in the area only one of these faults had been identified (Blake et al., 1982).

Interpretation of seismic reflection terminations against salt is a very important matter because many hydrocarbon traps are found in this structural position.

Downloaded 25 Jun 2012 to 95.28.162.50. Redistribution subject to SEG license or copyright; Terms of Use: http://segdl.org/

Numerous data collection and processing developments have been aimed at this problem (French, 1990). One-pass 3-D migration is considered preferable to the two-pass approach.

Case History 10 in Chapter 14 discusses the importance of precise definition of the salt/sediment interface and shows success in doing so. Figure 3-21 also addresses this issue and demonstrates that, by collecting the data in a direction strike to the salt/sediment interface, the definition of reflections terminating at the salt is significantly improved (O'Connell, Kohli, and Amos, 1990).

Figure 3-22 shows time slice 1500 ms from a circular 3-D survey in the North Sea. In the center a salt diapir is visible. Collecting data in circles around a circular salt body means that the collection direction is consistently strike to the salt/sediment interface. The myriad of short arcuate features on Figure 3-22 show the effects of shattering of a thin limestone layer encased in shale.

Depth migration and pre-stack depth migration in 3-D are now economically feasible and have been used extensively for imaging under salt (Chapter 10 and Appendix A). It is the abrupt large velocity contrasts that make this more elaborate migration necessary. After such processing the whole data volume is in depth and thus horizontal sections become **depth slices**. Figure 3-23 shows a depth slice under the Mahogany salt sill in the Gulf of Mexico and the successful wells.

Composite Displays

The interpreter of 3-D data is not restricted to single slice displays. Because the work is done with a data volume, composite displays can be helpful in appreciating three-dimensionality and also in concentrating attention on the precise pieces of data that provide insight into the problem at hand.

Figure 3-24 is a composite of horizontal and vertical sections spliced together along their line of intersection. The vertical section shows that the circular structure is a syncline. The horizontal section pinpoints the position of its lowest point. The fault on the left of this structure can be followed across the horizontal section. Figure 3-25 provides a different view of the structure. The same horizontal section is here spliced to the portion of the vertical section above in the volume.

It is possible to make cube displays showing, simultaneously, three orthogonal slices through the volume (Figures 1-20 and 3-26). These can certainly aid in the appreciation of three-dimensionality but two of the faces of any cube displayed in this way will always be distorted. An adaptation of the cube display concept is presented in Figure 3-27 and is known as the **chair**; it is really just the cube with a vertical section added above the horizontal section at the back. On Figure 3-27 the three-dimensional shape of a growth fault can be followed easily.

Figure 3-28 is a different kind of chair display. It is less dramatic than the chair of Figure 3-27 but probably more useful because none of the sections are distorted. The fault on the left can be followed clearly across the horizontal section indicating that the fault visible on line 75 (top, Figure 3-28) is the same as seen on line 110 (bottom, Figure 3-28). The other faults have a distinctly different azimuth and also traverse a shorter distance.

Figures 3-29 and 3-30 illustrate the study of a trio of normal faults. In Figure 3-29 one horizon has been tracked indicating the interpreted correlation across the faults. At the bottom of this figure a portion of the data from each of the four fault blocks is enlarged and again carries the interpreted track. Each block has been adjusted vertically to bring the track segments into continuity so that the correlation between these blocks of data can be assessed easily. Note how this display accentuates the apparent growth on the center fault of the three. In Figure 3-30 the composite horizontal and vertical section display permits the study of the horizontal extension of each of these three faults. A display customized to a problem usually helps significantly in the solution of that problem.

Downloaded 25 Jun 2012 to 95.28.162.50. Redistribution subject to SEG license or copyright; Terms of Use: http://segdl.org/

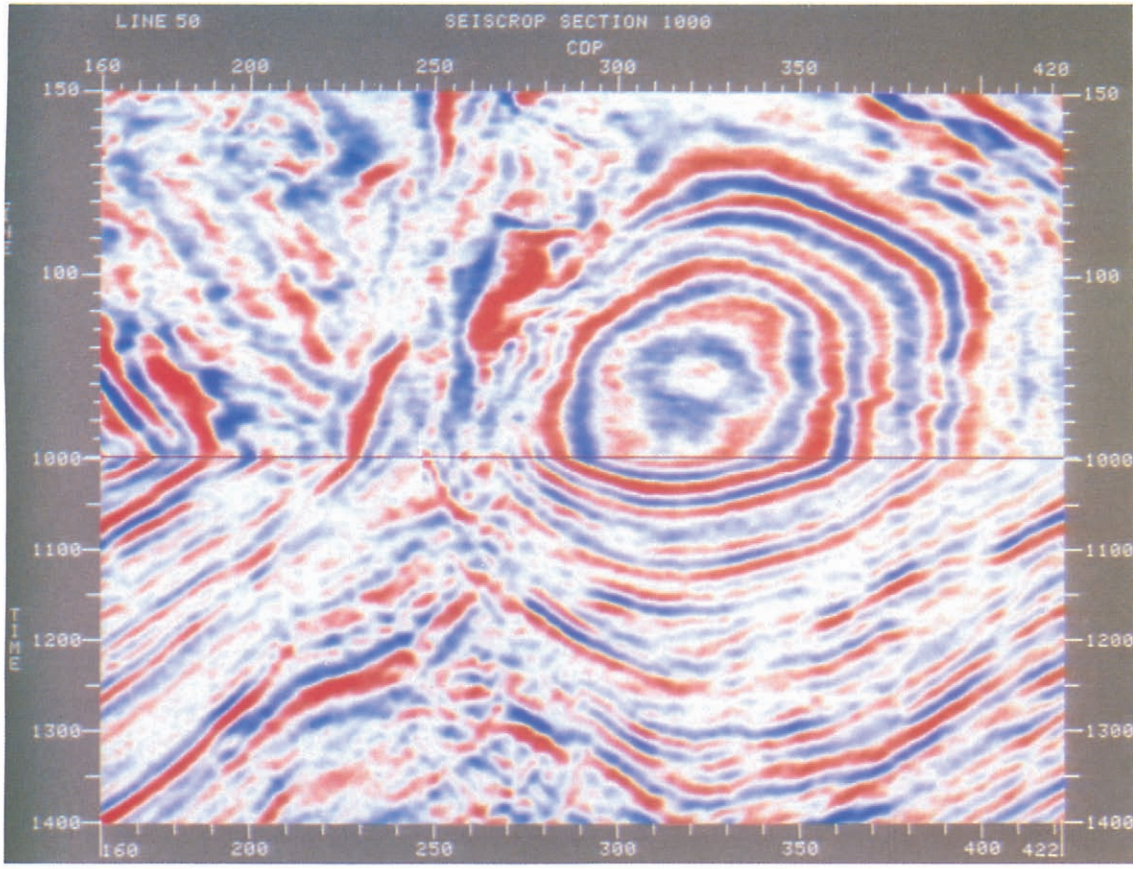

Fig. 3-24. Composite display of horizontal and vertical sections from onshore Europe. Vertical section segment lies beneath horizontal section.

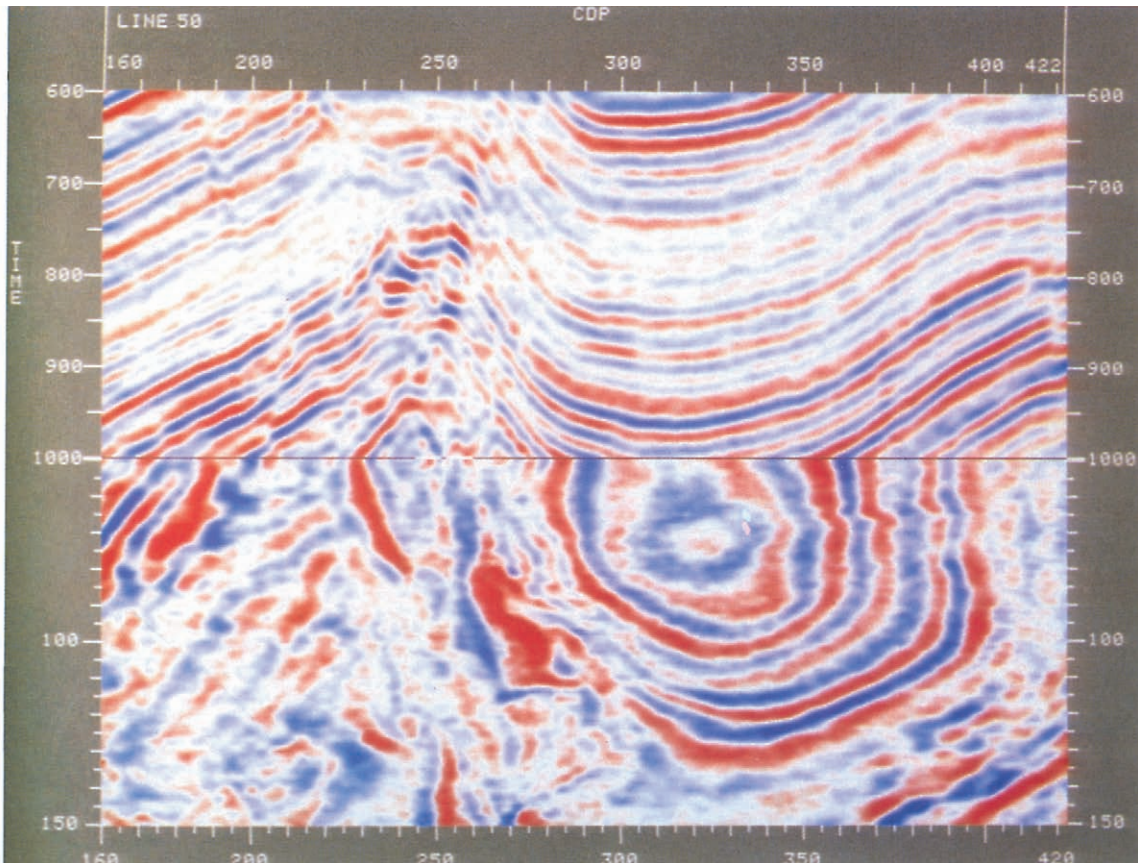

Fig. 3-25. Composite display of horizontal and vertical sections from onshore Europe. Vertical section segment lies above horizontal section.

Downloaded 25 Jun 2012 to 95.28.162.50. Redistribution subject to SEG license or copyright; Terms of Use: http://segdl.org/

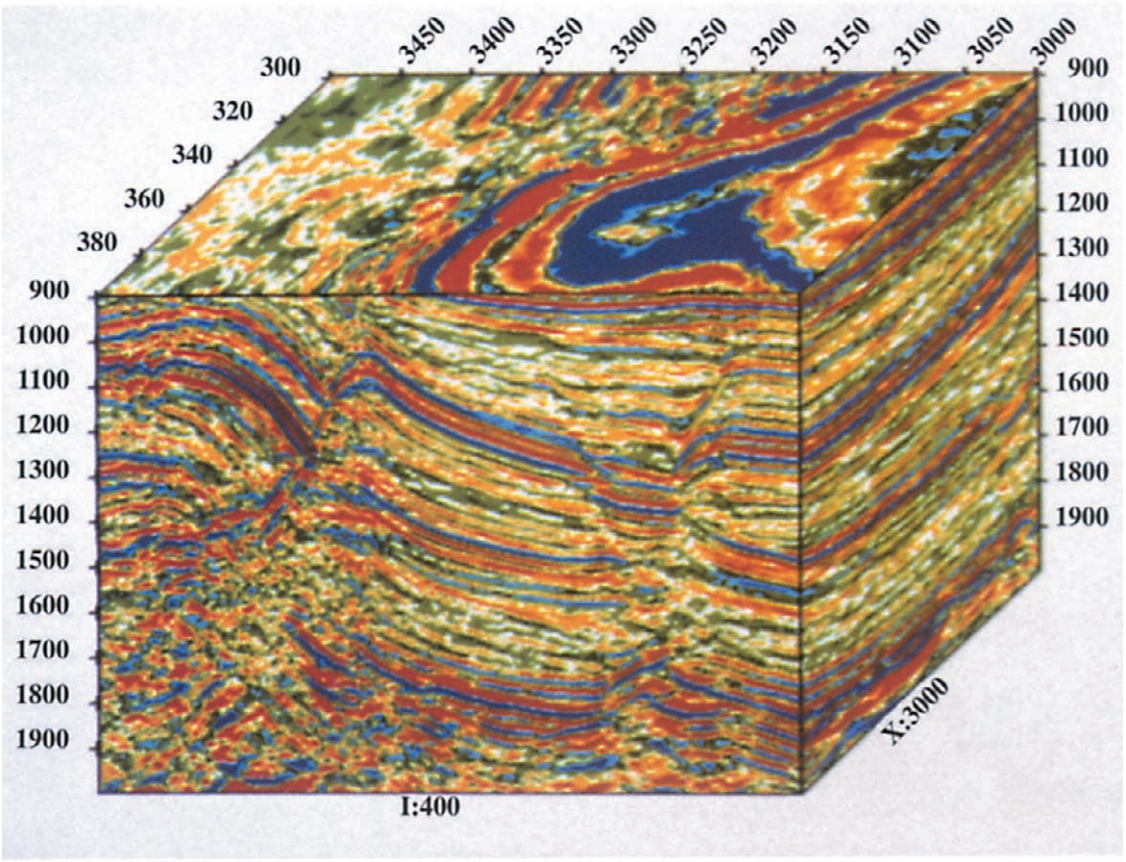

Fig. 3-26. Cube display made of two orthogonal vertical sections and one horizontal section. (Courtesy Western Atlas International.)

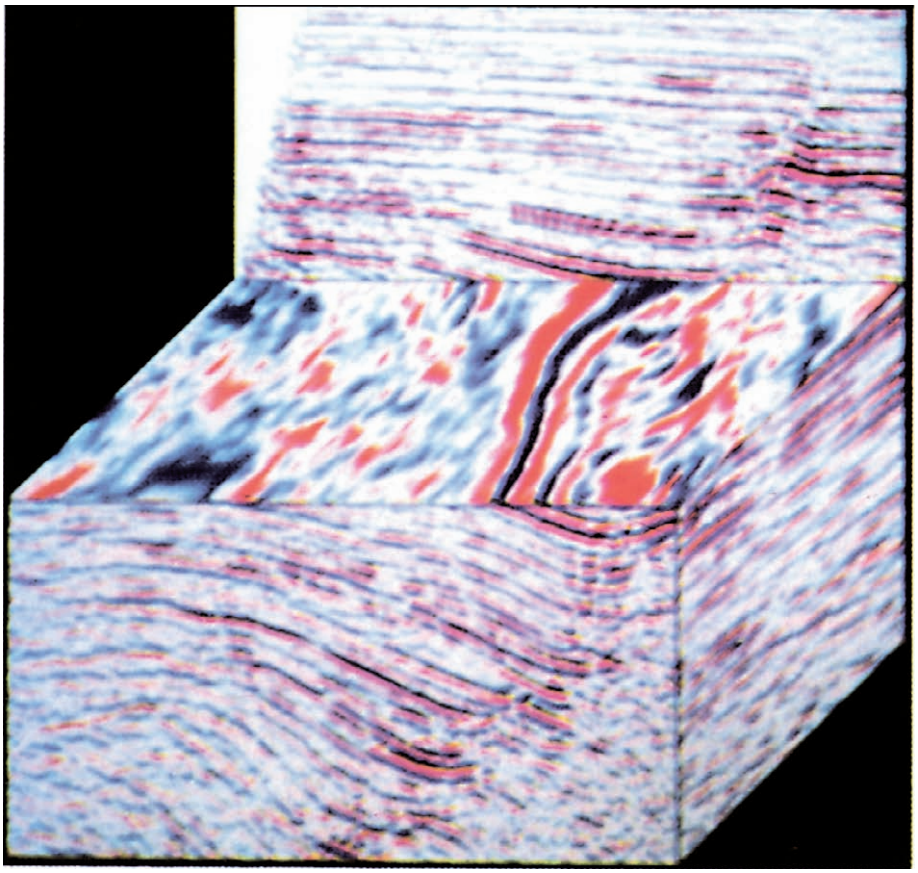

Fig. 3-27. Chair display of Gulf of Mexico data made of two lines, one crossline and one horizontal section. (Courtesy Geophysical Service Inc.)

Downloaded 25 Jun 2012 to 95.28.162.50. Redistribution subject to SEG license or copyright; Terms of Use: http://segdl.org/

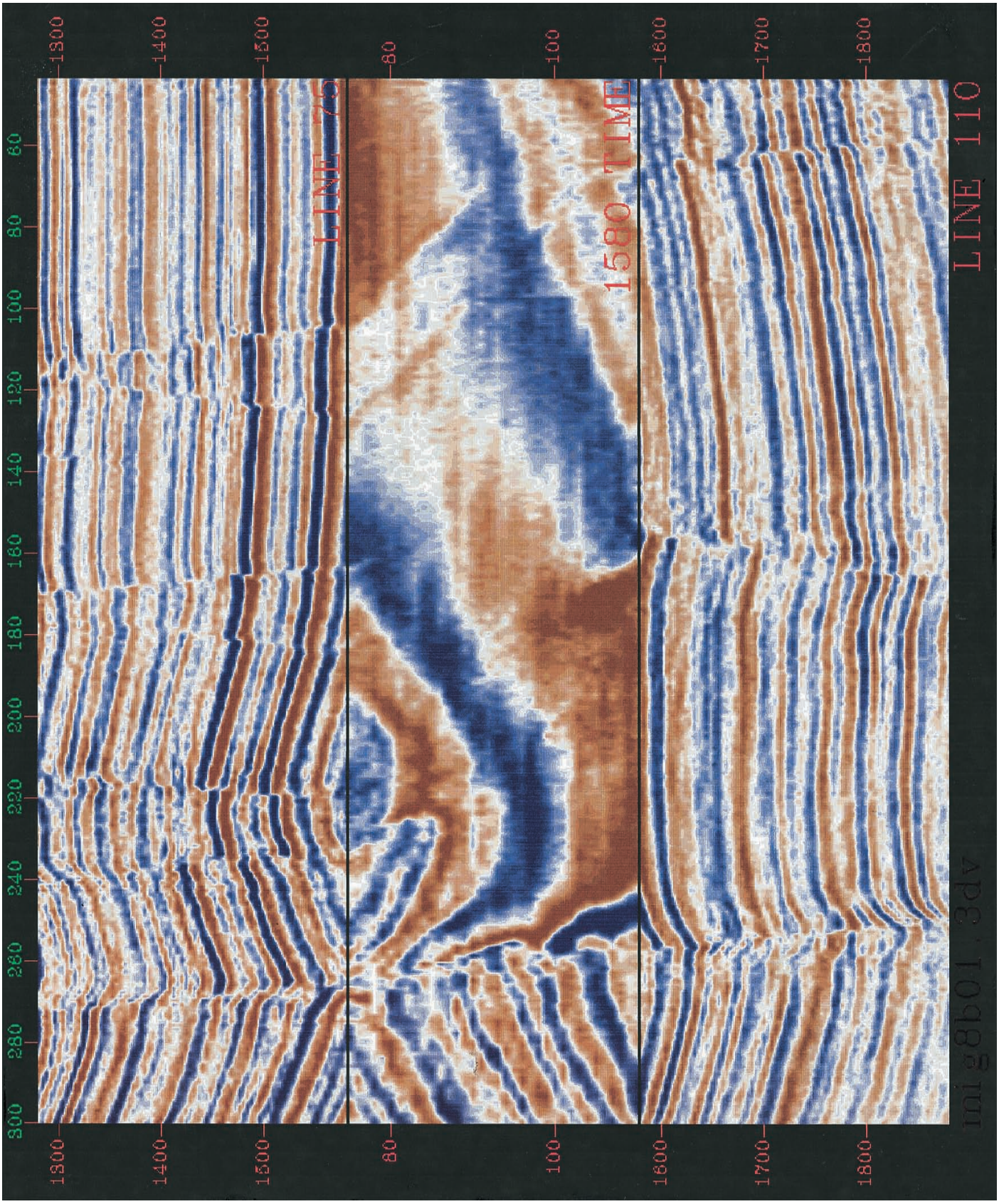

Fig. 3-28. Chair display made of two vertical sections and one horizontal section. Compare this with Figure 3-27 and note that here all the three sections are undistorted. (Courtesy Landmark Graphics Corporation.)

Downloaded 25 Jun 2012 to 95.28.162.50. Redistribution subject to SEG license or copyright; Terms of Use: http://segdl.org/

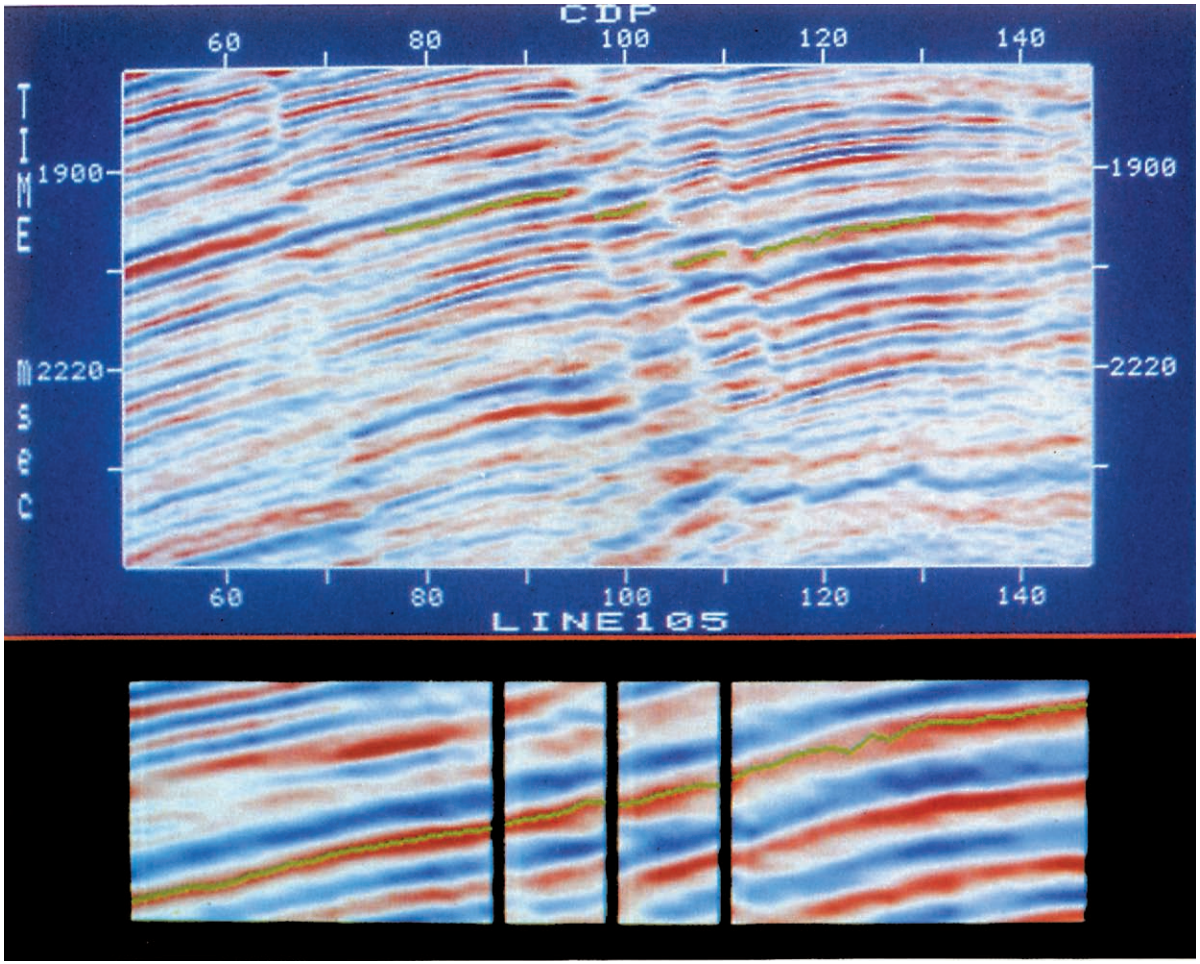

Fig. 3-29. Vertical section and magnified portions thereof designed to study fault correlations offshore Trinidad. (Courtesy Texaco Trinidad Inc.)

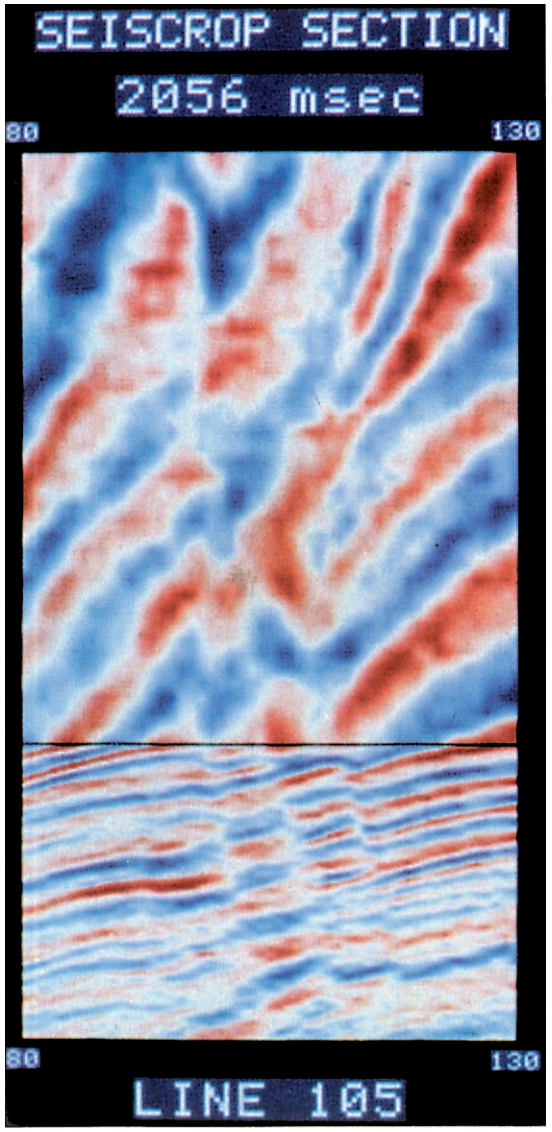

Fig. 3-30. Composite display of horizontal and vertical sections from offshore Trinidad showing horizontal extent of faults studied in Figure 3-28. (Courtesy Texaco Trinidad Inc.)

Downloaded 25 Jun 2012 to 95.28.162.50. Redistribution subject to SEG license or copyright; Terms of Use: http://segdl.org/

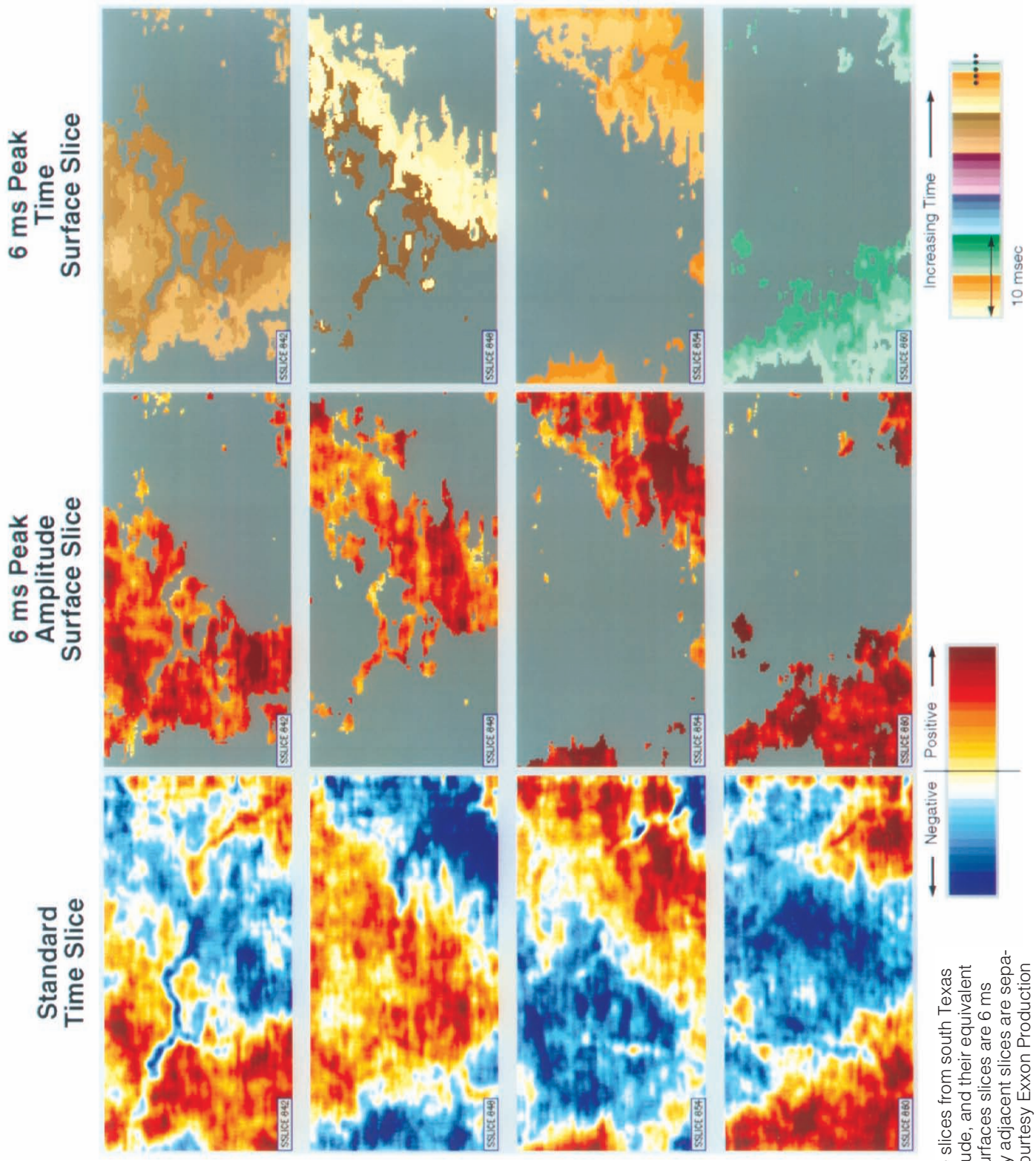

Fig. 3-31. Surface slices from south Texas in time and amplitude, and their equivalent time slices. The surfaces slices are 6 ms thick and vertically adjacent slices are separated by 6 ms. (Courtesy Exxon Production Research Company.)

Downloaded 25 Jun 2012 to 95.28.162.50. Redistribution subject to SEG license or copyright; Terms of Use: http://segdl.org/

Interpretation Procedures

The interpreter of 3-D data has a real opportunity to generate more accurate subsurface time and depth structure maps, but to do so a large amount of data must be studied. Furthermore *all* the data must be used to ensure proper information extraction. Thus the interactive workstation is an essential data management tool.

Initially the interpreter will pick major faults and make a preliminary horizon interpretation on a selected set of vertical sections in the line and crossline directions, for example on a one-kilometer grid. These fault and horizon picks will then be connected using a selected set of time slices. This framework becomes the seed points for input to the autotracker. The autotracker completes the horizon on every data point and provides necessary precision. When the interpreter encounters a problem in understanding the data at a particular location, reference to vertical sections through that point in line, crossline, and other directions is made. Arbitrary lines may be specially extracted from the data volume for that purpose. Experience with time slices (horizontal sections) underlines the value of the strike perspective discussed earlier. Continuing experience in 3-D interpretation consultation has taught the author that proper use of time slices is one of the most difficult but important hurdles for those wishing to master interpretation technology. Not only do time slices provide an essential view of the data which reveals various subtle features, they also add significant efficiency to the total project. Once some vertical sections have been examined to establish general structural relationships, spatial continuity should be followed on appropriate time slices. These directly drawn structural contours then give the autotracker plenty of seed points to tie it down. A successful way of building time slices into the interpretation procedure is to use composite displays such as Figures 3-24 and 3-25, chair displays such as Figure 3-28, or volumetric displays like Figures 3-26 and 3-27. In this way the relationship between horizontal and vertical section is apparent.

Another way of incorporating the efficiency of the strike view into interpretation procedures is to use **surface slices** (Stark, 1996). A surface slice displays either time or amplitude of one chosen point on the seismic waveform, for example the crest of a peak, over a defined time interval (typically three samples). A surface slice can thus, in a sense, be regarded as a thick time slice. However, the surface slice displays one data phase only over that thickness, in contrast to the time slice which shows all seismic phases at one unique time. A surface slice thus has no frequency dependence and provides true dip magnitude. Figure 3-31 contains a sequence of time slices and the equivalent amplitude surface slices and time surface slices. The surface slices are 6 ms thick and contain only peaks, either their horizon amplitudes or their travel times. Slices on the same row are from the same time, and the rows are separated by 6 ms. Vertically adjacent surface slices are thus independent and it can be seen that the edges of the colored areas fit together. This is the procedure with surface slices — a kind of jigsaw puzzle of horizon segments.

Figure 3-32 charts a recommended procedure for 3-D interpretation using an interactive workstation. The interactive capabilities required to follow this procedure include

(1) automatic and manual tracking of horizons on vertical and horizontal sections;
(2) automatic spatial horizon tracking and editing through a 3-D data volume;
(3) correlation of vertical sections with well data;
(4) extraction, storing and manipulation of seismic amplitudes;
(5) manipulation of maps;
(6) flexible use of color; and
(7) extraction and use of seismic attributes.

Downloaded 25 Jun 2012 to 95.28.162.50. Redistribution subject to SEG license or copyright; Terms of Use: http://segdl.org/

Fig. 3-32. Recommended interactive 3-D interpretation procedure.

RECOMMENDED PROCEDURE

1. Preview of data on composite displays and movies.

2. Horizon identification at wells.
   Assessment of data phase and polarity.

3. Recognition of major faults on widely-spaced vertical sections.

4. Fault framework by tying together with horizontal sections.

5. Initial horizon control using vertical and horizontal sections.
   Horizontal sections provide efficiency of coverage.

6. Automatic spatial tracking to complete horizon on every point.
   Autotracking provides precision picking.
   Get to this point as quickly as possible.

7. Scrutiny of intermediate horizon products for new features and for validation of tracking:
   - Color-posted time structure (including lineations of untracked points)
   - Color-posted horizon slice (for lineations and patterns in amplitude)
   - High spatial frequency residual
   - Dip magnitude and azimuth, difference, edge detection and illumination

8. Revision of horizons and faults, and rerun of autotracking.

9. Final time structure maps and horizon slices with chosen amounts of gridding or smoothing.

10. Isochron, isopach and depth maps.

11. Detailed stratigraphic and reservoir studies.

Some of the important principles implicit in the procedure of Figure 3-32 are that you

- understand the phase of data *before* embarking on the mainstream interpretation,
- use horizontal sections to full advantage; benefit from the efficiency of strike,
- study only as many vertical and horizontal sections as is necessary to provide initial input control for automatic spatial tracking,
- use intermediate horizon products to full advantage for refining the interpretation (Chapter 8),
- do not smooth any map or map-style product until degree of smoothing required can be judged intelligently, and
- engage in stratigraphic and reservoir studies in order to get the most out of the data (Chapters 4 and 7).

Autotracking is central to the procedure of Figure 3-32. More discussion on its use appears later in this chapter and also in Chapter 8. Today's autotrackers are fairly robust and will handle poorer data than many people think. However, there are always horizons of interest that have continuity too poor for acceptable autotracker performance.

In 3-D interpretation we studiously avoid drawing old-fashioned phantom horizons. Figure 3-33 shows the preferable alternative. We track a horizon above the objective horizon and displace it down with a constant time shift. Then we estimate

Downloaded 25 Jun 2012 to 95.28.162.50. Redistribution subject to SEG license or copyright; Terms of Use: http://segdl.org/

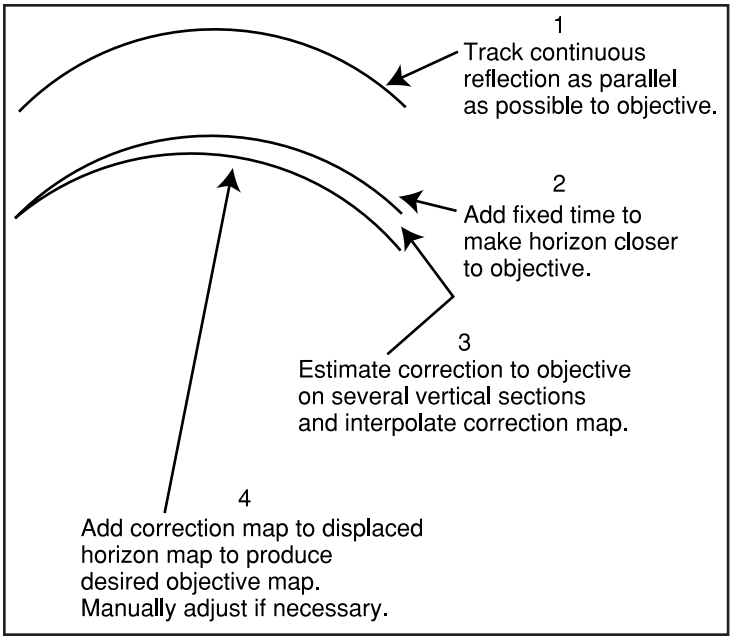
1
Track continuous reflection as parallel as possible to objective.
2
Add fixed time to make horizon closer to objective.
3
Estimate correction to objective on several vertical sections and interpolate correction map.
4
Add correction map to displaced horizon map to produce desired objective map. Manually adjust if necessary.

Fig. 3-33. Method for establishing a horizon through poor data or along an unconformity — the 3-D equivalent of a phantom horizon.

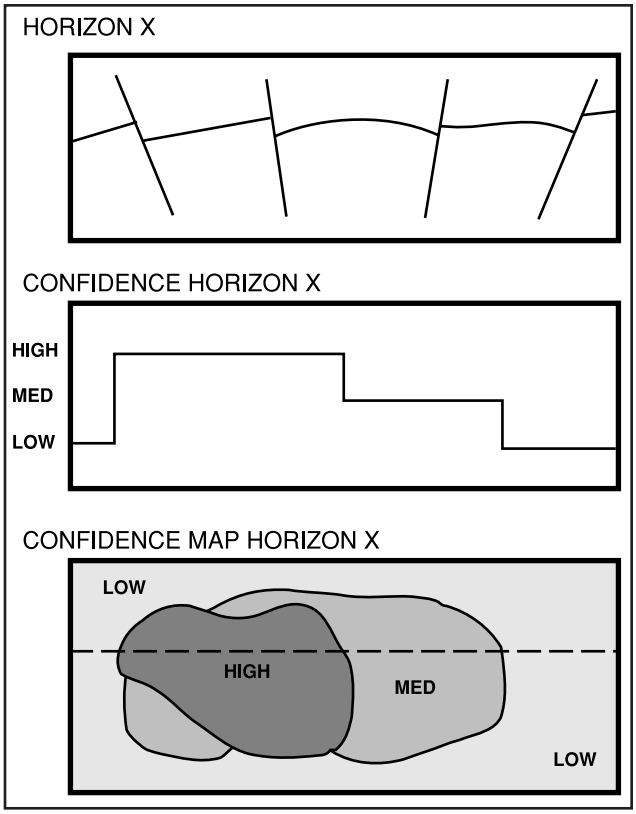

Fig. 3-34. Method for generating a confidence map to help qualify interpreted results.

the mistie between this and the desired horizon at several locations and interpolate a mistie, or correction, map. By adding this to the displaced horizon map we should obtain something close to what is desired. We can then manually adjust as necessary, but the amount of manual work should be small compared with the traditional manual approach for the whole project.

Figure 3-34 illustrates a way of generating a confidence map to communicate to managers, engineers, clients, and others the confidence we have in the interpreted maps we produce. Qualitative assessment of confidence, here using three levels, is made occasionally based on data quality and whatever interpretation difficulties may occur. The resultant interpolated confidence map can be included with final maps for the benefit of those who later use them.

Advantages and Disadvantages of Different Displays

With increasingly successful amplitude preservation in seismic processing, interpreters are increasingly suffering from the limited optical dynamic range of conventional seismic displays. Too common are the variable area sections where some events of interest are heavily saturated and others have barely enough trace deflection to be visible. This applies to all displays, vertical and horizontal, made with variable area techniques. Horizontal sections, historically, were first made with variable area using

Downloaded 25 Jun 2012 to 95.28.162.50. Redistribution subject to SEG license or copyright; Terms of Use: http://segdl.org/

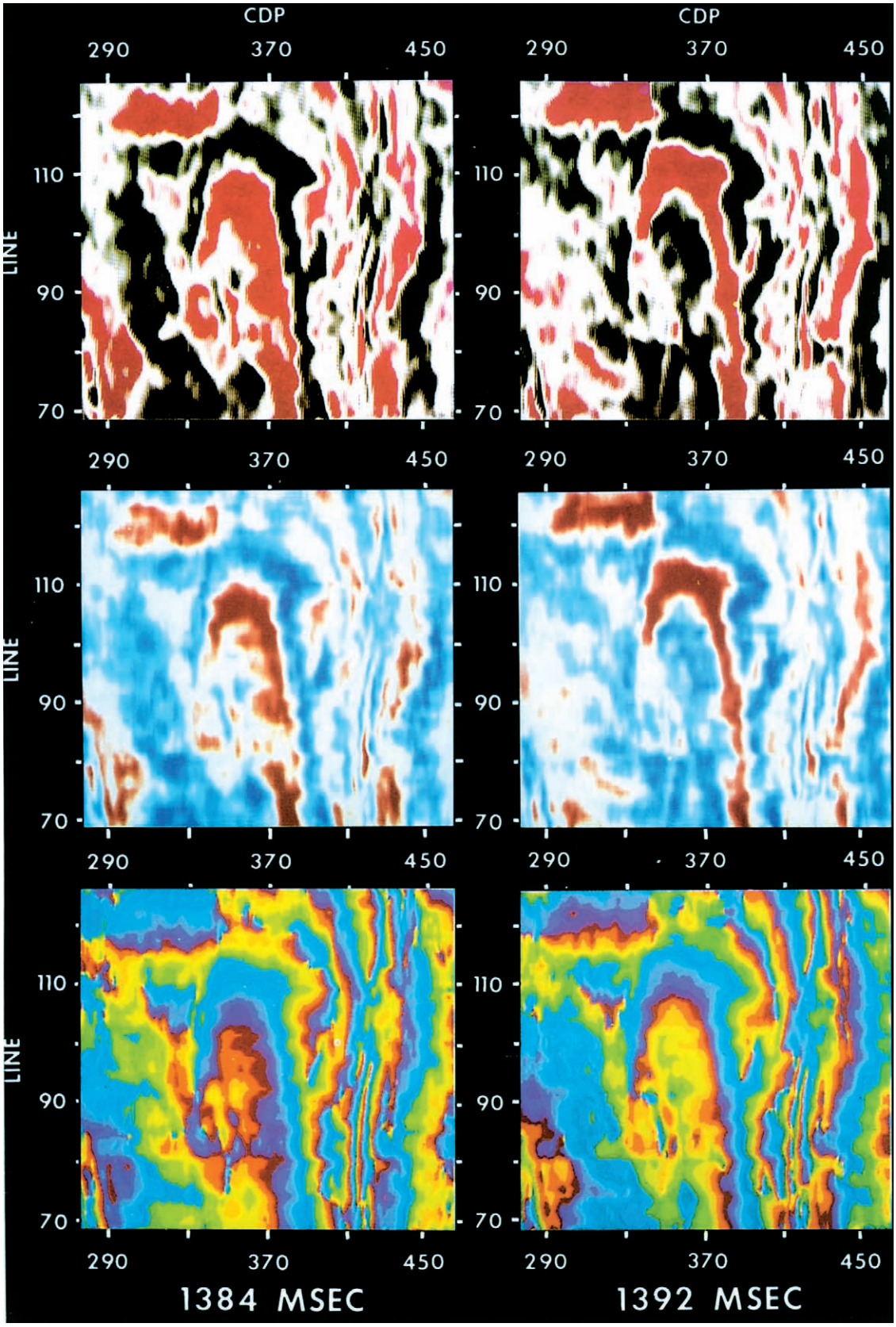

Fig. 3-35. Horizontal sections, 8 ms apart, from Gulf of Thailand, displayed in dual polarity variable area (upper row), with seismic amplitude coded to color (middle row), and with instantaneous phase coded to color (lower row). (Courtesy Texas Pacific Oil Company Inc.)

Downloaded 25 Jun 2012 to 95.28.162.50. Redistribution subject to SEG license or copyright; Terms of Use: http://segdl.org/

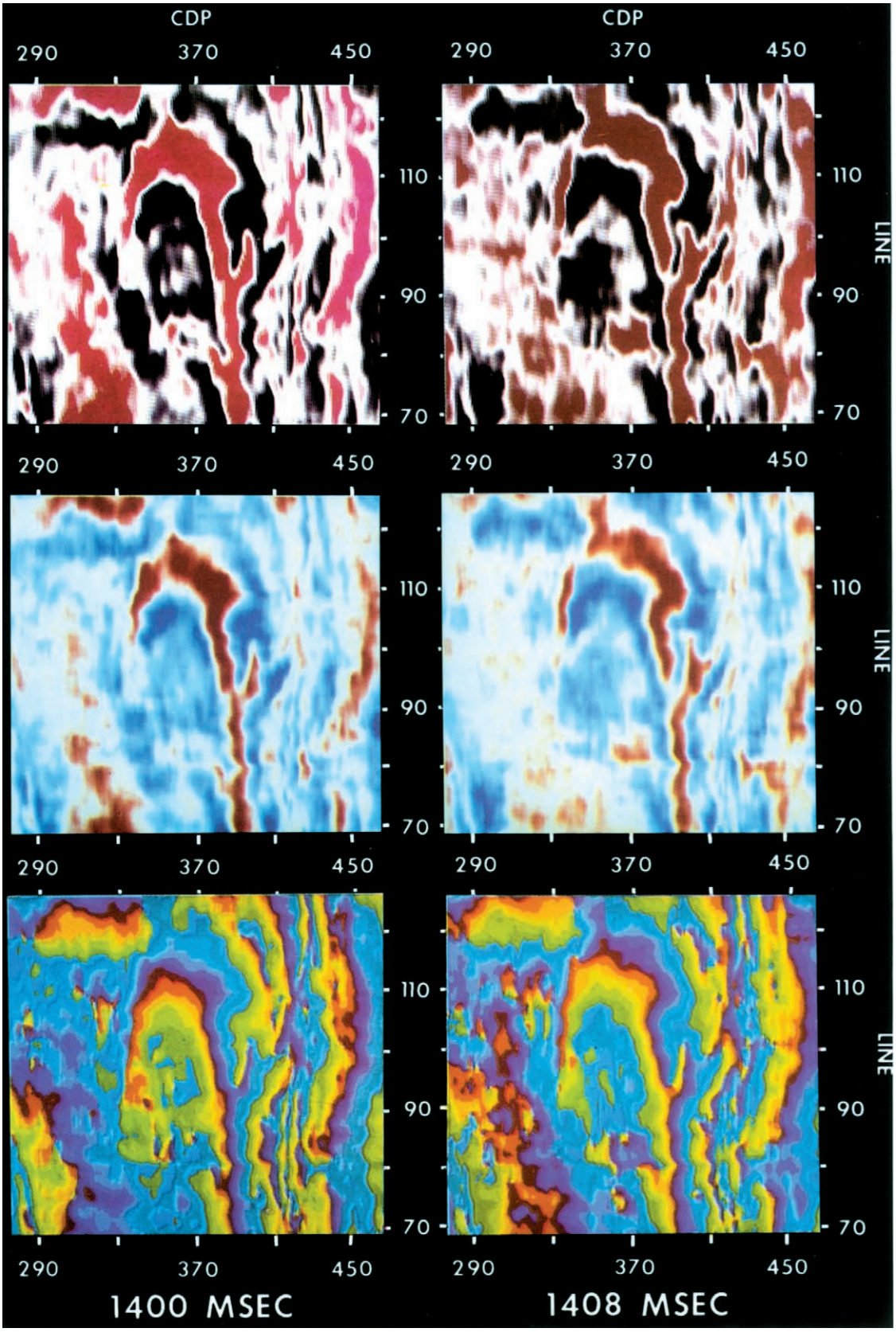

Downloaded 25 Jun 2012 to 95.28.162.50. Redistribution subject to SEG license or copyright; Terms of Use: http://segdl.org/

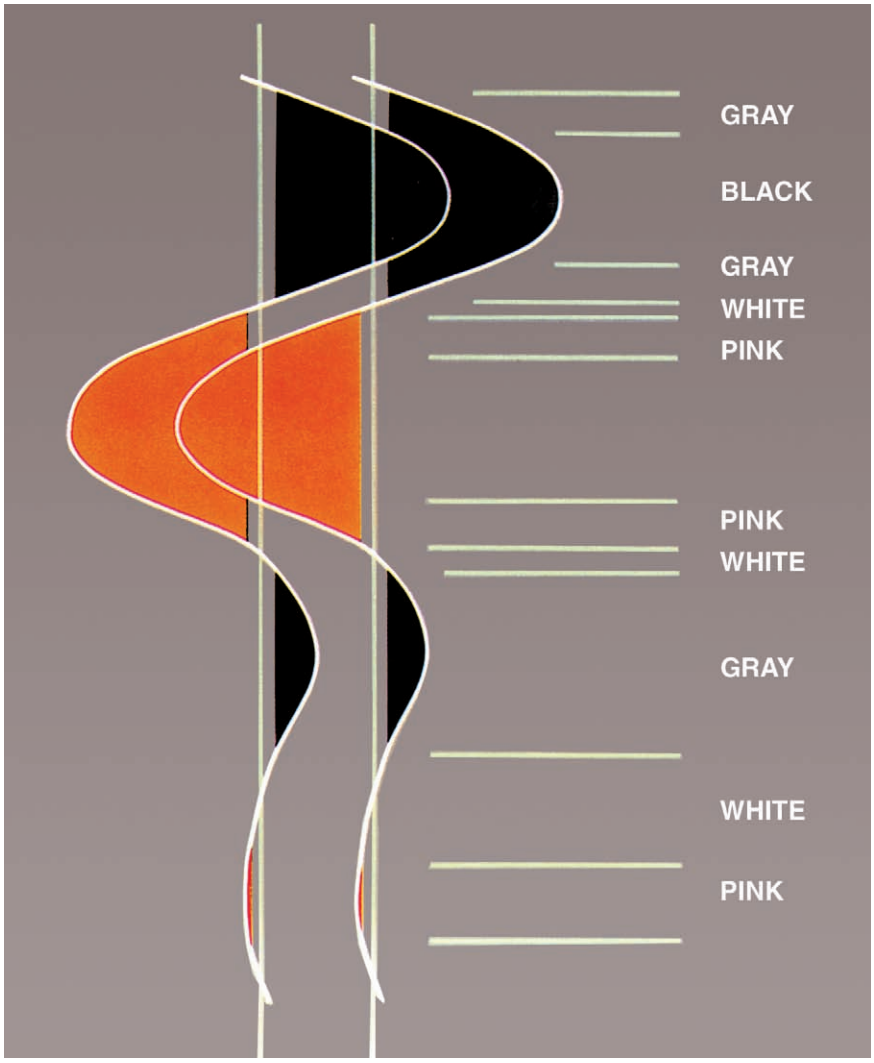

Fig. 3-36. Waveform definition using dual polarity variable area sections. The troughs are shown as excursions to the left; in practice sections are displayed with the troughs rectified and hence swinging to the right.

one polarity only, normally peaks. This soon evolved into dual polarity variable area giving equal weight to peaks and troughs (see Chapter 2). This is exemplified by the upper row of sections in Figure 3-35 and explained in detail by the diagram of Figure 3-36.

Dual polarity variable area provides five clearly discernible amplitude levels. The highest amplitude peaks are saturated and appear as continuous black areas; the medium amplitude peaks do not coalesce and appear as discontinuous black areas which look gray; the lowest amplitudes are below the variable area bias level and appear white; the medium amplitude troughs appear pink; and the highest amplitude troughs are continuous red areas.

If the detail in the seismic waveform provided by dual polarity variable area is inadequate, which is commonly the case today, then the increased dynamic range of full variable intensity color is required. The many ways of using color to interpretive advantage are discussed in Chapter 2. Gradational blue and red is the most useful application; this is illustrated in the middle row of sections in Figure 3-35 and explained in detail by the diagram of Figure 3-37. On such a display the interpreter can see the local amplitude maxima of a peak (or a trough) and draw a contour along the locus of those maxima, thus picking the crest of the seismic waveform.

A further option available to the structural interpreter is horizontal sections displayed in phase, using instantaneous phase derived from the complex trace (Taner, Koehler and Sheriff, 1979). This approach is illustrated by the lower row of sections

Downloaded 25 Jun 2012 to 95.28.162.50. Redistribution subject to SEG license or copyright; Terms of Use: http://segdl.org/

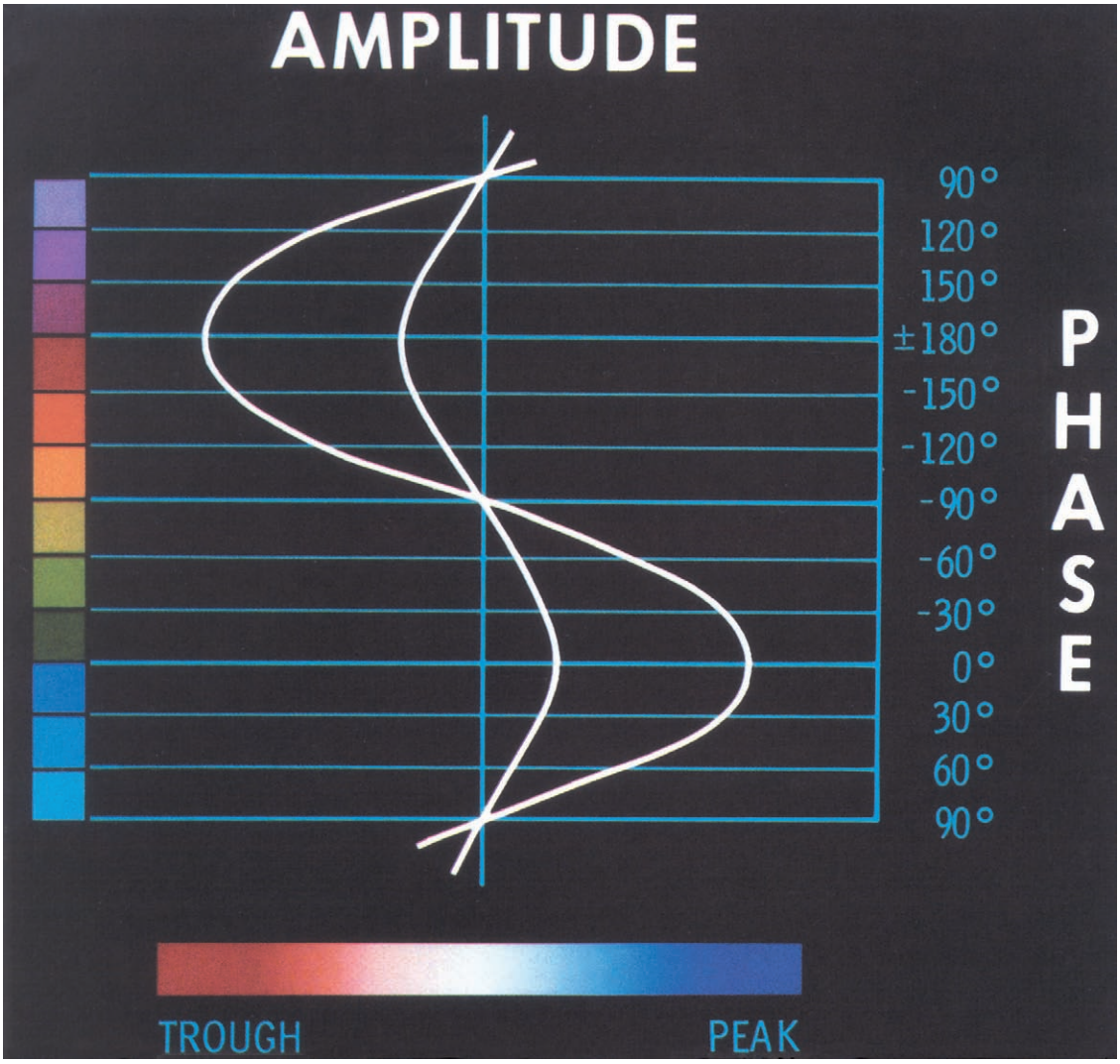

Fig. 3-37. Waveform definition using amplitude and phase color sections.

in Figure 3-35 and explained in detail by the diagram of Figure 3-37. Phase indicates position on the seismic waveform without regard to amplitude, making a phase section like one with fast AGC (Automatic Gain Control), destroying amplitude variations and enhancing structural continuity. A phase section is displayed with color encoded to phase over a given range, for example 30°. Color boundaries occur at significant phase values such as 0° (a peak), 180° (a trough), +90° and –90° (zero crossings). By following a chosen color boundary on a horizontal section displayed in this way, the interpreter is drawing a contour for his horizon map picked at a specific phase point. Thus the interpreter can also, if necessary, compensate for any estimated amount of phase distortion in the seismic wavelet.

Figure 3-38 is a horizontal phase section from a different area; the structural continuity is clear. Figure 3-39 shows the same section in edited phase, a simple modification of the display colors. A few degrees of phase centered on 0° have been colored black; a few degrees of phase centered on 180° have been colored red; and all other phases have been colored white. This gives the appearance of an automatically picked section with all the peaks and troughs at that level indicated. The interpreter simply selects the one he wants. A combination of these phase and amplitude displays is provided by Figure 3-40, where edited phase highlights the positions of the maximum amplitudes of peaks and troughs.

Downloaded 25 Jun 2012 to 95.28.162.50. Redistribution subject to SEG license or copyright; Terms of Use: http://segdl.org/

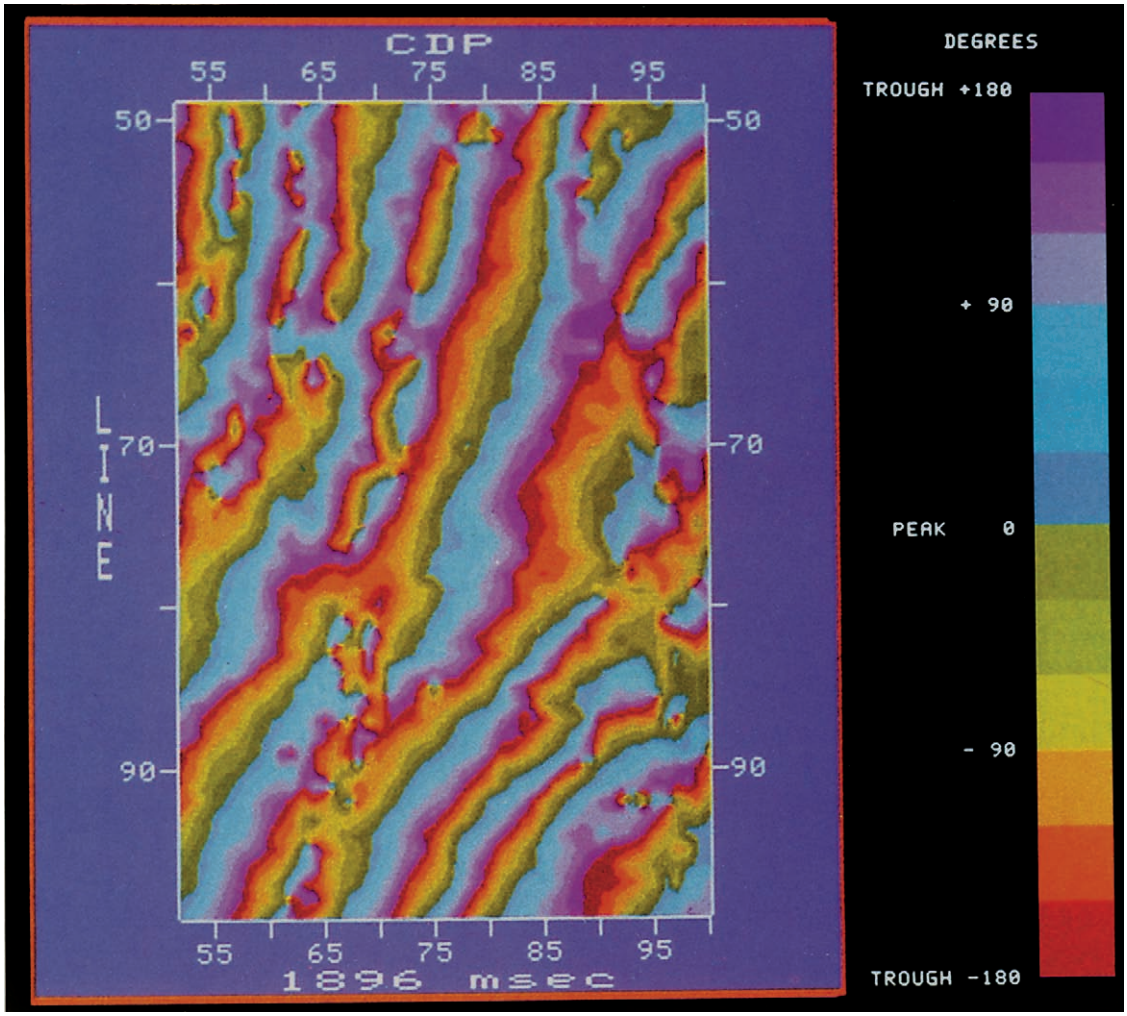

Fig. 3-38. Horizontal section at 1896 ms in instantaneous phase from offshore Trinidad. (Courtesy Texaco Trinidad Inc.)

Subtle Structural Features

Some form of strike view of the data is very helpful in recognizing subtle faults and establishing the spatial patterns of faulting. Figure 3-22 shows many small faults affecting a thin limestone that are much more easily recognized horizontally than vertically.

Figure 3-41 is a horizontal section, or time slice, from a data volume in which a subtle, small-throw fault became a significant part of the interpretation at the target level. Figure 3-42 shows the structure map and the fault under discussion running in a direction just east of north. By reference back to the time slice of Figure 3-41 it is possible to identify the small discontinuities which are the basis of interpreting this fault. The interpreter working on the data first noticed these on the horizontal sections and considered the fault real because it preserved its character over many contiguous sections.

Figure 3-43 shows several straight lineations, principally through the black structural event, that are caused by subtle faulting and jointing. These are so subtle that they would never be recognized on vertical sections. Here they are identified by the linear patterns that appear in the strike view.

Horizontal sections are thus undoubtedly valuable in the study of faults, subtle and not so subtle. Coherence applied to seismic data and then viewed in time slice form is an extension of this value for both fault recognition and mapping. Coherence as an aid to discontinuity detection is very powerful and is discussed at length in Chapter 8. Other attributes are also helpful, particularly when applied to horizon surfaces. These are also subjects of Chapter 8.

Downloaded 25 Jun 2012 to 95.28.162.50. Redistribution subject to SEG license or copyright; Terms of Use: http://segdl.org/

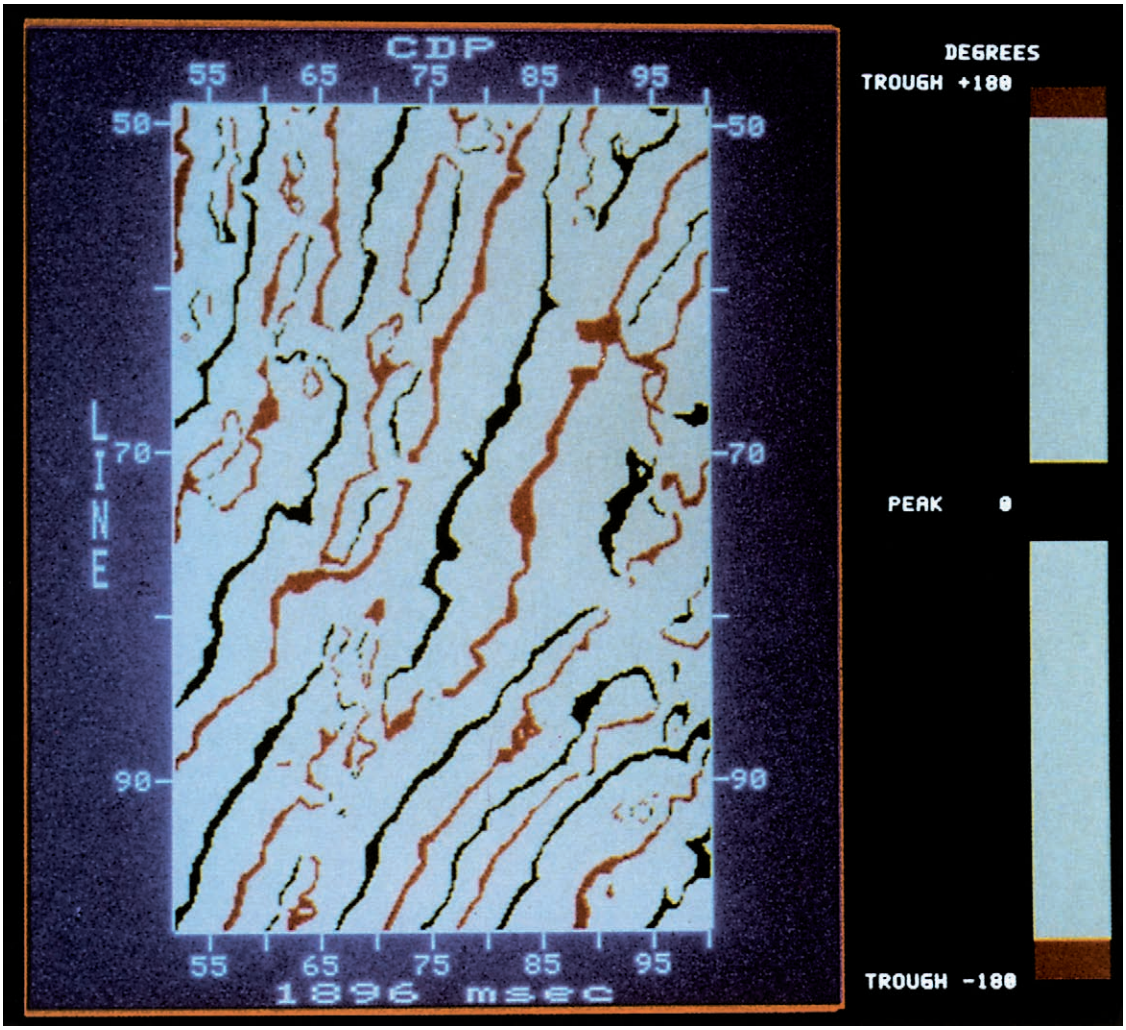

Fig. 3-39. Horizontal section at 1896 ms in edited phase from offshore Trinidad. (Courtesy Texaco Trinidad Inc.)

Visualization and Autotracking

Visualization pervades all stages of 3-D interpretation starting with the volume of data (Chapter 1) and concluding with the extensive discussion on horizon attributes (Chapter 8). The time slice, or horizontal section, so central to this chapter on structure, is itself a major visualization aid and should be used as such. One vertical section and one horizontal section often provide an early visualization of the structure under study.

Figure 3-44 is a time slice at 776 ms showing a distinctly circular feature about 3 km in diameter and occurring at a depth of about 1000 m. It is a very striking view of an impact crater, or astrobleme, of Devonian age. The radial patterns in the center strongly suggest ejecta from the central uplift.

Once horizons and faults have been interpreted they can be visualized as surfaces (Figure 3-45). The relationship between the surfaces can then be studied to help in validation of the interpretation and in placement of the wells to intersect multiple objectives. Many new tools for visualization have recently been created and these are the subject of Chapter 12.

The horizon surfaces above will have been produced using automatic spatial tracking starting from seed, or control, points on vertical and horizontal sections. This procedure, discussed earlier, uses the tracker in a controlled interpolatory manner, that is it is operating between points where the interpretation has been prescribed. With good data the automatic spatial tracker can be used in an extrapolatory manner from

Downloaded 25 Jun 2012 to 95.28.162.50. Redistribution subject to SEG license or copyright; Terms of Use: http://segdl.org/

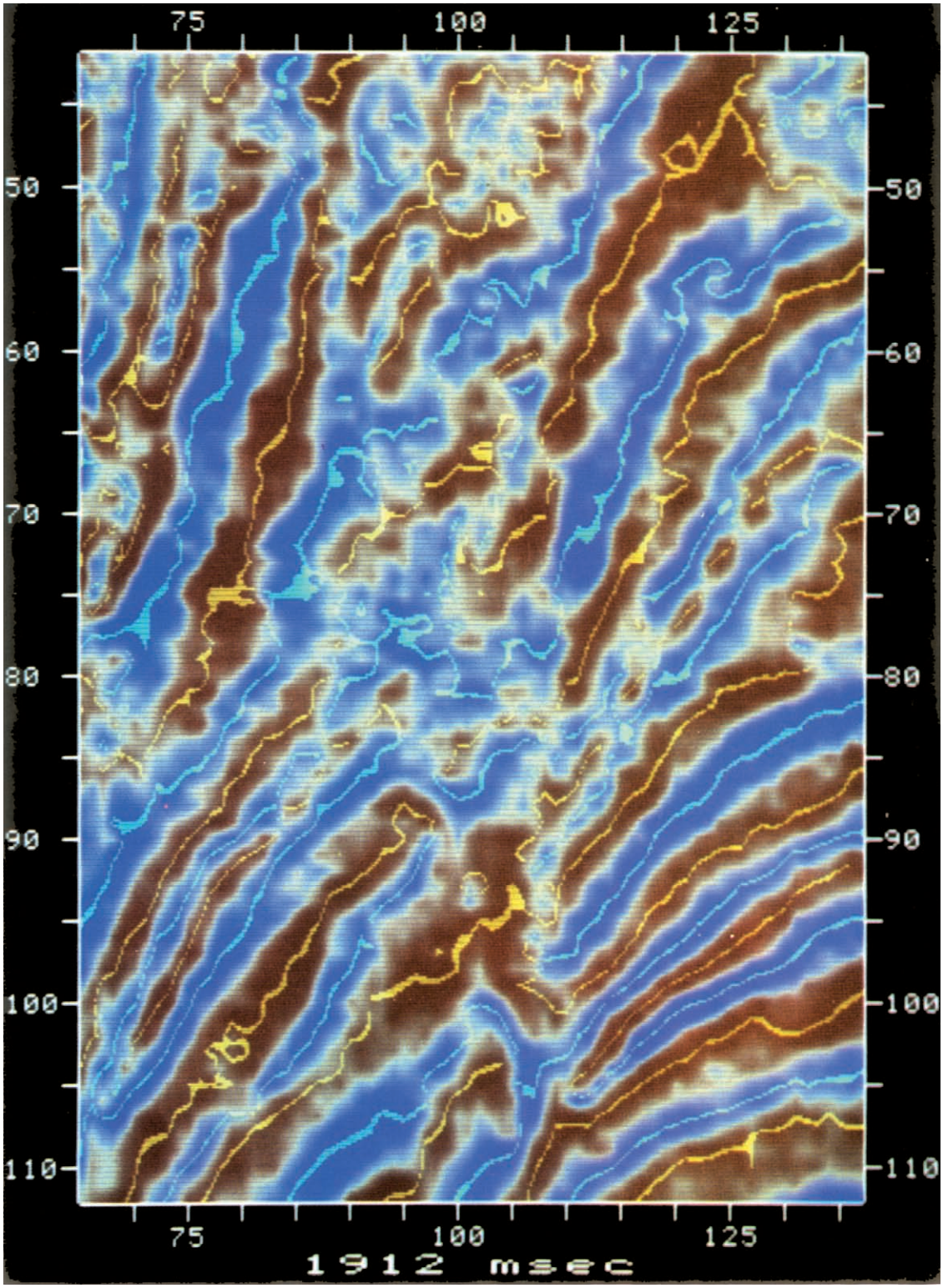

Fig. 3-40. Horizontal section in edited phase superimposed on amplitude. The edited phase in cyan follows the maximum amplitude of the peaks which are blue. The edited phase in yellow follows the maximum amplitude of the troughs which are red.

Downloaded 25 Jun 2012 to 95.28.162.50. Redistribution subject to SEG license or copyright; Terms of Use: http://segdl.org/

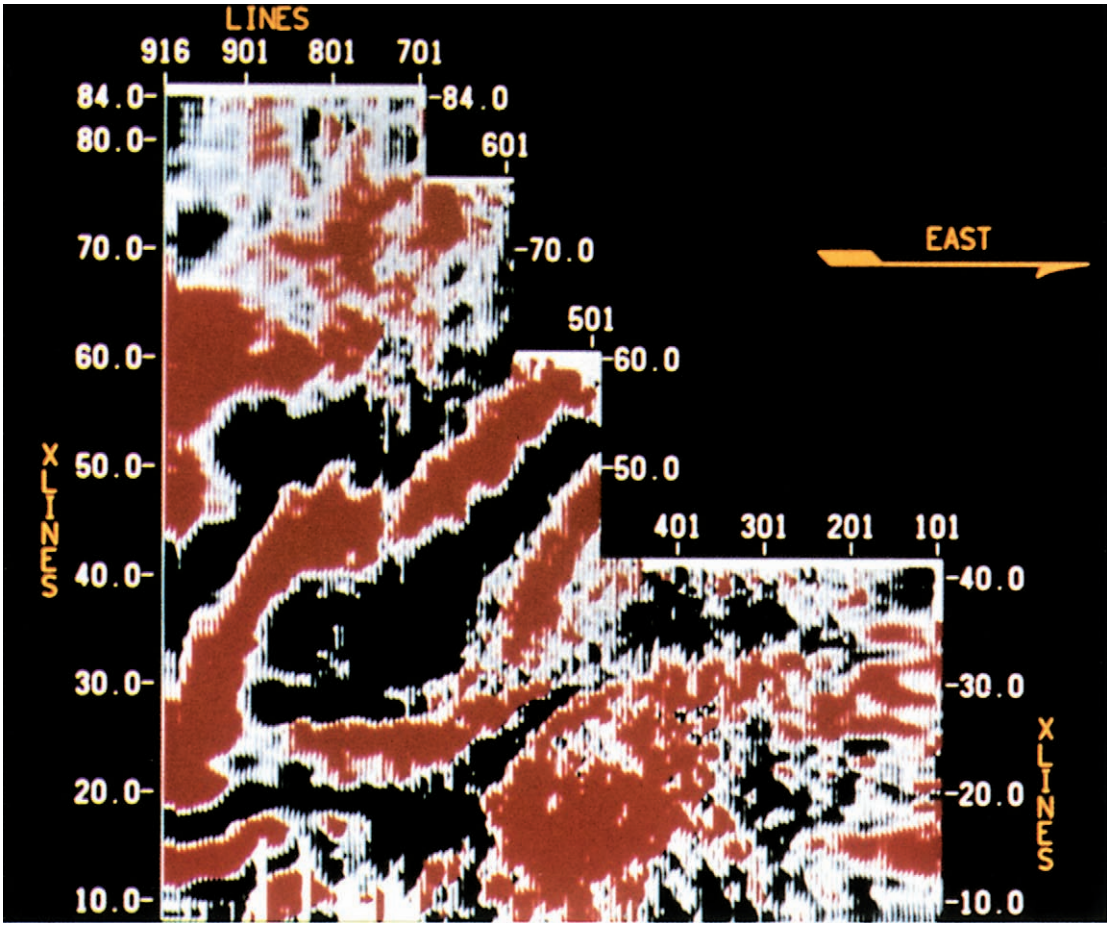

Fig. 3-41. Horizontal section at 2340 ms, from south Louisiana marsh terrain. (Courtesy Texaco Inc.)

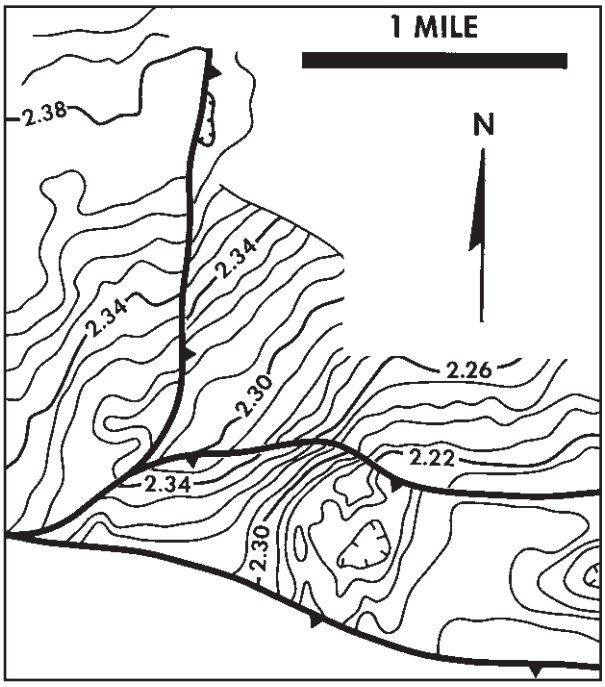

Fig. 3-42. Structural contour map showing subtle fault identified on horizontal section of Figure 3-41. (Courtesy Texaco Inc.)

Downloaded 25 Jun 2012 to 95.28.162.50. Redistribution subject to SEG license or copyright; Terms of Use: http://segdl.org/

Fig. 3-43. Horizontal section at 646 ms, from high-resolution 3-D survey at Ekofisk field in the North Sea. Note lineations due to faulting and jointing. (Courtesy Phillips Petroleum Company Norway.)

Downloaded 25 Jun 2012 to 95.28.162.50. Redistribution subject to SEG license or copyright; Terms of Use: http://segdl.org/

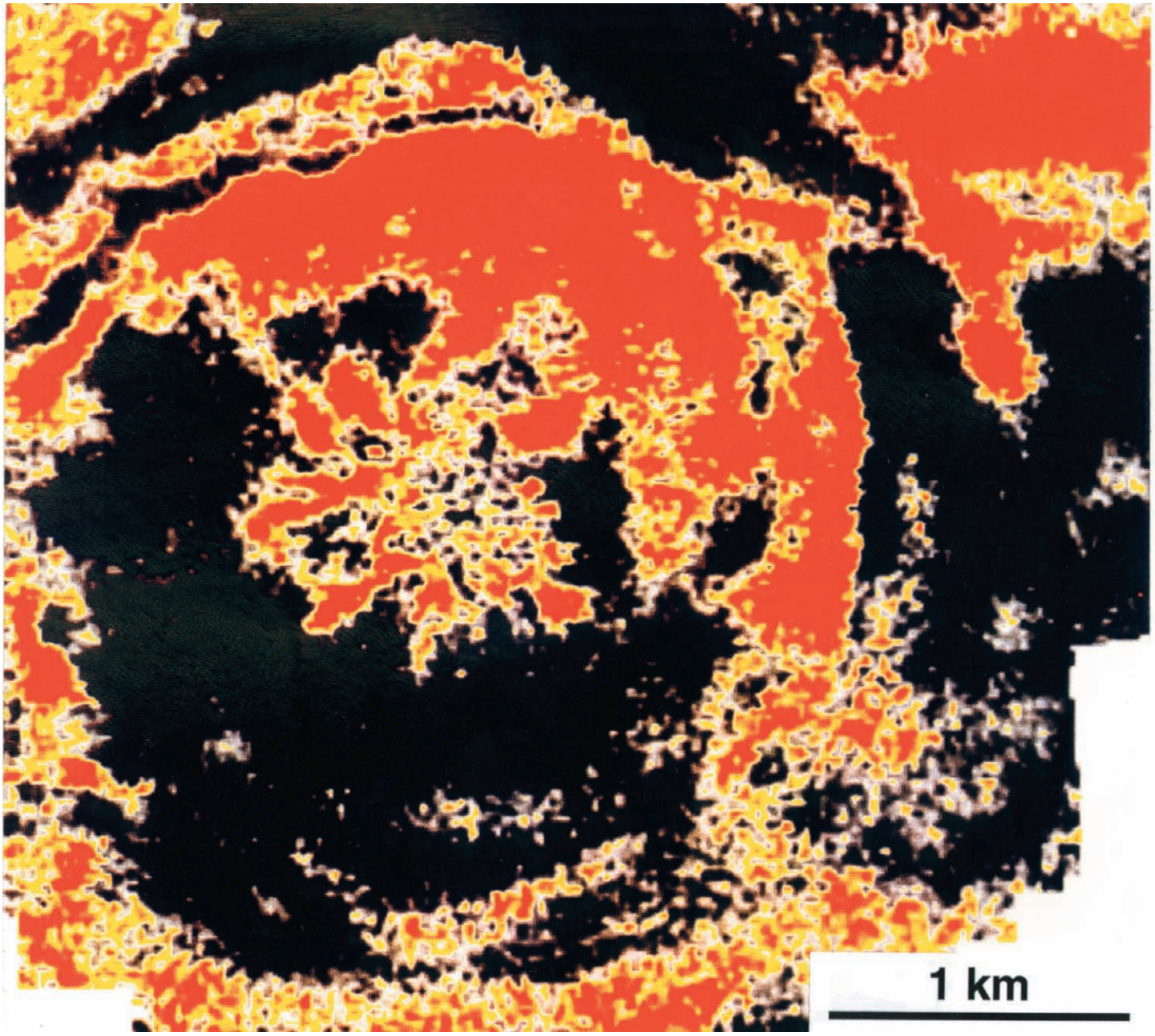

Fig. 3-44. Impact crater of Devonian age seen on time slice 776 ms, from the USA midcontinent. (Courtesy Texaco Exploration and Production Inc.)

minimum seed points. Figure 3-46 is an example where the tracker was seeded in the northeast and moved outwards independently to define several fault blocks and the faults between them. Notice along the faults, and in some other places, untracked points where the tracking criteria could not be satisfied.

Untracked points are also evident in Figure 3-47 and in several places they line up. These lineations of untracked points indicate places where the tracker had difficulty and may indicate subtle faults, sharp changes of dip, facies changes or other boundaries. Thus lineations of untracked points can be used as a source of geologic information.

Downloaded 25 Jun 2012 to 95.28.162.50. Redistribution subject to SEG license or copyright; Terms of Use: http://segdl.org/

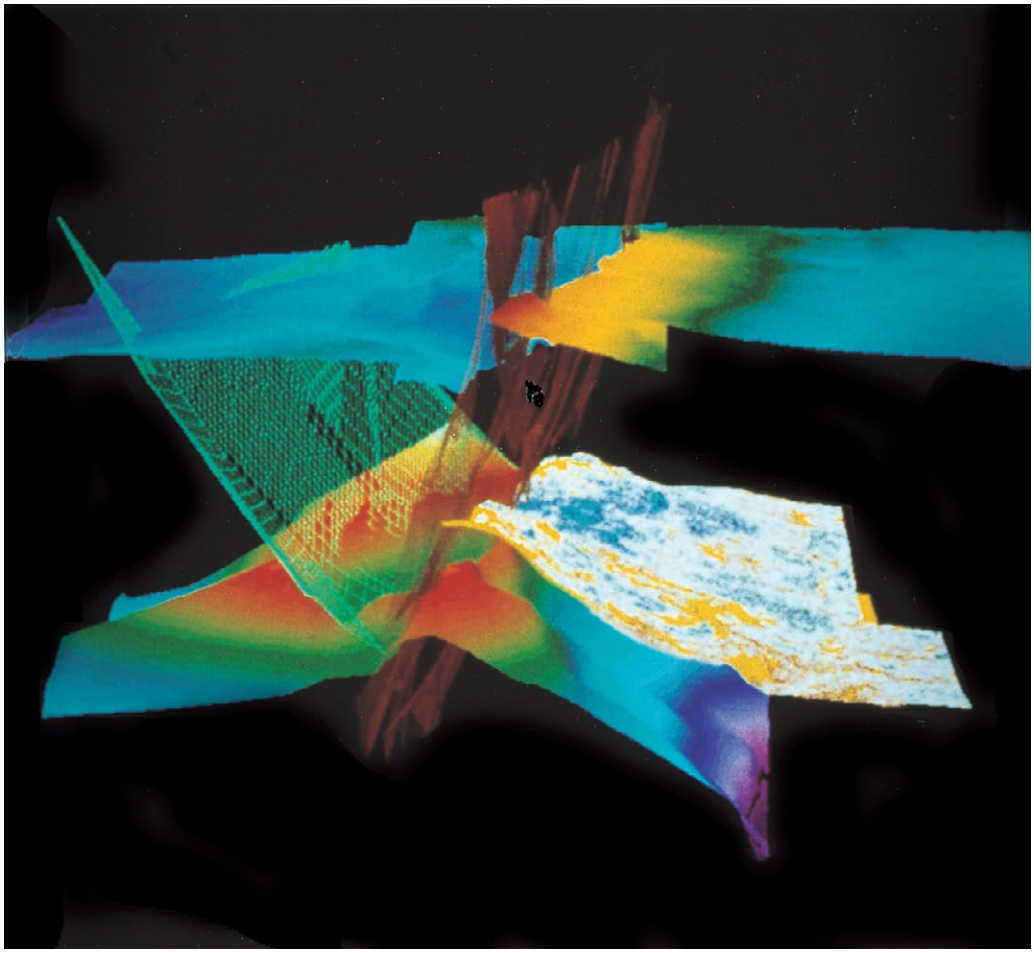

Fig. 3-45. Interpreted horizons and faults seen together as surfaces for validation and visualization. (Courtesy Landmark Graphics Corporation.)

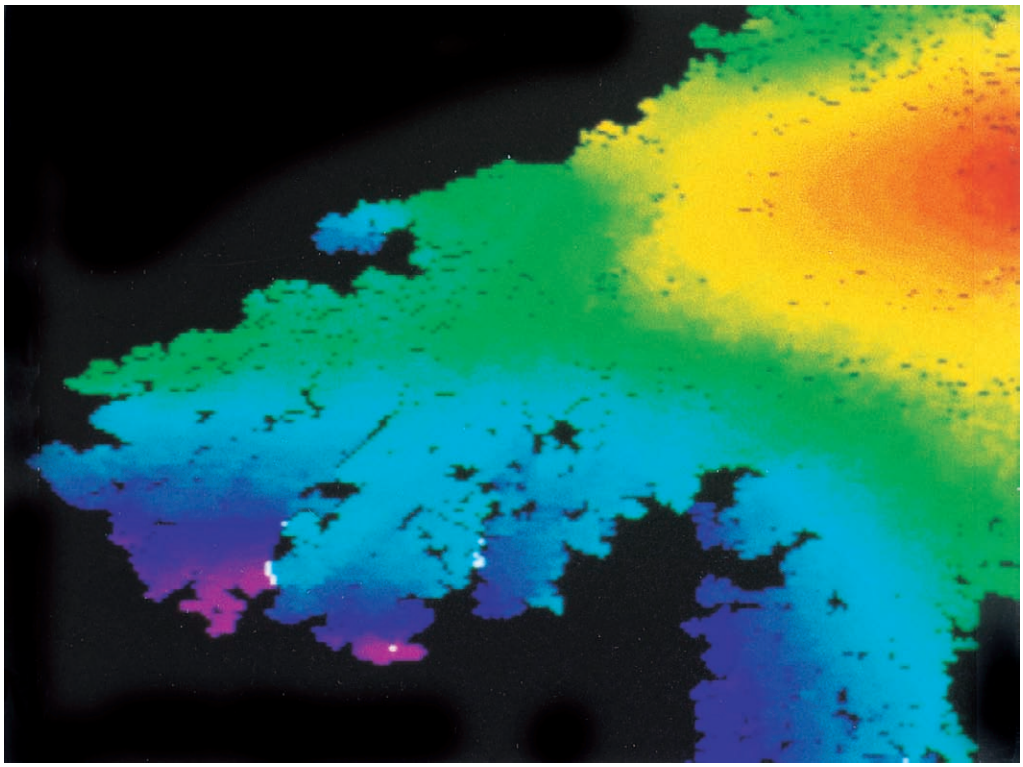

Fig. 3-46. Time structure map generated by automatic spatial tracking operating in an extrapolatory manner from minimum seed points located in the northeast. (Courtesy Landmark Graphics Corporation.)

Downloaded 25 Jun 2012 to 95.28.162.50. Redistribution subject to SEG license or copyright; Terms of Use: http://segdl.org/

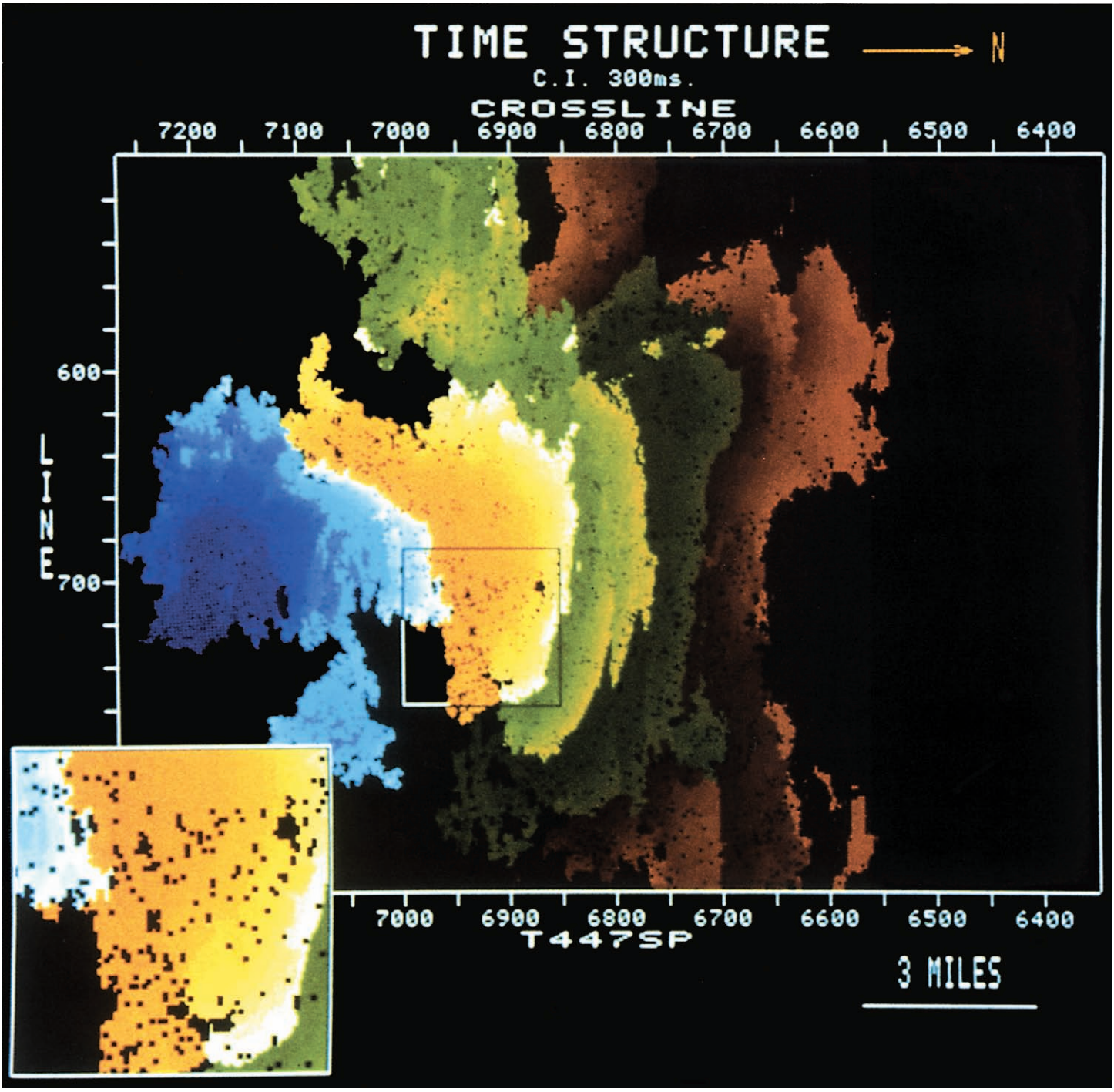

Fig. 3-47. Time structure map generated by automatic spatial tracking, showing lineations of untracked points. (Courtesy Geophysical Service Inc.)

Downloaded 25 Jun 2012 to 95.28.162.50. Redistribution subject to SEG license or copyright; Terms of Use: http://segdl.org/

References

Blake, B. A., J. B. Jennings, M. P. Curtis, and R. M. Phillipson, 1982, Three-dimensional seismic data reveals the finer structural details of a piercement salt dome: Offshore Technology Conference Paper 4258, p. 403–406.

French, W. S., 1990, Practical seismic imaging: The Leading Edge, v. 9, no. 8, p. 13–20.

Johnson, J. P., and M. R. Bone, 1980, Understanding field development history utilizing 3-D seismic: Offshore Technology Conference Paper 3849, p. 473–475.

O'Connell, J. K., M. Kohli, and S. W. Amos, 1990, Bullwinkle: a unique 3-D experiment: Proceedings, SEG 60th Annual Meeting, p. 756–757.

Stark, T. J., 1996, Surface slice generation and interpretation — a review: The Leading Edge, v. 15, p. 818–819.

Taner, M. T., F. Koehler, and R. E. Sheriff, 1979, Complex seismic trace analysis: Geophysics, v. 44, p. 1041–1063.

Downloaded 25 Jun 2012 to 95.28.162.50. Redistribution subject to SEG license or copyright; Terms of Use: http://segdl.org/

Stratigraphic Interpretation

Recognition of Characteristic Shape

Where a vertical seismic section intersects a stratigraphic feature the interpreter can normally find a small amplitude or character anomaly. The expression of a sand-filled channel or bar, for example, is therefore normally so subtle that it takes a considerable amount of interpretive skill to detect it. In contrast, a horizontal section reveals the spatial extent of an anomaly. The interpreter can thus observe characteristic shape and relate what he sees to geologic experience. A shape or pattern which is unrelated to structure may prove to be interpretable as a depositional, erosional, lithologic or other feature of significance. Klein (1985) and Broussard (1975), among others, have provided depositional models on which the interpreter can base his recognition of depositional features. The study of horizontal sections and horizon slices can provide a bird's-eye view of ancient stratigraphy, analogous to the view of modern stratigraphy obtained out of an airplane window.

Figure 4-1 shows five adjacent vertical seismic sections from a small 3-D survey in the Williston basin of North Dakota. Note that the reflections indicate largely flat-lying beds. At 1.8 seconds there is a very slight draping of reflections which is only just discernible. Figure 4-2 shows two single-polarity horizontal sections superimposed on each other. The data from both levels reveal the same almost circular shape. This is the outline of a carbonate buildup measuring approximately one kilometer in diameter.

Figures 4-3 and 4-4 are horizontal sections from a 3-D survey recorded in the Gippsland basin offshore southeastern Australia (Sanders and Steel, 1982). Many small circular features are strikingly evident. These appear as small depressions on the vertical sections which attract little attention. It is the characteristic circular shape when viewed horizontally that attracts the interpreter's eye. The circular features measure 200 to 500 m in diameter and are interpreted as sinkholes in a Miocene karst topography. The beds in which these features exist are dipping from upper left to lower right (east) in Figures 4-3 and 4-4. The width of the reflection is a function of seismic frequency and structural dip (see Chapter 3). The visibility of the sinkholes in the presence of this structure is because their diameters are each less than the reflection width.

Figure 4-5 shows a bifurcating channel close to a Gulf of Mexico salt dome. The salt dome's semi-circular expression results from the intersection of the horizontal section at 416 ms with the dipping structural reflections adjacent to the dome. Away from the salt dome the beds are close to flat-lying, so the horizontal section is sliced along the bedding plane. As a result, the channel is almost completely visible. In fact, the bedding is not exactly flat and some parts of the channel are more clearly seen on the adjacent section at 412 ms. Simple addition of these two horizontal sections improved the continuity of the channel (Figure 4-6). Adding together of horizontal sections is a useful approach to the enhancement of stratigraphic features if, *but only if*, the structural

Text continues on page 112.

Downloaded 25 Jun 2012 to 95.28.162.50. Redistribution subject to SEG license or copyright; Terms of Use: http://segdl.org/

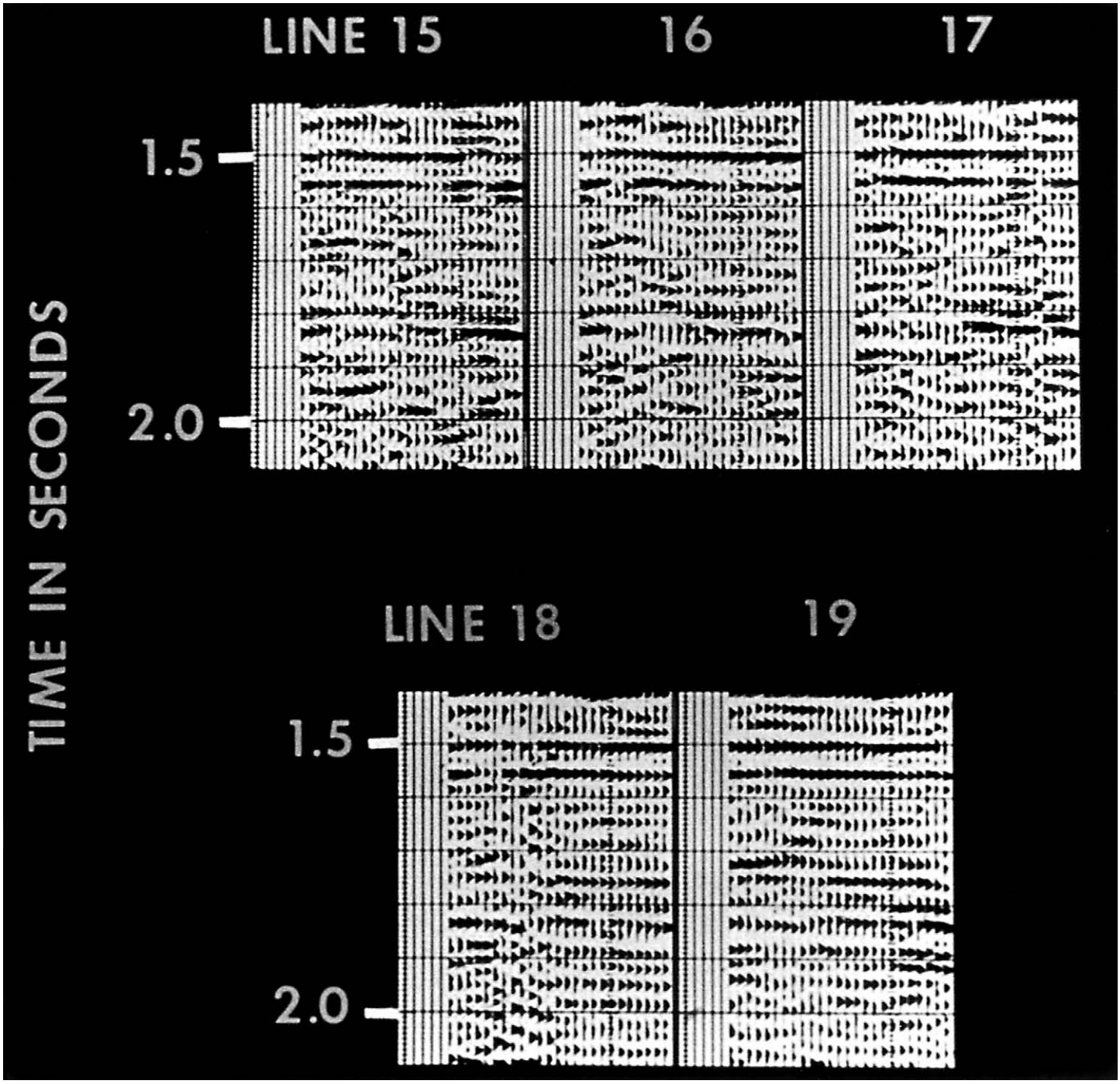

Fig. 4-1. Five adjacent vertical sections from 3-D survey in the Williston basin of North Dakota. (Courtesy Geophysical Service Inc.)

Downloaded 25 Jun 2012 to 95.28.162.50. Redistribution subject to SEG license or copyright; Terms of Use: http://segdl.org/

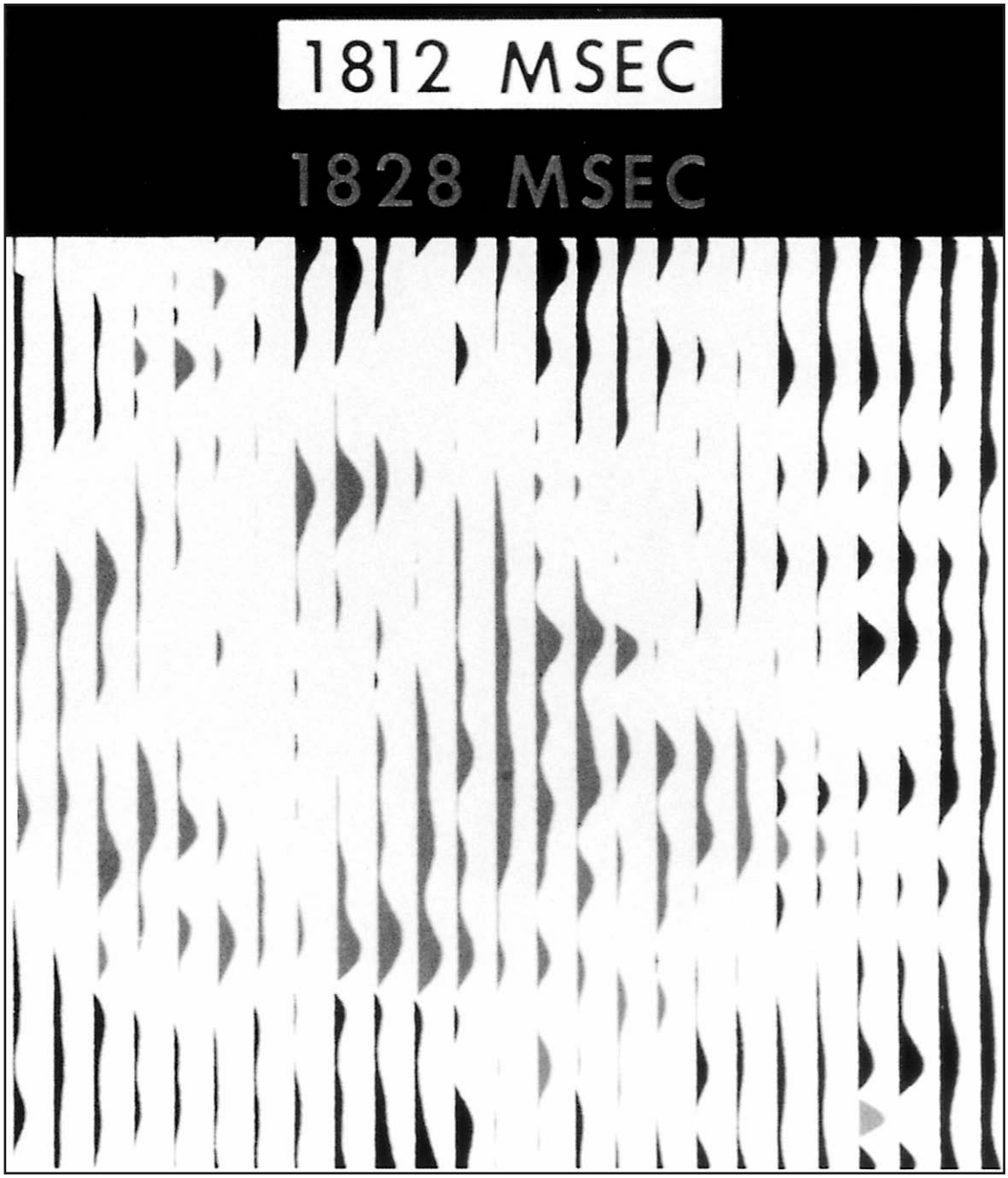

Fig. 4-2. Horizontal sections from 1812 and 1828 ms from North Dakota, each showing positive amplitudes only. The approximately circular outline between the black and the gray indicates the shape of a carbonate buildup. (Courtesy Geophysical Service Inc.)

Downloaded 25 Jun 2012 to 95.28.162.50. Redistribution subject to SEG license or copyright; Terms of Use: http://segdl.org/

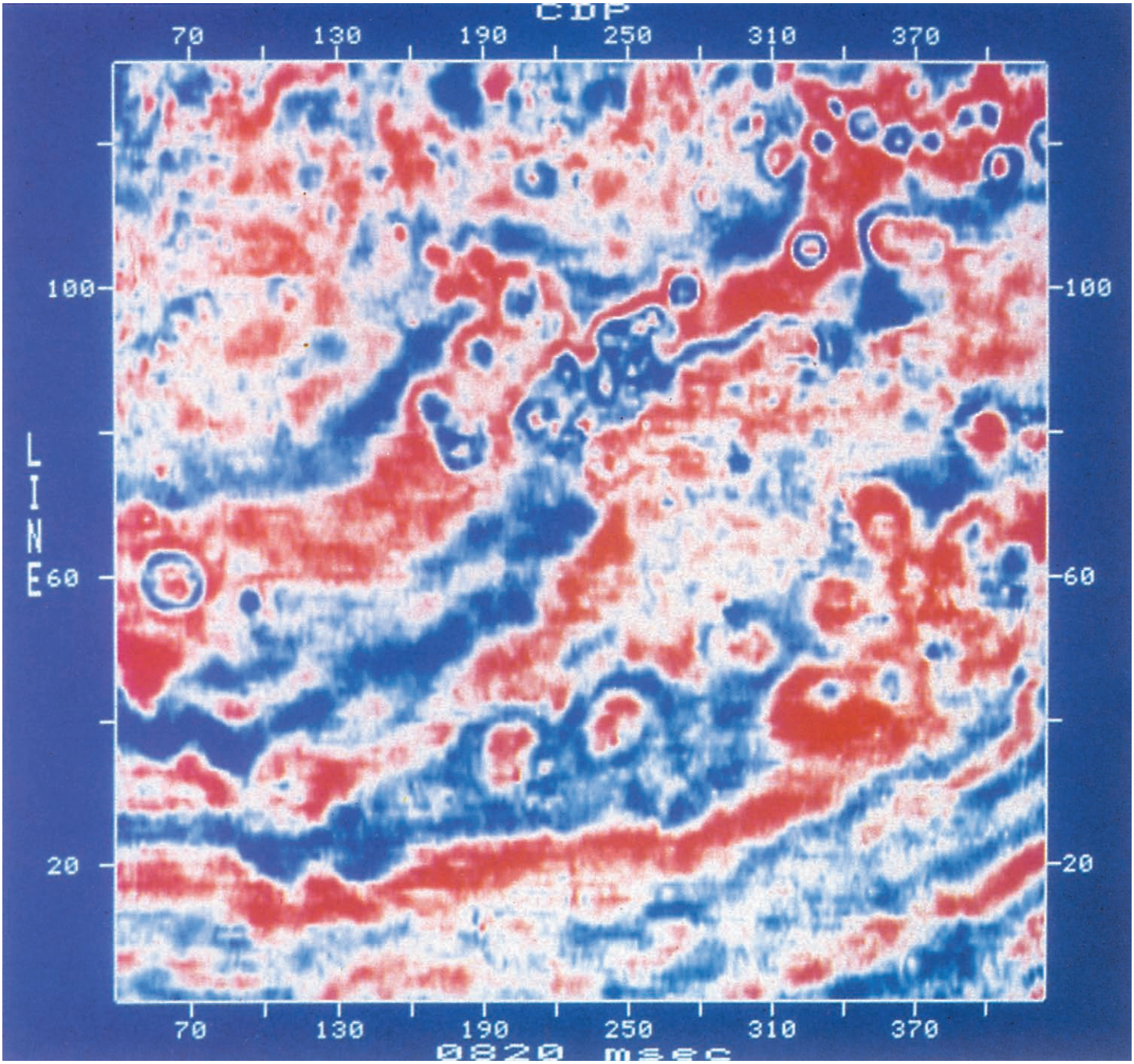

Fig. 4-3. Horizontal section at 820 ms from 3-D survey over Mackerel field in offshore Gippsland basin, southeastern Australia. Circular objects are interpreted as sinkholes in karst topography. (Courtesy Esso Australia Ltd.)

Downloaded 25 Jun 2012 to 95.28.162.50. Redistribution subject to SEG license or copyright; Terms of Use: http://segdl.org/

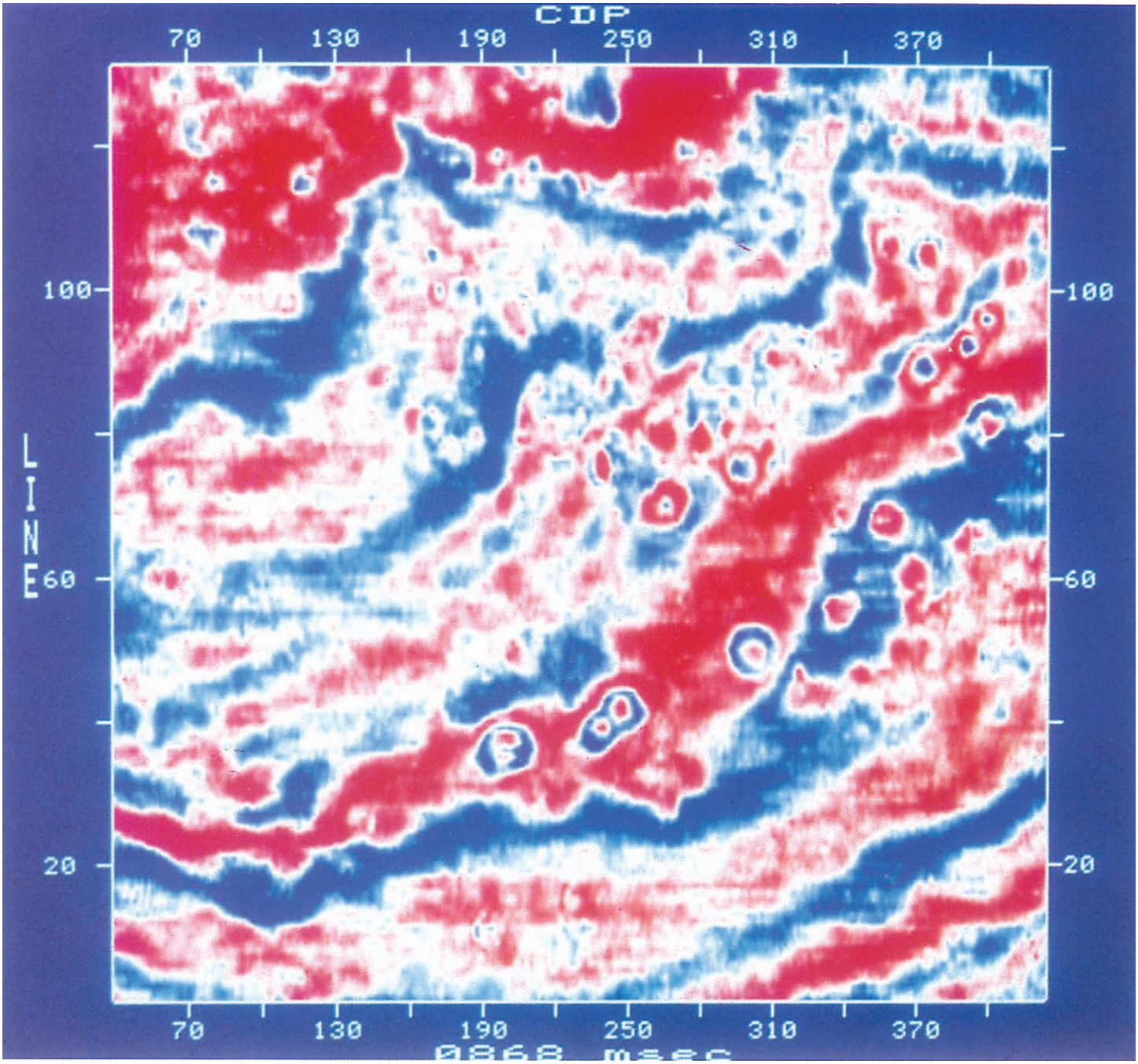

Fig. 4-4. Horizontal section at 868 ms from 3-D survey over Mackerel field in offshore Gippsland basin, southeastern Australia. Circular objects are interpreted as sinkholes in karst topography. (Courtesy Esso Australia Ltd.)

Downloaded 25 Jun 2012 to 95.28.162.50. Redistribution subject to SEG license or copyright; Terms of Use: http://segdl.org/

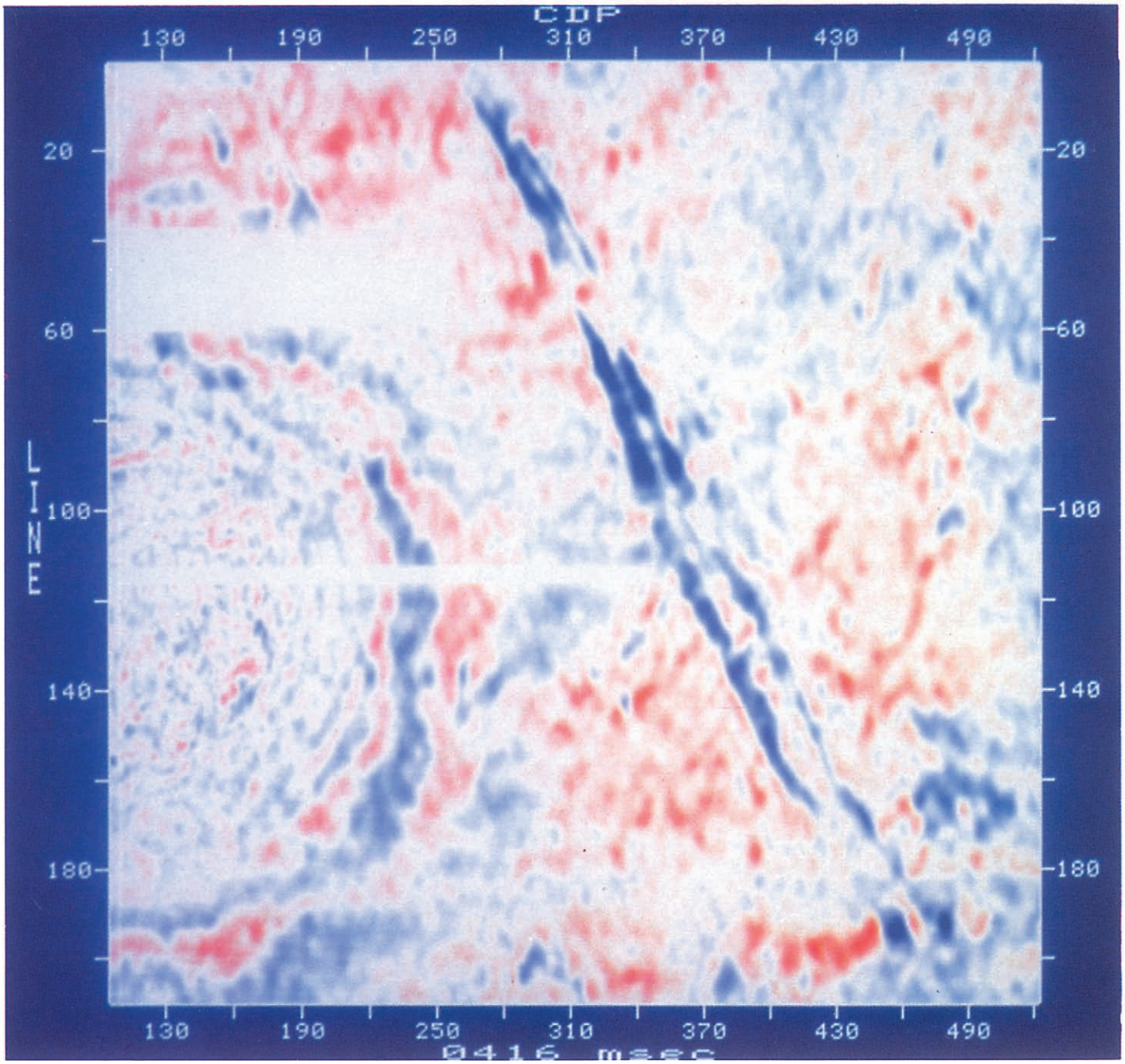

Fig. 4-5. Horizontal section at 416 ms from 3-D survey in the Gulf of Mexico. The bifurcating channel is seen close to the edge of a salt dome. (Courtesy Chevron U.S.A. Inc.)

Downloaded 25 Jun 2012 to 95.28.162.50. Redistribution subject to SEG license or copyright; Terms of Use: http://segdl.org/

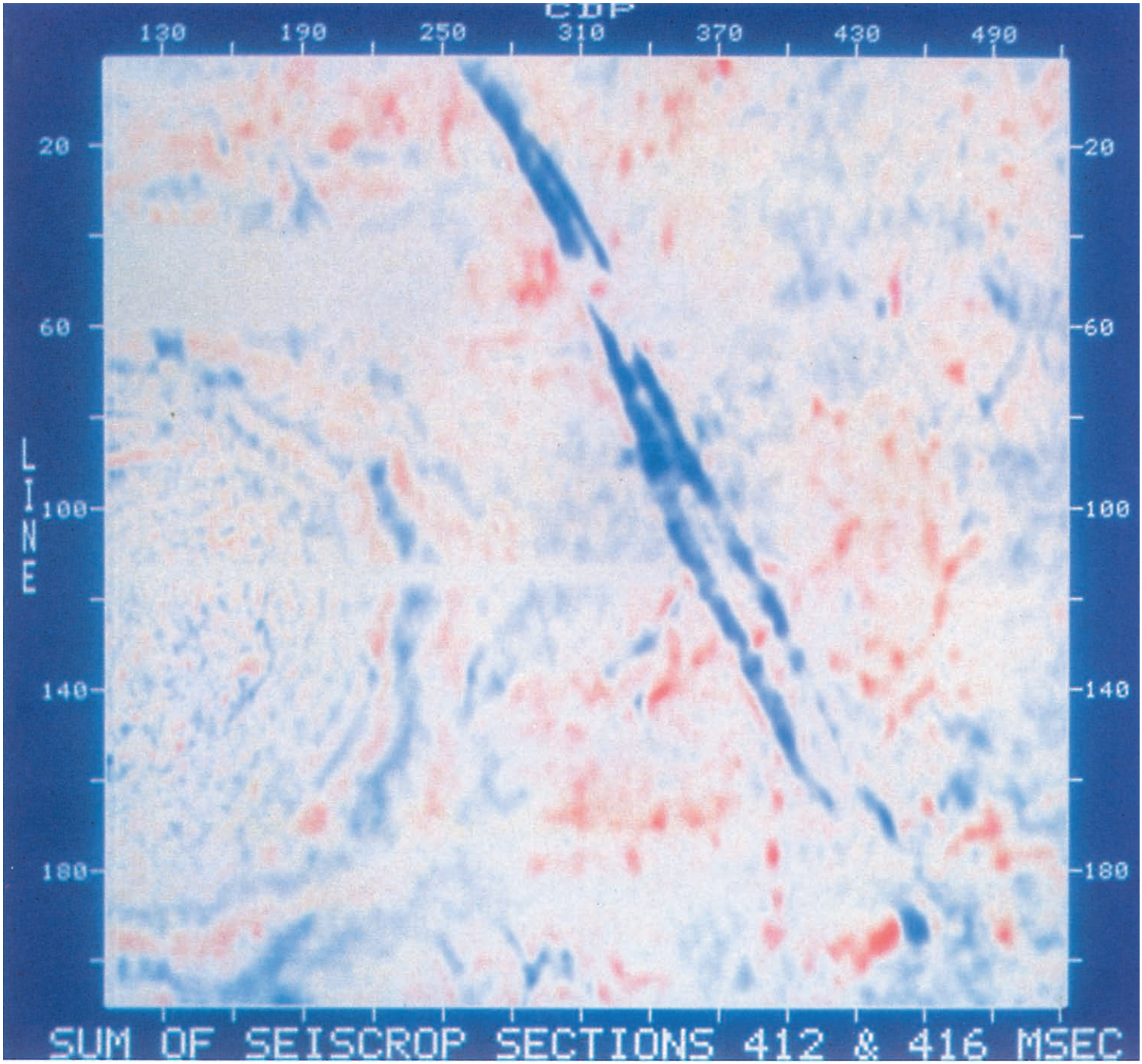

Fig. 4-6. Sum of horizontal sections at 412 and 416 ms from same survey as Figure 4-5 showing enhancement of the channel. (Courtesy Chevron U.S.A. Inc.)

Downloaded 25 Jun 2012 to 95.28.162.50. Redistribution subject to SEG license or copyright; Terms of Use: http://segdl.org/

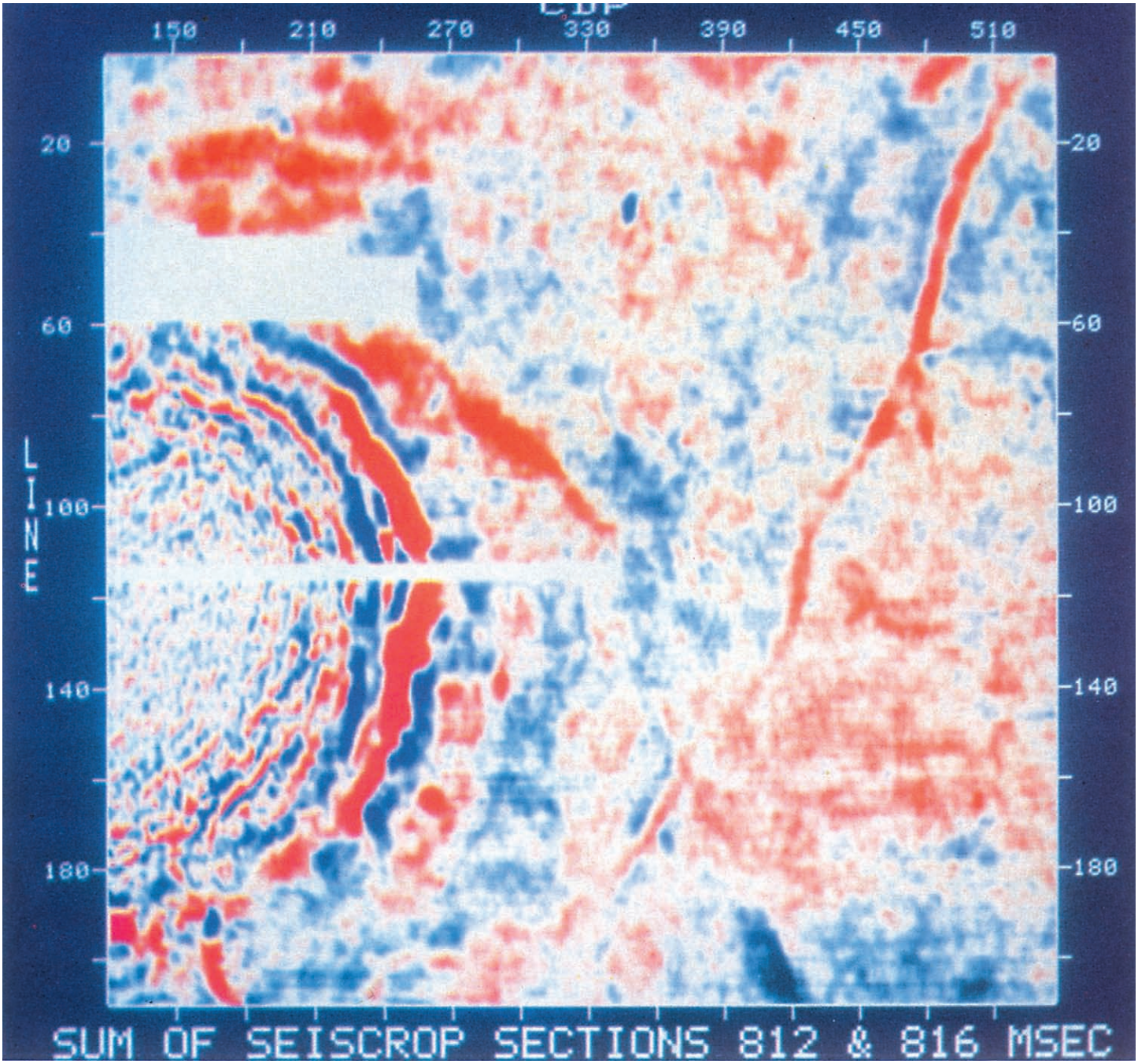

Fig. 4-7. Sum of horizontal sections at 812 and 816 ms from same survey as Figure 4-5 showing a branching channel. (Courtesy Chevron U.S.A. Inc.)

Downloaded 25 Jun 2012 to 95.28.162.50. Redistribution subject to SEG license or copyright; Terms of Use: http://segdl.org/

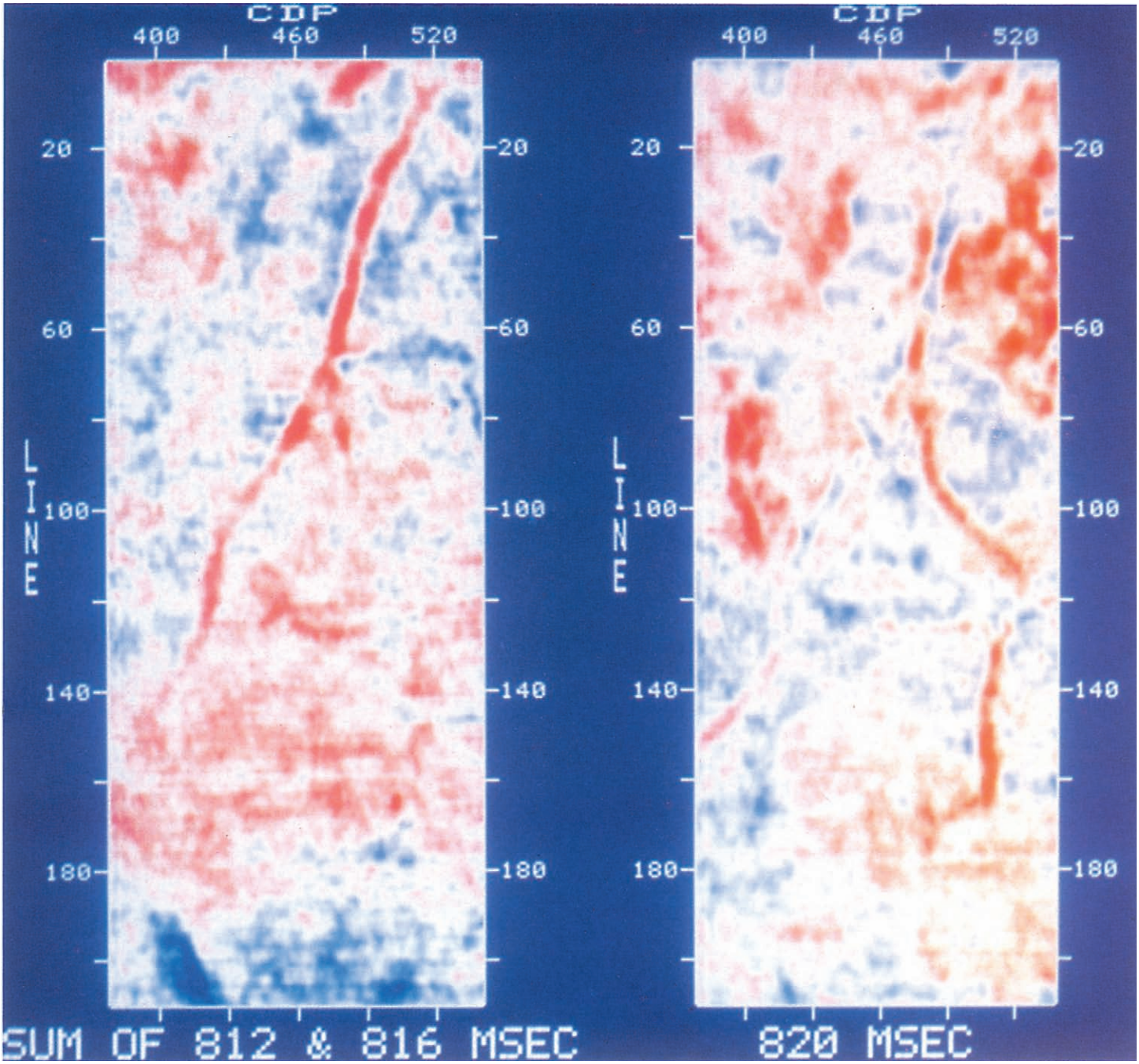

Fig. 4-8. Composite display of horizontal sections at 812 and 816 ms showing western branch of channel and at 820 ms showing eastern branch. (Courtesy Chevron U.S.A. Inc.)

Downloaded 25 Jun 2012 to 95.28.162.50. Redistribution subject to SEG license or copyright; Terms of Use: http://segdl.org/

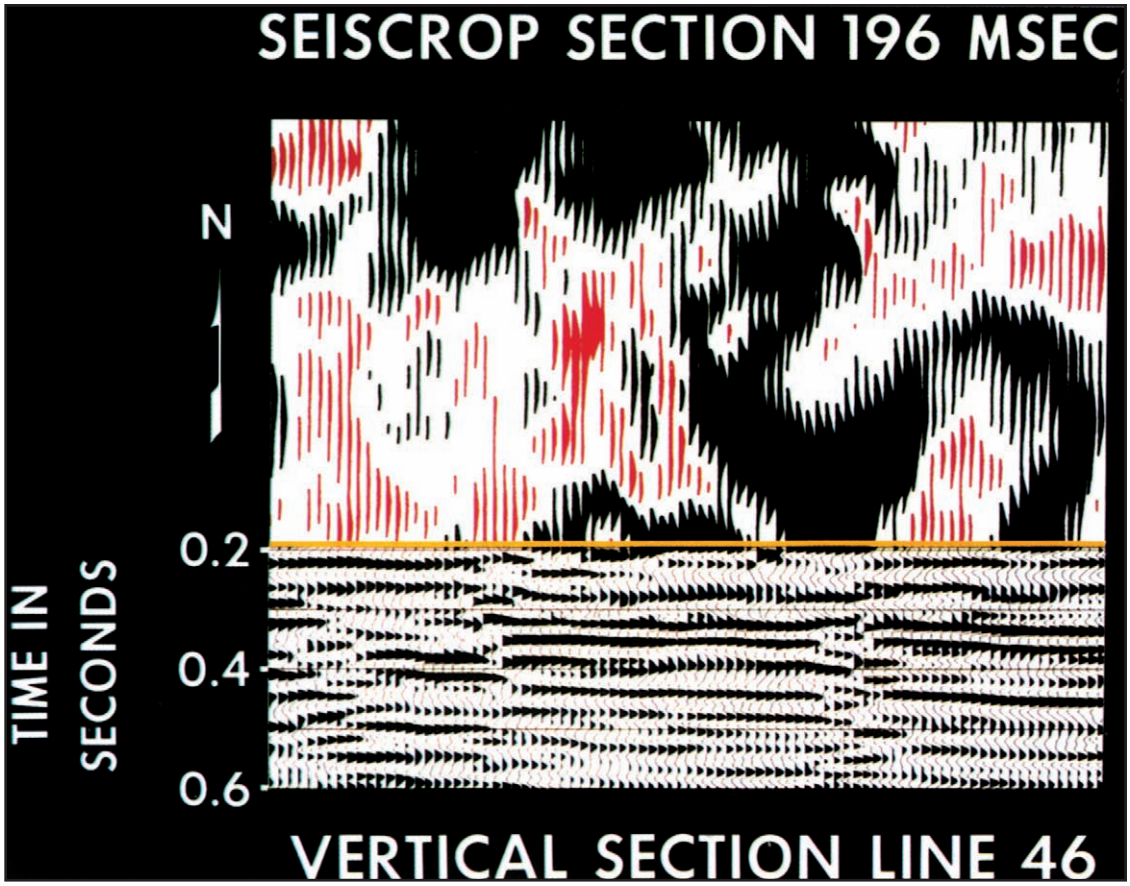

Fig. 4-9. Composite display of vertical and horizontal sections from Gulf of Thailand showing spatial continuity of vertical section event segments. (Courtesy Texas Pacific Oil Company Inc.)

variation across the feature is less than half a period of the appropriate seismic signal.

Figure 4-7 shows another channel deeper in the same data volume. Enhancement again resulted from adding together the horizontal sections from 812 and 816 ms. The channel branches at Line 70, CDP 470, but the eastern branch is not visible. Figure 4-8 shows just the portion of the survey area covering the channel system and includes the horizontal section at 820 ms. Here the eastern branch is clearly visible showing that it is structurally slightly deeper than the western branch. This indicates that the depositional surface containing this channel dips away from the salt dome, which dip was presumably induced by the movement of the salt. Thus, in order to view the entire channel system, several horizontal sections covering the structural range of this depositional surface are required.

Figures 4-9 through 4-16 show examples of depositional features observed on horizontal sections through flat-lying beds in the Gulf of Thailand. The vertical section in Figure 4-9 shows that the beds are flat-lying and that around 200 ms there are some abrupt character changes. The attached horizontal section shows that these reflection segments have spatial continuity. Figure 4-10, covering the whole prospect area, makes it clear that the continuity is part of a meandering channel system. Anyone who has flown over the Mississippi River will immediately relate Figure 4-10 to observations made from the airplane window.

In the Gulf of Thailand there is a regional unconformity in the mid-Miocene and above that unconformity the beds in this prospect area are largely flat-lying. Therefore, many horizontal sections above 900 ms directly reveal depositional features because the sections are parallel to bedding planes. Figure 4-11 is a schematic composite of the features observed. The interpretation of these in sequence indicated a delta prograding across the survey area from southwest to northeast during the mid-Miocene to Pleistocene.

Downloaded 25 Jun 2012 to 95.28.162.50. Redistribution subject to SEG license or copyright; Terms of Use: http://segdl.org/

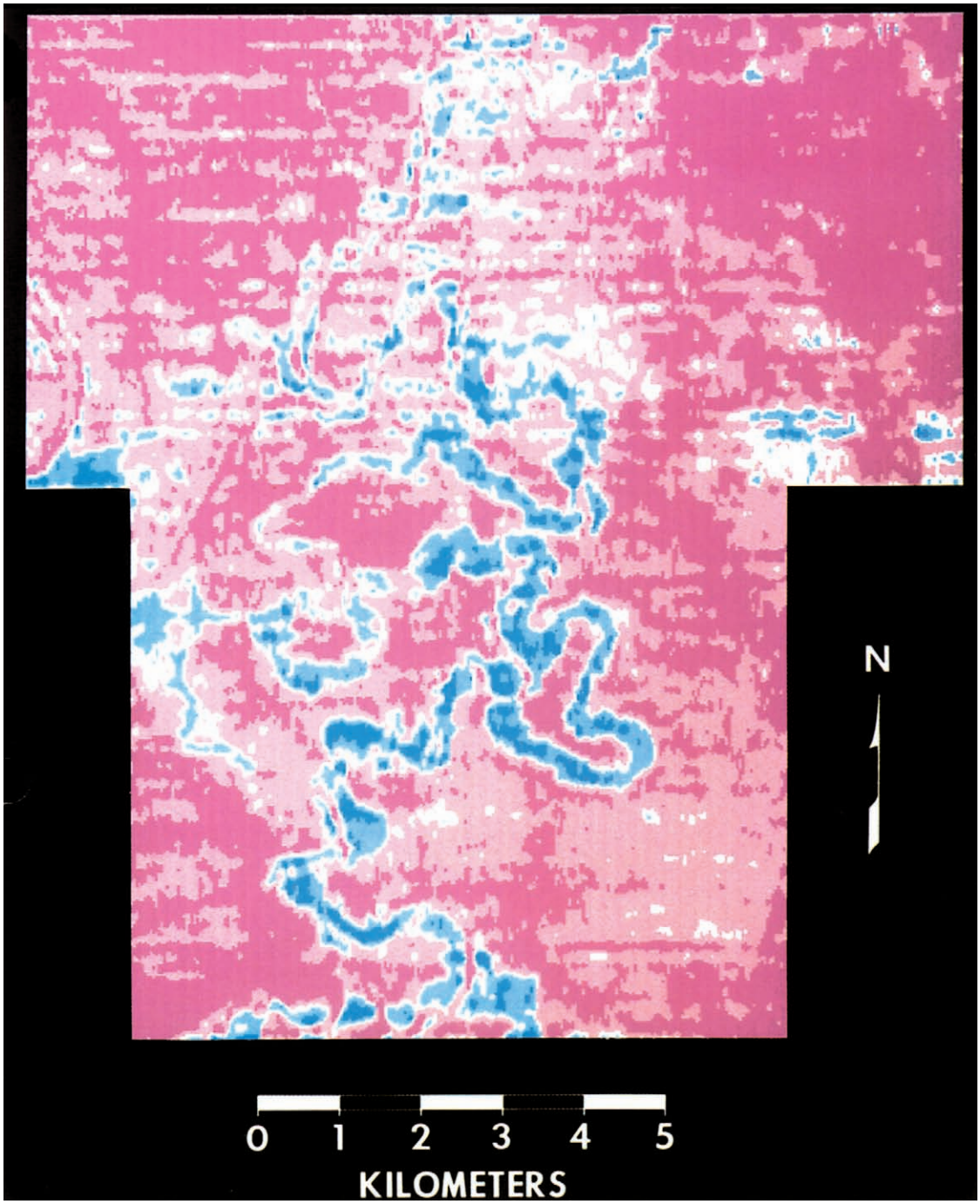

Fig. 4-10. Horizontal section at 196 ms from Gulf of Thailand showing meandering stream channel. (Courtesy Texas Pacific Oil Company Inc.)

Examples of the depositional features observed are presented in Figures 4-12 through 4-16. Figure 4-12 shows in the upper center a delta front channel. Figure 4-13 shows a large offshore bar trending northwest-southeast, transverse to the direction of delta progradation. Figure 4-14 shows two smaller bars, center and lower left, with the same orientation. Figure 4-15 shows, in the upper right, a reworked bar; toward the bottom are straight linear features suggestive of distributary channels. Figure 4-16 shows many twisting channels, some of them very narrow.

Figure 4-17 shows part of the Mahakam delta in Indonesia. At this time (about 18,000 years ago) deposition was clearly occurring in this part of the delta. Patterns are very similar to those visible in the present Mahakam delta (Figure 4-18). However, in another part of the ancient delta (Figure 4-19) erosion was occurring as evidenced by the dendritic patterns of canyons.

Text continues on page 121.

Downloaded 25 Jun 2012 to 95.28.162.50. Redistribution subject to SEG license or copyright; Terms of Use: http://segdl.org/

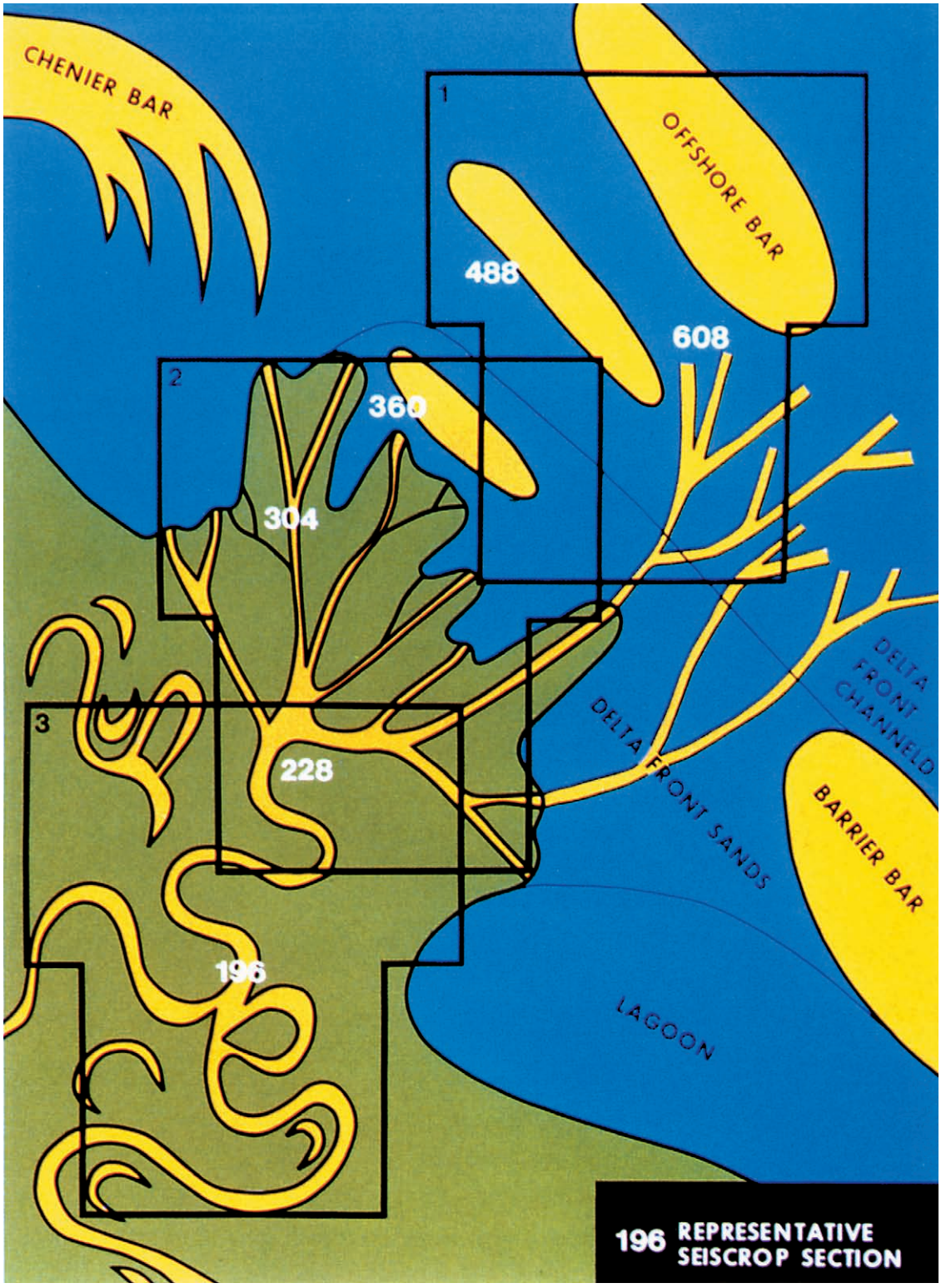

Fig. 4-11. Schematic diagram of delta prograding across the Gulf of Thailand 3-D survey area between mid-Miocene and Pleistocene.

Downloaded 25 Jun 2012 to 95.28.162.50. Redistribution subject to SEG license or copyright; Terms of Use: http://segdl.org/

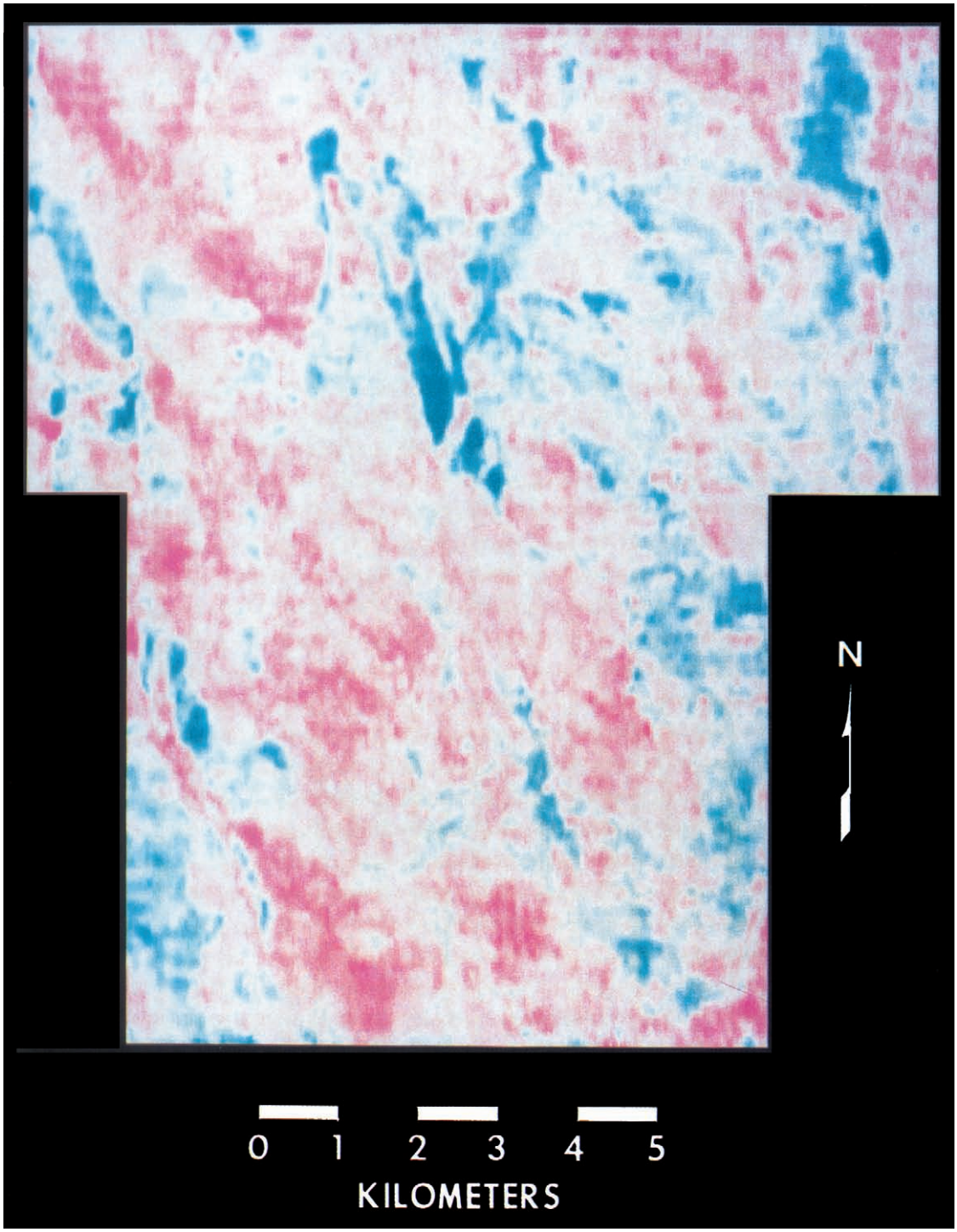

Fig. 4-12. Horizontal section at 608 ms from Gulf of Thailand showing delta front channel. (Courtesy Texas Pacific Oil Company Inc.)

Downloaded 25 Jun 2012 to 95.28.162.50. Redistribution subject to SEG license or copyright; Terms of Use: http://segdl.org/

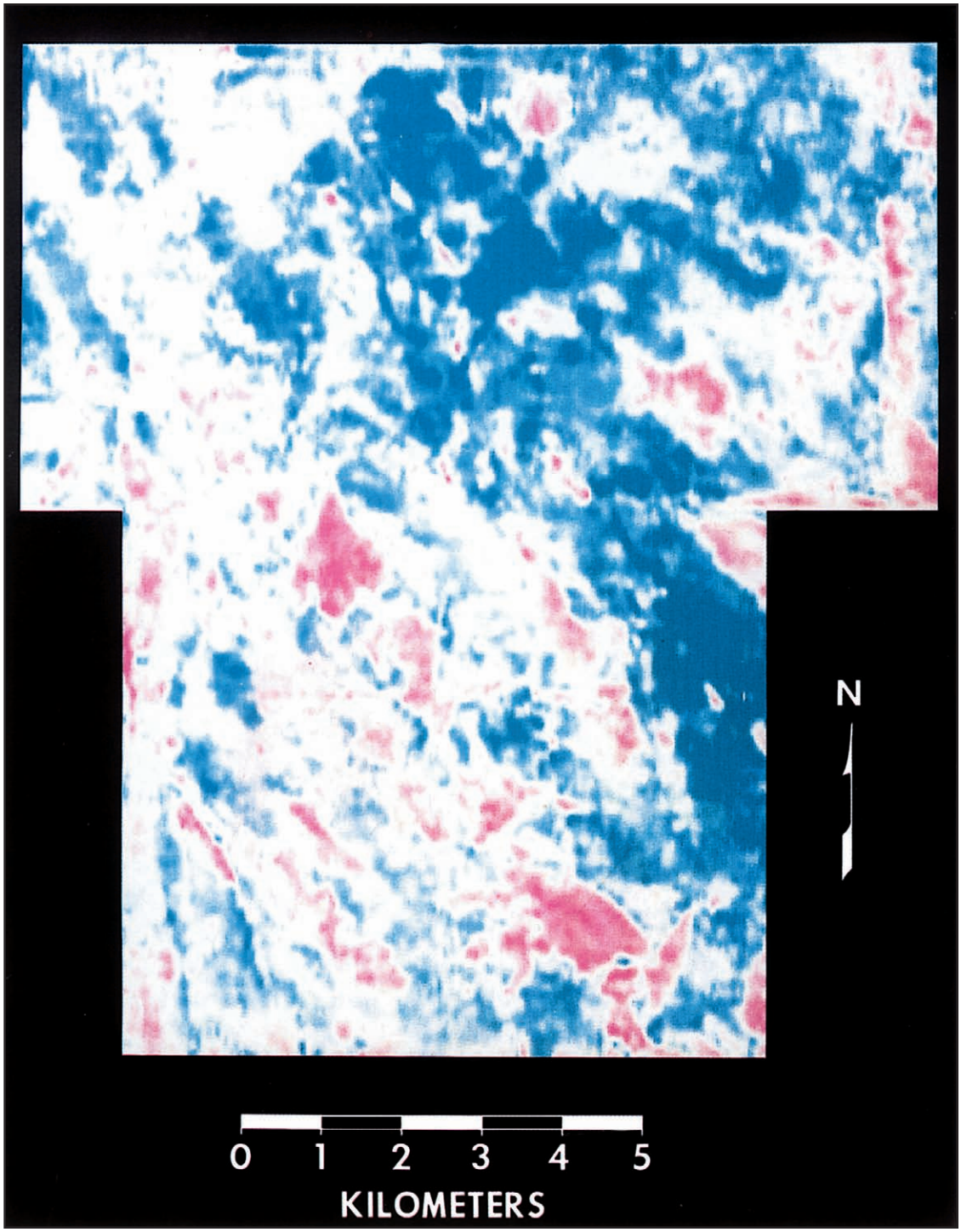

Fig. 4-13. Horizontal section at 488 ms from Gulf of Thailand showing large offshore sand bar. (Courtesy Texas Pacific Oil Company Inc.)

Downloaded 25 Jun 2012 to 95.28.162.50. Redistribution subject to SEG license or copyright; Terms of Use: http://segdl.org/

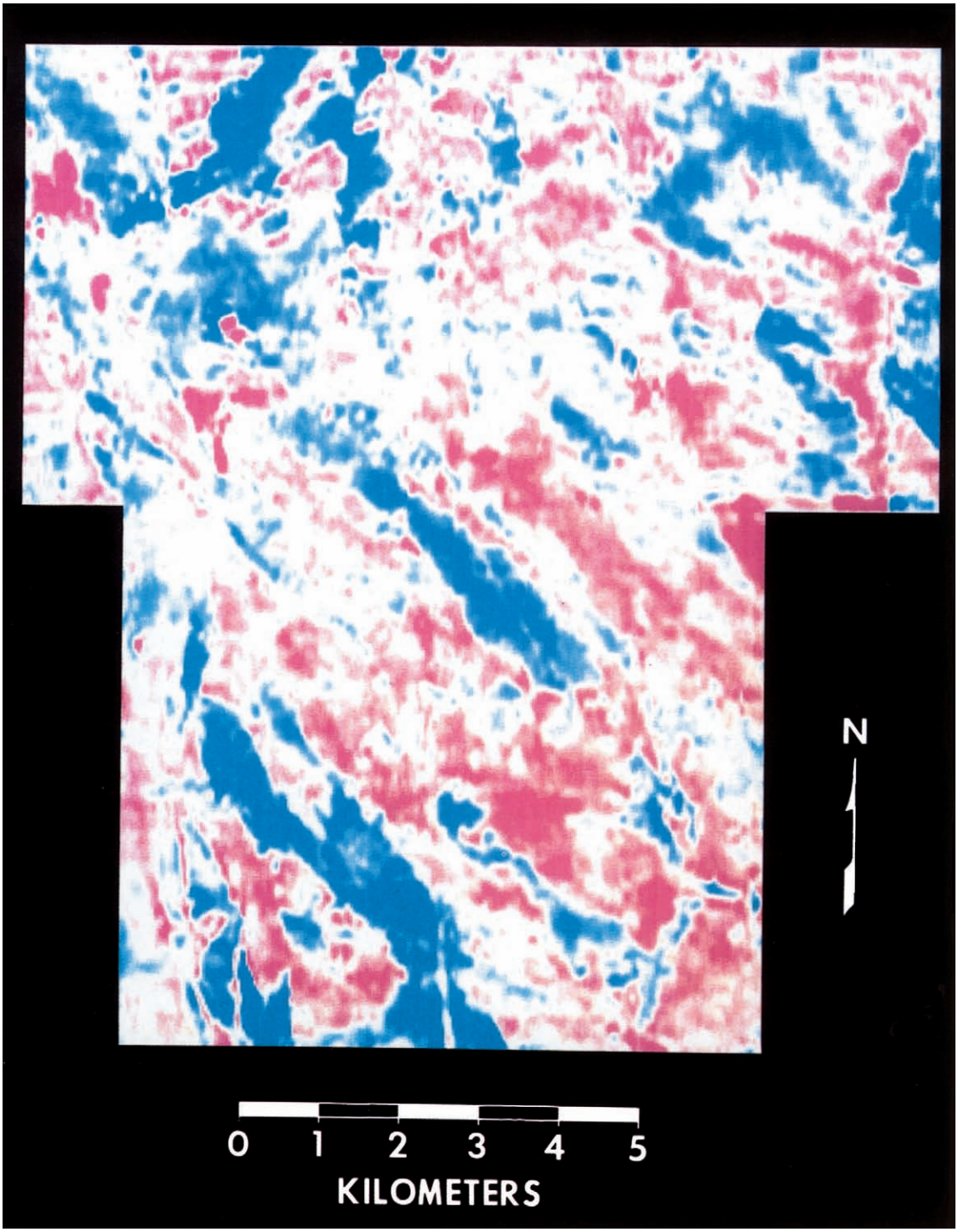

Fig. 4-14. Horizontal section at 360 ms from Gulf of Thailand showing small sand bars. (Courtesy Texas Pacific Oil Company Inc.)

Downloaded 25 Jun 2012 to 95.28.162.50. Redistribution subject to SEG license or copyright; Terms of Use: http://segdl.org/

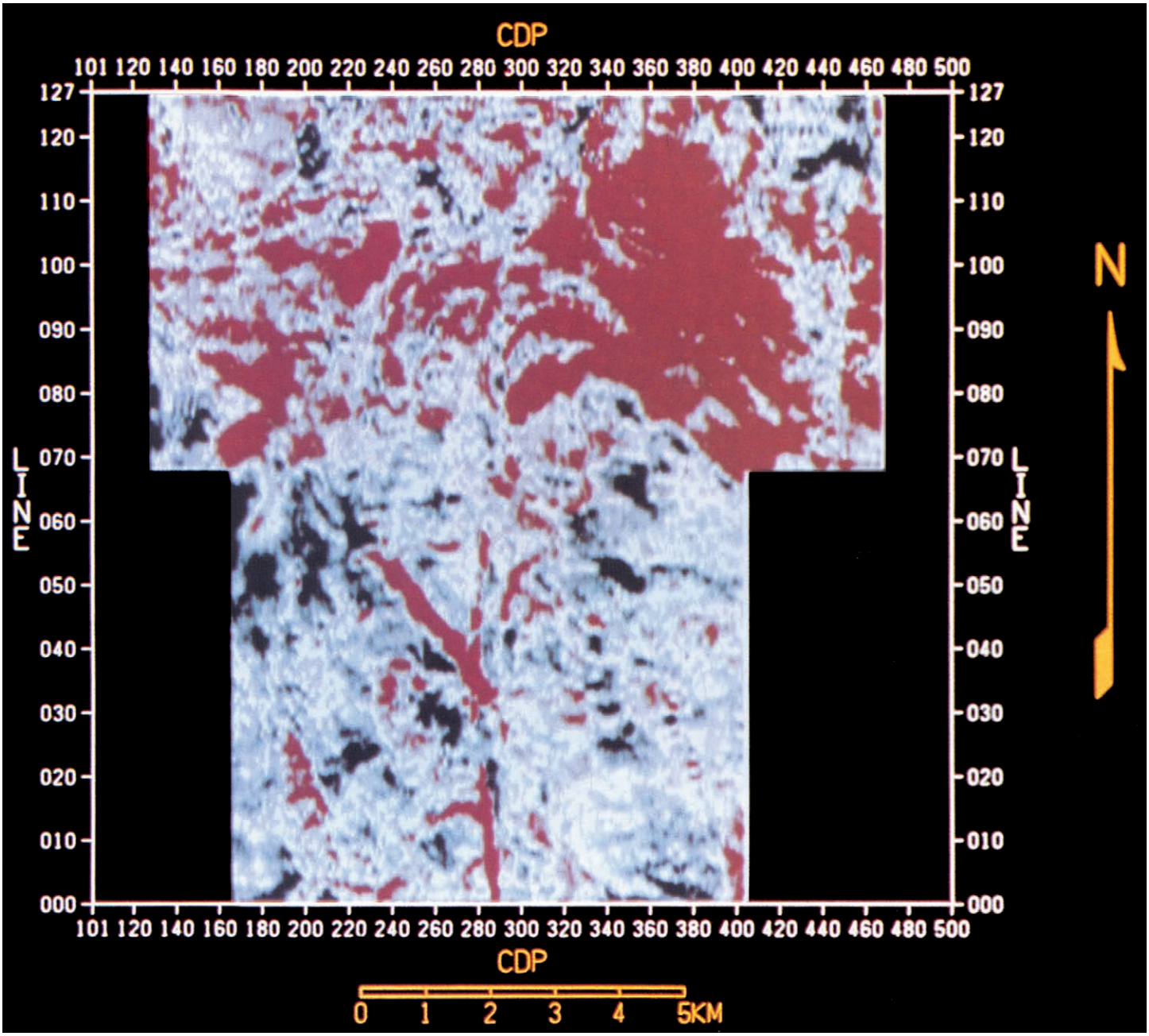

Fig. 4-15. Horizontal section at 304 ms from Gulf of Thailand showing a reworked bar and distributary channels. (Courtesy Texas Pacific Oil Company Inc.)

Downloaded 25 Jun 2012 to 95.28.162.50. Redistribution subject to SEG license or copyright; Terms of Use: http://segdl.org/

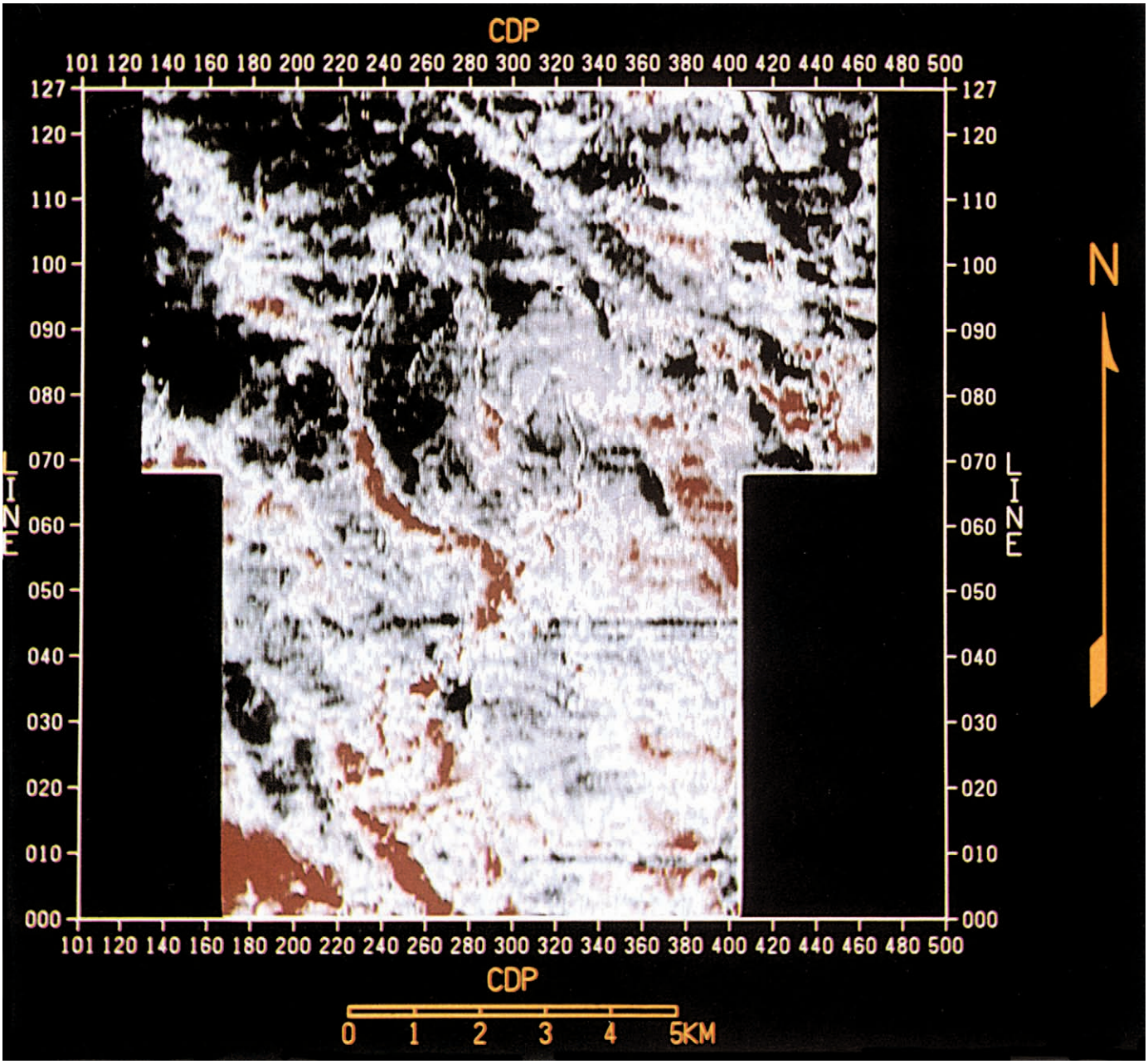

Fig. 4-16. Horizontal section at 228 ms from Gulf of Thailand showing several channels, large and small. (Courtesy Texas Pacific Oil Company Inc.)

Downloaded 25 Jun 2012 to 95.28.162.50. Redistribution subject to SEG license or copyright; Terms of Use: http://segdl.org/

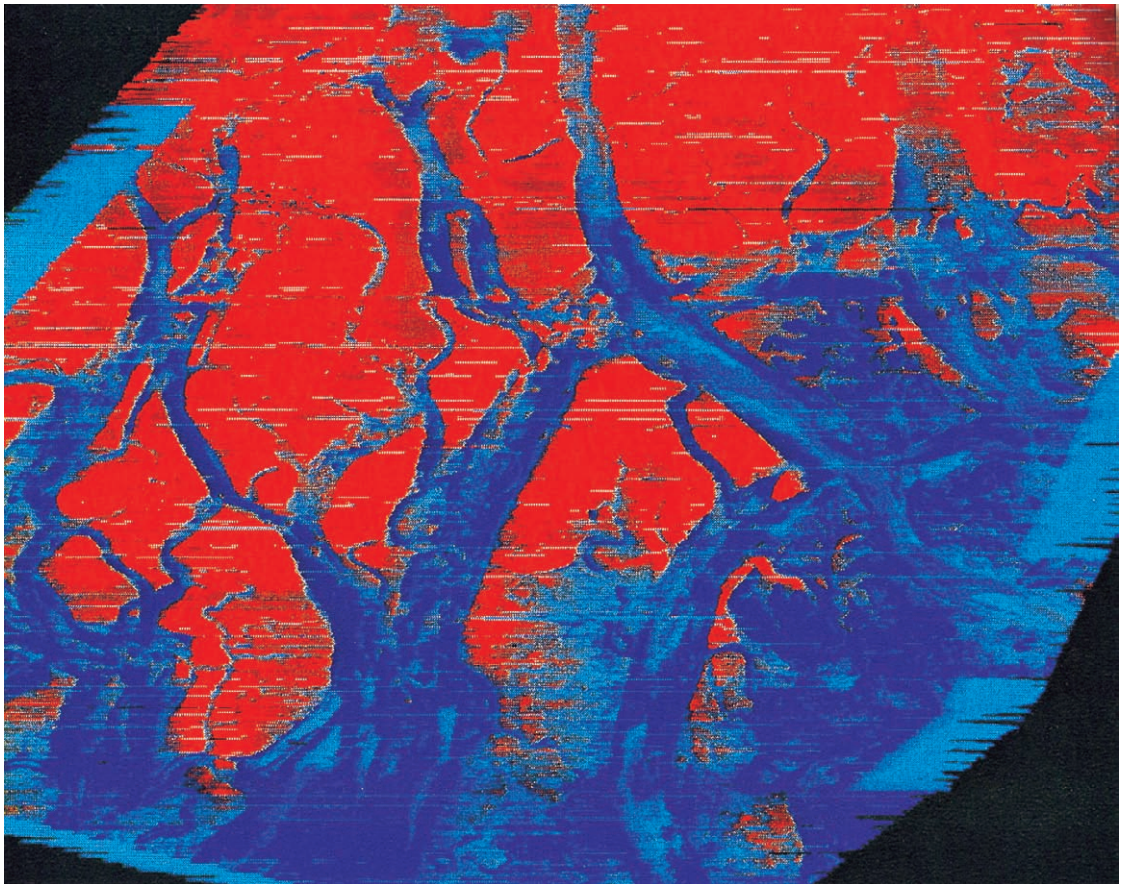

Fig. 4-17. Horizontal section at 100 ms from Peciko 3-D survey recorded in the Mahakam delta offshore Kalimantan, Indonesia. The deltaic features seen here are about 18,000 years old. (Courtesy Total Indonesie.)

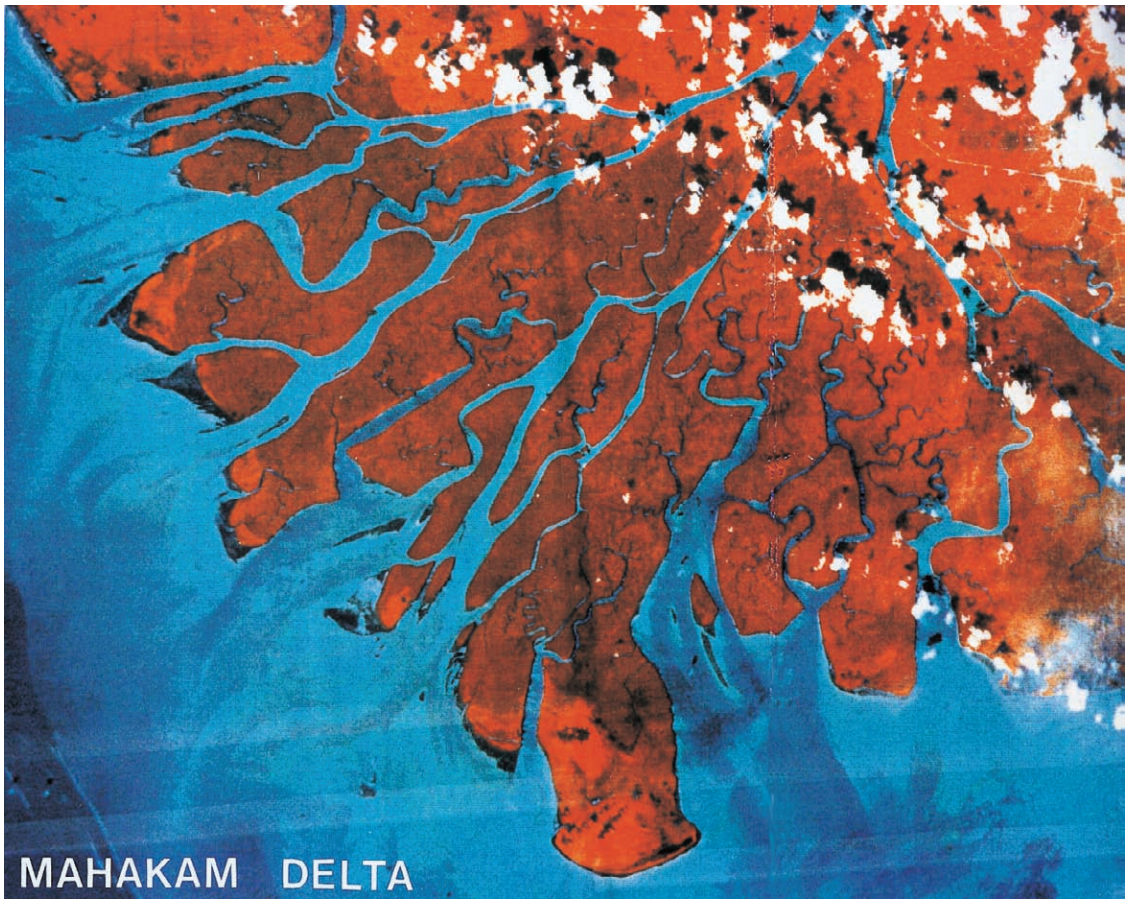

Fig. 4-18. Satellite photograph of part of present Mahakam delta for comparison with Figure 4-17. (Courtesy Total Indonesie.)

Downloaded 25 Jun 2012 to 95.28.162.50. Redistribution subject to SEG license or copyright; Terms of Use: http://segdl.org/

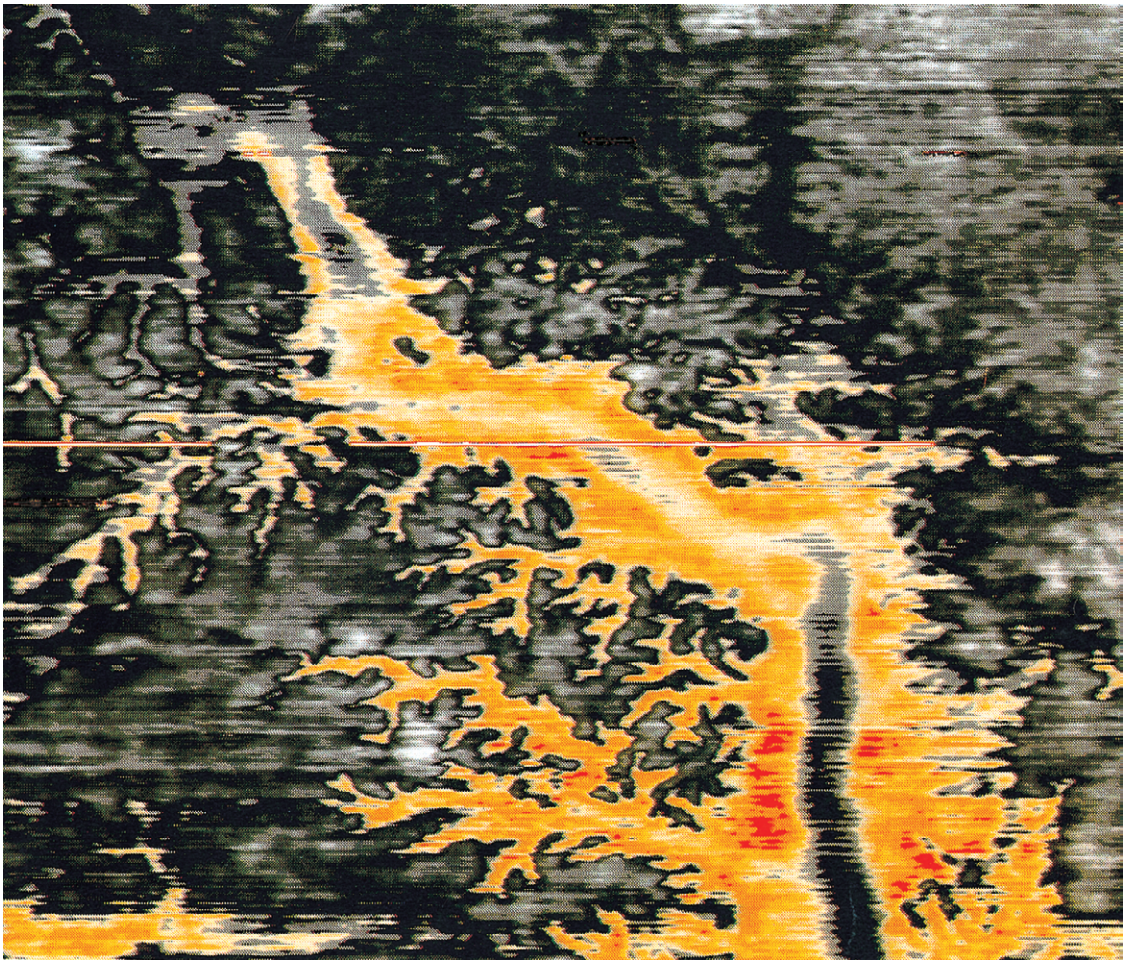

Fig. 4-19. Horizontal section at 104 ms from Nubi 3-D survey recorded in the Mahakam delta offshore Kalimantan, Indonesia. Note the dendritic patterns of incised canyons. (Courtesy Total Indonesie.)

Figure 4-20 shows a shallow horizontal section from a part of the Gulf of Thailand different from that discussed above; it covers a much larger area than other sections in this chapter, which is evidenced by the collage of eight panels. There is a plethora of depositional features clearly visible. In the lowermost and uppermost parts of the figure, channels cross each other. This is evidence that a horizontal section observes a slab of the subsurface of finite thickness (around a quarter of a wavelength) during the deposition of which, in this area, conditions changed significantly. On the right center of Figure 4-20 a meandering channel is visible. Where this channel turns into the center of the figure, it passes point bars inside the meander loops and crevasse splays outside them.

Figure 4-21 is a horizontal section from the Gulf of Mexico showing another clearly visible channel. The channel is fairly difficult to observe on the companion vertical section of Figure 4-22. This demonstrates again the unique value of the strike perspective in recognizing characteristic stratigraphic patterns.

Figure 4-23 shows the interpretation of several Miocene deltaic fans. They are visible on one horizontal section because the structural dip is very gentle. Figure 4-24 shows one deltaic fan from deeper within the same area. The single gray scale used for display of these two examples was beneficial for the overall fan morphology because much of the stratigraphic patterns were in low amplitudes (refer to the discussion of color schemes in Chapter 2).

Reconstituting a Depositional Surface

In general, stratigraphic features, after being deposited on a flat-lying surface, will be bent and broken by later tectonic movements. Stratigraphy and structure then become confused and the interpretive task comes in separating them. The structure must be interpreted before stratigraphy can be appreciated.

Downloaded 25 Jun 2012 to 95.28.162.50. Redistribution subject to SEG license or copyright; Terms of Use: http://segdl.org/

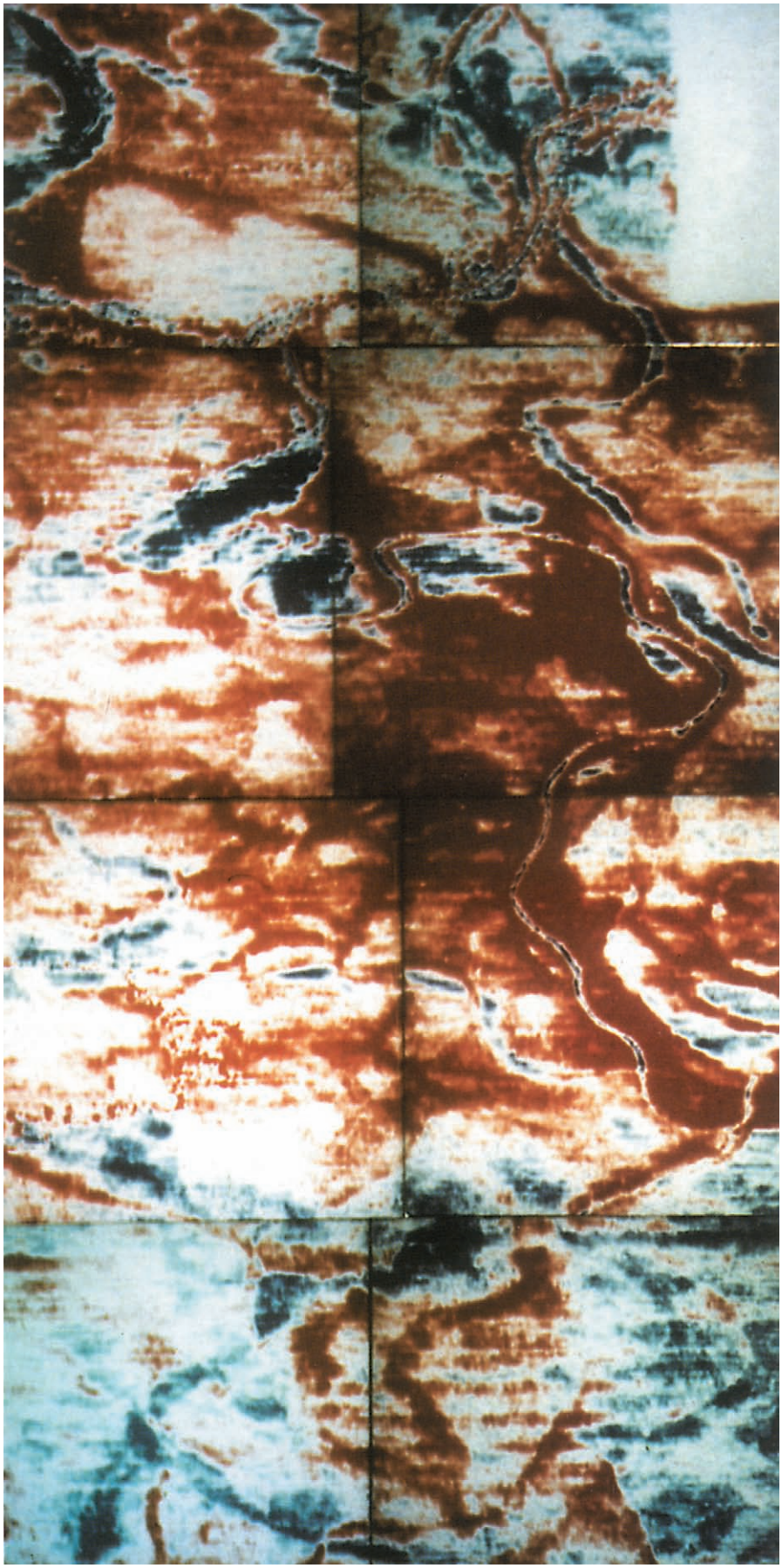

Fig. 4-20. Shallow horizontal section from Gulf of Thailand showing channels, point bars and crevasse splays. (Courtesy Unocal Thailand Ltd.)

Downloaded 25 Jun 2012 to 95.28.162.50. Redistribution subject to SEG license or copyright; Terms of Use: http://segdl.org/

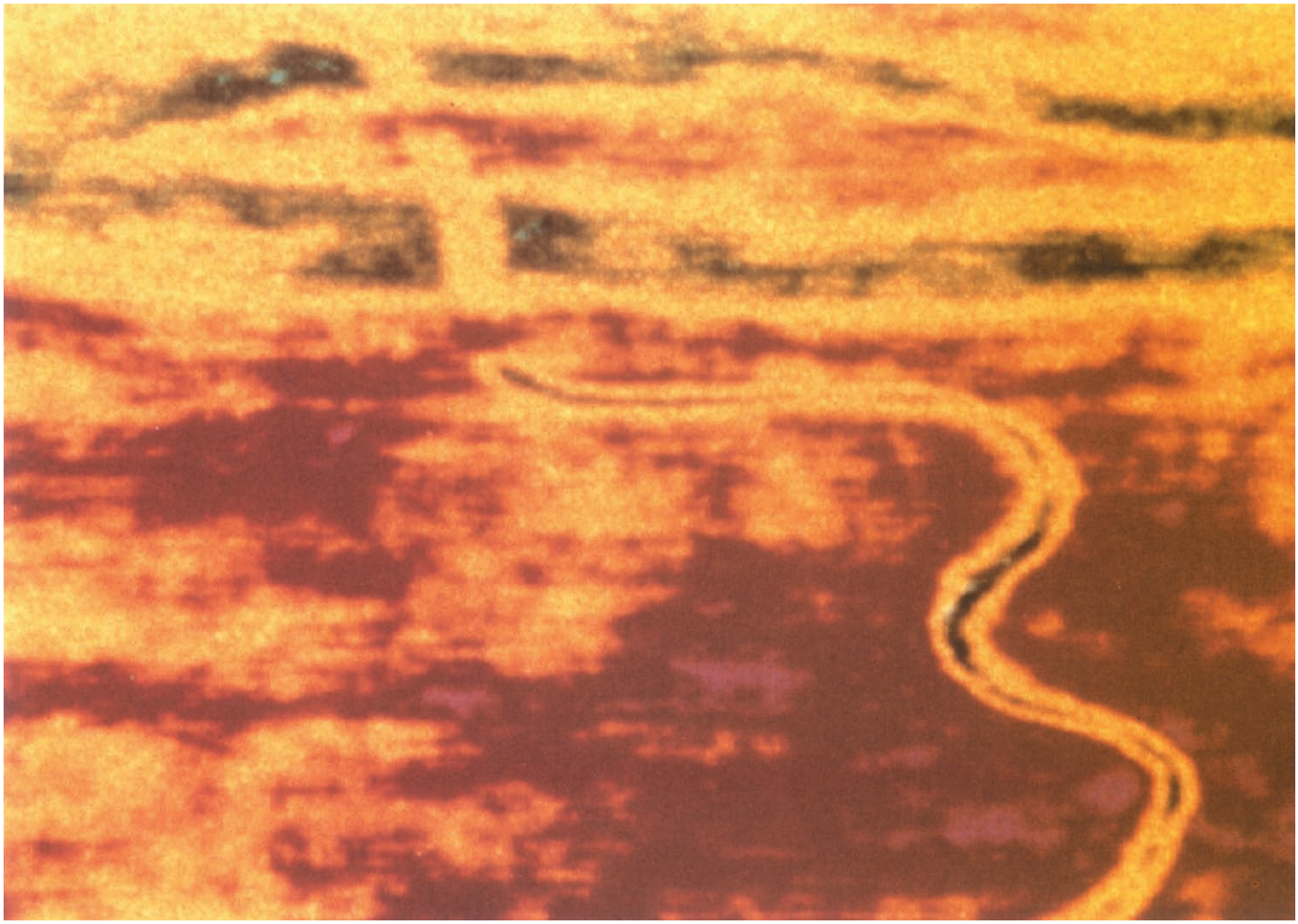

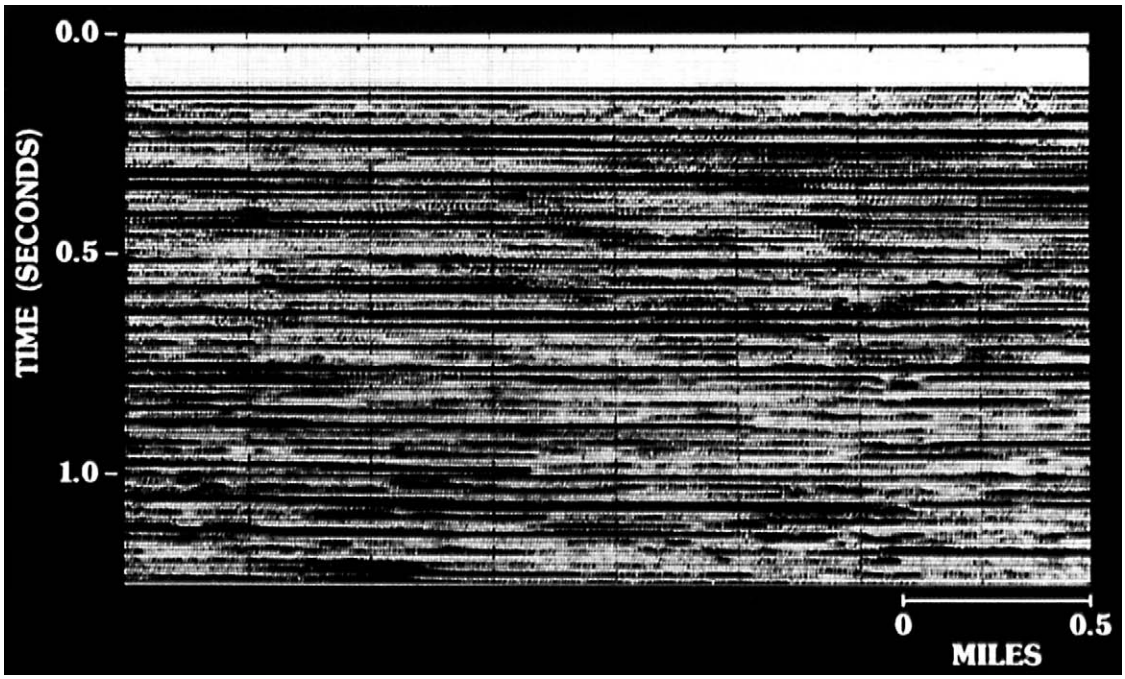

Fig. 4-21. Horizontal section from Matagorda Block 668, offshore Texas, showing prominent channel. It is a useful and interesting challenge to locate the channel intersection on the vertical section of Figure 4-22. (Courtesy ARCO Oil and Gas Company.)

Fig. 4-22. Vertical section from Matagorda Block 668, offshore Texas. (Courtesy ARCO Oil and Gas Company.)

Downloaded 25 Jun 2012 to 95.28.162.50. Redistribution subject to SEG license or copyright; Terms of Use: http://segdl.org/

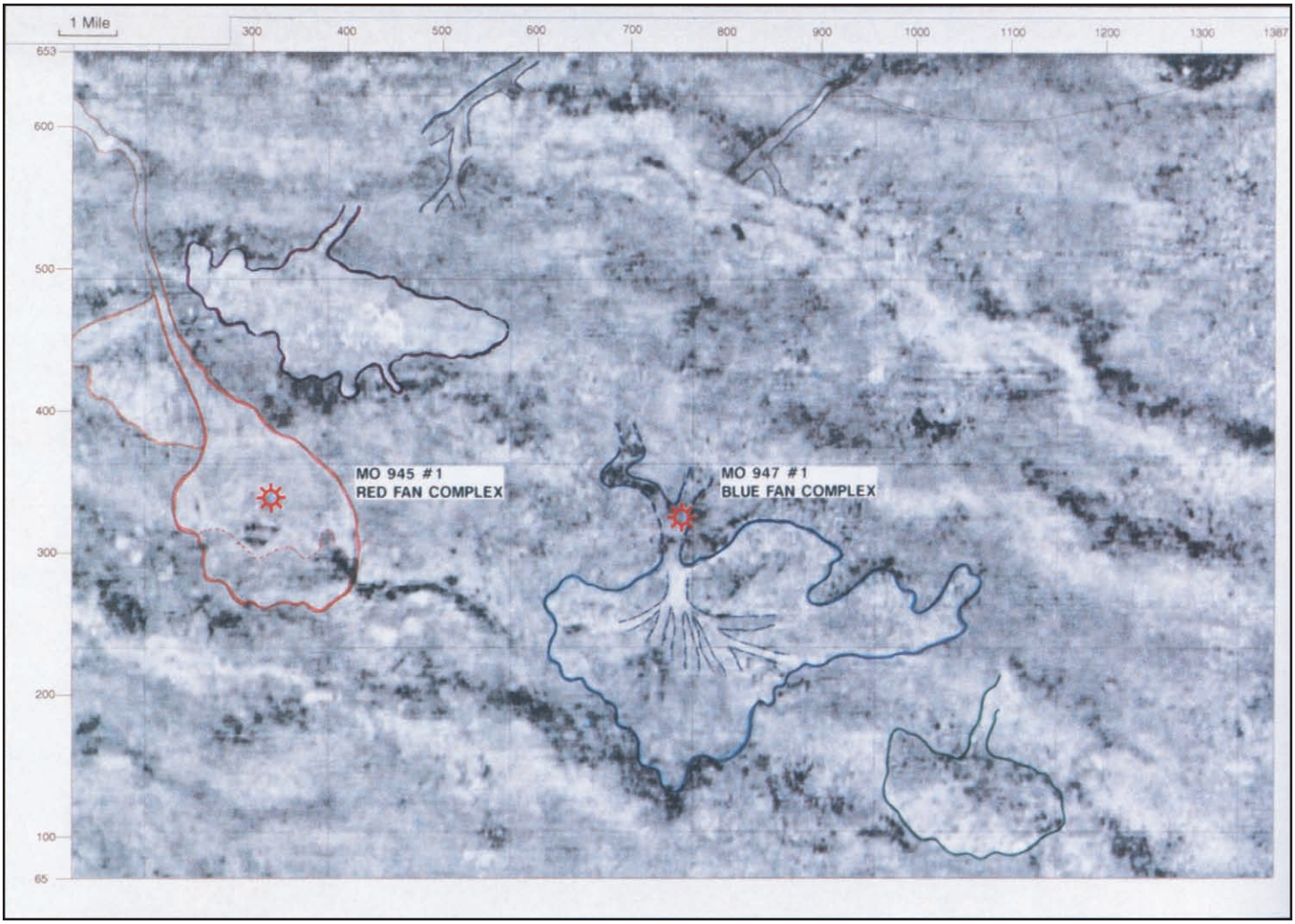

Fig. 4-23. Horizontal section at 936 ms from Mobile area, offshore Alabama, showing interpretation of numerous Miocene deltaic fans. (Courtesy Conoco Inc. and Digicon Geophysical Corp.)

Figure 4-25 illustrates schematically how a channel can be recognized and delineated in the presence of structure. In this example the interpreter has horizontal sections at 4 ms intervals from 1240 to 1260 ms. The selected event at 1240 ms for the horizon under study is traced to provide the contour as shown for 1240 ms. A high amplitude anomaly is recognized and marked at the position of the green blob. This procedure is repeated at 1244, 1248, 1252, 1256, and 1260 ms. At each of these levels the interpreter found an amplitude anomaly; together these arranged themselves into the curvilinear feature marked by the orange lines in Figure 4-25. This is manual amplitude mapping but the interactive workstation gives us several tools to do this in an efficient way.

Figure 4-26 shows a vertical section interpreted on three horizons. The Shallow Horizon, marked in blue, was selected on the basis of both structural and stratigraphic objectives. Figure 4-27 shows the structural contour map of the Shallow Horizon resulting from a full-scale structural interpretation of all the 3-D data. The desire then was to slice through the data volume along this structurally interpreted horizon in order to gather up all the seismic amplitudes associated with it. This is normally accomplished by the process of *amplitude extraction*, a menu-initiated search-and-gather operation on the interactive workstation. Alternatively, it is possible to flatten the data volume on the Shallow Horizon, as structurally interpreted in Figure 4-27, and then slice horizontally through the flattened volume at the level of the interpreted horizon.

The resultant section is known as a **horizon slice.** This type of section, following one horizon, must be along bedding planes or it loses its value for stratigraphic interpretation.

Downloaded 25 Jun 2012 to 95.28.162.50. Redistribution subject to SEG license or copyright; Terms of Use: http://segdl.org/

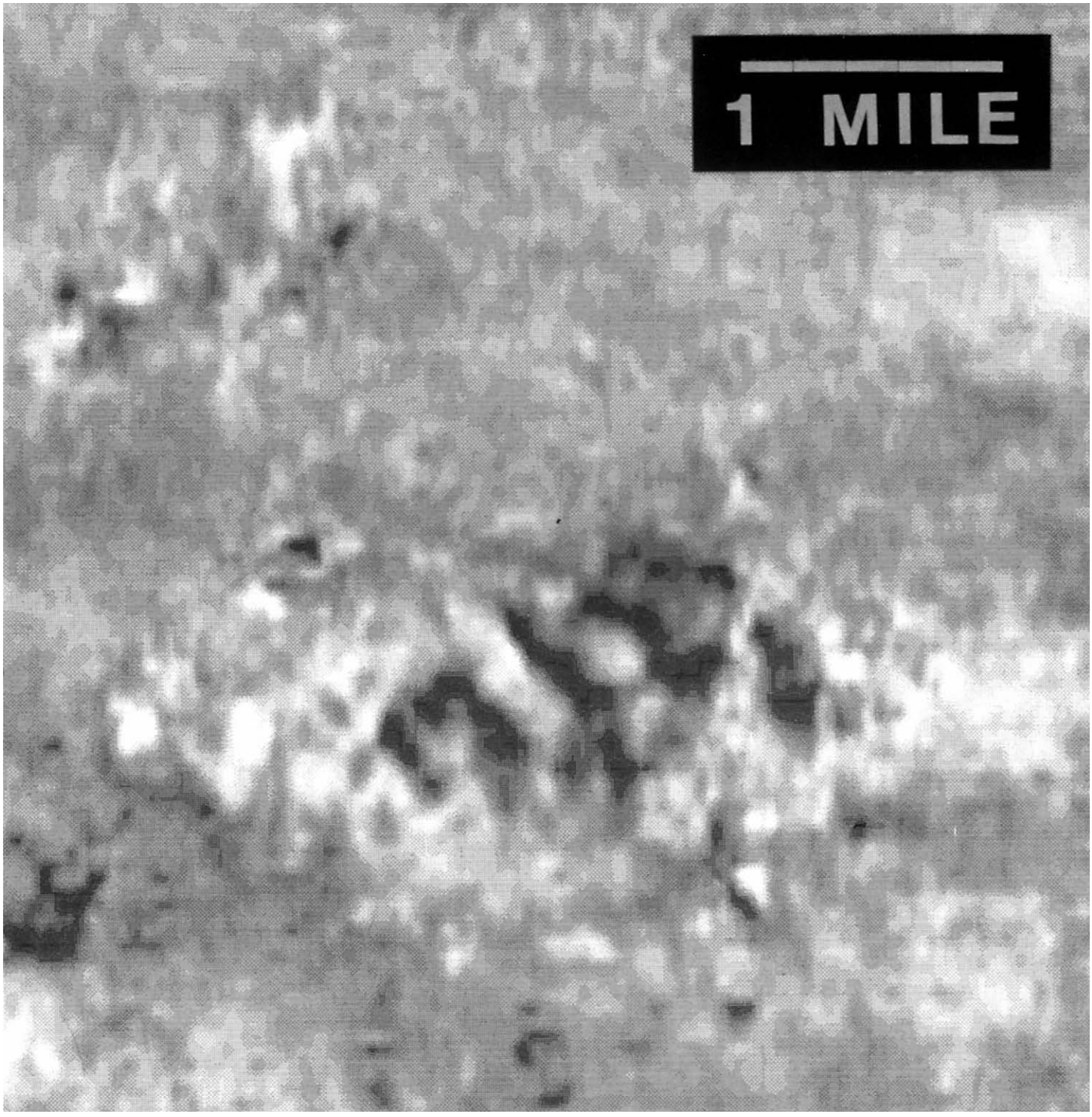

Fig. 4-24. Horizontal section at 1268 ms from Mobile area, offshore Alabama, showing one Miocene deltaic fan. Gas is being produced from one of the black channels. (Courtesy Conoco Inc. and Digicon Geophysical Corp.)

Downloaded 25 Jun 2012 to 95.28.162.50. Redistribution subject to SEG license or copyright; Terms of Use: http://segdl.org/

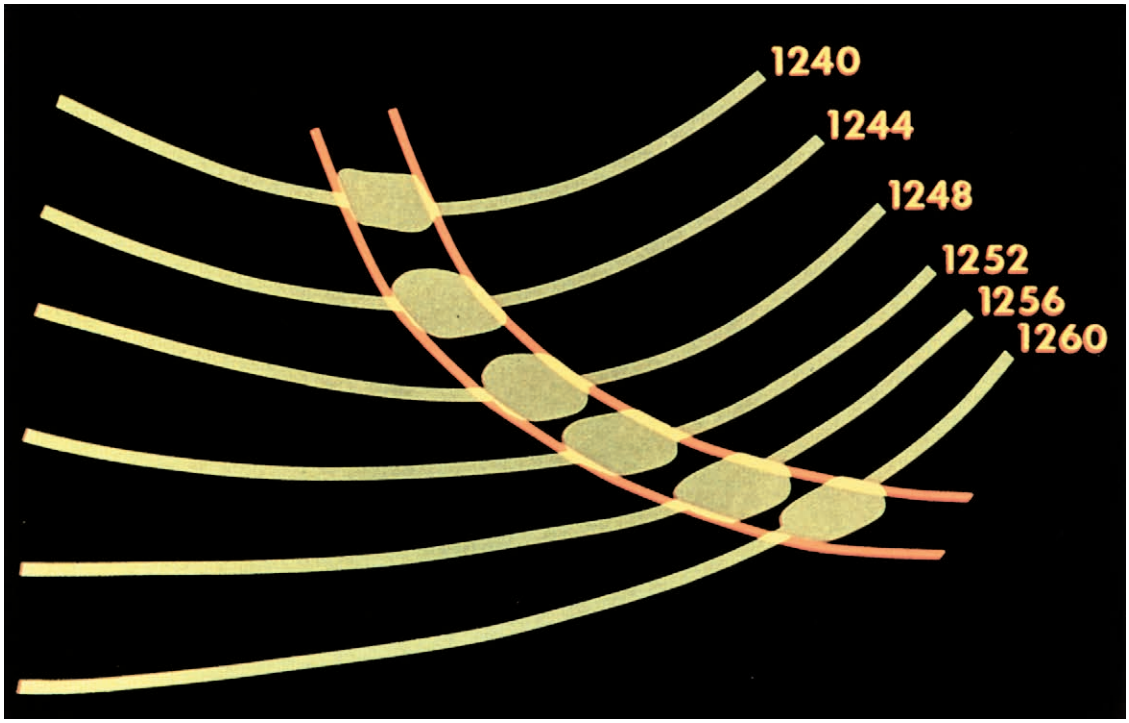

Fig. 4-25. How to follow an anomalous amplitude feature in the presence of structure on a sequence of horizontal sections.

The importance of this approach was first stressed by Brown, Dahm, and Graebner (1981).

Figures 4-28 and 4-29 are horizon slices through adjacent conformable horizons both following the structural configuration of Figure 4-27. Both were sliced through peaks and hence all amplitudes are positive and show as varying intensities of blue; the darker blues indicate the higher amplitudes. The approximately north-south light-colored streaks are the faults; the width of a streak gives an indication of fault heave.

Figure 4-28 shows a broad high amplitude trending northwest-southeast toward the left of the section. This is interpreted as a sand bar. It is evident that this inferred bar has been dissected by several faults. The process of constructing the horizon slice has put the bar back together. Hence the construction of a horizon slice amounts to the reconstitution of a depositional surface.

Figure 4-29 shows more spatial consistency of the darker blues, indicating that this horizon follows a sheet sand. There is a curvilinear feature, somewhat the shape of a shepherd's crook, which runs northwest-southeast just to the west of well 5X. This is interpreted as an erosion channel in the sheet sand. The fact that this inferred channel is continuous across the fault just west of well 5X lends support that this horizon slice has correctly reconstituted the depositional surface into which the channel was cut.

Figure 4-30 indicates by two black arrows the two seismic horizons followed in the construction of the horizon slices of Figure 4-31. The high amplitude feature shaped somewhat like a hockey stick appears very similar on the two sections. It is invisible on other adjacent horizon slices (not shown). Hence the seismic signature of this inferred channel is trough-over-peak, which implies high velocity material, given the polarity convention implicit in these data. After inverting the whole data volume to seismic logs (Chapter 9), a horizon slice through this velocity volume positioned between the horizon slices of Figure 4-31 generated the velocity horizon slice of Figure 4-32. The darker colors indicate the high velocity channel fill.

Methods of Making Horizon Slices

Automatic horizon tracking, now commonplace in interactive interpretation systems, has greatly facilitated the generation of horizon slices. When a horizon is tracked, the extreme amplitude as well as its time is stored in the digital database. Mapping of the times produces a structure map; mapping of the amplitudes produces a horizon slice. More commonly, only the time is stored as a result of horizon tracking and later the

Downloaded 25 Jun 2012 to 95.28.162.50. Redistribution subject to SEG license or copyright; Terms of Use: http://segdl.org/

amplitudes are extracted from the data. In addition, it is possible to extract the amplitudes not coincident with the tracked horizon but parallel to it and shifted by a chosen number of milliseconds.

Figure 4-33 shows two lines from a Gulf of Mexico 3-D prospect, where a horizon is tracked one-and-a-half periods above a red blob considered to be of stratigraphic interest. The structural continuity is better for the horizon being tracked than for the blob, so the structure was defined at this level and the horizon slice made parallel to it through the blob at a fixed time increment deeper.

The resulting horizon slice is shown in Figure 4-34 and the interpreter can readily infer the existence of another channel. The black horizontal lines indicate the positions of the two vertical sections of Figure 4-33. The amplitude of the channel reflection is greater to the northeast; a discussion of this relative to implied gas content appears in Chapter 5.

A horizon slice is by definition a slice along a bedding plane, but the methods by which an interpreter may make such a slice are many and varied (Figure 4-35). If the slice is made at the tracking level, following automatic horizon tracking, the horizon slice is made up of truly crestal amplitudes and should thus be accurately along the bedding plane. However, if the structure is defined by tracking at one level where the continuity is clear but the slice is made parallel to that at another level, then the slicing and tracking levels must be sufficiently conformable for the horizon slice to adequately follow the bedding plane. This approach beneficially segregates the stratigraphic and structural components of an interpretation. Minor irregularities at the tracking level may not be paralleled at the slicing level, so spatial smoothing of the tracked times may be desirable before displacing the horizon down or up to the slicing level.

When a tracked horizon is displaced down by a constant time shift, the option exists to snap the displaced horizon to the exact crestal amplitude of the new reflection. Sometimes this will be the right course of action and sometimes it will be wrong. Figure 4-36 illustrates diagrammatically a situation where it would be wrong. Good reflections exist at the sand/shale interface and the shale/limestone interface. However, at the latter patches of porosity form the exploration objective and also introduce character changes along the limestone reflection. The shale is of uniform thickness. The structure is followed on the sand/shale reflection, which is stratigraphically uncomplicated, and displaced down by a constant time shift to the top of the limestone. The amplitudes are then extracted *without snapping* to yield a horizon slice on which the porosity should show as low amplitude patches. Snapping would move the horizon down to the top of the unporous limestone and the low amplitude patches would be lost!

Slicing through a zone of poor reflection continuity (where tracking would have been impossible) parallel to a good reflection at the top or the base of the zone has in several cases yielded meaningful and interpretable stratigraphic patterns. This demonstrates that data that may appear poor and uninterpretable on vertical sections may in fact reveal significant stratigraphic information when viewed spatially over bedding plane surfaces. In the case of a poor continuity interval of nonuniform thickness it can be useful to track a reflection at the top and one at the base (Figure 4-37). Then the slice is made within that interval using a surface whose shape is based partly on the upper tracked surface and partly on the lower tracked surface, the proportions of each depending on where within the interval the slice is desired. This method yields **proportional slices**.

After amplitude has been extracted on the objective horizon corrections are sometimes required (Figure 4-35). Consider, for example, that a high amplitude bright spot on a deeper horizon slice is shadowed over part of its area by a shallower high amplitude anomaly. This is commonly referred to as transmission effect, and an example of this is discussed in Chapter 5. Some fraction of the amplitude extracted on the shallower horizon can be added to the amplitude on the deeper horizon to compensate for the shadowing effect. The fraction to use must be established empirically but the

Downloaded 25 Jun 2012 to 95.28.162.50. Redistribution subject to SEG license or copyright; Terms of Use: http://segdl.org/

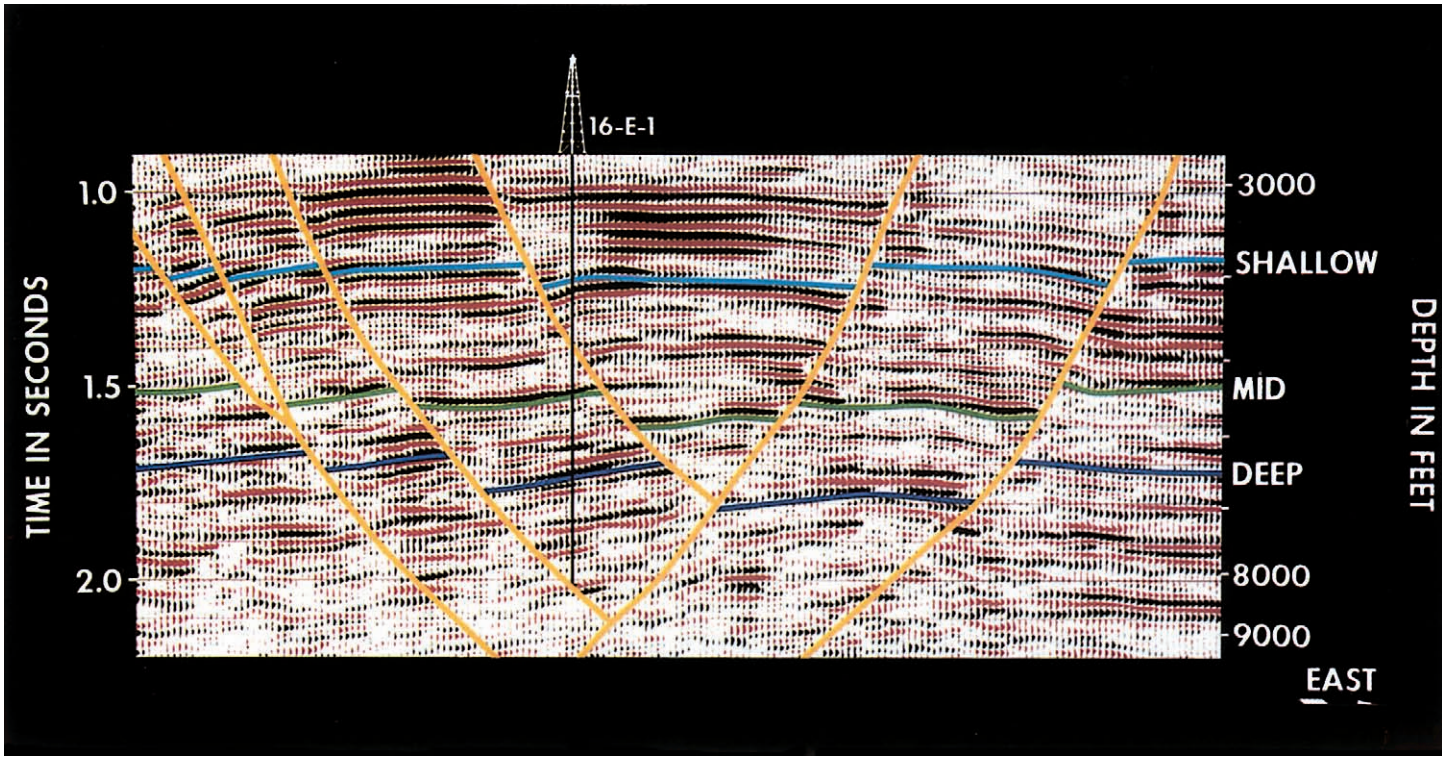

Fig. 4-26. Line 55 interpreted showing structure of Shallow Horizon. (Courtesy Texas Pacific Oil Company Inc.)

author has often used one-quarter. Lateral variations in amplitude caused by surface conditions or acquisition footprint can sometimes be removed successfully by normalization. The amplitude of a shallower horizon is assumed to be constant and then the amplitude ratio of the objective horizon to the shallow reference should remove the effect.

Horizon Slice Examples

Figure 4-38 shows a sequence of faults affecting one horizon interpreted on a vertical section from a 3-D survey in the Gulf of Thailand. Figure 4-39 shows the time structure map resulting from the complete structural interpretation of the same horizon. The faults trending north-northwest to south-southeast divide the area into seven fault blocks. The corresponding horizon slice is shown in Figure 4-40. A meandering stream channel is evident and gas production from the channel has been established in two of the fault blocks.

The continuity of the channel confirms that the depositional surface has been correctly reconstituted. Clearly the value of such a horizon slice for stratigraphic purposes is critically dependent on the accuracy of the structural interpretation that was involved in its derivation. Here the stratigraphic and structural interpretation actually impacted each other iteratively. The first horizon slice generated for this level did not show the channel continuity of Figure 4-40 in one of the fault blocks. This suggested miscorrelation into that block. After re-examining the correlation and retracking the data in that block, the horizon slice shown as Figure 4-40 was obtained. The improved channel continuity indicated the relative correctness of the updated structural interpretation.

Figures 4-41 and 4-42 show the time structure map and horizon slice for one interpreted horizon in a Gulf of Mexico shallow water prospect. Two channels are evident, one of them intersected by a fault. The deeper channel lies between 2100 and 2200 ms which converts to depths around 2500 m (8,200 ft).

Figure 4-43 shows a Gulf of Mexico horizon slice with overlain structural contours. This is a particularly valuable form of display (compare Figure 5-31) because it permits interpretation of stratigraphic/reservoir patterns in their present-day structural

Downloaded 25 Jun 2012 to 95.28.162.50. Redistribution subject to SEG license or copyright; Terms of Use: http://segdl.org/

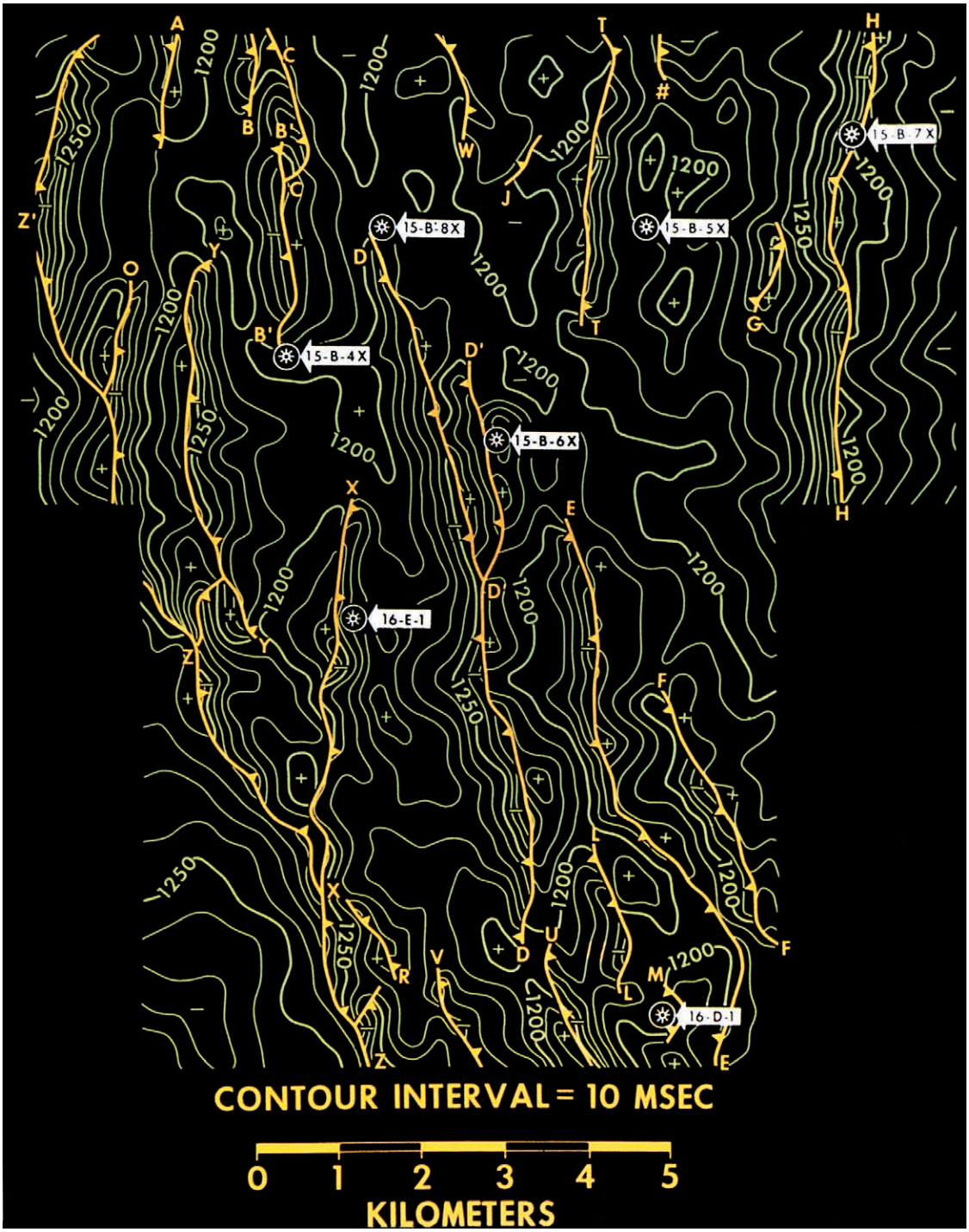

Fig. 4-27. Time structure map of Shallow Horizon. (Courtesy Texas Pacific Oil Company Inc.)

context. Here the high amplitudes (reds and oranges) are caused by gas in several sand bodies. Note the sharp amplitude terminations toward the south (downdip), indicating the position of the gas-water contacts.

Figure 4-44 is an arbitrary line through three wells from a 3-D survey in southern Canada. The structure was defined at the Base Bow Island reflection. A slice parallel to this through the Glauconite zone yielded the horizon slice of Figure 4-45. This approach was used in order to help distinguish stratigraphic variations from structural variations at the objective level. Even then the stratigraphic patterns were not clearly apparent, but a further interpretation tied to well intersections yielded the superimposed stratigraphic descriptions.

Downloaded 25 Jun 2012 to 95.28.162.50. Redistribution subject to SEG license or copyright; Terms of Use: http://segdl.org/

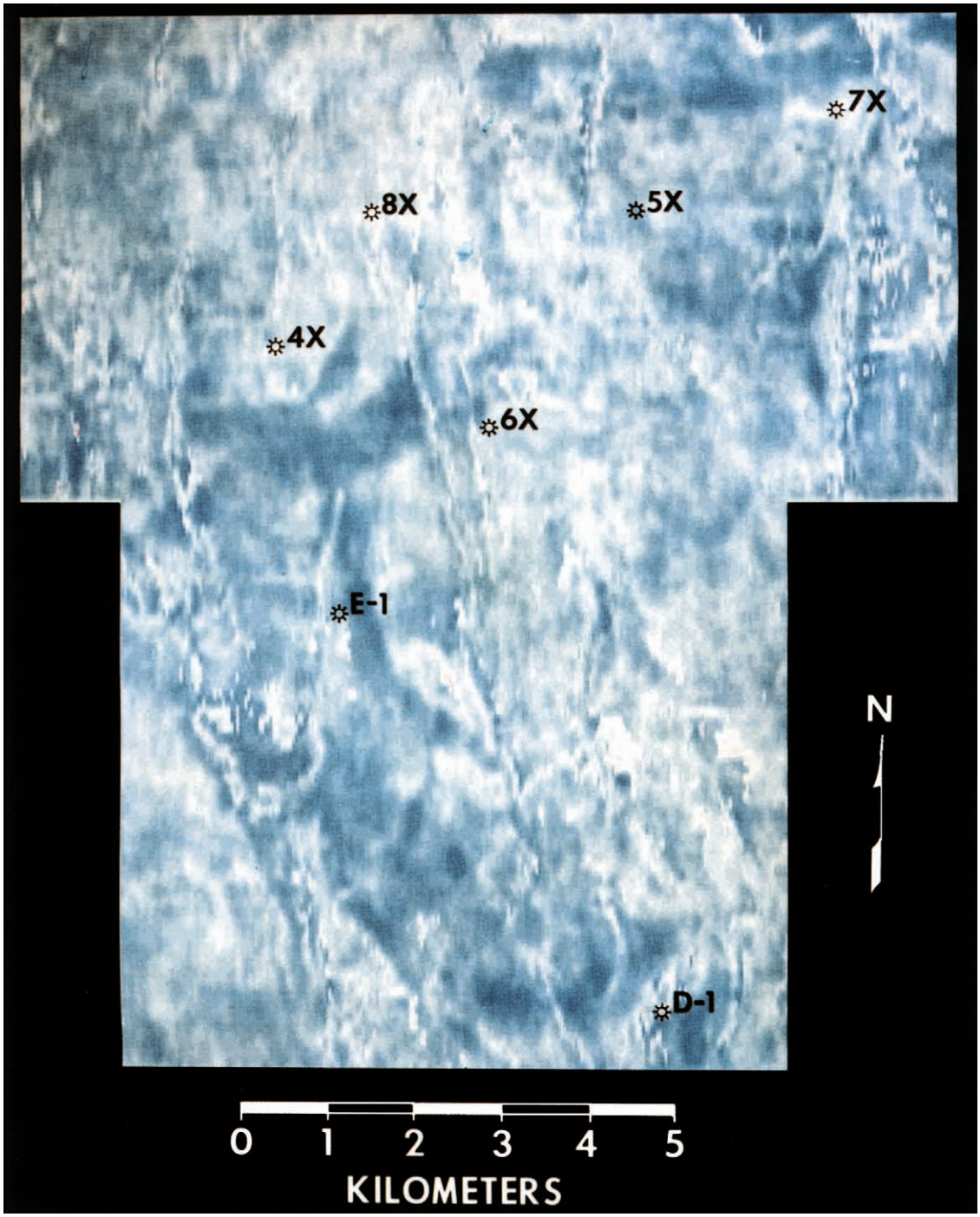

Fig. 4-28. Horizon slice 180 feet (60 m) below Shallow Horizon showing northwest-southeast-trending high amplitude interpreted as a sand bar. (Courtesy Texas Pacific Oil Company Inc.)

Figure 4-46 is a mosaic of amplitudes from 3-D and 2-D data from Argentina and demonstrates the increased stratigraphic detail available from 3-D data (Gerster, 1995). Three 3-D surveys are shown; seven others exist in the immediate area.

Figure 4-47 is a horizon slice from offshore eastern Canada between 2.4 and 2.8 seconds showing many channels and their levees, an old shore line and an abandoned lake (Enachescu, 1993).

Figure 4-48 is a horizon slice from the Norwegian North Sea. The interesting fan-shaped feature is interpreted as a mass flow in the Danian (basal Tertiary) chalk.

The majority of the horizon slices presented in this chapter display seismic amplitude, and this also reflects the author's usage. However, it is possible to make horizon slices in other attributes. Figure 4-32, for example, displays inversion velocity.

Downloaded 25 Jun 2012 to 95.28.162.50. Redistribution subject to SEG license or copyright; Terms of Use: http://segdl.org/

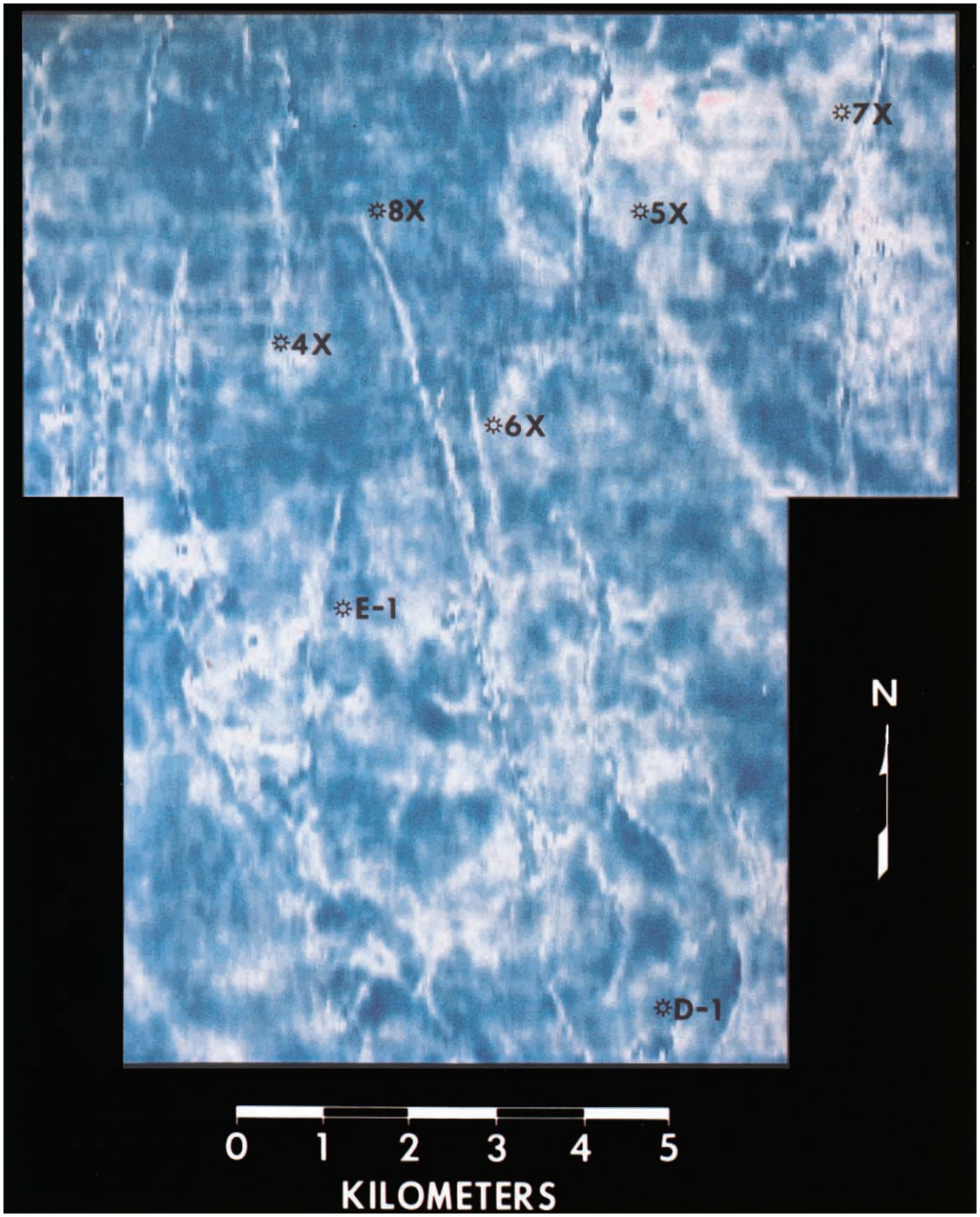

Fig. 4-29. Horizon slice through Shallow Horizon showing a partly eroded sheet sand. (Courtesy Texas Pacific Oil Company Inc.)

Unconformity Horizon Slices

Figure 4-49 shows a horizon slice from another Gulf of Mexico prospect. The amplitudes are in shades of blue and the time structure is superimposed as contour lines with an interval of 100 ms. Several amplitude lineations are apparent. The ones running approximately east-west are faults as evidenced by the displacement of the contours. The major lineation running north-northwest–south-southeast is apparently unrelated to the faulting. It is interpreted as the truncation of a sand dipping up from the east. It is probably a depositional edge but the erosional truncation of a sand at an unconformity would show in exactly the same manner. It is this lineation on the horizon slice which caught the interpreter's eye and thus begged for an explanation.

An excellent example of the variation in reflection character and amplitude across an angular unconformity comes from the Lisburne 3-D survey. The following

Text continues on page 140.

Downloaded 25 Jun 2012 to 95.28.162.50. Redistribution subject to SEG license or copyright; Terms of Use: http://segdl.org/

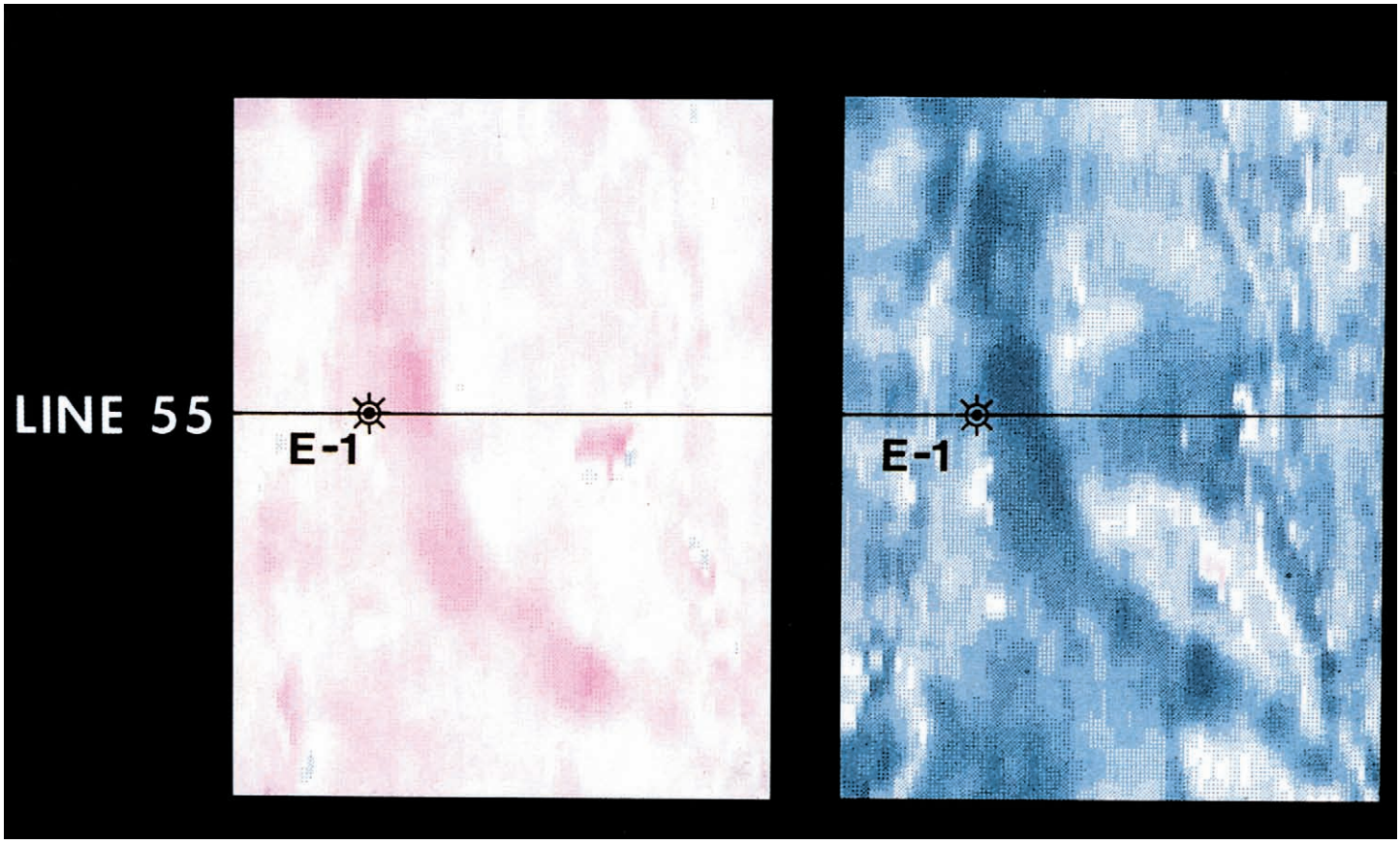

Fig. 4-31. Horizon slices through the two events marked with black arrows on Figure 4-30. The curvilinear features are interpreted as the reflections from the top and base of a channel. (Courtesy Texas Pacific Oil Company Inc.)

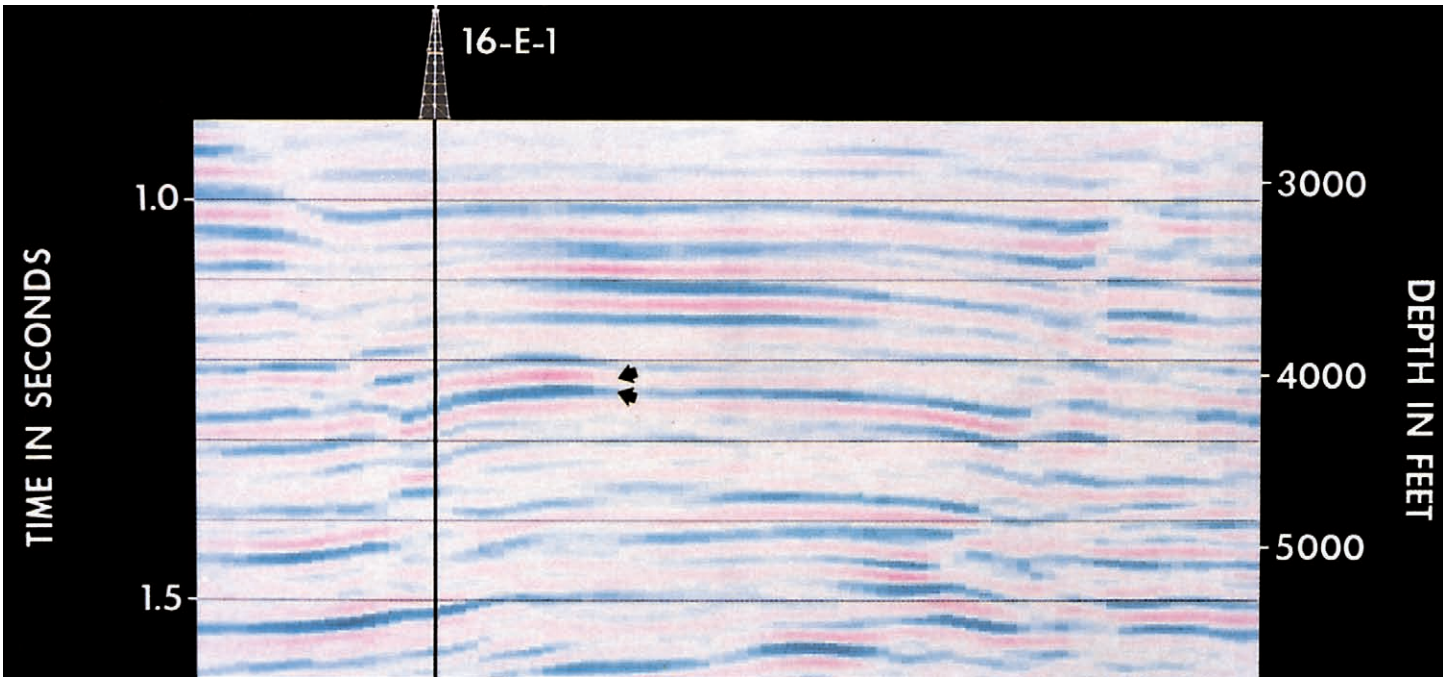

Fig. 4-30. A portion of Line 55 through the central graben of the 3-D prospect. (Courtesy Texas Pacific Oil Company Inc.)

Downloaded 25 Jun 2012 to 95.28.162.50. Redistribution subject to SEG license or copyright; Terms of Use: http://segdl.org/

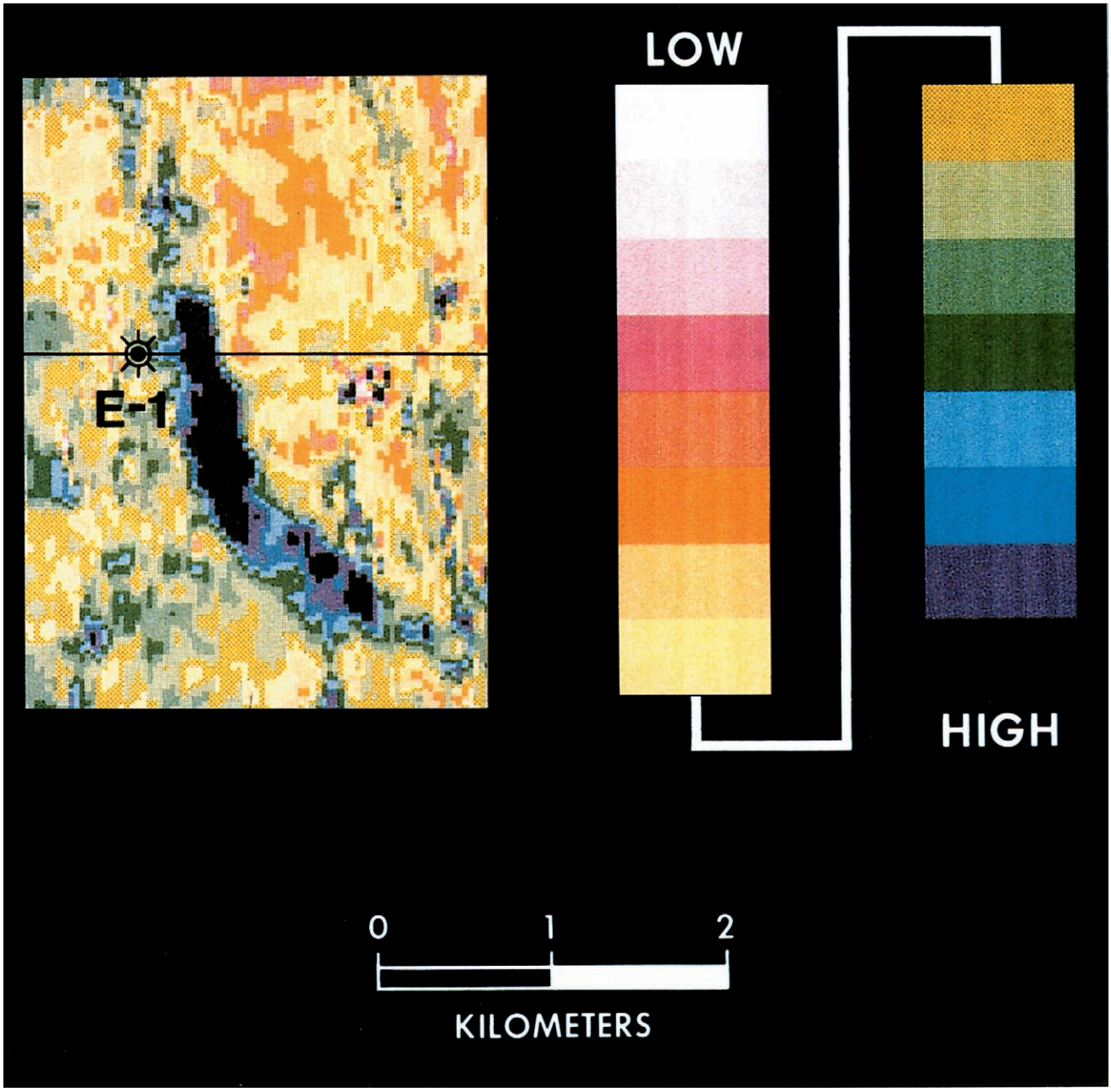

Fig. 4-32. Horizon slice in velocity positioned between the sections of Figure 4-31 and showing the extent of the high velocity channel fill. (Courtesy Texas Pacific Oil Company Inc.)

Downloaded 25 Jun 2012 to 95.28.162.50. Redistribution subject to SEG license or copyright; Terms of Use: http://segdl.org/

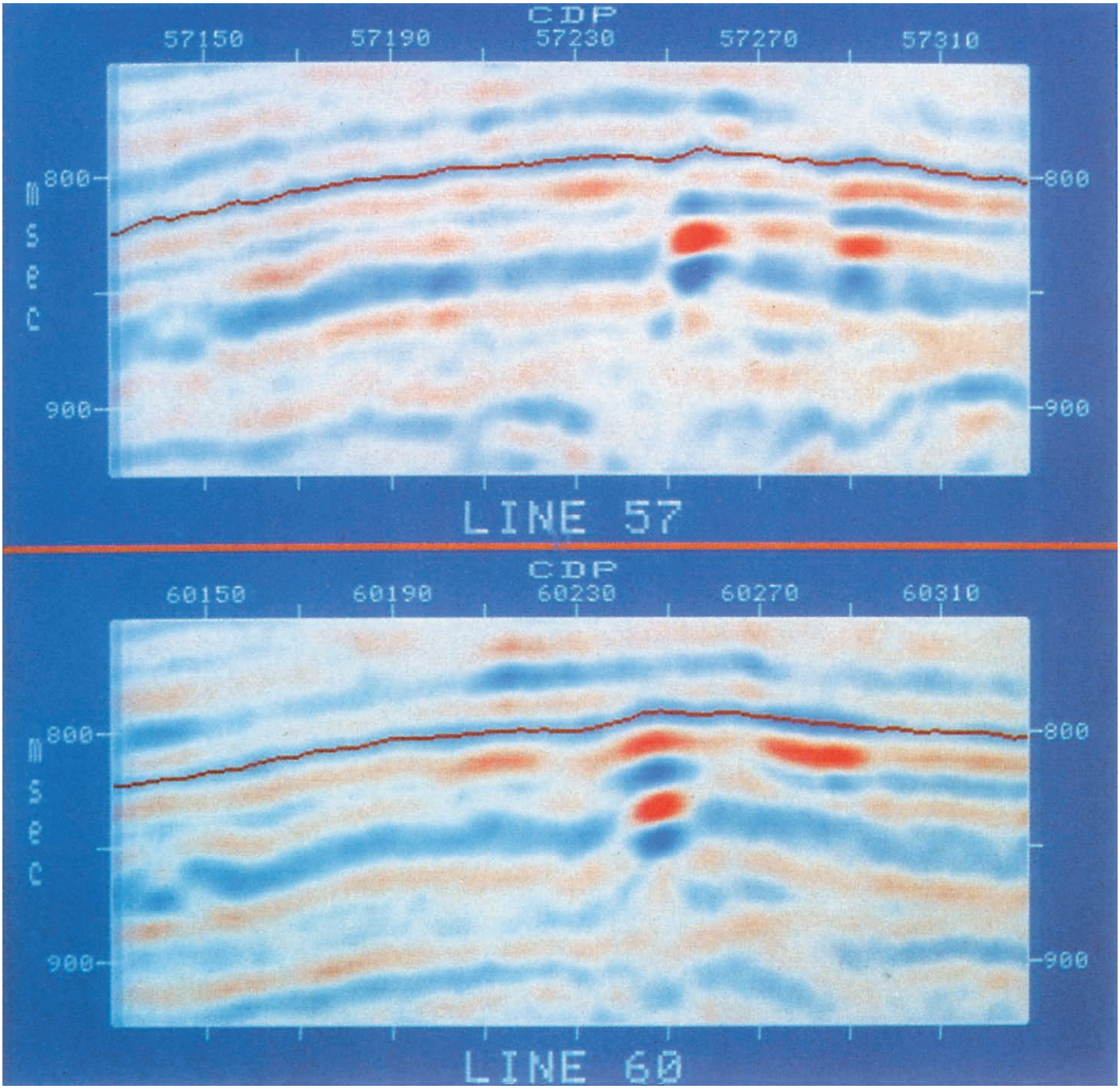

Fig. 4-33. Lines 57 and 60 from a 3-D survey in the Gulf of Mexico showing a tracked horizon above bright events indicating channel intersections. (Courtesy Chevron U.S.A. Inc.)

Downloaded 25 Jun 2012 to 95.28.162.50. Redistribution subject to SEG license or copyright; Terms of Use: http://segdl.org/

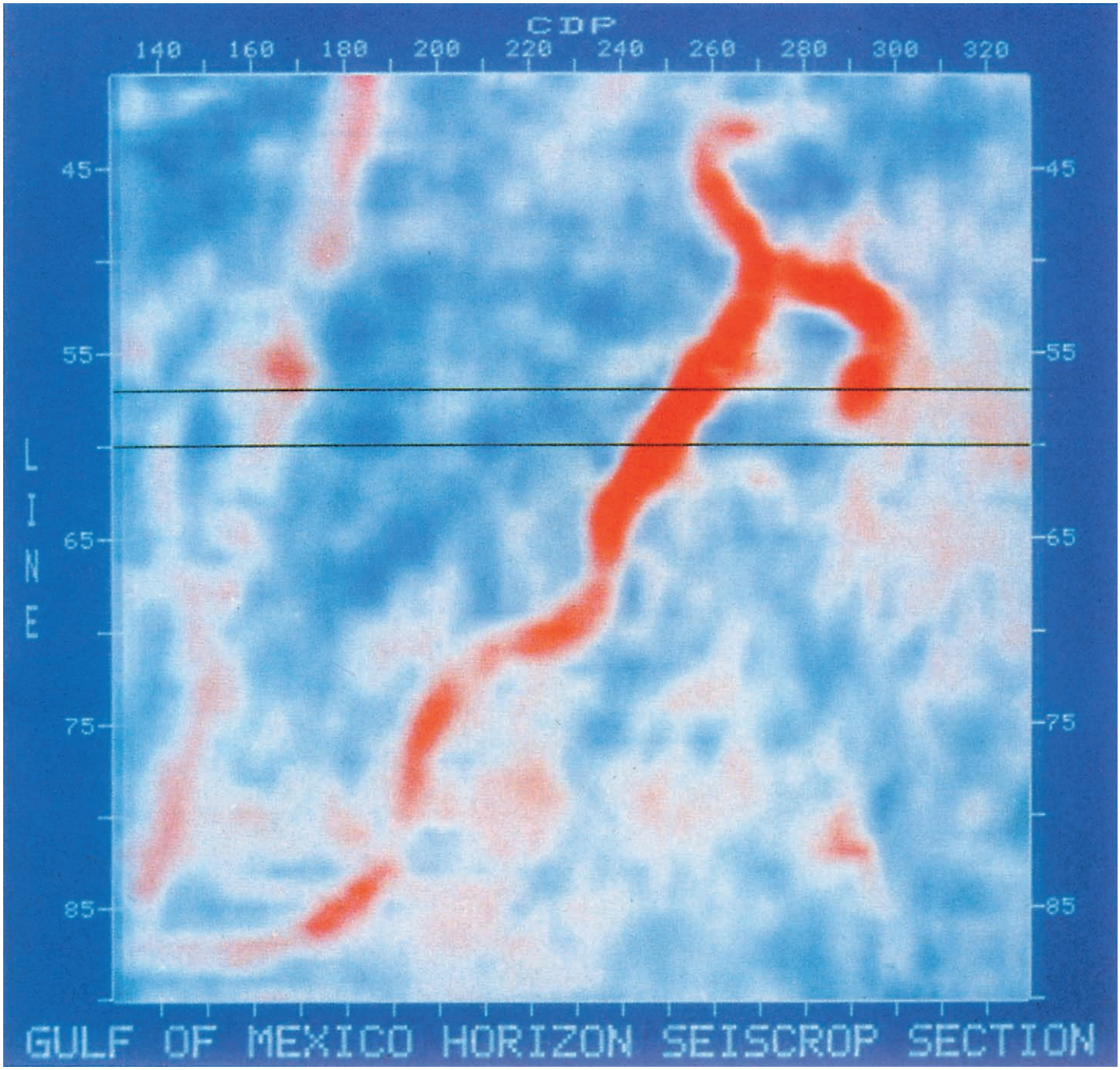

Fig. 4-34. Horizon slice showing channel intersected in Figure 4-33. (Courtesy Chevron U.S.A. Inc.)

Downloaded 25 Jun 2012 to 95.28.162.50. Redistribution subject to SEG license or copyright; Terms of Use: http://segdl.org/

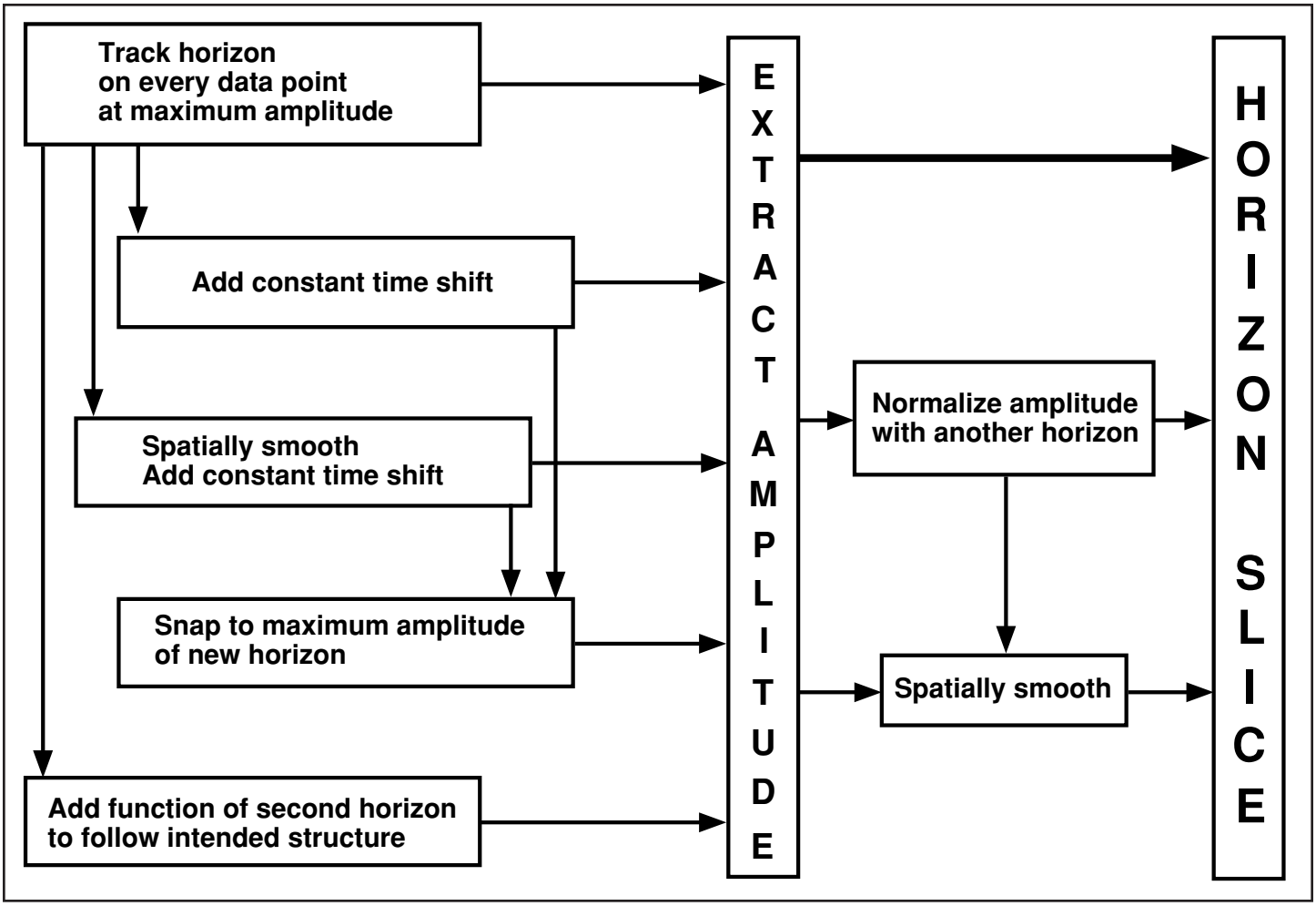

Fig. 4-35. Methods of making horizon slices. The tracking level and the slicing level need not be the same. Amplitude corrections may be necessary to compensate for shallower effects.

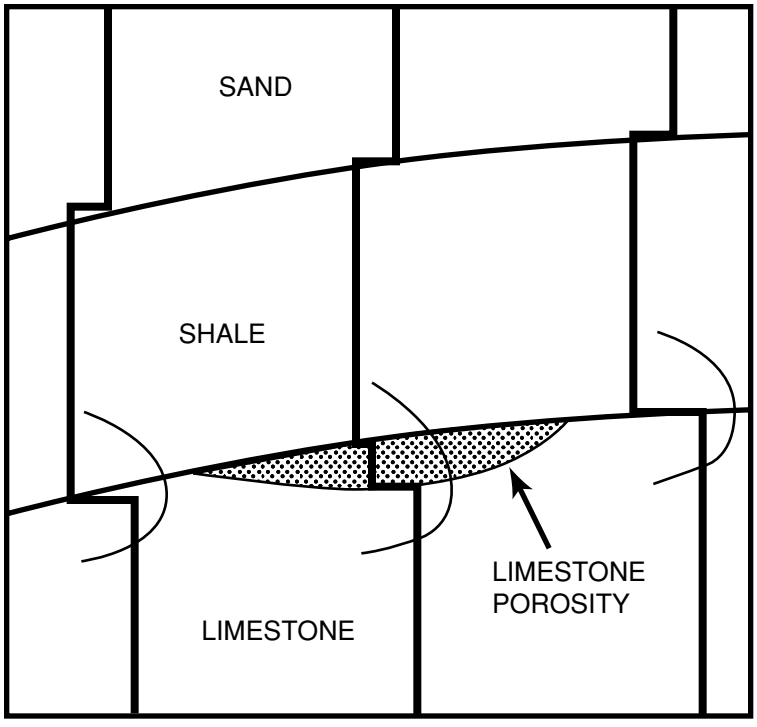

Fig. 4-36. Should a vertically-shifted horizon be snapped to the local amplitude maximum? In this situation the answer is 'no'. The heavy black vertical profiles are acoustic impedance and the exploration objective is the porosity patch at the top of the limestone layer.

Downloaded 25 Jun 2012 to 95.28.162.50. Redistribution subject to SEG license or copyright; Terms of Use: http://segdl.org/

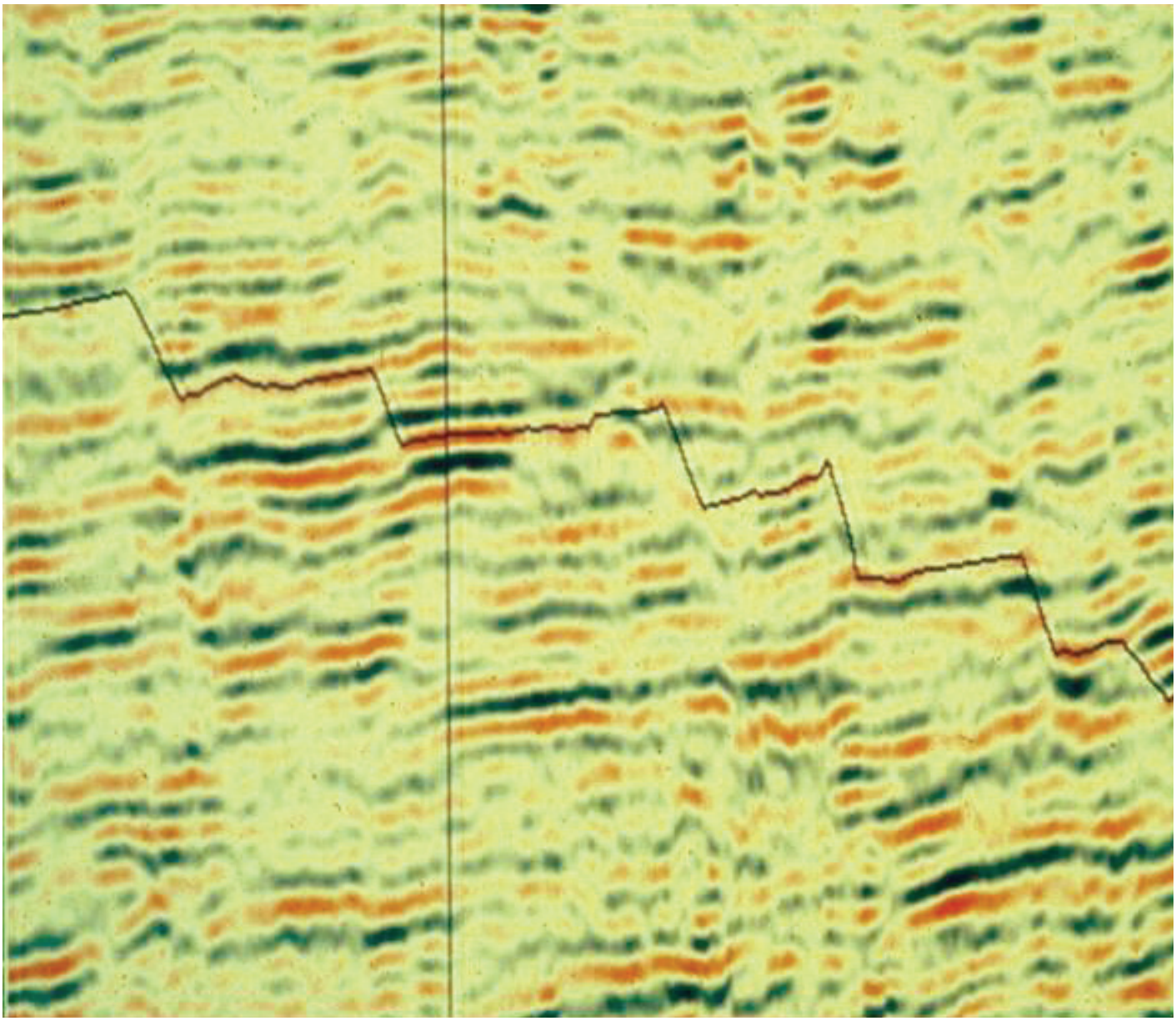

Fig. 4-38. Line 325 from 3-D survey in the Gulf of Thailand showing interpreted horizon through many fault blocks. (Courtesy Unocal Thailand Ltd.)

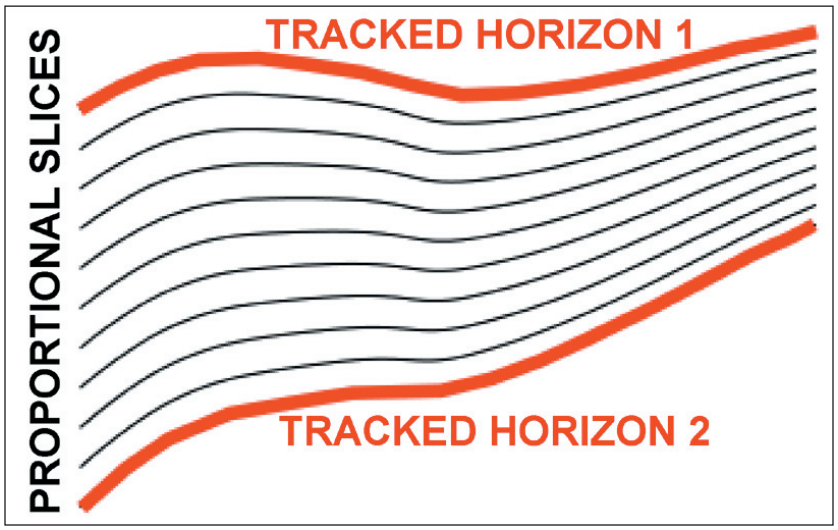

Fig. 4-37. Proportional slices are akin to horizon slices. The interval between two tracked horizons is divided proportionately into multiple increments in an attempt to slice along bedding planes when there is no horizon to follow at the level of interest.

Downloaded 25 Jun 2012 to 95.28.162.50. Redistribution subject to SEG license or copyright; Terms of Use: http://segdl.org/

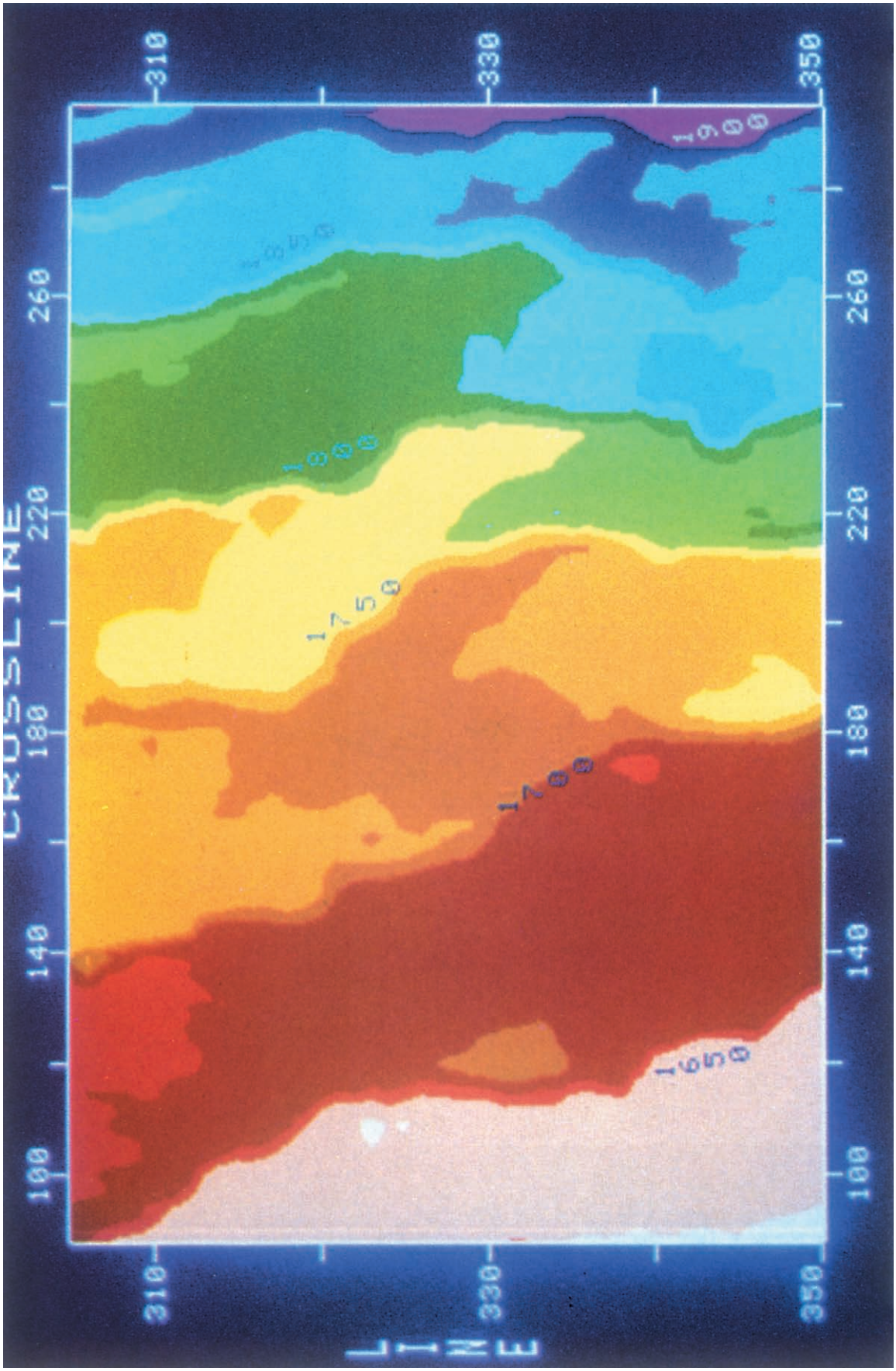

Fig. 4-39. Time-structure map of horizon tracked in Figure 4-38. (Courtesy Unocal Thailand Ltd.)

Downloaded 25 Jun 2012 to 95.28.162.50. Redistribution subject to SEG license or copyright; Terms of Use: http://segdl.org/

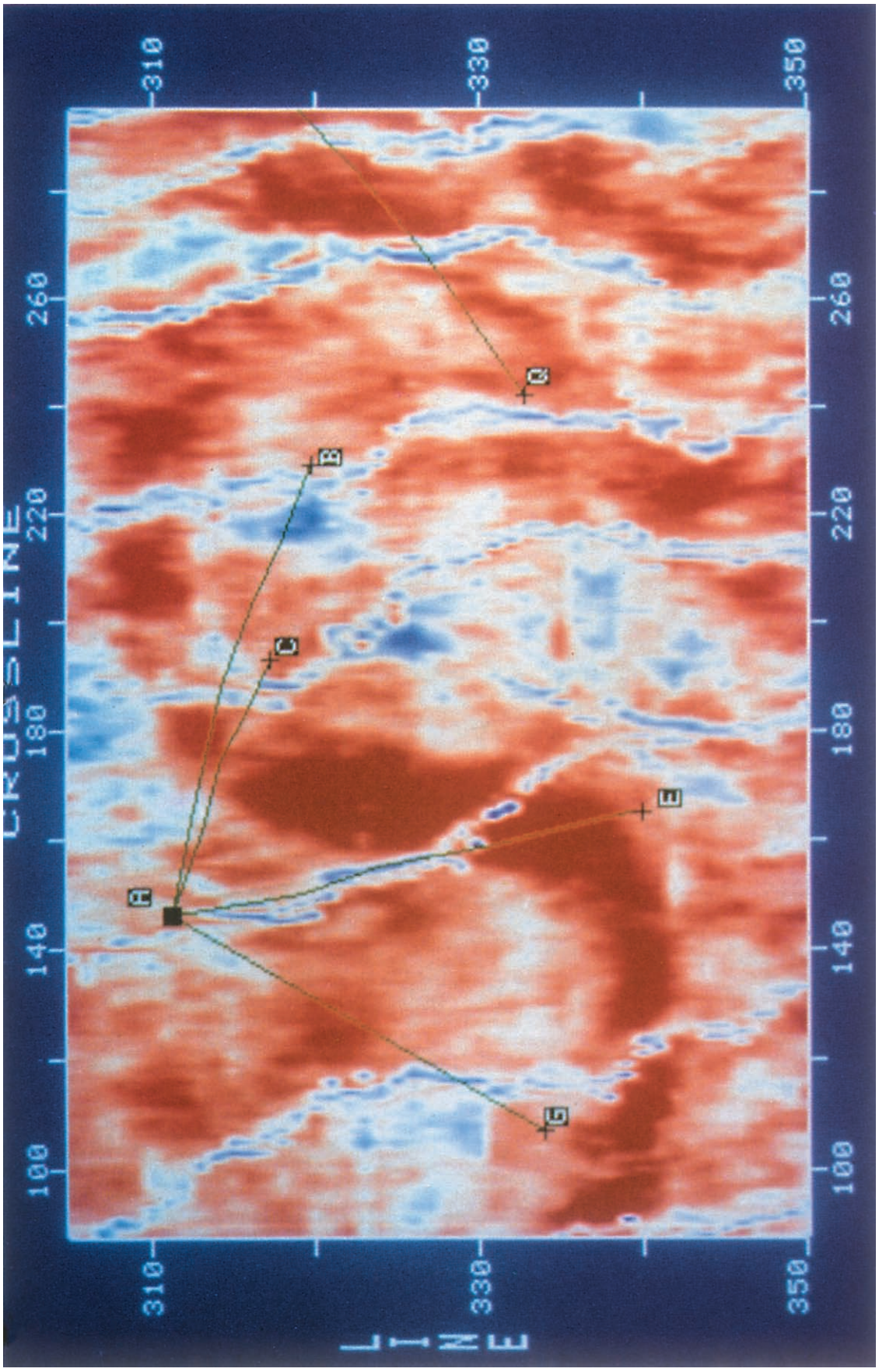

Fig. 4-40. Horizon slice showing spatial distribution of amplitude over the horizon mapped in Figure 4-39. Gas production has been established in the meandering channel. (Courtesy Unocal Thailand Ltd.)

Downloaded 25 Jun 2012 to 95.28.162.50. Redistribution subject to SEG license or copyright; Terms of Use: http://segdl.org/

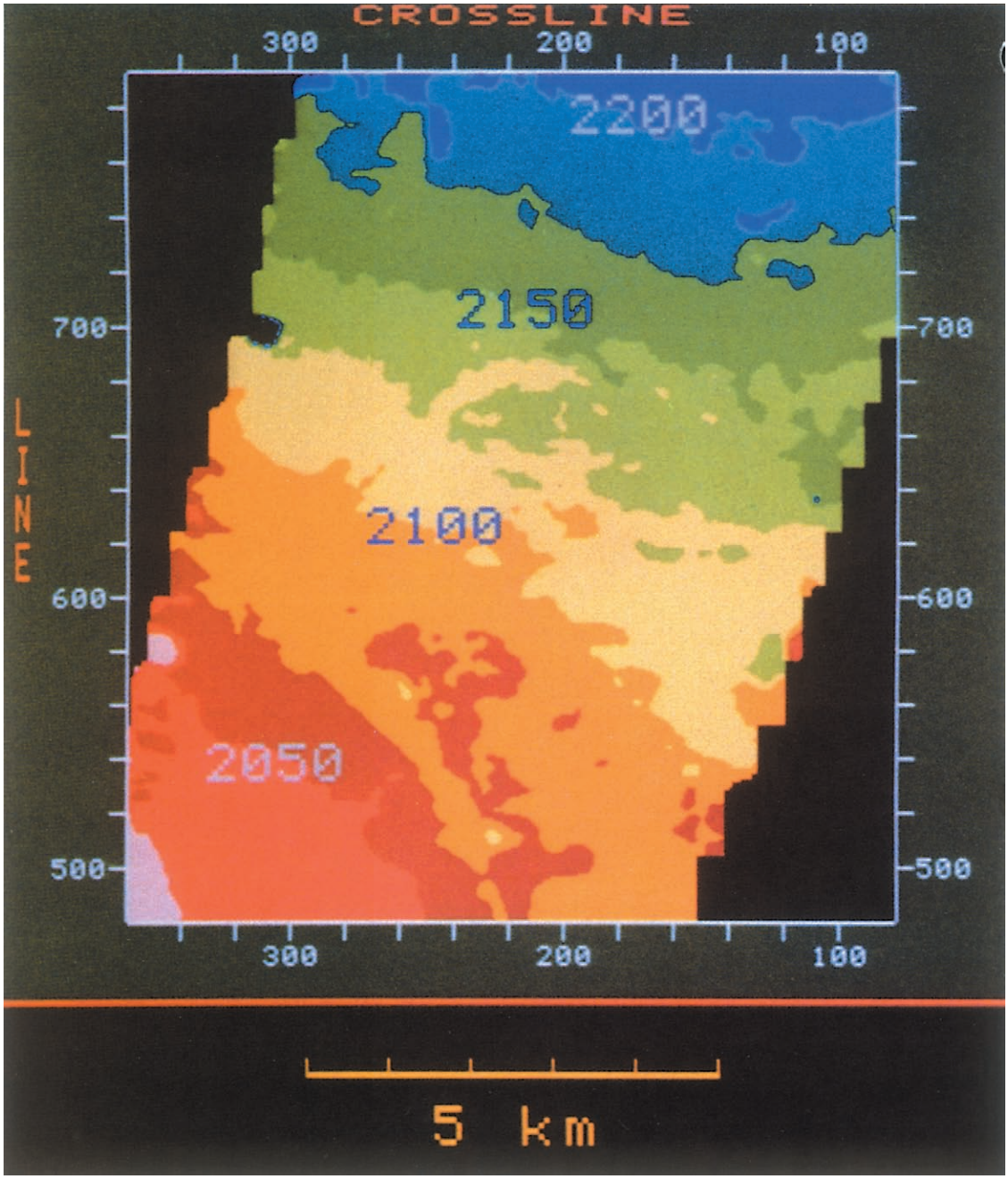

Fig. 4-41. Time-structure map for a horizon interpreted from a 3-D survey offshore Louisiana. The large numbers are contour designations in milliseconds. (Courtesy Geophysical Service Inc.)

description and Figures 4-50, 4-51, and 4-52 have been kindly provided by J. J. O'Brien of Standard Alaska Production Company, now BP Exploration (Alaska). The Lisburne Field is located on the North Slope of Alaska, adjacent to Prudhoe Bay Field and partly underlying the Prudhoe Bay gas cap. The Lisburne reservoir consists of a thin-bedded limestone/dolomite/shale sequence that was deposited in a subtidal to supratidal environment.

Prior to field startup in 1986, Standard Oil acquired a 3-D seismic survey over the eastern truncation zone of the field, where the Lisburne carbonate section is truncated by the Lower Cretaceous unconformity and the reservoir fluids are trapped by the overlying Cretaceous shale. Interpretation of the 3-D survey included tracking of key horizons on the migrated dataset using an interactive workstation and generation of time maps and horizon slices for these horizons. Horizon slices were found to possess significant information content. In particular, the amplitude of the reflection from the Lower Cretaceous unconformity (Figure 4-51) shows distinct lateral variations. Some

Downloaded 25 Jun 2012 to 95.28.162.50. Redistribution subject to SEG license or copyright; Terms of Use: http://segdl.org/

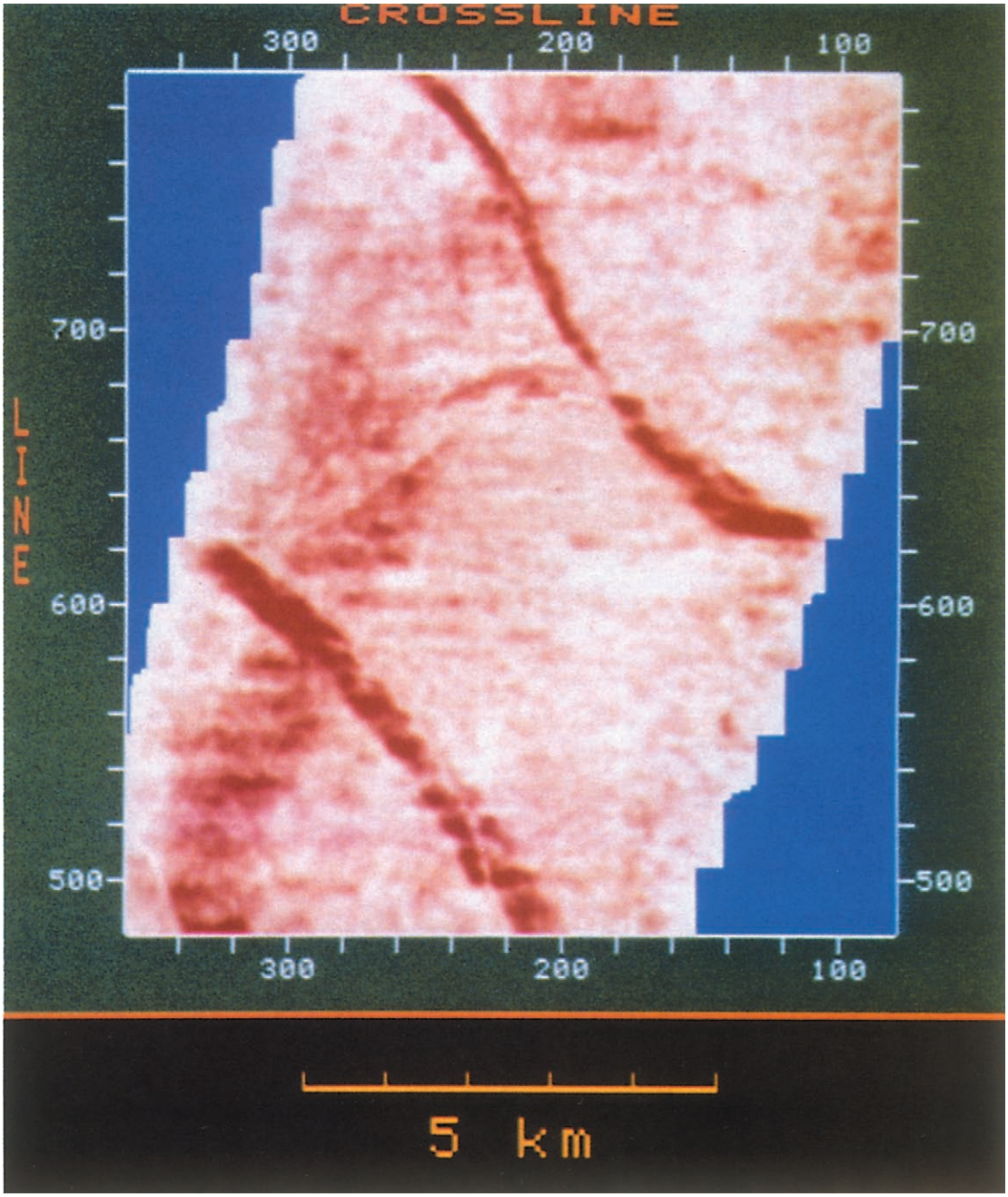

Fig. 4-42. Horizon slice showing spatial distribution of amplitude over the horizon mapped in Figure 4-41 and indicating two channels. (Courtesy Geophysical Service Inc.)

of these are interpreted in Figure 4-52 and are referenced to a vertical section in Figure 4-50.

In the western portion of the survey the Lower Cretaceous unconformity truncates the clastic section overlying the Lisburne carbonates. In this area, the unconformity surface represents a clastic/clastic interface with a relatively low acoustic impedance contrast, resulting in a low amplitude seismic reflection. Moving eastward, the Lower Cretaceous unconformity truncates the Lisburne carbonate section, and its surface represents an interface between a thick, uniform shale and an underlying carbonate section. There is, in general, a higher contrast in acoustic impedance across the unconformity in this area and reflection amplitudes are therefore greater.

In the area where the Lower Cretaceous unconformity truncates the Lisburne section, variations in reflection amplitude are seen. A lower amplitude feature is observed trending from northwest to southeast, subparalleling the truncation; time mapping indicates that this trend coincides with the truncation of Zone 5 of the Lisburne

Downloaded 25 Jun 2012 to 95.28.162.50. Redistribution subject to SEG license or copyright; Terms of Use: http://segdl.org/

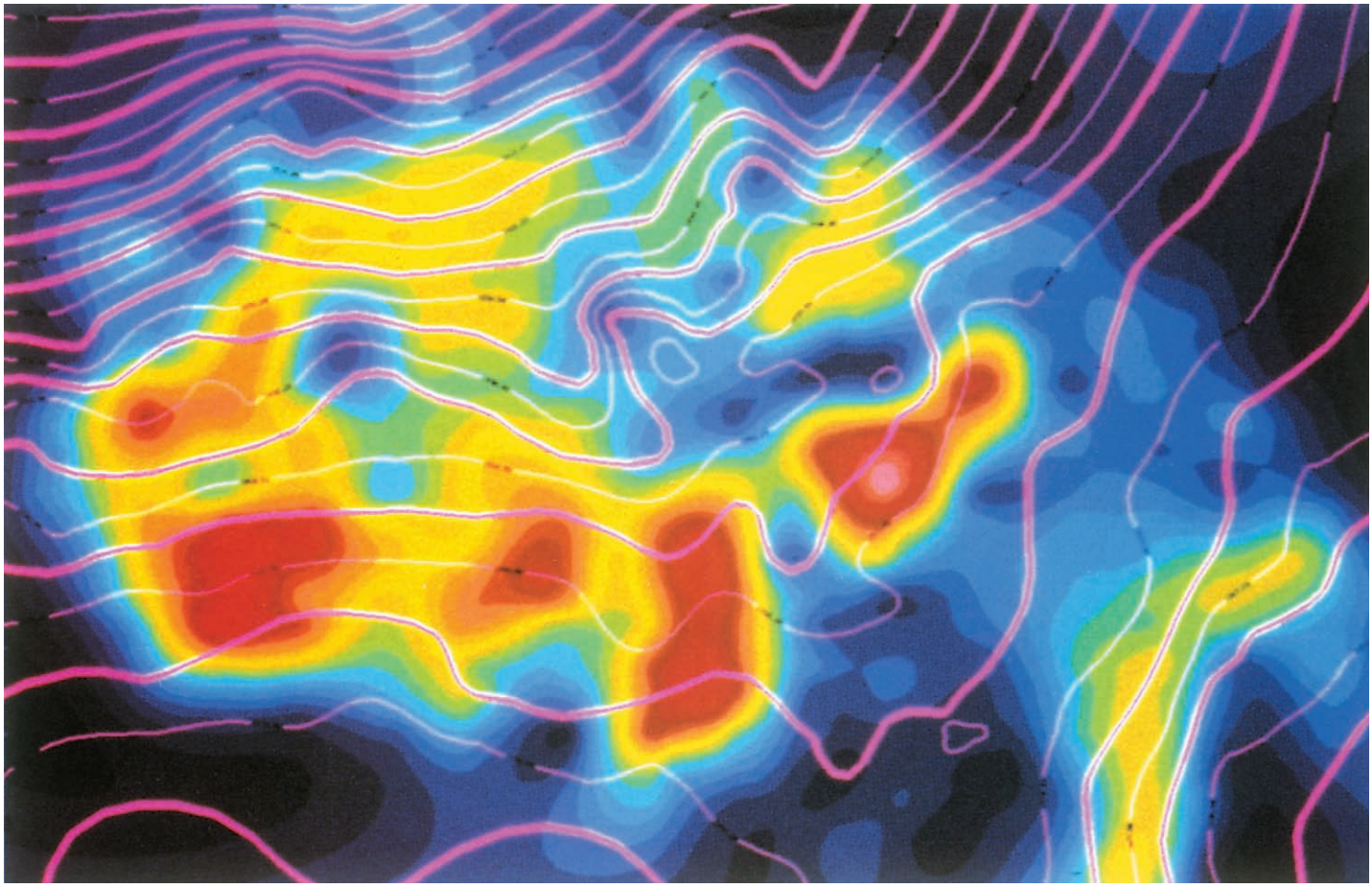

Fig. 4-43. Horizon slice from Gulf of Mexico with overlain structural contours showing high amplitudes caused by gas in several sand bodies. (Courtesy GeoQuest Systems Inc.)

reservoir. The L-7 well, which penetrated this amplitude trend, encountered a 29-m (95-ft)-thick section of Zone 5 with excellent porosity development immediately underlying the unconformity surface. Because the overlying formation is a marine shale that is uniformly low in acoustic impedance over the survey area, this low amplitude feature represents a lower acoustic impedance trend within the reservoir; the well data from L-7 suggest that it is an enhanced porosity trend.

Farther east another low amplitude lineament is seen trending from northwest to southeast. This feature coincides with the truncation of the Green Shale, a low impedance unit that is 9-18 m (30-60 ft) thick. In addition, a number of narrower east-west–trending lineaments are observed that correspond to faults cutting the unconformity surface and that have throws of up to 23 m (70 ft).

Windowed Amplitude

As an alternative to extracting amplitude along a horizon, amplitude can be extracted over a window, or time interval. The window can be flat, defined by a start time and an end time only; the window can be of a constant interval but defined relative to a structurally interpreted horizon; or the window can be the interval between two structurally interpreted horizons (Figure 4-53). The types of windowed amplitude in most widespread use are **average absolute amplitude** and **root-mean-square (RMS) amplitude**. In both of these, the amplitudes of the individual samples are added up without regard to their sign to give a gross amplitude for the whole interval. Average absolute and RMS amplitude are often considered to be amplitude-derived attributes, which subject will be discussed further in Chapter 8.

Amplitude extracted over a flat time window can be used very early in the interpretation because no horizon is required. Figure 4-54 shows a flat 100 ms time window straddling three high-amplitude features suspected as channels. Average absolute

Downloaded 25 Jun 2012 to 95.28.162.50. Redistribution subject to SEG license or copyright; Terms of Use: http://segdl.org/

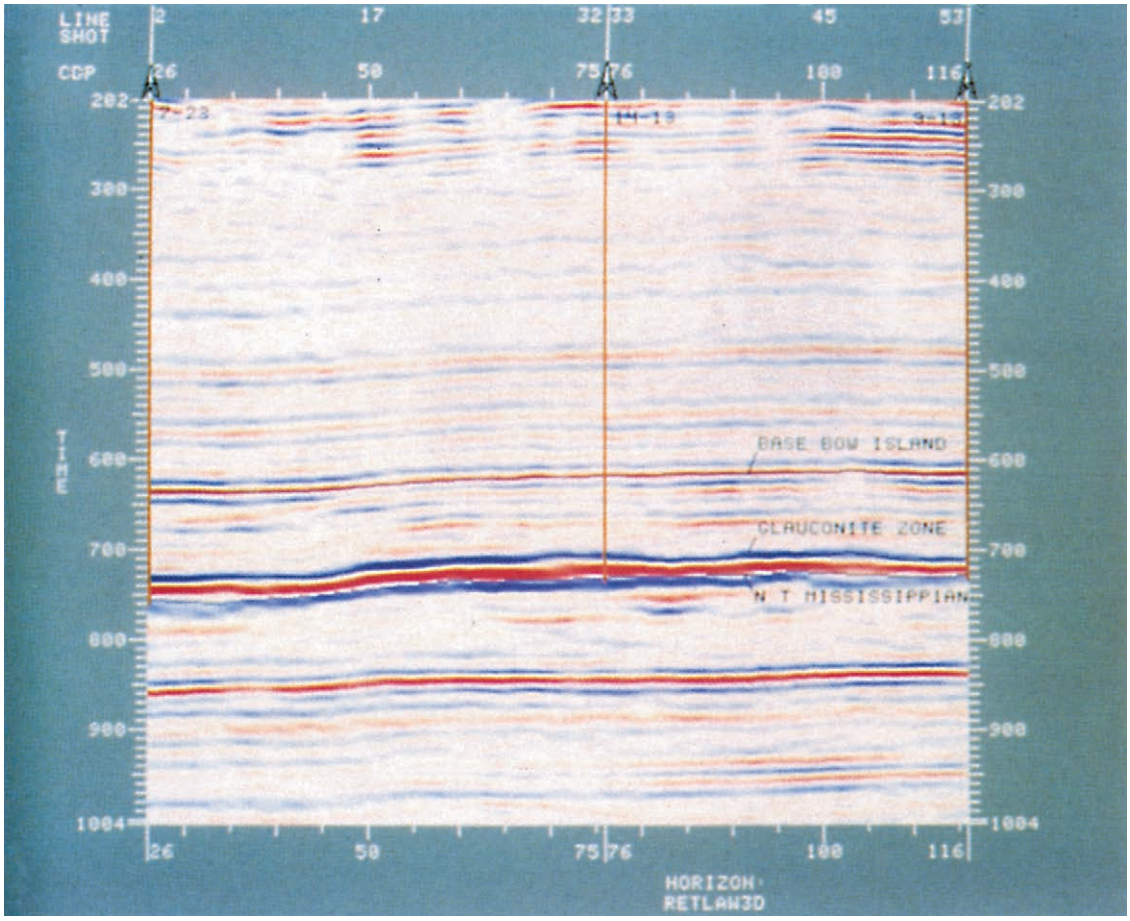

Fig. 4-44. Arbitrary line joining three wells in Retlaw prospect, southern Alberta, showing Base Bow Island reflection (the tracking level) and Glauconite Zone (the slicing level). (Courtesy Geophysical Service Inc.)

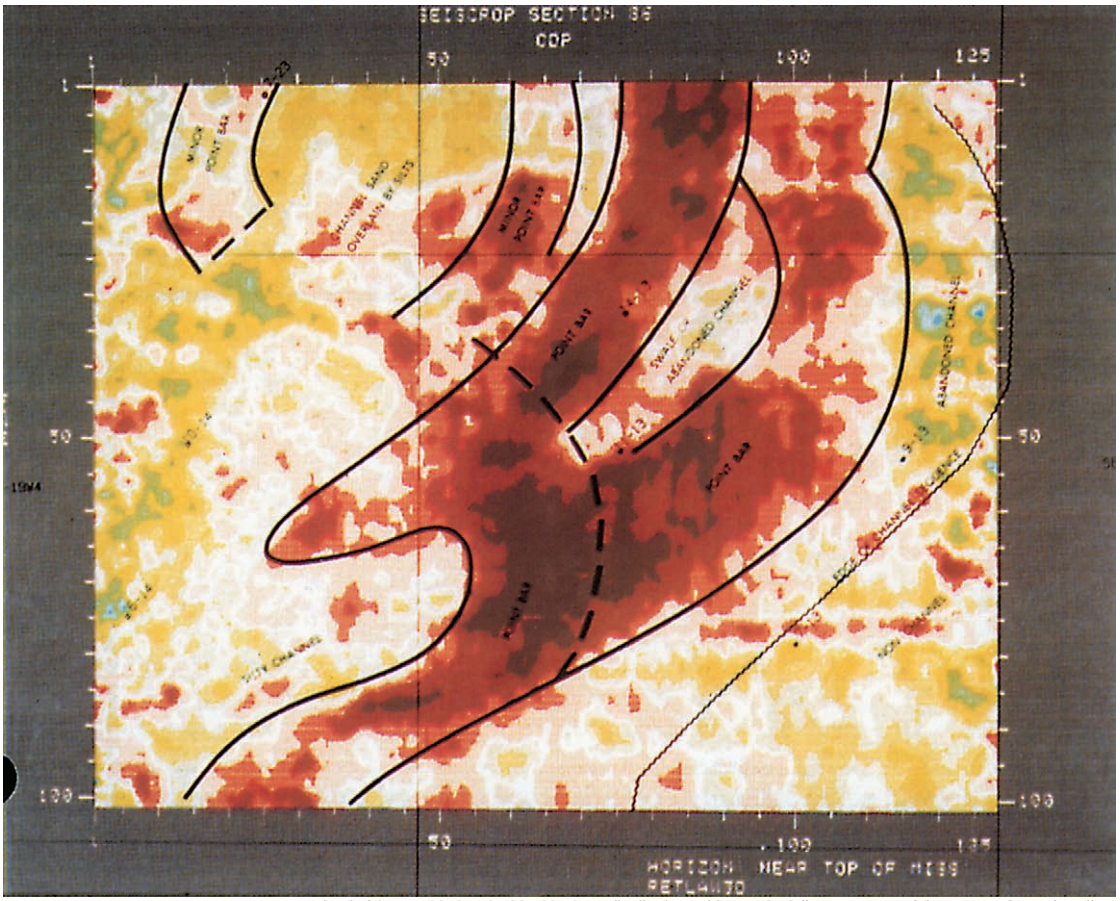

Fig. 4-45. Horizon slice through Glauconite Zone (near Top Mississippian) showing interpretation of depositional features. (Courtesy Geophysical Service Inc.)

Downloaded 25 Jun 2012 to 95.28.162.50. Redistribution subject to SEG license or copyright; Terms of Use: http://segdl.org/

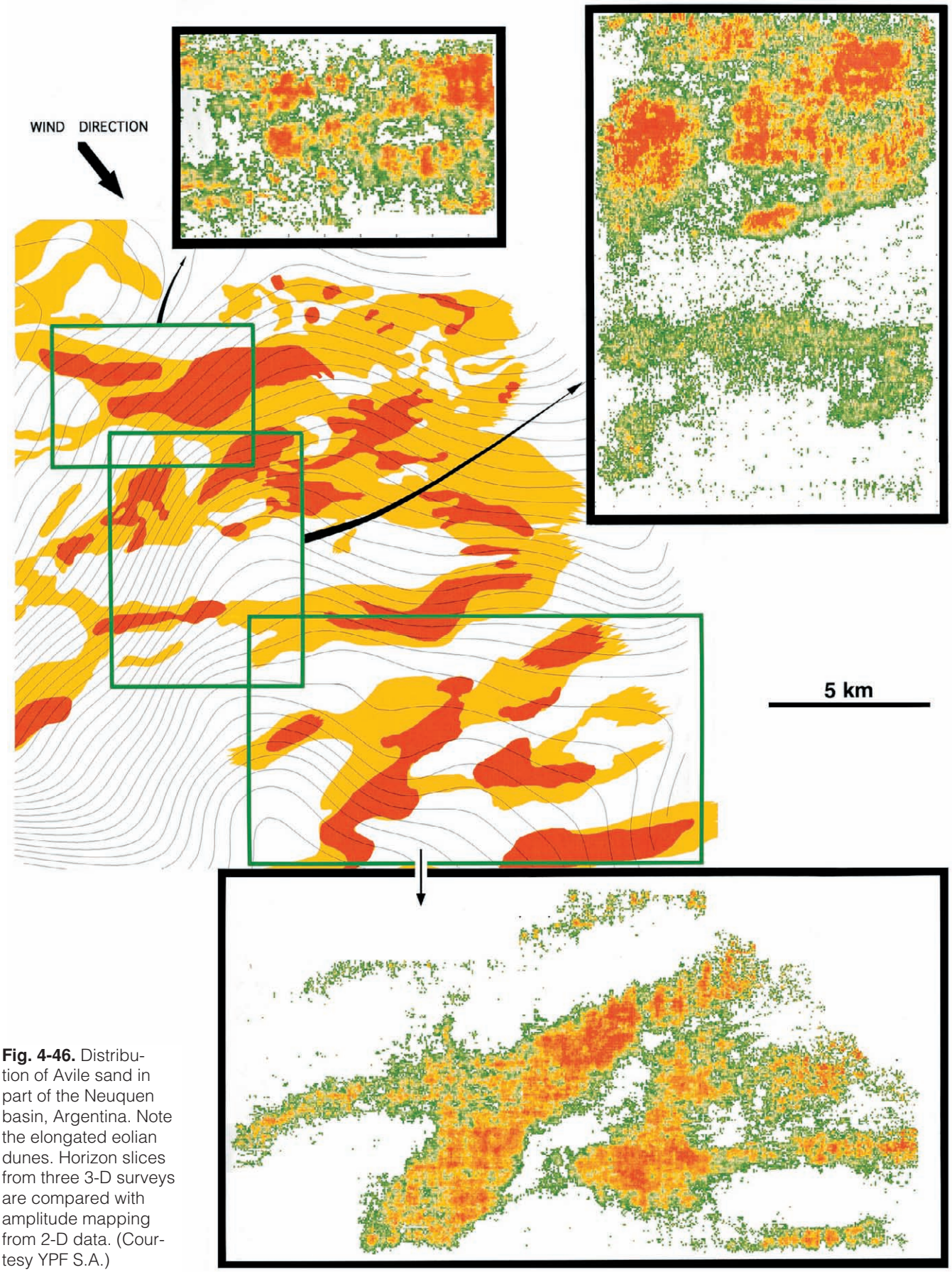

Fig. 4-46. Distribution of Avile sand in part of the Neuquen basin, Argentina. Note the elongated eolian dunes. Horizon slices from three 3-D surveys are compared with amplitude mapping from 2-D data. (Courtesy YPF S.A.)

Downloaded 25 Jun 2012 to 95.28.162.50. Redistribution subject to SEG license or copyright; Terms of Use: http://segdl.org/

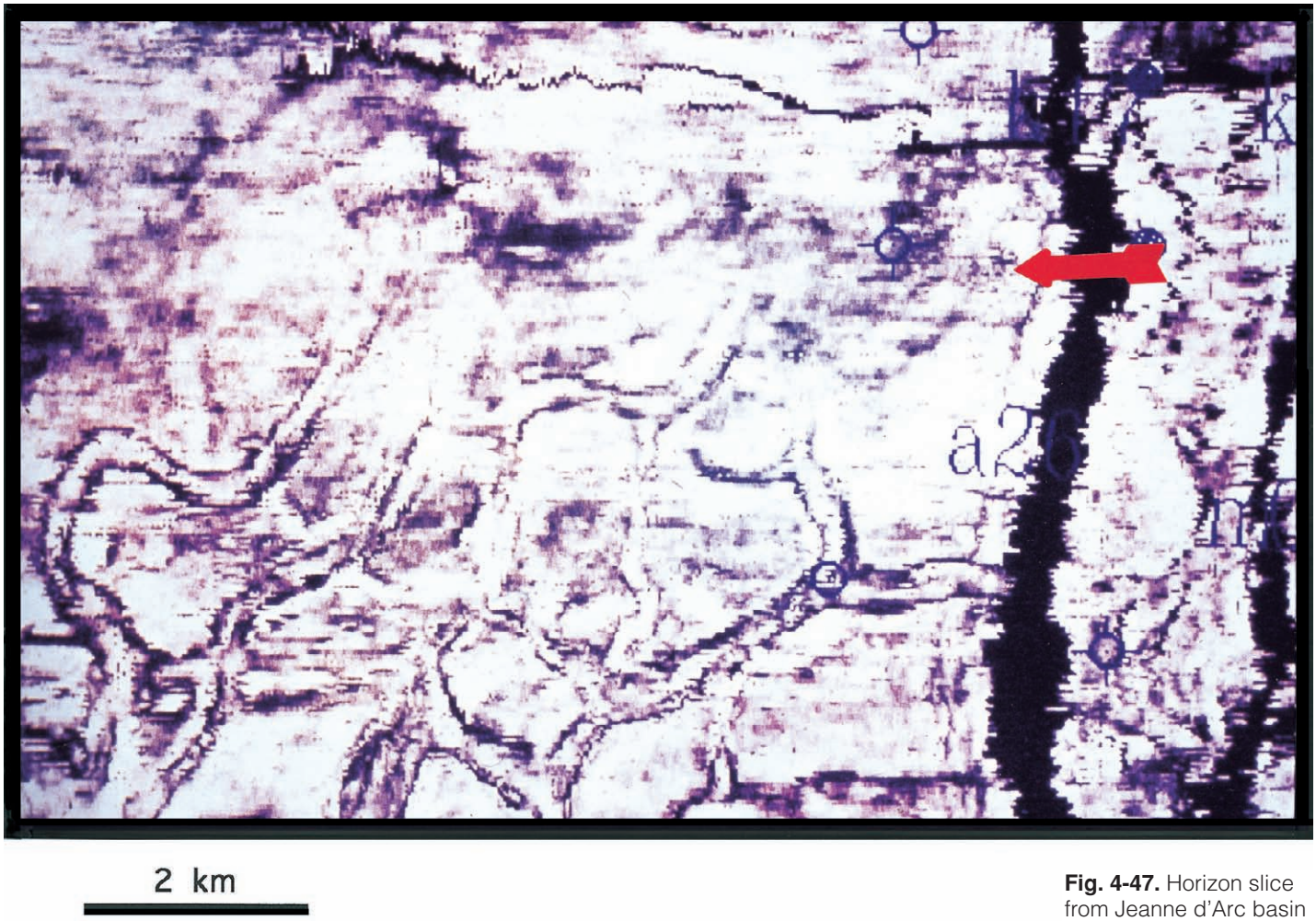

Fig. 4-47. Horizon slice from Jeanne d'Arc basin offshore eastern Canada showing a near-shore paleodrainage system. The arrow points along a possible ancient shore line. Note that the amplitude here shows the levees. (Courtesy Husky Oil.)

amplitude for this 100-ms window is mapped in Figure 4-55, and the extent of the two channels is evident. The two blue lines show the position of the two line segments of Figure 4-54. Clearly this is an easy approach, and, if the objective has structure, the window can be referenced to an interpreted horizon.

Windowed amplitude commonly suffers from contamination. Using Figures 4-54 and 4-55 as an example, the window is large enough to gather all the channel amplitudes, but it also gathers other amplitudes unrelated to the channels. These other amplitudes dilute the effect of the objective. However, the amplitude of the channel is dominant within the window, so the method worked effectively here.

Figure 4-56 shows RMS amplitude over a 500 ms window being used as a reconnaissance for bright spots in the Frio Formation of south Texas. Five hundred milliseconds is a very large window, but the RMS calculation helped overcome the contamination. The objectives were high-amplitude bright spots, and squaring them made them relatively even higher, helping them stand out against the background.

Figure 4-57 is again RMS amplitude but over a 50 ms window surrounding the relevant reflection. Here, Lamers and Carmichael (1999) have mapped the Top Balder reflection over multiple 3-D surveys in a reconnaissance of the Faroe Basin on the U.K. Atlantic margin. The patterns in amplitude have helped unravel the depositional history of the Faroe Basin and have provided a regional understanding of this Paleocene deep-water play.

Figure 4-58 shows a succession of three slump zones in a Mexican marine area. Apparently there is a hydrocarbon migration pathway into zone 3 but not into the

Text continues on page 156.

Downloaded 25 Jun 2012 to 95.28.162.50. Redistribution subject to SEG license or copyright; Terms of Use: http://segdl.org/

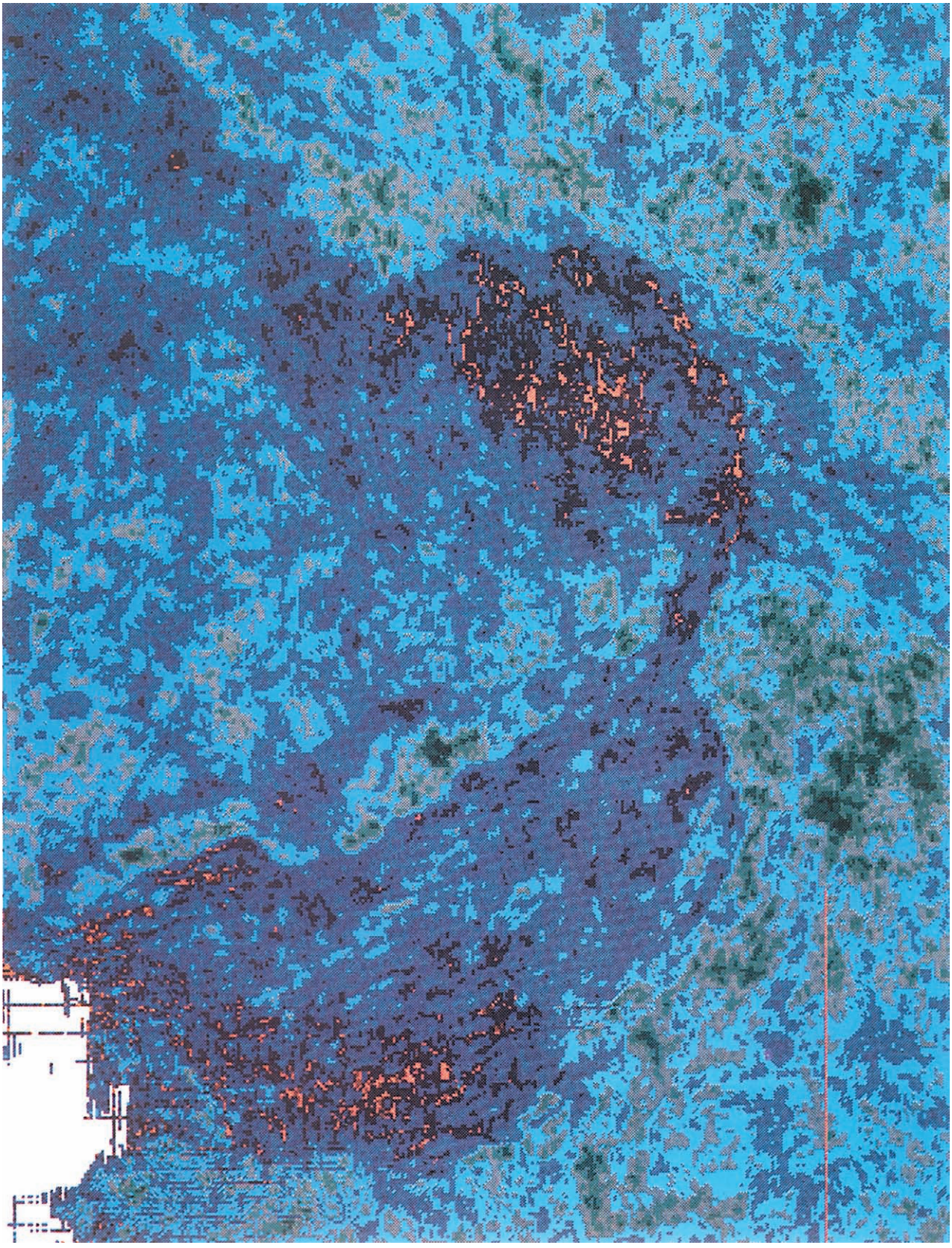

Fig. 4-48. Horizon slice from Central Graben area in Norwegian North Sea showing probable Danian intra-chalk mass flow. (Courtesy A/S Norske Shell.)

Downloaded 25 Jun 2012 to 95.28.162.50. Redistribution subject to SEG license or copyright; Terms of Use: http://segdl.org/

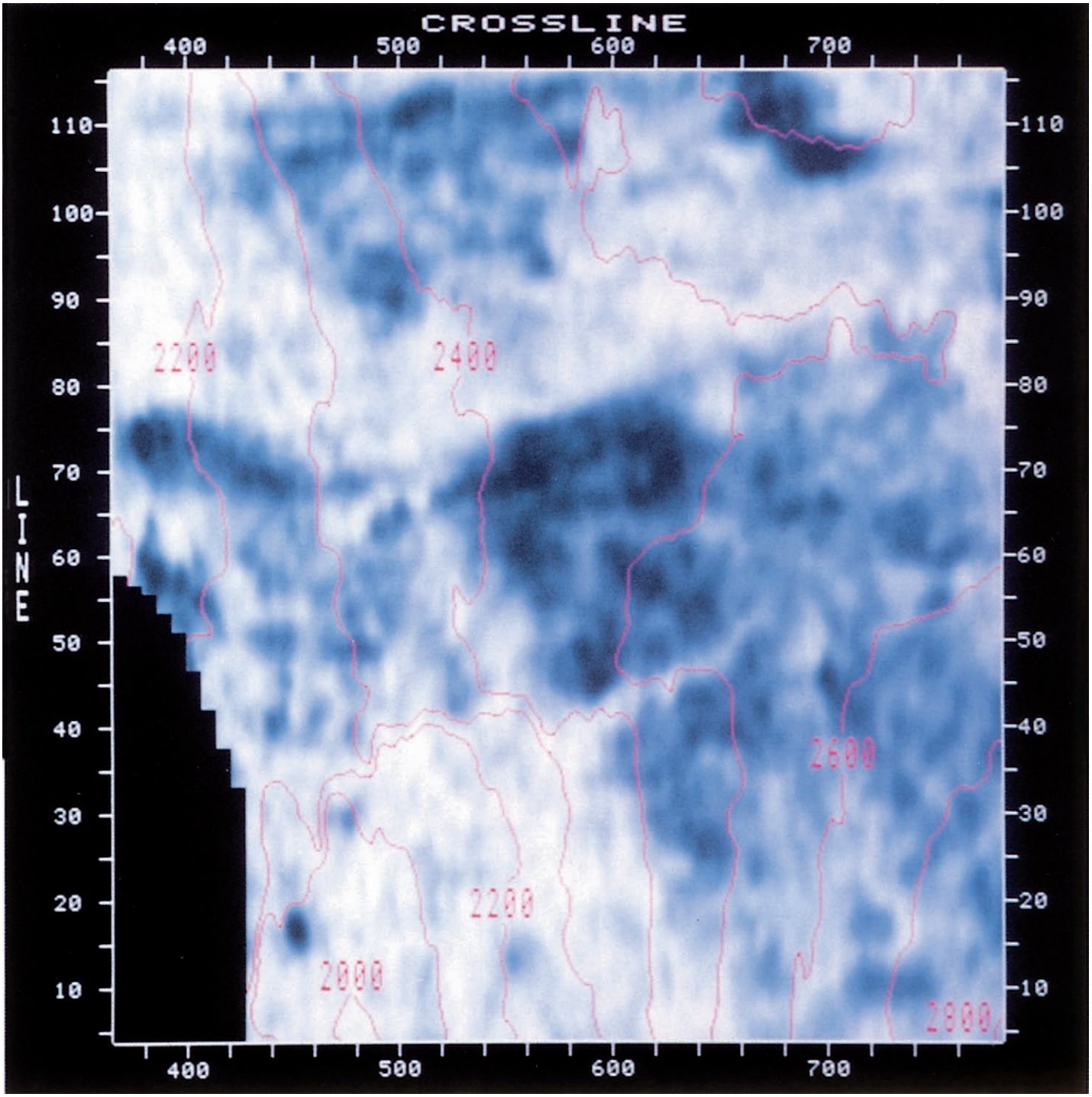

Fig. 4-49. Horizon slice and superimposed structural contours from a Gulf of Mexico 3-D survey. The ENE-WSW amplitude edges indicate faults. The NNW-SSE amplitude edge indicates a bed truncation. (Courtesy Chevron U.S.A. Inc.)

Downloaded 25 Jun 2012 to 95.28.162.50. Redistribution subject to SEG license or copyright; Terms of Use: http://segdl.org/

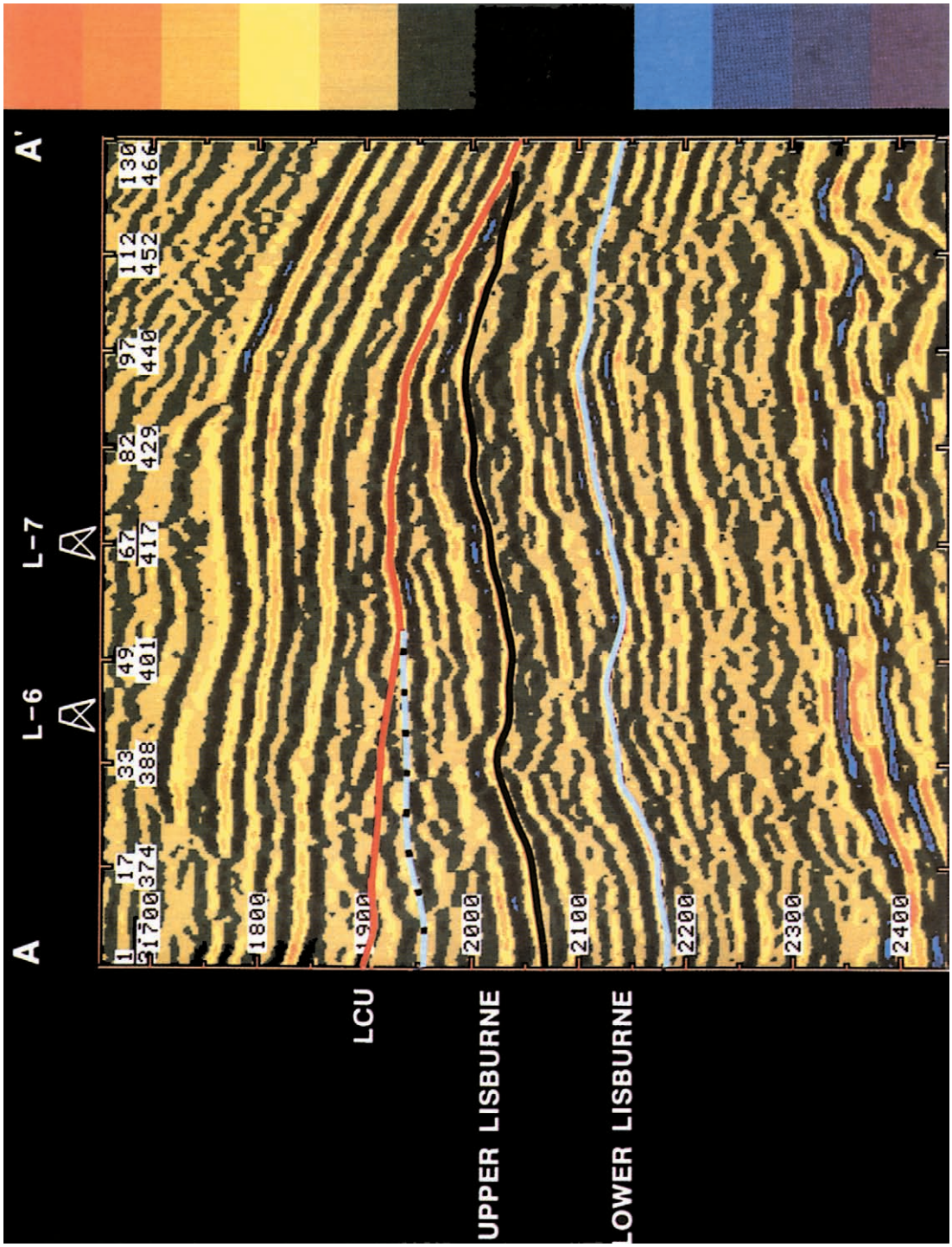

Fig. 4-50. Vertical section from Lisburne 3-D survey, North Slope of Alaska, showing Lower Cretaceous unconformity. (Courtesy Standard Alaska Production Company.)

Downloaded 25 Jun 2012 to 95.28.162.50. Redistribution subject to SEG license or copyright; Terms of Use: http://segdl.org/

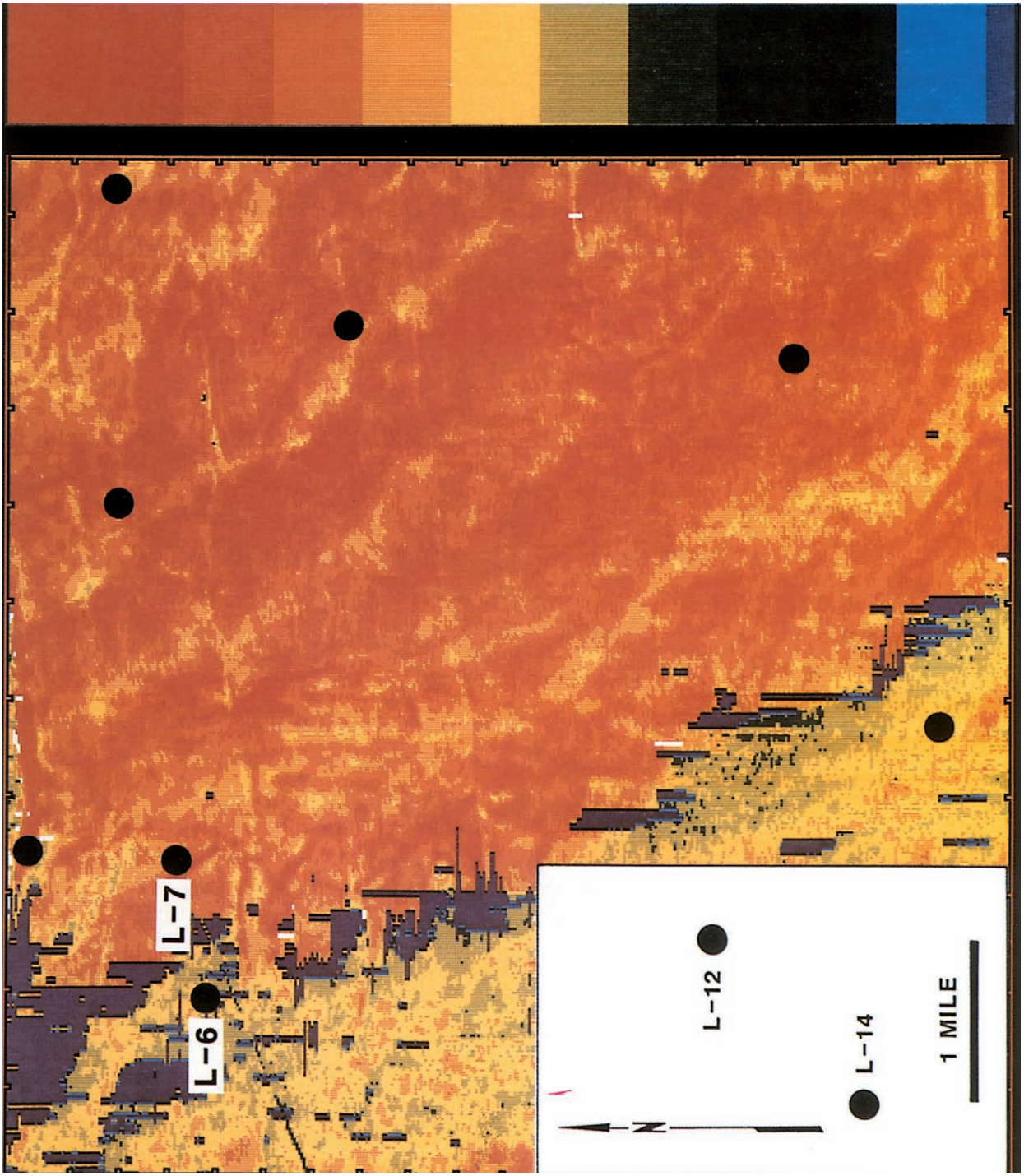

Fig. 4-51. Horizon slice along Lower Cretaceous unconformity showing amplitude lineations trending from northwest to southeast. (Courtesy Standard Alaska Production Company.)

Downloaded 25 Jun 2012 to 95.28.162.50. Redistribution subject to SEG license or copyright; Terms of Use: http://segdl.org/

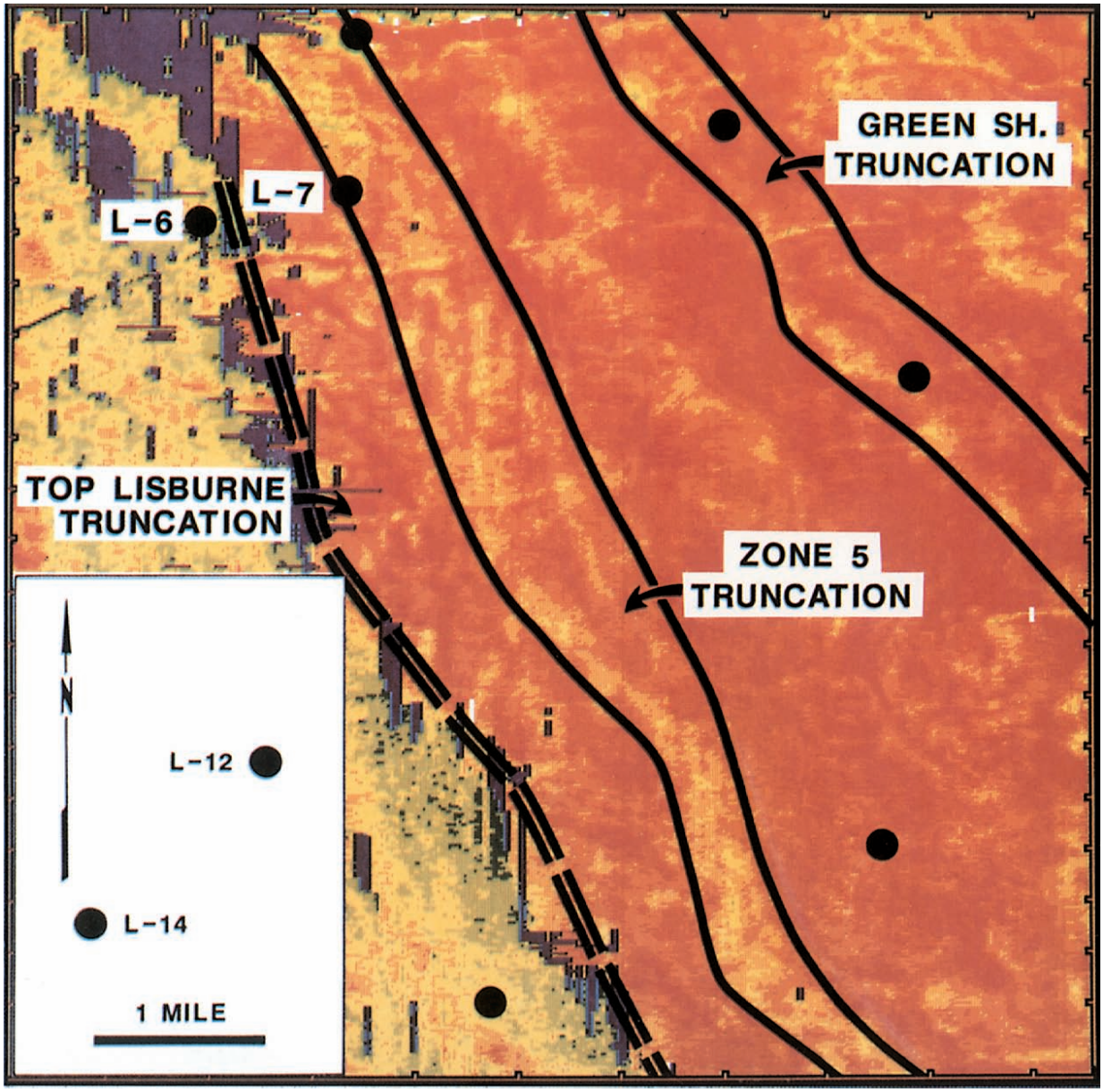

Fig. 4-52. Horizon slice from Figure 4-51 showing interpretation of amplitude lineations in terms of truncations of reservoir units. (Courtesy Standard Alaska Production Company.)

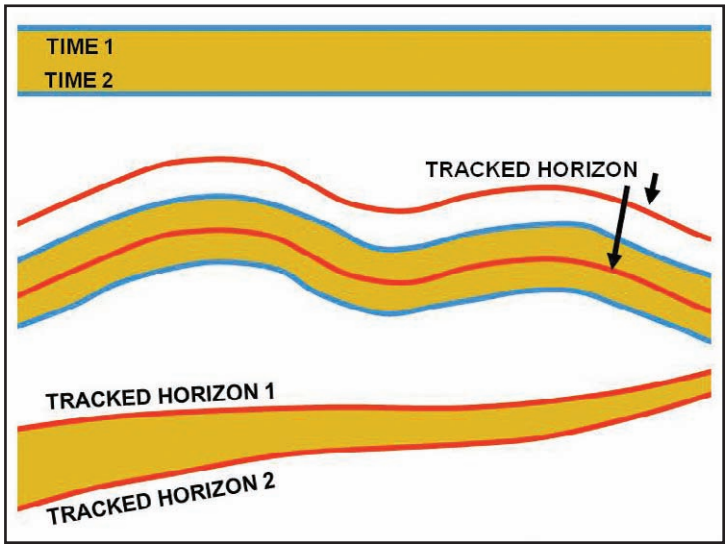

Fig. 4-53. Types of window for extracting amplitude or other attribute.

Downloaded 25 Jun 2012 to 95.28.162.50. Redistribution subject to SEG license or copyright; Terms of Use: http://segdl.org/

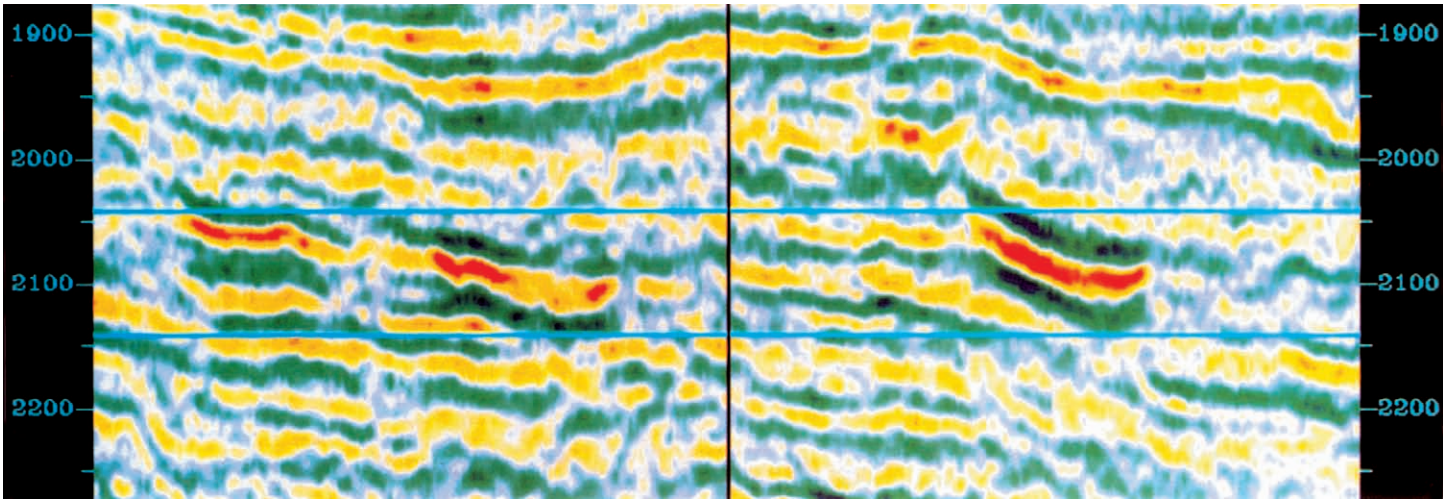

Fig. 4-54. Vertical seismic section from North Sea showing 100-ms time window enclosing high-amplitude channel reflections. (Courtesy Landmark UK, Phillips UK and Western Geophysical Corporation.)

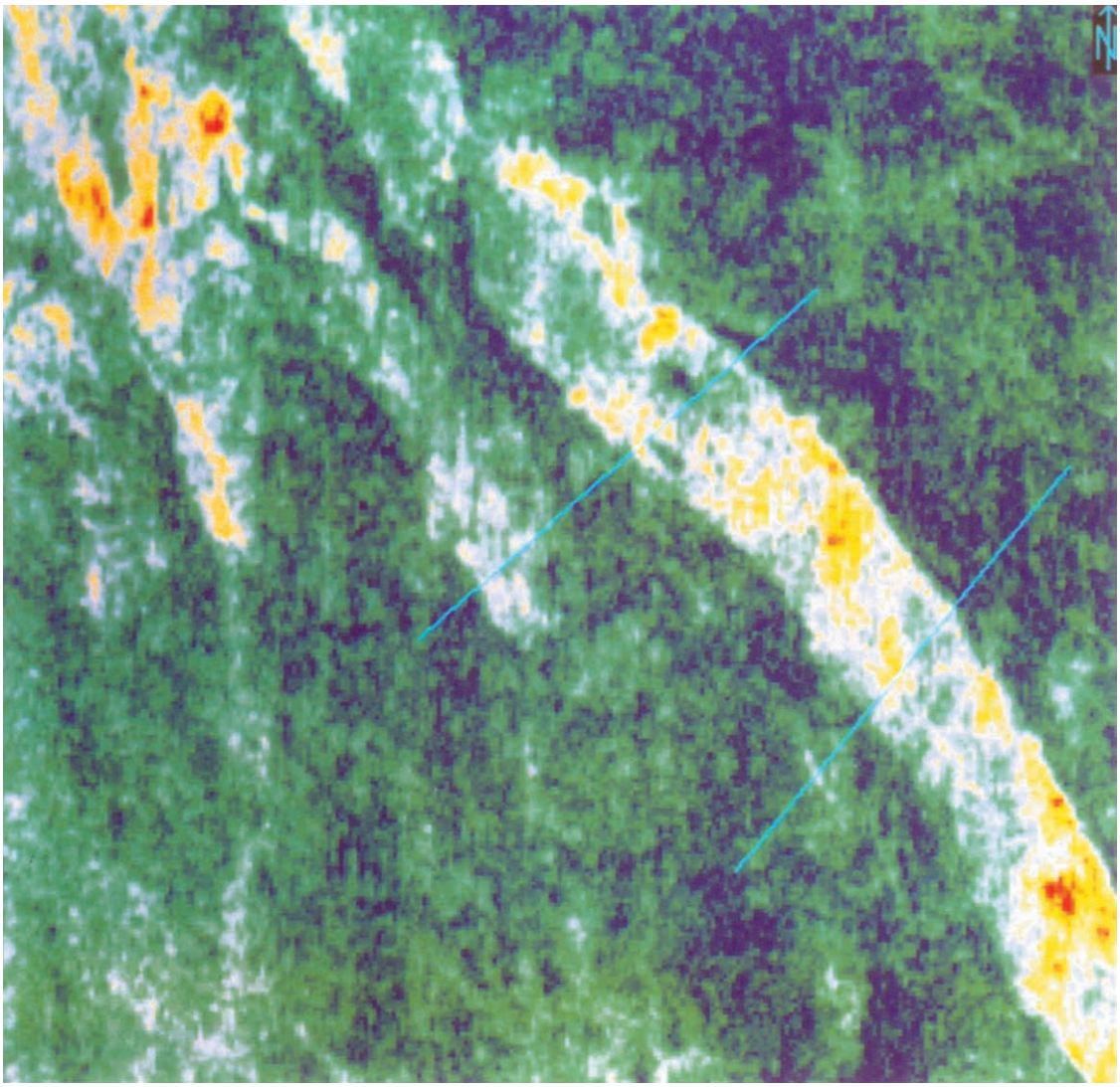

Fig. 4-55. Average absolute amplitude computed over time window indicated in Figure 4-54. Note definition of channels. (Courtesy Landmark UK, Phillips UK and Western Geophysical Corporation.)

Downloaded 25 Jun 2012 to 95.28.162.50. Redistribution subject to SEG license or copyright; Terms of Use: http://segdl.org/

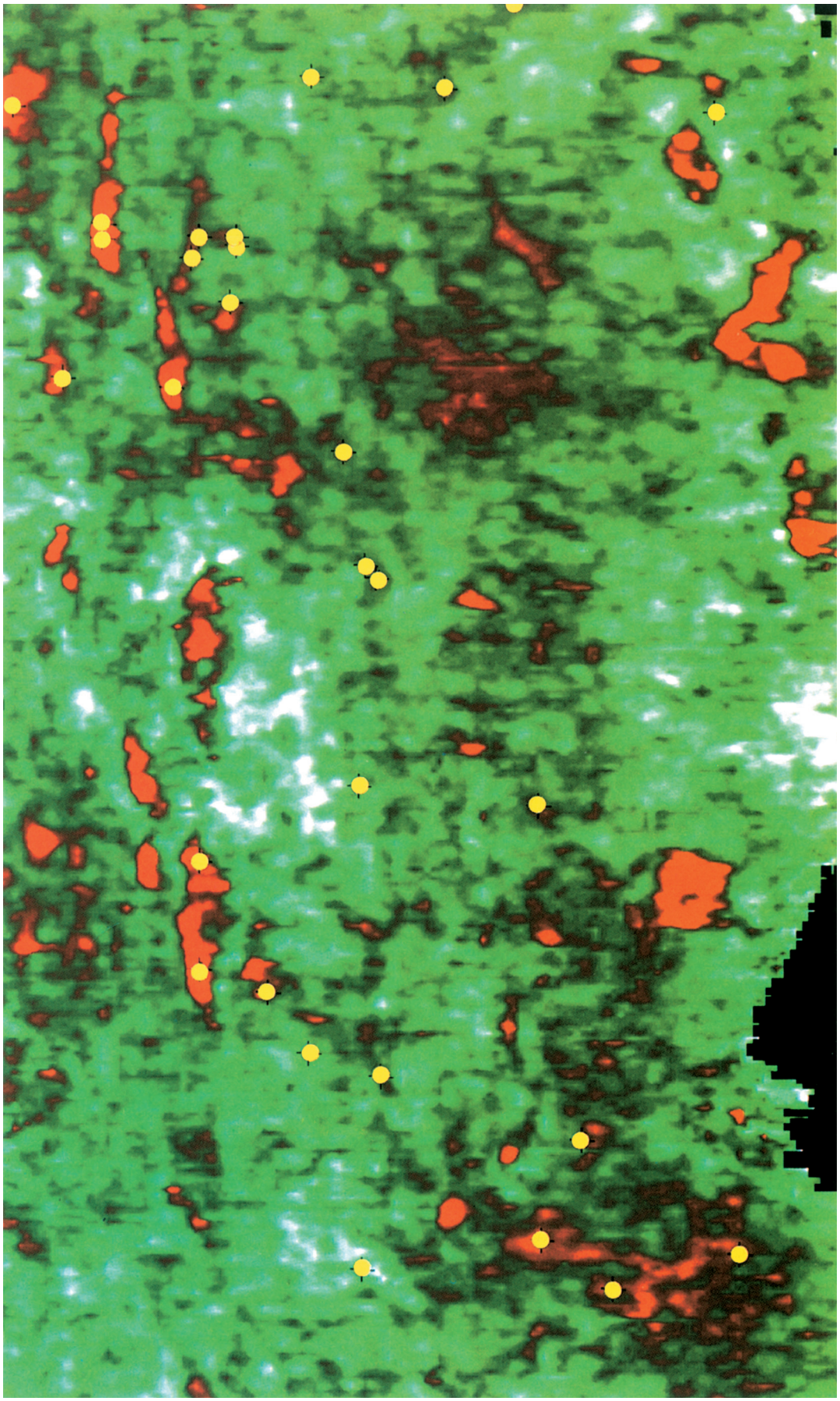

Fig. 4-56. RMS amplitude from a flat 500-ms window spanning Frio Formation bright spots in south Texas. The red patches of accumulated high amplitude can be seen in relation to the well penetrations shown in yellow. (Courtesy Edge Petroleum.)

Downloaded 25 Jun 2012 to 95.28.162.50. Redistribution subject to SEG license or copyright; Terms of Use: http://segdl.org/

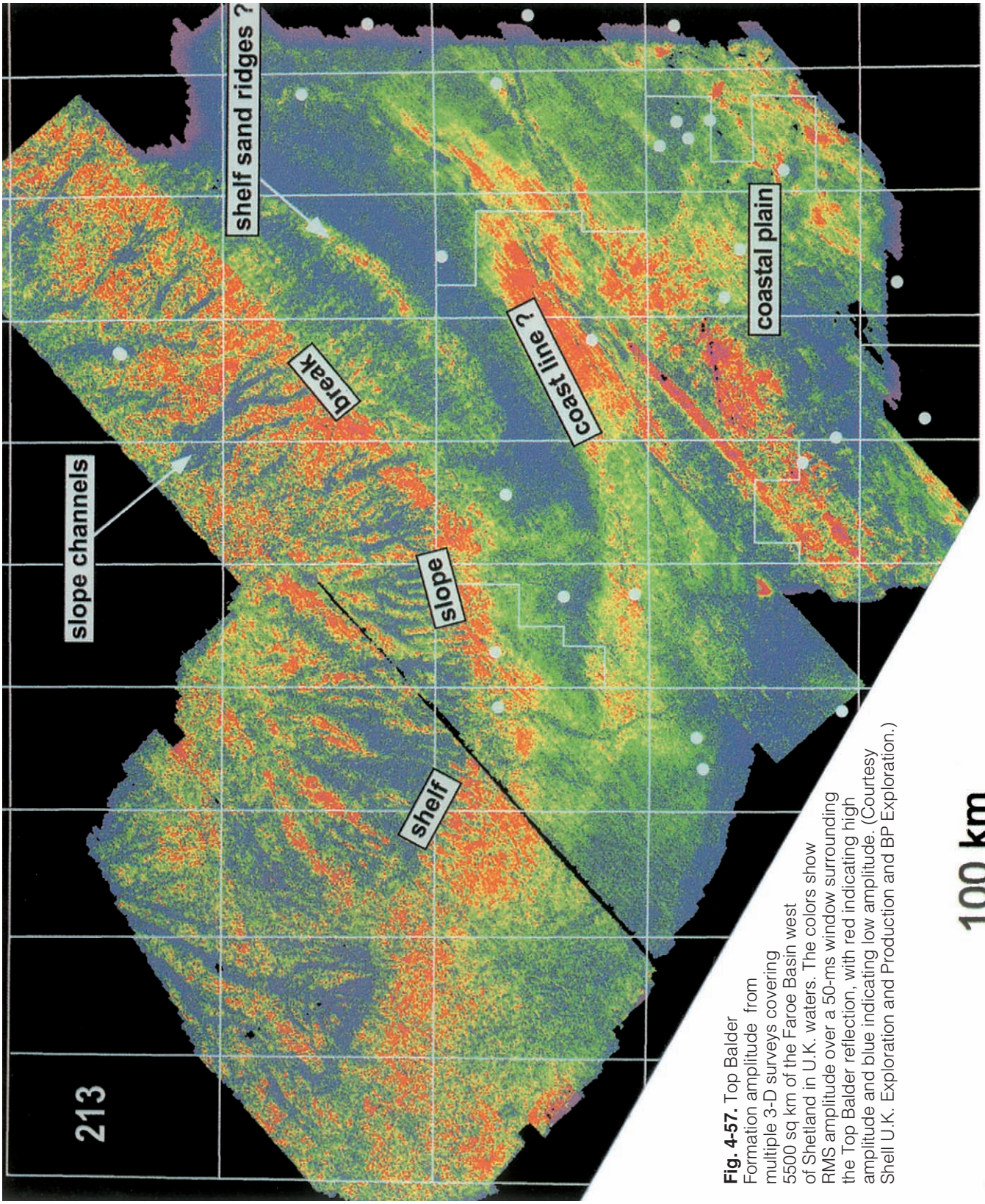

Fig. 4-57. Top Balder Formation amplitude from multiple 3-D surveys covering 5500 sq km of the Faroe Basin west of Shetland in U.K. waters. The colors show RMS amplitude over a 50-ms window surrounding the Top Balder reflection, with red indicating high amplitude and blue indicating low amplitude. (Courtesy Shell U.K. Exploration and Production and BP Exploration.)

Downloaded 25 Jun 2012 to 95.28.162.50. Redistribution subject to SEG license or copyright; Terms of Use: http://segdl.org/

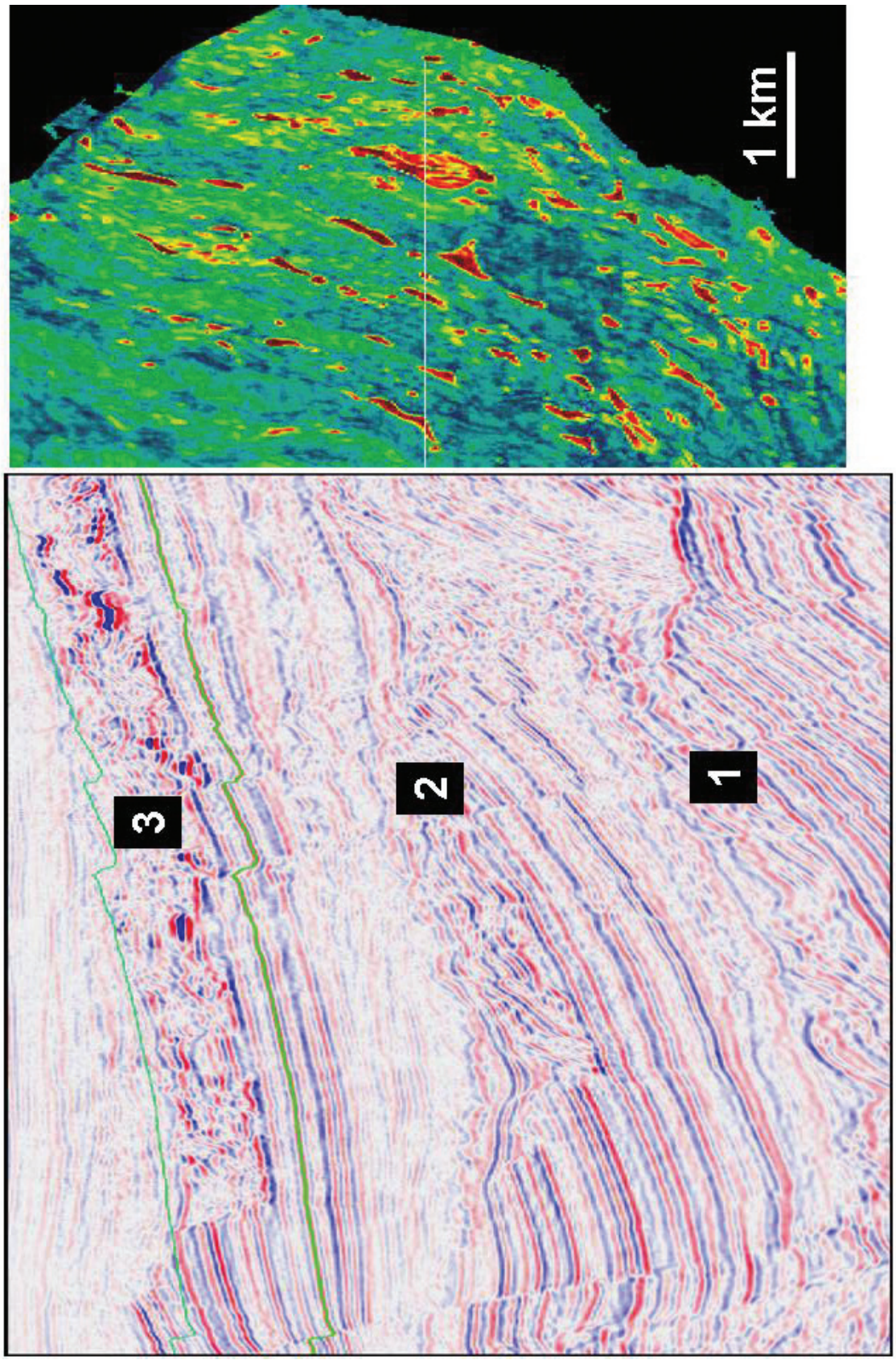

Fig. 4-58. Slump zone number 3 contains multiple bright spots, left. RMS amplitude over 200 ms window, right, demonstrates that all bright spots are too small to justify drilling. (Courtesy Pemex.)

Downloaded 25 Jun 2012 to 95.28.162.50. Redistribution subject to SEG license or copyright; Terms of Use: http://segdl.org/

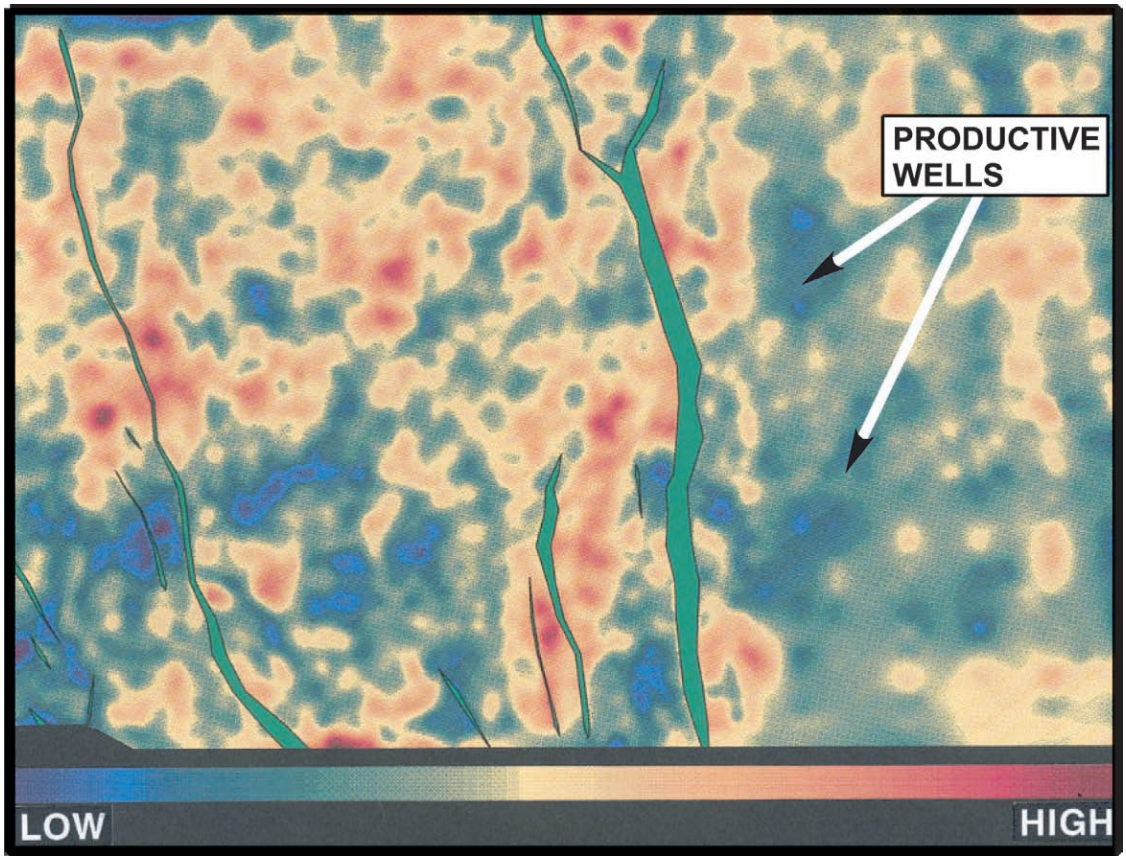

Fig. 4-59. Average absolute amplitude from San Jorge Basin of southern Argentina. The 250-ms window was tied to an interpreted horizon and spanned many thin reservoir sands. (Courtesy YPF S.A.)

HORIZON AMPLITUDE	WINDOWED AMPLITUDE
Reservoir study	Reconnaissance
No contamination	Subject to contamination by other amplitudes
Highly dependent on tracking accuracy	More immune to tracking errors
Horizon identification critical	Horizon identification less critical
Horizon name only required	Record required of window definition and type of amplitude extracted

Fig. 4-60. Comparison of horizon and windowed amplitude.

Downloaded 25 Jun 2012 to 95.28.162.30. Redistribution subject to SEG license or copyright; Terms of Use: http://segdl.org/

other two zones, as the high amplitudes in zone 3 are interpreted as hydrocarbon bright spots. The lower green horizon tracks the data, and the upper green horizon parallels it 200 ms above. The interval between the two green horizons is then the analysis window over which RMS amplitude was calculated. The spatial display of RMS amplitude on the right demonstrates that the inferred gas is trapped primarily by faults trending NNE-SSW. All of the hydrocarbon accumulations, however, are small, and even the largest has an area of only one-third of a square kilometer and is thus subeconomic.

Figure 4-59 shows average absolute amplitude from the San Jorge Basin of southern Argentina. Here there are many thin reservoir sands, but they occur over a very thick interval. The 250 ms window used here was referenced to an interpreted horizon just below the producing interval. The individual sands are very difficult to study seismically, but Figure 4-59 makes it clear that the productive wells are in areas of relatively low amplitude over the whole interval.

Average absolute amplitude, RMS amplitude, and other windowed amplitude attributes are, as illustrated above, most beneficially used for some kind of reconnaissance investigation. When reservoir reflections have been identified and the intent is to study the reservoir, then horizon amplitude is normally preferable. The author recommends tracking the top reflection and the base reflection and extracting the horizon amplitude on both of them. This idea is developed further in Chapter 7.

Figure 4-60 summarizes the advantages and disadvantages of horizon and windowed amplitude. Horizon amplitude is generally more precise and detailed, but it depends critically on the accuracy of the tracking, the horizon identification, and the data phase. In using windowed amplitude it is important that the interpreter keep an accurate record of the window definition and the type of amplitude extracted. The plethora of attributes and windows available today increases the need for full documentation.

References

Broussard, M. L., ed., 1975, Deltas: Houston Geological Society, 555 p.

Brown, A. R., C. G. Dahm, and R. J. Graebner, 1981, A stratigraphic case history using three-dimensional seismic data in the Gulf of Thailand: Geophysical Prospecting, v. 29, p. 327–349.

Enachescu, M. E., 1993, Amplitude interpretation of 3-D reflection data: The Leading Edge, v. 12, p. 678–685.

Gerster, R. L., 1995, The role played by 3-D and 2-D seismic data in the exploration and development of the largest oil field in Argentina: SEG Annual Meeting expanded abstract.

Klein, G. deV., 1985, Sandstone depositional models for exploration for fossil fuels, third edition: Boston, Massachusetts, International Human Resources Development Corporation, 209 p.

Lamers, E., and S. M. M. Carmichael, 1999, The Paleocene deepwater sandstone play West of Shetland, *in* A. J. Fleet and S. A. R. Boldy, eds., Petroleum geology of northwest Europe: Proceedings of the 5th Conference, The Geological Society, London, p. 645–659.

Sanders, J. I., and G. Steel, 1982, Improved structural resolution from 3D surveys in Australia: Australian Petroleum Exploration Association (APEA) Journal, v. 22, p. 17–41.

Downloaded 25 Jun 2012 to 95.28.162.50. Redistribution subject to SEG license or copyright; Terms of Use: http://segdl.org/

Reservoir Identification

Bright Spots As They Used To Be

Figure 5-1 shows a bright spot presented by Tegland (1973). This was one of the early examples studied and was observable because amplitude had been preserved in seismic processing. In earlier years, when records were normally made with automatic gain control, there was little opportunity for studying amplitudes. The bright spot of Figure 5-1 is actually a very good one for its era because it also shows a flat spot, presumably a fluid contact reflection. The flat spot terminates laterally at the same points as does the bright spot; we would consider this a simple form of bright spot validation, increasing the interpreter's confidence that the anomaly indicates the presence of hydrocarbons.

With the improvements in seismic processing over two decades, we can now consider polarity and phase as well as amplitude and spatial extent. Frequency, velocity, amplitude/offset and shear wave information can also help in the positive identification of hydrocarbon indicators. These are all subjects of this chapter and the direct observation of hydrocarbon fluids is now very widespread.

Most direct hydrocarbon indication relates to gas rather than oil reservoirs as the effect on acoustic properties of gas in the pore space is significantly greater than oil. Figure 5-2 (derived from Gardner, Gardner, and Gregory, 1974) summarizes the different effects of gas and oil and shows that the effect of either diminishes with depth.

Backus and Chen (1975) were very thorough in their discussion of the diagnostic benefits of flat spots, and Figure 5-3 shows a flat spot at 1.47 seconds that they discussed. Figure 5-4 is interpreted sufficiently to highlight the various hydrocarbon indicators on the section. The flat spot is easily identified by its flatness, and because it is unconformable with adjacent reflections. Hence it is a good indicator of the hydrocarbon/water contact. Nevertheless there is no high amplitude associated with it.

The reflection from the top of the reservoir (Figure 5-4) changes from a peak to a trough across the fluid contact and this again implies a significant change in acoustic properties between the gas sand above the hydrocarbon/water contact and the water sand beneath it. This phase change, or a polarity reversal, will be discussed in more detail in the next section.

The Character of Hydrocarbon Reflections

If the seismic data under interpretation have been processed to zero phase (see Chapter 2), then the detailed character of the bright spots, flat spots and other hydrocarbon indicators can be very diagnostic. Figure 5-5 shows diagrammatically the hydrocarbon indicators which may be associated with different relative acoustic impedances of gas sand, water sand and embedding shale. The polarity convention expressed diagrammatically in Figure 5-5 is that a decrease in acoustic impedance is expressed as a peak which is blue and an increase is expressed as a trough which is red. This is normally referred

Downloaded 25 Jun 2012 to 129.110.5.90. Redistribution subject to SEG license or copyright; Terms of Use: http://segdl.org/

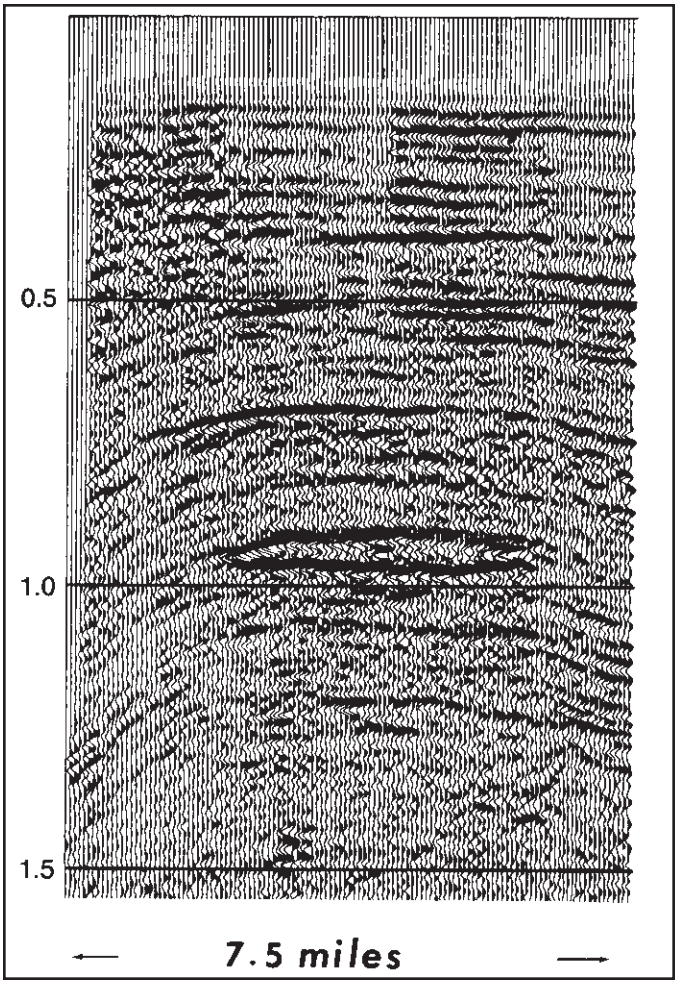

Fig. 5-1. A Gulf of Mexico bright spot and flat spot from the early 1970s.

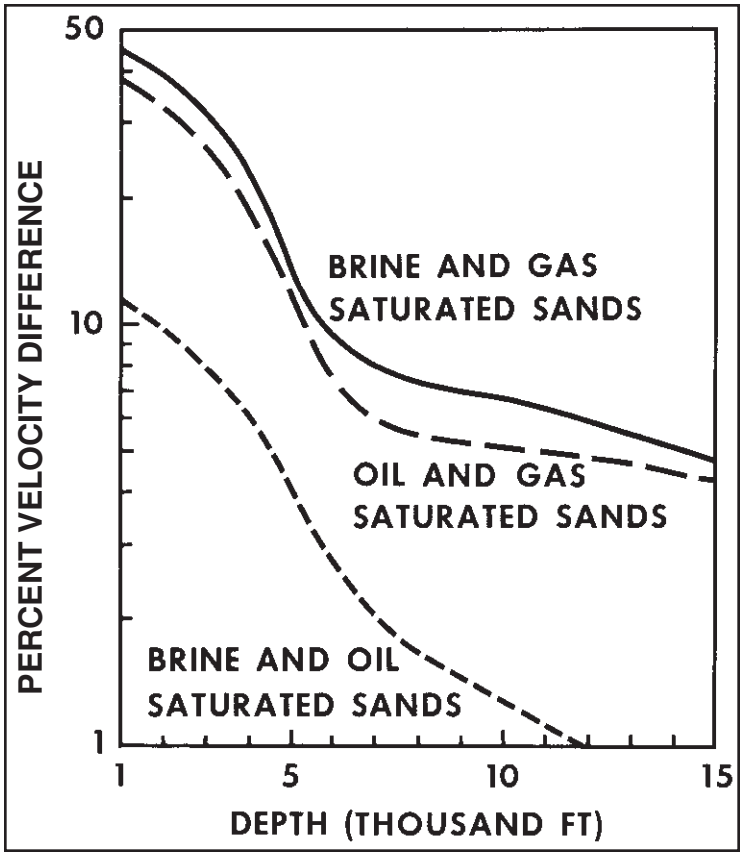

Fig. 5-2. Percent velocity difference between sands saturated with different fluids (derived from Gardner, Gardner, and Gregory, 1974).

to as European polarity. Peaks and troughs are symmetrical if they are the zero-phase expressions of single interfaces.

The top diagram of Figure 5-5 illustrates the most common situation: the water sand has an acoustic impedance lower than the embedding medium and the impedance of the gas sand is further reduced. For this situation the signature of the sand is peak-over-trough (blue-over-red) and, for the gas-filled portion, the amplitude is greater. This is the classical zero-phase bright spot with high amplitude for the top *and* base reflections. The simultaneous increase in top and base amplitudes is called **natural pairing**. If the sand is thick enough for the top and base reflections to be separated, then a flat spot or fluid contact reflection should be visible between the gas sand and the water sand, that is at the point where brightening occurs. The flat spot reflection will be a trough (red) because it must be an increase in acoustic impedance.

In the second diagram the situation is reversed; the water sand has a higher acoustic impedance than the embedding medium and hence has a signature of red-over-blue. When gas replaces some of the water in the pores of the sand, the acoustic impedance is reduced, the contrast is reduced at the upper and lower boundaries, and the reservoir is seen as a dim spot. Again, if the sand is thick enough, a flat spot can be expected at the point where the dimming occurs and this again will be red.

In the third diagram the reduction in acoustic impedance of the sand, because of gas saturation, causes the acoustic impedance to change from a value higher than that of the embedding medium to one lower than that of the embedding shale. Hence the polarities of the reflections for the top and the base of the sand switch. The signature changes from red-over-blue to blue-over-red across the fluid contact. In order to observe such a phase change, or polarity reversal, in practice, the structural dip must be clearly determined from non-reservoir reflections just above and/or just below the sand under study. Again, if the sand is

Downloaded 25 Jun 2012 to 129.110.5.90. Redistribution subject to SEG license or copyright; Terms of Use: http://segdl.org/

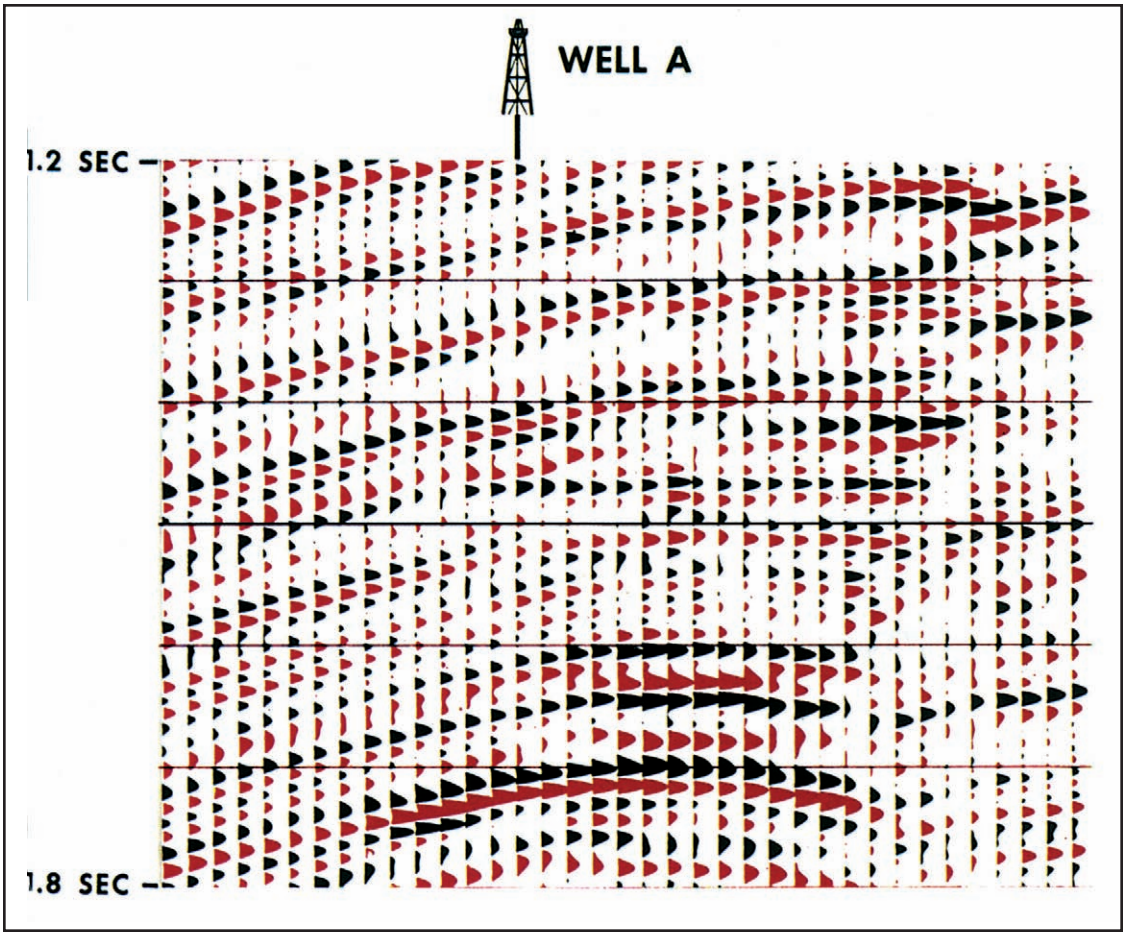

Fig. 5-3. Dual polarity section showing bright spots at 1.62 and 1.72 seconds and a flat spot at 1.47 seconds. (Courtesy Geophysical Service Inc.)

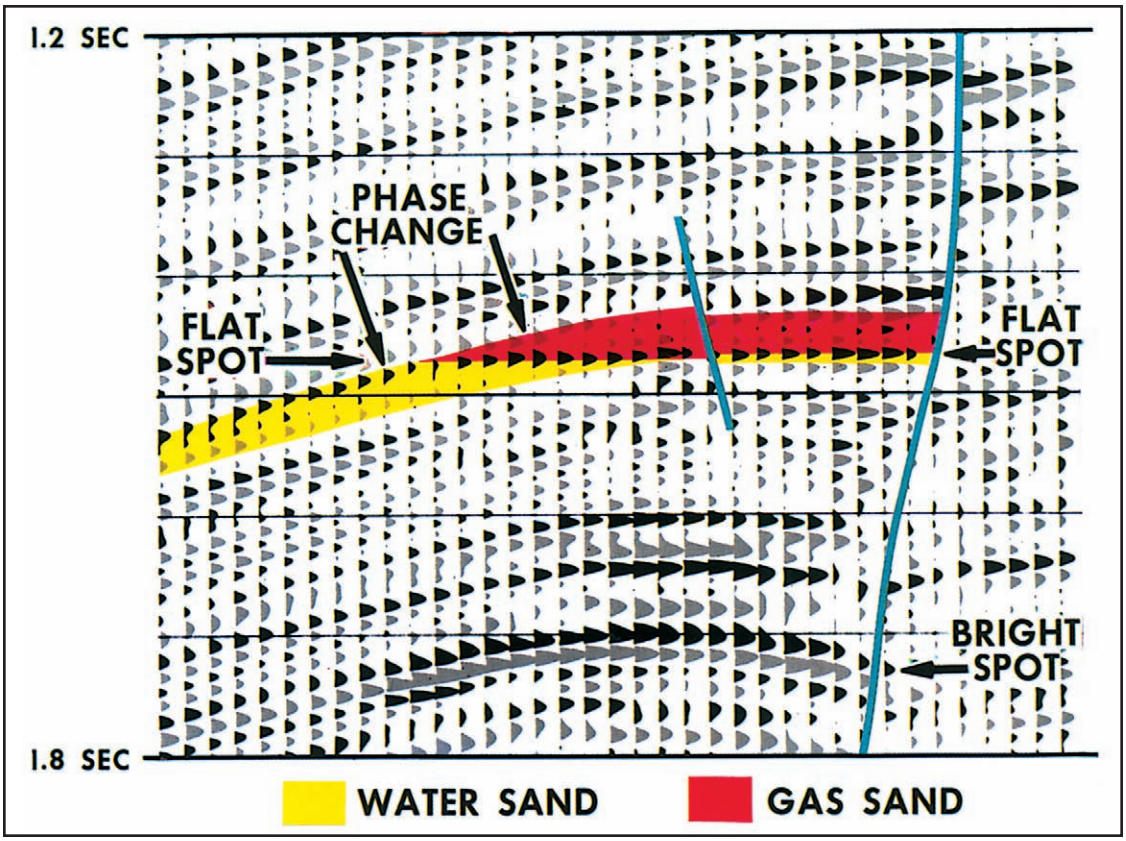

Fig. 5-4. Same section as Figure 5-3 showing the interpreted position of the gas reservoir and demonstrating a phase change between the reflections from the gas sand and the water sand. (Courtesy Geophysical Service Inc.)

Downloaded 25 Jun 2012 to 129.110.5.90. Redistribution subject to SEG license or copyright; Terms of Use: http://segdl.org/

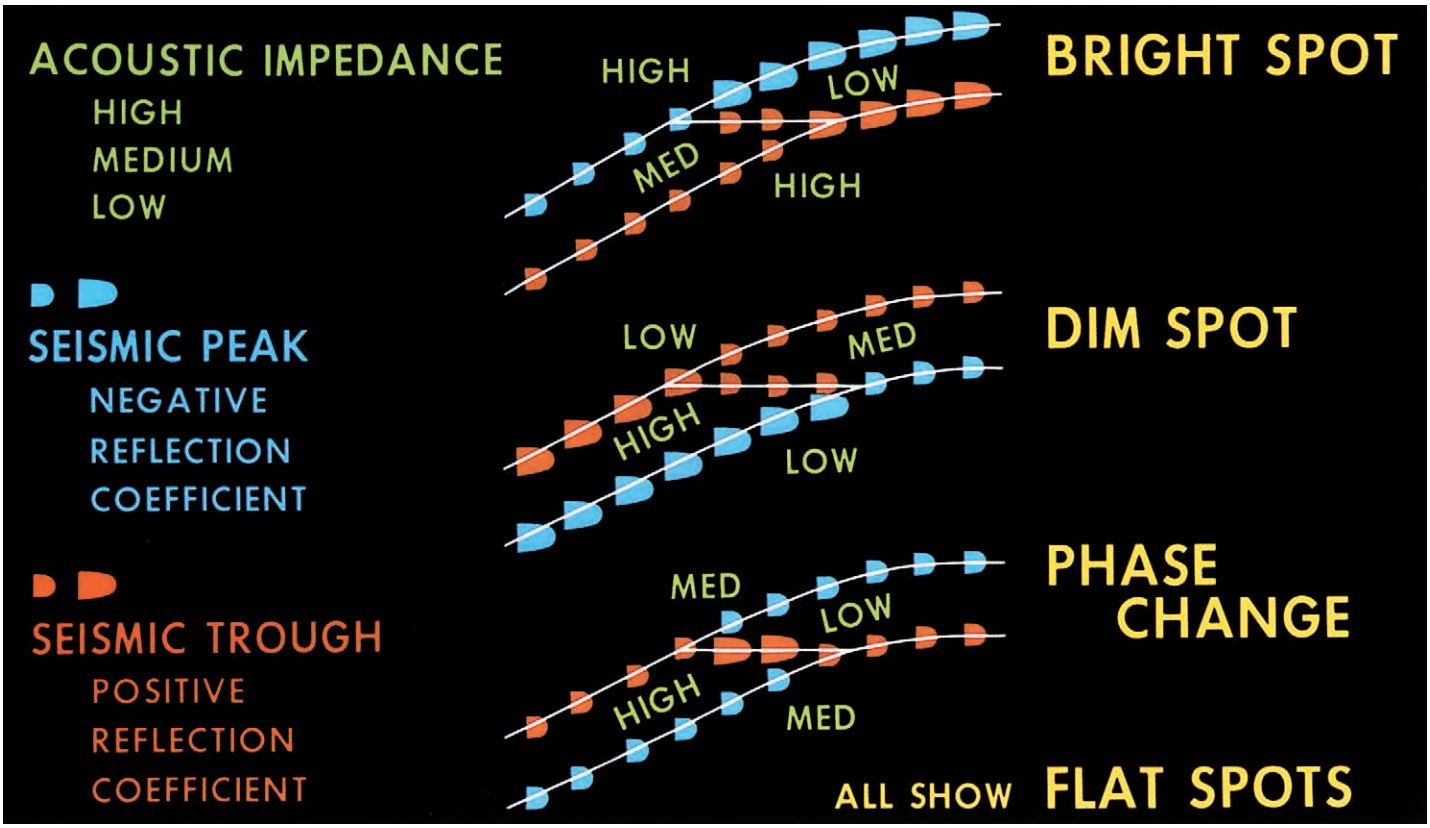

Fig. 5-5. Schematic diagram of the zero-phase response of hydrocarbon reservoirs for different acoustic contrasts between the reservoir and the embedding medium. Note these diagrams are drawn for European polarity. Some of the examples which follow are thus and some are American polarity. For definition of the two zero-phase polarities, see Figure 2-17.

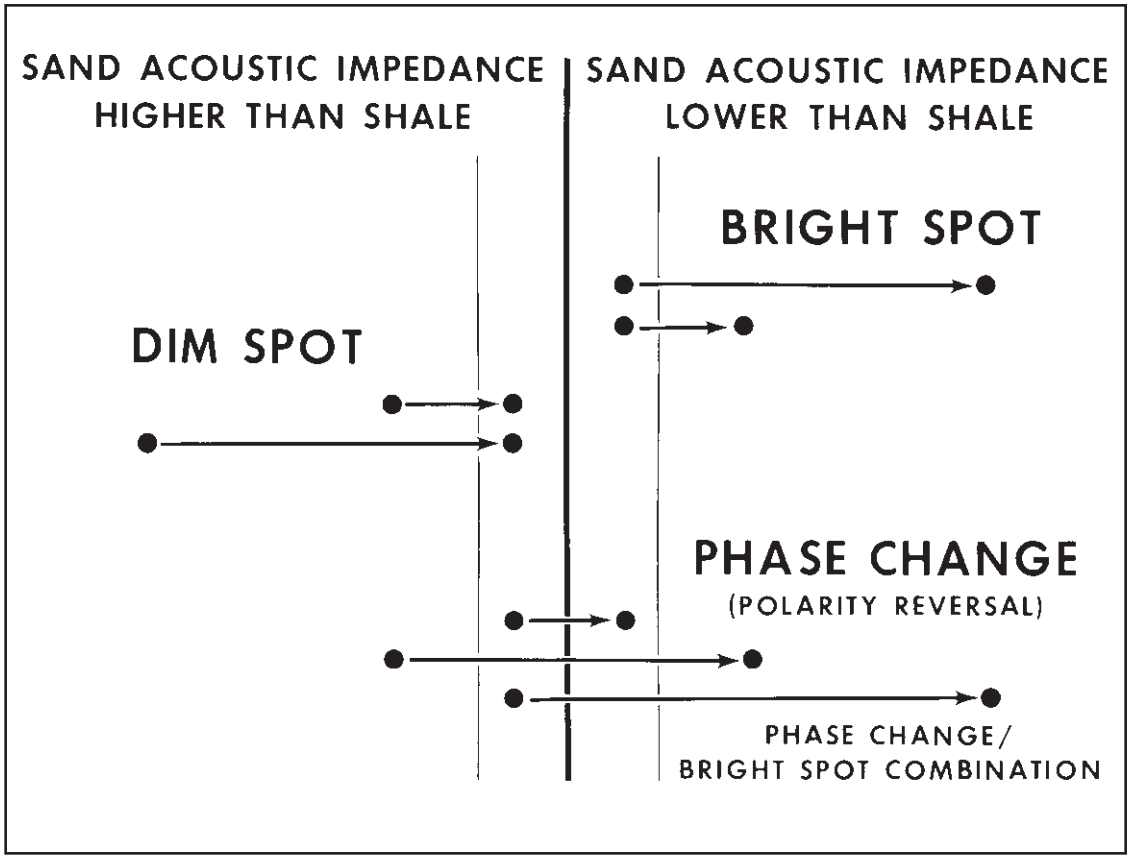

Fig. 5-6. The magnitude of acoustic impedance changes between water-filled and hydrocarbon-filled sands and the resulting observable indications.

Downloaded 25 Jun 2012 to 129.110.5.90. Redistribution subject to SEG license or copyright; Terms of Use: http://segdl.org/

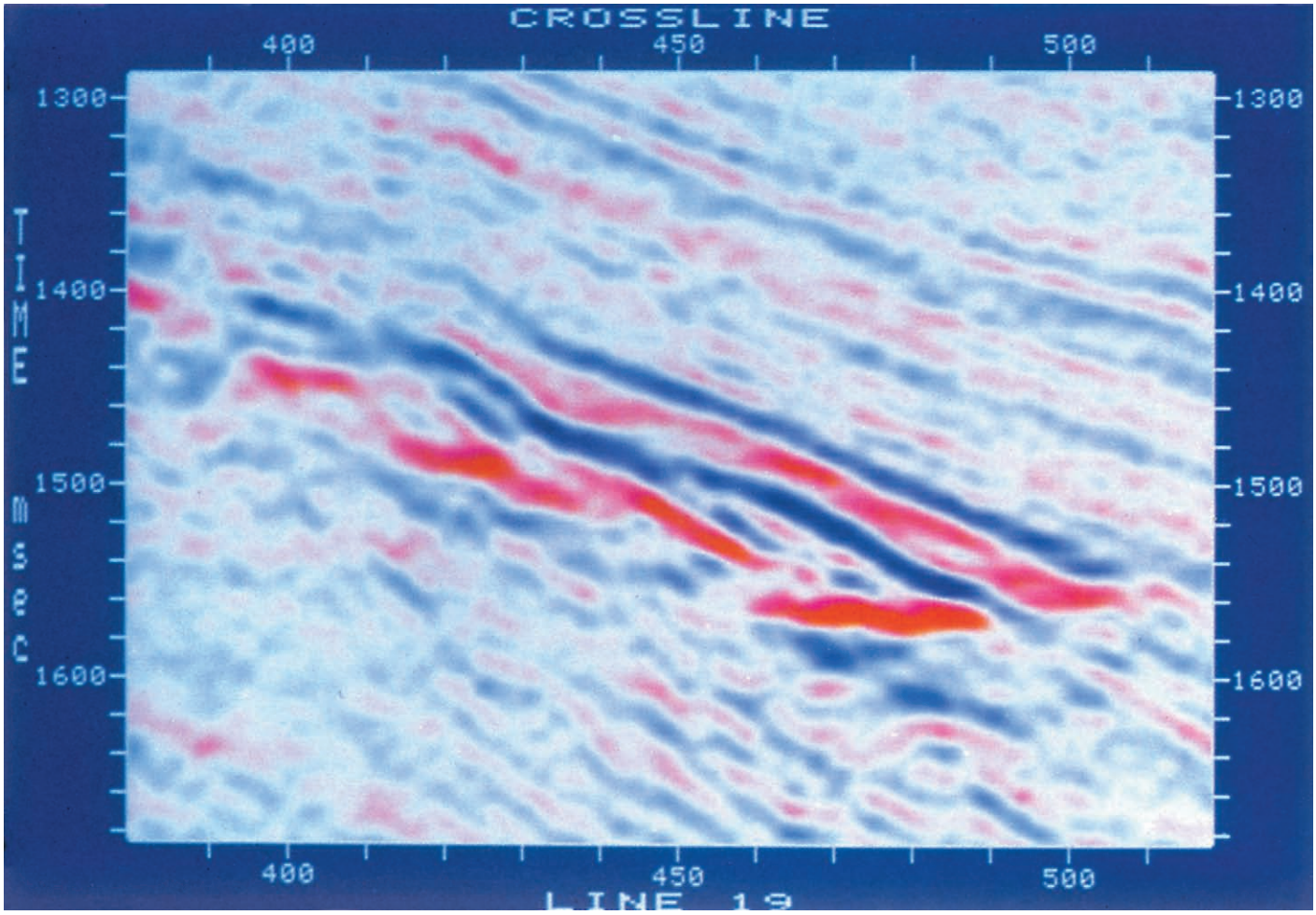

Fig. 5-7. Bright and flat reflections from a Gulf of Mexico gas reservoir known to be subdivided into upper and lower sand units. Data are zero-phase European polarity. (Courtesy Chevron U.S.A. Inc.)

thick enough, a fluid contact reflection should be visible and it will be red. Note that in this case the flat spot reflection has the highest amplitude locally.

Figure 5-6 shows the magnitude of acoustic impedance changes between water sand and hydrocarbon sand and hence the effect on seismic amplitude reflected from the interface between either of them and a uniform embedding medium. The diagram is drawn with clastics in mind, but it also has generality. Tertiary sands and shales normally have rather similar acoustic properties and thus on the relative scale of Figure 5-6 lie between the narrow lines, that is, not far from the heavy line of acoustic impedance equality in the center. For a bright spot (without phase change) the water sand is located just right of the center line and the gas sand is much farther to the right. For a phase change, or polarity reversal, the movement from water sand to gas sand must be from left to right across the center line. In the last situation illustrated in Figure 5-6, the bright spot is exactly the same in amplitude and phase as the one illustrated at the top of the figure; the difference is that the last one labeled *phase change/bright spot combination*, came from a water sand with higher acoustic impedance than the embedding shale and was thus located on the left of the center line. Dim spots must start from a water sand significantly to the left on the relative scale of Figure 5-6, so that a visible movement still leaves them left of center. This is unusual in Tertiary clastics and thus is the reason we do not see many dim spots in that environment. In older rocks, however, much greater differences in acoustic impedance between sands and shales are normal, so that dim spots are more commonly observable.

Examples of Bright Spots, Flat Spots, Dim Spots and Phase Changes

Figure 5-7 shows a Gulf of Mexico bright spot known to be a gas reservoir. The reservoir reflections have very high amplitude and hence the interference from other nearby reflections, multiples or noise is small. The bright reflections show the zero-phase response of two reservoir sands, each blue-over-red and located one on top of the other. The upper

Downloaded 25 Jun 2012 to 129.110.5.90. Redistribution subject to SEG license or copyright; Terms of Use: http://segdl.org/

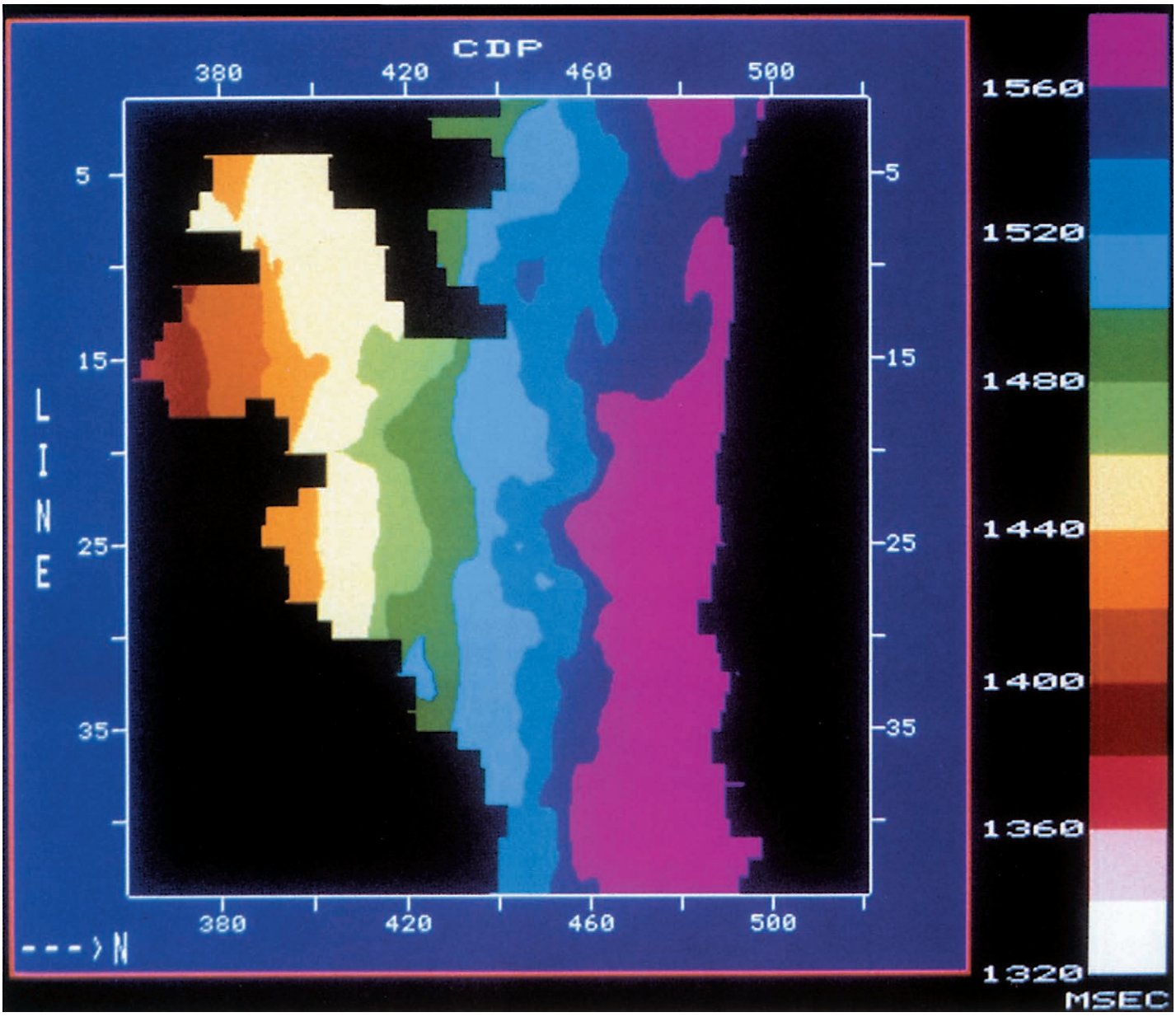

Fig. 5-8. Structure map of the base of the lower gas sand showing the areal extent of the flat spot seen in Figure 5-7. (Courtesy Chevron U.S.A. Inc.)

sand is fairly thin so there is only a hint of a flat spot reflection at the downdip limit of brightness. The lower sand is much thicker and the flat spot reflection is very clear. The natural pairing of top and base reflections is here striking for both reservoir sands.

Flat spot reflections are highly diagnostic indicators of gas but the interpreter should make several validity checks before drawing a conclusion. In Figure 5-7 the flat spot reflection is flat, bright and shows one symmetrical trough. It occurs at the downdip limit of the bright events and is unconformable with them. Figure 5-8 is a structure map of the base of the gas; it shows structural consistency for the flat spot reflection in the extent of the purple color.

Figure 5-9 illustrates other Gulf of Mexico bright spots and flat spots. These data are also zero phase, but the polarity is American. Hence, in Figure 5-9 flat spots are black and reflections from the top of gas reservoirs are red. Note particularly the prominent reservoir reflections between times of 1.5 and 1.6 on Line 49 and on Line 51 and on horizontal section 1.520 in the lower right against a salt dome.

Figure 5-10 shows bright spot reflections from a deep major gas field in the Garden Banks area of the Gulf of Mexico. The amplitudes from the gas are strong and they

Downloaded 25 Jun 2012 to 129.110.5.90. Redistribution subject to SEG license or copyright; Terms of Use: http://segdl.org/

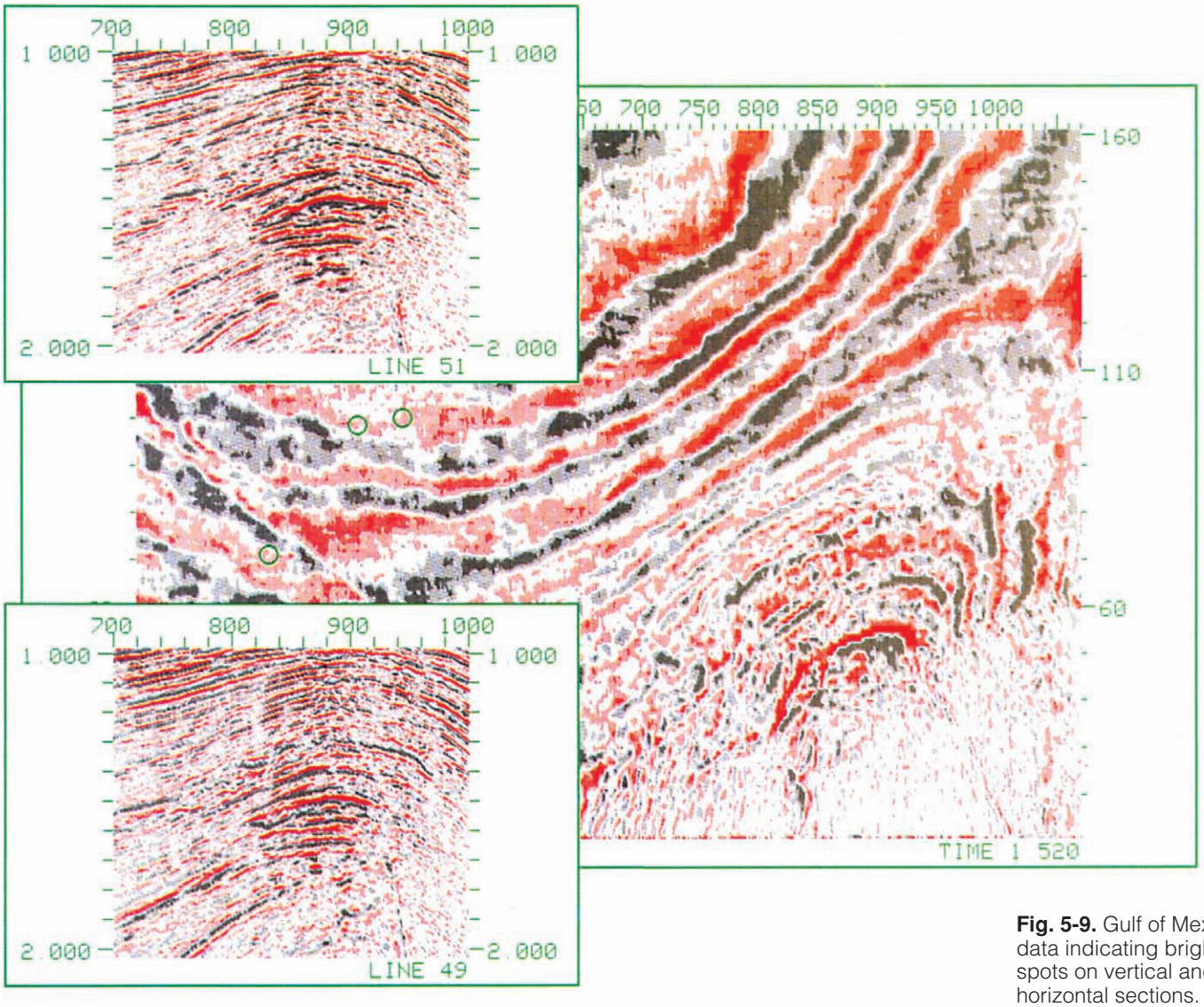

Fig. 5-9. Gulf of Mexico data indicating bright spots on vertical and horizontal sections. (Courtesy Texaco U.S.A. Inc.)

exhibit a very clear zero-phase character with American polarity. Figure 5-11 shows the exact same piece of data but with contrasting colors inserted into the ends of the color bar. The large areas of yellow and cyan demonstrate that this 8-bit data was significantly clipped when the data were loaded to the workstation. This type of clipping test was shown in Figure 1-27. The extreme clipping in Figure 5-11 shows that these reservoir amplitudes, originally intended for some reservoir evaluation study, are certainly not useable in this form.

Figures 5-12 and 5-13 both show good examples of bright spots/flat spots and in both cases the data are zero phase. However, in Figure 5-12 the data are European polarity, and in Figure 5-13 the data are American polarity.

Figure 5-14 shows a flat spot and associated bright spot from the Northwest Shelf of Australia. The flat spot, exhibiting 90° phase, is indicated by the green arrow and is quite clear. However, the well was dry, indicating that the hydrocarbons are no longer there and that this is a paleo-contact only. Several of these have been recognized recently by Ware and Burgess (1998).

Figures 5-15 and 5-16 illustrate two examples of bright and flat spots from parts of the Ha'py field offshore Egypt (Wigger et al., 1997). These Pliocene turbidite sands have an average porosity of 30% and reach a maximum thickness of 120 m.

Figure 5-17 illustrates a largely depleted gas field in the northern part of the Vienna

Downloaded 25 Jun 2012 to 129.110.5.90. Redistribution subject to SEG license or copyright; Terms of Use: http://segdl.org/

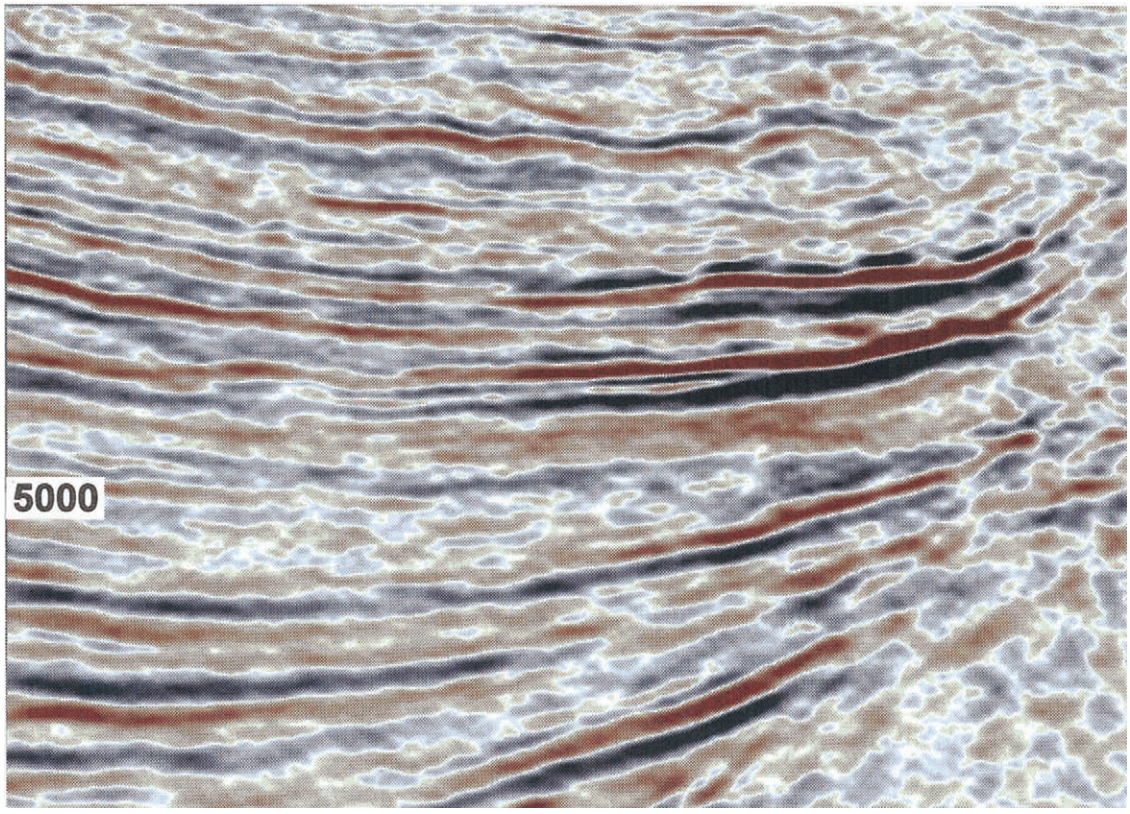

Fig. 5-10. Bright spots from four stacked Gulf of Mexico gas reservoirs. The productive sands are of Pliocene age and lie at depths between 5000 m and 6000 m. Data are zero-phase American polarity. (Courtesy Amoco Production Company.)

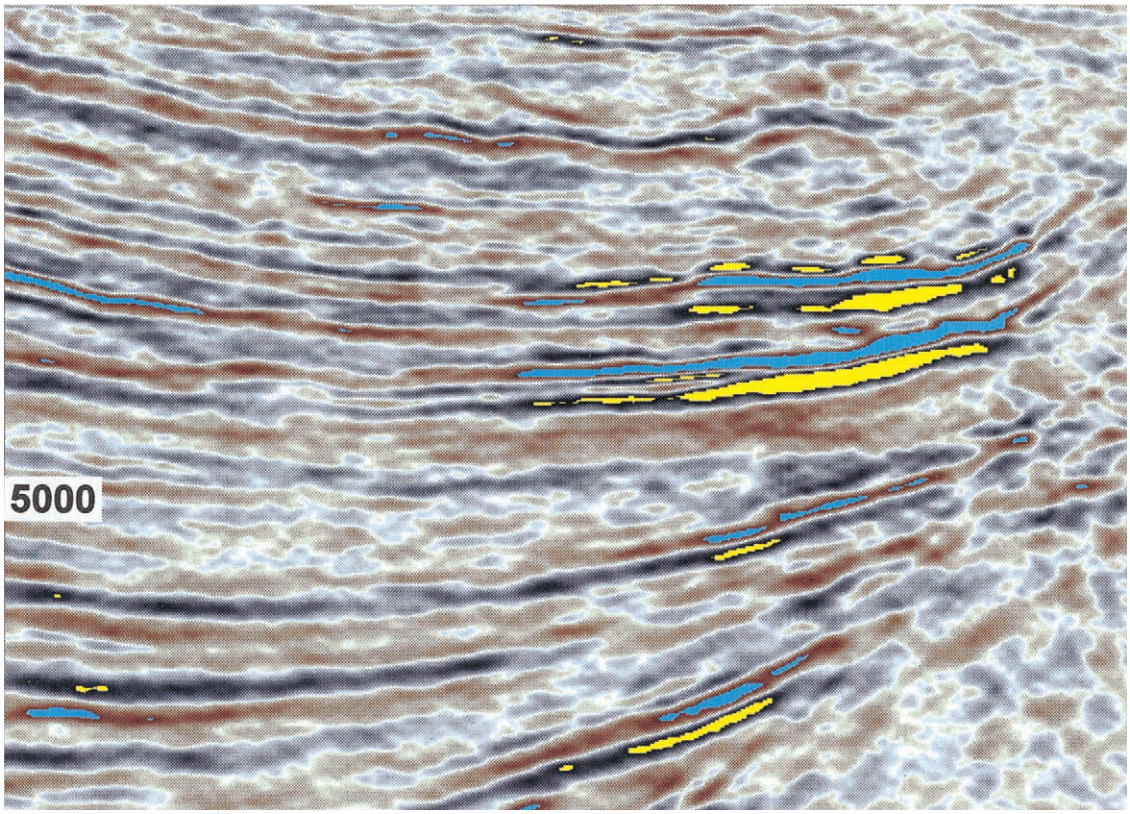

Fig. 5-11. Same bright spots as Figure 5-10, but contrasting colors have been inserted into the extremities of the color bar to demonstrate severe clipping of the reservoir reflections. (Courtesy Amoco Production Company.)

Downloaded 25 Jun 2012 to 129.110.5.90. Redistribution subject to SEG license or copyright; Terms of Use: http://segdl.org/

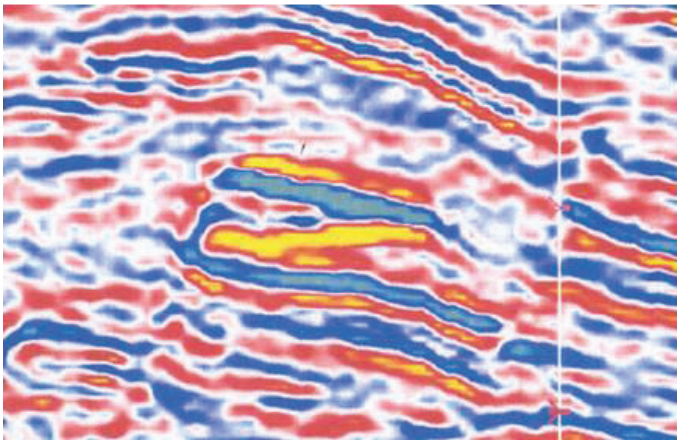

Fig. 5-12. Gas reservoir from Indonesia demonstrating zero-phase European polarity.

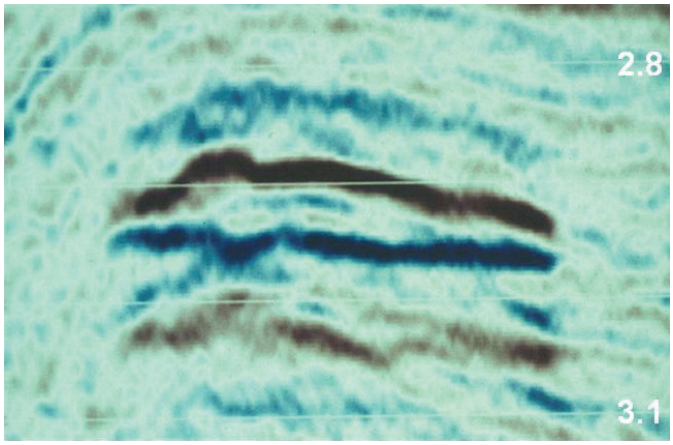

Fig. 5-13. Gas reservoir from the Gulf of Mexico demonstrating zero-phase American polarity. (Courtesy CNG Producing Company.)

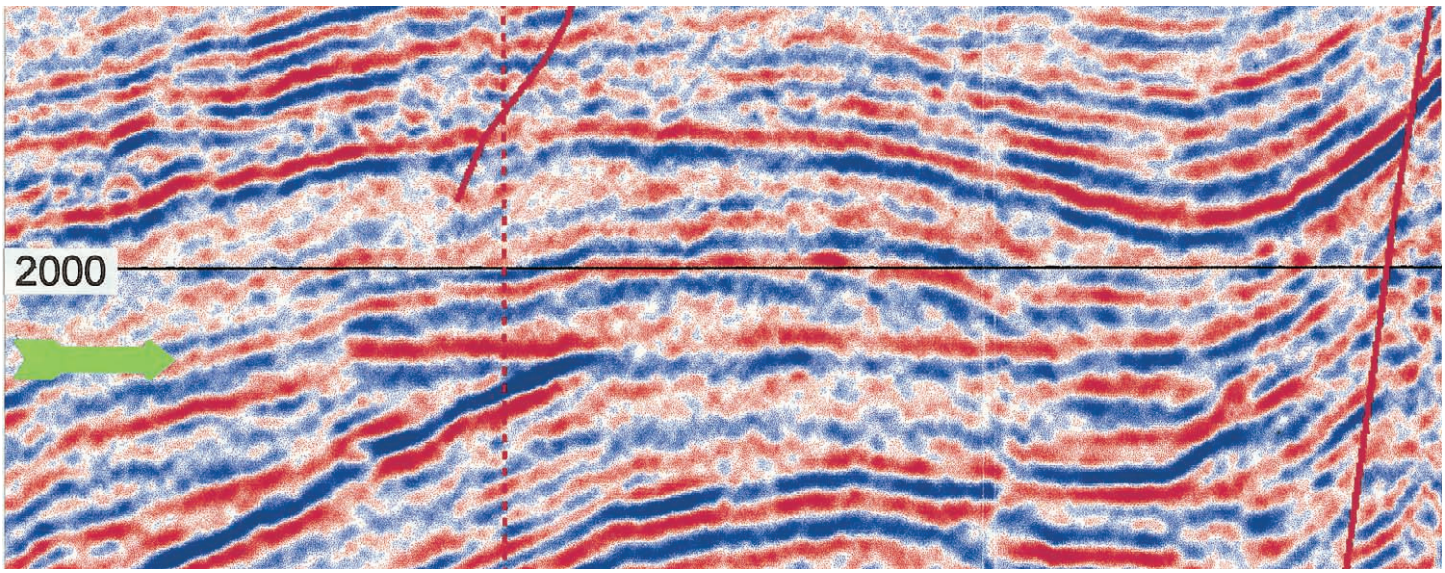

Fig. 5-14. Flat spot and associated bright spot on the Northwest Shelf of Australia. The well was dry so this is interpreted as a paleo-contact expressing diagenetic effects. (Courtesy Australian Geological Survey Organization and Santos Ltd.)

Basin in Austria. The porosity is about 30% and the depth is around 500 m. On the left of the vertical section the top reservoir reflection and the fluid contact reflection can still be seen, but the amplitude is much diminished because of a gas chimney. The full extent of the field can be clearly seen on the time slice.

Direct observation of hydrocarbon fluids through bright spots and flat spots is very well established in Tertiary clastic basins, of which the Gulf of Mexico is the most extensively studied. However, hydrocarbons are also directly observable in many older rocks. Figure 5-18 shows a fine flat spot and associated bright spot in Jurassic rocks offshore Norway. Early observation of this flat spot on 2-D data (Birtles, 1986) contributed to the discovery of the Troll Field. Now with 3-D data, zero-phaseness and color the flat spot is outstandingly clearer. The flat spot is not very flat because of the tuning effects and velocity effects but it is clearly unconformable with structural reflections. Often unconformability is a more important diagnostic than flatness in the identification of fluid contact reflections. Here the flat spot is almost 9 km long.

Downloaded 25 Jun 2012 to 129.110.5.90. Redistribution subject to SEG license or copyright; Terms of Use: http://segdl.org/

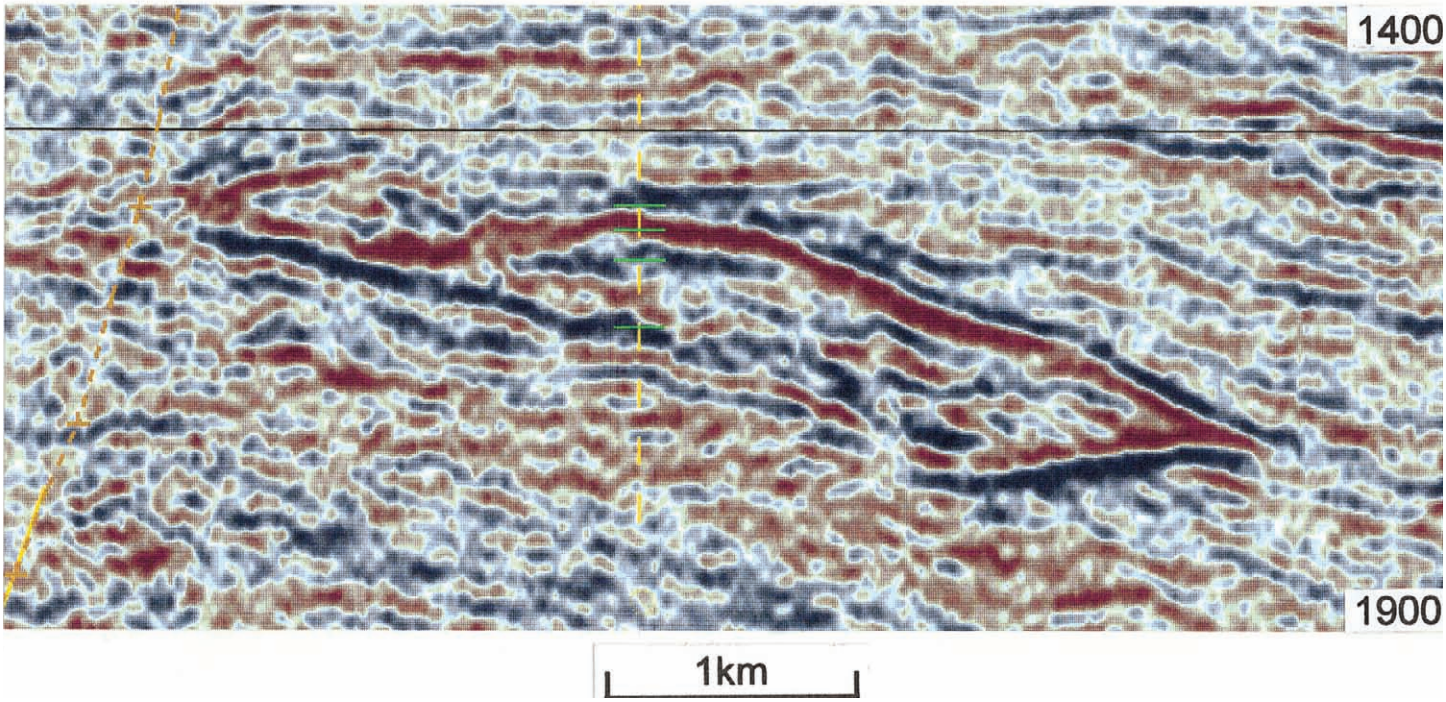

Fig. 5-15. Bright spot and flat spot from a Pliocene gas reservoir in the eastern Nile delta offshore Egypt. (Courtesy Amoco Egypt Oil Company.)

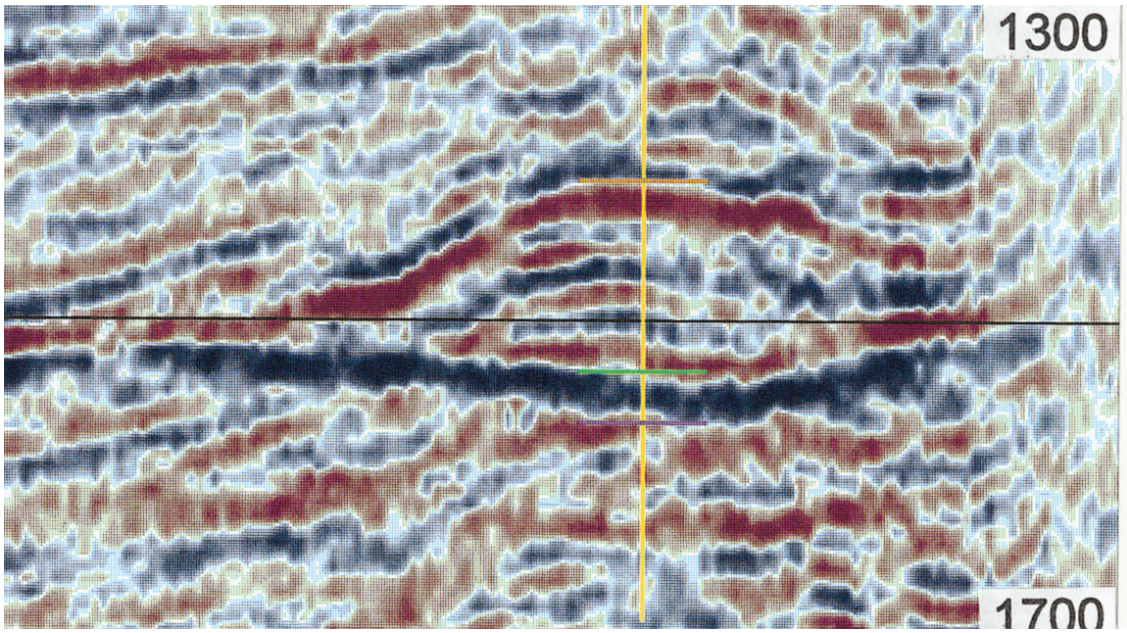

Fig. 5-16. Bright spot and flat spot from a Pliocene gas reservoir in the eastern Nile delta offshore Egypt. (Courtesy Amoco Egypt Oil Company.)

Figure 5-19 shows a flat spot and associated bright spot in Permian rocks in The Netherlands. (The strongest reflections on the section are from an anhydrite layer; be careful to look just under these strong reflections in the center to find the flat spot and bright spot.) The change in amplitude of the black (top reservoir) reflection coincident with the flat spot is an important diagnostic observation. The author is aware of direct observation of hydrocarbon fluids in rocks up to Pennsylvanian or Carboniferous in age. As the quality of seismic data improves further, the age theshold should be pushed to even greater ages.

Figure 5-20 shows two examples of bright spots and flat spots indicating the reflections from the top and base of proven hydrocarbons in the North Sea. Line 182 shows continuity of the fluid contact across the reservoir, whereas line 137 shows it interrupted

Downloaded 25 Jun 2012 to 129.110.5.90. Redistribution subject to SEG license or copyright; Terms of Use: http://segdl.org/

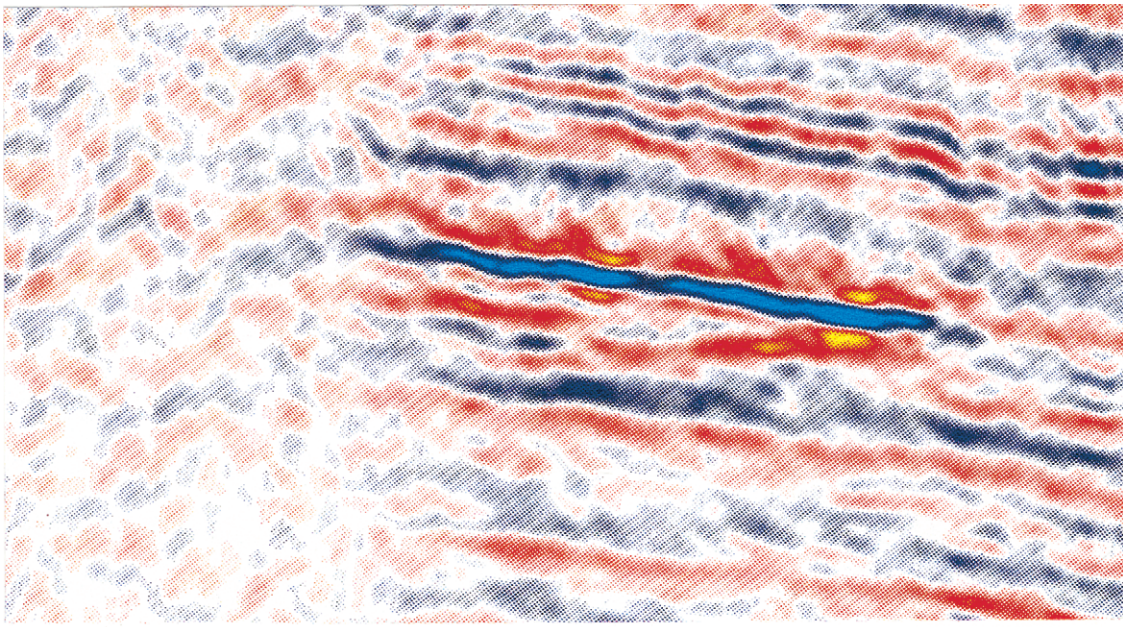

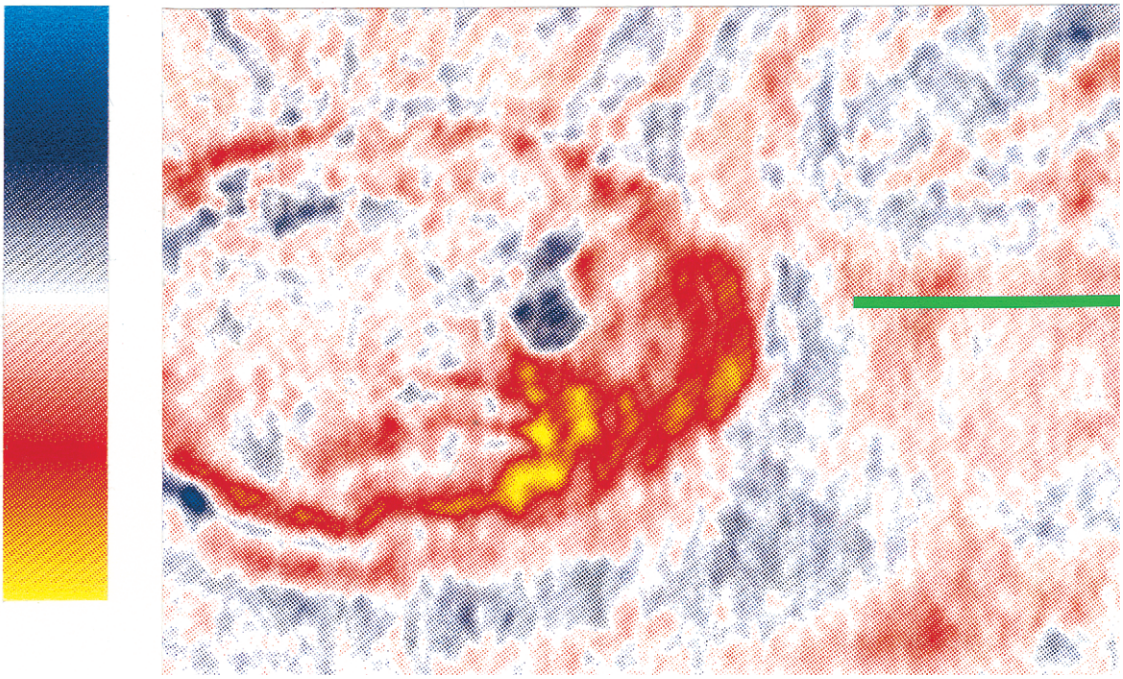

Fig. 5-17 (Upper). Vertical section showing bright spot and flat spot from a gas reservoir in upper Miocene sediments of the Vienna Basin, Austria. Amplitude is lost on the left because of a gas chimney effect. (Courtesy OMV Aktiengesellschaft.) **(Lower)**. Time slice at level of flat spot showing extent of high amplitude and extent of gas chimney. The green line shows the alignment of the vertical section above. (Courtesy OMV Aktiengesellschaft.)

in the center where the reservoir is full to base. Figure 5-21 shows horizon slices from the top reservoir reflection and from the fluid contact/base hydrocarbon sand reflection. Similar patterns in amplitude confirm that these horizon slices indeed follow the top and bottom of the same interval.

Figure 5-22 is a practical example of a dim spot. The discovery well penetrates a gas column of about 400 ft (130 m) but the acoustic contrast of the gas sand with its embedding medium is small. Outside the reservoir the contrast between the sand and the embedding medium is much greater, as the amplitudes indicate. Here the reservoir is cemented, so the increase in acoustic impedance is caused partly by lack of gas and partly by the cementation. Figures 5-23 and 5-24 illustrate dim spots from the Northwest Shelf of Australia. In both cases the reservoir sands truncate at an unconformity overlain

Downloaded 25 Jun 2012 to 129.110.5.90. Redistribution subject to SEG license or copyright; Terms of Use: http://segdl.org/

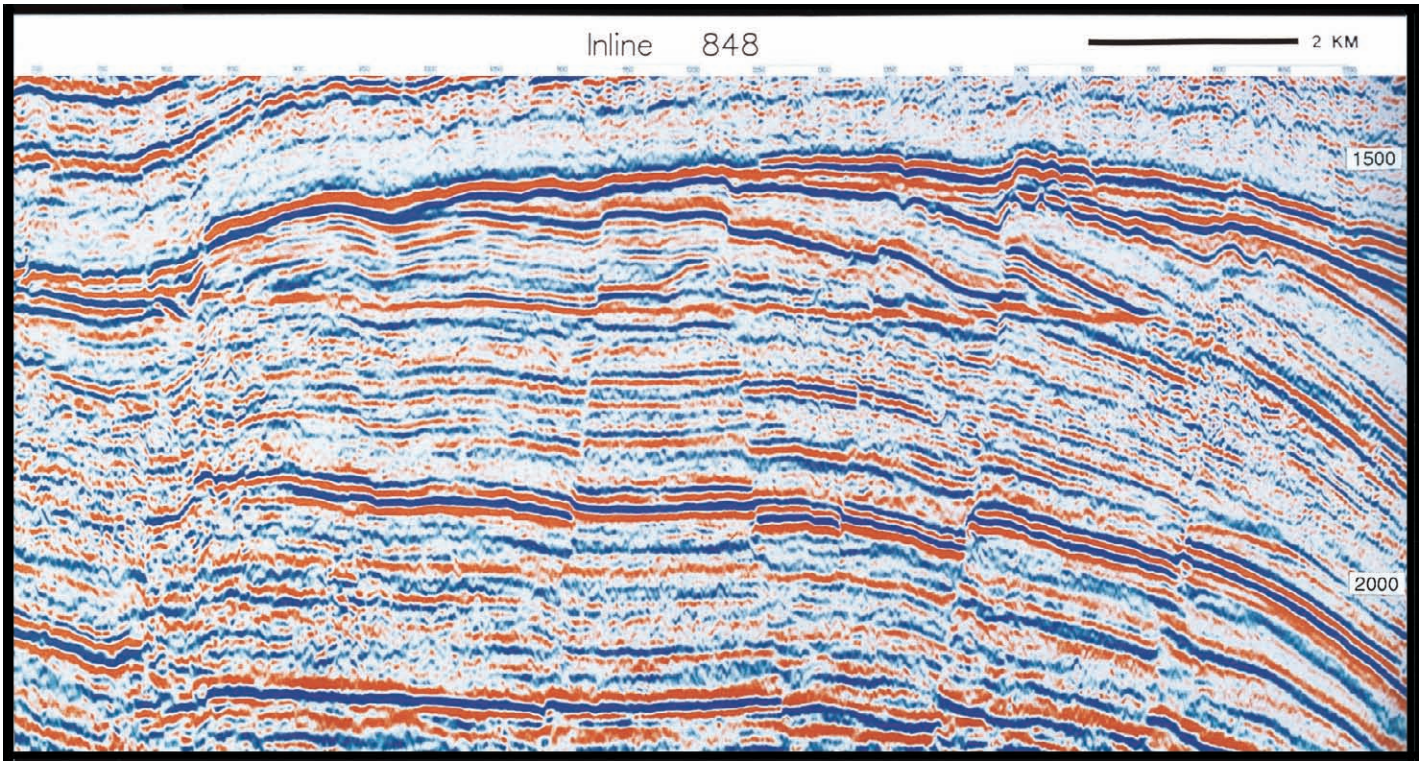

Fig. 5-18. Vertical section across Troll gas field offshore Norway. Note 9 km long flat spot at about 1700 ms. The reservoir is Jurassic in age with an average porosity of 28%. (Courtesy Norsk Hydro a.s.)

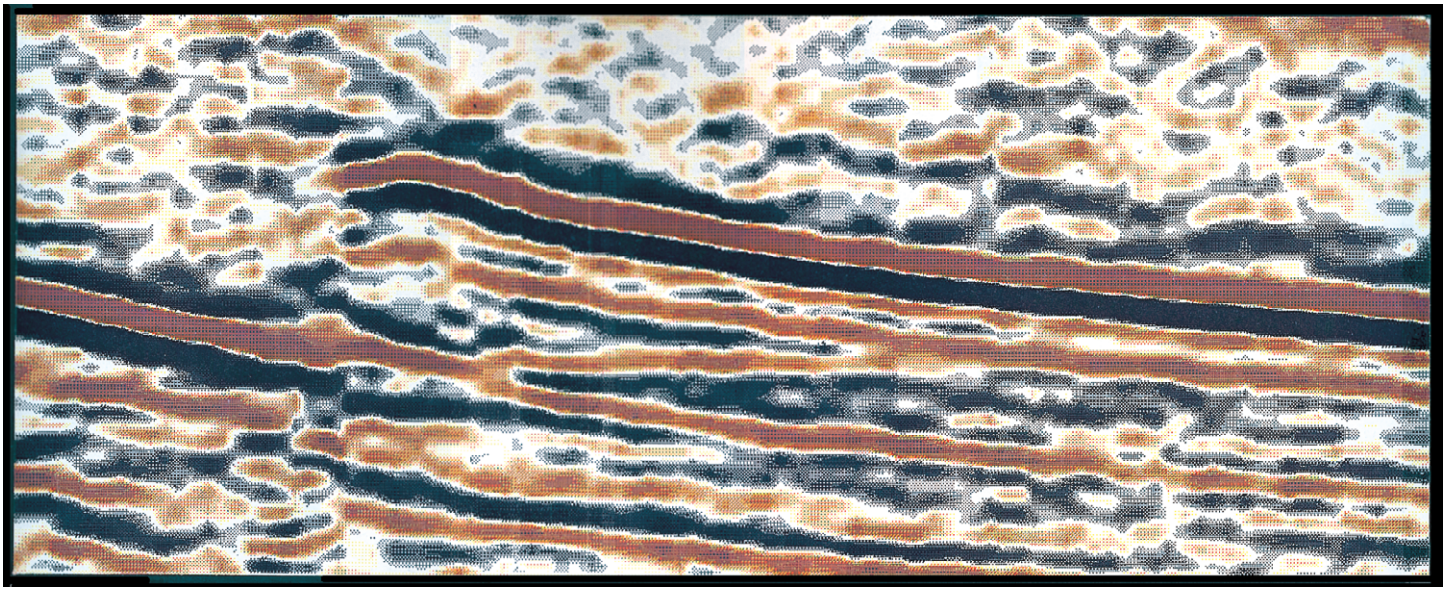

Fig. 5-19. Vertical section across a gas field in the Netherlands. The flat spot visible in the center is at a time of 1950 ms and a depth of 2850 m. The reservoir is within the Rotliegendes (lower Permian) sandstone and has an average porosity of 18%. (Courtesy Nederlandse Aardolie Maatschappij B. V.)

Downloaded 25 Jun 2012 to 129.110.5.90. Redistribution subject to SEG license or copyright; Terms of Use: http://segdl.org/

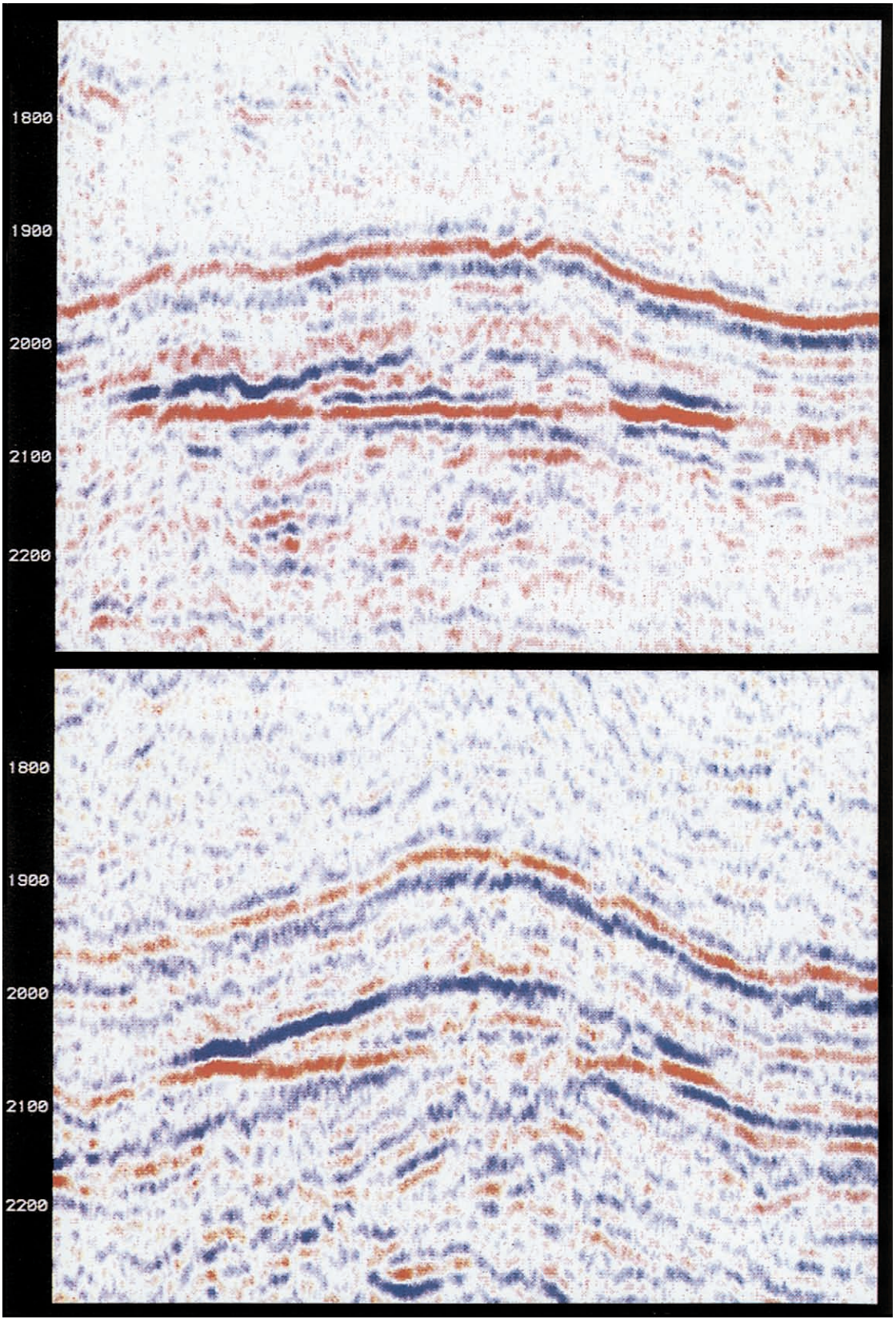

Fig. 5-20. Line 182 (upper) and line 137 (lower) over the Heimdal field in the Norwegian North Sea. The reflection from the top of the gas condensate reservoir is blue; the fluid contact reflection is red. (Courtesy Elf Aquitaine Norge a/s.)

Downloaded 25 Jun 2012 to 129.110.5.90. Redistribution subject to SEG license or copyright; Terms of Use: http://segdl.org/

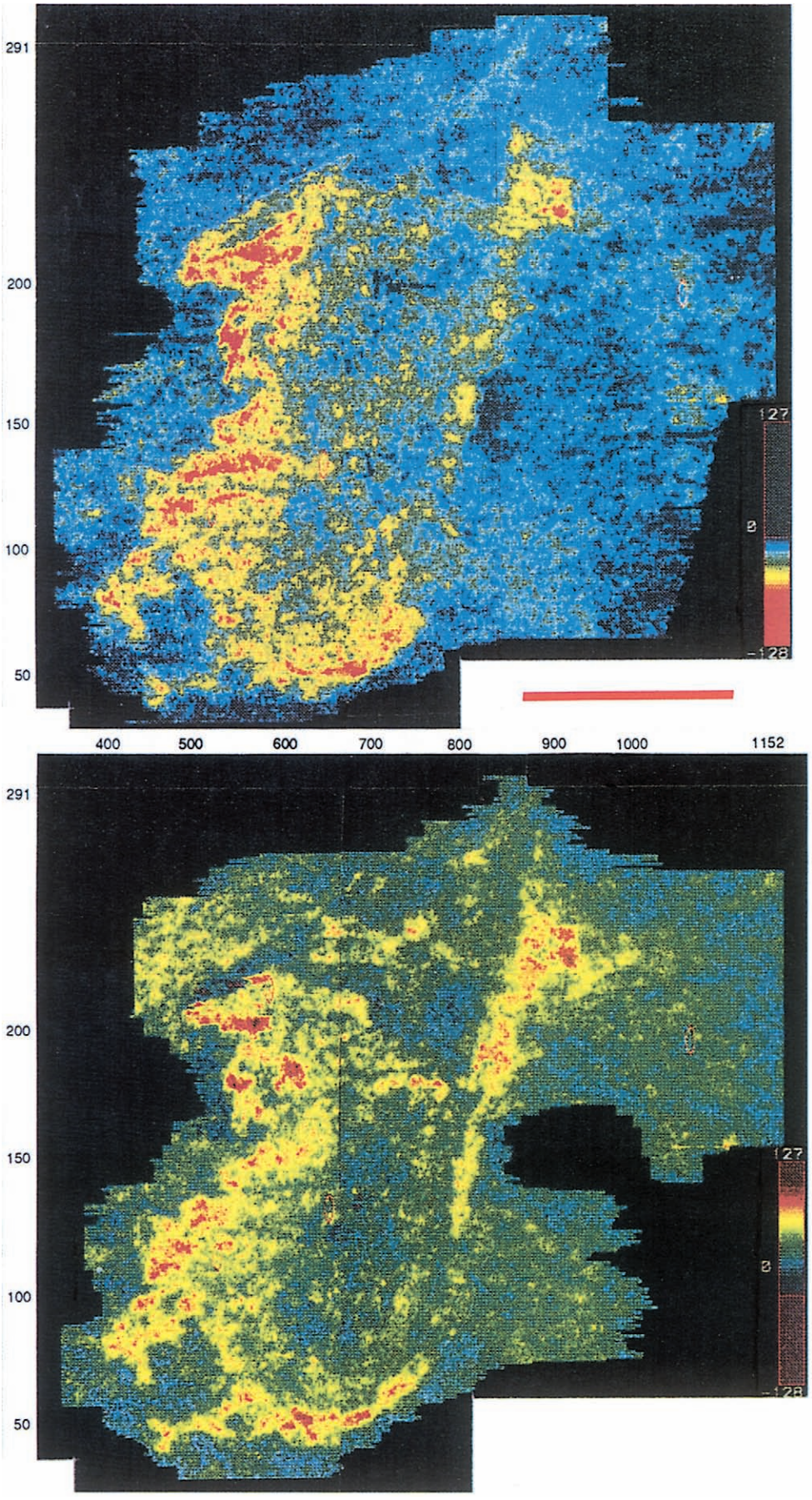

Fig. 5-21. Horizon slice through top reservoir reflection (upper) and through fluid contact reflection (lower) for the Heimdal field in the Norwegian North Sea. Red bar is 3 km. (Courtesy Elf Aquitaine Norge a/s.)

Downloaded 25 Jun 2012 to 129.110.5.90. Redistribution subject to SEG license or copyright; Terms of Use: http://segdl.org/

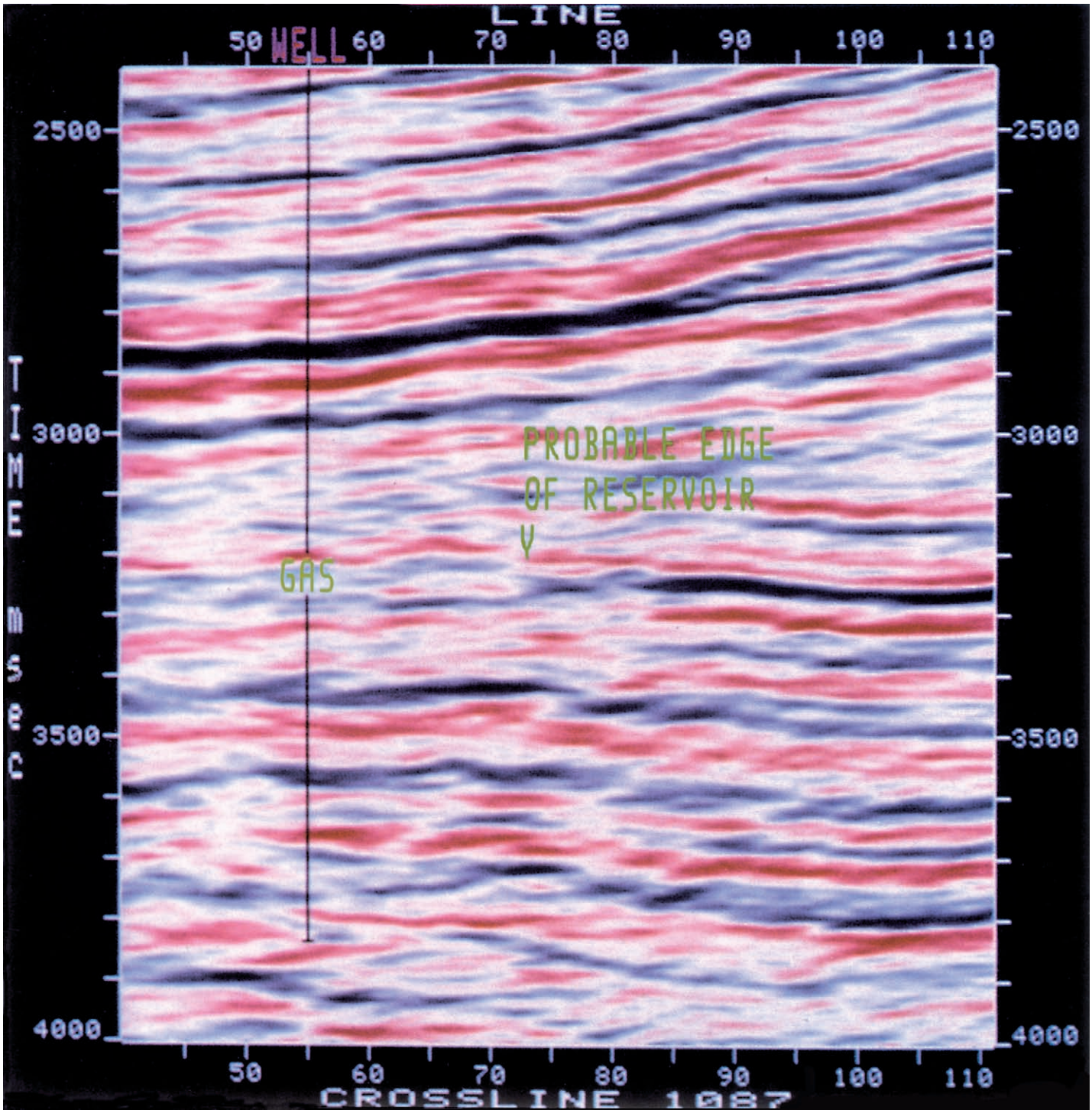

Fig. 5-22. A dim spot from a known gas reservoir offshore Trinidad. (Courtesy Texaco Trinidad Inc.)

by soft marine shale of acoustic impedance similar to, but in fact even slightly lower than, the gas sands. Hence, the amplitude of the reflection from the unconformity dims as an indication of the truncating gas reservoirs. Tilbury and Smith (1988) discuss the geology and seismic modeling in support of this interpretation.

Figures 5-25, 5-26, 5-27 and 5-28 illustrate a phase change; all four figures are exactly the same piece of data displayed with different colors and gains. Figure 5-25 uses the standard blue and red gradational scheme and the amplitude anomaly is clearly visible. Its visibility is perhaps enhanced further by the yellow, green and gray color scheme of Figure 5-26. In order to check for a phase change, or polarity reversal, it is necessary to judge the structural continuity from the bright reflections to their lower-amplitude

Downloaded 25 Jun 2012 to 129.110.5.90. Redistribution subject to SEG license or copyright; Terms of Use: http://segdl.org/

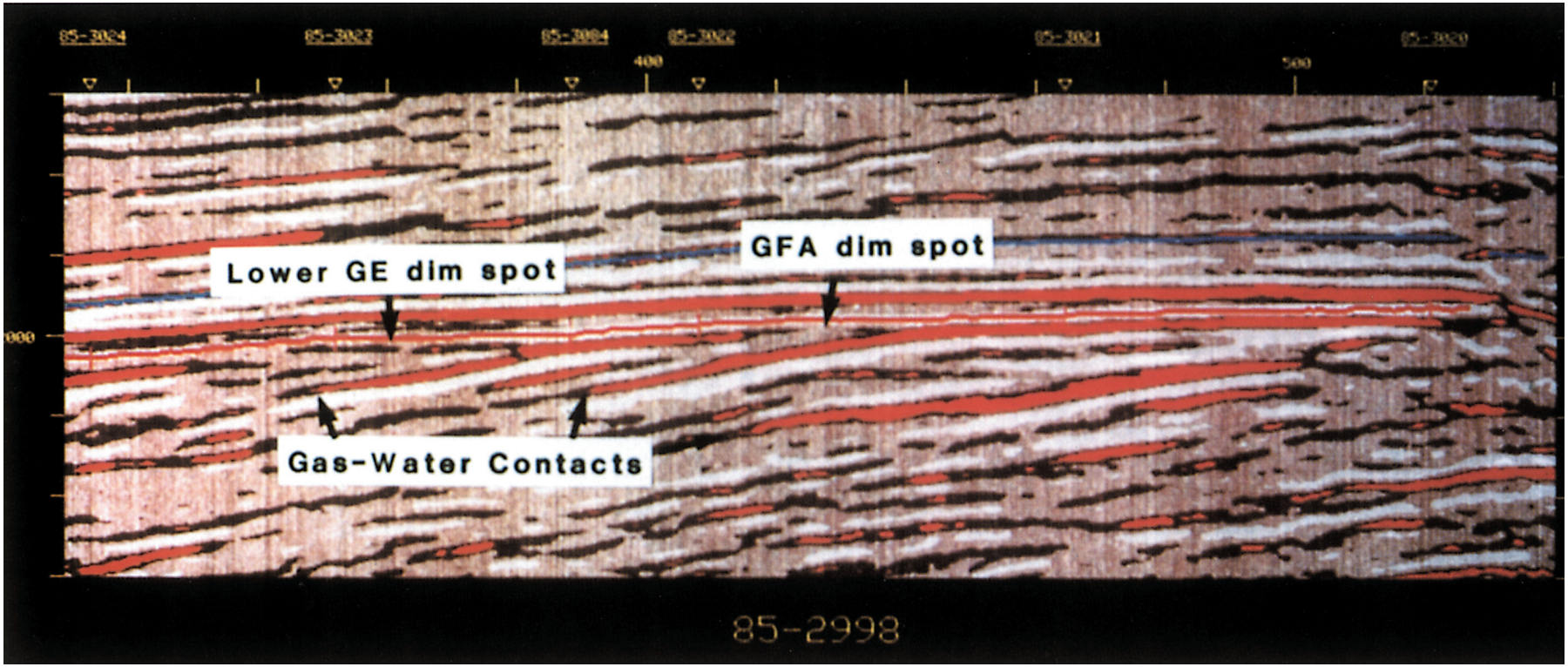

Fig. 5-23. Dim spots from Goodwyn gas field, Northwest Shelf, Australia, caused by gas sands truncating at an unconformity overlain by soft marine shale. (Courtesy Woodside Offshore Petroleum Pty., BP Development Australia Ltd., BHP Petroleum Pty. Ltd., Shell Development [Australia] Pty. Ltd., California Asiatic Oil Company, Japan Australia LNG [MIMI] Pty. Ltd., and Woodside Petroleum Ltd.)

Downloaded 25 Jun 2012 to 129.110.5.90. Redistribution subject to SEG license or copyright; Terms of Use: http://segdl.org/

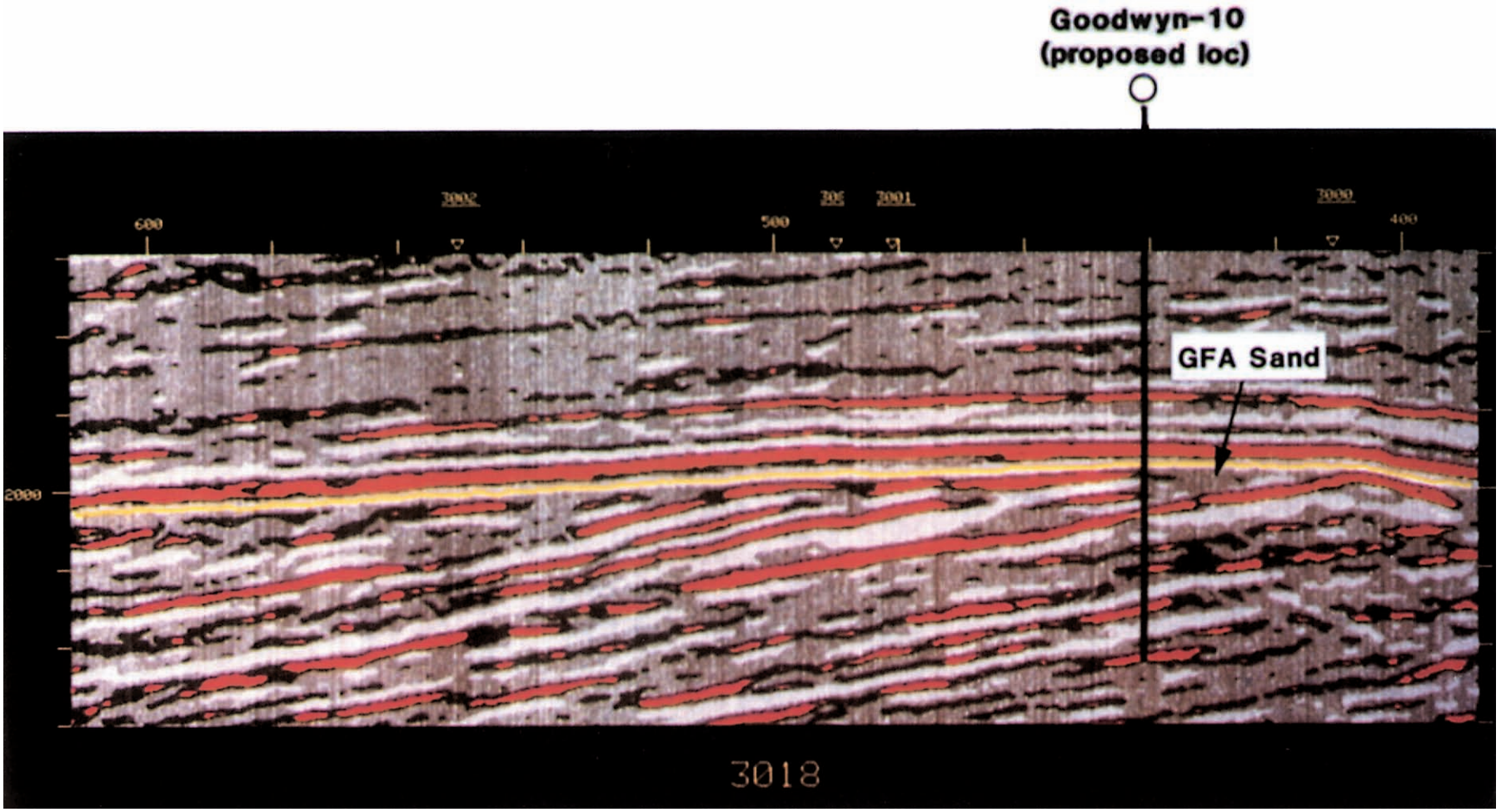

Fig. 5-24. Dim spot from Goodwyn gas field, Northwest Shelf, Australia, targeted as drilling location. (Courtesy Woodside Offshore Petroleum Pty., BP Development Australia Ltd., BHP Petroleum Pty. Ltd., Shell Development [Australia] Pty. Ltd., California Asiatic Oil Company, Japan Australia LNG [MIMI] Pty. Ltd., and Woodside Petroleum Ltd.)

Downloaded 25 Jun 2012 to 129.110.5.90. Redistribution subject to SEG license or copyright; Terms of Use: http://segdl.org/

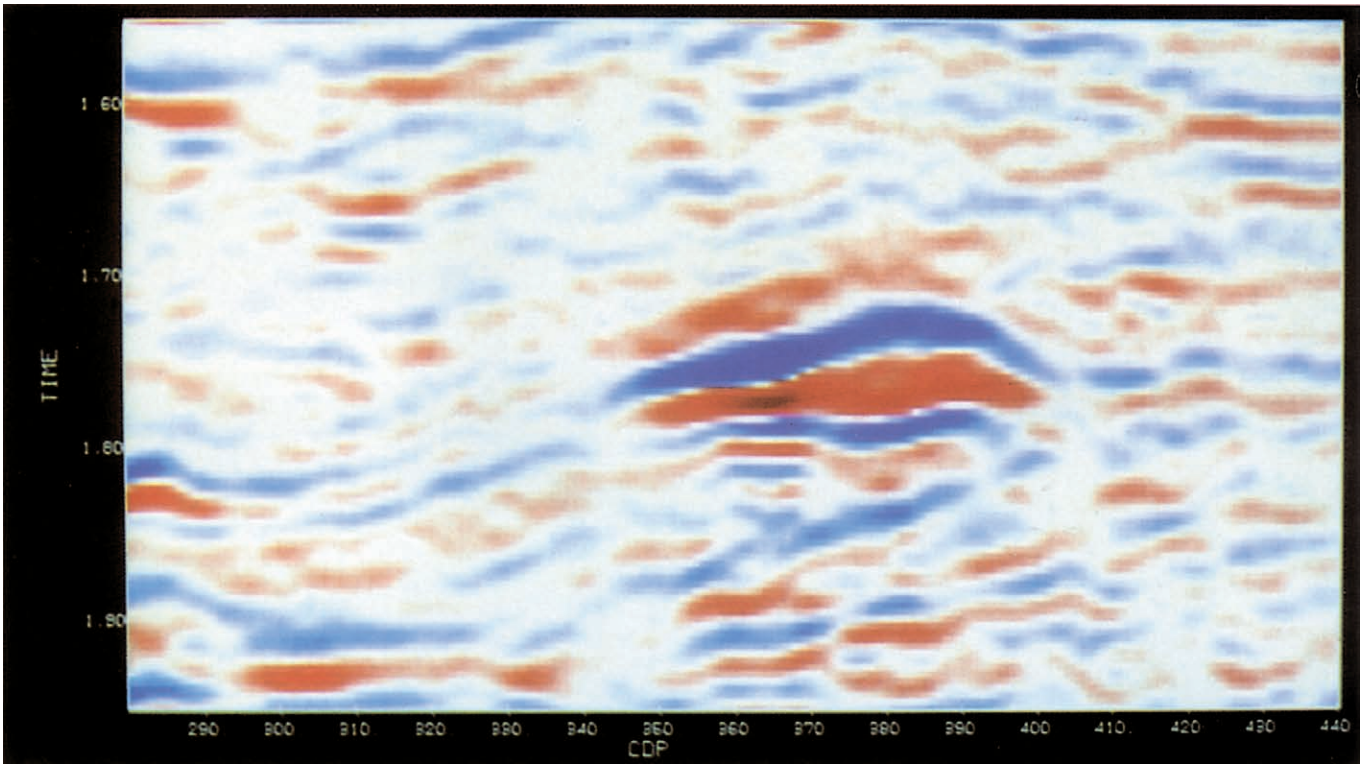

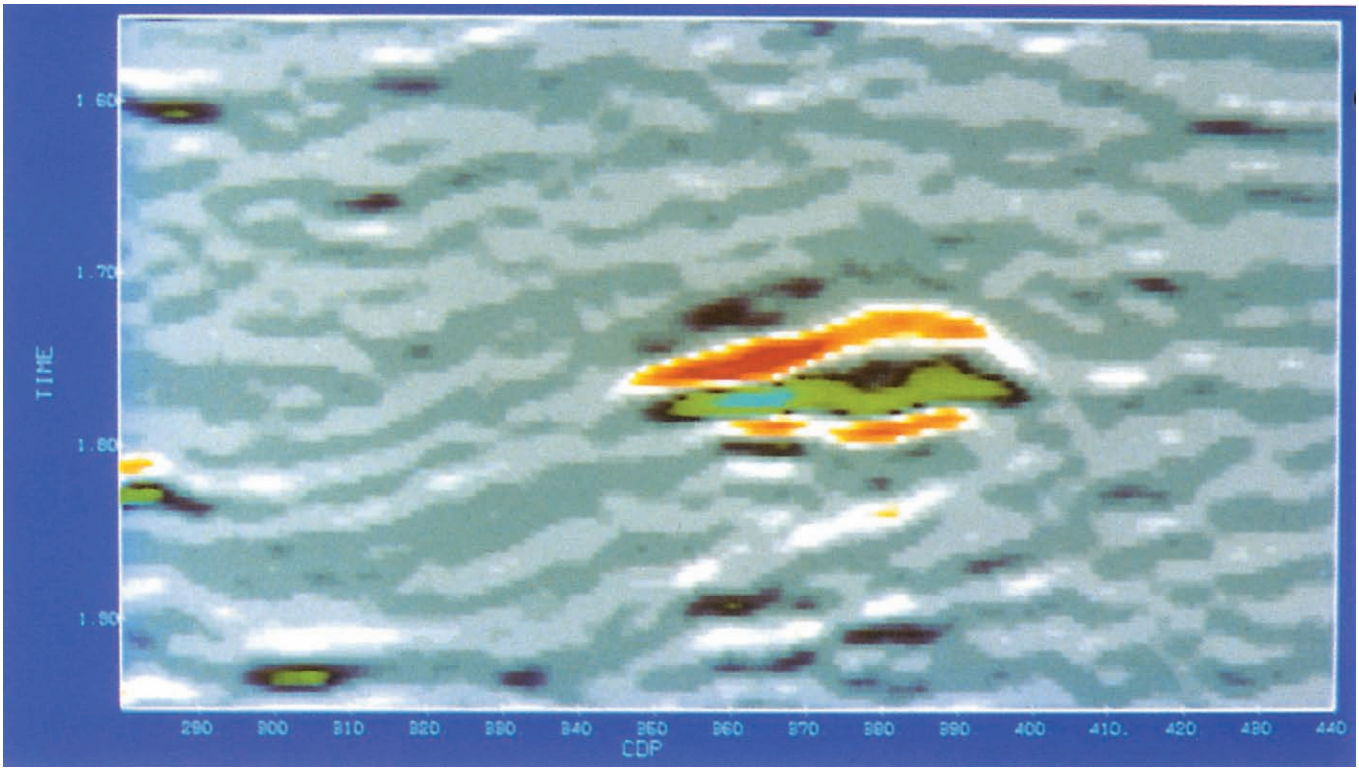

Fig. 5-25. (Top) Gulf of Mexico bright spot displayed in gradational blue and red with the gain set to maximize visual dynamic range and hence increase prominence of the amplitude anomaly. (Courtesy Chevron U.S.A. Inc.)

Fig. 5-26. (Bottom) Same bright spot as Figure 5-25 displayed in yellow, green and gray also in order to increase the prominence of the amplitude anomaly. (Courtesy Chevron U.S.A. Inc.)

Downloaded 25 Jun 2012 to 129.110.5.90. Redistribution subject to SEG license or copyright; Terms of Use: http://segdl.org/

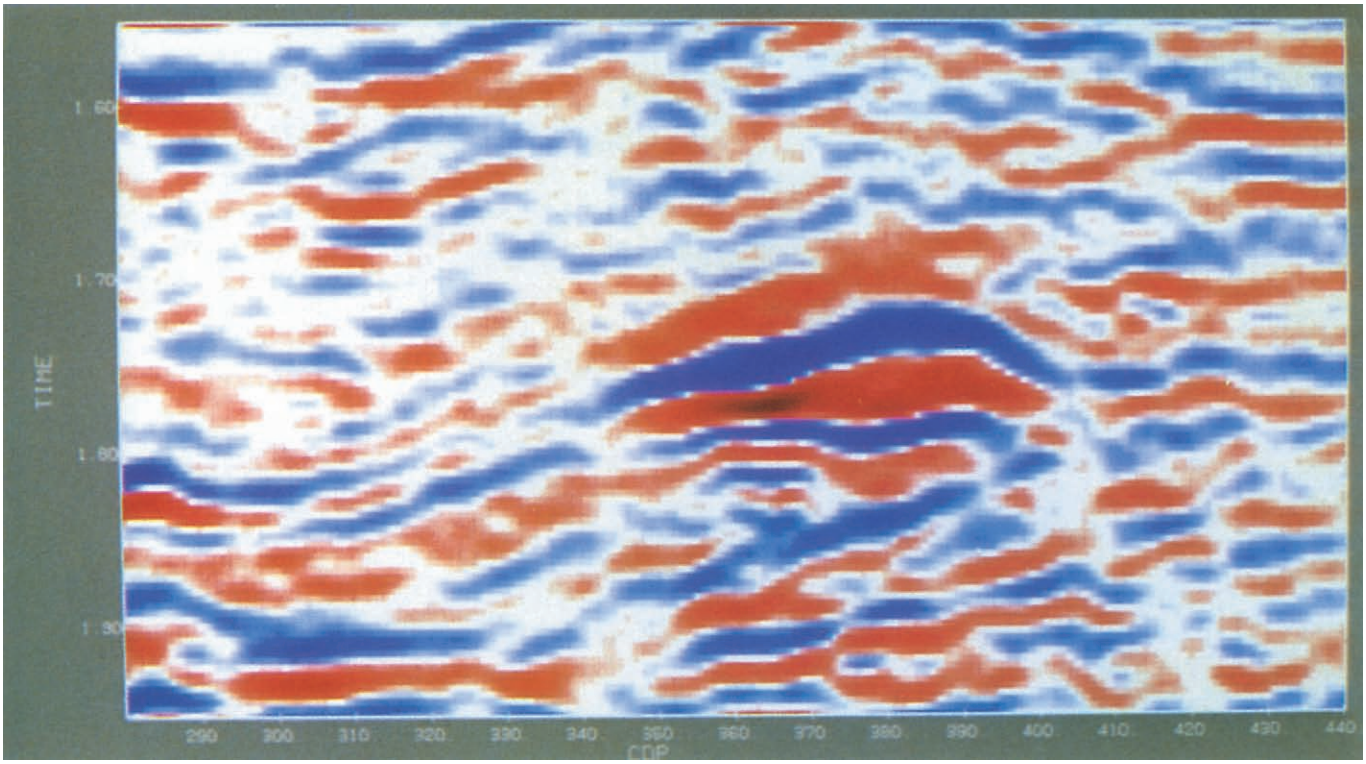

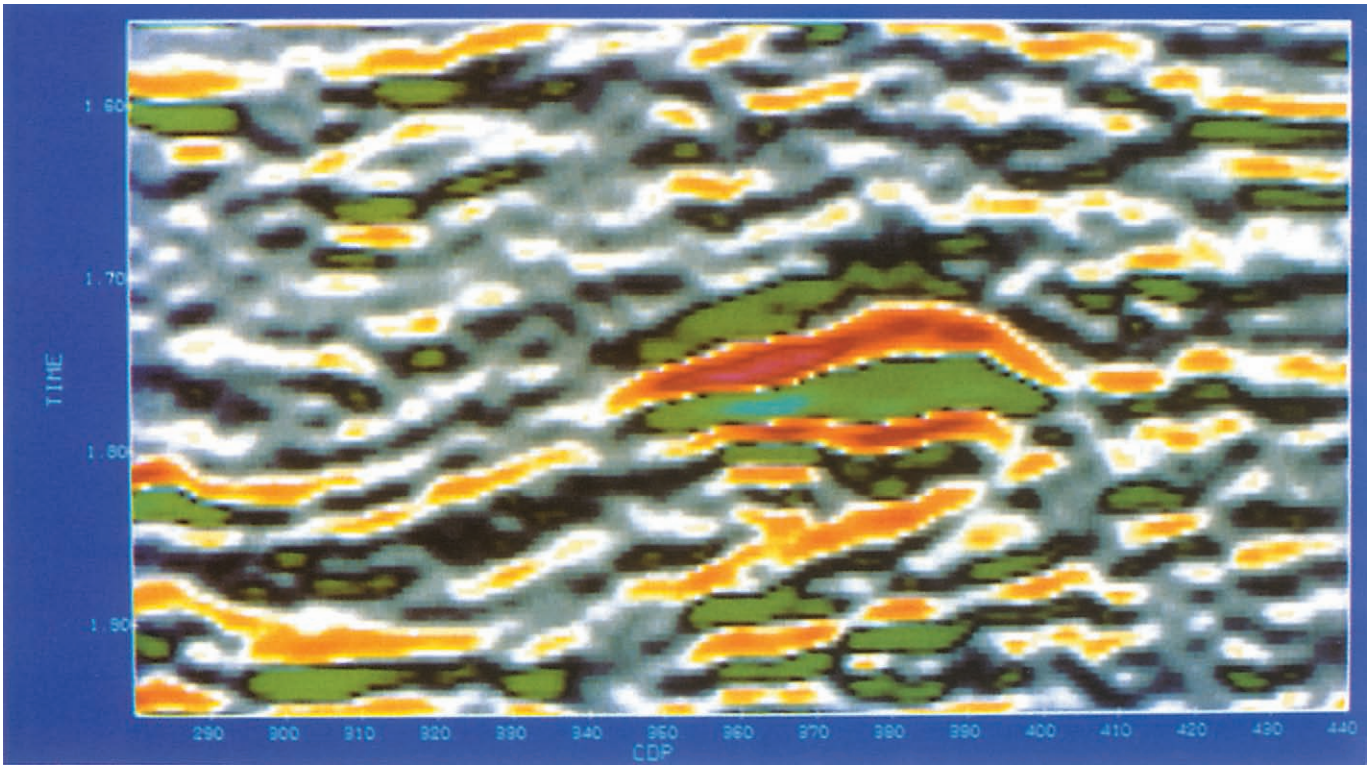

Fig. 5-27. (Top) Same bright spot and color scheme as Figure 5-25 but with the gain increased to study the continuity of reflections off the flank of the bright spot. Blue correlates with red and vice versa downdip indicating a phase change or polarity reversal at the edge of the bright spot. (Courtesy Chevron U.S.A. Inc.)

Fig. 5-28. (Bottom) Same bright spot as Figure 5-25, same color scheme as Figure 5-26 and same gain as Figure 5-27. The correlation of reflections downdip from the bright spot again indicates a phase change at the edge of the reservoir. (Courtesy Chevron U.S.A. Inc.)

Downloaded 25 Jun 2012 to 129.110.5.90. Redistribution subject to SEG license or copyright; Terms of Use: http://segdl.org/

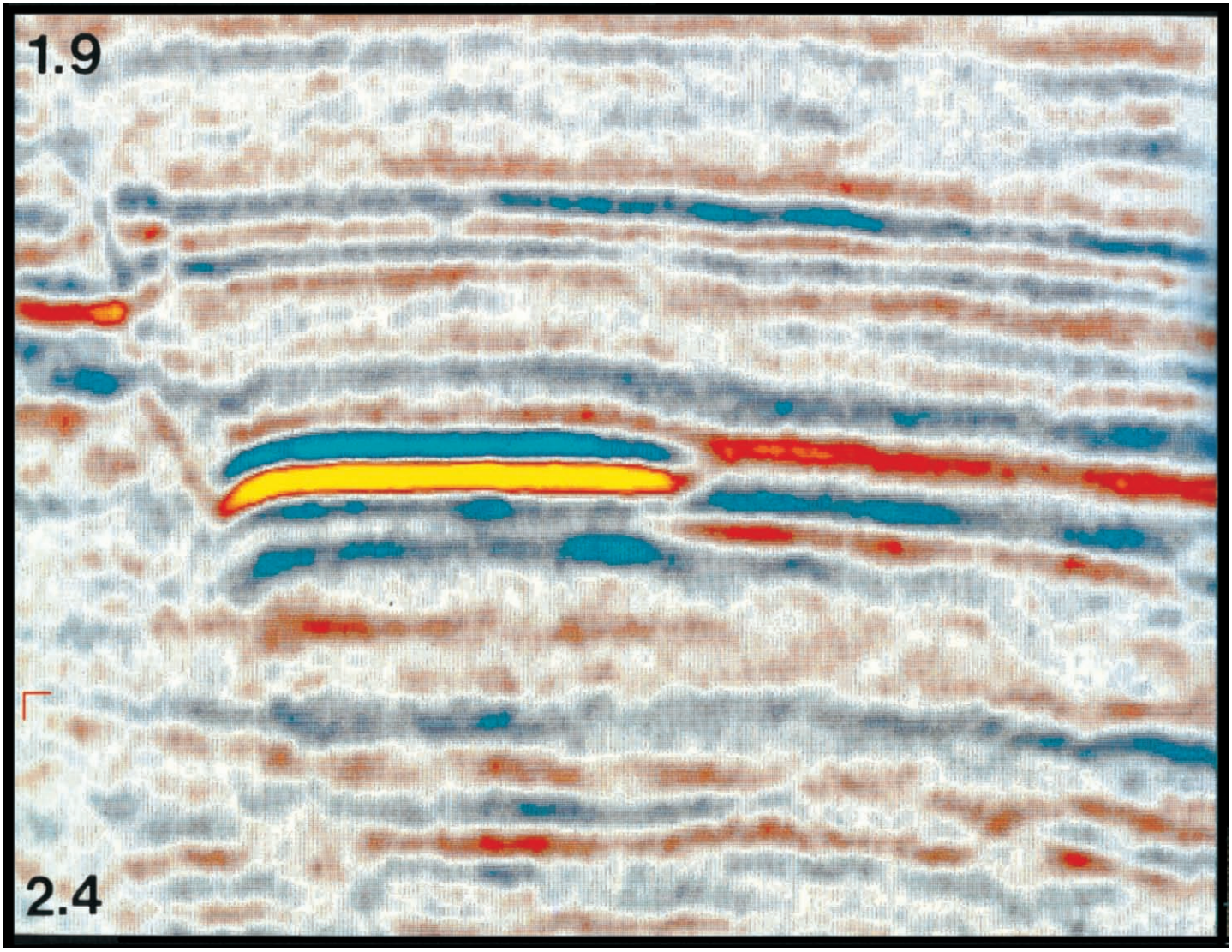

Fig. 5-29. Phase change (polarity reversal) caused by gas in unconsolidated sandstone of the Gulf of Mexico. Data are zero-phase European polarity.(Courtesy Conoco Inc.)

equivalents downdip. There is a very great difference in amplitude between these, causing a great difference in color intensity. Figures 5-27 and 5-28 use the same colors respectively as Figures 5-25 and 5-26 but with a higher gain applied to the data. This makes it easier to judge the downdip continuity on the left of the bright spot and hence to observe that red correlates with blue (Figure 5-27) and green correlates with yellow (Figure 5-28). In this way a polarity reversal is established.

Figures 5-29 and 5-30 show striking phase changes (polarity reversals) respectively in the Gulf of Mexico and on the Northwest Shelf of Australia. The two data sets are opposite polarity from each other. Figure 5-29 shows the gas, which is low impedance, as blue-over-red; this indicates European polarity. Figure 5-30 shows the gas as red-over-blue, which is American polarity. Figure 5-29 shows the gas contained by a fault on the west and the phase change on the east. Figure 5-30 shows the gas contained by a fault on the east and the phase change on the west. Some interpreters may feel inclined to identify both these phase changes as faults antithetic to the main faults. However, with experience the phase change explanation emerges as preferable. Structural/stratigraphic conflicts like this one are common and interpreters need to overcome their bias towards the structural solution.

Figure 5-31 shows the very unusual observation of a polarity reversal on the sea floor. With American polarity data, the blue reflection (with flanking red side lobes)

Downloaded 25 Jun 2012 to 129.110.5.90. Redistribution subject to SEG license or copyright; Terms of Use: http://segdl.org/

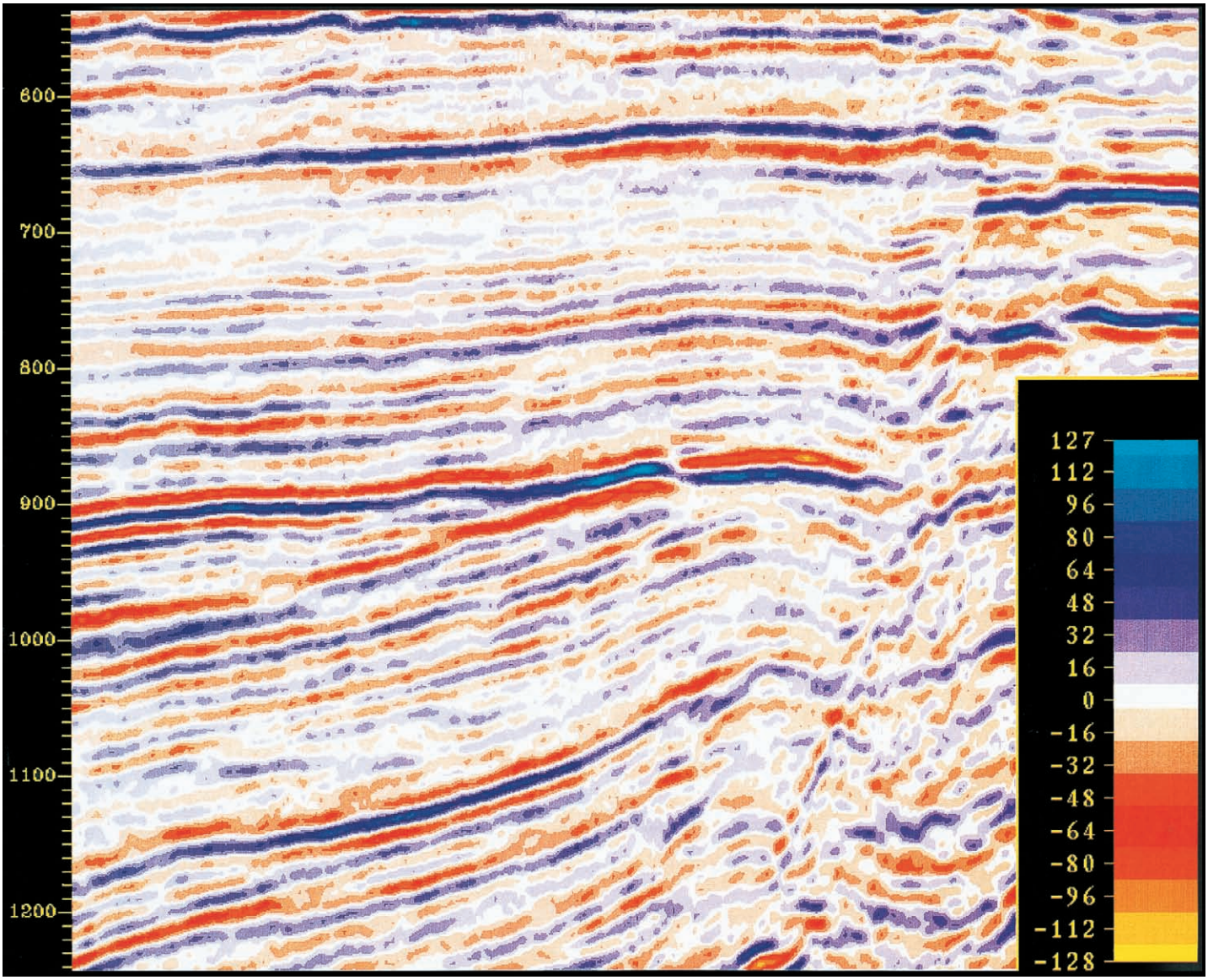

Fig. 5-30. Phase change (polarity reversal) caused by gas on the Northwest Shelf of Australia. Data are zero-phase American polarity. (Courtesy West Australian Petroleum Pty. Ltd.)

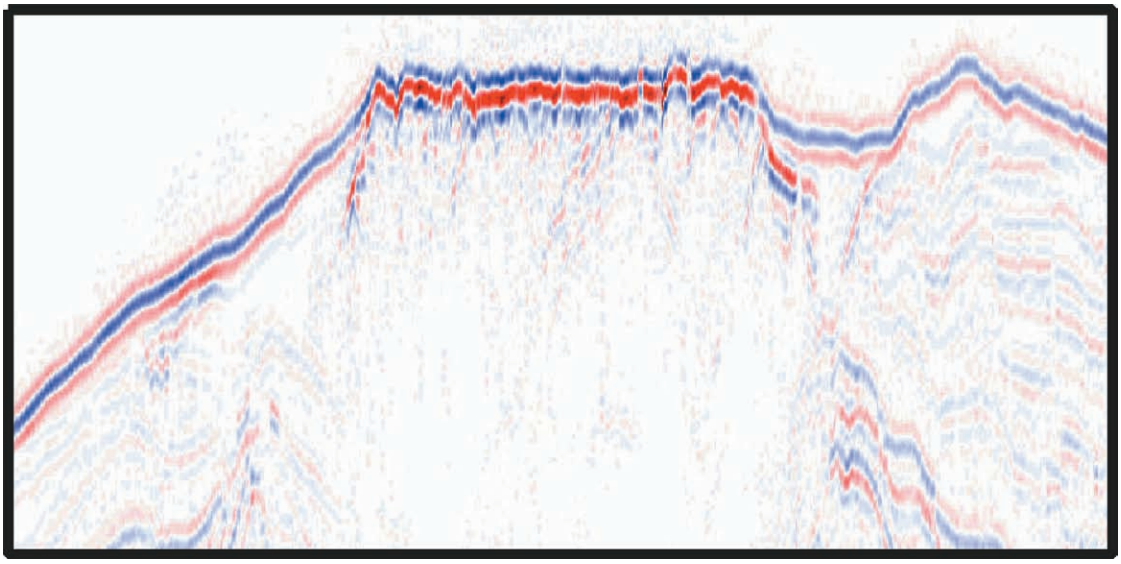

Fig. 5-31. Phase change (polarity reversal) on sea floor of Caspian Sea caused by gas-charged mud volcano. (Courtesy Azeri International Operating Co. and Fugro-Geoteam Limited.)

Downloaded 25 Jun 2012 to 129.110.5.90. Redistribution subject to SEG license or copyright; Terms of Use: http://segdl.org/

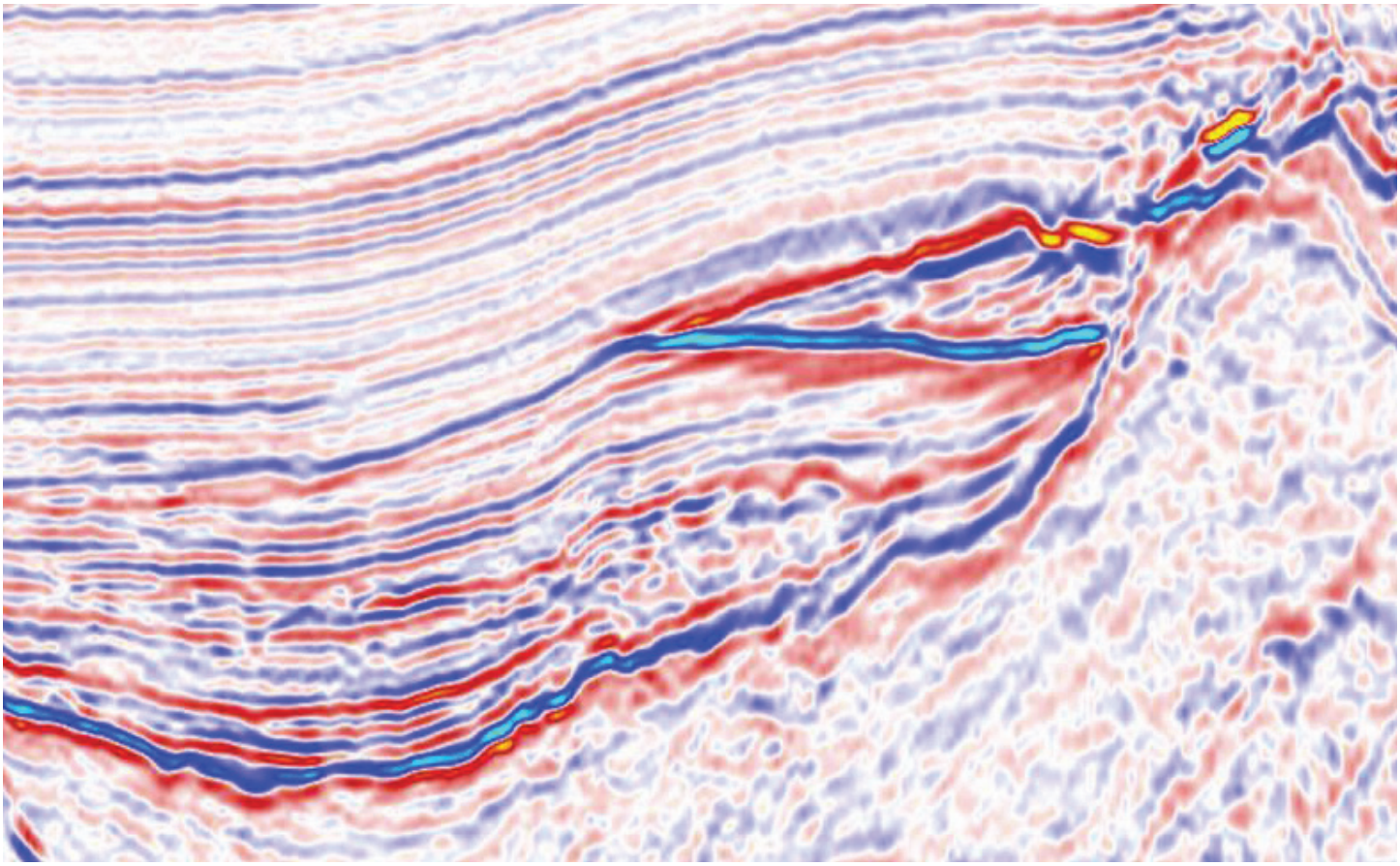

Fig. 5-32. Polarity reversal and flat spot from gas trapped against a high formed of mobile shale, offshore Sabah, Malaysia. (Courtesy Murphy Sabah Oil Co. Ltd.)

indicates a hard water bottom or an impedance increase. The water bottom over the mud volcano is red, which indicates an impedance decrease. The only reasonable explanation is that this impedance decrease is caused by a strong velocity decrease and a small density increase.

Hydrocarbon polarity reversals normally are difficult to interpret because geologic continuity has to be postulated from a blue reflection to a red reflection or vice versa. It is the natural inclination of seismic interpreters to stay on the same reflection as originally identified. Figure 5-32 shows a large gas accumulation trapped against mobile shale offshore Sabah. The bright spot amplitude on the top gas reflection is clear. The fluid contact reflection, or flat spot, is clear. The data are clearly American polarity. But is there a polarity reversal between top gas sand and top water sand reflections? At first both interpretations seem to have merit. The unequivocal factor influencing the interpretive decision is that the fluid contact reflection is the highest amplitude locally. This proves that there is a polarity reversal here (Figure 5-5).

Figure 5-33 shows a horizon slice indicating a channel. To the northeast the channel is bright, to the southwest it is not. The structural contours for this horizon have been superimposed and they demonstrate that the bright part of the channel is structurally above the dim part. This combination of structural and stratigraphic information helps validate gas content. Figure 5-34 is another way of graphically illustrating the same relationship; the representation of the channel in amplitude is superimposed on the structural configuration of the horizon surface.

The fit of amplitude to structure is a valuable hydrocarbon diagnostic. This is normally studied by displaying amplitude spatially and overlaying the structural contours. Both Figures 5-35 and 5-36 show some fit of amplitude to structure in this way. However, it should be remembered that this is just one of several important hydrocarbon diagnostics; it is not essential. Luchford (2001) discusses the subject in detail and presents three examples.

Downloaded 25 Jun 2012 to 129.110.5.90. Redistribution subject to SEG license or copyright; Terms of Use: http://segdl.org/

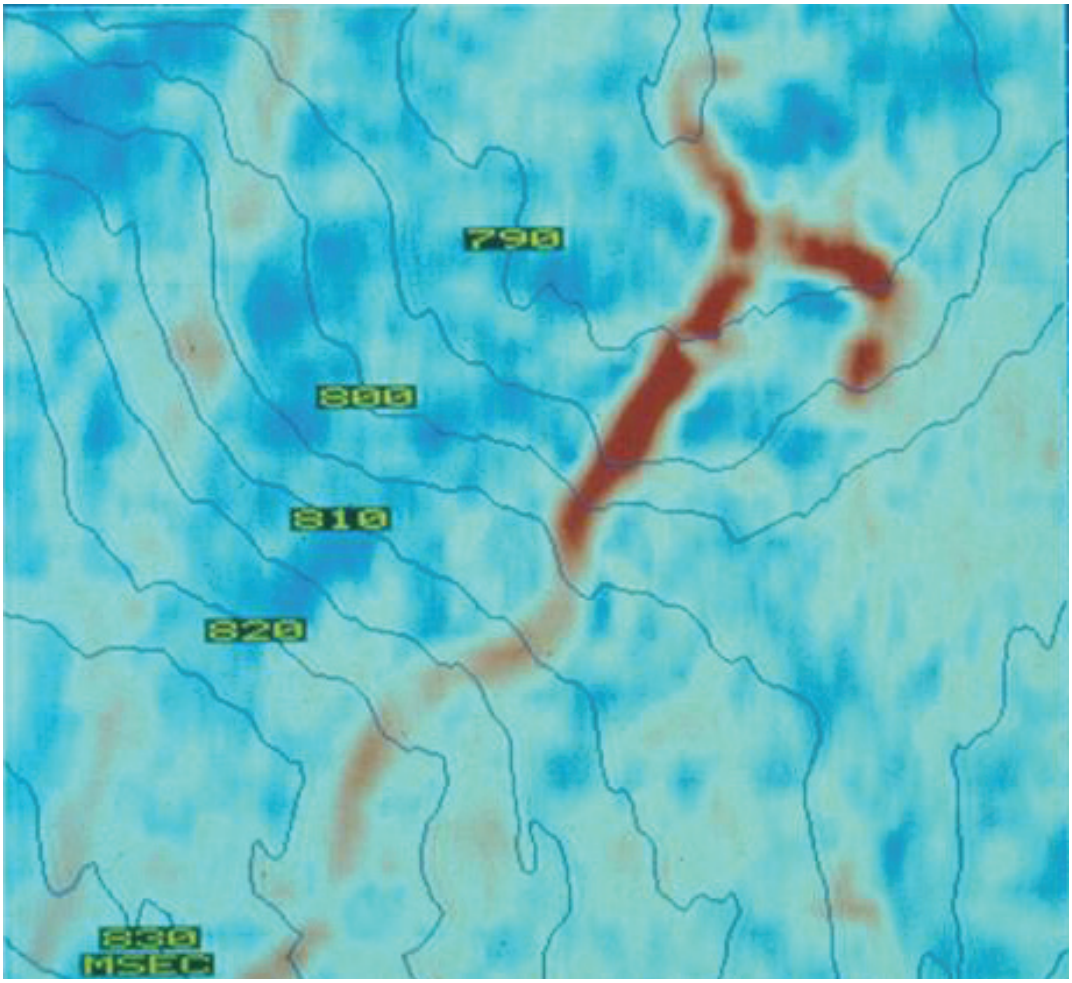

Fig. 5-33. Horizon slice showing the Gulf of Mexico channel discussed in Chapter 4. The superimposed contours show that the high amplitude in the channel is structurally above the lower amplitude in the channel. (Courtesy Chevron U.S.A. Inc.)

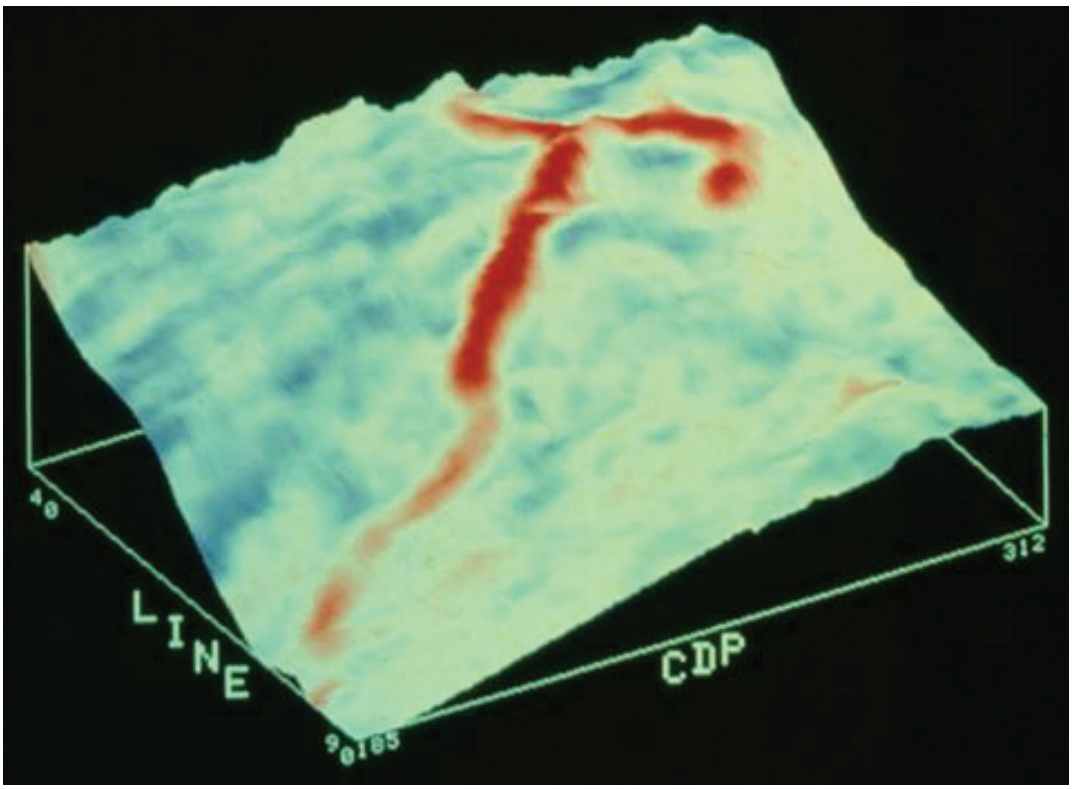

Fig. 5-34. Combination of the same horizon amplitude and structural information as Figure 5-31 using different colors and a three-dimensional perspective surface. (Courtesy Chevron U.S.A. Inc.)

Downloaded 25 Jun 2012 to 129.110.5.90. Redistribution subject to SEG license or copyright; Terms of Use: http://segdl.org/

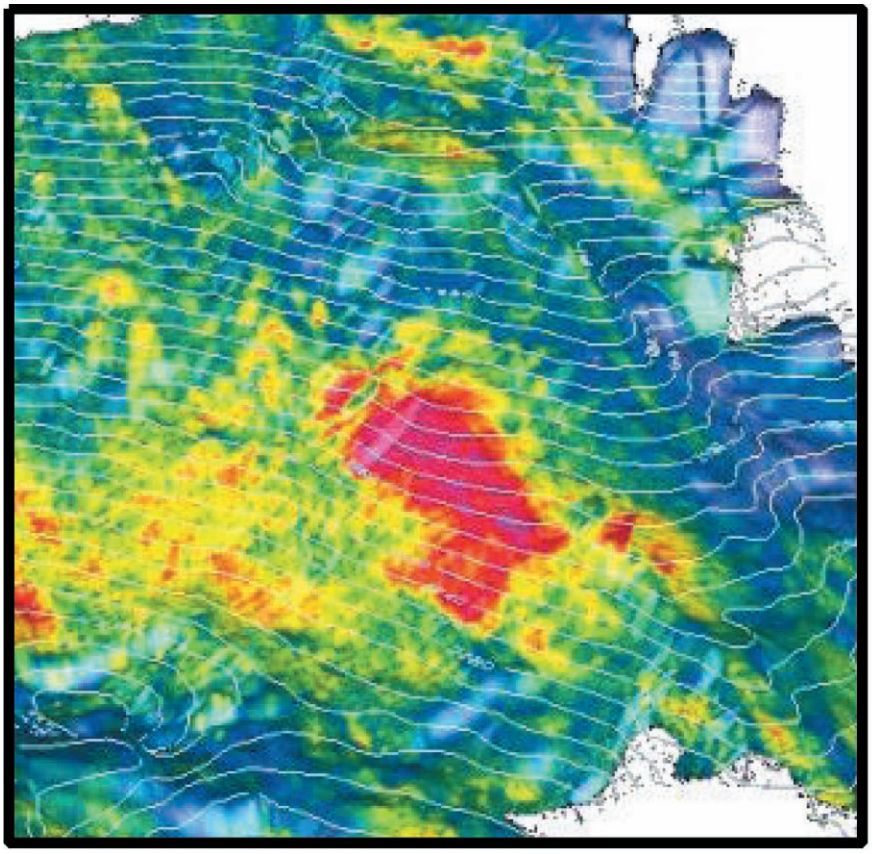

Fig. 5-35. Amplitude with superimposed structural contours from Mexico. The downdip edge of the high amplitude fits structure. (Courtesy Pemex.)

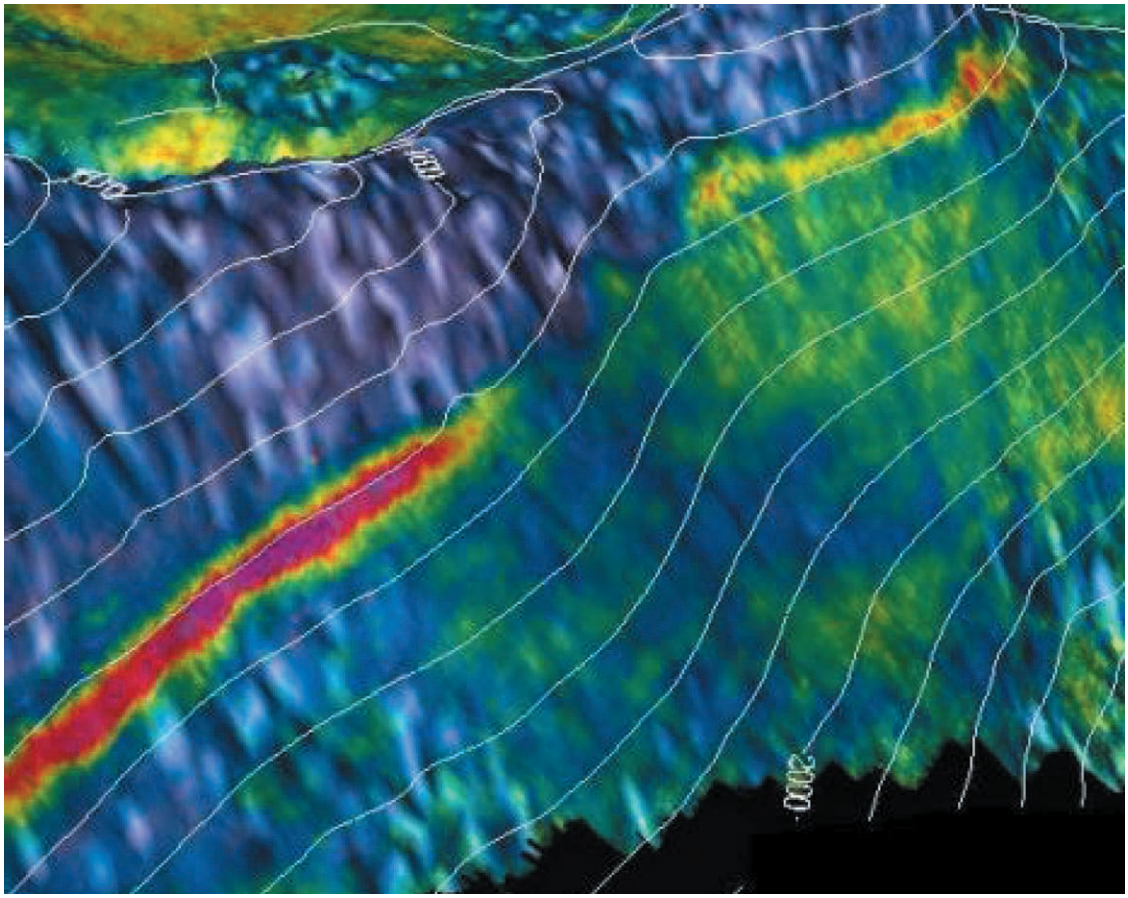

Fig. 5-36. Amplitude with superimposed structural contours from Mexico. The updip edge of the amplitude is a pinch out. The downdip edge is a fluid contact. (Courtesy Pemex.)

Downloaded 25 Jun 2012 to 129.110.5.90. Redistribution subject to SEG license or copyright; Terms of Use: http://segdl.org/

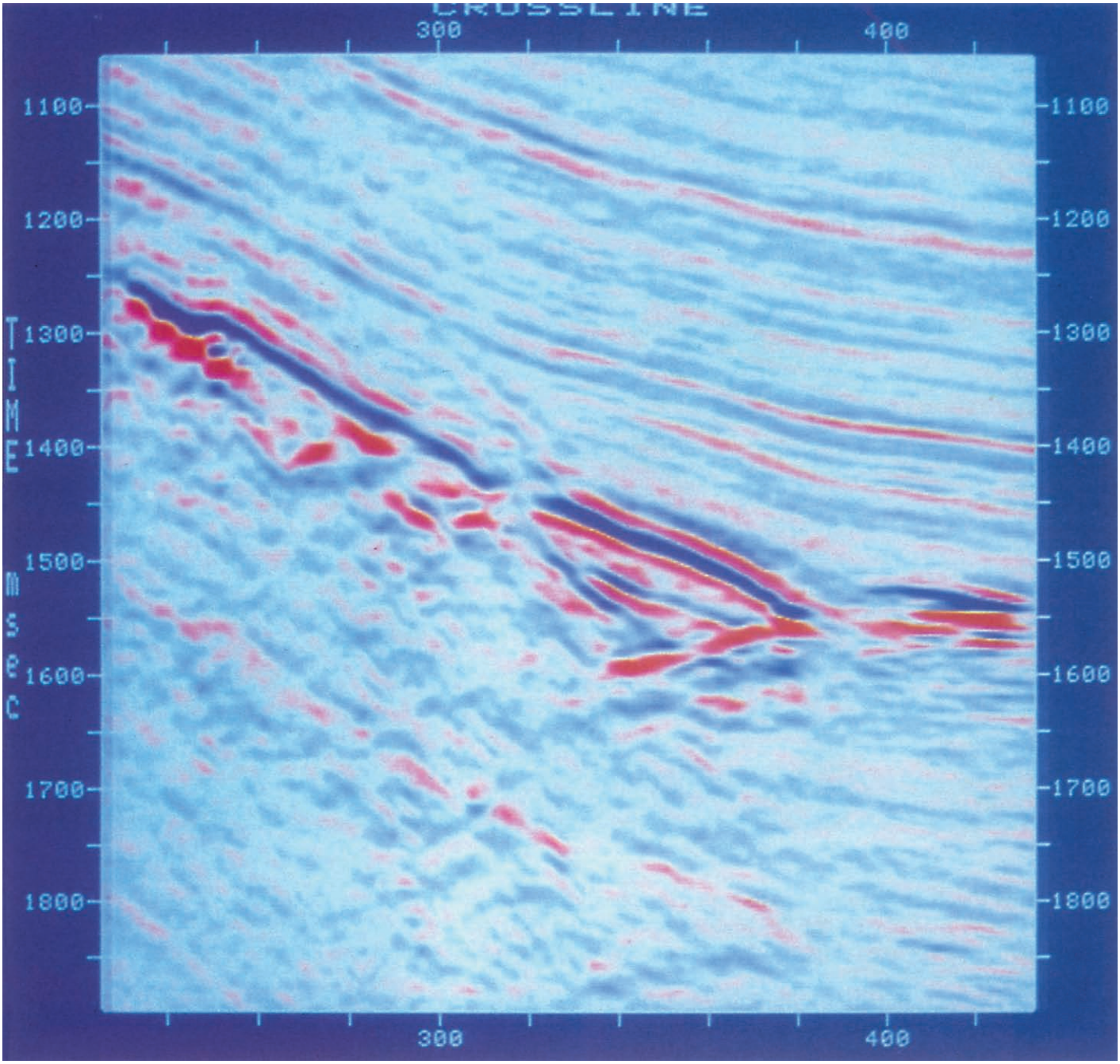

Figure 5-37 demonstrates gas velocity sag on a flat spot reflection. The trough (red event) dipping west between 1560 and 1600 ms should presumably be flat in depth but is depressed in time by the increased travel through the low velocity, wedge-shaped gas sand. Flat spot dip caused in this way will always be in the opposite direction to structural dip. This section also demonstrates another phenomenon: there are bright events *within* the reservoir which have little expression outside. This illumination of internal layering is fairly common in clastic reservoirs and is discussed further in Chapter 7.

Fig. 5-37. Bright spot from a rather thick and complex gas sand. The red event dipping right-to-left is a flat spot displaying gas velocity sag. (Courtesy Chevron U.S.A. Inc.)

Polarity and Phase Problems, Multiple Contacts and Transmission Effects

The character of paired high-amplitude reflections, red-over-blue or blue-over-red, is an important hydrocarbon diagnostic once the polarity of the data is known. This chapter has already presented examples of bright spots in both American and European polarity. Note the upper amplitude anomaly in Figure 5-38. The pairing is excellent, red-over-blue is the hydrocarbon bright spot character for American polarity, the

Downloaded 25 Jun 2012 to 129.110.3.90. Redistribution subject to SEG license or copyright; Terms of Use: http://segdl.org/

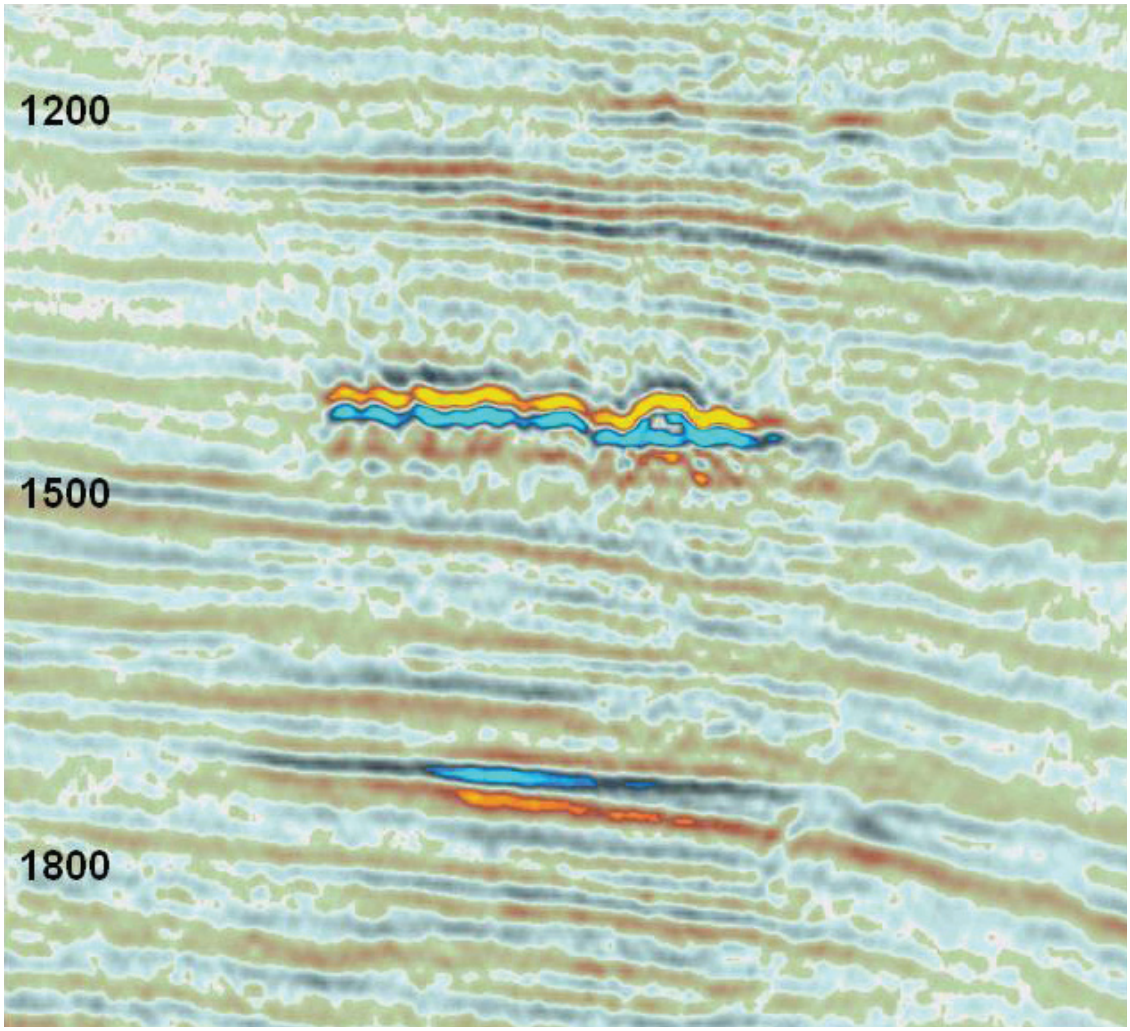

Fig. 5-38. Excellent bright spot prospect offshore Mexico. This is one prospect not two. Note pairing of upper anomaly is red-over-blue (soft) and pairing of the deeper one is blue-over-red (hard). (Courtesy Pemex.)

terminations are crisp, the amplitude is very high. Thus we can be very confident that there are hydrocabons here. Note the lower anomaly. It has high amplitude indeed but the character is blue-over-red. This indicates that it is a hard bed and consequently is unprospective. In Figure 5-39 two high-amplitude blue reflections were tracked and the amplitude extracted to produce two horizon slices. Both high-amplitude patches were drilled, but one well was successful and the other dry. These data are American polarity, so red-over-blue indicates a low-impedance layer and blue-over-red indicates a high-impedance layer. A hydrocarbon bright spot can only be caused by low impedance.

The majority of the discussion of the detailed character of hydrocarbon reflections so far in this chapter has been of zero-phase character. Unfortunately data phase is not always what it is supposed to be. Data processed to zero phase fairly often is close to 90˚ phase. Figure 2-25 shows a 90˚ phase flat spot and associated bright spot. It is the red and blue reflections together forming the flat spot that best demonstrates the 90˚-phaseness of these data. Figure 2-28 shows the 90˚ phase response of a thin gas reservoir. The three events for the two interfaces (top and base reservoir) indicate the 90˚-phaseness as discussed in Chapter 2.

Figure 5-40 shows a flat spot with 90˚ phase character, yellow-over-red, at the green arrow. This is further confused, e.g. by comparison with Figure 2-25, by the fact that here the flat spot appears to be broken into four pieces. This is in fact caused by interference of strong internal reflections with the fluid contact reflection.

When we observe what appears to be two flat spots (e.g. Figures 2-25 and 5-40) the question arises as to whether we could be seeing two fluid contact reflections, for example gas-oil and oil-water. In fact a fluid contact is always an increase in acoustic

Downloaded 25 Jun 2022 to 129.110.5.90. Redistribution subject to SEG license or copyright; Terms of Use: http://segdl.org/

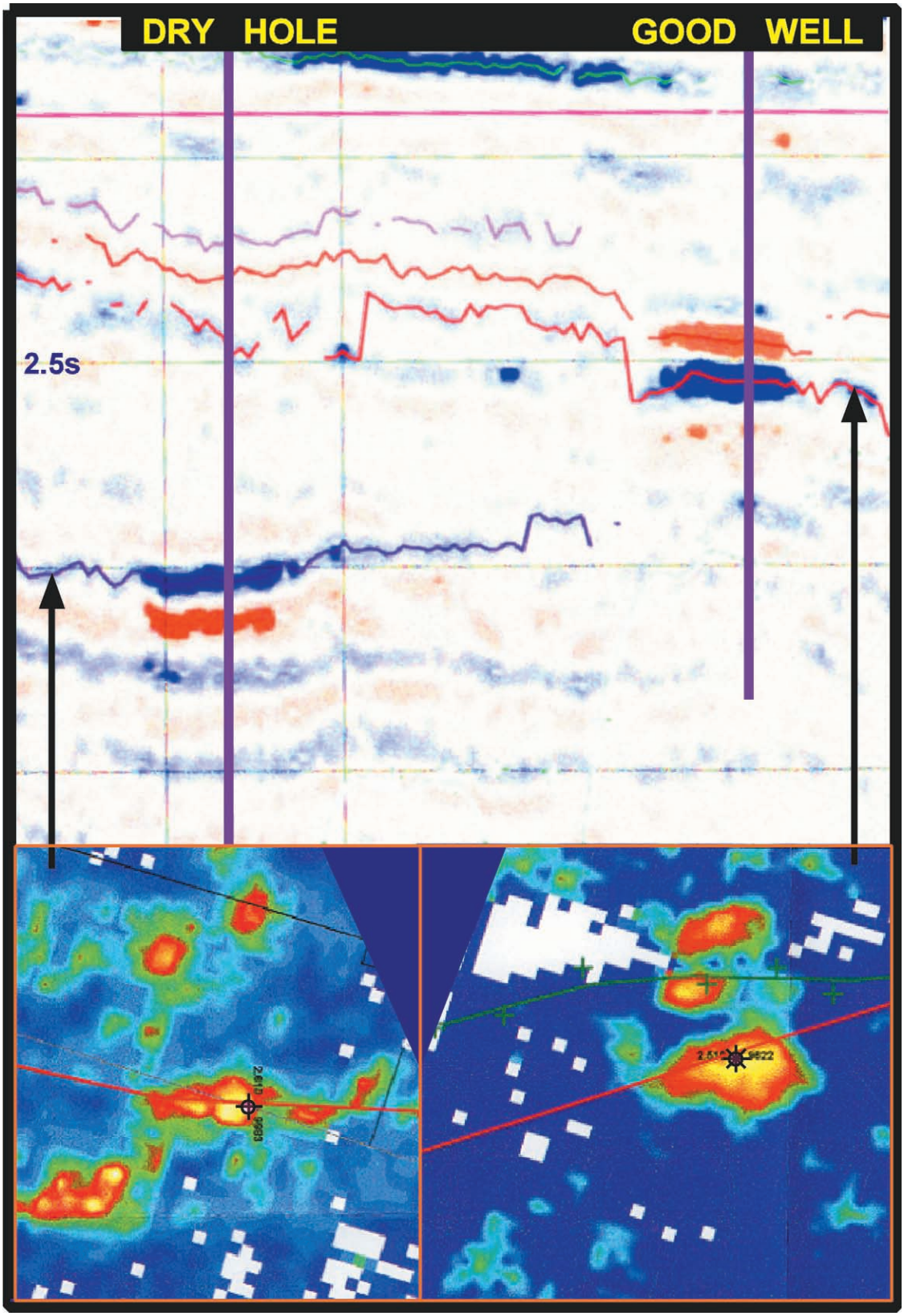

Fig. 5-39. Two horizon slices showing high-amplitude patches that were drilled. The arrows indicate the horizon tracks used. Both high amplitudes are blue on the vertical section but the natural pairing of top and base reflections is different. (Courtesy EnRe Corporation and Robert W. Buehler.)

Downloaded 25 Jun 2012 to 129.110.5.90. Redistribution subject to SEG license or copyright; Terms of Use: http://segdl.org/

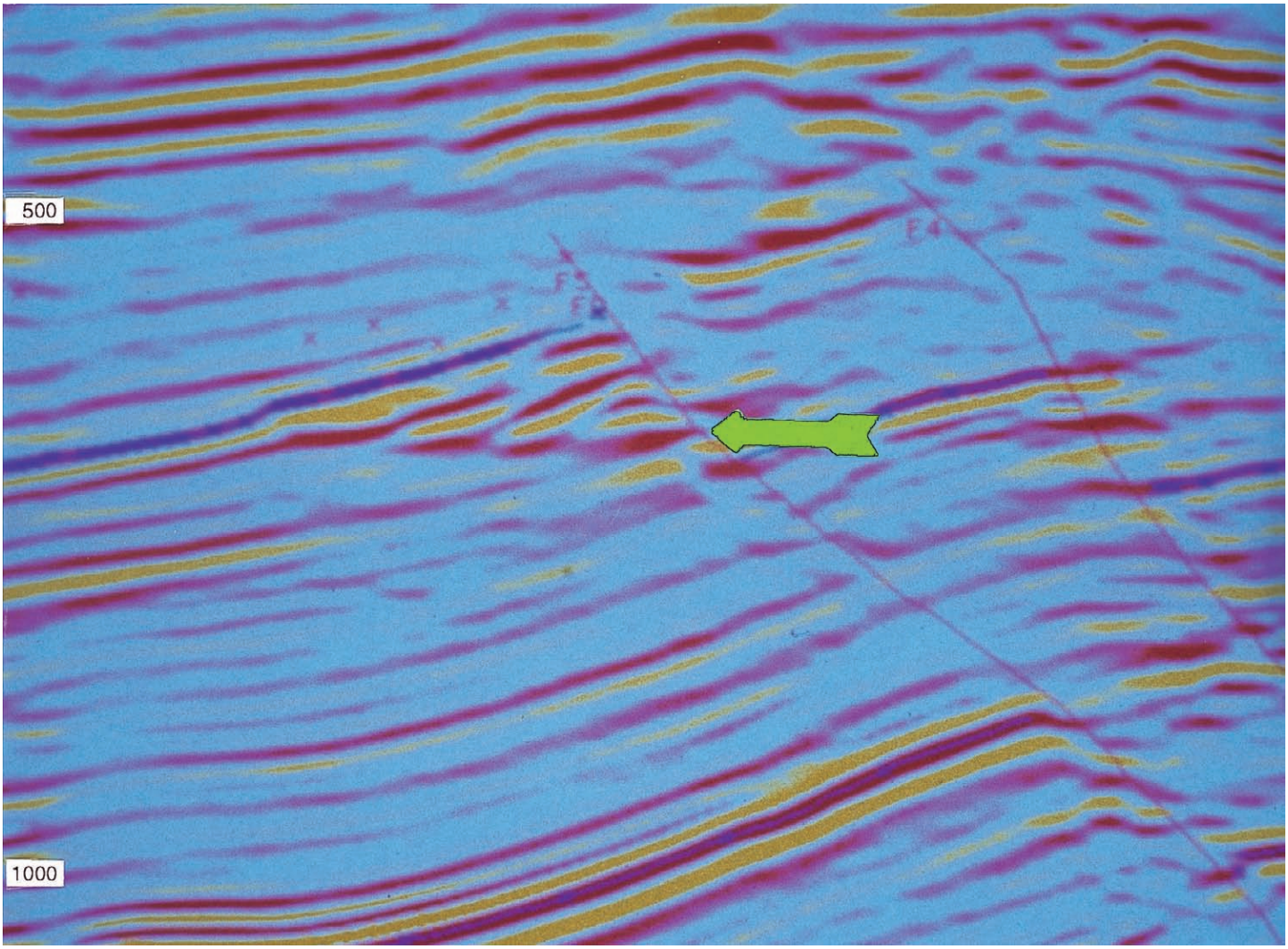

Fig. 5-40. Flat spot and bright spot visible in 90° phase data from offshore China. (Courtesy Bureau of Geophysical Prospecting, People's Republic of China.)

impedance and thus two contacts in the same reservoir will always have the same character; so one red contact and one blue contact is impossible.

Figure 5-41 shows two flat spots at the green arrows indicating two contacts in an Indonesian gas reservoir. They are both red. In fact the upper contact is at the base of producible gas and the lower contact is at the base of trapped gas, perhaps a paleo gas-water contact.

Figures 5-42 and 5-43 each show two flat spots from two separate contacts. The upper one is a gas-oil contact and the lower one an oil-water contact. Note that both fluid contact reflections are blue, as they should be for American polarity zero-phase data. Note the strong structurally dipping reflection separating the upper and lower reservoirs. They have a common oil-water contact, and the gas-oil contact is only in the upper reservoir. The somewhat high amplitude on the top reservoir reflection between the two flat spots demonstrates a bright response of oil. The difference in amplitude of the oil and the gas is clear with the higher dynamic range color scheme of Figure 5-43. Clark (1992) and Greenlee, Gaskins, and Johnson (1994) have both demonstrated bright spots caused by oil.

Figure 5-44 demonstrates a hydrocarbon transmission effect. The amplitude of the upper reservoir is very strong. This means that a large fraction of the incident energy is reflected, leaving little energy to be transmitted. This effect causes a marked reduction in amplitude for the lower reservoir. The coincidence of the high amplitude at the upper reservoir with lower amplitude at the lower reservoir is confirmed spatially with the two horizon slices of Figures 5-45 and 5-46.

Downloaded 25 Jun 2012 to 129.110.5.90. Redistribution subject to SEG license or copyright; Terms of Use: http://segdl.org/

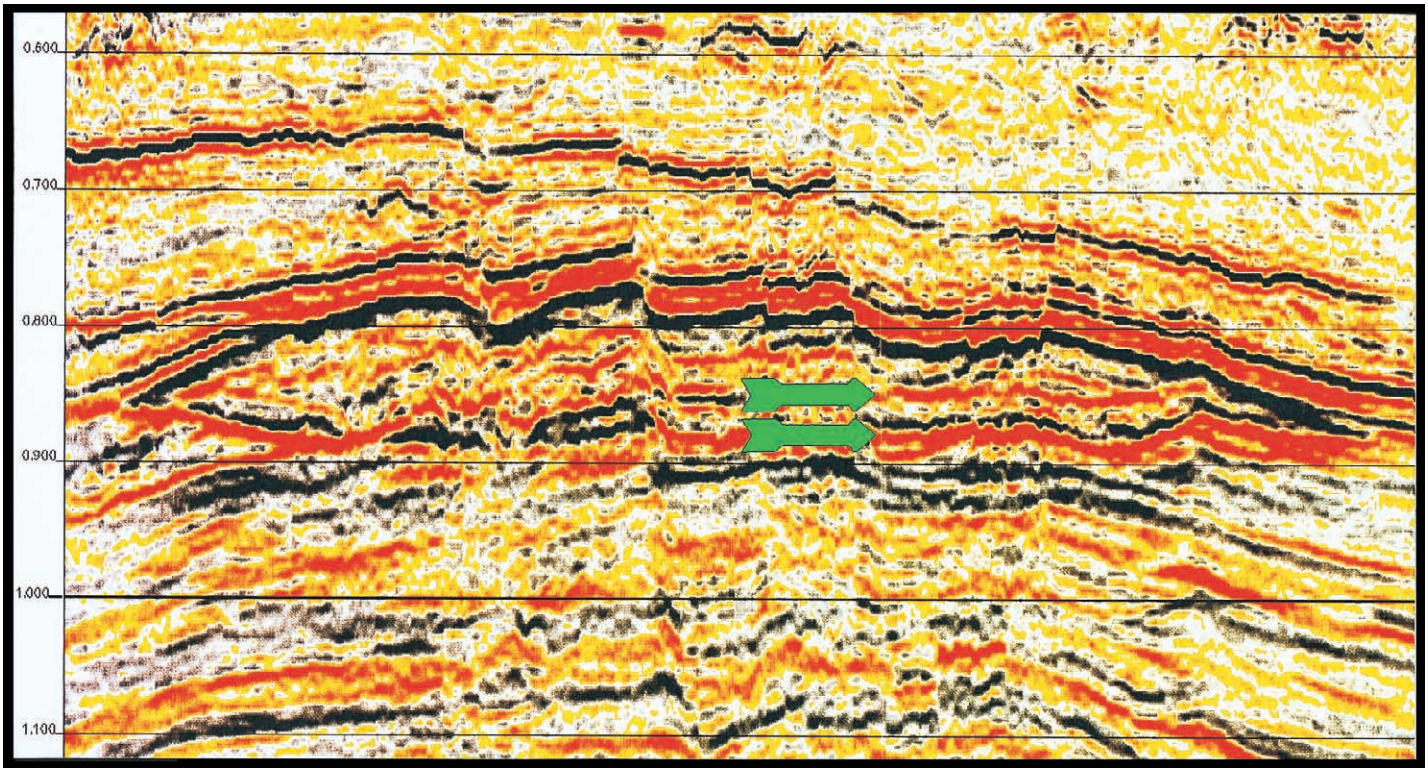

Fig. 5-41. Two flat spots in same gas reservoir offshore Indonesia indicating contact at the base of producible gas and at the base of trapped gas. (Courtesy Atlantic Richfield Bali North Inc.)

Use of Frequency, Amplitude Variations With Offset and Shear Waves

Gas reservoirs attenuate high frequencies more than do rocks without gas saturation. Following this principle, Taner, Koehler, and Sheriff (1979) have shown that low instantaneous frequency immediately below a suspected reservoir can be a good indicator of gas. The author has found this to be a rather unreliable indicator; several gas reservoirs studied with good data have yielded ambiguous results in instantaneous frequency. However, a good example where low instantaneous frequency anomalies indicate gas is shown in Figure 5-47. This lowering of frequency can often be observed as a simple broadening of the gas reservoir reflections. This is well illustrated in Figures 5-16 and 5-54.

Interval velocity is reduced if a low-velocity gas sand is included in the interval studied. For many years RMS velocities derived from normal moveout have been used to compute interval velocities, and for gross effects and trends this is valuable. However, the stability of interval velocities gets progressively worse for greater depths and also for thinner beds. This generally means that interval velocities are not sufficiently accurate to play a useful role in bright spot validation.

The variation of amplitude with recording offset has become a popular subject because of the possibility of extracting a significant amount of lithologic information from this kind of data. However, there are many difficulties both of a theoretical and practical nature (Backus and Goins, 1984). Among the practical issues, the data are prestack and hence have a lower signal-to-noise ratio, and, being multidimensional, there are many possible modes of display.

Ostrander (1984) demonstrated that in many practical cases gas sands show an increase of amplitude with offset and that this can be used as a means of identifying gas reservoirs. He studied the data in the form of common-depth-point gathers, normally

Downloaded 25 Jun 2012 to 129.110.5.90. Redistribution subject to SEG license or copyright; Terms of Use: http://segdl.org/

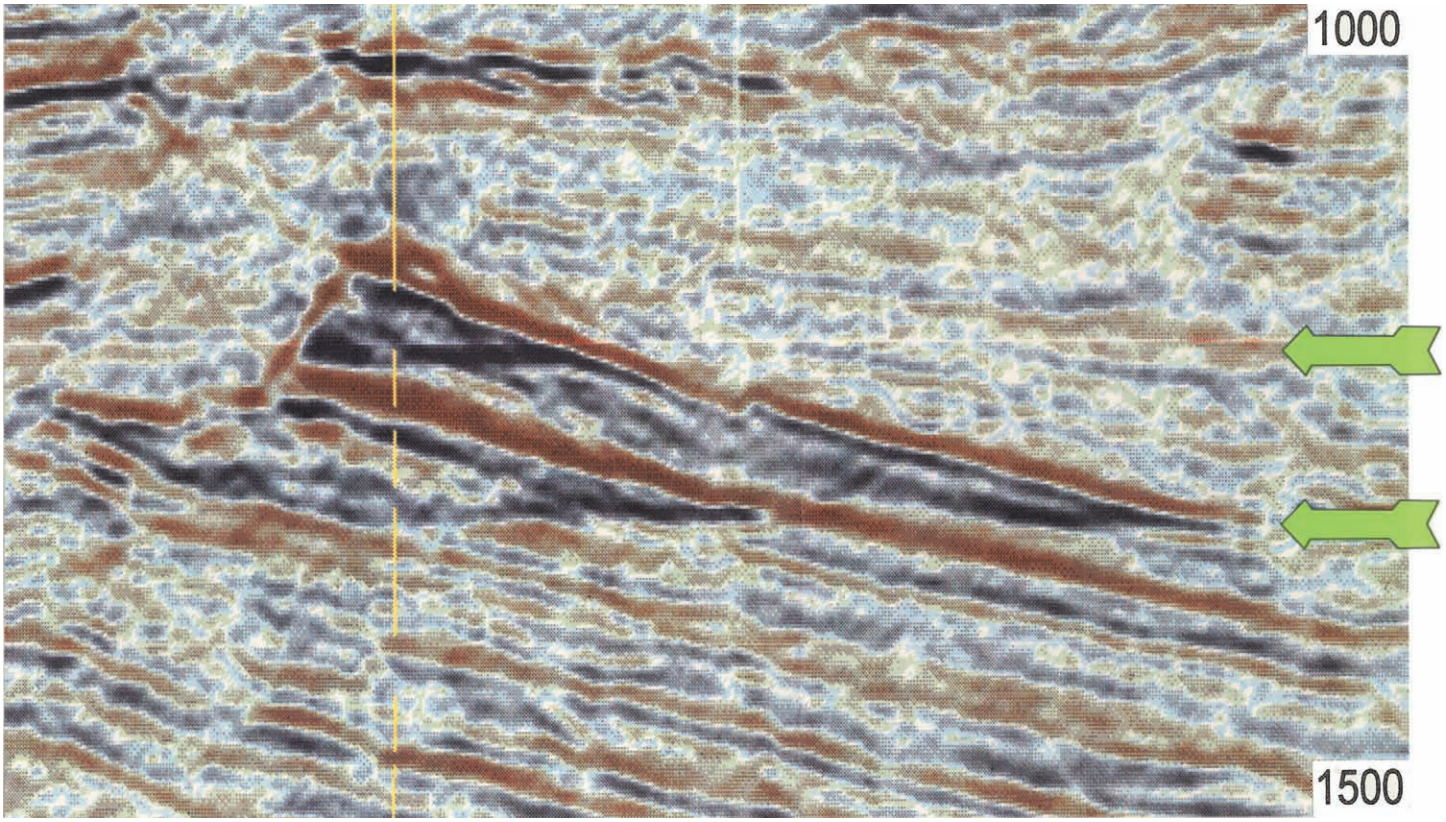

Fig. 5-42. Vertical section from offshore Nigeria showing flat spots from the gas-oil contact and the oil-water contact in the same reservoir. Note the significant bright spot from the oil. The flat spot from the oil-water contact is more than 2km long. (Courtesy Mobil Producing Nigeria Ltd.)

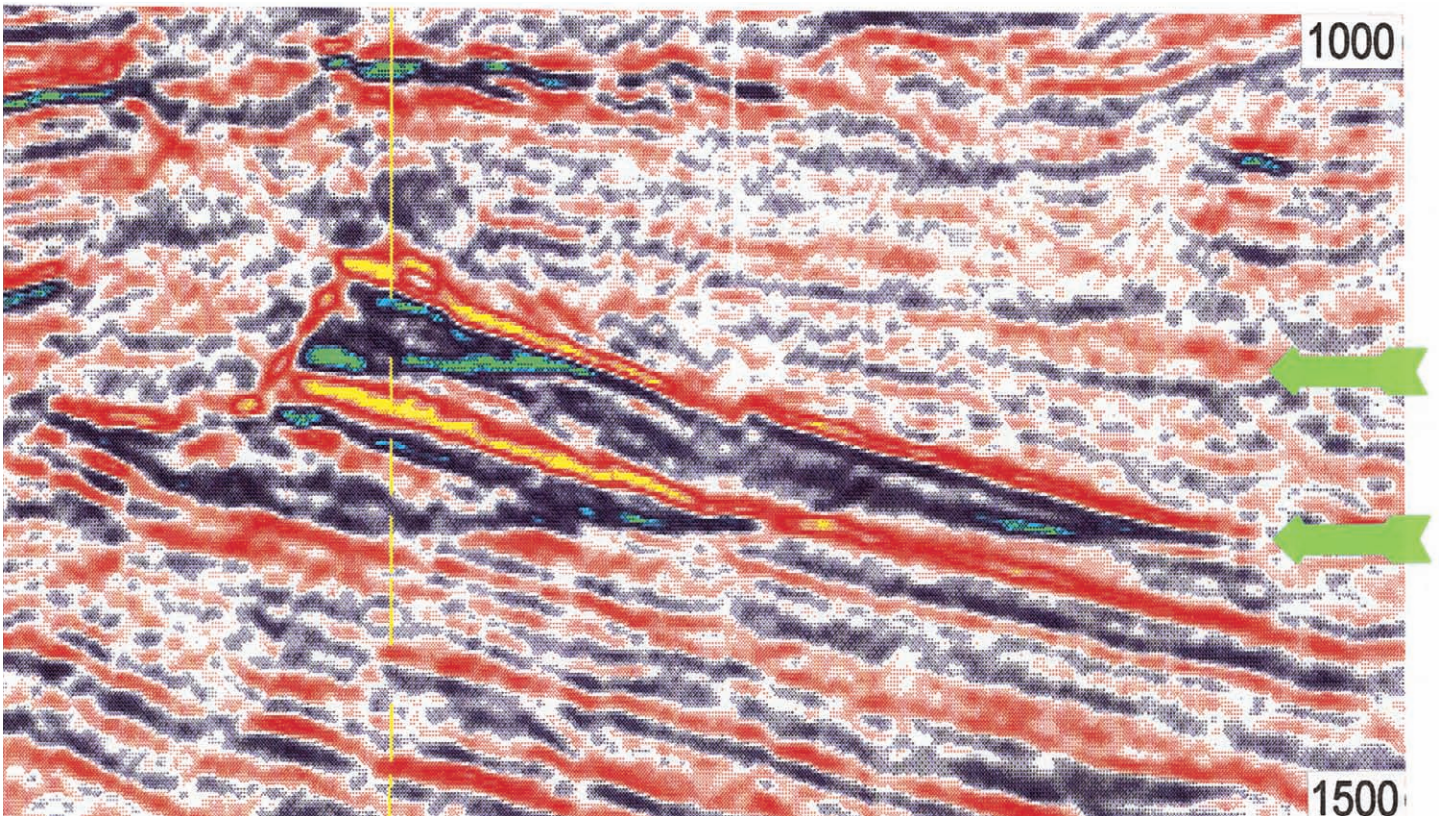

Fig. 5-43. Same section as Figure 5-42 but with higher dynamic range color scheme which more clearly distinguishes the amplitudes from the gas and from the oil. (Courtesy Mobil Producing Nigeria Ltd.)

Downloaded 25 Jun 2012 to 129.110.5.90. Redistribution subject to SEG license or copyright; Terms of Use: http://segdl.org/

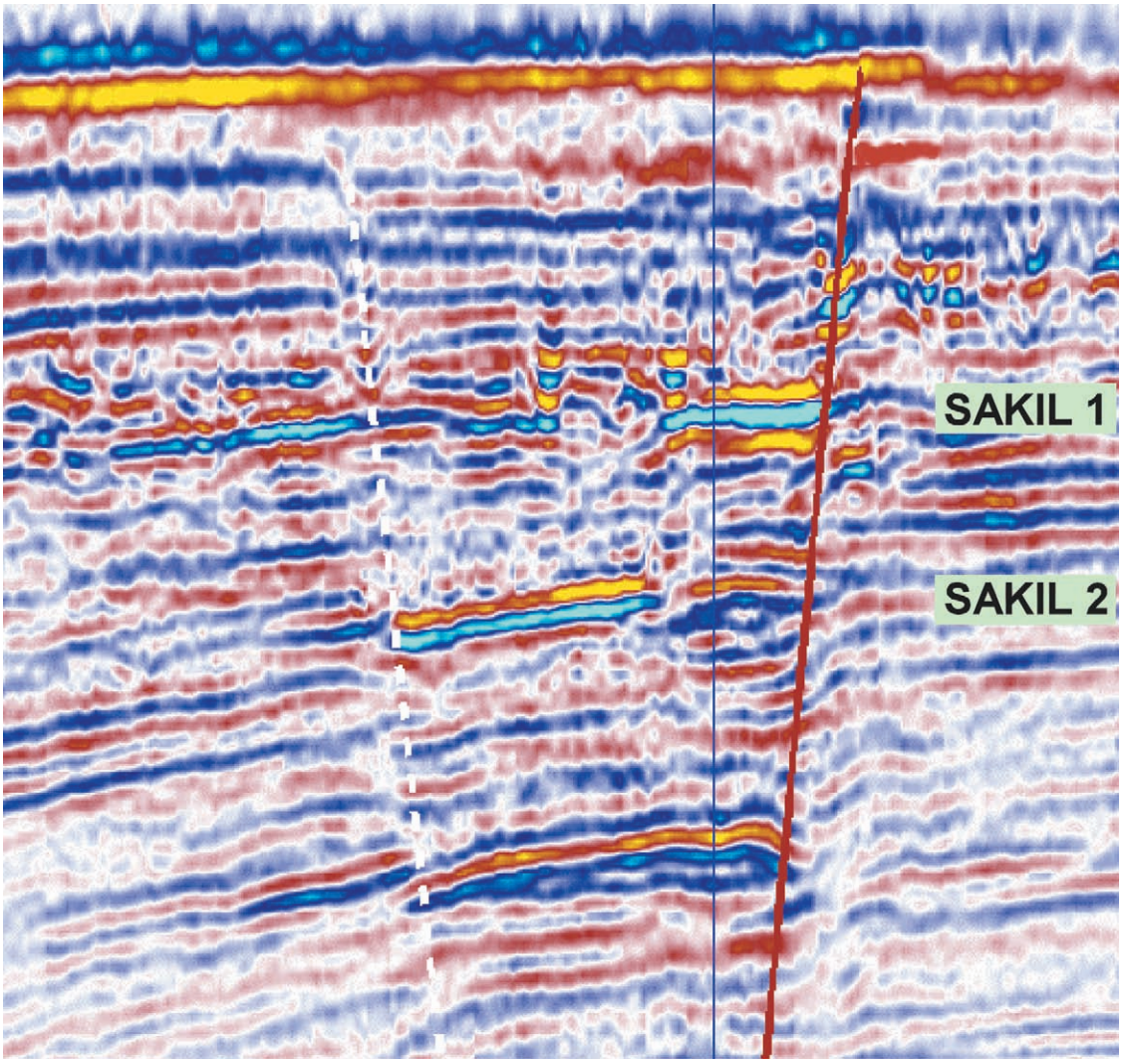

Fig. 5-44. Section from offshore Mexico demonstrating transmission effect. Because Sakil 1 gas reservoir has very high amplitude, little energy is transmitted, and Sakil 2 gas reservoir shows consequentially reduced amplitude. (Courtesy Pemex.)

Fig. 5-45. (Below) Horizon slice Sakil 1. The white lines are manually drawn around the high-amplitude areas. (Courtesy Pemex.)

Fig. 5-46. (Below) Horizon slice Sakil 2. The outlines are repeated from Fig. 5-45 demonstrating that high-amplitude areas at Sakil 1 correspond to low-amplitude areas at Sakil 2. (Courtesy Pemex.)

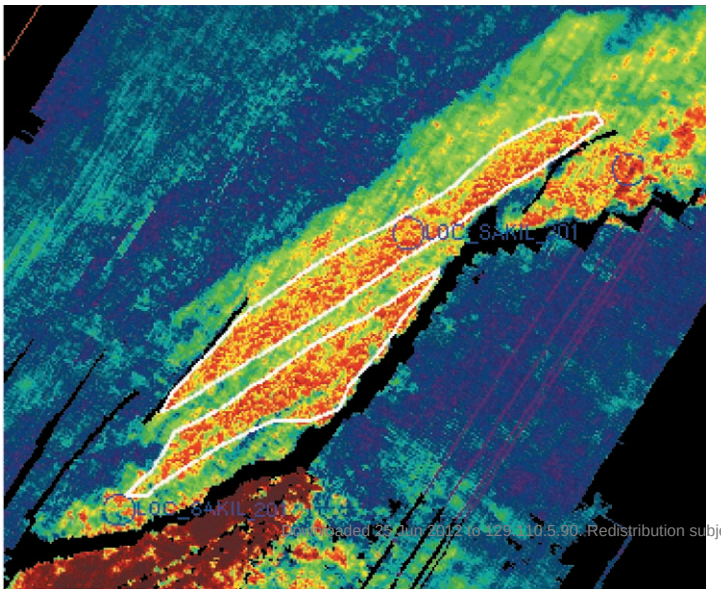

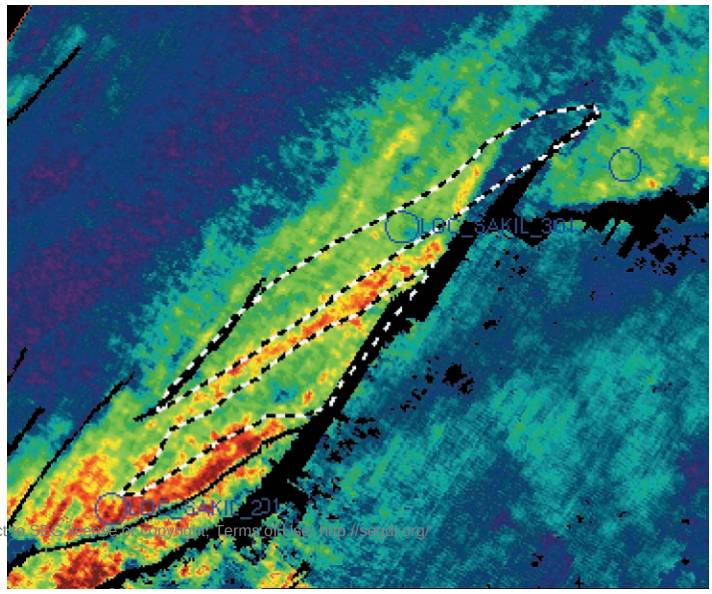

Downloaded 25 Jun 2012 to 129.110.5.90. Redistribution subject to SEG license or copyright; see Terms of Use at http://segd.org/

stacking together common and adjacent offsets to improve signal-to-noise ratio. Common-depth-point gathers corrected for normal moveout but without any stacking are shown in Figure 5-48. The somewhat bright reflections at and below the black arrow are from a known Gulf of Mexico gas sand. Increase of amplitude with offset is just visible.

The application of the horizon slice concept has increased the visibility of amplitude/offset effects for one horizon. Consider a volume of one line of prestack seismic data (Figure 5-49). The three dimensions are (1) CDP position along the line, (2) traveltime and (3) recording offset. The shape of one reflection without normal moveout correction is a cylindrical hyperbola as shown. By tracking this horizon and displaying the resultant amplitudes as if it were a horizon slice, a **horizon offset section** is obtained.

A horizon offset section prepared in this way is shown in Figure 5-50. The variation in amplitude with CDP position and with offset (approximately converted to incident angle) is shown for the trough immediately below the black arrow in Figure 5-48. The horizon offset section has been spatially smoothed, as an alternative to partial stacking, for increase of signal-to-noise ratio. The interpreter can observe, on this one section, the variation of amplitude with offset over many depth points for this horizon of interest. The amplitude increases with offset for most of the depth points and is hence consistent with gas content.

A full treatment of AVO is outside the scope of this book. Readers are referred to Castagna and Backus (1993). An AVO study should be undertaken only after normal stacked amplitude has been fully exploited. The application of AVO to 3-D data involves both 3-D imaging and 3-D display. It is a complicated and computationally-demanding activity. The variation of amplitude with offset can be expressed as a single gradient factor and horizon slices in AVO gradient can be produced. Far offset–near offset amplitude difference is similar to AVO gradient. This, as a 3-D AVO attribute, is discussed and illustrated in Chapter 8.

Interpretation of shear wave amplitudes in conjunction with conventional compressional wave amplitudes can provide another method of bright spot validation. On land, S-wave data have generally been collected in a separate operation. S-waves are not transmitted through water so, at sea, it is necessary to use waves mode-converted at the reflecting horizon and recorded by receivers placed on the water bottom.

Figure 5-51 summarizes the response of a water sand, a gas sand, a lignite bed, and a basalt bed to P- and S-wave energy; it should be studied in conjunction with Figure 5-5. Lignite has very low velocity and can be confused with a gas sand on the basis of P-wave response alone. Basalt, although high velocity, may also show a similar response if the polarity and phase of the data are not well understood.

The diagnostic comparison between P- and S-wave sections for a reflection from a gas sand is the presence of a P-wave bright spot and the absence of an amplitude anomaly for the correlative S-wave event. This comparison is illustrated in Figures 5-52 and 5-53 using data from a Gulf of Mexico 3-D 4-C survey (Nahm and Duhon, 2003).

In fact, the fundamental underlying principle is that compressional waves are sensitive to the type of pore fluid within rocks, whereas shear waves are only slightly affected. Hence the S-wave response of a reservoir sand will change little from below to above the gas/water contact, while the P-wave response normally changes greatly. Referring to Figure 5-5, it is clear that the P-wave dim spot would correlate on an S-section with a higher amplitude reflection. Where a phase change occurs across the gas/water contact on the P-section, the correlative P-wave and S-wave reflections from the gas sand will have opposite polarity. This is the situation interpreted by Ensley (1984). Any study using shear wave data is complicated by the extreme difficulty of reliably correlating P and S reflections.

Philosophy of Reflection Identification

Traditional approaches to reflection identification involve sliding a synthetic seismogram up and down on the real trace seeking a character match; we generally try to minimize the time mistie. With the all-too-common polarity and phase errors that may exist in our data, a more general and flexible approach will be more reliable. Let

Downloaded 25 Jun 2012 to 129.110.5.90. Redistribution subject to SEG license or copyright; Terms of Use: http://segdl.org/

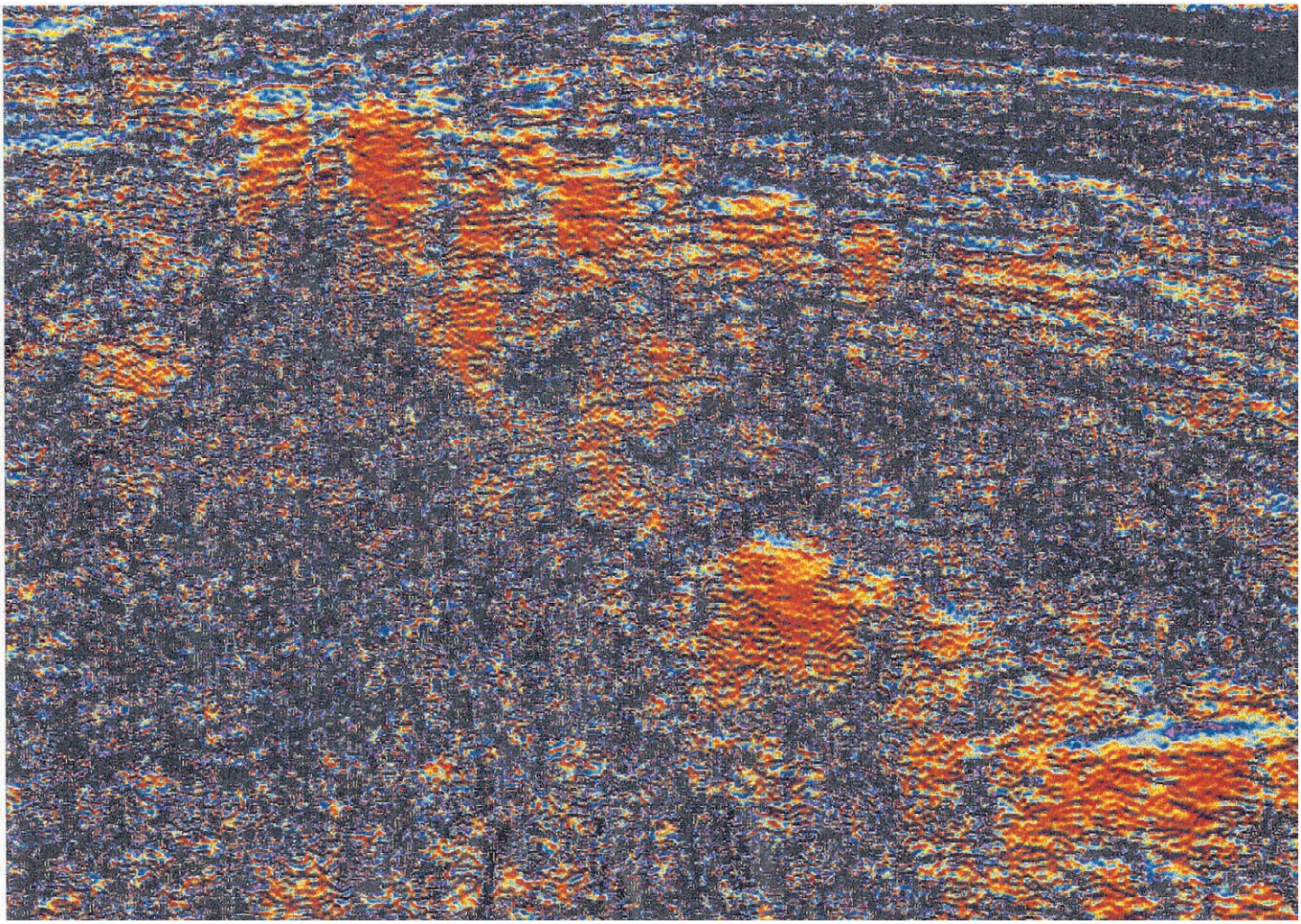

Fig. 5-47. Instantaneous frequency section showing several low-frequency indications of gas in red. (Courtesy Apache Corporation.)

us not simply assume that the data phase and polarity are what they are supposed to be. The interpreter should attempt to assess them in, for example, the ways discussed in Chapter 2. If synthetic seismograms are used, then ones made with many different phases of wavelet should be compared to the real data. Color is very helpful in detecting detailed character and recognizing phase and polarity errors.

The interpreter should be able to understand the complete character of the seismic data in the region of the geologic interface being tied. All the local reflections need to be understood; the more they cannot be understood, the more questions hang over the reflection identification. Clearly we must be confident of our reflection identification before any reservoir evaluation or characterization project, based on that reflection, can have any chance of success.

Let us consider an example: we find a seismic event of the right polarity (we think) at approximately the right time, so this becomes the top reservoir reflection. We know the approximate thickness of our reservoir so we look at the appropriate number of milliseconds deeper to find the reflection from the base. We find one of the right polarity at approximately the right time, so this becomes the base reservoir reflection. We know that we will need both top and base reflections for the study which is pending. All the wells show that the reservoir is a single, fairly massive unit so we would not expect any significant reflections from internal layers. However, on the seismic data, there is a reflection between top reservoir and base reservoir whose amplitude is greater than either top or base. Furthermore this "internal" reflection is widespread. The fact that we can then provide no satisfactory explanation for this reflection throws into question all the previous reflection identification!

Downloaded 25 Jun 2012 to 129.110.5.90. Redistribution subject to SEG license or copyright; Terms of Use: http://segdl.org/

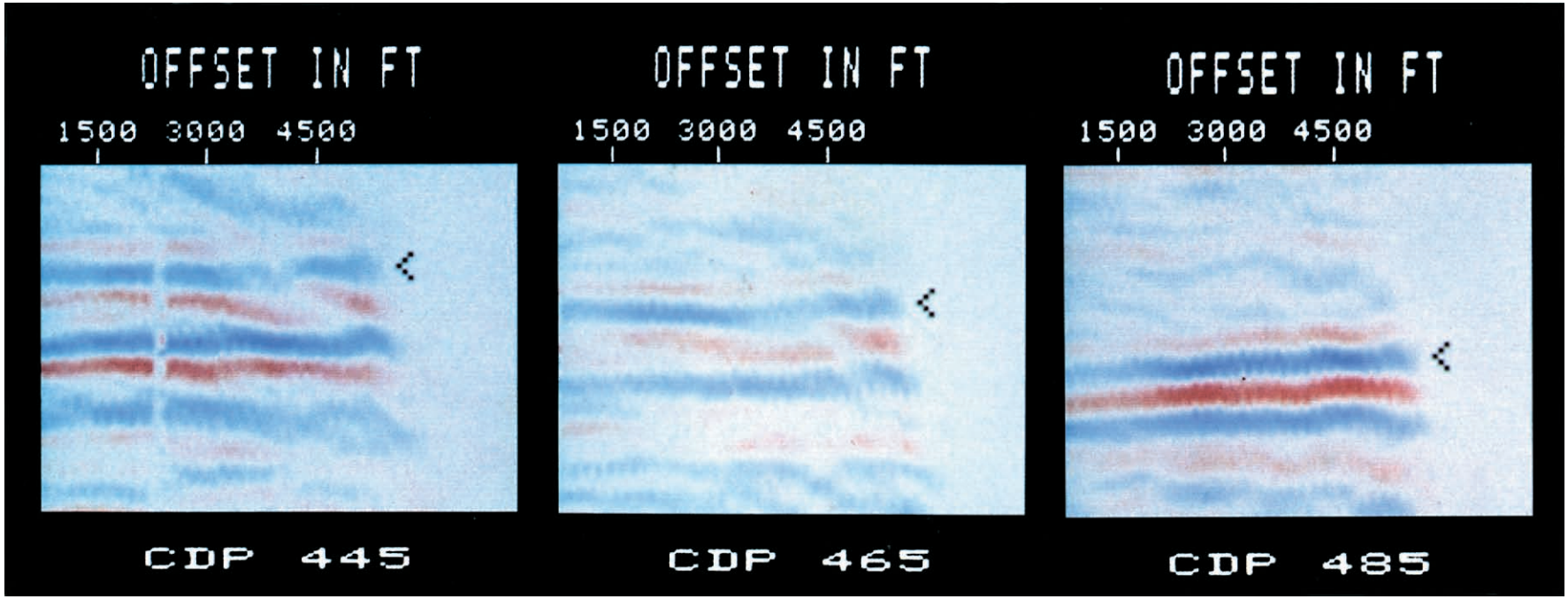

Fig. 5-48. Common-depth-point gathers corrected for moveout showing variation of amplitude with offset for several horizons.

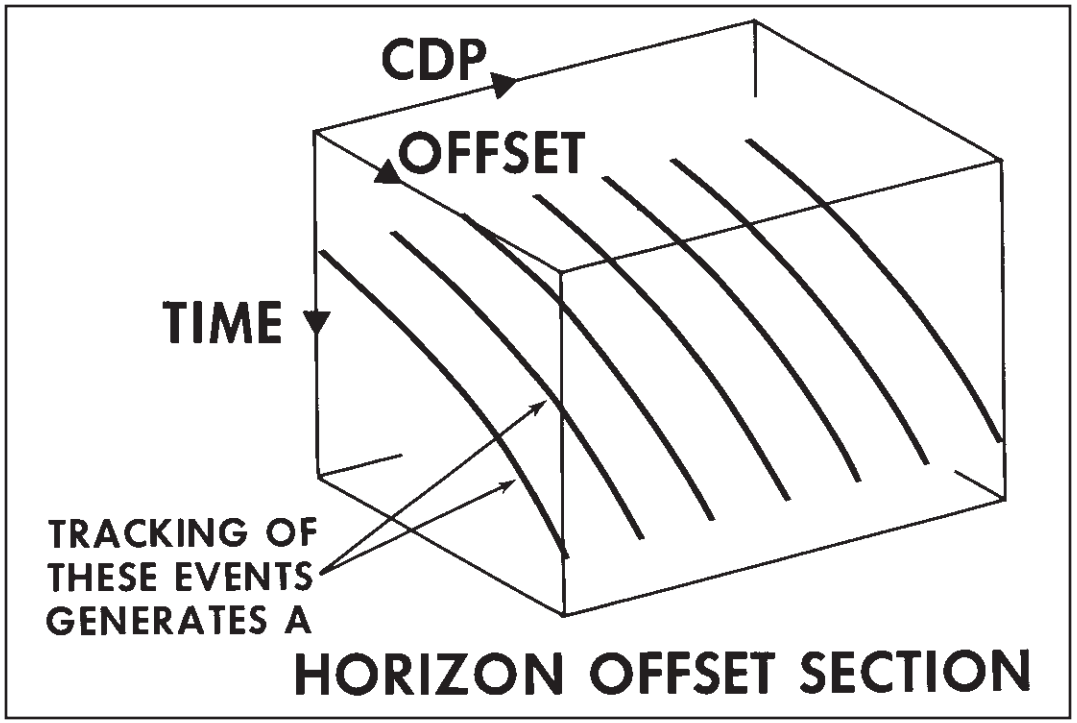

Fig. 5-49. The concept of a horizon offset section generated by tracking a horizon on a sequence of common-depth-point gathers.

Downloaded 25 Jun 2012 to 129.110.5.90. Redistribution subject to SEG license or copyright; Terms of Use: http://segdl.org/

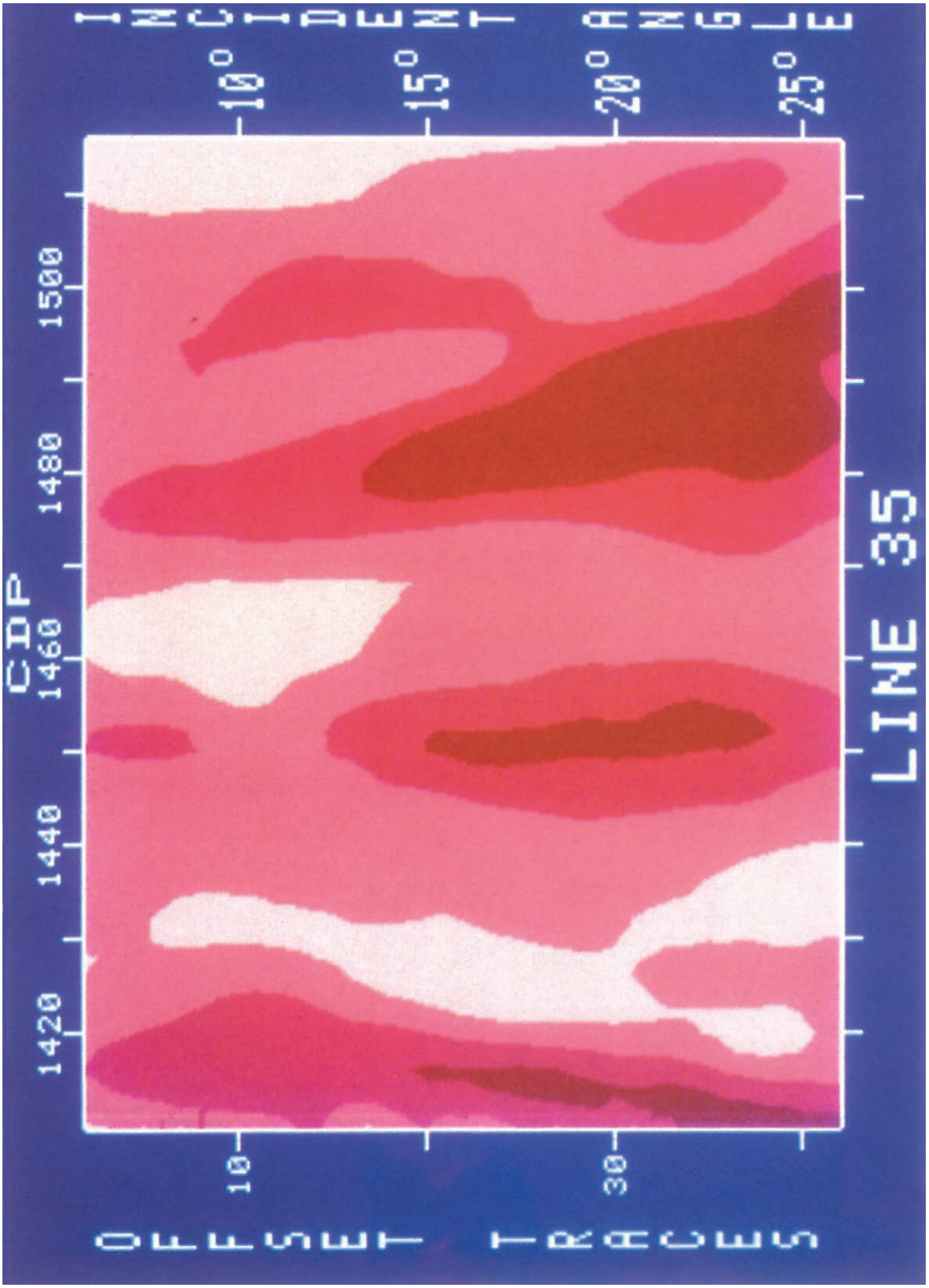

Fig. 5-50. Horizon offset section for a Gulf of Mexico bright spot showing increase of amplitude with offset for most depth points.

Downloaded 25 Jun 2012 to 129.110.5.90. Redistribution subject to SEG license or copyright; Terms of Use: http://segdl.org/

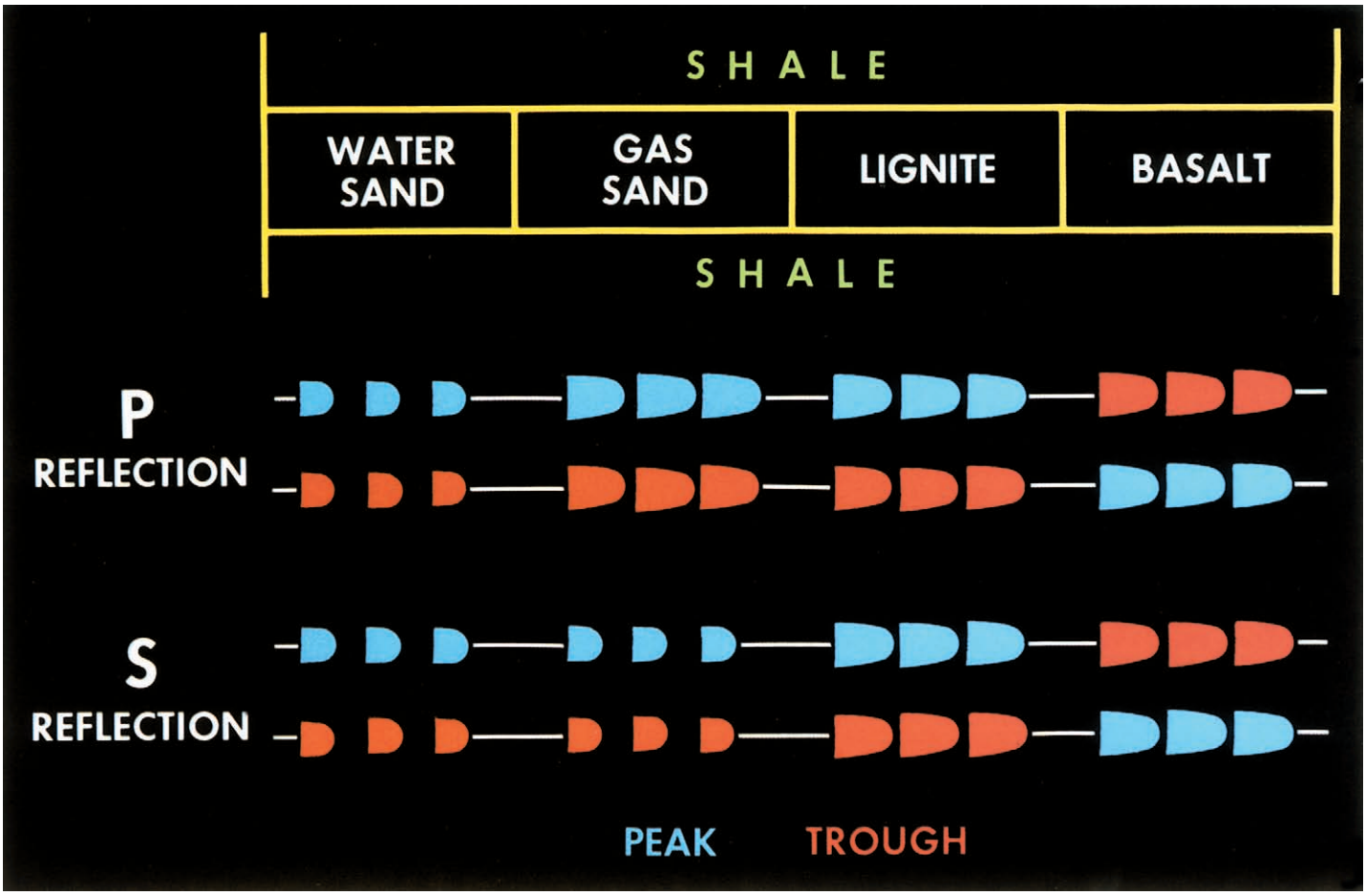

Fig. 5-51. Schematic diagram of the P-wave and S-wave zero-phase response for different beds encased in shale.

Some general recommendations for seismic reflection identification then include:

- Don't assume the data polarity and phase are what they are supposed to be.
- If you are going to use synthetic seismograms, use a suite of seismograms of various phases and of both polarities.
- Use a double-gradational color display which is balanced, because much more detailed character will be visible and you will more readily recognize polarity and phase problems.
- Consider all the local character, that is, seek to explain **all** the reflections in the neighborhood of the objective.
- Don't worry too much about time misties; they can usually be explained.

Downloaded 25 Jun 2012 to 129.110.5.90. Redistribution subject to SEG license or copyright; Terms of Use: http://segdl.org/

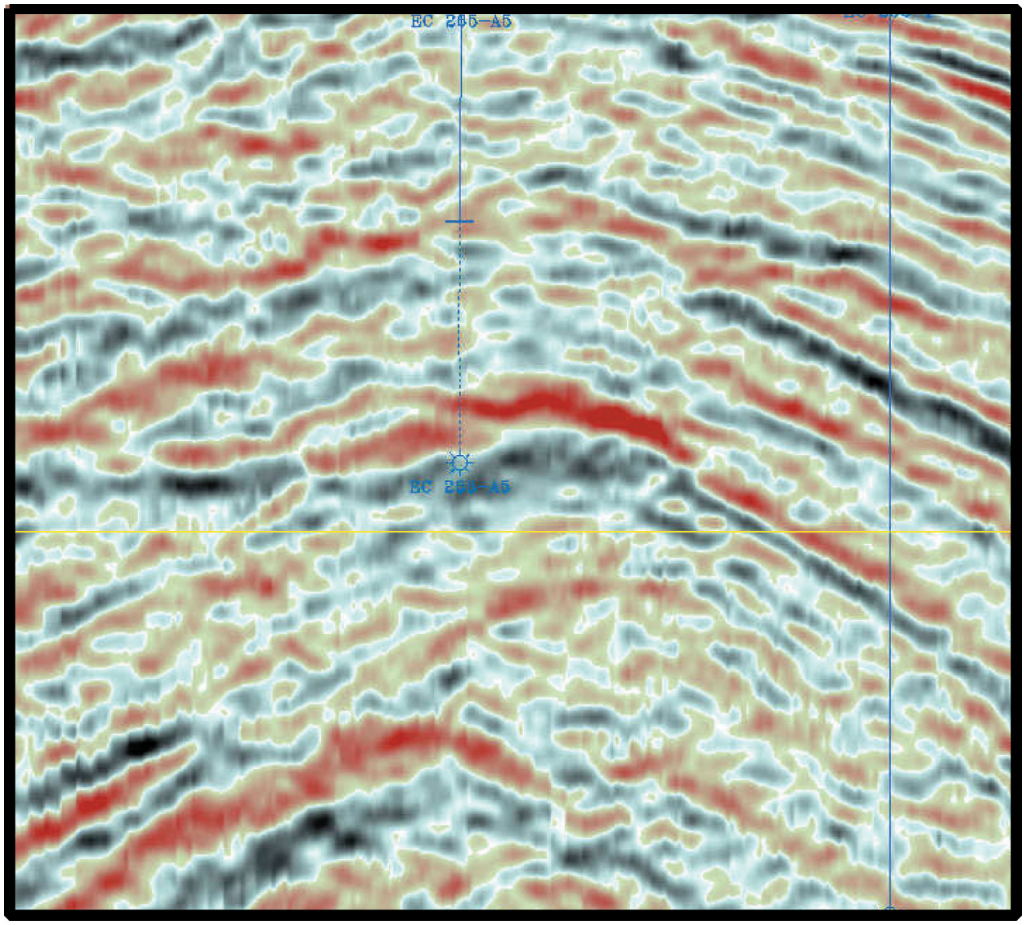

Fig. 5-52. Bright spot indicating gas from East Cameron area of Gulf of Mexico. This is the normal compressional wave section. (Courtesy BP.)

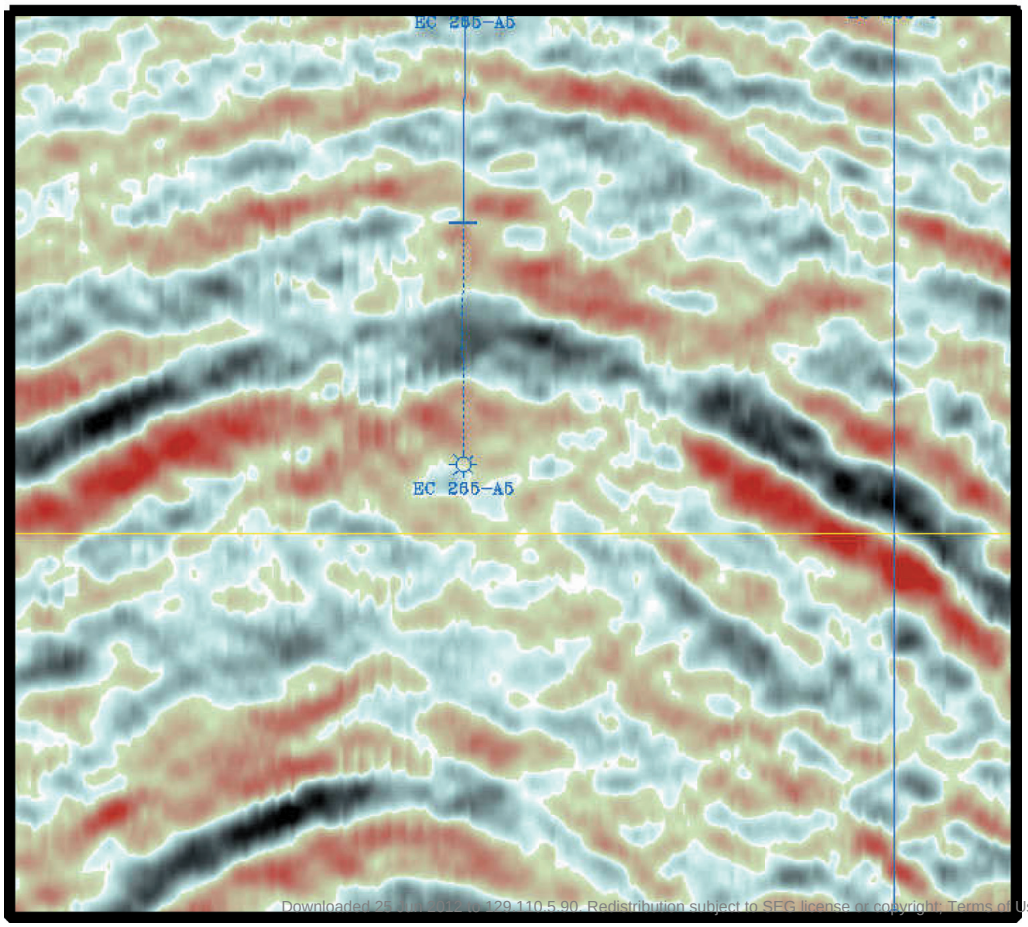

Fig. 5-53. Corresponding converted wave section from four-component survey. The gas bright spot is not present but rather a dimming in amplitude appears to occur. (Courtesy BP.)

Downloaded 25 Jul 2012 to 129.110.5.90. Redistribution subject to SEG license or copyright. Terms of Use: http://segdl.org/

Questions an Interpreter Should Ask in an Attempt to Validate the Presence of Hydrocarbons

(1) Is the reflection from the suspected reservoir anomalous in amplitude?
(2) Do the high-amplitude reflections have the character expected for hydrocarbons in these data?
(3) Is the amplitude anomaly structurally consistent?
(4) Is there one reflection from the top of the reservoir and one from the base?
(5) Do the top and base reflections exhibit natural pairing, dimming at the same point at the edge of the reservoir?
(6) Is the amplitude of the anomaly large relative to the background?
(7) Are the data zero phase and known polarity?
(8) Is a flat spot visible and is it discrete?
(9) Is the flat spot flat or dipping consistent with gas velocity sag or tuning?
(10) Is the flat spot unconformable with the structure but consistent with it?
(11) Does the flat spot have the correct zero-phase character?
(12) Is the flat spot located at the downdip limit of the anomaly?
(13) Is a phase change (polarity reversal) visible?
(14) Is the phase change structurally consistent and at the same level as the flat spot?
(15) Does bright spot, dim spot, or phase change show the appropriate zero-phase character?
(16) Is there a broadening of the reservoir reflections or a low-frequency shadow below?
(17) If the reservoir is thick, are there significant reflections inside?

(18) Do amplitude versus offset studies yield further validation evidence?
(19) Do shear wave or converted wave data provide further validation evidence?
(20) Do statistical crossplotting techniques indicate a flat spot?
(21) Is there an anomaly in moveout-derived interval velocity?

Every hydrocarbon indicator is potentially a reservoir, but any one indication can be spurious. Confident identification of a hydrocarbon necessarily involves the accumulation of evidence. The more questions on the above list to which you can answer "Yes," the greater should be your confidence. Every negative answer needs to be satisfactorily explained or the identification falls into question.

Figure 5-54 contains several suspected hydrocarbon reservoirs. Try asking the above questions for these data. You should find affirmative answers for questions 1 through 17 for many separate reservoirs. How many did you find? While scrutinizing these data, it is useful to bear in mind simple reservoir models, such as those portrayed in Figure 5-5. An effective way to interpret the reservoirs from Figure 5-54 is to draw an overlay for the reservoir reflections. On the assumption of zero-phaseness, interfaces should be drawn along crestal amplitudes, and it is important to mark the top and bottom of each suspected hydrocarbon reservoir *and* the top and bottom of the correlative aquifer in each case.

For comparison with Figure 5-54, Figure 5-55 presents the same data at a normal display aspect ratio and in variable area/wiggle trace. This demonstrates not only the value of color for identifying the reservoir reflections in Figure 5-54 but also the value of an expanded vertical scale.

Figure 5-56 presents the same section as Figure 5-54, but with the results of a well inserted. This demonstrates that there are at least seven stacked gas reservoirs at this offshore California location.

The Occurrence of Hydrocarbon Indicators

The nature of hydrocarbon indication — that is, whether the phenomenon is bright spot, phase change, or dim spot — depends on the relative acoustic impedances of hydrocarbon sand, water sand, and shale (Figure 5-5). Each of these acoustic impedances increases with depth (Figure 5-57) and they also each increase with rock age. It is difficult to be quantitative because they are also dependent on lithology, porosity, and local environment. Figure 5-57 is thus plotted for the qualitative product of depth and age. The effect of compaction on the shale causes its acoustic impedance to increase less rapidly

Downloaded 25 Jun 2012 to 129.110.5.90. Redistribution subject to SEG license or copyright; Terms of Use: http://segdl.org/

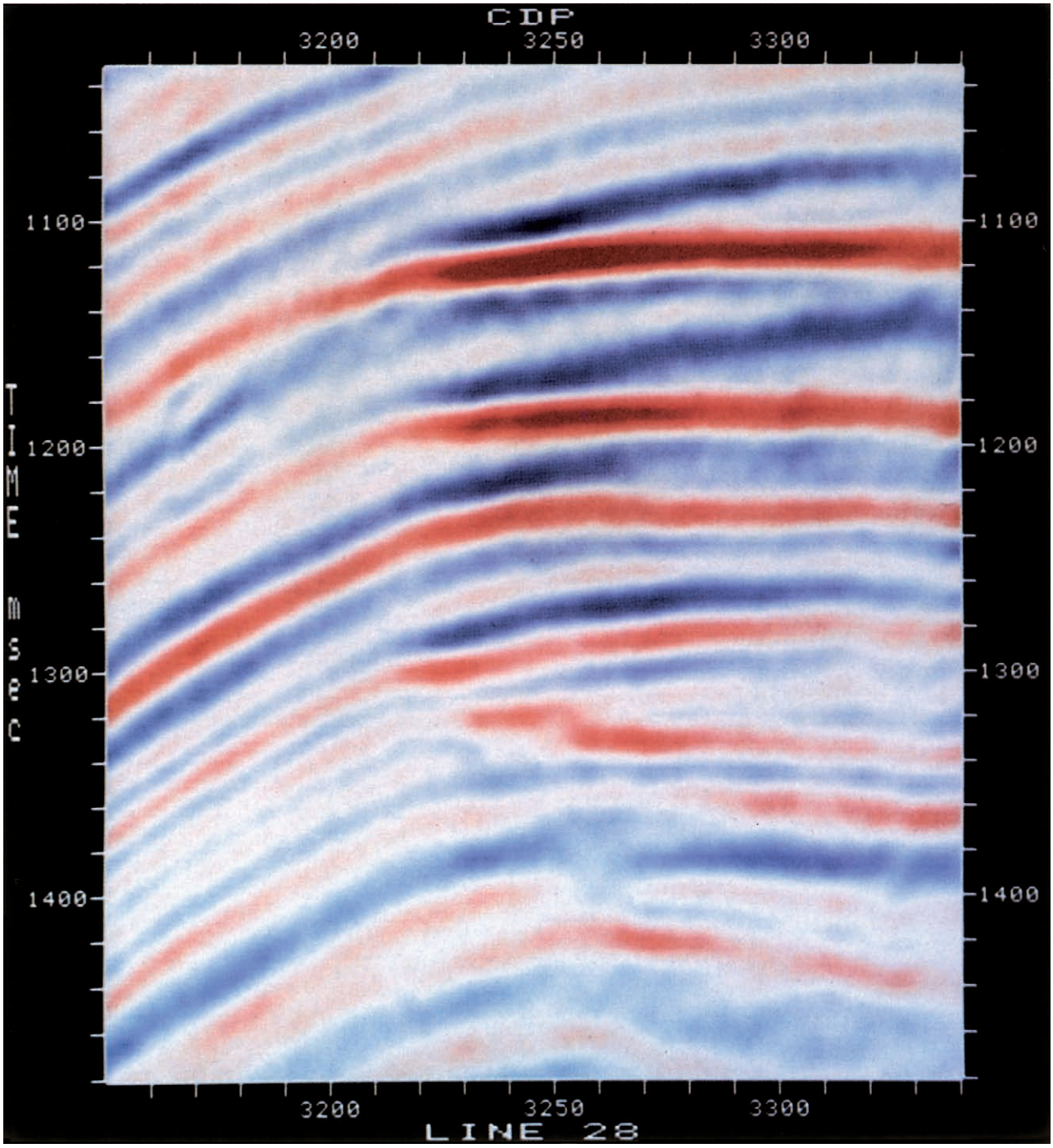

Fig. 5-54. Hydrocarbon indicators in Pliocene rocks offshore California. It is intended that the reader interrogate this section with the "Questions an interpreter should ask in an attempt to validate the presence of hydrocarbons."

Downloaded 25 Jun 2012 to 129.110.5.90. Redistribution subject to SEG license or copyright; Terms of Use: http://segdl.org/

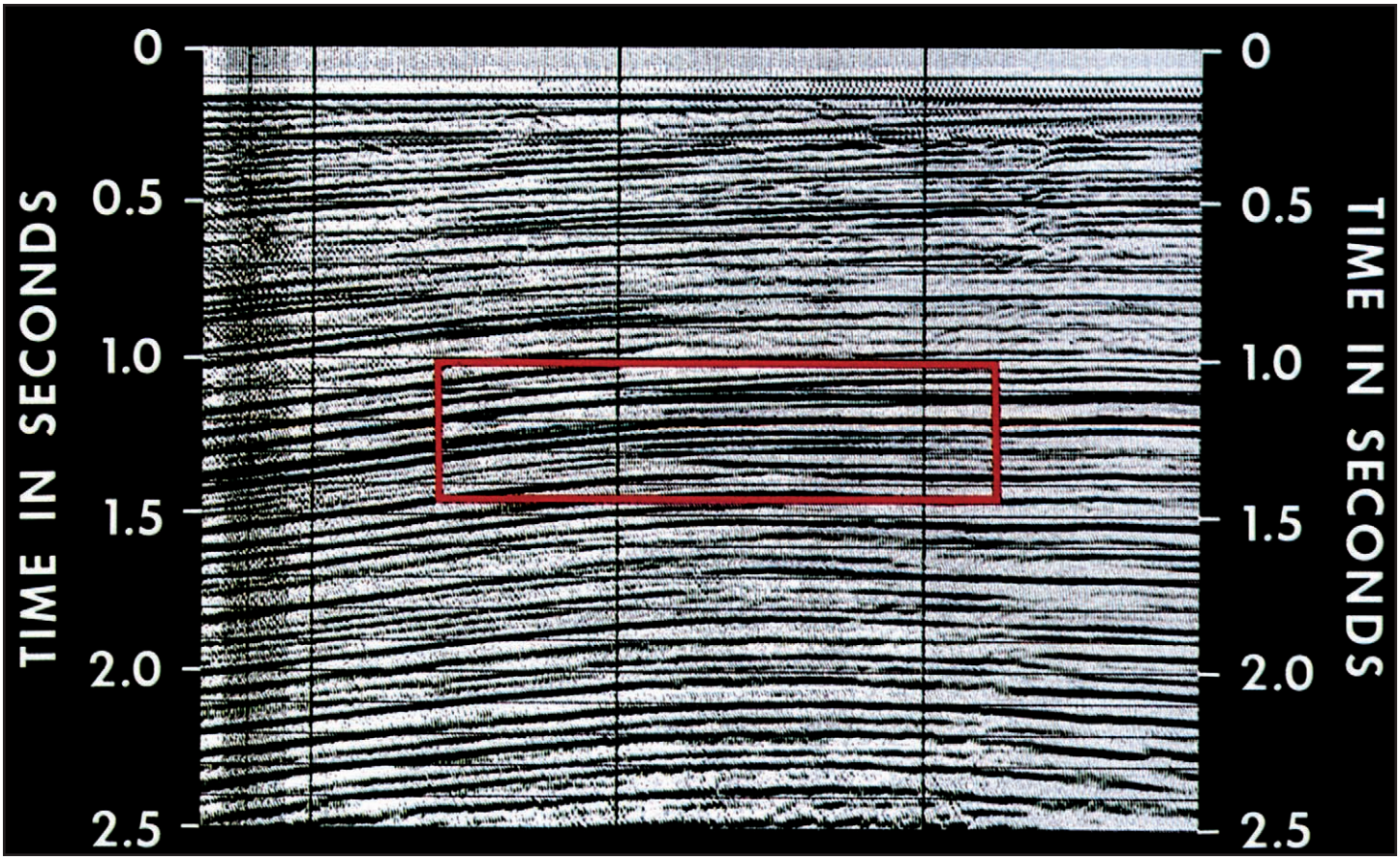

Fig. 5-55. Vertical section from offshore California in variable area/wiggle trace and normal aspect ratio. Data within red rectangle are the same as those presented in color in Figure 5-54, demonstrating that in the latter the vertical scale is exaggerated.

than that of the sand. Below the point where the shale acoustic impedance crosses that of the water sand, phase changes must occur. Below the point where the shale acoustic impedance crosses that of the hydrocarbon sand, dim spots must occur. Of course, all the phenomena are reducing in visibility with depth and age, and somewhere there is a cut-off below which no hydrocarbon observations will be possible. However, Figure 5-57 provides a likely pattern of occurrence within one basin. Once one direct observation has been made in a given area it is probable that deeper and older observations will fit the trend here illustrated. Figure 5-57 also demonstrates the effect of overpressure. This tends to be greater for the shale with the effect of enhancing dim spots and suppressing bright spots.

Figure 5-58 is an attempt to separate the effects of depth and age. The depth is the depth of maximum burial, and old rocks are unlikely to have been at a shallow depth for all their geologic history. Nevertheless, Figure 5-58 indicates that bright spots will occur at great depths for very young rocks. It also indicates that hydrocarbon phenomena will occur in older rocks that are reasonably shallow. Figure 5-10 shows striking bright spots in Pliocene rocks for depths well over 5000 m. Furthermore, hydrocarbon indicators have been observed in Permian rocks as previously discussed (Figure 5-19).

Figure 5-59 summarizes and integrates the subjects discussed in this chapter. Some of the diagrams are redrawn to coordinate with each other, and some of the data examples are new. The addition of acoustic impedance profiles to the reservoir models further increases understanding.

Downloaded 25 Jun 2012 to 129.110.5.90. Redistribution subject to SEG license or copyright; Terms of Use: http://segdl.org/

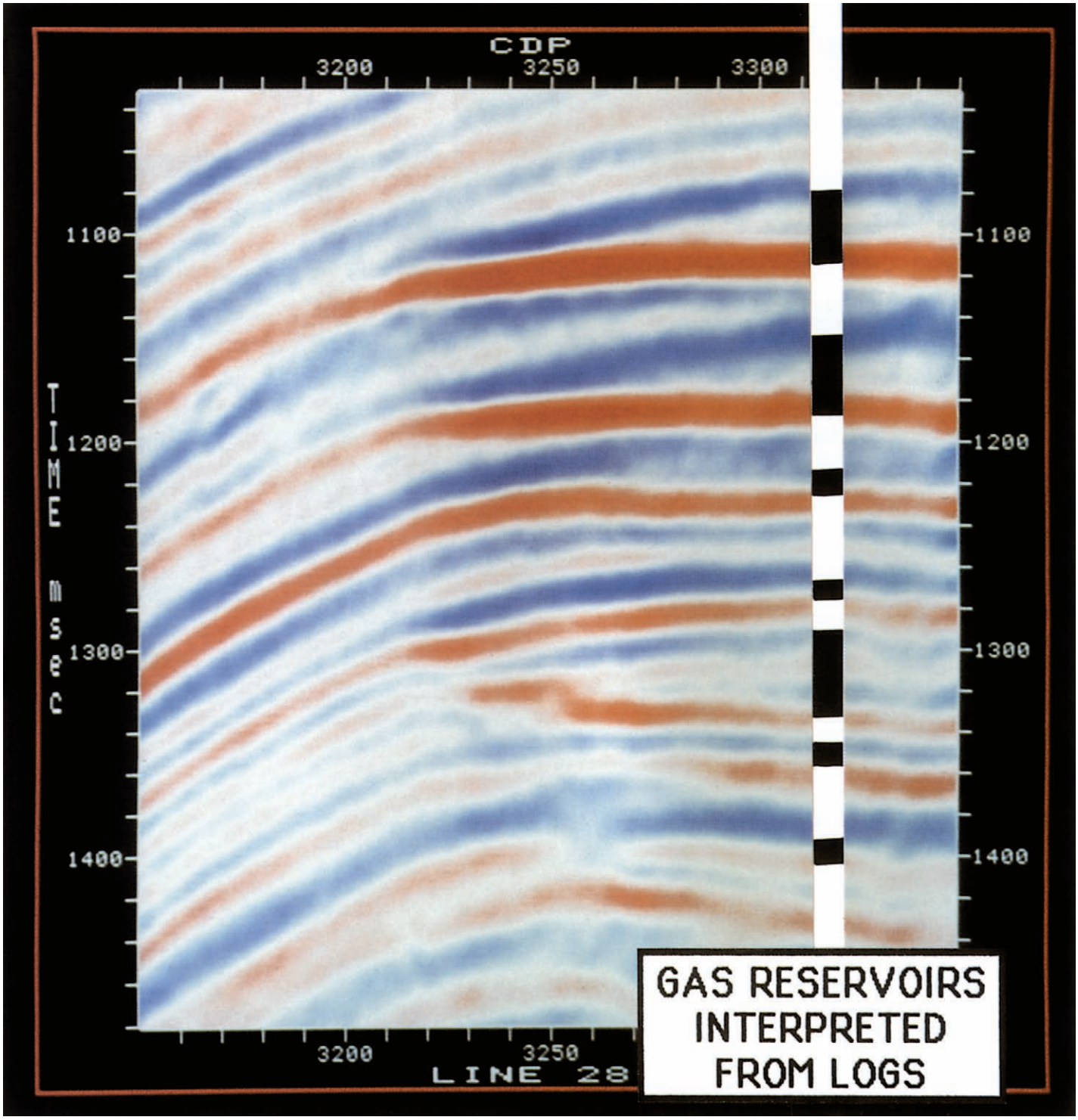

Fig. 5-56. Same section as Figure 5-54 with results of well inserted.

Downloaded 25 Jun 2012 to 129.110.5.90. Redistribution subject to SEG license or copyright; Terms of Use: http://segdl.org/

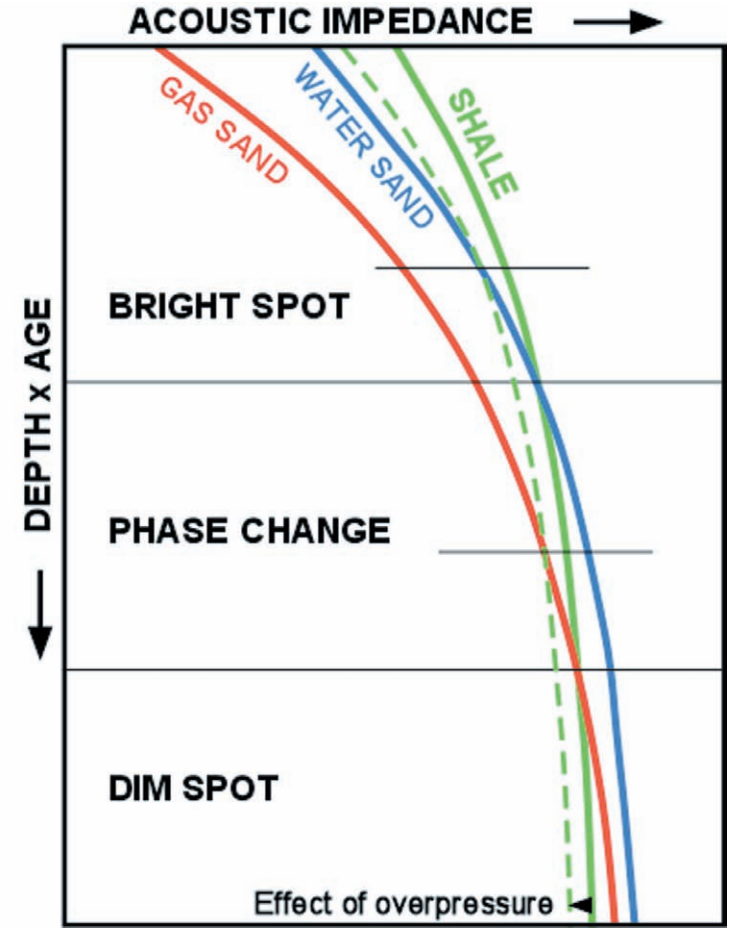

Fig. 5-57. Gas sand, water sand and shale acoustic impedances all increase with depth and age but at different rates. The crossover points define whether the hydrocarbon indication is bright spot, phase change (polarity reversal) or dim spot. The principal effect of overpressure moves the shale line to lower impedance, thus increasing the effect of dim spots and decreasing the effect of bright spots.

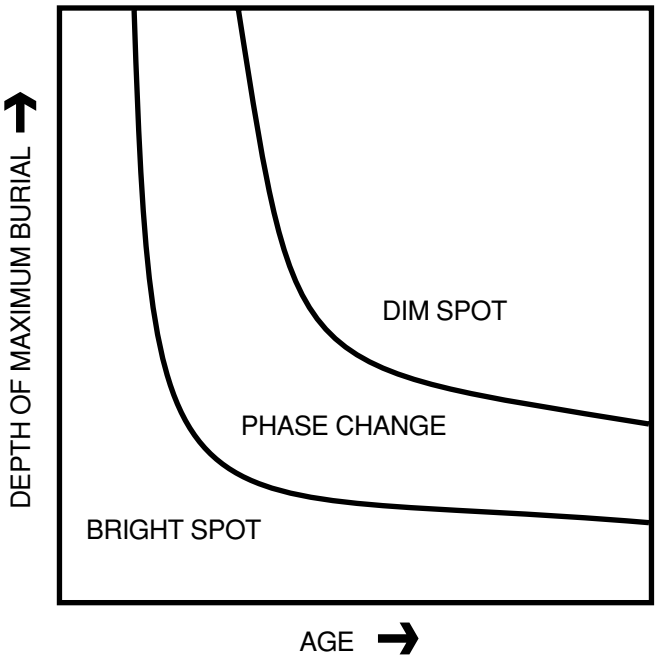

Fig. 5-58. Qualitative assessment of bright spot, phase change, and dim spot regions in terms of depth and age.

Downloaded 25 Jun 2012 to 129.110.5.90. Redistribution subject to SEG license or copyright; Terms of Use: http://segdl.org/

References

Backus, M. M., and R. L. Chen, 1975, Flat spot exploration: Geophysical Prospecting, v. 23, p. 533–577.

Backus, M. M., and N. Goins, 1984, Change in reflectivity with offset, Research Workshop report: Geophysics, v. 49, p. 838–839.

Birtles, R., 1986, The seismic flat spot and the discovery and delineation of the Troll Field, *in* Habitat of hydrocarbons on the Norwegian continental shelf, A.M. Spencer et al. (eds.): Graham and Trotman, p. 207–215.

Castagna, J. P., and M. M. Backus, 1993, Offset-dependent reflectivity — theory and practice of AVO analysis: SEG Investigations in Geophysics, No. 8, 348 p.

Clark, V. A., 1992, The effect of oil under in situ conditions on the seismic properties of rocks: Geophysics, v. 57, p. 894–901.

Ensley, R. A., 1984, Comparison of P- and S-wave seismic data: a new method for detecting gas reservoirs: Geophysics, v. 49, p. 1420–1431.

Gardner, G. H. F., L. W. Gardner, and A. R. Gregory, 1974, Formation velocity and density — the diagnostic basics for stratigraphic traps: Geophysics, v. 39, p. 770–780.

Greenlee, S.M., G. M. Gaskins, and M. G. Johnson, 1994, 3-D seismic benefits from exploration through development — an Exxon perspective: The Leading Edge, v. 13, p. 730–734.

Luchford, J., 2001, A view of amplitude fit to structure as a hydrocarbon-indicating attribute: First Break, v. 19, p. 411–417.

Nahm, J. W., and M. P. Duhon, 2003, Interpretation and practical applications of 4C-3D seismic data, East Cameron gas fields, Gulf of Mexico: The Leading Edge, v. 22, p. 300–309.

Ostrander, W. J., 1984, Plane-wave reflection coefficients for gas sands at non-normal angles of incidence: Geophysics, v. 49, p. 1637–1648.

Taner, M. T., F. Koehler, and R. E. Sheriff, 1979, Complex seismic trace analysis: Geophysics, v. 44, p. 1041–1063.

Tegland, E. R., 1973, Utilization of computer-derived seismic parameters in direct hydrocarbon exploration and development, *in* Lithology and direct detection of hydrocarbons using geophysical methods: Dallas Geophysical and Geological Societies symposium.

Tilbury, L. A., and P. M. Smith, 1988, Seismic reflection amplitude (dim spot) study over the Goodwyn Gas Field, Northwest Shelf, Australia: Proceedings, ASEG/SEG Conference (Adelaide), p. 179–183.

Ware, P.L.G., and C. Burgess, 1998, The problem of paleo-oil-water-contacts in seismic identification of hydrocarbon accumulations: AAPG International Conference, Rio de Janeiro, and Geophysical Society of Houston newsletter (January 1999).

Wigger, S.T., J. Bailey, M. Larsen, and M. Wallace, 1997, Ha'py Field: a Pliocene bright spot example from the Nile delta, Egypt: The Leading Edge, v. 16, p. 1827–1829.

Downloaded 25 Jun 2012 to 129.110.5.90. Redistribution subject to SEG license or copyright; Terms of Use: http://segdl.org/

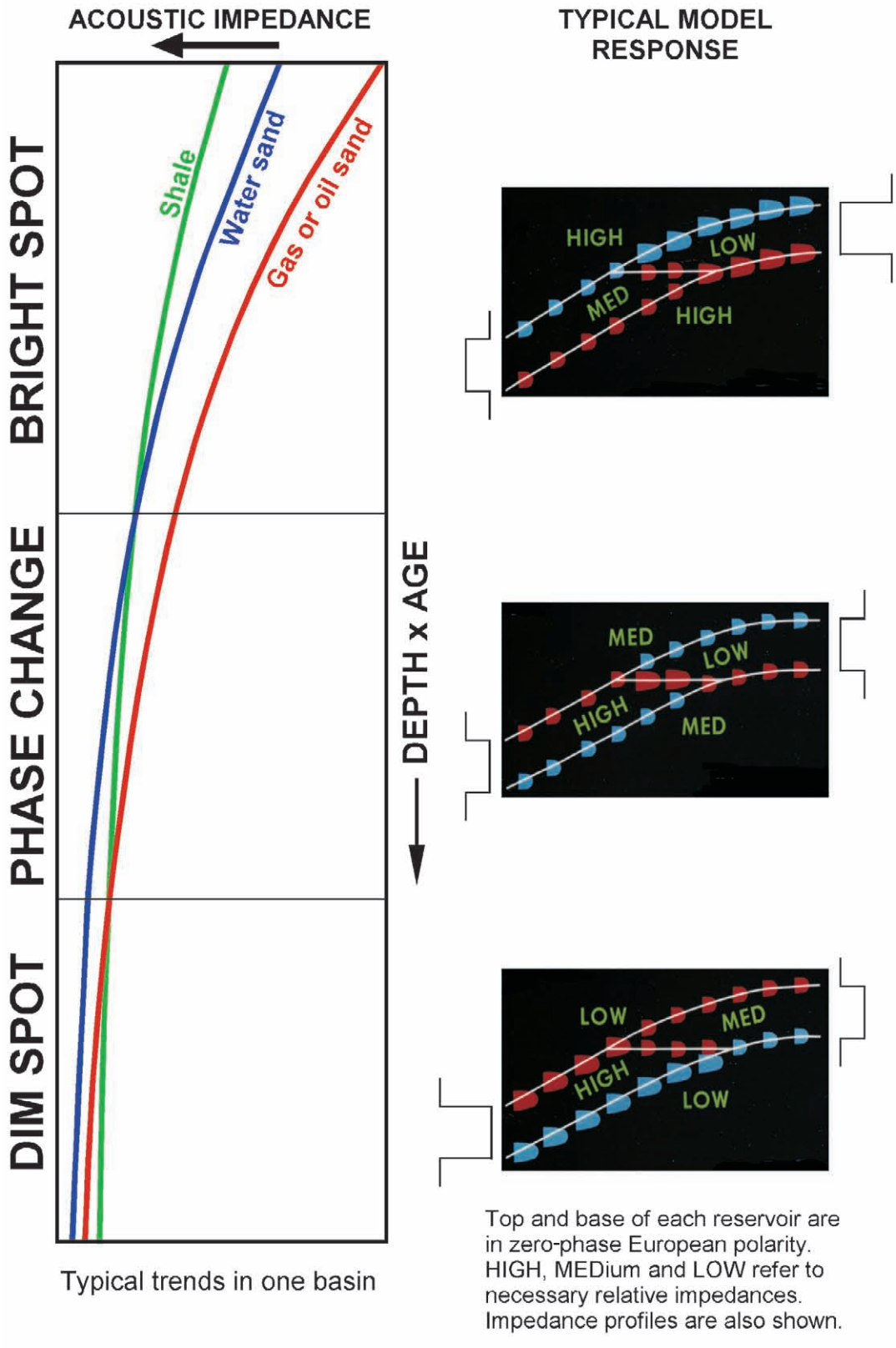

Fig. 5-59. Understanding hydrocarbon fluid effects in seismic data — a confluence of Figures 5-5, 5-6, and 5-57 and various data examples.

Downloaded 25 Jun 2012 to 129.110.5.90. Redistribution subject to SEG license or copyright; Terms of Use: http://segdl.org/

ACOUSTIC IMPEDANCE OF RESERVOIR RELATIVE TO EMBEDDING MATERIAL

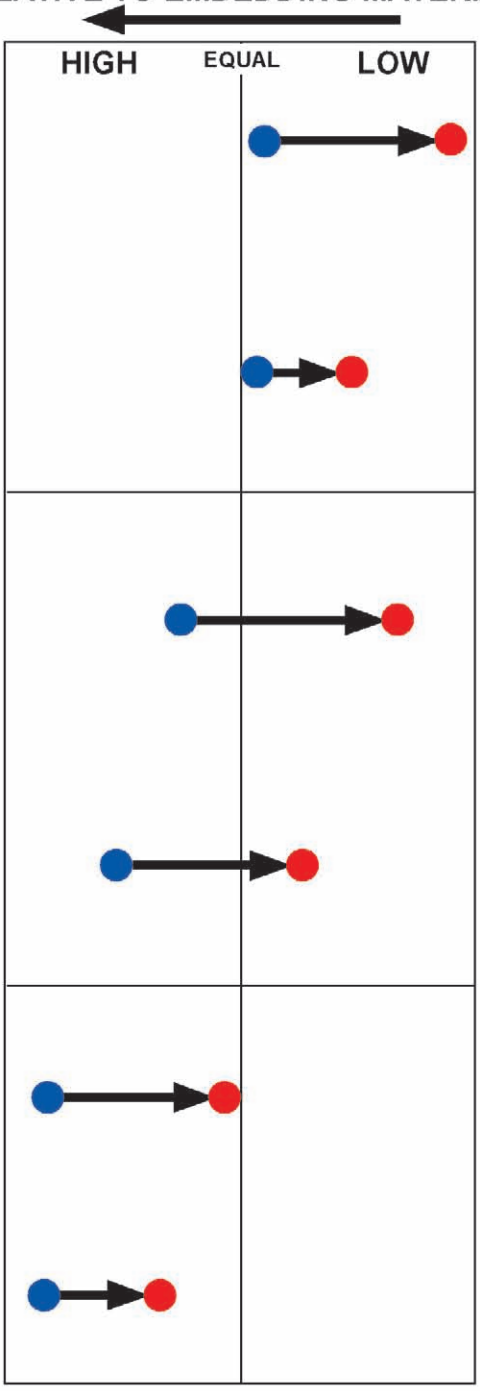

Water-filled reservoir

Hydrocarbon-filled reservoir

Length of arrow gives impedance change.
Distance from line of equality gives amplitude.

EXAMPLES FROM AROUND THE WORLD

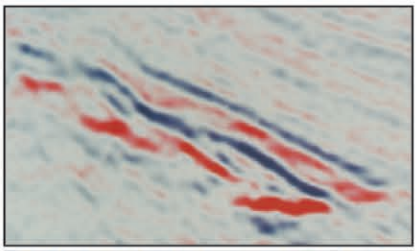

Bright spots from two stacked reservoirs in the Gulf of Mexico. Pleistocene sands at 1500m. (Courtesy Chevron)

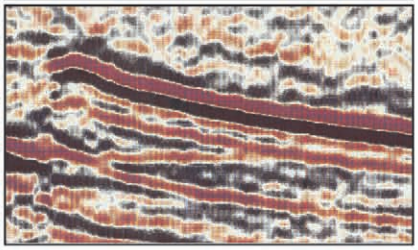

Bright spot and flat spot from onshore Netherlands. Permian sand at 2800m. (Courtesy NAM)

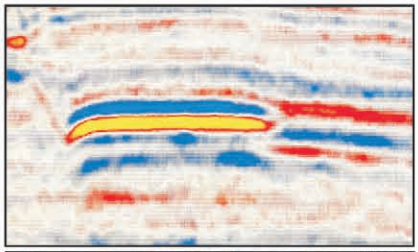

Phase change (polarity reversal) from Gulf of Mexico. Pliocene sand at 2200m. (Courtesy Conoco)

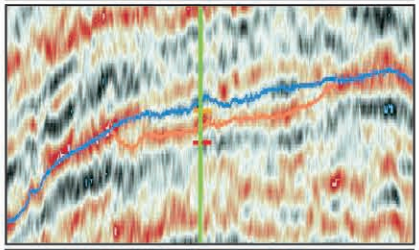

Phase change to lower amplitude from Northwest Shelf, Australia. Cretaceous sand at 2500m. (Courtesy Apache)

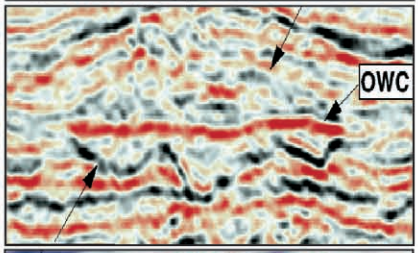

Dim spot and flat spot from UK sector, North Sea. Eocene sand at 1900m. (Courtesy Chevron)

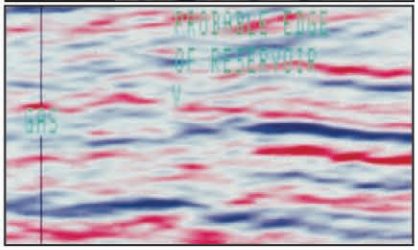

Dim spot from Trinidad. Miocene sand at 4200m. (Courtesy Texaco)

All data examples are zero phase European polarity except dim spot from Trinidad.

Downloaded 25 Jun 2012 to 129.110.5.90. Redistribution subject to SEG license or copyright; Terms of Use: http://segdl.org/

Downloaded 25 Jun 2012 to 129.110.5.90. Redistribution subject to SEG license or copyright; Terms of Use: http://segdl.org/

Tuning Phenomena in Reservoirs

Effect of Tuning on Stratigraphic Interpretation

Widess (1973) demonstrated the interaction of closely-spaced reflections. In his classic paper, "How thin is a thin bed?," he discussed the effect of bed thickness on seismic signature. For a bed thickness of the order of a seismic wavelength or greater there is little or no interference between the wavelets from the top and the bottom of the bed and each is recorded without modification. For thinner beds these wavelets interfere both constructively and destructively. Considering wavelets of opposite polarity, the amplitude of the composite wavelet reaches a maximum for a bed thickness of one-quarter wavelength (one-half period) and this is known as the tuning thickness. For beds thinner than this the shape of the composite wavelet stays the same but its amplitude decreases. Clearly, the bed thicknesses at which these phenomena occur depend on the shape of the wavelet in the data and hence on its frequency content.

These tuning phenomena are of considerable importance to the stratigraphic interpreter. They must be recognized as effects of bed geometry as opposed to variations in the acoustic properties of the medium. Figure 6-1 shows a sedimentary pod. As the reflections from the top and the base come together (within the black square) the amplitude abruptly increases; this is interpreted as tuning between the top and base reflections.

Convergence of reservoir reflections around the periphery of reservoirs is commonplace. Figure 6-2 illustrates the tuning phenomena in amplitude and time that occur between a top reservoir reflection and a fluid contact reflection near the downdip reservoir limit. At the tuning thickness the amplitude maximizes (for a given acoustic contrast), and for the parts of the reservoir thinner than this the amplitude will decrease. The tuning thickness is also the closest possible approach of the two seismic wavelets, so that, as the reservoir thins, the seismic reflections no longer will coincide with the reservoir interfaces. For zero-phase data this divergence will be disposed symmetrically between the top and fluid contact reflections, as shown in Figure 6-2.

The limit of seismic visibility indicated on Figure 6-2 is considered in more detail in Figure 6-3. For reservoirs with a higher acoustic contrast with the embedding medium, thinner parts of the reservoir will be visible, the exact thickness depending on the noise level in the data and the nature of the wavelet. Considering a common situation in Tertiary clastic reservoirs where the top and fluid contact reflections are equal in amplitude and opposite in polarity, the actual downdip limit is invisible but can be found by extrapolating to zero the amplitude gradient observed between the tuning thickness and the limit of visibility.

Figure 6-4 shows some bright spots which are reflections from the top and base of gas sands of variable thickness. The base of the gas sands (the bright red events) are fluid contacts at most of the downdip limits. Hence the top and base reflections in many places constitute thinning wedges. Close inspection of Figure 6-4 reveals several local amplitude maxima close to the downdip limits of brightness. At these points the apparent dip also changes. The interfering wavelets are unable to approach each other more closely than a half period. Therefore, the composite bed signature for each of these thin beds assumes a dip attitude which is the mean

Downloaded 25 Jun 2012 to 129.110.5.90. Redistribution subject to SEG license or copyright; Terms of Use: http://segdl.org/

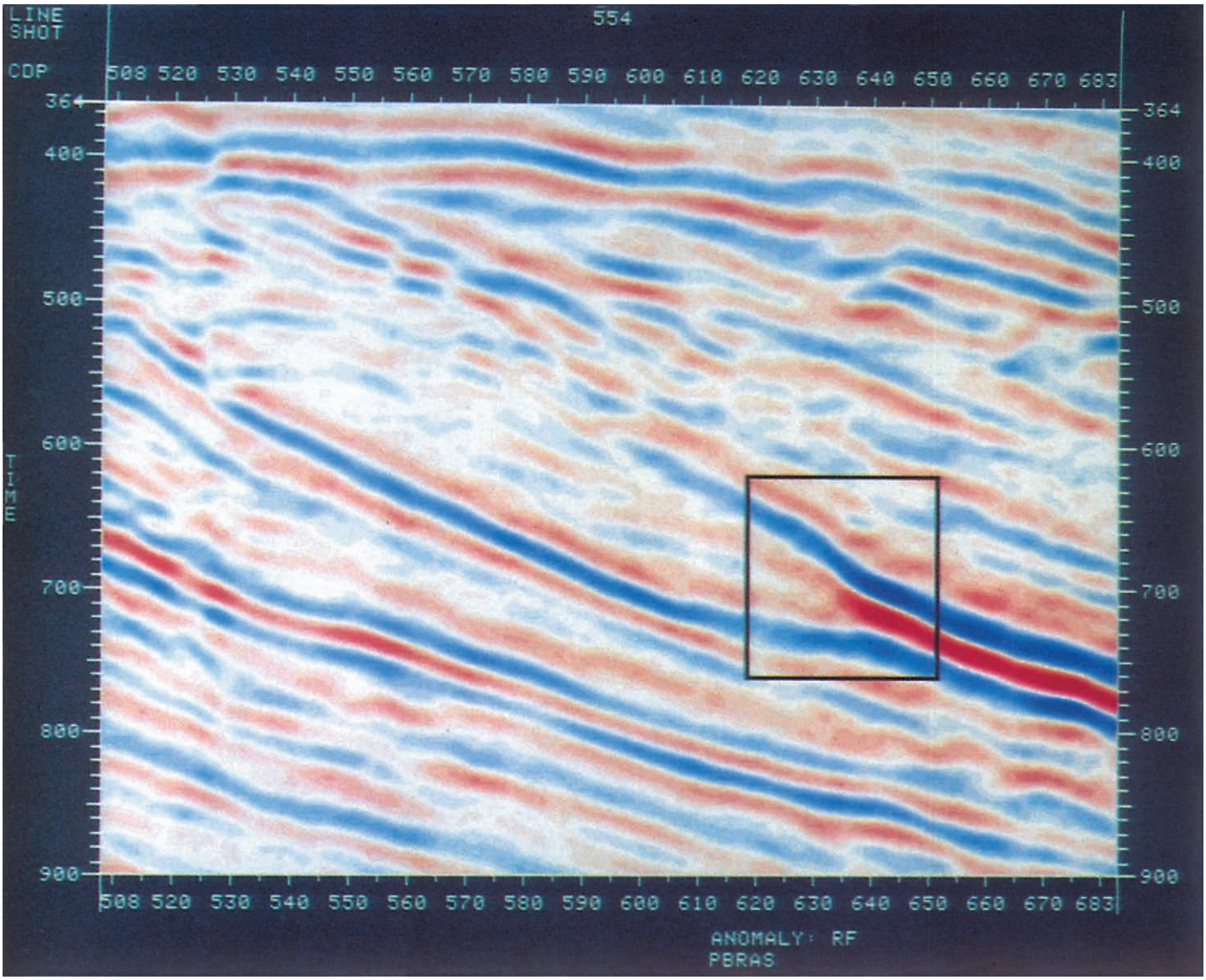

Fig. 6-1. Amplitude increases as reflections converge because of tuning. (Courtesy Petroleo Brasileiro.)

of the real dips of the top and the base of the interval. Because the base gas is flat at the down-dip pinchout, it is easy to see the dip of the composite wavelet turning to assume this intermediate value.

Tuning amplitudes are easily recognized on horizon slices. Figure 6-5 is a horizon slice over the reflection from the top of a Gulf of Mexico gas reservoir. Dip is to the north, which is to the right in this figure. Horizon tracking was stopped at the limit of visibility, which is the edge of the various shades of blue along the north. Close to that edge and parallel to it is a lineation of locally higher amplitudes, visible as locally darker blues and indicated by a red arrow. This is the tuning thickness trend along which the reservoir thickness is equal to one-half of the seismic period, namely about 15 m (49 ft).

Tuning effects are not always a nuisance; in fact, they can be used to increase the visibility of thin beds. Amplitude tuning occurs for a layer thickness of one-half period of the dominant seismic energy, as already discussed. Frequency tuning, on the other hand, occurs for layer thicknesses of one-quarter period or less. Robertson and Nogami (1984) used instantaneous frequency sections to study thin, porous sandstone lenses based on this phenomenon.

Deterministic Tuning Curves

Tuning phenomena are usually described by graphs such as those of Figure 6-6. In this simple form the principles of tuning are well understood and widely published (for example, see Neidell and Poggiagliolmi, 1977). Figure 6-6 shows that measured thickness, indicated by

Downloaded 25 Jun 2012 to 129.110.5.90. Redistribution subject to SEG license or copyright; Terms of Use: http://segdl.org/

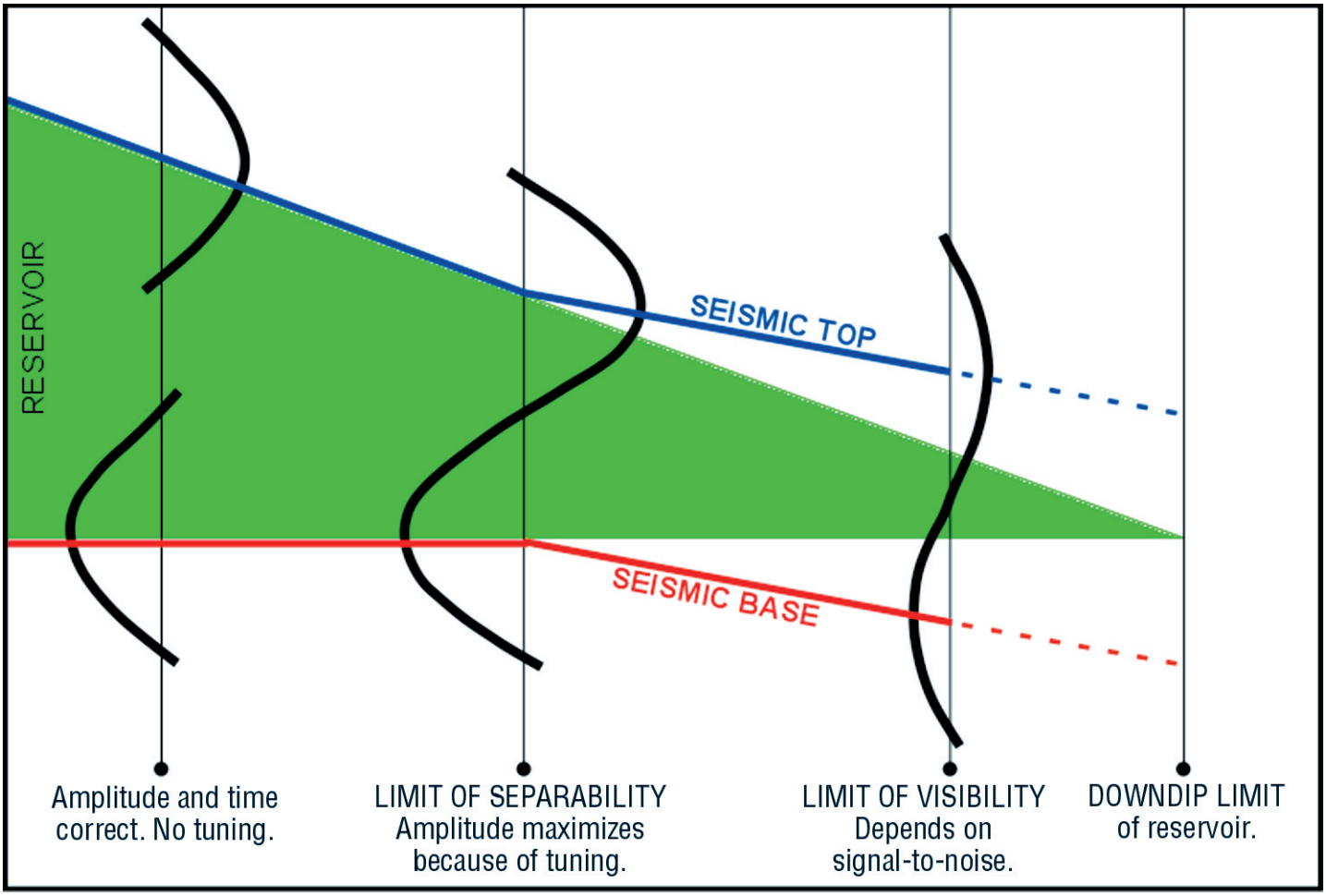
RESERVOIR
SEISMIC TOP
SEISMIC BASE
Amplitude and time correct. No tuning.
LIMIT OF SEPARABILITY Amplitude maximizes because of tuning.
LIMIT OF VISIBILITY Depends on signal-to-noise.
DOWNDIP LIMIT of reservoir.

Fig. 6-2. Tuning effects in both amplitude and time applicable to zero-phase wavelets for a thinning wedge such as occurs between reservoir top and fluid contact reflections near a downdip reservoir limit.

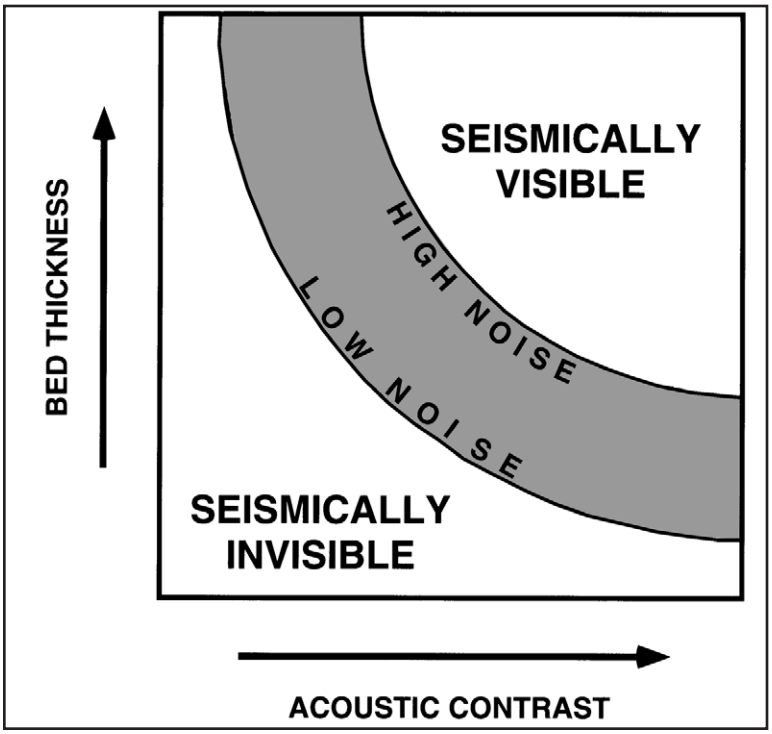

Fig. 6-3. Limit of seismic visibility depends on acoustic contrast of reservoir interfaces, noise level and wavelet shape. (After Meckel and Nath, 1977.)

Downloaded 25 Jun 2012 to 129.110.5.90. Redistribution subject to SEG license or copyright; Terms of Use: http://segdl.org/

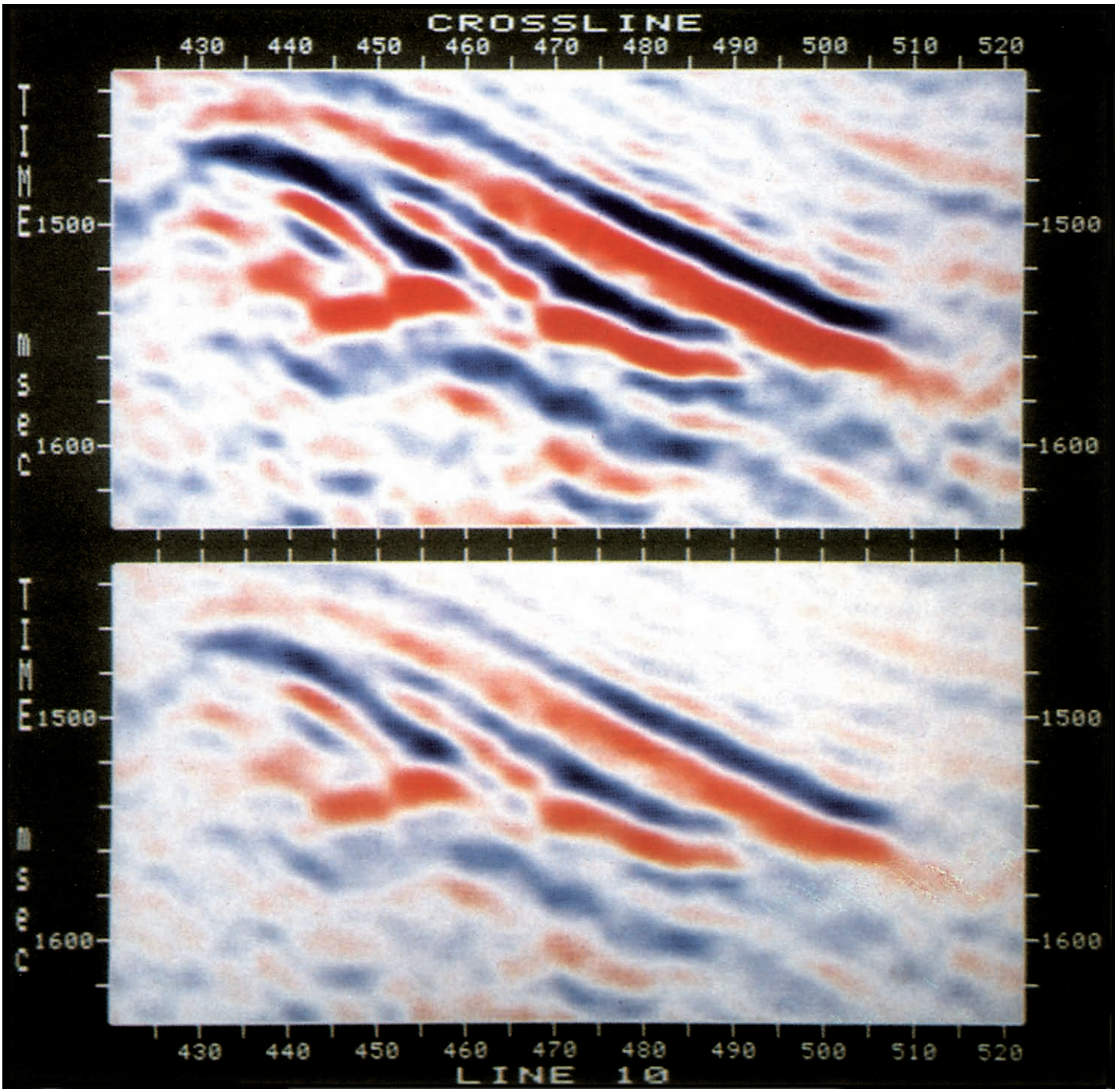

Fig. 6-4. High-amplitude reflections from gas sands of variable thickness showing tuning effects in amplitude and time as events converge. The two panels are the same data with different gains to aid the observation of some of the subtle amplitude effects on the printed page. (Courtesy Chevron U.S.A. Inc.)

the time separation of the reflections from the top and base of a bed, is only an acceptable measure of the true thickness of the bed for thicknesses above the tuning thickness. Also at tuning thickness the amplitude of the reflections reaches a maximum due to constructive interference between the reflected energy from the top and bottom of the bed.

The upper diagram of Figure 6-7 shows how the wavelets from the top and the base of a sand bed must be aligned to produce the principal tuning amplitude maximum; here it is assumed that the reflection coefficients are equal in magnitude and opposite in polarity. It is apparent that the shape of the tuning curve is dependent on the shape of the side lobes of the wavelet. Constructive interference occurs when the central peak of the wavelet from the base of the sand is aligned with the *first* negative side lobe of the wavelet from the top of the sand.

The lower diagram of Figure 6-7 shows how a second tuning maximum is caused. In this

Downloaded 25 Jun 2012 to 129.110.5.90. Redistribution subject to SEG license or copyright; Terms of Use: http://segdl.org/

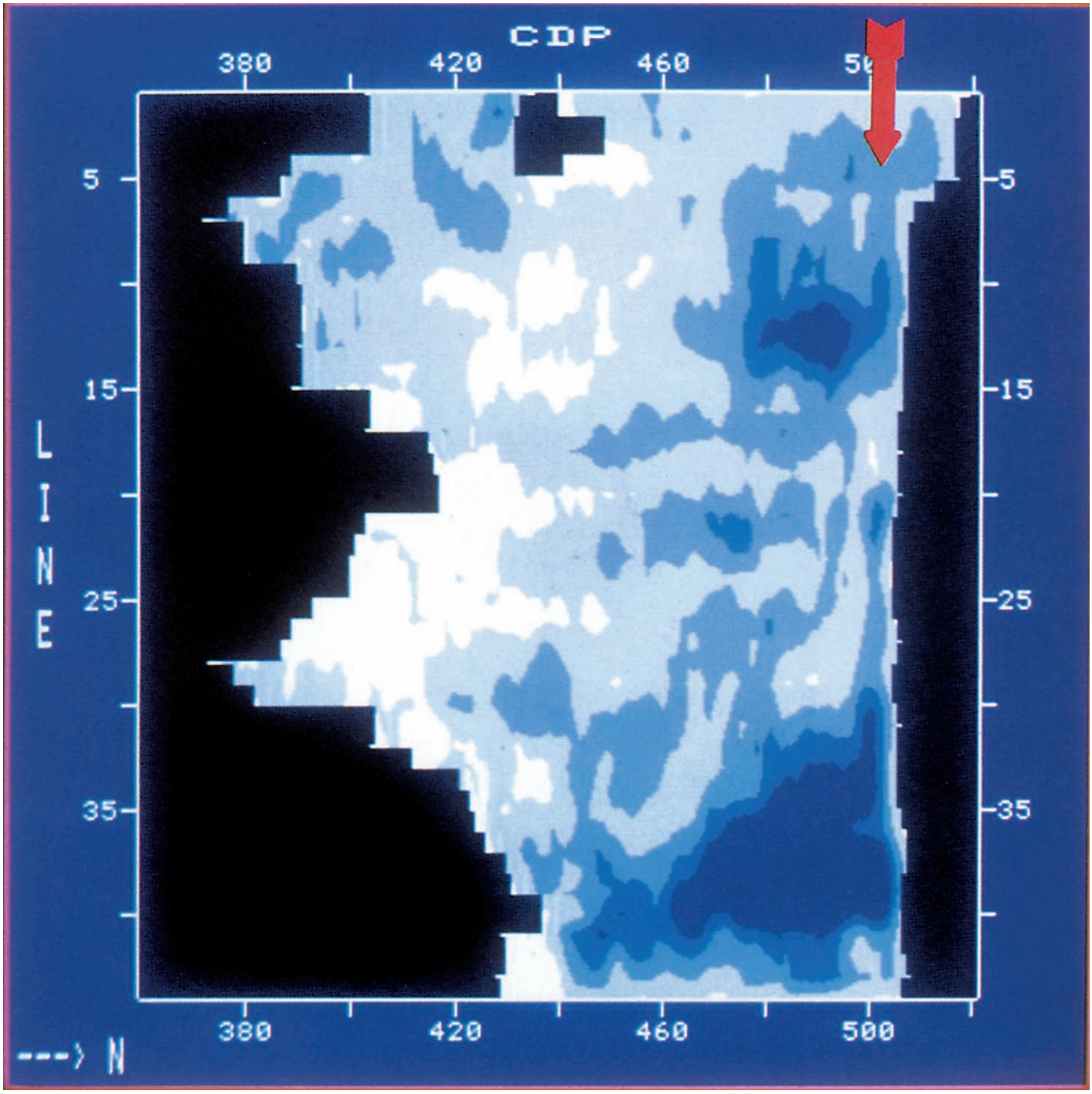

case the central peak of the wavelet from the base of the sand is aligned with the *second* negative side lobe of the wavelet from the top. Hence multiple wavelet side lobes generate multiple maxima in the tuning curve. Kallweit and Wood (1982) studied the resolving power of zero-phase wavelets and reported multiple maxima in their tuning curves (Figure 6-8).

Figure 6-9 illustrates deterministic tuning curves derived from four different wavelets. At the top of the page the Ricker wavelet has no side lobes beyond the first and consequently the tuning curve determined from it has only one maximum. This is the classical type of tuning curve, similar to that illustrated in Figure 6-6 and to that published by Meckel and Nath (1977).

The second wavelet in Figure 6-9 is a zero-phase wavelet derived from four corner frequencies defining a band-pass filter. It has, as can be seen, the same width of central peak as the Ricker wavelet but otherwise was randomly selected. This wavelet simply illustrates that multiple

Fig. 6-5. Horizon slice over reservoir top where structural dip is to the north (right). Close to the downdip limit, running top-to-bottom, an amplitude lineation in locally darker blues (in line with the red arrow) indicates the trend along which the reservoir thickness is equal to the tuning thickness. (Courtesy Chevron U.S.A. Inc.)

Downloaded 25 Jun 2012 to 129.110.5.90. Redistribution subject to SEG license or copyright; Terms of Use: http://segdl.org/

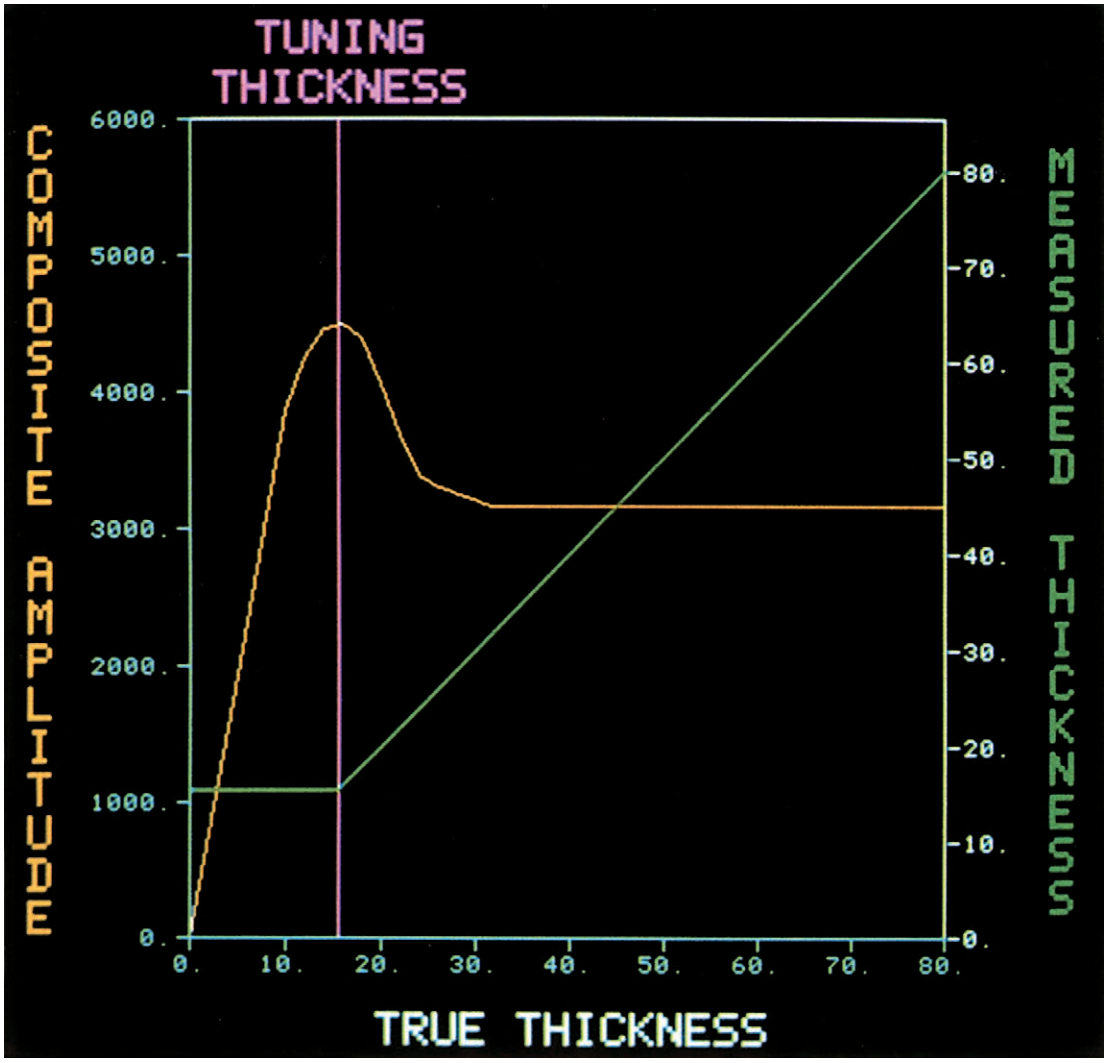

Fig. 6-6. Basic concepts of tuning for thin beds.

side lobes in the wavelet generate multiple maxima in the tuning curve. In fact it is interesting to note the similarity in shape between the tuning curve and half of the wavelet upside-down.

The third wavelet is again zero phase. Its simpler shape generated only two maxima in the tuning curve.

The fourth wavelet in Figure 6-9 was extracted from zero-phase data by a cross-correlation technique between the processed seismic trace and the synthetic seismogram at a well. The wavelet is seen to be almost, but not quite, zero phase. The deterministic tuning curve derived from the extracted wavelet shows some complexity but principally two maxima.

An amplitude spectrum was generated from this tuning curve. By interpreting this spectrum in terms of four corner frequencies it was possible to compute an ideal zero-phase equivalent wavelet and its tuning curve. For the extracted wavelet at the bottom of Figure 6-9 the ideal zero-phase equivalent wavelet is shown directly above as the third wavelet on the page.

In a practical situation the interpreter may be striving for a tuning curve applicable to the zone of interest over some broad area of a prospect. Inevitably, the interpreter will wonder whether a deviation from zero-phaseness such as that shown by the extracted wavelet at the bottom of Figure 6-9 is applicable to the whole area. He may reasonably consider the ideal zero-phase equivalent wavelet and its tuning curve to be more universal.

Statistical Tuning Curves

Tracked horizon data in time, amplitude and other attributes are normally mapped before drawing conclusions from it. It is also possible to crossplot one attribute against another from the same subsurface position. Crossplotting operates within a user-specified subsurface area.

Downloaded 25 Jun 2012 to 129.110.5.90. Redistribution subject to SEG license or copyright; Terms of Use: http://segdl.org/

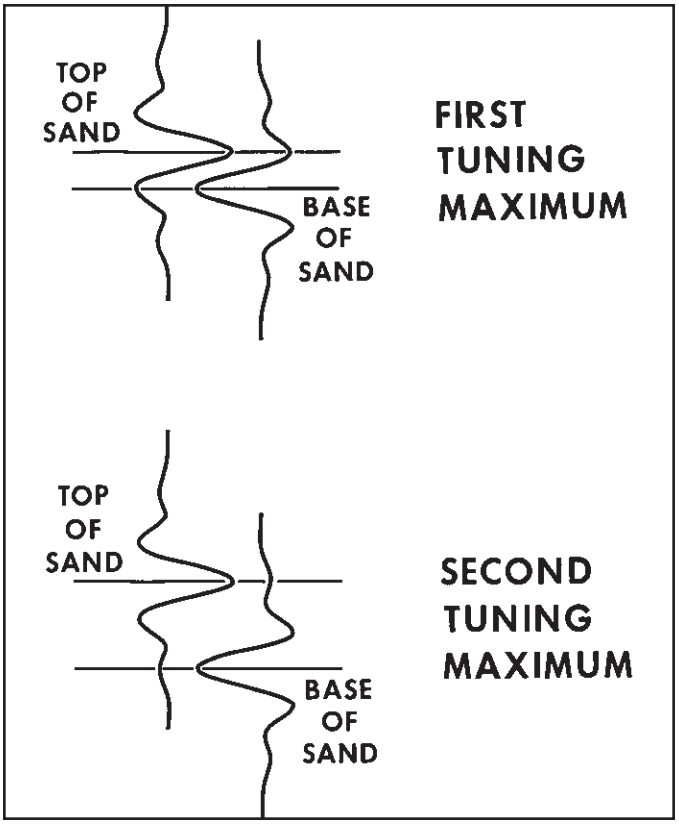

Fig. 6-7. Constructive interference of zero-phase wavelets to produce tuning maxima.

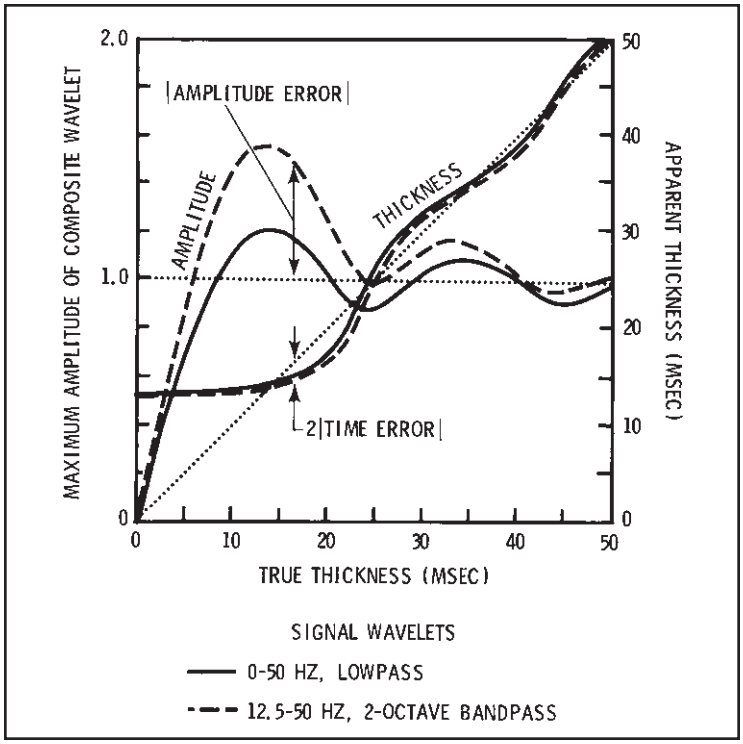

Fig. 6-8. Tuning curves for two zero-phase wavelets showing multiple-amplitude maxima (after Kallweit and Wood, 1982).

With this capability statistical analysis of horizon data can be an important part of interactive interpretation.

In studying the detailed character of bright spots and the tuning phenomena therein, it may be desirable to make the simplifying assumption that lateral variations in amplitude are due to lithologic changes in the reservoir or to tuning effects, and *not* due to changes in the acoustic properties of the embedding media. Figure 6-10 shows a crossplot of the top sand amplitudes against the base sand amplitudes for a particular reservoir. The general proportionality between the two as indicated by the extension of the points along the diagonal yellow line indicates that, to a first approximation, the lateral changes in amplitude do result from lateral changes within the reservoir rather than in the encasing material.

In pursuing the more quantitative study of reservoirs (Chapter 7), the absolute value summation of top and base reservoir amplitudes accentuates the properties of the reservoir, lithologic or geometric, relative to those of the encasing material. This absolute value summation is referred to as composite amplitude. Figure 6-11 shows a crossplot of composite amplitude against gross isochron (that is, measured thickness). These are the parameters for studying tuning (Figure 6-6), so Figure 6-11 is a statistical approach to the determination of tuning effects.

The principal maximum in composite amplitude (Figure 6-11) occurs at 16 ms, the tuning thickness. In addition there is a second maximum evident at about 35 ms. The meaning of these two maxima in terms of wavelet interaction was explained schematically in Figure 6-7. The first interpretation of a statistical tuning curve from this crossplot is then the envelope of the plotted points (Figure 6-12). This is based on the assumption that the highest amplitude points all indicate the maximum acoustic response of the interval under study and therefore that the variable shape of this envelope with isochron indicates geometric effects alone.

The horizontal blue line to the right of Figure 6-12 is the baseline and indicates the maximum untuned amplitude. The ratio of the amplitude of the tuning maximum to this baseline value is controlled by the side lobe levels of the interfering wavelets. On this basis the tuning maxima as

Downloaded 25 Jun 2012 to 129.110.5.90. Redistribution subject to SEG license or copyright; Terms of Use: http://segdl.org/

Fig. 6-9. Various wavelets and their corresponding deterministic tuning curves.

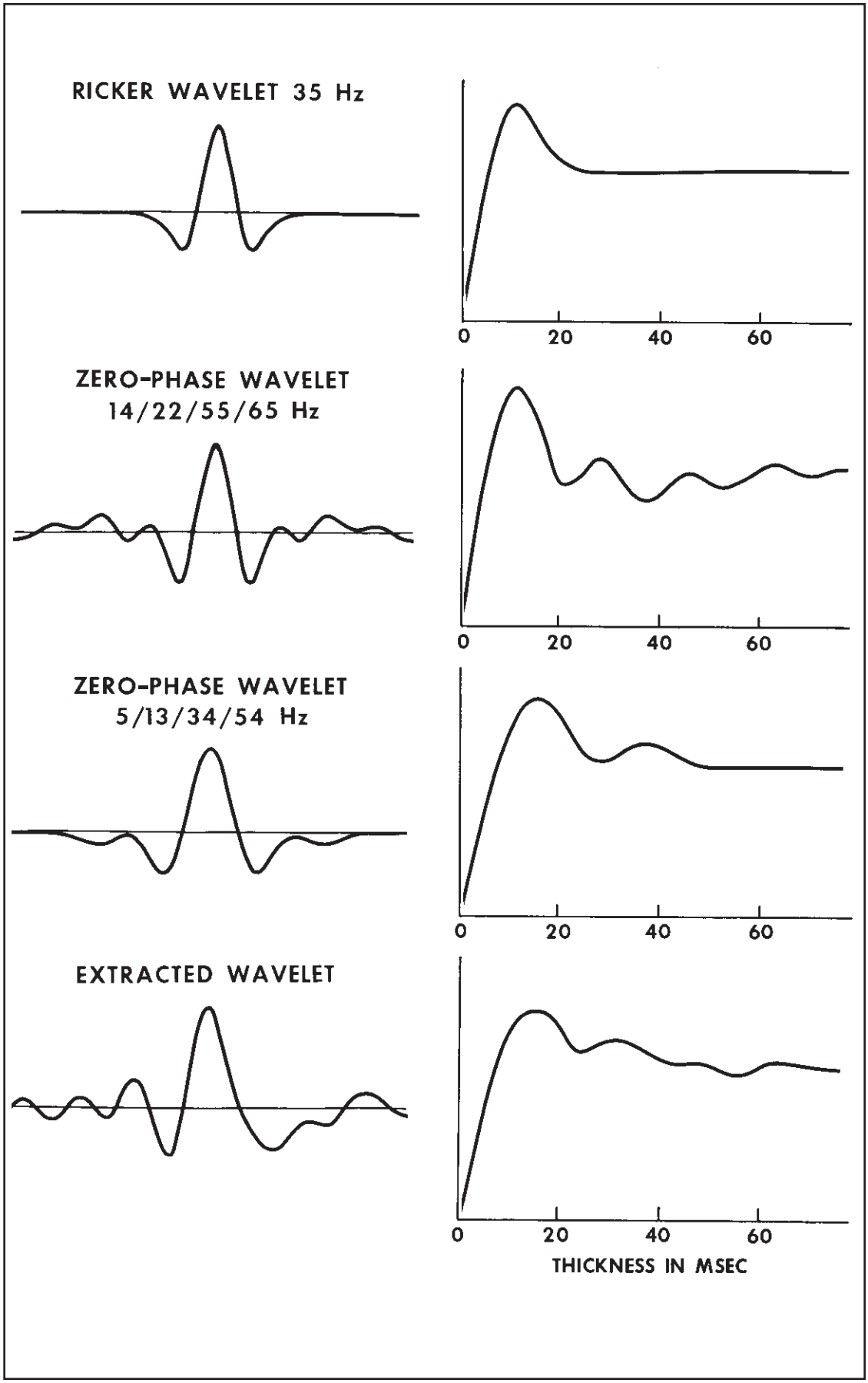

Downloaded 25 Jun 2012 to 129.110.5.90. Redistribution subject to SEG license or copyright; Terms of Use: http://segdl.org/

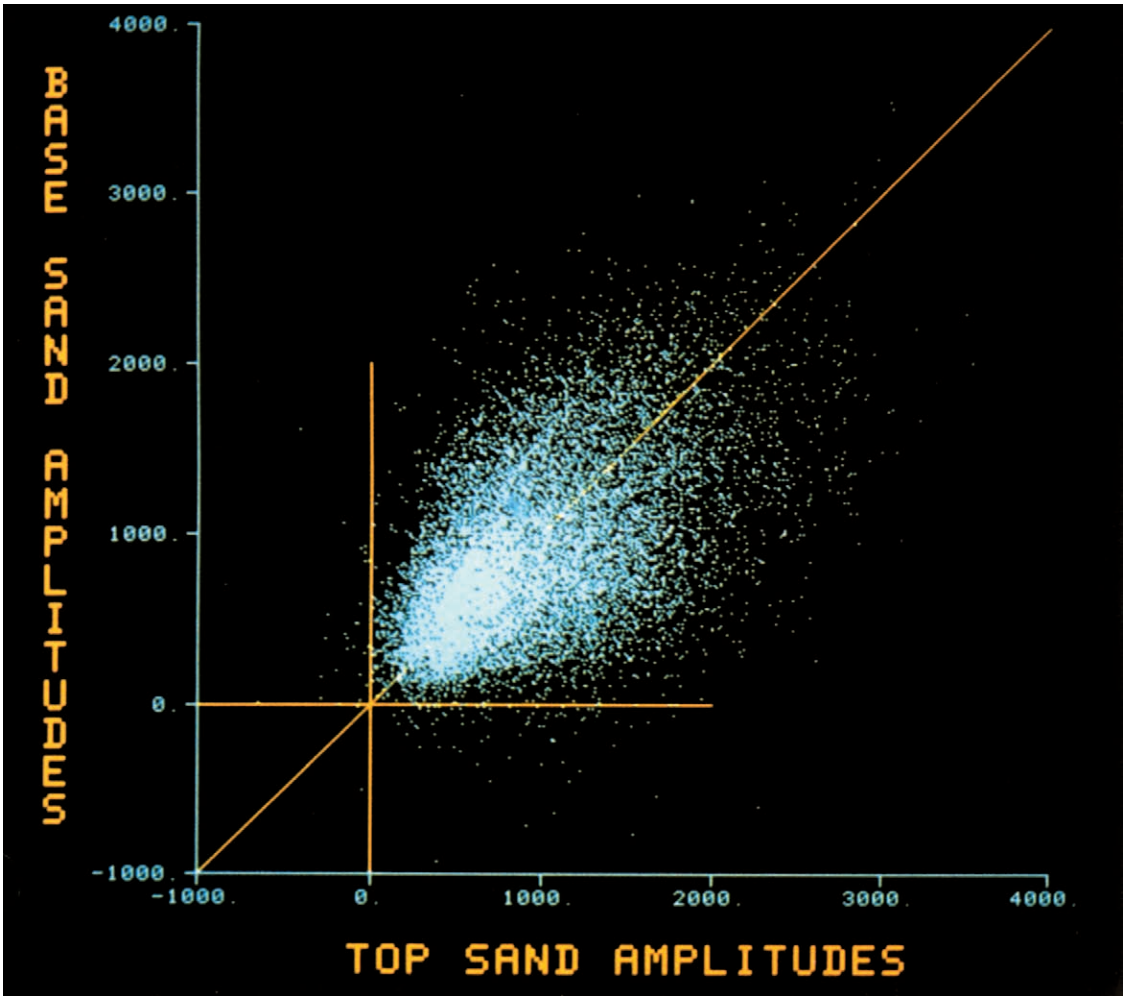

Fig. 6-10. Interactive crossplot of base sand amplitudes against top sand amplitudes, demonstrating approximate proportionality.

drawn in Figure 6-12 are too high. Considering the very large number of points plotted for isochrons in the 10-40 ms range, it is reasonable that some amplitudes are spuriously high because of constructive interference of the already-tuned reflections with nonreservoir interfaces, multiples or noise. In Figure 6-13, 99th percentile points computed over 2 ms isochron gates are plotted as blue asterisks. They fall at more reasonable levels relative to the untuned baseline.

Hence the existence of two maxima in the tuning curve was indicated by the raw crossplot, but a statistical analysis of the points guided by the knowledge of the deterministic tuning curve was required to establish the shape of the final curve. This final interpreted curve is shown in yellow in Figure 6-13.

Figure 6-14 shows the deterministic tuning curve points and the final interpreted curve superimposed on the same crossplot. Deterministic tuning curves have arbitrary vertical scales. Hence it was necessary to interpretively judge the factor by which the deterministic points must be scaled so that they could be plotted on the same composite amplitude axis as the crossplot points. This was done by matching the deterministic points to the crossplot envelope at the greater thicknesses where little or no tuning effect exists, and was confirmed by plotting the model response at a control well. The yellow curve in Figures 6-13 and 6-14 is the same. It is repeated to demonstrate how the final interpreted tuning curve for the area under study tied both the statistical and deterministic inputs.

Understanding the Magnitude of Tuning Effects

Interpreters sometimes try to explain as reservoir tuning effects amplitude phenomena which really cannot be explained that way. Understanding wavelet shape is the key to understanding what reasonably can or cannot be interpreted as a tuning effect.

Figure 6-15 shows four zero-phase wavelets of different bandwidths. The lowest frequency in the band is held the same while the highest frequency is progressively increased by a full

Downloaded 25 Jun 2012 to 129.110.5.90. Redistribution subject to SEG license or copyright; Terms of Use: http://segdl.org/

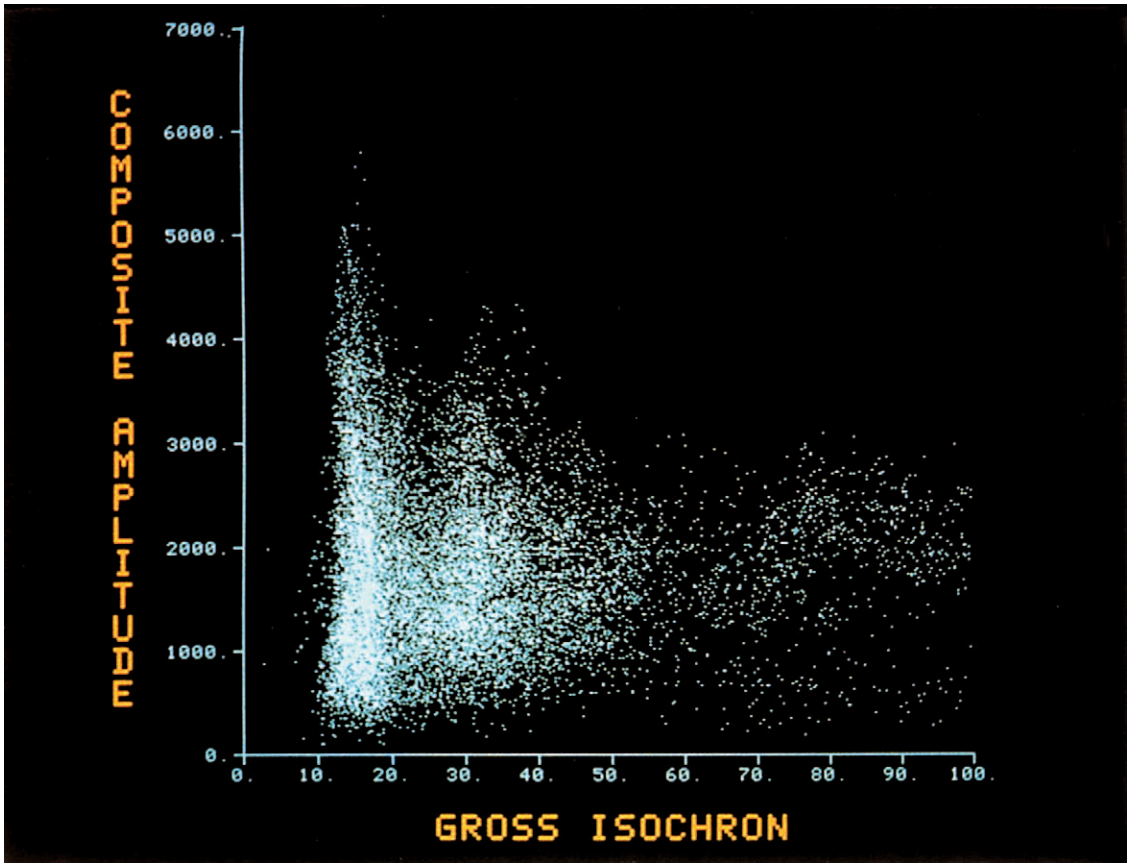

Fig. 6-11. Interactive crossplot of composite amplitude against gross thickness of a reservoir interval for all the interpreted data points in a prospect.

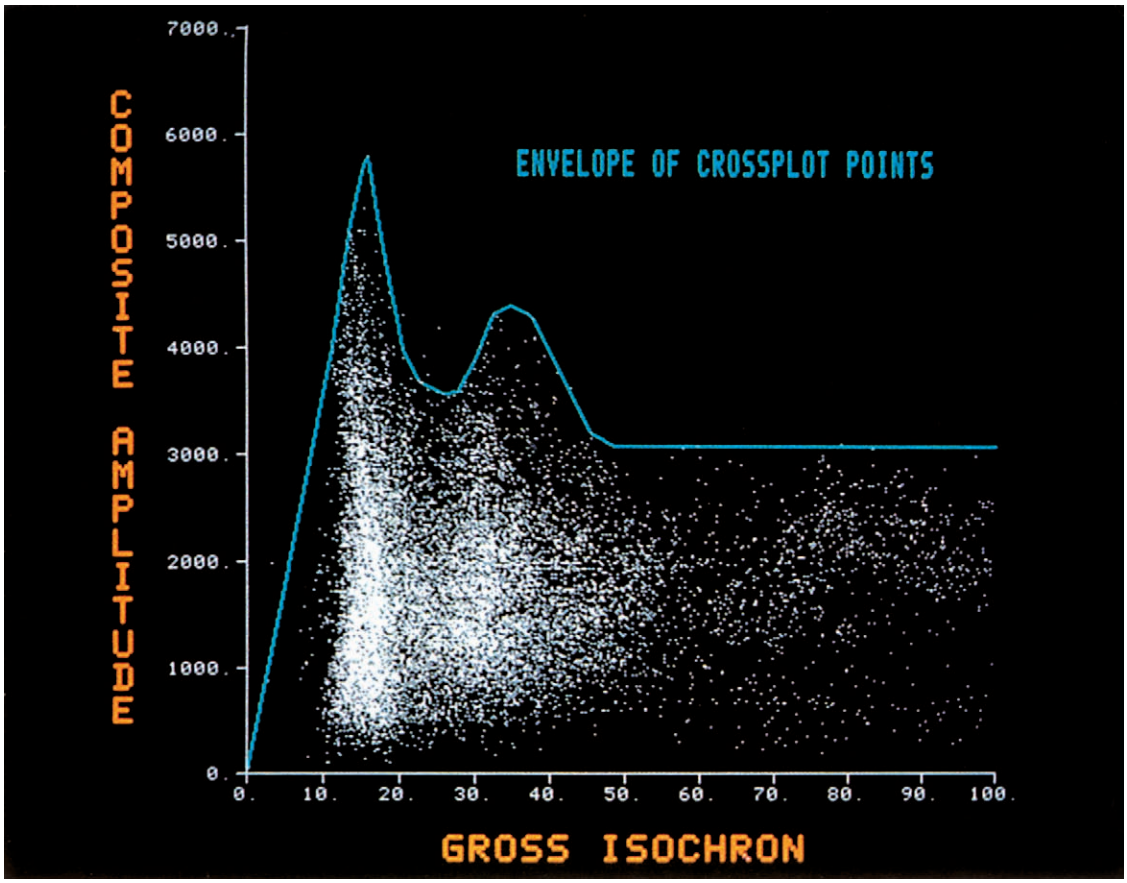

Fig. 6-12. Same crossplot as Figure 6-11 with upper envelope drawn as a first interpretation of a statistical tuning curve.

Downloaded 25 Jun 2012 to 129.110.5.90. Redistribution subject to SEG license or copyright; Terms of Use: http://segdl.org/

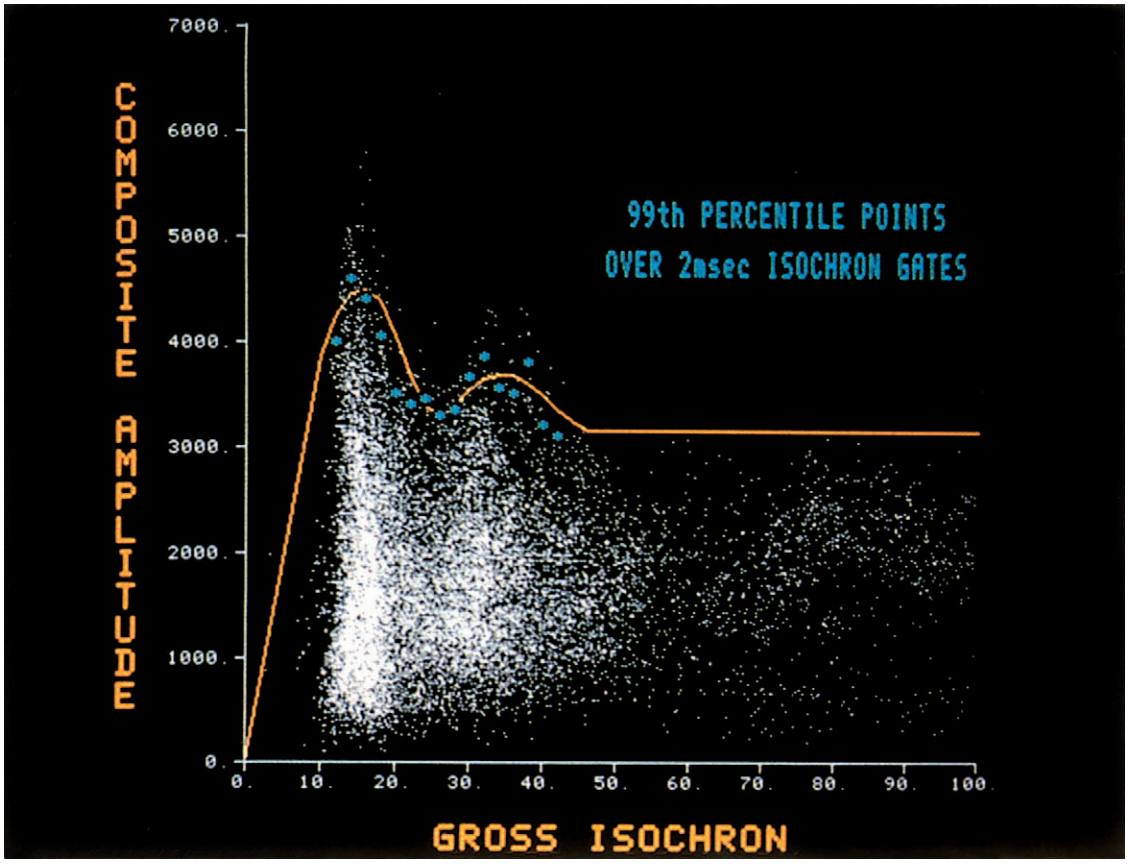

Fig. 6-13. Same crossplot as Figure 6-11 analyzed to yield 99th percentile points which show a more realistic peak-to-baseline ratio as required by deterministic studies.

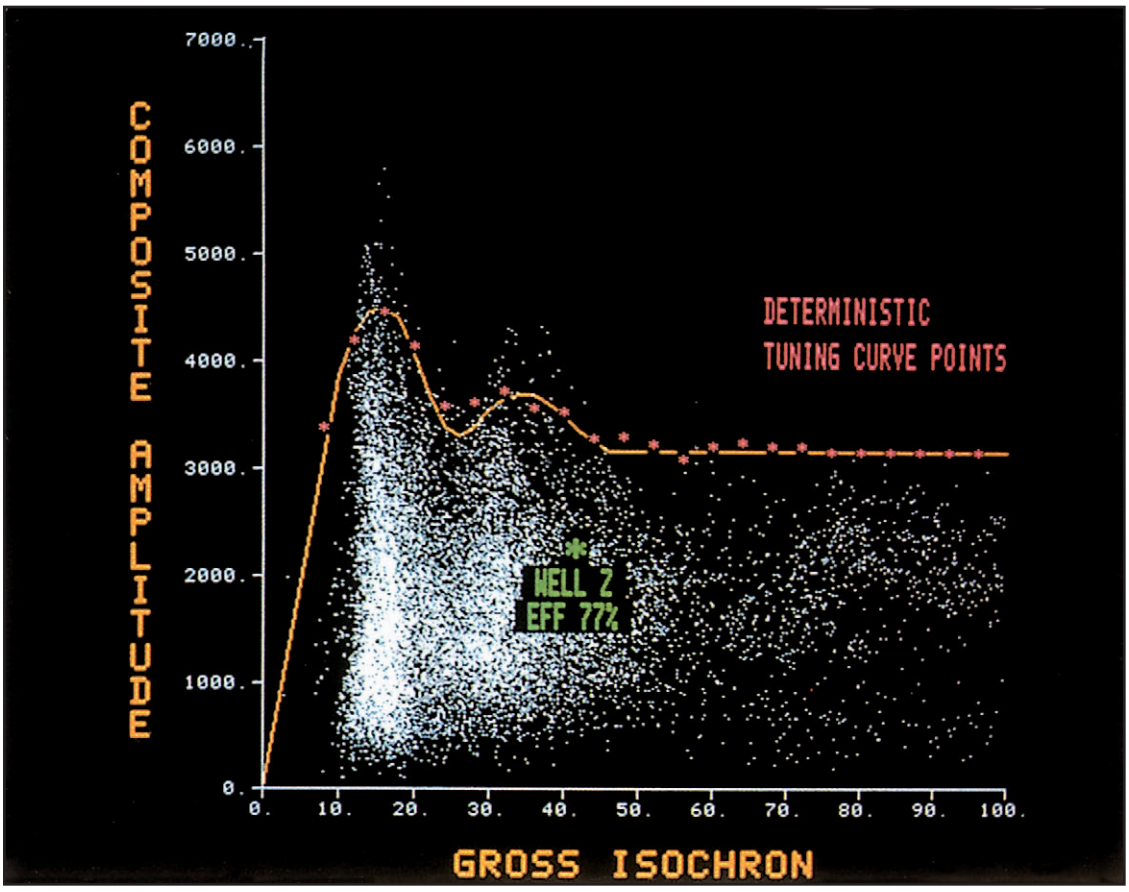

Fig. 6-14. Same crossplot as Figure 6-11 with deterministic tuning curve points computed from an extracted wavelet. The yellow final interpreted tuning curve is the same as in Figure 6-13 to provide comparison between statistical and deterministic tuning points.

Downloaded 25 Jun 2012 to 129.110.5.90. Redistribution subject to SEG license or copyright; Terms of Use: http://segdl.org/

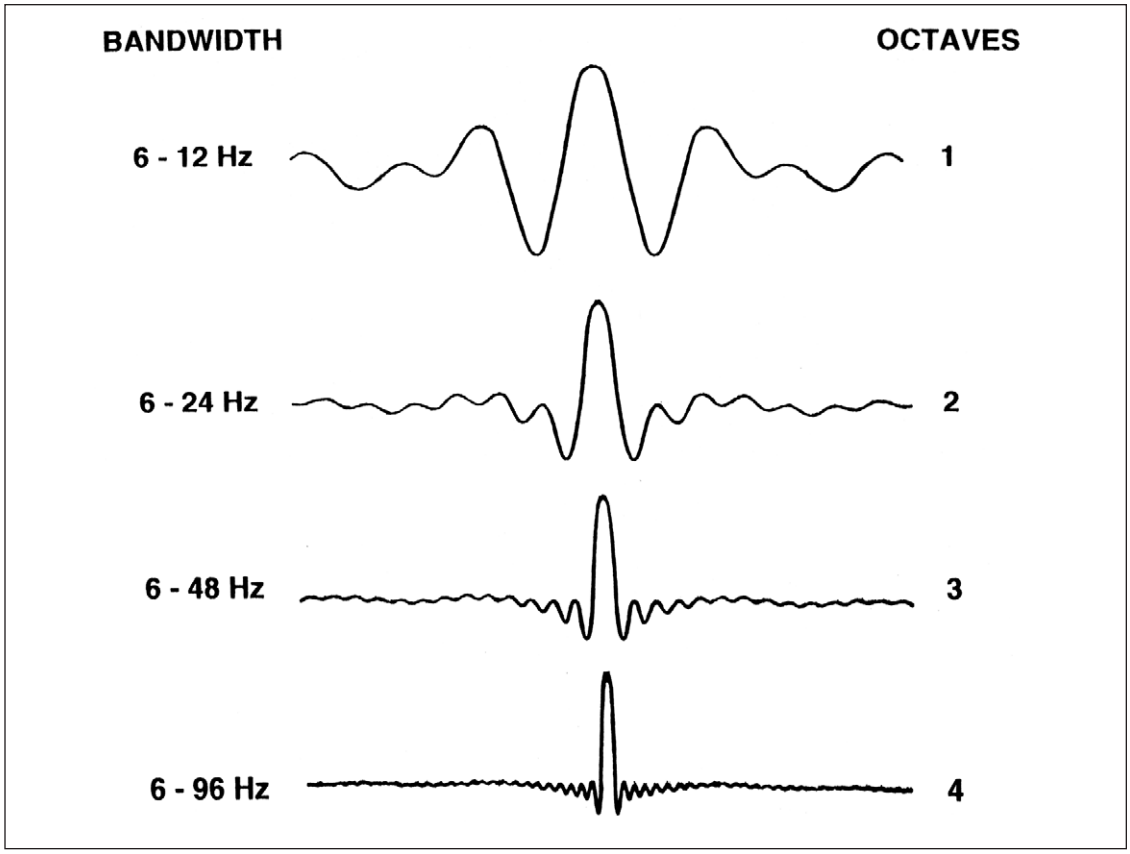

Fig. 6-15. Four zero-phase wavelets of different bandwidths demonstrating the effect of bandwidth on side lobe size and hence the magnitude of tuning effects.

octave from one wavelet to the next. The center lobe of the wavelet narrows considerably but what we are concerned with here is the size of the first side lobe. Notice that the first side lobe is about the same size as the center lobe for the one octave wavelet; the first side lobe is about half the center lobe for two octaves; it is about a third of the center lobe for three octaves; and it is about a quarter for four octaves. Thus we can establish a generalized rule-of-thumb, that *the first side lobe as a fraction of the center lobe of a zero-phase wavelet is the reciprocal of the octave bandwidth*. Furthermore a typical bandwidth for good but not exceptional seismic data today is two-and-one-half octaves; this gives a side lobe level of 40% relative to the wavelet's center lobe.

I call this the "40% rule"; it is an approximate but very useful rule-of-thumb. Figure 6-7 demonstrates that the size of the wavelet side lobe controls the magnitude of the tuning effects. Thus the 40% rule means that 40% is a common increase in amplitude at tuning for zero-phase wavelets reflected from the top and base of a reservoir layer. Increases in amplitude much greater than this must be explained some other way. A lateral amplitude increase of 40% is not dramatic even when using the highest dynamic range color scheme. It follows that dramatic amplitude changes which we observe in our data are unlikely to be simple tuning effects.

Well Tying and Tuning Effects

The mispositioning of reflections caused by tuning effects in time was discussed above and illustrated in Figure 6-2. Consider now Figure 6-16. The log on the left shows a good reservoir response and the seismic trace on the right shows high-amplitude reflections from top and base of this reservoir. The log was measured in depth and the seismic data in travel time, but here they have been laid accurately side-by-side using a perfect velocity relationship. Note that the seismic reflections at P and T do not exactly correspond to the top and base of the reservoir on the log because the reservoir is less than one-quarter wavelength in thickness. Thus the interpreter must match the seismic response to the well response *on character*, taking account of this tuning mispositioning. This situation is of course further complicated if the data are not zero phase or are of unknown polarity.

Downloaded 25 Jun 2012 to 129.110.5.90. Redistribution subject to SEG license or copyright; Terms of Use: http://segdl.org/

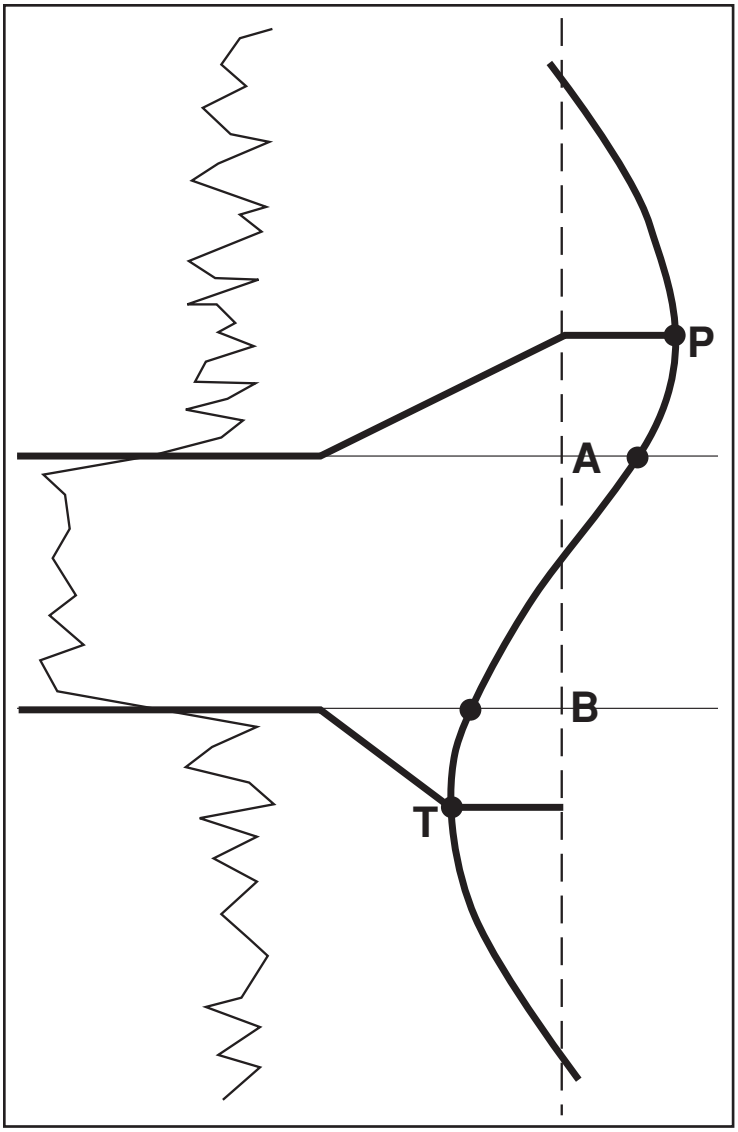

Fig. 6-16. Porous sand, with or without hydrocarbons, typically has a sonic or impedance log similar to that on the left. Corresponding seismic response in European polarity is shown on right. The amplitudes that should be used to characterize this reservoir are to be found at P and T, and not over the directly corresponding interval AB.

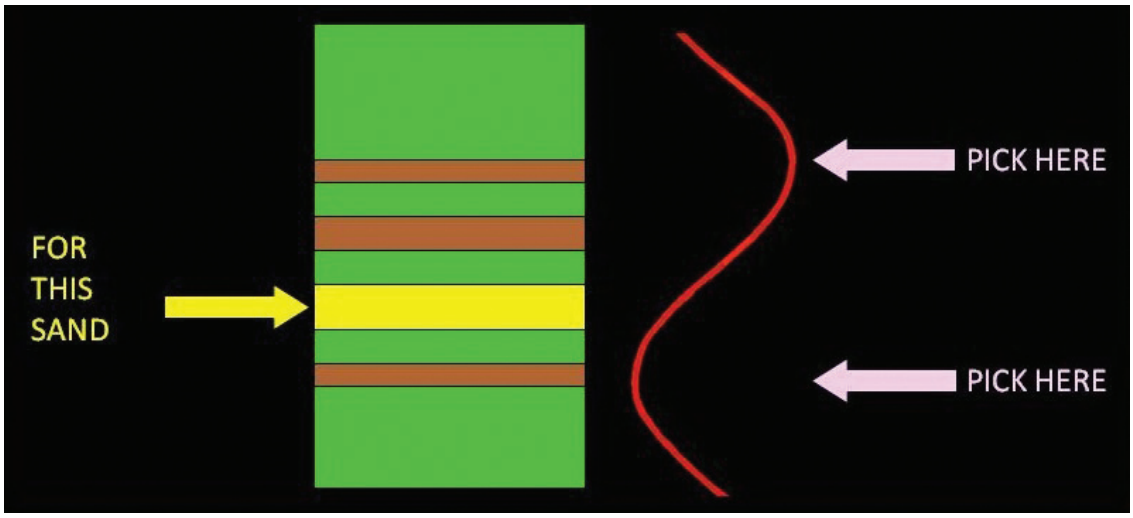

Fig. 6-17. Working with thin beds between the Limit of Separability and the Limit of Visibility. Pick on the waveform crest.

Downloaded 25 Jun 2012 to 129.110.5.90. Redistribution subject to SEG license or copyright; Terms of Use: http://segdl.org/

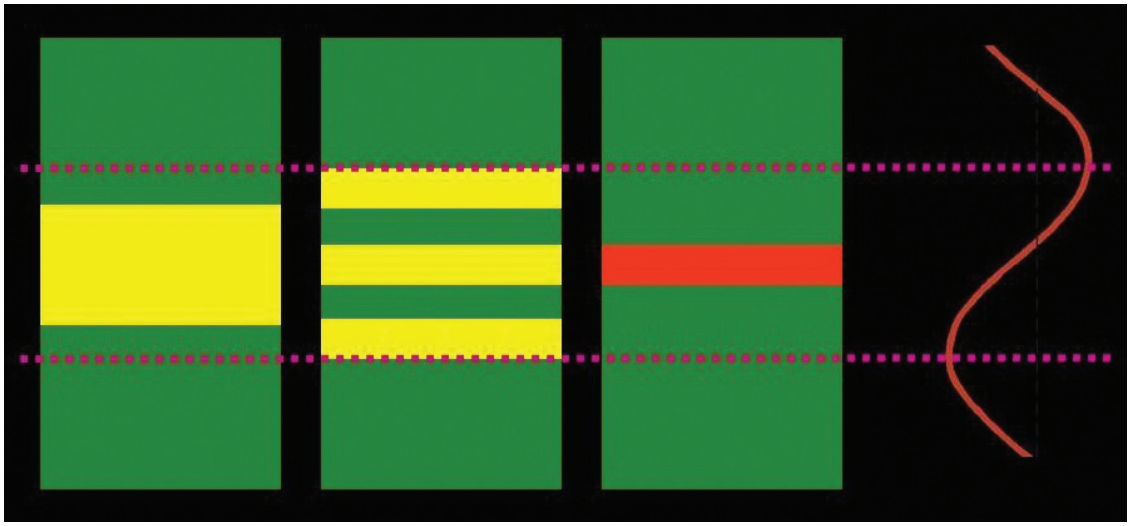

Fig. 6-18. Working with thin beds between the Limit of Separability and the Limit of Visibility. Ambiguities within the one-quarter wavelength.

Crestal points yield more reliable seismic amplitudes and attributes than do points on the waveform flank. Thus the best information to tell us about the internal nature of this reservoir in Figure 6-16 lies at points P and T. These are the amplitudes that should be extracted in a reservoir study. In fact, as will be discussed in Chapter 7, the best amplitude for the study of this reservoir is the absolute value summation of the amplitude at P and the amplitude at T. It is quite wrong to extract amplitude at points A and B, and the worst possible amplitude for the study of this reservoir is the windowed amplitude extracted over the interval AB exactly tying the reservoir on the log. This window completely misses the relevant information.

Tuning and resolution (Chapter 1) are closely related matters, the one-quarter wavelength being both the Limit of Separability and the Tuning Thickness. Because of the resolution limitations of the seismic data, reflections effectively occur at the top and base of one-quarter-wavelength-thick slabs. Thinner beds are seismically visible if they have good acoustic contrast with the embedding material. Figure 6-17 shows how we should study a thin bed whose thickness lies between the Limits of Separability and Visibility. The sand shown in yellow is our objective and we can see that its thickness is about one-twentieth of a wavelength. We should pick at the peak and trough indicated by the pink arrows; the amplitudes here are the best available for this sand but are of course contaminated by the effects of other sands within the one-quarter wavelength (shown in brown). The wrong place to pick would be at the exactly corresponding time/depth positions of the top and the base of the sand.

Because reflections are effectively from top and base of one-quarter-wavelength-thick slabs, there are ambiguities in determining the geology within these slabs. Figure 6-18 shows that one sand just below one-quarter wavelength in thickness, three thin sands of the same total thickness, and one thin gas sand with larger acoustic contrast, can all have the same seismic response.

References

Kallweit, R. S., and L. C. Wood, 1982, The limits of resolution of zero-phase wavelets: Geophysics, v. 47, p. 1035–1046.

Meckel, L. D., Jr., and A. K. Nath, 1977, Geologic considerations for stratigraphic modeling and interpretation, *in* C. E. Payton, ed., Seismic stratigraphy — applications to hydrocarbon exploration: AAPG Memoir 26, p. 417–438.

Neidell, N. S., and E. Poggiagliolmi, 1977, Stratigraphic modeling and interpretation — geophysical principles and techniques, *in* C. E. Payton, ed., Seismic stratigraphy — applications to hydrocarbon exploration: AAPG Memoir 26, p. 389–416.

Robertson, J. D., and H. H. Nogami, 1984, Complex seismic trace analysis of thin beds: Geophysics, v. 49, p. 344–352.

Widess, M. B., 1973, How thin is a thin bed?: Geophysics, v. 38, p. 1176–1180.

Downloaded 25 Jun 2012 to 129.110.5.90. Redistribution subject to SEG license or copyright; Terms of Use: http://segdl.org/

Reservoir Evaluation

Reservoir evaluation, reservoir characterization or reservoir property mapping is an important use of 3-D seismic data. As presented here it is an extension of reservoir reflection identification (Chapter 5), horizon slicing techniques (Chapter 4) and tuning phenomena (Chapter 6). Further issues on reservoir evaluation follow in Chapter 8.

Reservoir Properties Deducible from Seismic Data

Figure 7-1 gives a summary list of reservoir properties needed for effective development and production of hydrocarbon reserves. The basic information in seismic data is only time, amplitude and perhaps frequency, so there are many fewer measurements than there are unknowns. Seismic attributes (Chapter 8) may be helpful but they are not new additional information. Seismic traveltime addresses structure and structural boundaries. Amplitude and frequency are left to address the other properties. Amplitude is well understood and is used widely; frequency is less well understood and tends to be noisy.

The principal reservoir properties that affect seismic amplitude can be divided into two groups:

GROUP A	GROUP B
nature of fluid	porosity
gross lithology	net pay thickness or net-to-gross ratio
pressure	lithologic detail
temperature	hydrocarbon saturation

The properties in Group A are those which, to a first approximation, affect the reservoir as a whole. The difference between gas and oil was discussed in Chapter 5. The

RESERVOIR INFORMATION NEEDED	WILL 3-D SEISMIC PROVIDE ?
Structure	Generally yes
Reservoir boundaries	Generally yes
Fluid content & contacts	Yes for younger rocks
Porosity	Generally yes
Hydrocarbon saturation	Difficult but possible for younger rocks
Net pay or net sand	Generally yes
Permeability	No
Connectivity / flow units	Sometimes
Aquifer / drive mechanisms	Partially yes
Heterogeneities	all with resolution limitations

Fig. 7-1. Reservoir information needed for effective exploitation and the generalized ability of 3-D seismic data to help in providing it.

Downloaded 25 Jun 2012 to 129.110.5.90. Redistribution subject to SEG license or copyright; Terms of Use: http://segdl.org/

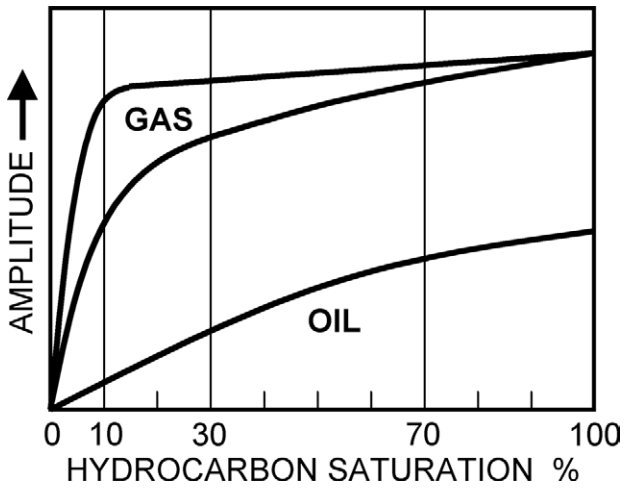

Fig. 7-2. Amplitude varies nonlinearly with hydrocarbon saturation, particularly for gas (Domenico, 1974).

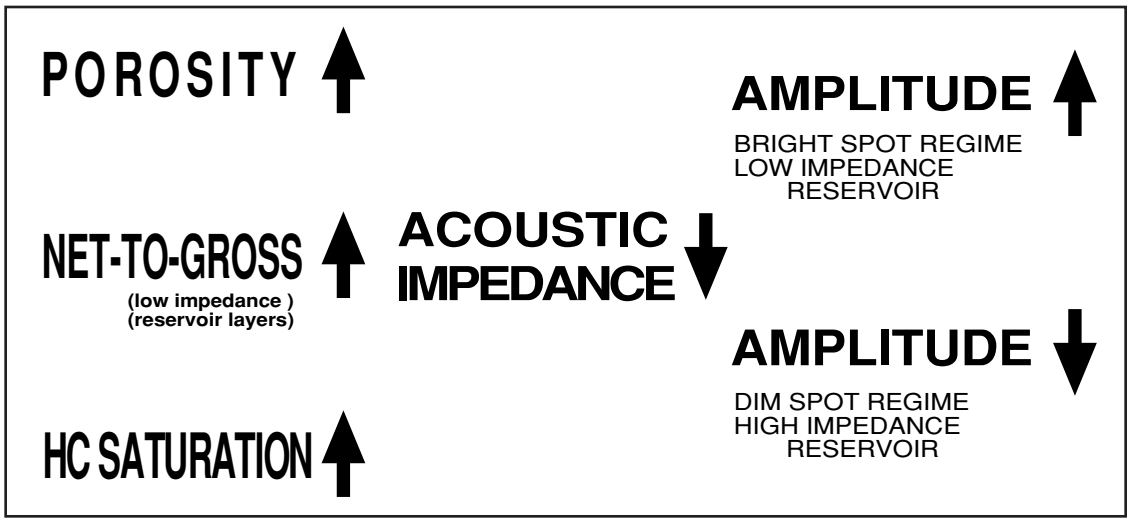

Fig. 7-3. Explanation of bright spot and dim spot regimes. In the bright spot regime high amplitude is desirable; in the dim spot regime low amplitude is desirable.

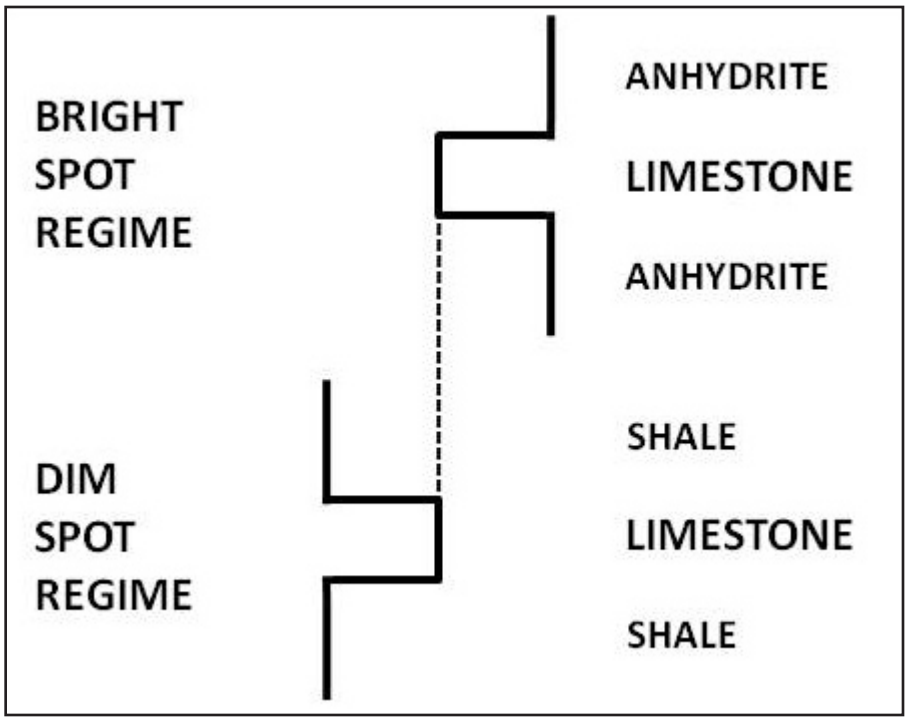

Fig. 7-4. A limestone reservoir can be either bright spot regime or dim spot regime, depending on the rock in which the limestone is embedded.

Downloaded 25 Jun 2012 to 129.110.5.90. Redistribution subject to SEG license or copyright; Terms of Use: http://segdl.org/

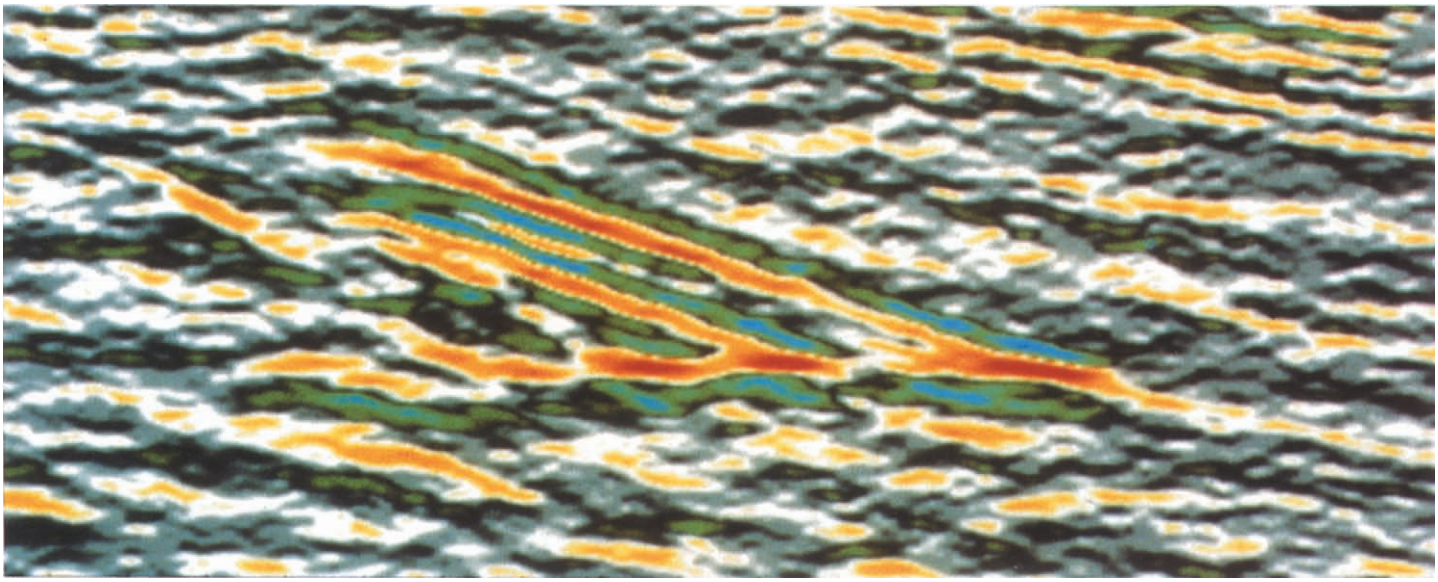

Fig. 7-5. Vertical section from Gulf of Mexico showing a thick gas reservoir filled with strong internal reflections. (Courtesy Chevron U.S.A. Inc.)

gross lithology of a reservoir rock generally does not change much within one reservoir; other related properties such as age, compaction and depth also will remain fairly constant. Anomalous reservoir pressure can affect seismic amplitude considerably but again this will generally affect the whole reservoir rather than only a part of it.

The properties in Group B are the ones which can vary laterally over short distances and therefore significantly affect the reserve estimates of a reservoir penetrated by a small number of wells. A major objective of development and production geophysics is to map these spatially-varying reservoir properties so that wells and platforms can be located optimally and reserve estimates can be made with greater precision.

Lateral changes in amplitude of reservoir reflections can be caused by changes in any one or more of these Group B properties, so there is an inherent ambiguity. The interpretive approach to reservoir evaluation thus requires that simplifying assumptions be made. Conveniently, the amplitude of a seismic bright spot is higher where hydrocarbon saturation is higher (although nonlinearly, as shown in Figure 7-2) where porosity is higher and where net pay thickness is greater (with some complications due to tuning). It normally follows, therefore, that the brighter the bright spot, the better the prospect. This relationship is generalized in Figure 7-3. Increasing porosity, net-to-gross and saturation all make the reservoir acoustic impedance lower. The reservoir "sweet spots" are thus the low-impedance areas. In the bright spot regime the amplitude of the reservoir reflections is then higher. This includes hydrocarbon bright spots but is not limited to them — any already low-impedance reservoir will get lower and thus generate more amplitude. In the dim spot regime the reverse occurs. Here the reservoir is higher acoustic impedance than the embedding medium, so reducing impedance reduces contrast and thus amplitude. Clearly the most important seismic property of a reservoir is whether it is bright spot or dim spot regime. In the former, high amplitude is good and the distribution of amplitude on the horizon slice guides development drilling (e.g., Figures 2-35 to 2-37). The reservoirs discussed in this chapter are in the bright spot regime. Case History 9 (Chapter 14) discusses a dim spot regime reservoir and another good example is illustrated in Figure 4-51.

Downloaded 25 Jun 2012 to 129.110.5.90. Redistribution subject to SEG license or copyright; Terms of Use: http://segdl.org/

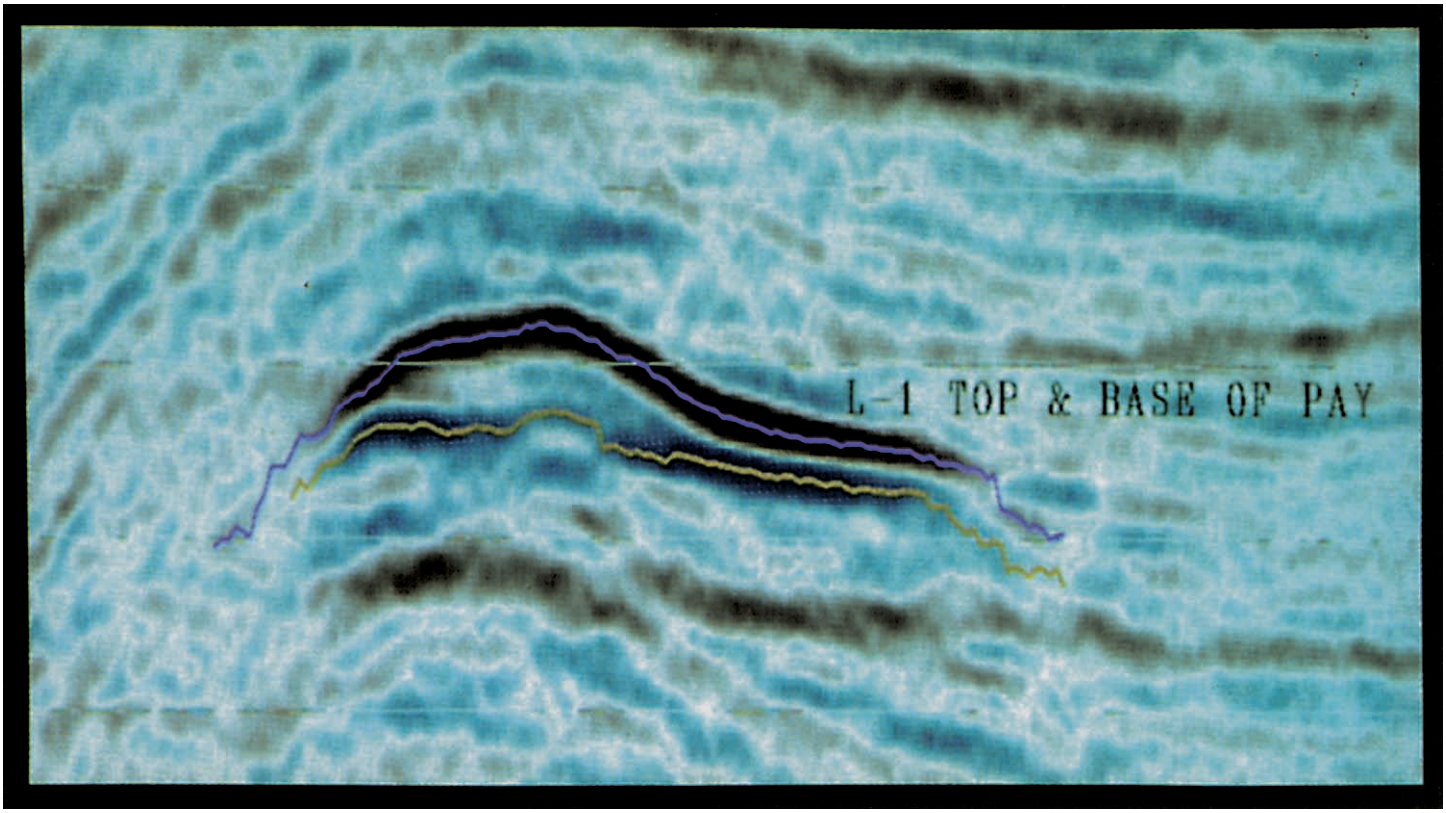

Fig. 7-6. Vertical section through a Gulf of Mexico gas reservoir showing high-amplitude reflections at the top and base of the gas. The automatic horizon track on the top reservoir reflection provided the amplitudes displayed in Figure 7-7. (Courtesy CNG Producing Company.)

Whether a reservoir exhibits bright spot regime properties or dim spot regime properties depends indeed on the impedance of the reservoir, but it also depends critically on the impedance of the embedding rocks. A limestone encased in shale (Figure 7-4) will be dim spot regime, and the sweet spots will be indicated by low amplitude, but the same limestone encased in anhydrite will be bright spot regime. An example of this latter situation is illustrated in Case History 4 (Chapter 14). For a high impedance reservoir, net-to-gross and porosity affect impedance and thus amplitude in opposite directions, thus complicating the simplicity of Figure 7-3.

Figure 7-5 illustrates a thick clastic reservoir with a strong fluid-contact reflection. The fluid-contact reflection (flat spot) appears to be stepped, suggesting the possibility of poor connectivity between reservoir compartments. In fact the steps are caused by internal reflections, illuminated by hydrocarbon (Chapter 5), tuning with the reflection from the fluid contact. This same phenomenon is visible along the flat spot of Figure 5-18.

Horizon Slices Over Reservoir Interfaces

A horizon slice showing the spatial distribution of seismic amplitude over a reservoir top or base is an enormously valuable aid for studying that reservoir. The value comes not only from spatial continuity but also from the faithful amplitude reconstruction resulting from 3-D migration. For a low acoustic impedance reservoir, high amplitude is good because it may be caused by higher net-to-gross ratio, higher porosity, or higher hydrocarbon saturation.

Figure 7-6 shows high-amplitude reflections from a Pleistocene gas reservoir. The red reflection is from the reservoir top and the blue reflection is from the fluid

Downloaded 25 Jun 2012 to 129.110.5.90. Redistribution subject to SEG license or copyright; Terms of Use: http://segdl.org/

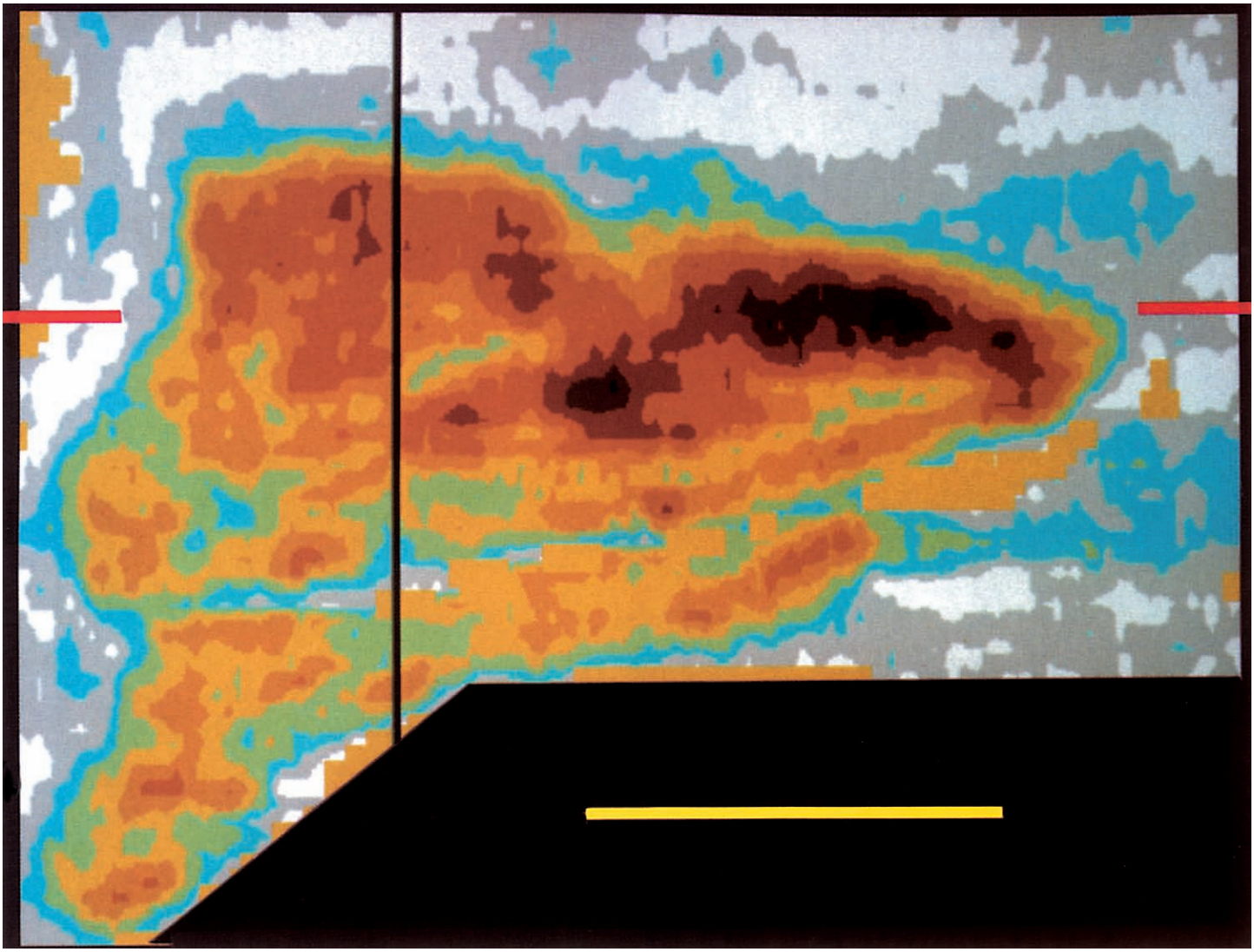

Fig. 7-7. Horizon slice from a Gulf of Mexico Pleistocene gas reservoir showing patterns in amplitude interpretable as the effects of hydrocarbon, faulting, porosity, and tuning. Yellow bar is one km. Red lines indicate the position of the vertical section in Figure 7-6. Black line is block boundary. (Courtesy CNG Producing Company.)

contact. The horizon slice in Figure 7-7 follows the maximum amplitude of the top reflection. The overall high-amplitude triangular shape indicates the extent of the gas. Along the northern dip-controlled boundary, the amplitude gradient can be extrapolated to find the actual downdip reservoir limit. Some internal roughly northeasterly lineations indicate faulting. A high-amplitude trend running N60˚E and crossing from the high-amplitude gas area into the low-amplitude surrounding area in the upper right corner is interpreted as a depositional trend of higher porosity. The high-amplitude trend running N80˚W parallel to and just south of the northern reservoir boundary is caused by tuning. Separation of different effects in this way on the basis of interlocking patterns should be a normal part of horizon slice interpretation.

Figures 7-8 and 7-9 show a structure map and horizon slice from another Gulf of Mexico field. Again, different effects can be interpreted based on their different amplitude patterns. Salt is to the northwest and gas is trapped against the salt, as indicated in red. Variable porosity in the wet sand is probably responsible for the irregular yellow patterns downdip. The high amplitudes, principally in red, following the upthrown side of fault A and spanning a structural range of 2,000 feet, can

Downloaded 25 Jun 2012 to 129.110.5.90. Redistribution subject to SEG license or copyright; Terms of Use: http://segdl.org/

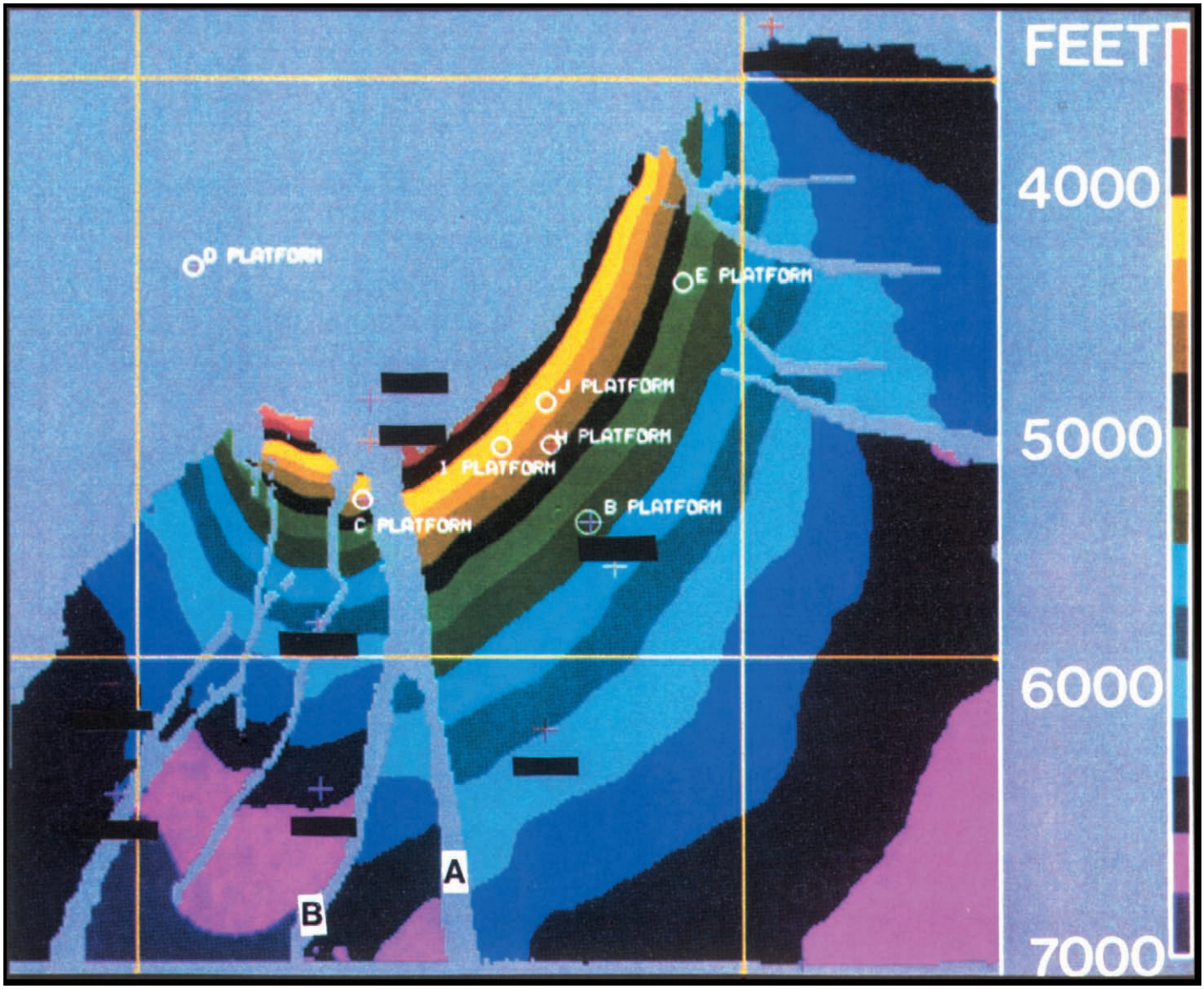

Fig. 7-8. Structure map of productive Gulf of Mexico sand showing the setting in a salt dome prospect. (Courtesy Chevron U.S.A. Inc.)

only be interpreted as gas actively migrating toward the trap. This same observation and interpretation has been made on several other horizon slices in Tertiary clastic basins, for example Figure 7-10.

Composite Amplitude

A reservoir has two seismic reflections: the one from the top and the one from the base; these constitute the available seismic information for this reservoir. Natural pairing was introduced in Chapter 2 and used extensively in Chapter 5; it is the observation that the amplitudes of the top and base reflections vary laterally in unison as reservoir properties vary. This observation should be used initially to help identify reservoir reflections.

Figure 7-11 shows top and base horizon slices for a variable clastic reservoir. Note the similarity of amplitude patterns. This is a spatial demonstration of natural pairing, and helps to confirm that the top and base reflections were correctly identified over the area. Both horizon slices show the effect of lateral variability in the reservoir, but

Downloaded 25 Jun 2012 to 129.110.5.90. Redistribution subject to SEG license or copyright; Terms of Use: http://segdl.org/

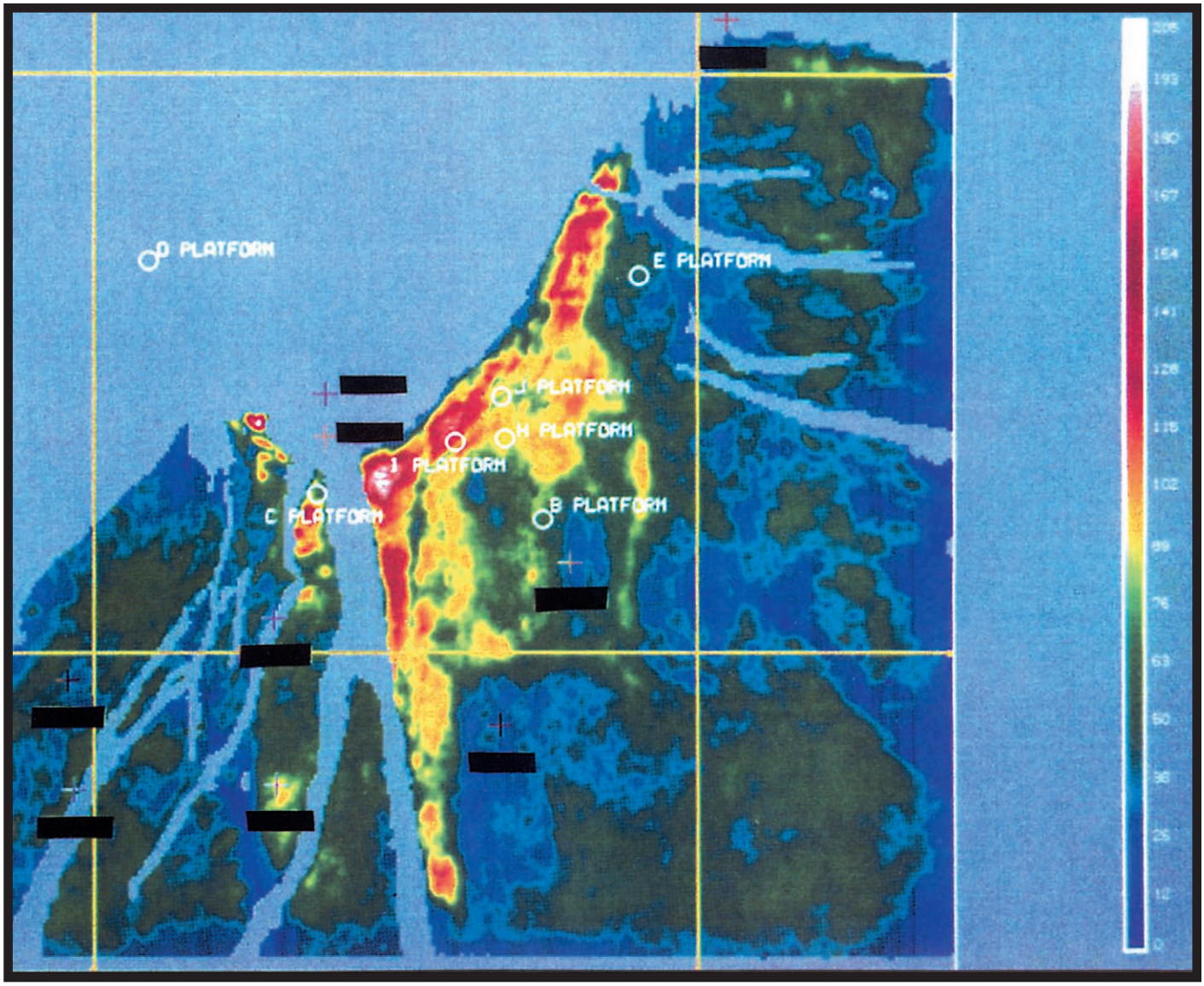

Fig. 7-9. Horizon slice corresponding to the structure map of Figure 7-8. The red colors close to the salt indicate gas. The yellows indicate a porosity overprint. The high amplitudes along the upthrown side of fault A are interpreted as hydrocarbons in migration after flowing up the fault. (Courtesy Chevron U.S.A. Inc.)

the top horizon slice also shows some effect of the overburden, and the base horizon slice also shows some effect of the underburden. Figure 7-12 is composite amplitude for this reservoir, the absolute value summation of the top and base horizon slices of Figure 7-11. This addition has emphasized the effect of the reservoir and deemphasized the effect of the embedding material. Figure 7-13 diagrams the principle of adding top and base to yield composite amplitude. In almost every situation composite amplitude is the best type of amplitude to use for the study of a reservoir.

Net Pay Thickness

In an area of Pleistocene sediments offshore Louisiana the wells indicated that each reservoir sand interval was composed of several thin productive lobes and that the position of these lobes within the sands and their thickness varied laterally over a short distance (Brown et al., 1984). The top and base of the gross sand intervals generate the seismic reflections and the nonproductive segments within them are caused by the sands becoming tight and shaly. The aggregate thickness of the productive lobes

Downloaded 25 Jun 2012 to 129.110.5.90. Redistribution subject to SEG license or copyright; Terms of Use: http://segdl.org/

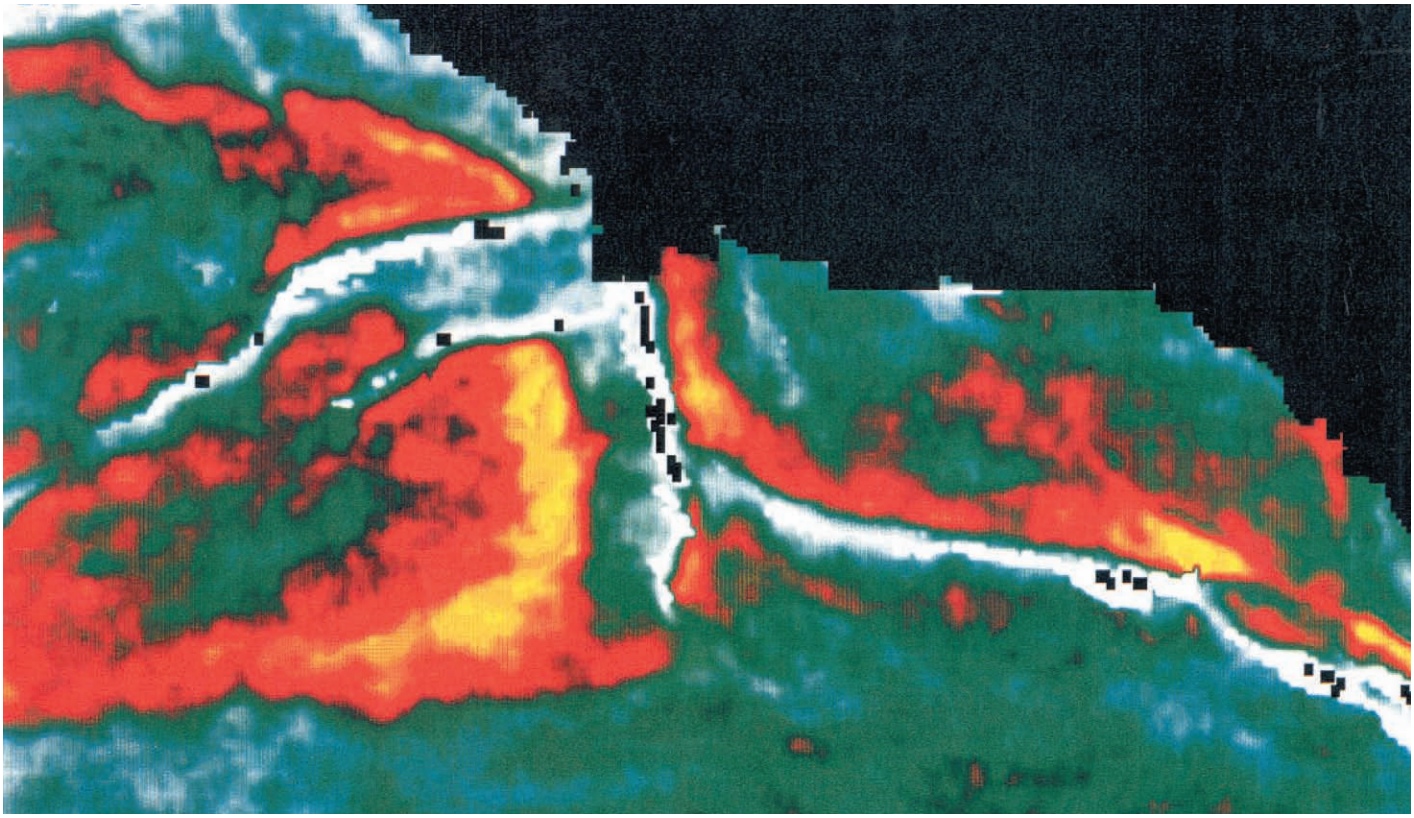

Fig. 7-10. Gulf of Mexico horizon slice. The high-amplitude lineations indicate hydrocarbon migration pathways. Note that high-amplitude lineations and low-amplitude lineations are both associated with the faults. (Courtesy Conoco Inc.)

is what matters economically. Therefore, the overall objective is to use amplitude measurements, coupled with time thickness measurements, to determine the spatial distribution of net producible gas sand from the seismic data.

The use of seismic amplitude to measure the proportion of sand within a sand/shale interval was demonstrated by Meckel and Nath (1977) for beds less than tuning thickness. Here the principle has been extended to thicker beds on the assumption that the individual lobes of producible gas sand are each below tuning thickness, that producible gas sand is a material of uniform acoustic properties, and that the internal layering is reasonably uniform.

Figure 7-14 shows bright reflections from one reservoir sand. The single blue-over-red signature indicates zero-phaseness and European polarity (see Chapter 2). Figure 7-15 shows two examples of two reservoir sands. Automatic tracking on an interactive interpretation system was used to track the bright reflection at the top and at the base of each reservoir interval. The tracker followed the maximum amplitude in the waveform while the interactive system stored the time and the amplitude of that pick in the digital database. Given that the data were zero phase, the time of the maximum amplitude is the correct time for the reservoir interface.

Figure 7-16 shows the workstation sequence which was then applied to the times and amplitudes provided by the horizon tracking. For any one sand, the horizon times provided structure maps for the top and the base reflections. Subtraction of these time maps yielded the gross isochron (or time thickness) map for the sand. The horizon amplitudes provided horizon slices for the top and base sand reflections. These were then added together in absolute value to yield the composite amplitude response of the sand.

Tuning effects remain as a distortion in this composite amplitude and should be removed. The key is to understand the shape of the tuning curve in detail; this can be obtained deterministically from an extracted wavelet or statistically from a crossplot (see Chapter 6). In this offshore Louisiana example both methods were used to yield the yellow tuning curve of Figure 7-17. Editing was then required to change the response from

Downloaded 25 Jun 2012 to 129.110.5.90. Redistribution subject to SEG license or copyright; Terms of Use: http://segdl.org/

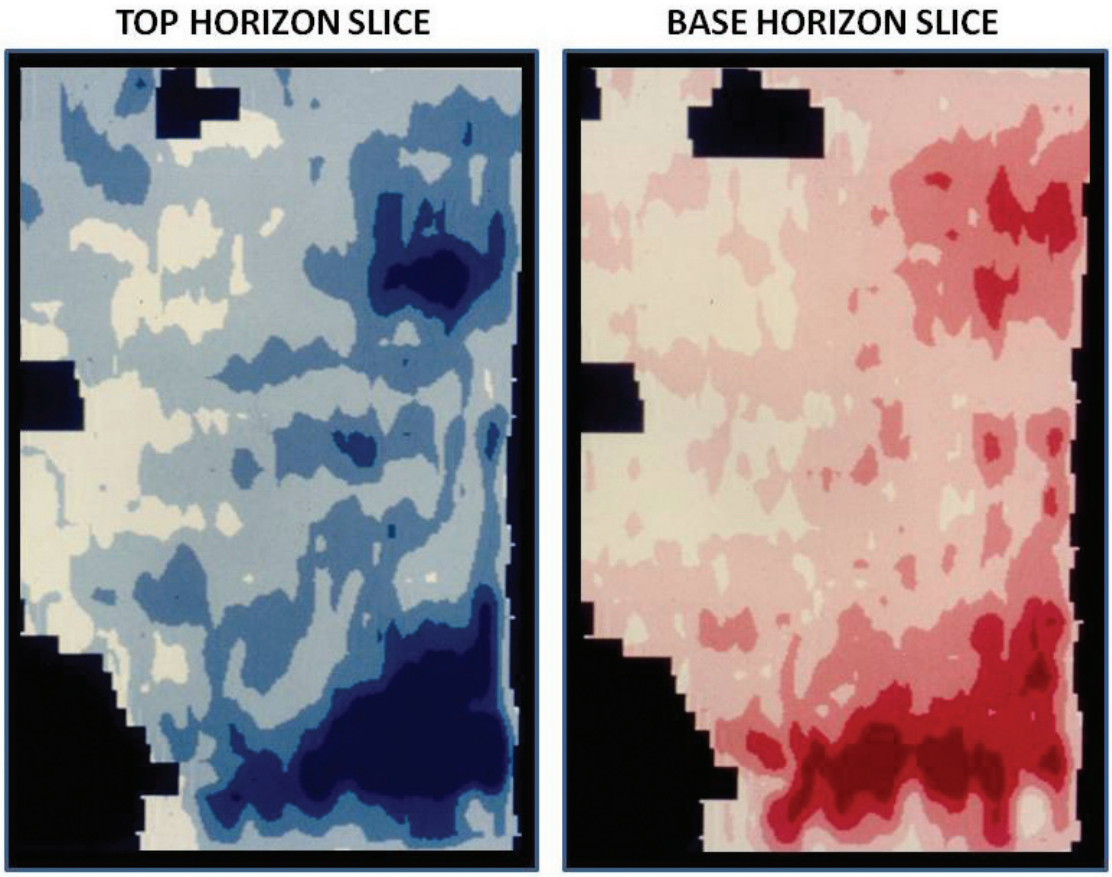

Fig. 7-11. Top and base horizon slices demonstrate natural pairing spatially.

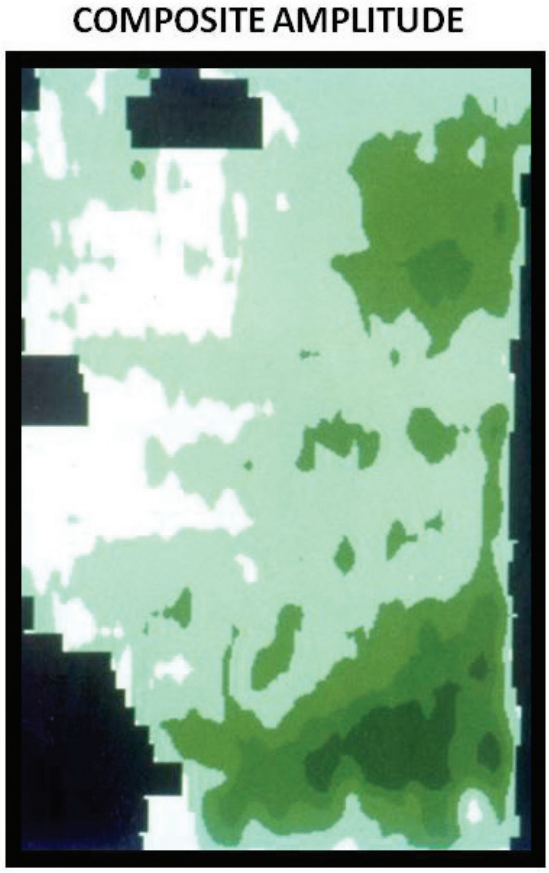

Fig. 7-12. Composite amplitude is the absolute-value summation of the two horizon slices in Figure 7-11.

Downloaded 25 Jun 2012 to 129.110.5.90. Redistribution subject to SEG license or copyright; Terms of Use: http://segdl.org/

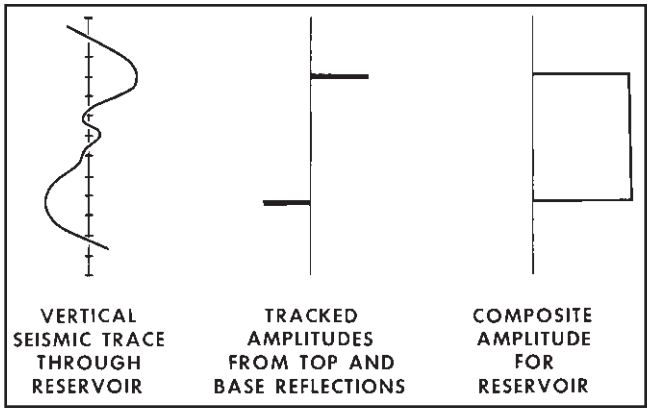
VERTICAL SEISMIC TRACE THROUGH RESERVOIR
TRACKED AMPLITUDES FROM TOP AND BASE REFLECTIONS
COMPOSITE AMPLITUDE FOR RESERVOIR

Fig. 7-13. The principle of tracking reservoir reflections and summing the absolute values of their maximum amplitudes to yield composite amplitude for the reservoir.

Fig. 7-14. Bright zero-phase reflections from the top and the base of one reservoir sand. (Courtesy Chevron U.S.A. Inc.)

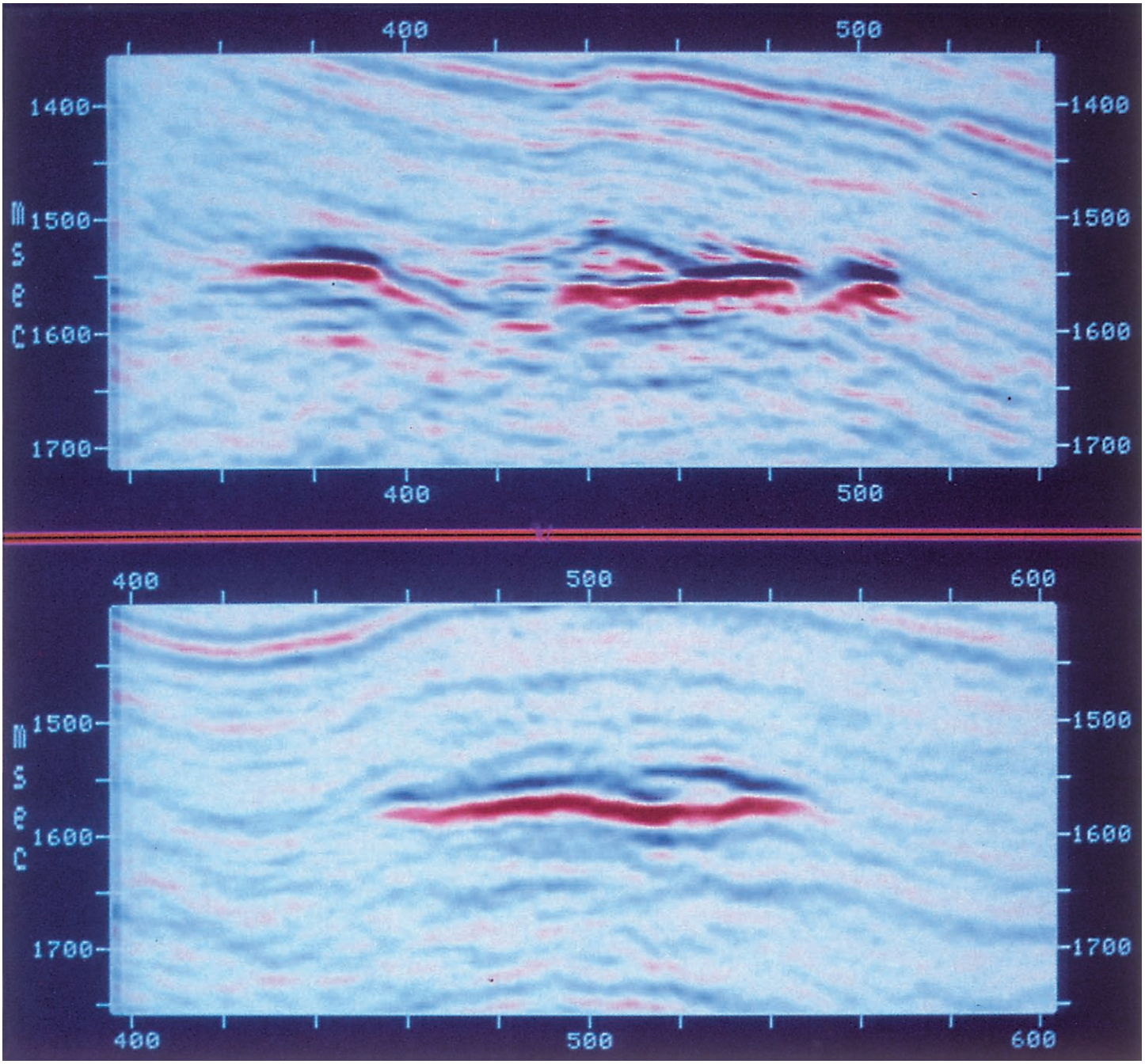

Downloaded 25 Jun 2012 to 129.110.5.90. Redistribution subject to SEG license or copyright; Terms of Use: http://segdl.org/

Fig. 7-15. Bright zero-phase reflections from the top and the base of two reservoir sands showing automatic tracks. (Courtesy Chevron U.S.A. Inc.)

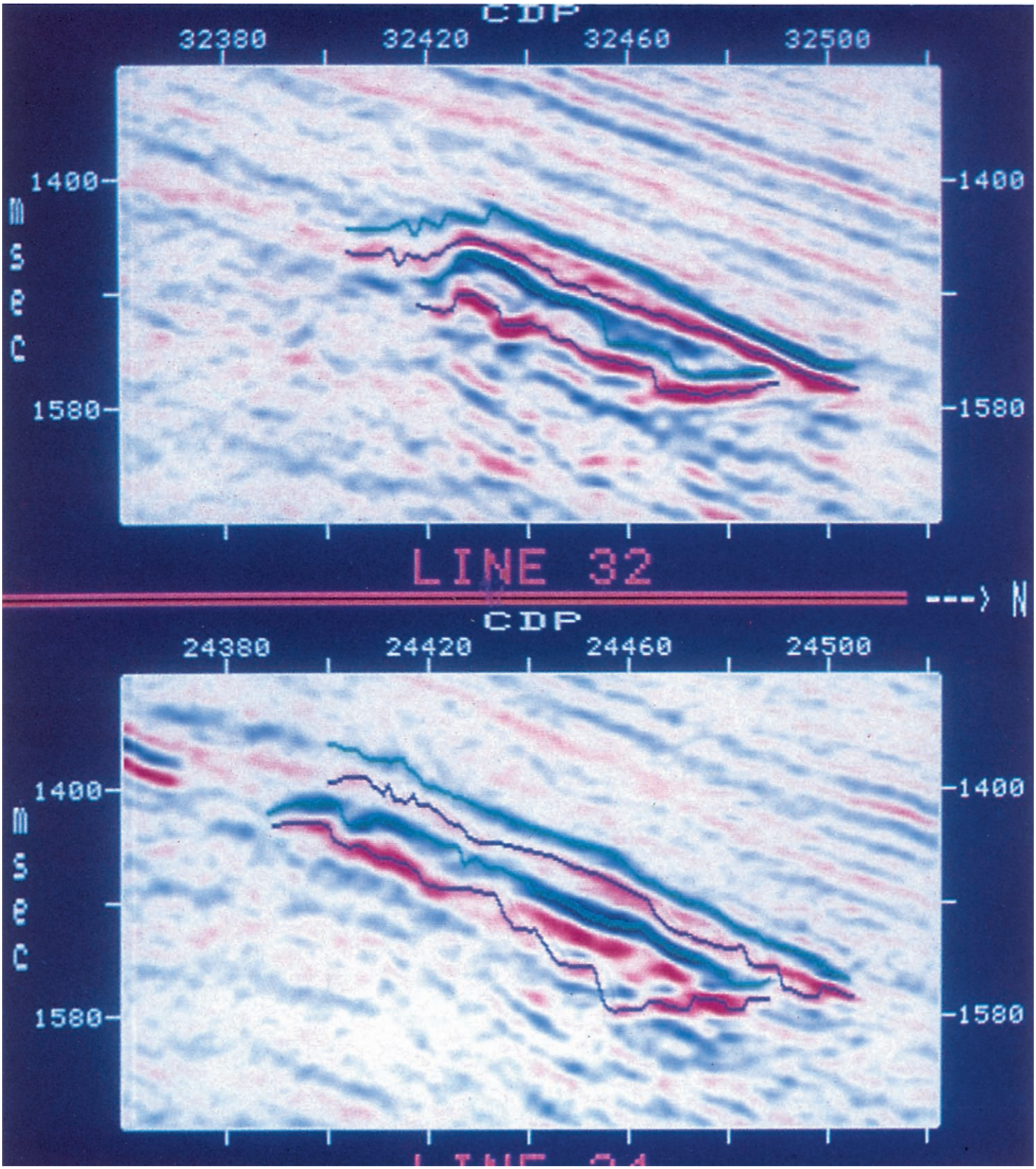

Downloaded 25 Jun 2012 to 129.110.5.90. Redistribution subject to SEG license or copyright; Terms of Use: http://segdl.org/

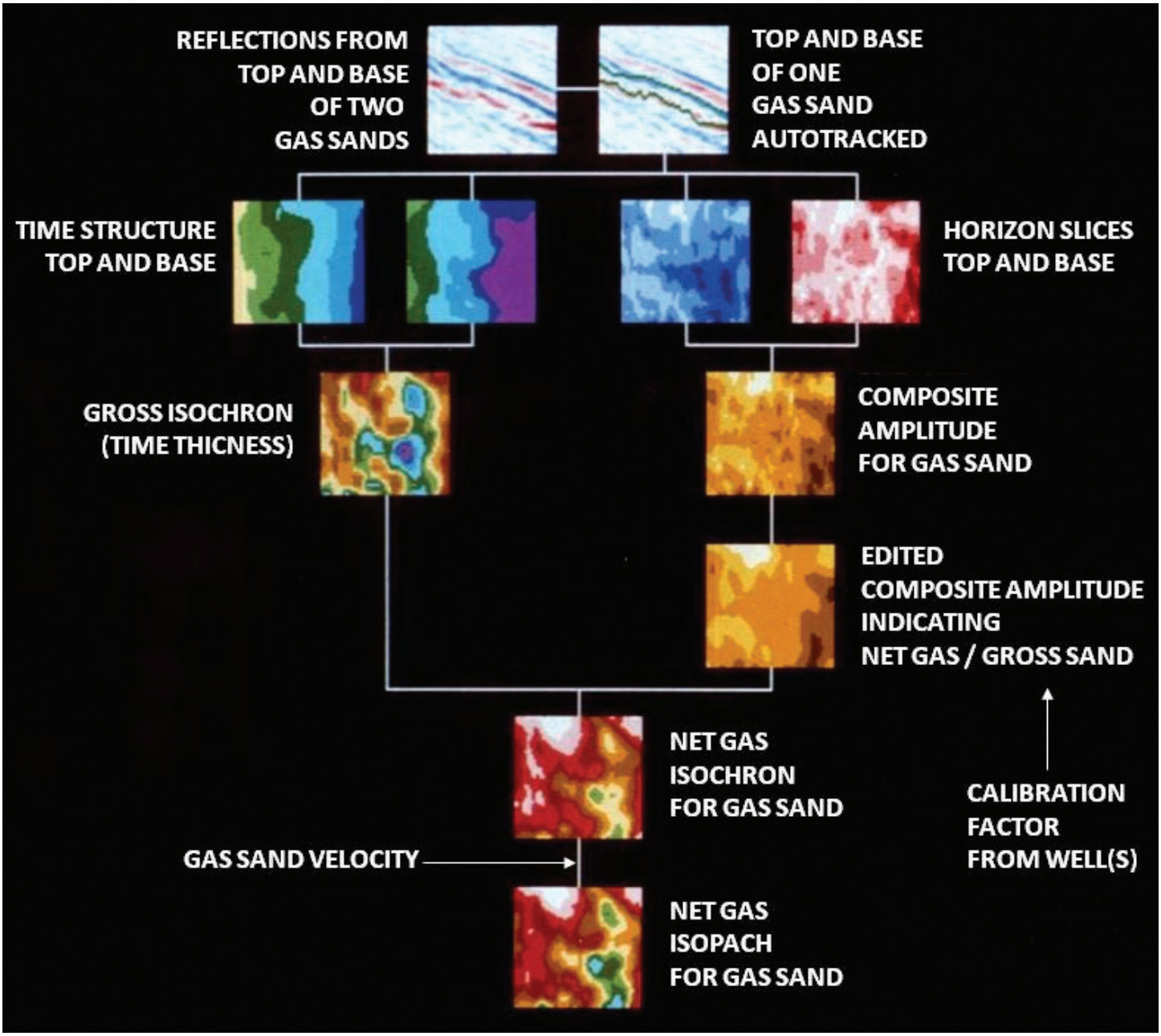
REFLECTIONS FROM TOP AND BASE OF TWO GAS SANDS
TOP AND BASE OF ONE GAS SAND AUTOTRACKED
TIME STRUCTURE TOP AND BASE
HORIZON SLICES TOP AND BASE
GROSS ISOCHRON (TIME THICNESS)
COMPOSITE AMPLITUDE FOR GAS SAND
EDITED COMPOSITE AMPLITUDE INDICATING NET GAS / GROSS SAND
NET GAS ISOCHRON FOR GAS SAND
CALIBRATION FACTOR FROM WELL(S)
GAS SAND VELOCITY
NET GAS ISOPACH FOR GAS SAND

Fig. 7-16. Interpretive sequence for deriving net pay thickness for gas sand. The isochrons and isopach have the thickest areas in green and blue. For all amplitude products the darker colors indicate higher values. In general this is the procedure for determining pore volume.

that shown in yellow to that shown in orange (using a multiplicative factor), so that the amplitude as a function of gross reservoir thickness alone is constant above tuning thickness and linearly decaying to zero for decreasing thickness below tuning.

In order to conclude the interpretive sequence of Figure 7-16, the composite amplitude response was edited according to Figure 7-17, and scaled with a single factor derived from one well to yield a map of net gas/gross sand ratio. Combining this by multiplication with the gross isochron map, a net gas isochron map was obtained. A

Downloaded 25 Jun 2012 to 129.110.5.90. Redistribution subject to SEG license or copyright; Terms of Use: http://segdl.org/

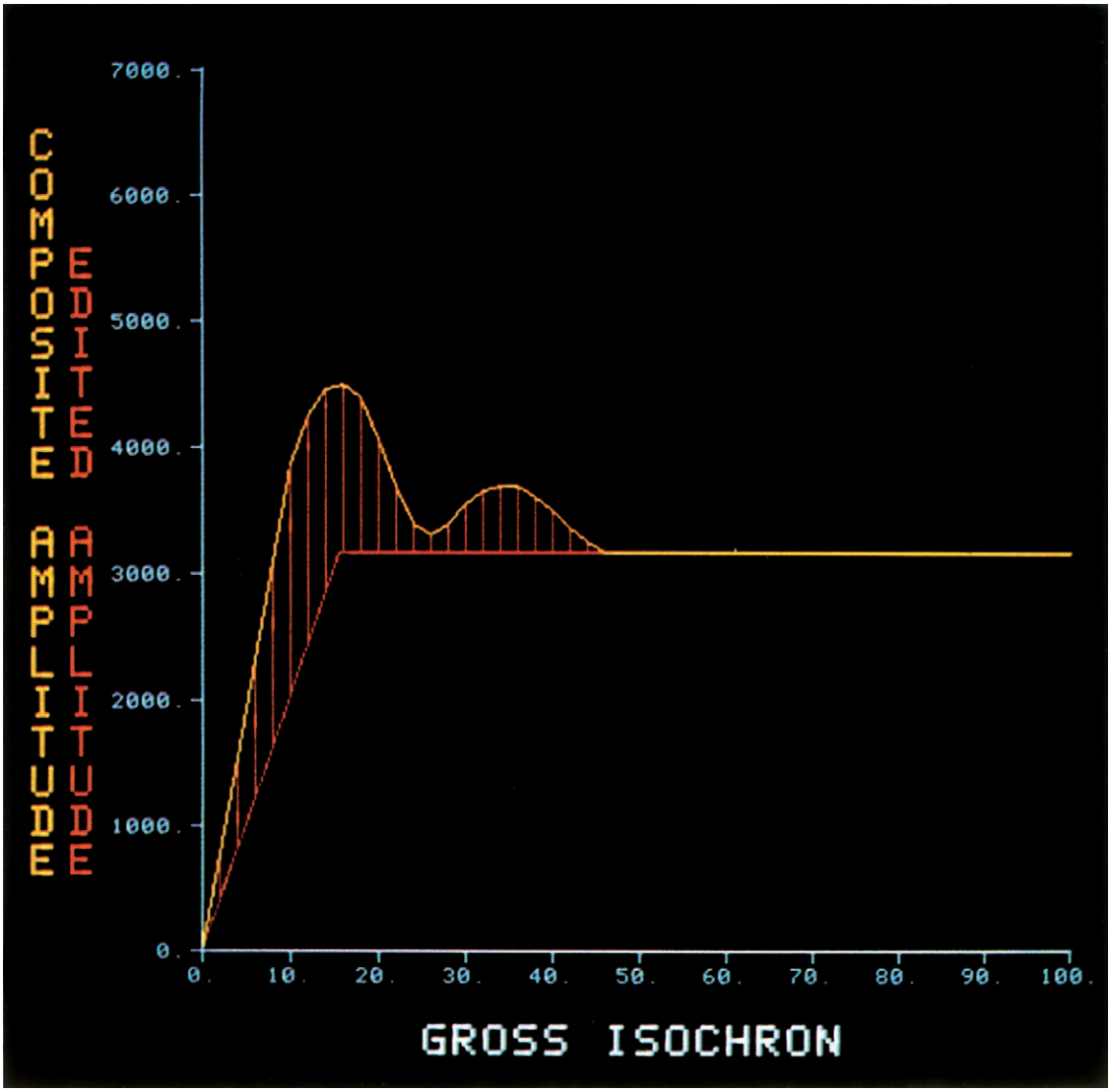

Fig. 7-17. The editing of tuning effects. The yellow is converted to the orange by a multiplier as a function of gross isochron.

constant gas sand interval velocity was then sufficient to convert this net gas isochron map to a net gas isopach map. In combining the gross isochron map with the net gas/gross sand ratio, it should be remembered that there are no gross isochrons less than tuning thickness because of the tuning phenomenon itself (Figure 6-2). For actual gas sand thicknesses less than tuning, all the net gas sand information is encoded in the amplitude.

Figures 7-18 and 7-19 show comparable gross and net isochron maps, making clear the contribution of the net gas/gross sand ratio derived from the composite amplitude. Note the two northwest-southeast thickness trends on the gross isochron map and then note that only one of them has survived in the net isochron map. This is caused directly by the higher amplitudes to the north and east. Net gas sand maps derived in this way have been shown to tie well data acceptably. In practice, relative values are more accurate than absolute values because of the difficulty of determining the scale factor connecting edited amplitude to net gas/gross sand ratio. Also note that the study was conducted only over the gas sand reflections. If a determination of net sand in the water zone were necessary, then a separate study would be required with a different calibration factor.

Downloaded 25 Jun 2012 to 129.110.5.90. Redistribution subject to SEG license or copyright; Terms of Use: http://segdl.org/

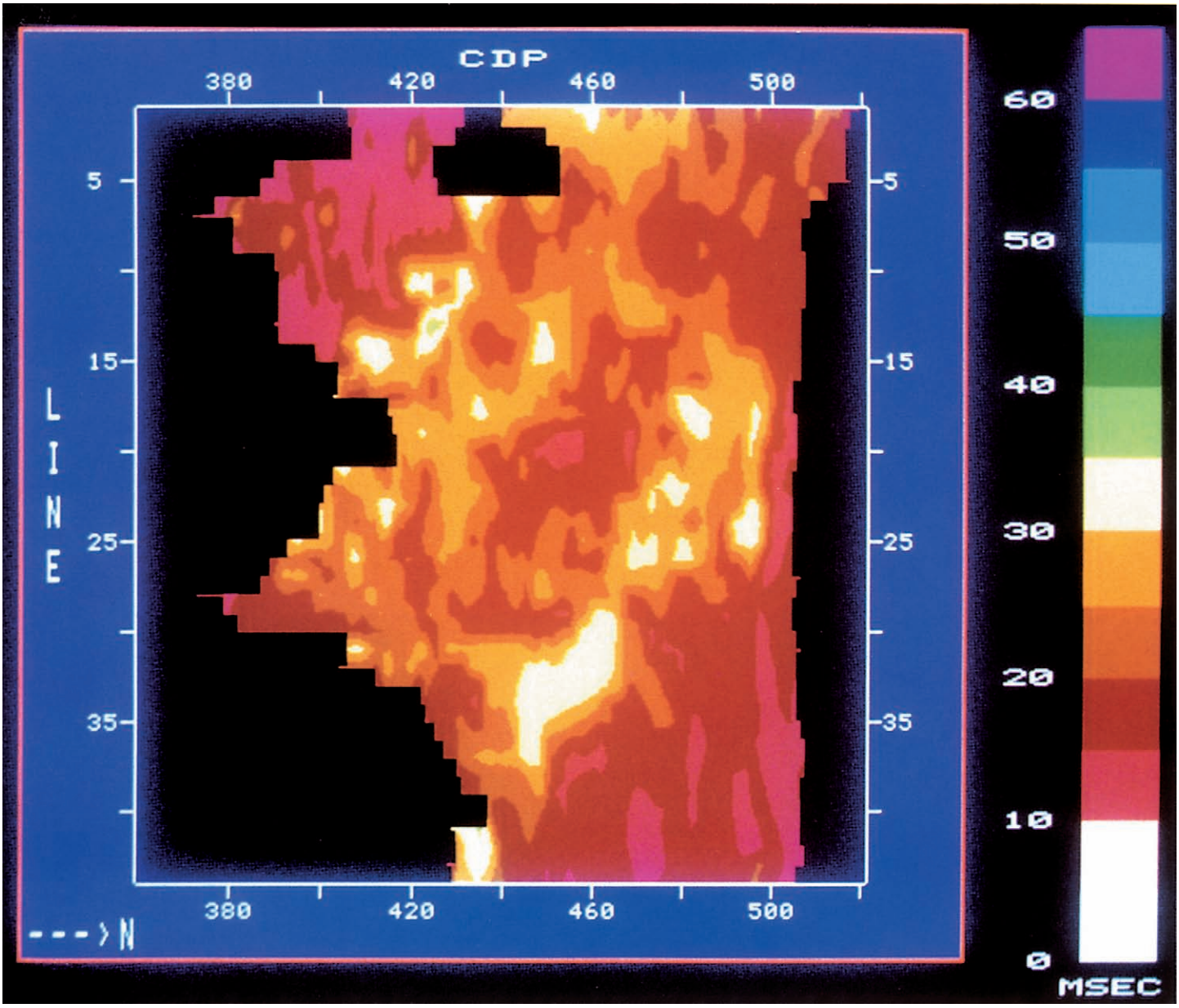

Fig. 7-18. Gross isochron map of Upper Sand showing two thickness trends. Area measures 2 × 2 km. (Courtesy Chevron U.S.A. Inc.)

When there is more than one mappable reservoir interval associated with the reservoir under study, each interval is treated separately and added together at net gas isopach stage. Figure 7-20 shows total net producible gas sand in color superimposed on the structural configuration of the top of the reservoir. Integration of net gas isopach maps yields the volume of the reservoir. By integrating over chosen sub-areas, the reservoir volume over different lease blocks or areas of special interest can be readily determined.

Case Histories 5 and 10 (Chapter 14) report on the use of net gas sand mapping in other prospects. Different approaches to mapping net pay have been presented by Woock and Kin (1987) and by McCarthy (1984).

Pore Volume

In the above section on net pay thickness, porosity was not mentioned because it was known to be constant in this area. In general for the bright spot regime, porosity multiplies with net pay thickness to give porosity–net thickness, or pore volume. So the general statement of the method becomes

Downloaded 25 Jun 2012 to 129.110.5.90. Redistribution subject to SEG license or copyright; Terms of Use: http://segdl.org/

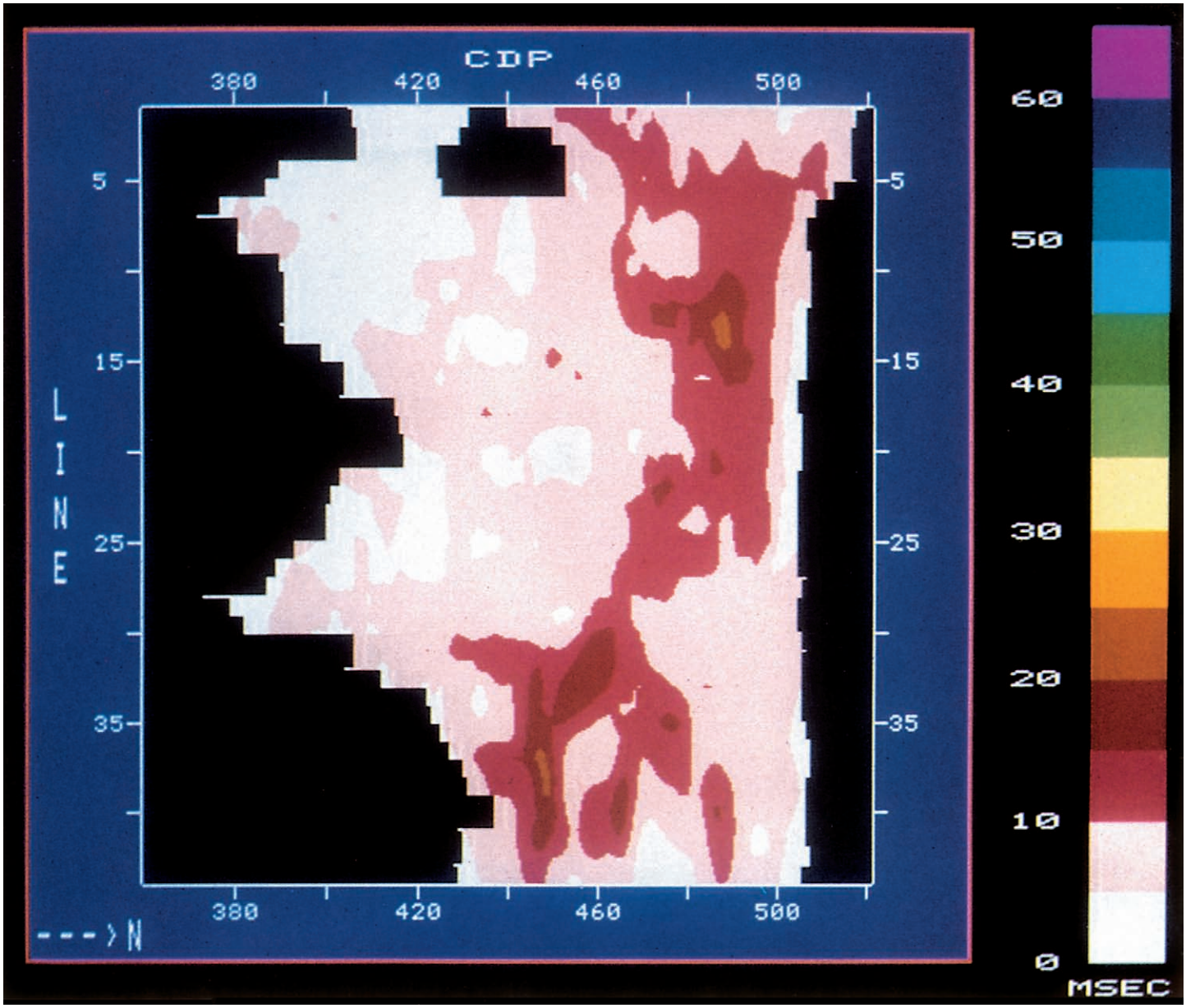

Fig. 7-19. Net gas isochron map of Upper Sand showing one thickness trend. (Courtesy Chevron U.S.A. Inc.)

PORE VOLUME = AMPLITUDE × ISOCHRON

This relationship, illustrated further in Figure 7-21, can be used with a calibration factor and the reservoir velocity to give quantitative numbers, or it can be used without calibration to give relative pore volume. It can be used with or without tuning correction. In whatever way it is used, the multiplication is important and has much generality. Matteucci (1996) tried many seismic attributes and concluded that the composite amplitude-isochron product is "the attribute most strongly related to hydrocarbon pore volume." The equivalent relationship for the dim spot regime is

PORE VOLUME = ISOCHRON ÷ AMPLITUDE

Downloaded 25 Jun 2012 to 129.110.5.90. Redistribution subject to SEG license or copyright; Terms of Use: http://segdl.org/

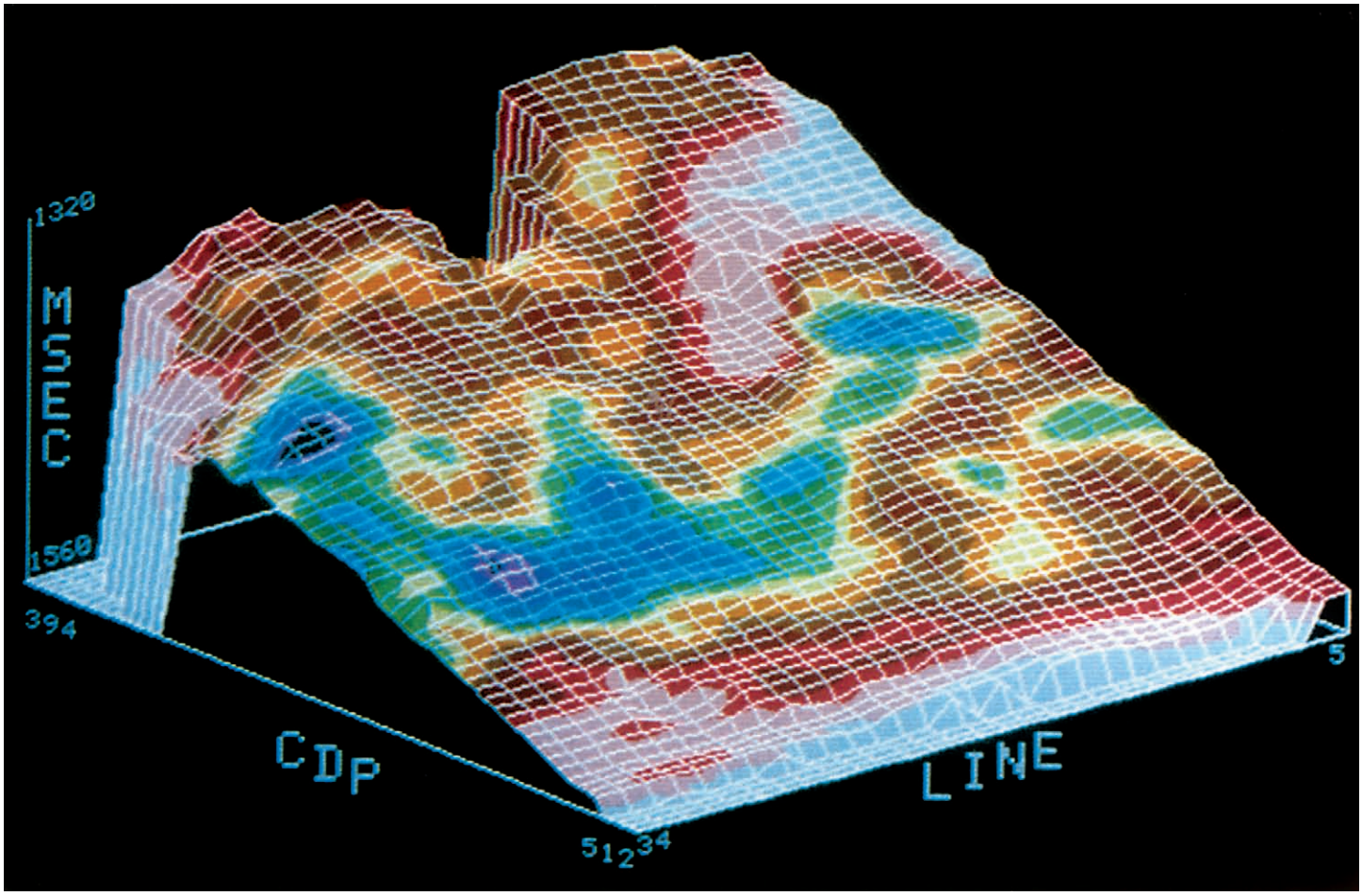

Fig. 7-20. Total net gas sand isopach superimposed on the structure of the top of the reservoir. The greens and blues indicate the thicker net gas zones. (Courtesy Chevron U.S.A. Inc.)

The Limit of Separability (one-quarter wavelength) was introduced in Chapter 1, and its equivalence to the Tuning Thickness was discussed in Chapter 6. Because of the wavelet interaction that occurs at this thickness and below, amplitude measures different properties for thicker and for thinner reservoirs (Figure 7-22). Net thickness is encoded into amplitude below the tuning thickness, but above the tuning thickness an independent thickness measurement can be obtained from the time separation of top and base reflections (the isochron). This means that amplitude is not a consistent measure when the reservoir thickness changes from below to above the quarter wavelength. When top and base reflections separate, we need a better indicator of reservoir productivity. A truly consistent measure for variable thickness reservoirs is, however, given by pore volume derived from one or other of the above formulas.

Consider the dilemma illustrated in Figure 7-23. Amplitude (actually here composite amplitude) indicates a bright area to the north; this suggests that the reservoir quality is best in this region. The measured thickness, or isochron, indicates thicker reservoir much further south. Neither of these is expected to be the most productive location. The maximum pore volume in the center of the area is the best place to drill.

Well Calibration

Seismic amplitude or other attributes extracted over one reservoir reflection from good quality data has high relative accuracy. However, it has no absolute accuracy and calibration with well data is necessary. There are many approaches and these are summarized in Figure 7-24. The author has had greatest success with the deterministic method using a single space-invariant scale factor. This factor can be determined

Downloaded 25 Jun 2012 to 129.110.5.90. Redistribution subject to SEG license or copyright; Terms of Use: http://segdl.org/

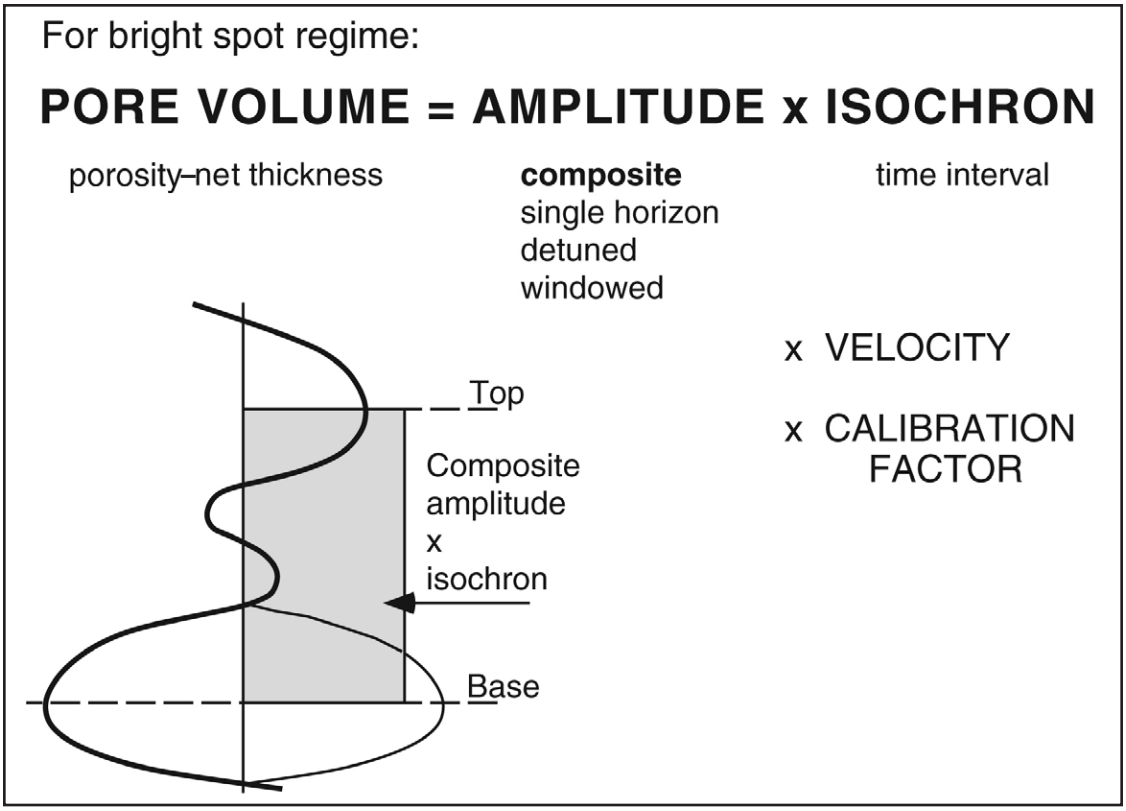

Fig. 7-21. Reflection amplitude, preferably a composite of reservoir top and base, times isochron thickness, is normally the best measure of reservoir pore volume.

from one well, where the amplitude is highest and the tie most reliable, from two wells, or from a crossplot using many wells. The single factor retains the relativities in the seismic data, its greatest strength.

If other properties of the reservoir and adjacent layers affect amplitude significantly and vary spatially, a space-variant scale factor, determined from the wells, will be necessary to remove them. A good discussion of secondary factors affecting amplitude and their removal appears in Case History 9. In projects like this one the relativities in the seismic amplitude are being changed by the different well ties. In general the uncertainties in the position of each well and its measured property need to be considered, and also the uncertainties in the seismic measurement. The tie in the desired reservoir property between the seismic value and the well value needs only to be within each other's uncertainty and thus distortion of seismic relativities or flexing can be minimized.

In geostatistical approaches to well calibration (Figure 7-24) several reservoir property maps may be desired and several seismic attributes may be considered as a source of information. Crossplots establish relationships and variograms guide the spatial interpolation or cokriging. However, good statistical correlations are not sufficient for reliable extraction of multiple reservoir property maps; support from petrophysics and modeling is also required. Matteucci (1996) summed up this situation nicely: "It is very simple and easy to find relationships. It is much harder to estimate if they are statistically significant, robust, and geologically meaningful." Use of various attributes and multiple attributes in reservoir studies is discussed further in Chapter 8.

Statistical Use of Tracked Horizon Data

Once the time and amplitude of the zero-phase reflections from the top and base of a reservoir are stored in a readily accessible digital database, statistical studies of the horizon data are straightforward. The value of interactive crossplotting for the statistical analysis of tuning phenomena was explained in Chapter 6.

Figure 7-25 shows an interactive crossplot of gross isochron against top sand time;

Downloaded 25 Jun 2012 to 129.110.5.90. Redistribution subject to SEG license or copyright; Terms of Use: http://segdl.org/

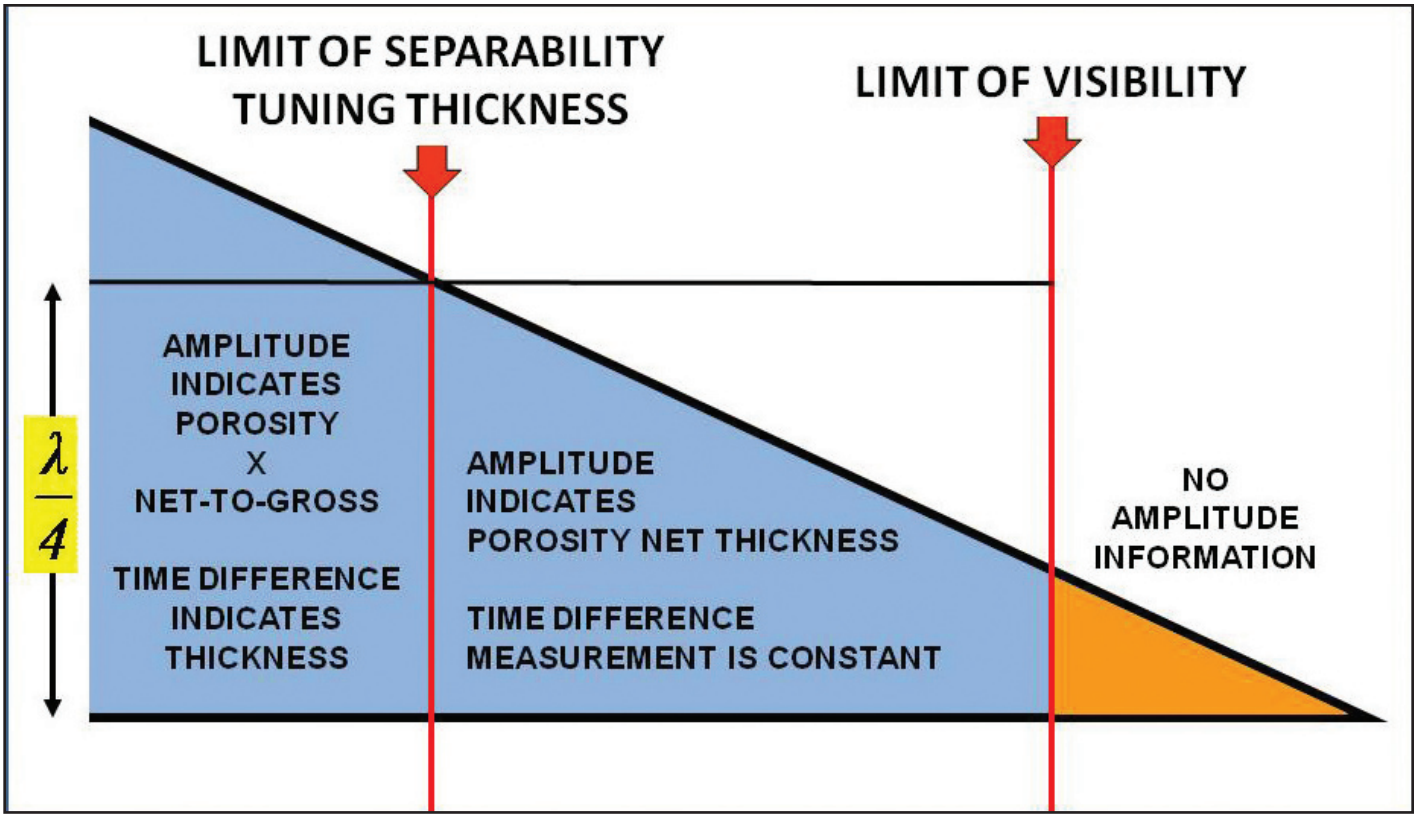

Fig. 7-22. Amplitude is a different measure of reservoir properties for thicknesses above and below the Limit of Separability / Tuning Thickness. No useable amplitude exists for thicknesses below the Limit of Visibility.

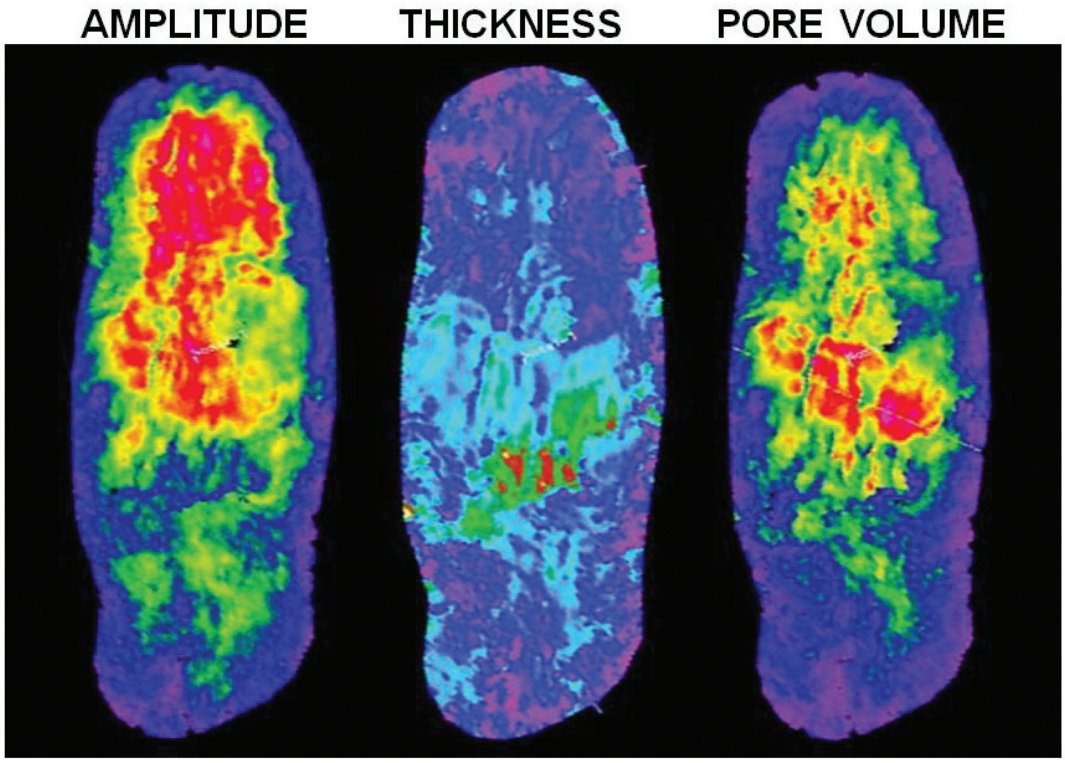

Fig. 7-23. Amplitude indicates reservoir quality, thickness indicates reservoir quantity, but pore volume indicates the best location to drill. (Courtesy Pemex.)

Downloaded 25 Jun 2012 to 129.110.5.90. Redistribution subject to SEG license or copyright; Terms of Use: http://segdl.org/

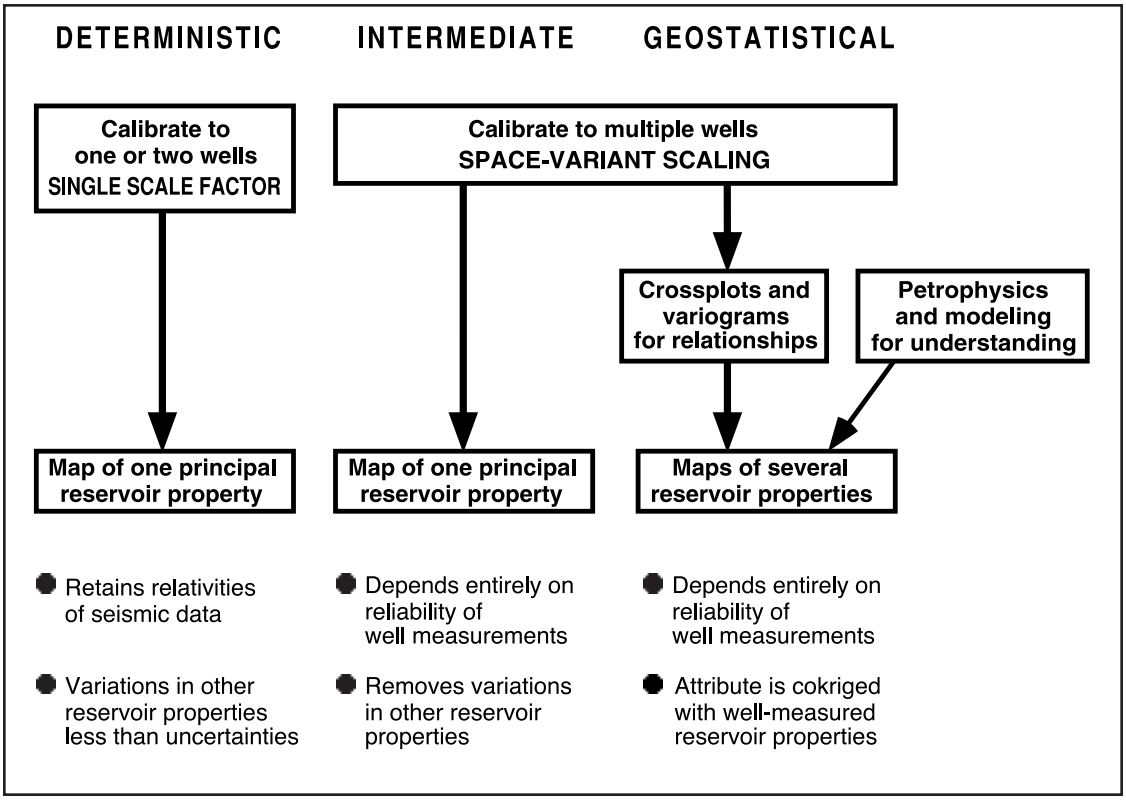
DETERMINISTIC
INTERMEDIATE
GEOSTATISTICAL
Calibrate to one or two wells SINGLE SCALE FACTOR
Calibrate to multiple wells SPACE-VARIANT SCALING
Crossplots and variograms for relationships
Petrophysics and modeling for understanding
Map of one principal reservoir property
Map of one principal reservoir property
Maps of several reservoir properties
Retains relativities of seismic data
Variations in other reservoir properties less than uncertainties
Depends entirely on reliability of well measurements
Removes variations in other reservoir properties
Depends entirely on reliability of well measurements
Attribute is cokriged with well-measured reservoir properties

Fig. 7-24. Methods of calibration of seismic amplitude or other attribute to reservoir properties at wells. Tie should minimize seismic flexing to fit well value within uncertainties.

that is, vertical thickness (in time) against structural position. The general effect is triangular with several clearly visible lineations. Interpretation of these lineations is a statistical assessment of the many thousands of data points included in this crossplot. Figures 7-26 and 7-27 are crossplots of sub-areas of the prospect, each accompanied by an exemplary data segment. Figure 7-26 makes it clear that the lineation along the bottom of the crossplot illustrates that thicknesses can only be measured down to just below tuning.

Sub-area C (Figure 7-26) includes many lines of data illustrating good flat spot reflections, one of which is illustrated in the data insert. The orange straight line labelled FLAT SPOT is a line of the form, $y = c - x$, that is, one representing equal increments of gross isochron and top sand time. Because top sand time plus gross isochron equals base sand time and because base sand time is approximately constant for a flat spot reflection, it is indeed expected that a flat spot would plot along such a diagonal line of unit gradient.

Sub-area B (Figure 7-27) is an area of thicker sands. An orange line represents the line of equal increments of gross isochron and top sand time as before. Most of the points fall to the right of this line, indicating varying degrees of gas velocity sag. Extreme sag is illustrated in the data insert and marked on the crossplot by a pink line.

An interpreted version of the total area crossplot of Figure 7-25 is shown in Figure 7-28. This interpretation incorporates the observations from several sub-areas including the two discussed here. The convergence of many of the lineations in the lower right corner and also the great concentration of crossplot points at the same location suggest a common gas/water contact over a large part of the reservoir. This in turn suggests that much of the reservoir is in communication, at least in terms of flow rates effective over geologic time. The concentration of points in a swath along the lower part of the triangular pattern suggests that many of the sands were preferentially deposited with thicknesses of 30 ms (approximately 25 m) or less.

Downloaded 25 Jun 2012 to 129.110.5.90. Redistribution subject to SEG license or copyright; Terms of Use: http://segdl.org/

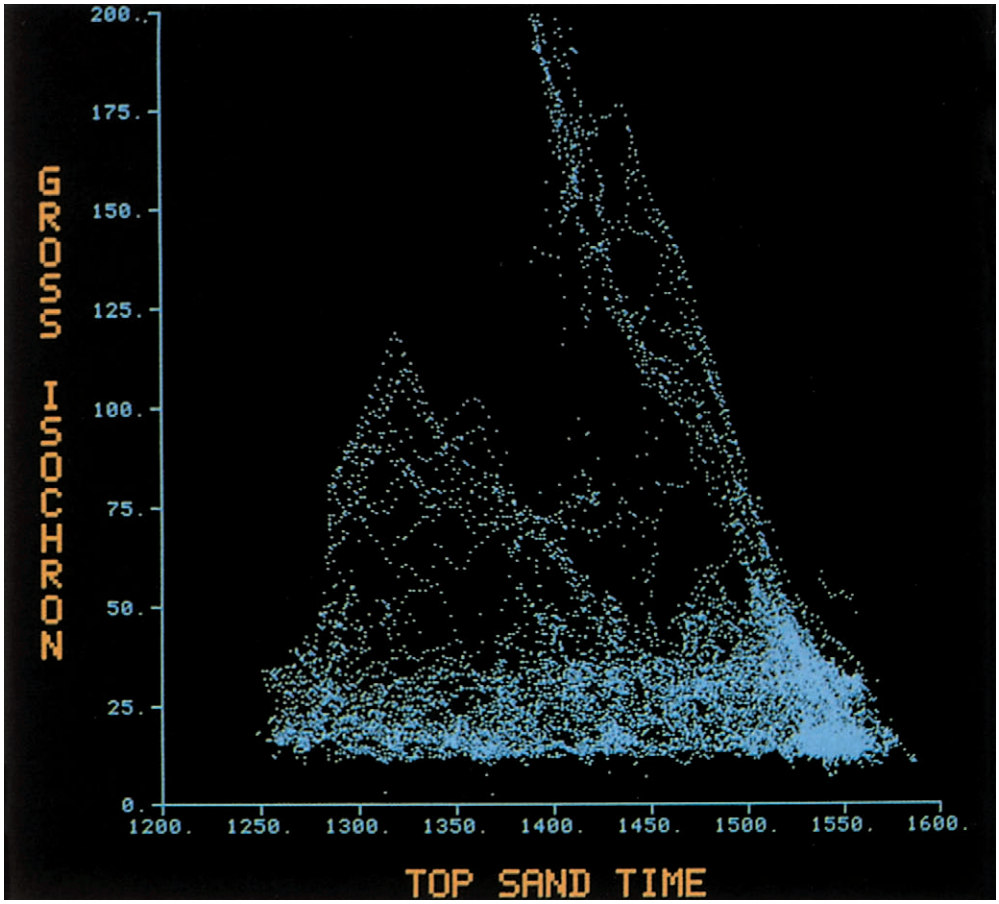

Fig. 7-25. Interactive crossplot of gross isochron against top sand time.

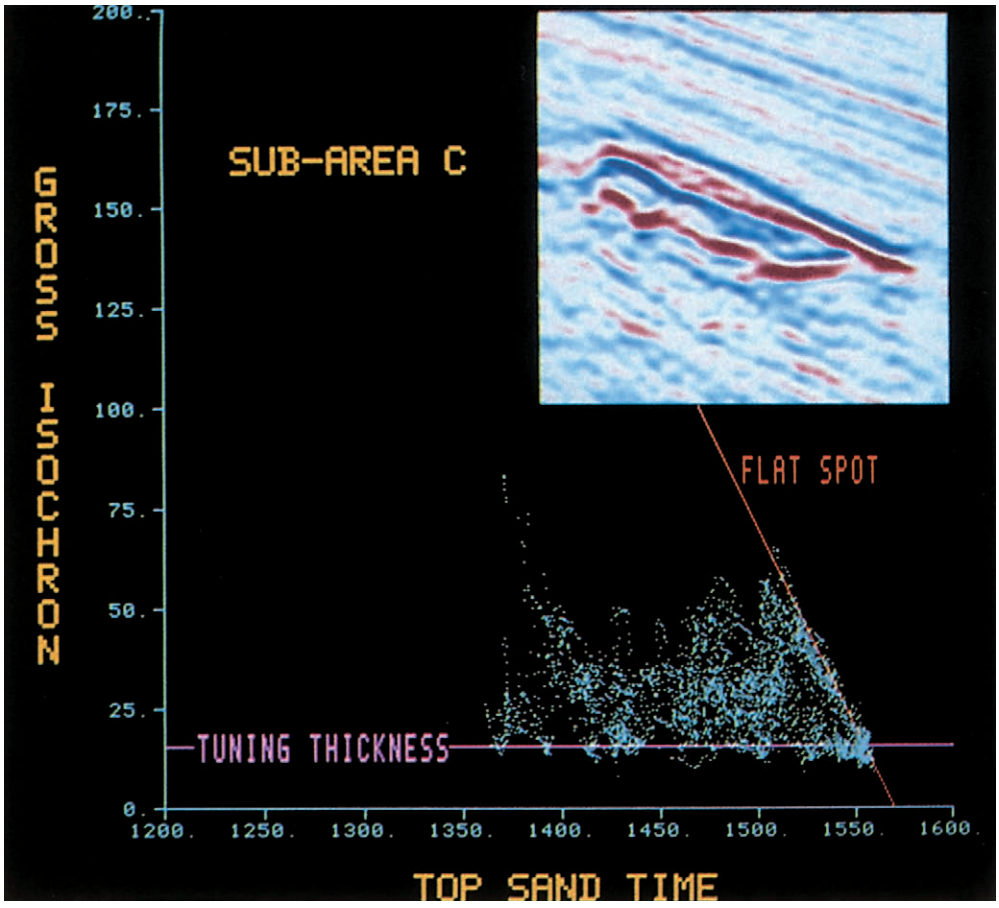

Fig. 7-26. Interactive crossplot of gross isochron against top sand time for sub-area C with exemplary data insert.

Downloaded 25 Jun 2012 to 129.110.5.90. Redistribution subject to SEG license or copyright; Terms of Use: http://segdl.org/

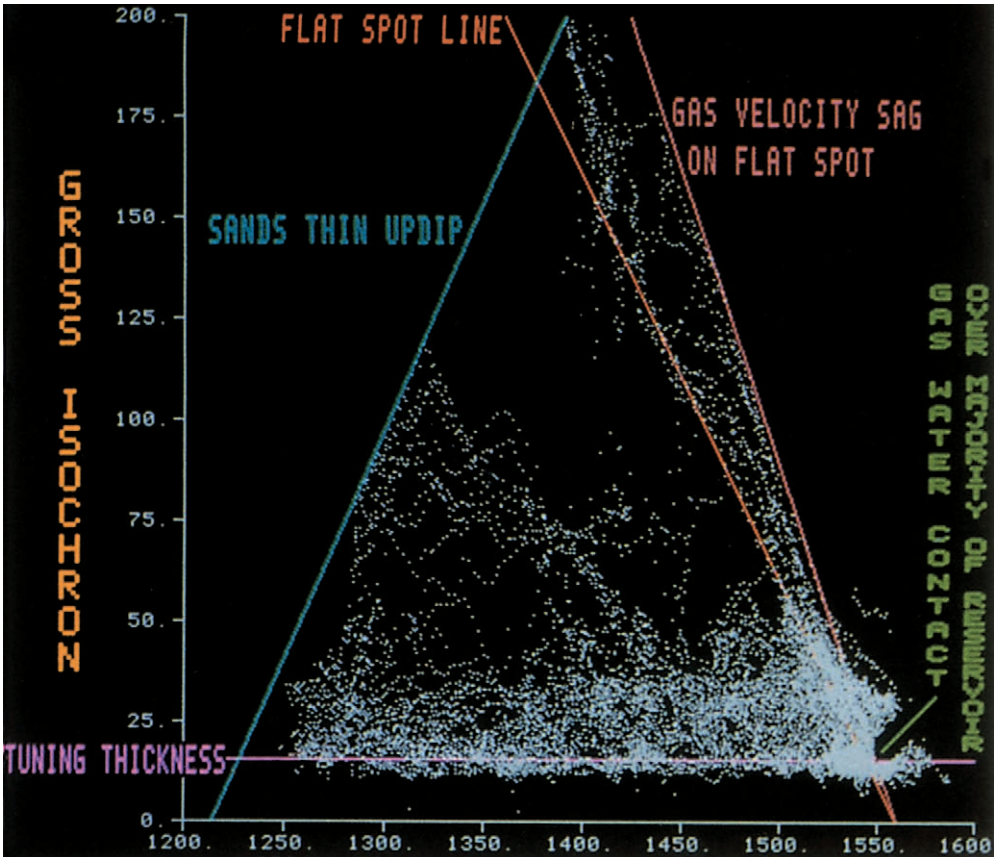

Fig. 7-28. Interactive crossplot of Figure 7-25 showing interpretation of lineations.

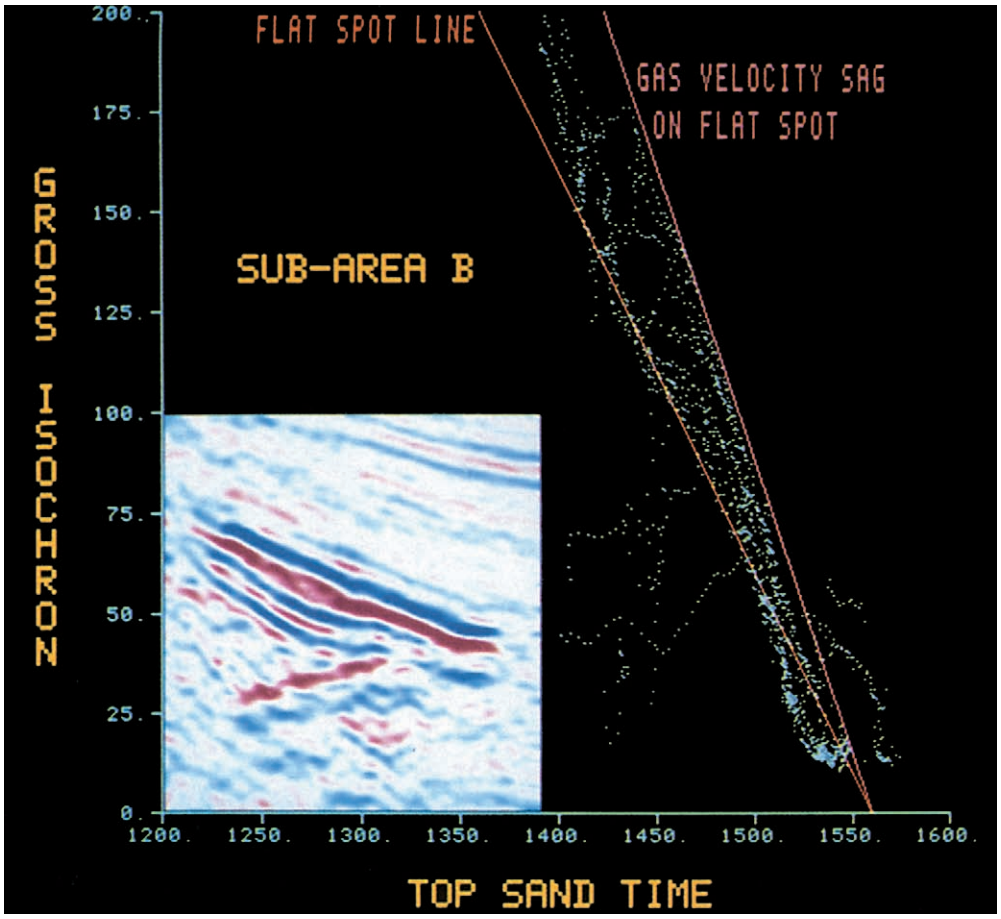

Fig. 7-27. Interactive crossplot of gross isochron against top sand time for sub-area B with exemplary data insert.

Downloaded 25 Jun 2012 to 129.110.5.90. Redistribution subject to SEG license or copyright; Terms of Use: http://segdl.org/

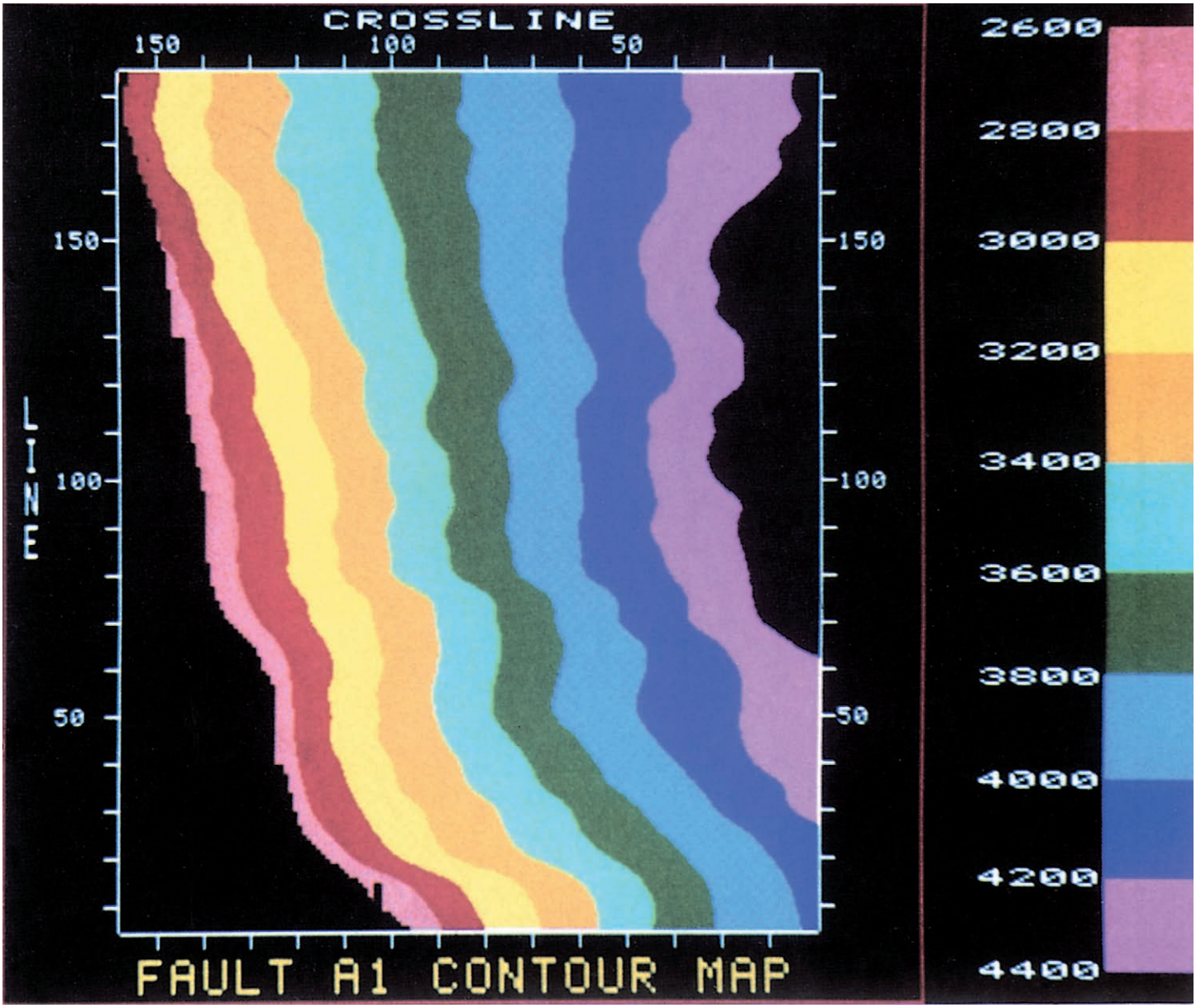

Fig. 7-29. Fault plane contour map, used as the reference surface for fault slicing. (Courtesy Texaco U.S.A. Inc.)

Downloaded 25 Jun 2012 to 129.110.5.90. Redistribution subject to SEG license or copyright; Terms of Use: http://segdl.org/

There is a suggestion of a lineation with the correct slope to be another flat spot reflection intersecting the top sand time axis at 1,440 ms. It is evident on both Figures 7-28 and 7-26. This observation can be considered to be the statistical identification of another possible fluid contact, which has obvious implications for segmentation of the reservoir.

Fault Slicing

A **fault slice** is a slice through a 3-D data volume parallel to the interpreted position of a fault plane of interest. Fault slices have applications for mapping structure very close to a fault and fault throw, for identifying splinter faults, and for studying fault sealing or leaking.

First of all, the fault under study must be mapped (Figure 7-29). This serves as the reference surface parallel to which all the fault slices in the upthrown and downthrown fault blocks are generated. One of these, eight data points from the fault on upthrown side, is shown in Figure 7-30. This slice and others parallel to it proved useful for observing steep dips that led to the mapping of growth structure in the upthrown block. This benefit resulted from the uniform proximity of the fault slices to the parent growth fault. Horizon tracks on Figure 7-30, and those judged correlative on the fault slice eight data points from the fault on the downthrown side, were subtracted from each other to yield a map of throw across the fault plane, as shown in Figure 7-31.

Secondary, or splinter, faults are generated by movement on a major growth fault and may extend only a short distance from it. A fault slice, remaining uniformly close to the growth fault, slices this zone and intersects splinter faults branching off the parent. Figure 7-32 shows the interpretation of thirty splinters on one fault slice, each being supported by at least six event terminations. Figure 7-33 shows the mapping of one of them on a range of five fault slices covering the splintered zone. The resultant map in coordinates relative to the parent growth fault shows, by the attitude of the contours, the relative strike or azimuth of the splinter fault and its parent. A more thorough treatment of the method and benefits of fault slicing is provided by Brown, Edwards and Howard (1987).

An application of fault slicing to fault sealing and leaking has been presented by Bouvier et al. (1989, reference in Chapter 8). Figure 7-34 is a fault slice from Nigeria. It is unrolled, meaning that it is presented in terms of distance along the actual fault plane, compared with Figure 7-30, which has vertical time as its axis. The fault slice of Figure 7-34 is in depth and it is inverted to display acoustic impedance. Three well logs are superimposed and the thin black lines indicate the interpretation of sands and shales. This interpretation is presented on Figure 7-35 with the sands in white and the shales in black. Hydrocarbon fluids, proven and probable, are in various colors. Shale interpreted from a fault slice in the juxtaposed fault block is superimposed in brown. The fluids still visible potentially will leak across the fault. However, shale may be smeared along the fault plane to seal these fluids also. Clay smear potential is a function of fault throw and shale-to-sand ratio. In this study, the fluids visible in red and green in the lower part of Figure 7-35 are in a region of high calculated clay smear potential (Bouvier et al., 1989, reference in Chapter 8).

Downloaded 25 Jun 2012 to 129.110.5.90. Redistribution subject to SEG license or copyright; Terms of Use: http://segdl.org/

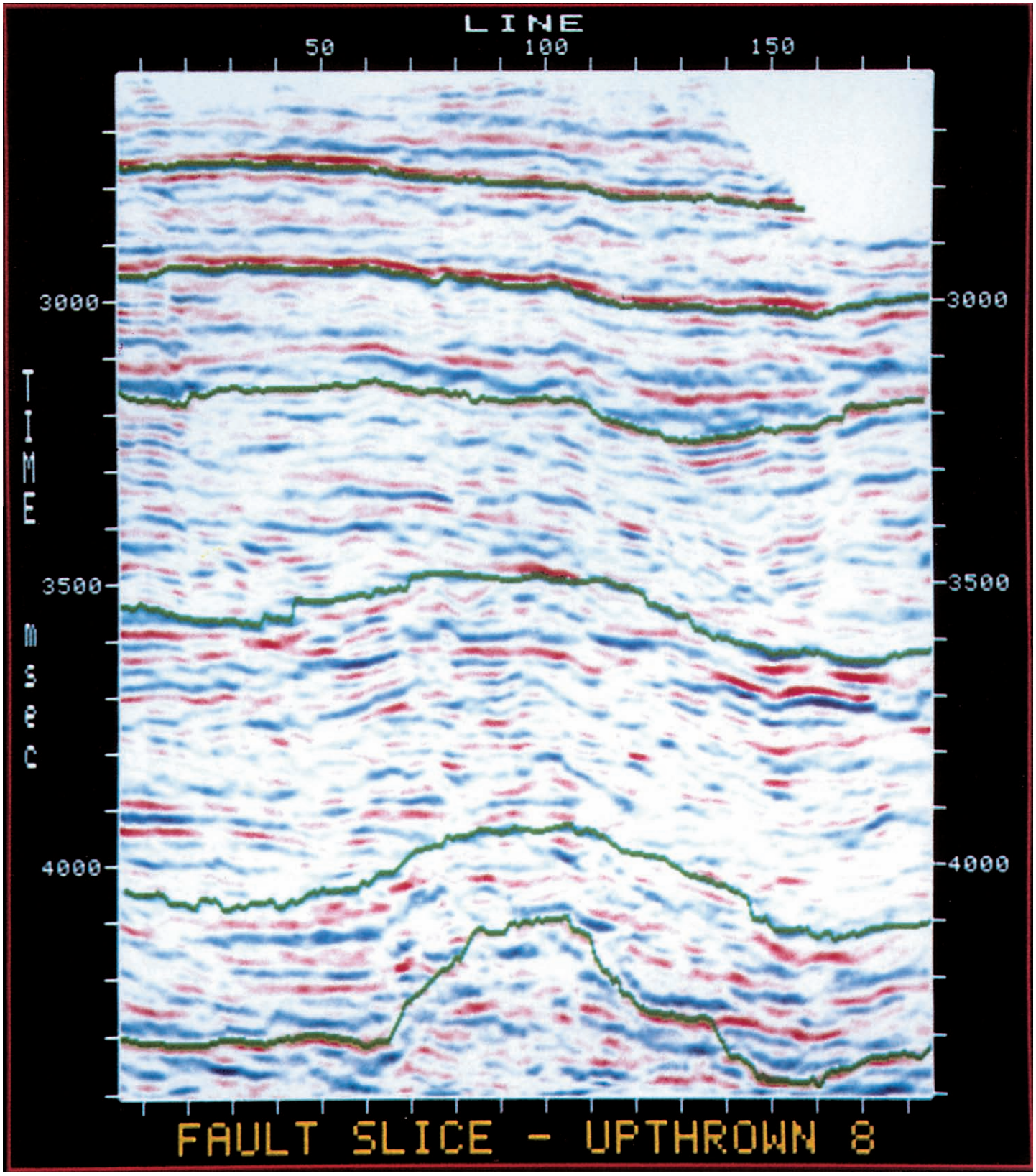

Fig. 7-30. Fault slice through Gulf of Mexico data volume parallel to the major growth fault mapped in Figure 7-29. Horizon tracks show deep structure caused by salt movement. (Courtesy Texaco U.S.A. Inc.)

Downloaded 25 Jun 2012 to 129.110.5.90. Redistribution subject to SEG license or copyright; Terms of Use: http://segdl.org/

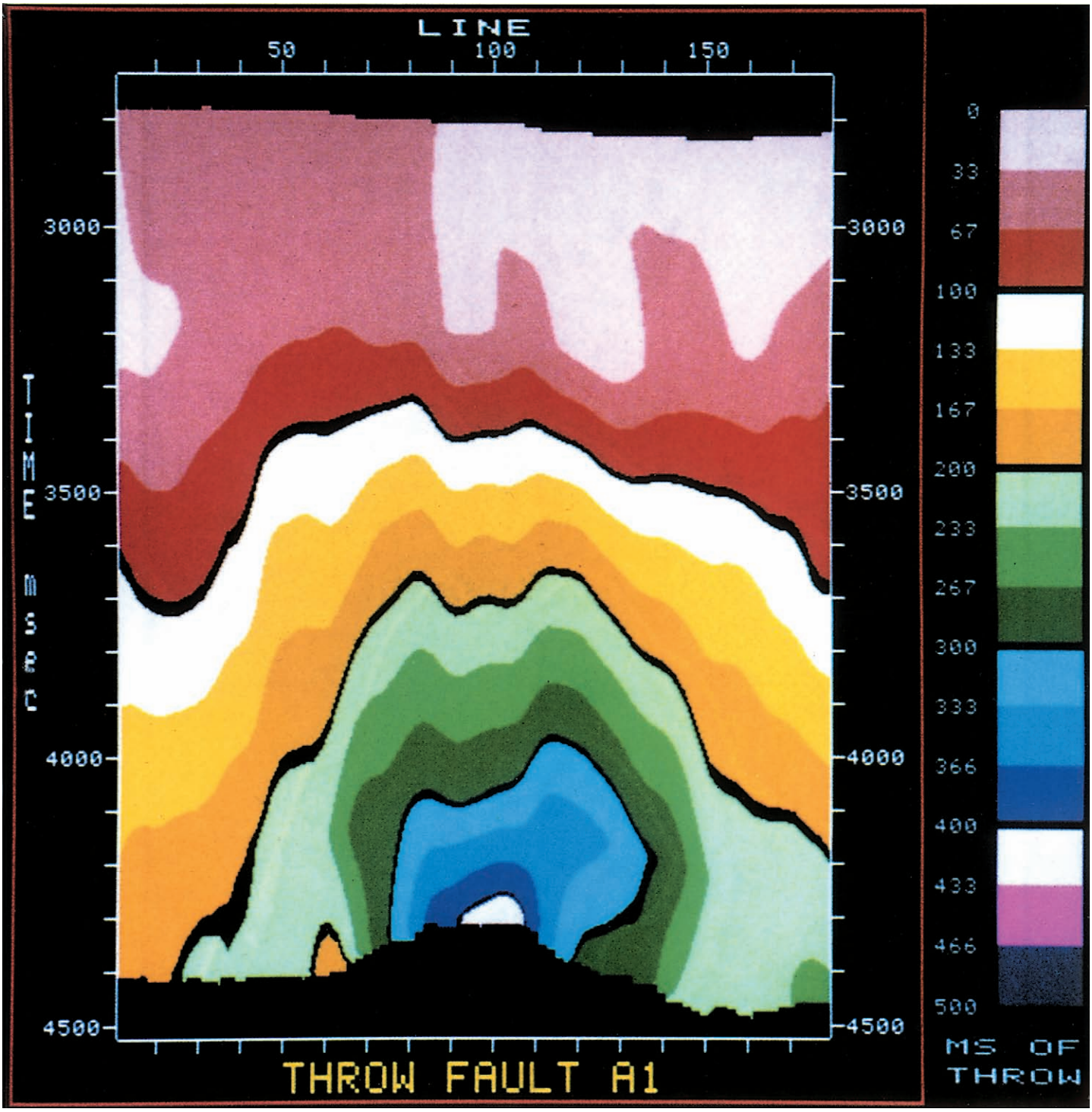

Fig. 7-31. Map of throw across the growth fault deduced from the horizon tracks in the upthrown fault block (Figure 7-30) and the correlative ones from a fault slice in the downthrown fault block. (Courtesy Texaco U.S.A. Inc.)

Downloaded 25 Jun 2012 to 129.110.5.90. Redistribution subject to SEG license or copyright; Terms of Use: http://segdl.org/

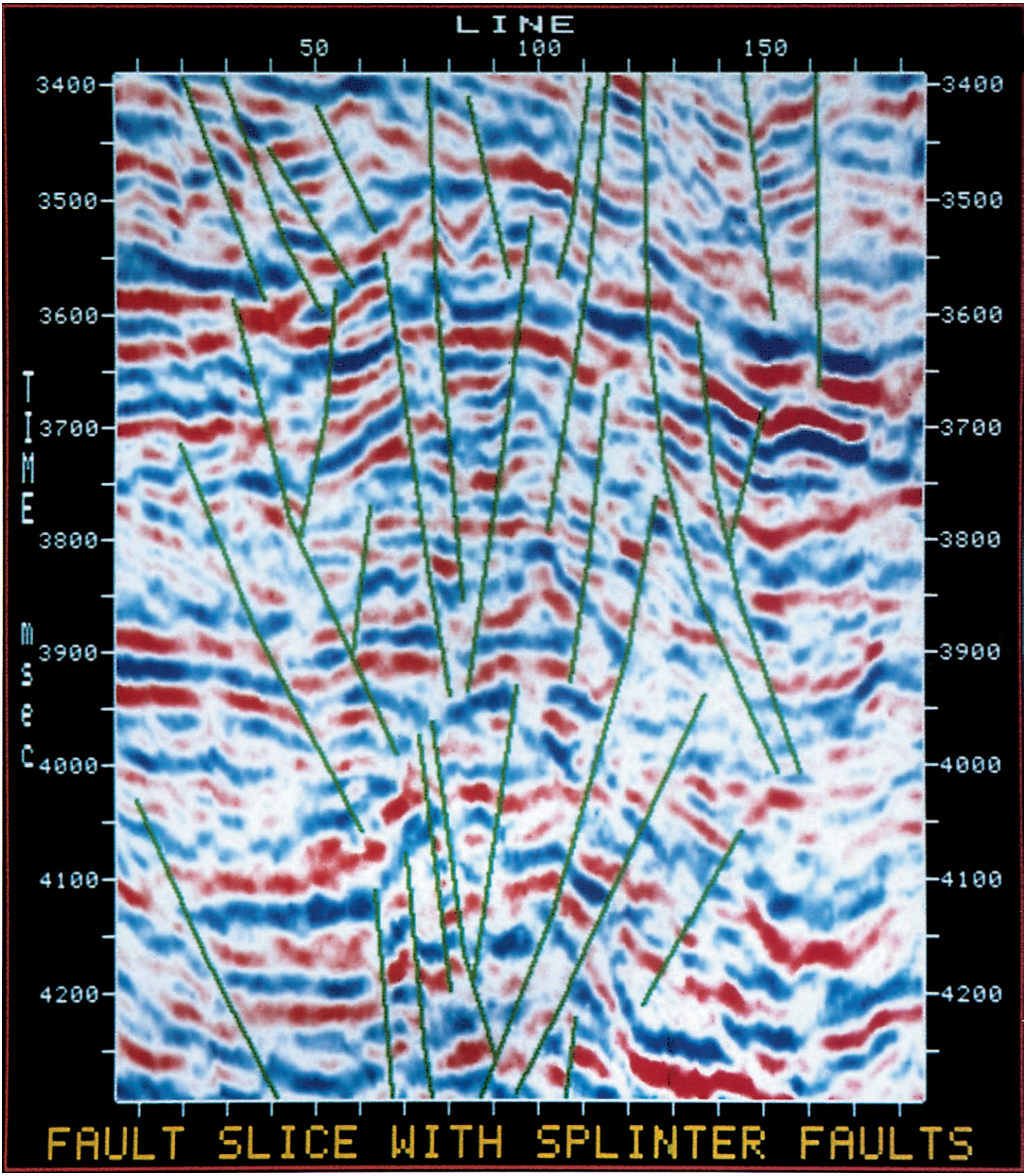

Fig. 7-32. Splinter faults generated by movement on the growth fault interpreted on one fault slice in the upthrown block. (Courtesy Texaco U.S.A. Inc.)

Downloaded 25 Jun 2012 to 129.110.5.90. Redistribution subject to SEG license or copyright; Terms of Use: http://segdl.org/

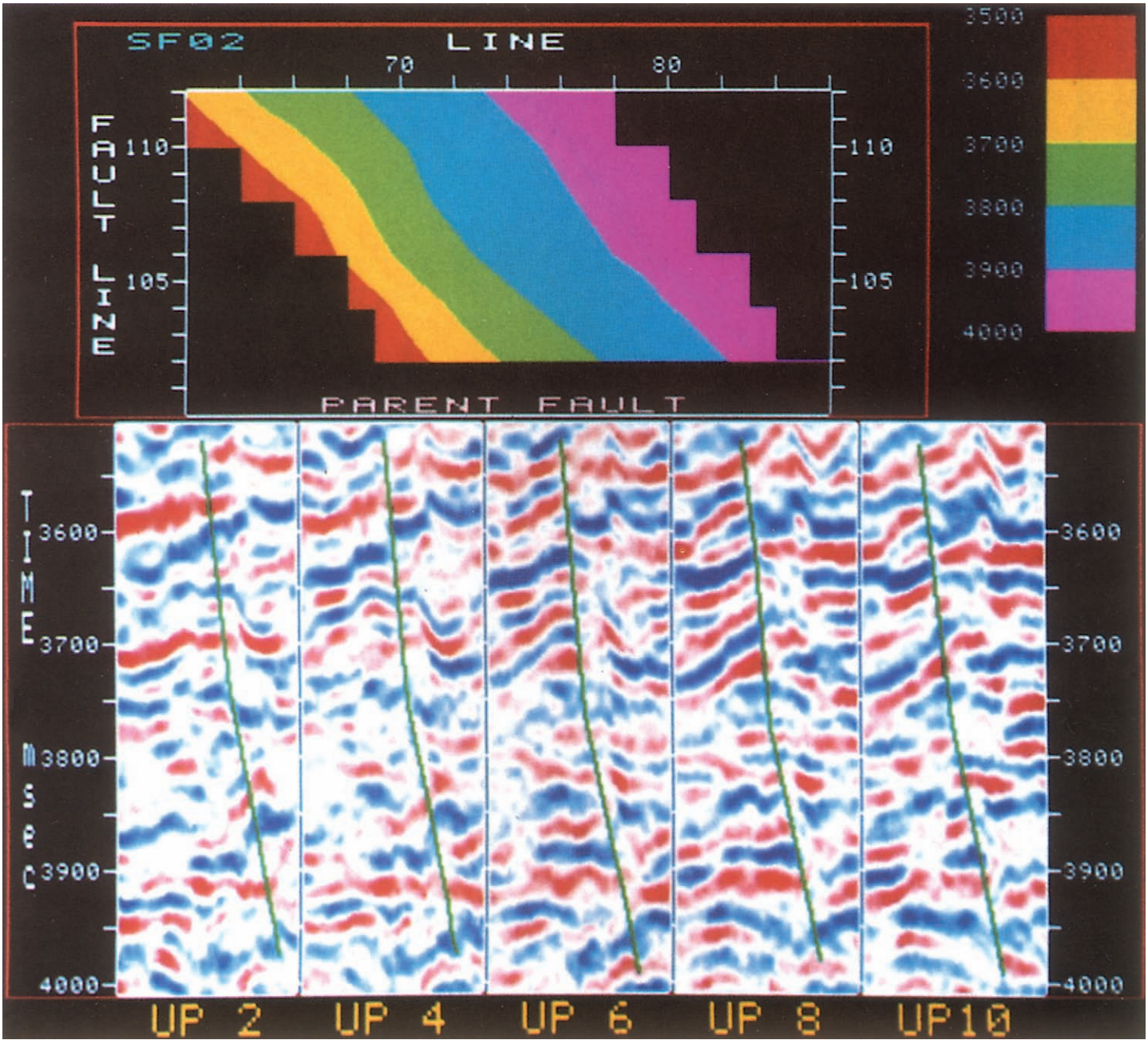

Fig. 7-33. Fault slice segments in the upthrown block used to map one splinter fault. The resultant map above is in coordinates relative to the growth fault, so that the contours show the relative strike of the splinter and its parent. (Courtesy Texaco U.S.A. Inc.)

Downloaded 25 Jun 2012 to 129.110.5.90. Redistribution subject to SEG license or copyright; Terms of Use: http://segdl.org/

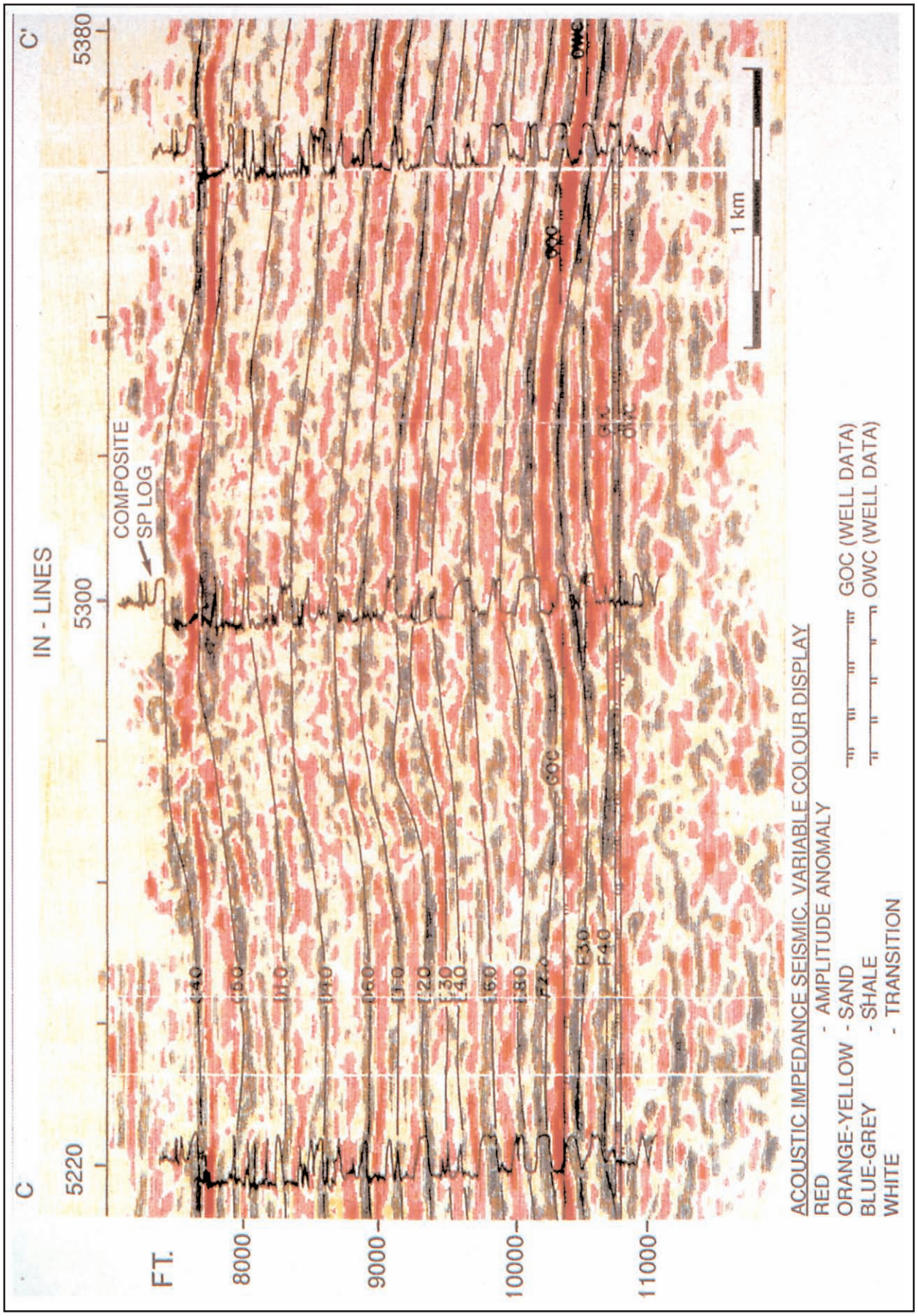

Fig. 7-34. Unrolled fault slice in depth along fault plane from Nigeria. Interpretation of sands and shales tied to three wells was for the study of fault sealing (Bouvier et al., 1989, reference in Chapter 8). (Courtesy Koninklijke/Shell.)

Downloaded 25 Jun 2012 to 129.110.5.90. Redistribution subject to SEG license or copyright; Terms of Use: http://segdl.org/

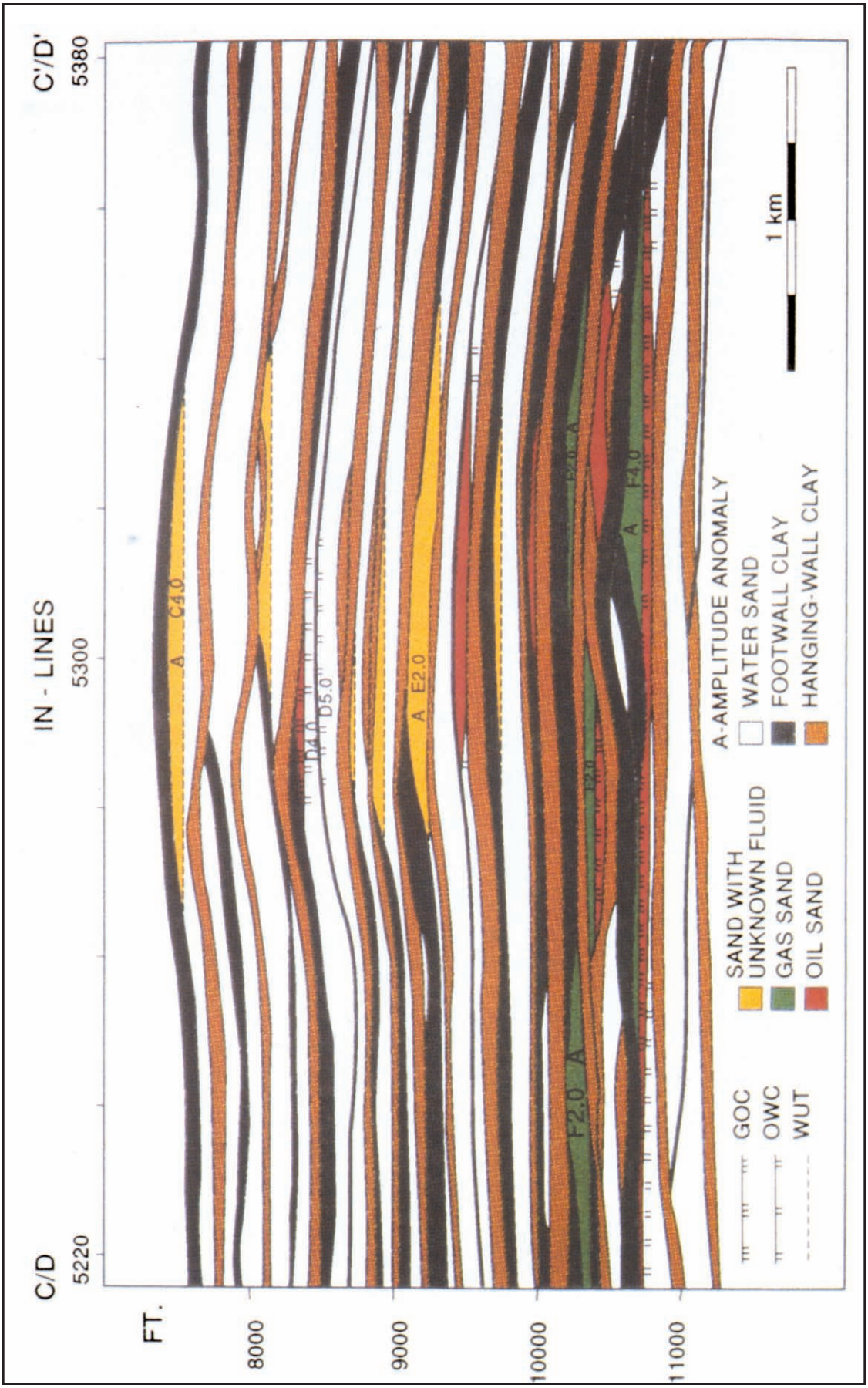

Fig. 7-35. Interpreted fault slice with colored fluids and black shale in one fault block. Superimposed in brown are the shale layers from the fault slice in the juxtaposed block. The fluids still visible potentially leak but may be sealed by clay smear (Bouvier et al., 1989, reference in Chapter 8). (Courtesy Koninklijke/Shell.)

Downloaded 25 Jun 2012 to 129.110.5.90. Redistribution subject to SEG license or copyright; Terms of Use: http://segdl.org/

References

Brown, A. R., G. S. Edwards, and R. E. Howard, 1987, Fault slicing — a new approach to the interpretation of fault detail: Geophysics, v. 52, p. 1319–1327.

Brown, A. R., R. M. Wright, K. D. Burkart, and W. L. Abriel, 1984, Interactive seismic mapping of net producible gas sand in the Gulf of Mexico: Geophysics, v. 49, p. 686–714.

Domenico, S. N., 1974, Effect of water saturation on seismic reflectivity of sand reservoirs encased in shale: Geophysics, v. 39, p. 759–769.

McCarthy, C. J., 1984, Seismic prediction of pore fluid and gas thickness: Proceedings, SEG 54th Annual Meeting, p. 326–328.

Matteucci, G., 1996, Seismic attribute analysis and calibration — a case study from the Gulf of Mexico: Geophysical Society of Houston Technical Workshop, April 17.

Meckel, L. D., Jr., and A. K. Nath, 1977, Geologic considerations for stratigraphic modeling and interpretation, *in* C. E. Payton, ed., Seismic stratigraphy — applications to hydrocarbon exploration: AAPG Memoir 26, p. 417–438.

Woock, R. D., and A. R. Kin, 1987, Predictive isopach mapping of gas sands from seismic impedance: modeled and empirical cases from Ship Shoal Block 134 field: AAPG Bulletin, v. 71, p. 1143–1151.

Downloaded 25 Jun 2012 to 129.110.5.90. Redistribution subject to SEG license or copyright; Terms of Use: http://segdl.org/

Horizon and Formation Attributes

Classification of Attributes

The last few years (since the publication of the Third Edition of this book) have seen an enormous increase in the number of attributes available and in their use. Attributes are used to pursue studies in structure, in stratigraphy and in reservoir properties. Therefore this chapter can be viewed as an extension of Chapters 3, 4 and 7.

An attribute is necessarily a derivative of a basic seismic measurement. All the horizon and formation attributes available (Figure 8-1) are not independent of each other but simply different ways of presenting and studying a limited amount of basic information. That basic information is **time**, **amplitude**, **frequency** and **attenuation** and these form the basis of our attribute classification.

As a broad generalization time-derived attributes provide structural information, amplitude-derived attributes provide stratigraphic and reservoir information. Frequency-derived attributes are not yet well understood but there is widespread optimism that they will provide additional useful stratigraphic and reservoir information. Attenuation is not used today but there is a possibility that in the future it will yield information on permeability. Most attributes are derived from the normal stacked and migrated data volume but variations of basic measurements as a function of angle of incidence (and hence source to receiver offset) provides a further source of information. The principal examples of these pre-stack attributes are AVO.

Post-stack attributes can be extracted along one **horizon** or summed over a **window** (Figure 8-1). The latter provides the concept of a formation attribute. In some cases the window is a constant flat time interval so that the display is effectively a thick time slice, sometimes termed a stat (statistical) slice. The window may be of a constant time interval but hung from one structurally-interpreted horizon so that the window properly follows a reservoir interval. The window may also be the interval between two structurally-interpreted horizons, for example the top and the base reservoir reflections. Within the window values may be summed to produce a **gross** attribute measurement, only some of the information may be extracted to provide a **selection** attribute, or the variation of the attribute within the window may be measured to assess a **distribution**. **Hybrid** attributes are an intriguing combination of amplitude and frequency information. Many examples of the uses of these different types of attributes are provided in this chapter, but not every attribute in Figure 8-1 is illustrated. Some of those listed have yet to be understood. A more extensive, but in the author's view less useful, attribute classification has been published by Chen and Sidney (1997).

Attributes normally are calculated and extracted from the data volume following

Text continues on page 256.

Downloaded 25 Jun 2012 to 95.28.162.50. Redistribution subject to SEG license or copyright; Terms of Use: http://segdl.org/

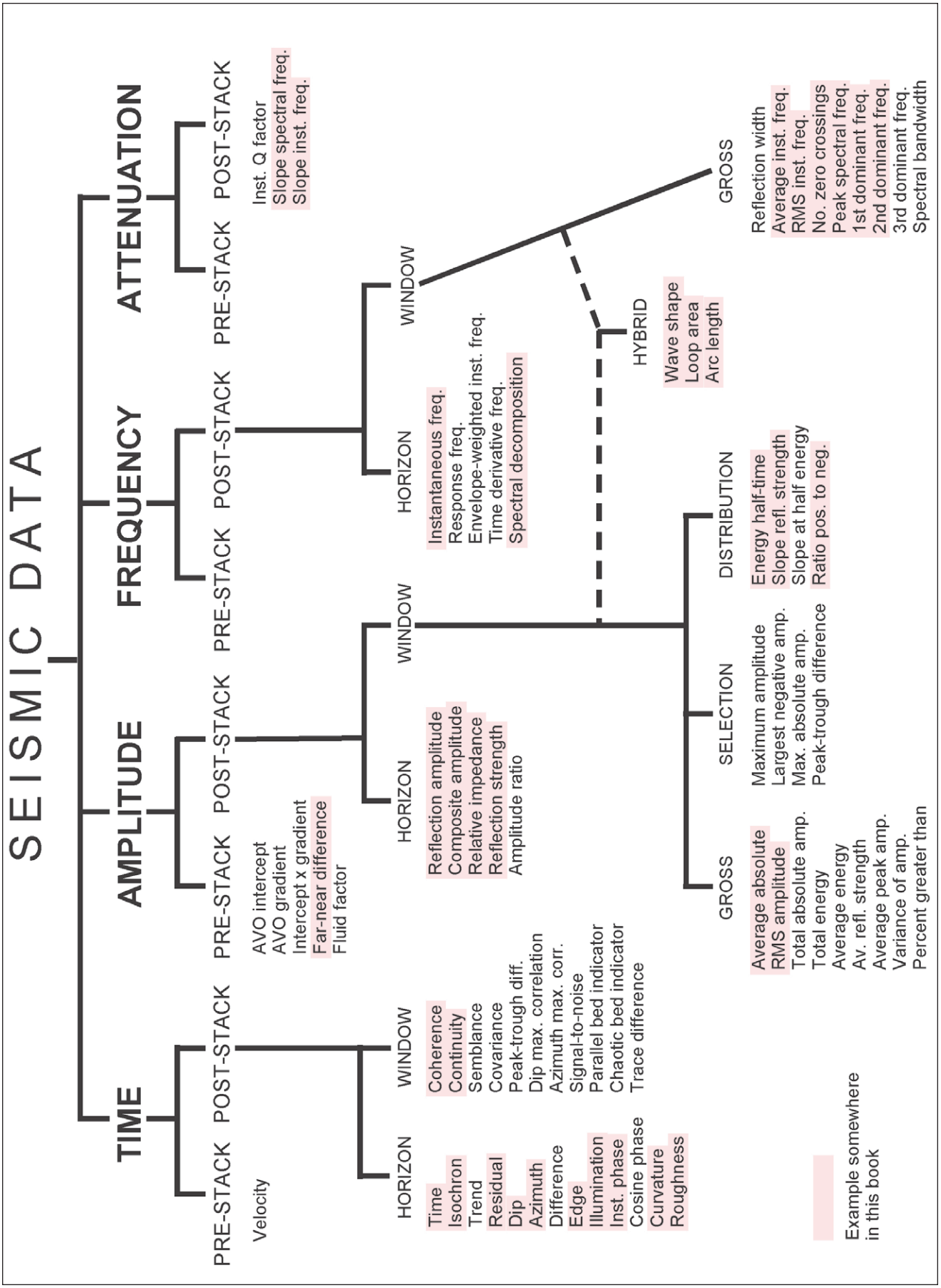

Fig. 8-1. Seismic attributes derived from or related to the basic seismic information of time, amplitude, frequency and attenuation. Window can be constant time interval, constant interval hung from one horizon or interval between two horizons.

Downloaded 25 Jun 2012 to 95.28.162.50. Redistribution subject to SEG license or copyright; Terms of Use: http://segdl.org/

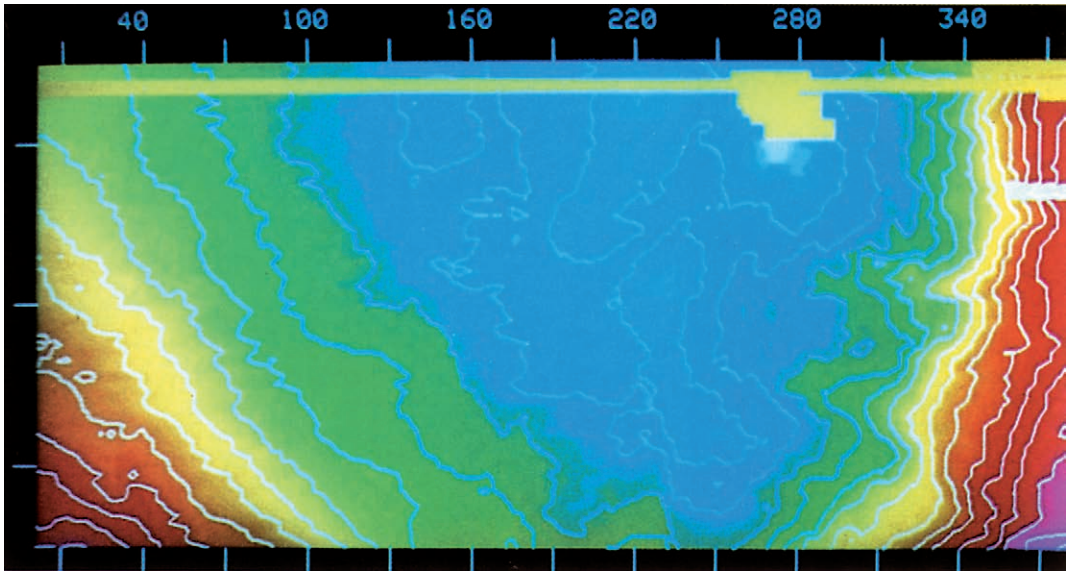

Fig. 8-2. Raw time structure map from Gippsland Basin, offshore SE Australia, with value from every live trace. Time range is 1100 ms to 1400 ms. (Courtesy Landmark Graphics Corporation and BHP Petroleum Pty. Ltd.)

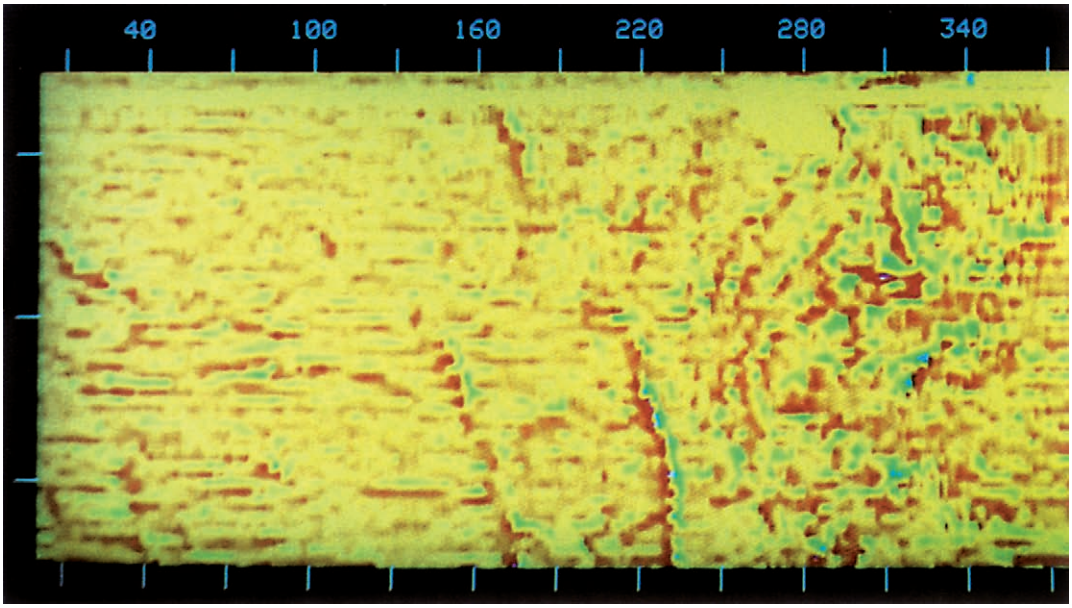

Fig.8-3. Residual map from Gippsland Basin, created by subtracting raw and spatially smoothed horizon times. The NNW-SSE trends around crosslines 160 and 220 are faults; blue is upthrown side and red is downthrown side. The E-W linear trends are caused by data collection irregularities. (Courtesy Landmark Graphics Corporation and BHP Petroleum Pty. Ltd.)

Downloaded 25 Jun 2012 to 95.28.162.50. Redistribution subject to SEG license or copyright; Terms of Use: http://segdl.org/

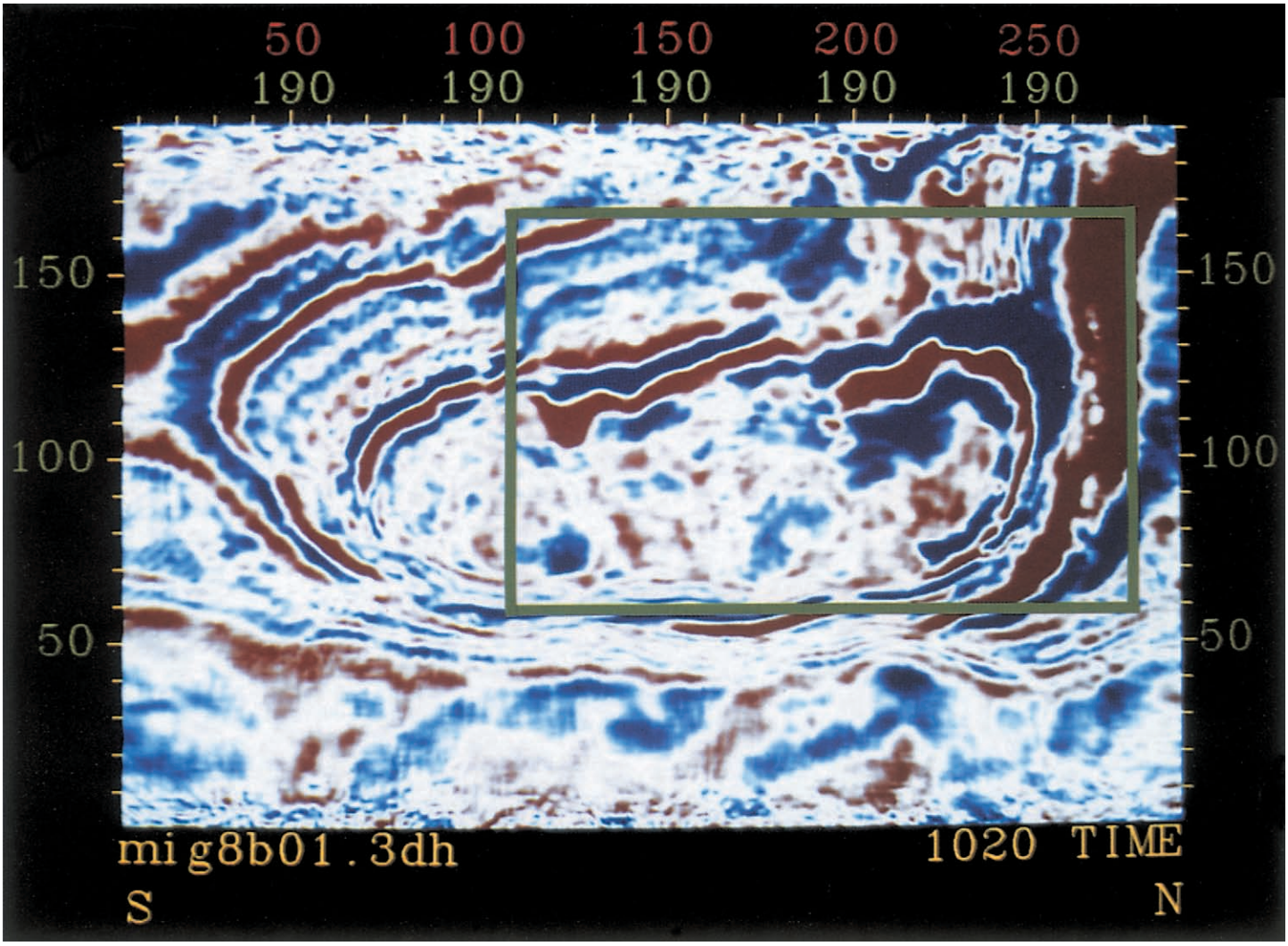

Fig. 8-4. Time slice at 1020 ms from Dollarhide field in west Texas, showing in green the outline of the area mapped in Figures 8-5 and 8-6. (Courtesy Unocal North American Oil & Gas Division.)

Fig. 8-5. (Opposite top) Time structure map on Devonian reflection, using raw times from automatic horizon tracking. (Courtesy Unocal North American Oil & Gas Division.)

Fig. 8-6. (Opposite bottom) Residual map created by subtracting the raw and spatially smoothed time maps. Note particularly the lineations which fit existing fault patterns. (Courtesy Unocal North American Oil & Gas Division.)

Downloaded 25 Jun 2012 to 95.28.162.50. Redistribution subject to SEG license or copyright; Terms of Use: http://segdl.org/

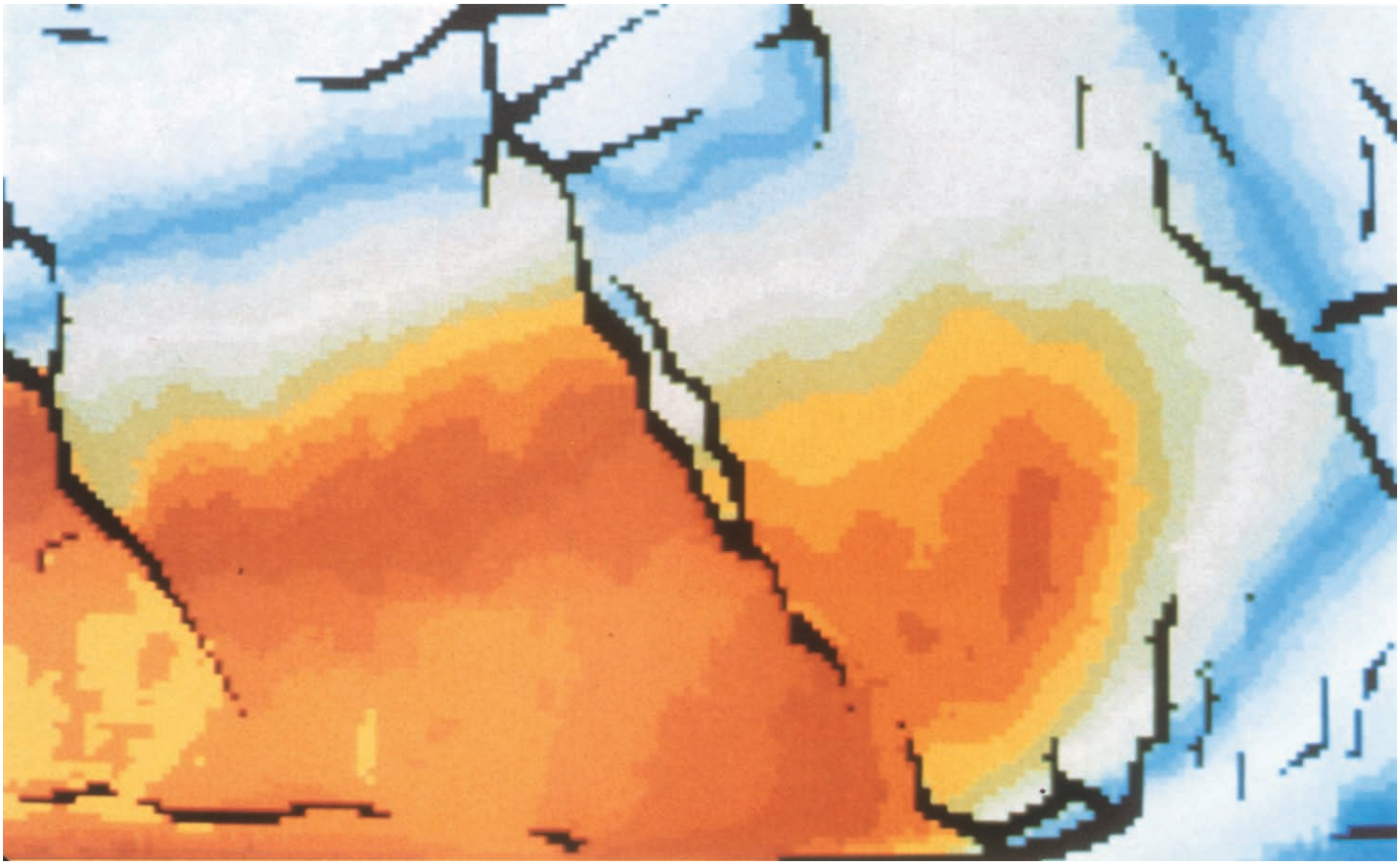

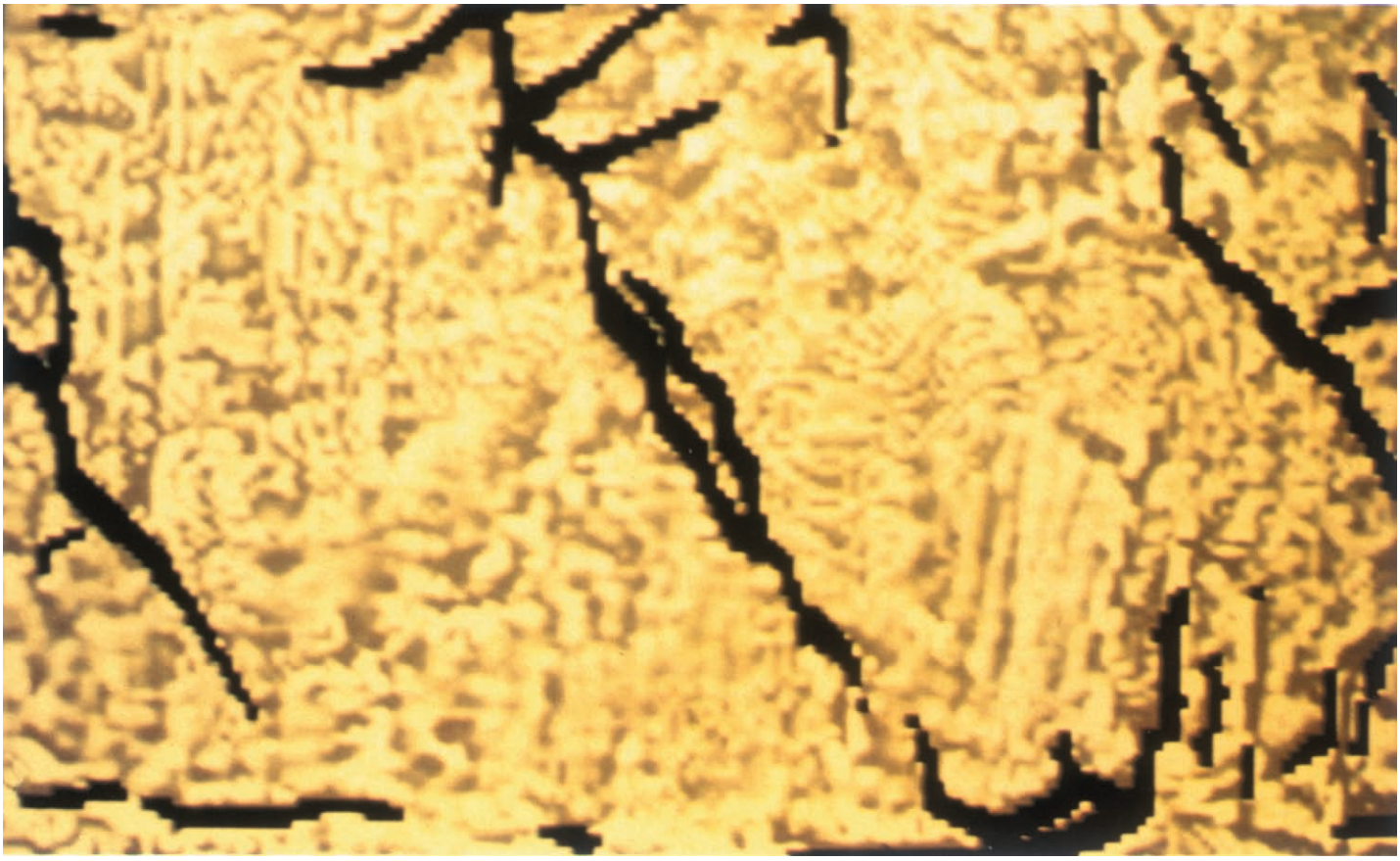

Downloaded 25 Jun 2012 to 95.28.162.50. Redistribution subject to SEG license or copyright; Terms of Use: http://segdl.org/

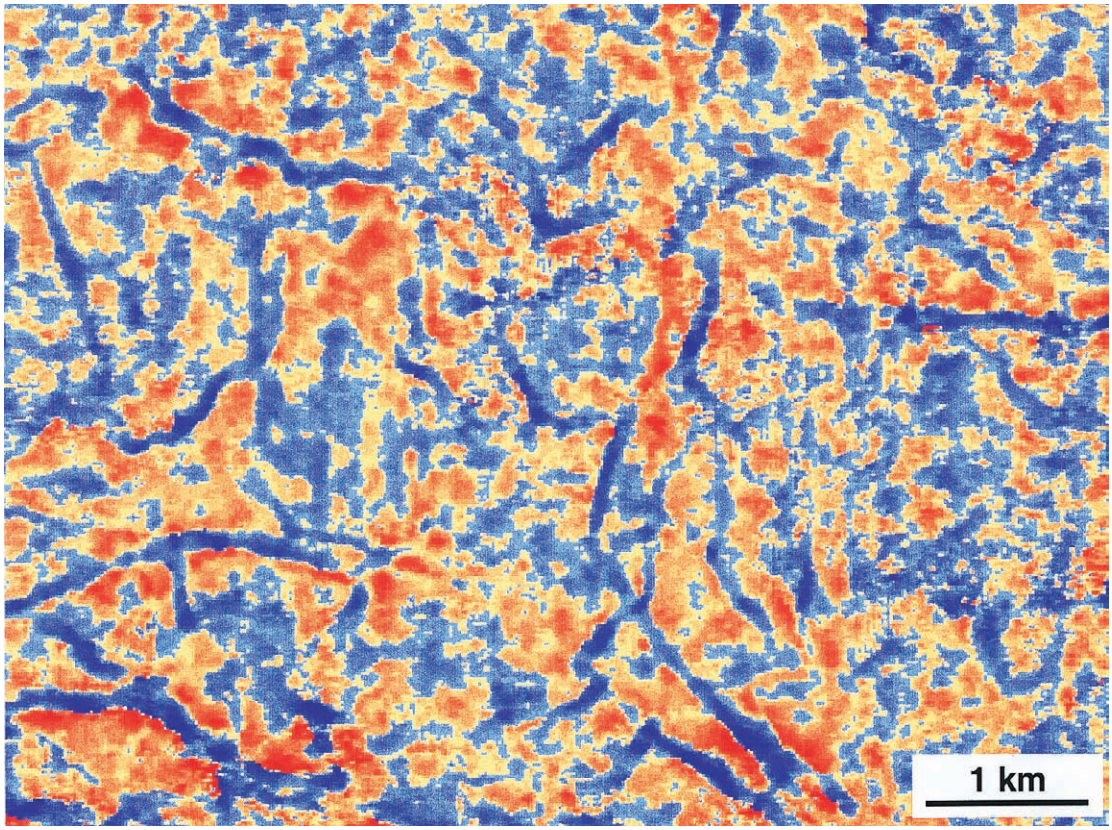

Fig. 8-7. Residual map from Eromanga Basin, South Australia. The linear blue features indicate grabens in the early Cretaceous C horizon occurring in this area around 1100 ms. (Courtesy Santos Ltd.)

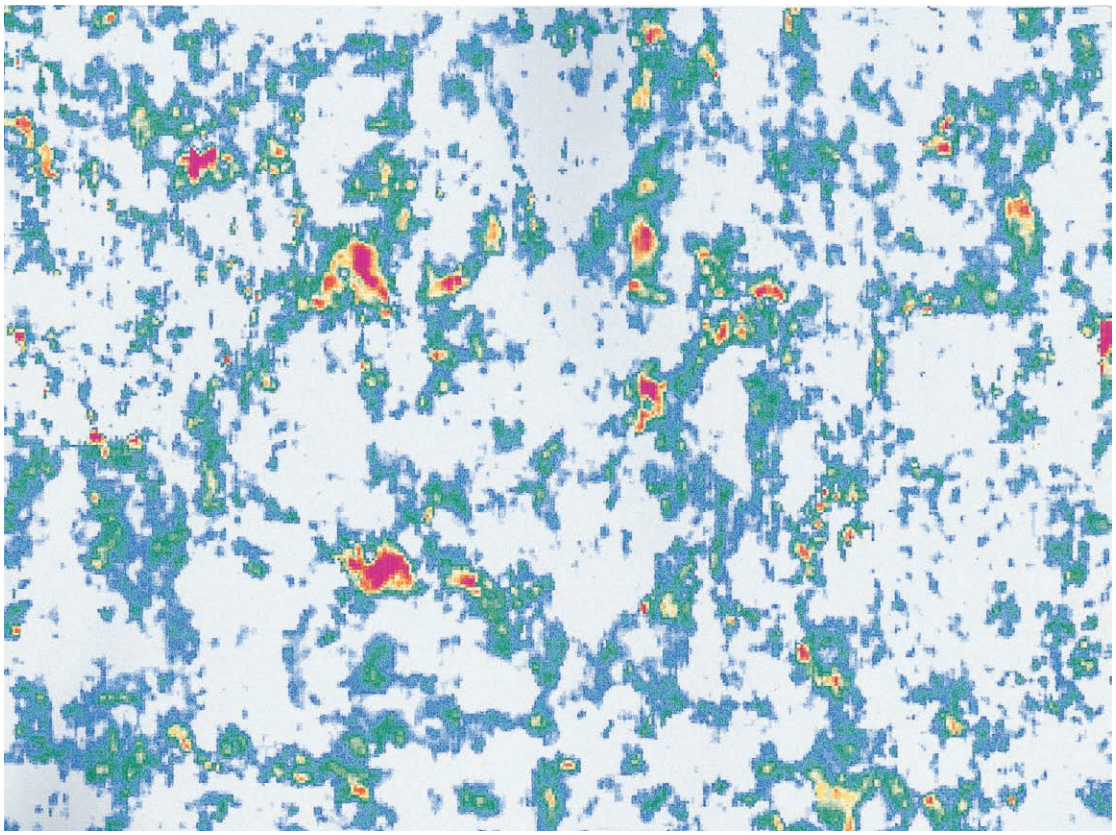

Fig. 8-8. Residual map on the DN horizon from Eromanga Basin, South Australia. The red and yellow patches indicate high spatial frequency drape over underlying bodies of calcified sandstone. (Courtesy Santos Ltd.)

Downloaded 25 Jun 2012 to 95.28.162.50. Redistribution subject to SEG license or copyright; Terms of Use: http://segdl.org/

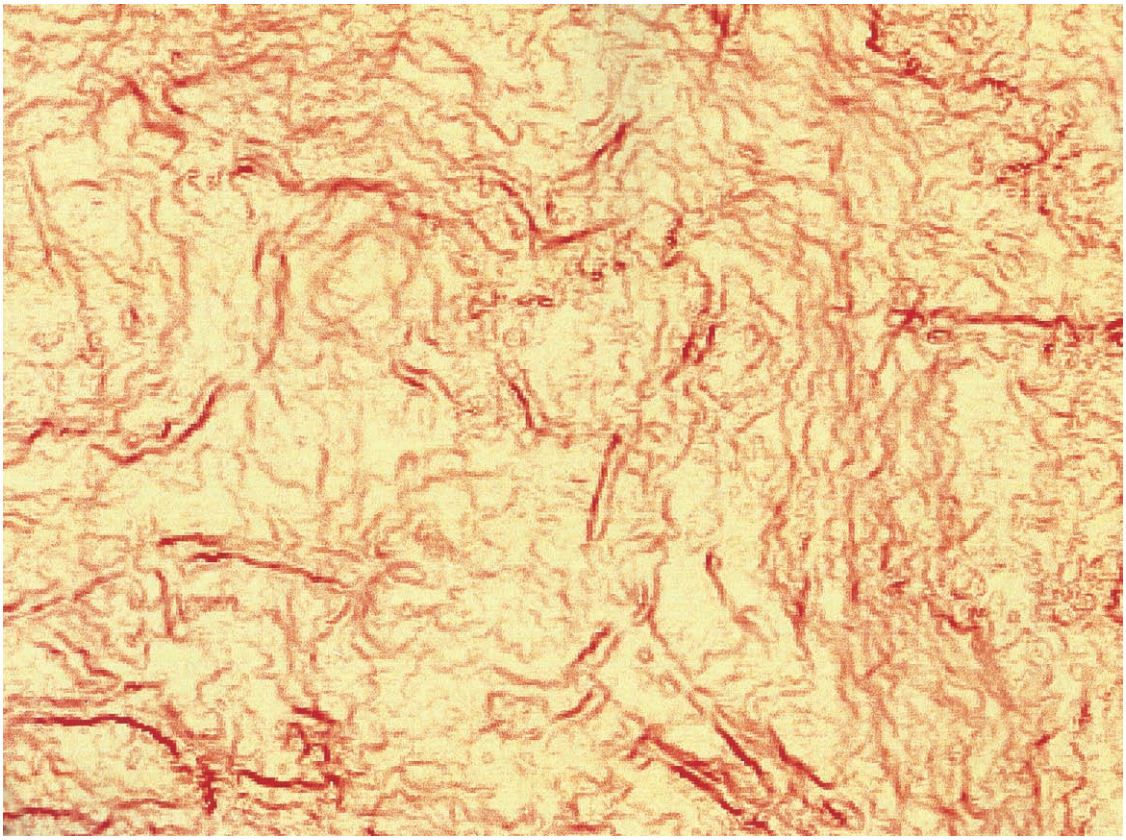

Fig. 8-9. Dip map on the C horizon from Eromanga Basin, South Australia. Note the double lineations indicating conjugate pairs of faults which correspond to the grabens of Figure 8-7. (Courtesy Santos Ltd.)

Downloaded 25 Jun 2012 to 95.28.162.50. Redistribution subject to SEG license or copyright; Terms of Use: http://segdl.org/

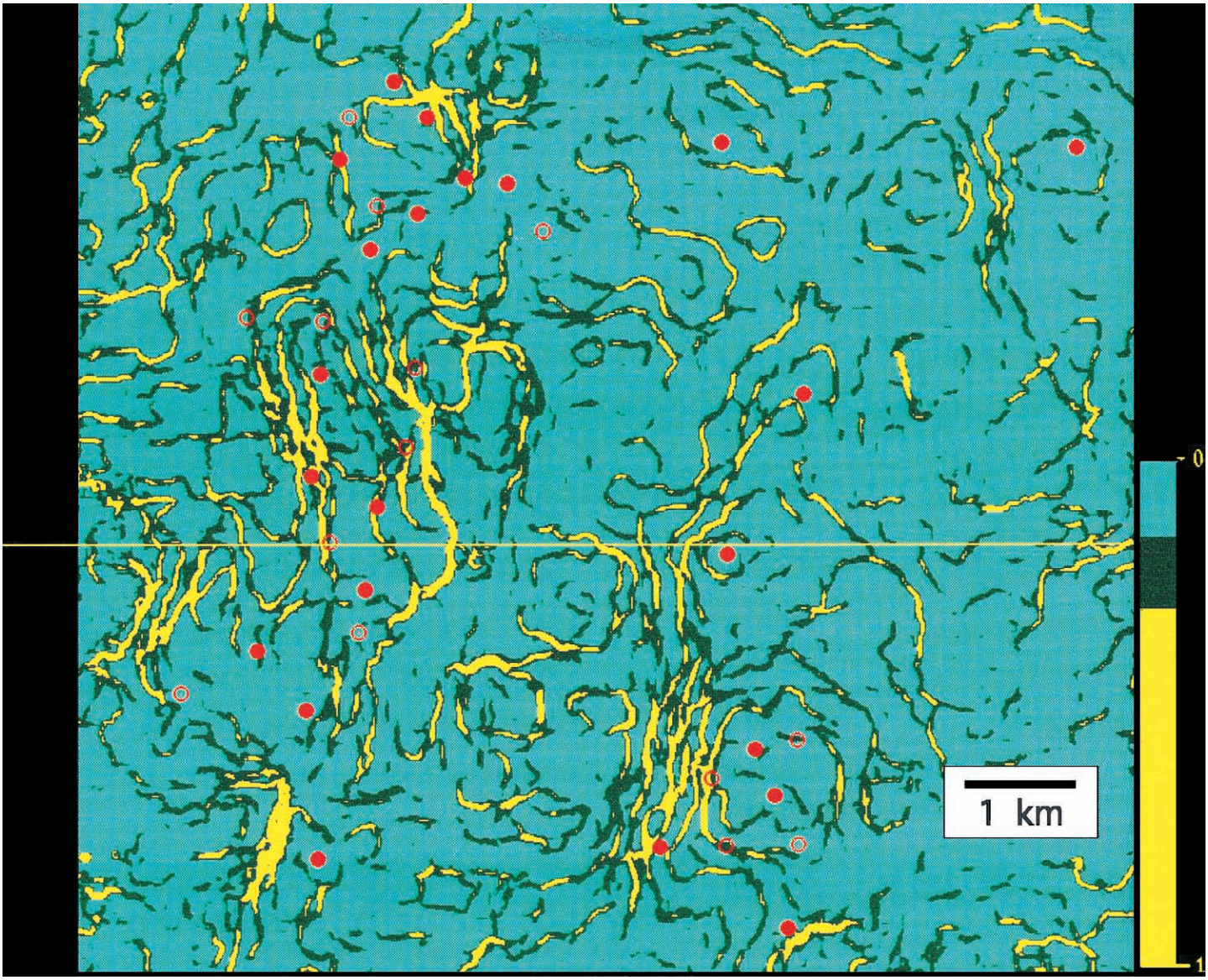

Fig. 8-10. Dip map of top reservoir reflection from Oman, indicating a large number of arcuate faults. (Courtesy Petroleum Development Oman LLC.)

Fig. 8-11. (Opposite top) Same dip map as Figure 8-10 with manually drawn red polygons around the significant dip anomalies. These polygons were then used in the final mapping of top reservoir. (Courtesy Petroleum Development Oman LLC.)

Fig. 8-12. (Opposite bottom) Vertical section along yellow line in Figures 8-10 and 8-11. The blue horizon is top of reservoir. A few sections like this one were used to validate faulting identified on the dip map. (Courtesy Petroleum Development Oman LLC.)

Downloaded 25 Jun 2012 to 95.28.162.50. Redistribution subject to SEG license or copyright; Terms of Use: http://segdl.org/

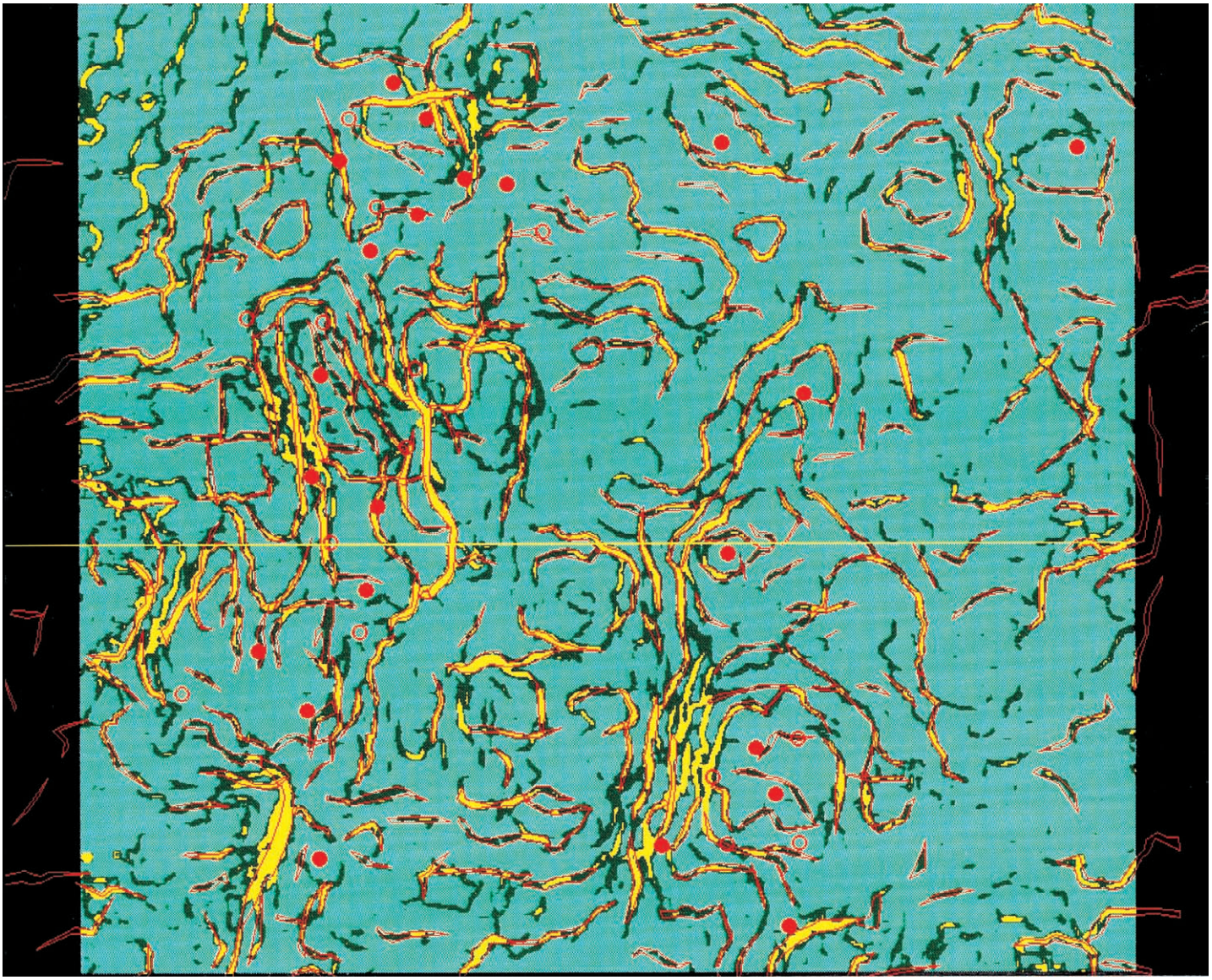

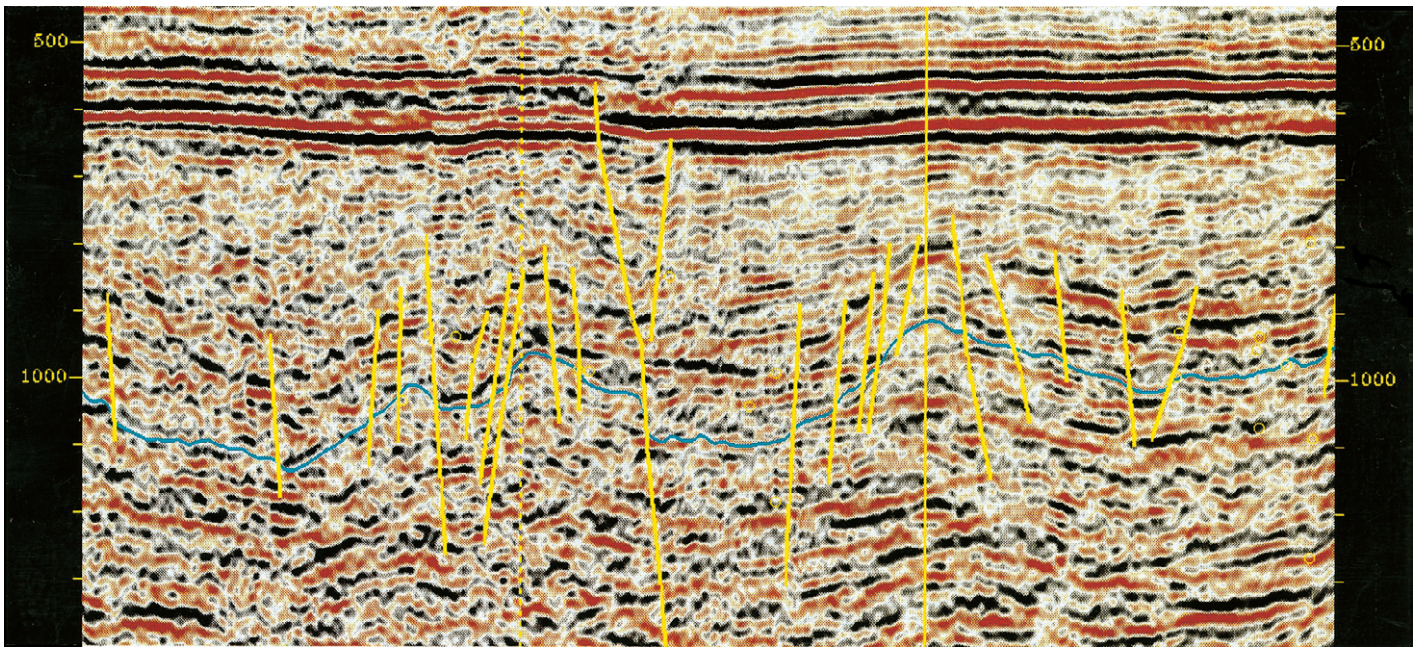

Downloaded 25 Jun 2012 to 95.28.162.50. Redistribution subject to SEG license or copyright; Terms of Use: http://segdl.org/

automatic spatial tracking or snapping. These workstation capabilities help the interpreter use all of the data and provide horizon time values at the crest of a reflection with a precision of about a quarter of a millisecond. The horizon attribute extracted at the crestal time carries a similar precision. Proper use of machine precision is a key part of seismic attribute analysis as the interpretation objective is normally a rather detailed one. The quotation at the front of this book, "Believe everything to be geology until proved otherwise," applies here. It is wise to put all detailed information into the interpretation in the early stages and consider later what is geology and what is noise. Attribute displays can be very helpful in this important decision. Windowed attributes generally use the sample values every 2 or 4 milliseconds.

Time-derived Horizon Attributes

Residual, or high spatial frequency residual map, is the arithmetic difference between a high-precision automatically-tracked time map and its spatially-smoothed equivalent. Figure 8-2 illustrates such a time map from Australia and Figure 8-3 is the corresponding residual map (Denham and Nelson, 1986). There are two types of linear patterns on this residual. The NNW-SSE lineations are faults, mostly too subtle to be seen as contour disturbances on the time map. The exactly-parallel east-west lineations are in the data collection direction and are clearly caused by data collection irregularities; this is a form of noise and is therefore unwanted.

Figure 8-4 shows the area under study in the next example; Figure 8-5 is the autotracked high-precision time map; Figure 8-6 is the residual. The black features are gaps in the interpreted horizon which were recognized as faults in the mainstream of the interpretation using vertical and horizontal sections. A linear pattern in the residual parallel to the existing faults and towards the east end of the area is a rather clear indication of another fault or similar geologic feature. In contrast, the north-south patterns towards the west end are highly regular and parallel and do not fit the existing fault patterns; they must be identified as data collection lineations or noise.

Figure 8-7 is a residual map from a land 3-D survey in South Australia; it is the time difference between a snapped and a smoothed version of this early Cretaceous horizon. The dark blue linear features are grabens. Blue means that the snapped horizon is below the smoothed horizon thus establishing that these features are structurally low.

Figure 8-8 is a similarly-produced residual map on another deeper horizon from the same survey. The red and yellow patches indicate high-spatial-frequency drape over underlying bodies of calcified sandstone. The calcite varies rapidly both horizontally and vertically in this interval and therefore constitutes a serious problem because of its effect on depth-conversion velocities for deeper horizons. This residual map is helping to address the problem.

Dip, or dip magnitude, is another time-derived horizon attribute addressing issues of structural detail (Dalley et al., 1989). On the high-precision automatically-tracked time surface one time value is considered in relation to its immediate neighbors to form a local plane. The true dip of that local plane is the attribute dip; the direction of that dip is the azimuth, or dip azimuth, which will be discussed later.

Figure 8-9 shows the dip map for the same horizon as used in Figure 8-7. The double lineations indicate conjugate pairs of faults which correspond to the grabens of Figure 8-7 (Oldham and Gibbins, 1995).

Figure 8-10 shows the dip map for a top reservoir reflection from Oman. Many arcuate features are evident. The color scheme was set so that all that was clearly noise was suppressed into the gray-green; everything else was considered as a potential real fault. The red polygons in Figure 8-11 were drawn around the majority of the dip anomalies and were then used directly in the mapping process. In drawing the red polygons and in deciding which dip anomalies were real, a few vertical

Downloaded 25 Jun 2012 to 95.28.162.50. Redistribution subject to SEG license or copyright; Terms of Use: http://segdl.org/

sections like Figure 8-12 were studied. The faults validated with a red polygon along the east-west yellow line in Figure 8-11 are shown in yellow in Figure 8-12.

Hesthammer (1998 and 1999) has studied subtle curvilinear features on dip and other attribute displays and concluded that many of them are noise. Coherent noise in the seismic data intersects the horizon under study and causes steps that can look like faults. Hesthammer concludes that the distinction between real, subtle faults and noise can be difficult, and this problem most likely exists in Figures 8-9 and 8-10. The basis for distinguishing must be geological reasonableness.

Figure 8-13 shows the dip map of a horizon which was autotracked with little vertical and horizontal section control. Although the tracking was successful over much of the area, the tracker jumped onto the wrong event in several places. These tracking busts show as very straight high-dip pseudo-faults primarily in green and blue. This demonstrates that time-derived attribute displays such as dip can be used to quality control the performance of an autotracker as well as to establish further structural detail.

Azimuth, or dip azimuth, is used in a similar way to dip. Figure 8-14 shows an example of an azimuth map from Lake Maracaibo, Venezuela. The data is clearly noisy but nonetheless several meaningful patterns can be seen. The red arrows indicate anomalies which conform with existing fault patterns and are thus probable additional faulting. Two of the indicated faults are magenta and blue and thus dip to the northeast; the third is red and yellow and thus dips to the southwest.

Figures 8-15 and 8-16 show a pair of dip and azimuth displays from Nigeria. Both show many faults which are generally the same. However, red arrows indicate two faults, each of which is visible on only one of the displays. For a subtle fault the dip of the fault can accidentally concur with the dip of the surrounding horizon surface; likewise separately for the azimuth. It is thus wise to look at more than one type of attribute display in order to reduce the chance of missing something significant.

A **dip-azimuth** combination map (Figure 8-17) combines the separate dip and azimuth attributes onto the one display and is thus an alternative approach to the fault visibility problem discussed above. In Figure 8-17 he dip is coded to color density and the azimuth is coded to hue according to the circular legend. Many faults associated with salt movement are visible.

Curvature and **roughness** are derivatives of dip and azimuth and thus serve as second derivatives of structure. Figure 8-18 illustrates these attributes and compares them with azimuth for the same horizon surface.

Edge, or edge detection, is a spatial operator usually occupying 9 points which operates like a spatial smoothing filter but has the opposite effect; spatial differences or edges are accentuated regardless of orientation. Figure 8-19 is an edge map on the top Tosca reflection in the Neuquen Basin of Argentina. In the west there is a swarm of north-south faults and several 7-km-long arcuate faults. These arcuate faults look impressive on the edge map but have a barely-visible displacement on vertical sections. Similar arcuate patterns on the edge maps from deeper horizons indicate that these faults are in fact conical in shape pointing downwards with their apexes on an igneous intrusion.

Figure 8-20 is an edge map from southern Alberta in Canada here being used to delineate a reef.

Illumination, lighting, shaded relief or sun shading is a display technique already well known from topographic and other kinds of mapping. Portions of the autotracked time surface pointing towards the source are highlighted, those pointing away from the source are in shadow. Figure 8-21 has an illumination direction from the northwest. The fault running north-south down the west side is highlighted. Just east of this is a sequence of en echelon faults in shadow. Just southeast of center is a clearly visible graben.

Figures 8-22 and 8-23 show the same time surface with different illumination directions

Text continues on page 274.

Downloaded 25 Jun 2012 to 95.28.162.50. Redistribution subject to SEG license or copyright; Terms of Use: http://segdl.org/

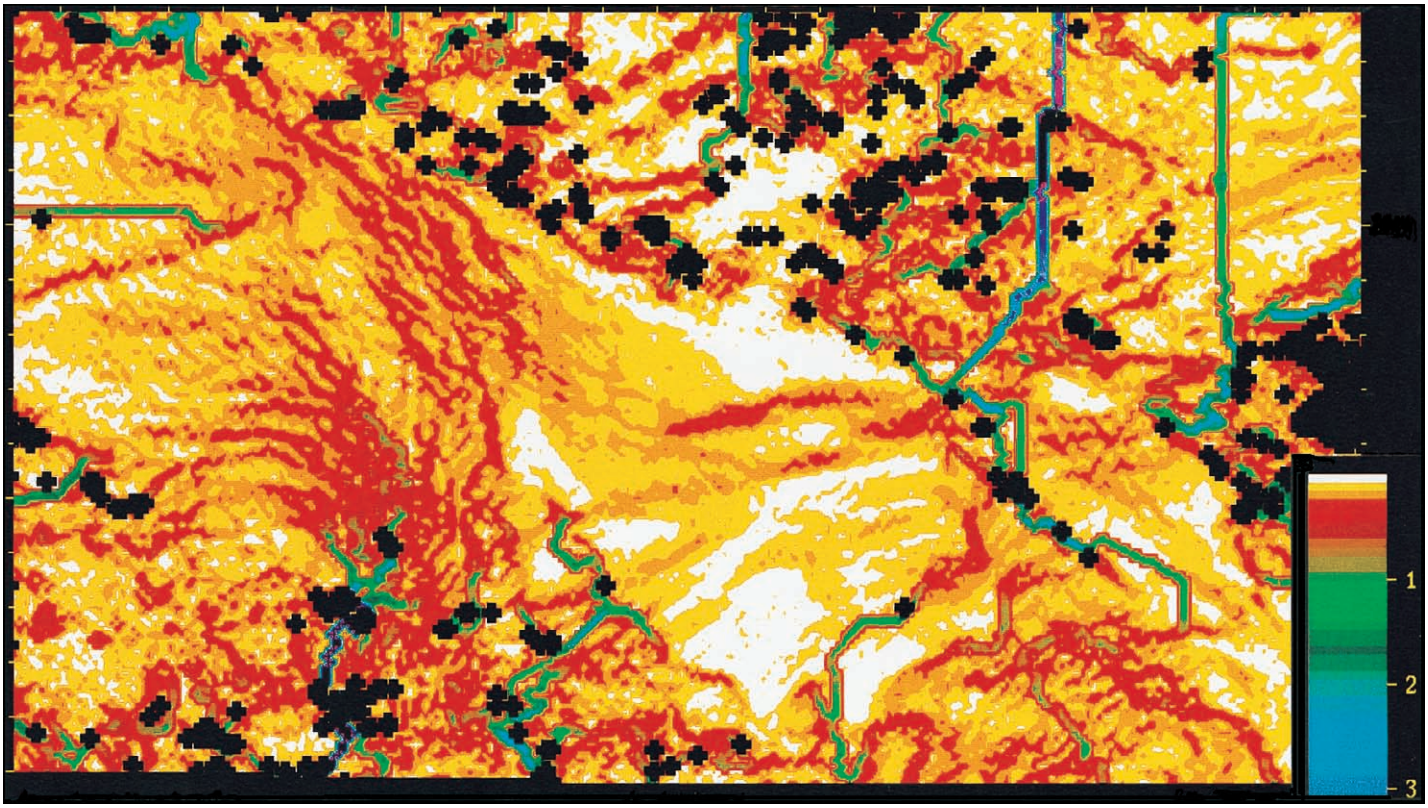

Fig. 8-13. Dip map used to check quality control of automatic tracker performance. The very straight, high-dip pseudo-faults are tracking busts. (Courtesy Nederlandse Aardolie Maatschappij B.V.)

Downloaded 25 Jun 2012 to 95.28.162.50. Redistribution subject to SEG license or copyright; Terms of Use: http://segdl.org/

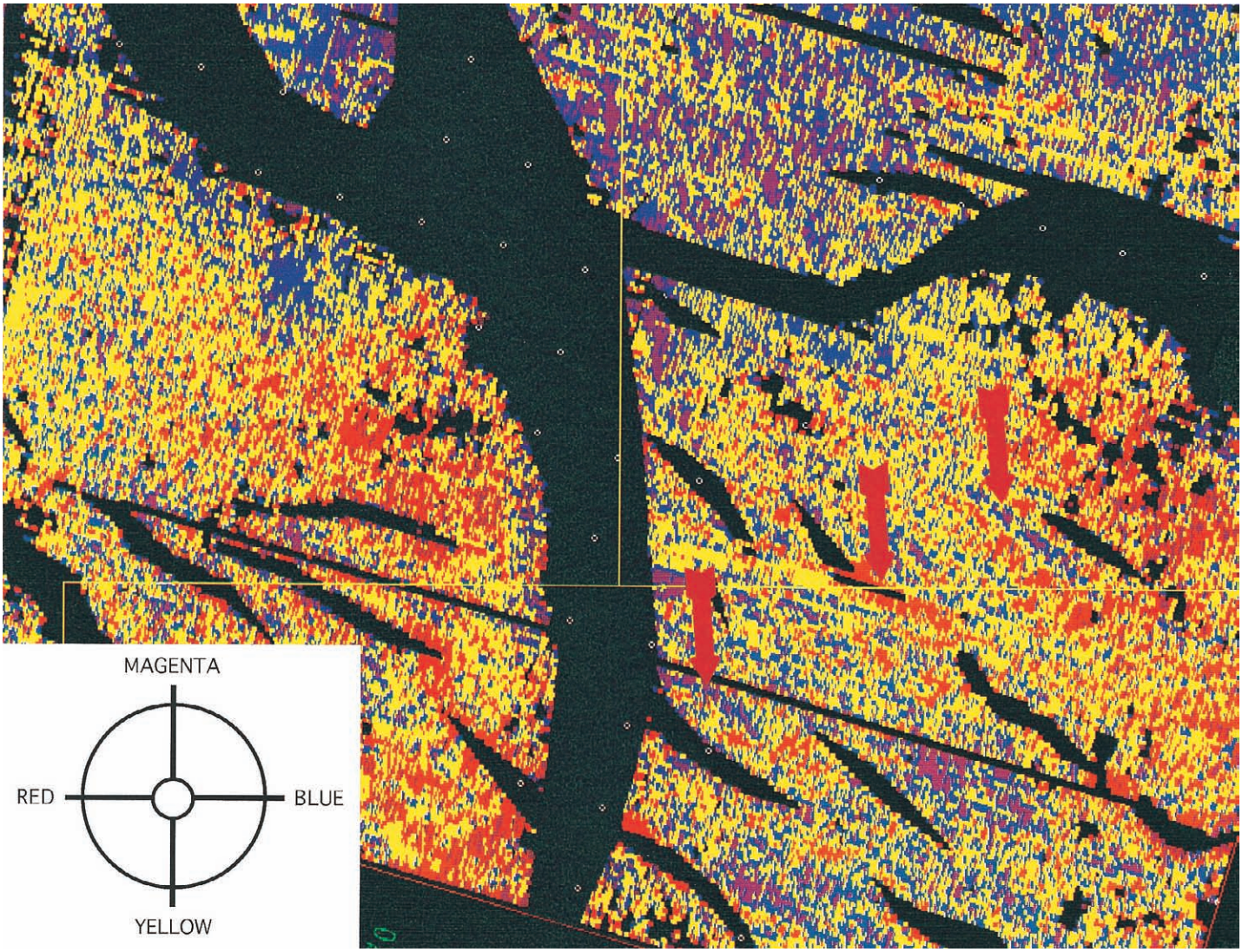

Fig. 8-14. Azimuth map from Lake Maracaibo, Venezuela. Red arrows indicate anomalies which conform well to existing fault patterns and are thus probable additional faulting. (Courtesy Maraven S.A.)

Downloaded 25 Jun 2012 to 95.28.162.50. Redistribution subject to SEG license or copyright; Terms of Use: http://segdl.org/

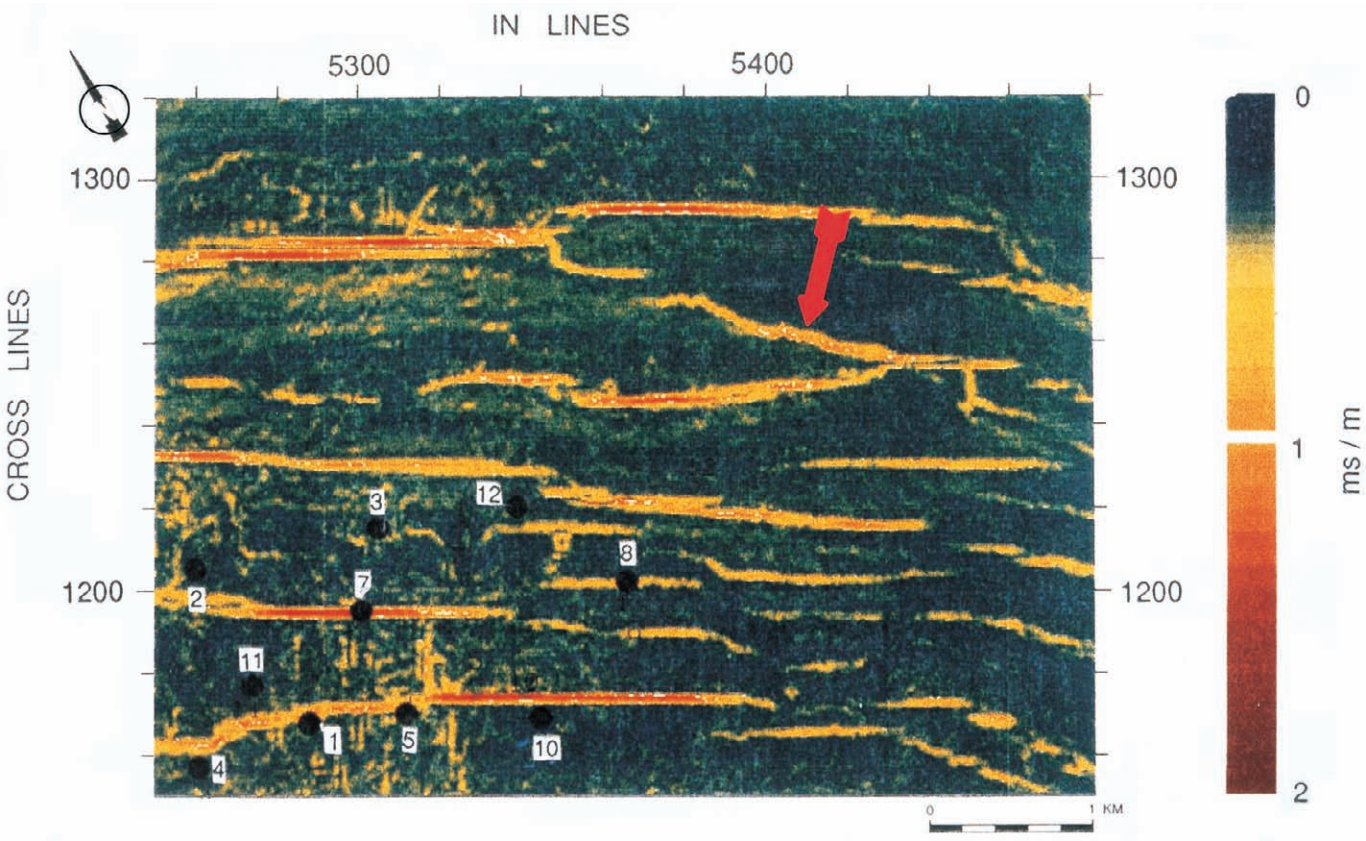

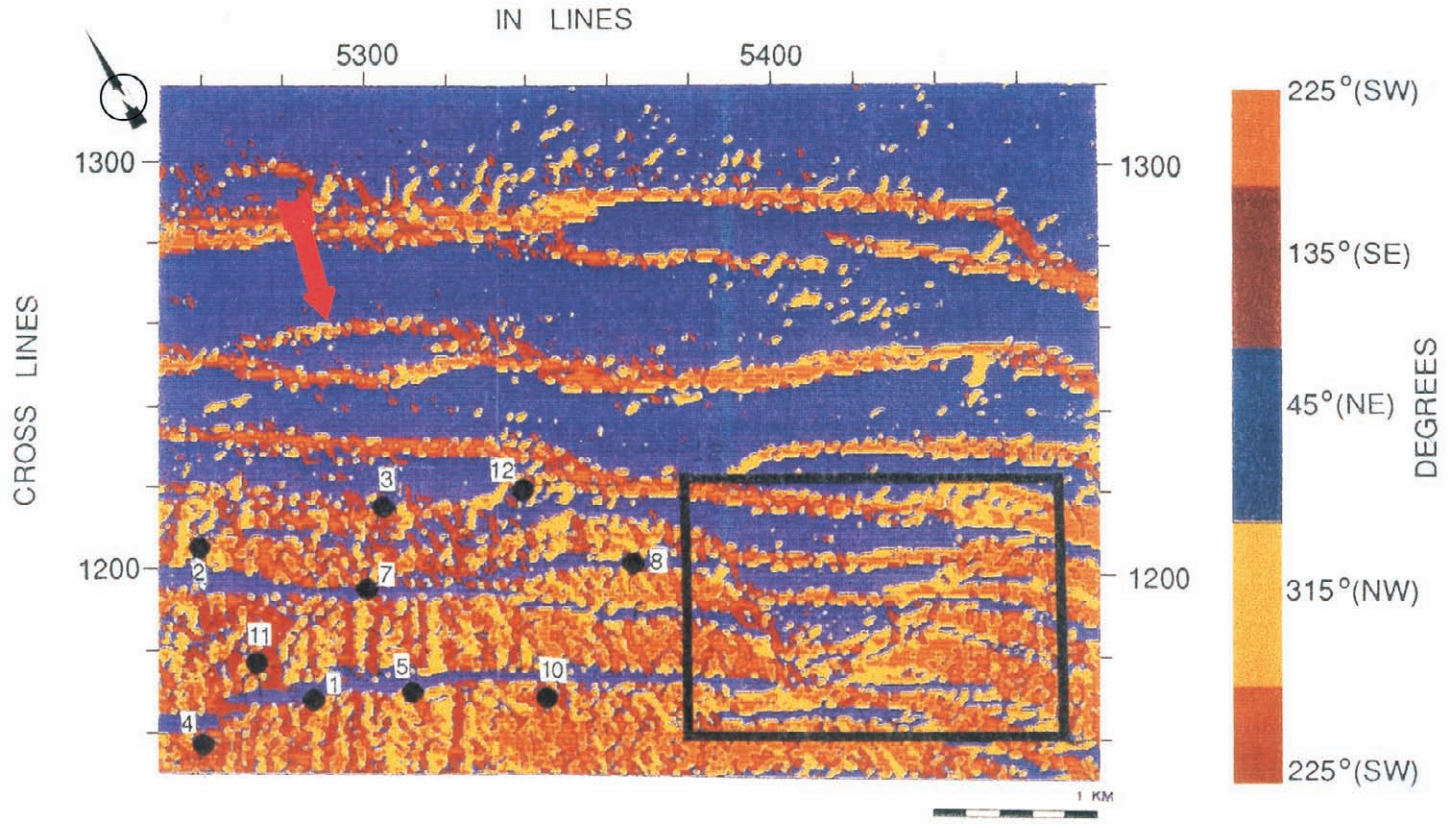

Downloaded 25 Jun 2012 to 95.28.162.50. Redistribution subject to SEG license or copyright; Terms of Use: http://segdl.org/

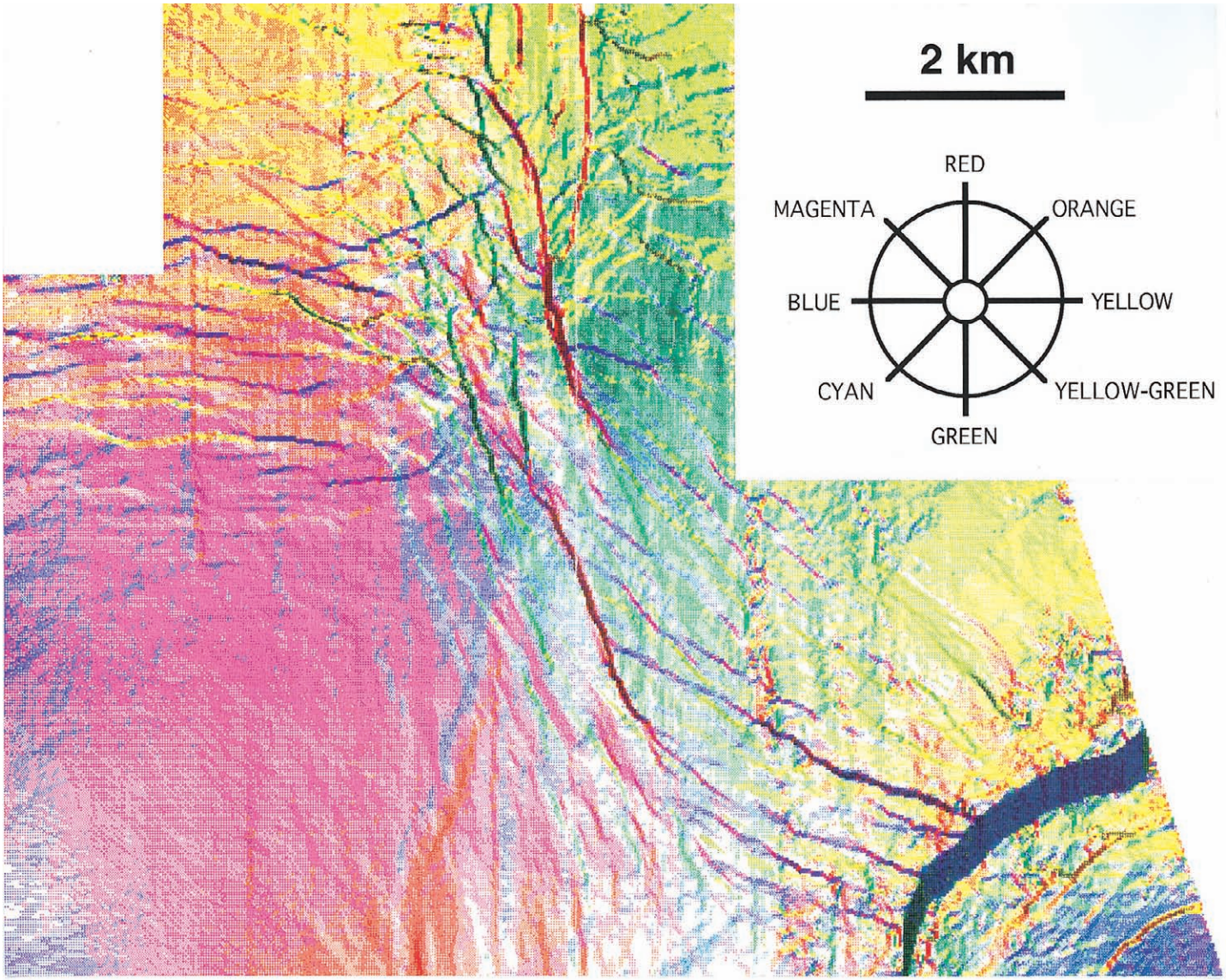

Fig. 8-15. (Opposite top) Dip map from Nun River field, Nigeria, showing many faults (from Bouvier et al., 1989). Arrow indicates one fault visible on dip map but not on azimuth map in Figure 8-16. (Courtesy Koninkljke / Shell.)

Fig. 8-16. (Opposite bottom) Azimuth map from Nun River field, Nigeria, showing generally the same faults as in Figure 8-15 (from Bouvier et al., 1989). Arrow indicates one fault visible in azimuth but not in dip. (Courtesy Koninklijke / Shell.)

Fig. 8-17. Dip-azimuth combination map from offshore The Netherlands. Azimuth is coded to hue according to legend; dip is coded to color density. The horizon is just above a salt dome located in the SW corner. (Courtesy Nederlandse Aardolie Maatschappij B.V.)

Downloaded 25 Jun 2012 to 95.28.162.50. Redistribution subject to SEG license or copyright; Terms of Use: http://segdl.org/

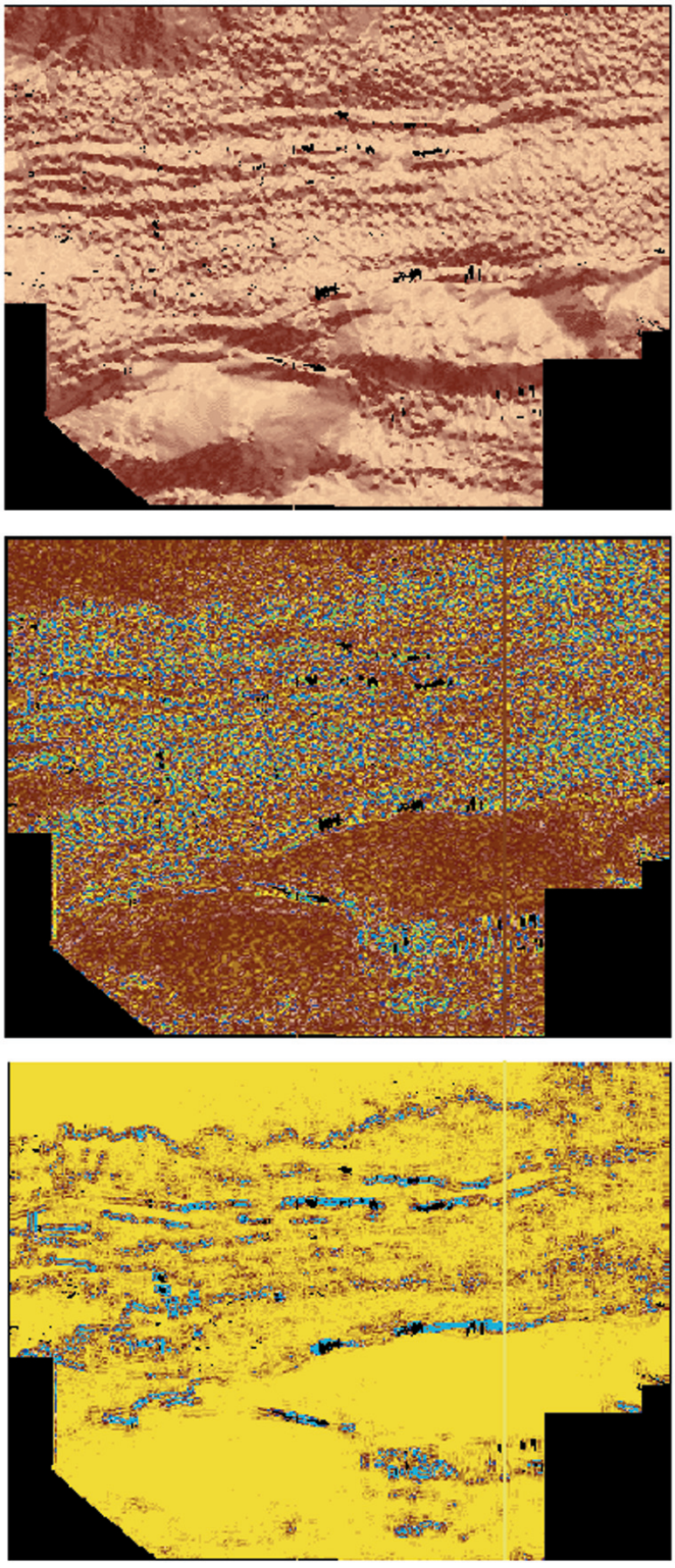

Fig. 8-18. Maps of azimuth (top), curvature (middle) and roughness (bottom) for same horizon. Curvature and roughness are the derivatives of dip and azimuth and help to highlight flexures. (Courtesy Flagship Geosciences L.L.C.)

Downloaded 25 Jun 2012 to 95.28.162.50. Redistribution subject to SEG license or copyright; Terms of Use: http://segdl.org/

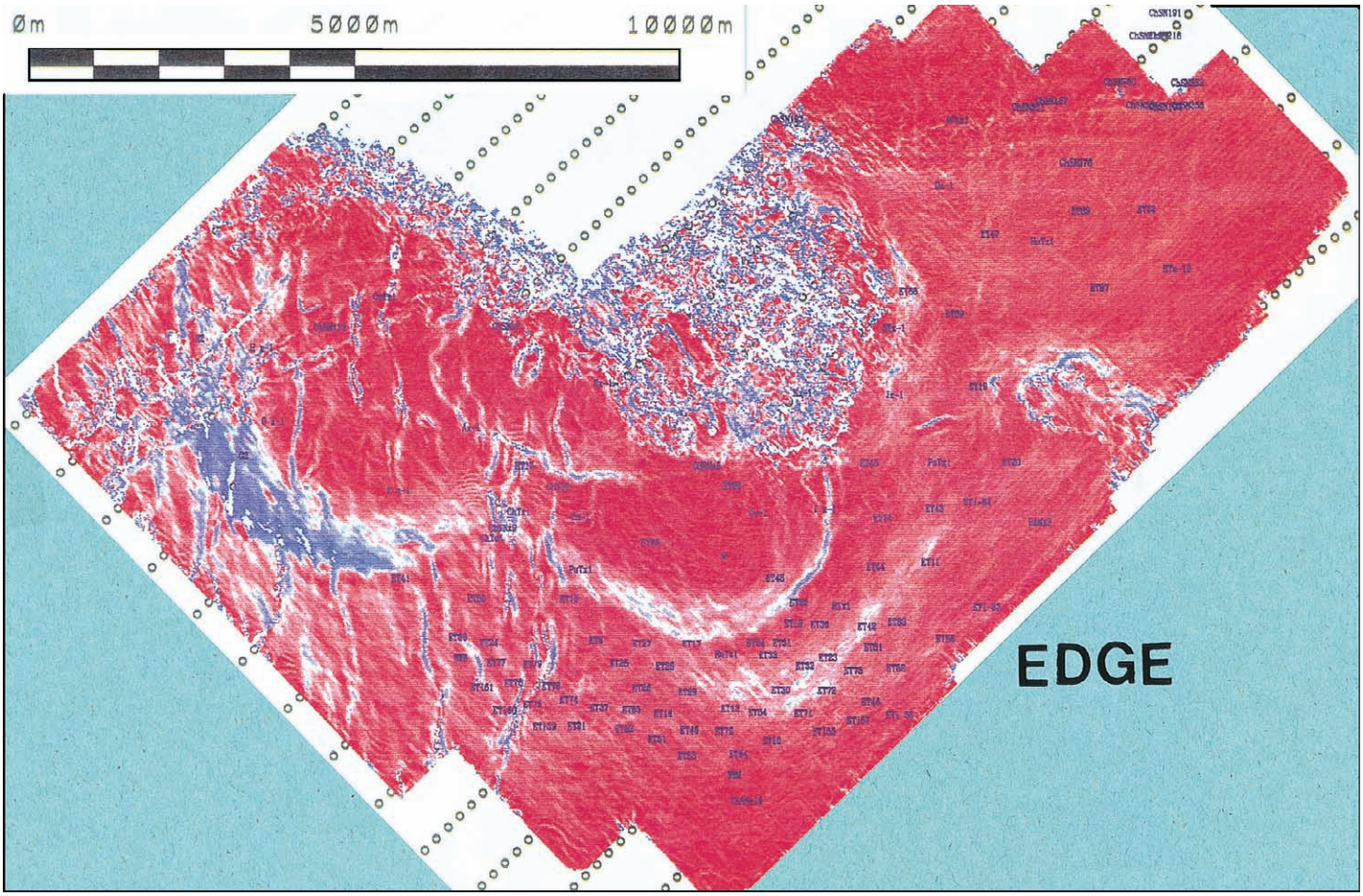

Fig. 8-19. Edge map from Neuquen Basin, Argentina. Arcuate faults about 7 km long have barely visible displacements on vertical sections. (Courtesy Petrolera Argentina San Jorge S.A.)

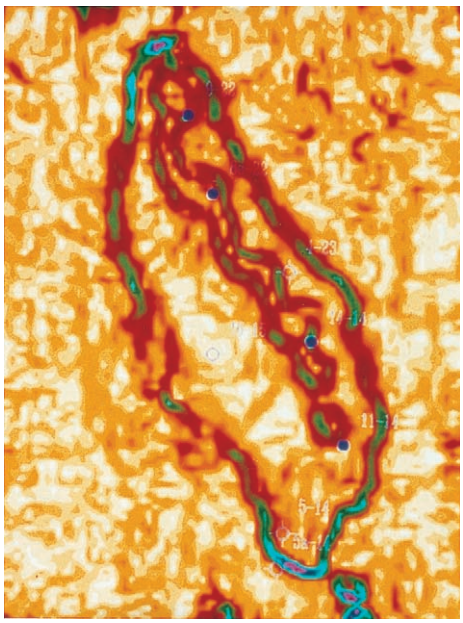

Fig. 8-20. Edge map from southern Alberta, Canada, outlining reef. (Courtesy Landmark Graphics Corporation.)

Downloaded 25 Jun 2012 to 95.28.162.50. Redistribution subject to SEG license or copyright; Terms of Use: http://segdl.org/

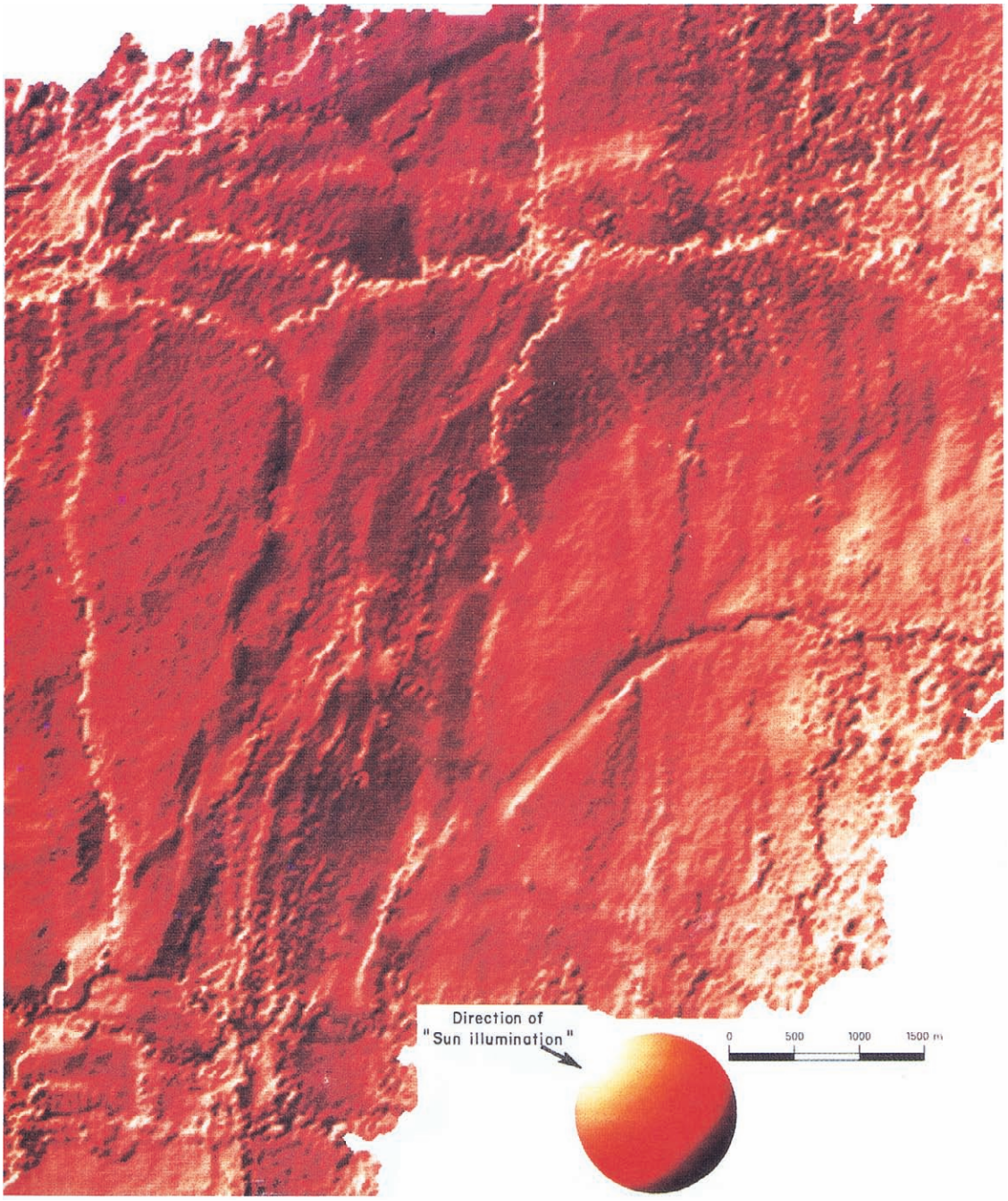

Fig. 8-21. Illumination display or shaded relief map on Base Zechstein reflection from Annerveen gas field, The Netherlands (from Hoetz and Watters, 1992). The direction of illumination is from the northwest. Note the graben just SE of center. (Courtesy Nederlandse Aardolie Maatschappij B.V.)

Downloaded 25 Jun 2012 to 95.28.162.50. Redistribution subject to SEG license or copyright; Terms of Use: http://segdl.org/

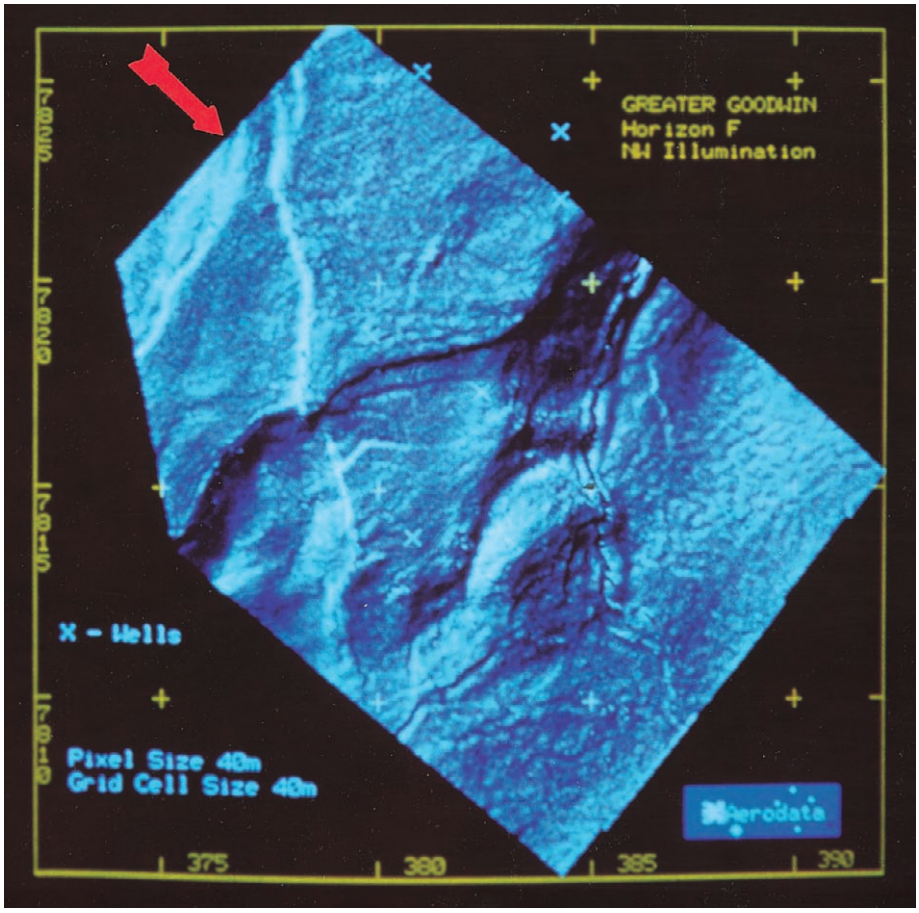

Fig. 8-22. Illumination display of horizon from Goodwyn field, Northwest Shelf, Australia. The direction of illumination is from the northwest. (Courtesy Woodside Offshore Petroleum Pty. Ltd.)

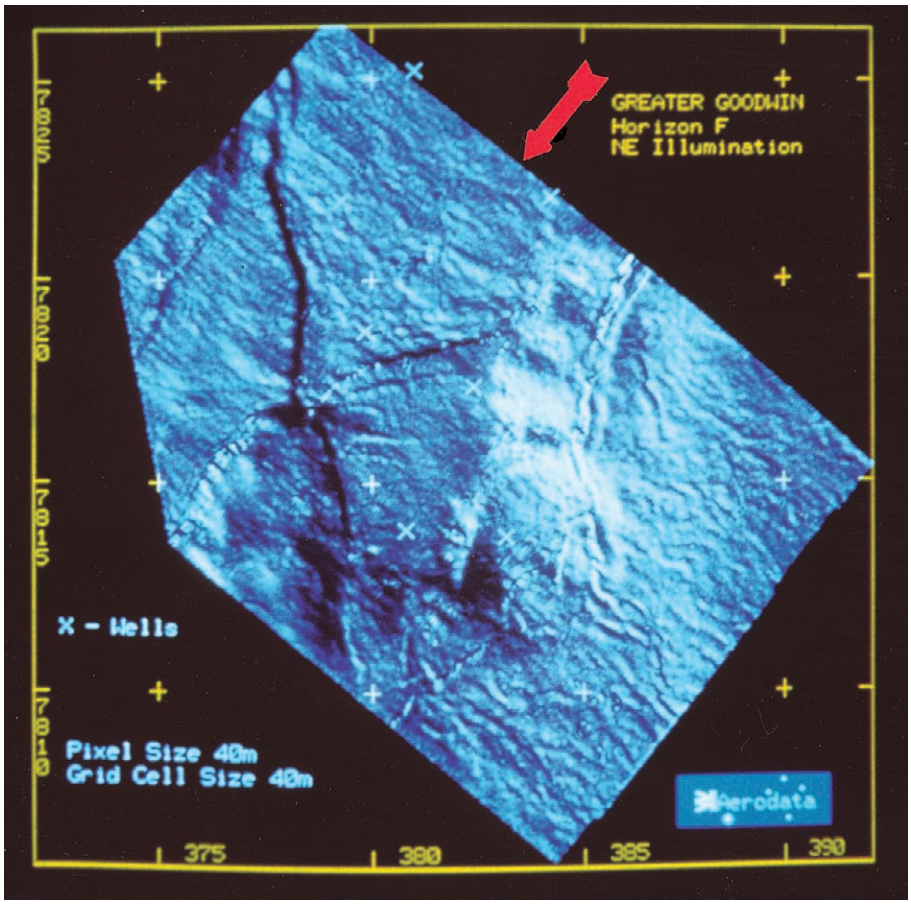

Fig. 8-23. Illumination display of horizon from Goodwyn field, Northwest Shelf, Australia. The direction of illumination is from the northeast, for comparison with Figure 8-22. Note how the data collection lineations are now visible. (Courtesy Woodside Offshore Petroleum Pty. Ltd.)

Downloaded 25 Jun 2012 to 95.28.162.50. Redistribution subject to SEG license or copyright; Terms of Use: http://segdl.org/

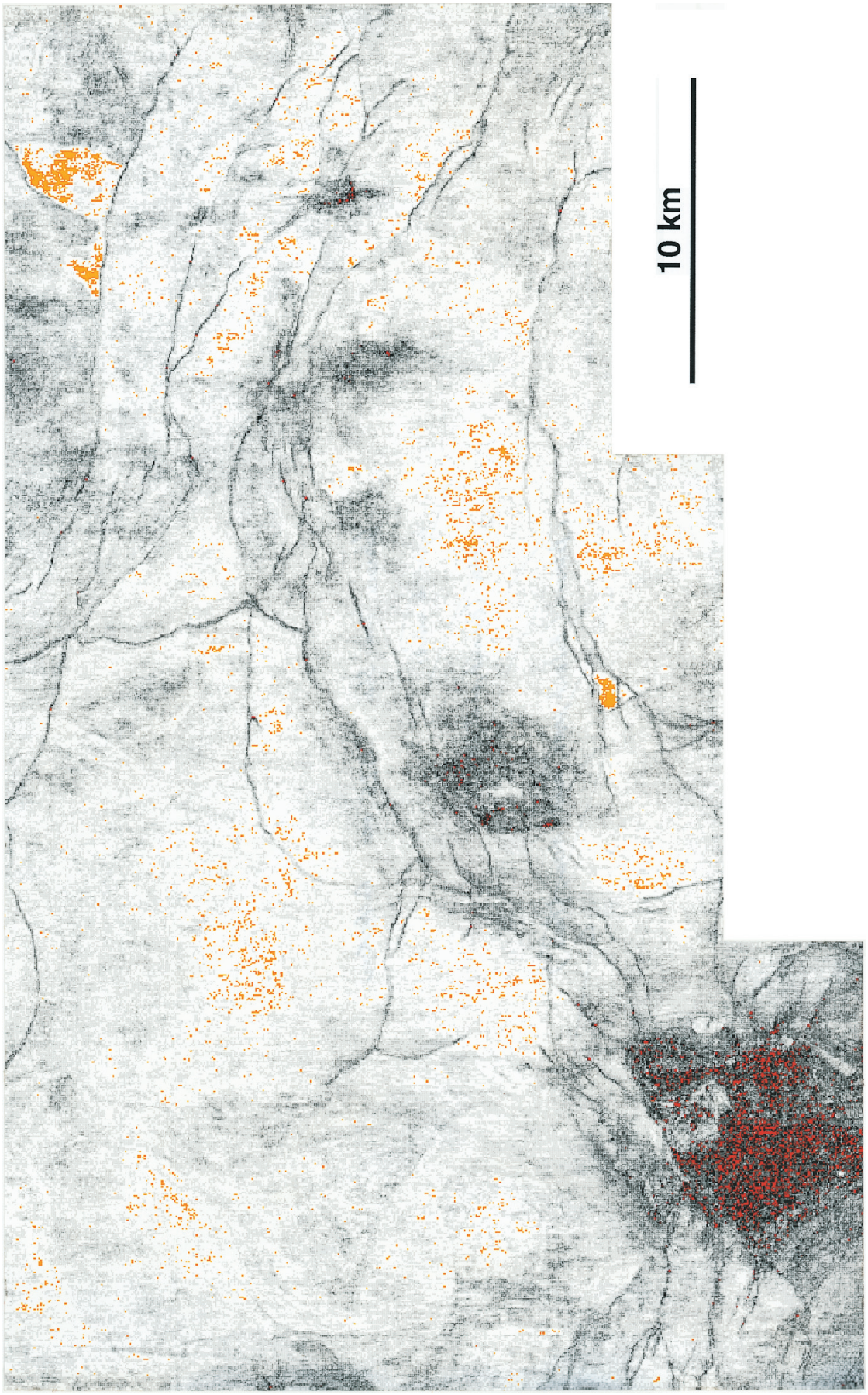

Fig. 8-24. Coherence time slice at 1525 ms from Gulf of Mexico. Area covers 60 blocks. Note, by comparison with Figure 8-25, how faults are equally visible when parallel to or perpendicular to structural strike. (Courtesy Amoco Corporation.)

Downloaded 25 Jun 2012 to 95.28.162.50. Redistribution subject to SEG license or copyright; Terms of Use: http://segdl.org/

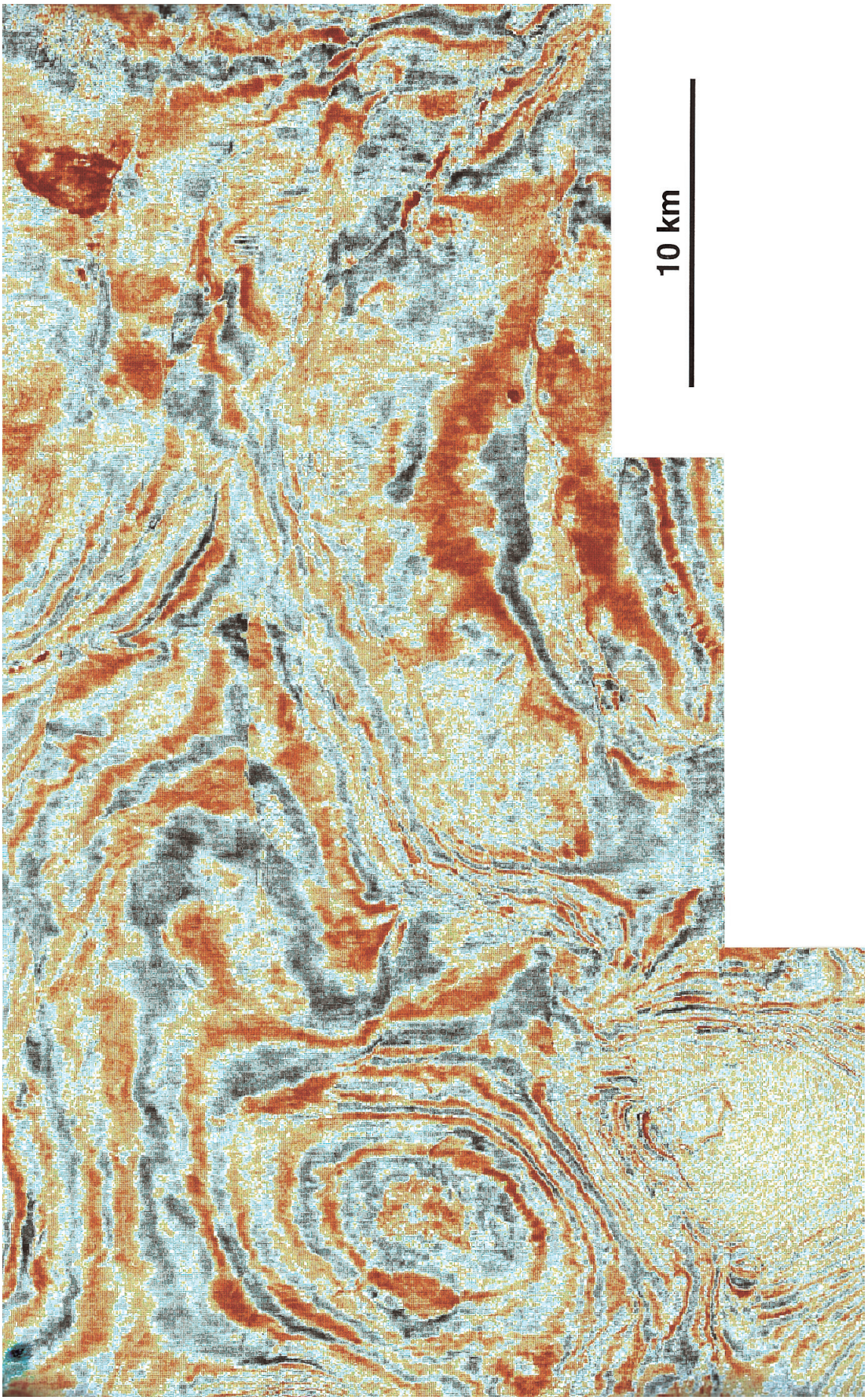

Fig. 8-25. Time slice at 1525 ms from Gulf of Mexico, for comparison with Figure 8-24. (Courtesy Amoco Corporation.)

Downloaded 25 Jun 2012 to 95.28.162.50. Redistribution subject to SEG license or copyright; Terms of Use: http://segdl.org/

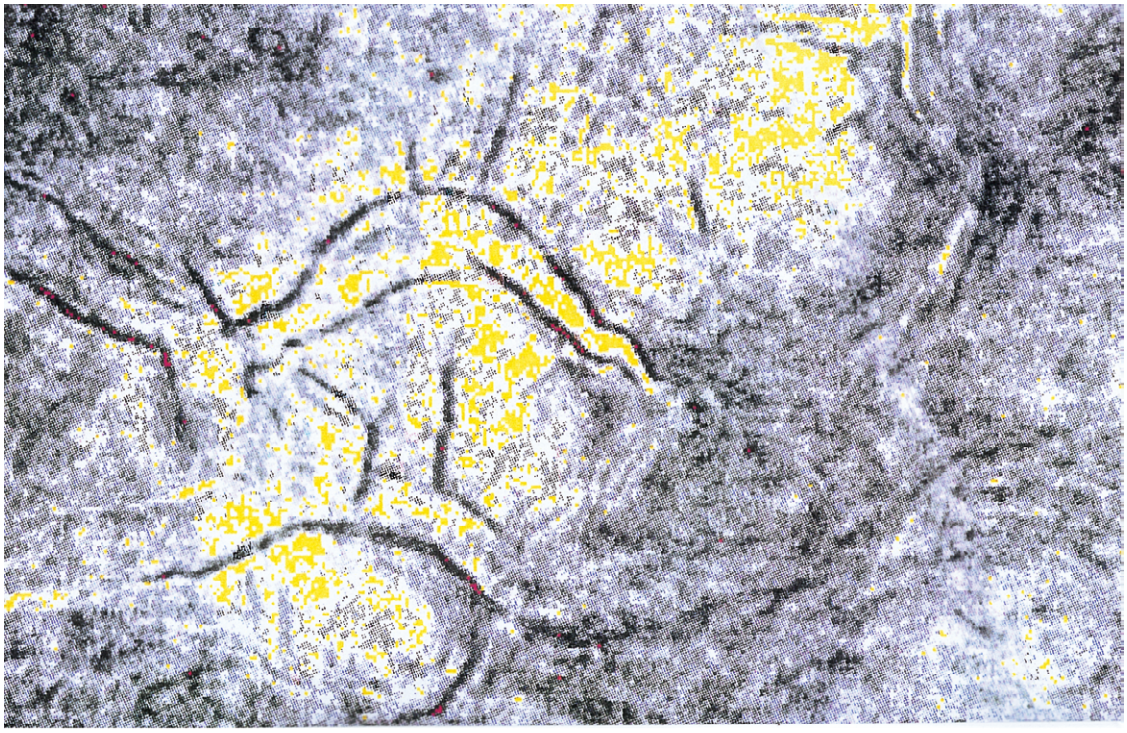

Fig. 8-26. Coherence time slice at 1640 ms from North Sea (from Bahorich et al., 1995). (Courtesy Amoco Corporation.)

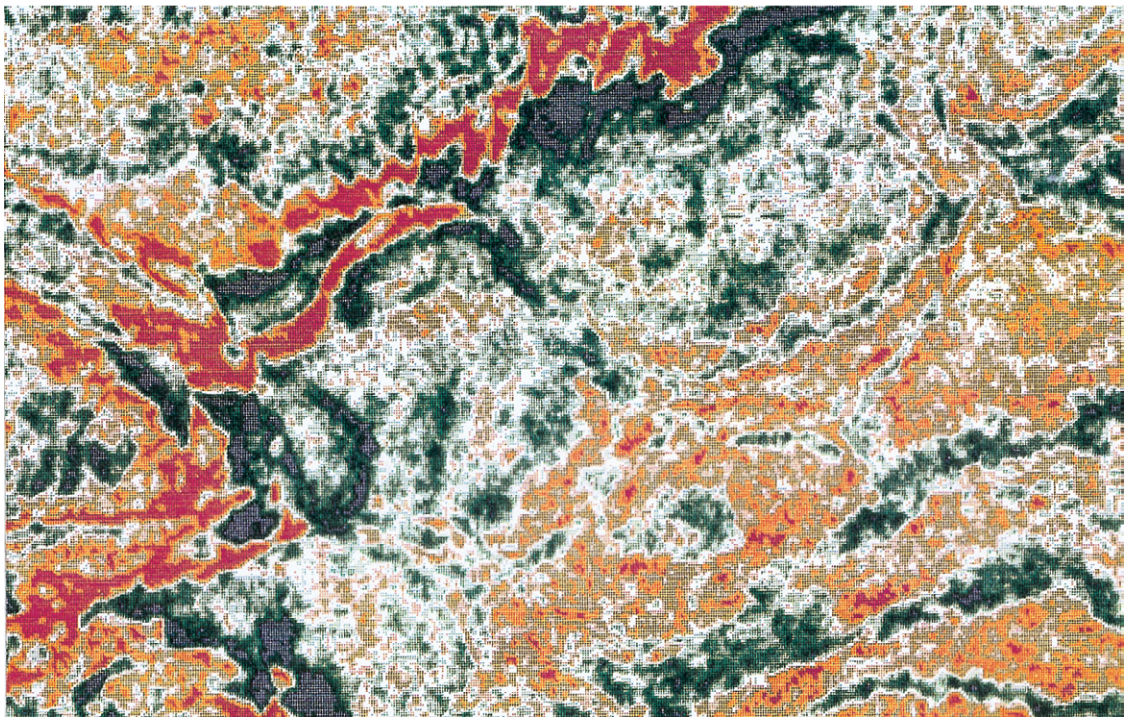

Fig. 8-27. Time slice at 1640 ms from North Sea, for comparison with Figure 8-26 (from Bahorich et al., 1995). (Courtesy Amoco Corporation.)

Downloaded 25 Jun 2012 to 95.28.162.50. Redistribution subject to SEG license or copyright; Terms of Use: http://segdl.org/

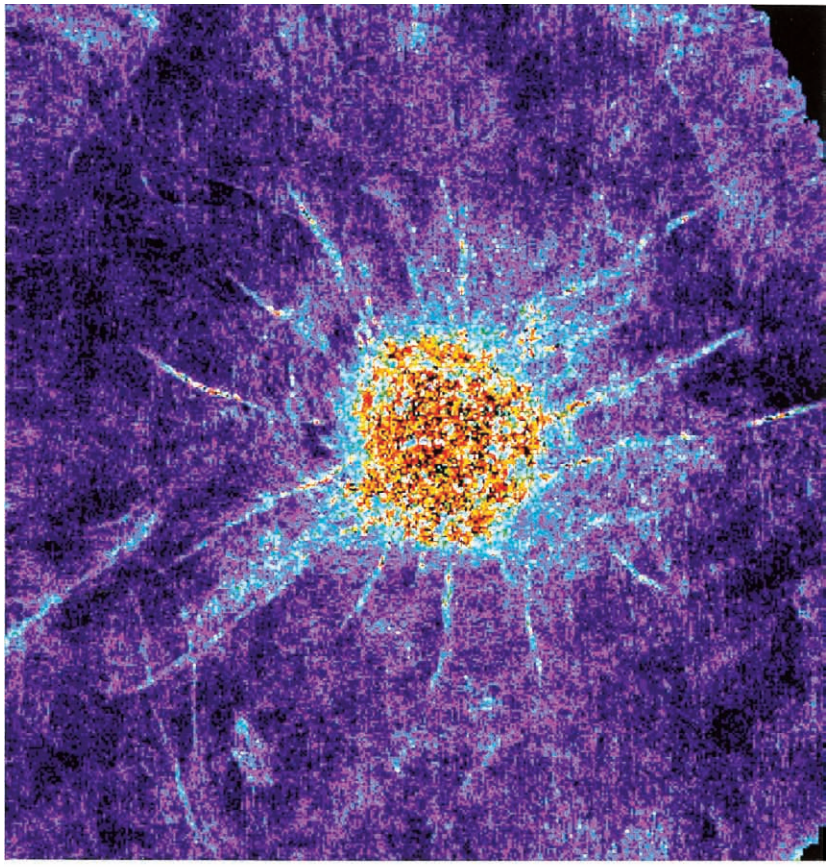

Fig. 8-28. Continuity time slice at about 1500 ms from Gulf of Mexico, showing many radial faults. (Courtesy CAEX Services and Landmark Advance Products Group.)

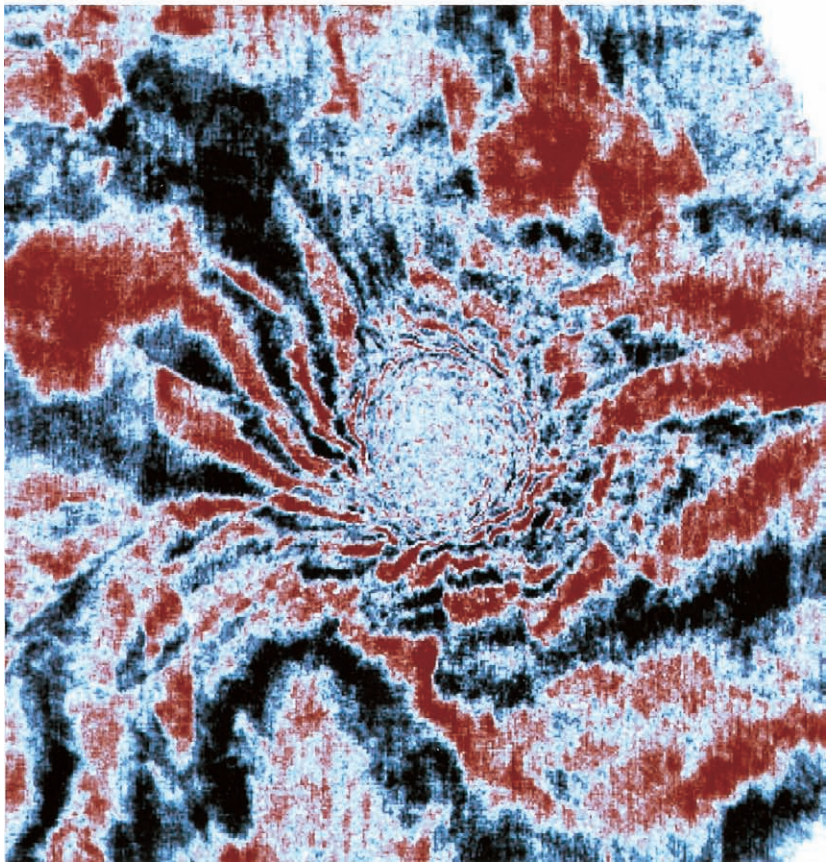

Fig. 8-29. Time slice at about 1500 ms from Gulf of Mexico, for comparison with Figure 8-28. (Courtesy CAEX Services and Landmark Advance Products Group.)

Downloaded 25 Jun 2012 to 95.28.162.50. Redistribution subject to SEG license or copyright; Terms of Use: http://segdl.org/

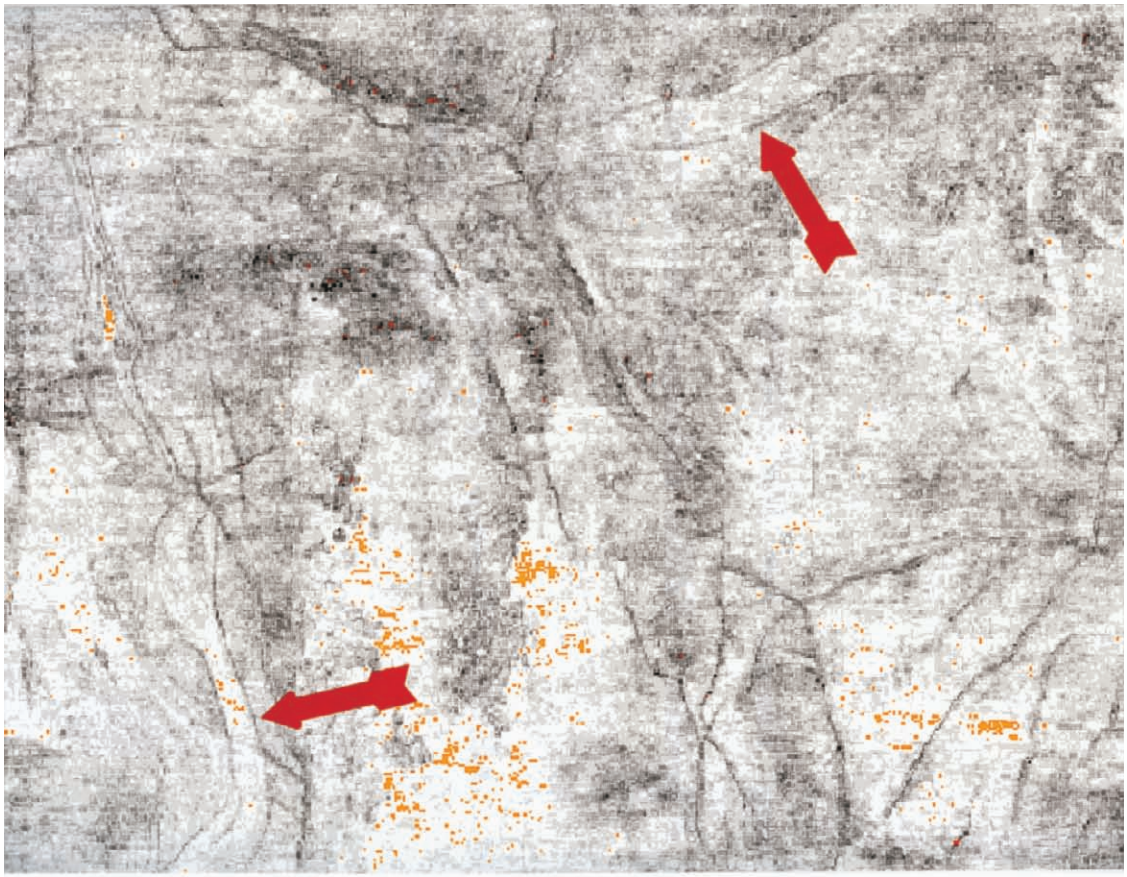

Fig. 8-30. Coherence time slice at 1250 ms from Gulf of Mexico, showing channels and faults (after Bahorich and Farmer, 1995). Note the channels indicated by the red arrows, how the channels are cut by faults, and also the point bars where one of the channels changes direction. (Courtesy Amoco Corporation. Data courtesy Geco-Prakla.)

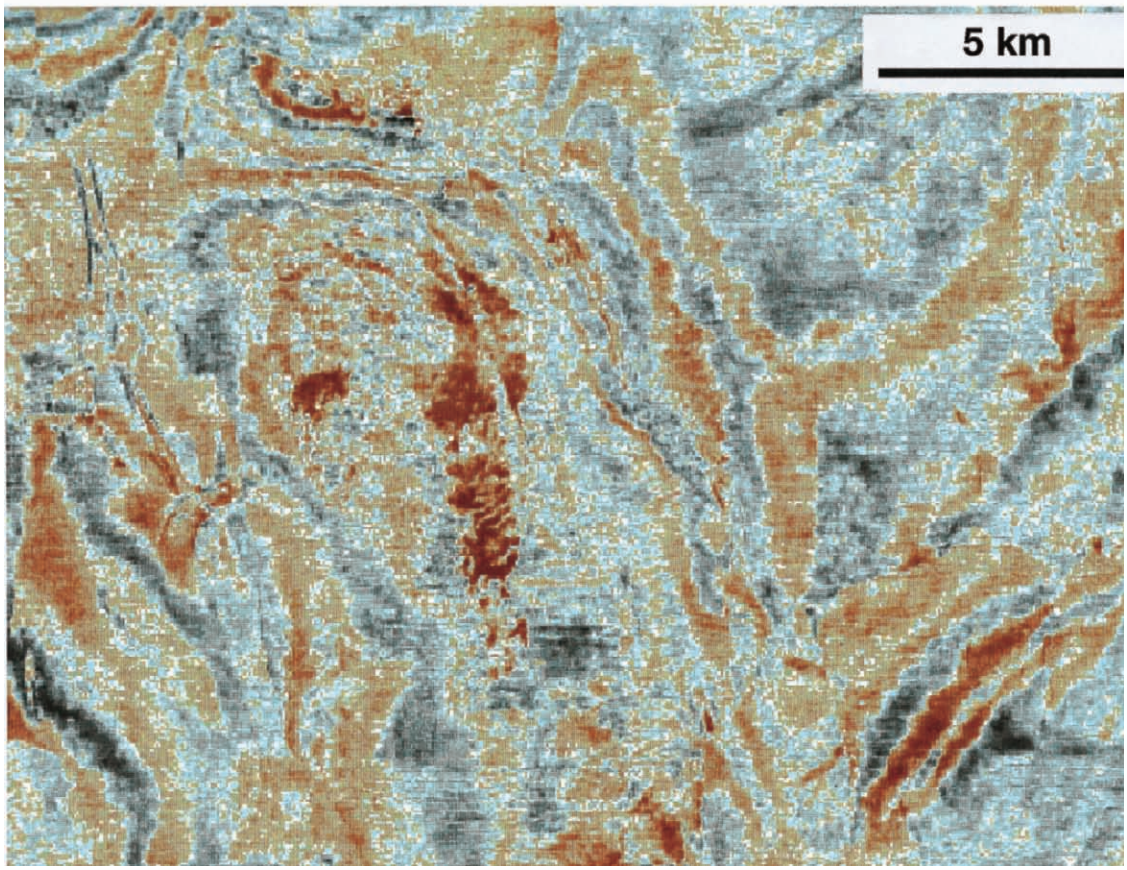

Fig. 8-31. Time slice at 1250 ms from Gulf of Mexico, for comparison with Figure 8-30 (after Bahorich and Farmer, 1995). (Courtesy Amoco Corporation. Data courtesy Geco-Prakla.)

Downloaded 25 Jun 2012 to 95.28.162.50. Redistribution subject to SEG license or copyright; Terms of Use: http://segdl.org/

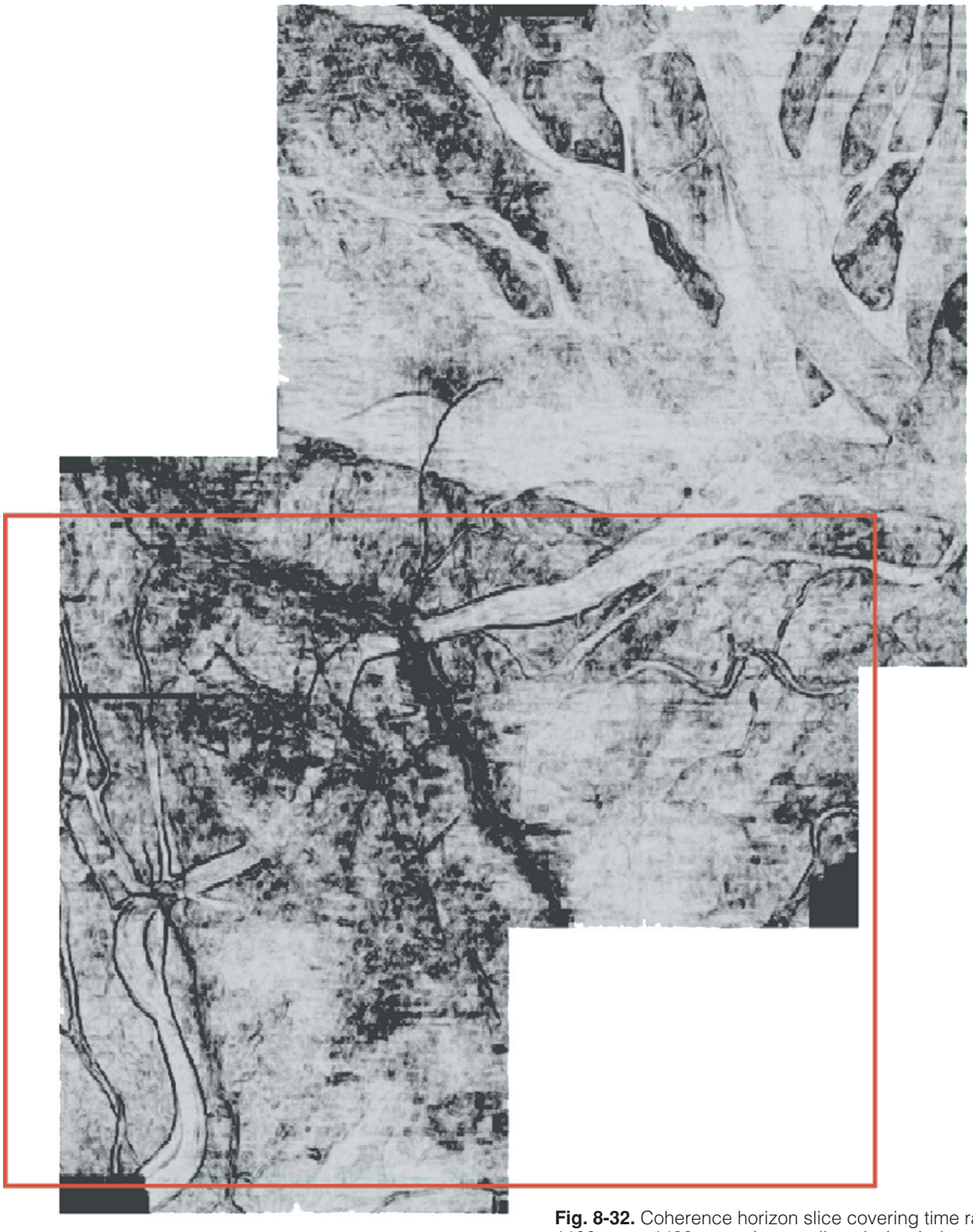

Fig. 8-32. Coherence horizon slice covering time range 1100 ms to 1400 ms, using small analysis window to further emphasize stratigraphic features seen in Figure 8-30. Scale is same as Figure 8-30 and its outline is here in red. Horizon slice is calculated over ±8-ms window around smoothed picked horizon. (Courtesy Amoco Corporation. Data courtesy Geco-Prakla.)

Downloaded 25 Jun 2012 to 95.28.162.50. Redistribution subject to SEG license or copyright; Terms of Use: http://segdl.org/

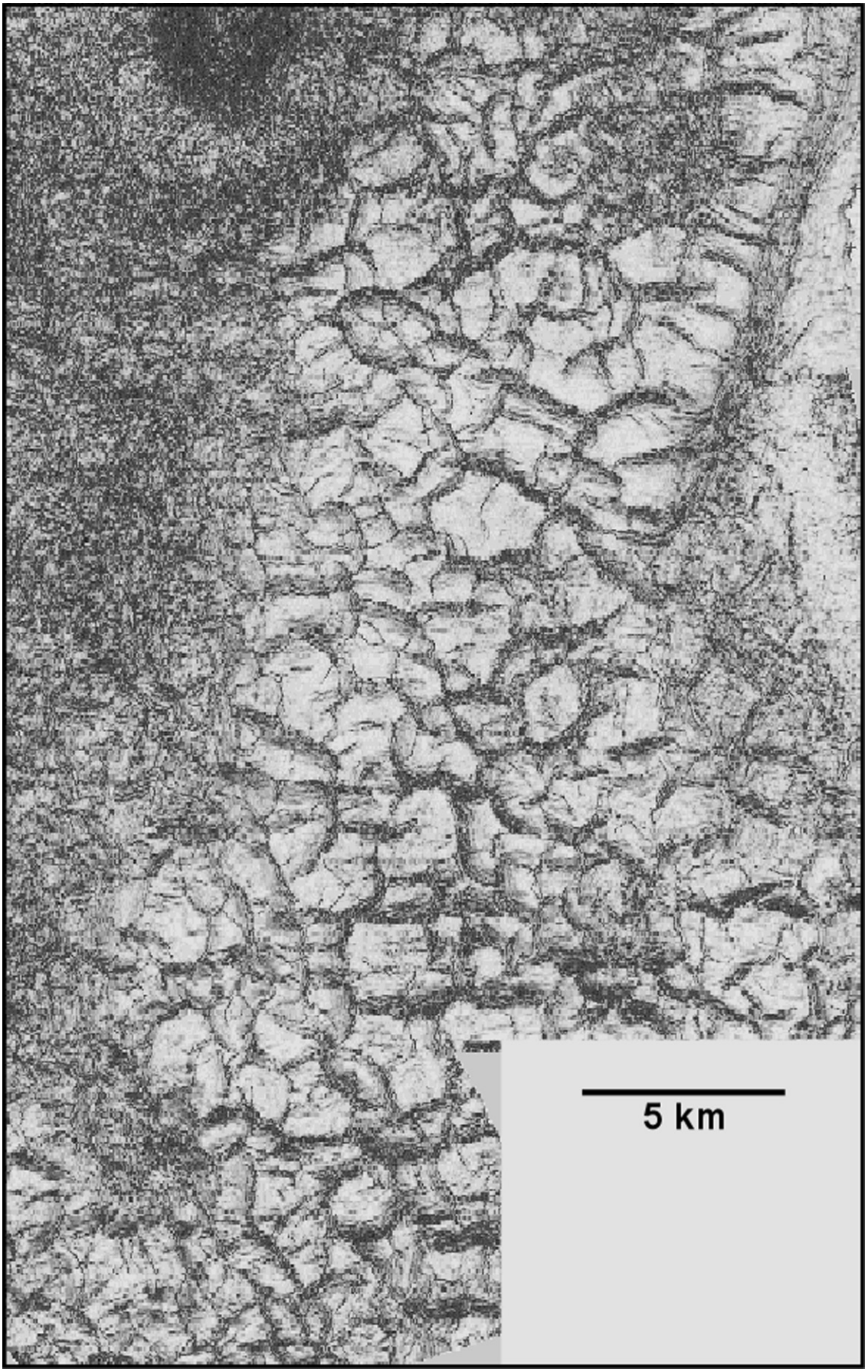

Fig. 8-33. Coherence time slice at 2800 ms from Valhall area of the North Sea. The polygonal fault pattern results from compactional dewatering of overpressured shales. (Courtesy Amoco Corporation.)

Downloaded 25 Jun 2012 to 95.28.162.50. Redistribution subject to SEG license or copyright; Terms of Use: http://segdl.org/

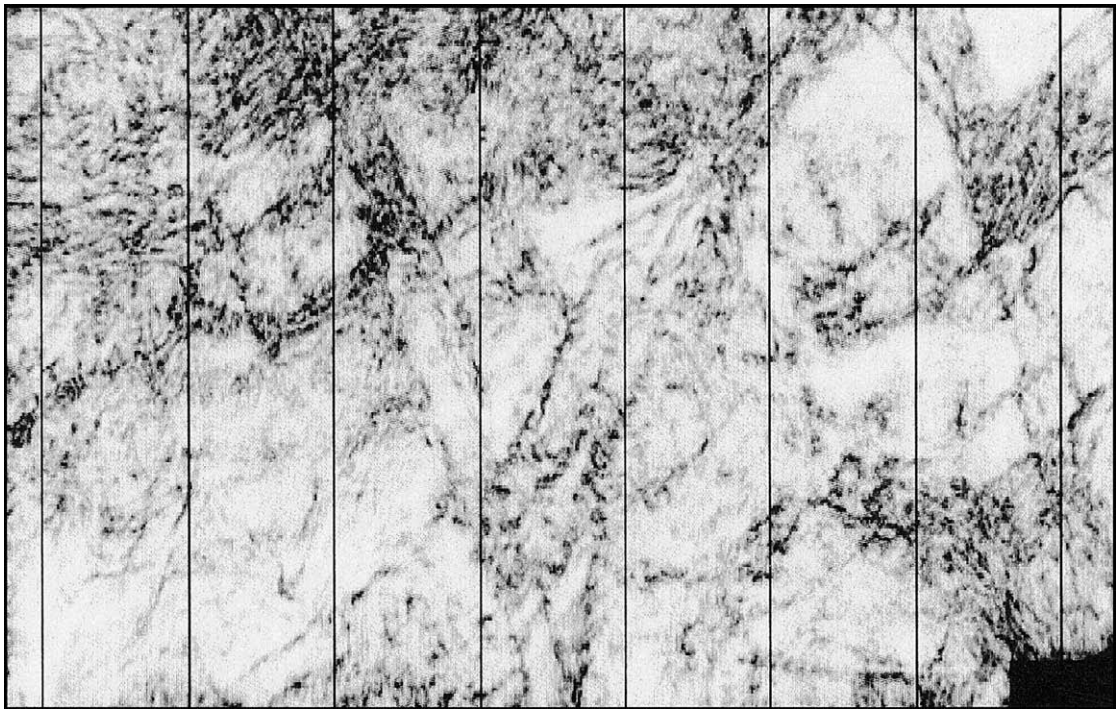

Fig. 8-34. Coherence time slice at 2600 ms from the North Sea, showing patterns of sub-salt Carboniferous faulting. (Courtesy Coherence Technology Company.)

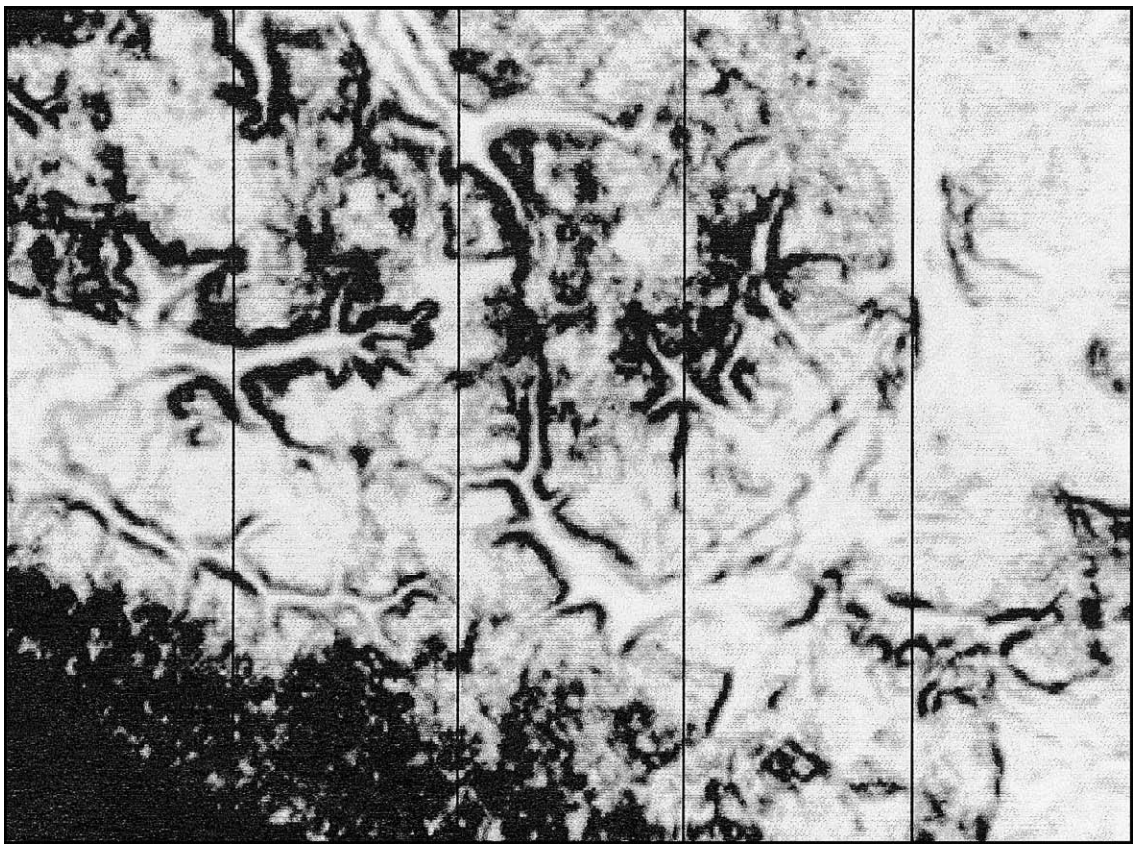

Fig. 8-35. Coherence time slice from Canada showing dendritic channel patterns. (Courtesy Coherence Technology Company.)

Downloaded 25 Jun 2012 to 95.28.162.50. Redistribution subject to SEG license or copyright; Terms of Use: http://segdl.org/

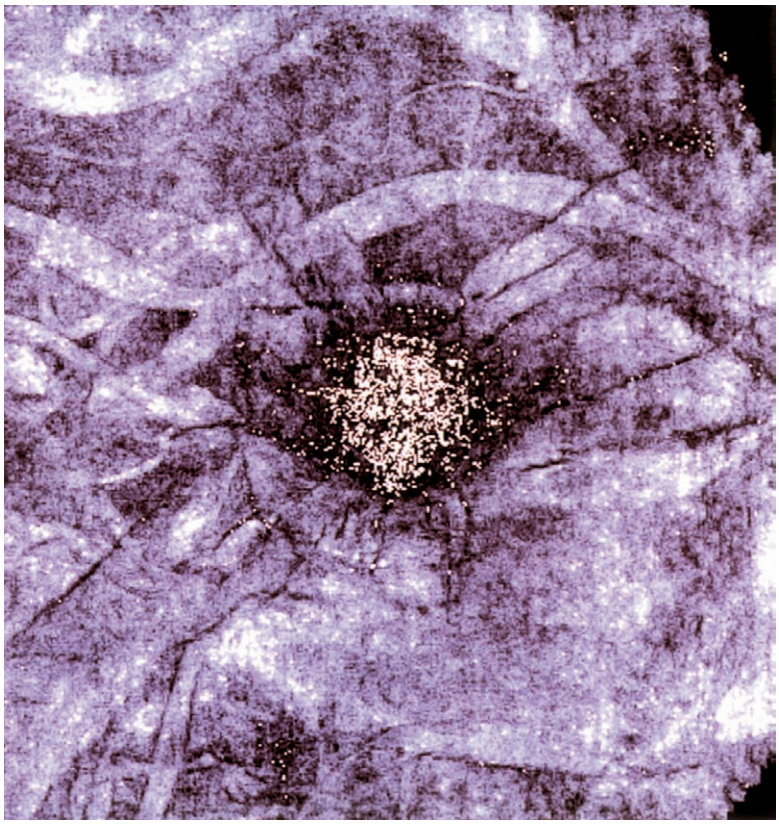

Fig. 8-36. Continuity time slice at about 1000 ms from Gulf of Mexico, showing channels and faults. (Courtesy CAEX Services and Landmark Advance Products Group.)

as shown by the red arrows. Faults highlighted on one are in shadow on the other and vice versa. These are marine data collected in the northwest-southeast direction. With the illumination direction perpendicular to this, the data collection lineations are visible (Figure 8-23); with the illumination direction parallel to the data collection, the lineations are not visible (Figure 8-22).

Coherence

Coherence, continuity, semblance and covariance are all rather similar. They aim to convert a volume of continuity (the normal reflections) into a volume of discontinuity (the faults and other boundaries). These attributes operate within a time window and use a variety of mathematical approaches similar to correlation. Because the attributes are derived direct from the processed data they are free of interpretive bias, in contrast to the horizon attributes discussed in the last section which require an interpreted horizon as their input. By producing a volume where discontinuities have been given an apparent continuity, the autotracking of faults now becomes a possibility.

Figure 8-24 is a **coherence** time slice covering a large area of the Gulf of Mexico. Many faults are outstandingly visible. Figure 8-25 provides the regular time slice for comparison. Some of the faults are visible here but, as is normal with time slices, the fault visibility depends greatly on relative strike of fault and structure. On the coherence time slice of Figure 8-24 it is clear that the faults are equally visible regardless of their orientation relative to structural strike. This value of a coherence time slice is further exemplified by comparison of Figures 8-26 and 8-27 from the North Sea. Here the faults are very curved but nevertheless are equally visible along their entire length.

Figure 8-28 is a continuity time slice from the Gulf of Mexico showing radial faults around a salt dome. Continuity involves a straightforward multiple cross-correlation calculation which also yields related attributes such as the dip and the azimuth of the maximum correlation. Comparison of Figures 8-28 and 8-29 shows again the improved fault visibility on the continuity time slice.

Downloaded 25 Jun 2012 to 95.28.162.50. Redistribution subject to SEG license or copyright; Terms of Use: http://segdl.org/

Figure 8-30 shows a coherence time slice delineating stratigraphic features that are actually channel edges. The channel is, for the most part, clear and the lower left point bars are visible where the channel changes direction. Figure 8-31 shows the normal time slice for comparison; here the red and blue structural reflections dominate the section, which is normally the case.

Figure 8-32 is a coherence horizon slice extracted along a smoothed picked horizon for comparison with Figure 8-30 (Marfurt et al., 1998). The channel visibility is improved because the structure has been removed. But also the analysis window for the coherence calculation has been reduced; it is here 16 ms, compared with a normal analysis window for structure of around 100 ms. Although the stratigraphic features here benefit greatly from the horizon slice display, in general the coherence time slice is the more valuable product. It is better for fault interpretation, is free of interpretive bias and is available much earlier in the interpretation project.

Figure 8-33 shows faults caused by the dewatering of overpressured shale, which can be a drilling hazard (Haskell et al., 1999). They are extremely difficult to map on any conventional views of the data, vertical or horizontal. Figures 8-34 and 8-35 show further examples of coherence time slices delineating features difficult to study in any other way. Figure 8-36 is a continuity time slice showing striking channels in the vicinity of a salt dome.

Post-stack Amplitude Attributes

Reflection amplitude measured at the crest of an identified reflection is by far the most widely-used amplitude attribute. Reflection amplitude extracted over one horizon produces a display normally called a horizon slice. Horizon slices and their value in stratigraphic interpretation are addressed at length in Chapter 4. **Composite amplitude** is the absolute value summation of the amplitudes of reflections identified at the top and base of a reservoir, or other, interval. Its use is discussed in Chapter 7. Composite amplitude is the author's favorite amplitude-derived attribute for reservoir studies. **Acoustic impedance** derived from amplitude by seismic inversion is another way of combining information from reservoir top and base (with thickness limitations) and some examples of this are also shown in Chapter 7.

Several of the attributes classified in Figure 8-1 are derivatives of the complex trace (Taner, Koehler and Sheriff, 1979, reference in Chapter 3). More recently the complex trace has been clearly explained by Barnes (1998). The amplitude derived from the complex trace is **reflection strength**, or envelope amplitude. It is a phase-independent, low-resolution type of amplitude and the author has seldom found it useful. However, Figures 8-37 to 8-40 show an example where reflection strength had a dramatic influence on the interpretation. The dips seen on the reflection strength section of Figure 8-38 are opposite to those seen on the regular section of Figure 8-37. These depositional clinoforms, if that is what they are, make sensible spatial patterns on the horizon slice of Figure 8-40 and can, to some extent, be discerned on the amplitude-enhanced section of Figure 8-39.

Various windowed amplitude attributes were discussed in Chapter 4. A comparison was there made between the merits of horizon amplitude and windowed amplitude.

For North Sea prospect Figure 8-41 maps the **total energy** over the reservoir interval defined as the time window between two structurally-interpreted horizons. Energy is the square of the seismic amplitude. The geologic environment here is shale-dominated so more reflection energy indicates more sand. The **number of zero crossings** mapped over the same area (Figure 8-42) indicates layering and thus should also be related to total quantity of sand. Because the top reflection here was a peak and the base a trough, the number of zero crossings between them must be an odd number. Even numbers thus indicate horizon mispicks, and the map of number of zero crossings was used as a quality control filter for mispicks based on this principle.

Energy half-time (Figure 8-43) for the same reservoir over the same area attempts to map vertical distribution of sand within the reservoir interval. Following the diagrammatic legend in Figure 8-43, energy half-time first sums energy over the interval

Downloaded 25 Jun 2012 to 95.28.162.50. Redistribution subject to SEG license or copyright; Terms of Use: http://segdl.org/

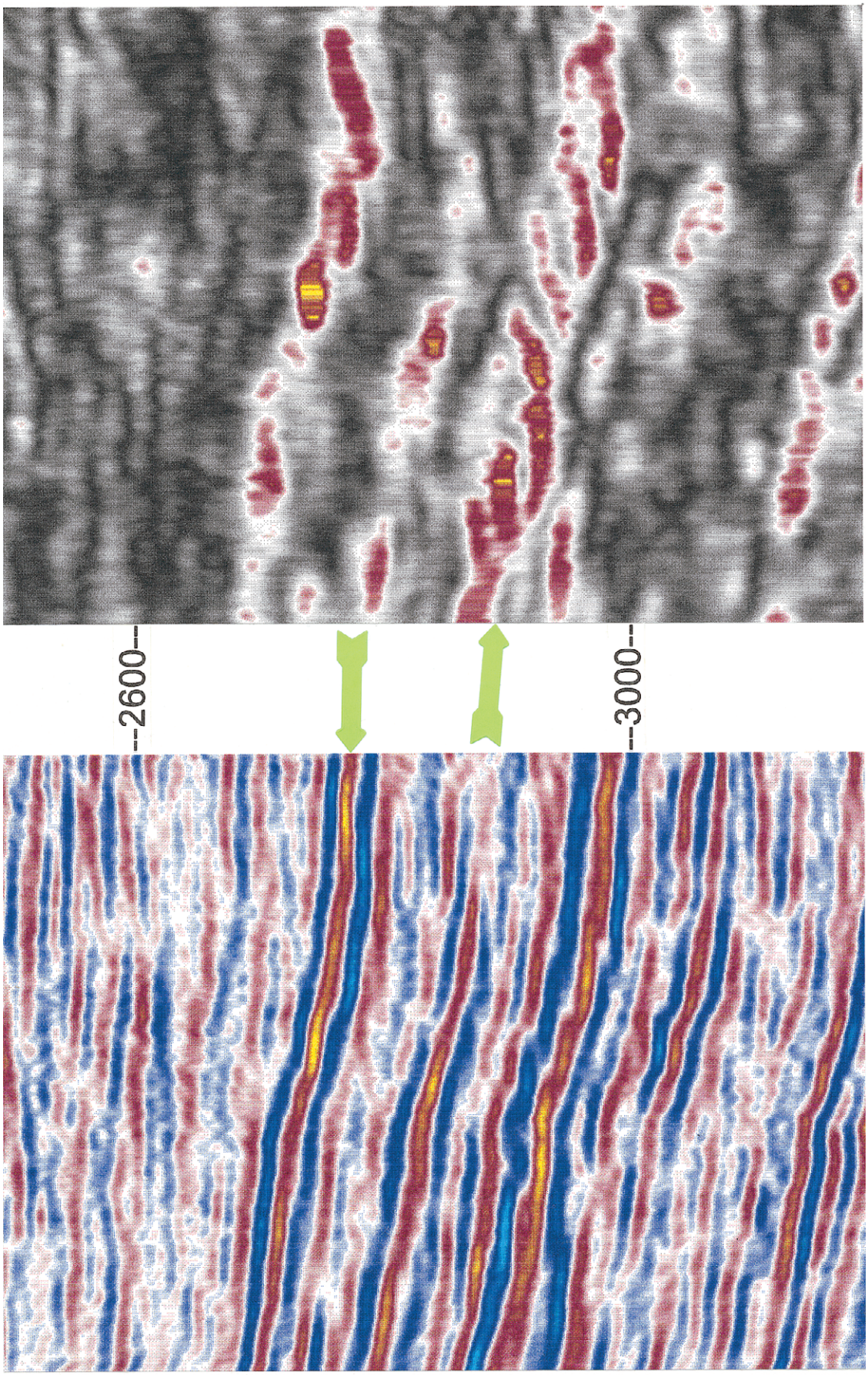

Fig. 8-38. Reflection strength display of same section as Figure 8-37, showing features dipping west which are thought to be depositional clinoforms. (Courtesy Apache Corporation.)

Fig. 8-37. Vertical section from 3-D survey onshore Texas showing strong reflections dipping east. (Courtesy Apache Corporation.)

Downloaded 25 Jun 2012 to 95.28.162.50. Redistribution subject to SEG license or copyright; Terms of Use: http://segdl.org/

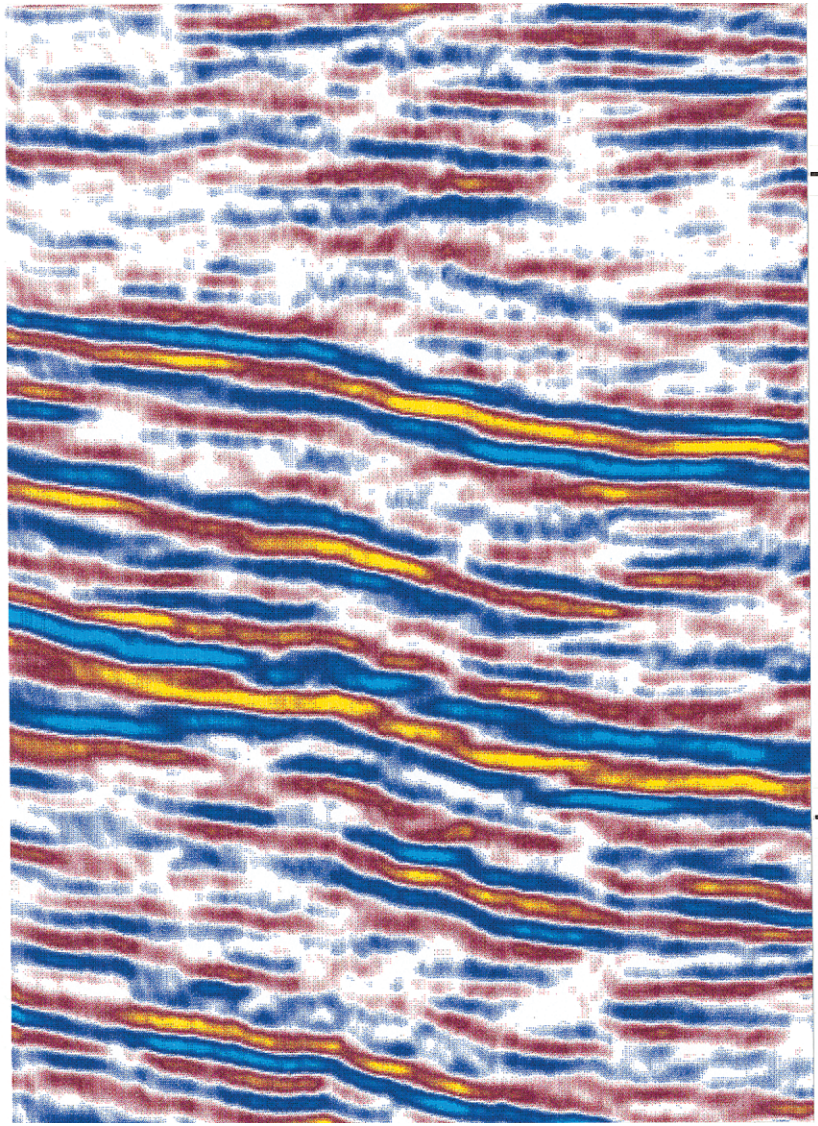

Fig. 8-39. Amplitude-enhanced version of Figure 8-37 showing west-dipping alignments of high amplitudes which give rise to the suspected clinoforms of Figure 8-38. (Courtesy Apache Corporation.)

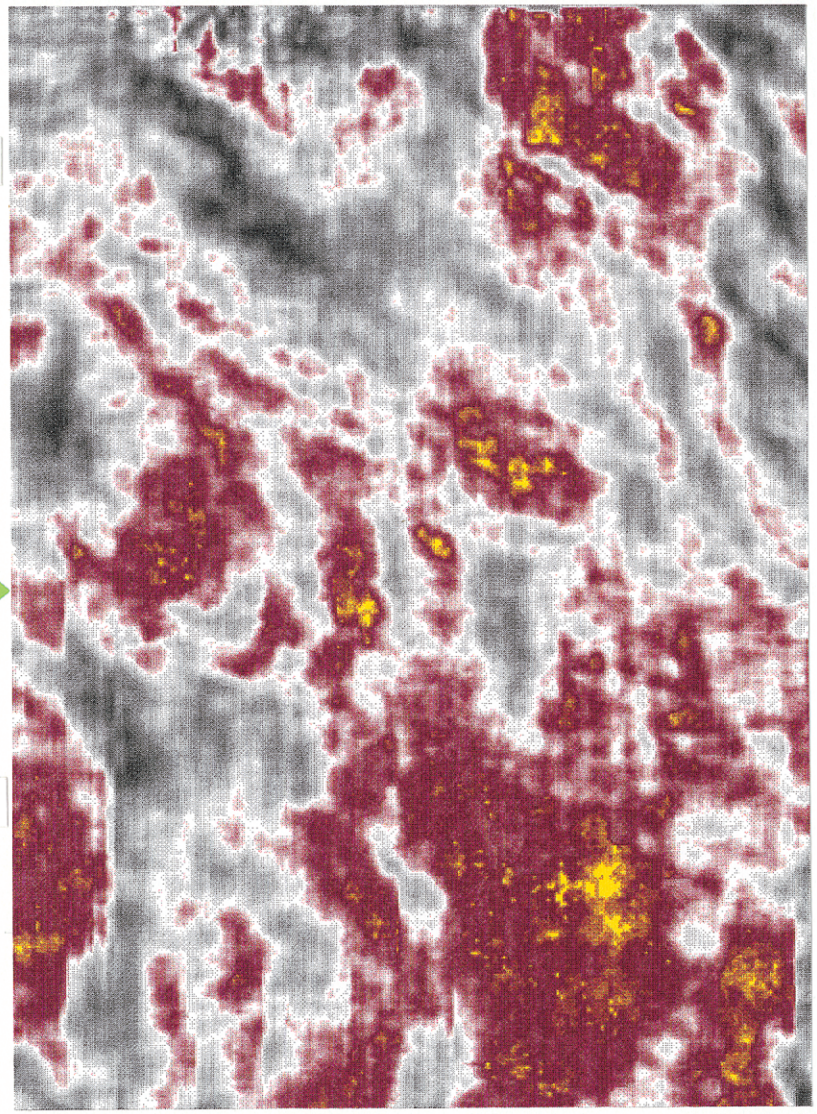

Fig. 8-40. Horizon slice in reflection strength showing spatial patterns of suspected clinoforms. The horizon that was tracked is indicated by the green arrow in Figure 8-37. After downward displacement this horizon was used for extraction of reflection strength at the position of the green arrow in Figure 8-38. The green arrow in this figure indicates the position of the vertical section of Figures 8-37, 8-38 and 8-39. (Courtesy Apache Corporation.)

Downloaded 25 Jun 2012 to 95.28.162.50. Redistribution subject to SEG license or copyright; Terms of Use: http://segdl.org/

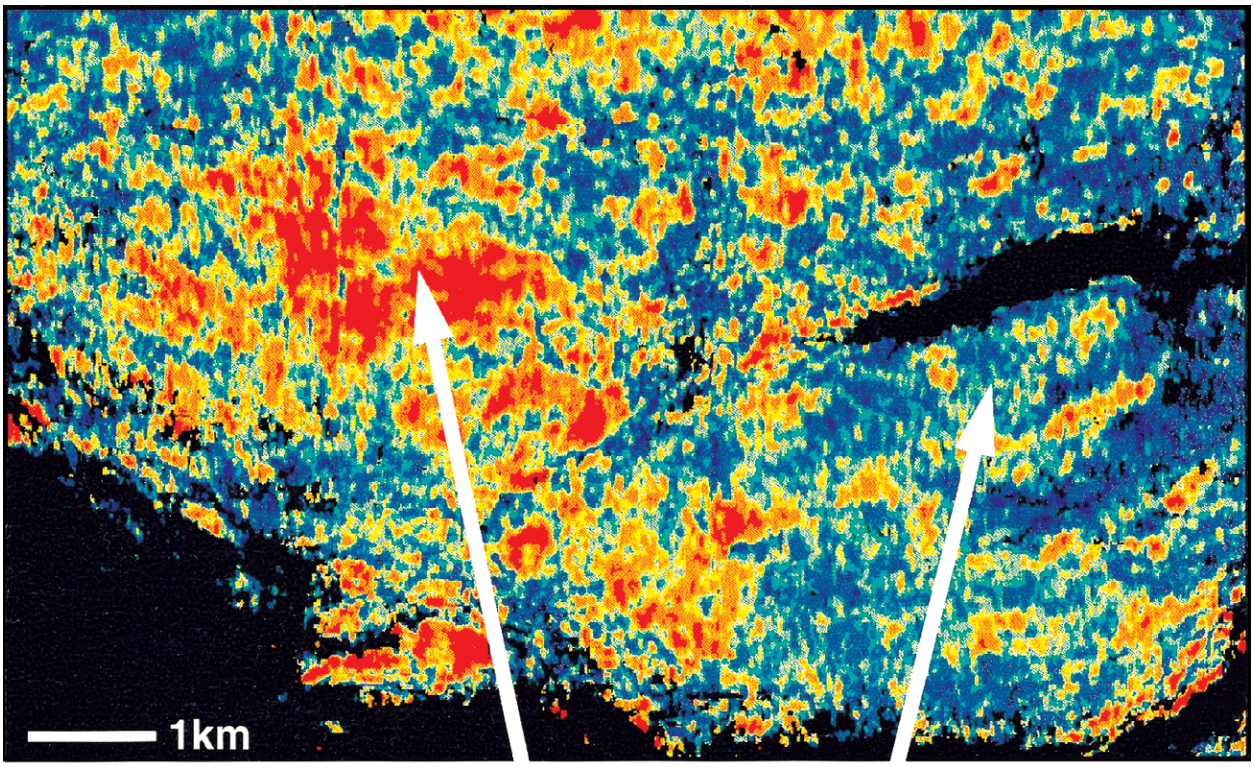

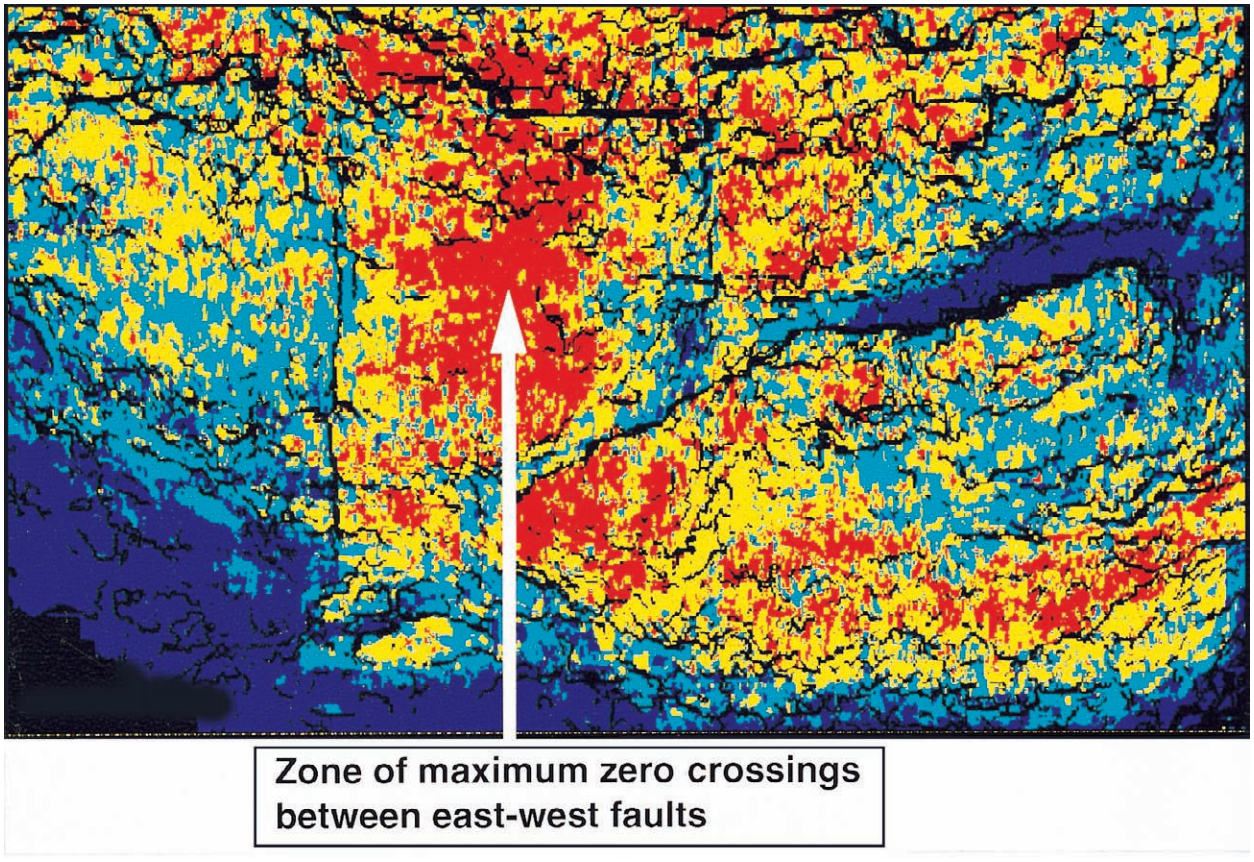

Downloaded 25 Jun 2012 to 95.28.162.50. Redistribution subject to SEG license or copyright; Terms of Use: http://segdl.org/

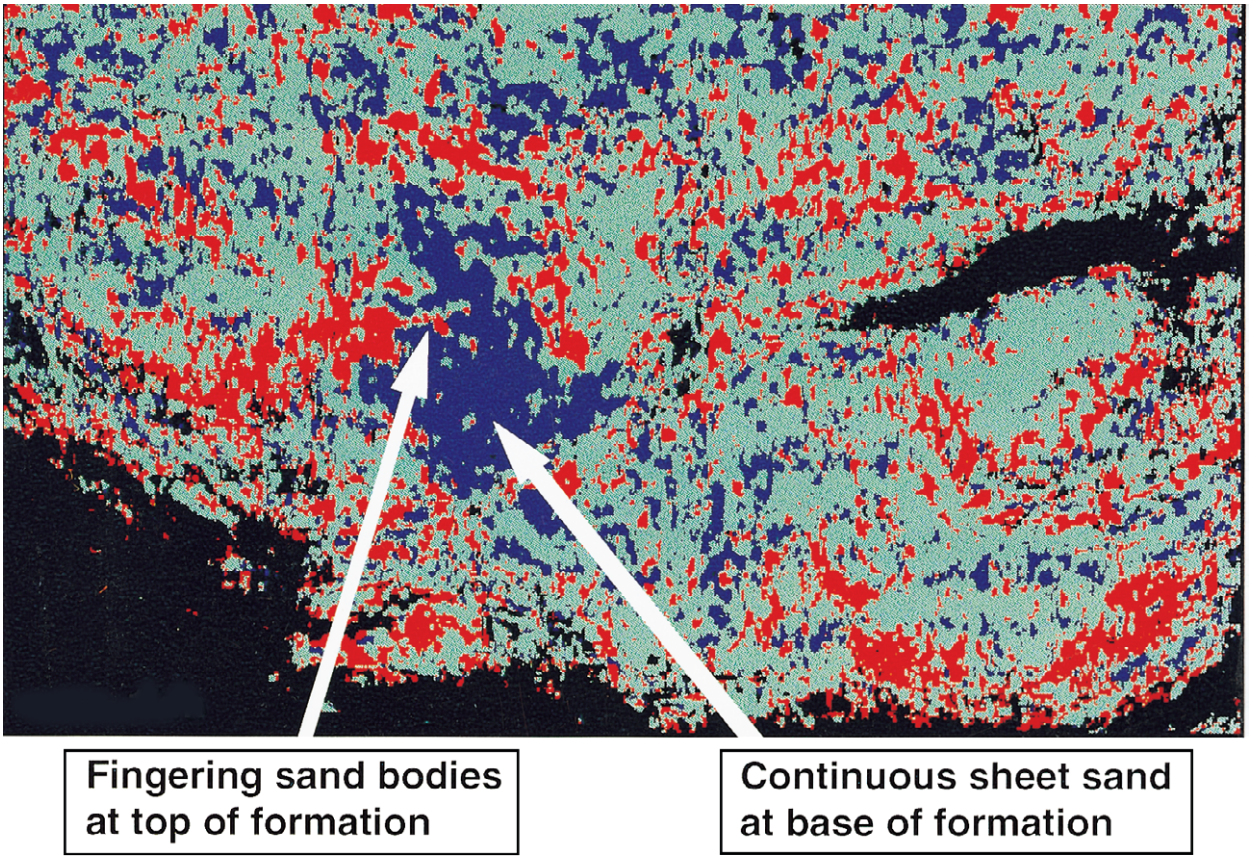

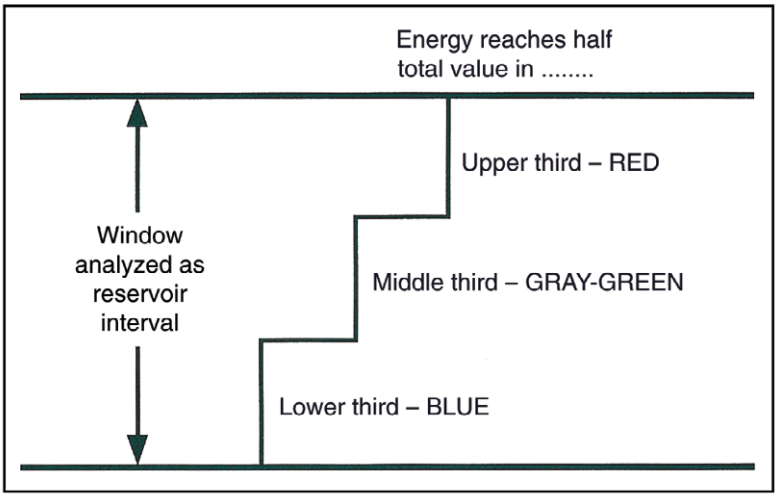

Fig. 8-43. Energy half-time map over reservoir interval from North Sea, indicating vertical distribution of sands within the reservoir. (Courtesy BP Exploration and P. Mulholland.)

Fig. 8-41. (Opposite top) Seismic energy map over reservoir interval from North Sea. High energy indicates sand in a shale-dominated environment. (Courtesy BP Exploration and P. Mulholland.)

Fig. 8-42. (Opposite bottom) Number of zero crossings over reservoir interval from North Sea. This map indicates layering and also serves as quality control filter for horizon mispicks. (Courtesy BP Exploration and P. Mulholland.)

Downloaded 25 Jun 2012 to 95.28.162.50. Redistribution subject to SEG license or copyright; Terms of Use: http://segdl.org/

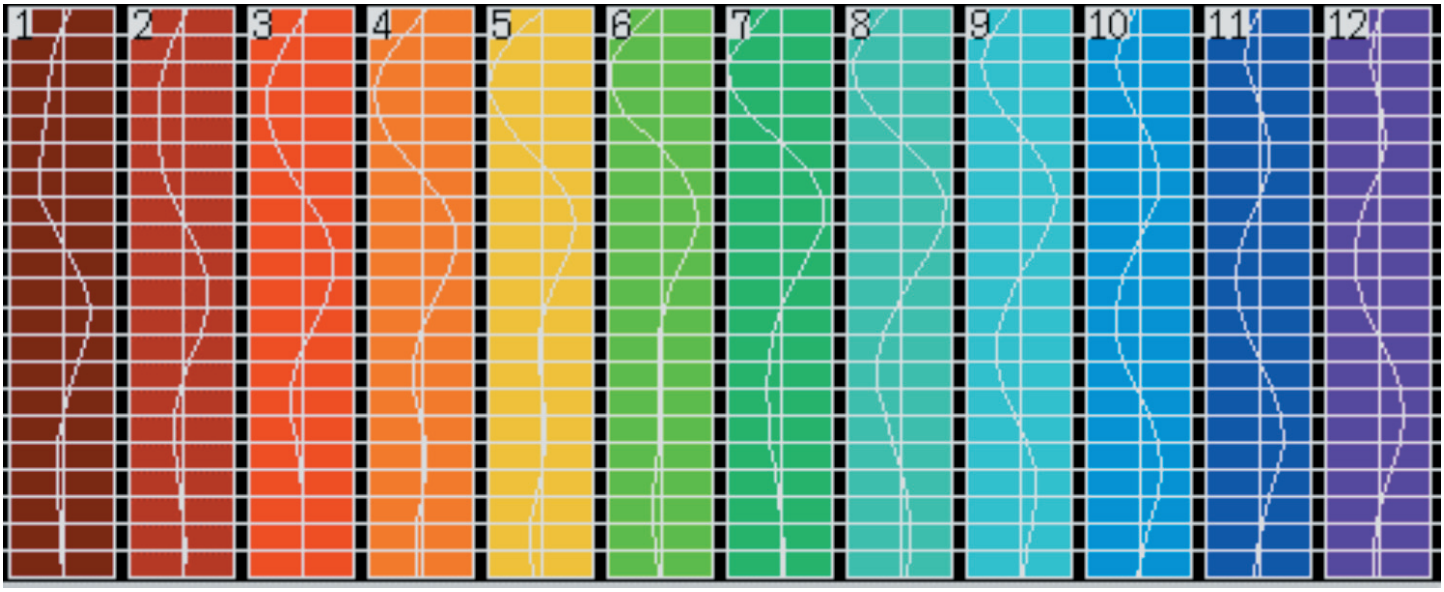

Fig. 8-44. Wave shape classification of seismic traces over an interval of 100 ms, for data from south Texas. The classification uses neural network pattern recognition technology. (Courtesy Flagship Geosciences L.L.C.)

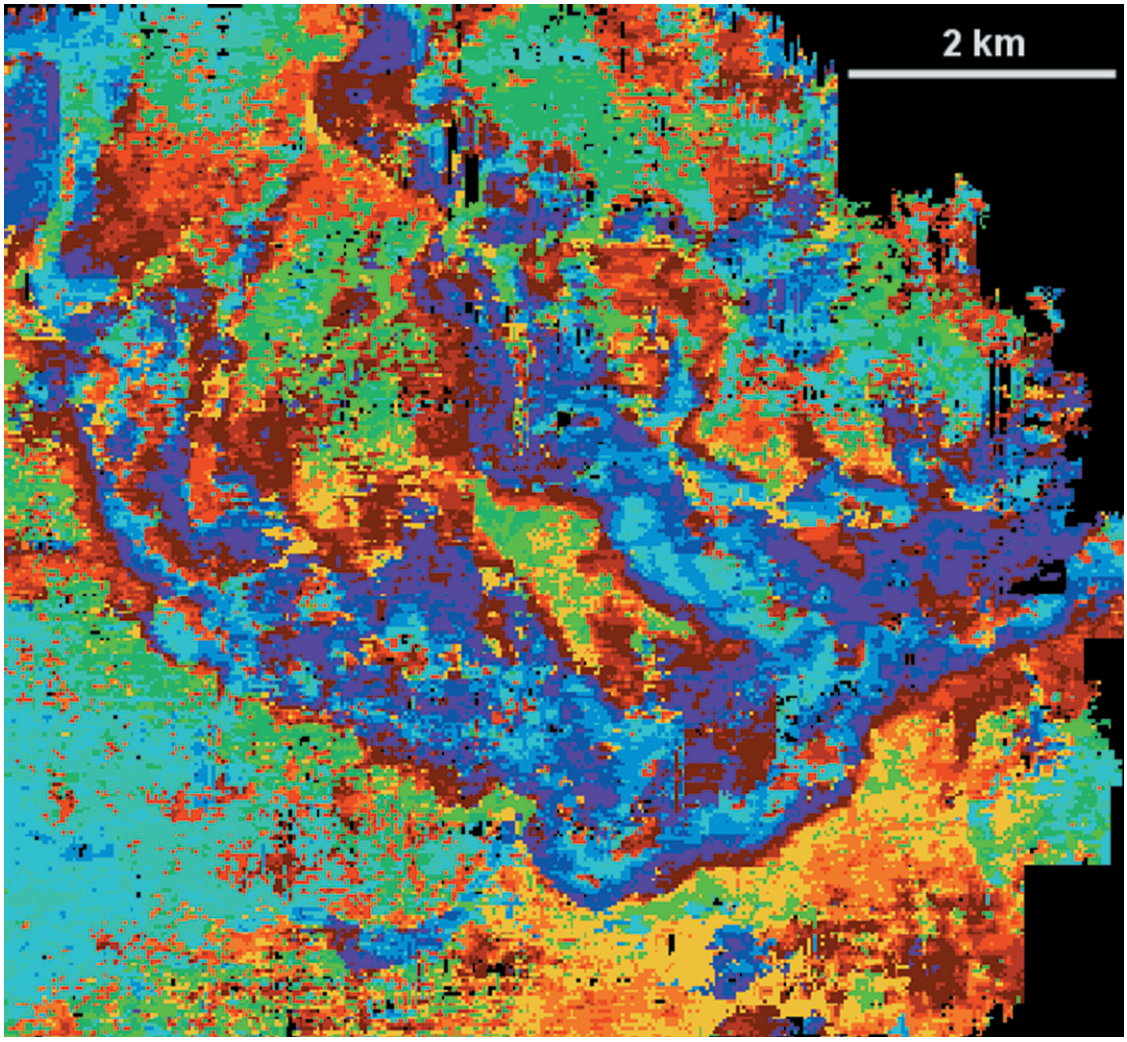

Fig. 8-45. Seismic facies map showing channel system where colors indicate the 12 different wave shapes classified in Figure 8-44. (Courtesy Flagship Geosciences L.L.C.)

Downloaded 25 Jun 2012 to 95.28.162.50. Redistribution subject to SEG license or copyright; Terms of Use: http://segdl.org/

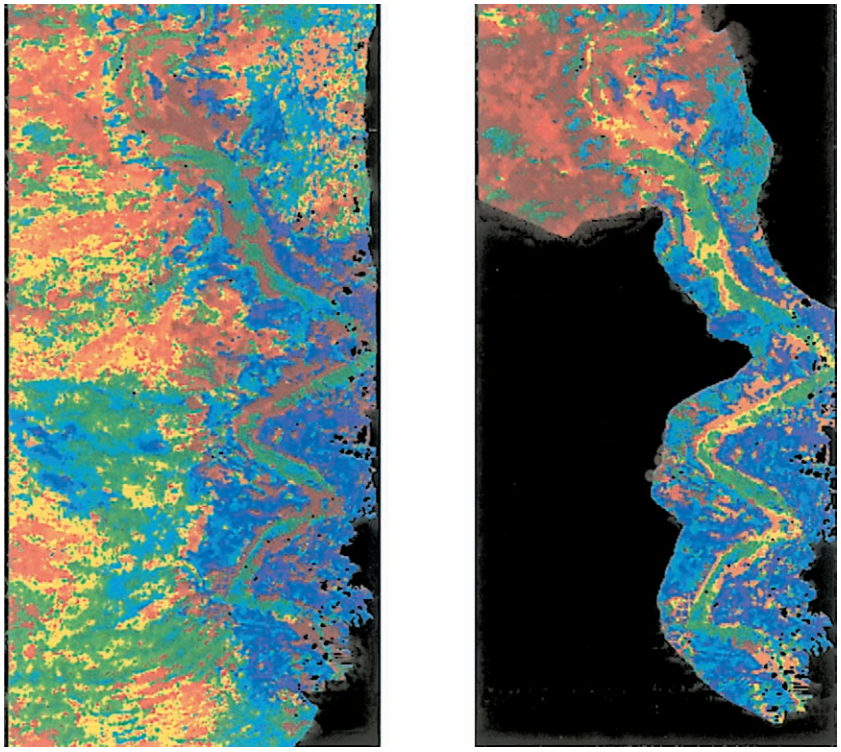

Fig. 8-46. Wave shape run over whole area shows a channel. Wave shape run over restricted area but with same number of classes shows facies along the channel. (Courtesy Paradigm Geophysical.)

starting from the top. Then the calculation sums again until half the previous total value is reached. If this point occurs above the midpoint of the interval, the sands are located primarily towards the top of the reservoir. If this point occurs below the midpoint of the interval, the sands are located primarily towards the base of the reservoir. Reds and blues, in Figure 8-43 (primarily within the high-energy area of Figure 8-41) indicate areas where these situations of internal distribution exist.

Energy half-time and other distribution attributes place even higher demands on data quality than other windowed attributes and, therefore, reliable results are difficult to obtain. **Amplitude ratio** (of top and base reflections) is a horizon-based amplitude attribute that addresses internal distribution. Relative to energy half-time it relies perhaps less on signal-to-noise but more on the zero-phaseness of the data.

Hybrid Attributes

Hybrid attributes combine components of amplitude *and* frequency, and for this reason have interesting potential. Seismic character is some mixture of amplitude and frequency; hence, a hybrid attribute has in principle the ability to be a good descriptor of seismic character. **Wave shape** is a neural network classification of trace character. A window of the seismic data, normally hung from an interpreted horizon, is analyzed, and some selected number of characteristic traces generated (Figure 8-44). The actual seismic traces within the area under study are then compared with the model traces and the best match is selected. Color indicates the model trace selected at each location and thus provides a seismic facies map. Hopefully with well control seismic facies can be related to actual depositional facies. Figure 8-45 shows a channel system delineated in this way. Addy (1998) provides several case history examples of this approach. The window size used should be large enough for the mathematical operations to be stable but small enough to provide adequate resolution of the geology; about one seismic period usually works well. Figure 8-46 shows the use of wave shape for studying a channel. The two panels show the effect of changing the size of the area studied while keeping the number of classes the same.

Downloaded 25 Jun 2012 to 95.28.162.50. Redistribution subject to SEG license or copyright; Terms of Use: http://segdl.org/

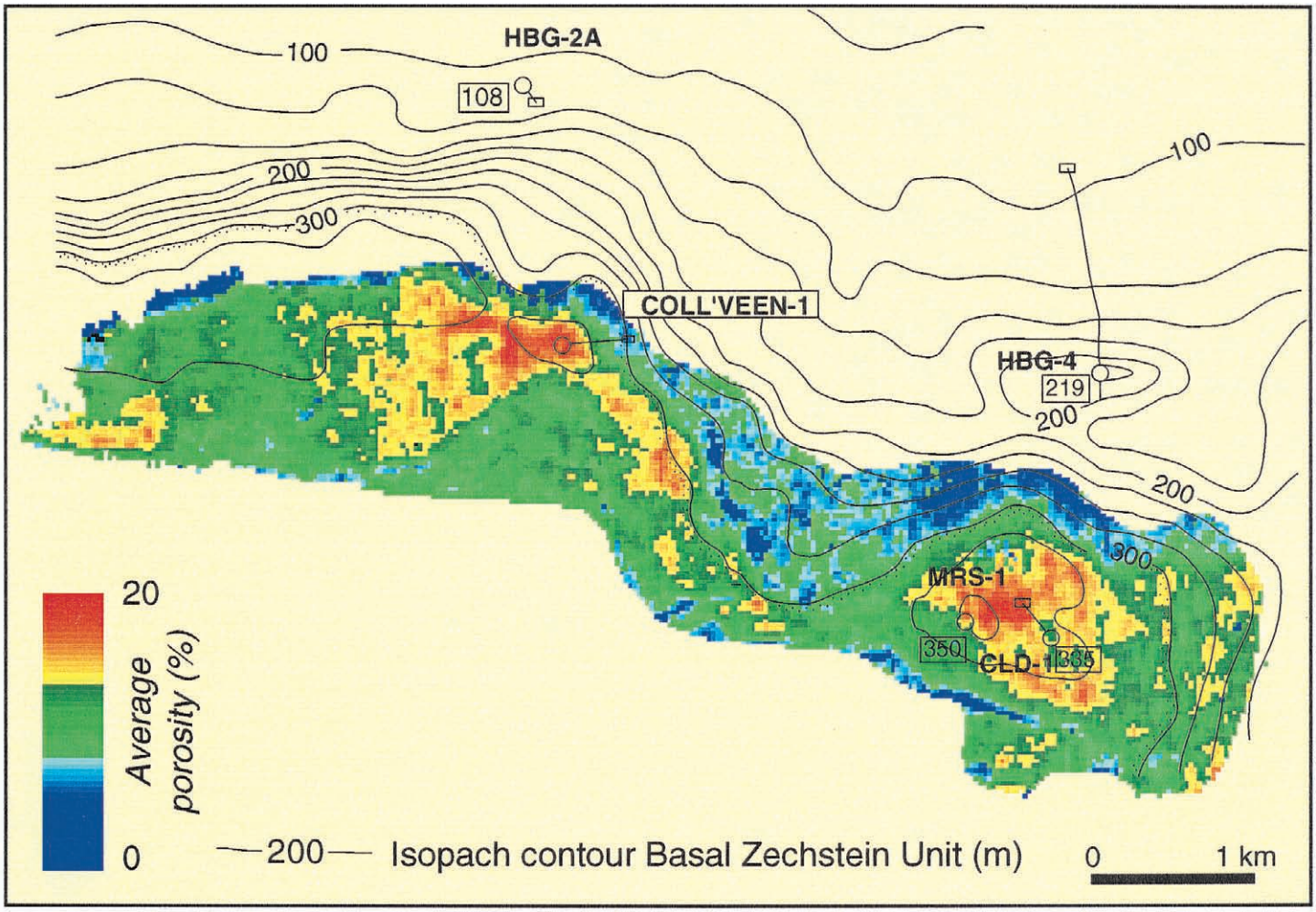

Fig. 8-47. Loop area was used to generate this average porosity map for a carbonate member of the Zechstein formation in Holland. (Courtesy Nederlandse Aardolie Maatschappij B.V.)

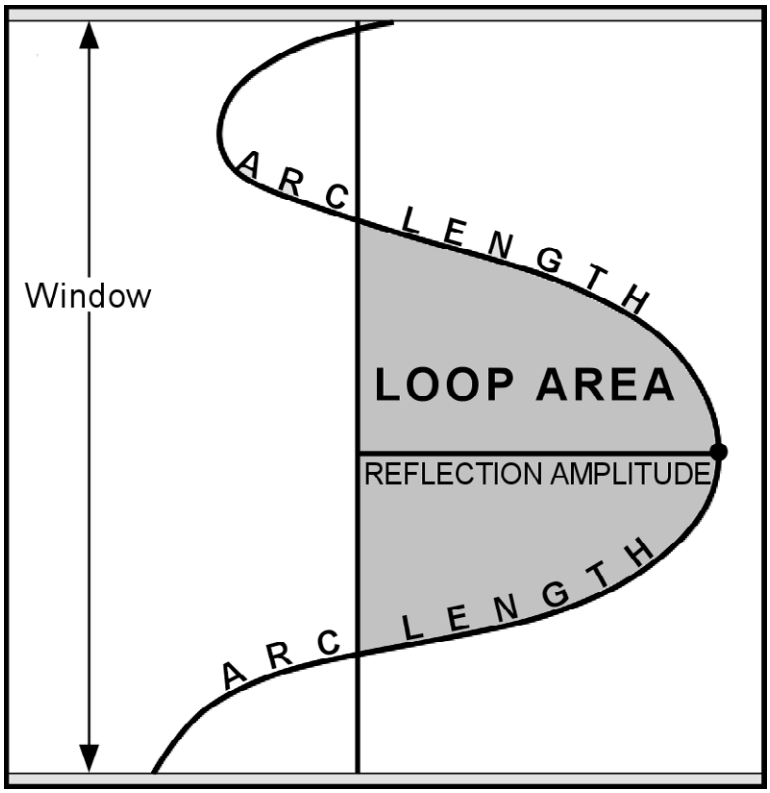

Fig. 8-48. Loop area and arc length explanation.

Downloaded 25 Jun 2012 to 95.28.162.50. Redistribution subject to SEG license or copyright; Terms of Use: http://segdl.org/

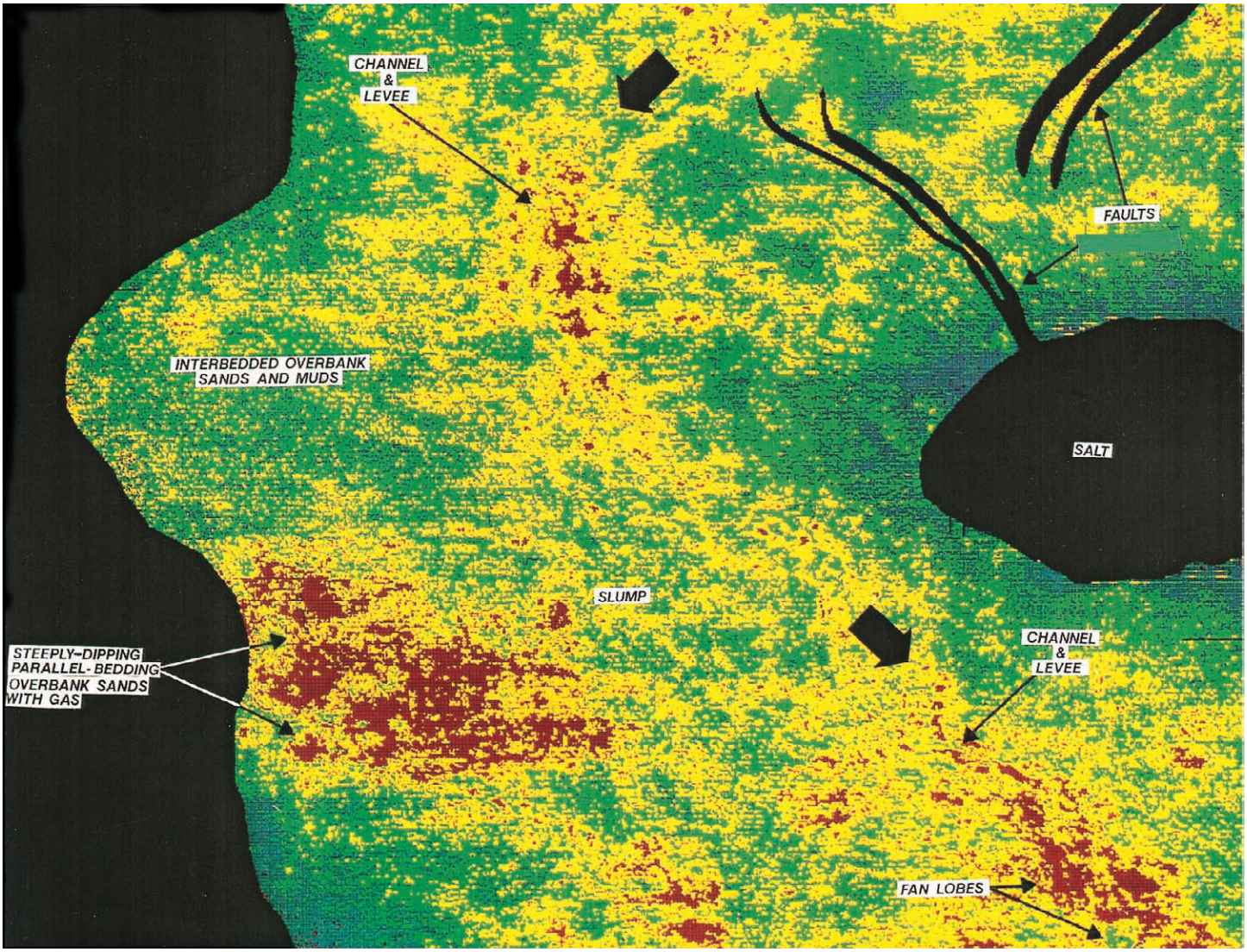

Fig. 8-49. Arc length, or reflection heterogeneity, used for mapping depositional facies in Gulf of Mexico. (Courtesy Geco-Prakla.)

Figure 8-47 shows a porosity map generated from the attribute **loop area**. Loop area is the area under the half-period of the seismic trace and is explained diagrammatically in Figure 8-48. In the project leading to Figure 8-47 (Van de Sande, 1996), loop area was found to correlate with porosity better than reflection amplitude.

Figure 8-49 shows depositional facies mapped from **arc length** in the Gulf of Mexico. Arc length is the total length of the seismic trace over a time window (Figure 8-48).

Frequency-derived Attributes

Use of instantaneous frequency to detect gas is discussed and illustrated in Chapter 5. However, it tends to be one of the less reliable approaches to the direct detection of hydrocarbons. In fact all frequency attributes tend to be noisy, and the industry has not yet really harnessed frequency for stratigraphic and reservoir studies. However, a few examples of their use do exist.

Figure 8-50 shows six different frequency-derived attributes displayed for the same small area. For comparison Figure 8-51 shows five amplitude-derived attributes over the same area and also the vertical section showing the window over which all these attributes were calculated. Three of the attributes in Figure 8-51 address vertical distribution within the interval.

Geologic frequency is simply the number of reflecting layers within unit thickness of rock. Higher geologic frequency means more layering. If it is detectable seismically,

Downloaded 25 Jun 2012 to 95.28.162.50. Redistribution subject to SEG license or copyright; Terms of Use: http://segdl.org/

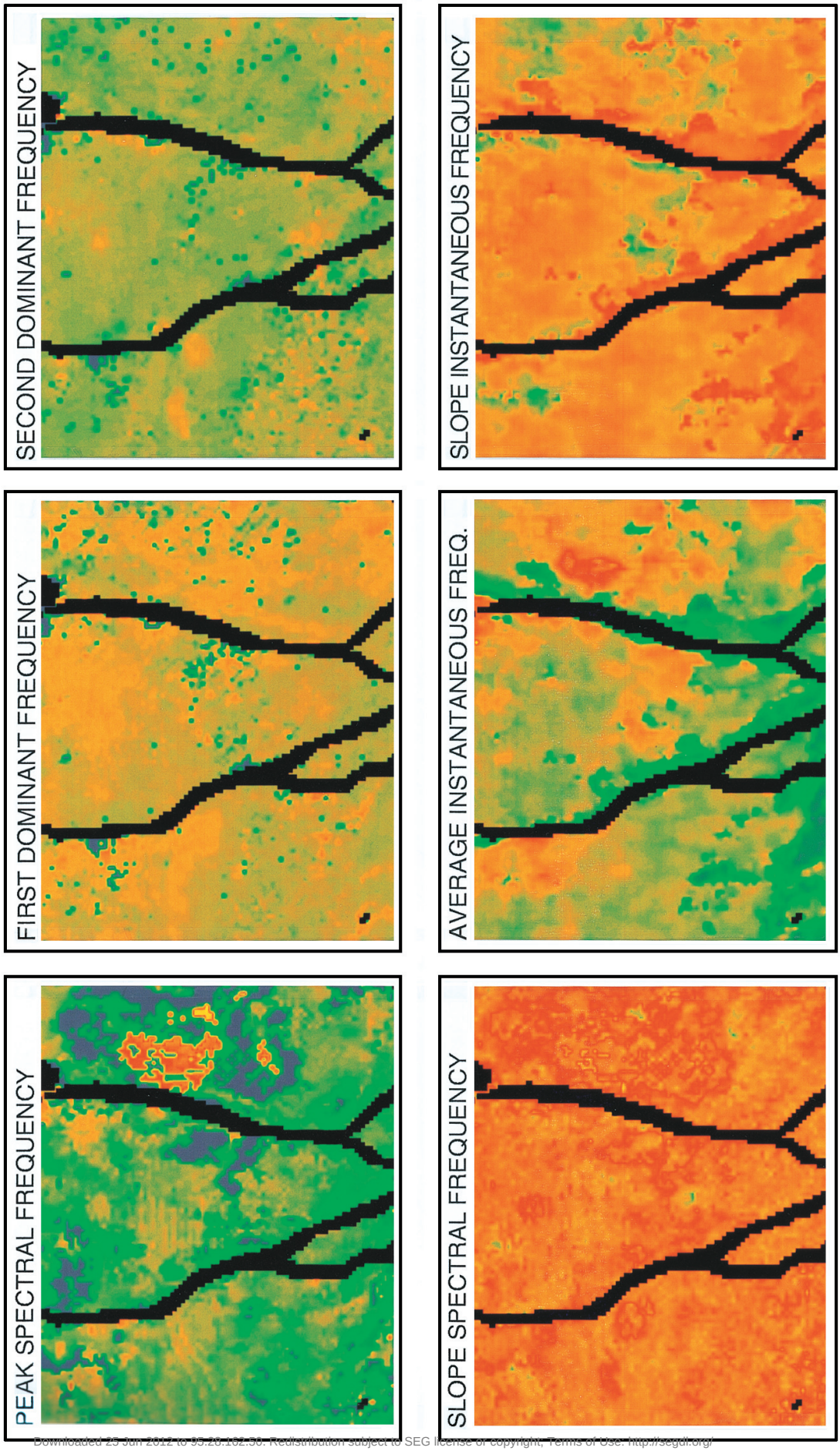

Fig. 8-50. Various frequency attributes displayed over the same area and for the same interval for comparison. (Courtesy Landmark Advance Products Group.)

Downloaded 25 Jun 2012 to 95.20.162.50. Redistribution subject to SEG license or copyright; Terms of Use: http://segdl.org/

Fig. 8-51. Various distribution and amplitude attributes displayed over the same area and for the interval shown in the lower left. (Courtesy Landmark Advance Products Group.)

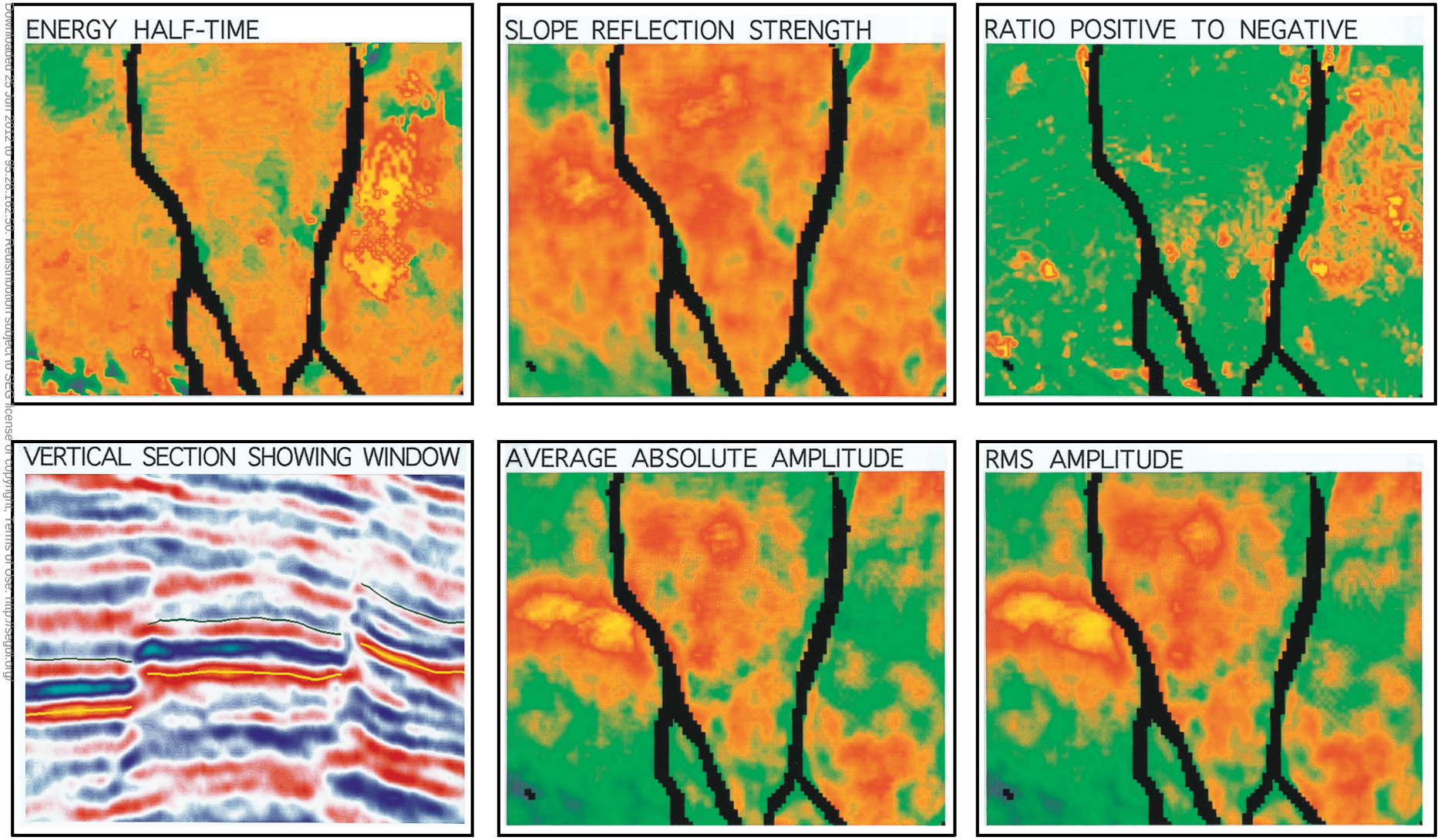

Downloaded 23 Jun 2012 to 65.26.162.90. Redistribution subject to SEG license or copyright. Terms of Use: http://segdl.org/

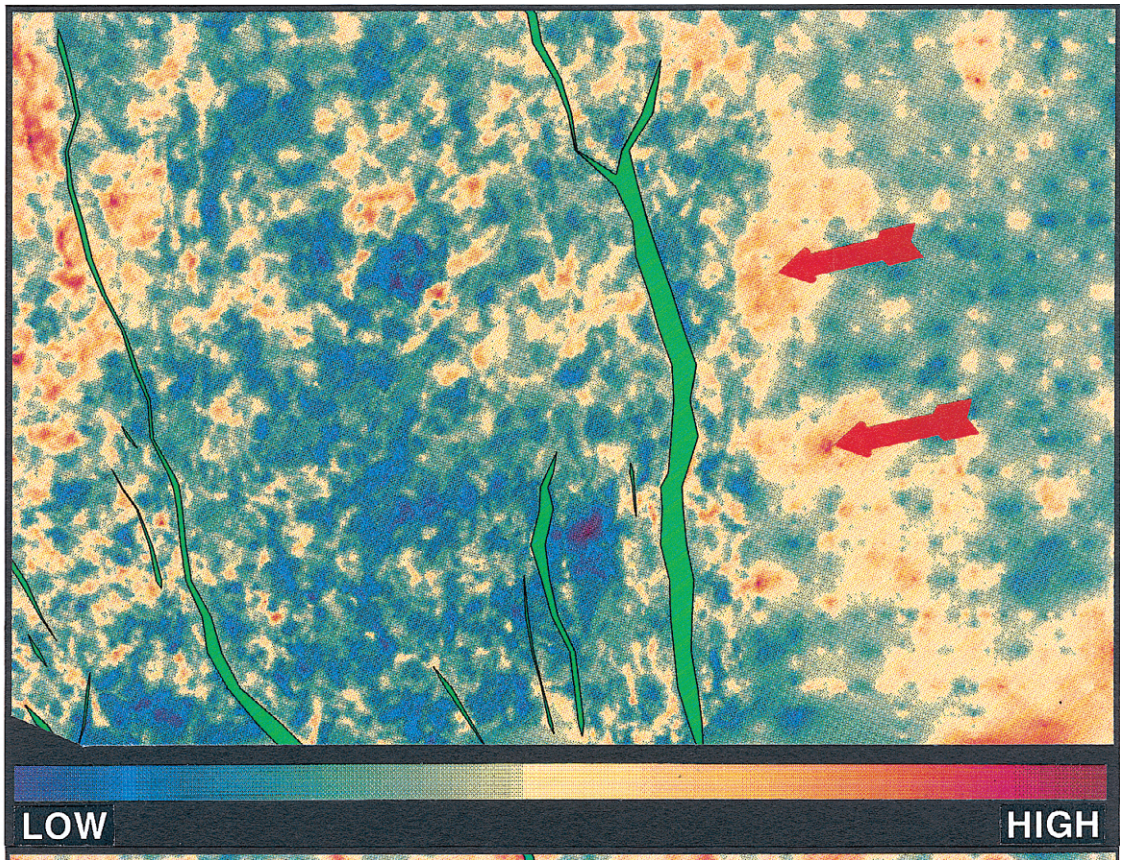

Fig. 8-52. Average instantaneous frequency map from the San Jorge Basin of southern Argentina. Productive wells are clustered in the areas indicated by red arrows. (Courtesy YPF S.A.)

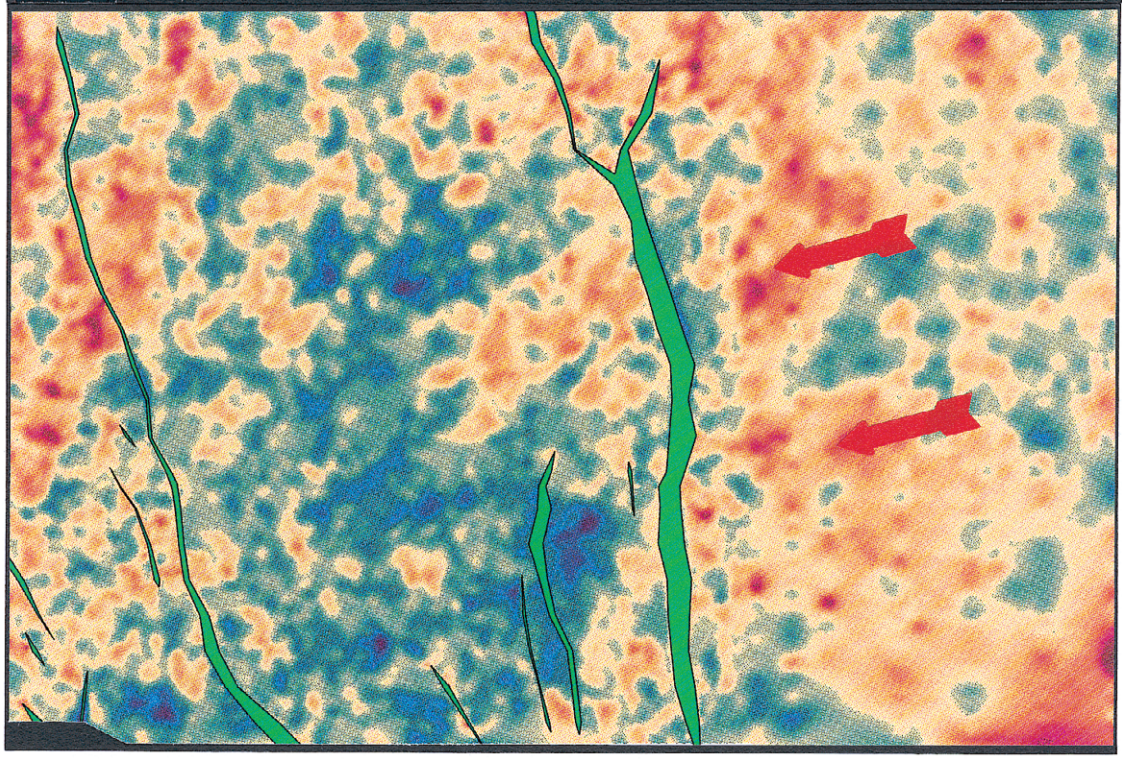

Fig. 8-53. Number of zero crossings map from the San Jorge Basin of southern Argentina. Productive wells are clustered in the areas indicated by red arrows. (Courtesy YPF S.A.)

Downloaded 25 Jun 2012 to 95.28.162.50. Redistribution subject to SEG license or copyright; Terms of Use: http://segdl.org/

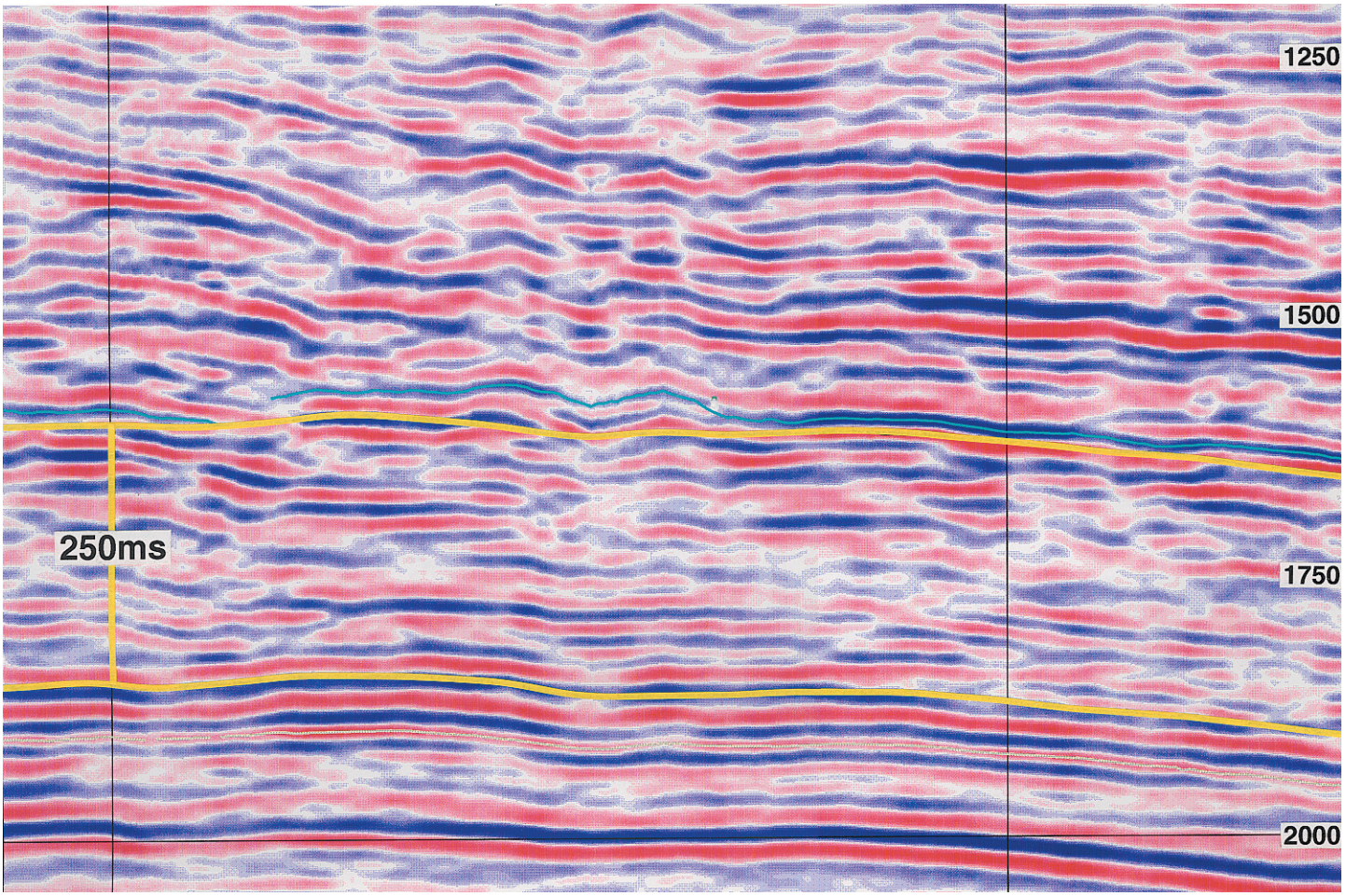

Fig. 8-54. Vertical section showing 250-ms window covering the productive sands. This window was used for the attribute calculations for Figures 8-52 and 8-53. (Courtesy YPF S.A.)

it must be secondary to the frequency characteristics of the propagating wavelet. In the three following examples it appears that geologic frequency is being expressed in a seismic frequency measurement.

Figures 8-52 and 8-53 show **average instantaneous frequency** and **number of zero crossings** for the oil-bearing interval shown as a 250-ms window in Figure 8-54. The field in southern Argentina has many wells producing from many thin sands of limited lateral extent. More layering should mean more sand. The wells were drilled on a regular pattern basis from the initial discovery, and are in fact clustered at the locations marked by red arrows. High frequency for both attributes thus correlates with better production from more sands.

A similar story is reported from south Texas by Horkowitz and Davis (1996). Figure 8-55 shows an RMS instantaneous-frequency map from an area with many wells. The wells with more sands lie in the areas of high instantaneous frequency.

First, second and third dominant frequencies involve completely different transform mathematics and notionally force-fit the spectrum to yield three maxima. First dominant frequency should primarily express the properties of the wavelet. **Second dominant frequency** should primarily express the geologic frequency and thus be the most useful. For the window of data shown in the small insert of Figure 8-51, second dominant frequency, first dominant frequency and composite amplitude were cross-plotted to yield Figure 8-56. The white points, well separated in second dominant frequency, are plotted in their proper geographic position in Figure 8-57. The color indicates amplitude and the existence of hydrocarbon. The white dots are believed to indicate additional layering and thus additional sand. In fact a well was drilled into one of the areas of white dots and found some previously bypassed reserves.

Downloaded 25 Jun 2012 to 95.28.162.50. Redistribution subject to SEG license or copyright; Terms of Use: http://segdl.org/

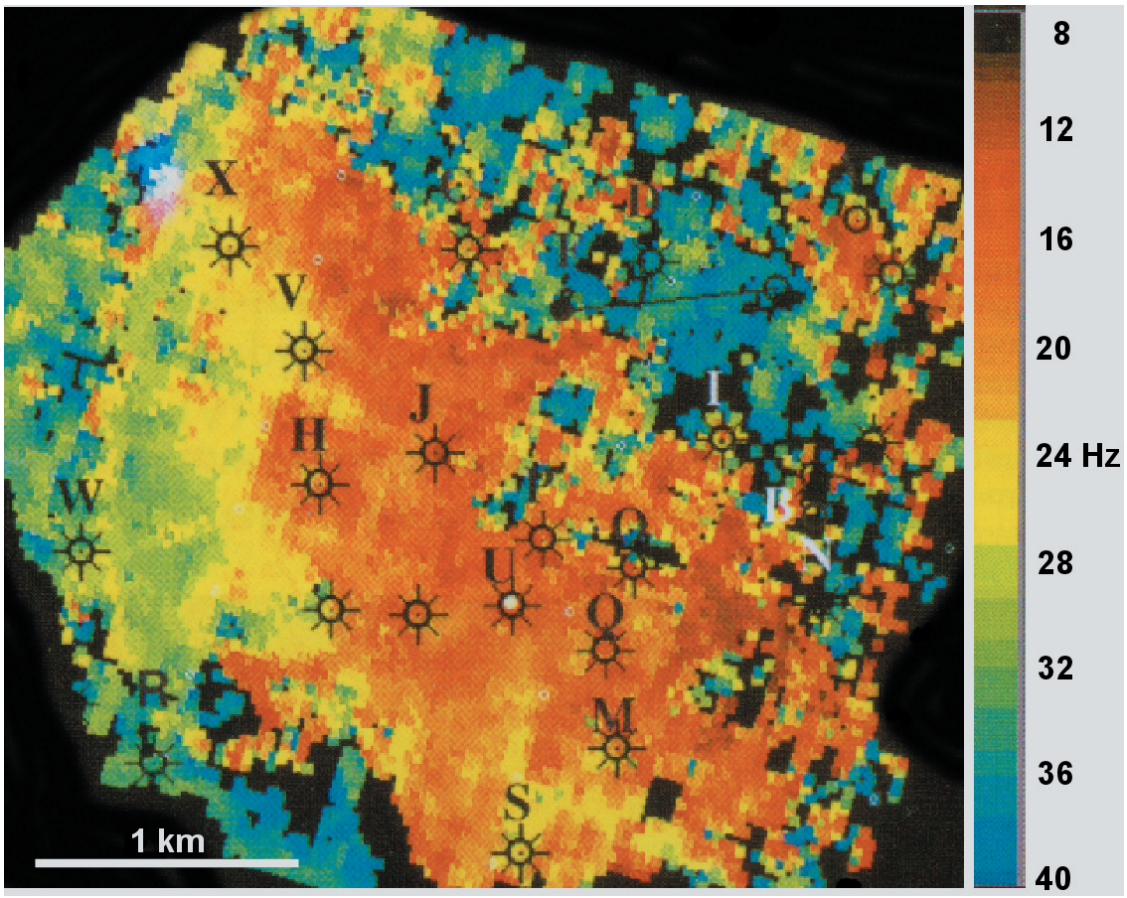

Fig. 8-55. RMS instantaneous-frequency map over 40-ms interval from south Texas. The wells in the high instantaneous-frequency areas contain more layers of sand. (Courtesy Sanchez-O'Brien Oil and Gas Corporation and K. O. Horkowitz.)

Downloaded 25 Jun 2012 to 95.28.162.50. Redistribution subject to SEG license or copyright; Terms of Use: http://segdl.org/

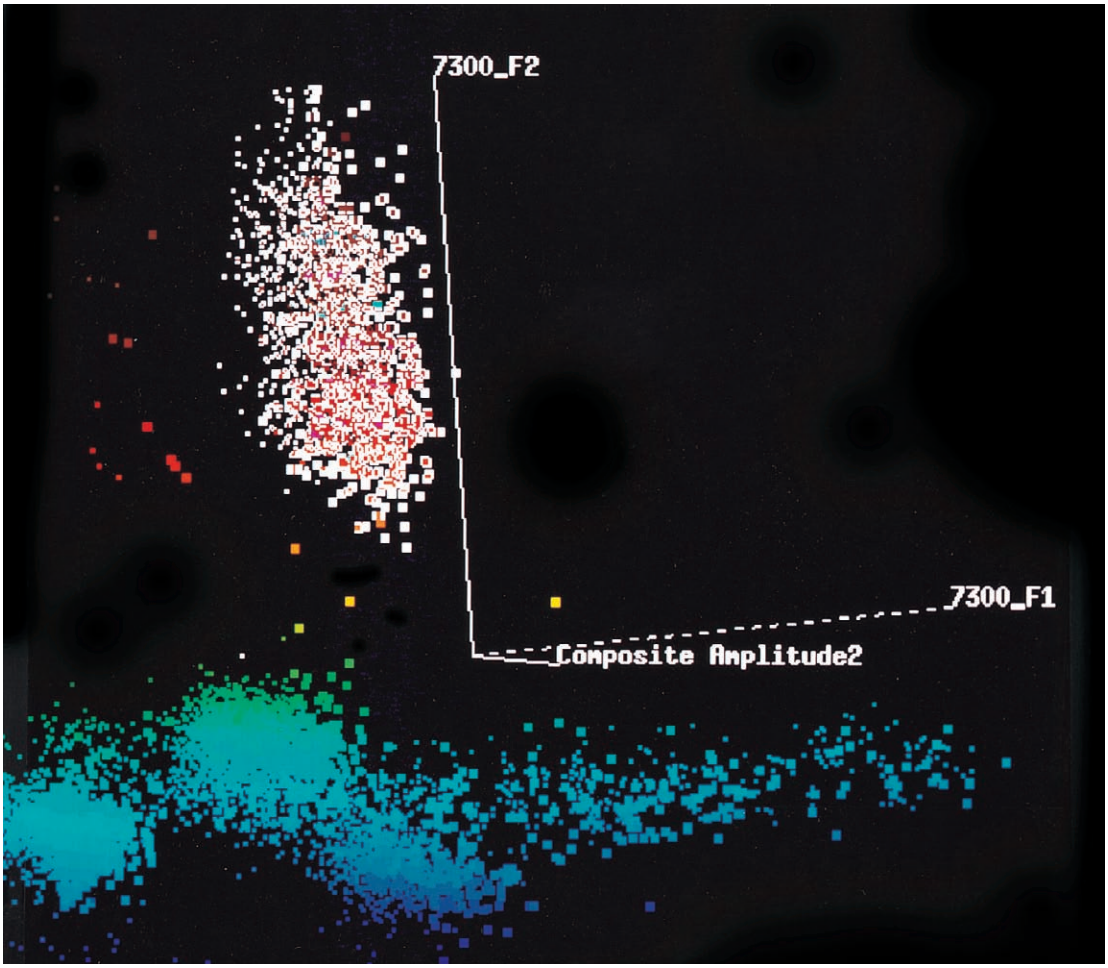

Fig. 8-56. Three-dimensional crossplot between composite amplitude, first dominant frequency and second dominant frequency, used to establish statistical separation of attributes. (Courtesy Landmark Advance Products Group.)

Fig. 8-57. High second dominant frequency, indicated by white dots, shows additional sand layering. High amplitude, indicated by reds and yellows, shows the presence of gas. The white dots were shown to be anomalously high in second dominant frequency on the crossplot of Figure 8-56. (Courtesy Landmark Advance Products Group.)

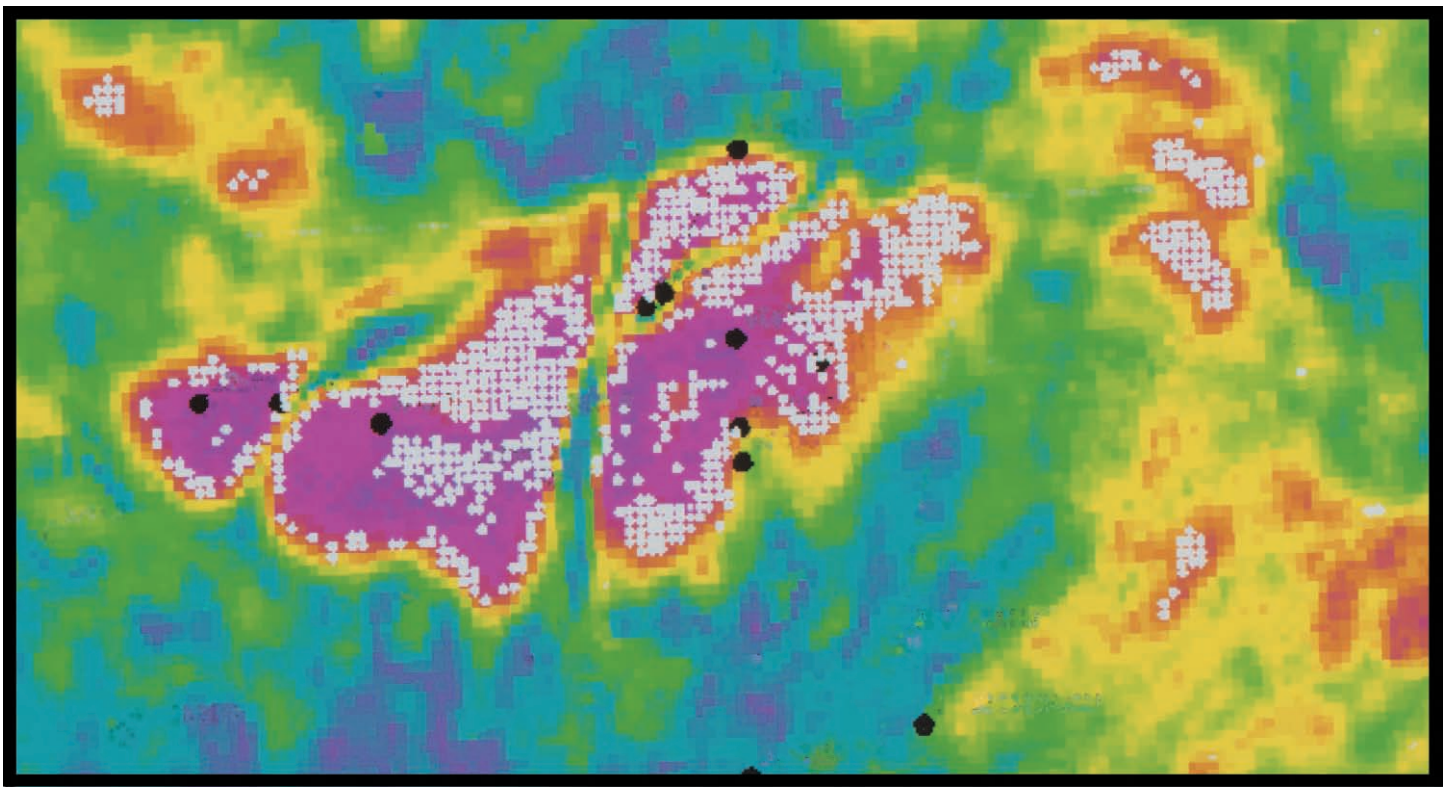

Downloaded 25 Jun 2012 to 95.28.162.50. Redistribution subject to SEG license or copyright; Terms of Use: http://segdl.org/

Volumetric Attributes and Curvature

Interpreters should distinguish between attributes which are properties of a horizon and attributes which are extracted from a volume of seismic data using a window. An attribute along a horizon obviously requires a structurally interpreted horizon, at least a preliminary one, and thus will be used after a significant amount of tracking has been completed. Much of this chapter has been addressing this type of attribute, and the uses have centered on verifying and enhancing the interpretation in progress.

Volumetric attributes, which operate directly on the data themselves, can be used earlier in the interpretation before a horizon exists. Coherence, which has been discussed at length in this chapter, is the best example of this type of attribute, and is used primarily for detecting faults. Other attributes can now also be extracted from the volume and the most significant of these is volumetric curvature. Chopra and Marfurt (2007) tell us that there are many ways of calculating **volumetric curvature** but that the most important are most-positive curvature and most-negative curvature. These can also be extracted from the curvature volume along a horizon surface to give a horizon slice in curvature.

Curvature has emerged as an attribute with many applications. It can be used in conjunction with dip, azimuth, or residual to cross-validate the presence of a subtle fault. It can be used to create a display emphasizing the relief on a horizon surface (Figure 8-58). For a brittle reservoir like a carbonate encased in shale, fracturing will probably be most pronounced where the layer is most bent. Thus a high value of curvature can be used as circumstantial evidence for fracturing in carbonate reservoirs. Figure 8-59 shows two types of volumetric curvature extracted along a horizon. Most-positive curvature shows lineations in red, indicating principally channel levees. Most-negative curvature shows lineations in blue, indicating principally channel thalwegs.

Amplitude Variation with Offset

Amplitude Variation with Offset for the identification of gas is discussed briefly in Chapter 5. AVO has become a very popular subject and is covered by Castagna and Backus (1993). However, the amount of AVO work performed in 3-D is extremely small, and Castagna and Backus barely mention the subject. Furthermore, the 3-D AVO projects which have been performed show little incremental benefit over the 3-D analysis of the post-stack amplitudes. The example presented in Figures 8-60 through 8-63 is one exception.

Figure 8-60 is the horizon slice displaying conventional stacked amplitude for a gas reservoir in the deepwater Gulf of Mexico. Figures 8-61 and 8-62 show horizon slices on the same horizon from individually migrated data volumes incorporating respectively near-offset traces only and far-offset traces only. The two are similar and both show separation into eastern and western lobes. The differences between the two do not at first appear significant.

Figure 8-63 is the arithmetic difference between the amplitudes of Figures 8-61 and 8-62; in other words Figure 8-63 is a display of the AVO attribute **far-near amplitude difference**. A channel is now clearly visible in yellow, red and green, which indicates increasing amplitude with offset. This channel, meandering across parts of both eastern and western lobes, is not visible on any normal amplitude display and is interpreted as the sand-filled channel facies of a slope fan. Furthermore, it probably indicates the areas of highest porosity and permeability within the reservoir.

Use of Multiple Attributes

This chapter has so far focused on the attributes available and their individual uses. Approaches are now in place for using multiple attributes together in the derivation of a reservoir property map. Attributes are normally extracted from the relevant level in the seismic data as horizon attributes and/or windowed attributes over at least one half-period. They are then selected on the basis of geophysical and petrophysical reasoning; that is, we use attributes which appear reasonable. Each attribute may be crossplotted against the reservoir property of interest using multiple wells and the one that correlates best is selected. The other attributes are then tested in turn to find

Downloaded 25 Jun 2012 to 95.28.162.50. Redistribution subject to SEG license or copyright; Terms of Use: http://segdl.org/

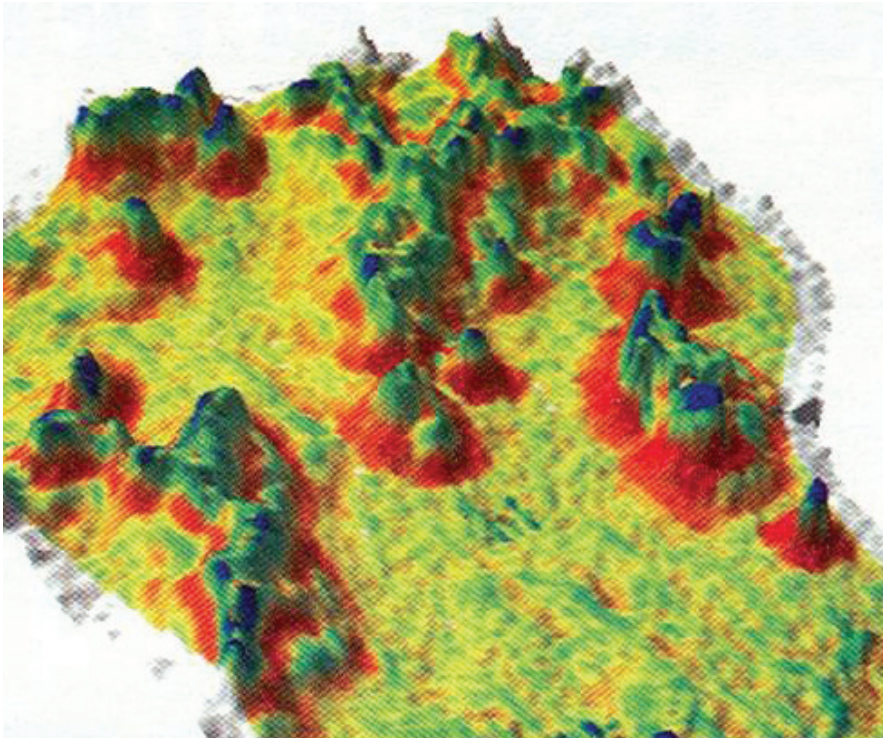

Fig. 8-58. Curvature on a horizon surface, emphasizing drape over pinnacle reefs.

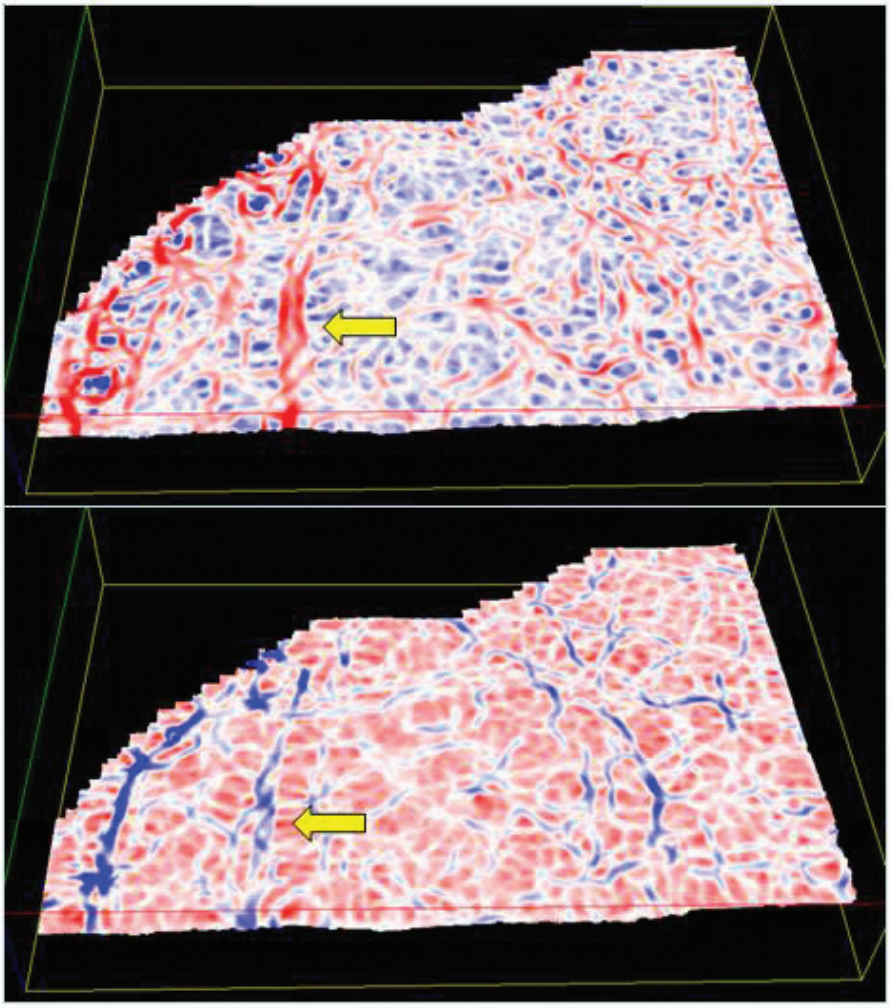

Fig. 8-59. Most-positive curvature extracted along a horizon (above) and most-negative curvature extracted along the same horizon (below), showing lineations associated with channels. (Courtesy Arcis Corporation.)

Downloaded 25 Jun 2012 to 95.28.162.50. Redistribution subject to SEG license or copyright; Terms of Use: http://segdl.org/

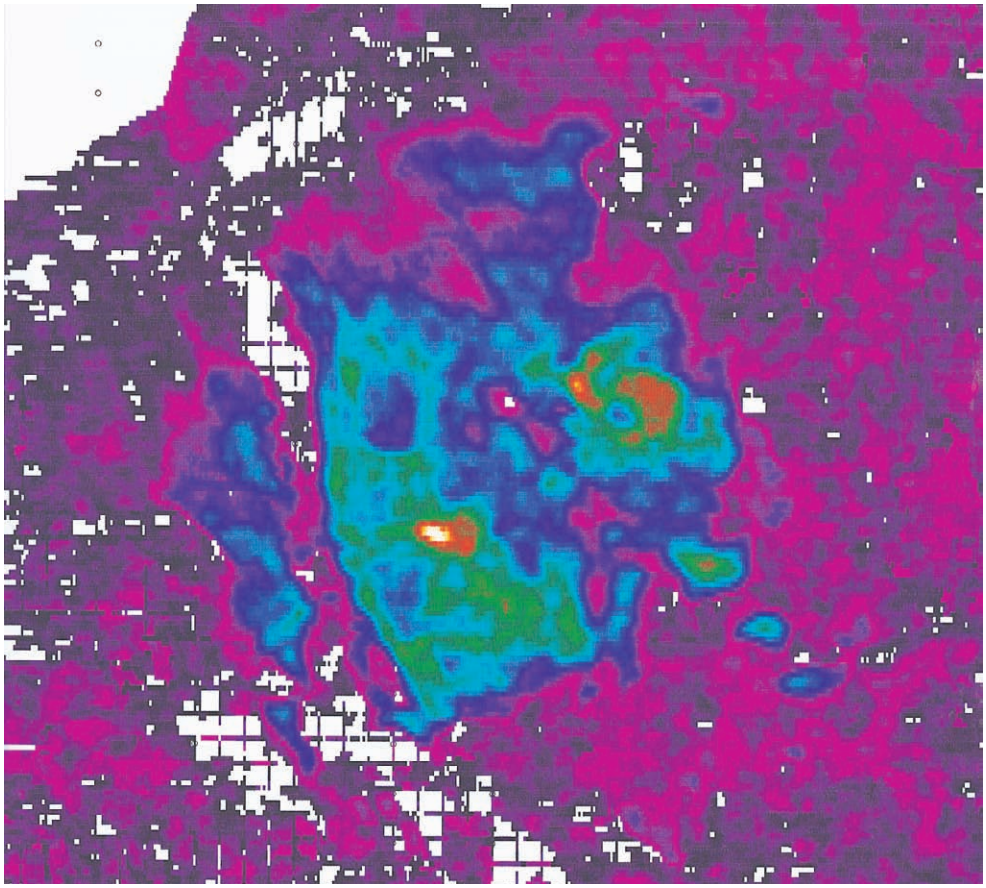

Fig. 8-61. Horizon slice in amplitude from near offsets only for a gas reservoir in the deepwater Gulf of Mexico. Note the separation of the reservoir into eastern and western lobes. (Courtesy Amoco Production Company.)

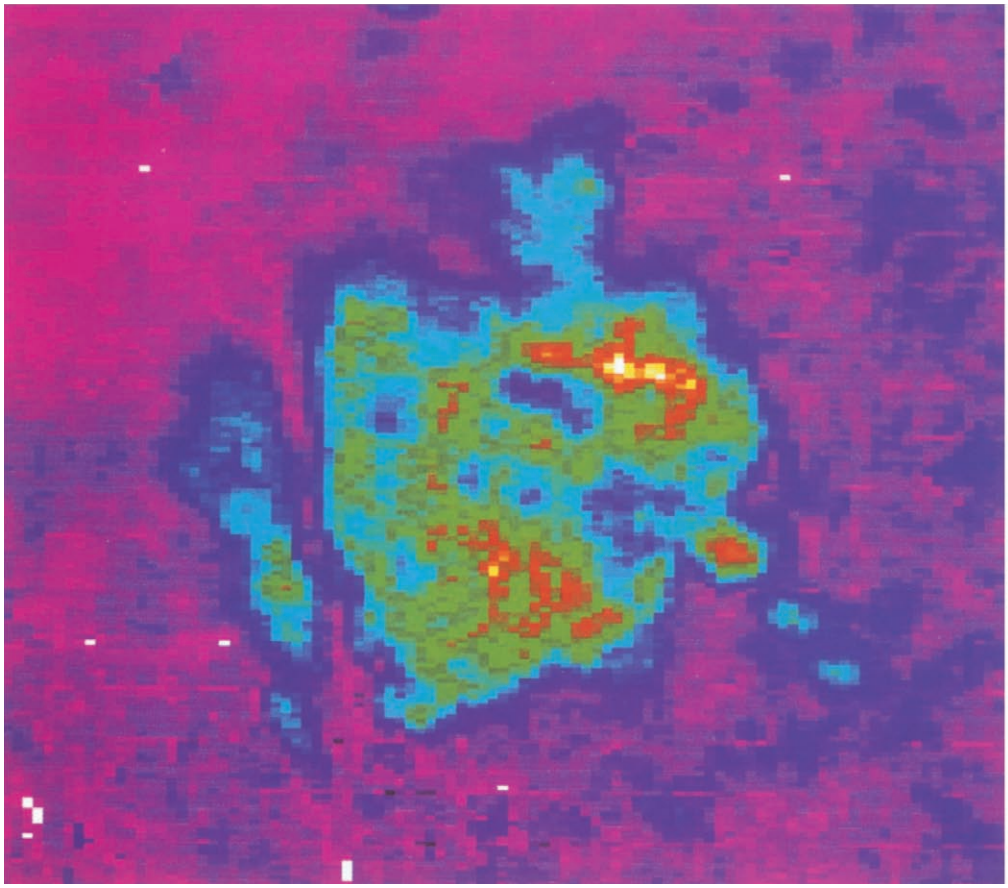

Fig. 8-60. Horizon slice in conventional stacked amplitude for a gas reservoir in the deepwater Gulf of Mexico. (Courtesy Amoco Production Company.)

Downloaded 25 Jun 2012 to 95.28.162.50. Redistribution subject to SEG license or copyright; Terms of Use: http://segdl.org/

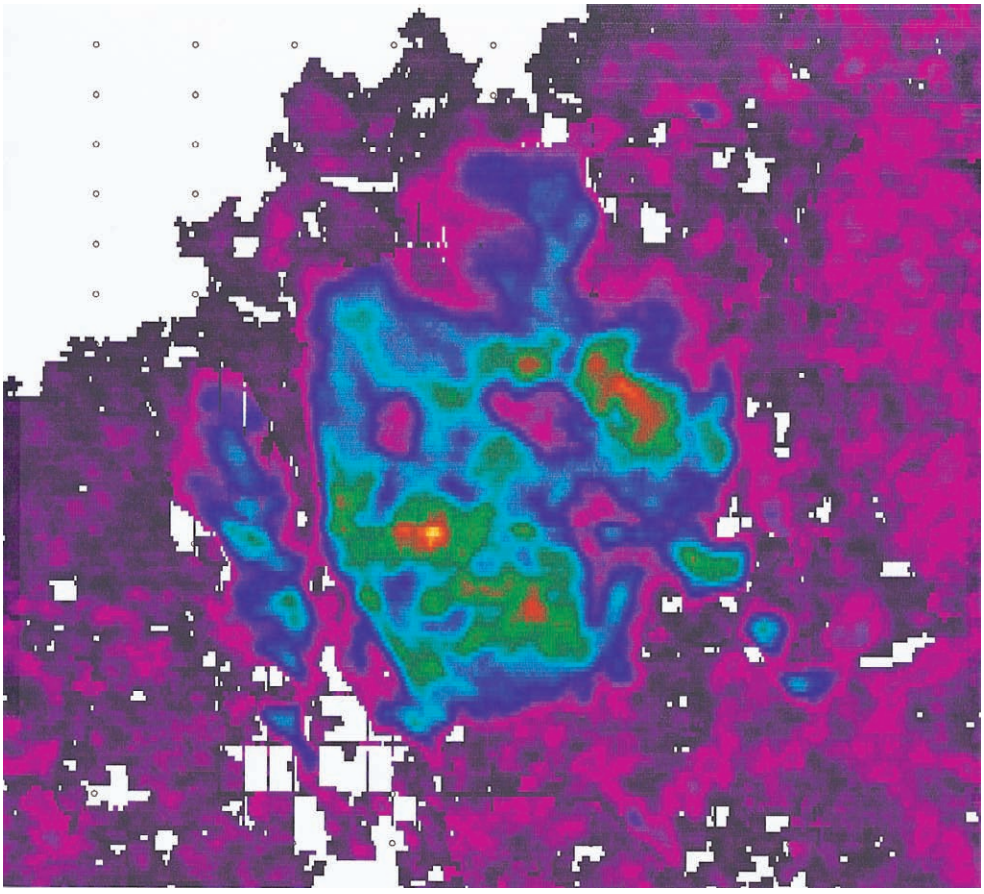

Fig. 8-62. Horizon slice in amplitude from far offsets only, for comparison with Figure 8-61. (Courtesy Amoco Production Company.)

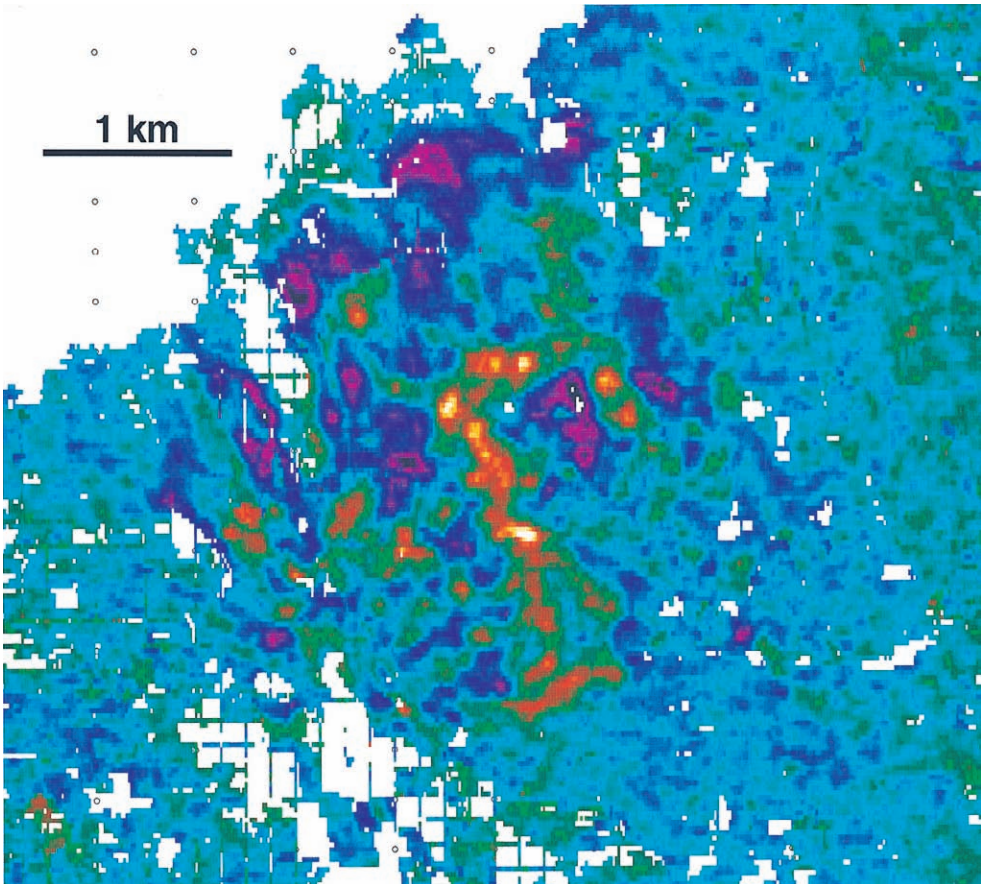

Fig. 8-63. 3-D AVO— horizon slice in far-near amplitude difference; that is, the subtraction of Figure 8-61 amplitudes from Figure 8-62 amplitudes. Reds, yellows and greens indicate amplitude increasing with offset. The pattern in these colors indicates a channel not visible in normal amplitude and probably containing the highest porosities and permeabilities in the fan. (Courtesy Amoco Production Company.)

Downloaded 25 Jun 2012 to 95.28.162.50. Redistribution subject to SEG license or copyright; Terms of Use: http://segdl.org/

how much of the remaining variance in the relationship they explain. The statistics then help with the selection on the basis of their contribution to variance reduction. The resultant attributes, one or several together, are then used in geostatistical cokriging to interpolate the reservoir property being mapped between wells.

There are many dangers in statistics, and much has recently been written about these dangers as applied to reservoir characterization. Hirsche et al. (1997 and 1998) have been particularly vocal with remarks including: *Neglecting geology and geophysics reduces geostatistics to a purely statistical process that may give false confidence in spurious results.* Schuelke and Quirein (1998) offer a similar caution: *The use of statistical methods without the foundation of a physical basis for the correlation between the seismic attribute(s) and the rock property … is very risky.* Hart (2002) makes the same point: *There must be a known or suspected link between the attribute and the log-based physical properties to be imaged.* Hart and Balch (1999) remind us that *the probability of obtaining a statistically significant but spurious correlation between an attribute and a log-derived property is proportional to the number of attributes tested and inversely proportional to the number of wells used in the calibration.* Kalkomey (1997) discusses this further and calculates alarmingly high probabilities.

In summary, for a geostatistical reservoir study we would like a large number of wells but we should not use a large number of attributes. Thus about three, or up to a maximum of five, attributes should be selected primarily on the basis of geophysical and petrophysical reasoning. Little reliance should be placed on correlation coefficients. The selected attributes are then submitted to the multiple regression analysis and cokriging.

Downloaded 25 Jun 2012 to 95.28.162.50. Redistribution subject to SEG license or copyright; Terms of Use: http://segdl.org/

Spectral Decomposition

Contributed by Gregory A. Partyka, Michael D. Bush, Paul G. A. Garossino, and Paul R. Gutowski, OpenGeoSolutions Inc.

Principles of Spectral Decomposition

Spectral decomposition (SD) is a technique that breaks down seismic signal into narrow frequency sub-bands. When these sub-bands are examined in a spatial context (i.e., plan view of a 3-D survey) they reveal interference that is occurring across the available bandwidth of signal. This approach is analogous to remote sensing techniques commonly used to image the surface of the earth. Whereas the remote sensing techniques rely on substantially higher electromagnetic frequencies to map interference at the surface of the earth, spectral decomposition makes use of much lower seismic frequencies to image the reflective nature of the subsurface rock mass. Such decomposition provides greater resolution and detection of the layer-stacking heterogeneity, boundaries, and thickness variability than are possible with traditional broadband seismic attributes.

The interference we observe in seismic data is controlled by the interaction of a band-limited signal with local distribution of impedance contrasts (Figure 8-64). This interaction causes geologic features to tune in at some frequencies and tune out at other frequencies (Figure 8-65). Finding frequencies at which the geologic features stand out (i.e., either tune in or tune out) from the background amplitude is the key to the successful application of spectral decomposition.

A reflective layer in the subsurface can be thought of as a "boxcar" in time. A boxcar in one domain transforms to a sinc function in the other domain. For example, a steep-sided boxcar-shaped filter in the frequency domain transforms to a sinc waveform in the time domain. A layer/boxcar in the time domain transforms to a sinc function in the frequency domain. Thus a single layer in time becomes a sinc function in frequency, and multiple layers form a summation of sincs. The mathematical expression of the layer-to-sinc transform allows examination of the relationship between layer-stacking combinations and the associated spectral signatures.

Interpretation using only full-bandwidth amplitude means disregarding the sub-band interference information that is available. This is much like the loss of information that occurs when stacking AVO gathers that exhibit significant amplitude changes with offset.

The goal of processing in preparation for SD work is to maintain as broad a signal bandwidth as possible. If possible, utilize AVO processing to preferentially image rock or fluid properties prior to SD analysis. This broad bandwidth can then be examined as a series of narrow bands to characterize a zone of interest with significantly more fidelity than is obtained from a combined full-bandwidth response.

Recommended Workflow

(1) Reconnaissance tuning cube (Figure 8-66):
Transform a short window around the zone of interest from time to frequency. Perform spectral balancing to suppress the wavelet overprint (Figure 8-67). Display the resulting (x,y,frequency) volume in plan view as a series of frequency slices—one slice per frequency sub-band.

(2) Running window spectral decomposition:
Select a few key frequency bands that reveal heterogeneity of interest. Generate isofrequency running window spectral decomposition volumes for the key frequencies. Perform spectral balancing to suppress the wavelet overprint. Animate up and down in time to identify temporal positions that best image the zone of interest.

Downloaded 25 Jun 2012 to 95.28.162.50. Redistribution subject to SEG license or copyright; Terms of Use: http://segdl.org/

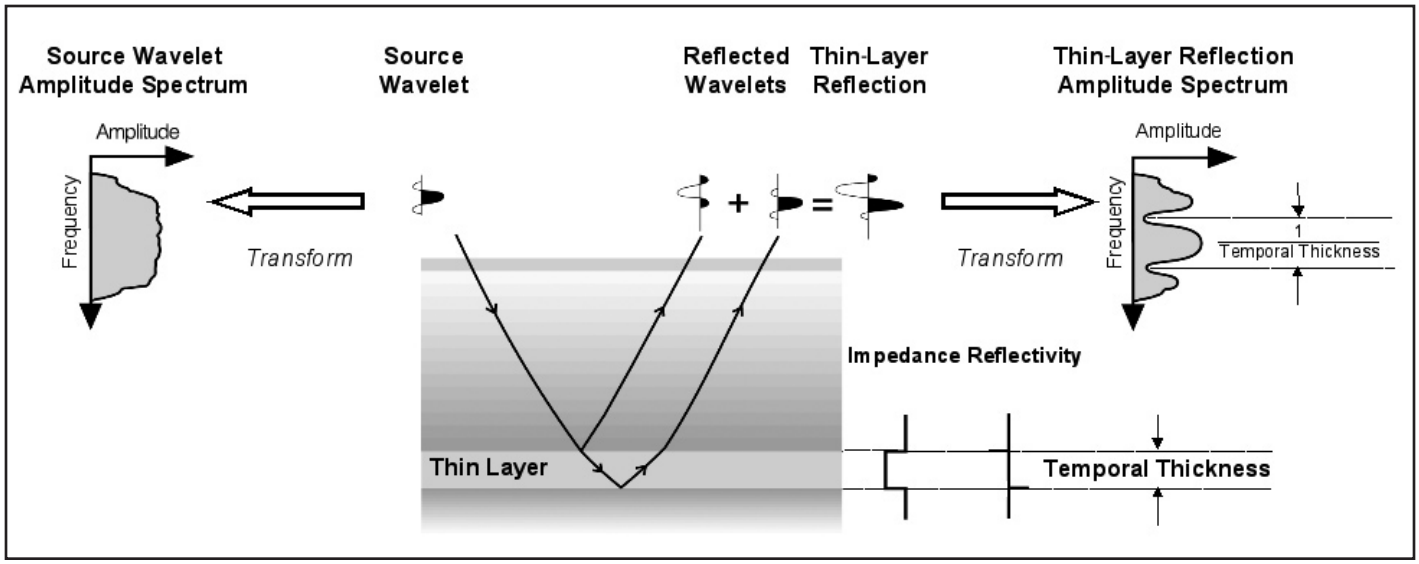

Fig. 8-64. Amplitude spectrum of a thin-bed reflection. From Partyka et al. (1999). Used by permission.

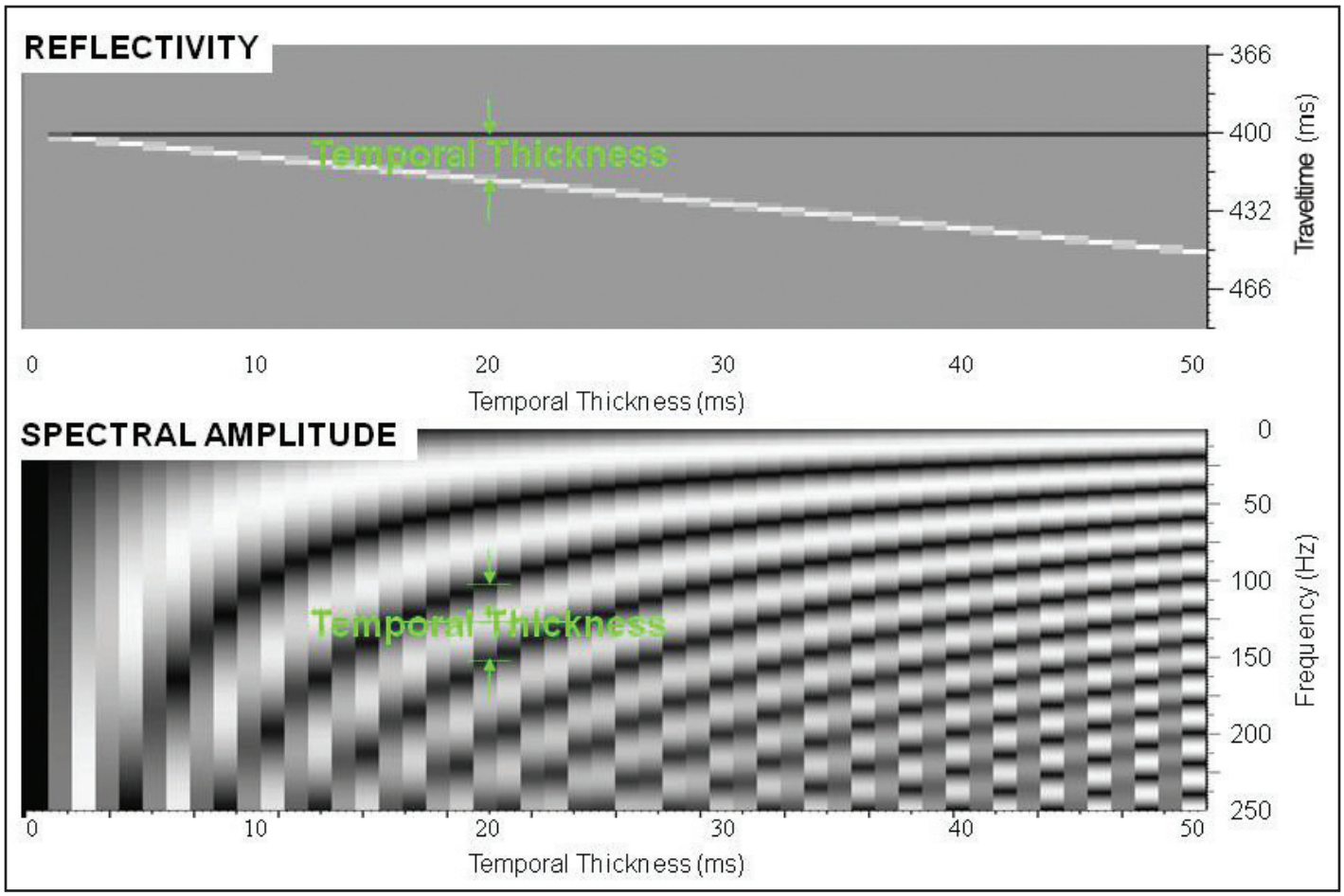

Fig. 8-65. A simple wedge model illustrates the interference that occurs as a function of temporal thickness and frequency. From Partyka et al. (1999). Used by permission.

Downloaded 25 Jun 2012 to 95.28.162.50. Redistribution subject to SEG license or copyright; Terms of Use: http://segdl.org/

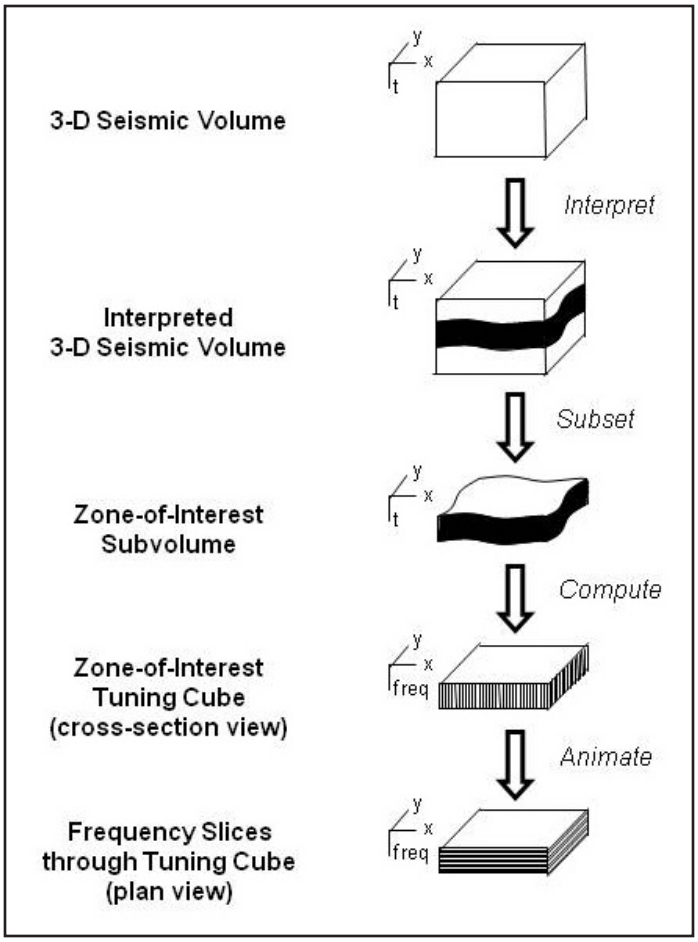

Fig. 8-66. The tuning cube is a frequency domain representation of a target zone within the seismic data. From Partyka et al. (1999). Used by permission.

Fig. 8-67. Spectral balancing removes the seismic wavelet shape in a way that does not destroy the spatial variations in interference. From Partyka et al. (1999). Used by permission.

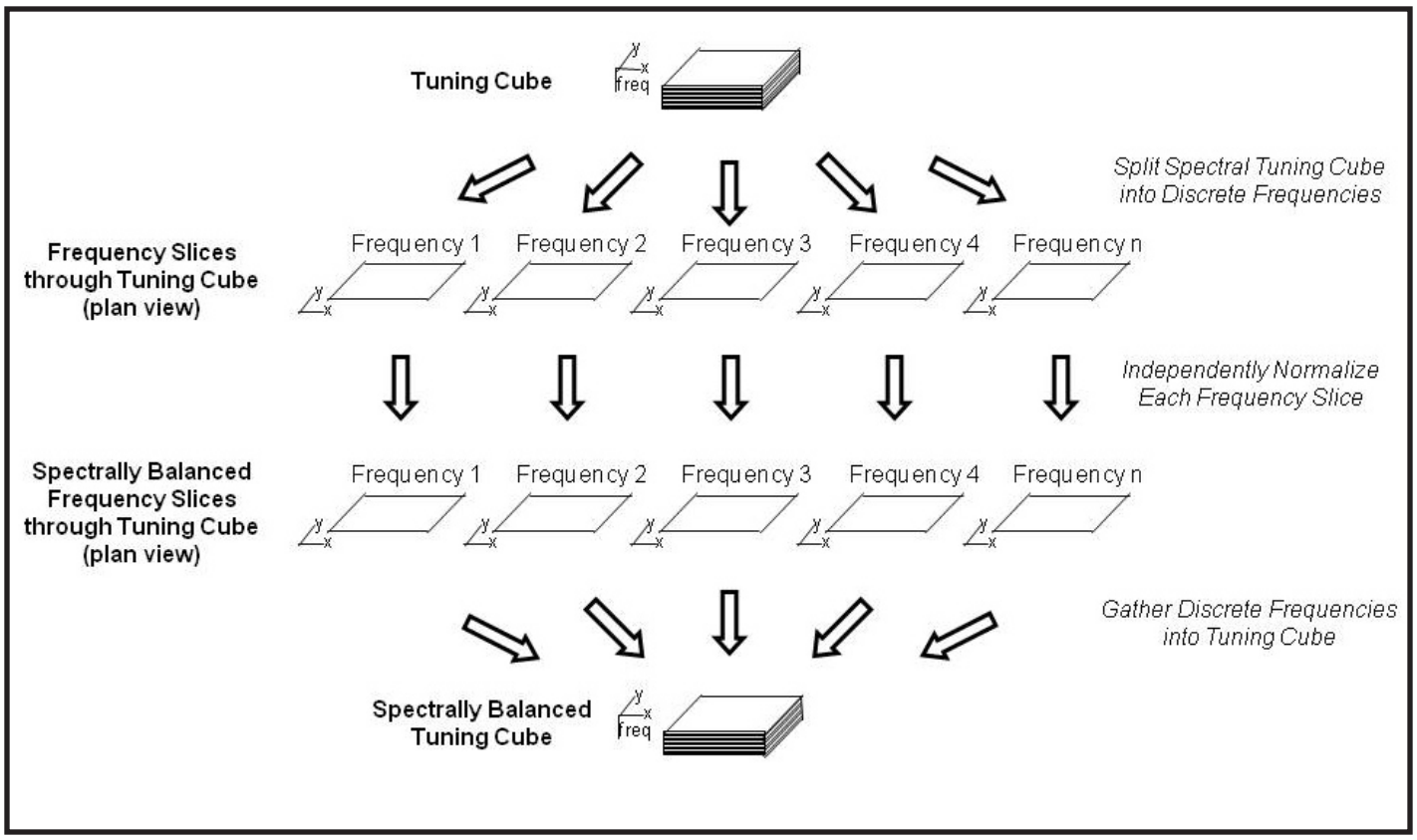

Downloaded 25 Jun 2012 to 95.28.162.50. Redistribution subject to SEG license or copyright; Terms of Use: http://segdl.org/

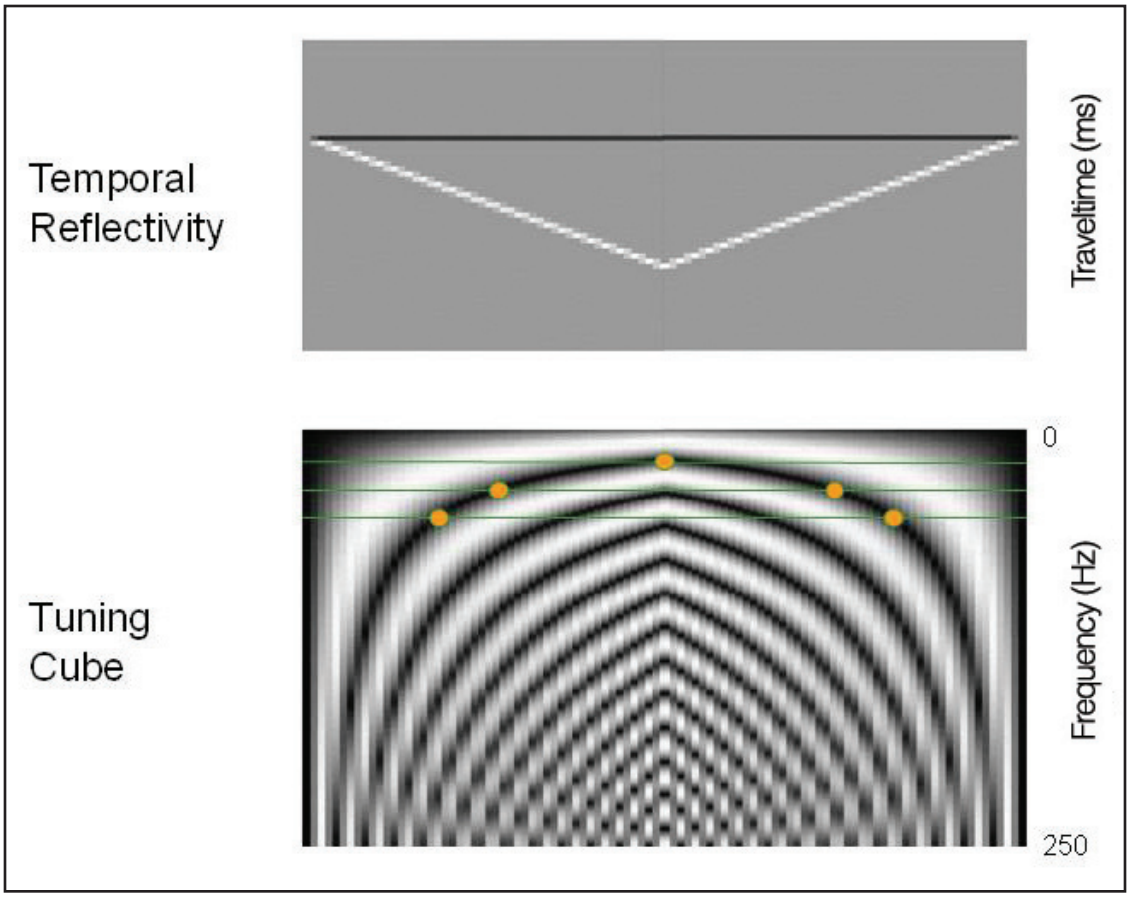

Fig. 8-68. A tuning cube view of a simple channel cross-section. Animating through the tuning cube from low to high frequency causes amplitude contours to move from thick to thin. From Partyka (2005). Used by permission.

(3) Targeted tuning cube:
Transform a short window around the zone of interest from time to frequency, using targeted parameters. Perform spectral balancing to suppress the wavelet overprint. Display the resulting (*x*,*y*,frequency) volume in plan view as a series of frequency slices—one slice per frequency sub-band.

Significance of Spectral Balancing

A raw tuning cube contains three main components:

- layer interference (the geologic heterogeneity part of most interest to the interpreter)
- noise, and
- the seismic wavelet

Frequency slices of amplitude in narrow frequency bands above and below the dominant frequency of the seismic wavelet will appear significantly weaker in amplitude than slices extracted at frequency bands near the dominant frequency. To remove this effect, spectral balancing is applied (Figure 8-67) by determining the median amplitude in each frequency slice and scaling to a target amplitude value. Spectral balancing suppresses the seismic wavelet overprint and reveals the underlying geologic heterogeneity while not destroying the spatial variations in interference. What is left behind is the reflective subsurface amplitude heterogeneity and noise. It provides a view of the zone-of-interest reflective energy that is no longer biased towards just the dominant frequency of the wavelet. In other words, the spectral balancing pro-cess allows every frequency band to be exposed to the same degree, although higher-frequency slices will tend to contain progressively more noise because the signal-to-noise ratio normally decreases with increasing frequency.

Downloaded 25 Jun 2012 to 95.28.162.50. Redistribution subject to SEG license or copyright; Terms of Use: http://segdl.org/

Interpretation Recommendations

(1) Don't limit the interpretation to one frequency band. Animate through a tuning cube after spectral balancing. Make sure to animate from the lowest frequency all the way through the usable frequency range. Geologic insight comes from the variations in amplitude from frequency to frequency (Figure 8-68). The first notch, marked in orange, is initially seen in the thickest part of the channel. This notch moves to thinner portions of the channel towards the outside with increasing frequency. Note all the channels visible on the horizon slice of Figure 8-69, and then note the different appearance of most of the channels on the frequency slices of Figures 8-70 and 8-71.

(2) Tuning out is just as important as tuning in. Don't limit the interpretation to features that are just tuning in (i.e., higher amplitude than the background). Subsurface features will tune in at certain frequencies and tune out at other frequencies. Examine the heterogeneity that is exposed in both the tuning-in and tuning-out cases.

(3) Consider red-green-blue blending of amplitude from different frequencies. Figure 8-72 combines three frequency slices, two of which are the slices shown in Figures 8-70 and 8-71. Although not as complete a picture of the zone-of-interest interference as a full tuning cube, RGB blending provides an image that is better than limiting the interpretation to a single band or to a single full-bandwidth attribute. Note, in Figure 8-72, that the centers of the channels are predominantly blue, indicating increased sedimentary thickness. Figures 8-73 and 8-74 both combine frequency slices from three frequencies in the same way and demonstrate a channel system at two different levels. Figure 8-75 combines three levels of the channel system for one frequency. The progression red to green to blue takes the observation from younger to older sediments and thus deeper into the valley fill.

(4) Interference is a first-order effect in seismic data. Attenuation does occur, but so does interference. Consider interference before jumping to the conclusion that a frequency anomaly is caused by attenuation. Consider, for example, a blocky, low-impedance, brine-filled reservoir layer embedded in a higher-impedance material. If we replace the brine with lower-impedance hydrocarbon, the time thickness and amplitude will both increase. For temporal thicknesses in the range shown in Figure 8-65 and frequencies less than 50 Hz, increasing the temporal thickness will cause a shift in the dominant frequency to a lower value. The higher-frequency content has not been attenuated, it is simply being tuned by the temporal thickness that is present.

(5) Strong amplitude events dominate the interference pattern. The spectral interference pattern is dominated by the strongest amplitude events in the analysis window, as demonstrated in Figure 8-76. If additional length does not include significant additional reflection energy, lengthening the analysis window will not change the overall interference pattern.

(6) Don't forget about the phase component. Transforming data from time to frequency domain produces both amplitude and phase spectra. The phase is very useful for imaging lateral discontinuities, both structural and stratigraphic, because phase instability exposes edges. Note the detailed information, especially the faults, in the frequency slice in phase shown in Figure 8-77.

(7) Tuning cube animations provide insight regarding stratigraphic and structural edges, as well as relative temporal thickness. Amplitude contours move from thicks toward thins as you proceed from low to high frequency. Subtle discontinuities and reflection heterogeneity are often best imaged at higher frequencies, as long as a reasonable signal-to-noise ratio exists at those higher frequencies.

(8) Low-frequency components often provide better imaging in poor data areas because the highest signal-to-noise ratio often exists at lower frequencies. Those lower-frequency slices are sometimes able to provide better images of the subsurface.

(9) Layer-stacking patterns exhibit characteristic spectral signatures. Changes in the reflective interfaces sampled by the analysis window show as changes in interference pattern. For the case of a single layer of reflective material in an analysis window, the period of the notching in the amplitude spectrum is inversely proportional to the temporal thickness of the layer. Changing the layering by shifting any one layer boundary within the layer stack alters the frequency domain interference profile in a characteristic manner.

Downloaded 25 Jun 2012 to 95.28.162.50. Redistribution subject to SEG license or copyright; Terms of Use: http://segdl.org/

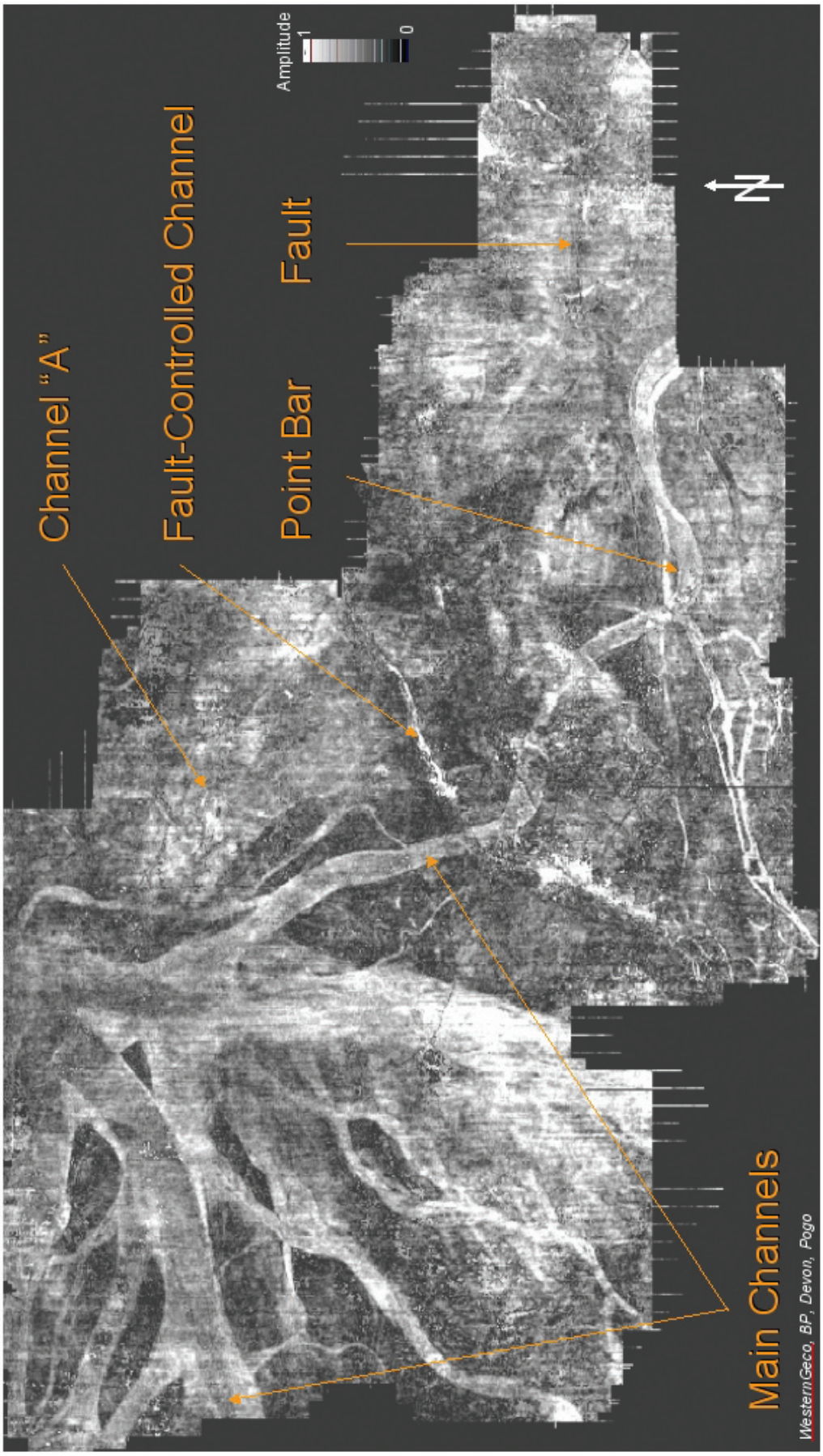

Fig. 8-69. Horizon slice showing full-bandwidth amplitude along a Pleistocene horizon from the Gulf of Mexico. From Partyka et al. (1999). Used by permission.

Downloaded 25 Jun 2012 to 95.28.162.50. Redistribution subject to SEG license or copyright; Terms of Use: http://segdl.org/

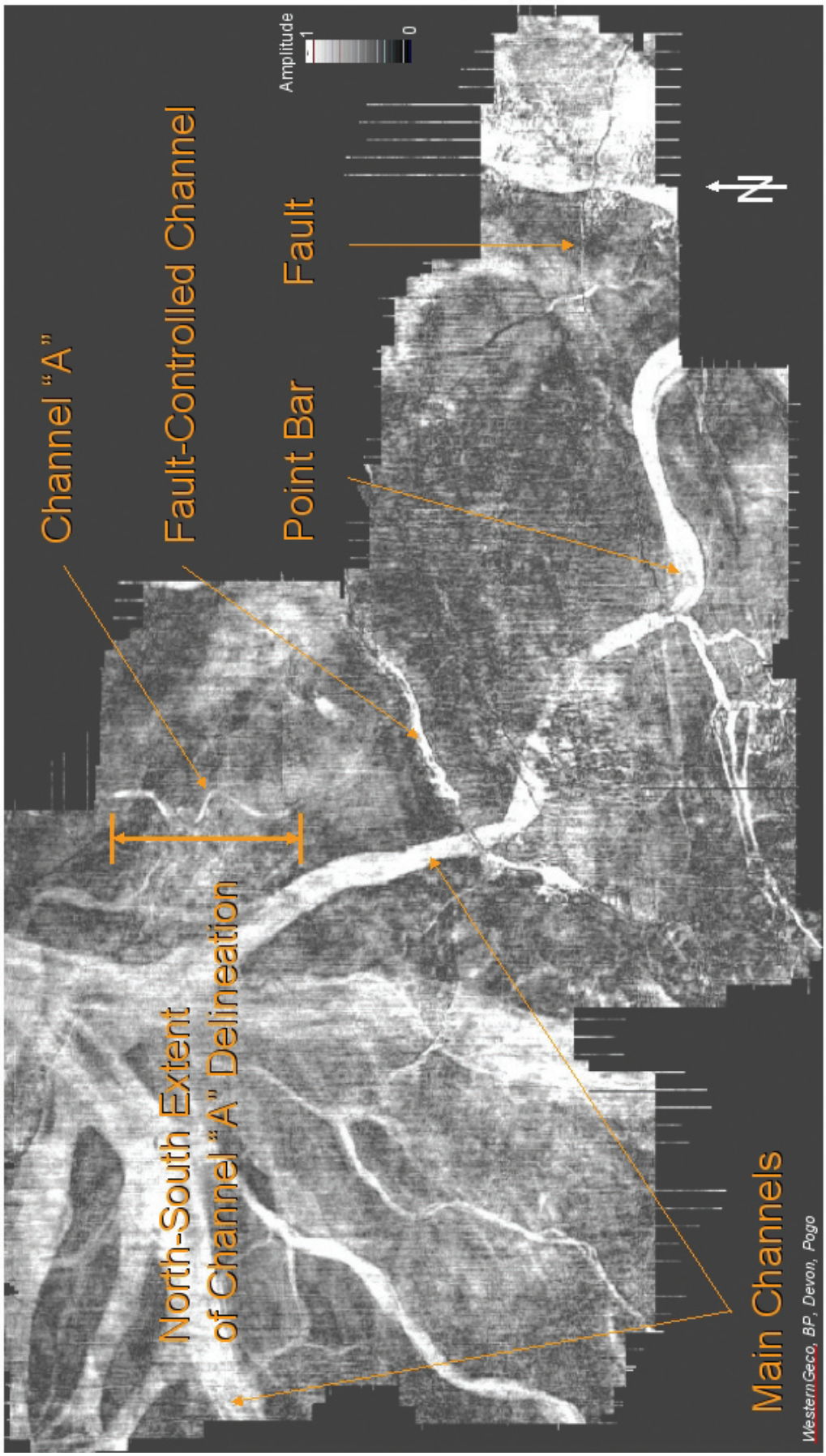

Fig. 8-70. Frequency slice showing amplitude in a narrow frequency band around 16 Hz, using the same horizon as Figure 8-69. From Partyka et al. (1999). Used by permission.

Downloaded 25 Jun 2012 to 95.28.162.50. Redistribution subject to SEG license or copyright; Terms of Use: http://segdl.org/

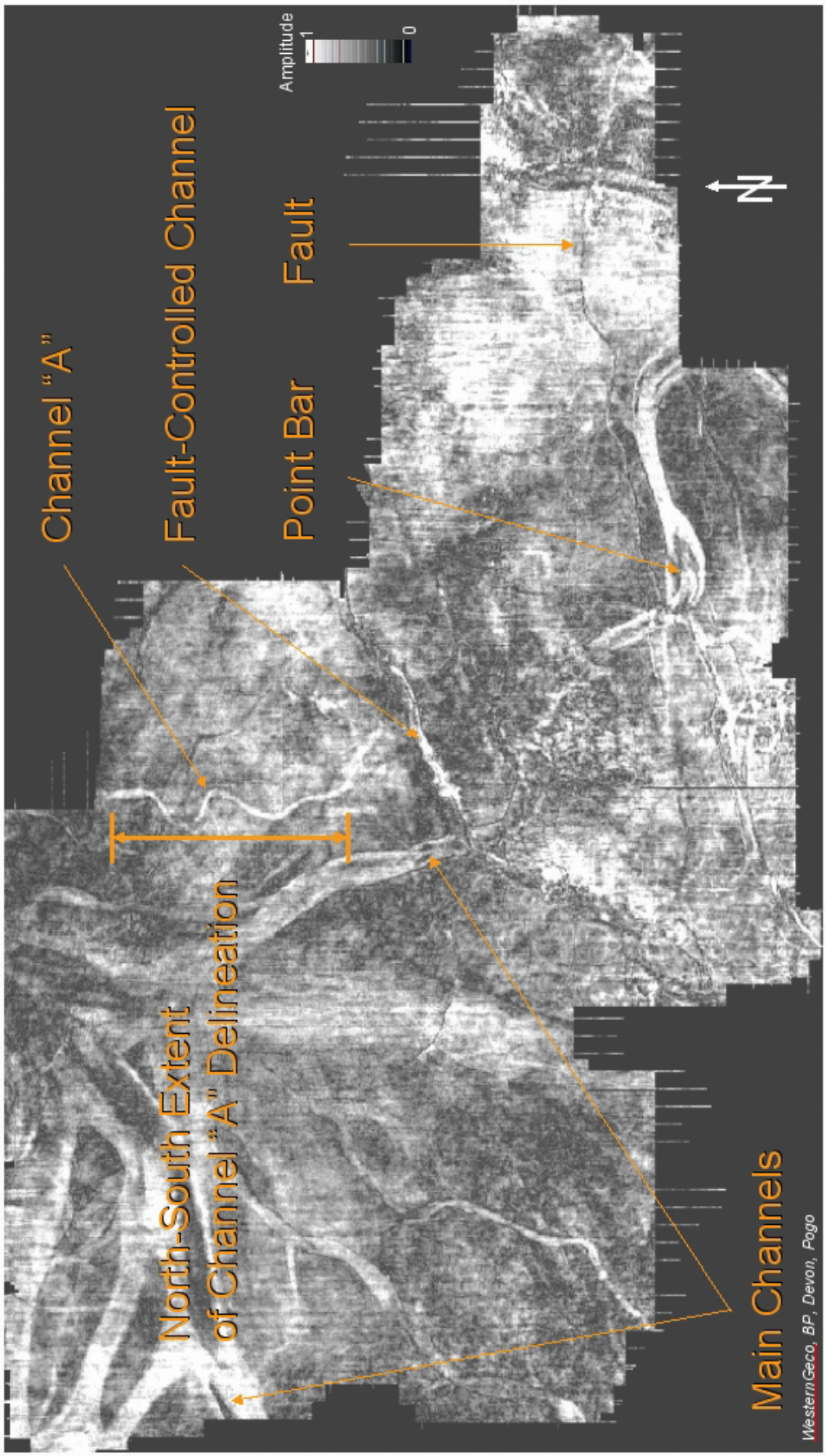

Fig. 8-71. Frequency slice showing amplitude in a narrow frequency band around 26 Hz, using the same horizon as Figure 8-69. From Partyka et al. (1999). Used by permission.

Downloaded 25 Jun 2012 to 95.28.162.50. Redistribution subject to SEG license or copyright; Terms of Use: http://segdl.org/

Fig. 8-72. Frequency slice showing amplitude in narrow frequency bands around 36 Hz as red, 26 Hz as green, and 16 Hz as blue, using the same horizon as Figure 8-69. Such Red-Green-Blue (RGB) blending provides a way to simultaneously view three frequency components. From Partyka (2005). Used by permission.

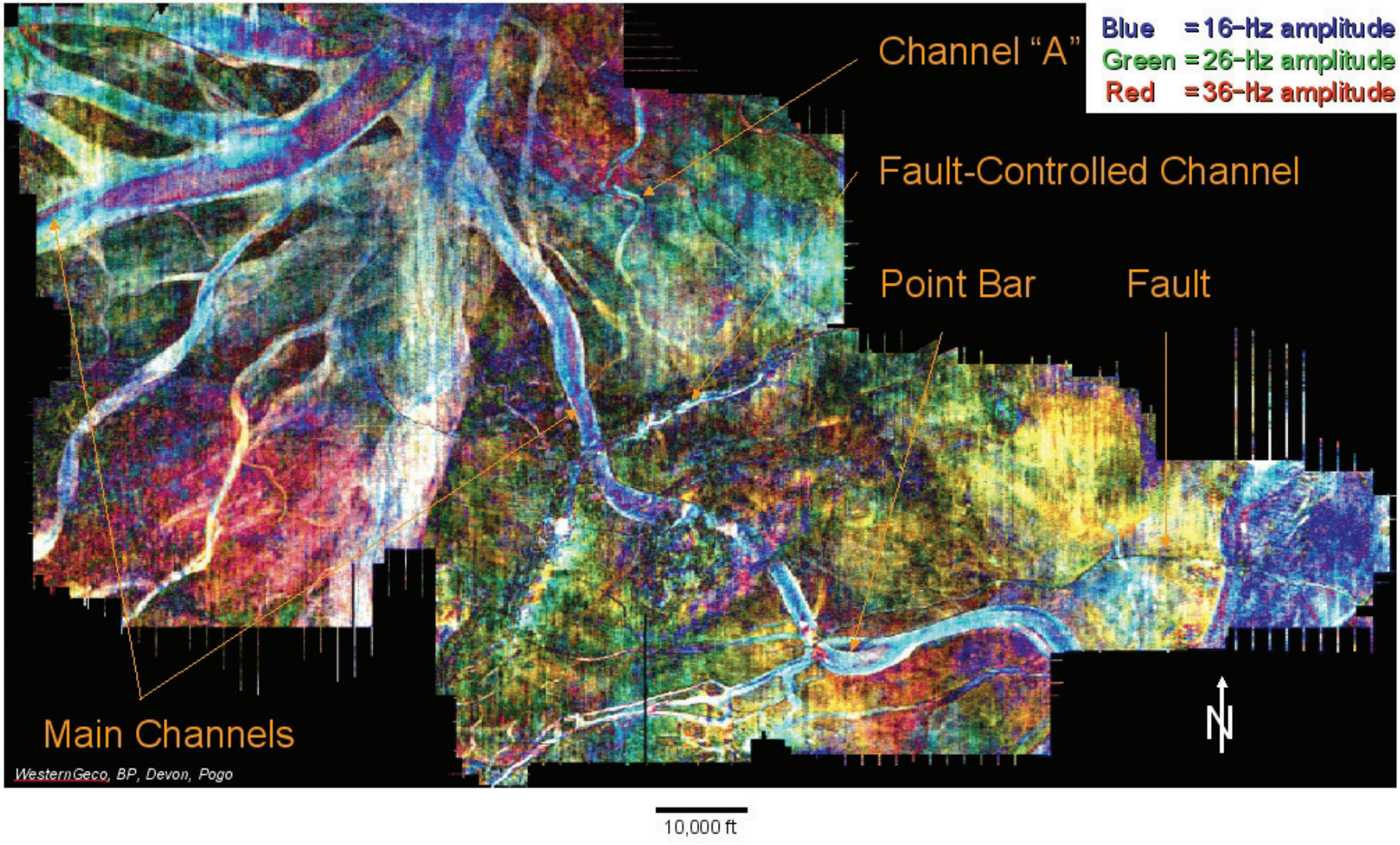

Downloaded 25 Jun 2012 to 95.28.162.50. Redistribution subject to SEG license or copyright; Terms of Use: http://segdl.org/

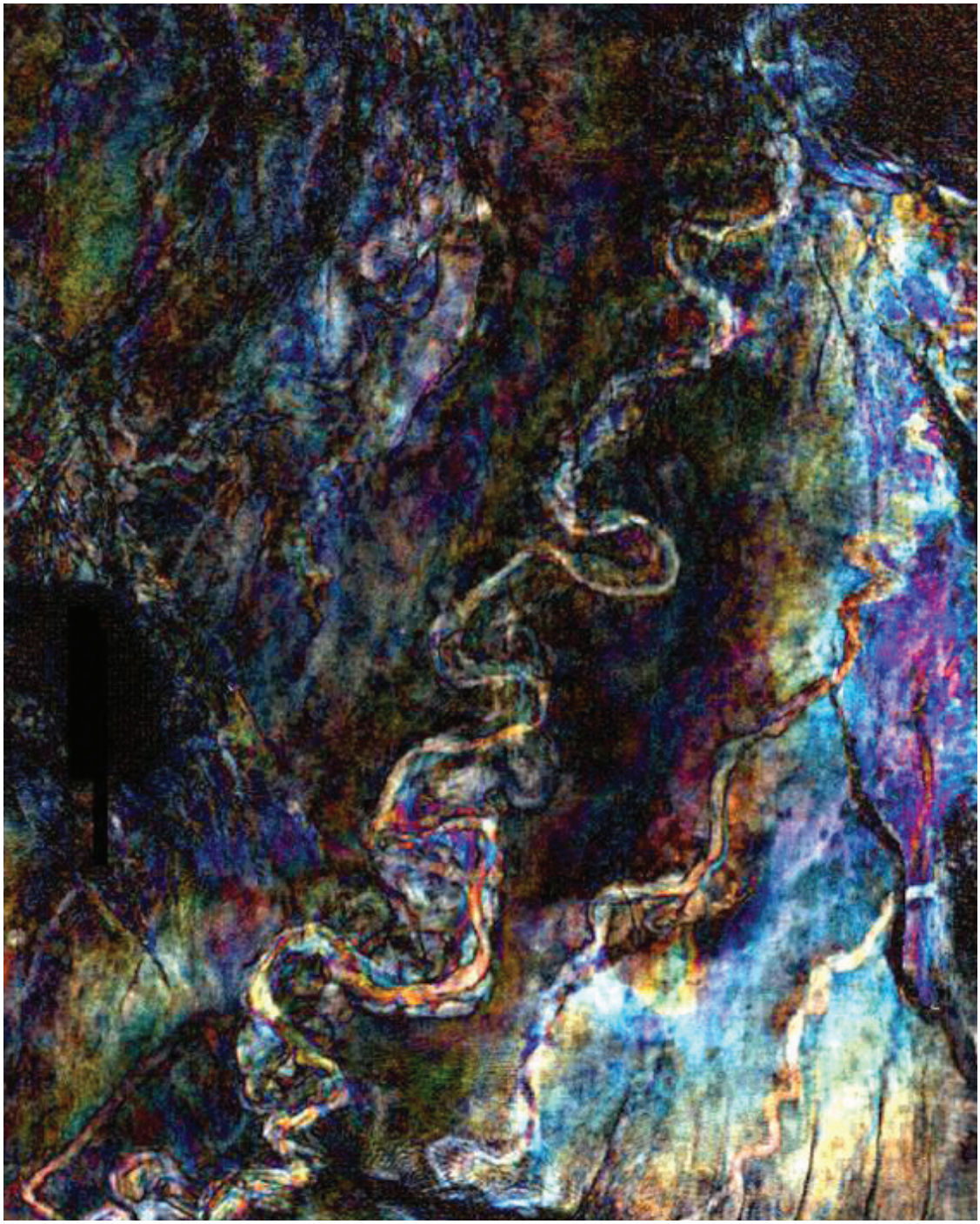

Fig. 8-73. Frequency slice from offshore Africa showing amplitude in narrow frequency bands around 60 Hz as red, 50 Hz as green, and 40 Hz as blue, at 80 ms above a picked horizon. From Partyka (2005). Used by permission.

Resolution Benefits of Spectral Decomposition

Traditional approaches to seismic resolution (separability and visibility) relate resolution limits to the seismic wavelet shape and its associated tuning frequency and tuning thickness (Chapters 1 and 6). With spectral decomposition the wavelet shape is removed during the spectral balancing step. Resolution is then no longer controlled by the wavelet. It is instead dependent on the available signal bandwidth (higher frequencies give increased resolution), signal-to-noise at each frequency (higher signal-to-noise ratio yields better imaging), complexity and gross thickness of the target (simpler layer-stacking patterns require less bandwidth to be detected), and the strength of the impedance contrasts (the higher the contrast, the stronger the reflected energy, and the higher the signal-to-noise).

Downloaded 25 Jun 2012 to 95.28.162.50. Redistribution subject to SEG license or copyright; Terms of Use: http://segdl.org/

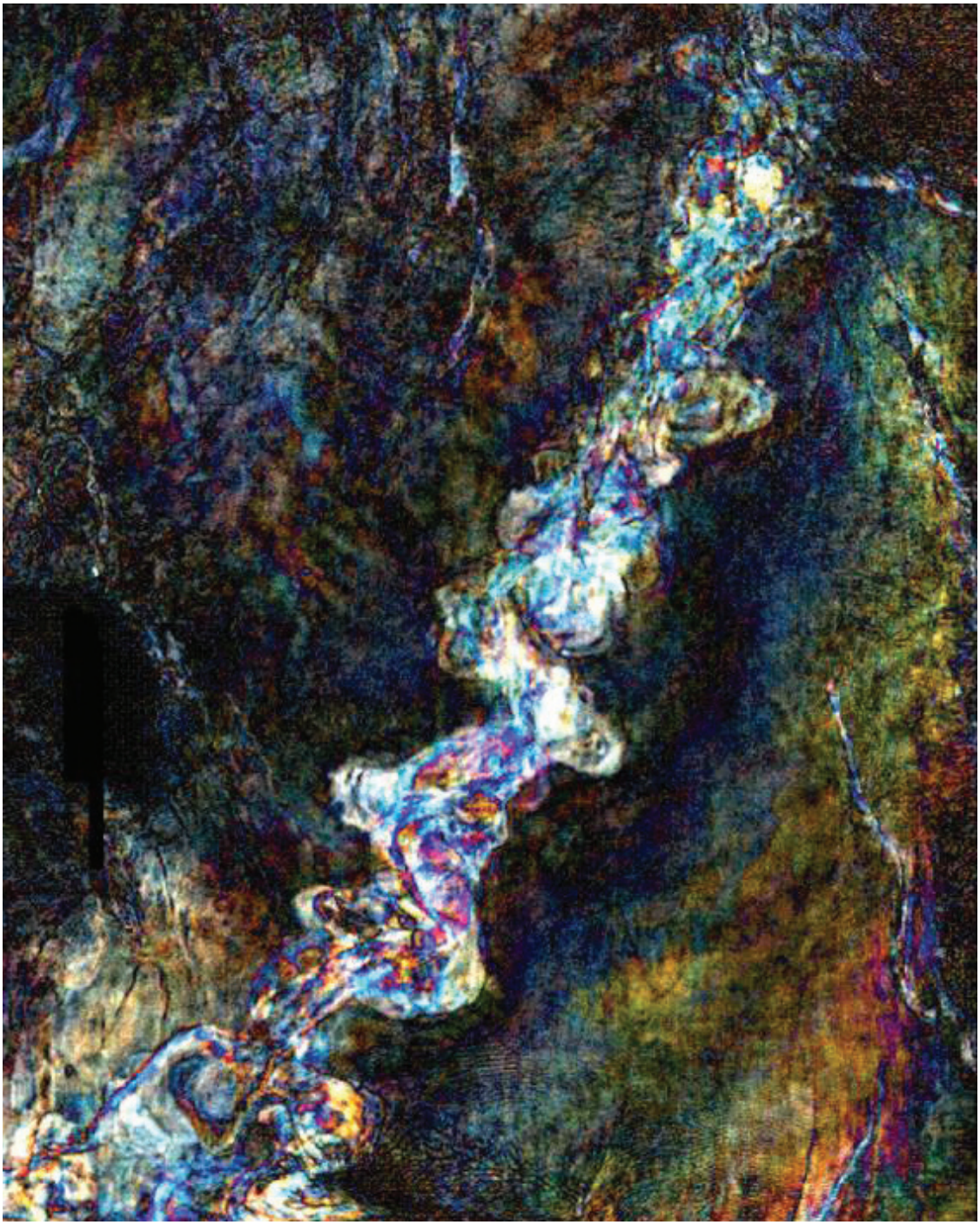

Fig. 8-74. Frequency slice showing amplitude in narrow frequency bands around 60 Hz as red, 50 Hz as green, and 40 Hz as blue, from 40 ms deeper than the level shown in Figure 8-73. From Partyka (2005). Used by permission.

Acknowledgments

We thank the SEG and the SEG Distinguished Lecture Program for permission to include material from the SEG Distinguished Lecture on Spectral Decomposition; BP for their permission to publish this material as part of the 2005 SEG Distinguished Lecture; teams at BP and Amoco for collaboration and support that led to the development of Spectral Decomposition; Chuck Webb and Craig Cooper for recognizing the value of this technology early and for providing the positive feedback and support that enabled its development, and OpenGeoSolutions Inc. for providing a framework for continued research and development of spectral decomposition and related technology.

Downloaded 25 Jun 2012 to 95.28.162.50. Redistribution subject to SEG license or copyright; Terms of Use: http://segdl.org/

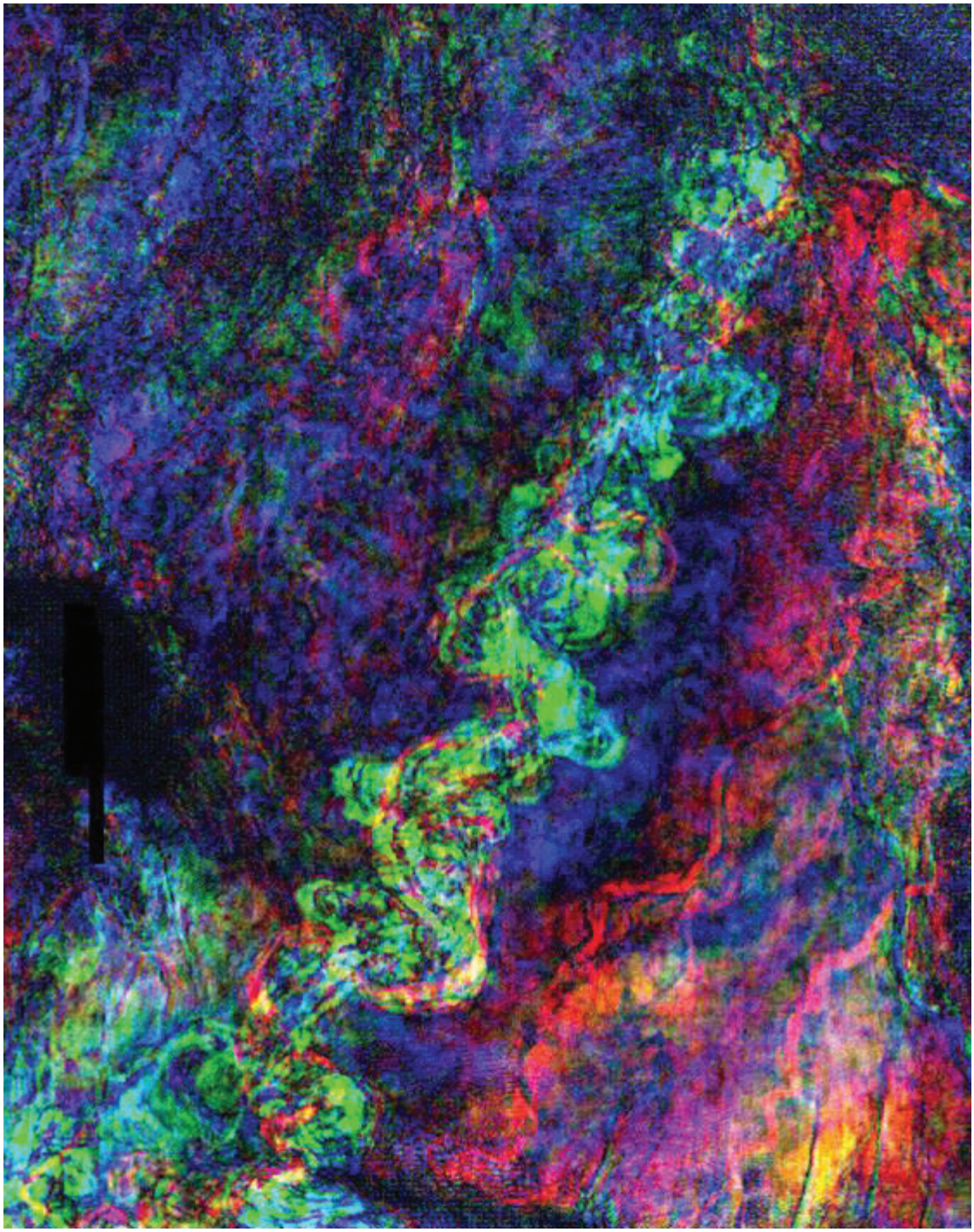

Fig. 8-75. Frequency slice showing amplitude in a narrow frequency band around 60 Hz at 80 ms above the picked horizon as red, at 40 ms above the picked horizon as green, and at picked horizon as blue. In this case, red, green, and blue allow you to look progressively deeper into the valley fill. From Partyka (2005). Used by permission.

References

Addy, S. K., 1998, Neural network classification method helps seismic interval interpretation: Oil & Gas Journal, v. 96, no. 37, p. 47–59.

Bahorich, M., and S. Farmer, 1995, 3-D seismic discontinuity for faults and stratigraphic features — the coherence cube: The Leading Edge, v.14, p. 1053–1058.

Bahorich, M., J. Lopez, N. Haskell, S. Nissen, and A. Poole, 1995, Stratigraphic and structural interpretation with 3-D coherence: SEG 65th Annual Meeting expanded abstracts, p. 97–99.

Barnes, A. E., 1998, The complex seismic trace made simple: The Leading Edge, v. 17, p. 473–476.

Downloaded 25 Jun 2012 to 95.28.162.50. Redistribution subject to SEG license or copyright; Terms of Use: http://segdl.org/

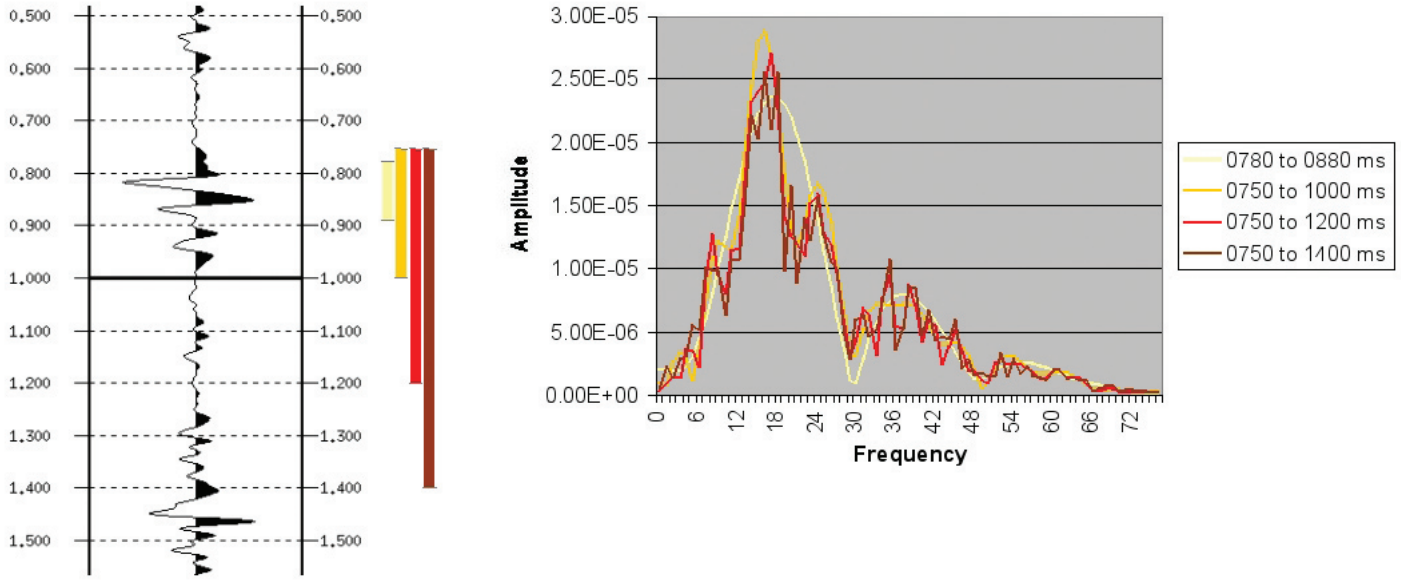

Fig. 8-76. Strong amplitude events dominate the spectrum. Whether we use a shorter analysis window or longer analysis window, the strong reflection dominates the interference pattern. From Partyka (2005). Used by permission.

Bouvier, J. D., C. H. Kaars-Sijpesteijn, D. F. Kluesner, C. C. Onyejekwe, and R. C. van der Pal, 1989, Three-dimensional seismic interpretation and fault sealing investigations, Nun River Field, Nigeria: AAPG Bulletin, v. 73, p. 1397–1414.

Castagna, J. P., and M. M. Backus, 1993, Offset-dependent reflectivity — theory and practice of AVO analysis: SEG Investigations in Geophysics no. 8.

Chen, Q., and S. Sidney, 1997, Seismic attribute technology for reservoir forecasting and monitoring: The Leading Edge, v. 16, p. 445–456.

Chopra, S., and K. J. Marfurt, 2007, Seismic attributes for prospect identification and reservoir characterization: SEG Geophysical Developments, No. 11, 464 p.

Dalley, R. M., E. C. A. Gevers, G. M. Stampfli, D. J. Davies, C. N. Gastaldi, P. A. Ruijtenberg, and G. J. O. Vermeer, 1989, Dip and azimuth displays for 3-D seismic interpretation: First Break, v. 7, no. 3, p. 86–95.

Denham, J. I., and H. R. Nelson, Jr., 1986, Map displays from an interactive interpretation: Geophysics, v. 51, p. 1999–2006.

Hart, B. S., and R. S. Balch, 1999, Approaches to defining reservoir physical properties from 3-D seismic attributes with limited well control: an example from the Jurassic Smackover Formation, Alabama: Geophysics.

Hart, B. S., 2002, Validating seismic attribute studies — beyond statistics: The Leading Edge, v. 21, p. 1016–1021.

Haskell, N., S. Nissen, M. Hughes, J. Grindhaug, S. Dhanani, R. Heath, J. Kantorowicz, L. Antrim, M. Cubanski, R. Nataraj, M. Schilly, and S. Wigger, 1999, Delineation of geologic drilling hazards using 3-D seismic attributes: The Leading Edge, v. 18, p. 373–382.

Hesthammer, J., 1998, Evaluation of the timedip, correlation and coherence maps for structural interpretation of seismic data: First Break, v. 16, p. 151–167.

Hesthammer, J., 1999, Improving seismic data for detailed structural interpretation: The Leading Edge, v. 18, p. 226–247.

Hirsche, K., S. Boerner, C. Kalkomey, and C. Gastaldi, 1998, Avoiding pitfalls in geostatistical reservoir characterization: a survival guide: The Leading Edge, v. 17, p. 493–504.

Hirsche, K., J. Porter-Hirsche, L. Mewhort, and R. Davis, 1997, The use and abuse of geostatistics: The Leading Edge, v. 16, p. 253–260.

Hoetz, H. L. J. G., and D. G. Watters, 1992, Seismic horizon attribute mapping for the Annerveen Gasfield, The Netherlands: First Break, v. 10, no. 2, p. 41–51.

Downloaded 25 Jun 2012 to 95.28.162.50. Redistribution subject to SEG license or copyright; Terms of Use: http://segdl.org/

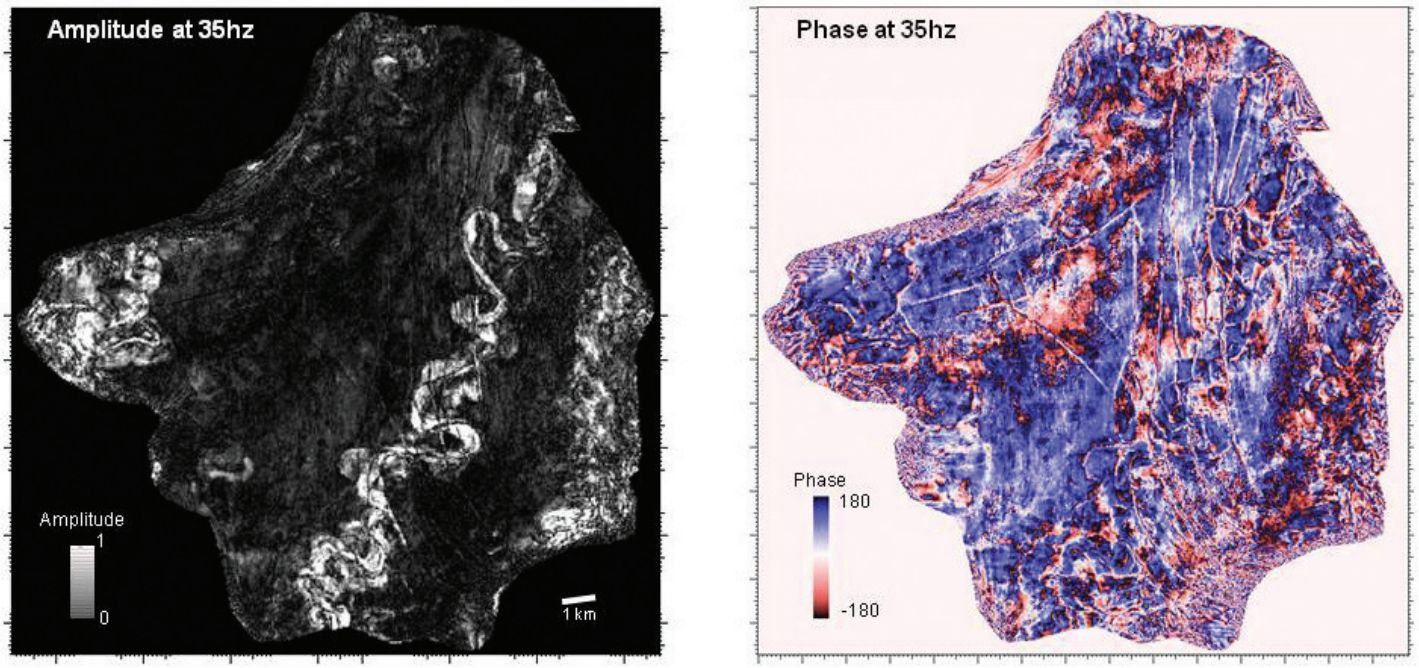

Fig. 8-77. Frequency slice showing amplitude on the left and phase on the right, in a narrow frequency band around 35 Hz along a picked horizon. Phase is particularly useful for imaging lateral discontinuities — both structural and stratigraphic. From Partyka (2005). Used by permission.

Horkowitz, K. O., and D. R. Davis, 1996, Seismic delineation of thin sandstone reservoirs in a shale-rich sequence using instantaneous frequency and reflection amplitude attributes from 3-D data, Texas Gulf Coast, *in* P. Weimer and T. L. Davis, eds., AAPG Studies in Geology No. 42 and SEG Geophysical Developments Series No. 5, AAPG/SEG, Tulsa, p. 35–44.

Kalkomey, C. T., 1997, Potential risks when using seismic attributes as predictors of reservoir properties: The Leading Edge, v. 16, p. 247–251.

Marfurt, K. J., R. L. Kirlin, S. L. Farmer, and M. S. Bahorich, 1998, 3-D seismic attributes using a semblance-based coherency algorithm: Geophysics, v. 63, p. 1150–1165.

Oldham, A. C., and N. M. Gibbins, 1995, Lake Hope 3-D — a case study: Exploration Geophysics, v. 26, p. 383–394.

Partyka, G. A., 2005, SEG Distinguished Lecture, http://eseg.org/staticcontent/presentations/partyka. Accessed September 15, 2009.

Partyka, G., J. Gridley, and J. Lopez, 1999, Interpretational applications of spectral decomposition in reservoir characterization: The Leading Edge, v. 18, p. 353–360.

Rijks, E. J. H., and J. C. E. M. Jauffred, 1991, Attribute extraction: An important application in any detailed 3-D interpretation study: The Leading Edge, v. 10, no. 9, p. 11–19.

Schuelke, J. S., and J. A. Quirein, 1998, Validation: a technique for selecting seismic attributes and verifying results: SEG Annual Meeting Expanded Abstracts, p. 936–939.

Taner, M. T., F. Koehler, and R. E. Sheriff, 1979, Complex seismic trace analysis: Geophysics, v. 44, p. 1041–1063.

Van de Sande, J. M. M., 1996, Prediction of reservoir parameters from 3-D seismic data for the Zechstein 2 carbonate play in the northeast Netherlands, *in* P. Weimer and T. L. Davis, eds., AAPG Studies in Geology No. 42 and SEG Geophysical Developments Series No. 5, AAPG/SEG, Tulsa, p. 197–204.

Downloaded 25 Jun 2012 to 95.28.162.50. Redistribution subject to SEG license or copyright; Terms of Use: http://segdl.org/

Inversion and Interpretation of Impedance Data

Contributed by Rebecca B. Latimer, Chevron U.S.A.

Introduction

Since the early to mid-1980s, inversion has been in discussion. Inversion is defined by Sheriff in his dictionary of geophysics terms as "Deriving from field data a model to describe the subsurface that is consistent with the data"(Sheriff, 2002, p. 194). My first exposure was at Amoco when I heard this topic discussed by Roy Lindseth. An excellent history of the topic is given in Lindseth (1979). The term *inversion* has always seemed to mean different things to different people. It also seemed to evoke very strong comments based on individuals' experiences on the topic. I was recently told that a "constrained sparse-spike inversion algorithm" was simply nothing more than a phase rotation of the seismic. When I mentioned the parameters that went into this type of algorithm, the individual did not want to discuss it because it did not support his argument against utilizing the process. I am forever amazed at how much confusion there still is and at how people can be so completely confused in their very definitive statements.

In 2000, I wrote an article in the Society of Exploration Geophysicists' *The Leading Edge* in an effort to present a guide to the interpreters who use inverted data (Latimer et al., 2000). A lot has happened since 2000, and it is time to update the interpreter community with added details and further explanations, which are featured in this chapter. I will expand the discussion from simply post-stack seismic-trace inversion to include pre-stack data and geostatistical inversion. I will provide a description of terminology and again a basis for comparison and usage of acoustic-impedance inversion products, and I will give the interpreter a methodology for quality control and interpretation of inverted data.

I still contend, as I did in 2000, that the first and foremost prerequisite in doing any type of inversion is to have the absolute best seismic processing completed prior to attempting an inversion. I will show, however, that a post-stack inverted data set may help you determine whether the data should be reprocessed, thereby indicating that it can sometimes also be used as a screening tool for further work.

The Nature of Impedance Data

Acoustic impedance (AI) is the product of rock density and *P*-wave velocity. This means that AI is a rock property and not an interface property (e.g., seismic reflection data). As I will illustrate, this distinction is the power of AI. Acoustic-impedance inversion is simply the transformation of seismic data into pseudo-acoustic-impedance logs at every trace. All information in the seismic data is retained. The wedge model

Downloaded 25 Jun 2012 to 95.28.162.50. Redistribution subject to SEG license or copyright; Terms of Use: http://segdl.org/

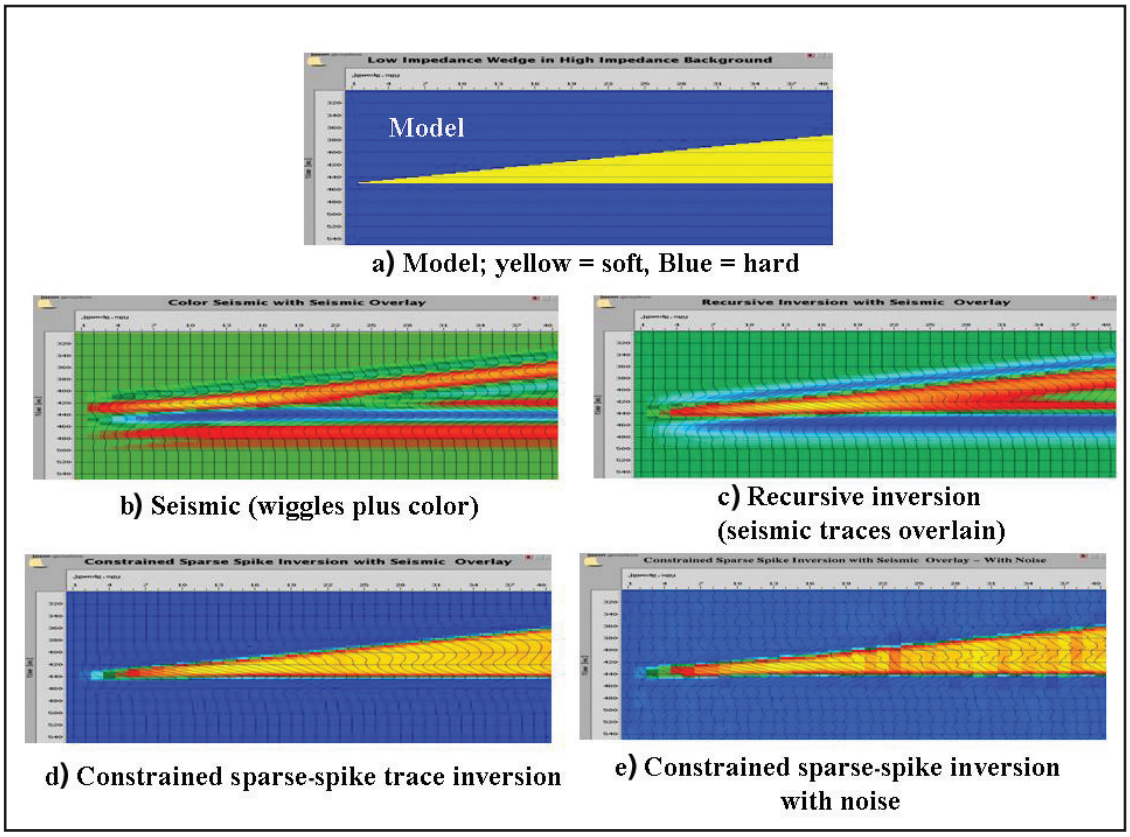
Low Impedance Wedge in High Impedance Background
Model
a) Model; yellow = soft, Blue = hard
Color Seismic with Seismic Overlay
b) Seismic (wiggles plus color)
Recursive Inversion with Seismic Overlay
c) Recursive inversion
(seismic traces overlain)
Constrained Sparse Spike Inversion with Seismic Overlay
d) Constrained sparse-spike trace inversion
Constrained Sparse Spike Inversion with Seismic Overlay – With Noise
e) Constrained sparse-spike inversion
with noise

Figure 9-1. Advantages of acoustic impedance over seismic data are illustrated in this figure. Structure is easy to derive from seismic data, but side lobes and tuning cause complications in interpretation. Using inverted data as the basis for stratigraphic interpretation can simplify interptetation of unconformities and condensed sections.

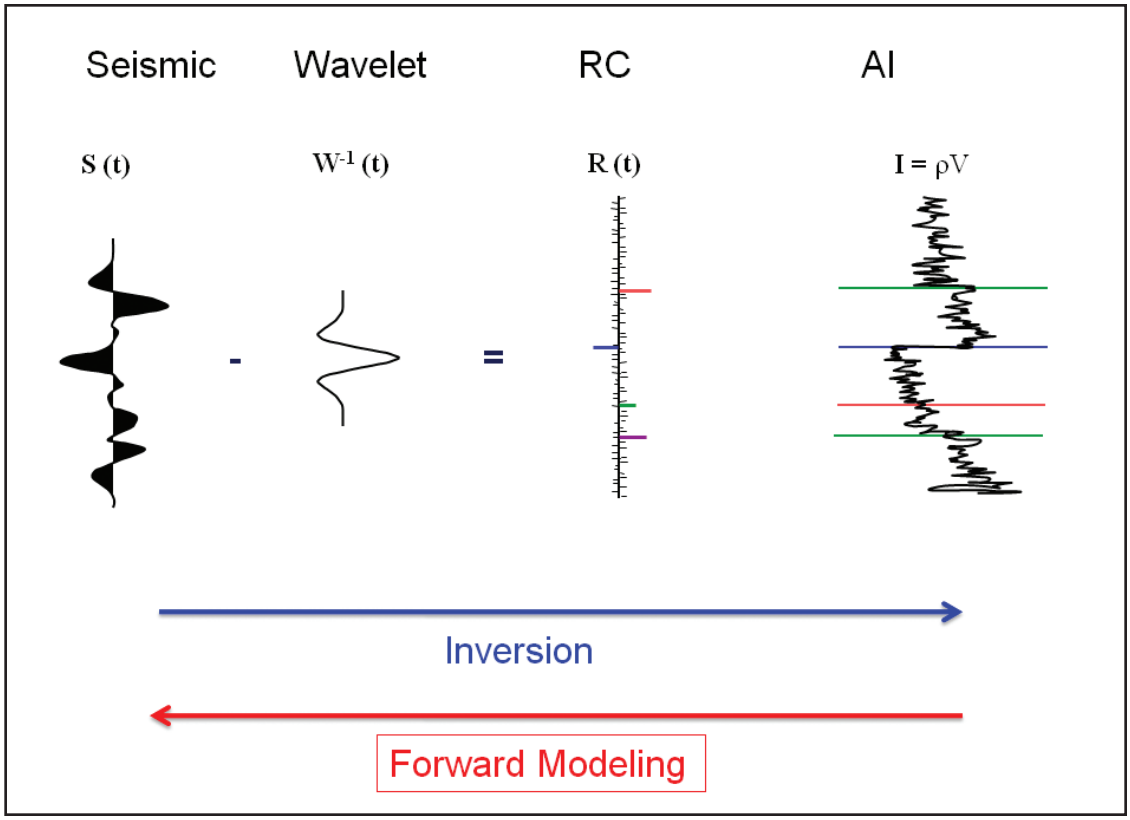

Figure 9-2. Schematic diagram graphically showing the process of inversion and forward modeling.

Downloaded 25 Jun 2012 to 95.28.162.50. Redistribution subject to SEG license or copyright; Terms of Use: http://segdl.org/

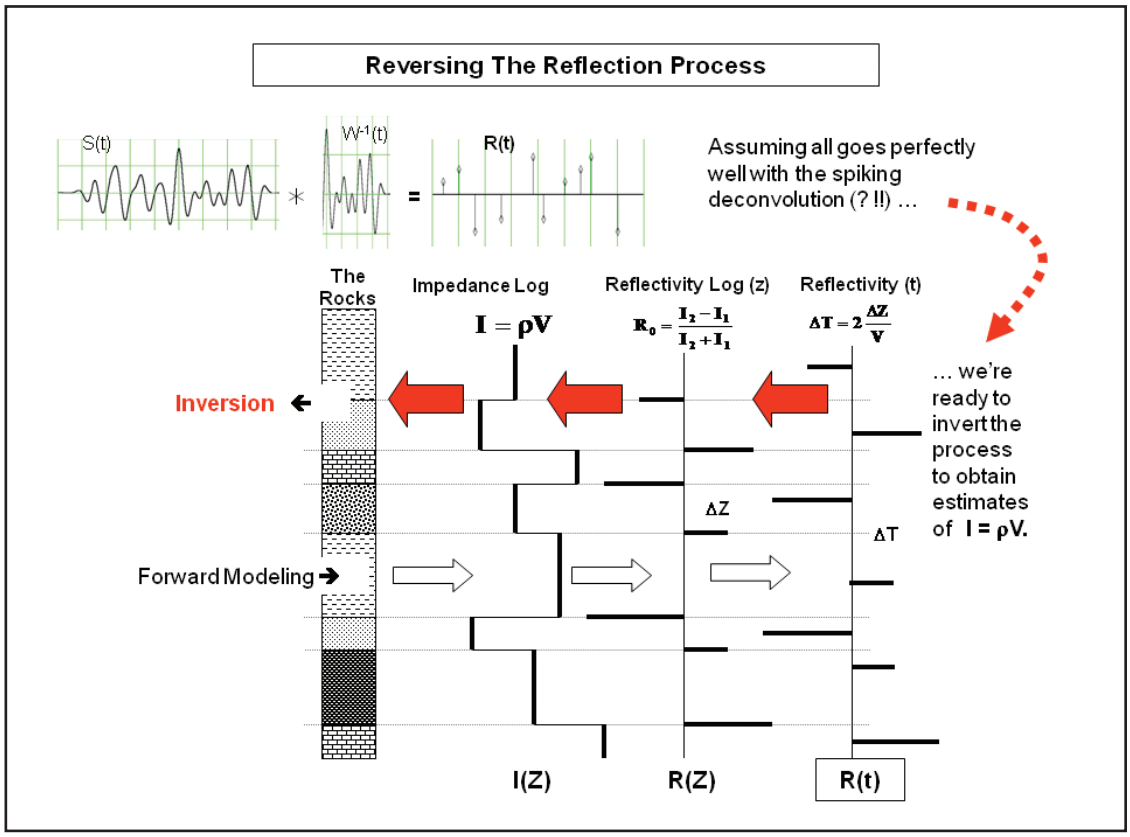

Figure 9-3. Graphic representation of trace inversion from the reflection series to the low-frequency earth model (Courtesy of Mike Graul.)

in Figure 9-1 is still a good starting point for discussion. Figure 9-1 shows an acoustic-impedance model and its representation with two imaging techniques. The model is simply a low-acoustic-impedance wedge embedded in a high-acoustic-impedance background (Figure 9-1a). Figure 9-1b shows zero-phase seismic representations of the model in standard color density, with wiggle traces overlain. Notice the tuning effects as the wedge thins, and note the side-lobe interference within the wedge itself. Figure 9-1c shows the results of a simple recursive inversion. Notice that this type of inversion does not help with tuning effects, and the side lobe effects are still present; however, the inversion has phase-rotated the data. Recursive inversion is available in many packages as a simple "push-button" inversion. This figure illustrates that not all inversions are the same. Refer to the section on "Methods of inverting seismic data" later in this chapter for details. Figure 9-1d shows the results of inverting the seismic data to AI by using a constrained sparse-spike inversion. Tuning is diminished, and the false internal geometry is eliminated. The resulting inverted wedge is a more accurate spatial representation of the original model and provides absolute AI values (shown in color) that match the original model. Figure 9-1e is the same as 9-1d, with noise introduced in the model prior to inversion. This figure is the simplest rendition of a post-stack trace inversion, computed from a constrained sparse-spike algorithm. It is meant to show the benefits of this very simple process.

A simple diagram showing what inversion means can be seen in Figures 9-2 and 9-3. In Figure 9-2, we see a seismic trace on the left where the correct wavelet is deconvolved to reveal a reflection series, RC. The seismic would yield only the bold black lines during the inversion, because of the band limitation. Therefore, inversion to rock properties yields only a low-frequency version of the rock data without the trend (increase in impedance with depth) because the low frequencies are not present in seismic data. In Figure 9-2, starting from the right, one could convolve the data with a wavelet to create a synthetic, thus doing a forward model. Figure 9-3 shows this in a different manner.

Downloaded 25 Jun 2012 to 95.28.162.50. Redistribution subject to SEG license or copyright; Terms of Use: http://segdl.org/

What are the benefits of this process? From where will we retrieve low-frequency information? Where can we obtain that information? When will the process fail? How do we determine whether the process will help in our area, without a costly inversion process? All of these questions and more will be answered in this chapter.

A compelling reason for inverting seismic data is illustrated in Figure 9-4. A synthetic seismic data set (colored seismic with wiggles overlain) is shown in panel b. The synthetic seismic is created from the acoustic-impedance model in panel d and the wavelet in panel a. The model contains three interfaces: 50 ms, 135 ms, and 230 ms. Note that each interface represents the same change in absolute AI units, but in varying gradational degrees. The seismic data identify the sharp interface at 50 ms. They identify the top of the second interface at 135 ms, but it is not apparent that the interface is a gradational coarsening-upward sequence because the seismic do not recognize the base of the event. The seismic fail to identify the most gradual interface at 230 ms. Compare the seismic response with that of the inverted traces in panel c. The inverted trace data can effectively model all these variations in rock properties because the inverted data utilize a complete frequency range of 0–80 Hz. Let us summarize some advantages of impedance data:

- A good-quality impedance inversion contains more information than seismic data do. It contains all the information that is present in the seismic data without the complicating factors caused by wavelets, as well as the essential information (generally low frequency) from the log data. The AI volume is a result of the integration of data from several different sources, typically seismic, well-log, and/or velocity data. The process involved in building an impedance model from an inverted data set is the most natural way to integrate data because it provides a medium understood by geologists, geophysicists, petrophysicists, and engineers.
- Acoustic impedance is a rock property. It is the product of density and velocity, both of which can be directly measured by well logging. Seismic data are an interface property, a close approximation to the convolution of a wavelet with a reflection-coefficient series, which reflects relative changes in acoustic impedance. AI is therefore the natural link between seismic data and well data.
- AI is closely related to lithology, porosity, pore fill, and other factors. It is common to find strong empirical relationships between acoustic impedance and one or more rock properties. AI models can provide the basis for generating 3-D facies models and 3-D petrophysical property models. Impedance volume results can be calibrated to reservoir properties and ported directly into reservoir simulators for flow analysis.
- AI is a layer property. Seismic amplitudes are attributes of layer boundaries. As a layer property, acoustic impedance can make sequence stratigraphic analysis more straightforward. Wavelet side lobes are attenuated, eliminating some false stratigraphiclike effects, as seen in Figures 9-1b and 9-1c.
- AI data can support fast and accurate volume-based interpretation techniques, allowing for rapid delineation of target bodies.
- The AI concept is readily generalized to handle the inversion of angle or offset stack data to elastic impedance or elastic parameters. Elastic impedance captures AVO information and, in conjunction with AI, improves interpretation power and the ability to discriminate lithology and fluids.

Quality Control of Seismic-Derived Inverted Data

The quality of the final inversion is a direct result of the quality of the input data. To objectively estimate the accuracy of an AI inversion cube, the interpreter must be familiar with the input data and with which algorithms were applied to process the data. A comprehensive processing report is a powerful source of information but, if one not available, some key items should be examined: type of acquisition, processing sequence, migration algorithm, filtering processes, etc. Obtaining a processing report or processing flow is more difficult today with 3D surveys. The post-stack data are

Downloaded 25 Jun 2012 to 95.28.162.50. Redistribution subject to SEG license or copyright; Terms of Use: http://segdl.org/

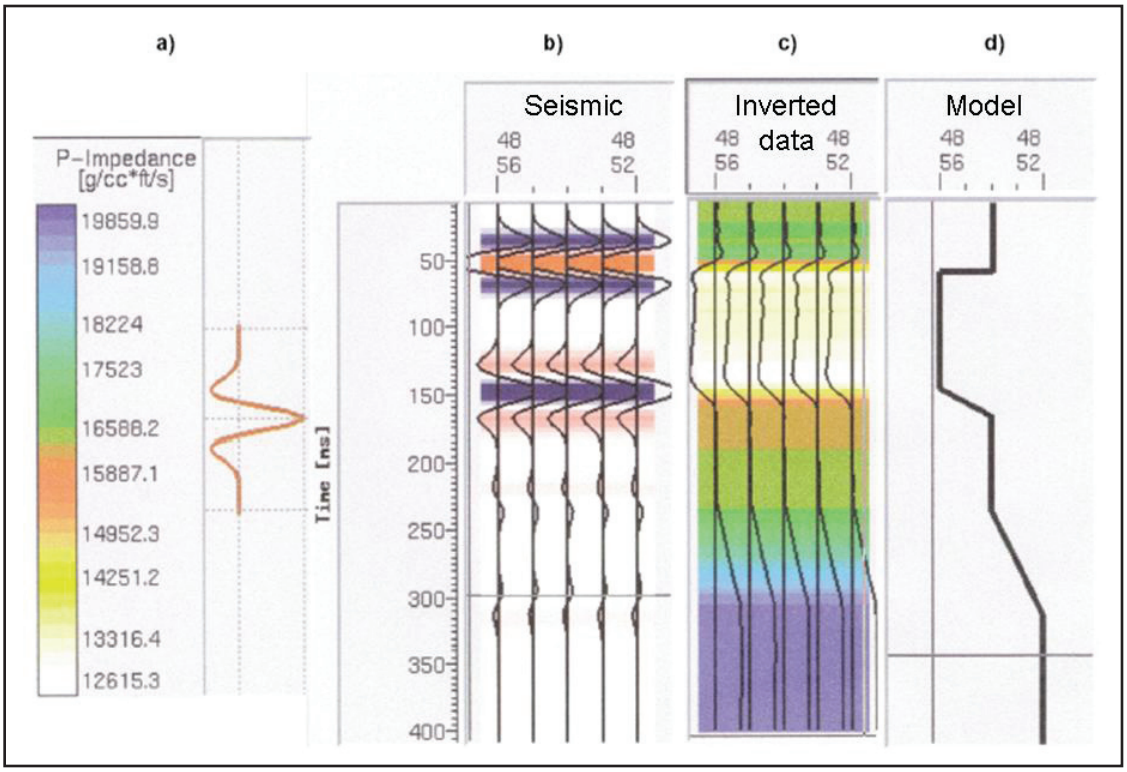

Figure 9-4. Impedance inversion data contain more information than seismic data because they have broader frequency content (low frequencies are replaced). There is a significant difference in the rock properties at 150 ms and 230 ms in the inverted panel, yet the differences are not clear from the synthetic seismic data because the low-frequency information is missing.

often collected and placed on a disk and the individual who is to create the inversion may have sketchy knowledge of the pre- and post-processing sequences. It is rare to find a description of the filtering in the file name or acquisition or processing parameters stored with the post-stack data. Once the inversion is complete, it is often more difficult for the interpreter to have any idea of the inversion process, let alone the seismic processing information.

If an interpreter gains access to a completed inversion volume, it is imperative, that he/she find out what went into the creation of the data — that he/she determine the inversion algorithm used to create the data, the date that the inversion was completed, and the workflow that was used. In order to quality control the inversion results, the interpreter should also collect all well data, well spud details, and log processing. Depending on the inversion method, the data types may include post-stack seismic data (full fold as well as angle stacks). The well-log data should include sonic, density, gamma-ray, water saturation, porosity, resistivity, and caliper data as a minimum. It is also a good idea to start with a set of preliminary time or depth horizons so that it can be cross checked with the time-to-depth data (check-shot data) in order to check the quality of the well tops with the marker surfaces.

Log Analysis, Editing, and Rock Properties

Prior to inversion, one should examine the well logs for suitable relationships between measured impedance logs (calculated by dividing the density by the sonic log) and other desirable properties, such as porosity and fluid fill. Well logs should be converted to time and filtered to the approximate bandwidth of the seismic to determine if zones of interest are recognizable at the frequencies expected after inversion. All well logs should be edited for borehole effects, balanced, and classified on the basis of quality. Logs that do not tie the seismic should be investigated for problems in log, wavelet, or seismic data.

Figure 9-5 shows a set of well logs. The logs on the panel are important for quality control in this area and will be discussed in relation to (1) pre-inversion analysis when considering the relationship between the rock properties in an area and the acoustic-

Downloaded 25 Jun 2012 to 95.28.162.50. Redistribution subject to SEG license or copyright; Terms of Use: http://segdl.org/

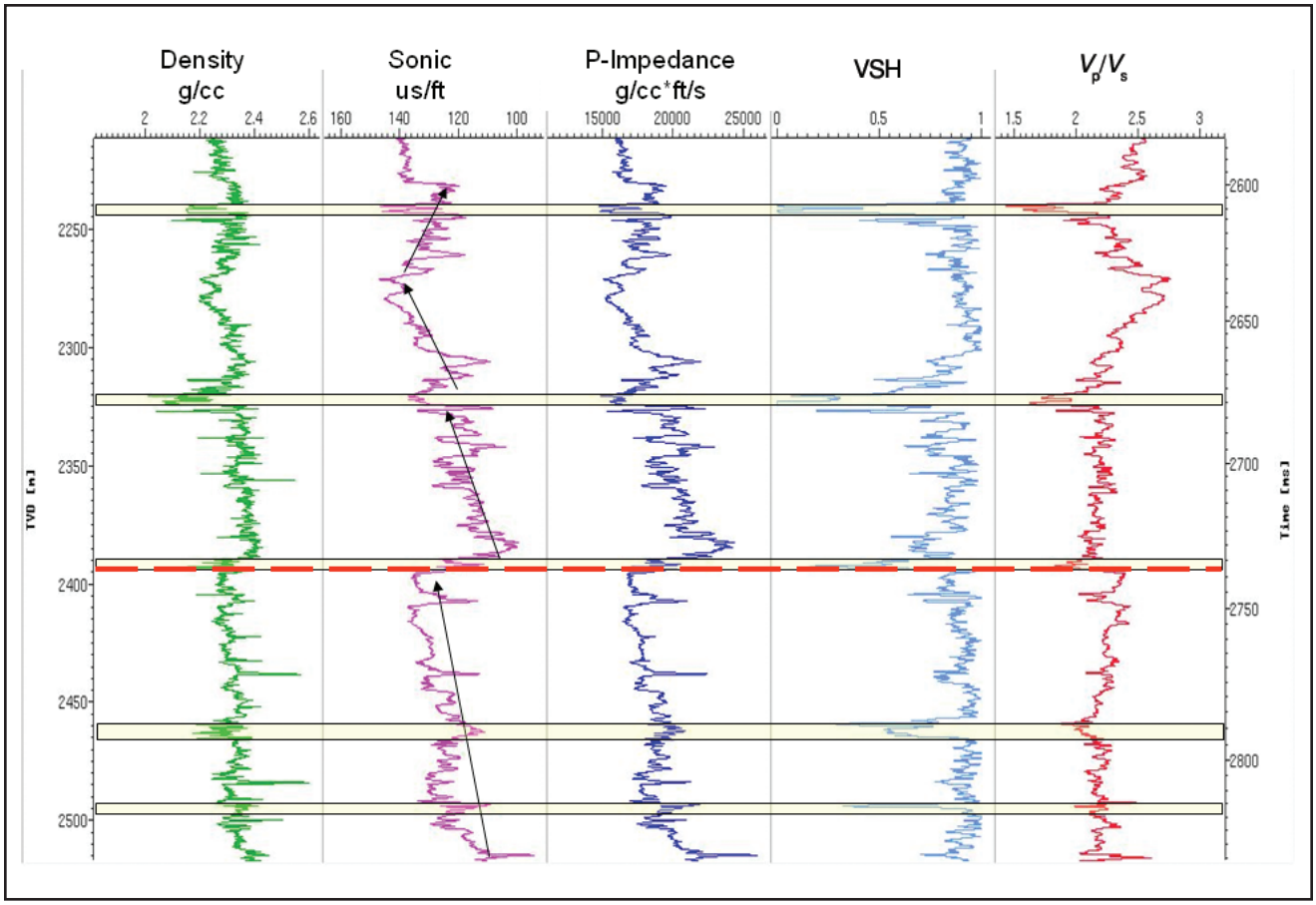

Figure 9-5. Panel showing a series of well logs used to assess the quality of the relationship between the impedance data and rock properties. Trends in the data are shown by the arrows. A large erosional unconformity is located at the red dashed line and sands are indicated by the light yellow boxes.

impedance data, (2) how the interpreter might use the data, and (3) whether further processing is necessary. Completing a pre-inversion analysis will prevent incorrect assumptions concerning the results the inversion may yield. This process should be completed in all areas being considered for an inversion, in order to determine what the inversion will yield from a rock property standpoint. The log data in Figure 9-5 show some interesting relationships. The sands, indicated by the yellow strips for low-volume shale (VSH), are thin and may be below seismic resolution. This will be tested. The data appear to be very different above and below the erosional unconformity (shown by the dashed red line). Above the unconformity, the sands have high sonic-log values (low velocity) and low values of density. Below the unconformity, the sands have low density but high velocity.

It is critical to understand the relationships between acoustic impedance and the other logs when analyzing the rock properties. It is also important to analyze the section above and below any major geologic change or unconformity separately in order to correctly understand the relationships between the impedance log data and other rock properties. The relationships may vary across the boundaries. A crossplot derived from the entire length of the log suite would lead you to believe that inverting the data for acoustic impedance will be fruitless. Many log and interpretation software packages do not allow the interpreter to select a time or depth range for analysis. Without doing so, the wrong conclusion can be derived. Shales and sands exist, in this data set, at all ranges of impedances.

In this particular area, we had shear sonic data and were able to calculate V_p/V_s log data. A comparison of P-impedance data, VSH, and V_p/V_s data can be seen in Figure 9-6. Note that sands (seen by the yellow and red dots) and shales (blue dots) are present for all ranges of P-impedance. However, with knowledge of our geology, we

Downloaded 25 Jun 2012 to 95.28.162.50. Redistribution subject to SEG license or copyright; Terms of Use: http://segdl.org/

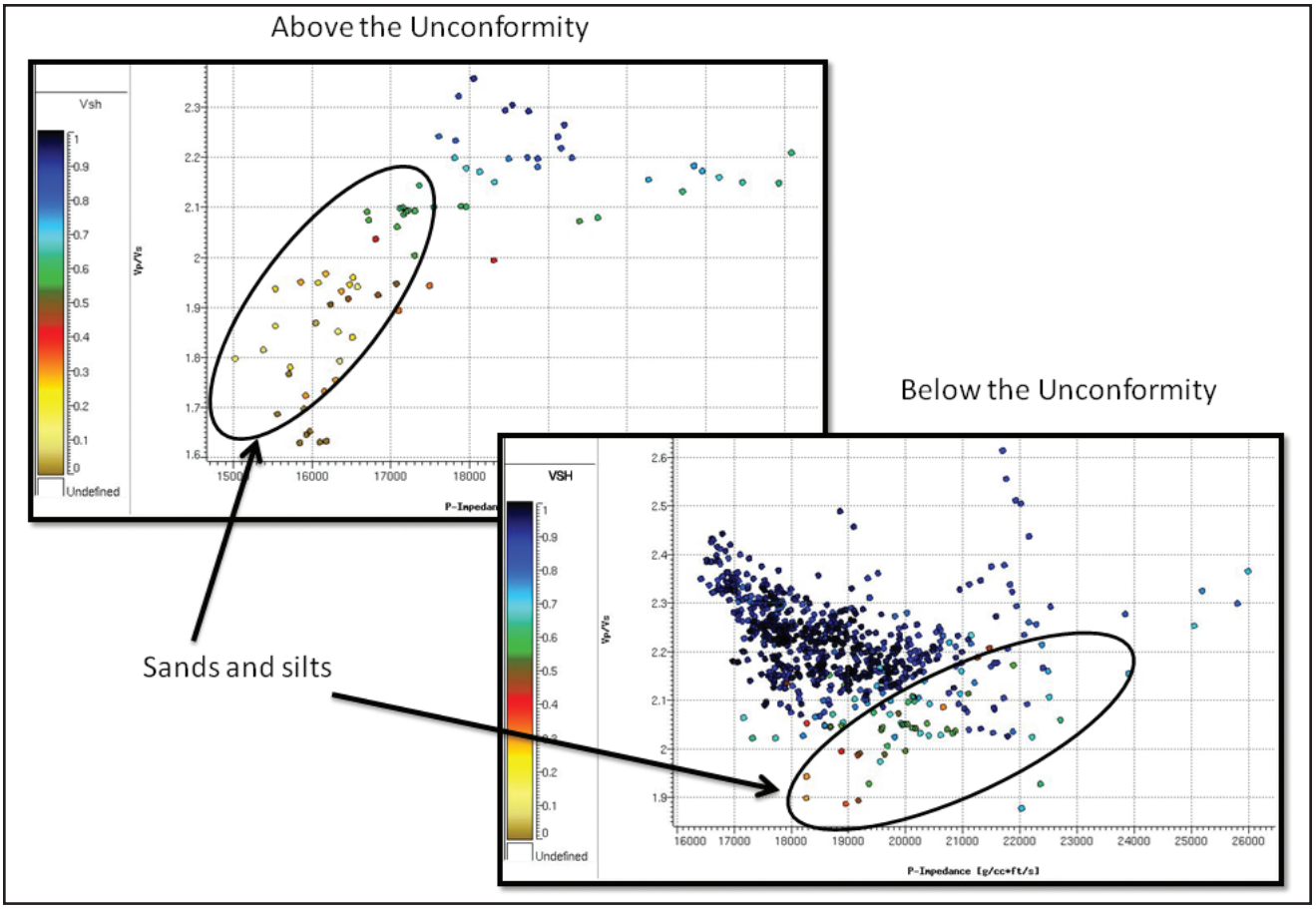

Figure 9-6. Crossplots showing the relationship between P-Impedance vs V_p/V_s with VSH color coded (yellows and golds indicate sands).

separate the analysis so that the crossplot analyzes the upper section and the lower section individually. Figure 9-6 shows the plots for the section above the unconformity (left) and below the unconformity (right). Above the unconformity, it is clear that the sands (in the oval) are of lower acoustic impedance than are the shales in blue. Therefore there is an assumption that it is possible to use an inverted data set to help locate the sands in this zone. This is a good start, but band-limitation issues must be examined before we make a definitive statement.

Below the unconformity, the issues are more difficult. The shales (in blue) are very soft when comparing them with the silts. The silts are very brittle and compacted. The silts are seen as having high or mid-range values on the crossplot. It is tempting to say that all of the silts could be identified by using a higher value of P-impedance cutoff. This assumption possibly would ignore a hydrocarbon-charged silt, because P-impedance is the product of velocity and density and P-impedance will decrease in value when charged by hydrocarbons. An area with rock properties such as this is the most difficult to analyze. Generally one can only hope to determine lithology, and that only when other attributes confirm the conclusion. This will be discussed later by an interpretation example.

All of the analyses above have been completed using log data with a full spectrum of frequencies. We now need to discuss the limitations of the data using seismic frequency ranges.

Band Limitation and Impedances

Seismic data are band limited, missing the highest and lowest frequency ranges. The band-limited nature of seismic data is often considered in terms of the high frequencies and the consequent lack of resolution. The lack of high frequencies is important and is the first item to check on log crossplots. Filtering the log data both on the

Downloaded 25 Jun 2012 to 95.28.162.50. Redistribution subject to SEG license or copyright; Terms of Use: http://segdl.org/

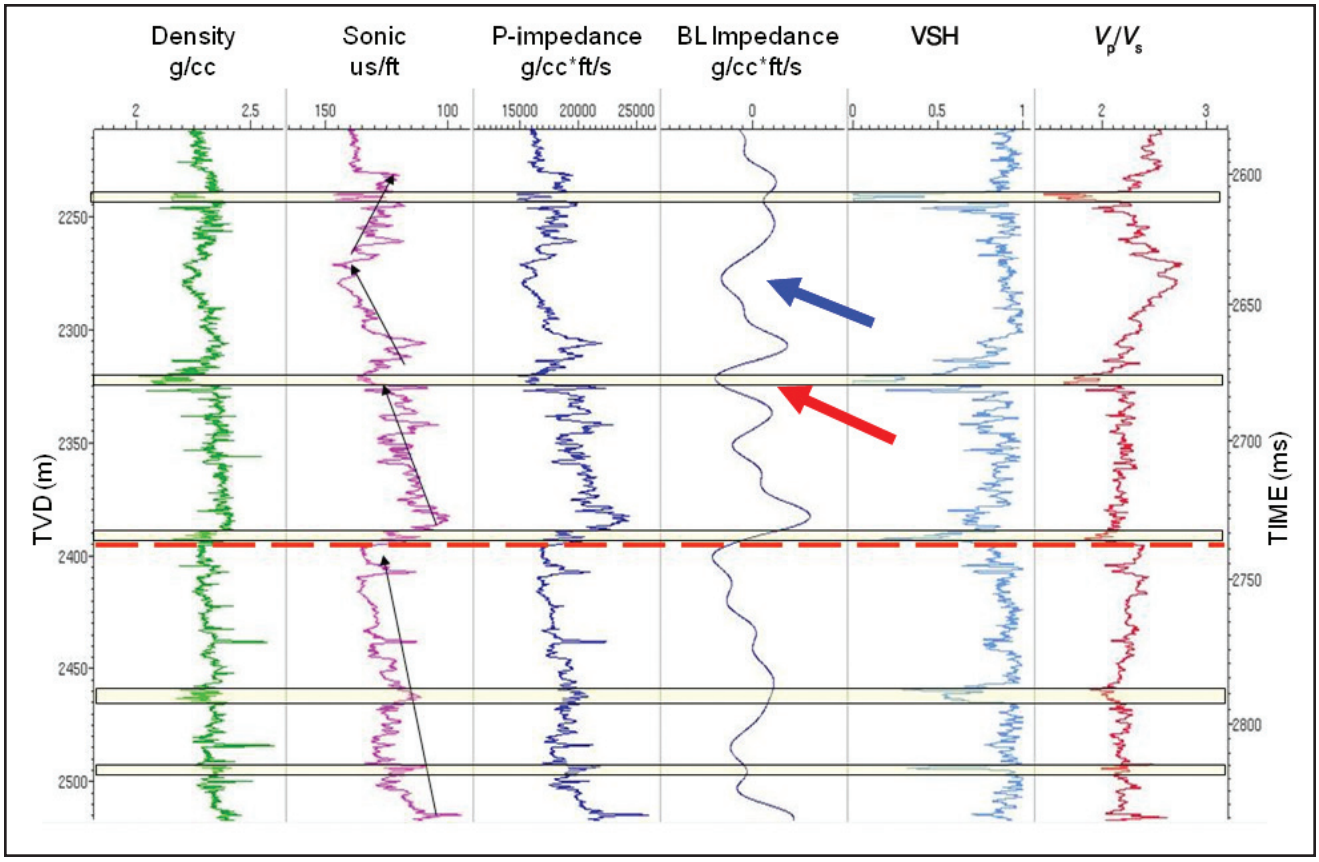

Figure 9-7. This figure is similar to Figure 9-5 except the fourth trace from the left has been added. It is a filtered version of the dark blue P-impedance log, both high and low cut. BL=band limited.

low and high end of the frequency range allows for the determination that the sands are or are not visible on the seismic data. Many factors can control whether sands at or near the limits of resolution are visible:

- Are thin sands clustered together, making them visible but mainly as thin stringers?
- Are the sands isolated in massive shale, making them visible?
- Are the sands very different from the shales (very porous sand in massive, tight shale)?
- What is the layer below the sand? Is it transitional or sharp?

In many of these cases, a very thin stringer, mathematically below resolution of the seismic data, may be visible on full-stack trace-inverted seismic data. In other cases, the sand is invisible due to the values of the surrounding shales. Figure 9-7 shows the data from Figure 9-5, but another trace called "band-limited impedance" has been added. This trace is simply the P-impedance log, high-cut and low-cut filtered, to include only data between 10 Hz and 60 Hz, similar to a range found in seismic data.

Notice on Figure 9-7 that the sand at 2320 m (red arrow) should be visible on the seismic data. The sand, although very thin, still causes the band-limited impedance data in column 4 to shift to the left. However, notice that an exact thickness of the sand and an exact value of impedance would not be possible. All the interpreter would know is that there is possibly a low-impedance sand or silt present in that section. Due to tuning, it would not be possible to determine whether the sand is hydrocarbon charged or not. Also look at the shale at 2275 m (blue arrow); it has almost the same value of band-limited impedance as the sand. Is this a log problem or a change in lithology? This should be investigated. The sand at 2240 m is also problematic. It is masked by a very high-density, high-velocity shale section. The resolution is too thin and the data appear as simply a wobble in the shale, yet it is just as thick as the sand at 2340 m. The sand at 2390 m is just above the unconformity and is being masked by

Downloaded 25 Jun 2012 to 95.28.162.50. Redistribution subject to SEG license or copyright; Terms of Use: http://segdl.org/

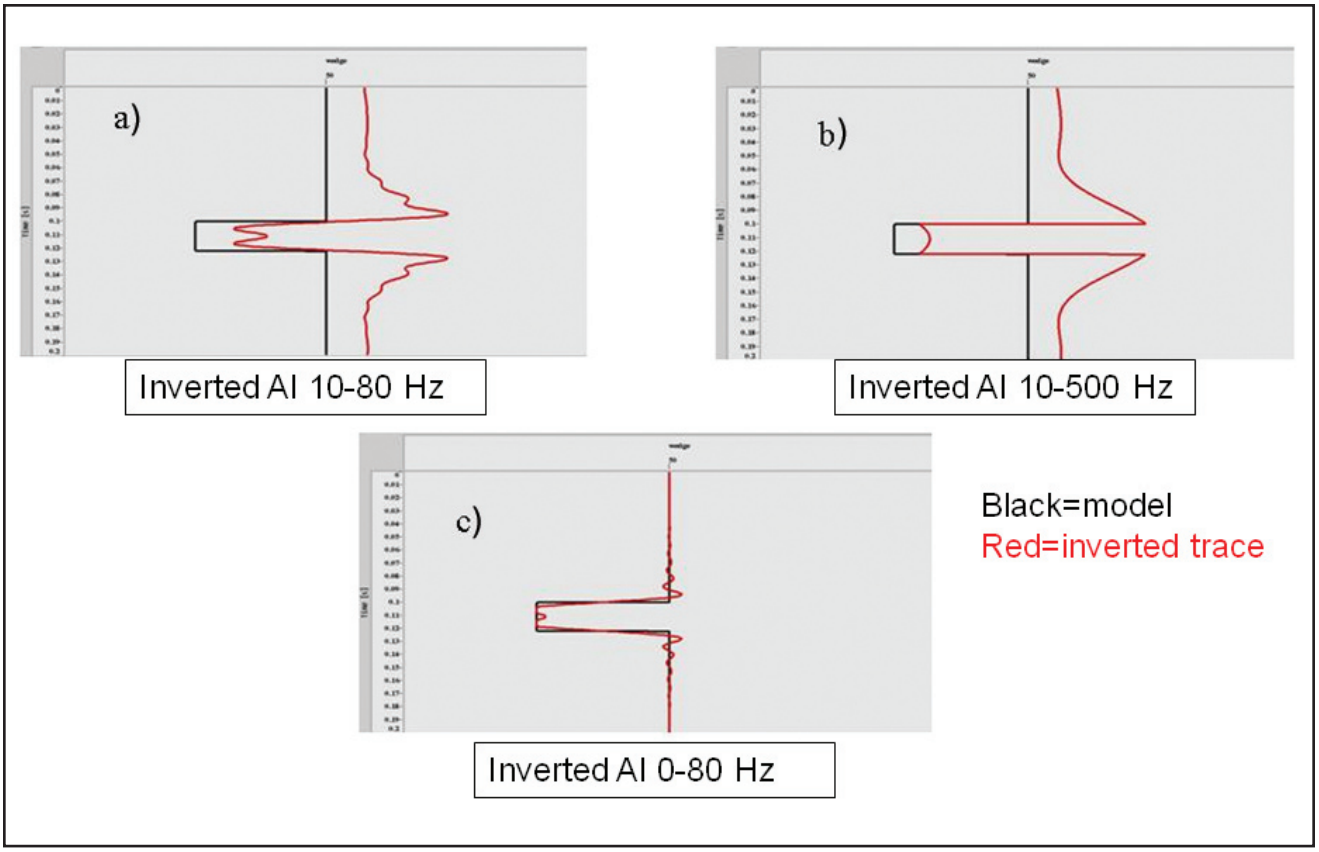

Figure 9-8. A simple impedance layer model, inverted for three different frequency ranges. The inclusion of the high frequencies (b) allows us to interpret the thickness of the layer boundaries more accurately, but it is the inclusion of the low frequencies (c) that allows us to obtain absolute values for use in the quantitative interpretation of the rock properties.

the change of geology and overall rock properties at the boundary. The final lower sand at 2460 m is low density but higher velocity and it appears as a high-impedance, tight sand or silt. This example was purposely utilized for this paper in order to show a worst-case scenario and to show the need for pre-inversion analysis of the log data, rock properties, and seismic data.

High-cut and low-cut filtering of the data (to the seismic range) yields a plot similar to that in Figure 9-6 but with fewer data points. The relationship still holds for the sand above the unconformity, but the relationship has additional uncertainty attached. Analysis such as this is very important when one is determining whether the band limitation of the data is masking all relationships with the P-impedance data.

Low frequencies that are inherently missing from the seismic data are extremely important if quantitative interpretation is required. This is illustrated in Figure 9-8 by a simple impedance layer model, inverted for three different frequency ranges: 10–80 Hz, 10–500 Hz, and 0–80 Hz. A modeled AI layer (well AI, in black) was used to derive a synthetic seismic data set utilizing a Ricker wavelet comprising the frequency range listed below each figure. The synthetic seismic was subsequently inverted back to AI. The resulting inverted AI traces are red, with the bandwidth of the inversion defined by the wavelet in the model.

When the seismic data are inverted using a wavelet with frequencies of 10–80 Hz (Figure 9-8a), the approximate thickness of the layer is accurately imaged, but the absolute impedance values and the interface shape are incorrect. When the wavelet frequency is increased to an extreme of 500 Hz (Figure 9-8b), the results are capable of resolving thinner beds but still do not accurately represent the model or the rock property values. However, when low-frequency information is included from additional sources, the inverted data best represent the model (Figure 9-8c). This demonstrates that low-frequency information is critical to a complete inversion result.

Most inversion methods incorporate external information to reconstruct the missing frequencies outside the seismic bandwidth, thereby producing broadband results.

Downloaded 25 Jun 2012 to 95.28.162.50. Redistribution subject to SEG license or copyright; Terms of Use: http://segdl.org/

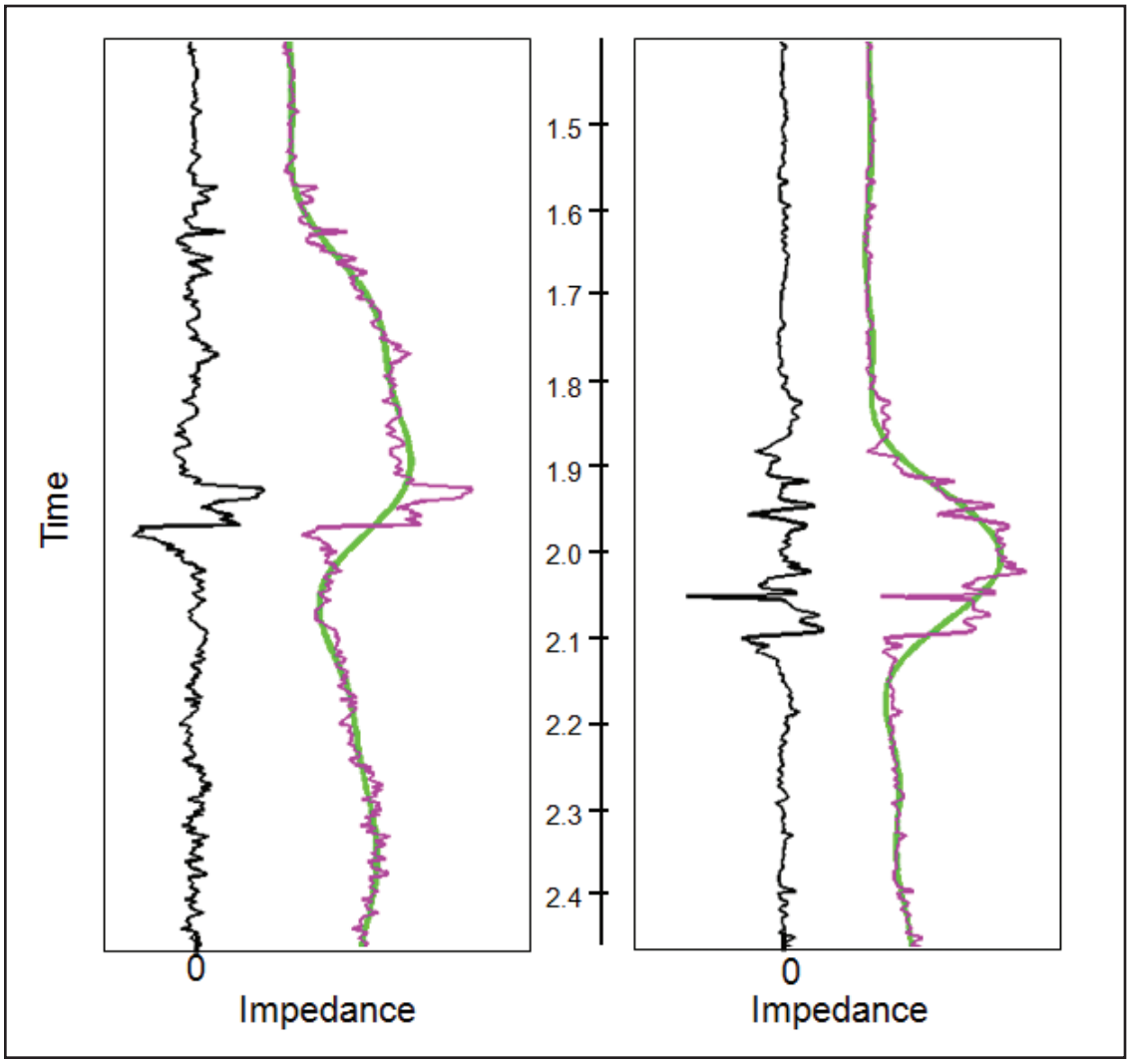

Figure 9-9. Impedance log (purple) and its low-frequency component (green). Relative impedance (black) is created by subtracting the low-frequency component from the impedance log. It is the inclusion of the low frequencies that allows us to obtain absolute values for use in the quantitative interpretation of the rock properties. (From Pedersen-Tatalovic et al., 2008. Used by permission.)

Different methods reconstruct the missing information in different ways and with varying degrees of success. Low-frequency information has traditionally been derived from log data, pre-stack depth, or time-migration velocities, and/or a regional gradient. Because many of these data are very low frequency (0–2 Hz), processing that preserves low frequencies is advantageous. Recently a number of articles have been written providing new methodologies. In 2007, *The Leading Edge* featured a special section devoted to low-frequency analysis.

A recent paper by Pedersen-Tatalovic et al. (2008) illustrates an excellent example of why low-frequency data are critical to the interpretation of certain rock types. It also illustrates how important it is to properly interpolate low frequencies and how incorrect evaluations can be derived from improperly interpolated low-frequency impedance data. The article discusses prospecting in a chalk section in the Danish sector of the North Sea. Figure 9-9 shows Figure 2 from the article. The figure reveals that removal of the low frequencies (or not having them present in the final inversion results) will mask the target zone. The target zone in this case is the chalk, which is between 1.6 and 2.0 on the left log and 1.85 and 2.1 on the right log. Notice that when the low frequencies are removed, the high-impedance chalk is not visible. The high-frequency porosity streaks become masked in the background.

Downloaded 25 Jun 2012 to 95.28.162.50. Redistribution subject to SEG license or copyright; Terms of Use: http://segdl.org/

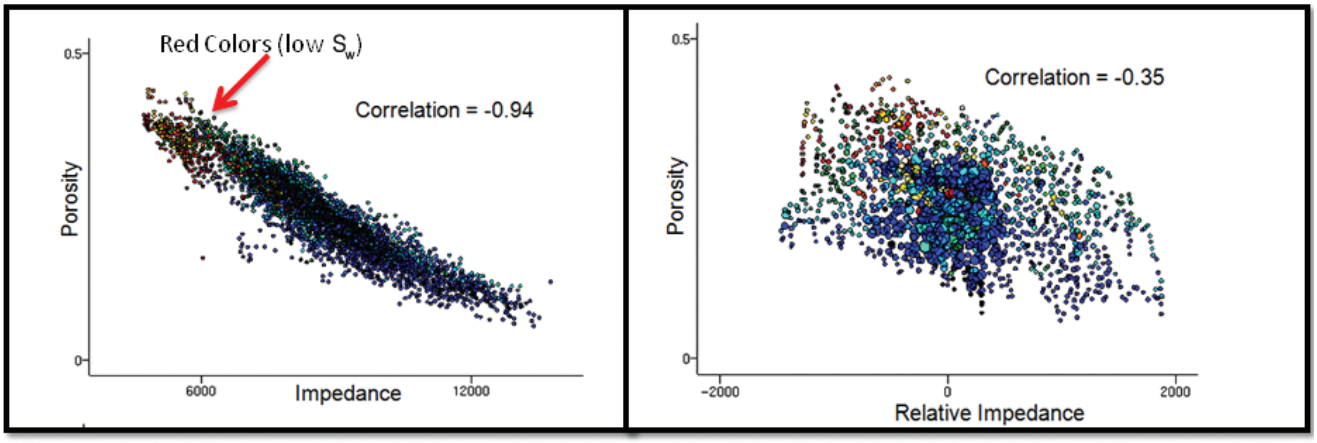

Figure 9-10. Crossplots showing chalk impedance vs. porosity log data for several wells in the Danish sector of the North Sea. Absolute impedance is shown on left panel and relative impedance on the right panel. Blue represents high water saturation. Yellow represents low water saturation. (From Pedersen-Tatalovic et al., 2008. Used by permission.)

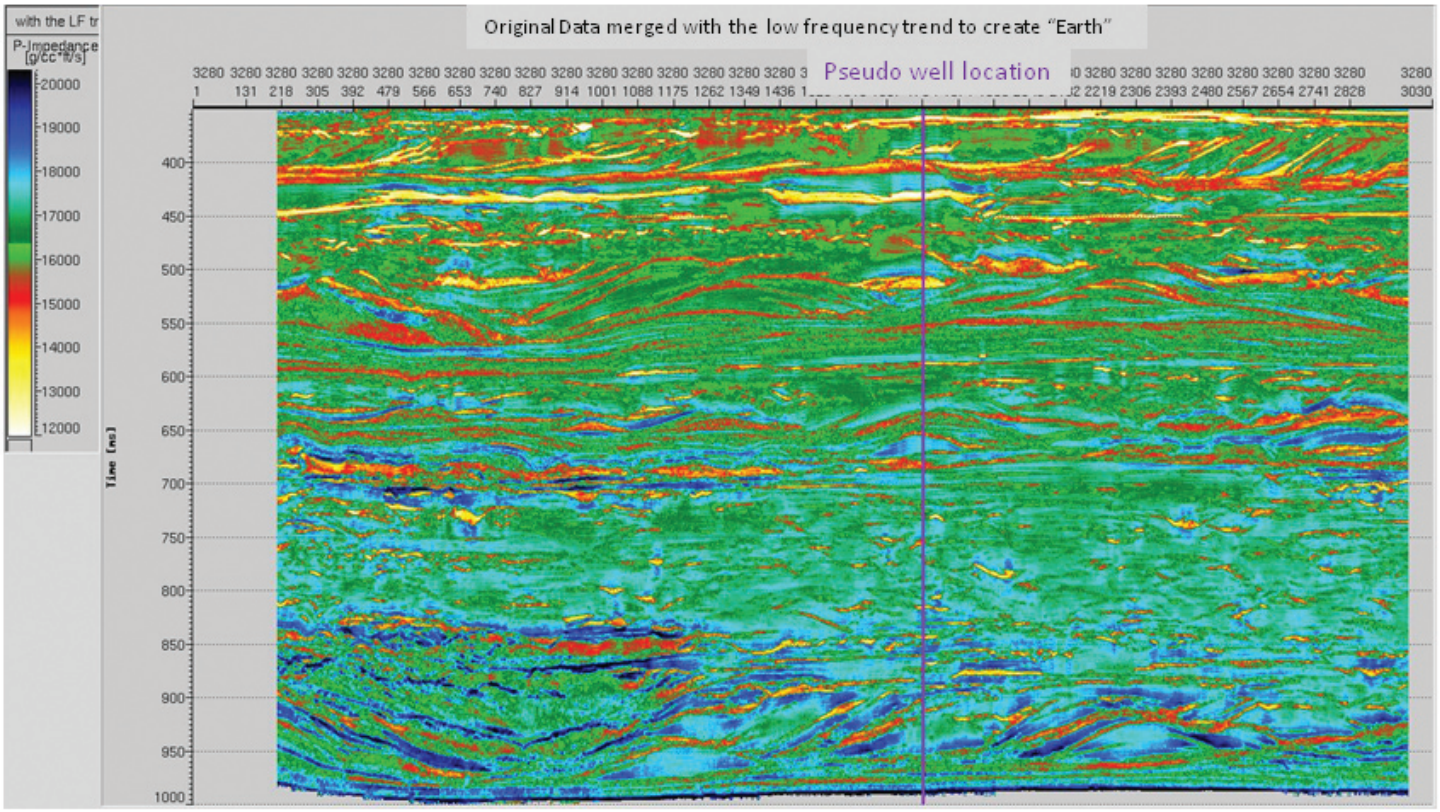

Figure 9-11. Impedance data created for testing on the Jurassic Tank data.

Downloaded 25 Jun 2012 to 95.28.162.50. Redistribution subject to SEG license or copyright; Terms of Use: http://segdl.org/

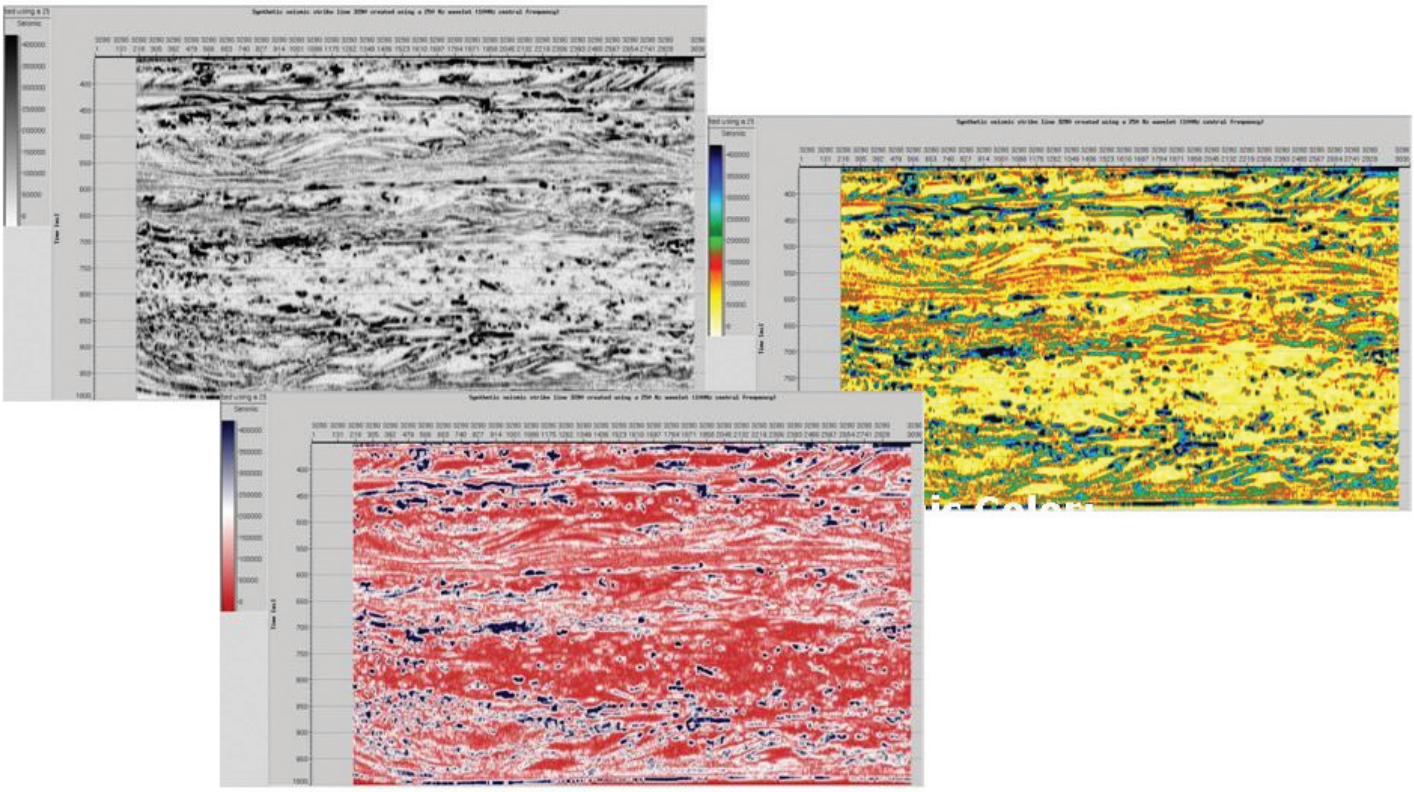

Figure 9-12. Seismic data from the Jurassic Tank experiment, created by convolving a zero-phase wavelet with the traces from the data shown in Figure 9-11.

As was stated in the article,

> *"In clean chalk, impedance can optimally be used to predict porosity, because it has a strong correlation to porosity, and because its sensitivity to presence of hydrocarbon fluids is limited. Presence of free gas or a high level of solution gas in the reservoir is normally handled by correcting the impedance level accordingly. Consequently, in order to derive porosity from impedance in chalk, it is essential to recover the low frequencies and establish the absolute impedance level."*

Figure 9-10 is also from that paper, but I have illustrated it with the red arrow (for clarity) in order to assist in the description and identification of the water saturation values. The crossplots show that the low frequencies (contained in the absolute impedance logs) are critical for identification of the hydrocarbon effect in the chalk. The article continues to discuss solutions for determining the missing low frequencies and methods of interpolation. The authors complete the article by proving their thesis with a case study.

High-frequency information is also problematic and will be discussed later in sections on model-based inversion methodologies.

In 2005, experiments were conducted on the Jurassic Tank data from the EarthScape facility experiment XES 02-1 at the University of Minnesota (Latimer, 2005). The tank data were reformatted to accommodate a typical seismic workstation. The digitized data from the tank were converted to time, scaled, and merged with a simple linear background trend to create a 3D volume of density. Details of the experiment can be found on the SEG website (www.seg.org) under Education/Professional Development/Distinguished Lecturer Program/Fall 2005 SEG AAPG Distinguished Lecturer.

Once a density cube was created, velocity was assumed to be unchanged because of the lack of compaction in the shallow tank. A linear compaction trend was created

Downloaded 25 Jun 2012 to 95.28.162.50. Redistribution subject to SEG license or copyright; Terms of Use: http://segdl.org/

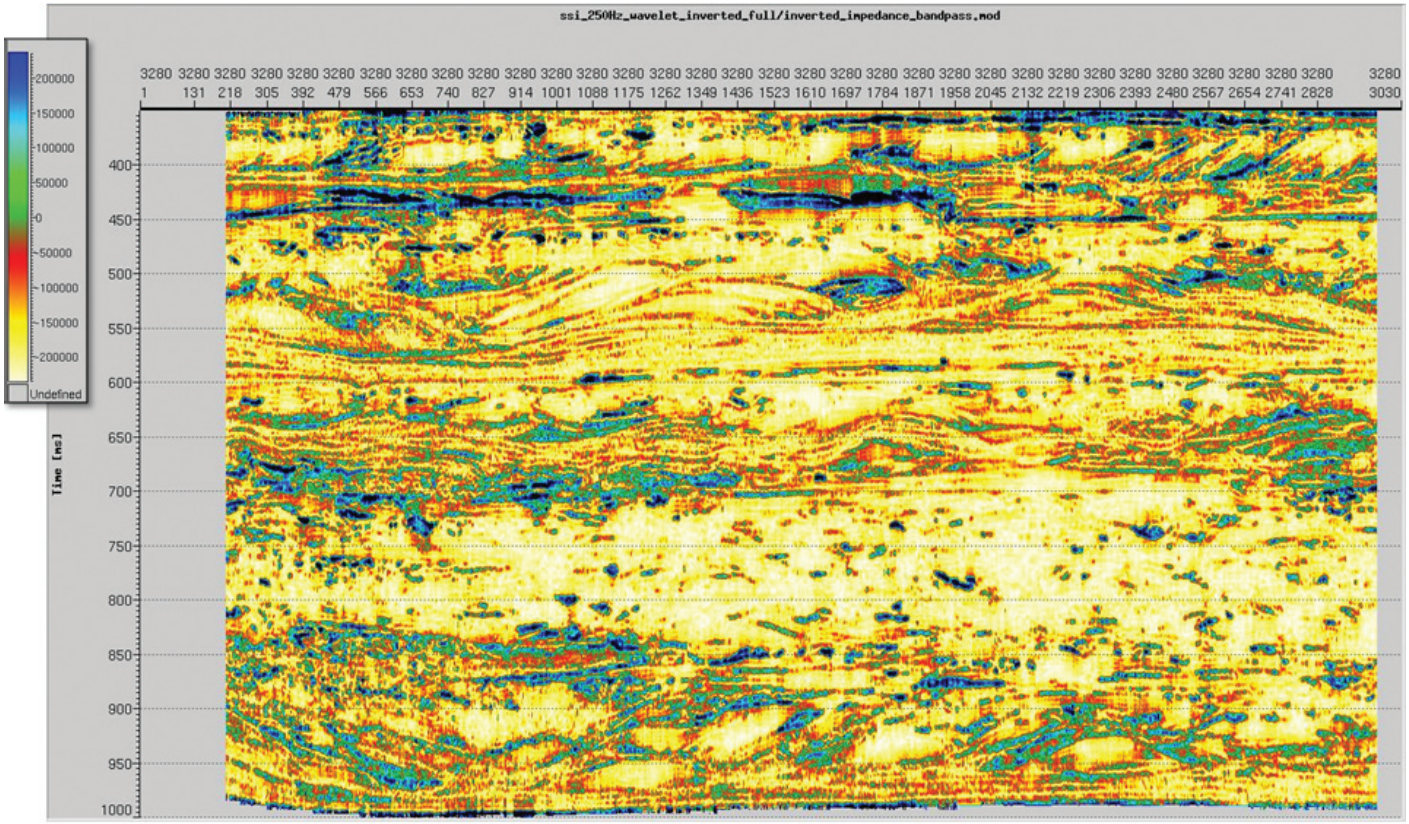

Figure 9-13. A constrained sparse-spike inversion (CSSI) was performed on the data in Figure 9-12. The results shown are a band-limited inversion.

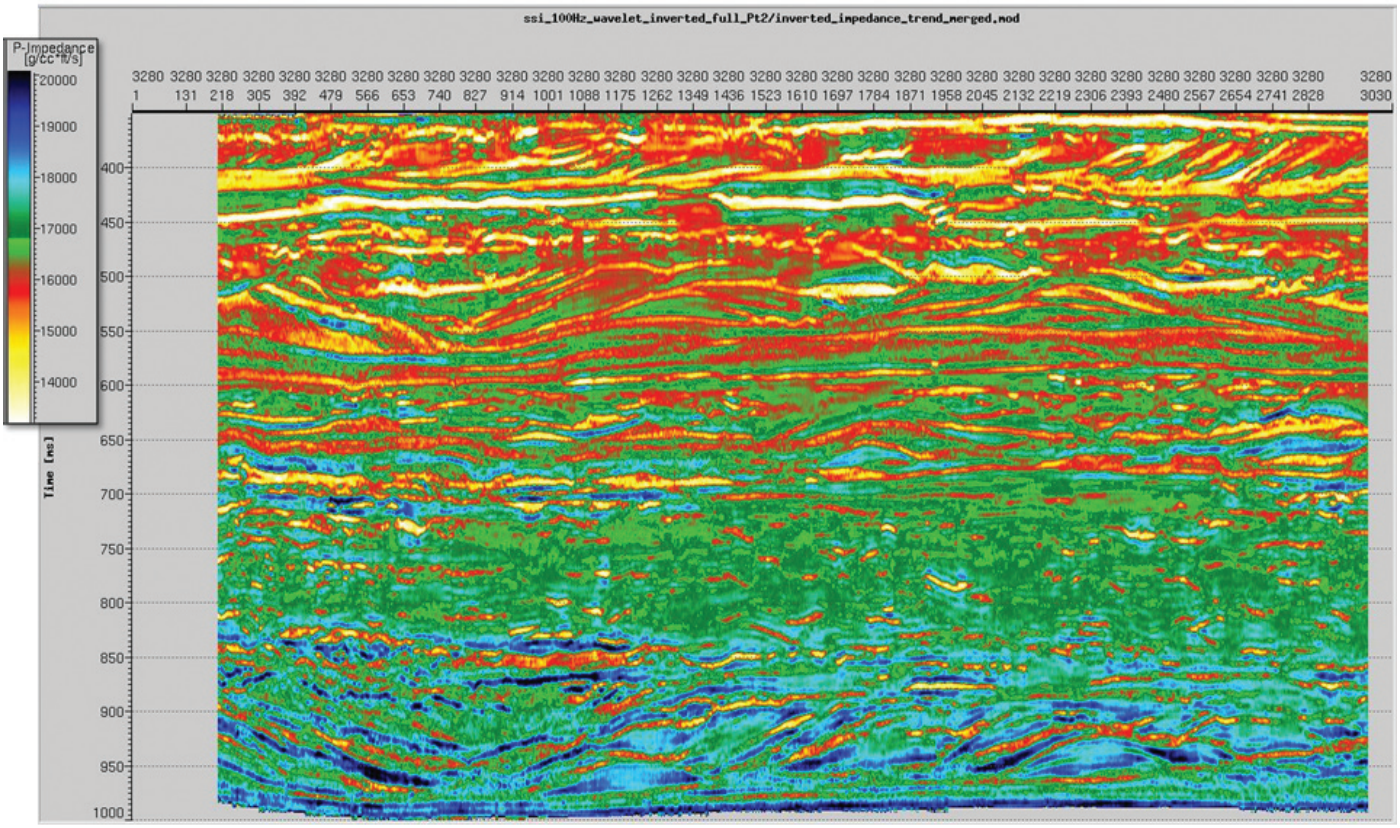

Figure 9-14. Merged acoustic-impedance data created by merging a linear trend with the data in Figure 9-13.

Downloaded 25 Jun 2012 to 95.28.162.50. Redistribution subject to SEG license or copyright; Terms of Use: http://segdl.org/

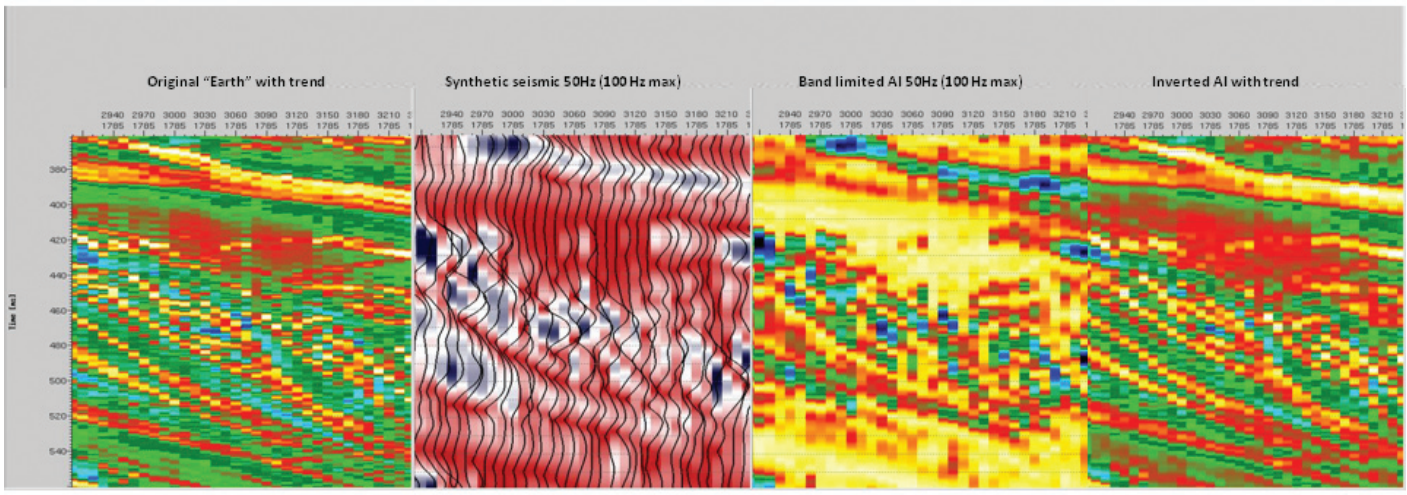

Figure 9-15. Inversion test from the Jurassic Tank experiments, using wavelet properties having frequencies of 50 Hz (100 Hz maximum) and zero phase. The blocky appearance is due to the sparse sampling of the data in the dip direction.

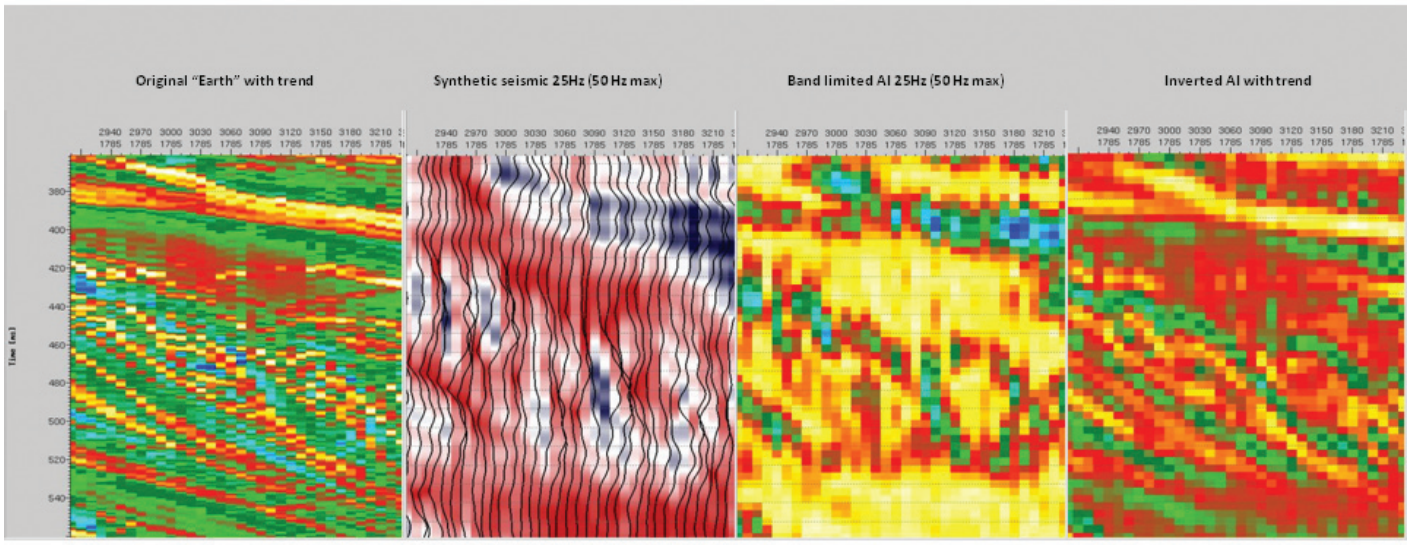

Figure 9-16. Inversion test from the Jurassic Tank experiments, using wavelet properties having a central frequency of 25 Hz (50 Hz maximum) and zero phase. The blocky appearance is due to the sparse sampling of the data in the dip direction.

(very low velocities) and multiplied with the density cube to create a cube of acoustic impedance. Using a series of Richter wavelets with different frequencies, synthetic seismic cubes were created. The data were inverted and compared with the original cube of acoustic impedance. Figure 9-11 shows a strike section through the Jurassic Tank impedance data. This is the "known" or model that was used as input into the testing.

The acoustic-impedance data in Figure 9-11 were convolved with a Richter wavelet to create a simple seismic cube. This was completed for two reasons: to check high-frequency differences and to check low-frequency differences. Three versions of the seismic data using three color bars are shown in Figure 9-12.

Downloaded 25 Jun 2012 to 95.28.162.50. Redistribution subject to SEG license or copyright; Terms of Use: http://segdl.org/

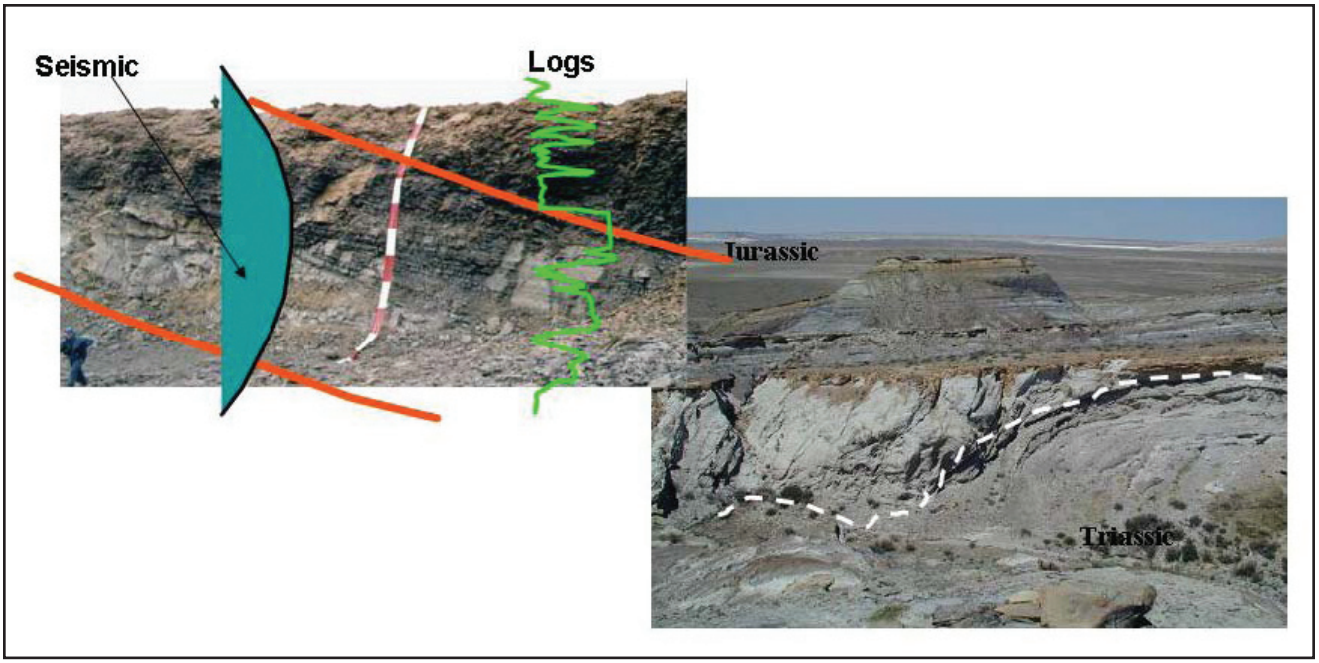

Figure 9-17. Scale differences between data used in interpretation exercises. Scale is basically frequency in the seismic domain.

After creating a seismic volume, inversion was computed using a constrained sparse-spike inversion algorithm (CSSI). The results of the CSSI were band-limited because seismic data do not contain the lowest frequencies. The band-limited inversion results are shown in Figure 9-13. There are a few items to note:

- The results are not substantially different from the seismic data.
- The band-limited inversion, because it is missing the lowest frequencies, has positive and negative numbers similar to seismic.
- The phase of the inverted data does not have to be known in order to interpret it, because the phase is taken care of during the CSSI inversion process. This makes interpretation easier because a change in color represents a change in velocity or density and thus a probable change in lithology.

The test was designed to determine whether a simple linear background trend (low frequencies), if known, would improve the results and arrive at an answer that is closer to the input data after inversion. In other words, would the merging of the low frequencies make the data easier to interpret, which was suggested by the theory? Figure 9-14 shows the results obtained by merging the data in Figure 9-13 with a simple linear background trend of low-frequency data derived from one pseudo-well in the Jurassic Tank experiment. These results show an improved volume over the results found in Figure 9-13. Note that the data are not all positive numbers. Sequence boundaries are easier to map, and again a change in color represents a change in rock properties.

The low-frequency test was repeated using synthetic seismic data with various frequencies. The results, using the Jurassic Tank data set, are shown on the SEG Distinguished Lecture video (Latimer, 2005). Figures 9-15 and 9-16 are dip sections from those data. Figure 9-15 shows the original data in the first panel, with the synthetic seismic using a 50-Hz wavelet (50-Hz central frequency, 100-Hz maximum) in the second panel. The third panel shows the band-limited results of an inversion of the seismic in panel two. The merged final inversion results are shown in far-right panel four.

Note how similar the final results on the far-right panel are to the input data on the far left. The original modeled data were higher frequency than the wavelet used in the creation of the synthetic seismic, so we would expect the apparent loss of resolution

Downloaded 25 Jun 2012 to 95.28.162.50. Redistribution subject to SEG license or copyright; Terms of Use: http://segdl.org/

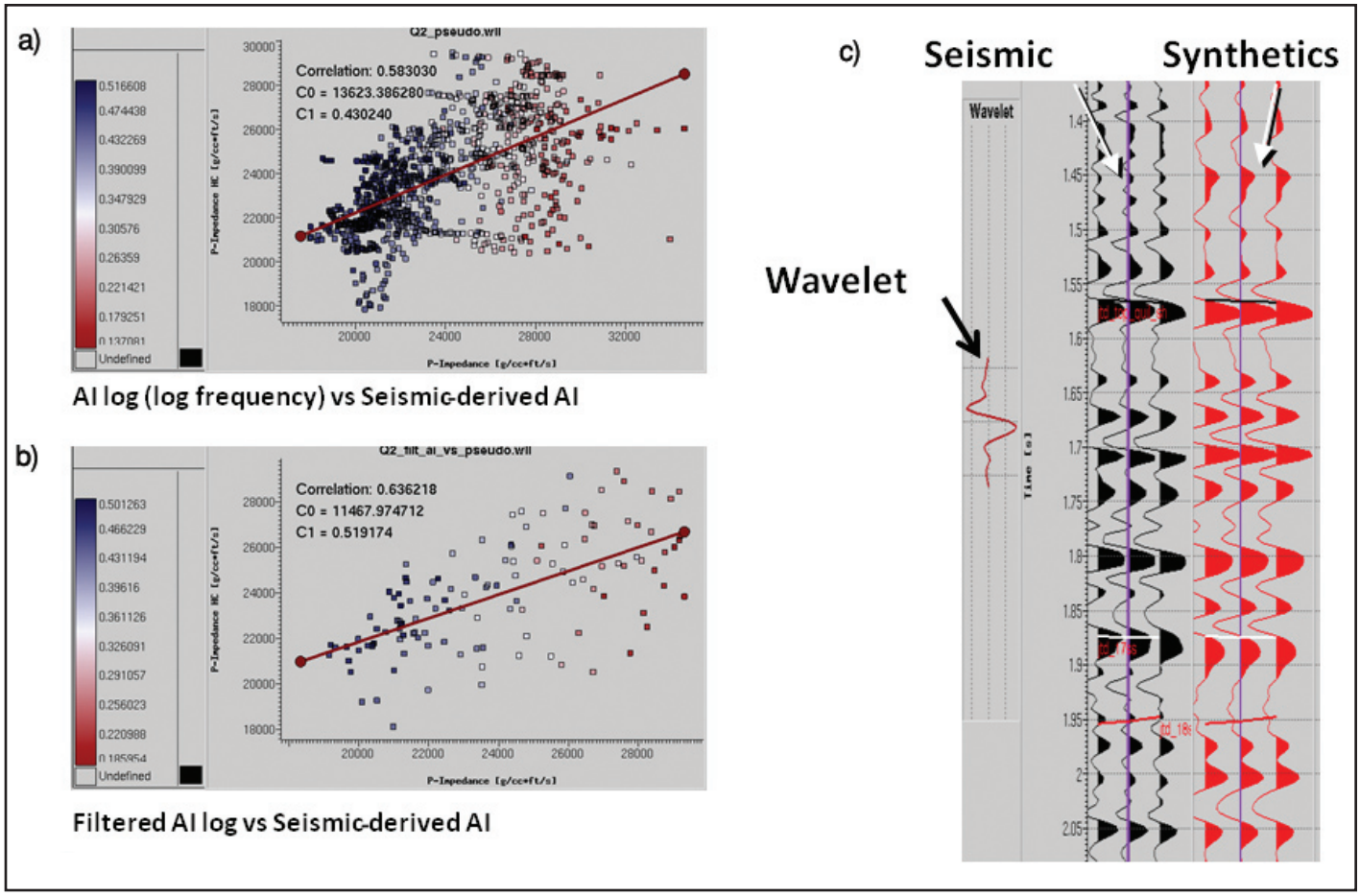

Figure 9-18. Seismic well tie and correlation. The excellent well tie, shown in 9-18c, yields a correlation coefficient of only 0.58 due to scale differences between the data.

(high frequencies). The synthetic seismic data show the prograding section, as do the band-limited inversion results in panel three, but not as clearly as the final merged volume in panel four. Numerous color bars were utilized, yielding the same general conclusions; the merged inversion on the right is superior to both the seismic data and the band-limited inversion. The merged inversion yields an answer that is closer to the "known" on the left.

Figure 9-16 shows the same test using a zero-phase wavelet having a central frequency of 25 Hz (50 Hz maximum). The results again indicate that the merged inversion yields a much easier section for interpreting. It would be difficult to interpret the section as prograding, by looking at either the seismic data or the band-limited inversion results.

Scale Differences

Scale differences are basically frequency differences but often are not thought of in this manner by interpreting geoscientists. Figure 9-17 shows a cartoon of the scale differences with relation to an outcrop. The image on the left shows the details of the outcrop. Overlain on the image are schematics showing a log curve and the lower- frequency seismic wiggle. The photo on the right shows a large sand-filled channel which, when seen on seismic, would be visible only if the data were shallow and of high frequency (10–60 or 70-Hz and 2-ms sampling). High frequencies of 70 Hz would yield approximately a 10-ms channel on seismic data, with thinning toward the edges.

The scale differences between these data do a lot more to our interpretation than just making items difficult to see. Seismic theory reminds us of the tuning curve. We need to use caution when analyzing our seismic data, and we must know the tuning thickness. Some inversion algorithms can improve the resolution, as we will see later in the chapter, but these data may contain additional uncertainty.

Downloaded 25 Jun 2012 to 95.28.162.50. Redistribution subject to SEG license or copyright; Terms of Use: http://segdl.org/

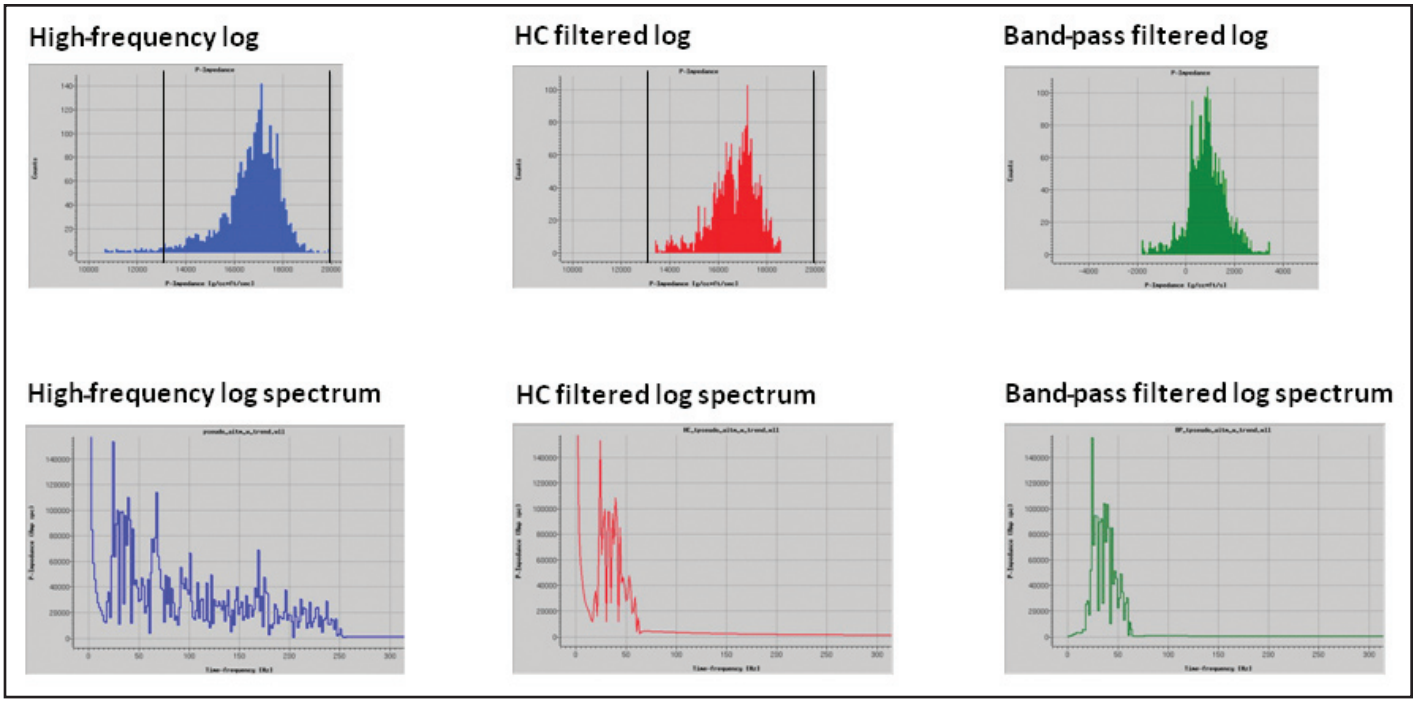

Figure 9-19. Effects of filtering on the statistics of data. Top row: Histograms of data from a pseudo-log used in the Jurassic Tank data set tests. Lower row: frequency-spectrum plots from the data that created the upper row histograms.

The tuning effect is defined in Sheriff's *Encyclopedic Dictionary of Applied Geophysics* (2002) as "Constructive or destructive interference resulting from two or more reflectors spaced closer than a quarter of the dominant wavelength. The composite wavelet exhibits amplitude and phase effects that depend on the time delays between the successive reflection events and the magnitude of the polarity of their associated reflection coefficients, and also on the shape of the embedded wavelet."

Tuning is covered thoroughly in Chapter 6. Creation of a tuning curve for the area, using wavelet attributes derived from the inversion process, is important because this is also an excellent test of the trace impedance results. The tuning curve can be used to determine whether the visual increase in resolution is actual or is an apparent resolution resulting from the inversion-induced change in the character of the display (inversion data are layer-based rather than interface-based).

The difference-of-scale problem can also be described in another way. Let's suppose we take a well log and plot it against a copy of itself. We have a perfect one to-one-correlation. Now let's suppose one of the copies is filtered to a frequency similar to the highest frequency that might be seen in most seismic sections (60 Hz). The correlation coefficient now becomes 0.9. The filtering has changed the statistics of the data as well as the accuracy, even though the data were identical prior to filtering.

Figure 9-18 shows what happens when one is comparing log data and seismic data. The crossplot on the left (Figure 9-18a) shows the relationship between P-impedance data derived from seismic (at the well location) and P-impedance data from the well log. The correlation coefficient is 0.58. The figure on the right (9-18c) shows three seismic traces around the well in black (the well location is in the center and is seen by the purple line) and three traces (repeated) from a convolution of the wavelet and the impedance log data (the normal way of making synthetic traces). There is a really excellent visual correlation between the well data synthetic and the seismic. Most interpreters would call this a "good well tie," yet due to the difference of scale between the two data sets, the correlation is marginal from a statistical standpoint. If the log data are preconditioned (filtered or resampled) prior to crossplotting, the correlation coefficient is improved to nearly 0.64 (Figure 9-18b).

The exercise in Figure 9-18 was designed to show how the scale differences between the seismic and well data can affect the statistics of the combined data and what should be expected when the two very different scales of data are compared.

Downloaded 25 Jun 2012 to 95.28.162.50. Redistribution subject to SEG license or copyright; Terms of Use: http://segdl.org/

The seismic should not be expected to correlate with well data with 90% accuracy or even close to that value. Sometimes geostatisticians comment that the seismic data do not match the well data because there is only a 0.6 correlation coefficient and thus the seismic data properties should not be used in a reservoir model. Because of the natural scale differences, a 0.6 correlation coefficient may be quite a good relationship.

An aside to the correlation of seismic-derived attributes and the correlation to well data is that seismic data are in time, and well data are in depth. Some of the correlation difficulties arise in the time-to-depth conversion of the seismic data cube or the depth-to-time conversion of the well data. Velocity data volumes are often computed from very-low-frequency checkshot data, pseudo-checkshot data from seismic, and synthetic correlations and/or velocities derived from processing. There is an inaccuracy in the process that will create errors in the depth or time match. The well data should also be edited carefully prior to interpretation, and the seismic processing should be of high quality.

In addition to the difficulties in depth conversion, the mechanics of putting a seismic data cube into a model-based system, such as reservoir modeling software, also causes inaccuracies. The seismic is at line-and-trace spacing, and the models are generally on a totally different grid system based on cells. Seismic is often painted onto the grid, smearing the seismic and causing traces to be relocated into the new grid system. If there was a correlation with the well data in time prior to regridding, chances are the correlation is even worse after gridding.

Filtering of all of these data causes the statistics of the data to be altered, thereby changing the original values and reducing accuracy. An example of this can be seen in Figure 9-19.

The lower row in Figure 9-19 illustrates three plots of the frequency spectrum from synthetic log data used in the Jurassic Tank Experiment. The upper row shows the histograms of the lower data. The blue data on the left contain the raw data without filtering. The red data in the center have been high-cut filtered. Notice the change in the statistics of the data in the histogram. The two black lines are located at the same values. The histogram in red has lost its low values and is now slightly bimodal. The lowest values of P-impedance were apparently at the highest frequency ranges as well as some of the mid-range values at 16800g/cc*ft/sec. In the green set of plots, we have filtered both the low and high frequencies (similarly to what would happen in seismic data). Notice the change in shape of the histogram as well as the range of numbers. The plot is narrower, and the values are around zero because the low-frequency "trend" is now missing.

An item of interest in Figure 9-19 is that when one is inverting data, the seismic is similar to the green data (limited in low and high frequencies). The goal is to reach either the red or blue data ranges. Replacing these missing unknown values, i.e., transforming from band-limited data back to full-band data, is nonunique and problematic. We do not have the exact values for the low-frequency or the high-frequency data; we have to make assumptions based on the geology, a probabilistic assumption, and so forth.

Another way of looking at how the scale differences or band limitation is affecting inverted data is to crossplot the log data by lithology type. Figure 9-20 is a crossplot of porosity versus impedance. It shows an example from real data in a carbonate environment. Figure 9-20a shows the log data (high-cut filtered to the frequency of the seismic data) with the low-frequency trend still in the data. The porous dolomite is the target for the reserves in this data set. The data have a 0.89 correlation and it is easy to separate out the porous from tight data. An easy test of what a band-limited inversion would yield is to filter the log data and remove the low frequencies. Figure 9-20b shows the same data set, with the low frequencies removed. The data now show that with respect to "relative" or band-limited impedance, the porous dolomites and tight limestones are indistinct. If the data were inverted using a trace inversion algorithm, it would be critical to replace the low-frequency data in some manner, either by calibrating the seismic-derived velocities to the well data and interpolating, or by using a statistical program to compute the values.

Downloaded 25 Jun 2012 to 95.28.162.50. Redistribution subject to SEG license or copyright; Terms of Use: http://segdl.org/

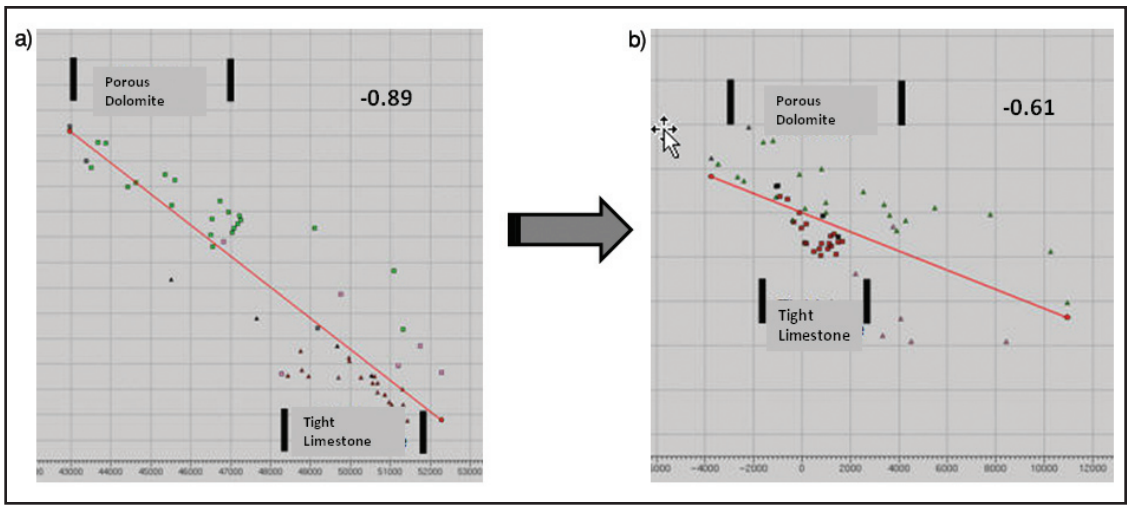

Figure 9-20. Low-frequency analysis. Transforming log data to band-limited data (removing low frequencies) changes the correlation and possibly the relationship between rock properties. Transforming from band-limited data back to full band is nonunique because values are known only at the well locations. In the case above, the low frequencies are critical to isolating the porous dolomite data.

Methods of Inverting Seismic data — General Considerations

There is no single best method for inverting all data. After defining the scope of the project, the next steps are to analyze the available data, determine the project objectives, consider the desired turnaround time, and then select the most suitable method for inversion. Some of the following points should be considered:

- An exploration project with huge volumes of data and little well control calls for application of quite a different method than does a development project with extensive well control and narrower production targets.
- From post-stack data, the output from inversion would be acoustic impedance (AI), the product of density and P-wave velocity, but from pre-stack data, both AI and shear impedance (SI) can be derived. Shear impedance is the product of S-wave velocity and density. With enough angle range or converted mode (PS) recordings, pre-stack data could also be inverted for density, allowing one to extract both P- and S-wave velocity from the impedances.
- Through log analysis, one can determine if the survey area has a unique relationship between AI and one's hydrocarbon target. Determine the thickness of the target section. Thin events may not be resolved when the frequency of the seismic is insufficient. Testing as discussed in Figures 9-7 and 9-20 will determine appropriateness of the inversion. When angle-stack data are necessary, determine whether the angles available in the seismic acquisition are sufficient to discriminate between lithology and fluids.

The earliest methodologies were developed for AI inversion and were based on recursive or trace-integration algorithms (RTI methods). These are truly trace-based, because the seismic trace is the sole input. They are also the simplest and most limited algorithms. For these algorithms to produce meaningful results, the wavelet embedded in the seismic must be zero phase. Such RTI methods are simple and fast. However, they produce results only within the seismic data bandwidth, and because the embedded wavelet is not removed, tuning and wavelet side-lobe effects are not reduced. If low frequencies are desired, then they must be added later through additional processing.

Why are so many inversion methods available, given the seemingly simple process of transforming data from the seismic-reflection domain to the acoustic-impedance domain? The fundamental reason is that when removing a wavelet from a seismic trace to arrive at an appropriate reflection-coefficient series, there are many answers;

Downloaded 25 Jun 2012 to 95.28.162.50. Redistribution subject to SEG license or copyright; Terms of Use: http://segdl.org/

i.e., the solution is not unique. To address this mathematical limitation, most modern inversion methods constrain the answer in some way and therefore produce broadband results that generally succeed in correctly inverting the seismic within the seismic bandwidth. How the constraints and the issues of sparsity (simplicity) and low-frequency replacement are handled determines the fundamental differences between algorithms. Because of their dependence upon a low-frequency model, all inversion methods can be thought of as being model-based, although, as we will see below, we reserve the term "model-based" for something else. Most model-based inversion algorithms available today can be divided into two major categories: post-stack and pre-stack inversions. Inversion types are described below. The description is intended to be simple, not exhaustive.

Inversion Methods — Post-stack

Recursive inversion (trace integration). This is the simplest and oldest form of inversion. It is sometimes referred to as "band-limited" inversion, or relative acoustic impedance (RAI), but there is a difference between a band-limited result from post-stack trace inversion and a band-limited recursive inversion. A band-limited result from a post-stack trace inversion can be computed via numerous algorithms but filtered to remove any low-frequency data that may be spurious. Recursive inversion was the first type of inversion and was discussed by Lindseth (1979). We assume that the seismic trace represents an approximation to the earth's reflectivity and can be written in the form

$$s_t = w_t * r_t \,, \tag{1}$$

where s_t is the seismic trace, r_t is the reflection coefficient series, and w_t is the seismic wavelet.

If we assume that the wavelet is zero phase and broadband, the seismic trace can be integrated to transform it from reflectivity to acoustic impedance. That is, the reflectivity can be inverted to represent impedance, as shown in Figures 9-2 and 9-3.

There are numerous recursive algorithms, but they are all similar to

$$Z_{i+1} = Z_i * \left[\frac{1 + r_i}{1 - r_i}\right] \tag{2}$$

where Z_i is the acoustic impedance and r_i are the reflection coefficient (seismic trace) samples.

For the algorithm to produce meaningful results, the input seismic trace must correspond to the band-limited earth reflectivity function (That is, $r_t = s_t$). These algorithms have numerous problems:

- The result is band-limited, being limited to the seismic frequency ranges,
- The algorithms require positive seismic trace amplitude data corresponding to a positive reflection coefficient, so the algorithms require zero-phase seismic,
- The wavelet in the seismic is ignored so tuning effects are not removed, and
- The inversion must be scaled to the proper range of impedances.

Band-limited inversion. A band-limited inversion can refer to **any inversion algorithm** that has the lowest and highest frequencies missing. It contains only those frequencies found in the seismic band. Band-limited inversions are also often referred to as **relative inversions**. The high-frequency component of the impedance can be recovered by a number of methods, such as deconvolution. The low-frequency model is commonly (but not necessarily) added later. It can be interpolated from the well data, calibrated to seismic-derived stacking velocities, or derived from a deterministic

Downloaded 25 Jun 2012 to 95.28.162.50. Redistribution subject to SEG license or copyright; Terms of Use: http://segdl.org/

or stochastic process. These lowest frequencies are used to extend the acoustic impedance from the low end of the seismic band down to 0 Hz. The advantage is that the impedance then is scaled to rock values. Disadvantages are that careful processing of the seismic data is needed for the derivation of accurate stacking velocities to fill in the very low frequencies (0–2 Hz), and incorrectly interpolated well data (in a nongeologic manner) can result in artifacts and very wrong rock properties.

Coloured inversion. The coloured inversion algorithm is similar to the recursive but approximates an unconstrained sparse-spike inversion by deriving an inversion operator that matches the amplitude spectrum of the seismic to that of the relative acoustic impedance data at the wells. The derived amplitude spectrum is combined with a –90° phase shift to create an operator. The operator is convolved with the seismic traces. The advantages of this method are its simplicity, short computation time, and robustness in the presence of noise, making it good for quick and preliminary inversions. The disadvantages again are that the results are band-limited and a wavelet is not used, so the input seismic must be zero phase. Additionally, the mean of the reflectivity spectra from the available wells is assumed to be representative of the true reflectivity across the project area.

Layer-based or blocky inversion. Layer-based or blocky inversion algorithms model the earth as layer blocks described by acoustic impedance and, optionally, time. This blocky model is broadband because of the assumption of layers with sharp boundaries. The link to the seismic is through the convolutional model, which can incorporate any wavelet. Nonuniqueness is countered by restricting the number of layers relative to the number of seismic samples. When the layers become thinner than the seismic resolution, nonuniqueness increases. These methods can be stabilized to an initial model, and it is in this context that we usually use the term "model-based inversion." The stabilization can be invoked in different bands, resulting in a variety of inversion strategies.

Sparse-spike inversion (SSI). Sparse-spike inversion is the collective name for a group of techniques in which the reflection coefficient series underlying the acoustic impedance is assumed to be sparse; i.e., the seismic trace data can be modeled with fewer reflection coefficients than can seismic trace data samples. A sparse-spike series is also broadband or attempts to retrieve a spiky (i.e. broadband) reflectivity series from band-limited seismic data. In these methods the link to the seismic is also through the convolutional model, which can incorporate any wavelet. Nonuniqueness is countered by applying the sparsity criterion. To provide further control on reconstructing frequencies outside the seismic data bandwidth, modern sparse-spike algorithms can also use model data for stabilization and/or constraint. These constraints effectively limit the range of potential solutions to those that have geophysical and geological significance.

Although there are similarities in the available sparse-spike algorithms, there are also many differences among them: how the sparsity is computed, how constraints are defined, how the L1 (sparsity) and L2 (match with the seismic) norms are utilized, and how the local minima are avoided. These algorithms are beneficial because they are fast and they are an improvement over recursive inversions.

Least-squares inversion. Least-squares inversion methods are similar to SSI, except a sparsity criterion is not used. Instead, these methods start with a model of the subsurface and then update this model until the synthetic seismic response from the final model fits the seismic data with the smallest least-squares error. To start the process, both an initial model and an estimated wavelet are required. The model is usually built from sonic and density logs and/or or RMS velocity control, using the picked seismic horizons to stretch the impedance values laterally. Using the extracted wavelet and the sonic log, a synthetic match is also done at each well location, allowing the interpreter to perform vertical stretching. It is important not to bias the final result too much using the initial model, and for this reason a low-pass filter is often applied so that the higher frequencies can be extracted from the seismic data. The methods can be applied to either post-stack or pre-stack data and sometimes (but not always) can be rightly termed to be model-based.

Downloaded 25 Jun 2012 to 95.28.162.50. Redistribution subject to SEG license or copyright; Terms of Use: http://segdl.org/

Important considerations when one is performing this type of inversion are the quality of the initial model and initial wavelet, the number of iterations needed to converge to a good answer, and the types of constraints used for pre-stack inversion.

Inversion Methods — Based on 3-D Stratigraphic Models

Modern computers allow for the construction of complex 3-D geologic models using a parametric approach, in which the model is parameterized into layers described by acoustic-impedance values and traveltimes. The key with these programs is in combining intelligent parameterization with constraints to impose the 3-D behavior of layer parameterization. It can be formulated in such a manner that the optimization problem has only one minimum so that the global minimum corresponds to the local minimum. The implication is that global optimization can be achieved with fast, robust local search algorithms that are guaranteed to find the optimum solution. One example utilizes a model based on input logs, lateral distribution of log weights, time-structure maps, and velocity corrections to control geologic-layer thickness. These inversions can utilize seismic, where log information is sparse. The advantages are that the results are high-resolution, and broadband and geologic input is included from the "initial model" by way of the horizon interpretation and the well data. Because the initial geologic model is heavily utilized (strongly model-based), successful application requires multiple wells with excellent fit to the seismic and good control on the geologic model.

Geostatistical inversion. The geostatistical inversion algorithm combines geostatistical data analysis and modeling with seismic inversion. In geostatistical analysis, the spatial statistics of the data are generated. Geostatistical modeling simulates data at grid points starting from known control points, typically well logs. Geostatistical modeling preserves the spatial statistics of the data but does not guarantee that any simulations are consistent with seismic data. In geostatistical inversion, the simulation algorithm is modified to simultaneously honor both the wellbore and the seismic data while producing estimates of reservoir parameters between wells. Geostatistical inversion provides an alternative method for including information not found in the seismic bandwidth (lower and higher frequencies). These algorithms utilize both well control and geologic control spatially described by the stochastic algorithm. They also have the benefit of the "model" parameters in three dimensions. The benefits of this modeling are that the results provide multiple possible solutions, are broadband (possibly higher frequency than the seismic data), and include one's initial geologic interpretation and well data as well as one's seismic data. However, when the initial geologic model is heavily utilized, successful application requires an excellent fit between the wells and the seismic and good control on the geologic model (excellent and detailed interpretation of both structure and stratigraphy) prior to running the inversion. Geostatistical inversion can optionally be run without well data, with only a model to define layers. It will then run blind-to-the-wells. The well data can be used subsequently for a quality assessment of the results.

Inversion Methods — Pre-stack or Angle-stack

Elastic-impedance inversion. The elastic-impedance (EI) approach formulated by Connolly (1999) inverts stacked data for a range of angles. Elastic impedance is mathematical impedance that produces the Aki-Richards linearized reflectivity function, assuming the small-term reflectivity approximation (that is, the reflectivity is the derivative of the logarithm of impedance). It implies a constant V_p/V_s ratio. I will use the term "elastic inversion" for any pre-stack inversion in which elastic parameters are the result. These may not be formulated exactly as Connolly describes and are an offshoot of the concepts. Below are some methods that derive elastic parameters.

In post-stack inversion, we make the assumption that the seismic rays hit the reflector at a near-zero angle. These normal-incidence seismic rays respond to the acoustic impedance of the geology. At nonzero incident angles, however, the seismic data are the response to the elastic impedance. This effect can be calculated using the Zoeppritz

Downloaded 25 Jun 2012 to 95.28.162.50. Redistribution subject to SEG license or copyright; Terms of Use: http://segdl.org/

equations. Typically we use AVO in a qualitative manner and inversion in a more quantitative manner, but this does not have to be the case.

Pre-stack inversion methods (for angles greater than zero) began to be developed around 1995–2000. These methods have improved and been refined since that time. In pre-stack inversion, both P- and S-impedances are calculated to obtain elastic models. When they are calculated together with density, the process is called "simultaneous inversion." Pre-stack inversions are especially useful when attempting to derive fluid properties from seismic data. The process is often performed on multiple angle-stack data or on pre-stack data in the angle domain (CDP gathers or angle stacks). The process creates P-wave impedance (I_p) and S-wave impedance (I_s) or V_p/V_s. For additional theory on simultaneous inversion see Simmons and Backus (1996), Pendrel et al. (2000), Savic et al. (2000), Aki and Richards (2002), Luo et al. (2003), and Hampson et al. (2005).

A number of commercial companies perform these processes. They are all slightly different in their theory and algorithms. They may use Zoeppritz-Knott, the full nonlinear Aki-Richards approximation, or the exact Zoeppritz. Many of the commercial packages have fairly exhaustive discussions of the theory in their software manuals. Some examples of pre-stack inversion algorithms follow.

Angle-dependent inversion. Angle-dependent inversion (ADI) is a method that was first introduced in 2000. This inversion integrates a detailed geologic interpretation (the model) with multiple partial angle-stack seismic data and well-log data to generate a 3-D acoustic-impedance volume having an increased bandwidth compared with the input seismic data (low frequencies are added from the model and the stacking velocity data). The process works by inverting each of the angle stacks using their associated unique wavelet, converting seismic interface properties into layer properties, and by integrating a low-frequency model, as described in Anderson and Bogaards (2000) and Jarvis et al. (2004). The near-stack amplitude information relates to changes in density and compressional velocity. The far-stack amplitude information relates to density, compressional velocity, and shear-wave velocity (elastic properties). Rock property constraints and geologic insight are incorporated in order to calculate reservoir NTG ratios and porosities. This is discussed in Glenn et al. (2005). The ADI approach involves splitting all the CDPs into constant angle groups, stacking them, and performing an inversion on the results. The data can be calibrated to brine, oil, and gas, by modeling using a probability density function (pdf), thus allowing for a relative fluid discrimination. This method is described in detail in Anderson and Bogaards (2000) Dubucq et al. (2001). The process is fast and often is sufficient to define the possibility of hydrocarbons for exploration purposes.

Angle-impedance inversion. I separate the topic of angle-impedance inversion only to highlight that a generic method of inversion similar to the one above is also possible in which the user inverts different CDP gathers or angle stacks on purely band-limited data. The user inverts the data for the near traces and then inverts the data for the far traces (elastic impedances; Dubucq et al., 2001). This can also be a benefit even though the results yield relative values and must be calibrated to the log data and used with caution. In the interpretation section of this chapter, I will show how these data can be utilized in a regional project and can improve the overall interpretation of the area.

When inverting different angles to compare AI and EI, problems exist as a result of different frequencies of the volumes (near traces are generally higher frequency than far traces), the positioning of the individual trace data due to velocity differences, and the possible changes in phase due to fluids. Numerous methods can be employed to account for this, and in many cases, this quick inversion of the different angle data is sufficient for exploration. From this quick inversion of the nears and the fars, a pseudo-volume of shale (VSH) can be generated from individual angle impedances. The VSH volume can be created using an equation that combines band-limited near- and far-angle elastic impedances with the intercept and slope of a shale fit-line in a crossplot view of elastic impedances.

The procedure is based on petrophysical lithotype discrimination through coordinate translation and rotation to principal directions. Figure 9-21 illustrates crossplots

Downloaded 25 Jun 2012 to 95.28.162.50. Redistribution subject to SEG license or copyright; Terms of Use: http://segdl.org/

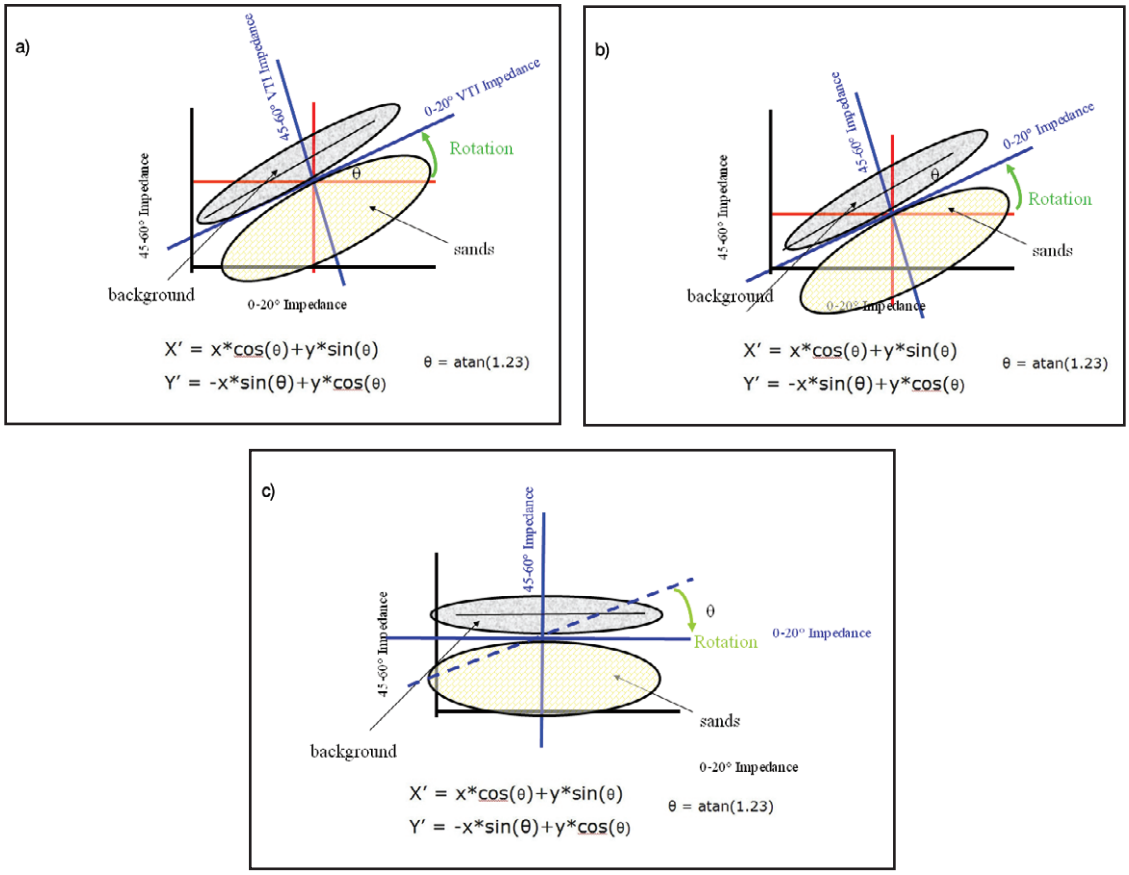

Figure 9-21. A VSH volume can be created using an equation that combines band-limited near- and far-angle elastic impedances with the intercept and slope of a shale fit-line. The procedure is based on petrophysical lithotype discrimination through coordinate translation and rotation to principal directions (Courtesy of Brian Cerney.)

showing petrophysical relationships of sands and shales from real well data. To separate out the sands from the shales, a line is fit to the shale data (thin black line) as in Figure 9-21a. A line drawn orthogonally to the shale line will pass through the sand region (circled yellow). The shale line is a principal-component direction and its orthogonal is also one. If we rotate the data (x- and y-axes) to their principal directions, then we can separate the sands from the shales while looking at a single dataset. Rotation of the data to their principal directions is shown in Figure 9-21b. The equations to rotate from the original axes (x and y) to new principal component directions (x' and y') are shown. Prior to rotation, the line that fits the data has to have a y-intercept of zero. This is done by shifting the data in the y-direction by the y-intercept amount of the original shale-line fit to the data (9-21b). The data are then rotated (Figure 9-21c). The rotation angle is the inverse tangent of the slope of the shale-line (e.g., 1.23 in this case). After rotation, the data will fall along the principal directions and we can look at the new y'-direction.

Simultaneous inversion. Simultaneous AVO inversion uses a set of partial-offset or angle stacks, each with their own wavelets, plus low-frequency models for P-impedance, a shear measure (e.g., S-impedance) and density to estimate simultaneously, inversion volumes for P-impedance, the shear measure and density. This algorithm, described by Mesdag et al. (2003) and Pendrel et al. (2000) uses the exact Zoeppritz equations in a mixed-norm, non-model-based, sparse-spike implementation with arbitrary low-frequency control from a geologic model.

A pre-stack model-based simultaneous inversion algorithm to estimate P-impedance and S-impedance from PP angle gathers has been described by Hampson et al. (2005). The method is based on a linearized AVO inversion as described by Buland and Omre (2003). The constraints are used in a non-Bayesian way, and the inversion is for impedance and density rather than velocity and density. The algorithm is based on

Downloaded 25 Jun 2012 to 95.28.162.50. Redistribution subject to SEG license or copyright; Terms of Use: http://segdl.org/

three assumptions: reflectivity is a linear process, PP and PS reflectivity are described as a function of an incident angle, and there is a linear relationship between P- and S-impedance and density.

Inversion results (P-impedance, S-impedance, and the V_p/V_s) can be transformed to the elastic attributes of lambda-rho (λ-ρ) and mu-rho (μ-ρ). These elastic attributes are helpful in discriminating between lithologies and fluid properties. Density, itself, is difficult to estimate with certainty from most seismic surveys, since, for angles less than 50°, it usually is not possible to differentiate between density and shear effects.

It is advantageous to invert all the stacks simultaneously because the results can yield compressional- and shear-wave velocities and density or any combination of those, as well as the acoustic impedance and shear impedances. When using only a post-stack seismic inversion, there is often overlap in lithologies and fluids, and these can be discriminated with pre-stack inversion methods. Simultaneous inversion, however, requires an a priori model of the low frequencies for P-impedance, S-impedance, and density. It is also important to have excellent preprocessing of the seismic data. Accurate moveout to subsample accuracy is critical in achieving reliable quantitative results. Knowledge of the basin is imperative, and any information that is known should be included in the model, along with a detailed stratigraphic interpretation.

AVA (amplitude variarion with angle) geostatistical inversion. Advanced methods are also available that will allow the user to analyze the uncertainty associated with the final volumes. This is critically important in deciding whether to drill in an area. The applications combine the advantages of AVA analysis with those of geostatistical inversion. For a discussion of the process and uses, see Eidsvik et al. (2004), Contreras et al. (2005), and Merletti and Torres-Verdín (2006). This process, because it combines seismic with a stochastically derived model, can increase the resolution (on the upper end of the frequency as well as on the lower end). The increase in resolution is where much of the uncertainty lies. The results are a set of realizations, which are all possible, based on the input data. Uncertainty information can be derived from an analysis of the variance in the realizations.

Which Inversion Method Do I Use?

Because so many inversion methods are available to the interpreter, it may appear to be a daunting task to determine which inversion method is appropriate for a given area and data set. The easy answer is to always start simply. Working from the top of the list will allow the interpreter to analyze the data and determine whether they are suited to a certain type of inversion. The first question to ask is: What do I want to learn? Some additional questions are

- When I look at the log data and analyze acoustic impedance versus a lithology log, do target lithologies become apparent? Does this remain the case at seismic frequency ranges (band-limited data)?
- When I look at the log data and analyze acoustic impedance versus fluid data, can water, oil, and gas be discriminated?
- What are the frequencies in the seismic data? What are the tuning frequencies? Am I interested in beds that are below resolution of the seismic?
- Do I have a good understanding of my geology and can I create a reasonable three-dimensional structural and stratigraphic model?
- Am I looking for stratigraphic events? Will I want to see channeling, or channel fill, or am I trying to create the regional picture to determine what play types are present?

Inverting the data using one of the post-stack simple methods may aid in answering most of these questions. I would start with one of the first six methods above, using the inversion results to help refine the interpretation. In that process, by necessity, the wells will be tied to the seismic, the phase of the seismic will be determined, crossplots of the well data will be analyzed, and knowledge of the rock property relationships will be derived.

Downloaded 25 Jun 2012 to 95.28.162.50. Redistribution subject to SEG license or copyright; Terms of Use: http://segdl.org/

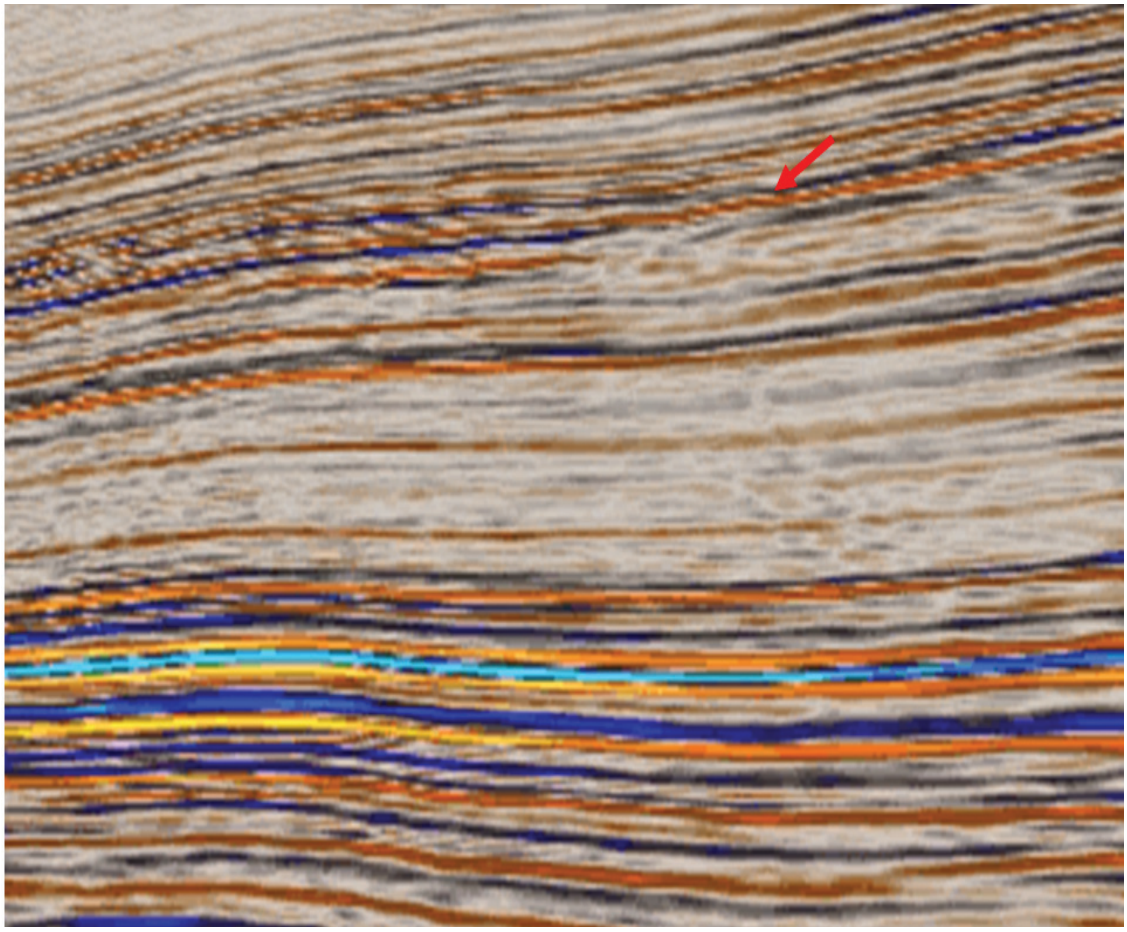

Figure 9-22. Migrated seismic amplitude data. Can you see the migration problems? The red arrow indicates where the parallel reflectors change to "hummocky." (From Sheffield and Payne, 2008. Used by permission.)

Analysis of the data will allow the interpreter to choose one of the more advanced algorithms, again starting simply with model-based and/or an angle inversion and moving to the more advanced and detailed process as knowledge is increased. Prospect delineation is well suited to the advanced methods. The faster and simpler inversions can be used for reconnaissance, and the more computer-intensive inversions can be used for 3-D or 4-D development or delineation.

In the first section of this chapter, we discuss the impact of converting from band-limited seismic data to broadband impedance data. It is important to understand which data you have available (band-limited or full-band).

When one is working with band-limited or relative data, there are pitfalls:

- the data are *relative* elastic values and therefore will not match the *absolute* values at the well,
- the data are only valid where you can calibrate to well data and will be relative elsewhere. An identical value of a band-limited impedance may mean something quite different, shallow versus deep or laterally away from the calibration well, and
- the data are similar to seismic and thus will have the same difficulties as seismic data, in that lithologies or fluids may be very difficult to determine and there may be lots of crossplot overlap in values.

When one is working with full-band data in which the low frequencies have been replaced in some manner, there are also pitfalls:

- artifacts might result from an incorrect or inaccurate interpolation of the low-frequency data,

Downloaded 25 Jun 2012 to 95.28.162.50. Redistribution subject to SEG license or copyright; Terms of Use: http://segdl.org/

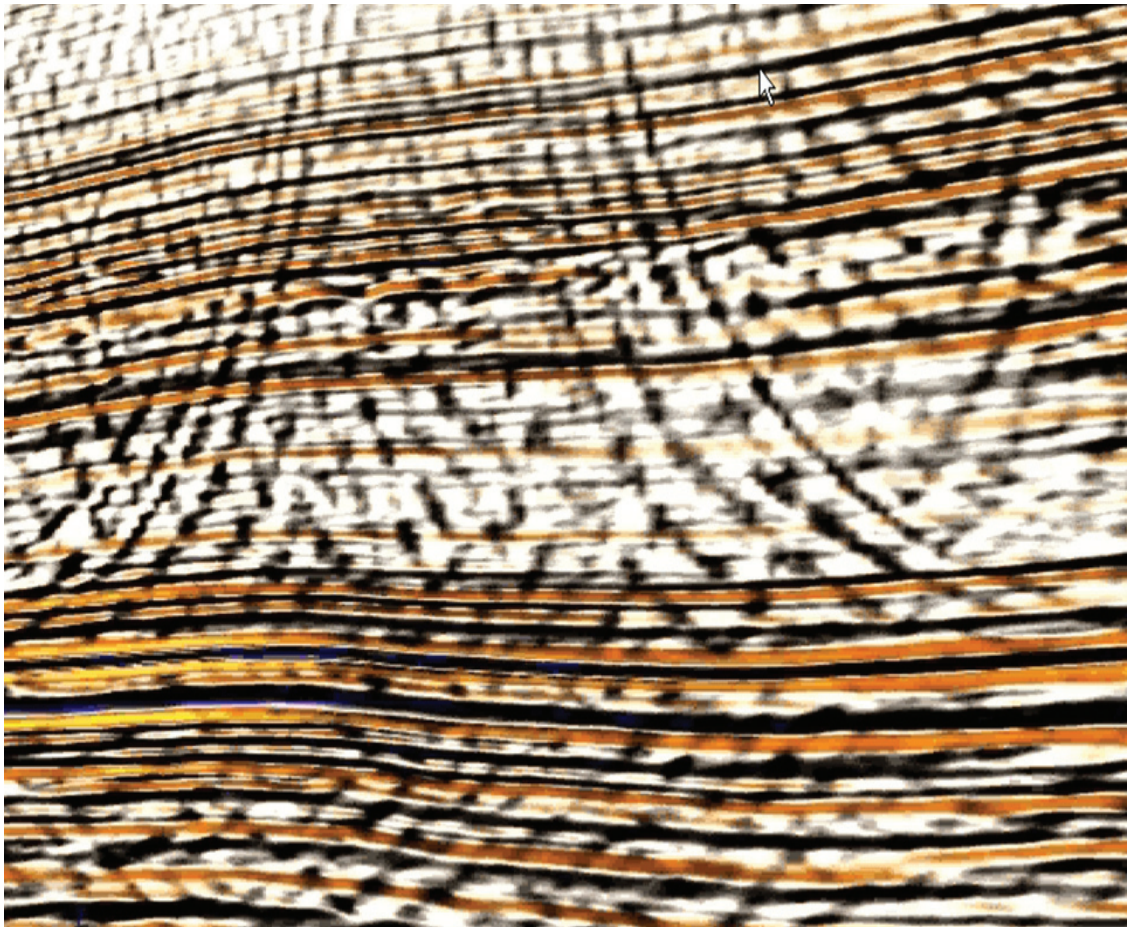

Figure 9-23. Migrated seismic amplitude data from Figure 9-22, with relative acoustic impedance (RAI) data overlain as a light texture. This technique is used as a quality-control tool prior to completion of a full inversion or any attribute analysis. (From Sheffield and Payne, 2008. Used by permission.)

- it may be difficult to display full-band seismic on a traditional workstation that is designed for seismic data and displays only positive and negative values. The entire dynamic range of the data may not be visible. The data may also be clipped when loaded onto a traditional workstation. A work around to this problem is to subtract a constant value prior to loading to ensure that the data-loading operation does not include a large "scale and clip" process, and
- often the low frequencies are overcompensated for and the results "overprint" the details of the inversion.

The best way to solve the pitfalls above is to use the band-limited and full-band data together to understand the rock properties and assess the quality of the inversion products. If the inversions look unusual (do not match well data, have large and quick lateral changes not found in the geologic concepts, are not as high resolution as the seismic), ask about the process. Inversion is NOT a black box and many things can go wrong. The interpreter is the best person to assist the processor with the inversion process. Inversions use seismic data, so if the seismic is of poor quality, the inversion result will also be of poor quality.

Inversion data can be a wonderful interpretation tool if used correctly. They can clarify well ties, assist in correlation problems, and provide an additional medium for interpreting channels, lithologies, fluids, and velocities. Inversion is not just a tool for quantification of lithology and fluids; it can qualitatively assist the interpreter. Below are some examples.

Quality Control of Input Data

The quality of the final inversion is a direct result of the quality of the input data. To objectively estimate the accuracy of any inversion cube, the interpreter should be

Downloaded 25 Jun 2012 to 95.28.162.50. Redistribution subject to SEG license or copyright; Terms of Use: http://segdl.org/

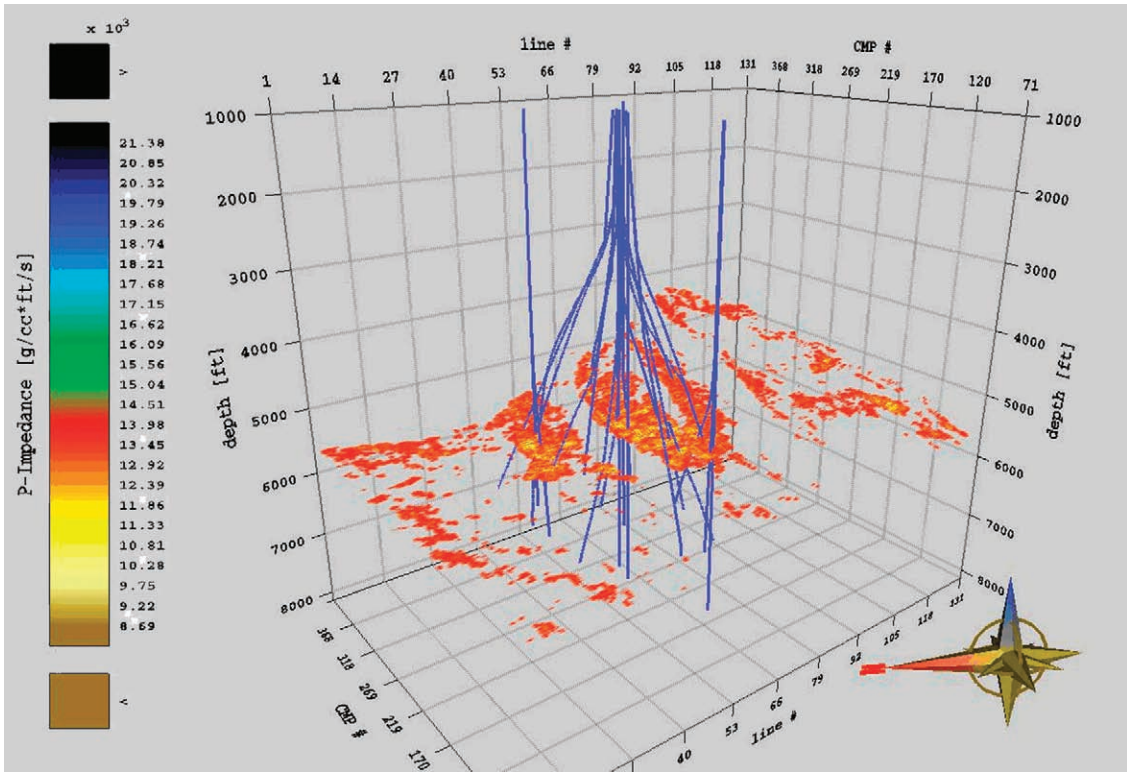

Figure 9-24.
Transparency applied to the nondesired acoustic-impedance range. This analysis highlights only the target reservoir or target rock property. (From Latimer et al., 2000. Used by permission.)

familiar with the input data and what processes were applied to invert the data. A comprehensive inversion report is a powerful source of information, but if it is not available some key items should be examined: seismic processing information, inversion algorithm, date and workflow, well-spud details, and log processing. Depending on the inversion method, the data types may include post-stack seismic data (full fold as well as angle stacks), well-log data, and a set of preliminary time or depth horizons.

A recursive or trace integration can be utilized when one is assessing the quality of seismic data for acquisition or migration artifacts. Many seismic-attribute packages have very easy and quick algorithms with what they call RTI (recursive trace inversion) or RAI (relative acoustic impedance) available. Figures 9-22 and 9-23 show a recent example of utilization of recursive trace inversion as a seismic quality-control tool. Figure 9-22 displays a vertical seismic section. The events show a character that is sometimes referred to as "hummocky" and is often interpreted as indicative of sand-filled events. See the location of the red arrow, where the parallel reflectors change to hummocky.

Figure 9-23 shows the same line and the same amplitude data in black and white, with an RAI data set overlain. The peak values are corendered with a light texture display. Note the large data artifacts. The "hummocky sands" are in fact artifacts of the data acquisition and processing.

Prior to inversion, examine the well logs for suitable relationships between measured impedance logs (calculated by dividing the density by the sonic log) and other desirable properties, such as porosity and fluid fill. Well logs should be converted to time and filtered to the approximate bandwidth of the seismic to determine if zones of interest are recognizable at the frequencies expected after inversion. All well logs should be edited for borehole effects, balanced, and classified on the basis of quality. Logs that do not tie the seismic should be investigated for problems in log, wavelet, or seismic data.

When one is inverting, it generally is preferable to run a loosely constrained, trace-based inversion first. The inversion can then be used for a more thorough interpretation. This initial inversion can be followed by a more tightly constrained or model-based inversion, as the need arises, to meet the particular project's interpretation objectives. With trace-based inversion, the process begins with the seismic

Downloaded 25 Jun 2012 to 95.28.162.50. Redistribution subject to SEG license or copyright; Terms of Use: http://segdl.org/

data, possibly augmented with limited nonseismic data (trend data derived from velocities or wells). With model-based inversion, additional weight is given to the nonseismic data in addition to the seismic trace data. Nonseismic data do not necessarily need to be captured in the form of a model. For example, methods that also use constraints or information about statistical distributions are also considered model-based. This distinction between trace-based and model-based is important with regard to the quality assessment of the results, as will be shown in the next section.

Interpretation of Impedance Data — General Considerations

The first item to notice about full-bandwidth AI data is that all the values are positive. The positive values should tie with the well impedance values when the well impedance data are high-cut filtered to the seismic data range. As pointed out above, these positive values pose a problem when one is attempting to analyze the results on a traditional seismic interpretation workstation designed for the positive and negative values found in seismic data. Filtering the data to create a relative impedance data set will allow improved visualization of the data, since the data now contain positive and negative values that allow for seismic-type tracking.

The problem with the traditional workstation approach is that AI data are treated as though they are seismic. Once it is understood that inverted AI data represent rock properties, it becomes much easier to extend methods of interpretation beyond traditional 2-D or 2.5-D interpretation. In fact, impedance data make true 3-D interpretation not only possible but also the technique of choice. With a known relationship between AI and a desirable lithologic parameter such as porosity or sand/shale fraction, the entire AI volume can be examined. Targets of interest may be quickly extracted from the inverted data by capturing the top, bottom, and areal extent of the target body (Figure 9-24).

Variations of the lithologic property within these "geobodies" can be included in volumetric calculations. Generally, this type of analysis is done using well data to establish a relationship among reservoir elastic impedances and density and known rock properties within specific target zones and within the frequency range of the inverted data set. For example, in post-stack inversion work, establish the cutoff value using a crossplot between AI and another parameter, for example a lithology or fluid. Limit the lateral and vertical range of the AI volume to the zone of interest, either by defining a time or depth range around a horizon, or by focusing around a specific lithologic unit. As seen in Figures 9-5 through 9-7, limiting the target zone can be critical to proper analysis. Finally, apply the cutoff to the target zone. It may be important to apply a size or economic threshold to the data after the bodies are visible, in order to eliminate the very small bodies or the scatter.

When analysis can be completed in this manner, it makes interpretation of acoustic impedance very easy. A relationship between the well data is known and the effect of frequency limitations is obvious. All of the interpretative advantages listed above also apply to the inversion of angle-stack data into elastic impedance (EI). Discrimination of lithology and fluid content is further enhanced when comparing AI (near-angle) and EI (mid- or far-angle) data.

Impedance Interpretation When the Relationship Is Unclear

Sometimes when one is using the simplest of post-stack inversions, the relationship between rock properties and impedance results are not clear, especially when using "band-limited" impedance data. When this happens, I often hear interpreters say *"We didn't use the inversion in my area, it doesn't work."* Whether or not the inversion arrives at a clear quantitative relationship, it can still be used qualitatively. Generally, it can be utilized as an additional data volume to clarify stratigraphic relationships.

In a recent project, the following workflow was utilized, thereby improving the interpretations greatly:

- Tie the well logs to the seismic. Make a first-pass interpretation of the seismic

Downloaded 25 Jun 2012 to 95.28.162.50. Redistribution subject to SEG license or copyright; Terms of Use: http://segdl.org/

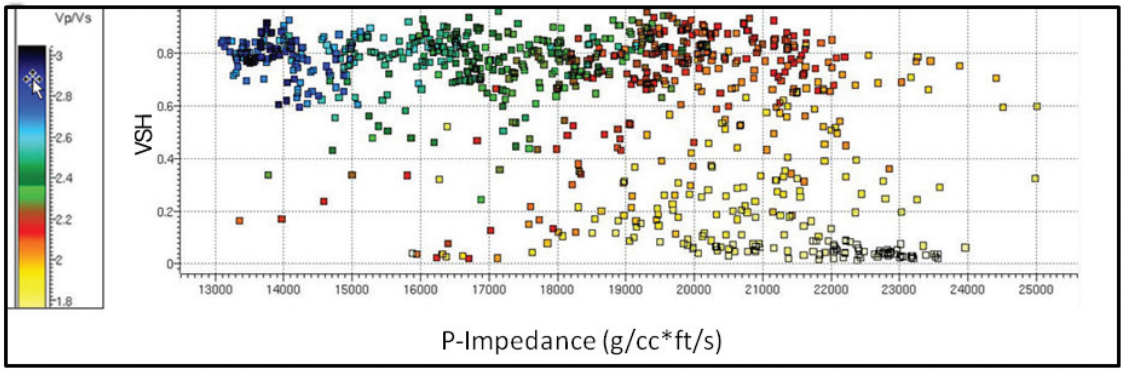

Figure 9-25. Crossplot of VSH vs acoustic impedance. Notice that in this case lithology is not distinct. The plot is color coded by V_p/V_s.

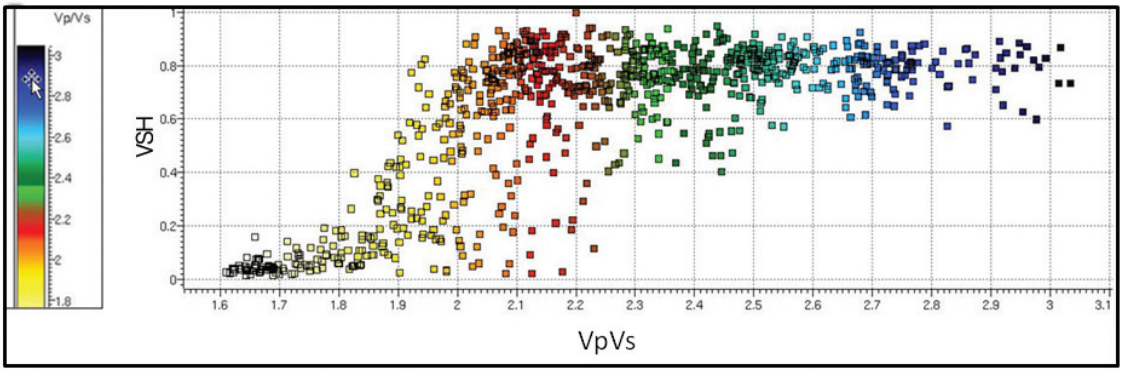

Figure 9-26. Crossplot of VSH vs V_p/V_s. Notice that the sands in yellow and light reds are easily separated from the shales in the dark colors.

using the most obvious events (usually the condensed sections if in deep water and the flooding surfaces in shallow marine data).

- Create a first-pass inversion. The regional surfaces created above are utilized in constraining the inversion. Create a synthetic and extract a wavelet. Petrophysical editing and calibration of the sonic (acoustic-log) and the density-log data will improve the impedance logs and wavelet extraction. Extract velocity data at the well location, to be utilized in depth-to-time conversion.
- Utilizing the band-limited inversion results (post-stack), refine the interpretation of the surfaces. Determine a relationship among sands, shales, wet sands, or hydrocarbon-filled sands, using crossplots. High-cut filter the well data back to the seismic frequency range to create the crossplots and to determine if a relationship exists between AI and any of the lithologies or fluids in the range of the seismic frequencies.
- Once a stratigraphic framework is complete, utilize stratal slicing between the major sequences, to visualize the channel complexes (using the AI data volume). Even if the cutoff relationship is not clear, geologic features can often still be seen. If this does not work well, there are some common errors to consider:

  1) The interpretation of the surfaces MUST follow stratigraphic surfaces and should not cross stratigraphy.
  2) Extract values in a small enough interval. In other words, when one is averaging too many data points (cells) together vertically, geologic features may be obscured.

- If the crossplots and these processes above do not highlight the stratigraphy, I would suggest embarking on a higher-order inversion. I would start with the simple angle-impedance inversion but would probably calibrate it to a very small simultaneous inversion. Simultaneous inversion is computer intensive, and it is

Downloaded 25 Jun 2012 to 95.28.162.50. Redistribution subject to SEG license or copyright; Terms of Use: http://segdl.org/

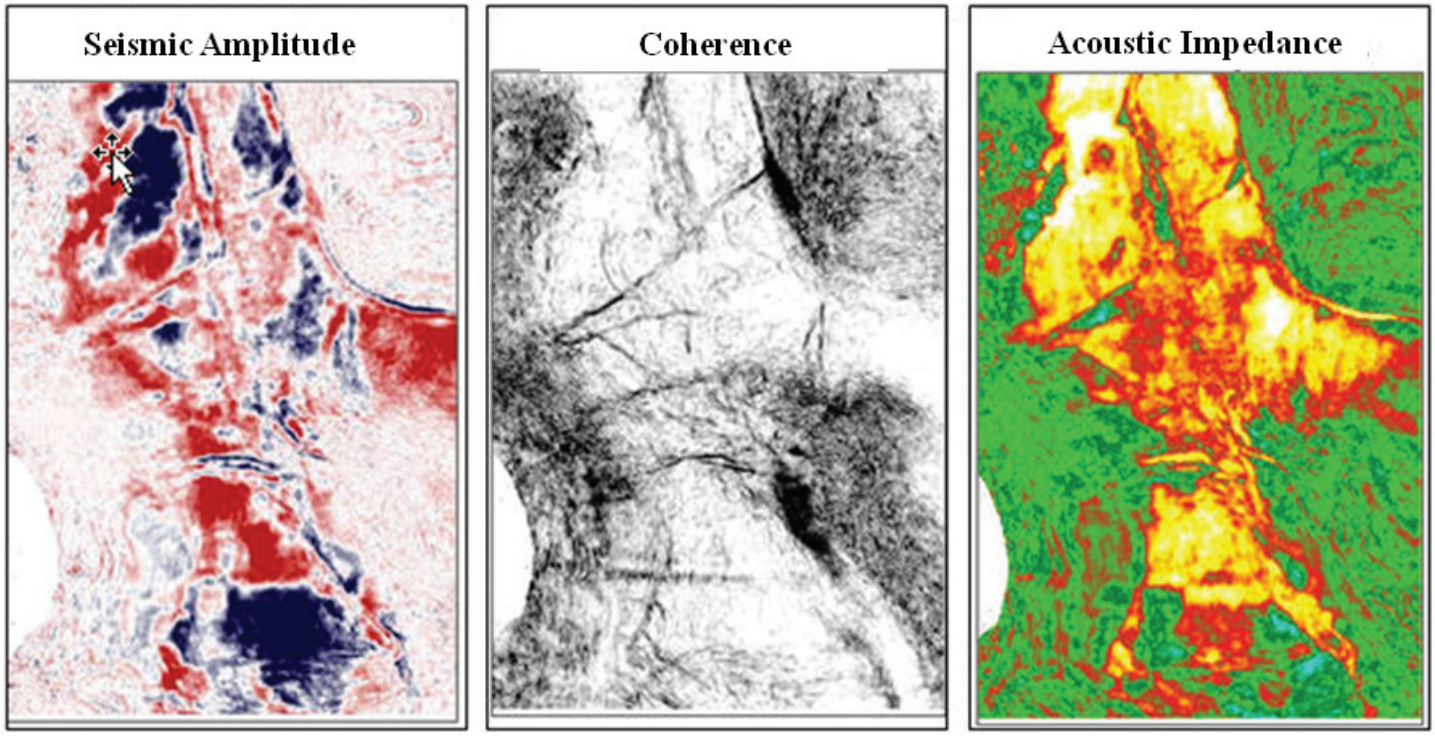

Figure 9-27. Three examples of stratal slices: seismic amplitude data (left), Coherence data (middle) and inverted acoustic impedance data (right) to help unravel the interpretation. Each adds to the story.

possible that the angle inversion will be sufficient. To point out a recent example, the angle inversion ran overnight for an entire block, but the simultaneous inversion took nine days for a much smaller area. Figure 9-25 shows a crossplot of VSH versus acoustic impedance (P-impedance). Note that there is not a clear relationship between VSH and impedance. Figure 9-26 shows a plot of VSH versus V_p/V_s where a relationship between low values of shale and V_p/V_s can easily be extracted.

- Once the angle inversion is complete, the method in Figure 9-21 can be used to create a pseudo-lithology cube.
- The pseudo-lithology cube can be used to corender with the seismic data. A pseudo-lithology cube created in this manner will have a lower frequency than the seismic data but should contain an indication of your sands or shales.

Figure 9-27 shows three sets of stratal slices. The left panel shows a stratal slice from seismic amplitude data. The center panel is a type of coherence display of the same slice, and the right panel is the slice from the inverted acoustic-impedance data. Each attribute shows distinct differences and highlights different important characteristics. Seismic data typically can yield stratigraphic information (onlap, toplap, and various internal configurations), as well as aid in determining the stratigraphic relationships. Seismic will assist in developing the regional picture, will show changing sea levels, and will add to the determination of lithology when the phase and rock property information is known. The amplitude slices must be used with caution, avoiding interpretation of tuning as being hydrocarbon-bearing units. The coherence display is useful in highlighting the sides of channels, faults, or any abrupt changes seen in the data. In this case, a sinuous channel and crosscutting (E-W) faults can be seen. The acoustic-impedance data, or the pseudo-VSH or the V_p/V_s, is useful in determining the lithology type or the fluid content. Using all three of these data sets simultaneously yields a clearer picture of the geology than any of these data sets can yield in isolation.

Downloaded 25 Jun 2012 to 95.28.162.50. Redistribution subject to SEG license or copyright; Terms of Use: http://segdl.org/

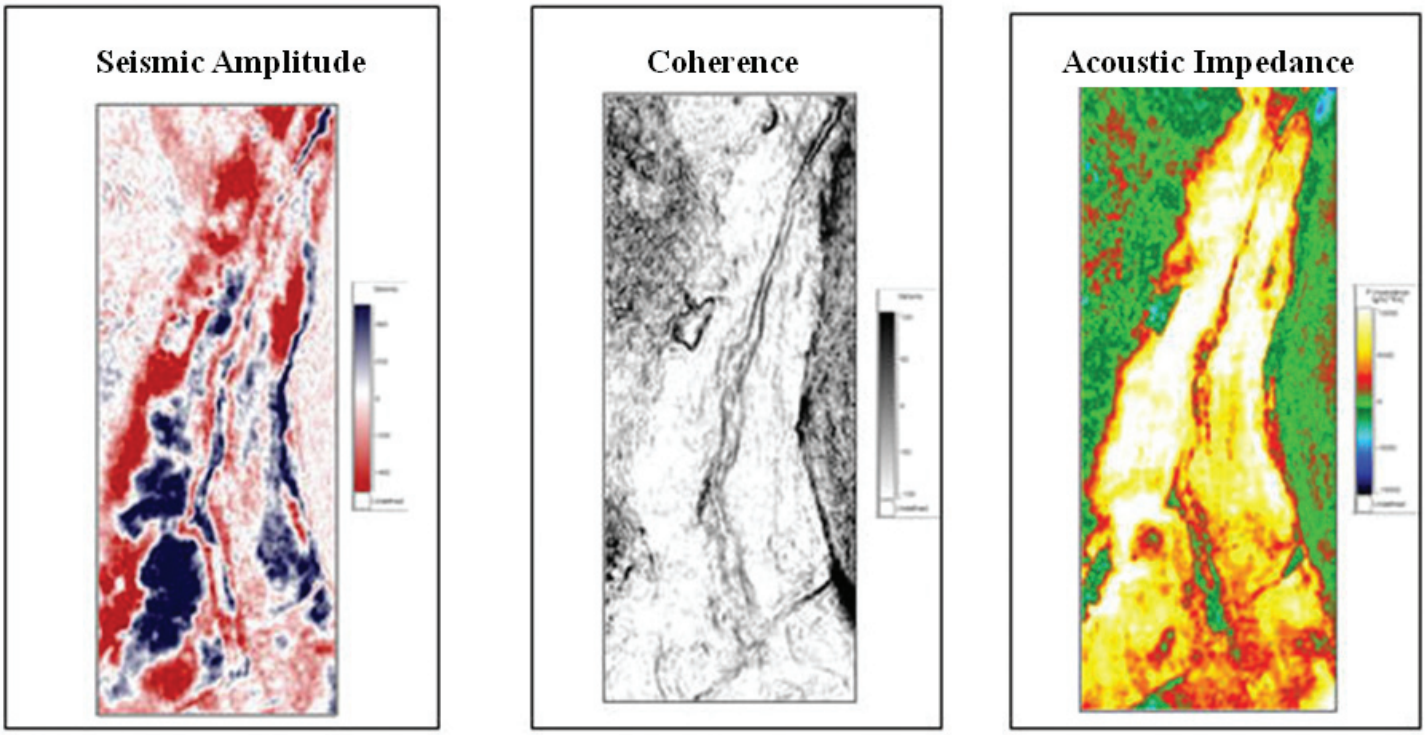

Figure 9-28. Three examples of stratal slicing: seismic amplitude data (left), coherence data (middle), and inverted acoustic-impedance data (right) to help unravel the interpretation.

The amplitude data in Figure 9-27 show areas of peak and trough amplitudes, both appearing bright. In this area of the world, the amplitudes are not diagnostic of lithologies or hydrocarbons. The acoustic-impedance data were derived using near and far trace volumes and have been converted into a pseudo-VSH using the technique in Figure 9-21. The bright yellow therefore represents probable sands. Because the data are not perfect in that they do not have extra-long offsets and because calibration is difficult due to sparse well control, a number of assumptions must be made.

Even with the less-than-perfect data, some interpretations can be made using all of the available data:

- The amplitude cannot yield lithologies accurately. Both the peaks (blue) and the troughs (red) are interpreted as sands in the VSH volume.
- The channel in the coherence slice appears on the VSH volume as shale filled in the upper portion and sand filled where it becomes sinuous.
- The container has sharp edges.

Figure 9-28 is from the same area, only the image is zoomed out to gain a larger view of the area. The container is now seen as being expanded to the south and has become less constrained. The section to the top of the slice seems to contain thicker sands. The central channel carries sands until a change in slope occurs where it shales outward, and a bypass in the channel merges. All three slices contribute to the story. The overbank is apparent on the amplitude data, the channel is clear on the coherence data, and the fill is easier to see on the VSH from impedance data.

Figure 9-29 is an example from another block. Notice the sinuous channel that is

Downloaded 25 Jun 2012 to 95.28.162.50. Redistribution subject to SEG license or copyright; Terms of Use: http://segdl.org/

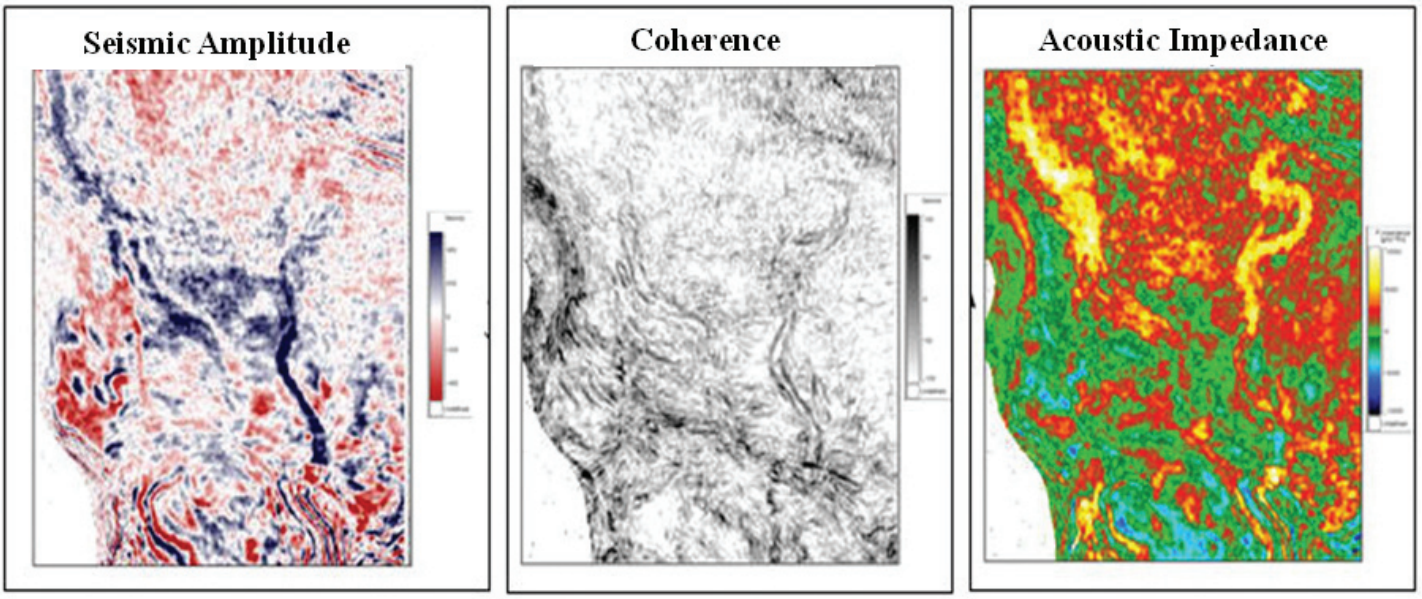

Figure 9-29. Three examples of stratigraphic slicing: seismic amplitude data (left), coherence data (middle), and inverted acoustic-impedance data (right) to help unravel the interpretation.

clear on all three slices. The amplitude data do not display the curve in the channel as well as the coherence data do, and since the channel appears to be sand filled, the VSH from impedance data highlights the channel clearly. The southernmost portion of the channel turns blue on the seismic and appears to become shalier on the inversion.

Utilizing the amplitude data for the fine details, the coherence data for highlighting faults and channel boundaries, and the impedance results for lithology, helps one to complete a stratigraphic history of the area. In section view, the seismic is used as a backdrop with the VSH from impedance as a corendered volume with shales as transparent.

Acoustic impedance can often be used as a tool to improve the structural and stratigraphic interpretation. The example shown in Figures 9-30 through 9-33 illustrates the use of acoustic impedance for well tie. Figure 9-30 is a base map showing a field area with deviated wells. Deviated wells are often difficult to tie to seismic. In this case, traces have been pulled along the boreholes shown in black to the center of the platform, and along the direction of the arrow, in order to unfold the seismic and check the well tie to seismic. Figure 9-31 shows the seismic data along these traces.

The interpreter has made a first pass at an interpretation based on the seismic character and the well-marker data that were provided. Clear, mappable events are not apparent. The area contains a large carbonate bank. The seismic rock properties do not indicate that acoustic impedance would be diagnostic of lithology or hydrocarbons. The carbonates are very hard (high velocity and density), so with the introduction of porosity or hydrocarbons, the acoustic impedance would decrease and might overlap with the background shale. An inversion was performed in order to assist in tying the well data and to provide pseudo-checkshot data. The results of the band-limited inversion are shown in Figure 9-32.

Downloaded 25 Jun 2012 to 95.28.162.50. Redistribution subject to SEG license or copyright; Terms of Use: http://segdl.org/

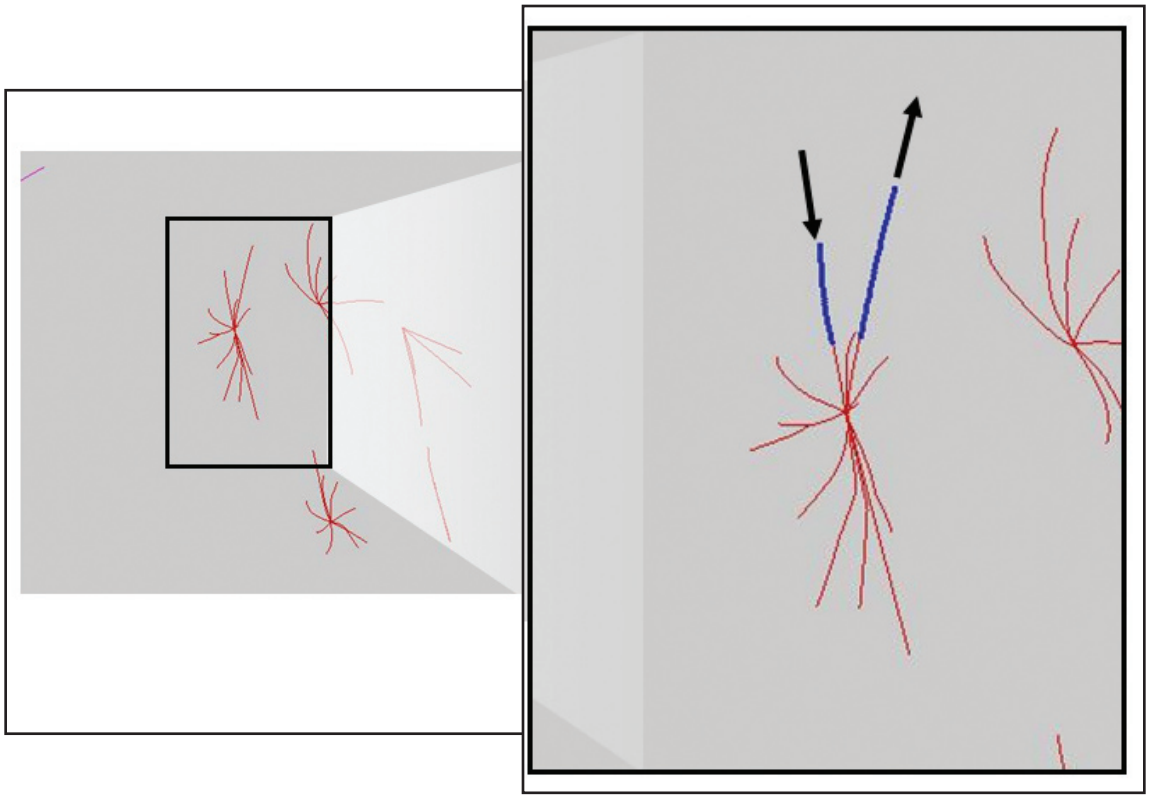

Figure 9-30. Base map for Figures 9-31 through 9-33. Each platform contains numerous deviated wells.

Well-log data overlain on the inversion show that the wells are not tied correctly to the seismic or inversion results. These wells were not used in the inversion process. Well #1 (left) appears to be tied correctly around 1950 ms but not at 2000 ms. When the checkshot data were investigated, it was found that the interpreter used only one checkshot for all wells in the region. Correct checkshot data (located in paper form in a box) for this well moved the well slightly to the right, tying it exactly with the impedance data. Well #2 (center) has nearly the correct TD relationship, but the density log required petrophysical editing. Once that was completed, the well data tied the seismic. Well #3 (right) had an incorrect marker for the top of the carbonate bank. The marker was moved to a shallower position, at the top of the orange event at 1940 ms.

When one is learning to use acoustic-impedance data as an interpretation tool, it is advantageous to overlay the seismic data as wiggle traces. Corendering the data can allow the interpreter to visualize the impedance data with respect to the seismic data that he or she is comfortable with and used to seeing. In Figure 9-33, the wiggle traces are overlain by skipping every two lines and traces so that the impedance data are visible below the seismic traces.

Figure 9-33 illustrates why the interpreter had difficulties mapping the top of the carbonate bank in yellow. The seismic does not image the event clearly. There is a decrease in impedance, due to the pososity, but the decrease is subtle. When the seismic is properly tied to the well data, the carbonate bank is easier to discern. The act of creating the inversion, correcting the well data, and inverting the seismic, has improved the interpretation. The process of inversion caused minor details to be revisited, resulting in a new and improved understanding of the basin. Since the carbonate bank is similar in rock properties to a variety of geologies in this section, prescreening the rock properties in the well data did not tell the entire story.

Downloaded 25 Jun 2012 to 95.28.162.50. Redistribution subject to SEG license or copyright; Terms of Use: http://segdl.org/

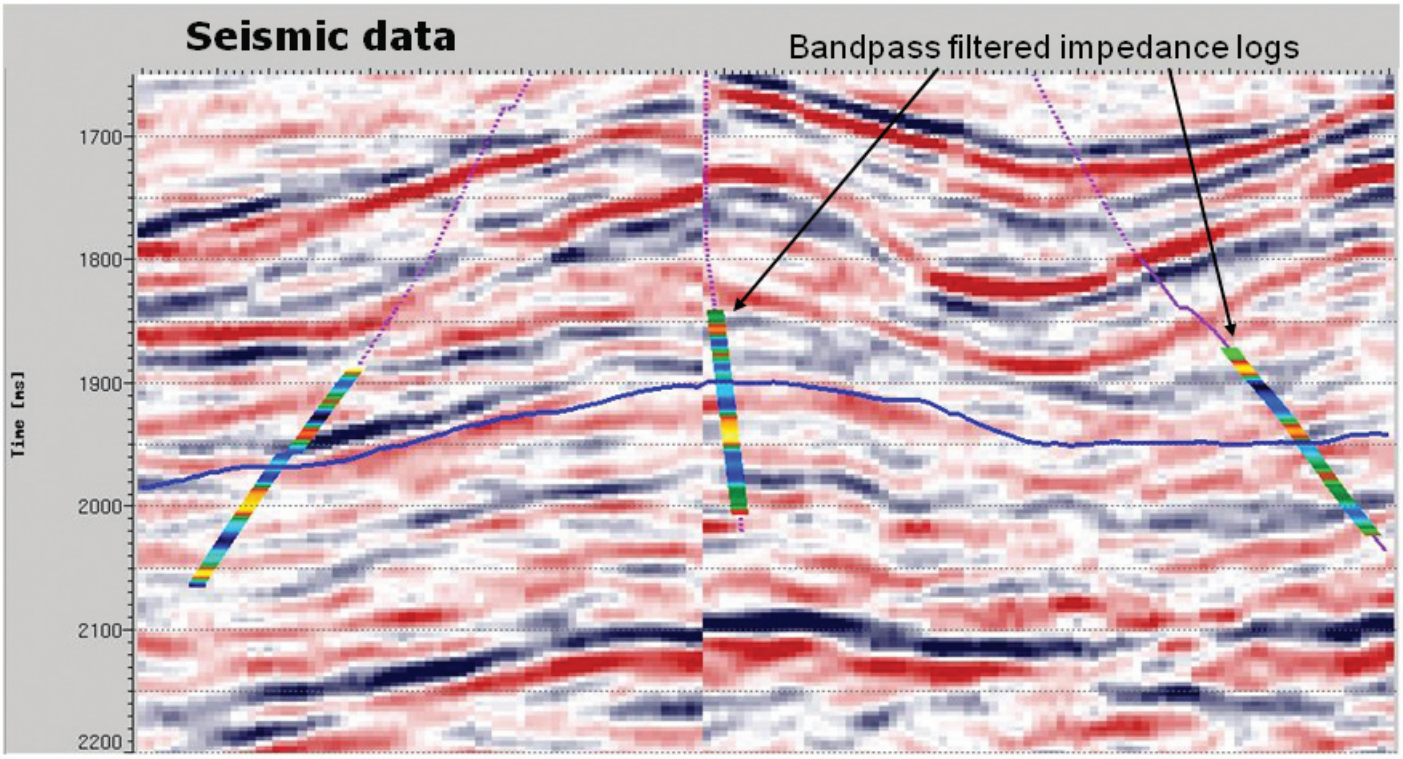

Figure 9-31. Seismic data displayed along the deviated track, through the center borehole, and along the second deviated track. Note the first pass of interpretation, honoring the well picks and a skipped trace at the center fold.

Key Messages

- Success of an inversion depends on data quality and on successful extraction of the proper wavelet.
- Scale differences between seismic, well data, and outcrop models can adversely affect statistics.
- Acoustic-impedance inversion can significantly improve data interpretation because:
  - it is not critical whether the inversion is diagnostic of rock properties or porosity,
  - interpreting on rock layers (changes), not interfaces, is an important benefit, and
  - interpretation of AI data can be automated in 3D.
- Low-frequency data are difficult to obtain but important in creation of accurate full-band data.
- One should use both inversion data and seismic data together because:
  - one is forced to tie well data for wavelet extraction,
  - it is much easier to compare well data with impedance results, and
  - one does not need to deal with the data phase because it is already handled in the wavelet extraction process.

Downloaded 25 Jun 2012 to 95.28.162.50. Redistribution subject to SEG license or copyright; Terms of Use: http://segdl.org/

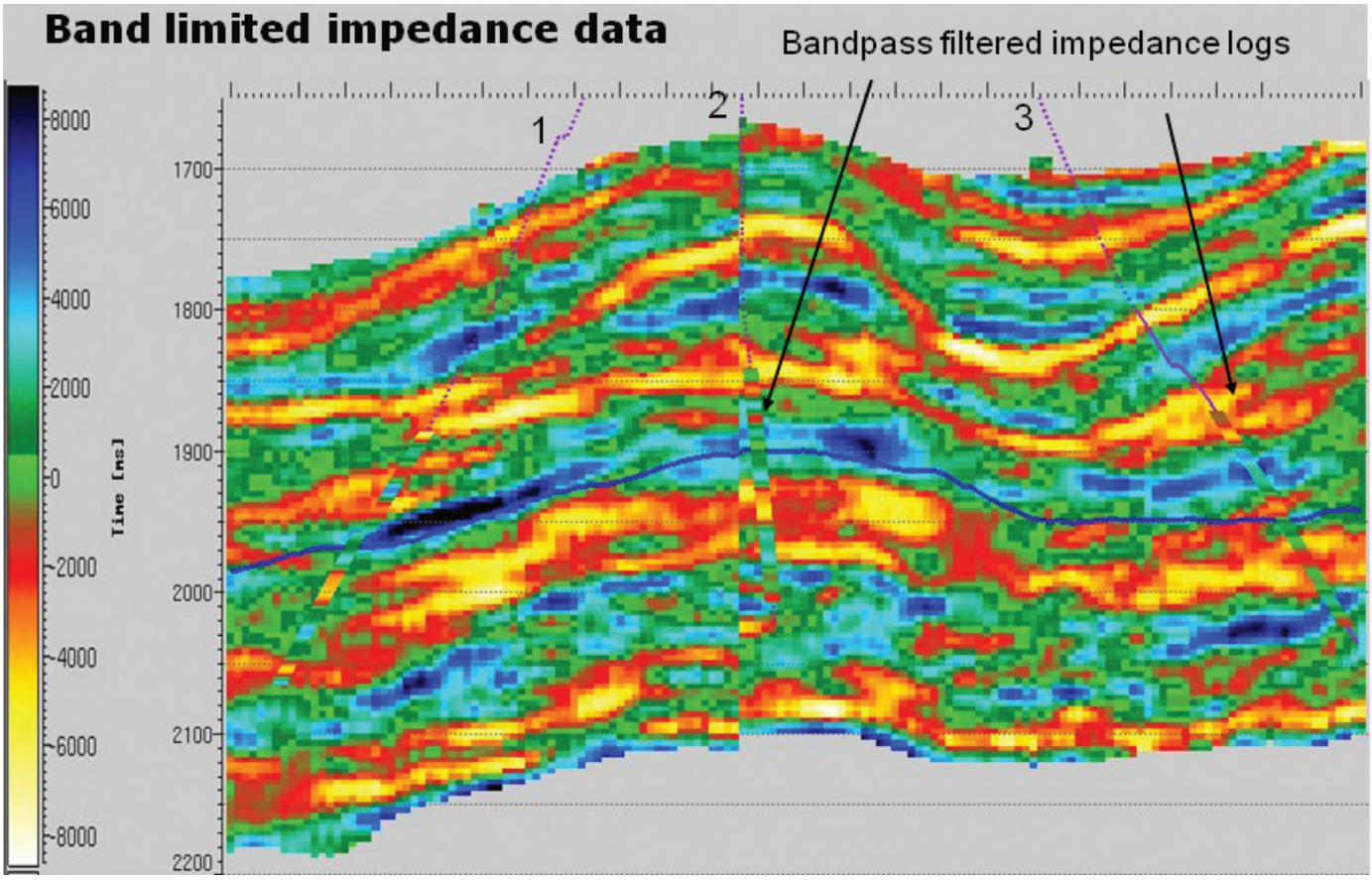

Figure 9-32. Band-limited inversion created using a constrained sparse-spike inversion (CSSI). Band-pass filtered well-log data are overlain.

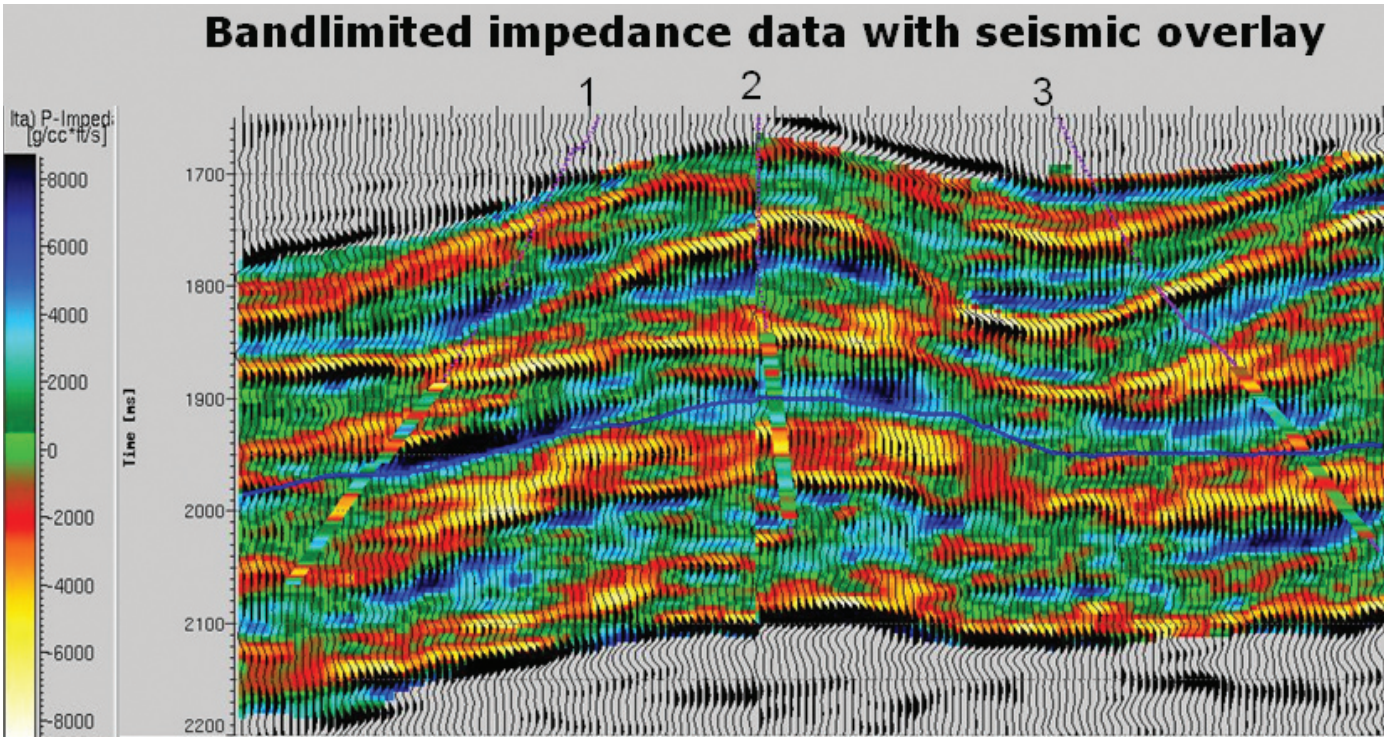

Figure 9-33. Band-limited inversion from Figure 9-32, with seismic traces overlain.

Downloaded 25 Jun 2012 to 95.28.162.50. Redistribution subject to SEG license or copyright; Terms of Use: http://segdl.org/

Acknowledgments

I would like to acknowledge John Pendrel, Brian Russell, Bill Abriel, and Madonna Smith for their suggestions and review of the manuscript. Their encouragement is most appreciated.

References

Aki, K., and P. G. Richards, 2002, Quantitative seismology, 2nd edition: University Science Books, 704 p.

Anderson, J. W., and M. A. Bogaards, 2000, Quantifying fluid prediction using angle-dependent inversion measured against log fluid substitutions: SEG, Expanded Abstracts, v. 19, p. 1493–1496.

Buland, A., and H. Omre, 2003, Bayesian linearized AVO inversion: Geophysics, v. 68, no. 1, p. 185–198.

Connolly, P., 1999, Elastic impedance: The Leading Edge, v. 18, p. 438–452.

Contreras, A., C. Torres-Verdín, W. Chesters, K. Kvien, and T. Fasnacht, 2005, Joint stochastic inversion of 3D pre-stack seismic data and well logs for high-resolution reservoir characterization and petrophysical modeling: Application to deepwater hydrocarbon reservoirs in the central Gulf of Mexico: 75th Annual International Meeting, SEG, Expanded Abstracts, v. 24, p. 1343–1346.

Dubucq, D., S. Busman, and P. Van Riel, 2001, Turbidite reservoir characterization: Multi-offset stack inversion for reservoir delineation and porosity estimation; A Gulf of Guinea example: SEG, Expanded Abstracts, v. 20, no. 1, p. 609–612.

Eidsvik, J., P. Avseth, H. Omre, T. Mukerji, and G. Mavko, 2004, Stochastic reservoir characterization using prestack seismic data: Geophysics, v. 69, no. 4, p. 978–993.

Glenn, D., K. Hariyannugraha, R. Schneinder, K. Kirschner, S. Walden, S. Smith, E. Berendson, C. Skelt, L. Lisapaly, R. van Eykenhof, and M. Sams, 2005, Enhancing consistency between geological modeling and seismic pre-stack amplitude inversion with pseudo-wells: An example from the Gendalo field: Proceedings, Indonesian Petroleum Association Thirteenth Annual Convention and Exhibition, IPA05–G-029, p. 433–445.

Hampson, D. P., B. H. Russell, and B. Bankhead, 2005, Simultaneous inversion of pre-stack seismic data: 75th Annual International Meeting SEG, Expanded abstracts, v. 24, p. 1633–1637.

Jarvis, K., A. Folkers, and P. Mesdag, 2004, Reservoir characterization of the Flag Sandstone, Barrow sub-basin, using an integrated, multiparameter seismic AVO inversion technique: The Leading Edge, v. 23, no. 8, p. 798–800.

Latimer, R. B., 2005, Uses, abuses, and examples of seismic-derived acoustic impedance data: What does the interpreter need to know, AAPG/SEG Distinguished Lecture: http://www.seg.org/SEGportalWEBproject/portals/SEG_Online.portal?_nfpb=true&_pageLabel=pg_gen_content&doc_URL=prod/SEG-Education/Ed-Presentation-Library/Dl-Presentations/fall2005/presentation.htm, accessed December 2009.

Latimer, R. B., R. Davison, P. van Riel, 2000, An interpreter's guide to understanding and working with seismic derived acoustic impedance data: The Leading Edge, v. 19, p. 242–256.

Lindseth, R. O., 1979, Synthetic sonic logs — A process for stratigraphic interpretation: Geophysics, v. 44, p. 3–26.

Luo, Y., P. G. Kelamis, and Y. Wang, 2003, Simultaneous inversion of multiples and primaries: Inversion versus subtraction: The Leading Edge, v. 22, no. 9, p. 814–818, 891.

Merletti, G. D., and C. Torres-Verdín, 2006, Accurate detection and spatial delineation of thin-sand sedimentary sequences via joint stochastic inversion of well logs and 3D pre-stack seismic amplitude data: Presented at the Annual Technical Conference and Exhibition, Society of Petroleum Engineers, SPE paper no. 102444.

Mesdag, P. R., R. Van Eykenhof, L. Harvidya, P. Van Riel, M. Sams, and W. E. Harmony, 2003, Integrated AVO reservoir characterization and time-lapse analysis of the Widuri Field: 66th EAGE Conference and Exhibitory, Extended Abstracts, A19.

Downloaded 25 Jun 2012 to 95.28.162.50. Redistribution subject to SEG license or copyright; Terms of Use: http://segdl.org/

Pedersen-Tatalovic, R., A. Uldall, N. L. Jacobsen, T. M. Hansen, and K. Mosegaard, 2008, Event-based low-frequency impedance modeling using well logs and seismic attributes: The Leading Edge, v. **27**, no. 5, p. 592–603.

Pendrel, J., et al., 2000, Estimation and interpretation of P and S impedance volumes from the simultaneous inversion of P-wave offset seismic data: 70th Annual. International Meeting, SEG, Expanded Abstracts, v. 19, p. 200–201.

Savic, M., B. VerWest, R. Masters, A. Sena, and D. Gingrich, 2000, Elastic impedance inversion in practice: 70th Annual International Meeting, SEG, Expanded Abstracts, v. 19, p. 689.

Sheffield, T. M., and B. A. Payne, 2008, Geovolume visualization and interpretation: what makes a useful visualization seismic attribute?: 78th Annual International Meeting, SEG, Expanded Abstracts, v. 27, p. 849-853.

Sheriff, R. E., 2002, Encyclopedic dictionary of applied geophysics, 4th edition: Society of Exploration Geophysicists, 429 p.

Simmons, J. L., and M. M. Backus, 1996, Waveform-based AVO inversion and AVO prediction-error: Geophysics, v. 61, p. 1575–1588.

Additional Reading

Aki, K., and P. G. Richards, 1980, Quantitative seismology, 1st edition: W. H. Freeman and Company, 2 volumes.

Bachrach, R., S. Noeth, N. Banik, M. Sengupta, G. Bunge, B. Flack, R. Utech, S. Mallick, 2001, AVO and elastic impedance: The Leading Edge, v. 20, p. 1094–1104.

Bachrach, R., S. Noeth, N. Banik, M. Sengupta, G. Bunge, B. Flack, R. Utech, C. Sayers, P. Hooyman, L. den Boer, L. Leu, B. Troyer, and J. Moore, 2007, From pore-pressure prediction to reservoir characterization: A combined geomechanics-seismic inversion workflow using trend-kriging techniques in a deepwater basin: The Leading Edge, v. 26, p. 590–595.

Benabentos, M., M. Silva, F. Ortigosa, and V. Mercado, 2007, Reservoir characterization in Burgos Basin using simultaneous inversion: The Leading Edge, v. 26, no. 5, p. 556–561.

Berkhout, A. J., 1992, Editorial: SEG Annual Meeting 1992: a successful meeting characterised by progress and uncertainty: Journal of Seismic Exploration, v. 1, p. 311–314.

Berkhout, A. J., and C. P. A. Wapenaar, 1990a, Delphi: Delft philosophy on acoustic and elastic inversion: The Leading Edge, v. 9, p. 30–33.

Berkhout, A. J., and C. P. A. Wapenaar, 1990b, Part 2—Delphi: Delft philosophy on acoustic and elastic inversion: The Leading Edge, v. 9, p. 53–59.

Bleistein, N., 1999, Hagedoorn told us how to do Kirchhoff migration and inversion: The Leading Edge, v., 18, p. 918–927.

Calderon, J. E., and J. Castagna, 2007, Porosity and lithologic estimation using rock physics and multi-attribute transforms in Balcon Field, Colombia: The Leading Edge, v. 26, no. 2, p. 142–150.

Castagna, J. P., M. L. Batzle, and R. L. Eastwood, 1985, Relationships between compressional-wave and shear-wave velocities in clastic silicate rocks: Geophysics, v. 50, p. 571–581.

Castagna, J. P., 1993, Petrophysical imaging using AVO: The Leading Edge, v. 12, p. 172–178.

Castagna, J. P., And H. W. Swan, 1997, Principles of AVO crossplotting: The Leading Edge, Interpreter's Corner, v. 16, no. 4, p. 337–342.

Chimblo, R. D., S. N. Dasgupta, and J. T. Foote, 1992, E & P information management: a user's view: Journal of Seismic Exploration, v. 1, p. 337–345.

Connolly, P., 2007, A simple, robust algorithm for seismic net pay estimation: The Leading Edge, v. 26, no. 10, p. 1278–1282.

Downloaded 25 Jun 2012 to 95.28.162.50. Redistribution subject to SEG license or copyright; Terms of Use: http://segdl.org/

Contreras, A., and C. Torres-Verdín, 2005, Sensitivity analysis of factors controlling AVA simultaneous inversion of 3D partially stacked seismic data: application to deepwater hydrocarbon reservoirs in the central Gulf of Mexico: 75th Annual International Meeting, SEG, Expanded Abstracts, v. 24, p. 464–467.
Dobrin, M. B., 1976, Introduction to geophysical prospecting: McGraw-Hill, Inc., 576 p.
Dragoset, B., and J. Gabitzsch, 2007, Introduction to this special section: Low-frequency seismic: The Leading Edge, v. 26, no. 1, p. 34–35.
Dubrule, O., and The Leading Edge, 2003, CSEG interviews Olivier Dubrule: The Leading Edge, v. 22, p. 850–854.
Egreteau, A., and P. Thierry, 2003, Postmigration processing for AVA inversion: The Leading Edge, v. 22, no. 10, 1016–1023.
Eidsvik, J., H. Omre, T. Mukerji, G. Mavko, and P. Avseth, 2002, Seismic reservoir prediction using Bayesian integration of rock physics and Markov random fields: A North Sea example: The Leading Edge, v. 21, no. 3, p. 290–294.
Francis, A., 1997, Acoustic impedance inversion pitfalls and some fuzzy analysis: The Leading Edge, v. 16, p. 275–278.
Gidlow, P. M., G. C. Smith, and P. J. Vail, 1992, Hydrocarbon detection using fluid factor traces: A case history: Joint SEG/EAEG Summer Research Workshop on "How Useful Is Amplitude Versus Offset (AVO) Analysis?": Expanded Abstracts, p. 78–89.
Giroldi, L., A. L. Angriman, JP Blangy, J. C. Cordova, and E. Martinez, 2005, Seismically-driven appraisal and development: A case study from Bolivia's Chaco Basin; The Leading Edge, v. 24, no. 11, 1099–1108.
Goodway, W., T. Chen, and J. Downton, 1997, Improved AVO fluid detection and lithology discrimination using Lamé petrophysical parameters: 67th Annual International Meeting, SEG, Expanded Abstracts, v. 16, no. 1, p. 183–186.
Gray, S., and L. Lines, 1992, Cross-borehole tomographic migration: Journal of Seismic Exploration, v. 1, p. 315–324.
Hampson, D., 1991, AVO inversion, theory and practice: The Leading Edge, v. 10, p. 39–42.
Hampson, D. P., J. S. Schuelke, and J. A. Quirein, 2001, Use of multiattribute transforms to predict log properties from seismic data: Geophysics, v. 66, p. 220–229.
Herrera, V. M., B. Russell, and A. Flores, 2006, Neural networks in reservoir characterization: The Leading Edge, v. 25, no. 4, p. 402–411.
Hill, S. J., 2005, Inversion-based thickness determination: The Leading Edge, v. 24, no. 5, p. 477–480.
Hill, S. J., 2007a, Geophysics bright spots: The Leading Edge, v. 26, no. 2, p. 132–133.
Hill, S. J., 2007b, Geophysics bright spots: The Leading Edge, v. 26, no. 8, p. 952–953.
Hubral, P., J. Schleicher, and M. Tygel, 1992, Three-dimensional paraxial ray properties, Part II: Applications: Journal of Seismic Exploration, v. 1, p. 347–362.
Keys, R. G., and D. J. Foster, eds., 1998, Comparison of seismic inversion methods on a single real data set: SEG, Open File Publications, no. 4, 213 p.
Kowalsky, M. B., J. Chen, and S. S. Hubbard, 2006, Joint inversion of geophysical and hydrological data for improved subsurface characterization: The Leading Edge, v. 25, no. 6, p. 730–734.
Landro, M., A. Buland, and R. D'Angelo, 1995, Target-oriented AVO inversion of data from Valhall and Hod fields: The Leading Edge, v. 14, p. 855–861.
Latimer, R. B., P. van Riel, 1996, Integrated seismic reservoir characterization and modeling: A Gulf of Mexico 3D case history: Paper presentated at the Gulf Coast Society SEPM Research Conference: http://www.fugro-jason.com/readingroom/techpapers/GOM_1996_GCSSEPM.pdf, accessed November 2009.
Lau, K. W. H., R. S. White, and P. A. F. Christie, 2007, Low-frequency source for long-offset, sub-basalt and deep crustal penetration: The Leading Edge, v. 26, no. 1, p. 36–39.

Downloaded 25 Jun 2012 to 95.28.162.50. Redistribution subject to SEG license or copyright; Terms of Use: http://segdl.org/

Mallick, S., X. Huang, J. Lauve, and R. Ahmad, 2000, Hybrid seismic inversion: A reconnaissance tool for deepwater exploration: The Leading Edge, v. 19, p. 1230–1237.

Margrave, G. F., R. R. Stewart, and J. A. Larsen, 2001, Joint *PP* and *PS* seismic inversion: The Leading Edge, v. 20, p. 1048–1052.

Mavko, G., C. Chan, and T. Mukerji, 1995, Fluid substitution: Estimating changes in V_P without knowing V_S: Geophysics, v. 60, p. 1750–1755.

Merletti, G., J. Hlebszevitsch, and C. Torres-Verdín, 2003, Geostatistical inversion for the lateral delineation of thin-layer hydrocarbon reservoirs: A case study in San Jorge basin, Argentina: 73rd Annual International Meeting, SEG, Expanded abstracts, p. 662-665.

Nammour, R., 2008, Approximate inverse scattering: using pseudodifferential scaling: MA. thesis, Rice University: http://www.trip.caam.rice.edu/reports/2008/trip08_report.html, accessed December 10, 2009.

Puryear, C. I., and J. P. Castagna, 2008, Layer-thickness determination and stratigraphic interpretation using spectral inversion: Theory and application: Geophysics, v. 73, no. 2, p. R37–R48.

Richards, P. G., and C. W. Frasier, 1976, Scattering of elastic waves from depth-dependent inhomogeneities: Geophysics, v. 41, p. 441–458.

Roberts, R., J. Bedingfield, D. Phelps, A. Lau, B. Godfrey, S. Volterrani, F. Engelmark, and K. Hughes, 2005, Hybrid inversion techniques used to derive key elastic parameters: A case study from the Nile Delta: The Leading Edge, v. 24, no. 1, p. 86–92.

Russell, B. H., 1988, Introduction to seismic inversion methods: SEG Course Notes no. 2, 90 p.

Russell, B. H., and D. P. Hampson, 1991, A comparison of post-stack seismic inversion methods: 61st annual International Meeting, SEG, Expanded Abstracts, p. 876–878.

Russell, B. H., K. Hedlin, F. J. Hilterman, and L. R. Lines, 2003, Fluid-property discrimination with AVO: A Biot-Gassmann perspective: Geophysics, v. 68, p. 29-39.

Saltzer, R., C. Finn, and O. Burtz, 2005, Predicting V_{shale} and porosity using cascaded seismic and rock physics inversion: The Leading Edge, v. 24, p. 732–736.

Sancevero, S. S., A. Z. Remacre, R. de Souza, and E. C. Mundim, 2005, Comparing deterministic and stochastic seismic inversion for thin-bed reservoir characterization in a turbidite synthetic reference model of Campos Basin, Brazil: The Leading Edge, v. 24, no. 11, p. 1168–1172.

Sayers, C., P. Hooyman, L. den Boer, L. Leu, B. Troyer, and J. Moore, 2007, From pore-pressure prediction to reservoir characterization: A combined geomechanics-seismic inversion workflow using trend-kriging techniques in a deepwater basin: The Leading Edge, v. 26, no. 5, p. 590–595.

Shuey, R. T., 1985, A simplification of the Zoeppritz equations: Geophysics, v. 50, p. 609–614.

Singh, Y., 2007, Lithofacies detection through simultaneous inversion and principal component attributes: The Leading Edge, v. 26, no. 12, p. 1568–1575.

Symes, W. W., 2007, Model extensions and inverse scattering: inversion for seismic velocities: The Rice Inversion Project: http://www.trip.caam.rice.edu/downloads/downloads/html, click on the link for seismic Inversion: Progress and Prospects, accessed December, 2009.

Symes, W. W., 2008, Migration velocity analysis and waveform inversion: Geophysical Prospecting, v. 56, p. 765-790.

Toxopeus, G., J. Thorbecke, K. Wapenaar, S. Petersen, E. Slob, and J. Fokkema, 2008, Simulating migrated and inverted seismic data by filtering a geologic model: Geophysics, v. 73, no. 2, p. T1–T10.

Treitel, S., 1989, Quo vadit inversio?: The Leading Edge, v. 8, p. 38–42.

Wapenaar, K., J. Goudswaard, and A.-J van Wijngaarden, 1999, Multiangle, multiscale inversion of migrated seismic data: The Leading Edge, v. 18, p. 928–932.

Widess, M. B., 1973, How thin is a thin bed?: Geophysics, v. 38, p. 1176–1180.

Downloaded 25 Jun 2012 to 95.28.162.50. Redistribution subject to SEG license or copyright; Terms of Use: http://segdl.org/

Yarus, J. M., and R. L. Chambers, eds., 1994, Stochastic modeling and geostatistics: Principles, methods, and case studies: AAPG Computer Applications in Geology, no. 3, American Association of Petroleum Geologists, 379 p.
Zou, Y., L. R. Bentley, L. R. Lines, and D. Coombe, 2006, Integration of seismic methods with reservoir simulation, Pikes Peak heavy-oil field, Saskatchewan: The Leading Edge, v. 25, no. 6, p. 764–781.

Downloaded 25 Jun 2012 to 95.28.162.50. Redistribution subject to SEG license or copyright; Terms of Use: http://segdl.org/

Downloaded 25 Jun 2012 to 95.28.162.50. Redistribution subject to SEG license or copyright; Terms of Use: http://segdl.org/

Depth Conversion and Depth Imaging

Introduction

Depth conversion concerns the seismic interpreter because seismic measurements are made in time, but the wells based on a seismic interpretation are drilled in depth. The depth conversion can now be carried out as part of the data processing, but this depth imaging is only done in special circumstances. Historically, geophysical interpreters have relied more and more on automatic data processing to prepare the data for interpretation. The way this has occurred for depth conversion is shown in Figure 10-1. Depth imaging is used when the velocity distribution and structural complexity are such that the time image of the subsurface does not permit the interpreter to understand the geology (Figure 10-2).

Depth imaging is difficult, expensive and never completely accurate. The most accurate depth imaging uses pre-stack depth migration of the 3-D seismic data volume, a computationally intensive task which is critically dependent on an accurate velocity field. The velocity field cannot be known until the geological structure is known, and

1972	1974	1994	1996
STACK	STACK	STACK	MIGRATE DATA IN DEPTH
HORIZON TRACKING	MIGRATE DATA IN TIME	MIGRATE DATA IN DEPTH	STACK
MIGRATE MAP	HORIZON TRACKING	HORIZON TRACKING and MAPPING	HORIZON TRACKING and MAPPING
DEPTH CONVERT MAP	DEPTH CONVERT MAP		
	still the most common today		

Fig. 10-1. Evolution of depth conversion approaches, with the year in which each became practical.

Downloaded 25 Jun 2012 to 95.28.162.50. Redistribution subject to SEG license or copyright; Terms of Use: http://segdl.org/

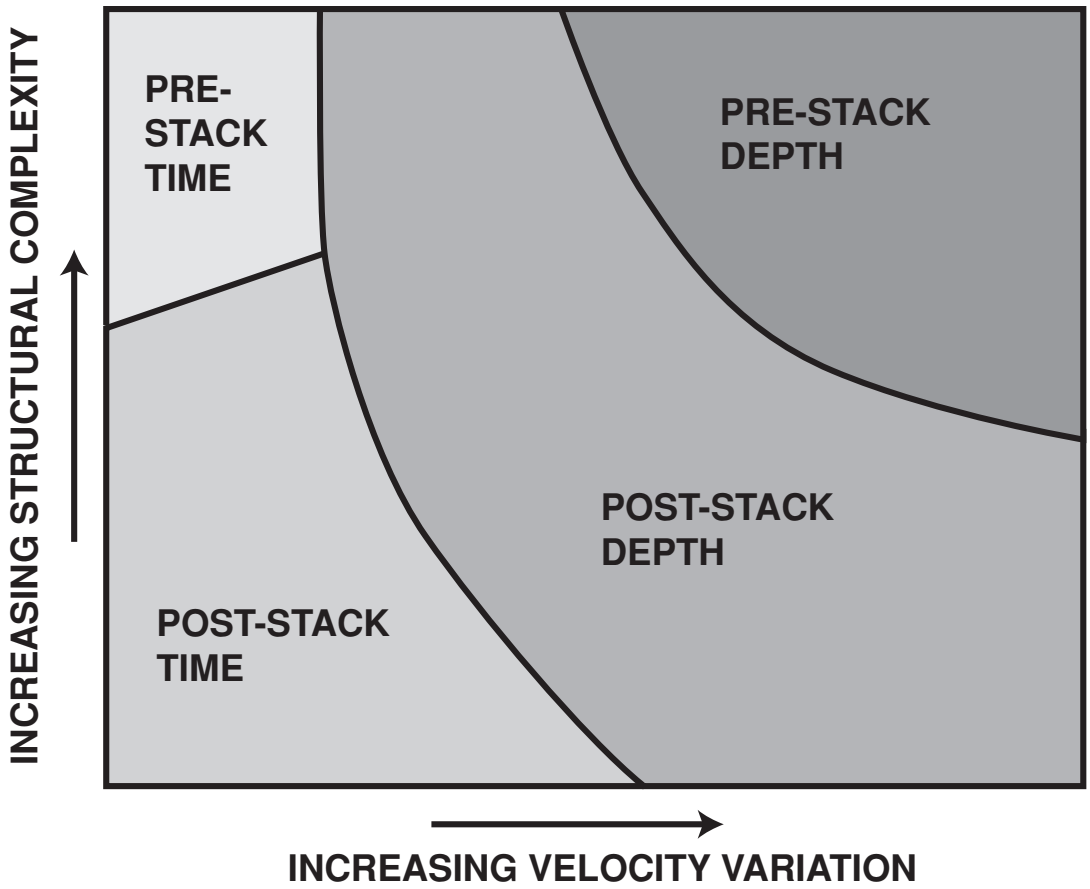

Fig. 10-2. Appropriate kind of migration as a function of structure and velocity variation. (After Liner, 1996. Used by permission.)

the geological structure cannot be known until the seismic volume has been migrated. Consequently, the depth imaging process usually involves iteration.

Depth conversion of a time interpretation, on the other hand, is computationally simple, and can be quickly repeated whenever new information becomes available. The most common procedure for preparing a depth image of the earth from 3-D seismic data is to time-migrate the 3-D data volume, usually after stack, and convert the time interpretation into a depth model of the earth. Accurate depth conversion is particularly important because the 3-D data volume presents the promise of much more reliable interpretation than with 2-D seismic methods, so errors in depth conversion can be the largest errors in the final interpretation.

The physical quantity that relates time to depth is velocity. In most seismic interpretation, we are concerned with the velocity of compressional (P) waves through the earth, because conventional seismic processing attempts to eliminate all seismic energy except that which represents a simple P-wave reflection. The velocity required for converting time to depth is the P-wave velocity in the vertical direction. It can be measured directly in a well, or extracted indirectly from surface seismic measurements, or deduced from a combination of seismic and well measurements. Conventional time-to-depth conversion is the subject of the first half of this chapter.

Downloaded 25 Jun 2012 to 95.28.162.50. Redistribution subject to SEG license or copyright; Terms of Use: http://segdl.org/

Depth Conversion

Contributed by Leslie R. Denham and Dave K. Agarwal, Interactive Interpretation and Training

Sources and Computation of Velocity

Seismic P-wave velocity may be measured directly by recording a conventional seismic energy source (such as a dynamite charge, a vibrator, or an air gun) with a special geophone lowered down an exploration well. This conventional well velocity survey (or checkshot survey) records a small number of shots at large geophone depth intervals (usually 100 m or more) from a single source position. The arrival time of the first energy from each shot is assumed to be the P-wave arrival, and the relationship of time to depth given by the survey can be used to convert time to depth directly. Some corrections are usually needed: a correction for a near-surface low velocity layer at the source; corrections of source elevation and drilling reference elevation to the seismic reference elevation; and corrections for a non-vertical path.

Sometimes a vertical seismic profile (VSP) is recorded, with much closer geophone depth intervals and perhaps several source positions for each geophone depth (a walk-away VSP). A VSP is intended to image the subsurface in the vicinity of the well bore, but it also provides vertical velocity information in the same way as a checkshot survey does, and usually more accurately.

Seismic data themselves provide velocity information through measurement of normal moveout (NMO). If a seismic reflection is recorded from a horizontal reflector, and the earth above the reflector (the overburden) has a uniform P-wave velocity V, the traveltime $T(x)$ for a source-receiver separation of x is given by the hyperbolic equation

$$T^2(x) = T^2(0) + \frac{x^2}{V^2}$$

Given the relationship between $T(x)$ and x for a reflector, the overburden velocity can be computed. Conventional seismic processing stacks or sums data recorded with varying source-receiver separation. The reflection time is corrected to zero source-receiver separation by fitting such a hyperbola to the arrival time curve of the reflection, even though the overburden velocity is not uniform and the reflector is not horizontal. The value of V for such a "best fit" hyperbola is called the "stacking velocity," because it has the dimensions of velocity (distance divided by time) even though it is not a velocity in a real sense.

C. Hewitt Dix (1955) pointed out that if the overburden is considered to be not uniform but made up of several horizontal layers, the stacking velocity (although he did not use that term) is approximately equal to the "root mean square" of the layer velocities. The velocity V of a uniform layer between two horizontal reflections with zero-offset times of t_1 and t_2 and stacking velocities of V_1 and V_2 is then given by

$$V^2 = \frac{V_2^2 t_2 - V_1^2 t_1}{t_2 - t_1}$$

With some approximations then, we can compute interval velocities between reflections from the "velocities" used by the processing center to stack the data. These stacking velocity values are readily available from the processing geophysicist, and are typically supplied to the interpreter as a listing of time-velocity pairs.

Interval velocities computed using the Dix equation can, in principle, be used directly for depth conversion. There is a great gulf between principle and practice. Firstly, both the top and bottom parts of the equation are differences, so the thinner

Downloaded 25 Jun 2012 to 95.28.162.50. Redistribution subject to SEG license or copyright; Terms of Use: http://segdl.org/

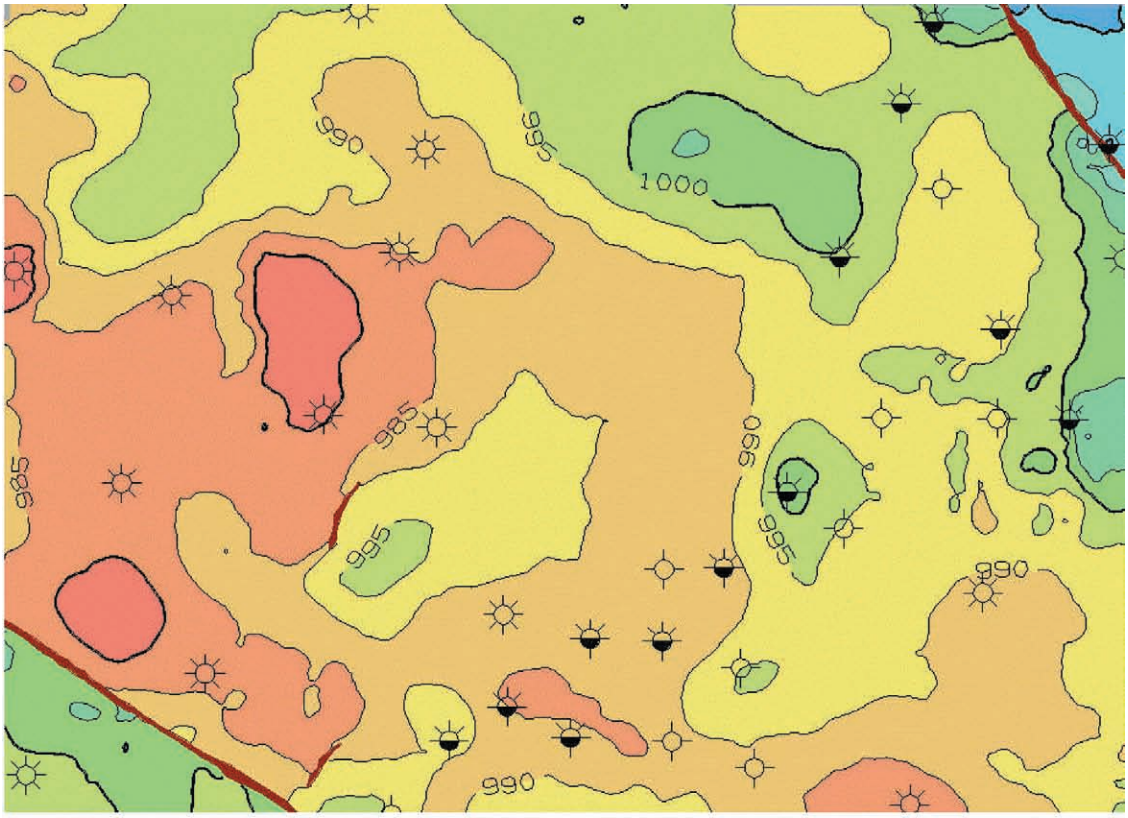

Fig. 10-3. The interpreted time map for a reflection in the Fort Worth basin in north Texas. Not all the wells posted on the map are deep enough to penetrate this horizon.

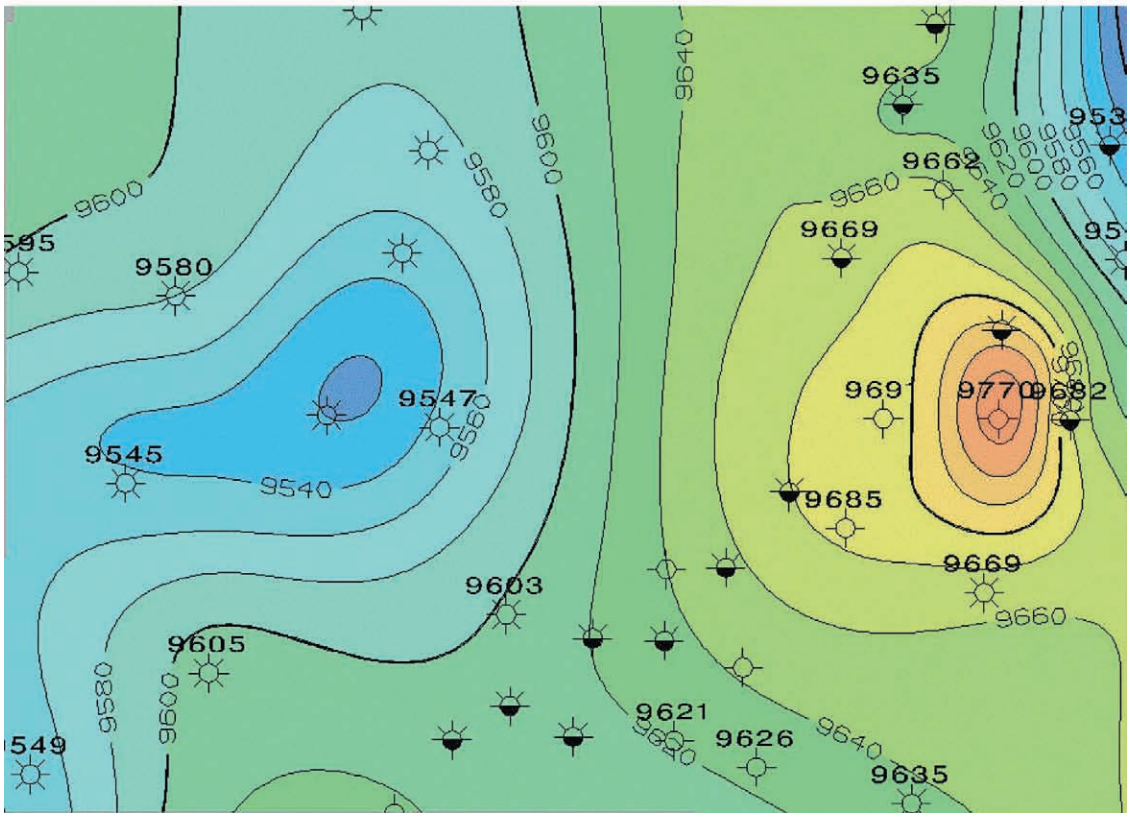

Fig. 10-4. The pseudovelocity map produced by dividing the depth to a marker in a well by half the mapped reflection time at the well. The depth is below sea level, while the reflection time is measured relative to a +900 ft datum, so the pseudovelocities have no physical meaning.

Downloaded 25 Jun 2012 to 95.28.162.50. Redistribution subject to SEG license or copyright; Terms of Use: http://segdl.org/

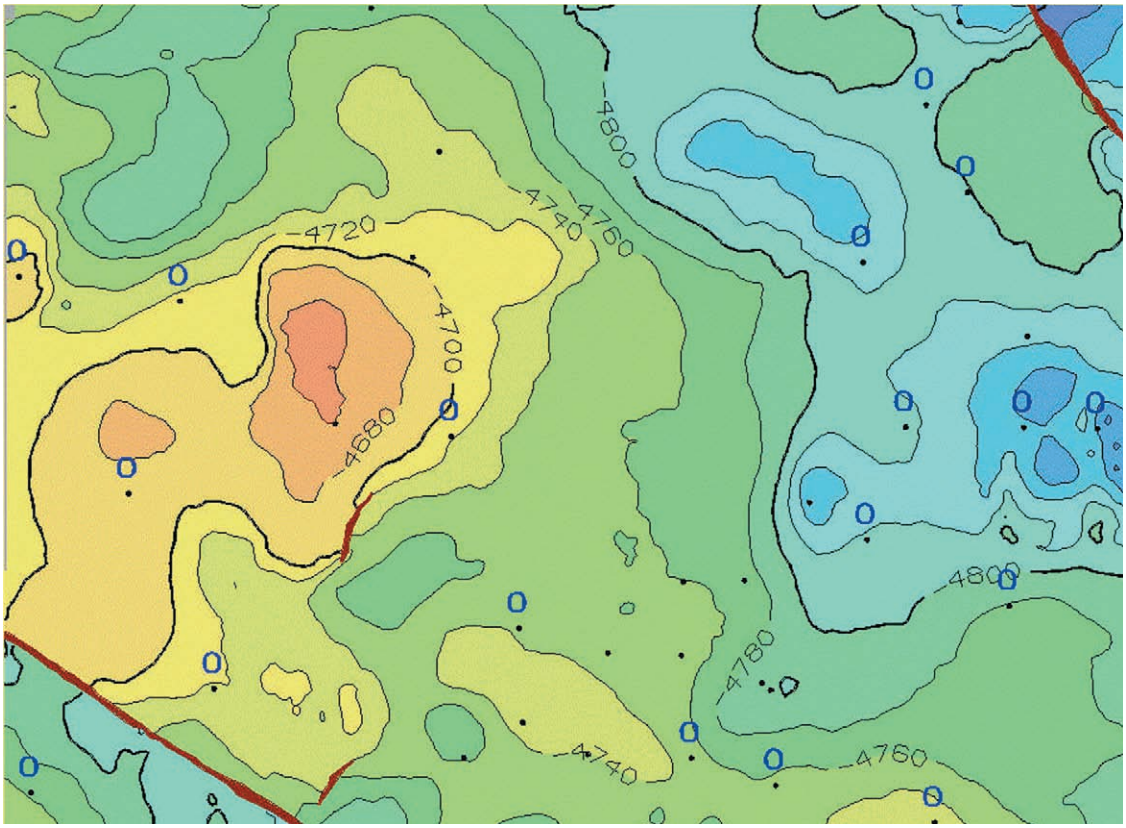

Fig. 10-5. The depth map produced by multiplying the times in Figure 10-3 (divided by 2 to give one-way time) by the velocities in Figure 10-4. The posted values, all zero, show the difference between the map depth and the depth of the horizon in the well. Depths are shown as elevations relative to sea level.

the layer, the greater the error in the computed velocity. The uncertainty in the velocity is inversely proportional to the time interval: for an interval velocity calculated over a 1000-ms interval in a simple model, a 1% error in either RMS velocity gives 1% error in the interval velocity, the same 1% error in RMS velocity gives a 20% error if the time interval is only 50 ms. The reflections used by the processing center to compute stacking velocities are rarely those mapped by the interpreter, and in any case they are unmigrated reflections. Furthermore, the interval velocities computed are really horizontal velocities, not vertical velocities. The earth rarely has the same velocity vertically as horizontally (it is not isotropic). And the layers used for velocity analysis are rarely uniform. Finally, the reflections are not, in general, horizontal, and the closer they are to horizontal the less interesting they are to the explorationist. Either dip or curvature in the reflector alters the measurement of stacking velocity. One simplification shows that the stacking velocity is equal to the RMS velocity divided by the cosine of the dip of the reflector, so that a dip of 10° introduces an error of 1.5%, and a dip of 20° introduces an error of over 6%. Still, the stacking velocity data are available throughout the 3-D data volume, while real (checkshot) velocities may be available only in one or two wells, or not at all. Errors in stacking velocities increase with depth: the moveout becomes smaller at the maximum source-receiver separation, the reflection quality deteriorates, the resolution of reflections is lower as high frequencies are attenuated (so the moveout can be measured with less accuracy), and dip and curvature are usually greater. The stacking velocity pairs given by the processing center provide a function of stacking velocity as a function of depth, and the value for the time of each mapped horizon can be interpolated and the interpolated values used in the Dix equation to give interval velocities between mapped horizons. The processing center can often supply a velocity volume used for migration, especially where prestack migration is used, and this gives average velocities directly. However, it is still, like stacking velocities, horizontal velocity, not vertical velocity.

If a mapped reflection is known to be a marker that can be identified in wells, then wells which have penetrated the marker have both a depth (from log interpretation in

Downloaded 25 Jun 2012 to 95.28.162.50. Redistribution subject to SEG license or copyright; Terms of Use: http://segdl.org/

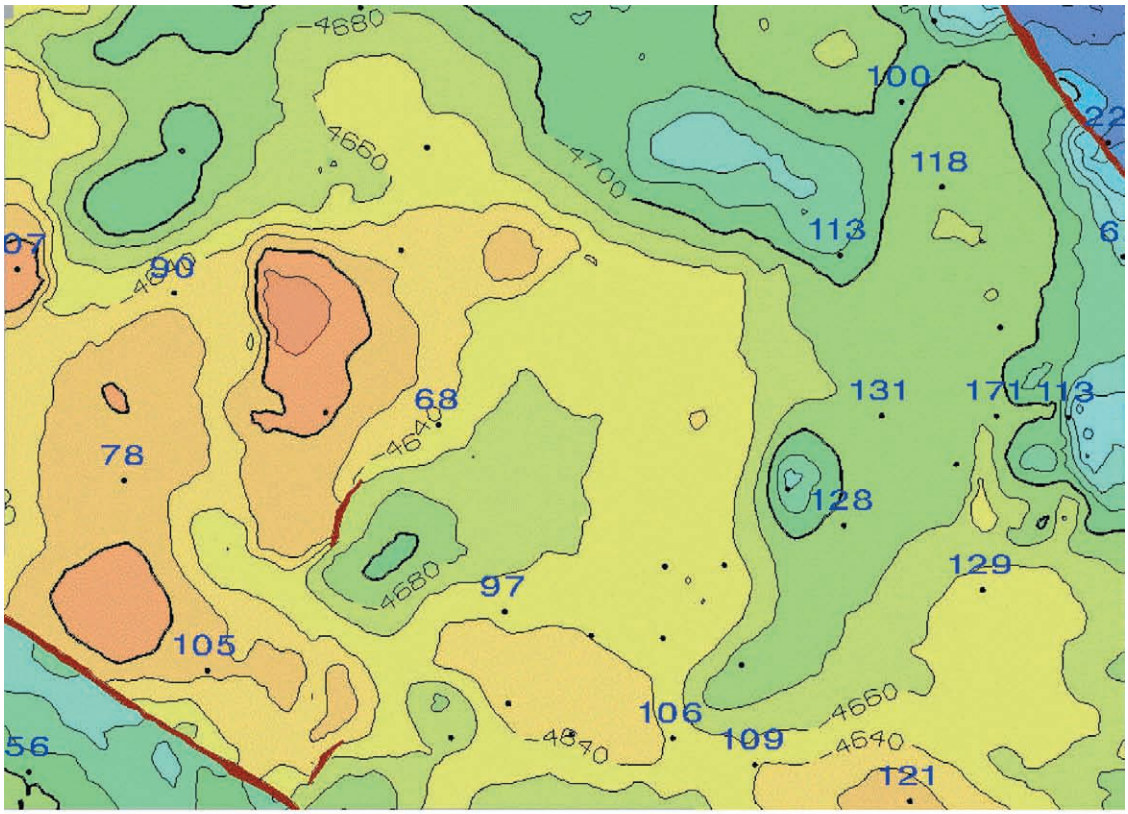

Fig. 10-6. The depth map produced by converting the time map in Figure 10-3 to depth using the velocity measured in a single well. The numbers indicate the mistie at wells.

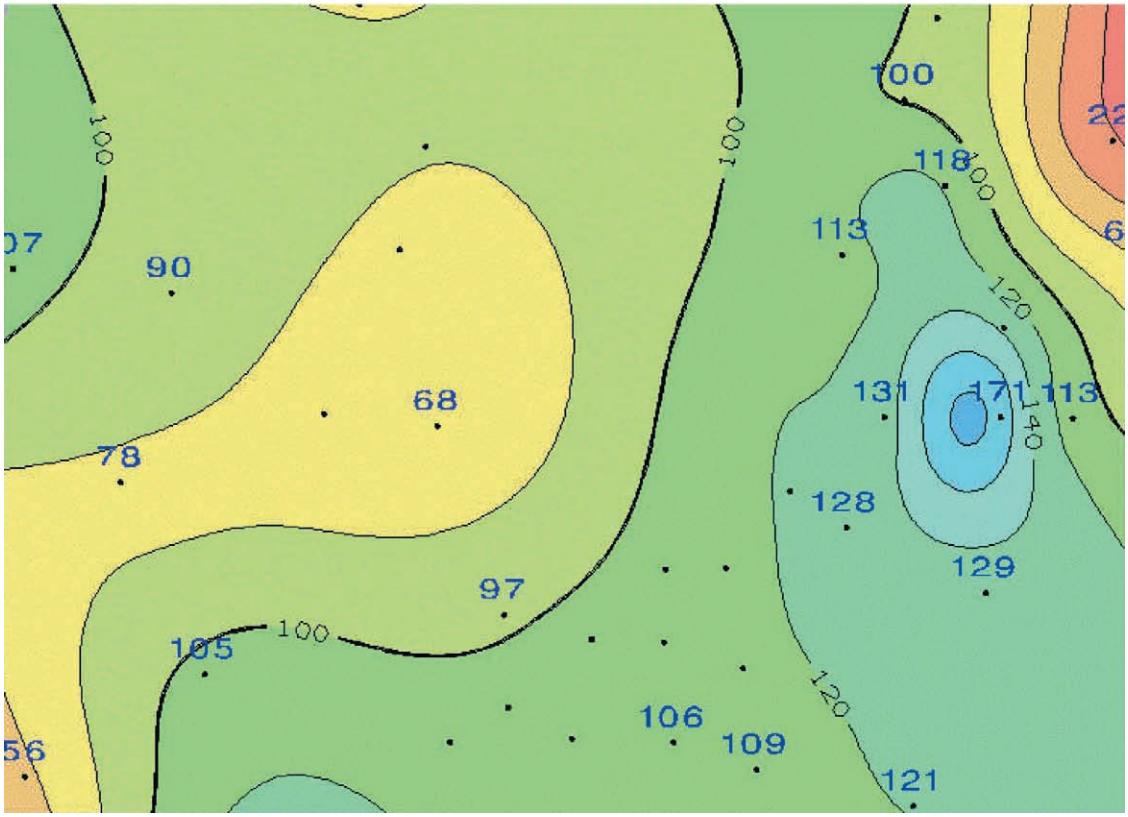

Fig. 10-7. The difference between the depth map in Figure 10-6 and the depth of the horizon in the well. The contoured surface fits each mistie exactly.

Downloaded 25 Jun 2012 to 95.28.162.50. Redistribution subject to SEG license or copyright; Terms of Use: http://segdl.org/

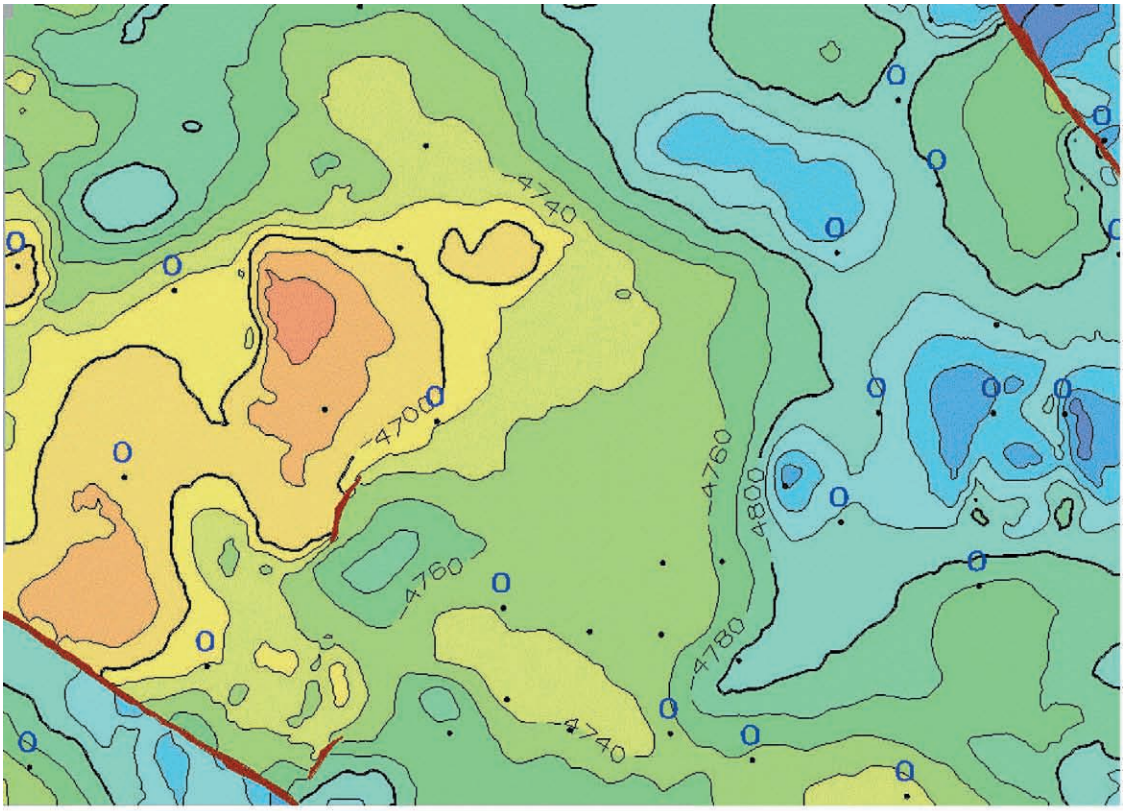

Fig. 10-8. The corrected depth map produced by subtracting the error surface in Figure 10-7 from the depth map in Figure 10-6. Posted values, all zero, show the misties with well depths.

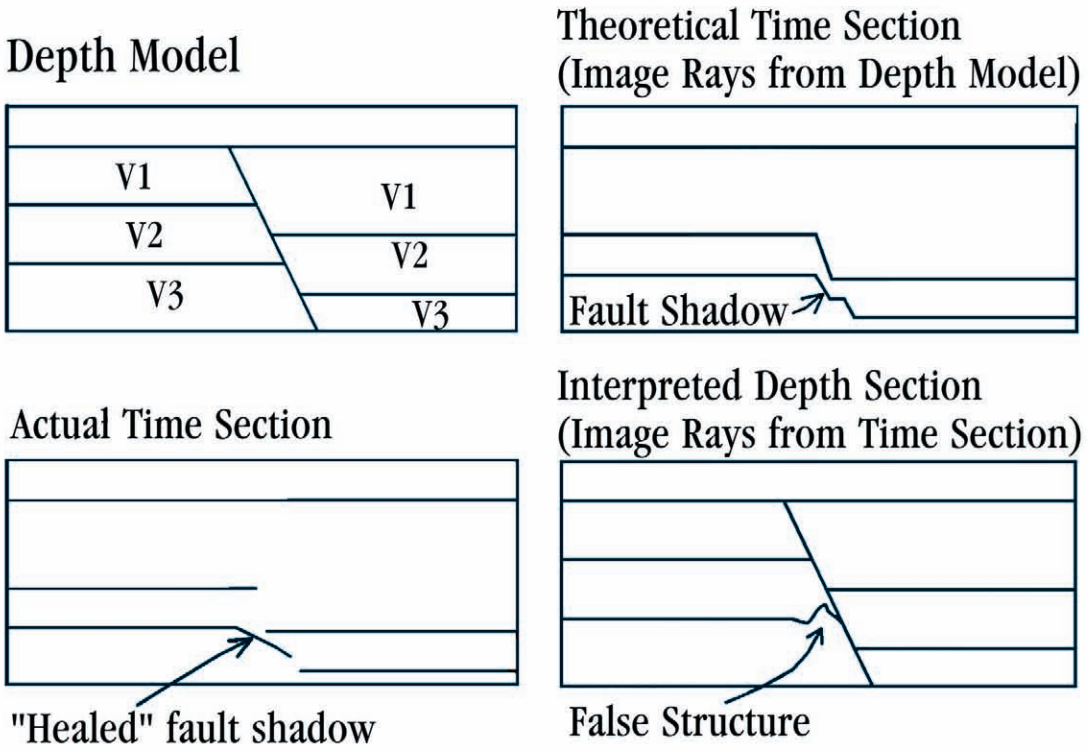

Fig. 10-9. The fault healing effect, and how it distorts depth conversion.

Downloaded 25 Jun 2012 to 95.28.162.50. Redistribution subject to SEG license or copyright; Terms of Use: http://segdl.org/

the well) and a time (from the 3-D seismic interpretation). Figure 10-3 shows a time map over an area with about 20 wells that have penetrated the mapped marker. If we divide the depth below datum of the marker by the interpreted time at the well, we have calculated an empirical velocity, often termed "pseudovelocity," which will convert the time of this event to the depth of the well marker at this well. With enough wells, we can map changes of the pseudovelocity, so that a velocity is available over the whole of the survey as shown in Figure 10-4. The depth map (Figure 10-5) computed from the interpreted time map and the pseudovelocity map, must tie exactly at each well used for pseudovelocities, but there is no way of estimating the accuracy of the map away from these wells.

Geostatistical cokriging is a statistical technique for using a measured value of one quantity at many points to estimate the value of another quantity at those many points, given a few measurements of the second quantity. Because depth is closely related to time the technique works quite well for direct conversion of time to depth without computing velocity. The results are very similar to using pseudovelocities, with the advantage of giving an estimate of the accuracy of the final depth map, but this requires special software. Geostatistical software has not been integrated into commonly used interpretation or mapping systems, and stand-alone geostatistical software tends to have user manuals and a user interface that only a mathematician could love (Wolf, 1990).

Velocities may be available from several sources: well velocity surveys, VSPs, stacking velocities, and pseudovelocities. The interpreter typically combines them by using the sparse, accurate data points at wells to calibrate maps generated from numerous but less accurate stacking velocity measurements. Often the interpreter must reject anomalous values, using the criteria of geological reason. The final velocity field used for depth conversion must represent a reasonable approximation to the geological model represented by the final interpretation. Velocities must be realistic for the lithologies known or presumed to be present, and any lateral or vertical changes in velocity must have a geological explanation.

General Considerations in Depth Conversion

The velocities available for depth conversion may have varying accuracy. Actual measurements in a well, whether a velocity survey or a VSP, are usually very accurate, with errors often as small as 0.1% or better, but velocities computed from moveout are often in error by 5% or more. One of the subtler characteristics of time migrated data is that a vertical line through the time-migrated data volume (along the time axis) does not necessarily represent a vertical line through the earth. In fact, it only represents a vertical line through the earth when there is no horizontal velocity gradient, when all isovelocity surfaces are horizontal. This was first published by Peter Hubral (1977). In other cases, the true position of a point on a time-vertical trace can be found by tracing the ray into the earth from the surface (or from the seismic datum plane), starting with a vertical ray and bending it according to Snell's Law at all velocity boundaries. This process is called "image ray migration."

If there is an abrupt lateral change in velocity, as at a fault, the approximation that the stacked seismic trace is the same as the zero-offset seismic trace, and that the migrated seismic trace represents data along an image ray, would lead the interpreter to expect a discontinuity in deeper reflections, a "fault shadow," even when they are not faulted (Figure 10-9). In real data, any discontinuity disappears rapidly with increasing depth below the discontinuous velocity surface: the samples which make up the time-migrated trace come from the stacked data volume within a cone expanding upwards from the sample time, so samples below the discontinuity soon include data from both sides. In effect, the fault shadow is "healed" with depth, becoming a broader and broader monocline.

When using any layer-based depth conversion technique, we must simulate this fault

Downloaded 25 Jun 2012 to 95.28.162.50. Redistribution subject to SEG license or copyright; Terms of Use: http://segdl.org/

shadow healing by smoothing a layer before building downwards from it. A technique that works well is to remove wavelengths shorter than the layer thickness, from both the time and the depth maps of the top of the layer. The exact tie of a well to a seismic trace should be represented by the synthetic seismogram computed from sonic and density logs in the well, calibrated by a velocity survey or a VSP. In real life, the synthetic seismogram is rarely a good match to the processed seismic trace. The well tie of a reflection is usually best determined by answering two questions:

Is there a noticeable change in acoustic impedance as measured by the well logs at about the correct time as defined by velocity survey?

Is the mapped seismic event of the expected polarity for the direction of change of the acoustic impedance, taking into account the polarity conventions assumed by the processing center, and the phase manipulations in the processing sequence?

If the answer to both of these questions is "yes", then the mapped event probably represents the acoustic impedance change. If either answer is "no", the mapped event may not be reliably identified. If a horizon can be accurately identified at one well, and is reliably identified throughout the survey by its distinctive character, it will in most areas be correct to assume that it is the same geological marker throughout the area. However, seismic reflections in general follow geological time lines, often representing thin but persistent chronostratigraphic units representing widespread geological phenomena such as maximum sea level fluctuations or volcanic eruptions. On the other hand, the formations identified in wells by geologists are often lithostratigraphic units, which may or may not have been deposited at the same time throughout the area.

Depth Conversion Using a Single Velocity Function

Many small 3-D interpretations can be converted from time to depth using a single velocity function, often from a velocity survey in one well, either in the area of the 3-D survey or nearby. Such a function is usually a series of time-depth pairs, with the time recorded from the surface to several widely-spaced points down the well. Depth conversion uses the grid manipulation functions of the mapping system. Because these are usually limited to a few arithmetic operations, the interpreter often approximates the measured time-depth function with a mathematical function such as a straight line fitted to the time-depth points within the time range of the time map. A non-linear time-depth function may also be used, and could be any mathematical expression which fits the data and which can be evaluated using the grid manipulation functions of the mapping system.

The results of such a conversion are shown in Figure 10-6. Because the measured time-depth function is accurate only at one point (the well where it was recorded), the depth map does not usually tie to the depths for the mapped formation measured in other wells. To correct for the mistie, the interpreter can fit a smooth surface to the mistie values, shown in Figure 10-7, and subtract this surface from the depth map to give a corrected depth map, Figure 10-8, which ties exactly at each well.

Depth Conversion Using Mapped Velocity Function

Where several wells have velocity surveys, or where other methods provide velocities, some way of handling the varying velocities must be used. The easiest way to do this is to map the velocity in some way: either the actual average velocity at each point (as was done in Figure 10-4) or constants in the velocity function fitted to the data points at each well. If a straight line time-depth function of the form $Z=a + bT$ is used, where Z is depth and T is time and a and b are constants, the interpreter could map either a or b, and hold the other constant over the whole area, or could map both of the constants. With both constants mapped, the depth map would be produced by multiplying the time map grid by the b map grid, and adding the a map grid. This depth map requires residual corrections in the same way as the map prepared using a single velocity function, unless the only velocities used are pseudovelocities.

Downloaded 25 Jun 2012 to 95.28.162.50. Redistribution subject to SEG license or copyright; Terms of Use: http://segdl.org/

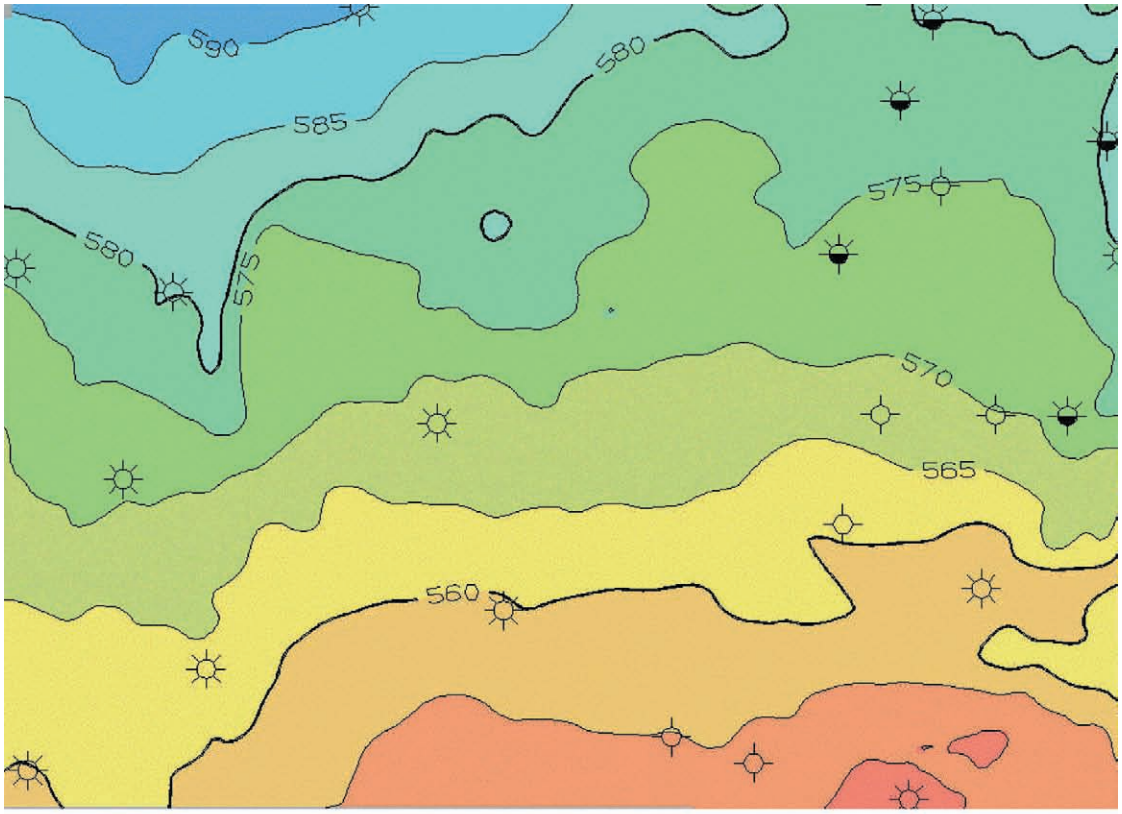

Fig. 10-10. The interpreted time map for a shallow horizon marking the boundary between two velocity layers.

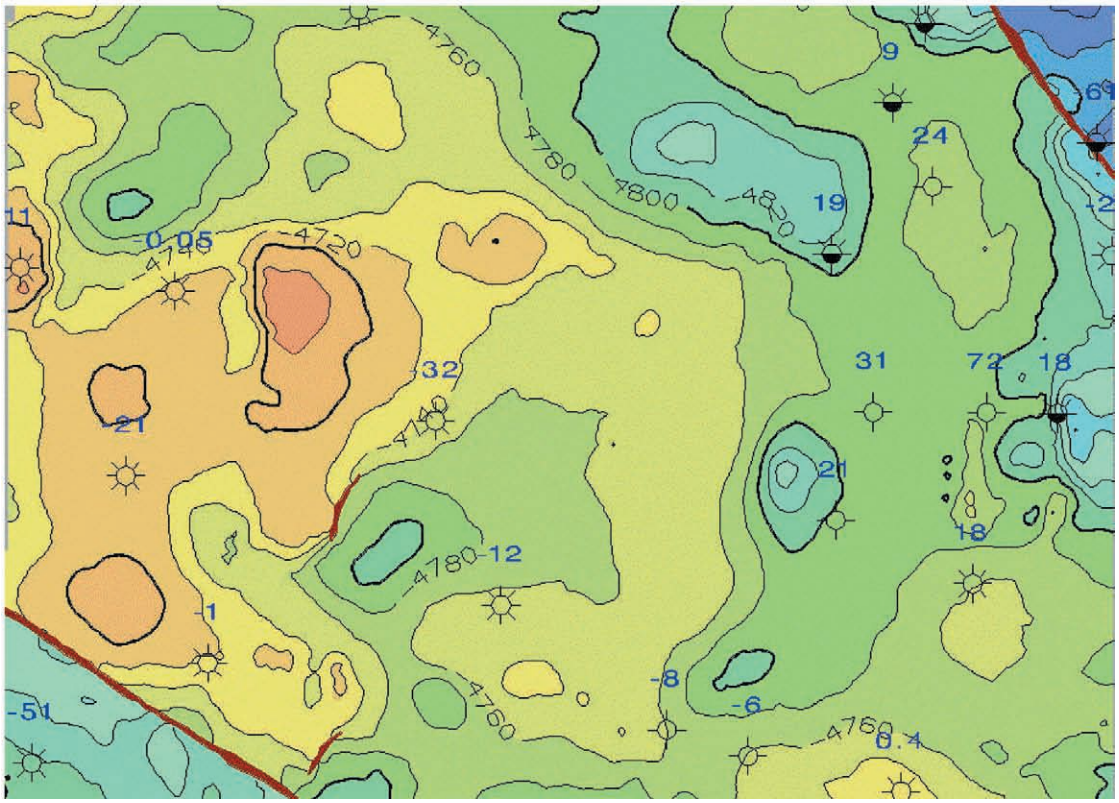

Fig. 10-11. A depth map produced by conversion from time to depth in two layers. The velocity used from seismic datum to the horizon mapped in Figure 10-10 is 10204 ft/s, and the velocity used from this shallow horizon to the horizon shown in Figure 10-3 is 12107 ft/s. A constant correction of -208 ft was applied to give an average mistie of zero, and the posted values show the residual misties. The standard deviation of the misties is 30 ft.

Downloaded 25 Jun 2012 to 95.28.162.50. Redistribution subject to SEG license or copyright; Terms of Use: http://segdl.org/

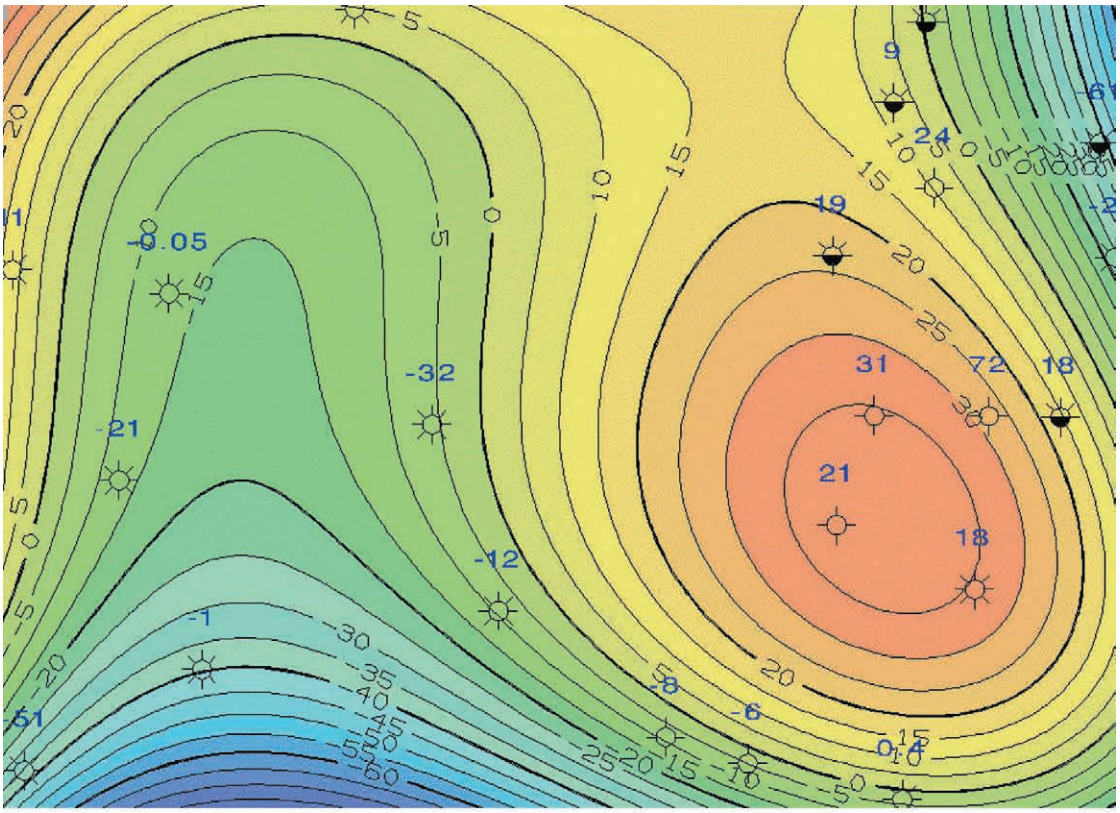

Fig. 10-12. A third order trend surface fitted to the residual errors shown in Figure 10-11.

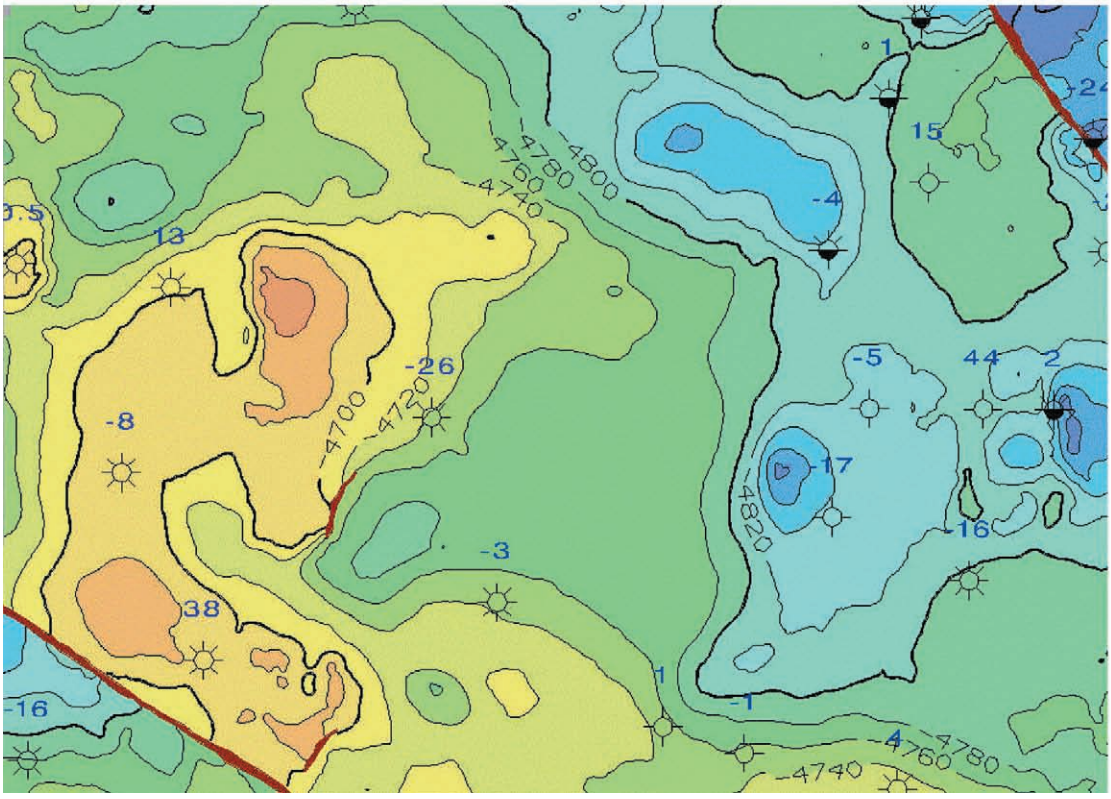

Fig. 10-13. The corrected depth map produced by subtracting the trend surface in Figure 10-12 from the depth map in Figure 10-11. The residual misties are posted on the map. The standard deviation of the residual mistie is 18 ft.

Downloaded 25 Jun 2012 to 95.28.162.50. Redistribution subject to SEG license or copyright; Terms of Use: http://segdl.org/

Depth Conversion Using Layers

Where there are major velocity changes in the overburden which result largely from changes in lithology rather than from depth of burial, interpolation between control points should use a series of layers with different velocities for each layer. The simplest case is where the velocity for each layer is constant. In this case, the interval from the surface to the base of the first layer is converted to depth using one of the methods described above. Then the time interval over the next layer is converted to a depth interval using a constant velocity (or single velocity function) and added to the depth to the base of the first layer to give the depth to the base of the second layer, and the process repeated for each subsequent layer. Figure 10-10 shows the time map for a shallow reflection marking a major velocity break. At the one well with a velocity survey, the velocity for the interval above the shallow reflection is 10204 ft/s, and from that reflection to the deep reflection (Figure 10-3) the velocity is 12107 ft/s. The depth map from the layer method, with a constant added to give zero average mistie, is Figure 10-11.

If there were significant faulting in the shallow layer, we would need to smooth the time map for the top of each layer before computing the time interval, and the depth map for the top of each layer before adding the depth interval. This is to remove the effect of "fault healing", shown in Figure 10-9. Abrupt lateral changes in velocity in the overburden, such as might occur at a fault, should produce apparent faulting in deeper reflectors; but in real seismic data this effect is rarely seen. The time migration process, where recorded data from both sides of an abrupt velocity variation are used to produce the migrated image below the anomaly, mixes data actually recorded over a circular area above the imaged subsurface point.

Lateral velocity variations in the layers are accommodated in the same way that they are in a single layer case: by mapping the variations, either directly as variations in the velocity over the interval of the layer, or by variations in parameters of a mathematical function. As for a single layer, the velocity may change with depth. However, such functions introduce complications in depth conversion. The time map to be converted to depth must be the pseudotime map that would be recorded if the velocity function for the layer held for the total depth interval from the survey datum to the base of the current layer. If there are abrupt lateral thickness changes in the shallower section, these must be smoothed out to simulate the smoothing inherent in processing. The procedure then for each layer is this:

1. Smooth time and depth maps for the top of the layer.
2. Convert the smoothed depth map to the top of the layer to a pseudotime map, using the (possibly mapped) time-depth function for the layer.
3. Compute the time interval from the smoothed time map at the top of the layer to the unsmoothed time map of the base of the layer.
4. Add this time interval to the pseudotime map for the top of the layer to give a pseudotime map for the base of the layer.
5. Convert this pseudotime map to depth using the (possibly mapped) time-depth relationship for the layer.

As with the single-layer case, the final map will not tie to the wells. The constant part of the error is easily removed, as in Figure 10-11, and the residual error can either be left in the final map or removed by subtracting an error grid as in Figure 10-7.

Map Migration

Where the Hubral effect becomes significant, usually where the dip on velocity interfaces exceeds about 15°, the most accurate solution to depth conversion of a time map is image-ray migration. This is done with map-migration software designed for the purpose starting with a horizon map picked on unmigrated data. The magnitude of the Hubral effect can be calculated by applying Snell's Law to a ray projected vertically down from the surface through the velocity structure proposed for depth conversion.

In principle, an interpreter could produce a more accurate map of a complex area by interpreting unmigrated seismic data and using map migration. In real exploration situations, this is almost always impossible, because crossing reflections become impractical to map. Where this approach might have been the only way of resolving complex

Downloaded 25 Jun 2012 to 95.28.162.50. Redistribution subject to SEG license or copyright; Terms of Use: http://segdl.org/

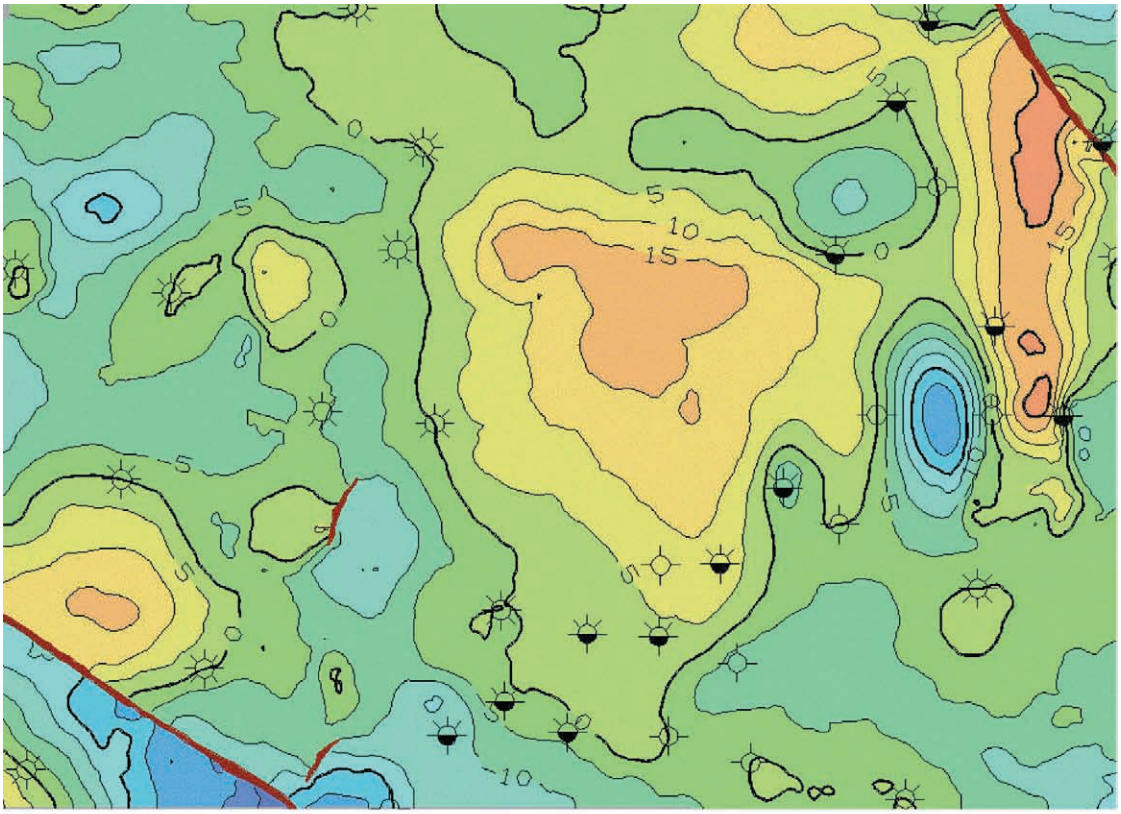

Fig. 10-14. Difference between the depth maps of Figure 10-5, generated using pseudovelocities, and Figure 10-8, generated using a single velocity function.

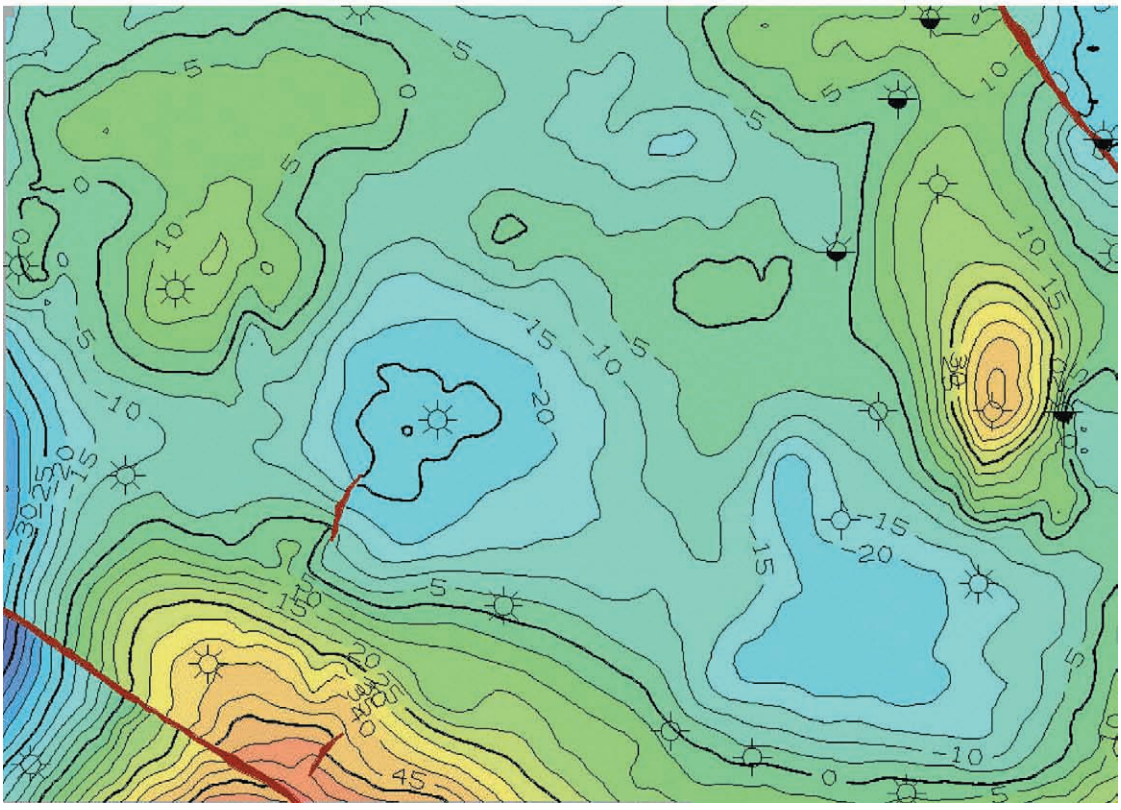

Fig. 10-15. Difference between the depth maps of Figure 10-5, generated using pseudovelocities, and Figure 10-11, generated using layers. Note that this map is not very similar to Figure 10-14.

Downloaded 25 Jun 2012 to 95.28.162.50. Redistribution subject to SEG license or copyright; Terms of Use: http://segdl.org/

structure with 2-D seismic exploration, 3-D seismic surveys allow 3-D depth migration, which, although expensive, may be the only practical technique where velocity structure is complex. Depth imaging is discussed in the next part of this chapter.

Dealing with Conversion Errors

All the depth conversion methods described here, with the exception of the pseudovelocity method, fail to tie exactly at wells. The amount of this well mistie can show how accurate the map is likely to be away from the well ties, where a new well is likely to be drilled. The constant component of all well misties should be subtracted from the depth map to give a map such as Figure 10-8 where the average mistie is zero. The residual misties are a measure of the accuracy of the final map. The misties posted on the map in Figure 10-11 have a standard deviation of 30 ft. In other words, a well drilled has a 95% chance of finding the mapped formation within 60 ft of the mapped depth. For a map with a total range of 220 ft, that is not reassuring.

The estimated errors for a map can be reduced in several ways. Firstly, some of the misties may be incorrect because either the depth in the well is incorrect, or because the interpreter has picked locally on the wrong reflection. The interpreter should check carefully both the seismic interpretation and the well depth at any wells where the mistie is much larger than average. Once this possibility has been eliminated, the remaining errors may be largely due to errors in the velocities, usually due to inadequate control points. Such errors could be expected to vary slowly across the map, so fitting a smooth trend to the misties should correct for them. Figure 10-12 is an example of such an error trend. Subtracting this error produced the corrected depth map in Figure 10-13. The standard deviation of the errors posted on this map is 18 ft, a significant improvement.

Once the interpreter has made a best estimate for a corrected depth map, there are still misties at wells. A final presentation map that has no errors at wells is made by gridding a residual error surface from the final misties, and subtracting this from the final depth map. Persons using this map must not assume that just because it shows the correct depth at all the wells it is completely accurate. Both Figure 10-5 and Figure 10-8 tie all the wells exactly. But they are not the same maps. The difference between the two is shown in Figure 10-14. The most accurate uncorrected map shown for this project is possibly Figure 10-11 and the difference between this and Figure 10-5 is shown in Figure 10-15. This difference map shows little resemblance to the trend surface used to refine the depth conversion to produce Figure 10-13. The comparison underscores the difficulty in evaluating the accuracy of any depth conversion.

Discussion

The very nature of seismic data, recorded in a typical nonisotropic medium, does not permit the derived depth surface to be accurate at all points in a given area. Some advantages and disadvantages of each technique are:

- Depth conversion with a single velocity function may be satisfactory over a very limited area, perhaps just around the well where the velocity data were acquired; this method often minimizes local errors in absolute depth for a single horizon.

- Where velocities vary with depth of burial more than with stratigraphic units, using a mapped velocity function is often the simplest and most accurate technique.

- Pseudovelocities and other techniques which convert each horizon independently often give small absolute errors for each horizon, but if the horizons are closely spaced the intervals can be grossly in error: the interpreter may even produce maps which imply crossing horizons.

Downloaded 25 Jun 2012 to 95.28.162.50. Redistribution subject to SEG license or copyright; Terms of Use: http://segdl.org/

- Image-ray map migration suffers from errors in velocities and the assumption that the stacked seismic trace is a zero-offset trace, but it may be needed in areas with both steep dip and large velocity variations.

- The layer-cake method minimizes the errors in the thickness of individual layers but may introduce large errors in the cumulative depth when several layers are added together. This velocity model is geologically more realistic where velocities change rather abruptly across the stratigraphic boundaries, but less realistic where velocity variation depends more on depth of burial than on stratigraphic position. Most commercial software packages appear to use this technique, sometimes with image-ray map migration as an option. Layer-cake depth conversion has two disadvantages:
    1. Abrupt horizontal changes in velocity often produce false structures in the underlying horizons.
    2. This technique is unnecessarily complex and prone to errors where velocity is more a function of depth of burial than of stratigraphy.

The best one can do is to make full use of the available velocity data and to ensure that all information available in each well is fully consistent with the geophysical interpretation within the statistical probable error. The interpretation must not be forced to tie exactly to the well information; the most accurate depth surface is the one that statistically gives a minimum standard deviation. Statistical adjustments ensure that the residual misties are a true indication of the accuracy of the interpretation. Depth conversion software packages often ease the mechanics of complex depth conversion techniques, but the interpreter must understand exactly how the software works before relying on the output.

References

Dix, C. H., 1955, Seismic velocities from surface measurements: Geophysics, v. 20, p. 68–86.

Hubral, P., 1977, Time migration — some ray-theoretical aspects: Geophysical prospecting, v. 25, p. 738–745.

Liner, C. L., 1996, Seismos — a free-form column on the history and culture of geophysics: The Leading Edge, v. 15, p. 1156–1158.

Wolf, D. J., 1990, Mathematics and geostatistics: A Tutorial for geoscientists without the Ph.D. in mathematics (geostatistics for poets): SEG 60th Annual Meeting expanded abstracts, p. 336–338.

Downloaded 25 Jun 2012 to 95.28.162.50. Redistribution subject to SEG license or copyright; Terms of Use: http://segdl.org/

Downloaded 25 Jun 2012 to 95.28.162.50. Redistribution subject to SEG license or copyright; Terms of Use: http://segdl.org/

3-D Depth Image Interpretation

Contributed by William L. Abriel, Joseph P. Stefani, Robert D. Shank, and David C. Bartel,
Chevron U.S.A.

Concept of 3-D Depth Imaging

The purpose of our paper is to illustrate the concept of 3-D depth imaging in seismic exploration and development. Our experience is concentrated in the Gulf of Mexico subsalt where depth imaging is an integral part of that play. Through the use of models and live data examples, it is our intent to communicate why and how depth imaging works, as well as some of the pitfalls.

Depth imaging has grown significantly in the past decade as a percent of the seismic processing industry. Geologists, engineers and geophysicists are more commonly utilizing depth-imaged seismic data in daily activities to find and understand hydrocarbon reservoirs. And although the tradition of depth imaging grows from interests in structural definition of hydrocarbon traps, the quality of depth imaging in 3-D is high enough to also have significant impact in reservoir definition and stratigraphic imaging. As depth imaging moves further into the mainstream of our business, it becomes important to describe and even quantify the uncertainties of the earth descriptions we derive from these data.

It is not necessary for users of depth images to be high-powered seismic data processors. However, it is important for users to understand the required elements of successful depth imaging, and how these elements contribute to the success or failure of the imaging process. One very important concept that needs to be understood is the sensitivity of seismic imaging to variations in overlying earth velocity, and why depth images can be significantly different from time-imaged data. An extension of this concept also shows why 3-D pre-stack depth imaging may be necessary instead of post-stack. Another signal-based concept requiring clear understanding is that of incomplete seismic illumination in shadow zones. These must not be mistaken for changes in reflection amplitude variation caused by changes in lithology, fluids or pressure. In addition to understanding the signal concepts, it is also important to understand coherent noise and how it should appear in depth-imaged data.

The models and data examples shown in the sections that follow are intended to illustrate the above points. In order to cover them all, we have compiled data from a series of different projects. We have concentrated on illustrating one play type (Gulf of Mexico subsalt) for consistency and focus. The basic concepts illustrated here are useful when understanding other plays where depth imaging is used, but it should be noted that the relative importance of the elements constituting depth imaging varies among plays.

Why Time Imaging Is Not Depth Imaging

The imaging of seismic data is intended to represent the earth subsurface reflectivity with sufficient accuracy for rendering structural geology, stratigraphy, and reservoir properties. Field data are recorded in the time domain with varying source-receiver offsets to reflect energy from the subsurface at multiple angles.

Time imaging of these data attempts to add together the subsurface reflections and position (migrate) them to the appropriate 3-D *xyz* positions while still retaining time as the *z* axis. Time imaging generally employs elements of a "flat earth" processing model, and cannot correct for rapid variations in earth velocity. Therefore time imaging is forgiving of small earth-model errors but fails when velocity

Downloaded 25 Jun 2012 to 95.28.162.50. Redistribution subject to SEG license or copyright; Terms of Use: http://segdl.org/

varies rapidly. Standard practice of using these time data is to interpret them in the time domain, and convert the resulting map to depth, as described in the first part of this chapter. Alternately, the seismic time data are depth "stretched" either vertically or along raypaths dictated by the velocity model. However, depth stretching of traces should not be confused with depth imaging.

Depth imaging uses a velocity model in the depth domain to compensate for propagation effects. Each vertical and horizontal change in the velocity field is honored in a specialized migration algorithm to account for the bending of the energy down to reflection wavelength scales. In this sense, depth imaging is a correcting lens attempting to place the reflected energy in its correct *xyz* depth position. Although costlier, depth imaging is generally more accurate than time imaging. As a result, depth imaging is fast becoming the process of choice in areas of high velocity complexity.

But along with the increase in image accuracy, comes the danger of not having the right earth velocity to make the corrections. Because depth imaging does such exact calculations of the ray paths, it is very sensitive to errors in our interval velocity model of the earth. While small distributed errors in spatially smooth RMS velocities are generally not harmful in time migration, cumulative errors in the local interval velocity are leveraged and magnified in the depth imaging process. These can be so bad as to degrade the depth image to the extent that it gives less information than a depth stretch of the time-imaged data! Depth imaging, then, must be considered in a context much wider than a migration algorithm, and must at least also include velocity analysis, accuracy, and representation.

As a representation of the principles behind depth imaging, refer to the model of seismic ray propagation in Figure 10-16. The 2-D cross-section shows a salt ledge buried in sediments of modest velocity variation represented by multicolored layers. Imaging of the subsurface typically employs seismic traces from shots and receivers whose midpoint at the surface is the same (common mid point: CMP). This allows subsurface reflection points (common reflection point: CRP) to add together when the earth velocity can be approximated by flat layers. However, when the earth velocity layers are not very flat, the subsurface reflection points are not in common, and the image can become seriously distorted.

In Figure 10-16, the individual CMP rays in black illustrate how the seismic energy travel path through sediments suffers small "kinks" at the interfaces where the velocity changes. In contrast, at the salt boundaries the change in angle is quite large, and so this body acts as a distorting lens for imaging the reflectors below. The cross-section shows how rays constituting a single CMP gather hit the subsurface irregularly over a 5000-foot horizontal area. The theory for time imaging generally assumes that the kinks are small and not important at the small scale. It also assumes that no large ray bending occurs like we see at the salt interfaces.

The inset in Figure 10-16 helps illustrate this difference in time and depth imaging. The plot of offset versus time shows the ray arrivals as recorded at the surface. Ideal time imaging requires the arrivals to fall along a hyperbola, but complex ray bending scatters individual arrivals about a hyperbolic trajectory. In this case time imaging is unsatisfactory, precisely because it assumes straight rays, and because it further assumes the reflection comes from the horizontal location of the midpoint at x = 15,000 feet.

Correct depth imaging, however, is designed to correct for these distortions and place the events in their appropriate horizontal and vertical position. The effect of depth imaging is to use the source-receiver pairs whose common reflection points are the same, based on good knowledge of the velocity through which the rays travel. The small kinks are honored directly, and all ray bending is taken into account. Where no salt exists in Figure 10-16, the rays generally make it to the surface without much distortion. Through the salt, however, the salt/sediment velocity contrast of 2 has a large effect where the rays intersect the salt interface at a non-normal angle. Rays can emerge from the salt displaced thousands of feet

Downloaded 25 Jun 2012 to 95.28.162.50. Redistribution subject to SEG license or copyright; Terms of Use: http://segdl.org/

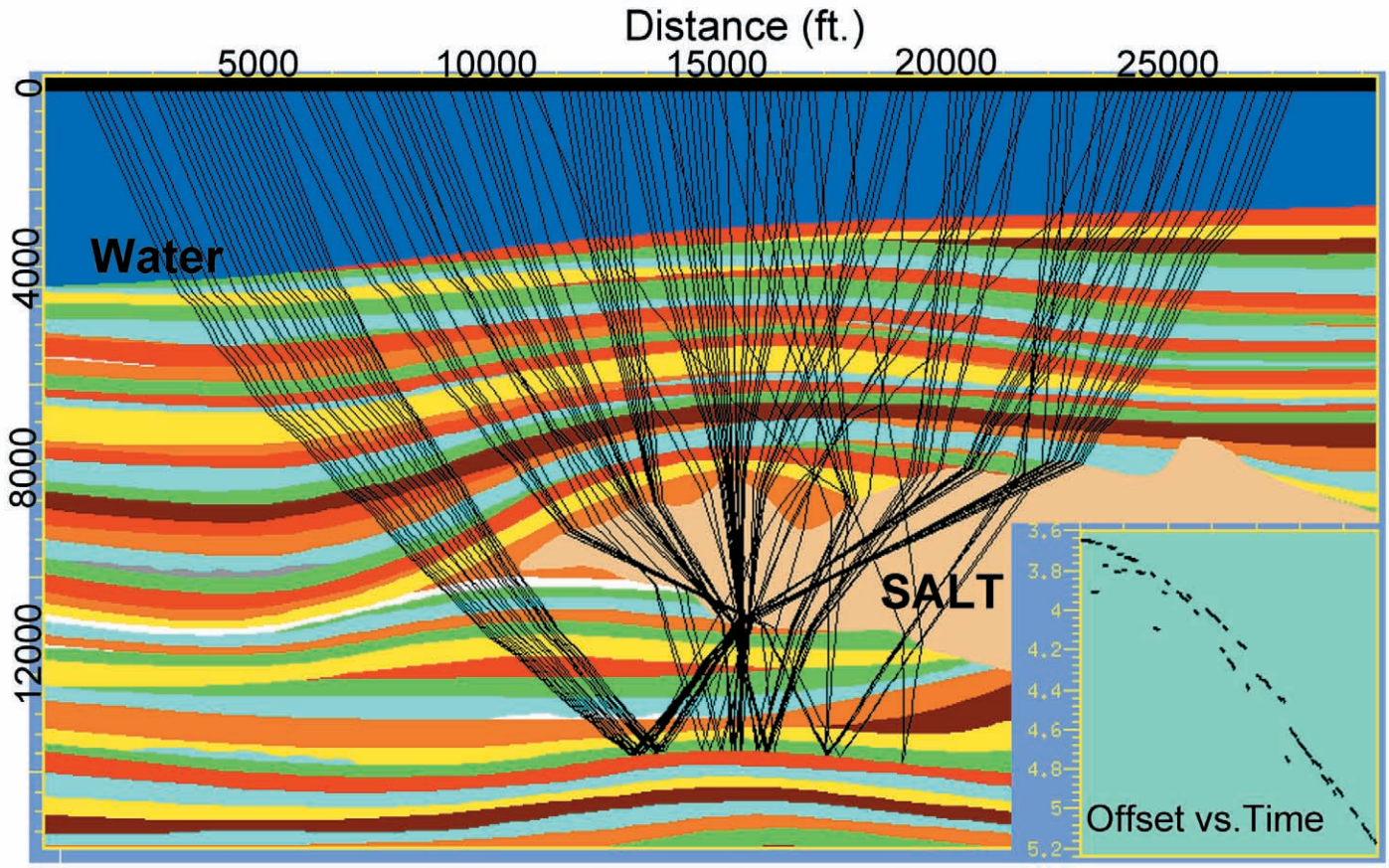

Fig. 10-16. 2-D cross-section of seismic ray paths for one common midpoint gather (CMP). Note the distortion of ray paths due to a strong velocity contrast at the rugose salt-sediment interface and the scatter of reflection points along the subsurface reflector. Inset: A CMP gather of arrival times versus offset as recorded at the surface, covering source-to-receiver offset from 0 to 26,000 feet.

Downloaded 25 Jun 2012 to 95.28.162.50. Redistribution subject to SEG license or copyright; Terms of Use: http://segdl.org/

horizontally. Depth imaging corrects for these variations whereas time imaging does not.

The benefit of the correction process inherent in depth imaging comes at a substantial price. Significant interpreter effort is required build the interval velocity model and to update the velocity estimates while honoring geologic constraints. Also, much greater raw computational effort is required in depth migration, especially in its 3-D and pre-stack manifestations.

Required Elements of 3-D Depth Imaging

Effective 3-D depth imaging of surface seismic data can be accomplished using the required elements of (1) appropriate acquisition coverage, (2) a robust and accurate velocity representation of the subsurface, (3) 3-D ray tracing, (4) a depth migration algorithm, and (5) an imaging expert. High-quality imaging results can be obtained when each of these elements is also of high quality.

Even with optimal acquisition, depth imaging cannot overcome the shortcomings of blind spots in the subsurface. Although 3-D seismic coverage at the surface may be evenly distributed, substantial ray bending through lenses like rugose salt often prevents parts of lower reflecting surfaces from being touched by penetrating energy. As Figure 10-16 shows for a single surface CMP, there are gaps in the subsalt illumination. Seismic processing alone cannot heal these gaps. Another effect can occur when energy is not reflected back from the subsurface, but enters a layer of high contrast at what is known as the critical angle, where the wave energy is blocked. An example of this is shown in Figure 10-17; shots from outside a salt body travel to the reflector, but only some of them return to the surface. With a valid model of the subsurface velocity, maps can be generated showing where and why this takes place based on counting the hits from ray tracing.

Another approach to understanding illumination variations is to model them using full wavefields. This approach offers a volumetric view and understanding of lost data zones, and also calibrates troublesome variations in amplitude that do not represent geology. Figure 10-18 shows slices from a 3-D volume of zero-offset-wavefield depth migration amplitudes. Input to the migration consists of the simulated surface wavefield from a grid of point sources of equal strength distributed throughout the earth model. The migration amplitudes have variations solely due to variations of wave propagation in the earth, migration aperture, and migration algorithm, but are independent of reflector lithology and reflectivity. Therefore, the value of such maps for interpretation is to distinguish between incomplete illumination effects and geology.

For our examples in the Gulf of Mexico, the velocity representation of the salt bodies and the enclosing sedimentary section require a robust representation of the salt interface. The exact topology of the salt interface is critical to imaging success, as the ray bending there is so large. Even small errors in the local dip of the interface will fail to adequately place the subsurface energy. 3-D software is used to build, edit, and update the salt interfaces in great detail. Then, to complete the 3-D velocity model, the software is also required to handle additional velocity objects, velocity gradients, and gridded small-scale changes in the sedimentary section. Speed and accuracy are important in this process, but just as important is the ability to communicate the model to geophysicists, geologists, managers and partners, so 3-D visualization software is employed.

The resulting velocity model is then used to calculate the ray paths that are needed to illuminate the subsurface and correct for the bending of the reflection energy. The travel paths of the rays are also visualized to show where and why the subsurface corrections take place. The ray calculations are then used by a migration program to 3-D propagate the seismic energy recorded at the surface back through the earth model to illuminate the subsurface. Aspects of a good migration algorithm for depth imaging are speed, accuracy, low cost, and good noise handling characteristics.

Downloaded 25 Jun 2012 to 95.28.162.50. Redistribution subject to SEG license or copyright; Terms of Use: http://segdl.org/

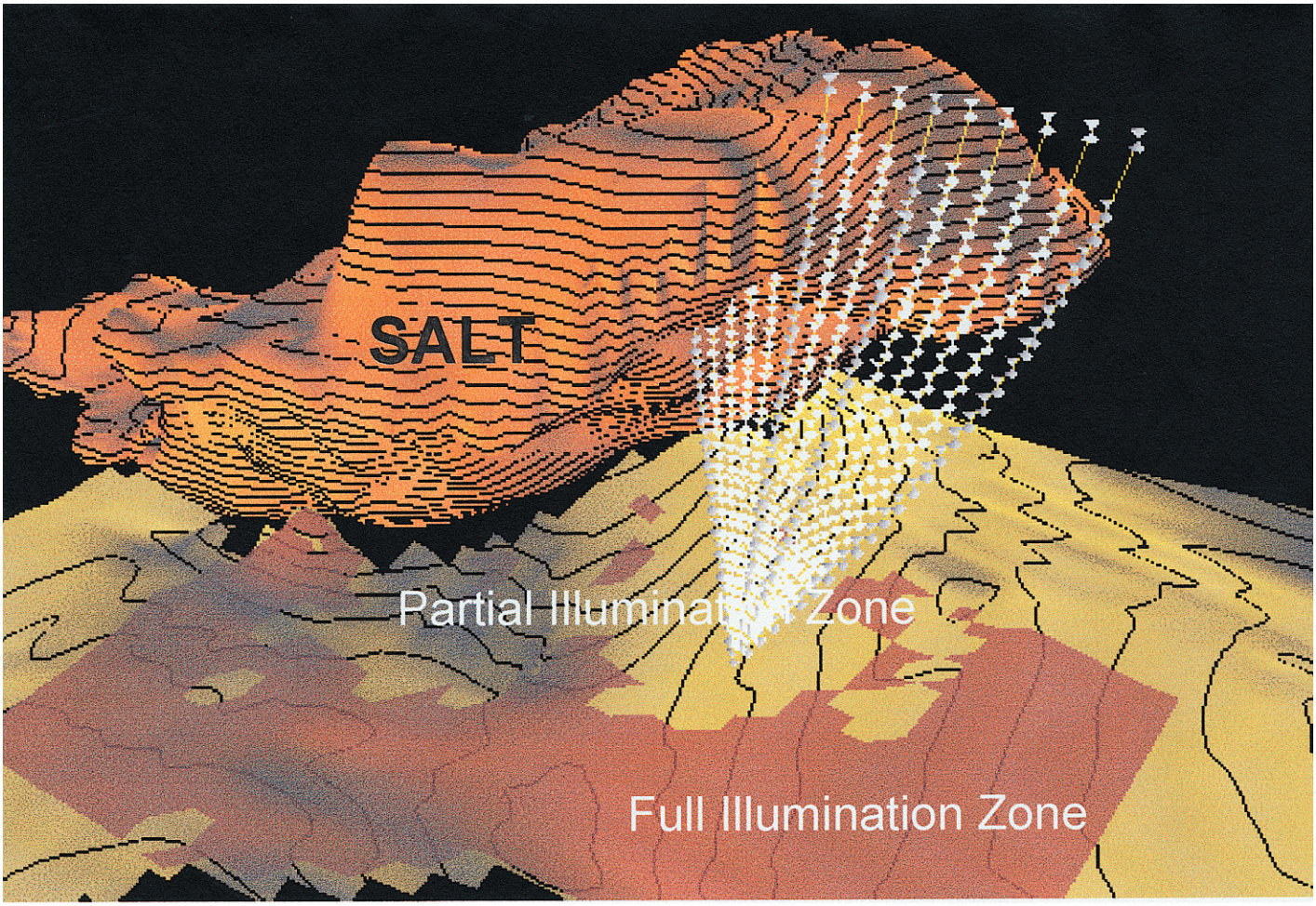

Fig. 10-17. 3-D illustration of a partially illuminated reflector. In this case, the near-offset rays travel successfully from source to reflector and back to the receiver. Rays for the farther offsets are stopped at the salt base due to postcritical incidence.

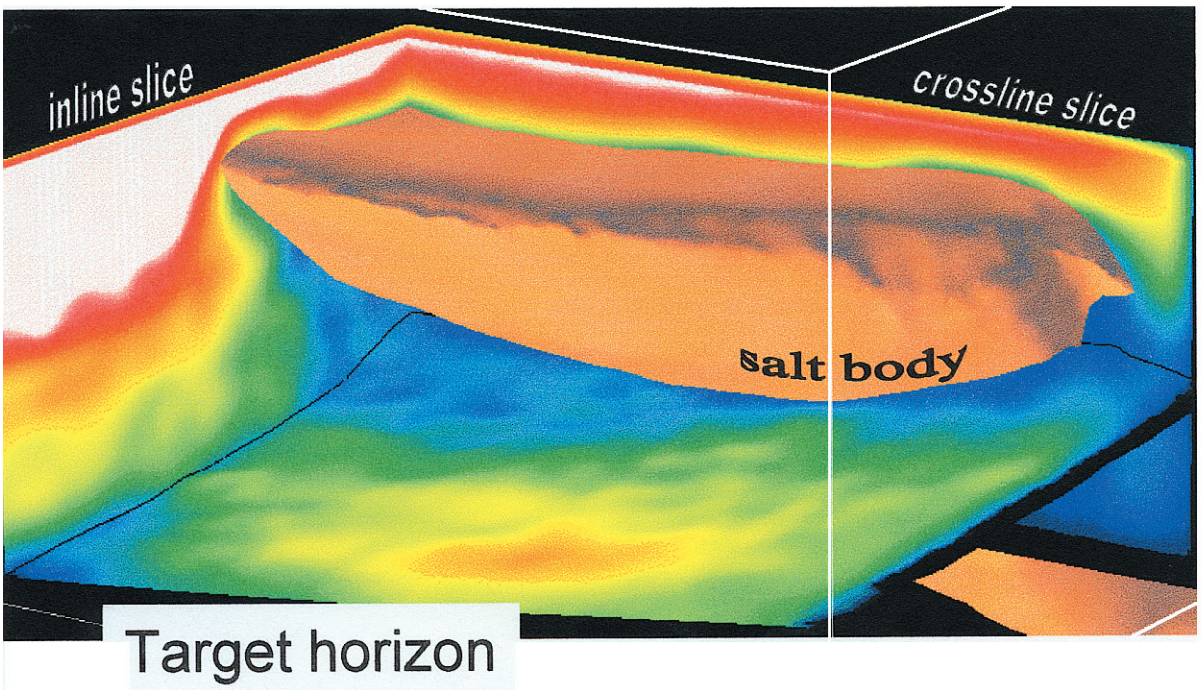

Fig. 10-18. 3-D perspective of illumination of the subsurface as calculated from full wavefield modeling. White areas are completely illuminated, blue the least. Note the low illumination just below salt. Also note the amplitude changes on the horizon of interest not due to lithology changes.

Downloaded 25 Jun 2012 to 95.28.162.50. Redistribution subject to SEG license or copyright; Terms of Use: http://segdl.org/

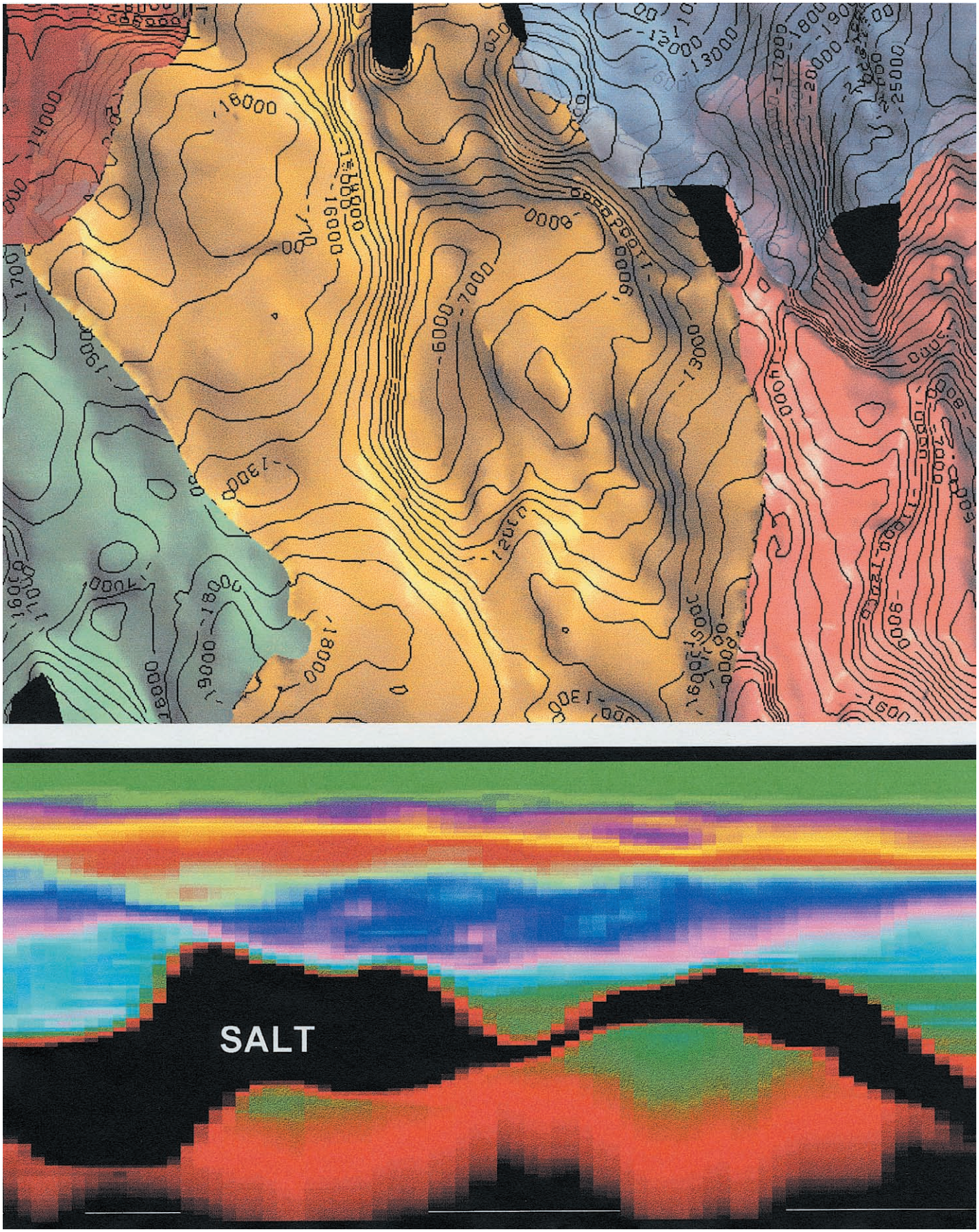

Downloaded 25 Jun 2012 to 95.28.162.50. Redistribution subject to SEG license or copyright; Terms of Use: http://segdl.org/

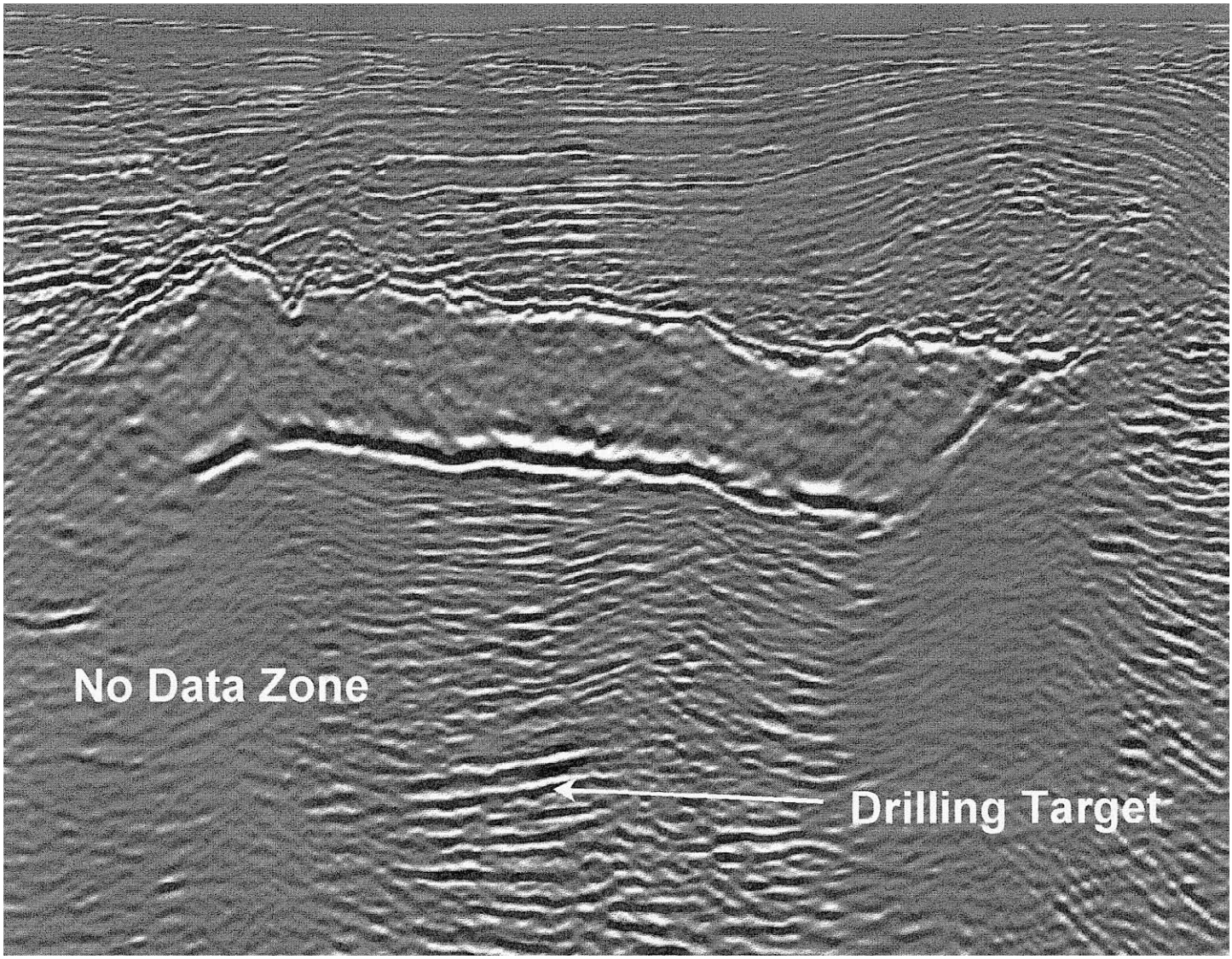

Fig. 10-19. (Opposite, top) Overlapping 3-D salt bodies as represented in Gocad. Horizontal extent covers tens of thousands of feet.

Fig. 10-20. (Opposite, bottom) Cross-section of salt bodies as seen in Figure 10-19, with velocity field included. Horizontal velocity variations in the sedimentary section span a few thousand feet, and vary in magnitude over several hundreds of feet per second.

Fig. 10-21. 3-D depth-migrated seismic image. Note interaction of the top salt and the sedimentary faults and folds. In the central zone, higher amplitude reflectors suggest potential reservoir sands. Shadow zones tend to occur where base salt is discordant with reflector dip.

Downloaded 25 Jun 2012 to 95.28.162.50. Redistribution subject to SEG license or copyright; Terms of Use: http://segdl.org/

Because the depth imaging process is employed in areas of high geological complexity (from a velocity perspective), maximum information of the resulting images is gained when the experience of the depth imager is used in the interpretation. Signal, noise, shadow zones, depth uncertainty and position uncertainty can be validly assessed when using the specific knowledge of how the image was formed and how it can be modified.

Figures 10-19 to 10-21 illustrate some of the elements of the depth imaging process. In one step, the tops of a series of overlapping salt bodies with high complexity (Figure 10-19) are represented with Gocad software. Notice that the surface contours in 3-D show a great deal of structure at both the large and the fine scale. Both faulting and folding of the salt is represented faithfully to be sure that all of the ray bending can be accounted for in seismic processing. An east-west cross-section (Figure 10-20) illustrates the sedimentary velocity surrounding these complex salt bodies. Variation in the velocity of the surrounding sediments is a complex function of depth, geological age, deposition rate, compaction, lithology, pressure, and fluids. Accurate analysis and representation of the sediment velocity is important in imaging, as these changes determine the path of the seismic energy.

With adequately recorded seismic data and the appropriate velocity model, seismic imaging via high quality migration is then possible. An example of a depth-migrated subsalt image from a similar but different area is shown in Figure 10-21. Several good points can be made from this seismic image. Notice the complexity of the salt-sediment interface at the top. Faults and small-scale folds with 3-D geometry make the interface have local dips up to 45° immediately adjacent to planar salt sections.

Below the salt, prospective reflections (marked) can be seen that terminate both to the left and right under non-illuminated shadow zones. Imaging may not be possible in the no-data locations as calculated from ray tracing. These shadow zones, apparently due to postcritical ray blockage, are common when the dips of the reflector and the base salt become too discordant. Even so, the imaging below salt shows very encouraging events that resemble the type of deepwater turbidite sands expected in a stratigraphic trapping position. The consistent higher amplitude events lose reflectivity up the paleo-dip as would be expected if they are deposited in a paleo-low. Utilizing the depth image, then, the prospective horizons under the salt were drilled. Sands were encountered in the zone of interest at the dip rates shown in the cross section.

3-D Post-stack Depth vs. 3-D Post-stack Time Imaging

Depth imaging is not only converting the time recordings to depth, but is also positioning the data at the appropriate horizontal and vertical depth location. When comparing the two approaches in a simple velocity area, they should give comparable results. However, comparisons in complex velocity areas will be different. Inadequate time imaging can be corrected through depth migration. Depth migration affects both the structural and the amplitude information of the image.

An analogy of the impact of depth imaging over time imaging would be a similar comparison of migrated time vs. unmigrated time data. An example would be when unmigrated data can have large smooth anticlines that are really synclines when migrated! Depth imaging can sometimes have this much impact when the velocity of the earth is complicated and highly three-dimensional. Therefore, differences in migrated time and migrated depth images will exist in areas of highly contrasting and varying velocity where the lens effects are greatest. The Gulf of Mexico subsalt play is a good example of just such an area.

As previously noted, depth imaging is not an improvement over time imaging when an inaccurate (or even a moderately wrong) velocity model is used. Given the precision of the migration algorithms to act as lens correctors, errors in the velocity model can propagate odd-looking distortions that can be confused with geology. An example of this would be false faults or fold axes caused by inappropriate breaks in the velocity model. An additional caution should be noted. Noise in depth images appears different from the same noise in time images, and in both cases the noise can be either similar

Downloaded 25 Jun 2012 to 95.28.162.50. Redistribution subject to SEG license or copyright; Terms of Use: http://segdl.org/

to or distinct from the signal. This becomes very important, when depth imaging is employed in noisier than normal areas to bring out signal. When both the processing and the interpretation of the data are well connected, experience allows the avoidance of pitfalls in velocity, noise and poor illumination zones.

As an example of post-stack time versus depth 3-D imaging, refer to Figures 10-22 and 10-23. The difference between these sections is the migration velocity and the migration algorithms. In both cases, the input data are stacked in the time domain. The geology of the area is quite interesting. As observed in the time section of Figure 10-22, the shallow central anticline is underlain by a salt diapir. Deeper, the east dip extends from the center to the edge of the data and a no-data zone extends under the salt from the center to the west.

Comparing the 3-D depth-migrated data (Figure 10-23), one sees significantly new information. First, a base of the salt can be seen in the depth-migrated data (A). Although the reflectivity of the base is not as stable as the top salt reflector, the base can be mapped in 3-D. The reason one can now see this reflector is that depth migration is honoring salt velocity and structure. It has correctly assembled the appropriate data, from both within and out of the plane of the section, into its coherent *xyz* location.

Deeper events in the depth image (B) imply a quite different structural history. The possibility of deep block faulting is suggested. This also sets the structural framework of the middle section (C) where dips have changed from monoclinal east to that of a half anticline. This is a significant change to the understanding of the structure. In addition, the characteristics of the reflectors on the east flank are also different in the depth image. Unfortunately, in the west flank of the subsalt, the noise characteristics have not improved sufficiently to complete the subsalt picture. The attractive west dip segment (D) is a multiple! The subsalt section here probably cannot be improved using the stacked data as input to migration.

The high impact of depth migration is due to its application where the velocity model is complex. The salt velocity is about twice that of the sediments, and waves traveling through salt rapidly deviate from trajectories appropriate to the time processing model of a layered earth. Additional differences are due to horizontally changing velocity in the sedimentary section. Although lateral sedimentary velocity variation is often modest, in some areas it can vary by up to a few thousand feet per second over several thousand feet, as it does below salt in Figure 10-23. Thus the impact of depth imaging is fairly small above salt but quite large in the deeper central section where imaging is greatly affected by the rapid velocity contrasts of the geology.

Noise Characteristics of Depth-imaged Data

As noted in the prior examples, depth migration is often applied in complex velocity environments where signal is desired in otherwise noisy areas. Because this is so, an understanding of the noise characteristics of these areas and how the imaging algorithm handles them becomes important.

Reflections of the subsurface that are correctly imaged are the signal we desire. Coherent energy that does not represent the earth reflectivity is a danger in our interpretation efforts. Mispositioned signal does not qualify as noise. Given the right velocity model and acquisition sampling, this can be handled correctly. What we do need to classify as coherent noise includes surface waves, refractions, mode conversions, multipaths and multiples. These are most common in areas of complex structure and high velocity contrasts, to the degree that the noise may be ten times stronger than the signal itself! The noise is not inherent in depth imaging, but depth imaging is more commonly used in areas with these noise characteristics, thus we can expect depth images to commonly contain noise.

Surface-generated coherent noise is common in land data, and especially troublesome where the wavefield is strongly reflected or diffracted by surface objects (dunes, valleys, karst, etc.). Marine data also have surface-generated noise caused by sea bottom diffractors and waves trapped in near-surface low velocity zones. Surface generated noise can sometimes be localized but often affects the entire seismic section.

Downloaded 25 Jun 2012 to 95.28.162.50. Redistribution subject to SEG license or copyright; Terms of Use: http://segdl.org/

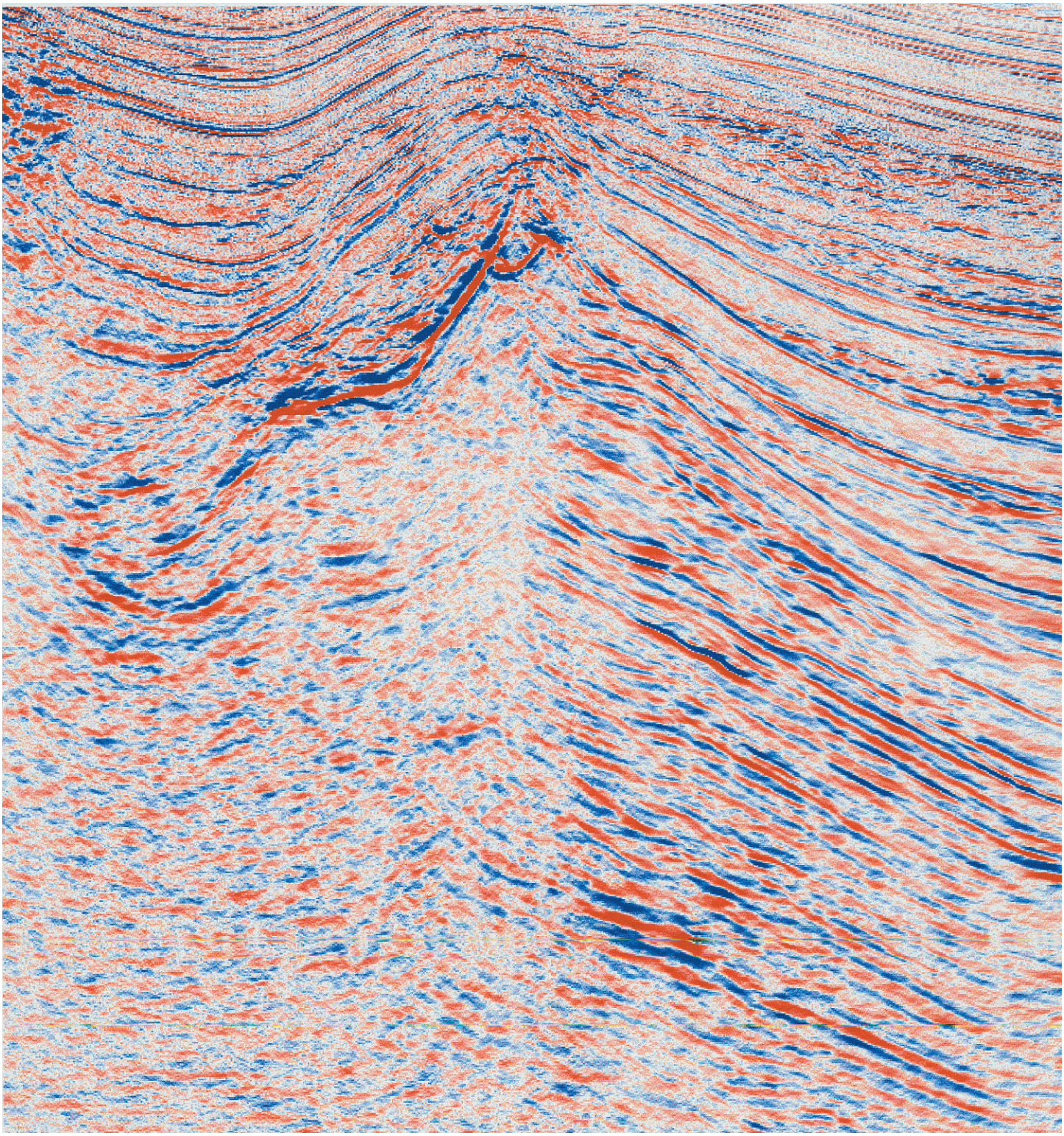

Fig. 10-22. 3-D post-stack time migration. Compare with Figure 10-23.

Downloaded 25 Jun 2012 to 95.28.162.50. Redistribution subject to SEG license or copyright; Terms of Use: http://segdl.org/

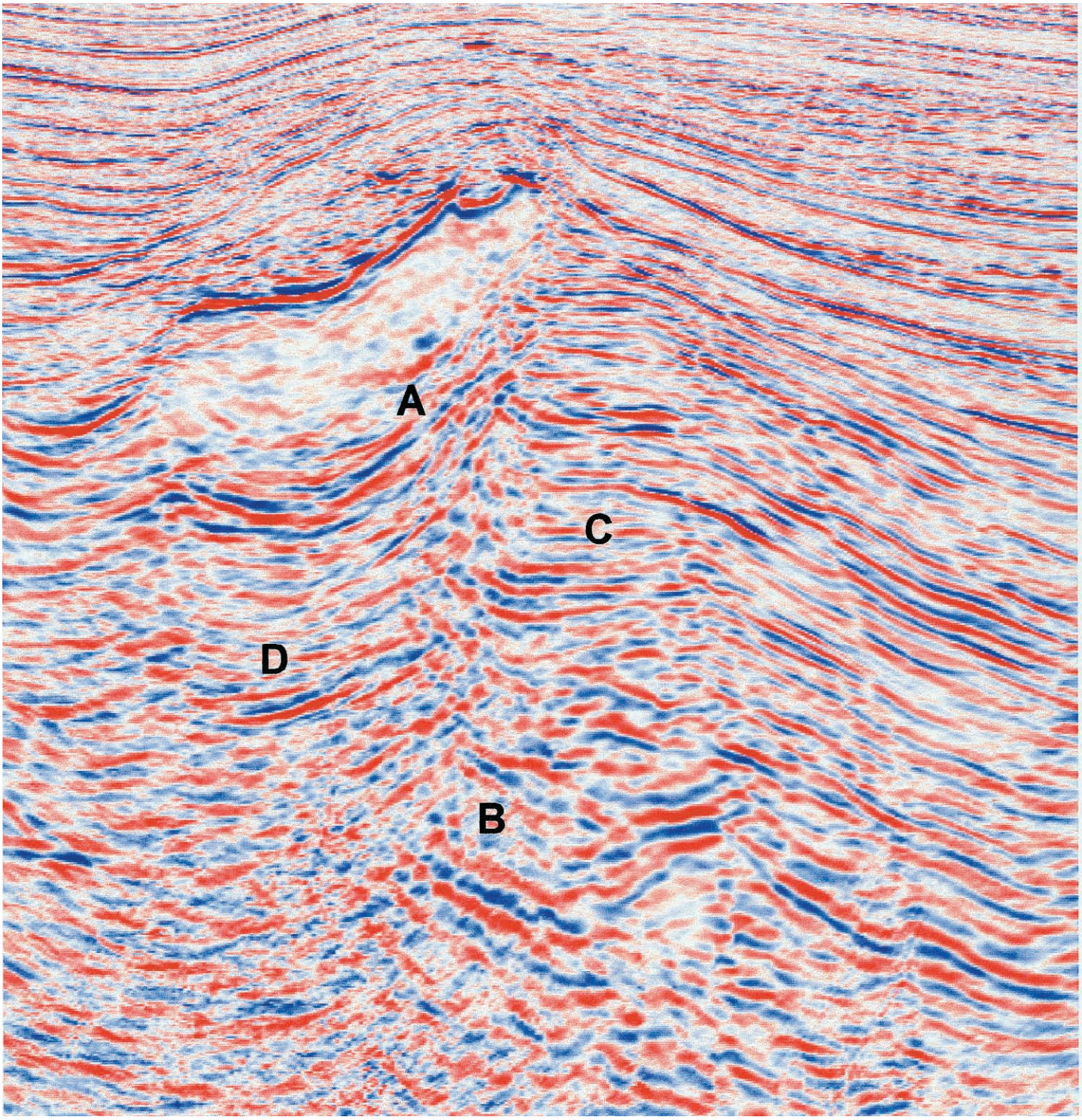

Fig. 10-23. 3-D post-stack depth migration of same input data as for Figure 10-22.

Downloaded 25 Jun 2012 to 95.28.162.50. Redistribution subject to SEG license or copyright; Terms of Use: http://segdl.org/

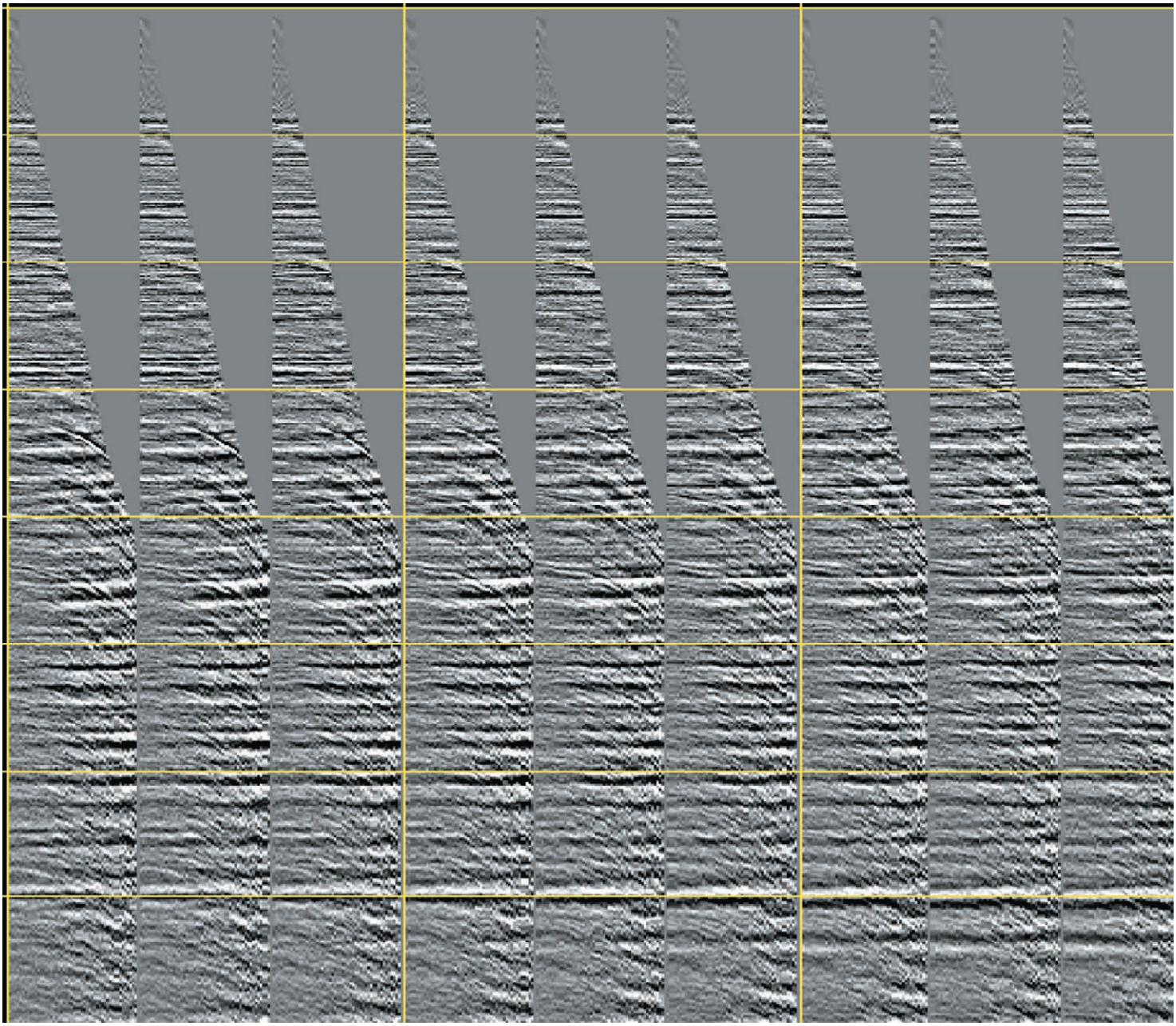

Fig. 10-24. 3-D depth-migrated common reflection point (CRP) gathers (no salt). Flat events within each gather are indicative of correctly imaged primary signal. Note multiples in the central portion of the section that curve downward due to slower propagation. During stacking these cancel well.

Seismic reflection energy converted to refractions is another coherent noise in our imaging, and is caused by energy traveling along high velocity layer boundaries. Although this energy is not dominant in depth imaging, it can easily be misinterpreted as signal especially at critical locations like the salt-sediment interface.

Some reflections do not fit the migration theory and so are considered coherent noise. Included are multipaths and multiples. Multipaths are waves that reflect from several single interfaces much like hitting a pool ball off three cushions. This energy does not conform to migration implementations, and can be quite strong. Conversion of compressional energy to shear energy also represents a significant noise characteristic of our data. This mode conversion is especially strong at the carbonate and salt interfaces and can contribute significantly to a low signal-to-noise ratio in the seismic image.

Another type of unwanted reflection energy is multiples. These reflections travel several times in the layers of the earth bouncing up and down repetitively. Simple first-order free-surface multiples are commonly recognized in unmigrated time data as having approximately twice the reflection time of their primaries. Examples of strong

Downloaded 25 Jun 2012 to 95.28.162.50. Redistribution subject to SEG license or copyright; Terms of Use: http://segdl.org/

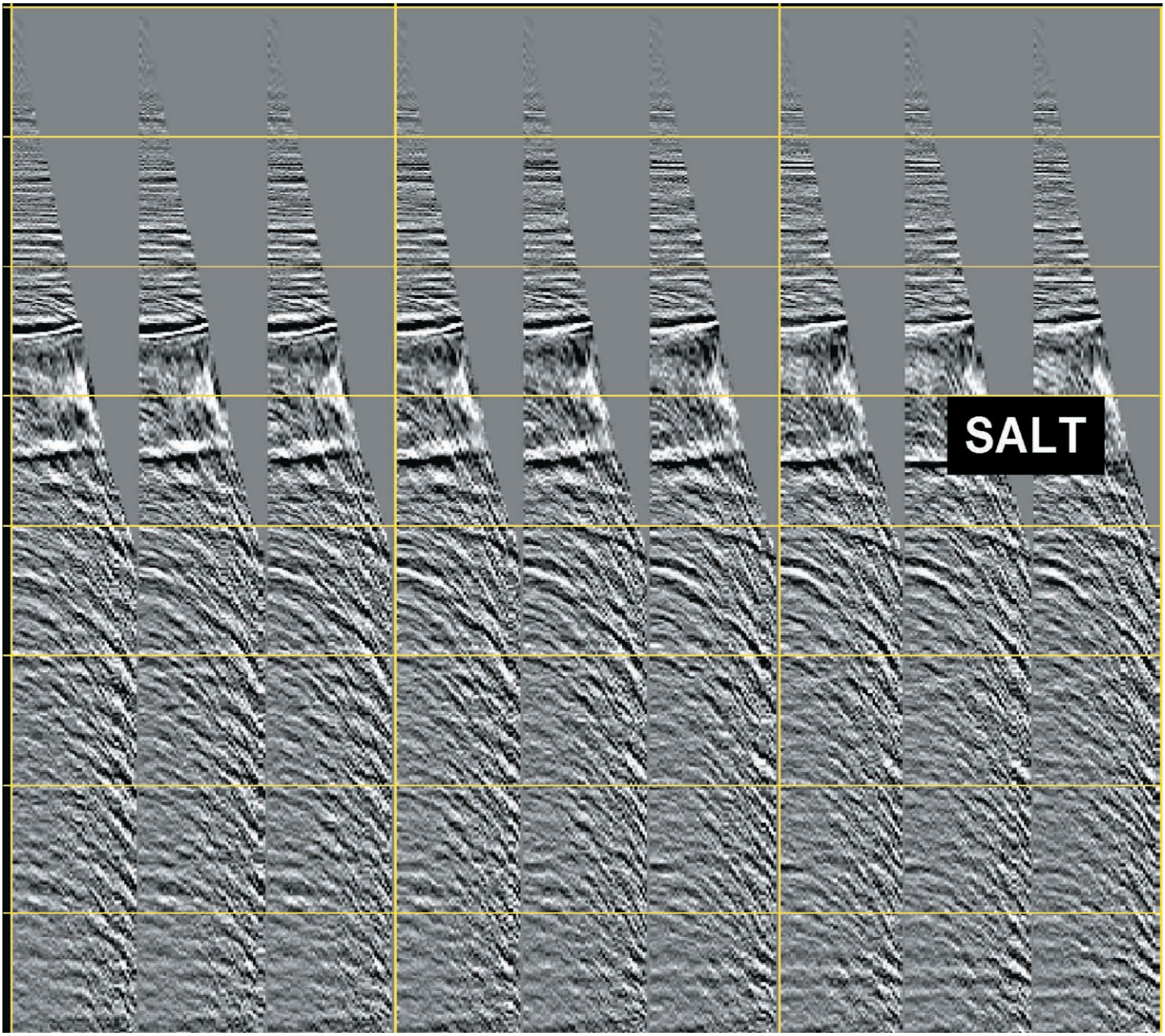

Fig. 10-25. 3-D depth-migrated CRP gathers with intervening salt. Although stratigraphically continuous with the nearby gathers of Figure 10-24, here flat subsalt signal is much weaker than the curving coherent noise (multiples).

multiple generators are the air-water interface, ocean bottom, carbonate layers and salt. Complicating this situation are the shorter path, interbed multiples spawned among the brighter reflectors. Although they are no stronger individually than free-surface multiples, the interbed population increases geometrically with the number of bright multiple generating interfaces, instead of proportionately as do the simple multiples. This is the coherent noise challenge in subsalt imaging.

Figures 10-24 and 10-25 show 3-D depth-migrated traces of data before stacking. In Figure 10-24, the sedimentary signal is very strong, the velocity is well behaved, and the gathers are quite flat prior to stacking. With close inspection, some noise (multiples) can be seen that appears to be parabolic and turning down at the far offsets (to the right). In Figure 10-25 a continuation of the same sedimentary section is represented subsalt, where extensive mode conversions and multiples exist. Look hard and you will see the same flat reflectors are in these data, but they are about ten times weaker than the coherent noise. The subsalt seismic signal is weaker due to the conversion of much of the energy to noise.

Downloaded 25 Jun 2012 to 95.28.162.50. Redistribution subject to SEG license or copyright; Terms of Use: http://segdl.org/

All of the coherent noises described above exist in the time-imaged seismic sections, because they are a result of the seismic acquisition and the wavefield paths over which they travel. The depth imaging does not create the noise, but does distribute it differently than does time imaging. In the poor image portions of Figures 10-21 and 10-23, the section is dominated by coherent noise. The energy there has a characteristic that is important to understand – it generally does not map in 3-D. This characteristic is most easily evaluated by using rapid 3-D movie views, and is very important in sorting out noise from signal when they exist in equal strength.

Much of the noise characteristics of depth-imaged areas can be better understood by employing seismic modeling. 3-D ray tracing can predict where the shadow zones are. The position and strength of multiples and mode conversions are also predictable. These predictions should be confirmed on the time-migrated data, and aid in the interpretation of time-imaged data. However, to understand noise in depth-imaged data, one must also account for the fact that the noise has been pushed though a depth migration process that can scatter or collect noise in ways more complex than for time migration.

As an example, Figure 10-26 illustrates a subsalt depth migration containing both signal and noise. The velocity model used is one of a simple sedimentary velocity encasing salt. However, the salt velocity layer is made infinitely thick below its top, so that the depth migration is used to image and identify the base of the salt. Seismic ray trace modeling of the multiple generated from the top of the salt plus an extra bounce in the water layer shows complexity in 3-D. To match the depth-migrated wavefield image, the ray traced multiple was also "ray" depth migrated, and posted on the seismic cross-section in yellow. Where its overburden is simple, the multiple is very continuous and can be wrongly identified as base salt. Where the 3-D ray paths are complex, the multiple incoherently migrates into alternately scattered and convergent zones. Having the ray migrated multiple in this case allowed us to avoid a wrong interpretation of the salt base and proceed with completing the salt velocity model and then imaging the subsalt section.

Pre-stack Depth Imaging

Post-stack depth imaging uses the time stack as input to a depth migration. This is a reasonable thing to do when the uncertainties of the velocity model are large, or cost is a major issue. However, it is an imaging compromise. Stacking seismic data is the wrong thing to do in complex velocity areas, and depth migrating this simply moves the wrong data around without constructing the right image. Referring back to the inset in Figure 10-16, adding this erratically arriving signal along a hyperbola will produce a fuzzy stack of the data, which can then be migrated. Pre-stack depth migration handles each trace independently to create more precise image points in the subsurface.

It is important to note, for example, that the existence of an amplitude in stacked data at a particular trace and time does not guarantee that it will find a place in the post-stack depth image. Assume that the stack amplitude comes mostly from the farther offsets, while because of salt geometry the nearest offset ray experiences a quite different trajectory (or attenuates in a shadow zone). Then, because a post-stack migration algorithm maps data back along the zero-offset ray, a bias in its trajectory may misplace the entire stack amplitude or even carry it into oblivion.

With a good earth velocity model in areas of complex geometry and velocity, imaging accuracy and precision are improved by pre-stack depth migration, which puts the signal in the right location for each separate seismic trace and corrects for the lens effects of large velocity contrasts. Because the depth imaging areas are challenging, however, the signal-to-noise ratio can vary greatly. The signal is placed in the correct CRP prior to stacking the traces, and gathers are more important in the interpretation process. It becomes important to recognize noise and improperly positioned signal on the gather data, and relate these back to the 3-D stacked volume to complete an effective interpretation.

Downloaded 25 Jun 2012 to 95.28.162.50. Redistribution subject to SEG license or copyright; Terms of Use: http://segdl.org/

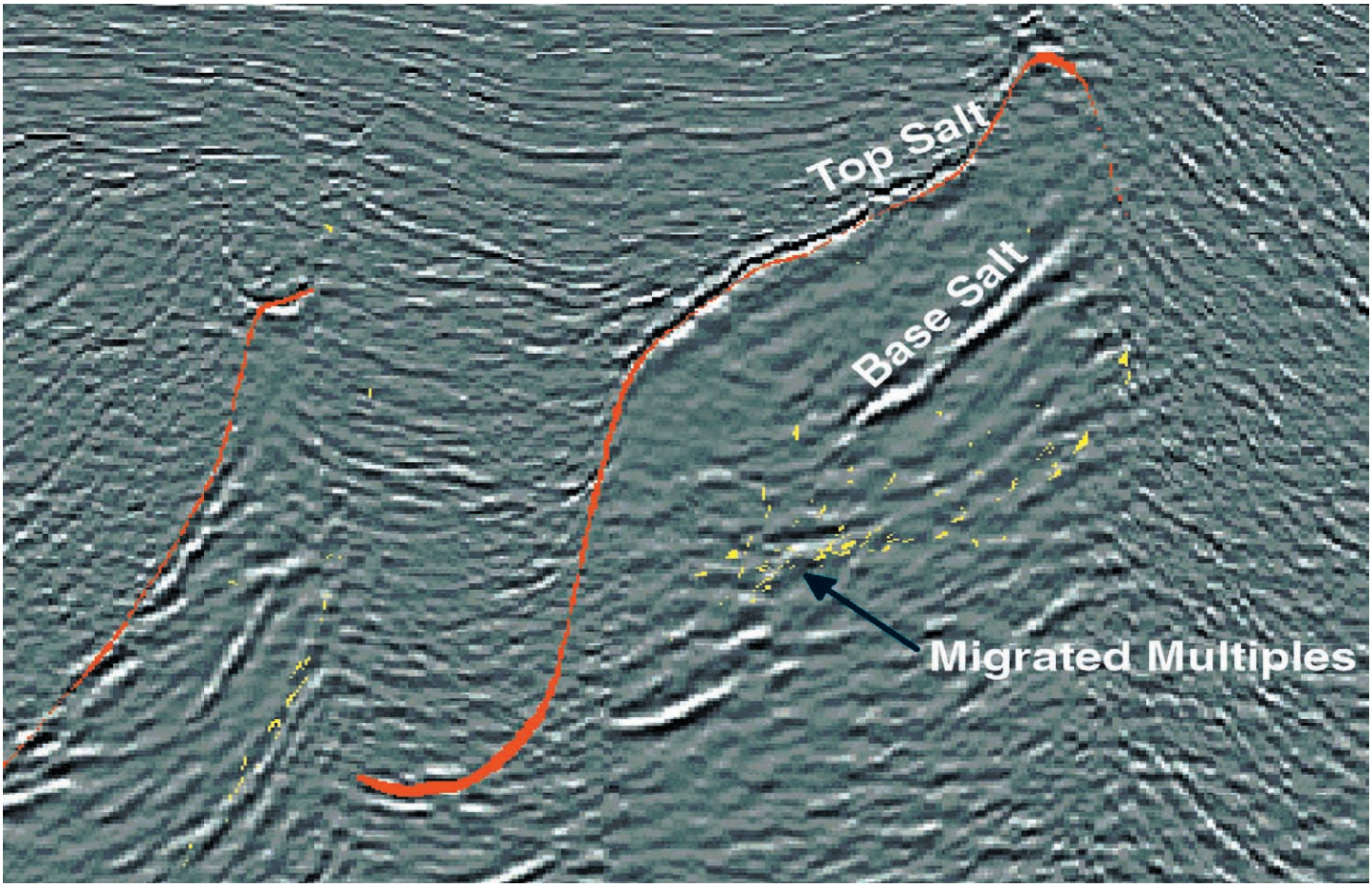

Fig. 10-26. 3-D depth-migrated seismic data. The superposed ray-migrated dip bars were initially created in the time domain by ray tracing. Red dip bars represent top salt primary signal. The yellow dip bars represent top salt - water pegleg multiples, both coherent (left half of figure) and incoherent (right half of figure).

As an example of using pre-stack gathers in evaluating depth imaging, refer to Figures 10-27 and 10-28. In Figure 10-27, the traces are 3-D pre-stack depth migrated and plotted prior to stacking. Figure 10-28 is a stack of the traces, and represents one of the cross-sections of the 3-D project. Each of the 19 common reflection gathers shown in Figure 10-27 has the short offsets located on the left with increasing offset distance to the right. Looking at the gathers above the salt, one can see they are very nearly flat, but on the far right of the line, the far offsets are a bit delayed, suggesting that a slightly slower velocity model should be used to image these. The signal-to-noise ratio of these gathers is very high, and one can readily relate the same signal from the gathers to the stacked seismic section.

The top salt reflector is only slightly more complicated. The 13th gather shows one complication of noise. The far offsets appear to be "pulled up" and improperly imaged as though the imaging velocity used was too slow. However, it is known that these far offsets are contaminated with the refracted wave. These traces contain this noise because, for those traces, the energy is no longer reflecting directly form the source to the receiver but traveling along the salt boundary before emerging at the seismic receiver. This is one of the reasons why the stacked amplitude of the top salt at that location is weaker than at others. Note that the base salt is flat on the gathers and does not show a contaminating refractor.

The subsalt signal is also flat on the gathers, and is marked on both the gathers and their stack in yellow. It is easy to follow the first subsalt reflector from the west, but note how the signal on the gathers becomes lost at it approaches the salt edge to the east. The gathers there become dominated with multiples, converted waves and possibly improperly placed signal. The pattern of the stacked data takes on a characteristic "wormy" appearance in this low signal/noise area. The second reflector, also in yellow,

Downloaded 25 Jun 2012 to 95.28.162.50. Redistribution subject to SEG license or copyright; Terms of Use: http://segdl.org/

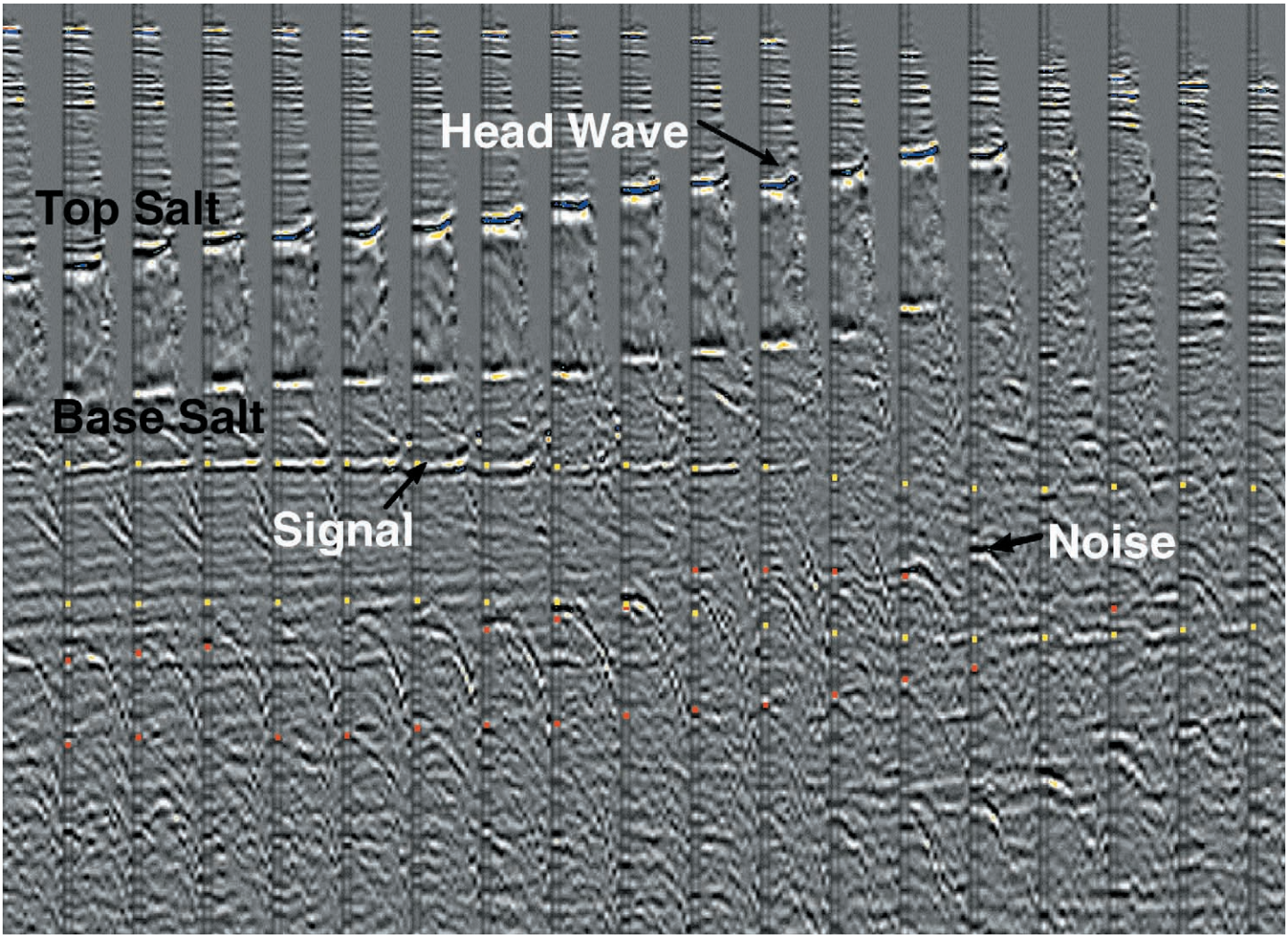

Fig. 10-27. 3-D pre-stack depth-migrated common reflection point gathers. The yellow and red dots superposed at zero offset (left side of each gather) represent the zero-offset depth location of primaries and multiples respectively. Note the excessive residual moveout associated with the red dots that represents multiples.

can be tracked from west to east along high, low, and then medium signal/noise areas.

A model of noise is also posted on the imaged data. As an example, the top and base salt multiples from the water bottom are posted in red on both the gathers and the stack. Notice the strong curvature of the noise on the gathers and their strong amplitude response on the stacked section. The noise cuts straight across the signal on the stacked data, and damages the ability to draw stratigraphic information from the image. Worse, one could be drawn to an incorrect structural interpretation. Using the gathers, the stack, and the modeling together avoids this pitfall.

Example of Pre-stack vs. Post-stack 3-D Depth Imaging — Model Data

As mentioned previously, the advantage of pre-stack depth imaging over post-stack relates to the need for correcting the effects of the velocity lens through which the seismic energy has passed for each separate seismic trace. An example of this is correcting for salt bodies with medium to high rugosity. The following example shows a direct comparison of pre-stack and post-stack imaging of data from a 3-D physical model resembling bodies of the Gulf of Mexico. 3-D seismic data was acquired in the tank of the Allied Geophysical Laboratory (AGL) at the University of Houston and imaged to measure the differences of pre-stack and post-stack imaging. The model was built of a flat Plexiglas sheet of constant initial thickness milled to specifications of predefined statistical roughness as noted in faulted and folded

Downloaded 25 Jun 2012 to 95.28.162.50. Redistribution subject to SEG license or copyright; Terms of Use: http://segdl.org/

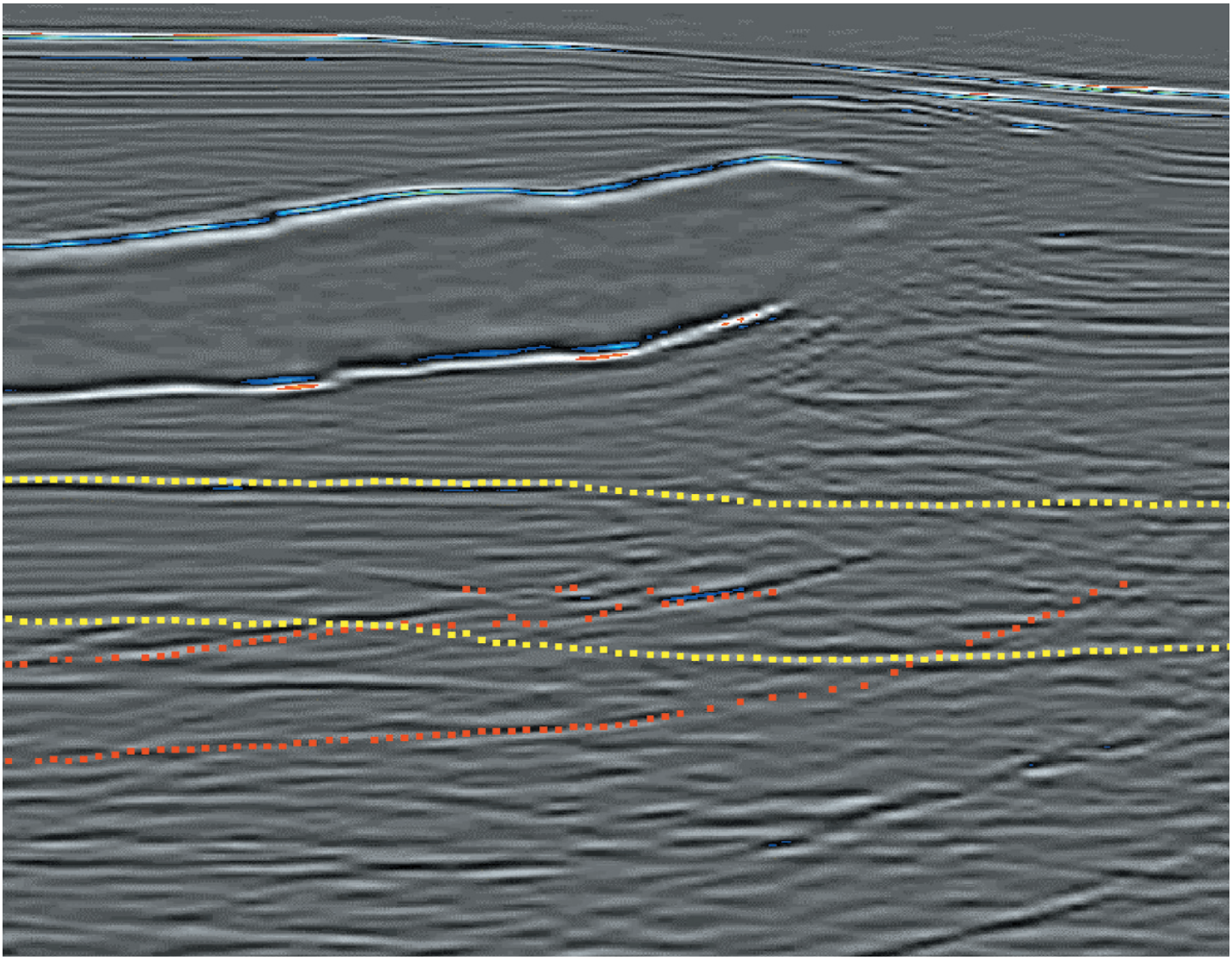

Fig. 10-28. Stack of the CRP gathers of Figure 10-27. The trains of yellow and red dots exactly correspond to those in the previous figure and are simultaneously posted in both views in practice. This assists the interpreter in discriminating between reflection signal (yellow) and coherent multiples (red). Note the wormy zone beneath the salt pinchout.

real salt bodies exhibiting topological self-similarity (Figure 10-21). The Plexiglas sheet was placed over a reflector model of a fault and two small anticlines, with four rods inserted below to act as line diffractors (Figure 10-29). 3-D linear marine seismic acquisition was then performed over the model (AGL Model 93).

A digital representation of the model shows how the seismic energy is bent at the salt-sediment interface (Figure 10-30). The top and base layers of the salt are represented in a cut-away view to show the 3-D rays traveling through the salt. Notice that the CMP at the surface collects data from different locations on the reflector, so that a pre-stack process will be required to correct for this.

Seismic CMP gathers (Figure 10-31) show low signal/noise prior to stack, especially at the target horizon. Note that the physical model data has noise characteristics much like live data, in that it contains multiples and other noise like the mode conversion from P to S energy at the salt as noted. Although much of this noise is attenuated as a result of the power of stacking in the time domain, nevertheless stacking before migration degrades much of the signal, as we next illustrate.

Comparing an enlarged portion of the post-stack and pre-stack 3-D depth-migrated data on a cross section of the model (Figures 10-32 and 10-33 respectively) shows why pre-stack imaging is preferred for stratigraphic quality imaging. The target horizon, anticline and fault are much clearer on the pre-stack data, and the lateral resolution of

Downloaded 25 Jun 2012 to 95.28.162.50. Redistribution subject to SEG license or copyright; Terms of Use: http://segdl.org/

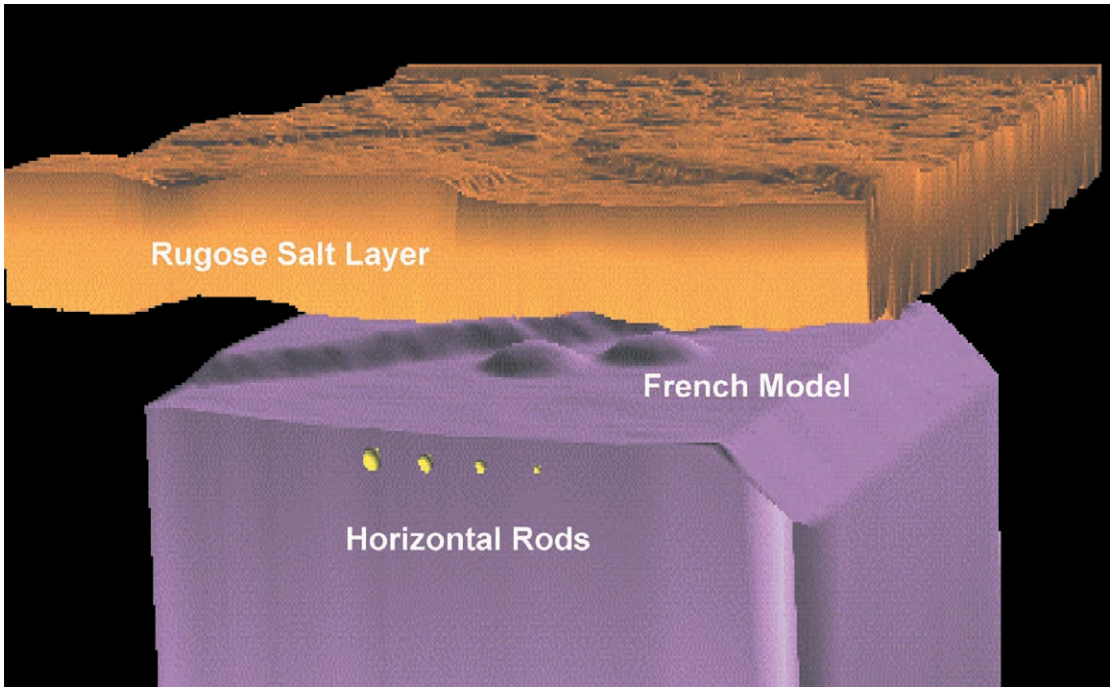

Fig. 10-29. Perspective Gocad view of rugose salt above a structural geology model. This digital representation guided the milling of the physical Model 93 of the Allied Geophysical Laboratories (AGL) of the University of Houston.

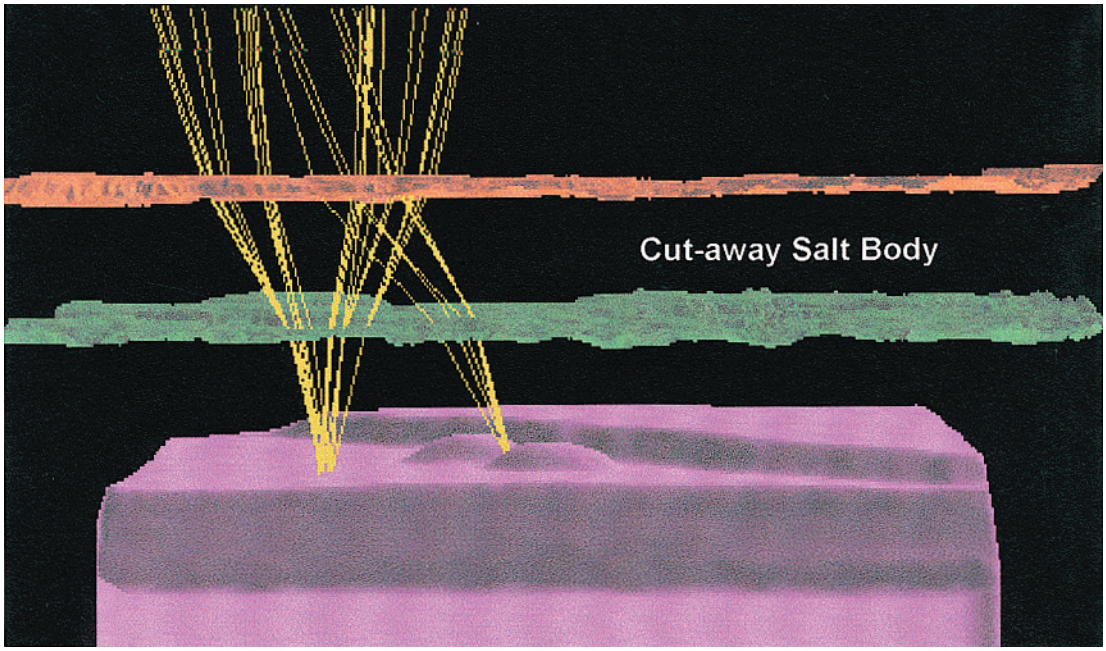

Fig. 10-30. Common midpoint ray trajectories in 3-D reflecting from the target horizon and traveling through the intervening rugose salt. Geostatistically appropriate bumps and dimples of various scales on the salt boundary cause erratic ray distortion.

Downloaded 25 Jun 2012 to 95.28.162.50. Redistribution subject to SEG license or copyright; Terms of Use: http://segdl.org/

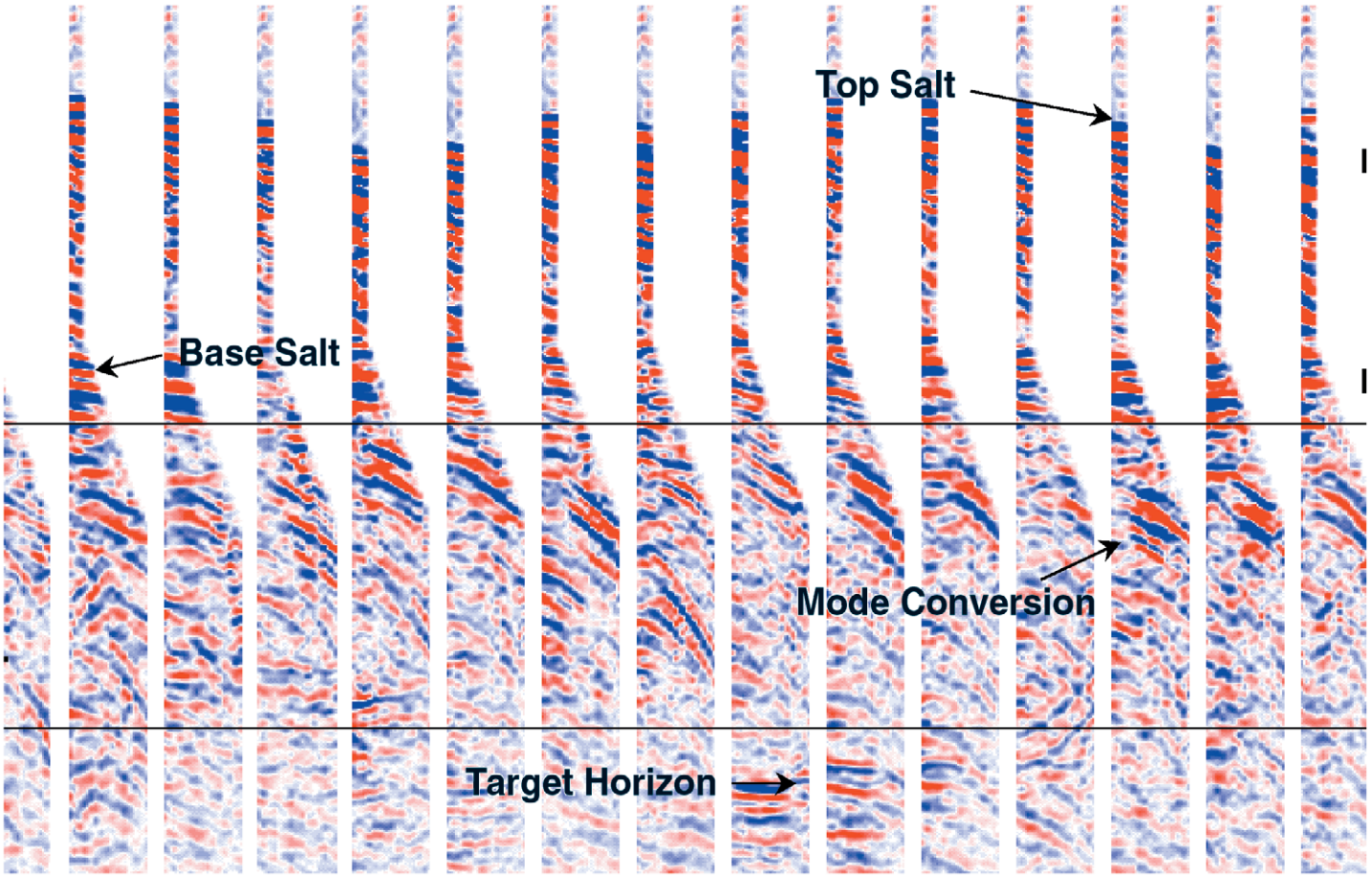

Fig. 10-31. CMP time gathers prior to stack and migration for AGL subsalt Model 93.

the four rods is clearly superior. Despite the fact that the model is of constant reflectivity, the post-stack depth image of the target horizon is too poor to pick, and a horizon slice would be meaningless. Compare this with the same blue event on the pre-stack imaged data. The pre-stack image is structurally superior and also more appropriate for stratigraphic interpretation.

Example of Pre-stack vs. Post-stack 3-D Depth Imaging — Live Data

In an example similar to the model salt ledge, live data shows how pre-stack depth imaging can be an advantage over post-stack depth imaging beneath and around a salt tongue. In Figure 10-34, a cross-section of the salt ledge overlies a prospective sedimentary structure. The subsalt image of this post-stack depth-migrated section shows significant coherent noise (predominantly multiples) and little recognizable signal. The same pre-stack data were depth migrated prior to stack, and the subsalt image was improved (Figure 10-35). The prospective reservoir was revealed in the area of the tip of the salt ledge.

Left of the prospective reservoir, even the pre-stack depth-migrated data are not very high signal/noise. Significant multiples remain in the subsalt data, and determining what is signal is impossible by inspection of the stacked data volume only. However, by using modeling and the gathers, even these data can be interpreted. Gathers of the pre-stack depth-migrated data are shown in Figure 10-24 outside of the salt and in Figure 10-25 under the salt.

The pre-stack data from this project were used in the selection of a drilling target. At the reflector noted hydrocarbons were found. The dip of the reflector (approximately flat) was found to be correct from dip meter logs. Downhole acoustic and petrophysical log data also show that the reflection characteristic of the reservoir is correct, as the

Downloaded 25 Jun 2012 to 95.28.162.50. Redistribution subject to SEG license or copyright; Terms of Use: http://segdl.org/

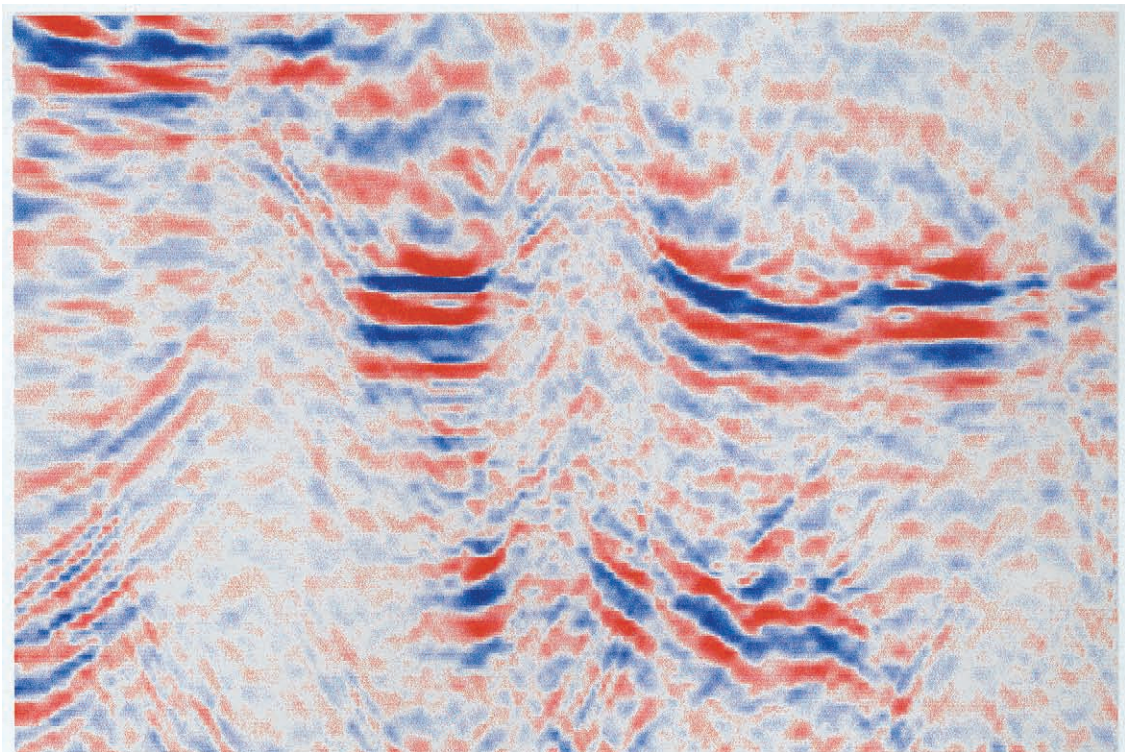

Fig. 10-32. 3-D post-stack depth migration of AGL data at the target level below salt.

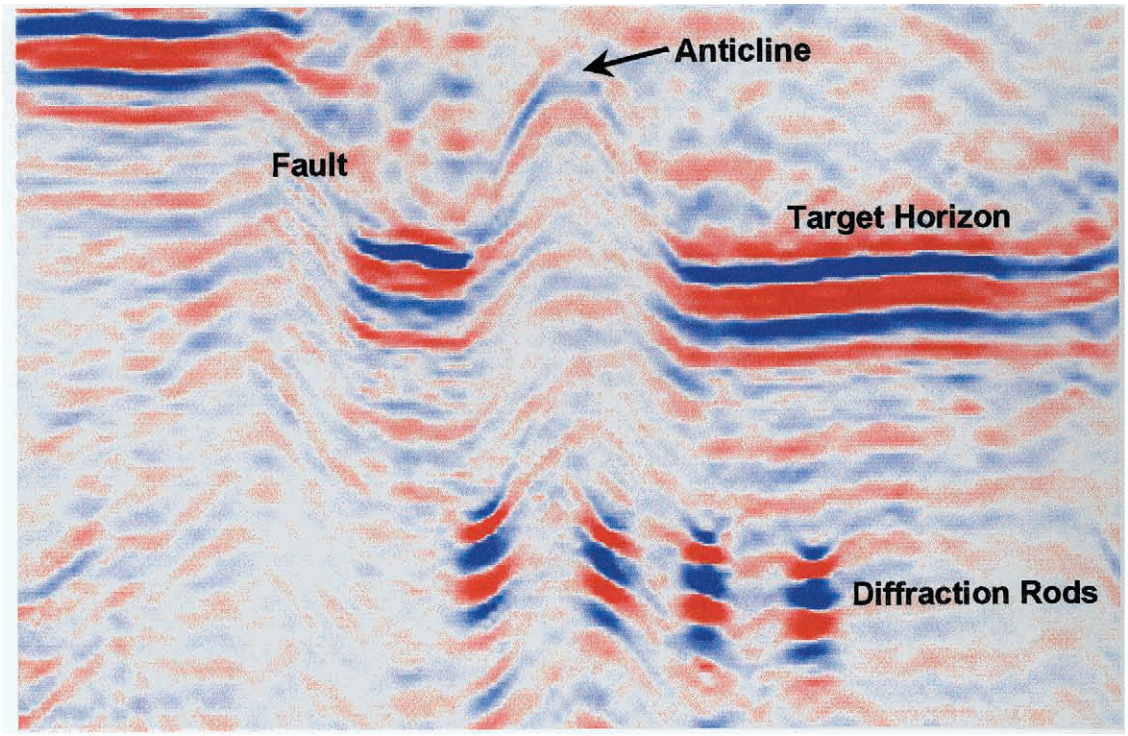

Fig. 10-33. 3-D pre-stack depth migration of the same region as Figure 10-32. Note the sharper and brighter images of the target horizon, anticline, fault, and diffraction rods.

Downloaded 25 Jun 2012 to 95.28.162.50. Redistribution subject to SEG license or copyright; Terms of Use: http://segdl.org/

hydrocarbons cause a bright spot relative to the surrounding section.

Interpretation of subsalt amplitude anomalies is an especially tricky practice. As the prior sections have noted, the pitfalls in trusting subsalt amplitudes are many. Incomplete illumination, energy partitioning, coherent noise, improper velocity and inadequate imaging algorithms can all contribute to poor subsalt signal response, and destroy the quality of the imaging so that it falls well below what is needed for stratigraphic work.

But the good news is that understanding and accounting for these effects may also provide satisfactory results. Figures 10-36 through 10-39 show a comparison of post-stack and pre-stack subsalt imaging where stratigraphic interpretation quality can be achieved. Figures 10-36 and 10-37 are post-stack and pre-stack sections, respectively, cutting through salt and an event of interest. The pre-stack image improves upon the post-stack image throughout the cross-section, but nowhere is the interpretational gain more pronounced than under and adjacent to the salt body. This is because the subsalt data area was initially in need of the most improvement, which the pre-stack process delivered and the post-stack process could not. In particular, the events below salt are both sharper and more continuous on the pre-stack section. Of special note, because the pre-stack process does not rely on just the zero-offset ray to place amplitudes at depth but allows all ray trajectories to contribute to the image, there is much less probability of subsalt event discontinuity. This is well illustrated by the discontinuity in the event of interest below the tip of salt. On the post-stack section the gap is wide and the interpretation suffers, but on the pre-stack section the gap is reduced to a narrow suture zone with less risk of misinterpretation.

As compelling as the cross-sectional comparison is, the dramatic improvement of pre-stack over post-stack imaging is best seen in this case by comparing horizon slices on the event of interest identified in the previous two figures. In Figure 10-38, the horizon slice of post-stack 3-D depth-migrated data shows probable turbidite channel and overbank sands that are hard to follow under the salt ledge. Once under the ledge, the event discontinuity first observed on the cross-section cuts a wide and incoherent gash across the horizon, rendering interpretation risky. In Figure 10-39, the same horizon sliced from the pre-stack image volume exhibits vastly greater geologic continuity and integrity of the channel and overbank system. The event continuity is much improved and can be followed with little risk.

In these examples, high quality 3-D pre-stack depth migration completes the necessary imaging process required to clarify the subsalt amplitudes. The horizon map is then sufficient to define the limits of a potential reservoir for exploration and development purposes. A better understanding of the structural and stratigraphic context gives the interpreter greater confidence in defining the geologic model and reducing risk.

Discussion

Depth imaging is rapidly increasing in use in exploratory and development areas. For complex velocity and structural regimes, large differences can sometimes be seen from depth versus time imaging, as depth imaging can change the position, dip and amplitude of reflectors. Pre-stack depth imaging can also be advantageous over post-stack depth imaging under the right conditions. In either case, the noise characteristics of the depth-imaged data are different from those of the time-imaged data, and must be taken into account during interpretation.

Depth imaging can be expensive due to the computational effort of getting the lens effects corrected. An additional cost is incurred in getting a reasonable velocity model to ensure imaging success. Another consideration is that the data are complex, and interpretation is most valuable when the signal can be separated from the noise, another potentially costly procedure. Success in depth imaging can be achieved by using:

- A versatile 3-D earth model and robust model editor
- Accurate velocity analysis and representation

Downloaded 25 Jun 2012 to 95.28.162.50. Redistribution subject to SEG license or copyright; Terms of Use: http://segdl.org/

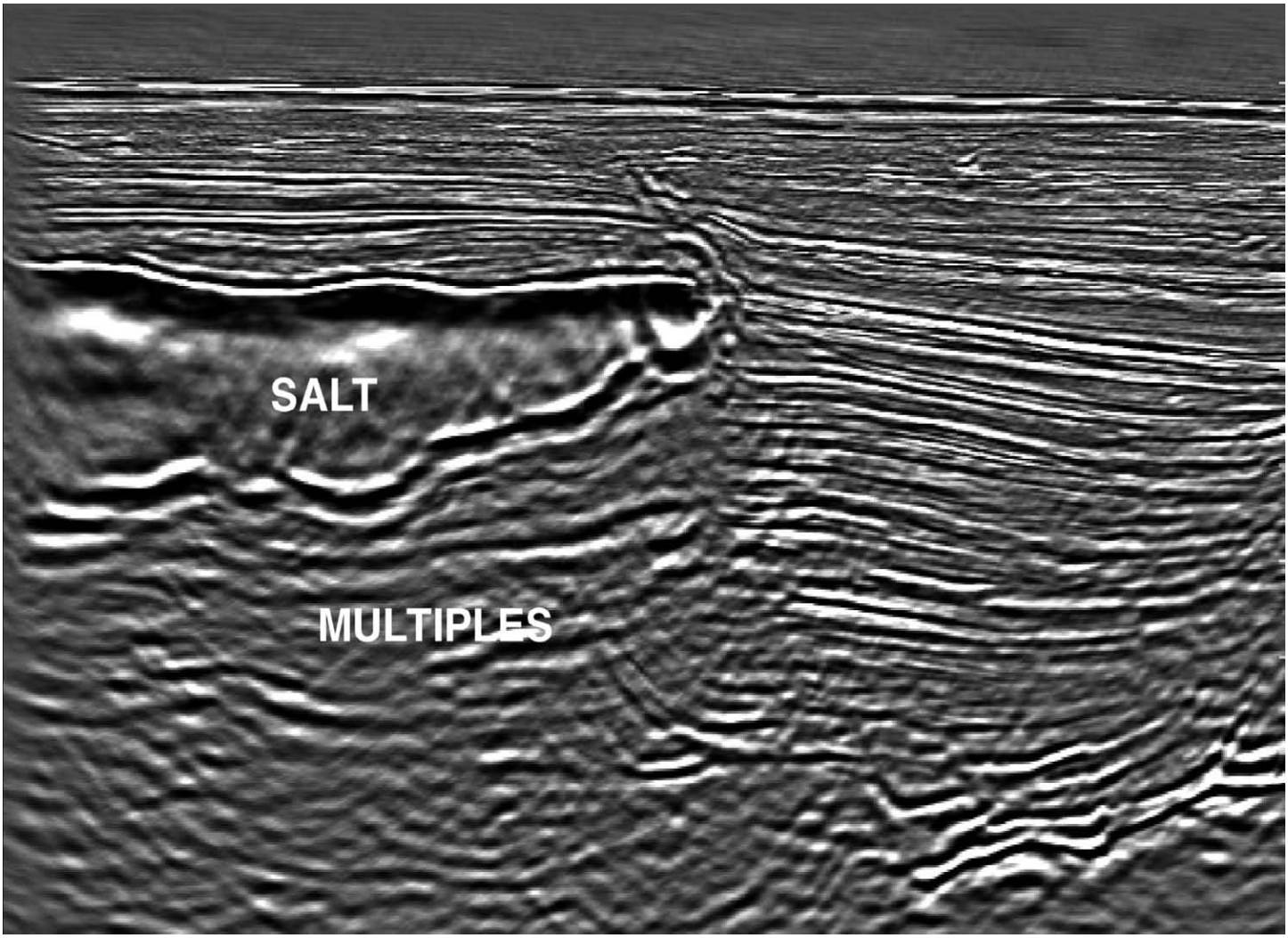

Fig. 10-34. Cross-section of a 3-D post-stack depth migration through a salt ledge.

- Robust 3-D forward modeling of rays and waves
- Visualization of ray tracing
- Gather and stack interpretation tools
- An accurate and efficient migration algorithm
- High-quality geological/geophysical interpretation capabilities
- Imaging specialists with sufficient amounts of courage

Depth imaging is currently common in several plays around the world, including over-thrusts, subsalt, the West African offshore, and the North Sea. As depth imaging matures, it will become increasingly useful in older exploration areas and applications where stratigraphic quality is important. The trends that have made 3-D depth imaging possible (advances in hardware, software, and imaging expertise) will continue and cause this technology to spread. As it does, we will be challenged to produce the best possible quality images and required to adequately describe their uncertainties.

Acknowledgments

We thank our imaging colleagues, both theoretical and applied, for their useful and ongoing collaboration, and also Chevron North America E. & P. and Chevron Petroleum Technology Company for permission to publish this paper. Gocad is a software product of ASGA (Association Scientifique pour la Geologie et ses Applications).

Downloaded 25 Jun 2012 to 95.28.162.50. Redistribution subject to SEG license or copyright; Terms of Use: http://segdl.org/

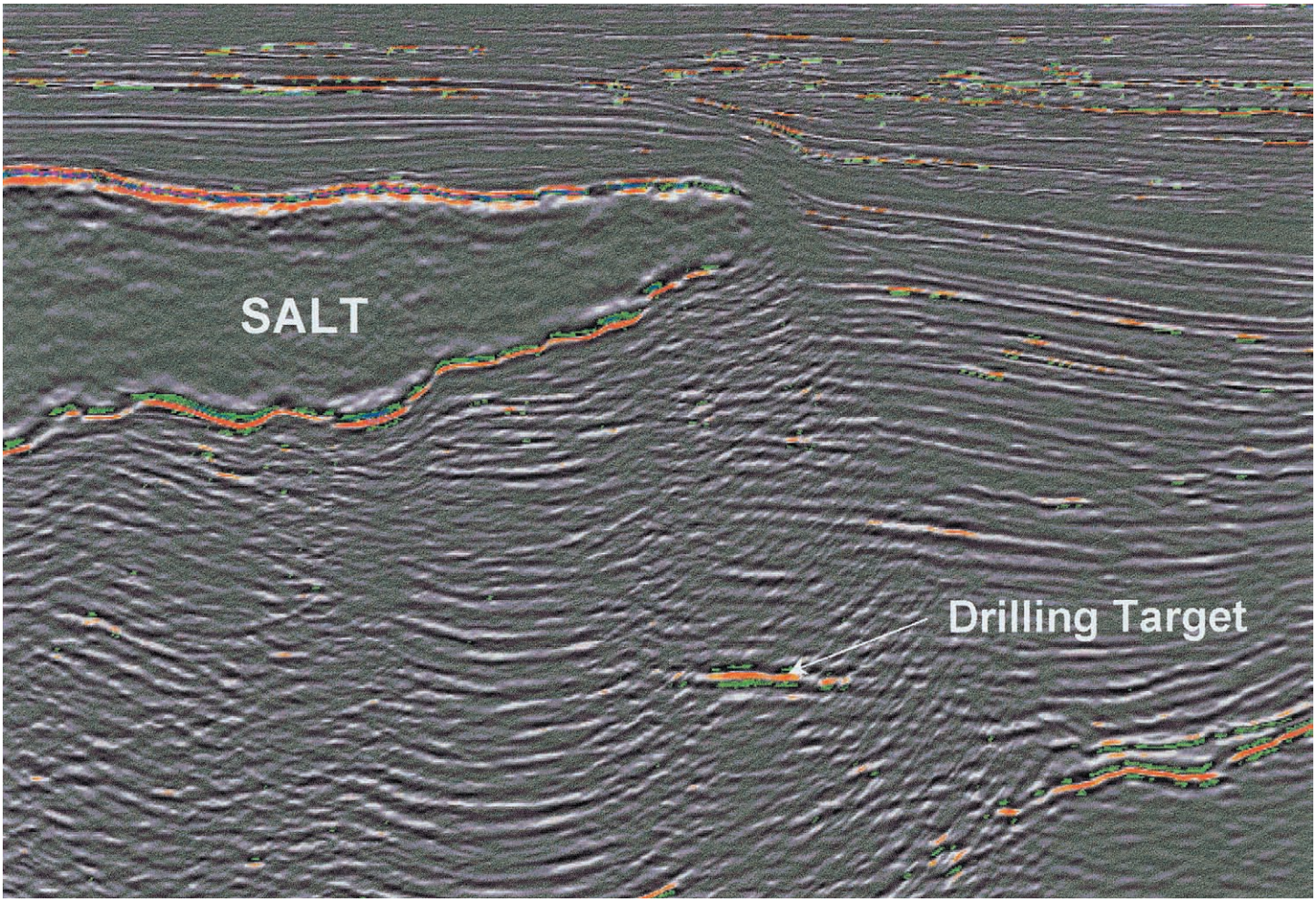

Fig. 10-35. Same as Figure 10-34, but pre-stack depth migrated.

Downloaded 25 Jun 2012 to 95.28.162.50. Redistribution subject to SEG license or copyright; Terms of Use: http://segdl.org/

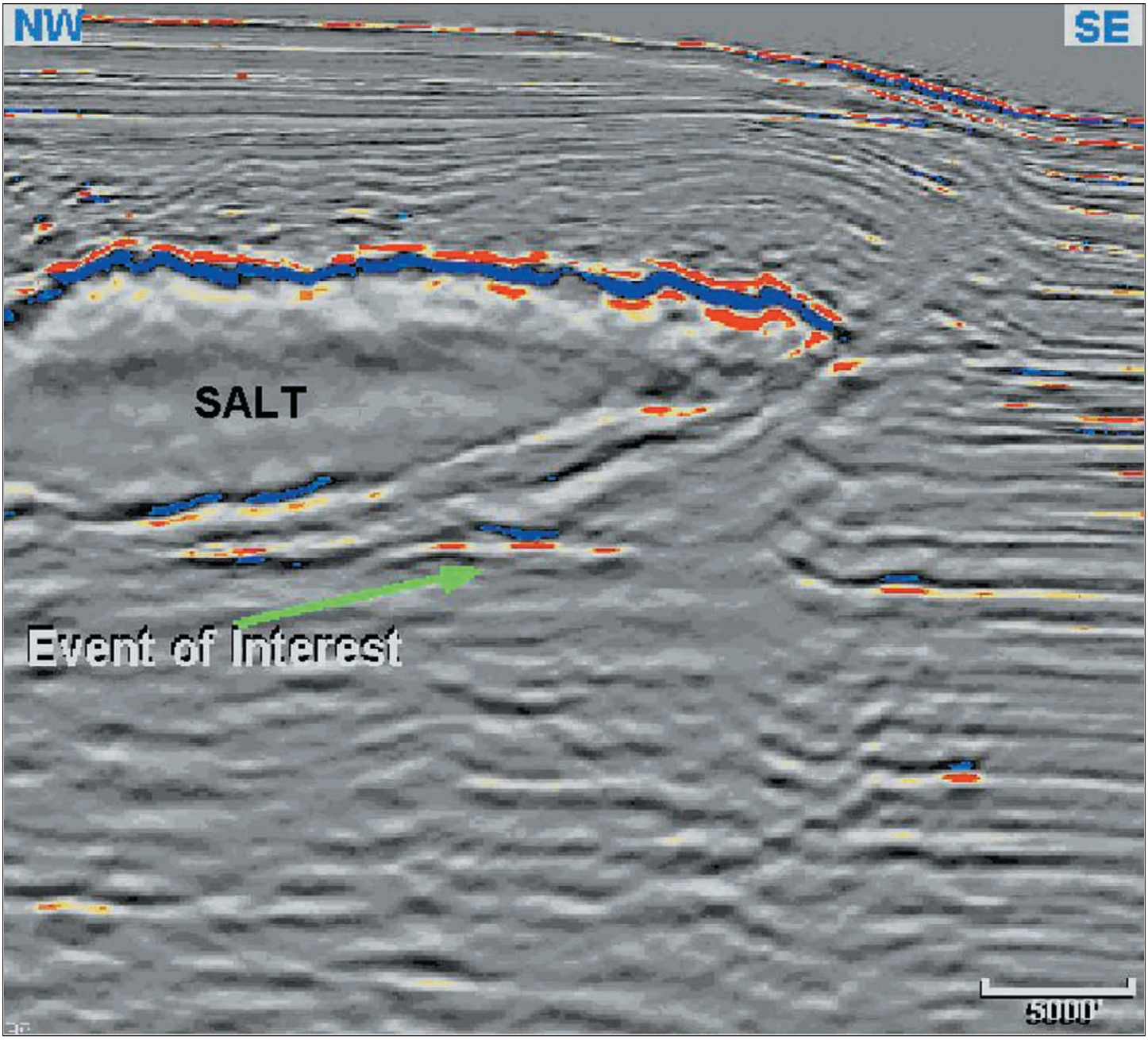

Fig. 10-36. Cross-section of post-stack depth-migrated seismic data along line UT1 of Figure 10-38. Note the wide signal gap in the event of interest below the tip of salt.

Downloaded 25 Jun 2012 to 95.28.162.50. Redistribution subject to SEG license or copyright; Terms of Use: http://segdl.org/

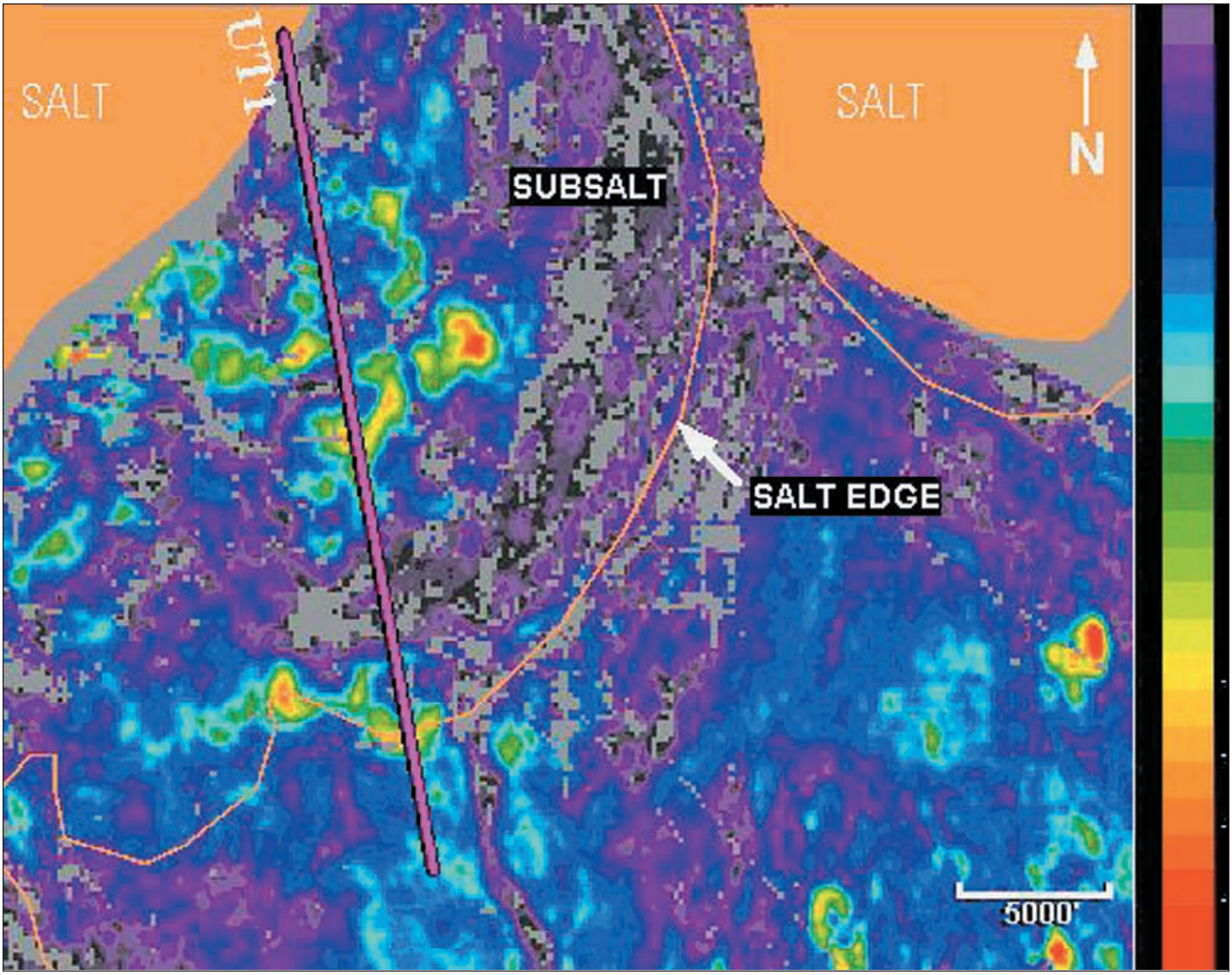

Fig. 10-38. Horizon slice (amplitude map) at the event of interest, from post-stack depth-migrated seismic data.

Downloaded 25 Jun 2012 to 95.28.162.50. Redistribution subject to SEG license or copyright; Terms of Use: http://segdl.org/

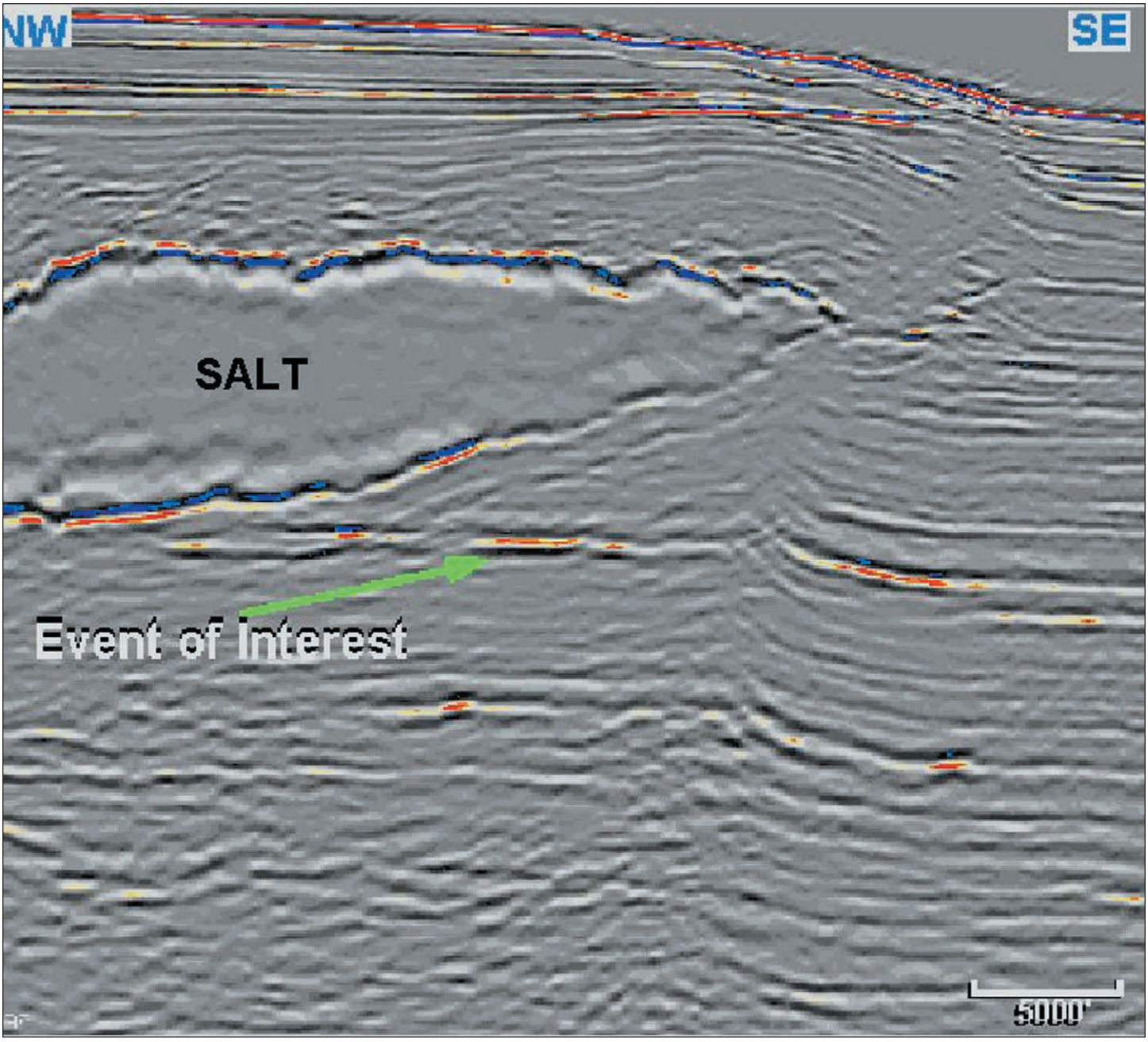

Fig. 10-37. Cross-section of pre-stack depth-migrated seismic data along line UT1 of Figure 10-39. The signal gap in the event of interest below salt is reduced to a narrow suture zone, and base salt and other events are much better defined.

Downloaded 25 Jun 2012 to 95.28.162.50. Redistribution subject to SEG license or copyright; Terms of Use: http://segdl.org/

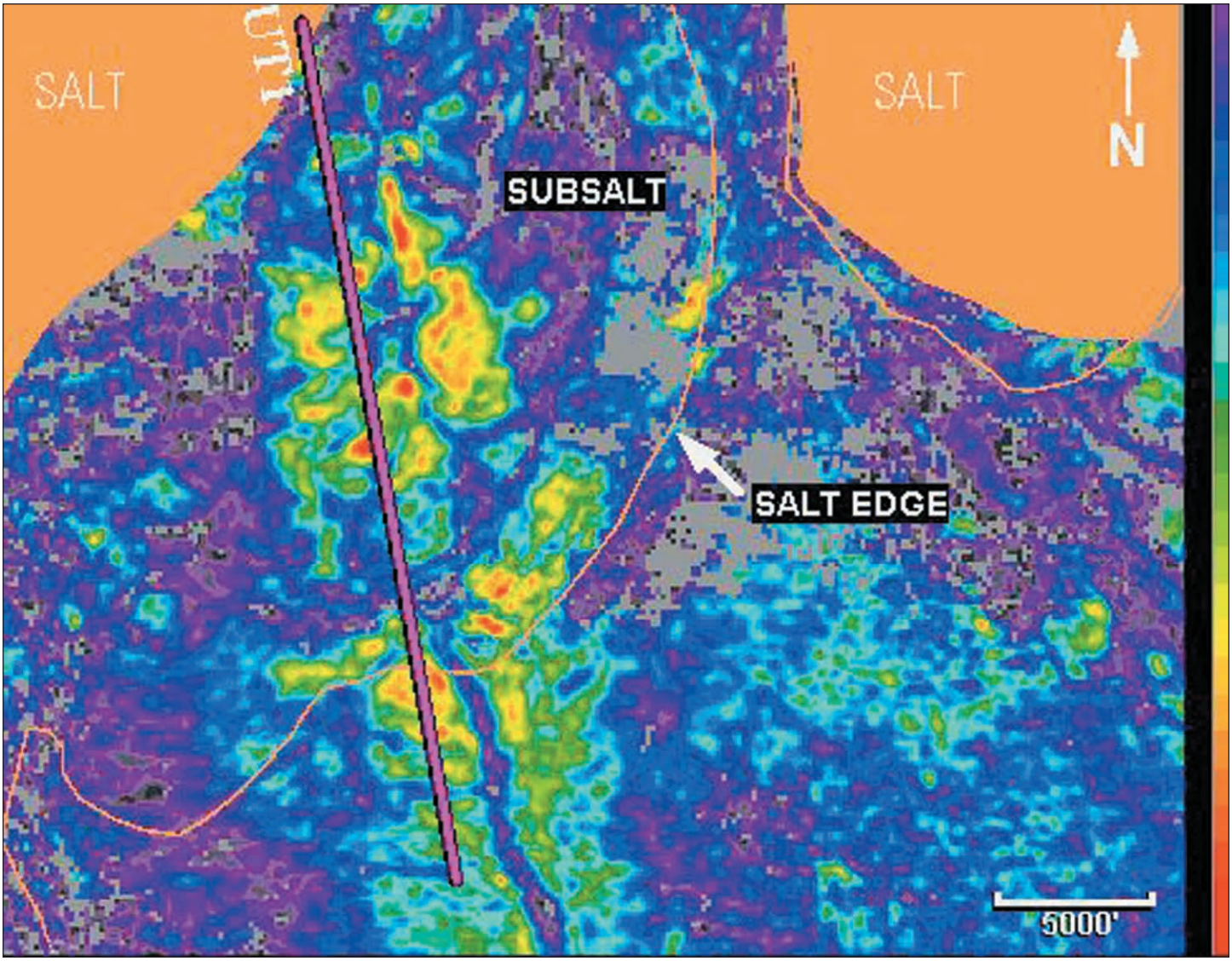

Fig. 10-39. Horizon slice (amplitude map) at the event of interest, from pre-stack depth-migrated seismic data. Note the improved reflection continuity crossing beneath the salt edge.

Downloaded 25 Jun 2012 to 95.28.162.50. Redistribution subject to SEG license or copyright; Terms of Use: http://segdl.org/

Downloaded 25 Jun 2012 to 95.28.162.50. Redistribution subject to SEG license or copyright; Terms of Use: http://segdl.org/

Regional and Reconnaissance Use of 3-D Data

Three-D seismic coverage is now very extensive in both land and marine environments, making practical the regional and reconnaissance use of 3-D data. This has led to more exploration applications of 3-D surveys. More than 10 years ago there was a type of "Exploration 3-D" which involved widely spaced acquisition and interpolation in processing. Today all 3-D data are properly sampled and data acquisition is fast and highly efficient, particularly at sea.

Figures 11-1 through 11-4 show time slices from 1600 sq. km. of speculative 3-D seismic coverage in the Gulf of Mexico, and this is only a small portion of the total data available. The four salt domes change with depth and the structural complexity increases. Regional studies of salt tectonics are made possible with this kind of display, and time slices are key in revealing the spatial patterns of faulting. Coherence data displayed in time slices often provide improved visibility of fault patterns. Figure 8-24 shows many faults clearly delineated in coherence over an area of 1400 sq. km.

Figure 11-5 covers 23,000 sq. km. offshore Louisiana and Texas, giving a thoroughly regional view. The NE-SW Texas trend is clearly visible in the west, but over most of the time slice the E-W Louisiana trend is evident. Both these trends are consistent with salt dome distribution, with fault orientation, and with gravity and magnetic data (J. S. Watkins, pers. comm., 2003). A prominent magnetic lineation is at the junction of the two trends, suggesting that the trends are caused by basement tectonics. A. W. Bally (1999) has long been promoting regional 3-D seismic coverage. He believes "that regional tectonics will be completely recast as soon as regional 3-D seismic surveys become available to a larger community."

Reconnaissance of 3-D data for amplitude anomalies can be accomplished quickly with various carefully chosen displays. Figures 11-6 and 11-7 show a data volume from south Texas displayed with voxel transparency so that only the highest amplitudes are visible. The volume can be rotated and the best angle of view selected. The exact amplitude threshold can also be adjusted as the interpreter's understanding of the amplitude corresponding to gas develops. The data here are zero phase and normal American polarity. This is why the gas bright spots appear red in Figure 11-6 when we are looking down on them from the top, but blue in Figure 11-7 when we are looking up at them from the bottom. We can here quickly review which bright spots have been penetrated by wells and which have not.

Extensive joining, splicing, and merging of 3-D surveys to give regional coverage have been accomplished in many parts of the world. PGS Geophysical has been heavily involved in three areas offshore northwest Europe. The Central North Sea Mega Survey has merged more than 150 separate surveys onto a standard north-south grid. The time slice of Figure 11-8 shows 35,000 sq. km. of coverage, but eventually this

Downloaded 25 Jun 2012 to 95.28.162.50. Redistribution subject to SEG license or copyright; Terms of Use: http://segdl.org/

Text continued on page 412.

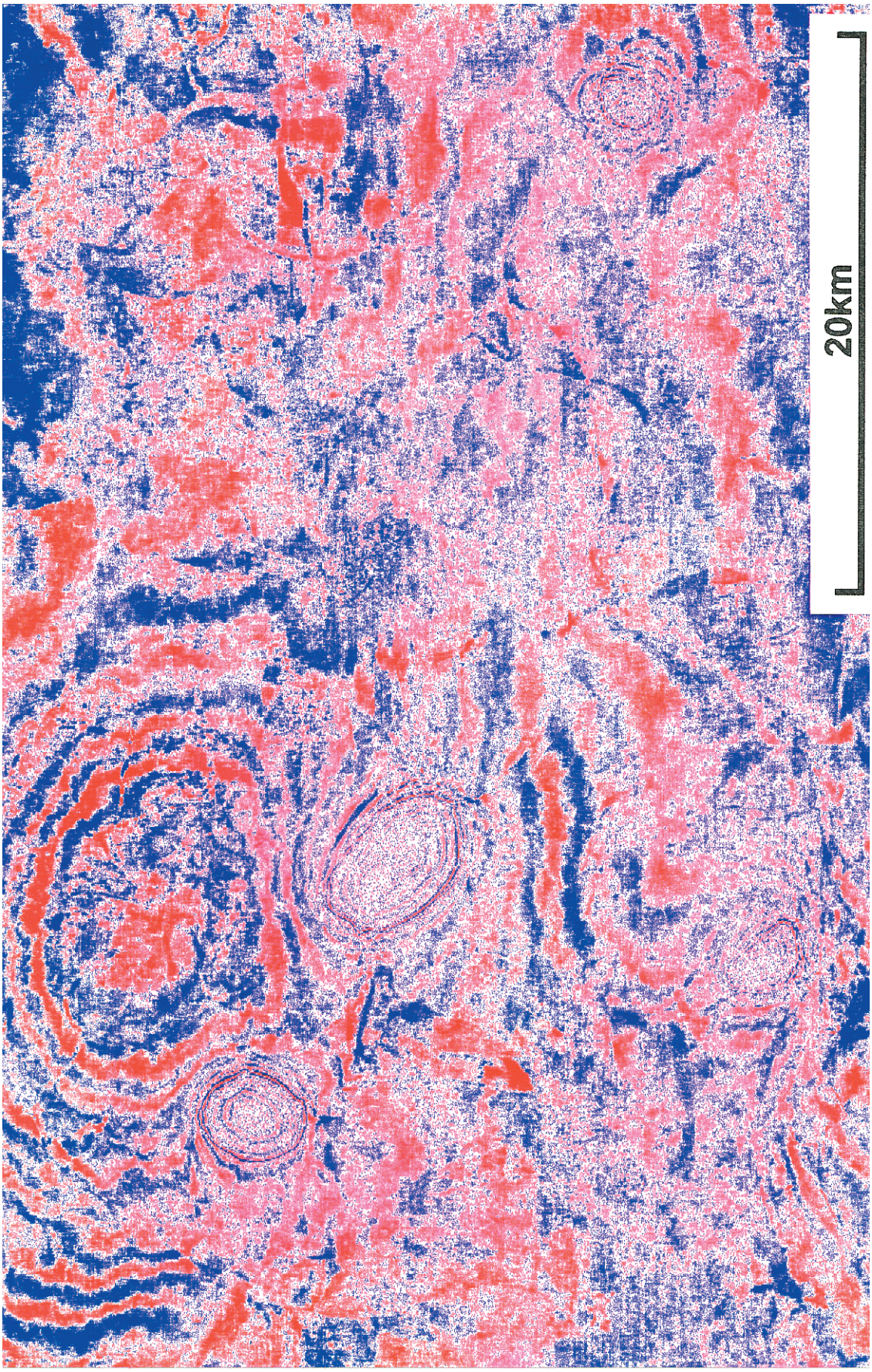

Fig. 11-1. Time slice at 1000 ms from Gulf of Mexico speculative 3-D survey. Area covers 1600 sq. km. Note several channel patterns. (Courtesy Western Geophysical, a division of Baker Hughes.)

Downloaded 25 Jun 2012 to 95.28.162.50. Redistribution subject to SEG license or copyright; Terms of Use: http://segdl.org/

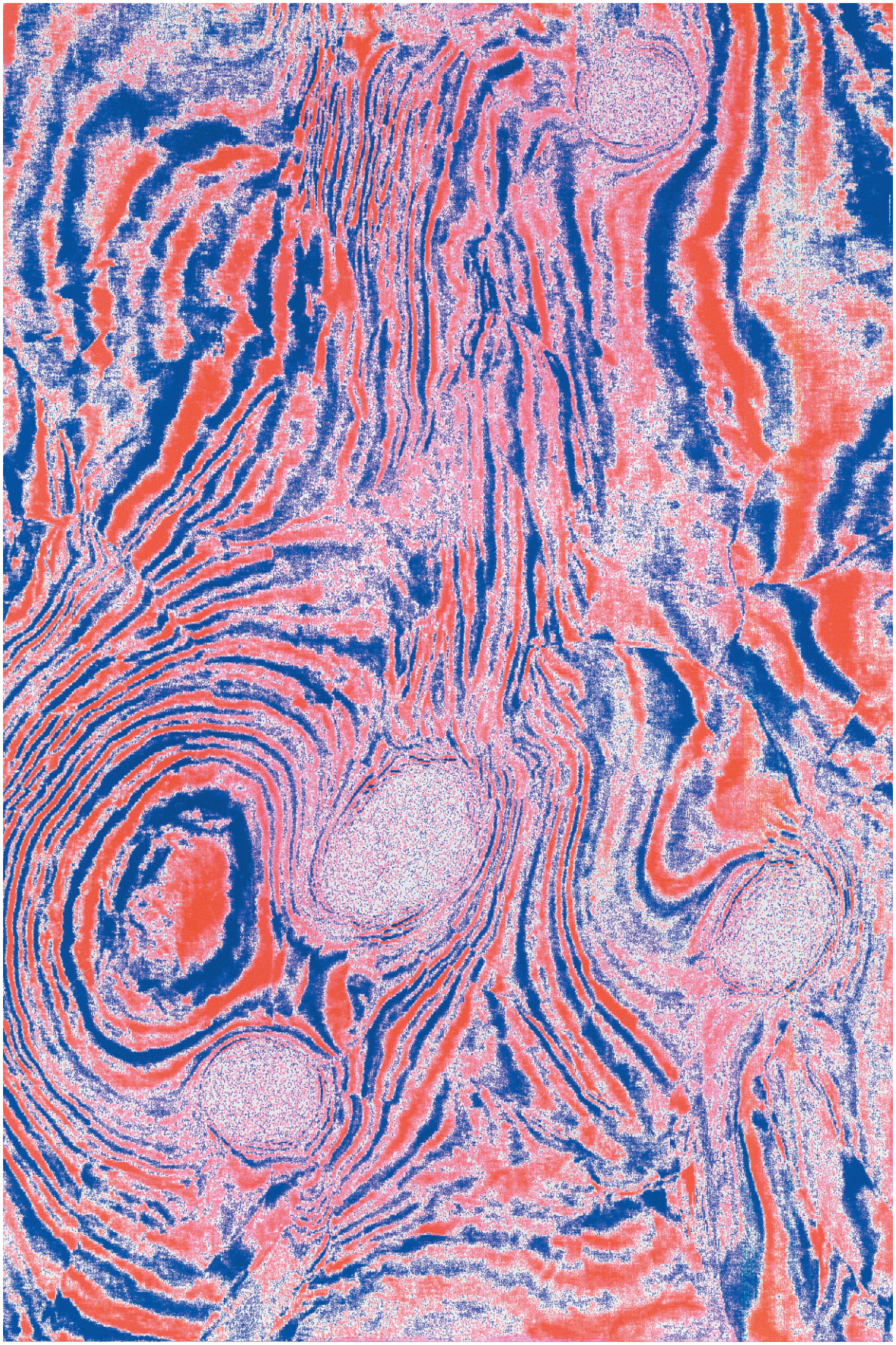

Fig. 11-2. Time slice at 2000 ms from Gulf of Mexico speculative 3-D survey. Area and scale are the same as Figure 11-1. Note four salt domes. (Courtesy Western Geophysical, a division of Baker Hughes.)

Downloaded 25 Jun 2012 to 95.28.162.50. Redistribution subject to SEG license or copyright; Terms of Use: http://segdl.org/

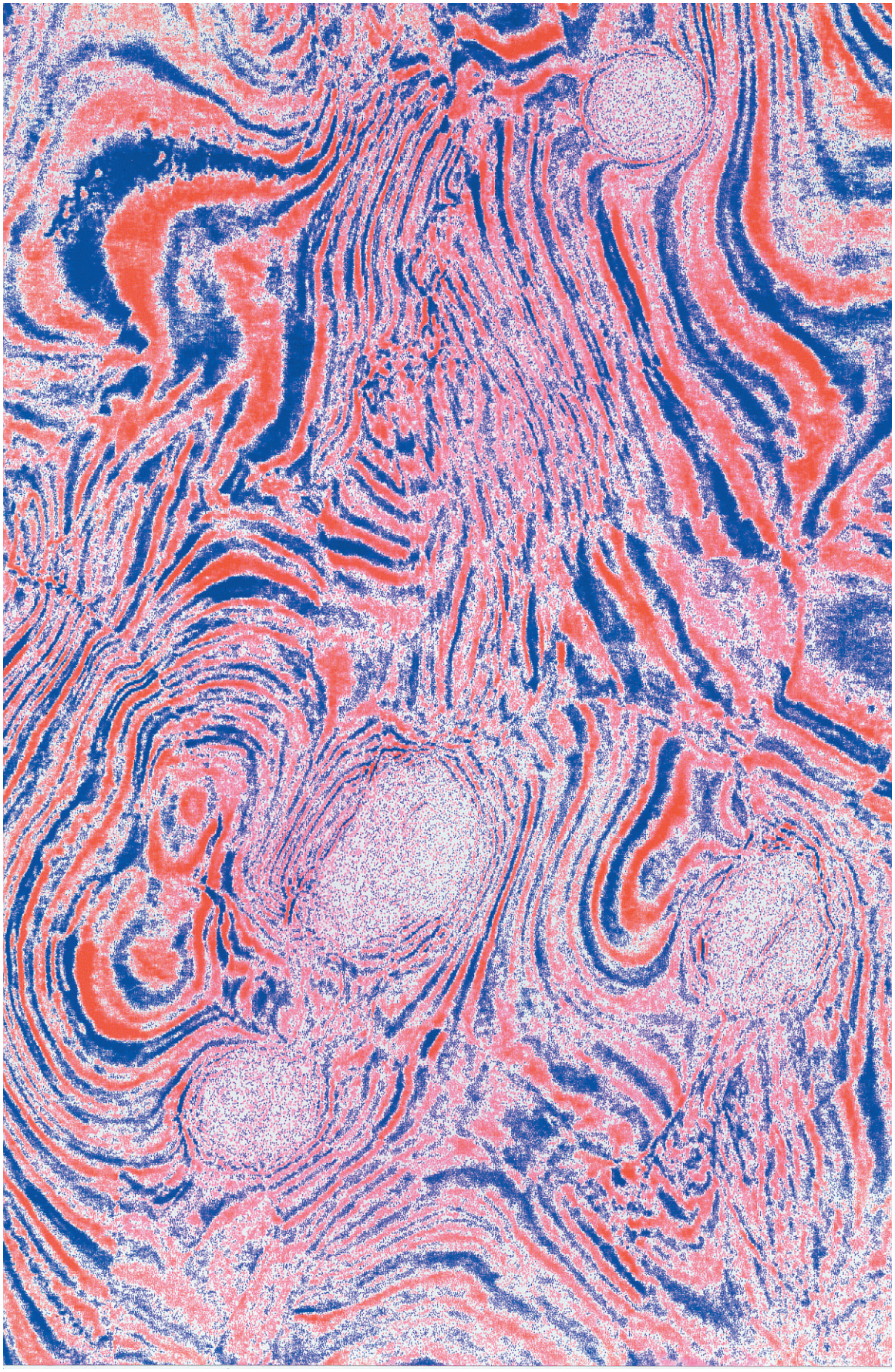

Fig. 11-3. Time slice at 3000 ms from Gulf of Mexico speculative 3-D survey. Area and scale are the same as Figure 11-1. Note syncline in north is now double syncline. (Courtesy Western Geophysical, a division of Baker Hughes.)

Downloaded 25 Jun 2012 to 95.28.162.50. Redistribution subject to SEG license or copyright; Terms of Use: http://segdl.org/

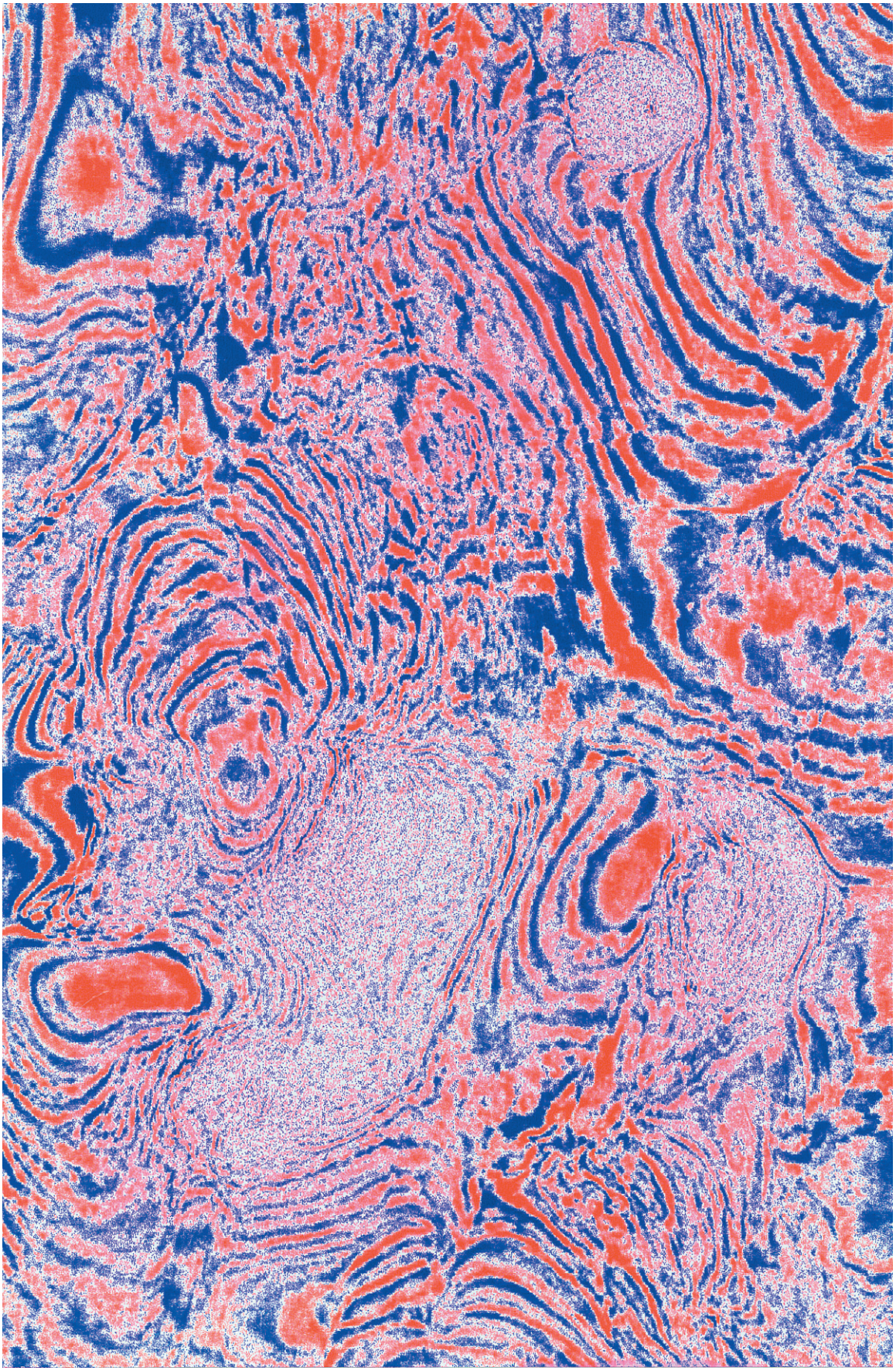

Fig. 11-4. Time slice at 4000 ms from Gulf of Mexico speculative 3-D survey. Area and scale are the same as Figure 11-1. Note increased area of salt and more faulting. (Courtesy Western Geophysical, a division of Baker Hughes.)

Downloaded 25 Jun 2012 to 95.28.162.50. Redistribution subject to SEG license or copyright; Terms of Use: http://segdl.org/

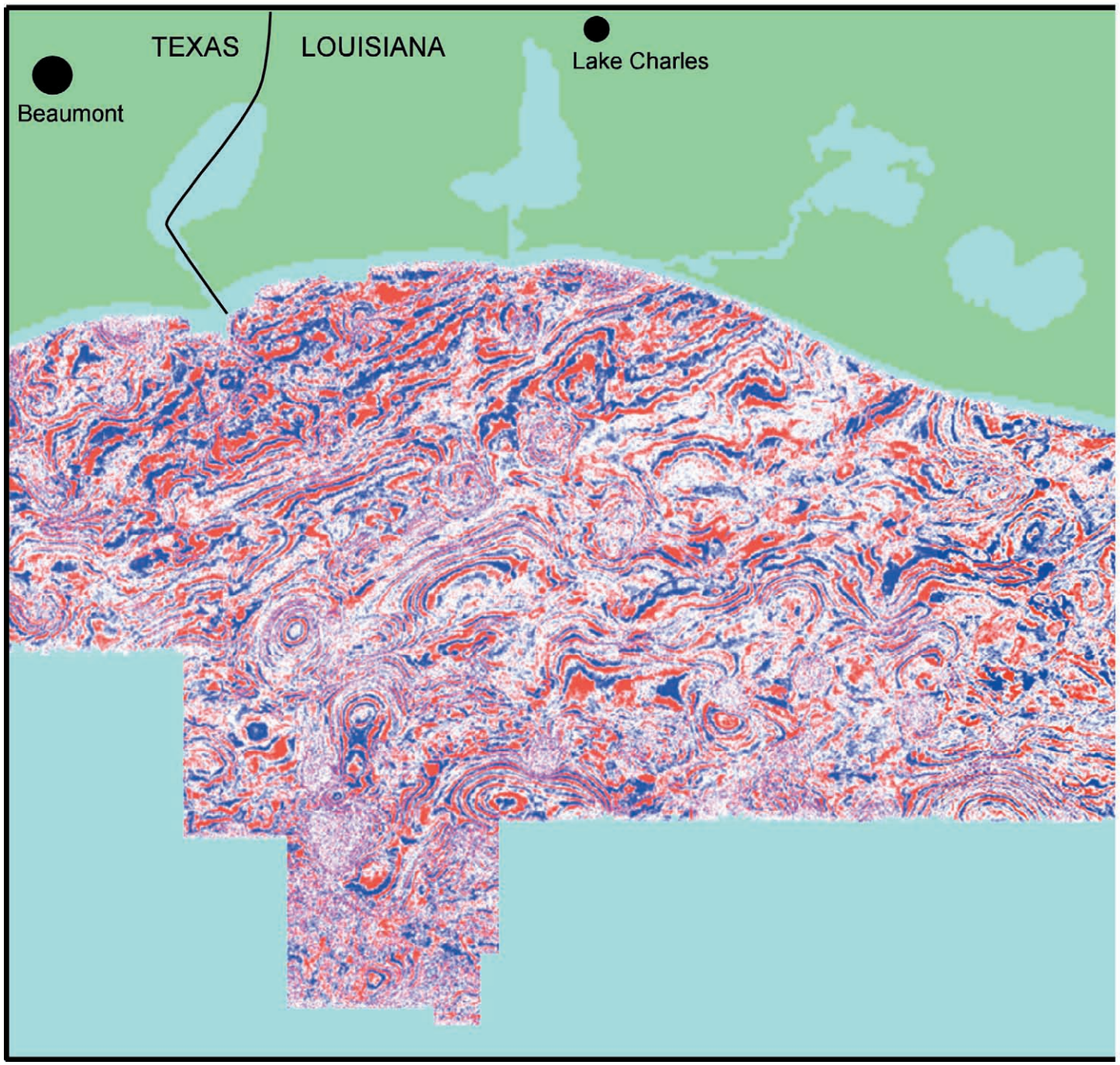

Fig. 11-5. Time slice at about 2 seconds from 3-D survey on the Gulf of Mexico shelf. The time slice measures 356 km from east to west and covers an area of 23,000 sq. km. Note NE-SW trend in west and E-W trend in east. (Courtesy Fairfield Industries.)

Downloaded 25 Jun 2012 to 95.28.162.50. Redistribution subject to SEG license or copyright; Terms of Use: http://segdl.org/

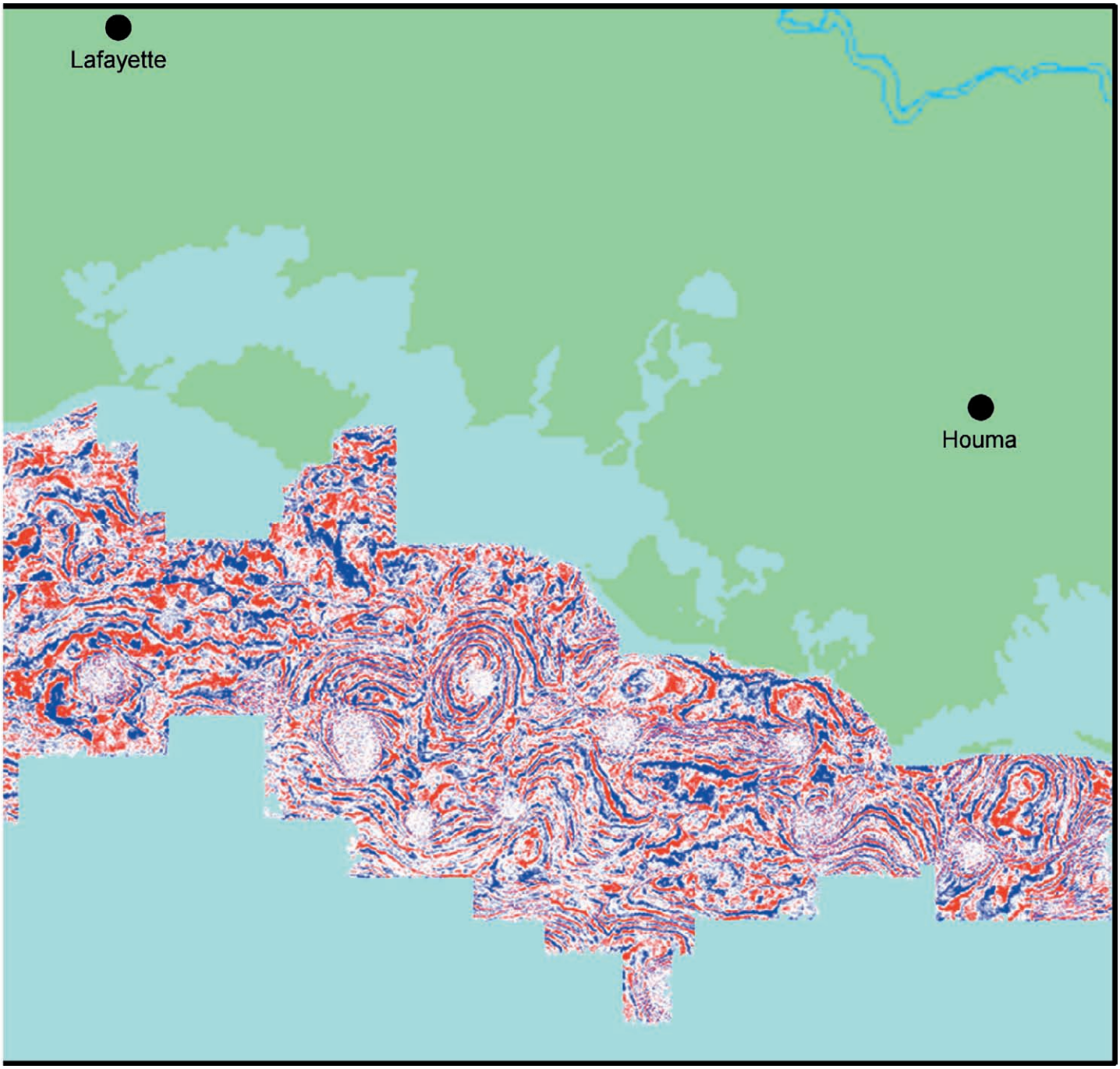

Fig. 11-5. Continued.

Downloaded 25 Jun 2012 to 95.28.162.50. Redistribution subject to SEG license or copyright; Terms of Use: http://segdl.org/

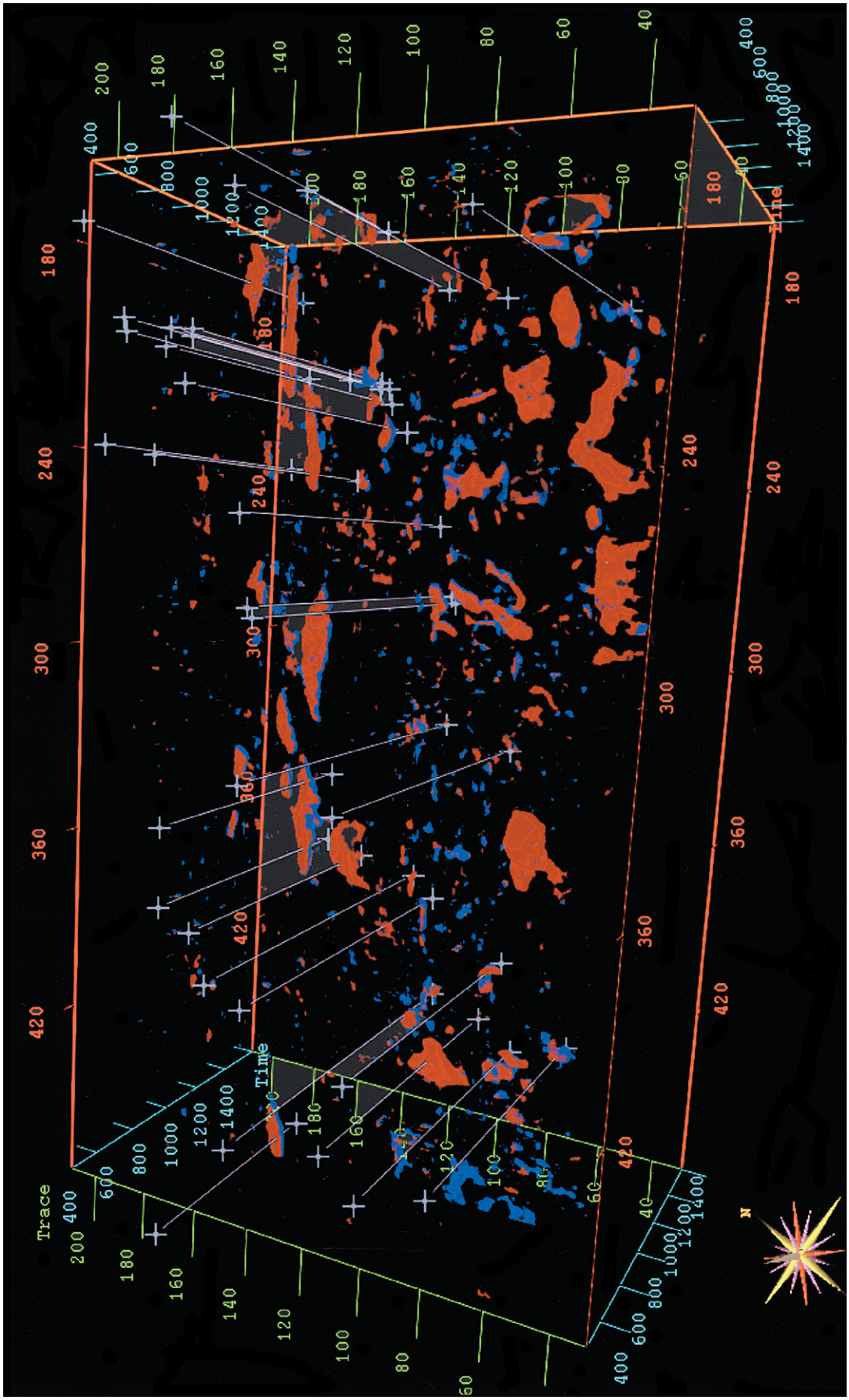

Fig. 11-6. Volumetric view of bright spots in the Frio Formation of south Texas. The volume has been made transparent except for the highest amplitudes from the gas accumulations. The view is from above, so the red top-gas reflections are the principal ones seen. The white lines are wells. (Courtesy Edge Petroleum.)

Downloaded 25 Jun 2012 to 95.28.162.50. Redistribution subject to SEG license or copyright; Terms of Use: http://segdl.org/

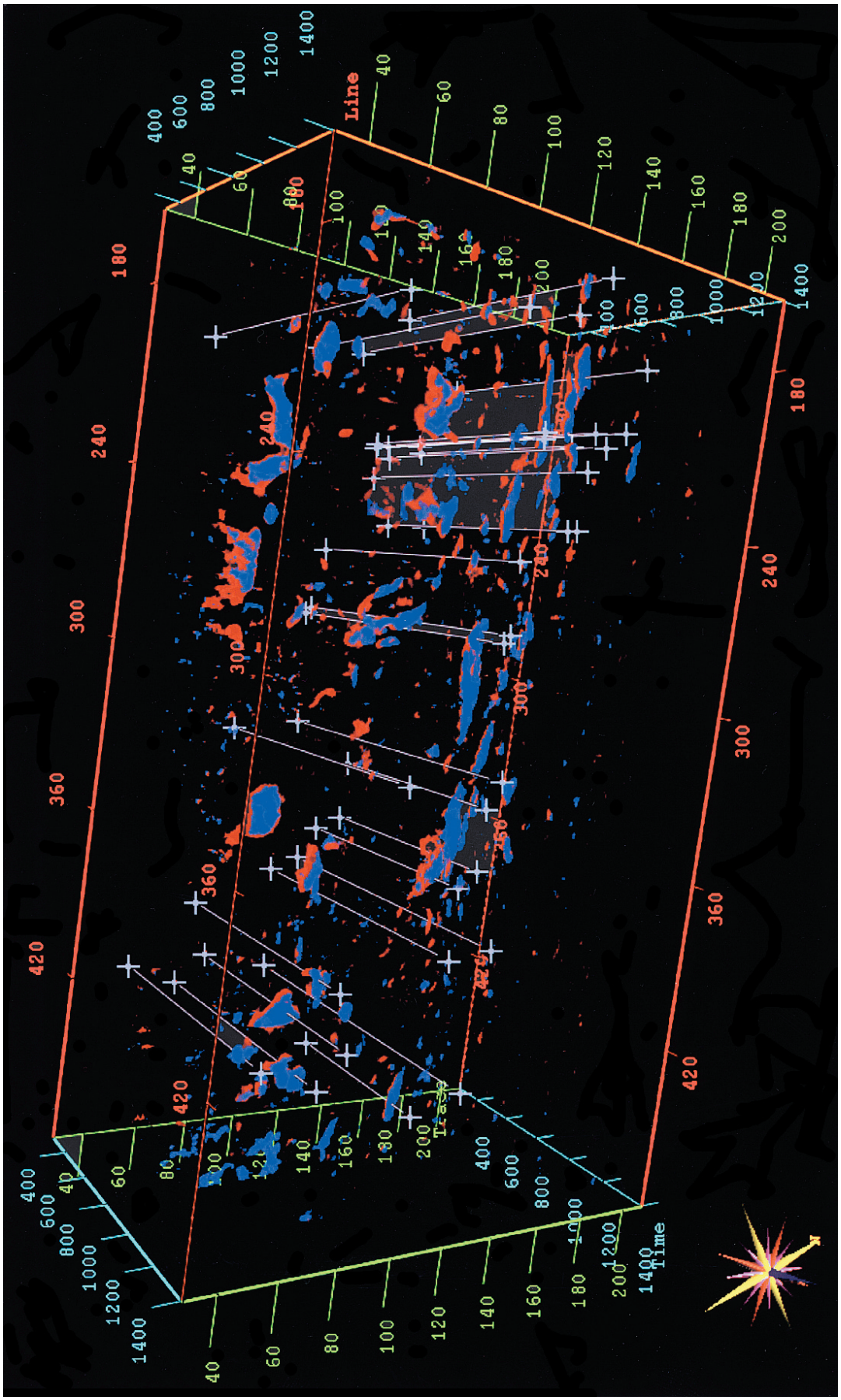

Fig. 11-7. Same as Figure 11-6 but viewed from below, so the blue base-gas reflections are the principal ones seen. (Courtesy Edge Petroleum.)

Downloaded 25 Jun 2012 to 95.28.162.50. Redistribution subject to SEG license or copyright; Terms of Use: http://segdl.org/

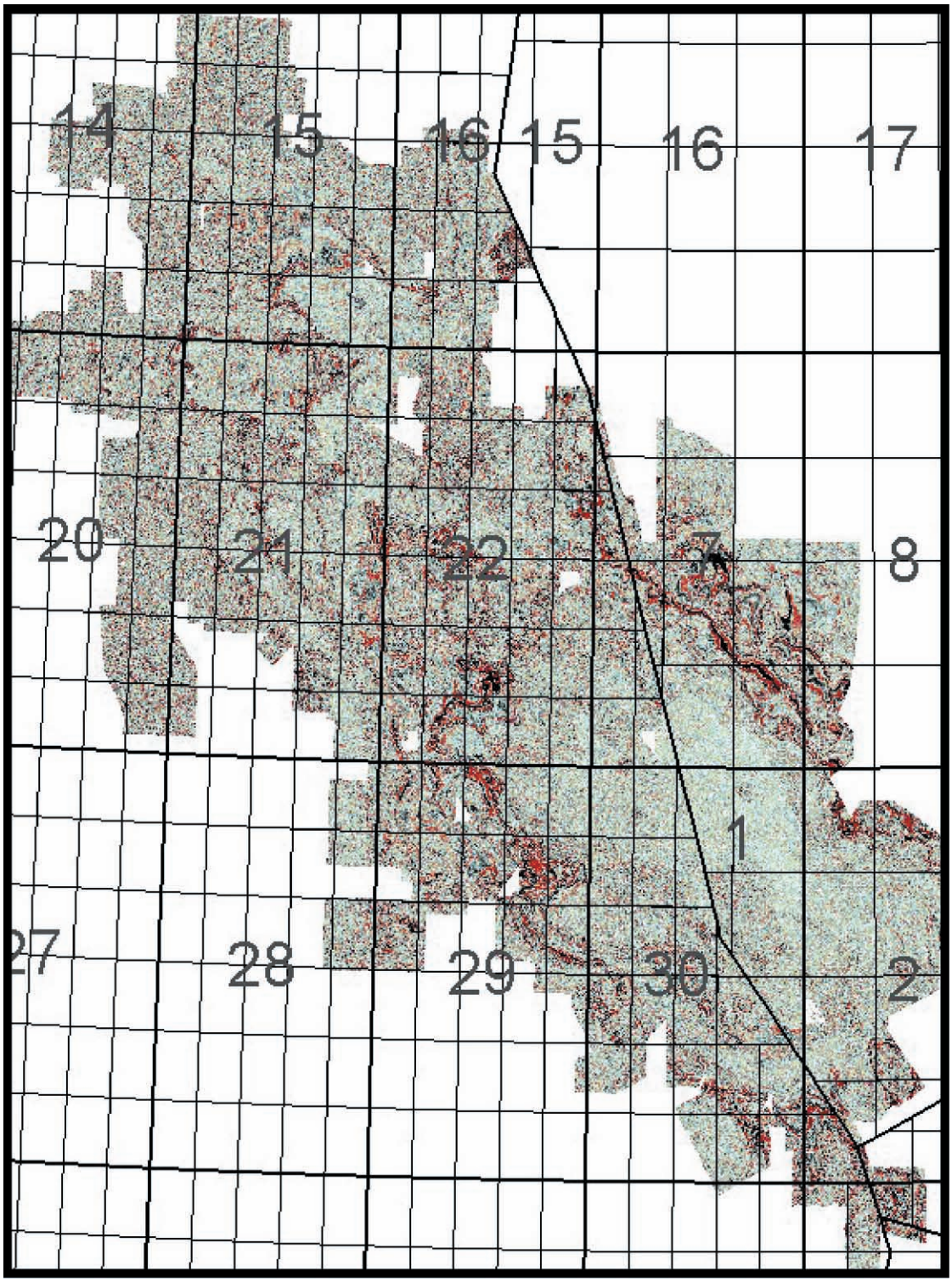

Fig. 11-8. Time slice from Central North Sea Mega Survey covering 35,000 sq. km. in the offshore of U.K., Norway, and Denmark. (Courtesy PGS Geophysical.)

Downloaded 25 Jun 2012 to 95.28.162.50. Redistribution subject to SEG license or copyright; Terms of Use: http://segdl.org/

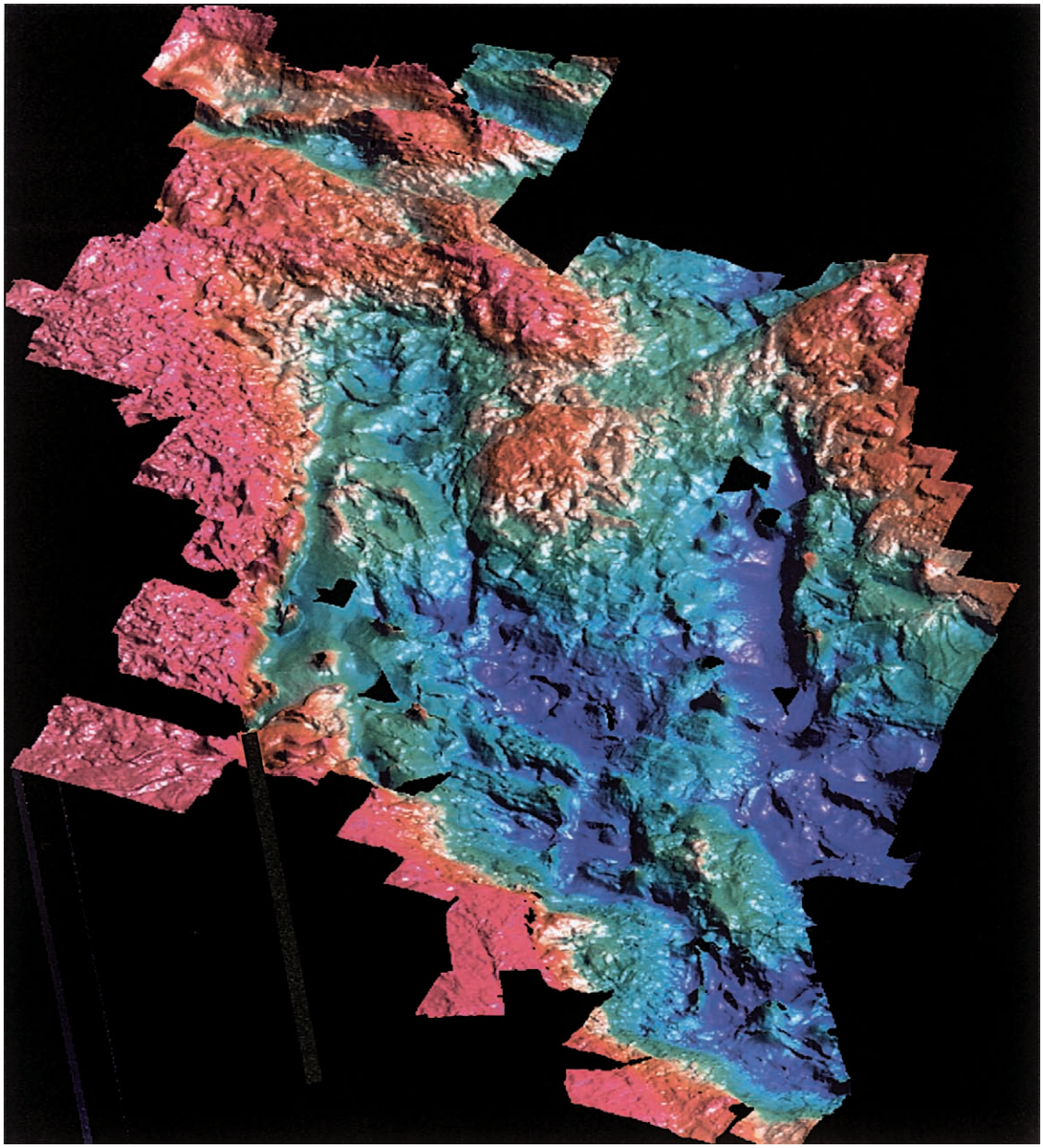

Fig. 11-9. Perspective structure of Base Cretaceous Unconformity from Central North Sea Mega Survey. Area covers 20,000 sq. km. of U.K.'s Central Graben. (Courtesy PGS Geophysical.)

Downloaded 25 Jun 2012 to 95.28.162.50. Redistribution subject to SEG license or copyright; Terms of Use: http://segdl.org/

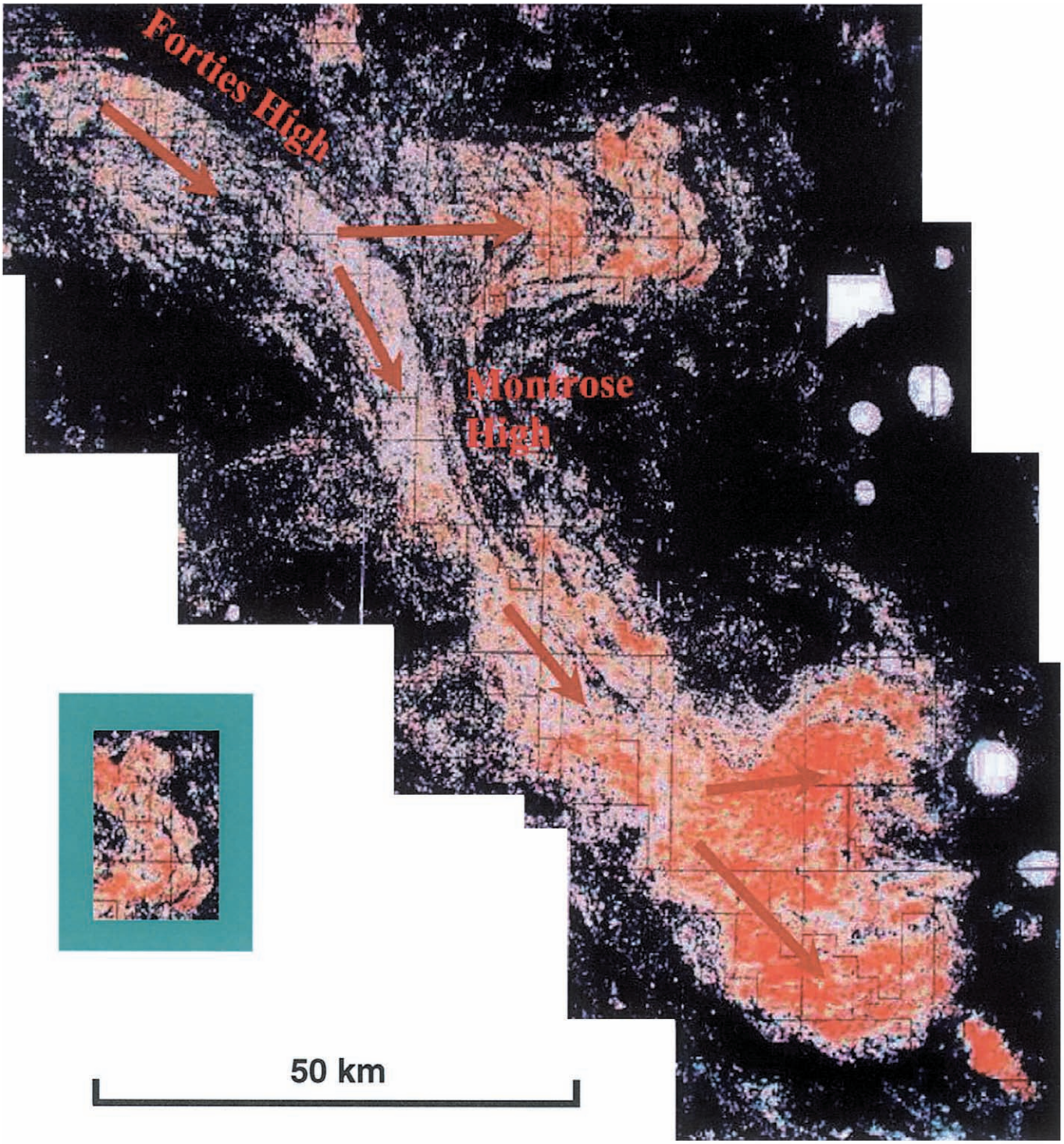

Fig. 11-10. RMS amplitude map over 100-ms window in lower Paleocene from Central North Sea Mega Survey. Color shows distribution and depositional morphology of Maureen Sand over an area of 15,000 sq. km. For comparison, inset is one U.K. block of 250 sq. km., commonly the size of an individual 3-D survey. (Courtesy PGS Geophysical.)

Downloaded 25 Jun 2012 to 95.28.162.50. Redistribution subject to SEG license or copyright; Terms of Use: http://segdl.org/

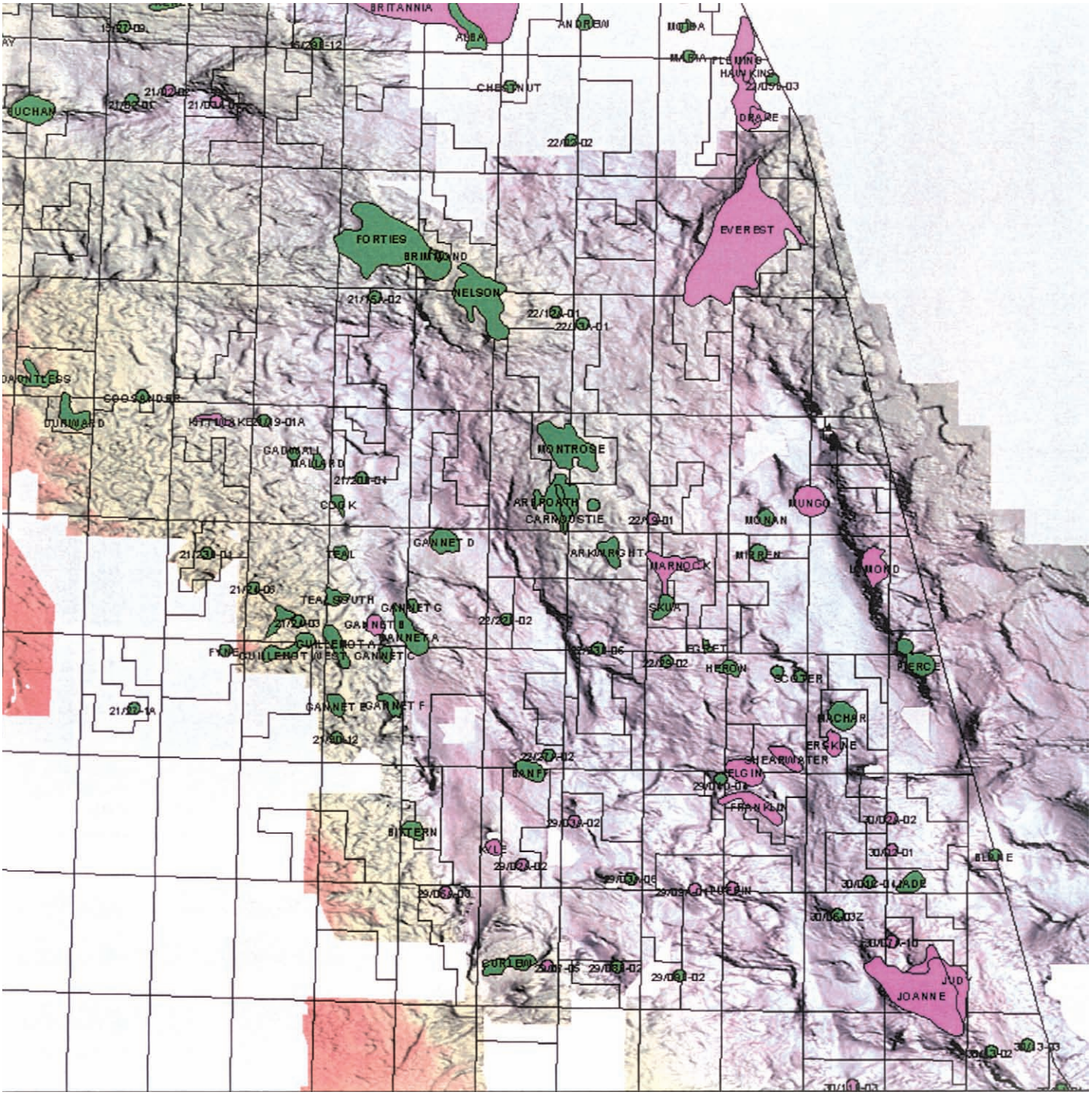

Fig. 11-11. Edge display of Base Cretaceous Unconformity horizon from Central North Sea Mega Survey, showing the relation of oil (green) and gas (magenta) fields to the structural trends. Area covers more than 20,000 sq. km. (Courtesy PGS Geophysical.)

Downloaded 25 Jun 2012 to 95.28.162.50. Redistribution subject to SEG license or copyright; Terms of Use: http://segdl.org/

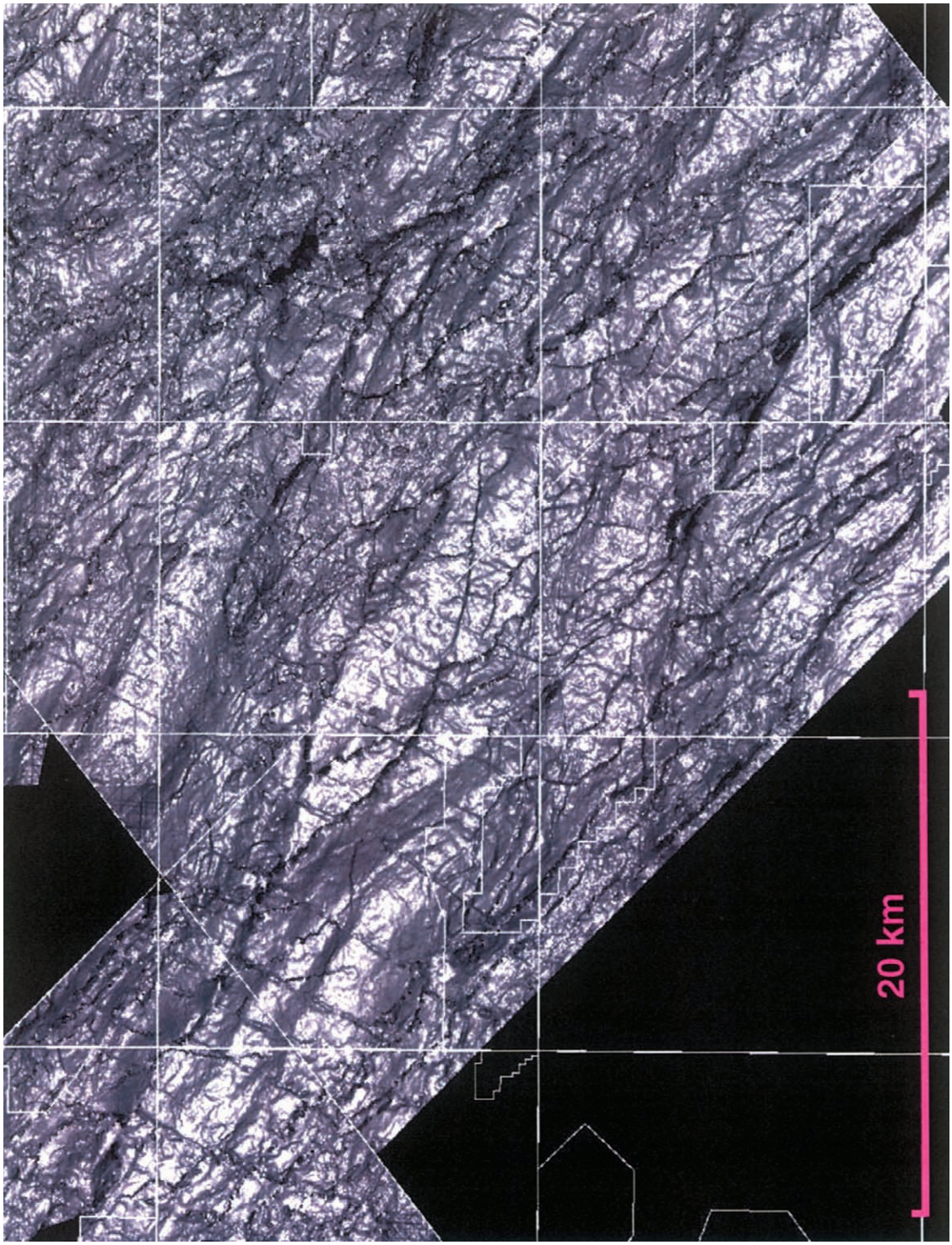

Fig. 11-12. Edge display of Base Zechstein horizon from Southern North Sea Mega Survey. Area covers about 2000 sq. km. of U.K. waters. (Courtesy PGS Geophysical.)

Downloaded 25 Jun 2012 to 95.28.162.50. Redistribution subject to SEG license or copyright; Terms of Use: http://segdl.org/

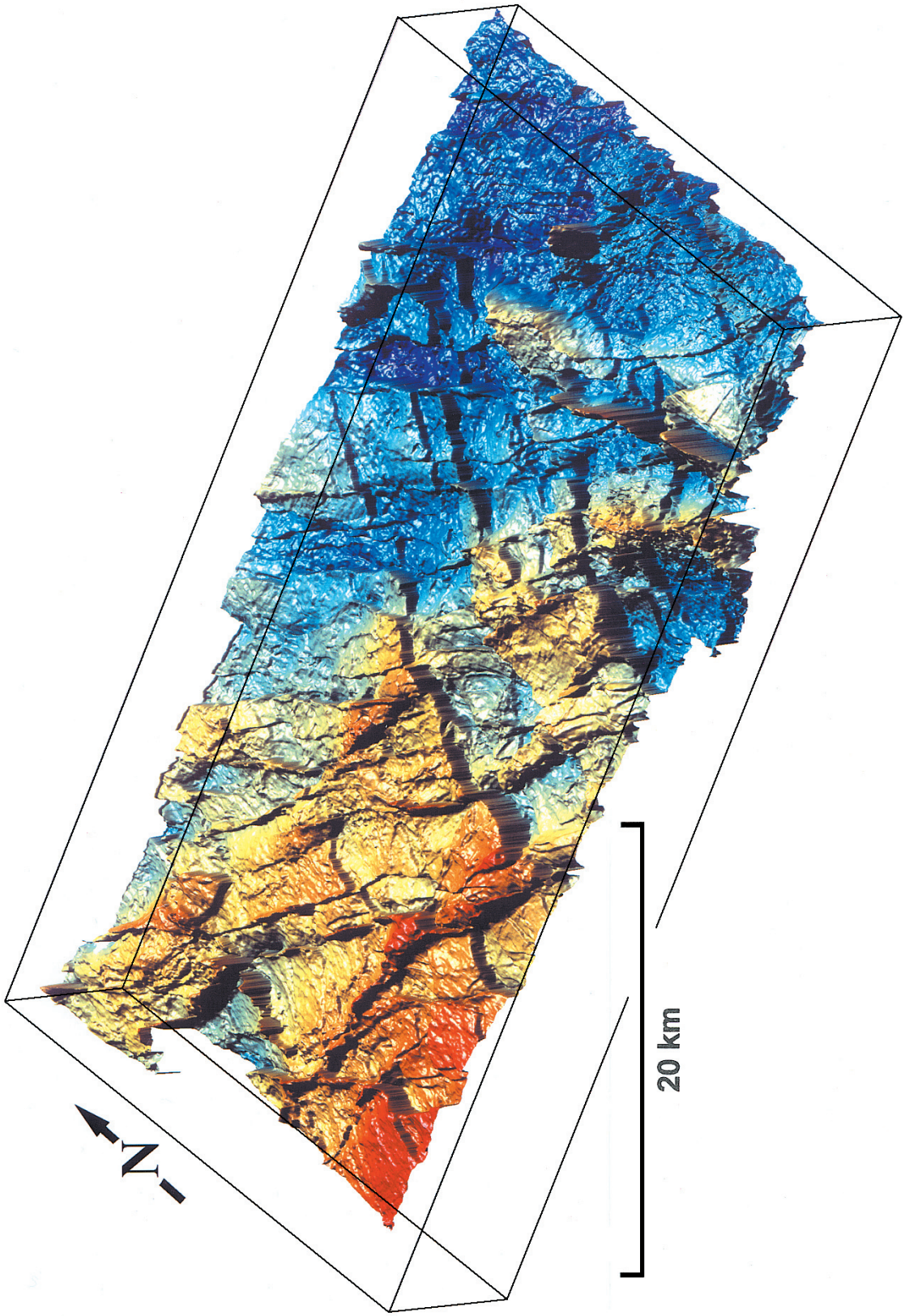

Fig. 11-13. Perspective view with illumination of Base Zechstein offshore Netherlands. The area covers 1100 sq. km. and is composed of seven 3-D surveys. This typical structural style here ranges in depth from 2700 m (red) to 4200 m (blue). (Courtesy Nederlandse Aardolie Maatschappij B. V.)

Downloaded 25 Jun 2012 to 95.28.162.50. Redistribution subject to SEG license or copyright; Terms of Use: http://segdl.org/

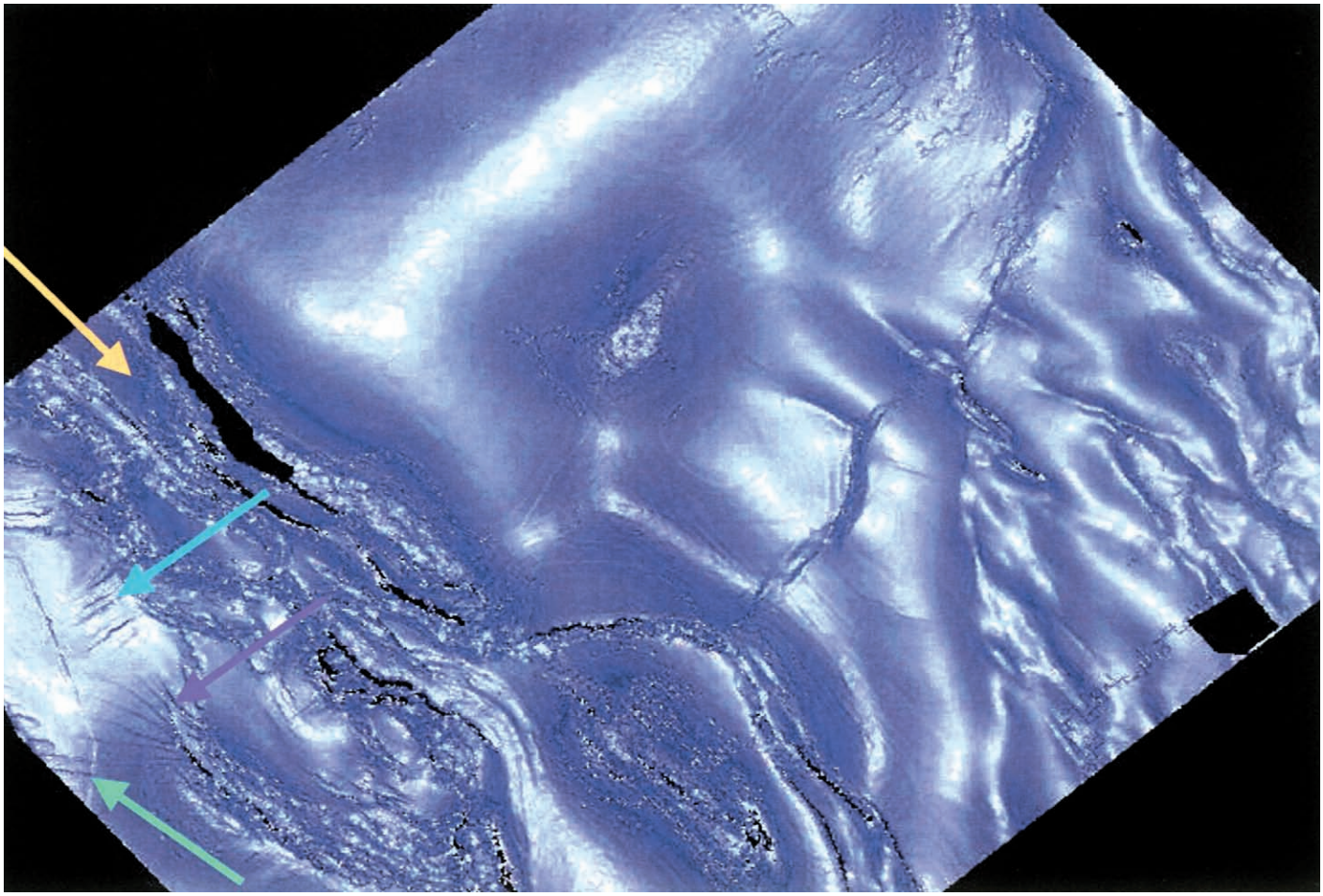

Fig. 11-14. Top Triassic structure from Southern North Sea Mega Survey. Area covers 3000 sq. km. The patterns are caused by underlying mobile salt. (Courtesy PGS Geophysical.)

Downloaded 25 Jun 2012 to 95.28.162.50. Redistribution subject to SEG license or copyright; Terms of Use: http://segdl.org/

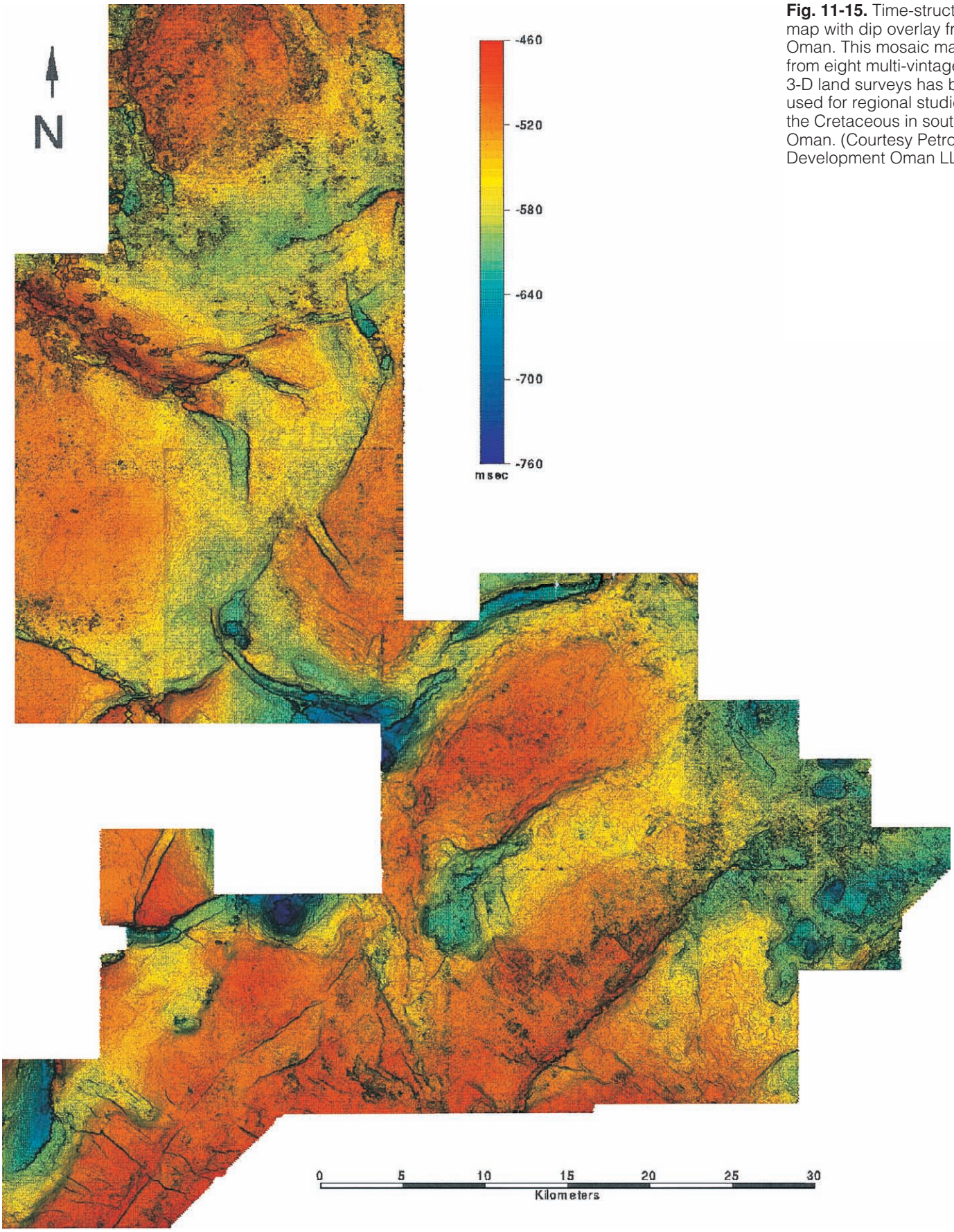

Fig. 11-15. Time-structure map with dip overlay from Oman. This mosaic made from eight multi-vintage 3-D land surveys has been used for regional studies of the Cretaceous in southern Oman. (Courtesy Petroleum Development Oman LLC.)

Downloaded 25 Jun 2012 to 95.28.162.50. Redistribution subject to SEG license or copyright; Terms of Use: http://segdl.org/

total will be extended to 60,000 sq. km. (Edwards and Witney, 2002). Some of these data were used to generate the regional view of the Base Cretaceous Unconformity in Figure 11-9.

A wonderful demonstration of the value of regional coverage is shown in Figure 11-10. Here, using the Top Chalk reflection as the reference horizon, a window from 120 ms above to 20 ms above produced this amplitude map of the Maureen Sand. The fan comes from the northwest, flows around the Forties and Montrose Highs and then terminates in the deepest part of the Central Graben, where its forward progress is impeded by the Josephine High. For comparison in Figure 11-10, one U.K. block of the amplitude map is shown. This makes it clear that the nature and extent of the deposition can only be understood by studying regional displays.

Figure 11-10 uses RMS (root-mean-square) amplitude over a 100-ms window. RMS amplitude is well suited to reconnaissance studies, as discussed in Chapter 4. The reader is referred to the comparison between horizon and windowed amplitude in Figure 4-58.

Figure 11-11 is another interesting regional display from the Central North Sea Mega Survey. The whole of the central North Sea may be viewed at once and the relationship between Base Cretaceous structure and the existing fields can be studied easily. The NW-SE structural trend apparently controls the oil and gas accumulations.

Figure 11-12 is from the Southern North Sea Mega Survey and shows part of the southern U.K. gas area. The orientation of the principal faults is northwest-southeast. This edge display clearly shows a secondary younger fault set running at right angles to this primary trend, and the Mega Survey interpretation concludes that these younger faults are 50 km or more long. The structural style is evidently very similar to that across the median line in offshore Netherlands (Figure 11-13).

Figure 11-14 is from the Southern North Sea Mega Survey and shows the effect of the Zechstein salt movement at the Top Triassic level. The major disturbances trending northwest-southeast (aligned with the yellow arrow) are caused by underlying elongated salt walls. At the end of one of the walls faults can be seen radiating outwards (the magenta arrow). Adjacent to another wall the faults are perpendicular (the blue arrow). The green arrow indicates a merge boundary between input 3-D surveys.

Figure 11-15 shows how the same joining of 3-D surveys has been accomplished with land data. Here eight surveys have facilitated the regional study of the Cretaceous in southern Oman. Note various grabens oriented in a variety of directions. These eight surveys are part of a continuous swath of more than 40 surveys in the area. Petroleum Development Oman, whose concession covers about half the country, now have so many 3-D surveys that they have introduced the 3-D MegaProject (Ligtendag, 1999). Data are stored, manipulated, displayed and interpreted as MegaCells measuring 10 × 10 km each, rather than as individual surveys. Each MegaCell is part of one of four MegaGrids, and a huge variety of regional displays is possible.

References

Bally, A. W., 1999, About geophysics, geology and regional hydrocarbon systems — a discussion that contrasts the Gulf of Mexico with northeastern Venezuela: address to Geophysical Society of Houston and Houston Geological Society.

Edwards, H., and J. Witney, 2002, The 'mega survey' route to understanding reservoir potential: First Break, v. 20, p. 571–575.

Ligtendag, M. H. P., 1999, The 3-D MegaProject in Petroleum Development Oman: A 3-D data management concept for seismic, workstation support and interpretation: The Leading Edge, v. 18, p. 330–337.

Downloaded 25 Jun 2012 to 95.28.162.50. Redistribution subject to SEG license or copyright; Terms of Use: http://segdl.org/

Visualization and Visual Integration

Contributed by David M. Roberts
3-DMR

Introduction

Three-dimensional visualization technology has been used in the oil industry for many years. However, until recently, it required powerful, expensive computer hardware that generally was not accessible to most geoscientists. More recently, much cheaper and much more powerful PC hardware has made 3-D visualization possible on every geoscientist's desktop.

Seismic interpreters have always needed to visualize, simply because the Earth that we seek to study is three dimensional. The simplest form of visualization that 3-D data provides is one vertical section and one horizontal section, or time slice, side-by-side. This was discussed in Chapter 3. Early extensions of this idea included composite displays of one vertical and one horizontal section spliced together, chair displays and volumetric displays of various kinds, again discussed in Chapter 3. Color is of course vital to visualizing and understanding data, and this is discussed at length in Chapter 2. Visualizing amplitude and structure together is introduced in Chapters 4 and 5, and is further developed in Chapter 8. Visualization of large volumes using voxel display is introduced in Chapter 11. The current chapter extends all these ideas and demonstrates the full power of modern visualization technology to understand, interpret, and integrate seismic data better.

The topic of visualization extends well beyond 3-D seismic and associated subsurface data, but I have limited the focus of this chapter to the use of 3-D visualization for 3-D seismic interpretation — data inspection, data interpretation, and interpretation quality control — followed by several examples of visual integration. I have largely avoided conventional seismic interpretation techniques and have focused on techniques that are unique to visualization applications and technology. I also have not delved deeply into the topic of visualization hardware, as this would probably require a book in its own right. Suffice it to say that I have worked very successfully using hardware ranging from twin-screen desktop workstations to room-sized visualization centers like that shown in Figure 12-1.

Computer Hardware

Although computer hardware technology advances very quickly, currently there are still two fundamental hardware components that are critical. These are the size of the memory and the power of the graphics card. At press time, a typical workstation used for 3-D visualization will probably have 32GB RAM and a powerful NVIDIA graphics card, such that several complete 3-D surveys can be visualized and interpreted in real time.

Downloaded 25 Jun 2012 to 95.28.162.50. Redistribution subject to SEG license or copyright; Terms of Use: http://segdl.org/

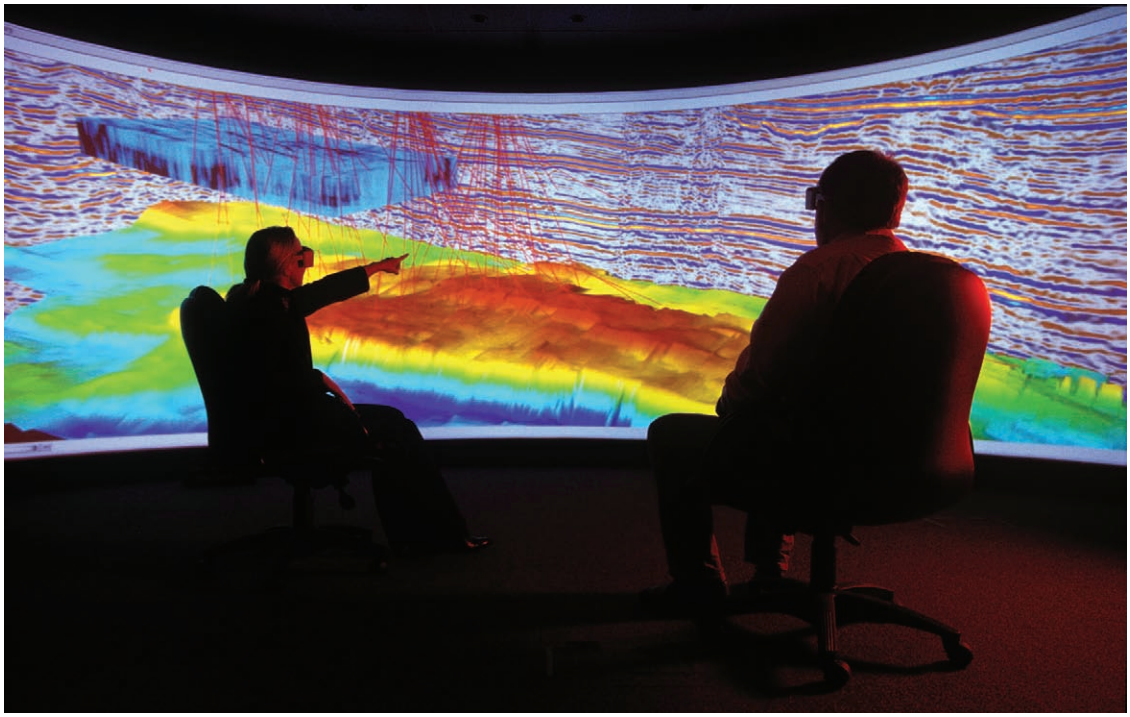

Fig. 12-1. Working in a visualization center. (Courtesy BP Exploration and Chris Sattlberger.)

In order to allow the viewing of much larger 3-D surveys that will not fit into the memory of the computer, most software vendors have also developed ways of accessing data very quickly from a hard disk using advanced disk caching and data compression algorithms.

In addition to enabling the interpreter to view 3-D seismic data in three dimensions, visualization hardware and software offer the significant benefit of usually providing him instant access to all of his seismic data. Thus equipped, he is able to interpret his 3-D data sets more efficiently.

The Power of Visualization

The power and value of 3-D visualization are illustrated by three examples. The first compares a conventional top reservoir contour map of the Lan Tay field carbonate platform in the Far East (Figure 12-2) with a 3-D visualization of the same information (Figure 12-3). I suggest that it is much easier to understand the geometry of the top reservoir structure and its seismic expression by viewing the surface in 3-D than by examining the conventional contour map. Visualization has allowed appraisal and development planning of this field to proceed more efficiently and effectively.

The second example, illustrated by Figure 12-4, shows a 3-D visualization of bathymetry data in the Caspian Sea. In this example the severity and potential instability of some of the seabed features are only really clear using 3-D visualization. The use of visualization played a particularly important role in communicating to the staff involved the location and extent of these potential engineering hazards.

The third example shows a visualization of a multipay oilfield in the Gulf of Mexico. Figure 12-5 is a scene taken from one of the first BP workstation well-planning sessions. The session showed the best way for a multidisciplinary team to plan wells to intersect multiple reservoirs lying between several salt bodies.

Data Inspection

When a new 3-D survey arrives in the office, I believe that visualization should be used by the interpreter to scan back and forth through the new data set in the inline, crossline, and time or depth directions, as shown in Figure 12-6. In this way the interpreter can quickly become familiar with both the quality of the data and the geologic

Downloaded 25 Jun 2012 to 95.28.162.50. Redistribution subject to SEG license or copyright; Terms of Use: http://segdl.org/

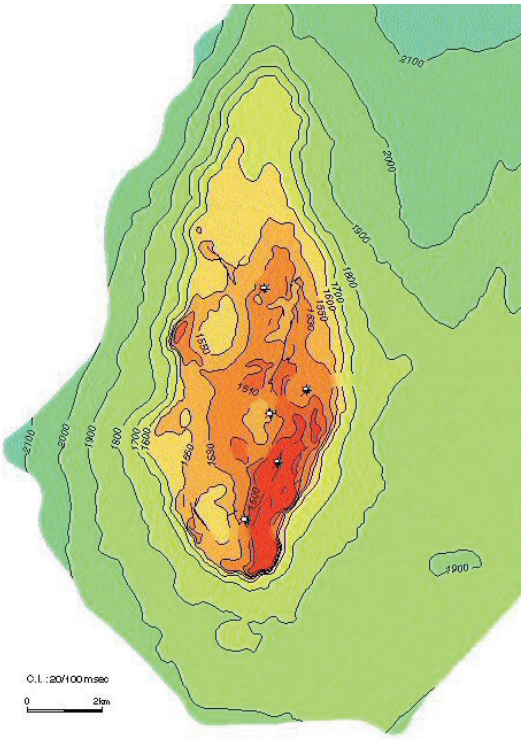

Fig. 12-2. Traditional structural contour map of Lan Tay Field. (Courtesy BP Exploration.)

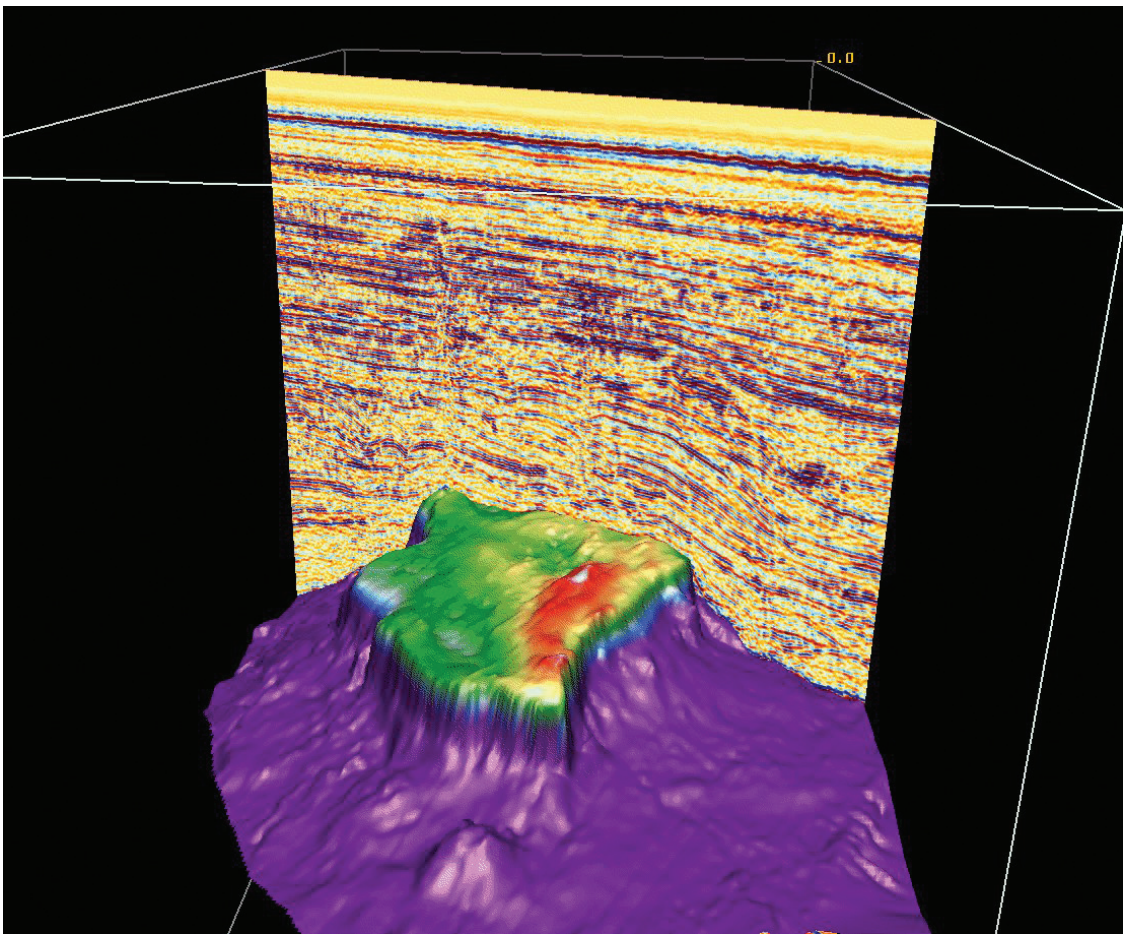

Fig. 12-3. Three-dimensional surface representation of Lan Tay field structure, for comparison with Figure 12-2 (Courtesy BP Exploration.)

Downloaded 25 Jun 2012 to 95.28.162.50. Redistribution subject to SEG license or copyright; Terms of Use: http://segdl.org/

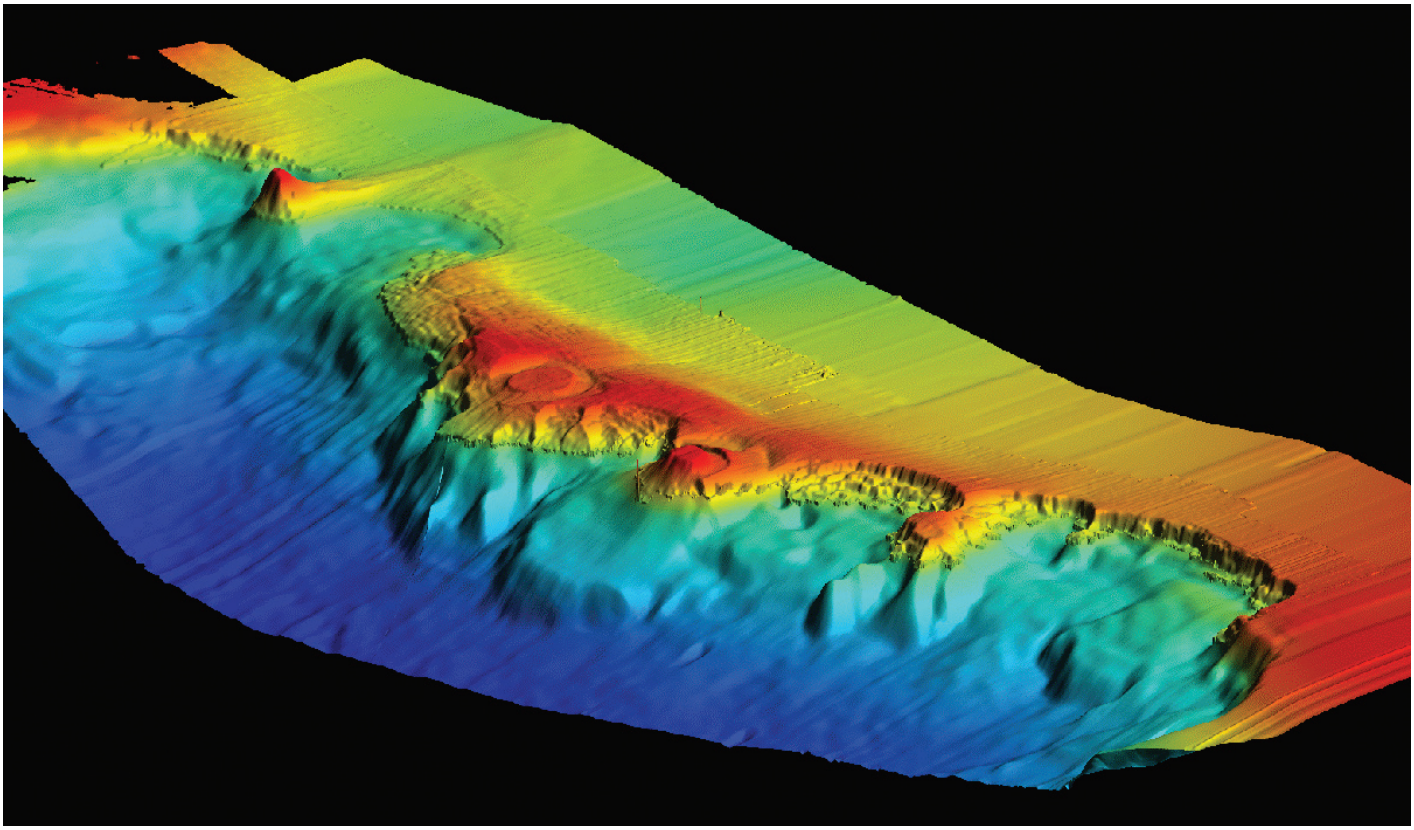

Fig. 12-4. Caspian Sea bathymetry. The severity and potential instability of some of the seabed features are only really clear from the 3-D visualization. (Courtesy BP Exploration and the AIOC partners.)

features shown, prior to the start of any actual interpretation. A team review of the data at this stage can often also allow an interpretation strategy to be defined, leading to a more efficient and fit-for-purpose interpretation.

Animation and motion are currently underutilized by interpreters. The process of animating back and forth through a 3-D data set can be very instructive and can provide early information about, for example, channel and fault continuity. It is also particularly useful in areas of poor data quality where the motion creates a visual stacking effect which enhances weak, noise-obscured reflection events.

Opacity

The use of opacity is another powerful visualization technique, which allows the interpreter to examine a volume of seismic data using varying transparency, so that only the very highest-amplitude reflections are visible. This can quickly reveal the shape of the high-amplitude features in 3-D and provide insight as to whether the shapes are depositional or perhaps hydrocarbon related. Figure 12-7 shows how the opacity and size of a small cube of seismic data can be adjusted to reveal the morphology of high-amplitude channel features.

I often find interpreters working with only a single cube of semitransparent seismic data. A better way is also to display a vertical profile so that the 3-D features "grow out of the vertical profile." This immediately allows the interpreter to better understand how the 3-D geometries tie with the vertical data, as shown in Figure 12-8.

The interpreter should check that the amplitude feature being examined is fully contained within the semitransparent seismic volume; otherwise, some very misleading conclusions about the shape and interpretation of the amplitude feature might be reached. Figure 12-9 shows an example of the way opacity has been used to visualize the geometry of a complex channel system by first sculpting the target interval.

Downloaded 25 Jun 2012 to 95.28.162.50. Redistribution subject to SEG license or copyright; Terms of Use: http://segdl.org/

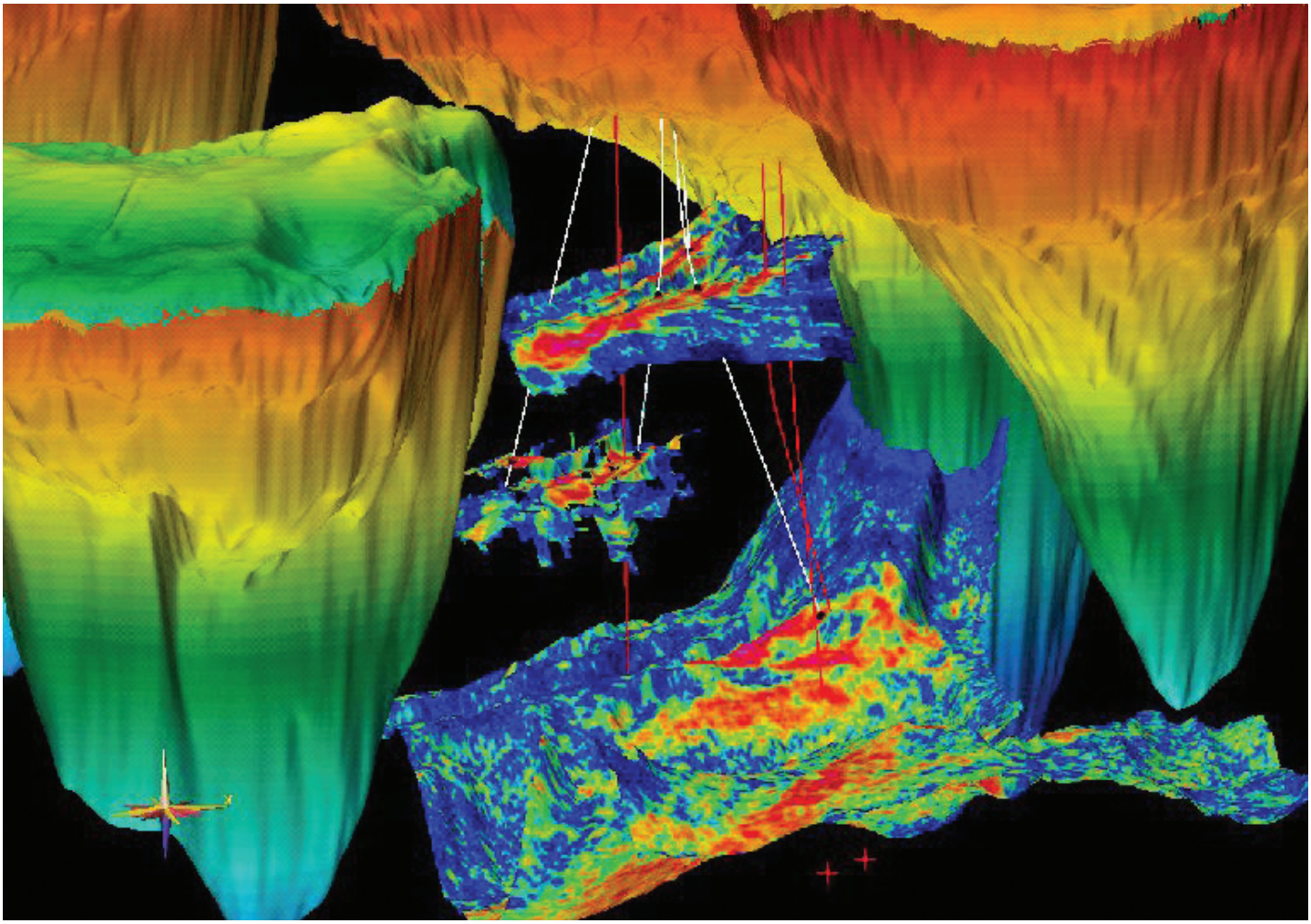

Fig. 12-5. Gulf of Mexico development well planning. The reservoirs are color-coded by amplitude, and salt bodies lie to the left and right of the image. (Courtesy BP Exploration.)

A special application of the use of opacity, called optical stacking, can be used to scan 3-D data sets for flat spots. A fairly thin semitransparent seismic cube is viewed from the side — and any flat spots tend to "optically stack" and become more easily identifiable than they are on individual conventionally displayed inlines and crosslines, particularly if the flat spots are subtle.

Data Interpretation

Most of the first 3-D seismic visualization applications included very basic interpretation tools that allowed the connectivity of high-amplitude seismic reflections to be examined and mapped. This worked well in areas where seismic quality was good and reservoirs were associated with fairly simple high-amplitude reflections. Unfortunately, this has led to a popular misconception that visualization software "only works on very good quality 3-D seismic data." Nothing could be farther from the truth! Most modern visualization and interpretation applications now include a variety of interpretation tools, thereby permitting the interpretation of any quality of seismic data. These tools typically range from sophisticated wavelet autotrackers to simple manual picking. Many software applications now handle multiple 3-D surveys and also 2-D data.

Downloaded 25 Jun 2012 to 95.28.162.50. Redistribution subject to SEG license or copyright; Terms of Use: http://segdl.org/

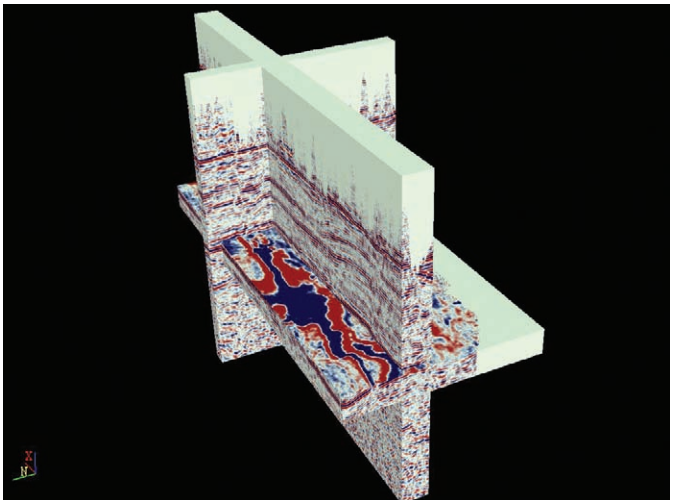

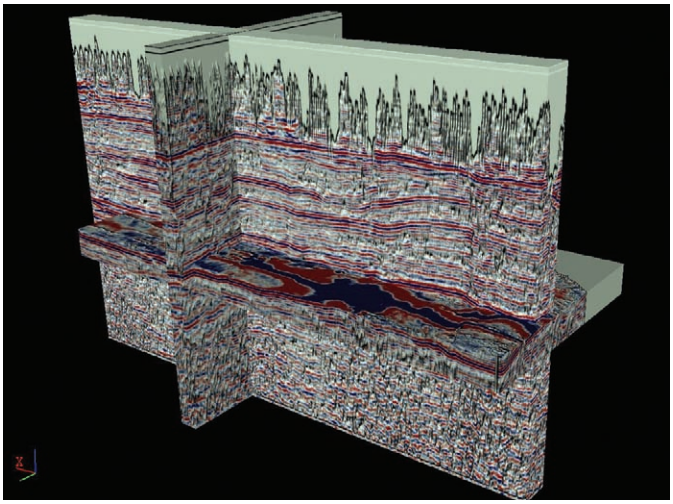

Fig. 12-6. Data inspection by scanning inlines, crosslines, and time slices (Courtesy BP Exploration and the Wytch Farm partners.)

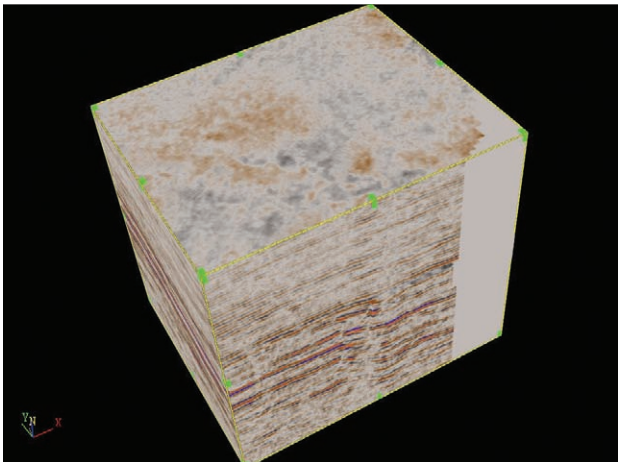

(a)

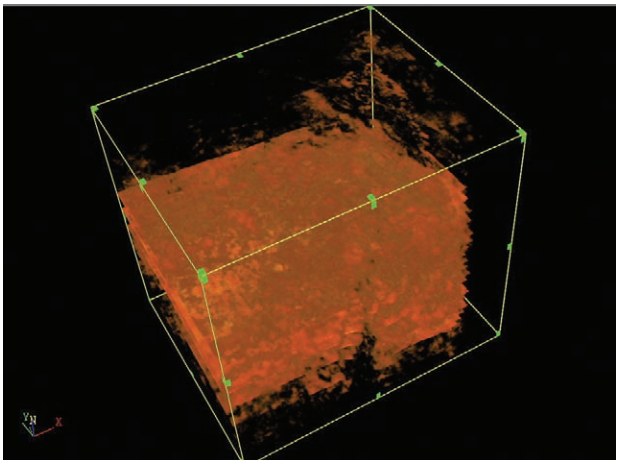

(b)

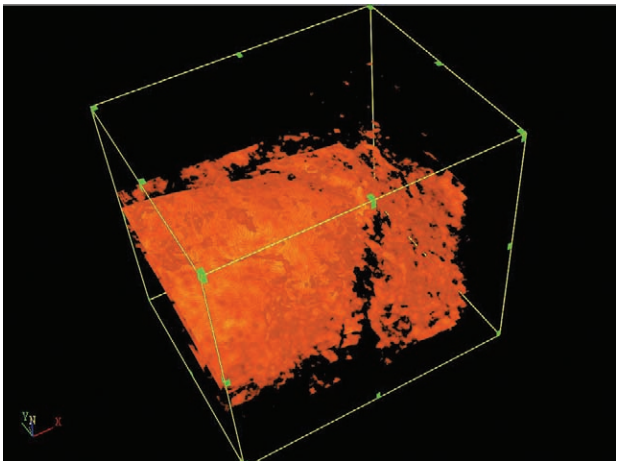

(c)

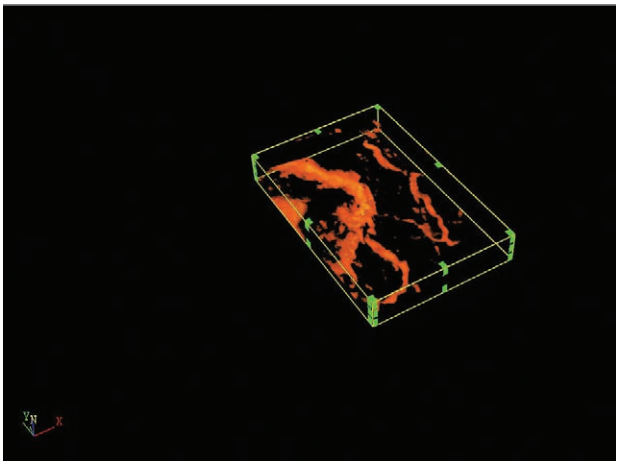

(d)

Fig. 12-7. Isolating and identifying the morphology of high-amplitude channel features: (a) the data volume, (b) the opacity adjusted to show only the high amplitudes, (c) the opacity adjusted to show only the highest amplitudes, and (d) the size of the displayed volume, reduced to isolate the body geometries. (Courtesy Landmark.)

Downloaded 25 Jun 2012 to 95.28.162.50. Redistribution subject to SEG license or copyright; Terms of Use: http://segdl.org/

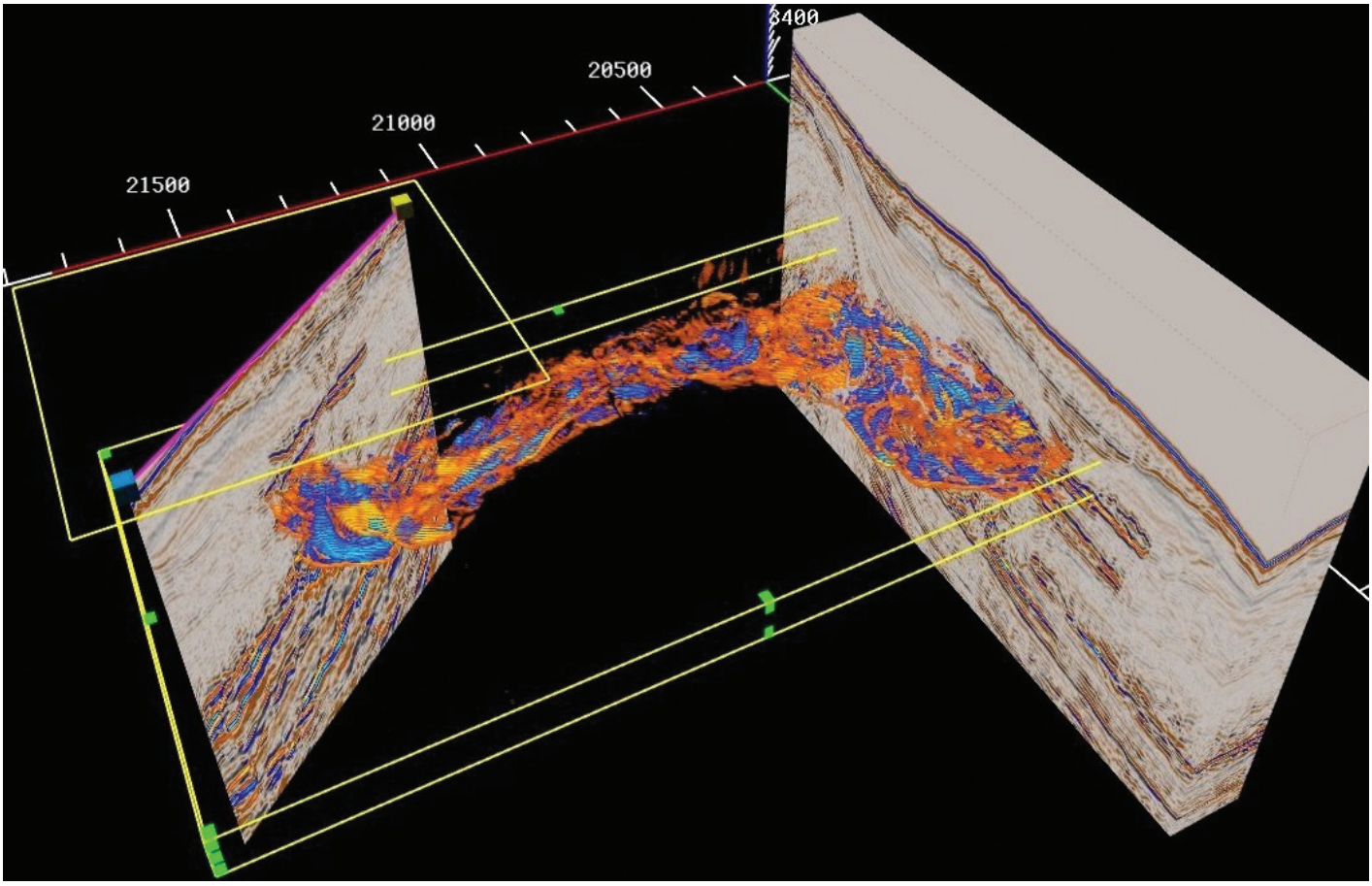

Fig. 12-8. The use of opacity cubes in conjunction with vertical seismic data to visualize high-amplitude depositional features and their 3-D geometry. (Courtesy BP Exploration.)

Downloaded 25 Jun 2012 to 95.28.162.50. Redistribution subject to SEG license or copyright; Terms of Use: http://segdl.org/

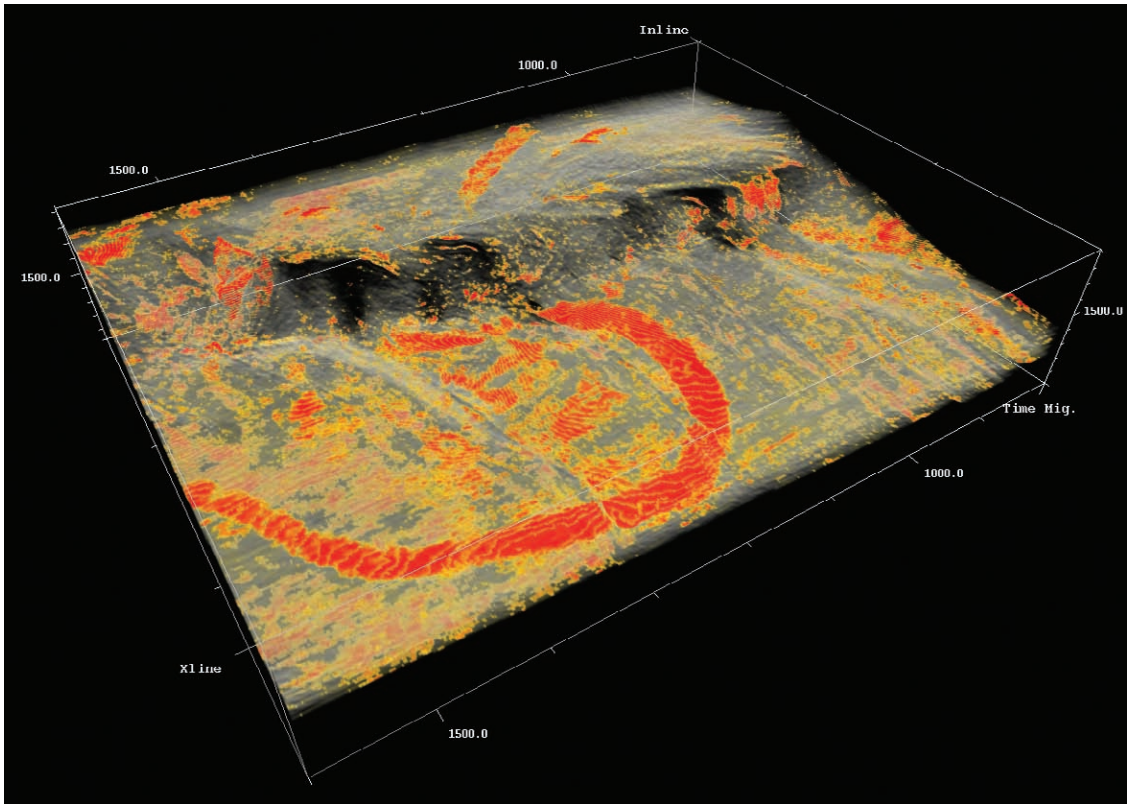

Fig. 12-9. Opacity applied to a channel feature by first sculpting the target interval. (Courtesy Clyde Petroleum and Paradigm.)

Coloring Surfaces by Amplitude

An effective technique for checking amplitude conformance with structure while trying to identify hydrocarbon reflections (Chapter 5) is to color a structural surface with either horizon amplitude or a windowed attribute, as shown in Figure 12-11. It is usually easy to determine if there is conformance with structure, by simply adding contours to the surface (not done in this example). This work is better carried out in 3-D because the conformance of amplitude with structure is usually more obvious. However, care should be taken if the overburden contains lateral velocity changes — in which case, the interpreter should work with depth surfaces.

Stratigraphic Interpretation

In the right geologic environment and with good quality 3-D seismic data, 3-D visualization can be a powerful tool to reveal details of complex depositional environments. Figure 12-12 shows RMS amplitude draped over a structural surface. The surface intersects a 3-D seismic profile showing the data from which the windowed attribute was extracted. Figures 12-13 and 12-14 show two further examples of the definition of channel and mud volcano geometries using 3-D visualization.

Coherence Data

Coherence data are interpreted effectively in a visualization environment. This allows the coherence data, in time-slice mode, to be covisualized with conventional vertical section data. This type of data integration allows the interpreter to see, manipulate, and interpret both data sets at the same time. In this way it is easier to judge whether anomalies identified on coherence time slices represent faults, channel edges, facies changes, or noise.

Text continues on page 424.

Downloaded 25 Jun 2012 to 85.29.162.50. Redistribution subject to SEG license or copyright; Terms of Use: http://segdl.org/

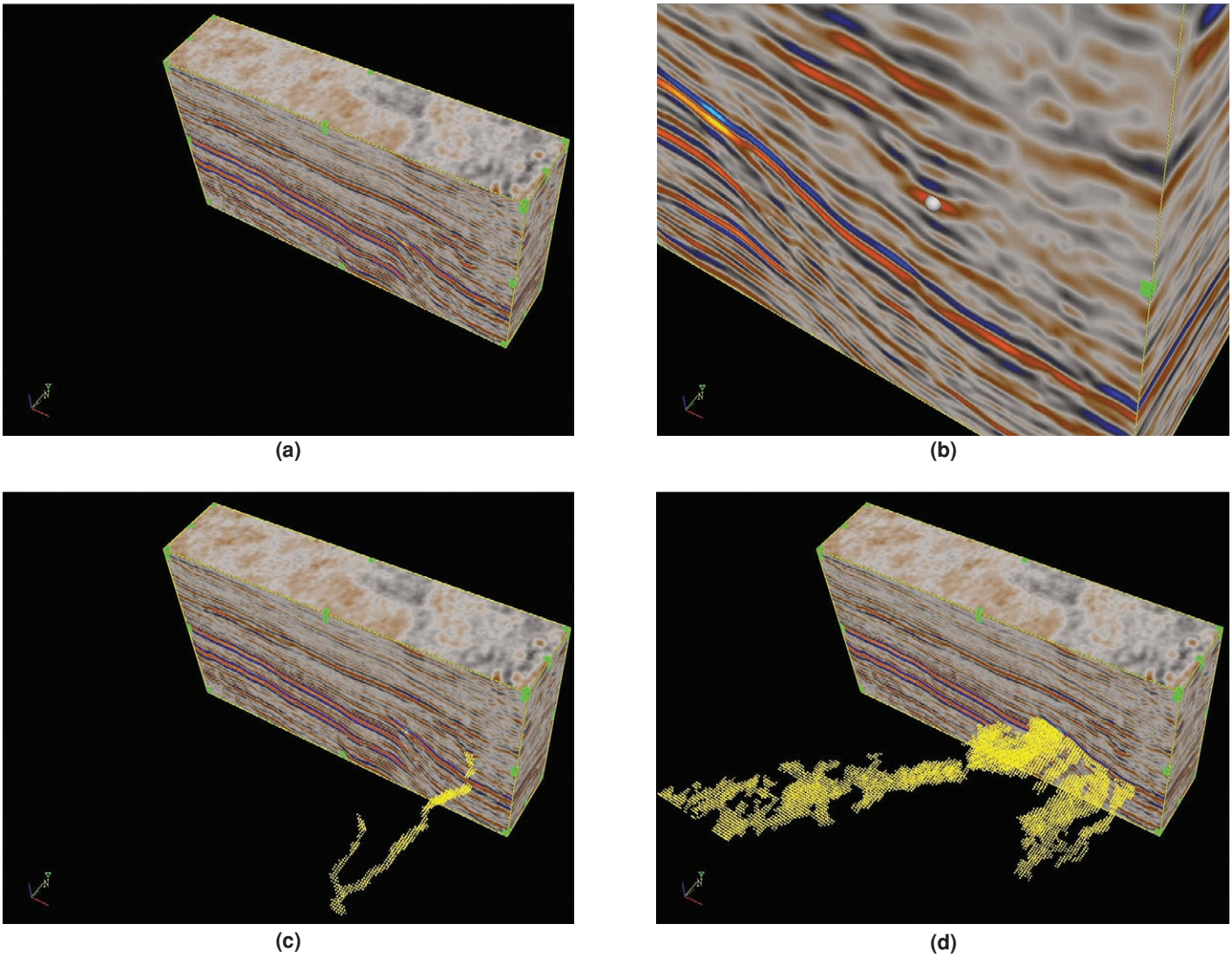

Fig. 12-10. Connectivity analysis using an autotracker and visualization: (a) the data volume, (b) a seed point, (c) the corresponding autotracked channel feature, and (d) another channel feature using a different seed point and different amplitude criteria. (Courtesy Landmark.)

Downloaded 25 Jun 2012 to 95.28.162.50. Redistribution subject to SEG license or copyright; Terms of Use: http://segdl.org/

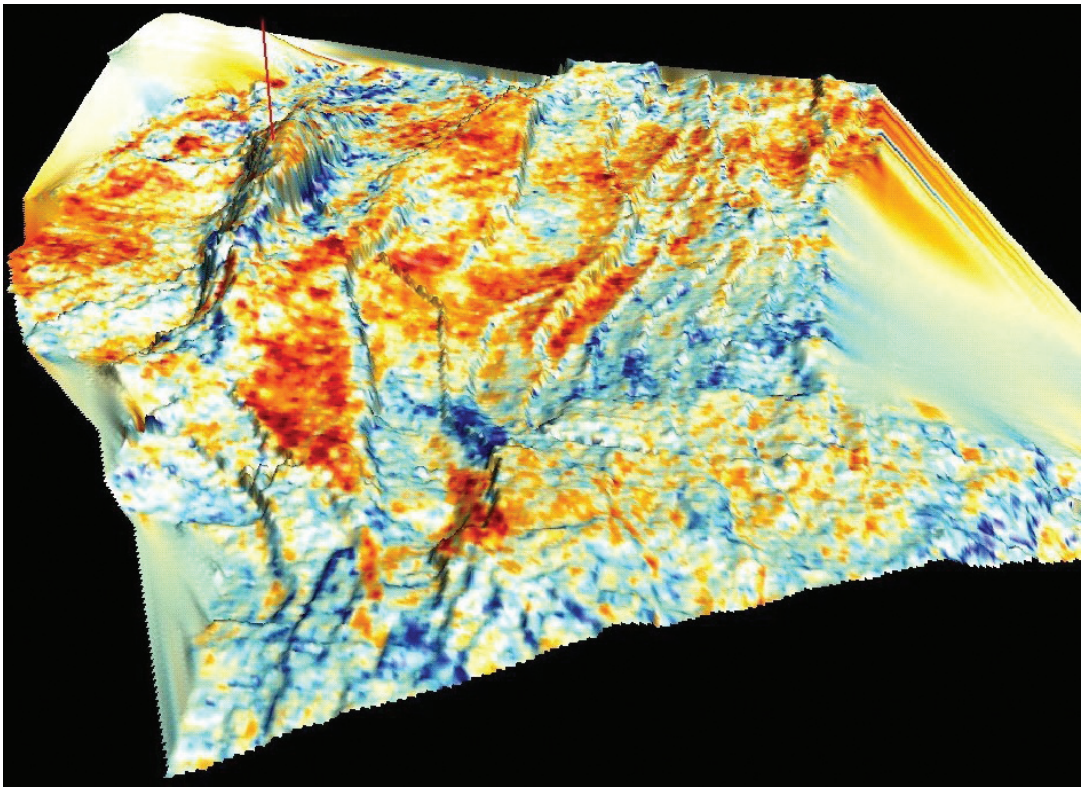

Fig. 12-11. Structural surface colored with amplitude, showing areas where amplitude appears to conform to structure. (Courtesy BP Exploration.)

Fig. 12-12. RMS amplitude draped over structure, clearly showing depositional geometries. The surface with draped amplitude is covisualized with a vertical seismic section. (Courtesy BP Exploration.)

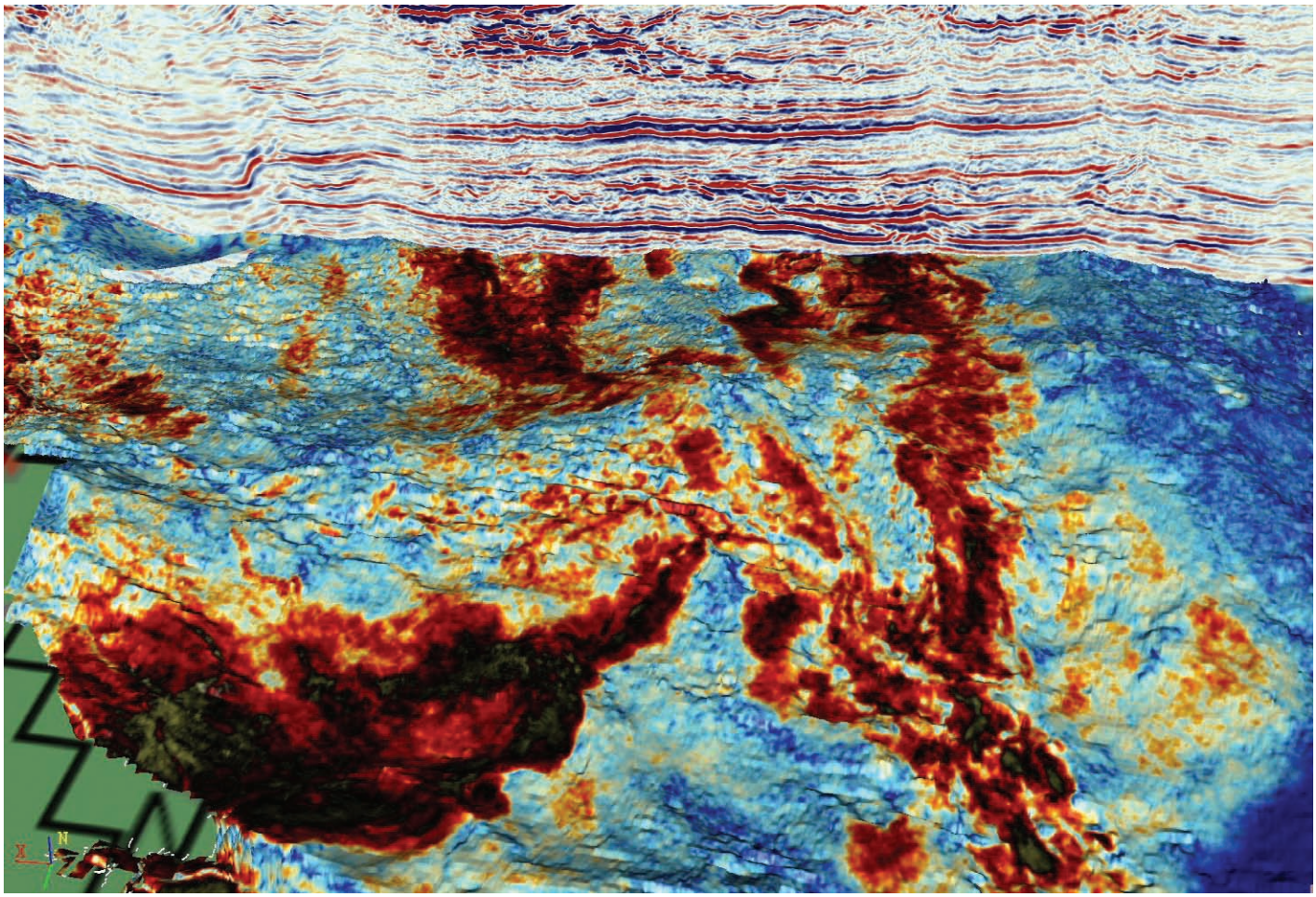

Downloaded 25 Jun 2012 to 95.28.162.50. Redistribution subject to SEG license or copyright; Terms of Use: http://segdl.org/

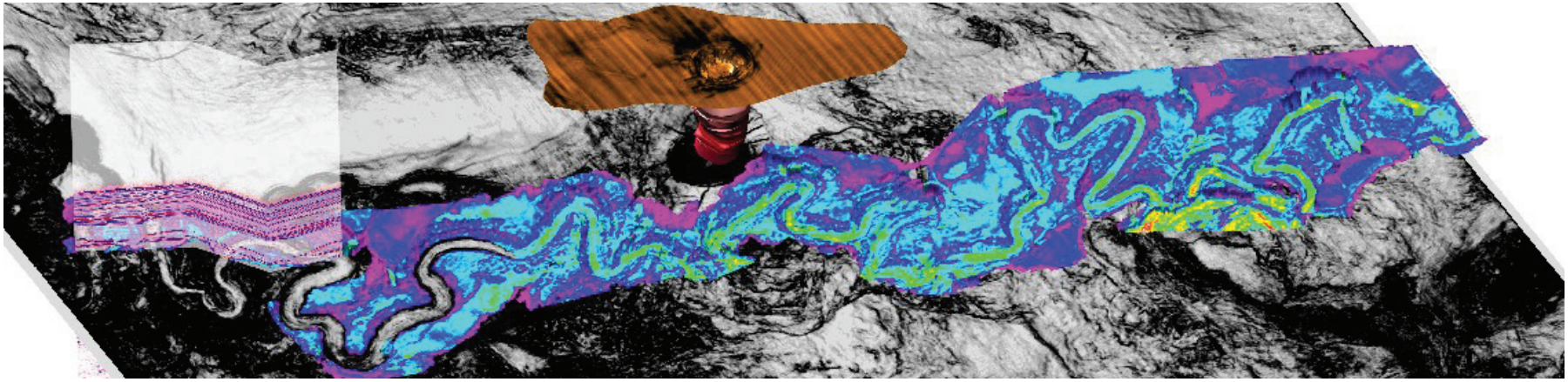

Fig. 12-13. Visualization of a deepwater channel system in South Asia. The high sinuosity of the system is depicted by amplitude (in rainbow colors) that dips to the left into a black-and-white shaded time slice of the coherence attribute. The scene center is dominated by the collapsed vertical feeder system of a mud volcano to seabed. The coherence slice highlights the radial fracture pattern away from the feeder. The seabed image (brown, with amplitude drape) indicates mud flow to the left and the pronounced depression following the mud feeder collapse. (Courtesy Shell.)

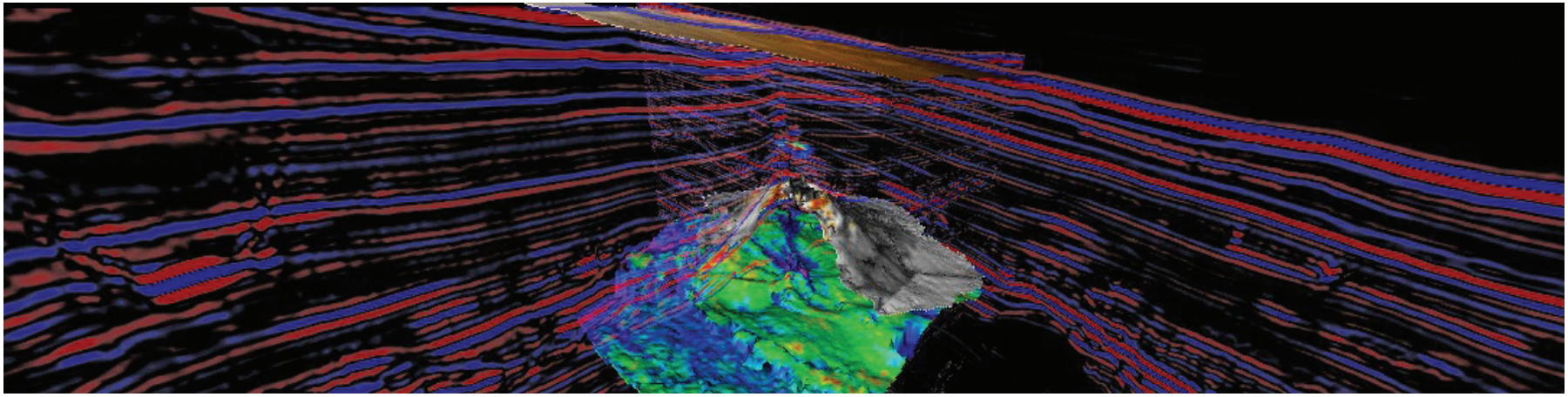

Fig. 12-14. In a different location of the same geologic setting, a mud volcano with a fully developed cone was interpreted. It is located at the intersection of the two partially transparent seismic sections. The amplitude (in rainbow colors) is the horizon slice of seabed prior to the occurrence of the mud eruption. The mud feeder system utilizes a deep-seated fault as a migration route. The eruptions occurred in two phases, each of which is represented by a distinct mud flow. Subsequently, the cone surface (gray) was buried by deepwater sediments which onlap. (Courtesy Shell.)

Downloaded 25 Jun 2012 to 95.28.162.50. Redistribution subject to SEG license or copyright; Terms of Use: http://segdl.org/

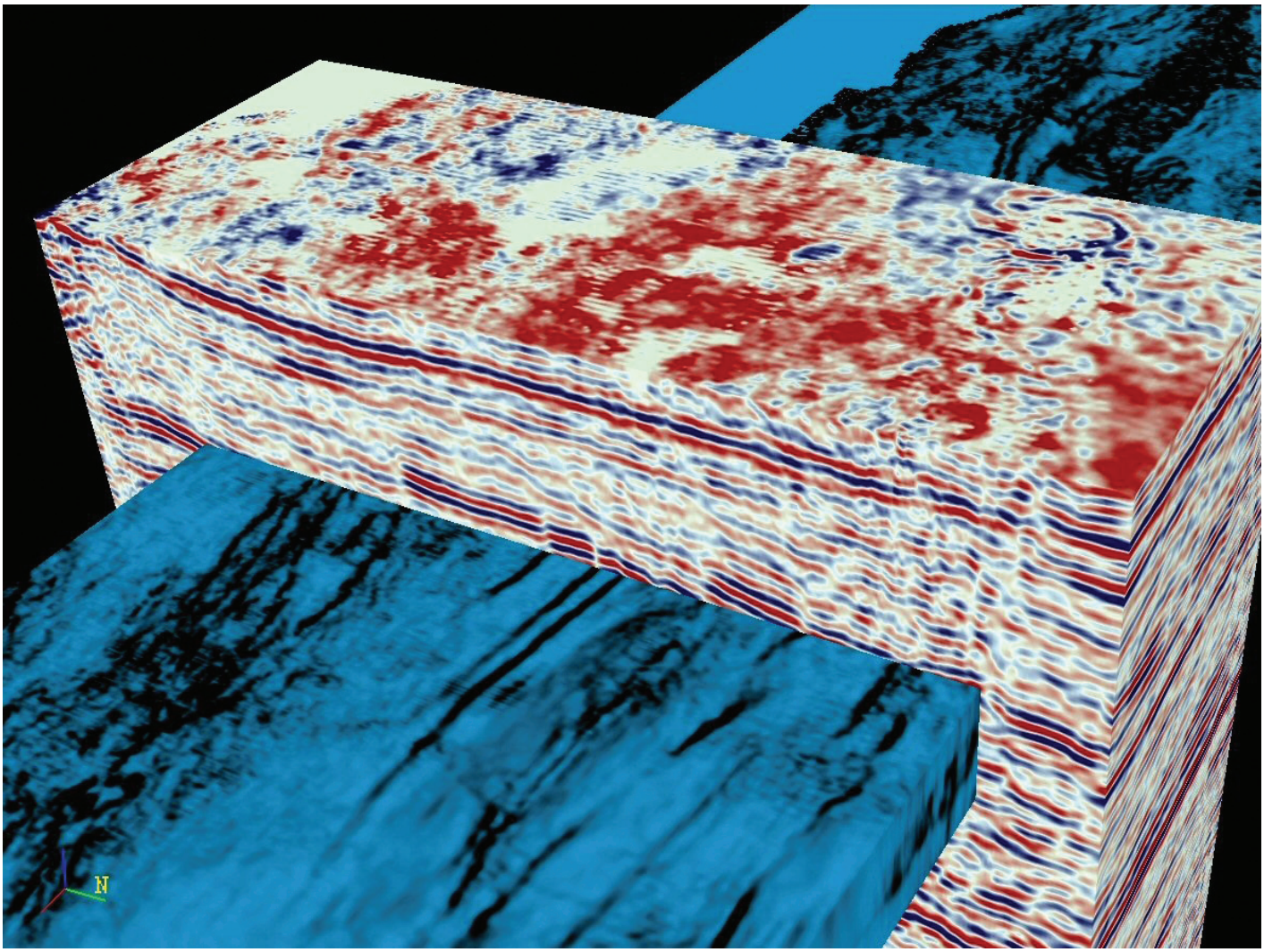

Fig. 12-15. Coherence data covisualized with conventional seismic data. This technique allows the interpreter to identify the origin of the coherence anomaly. In this example, clear faulting on the vertical section correlates well with the discontinuities shown in black on the coherence data. (Courtesy BP Exploration and the Wytch Farm partners.)

Figure 12-15 shows an example of 3-D seismic data and horizontal coherence data visualized together to provide an excellent environment in which to interpret faults with confidence. Using the same data set, Figure 12-16 shows how several different attributes can be used to aid fault interpretation.

Figure 12-17 show a 3-D opacity-rendered fault volume with color variation representing orientation of the faults. The underlying fault attribute highlights discontinuities in the data, whereas the volume at the back shows the faults embedded into the reflectivity data, thereby providing a template for manual or automatic fault interpretation. Figure 12-18 shows a rather unusual display of opacity applied to coherence data blended with amplitude data to isolate structural and stratigraphic information around a wellbore.

Surface Illumination

Surface illumination is a visualization technique used to reveal various subtle features. Simply "moving the sun down to the sunset position" can reveal subtle fault trends which may otherwise not have been detected. Figures 12-19 and 12-20 show a

Downloaded 25 Jun 2012 to 95.28.162.50. Redistribution subject to SEG license or copyright; Terms of Use: http://segdl.org/

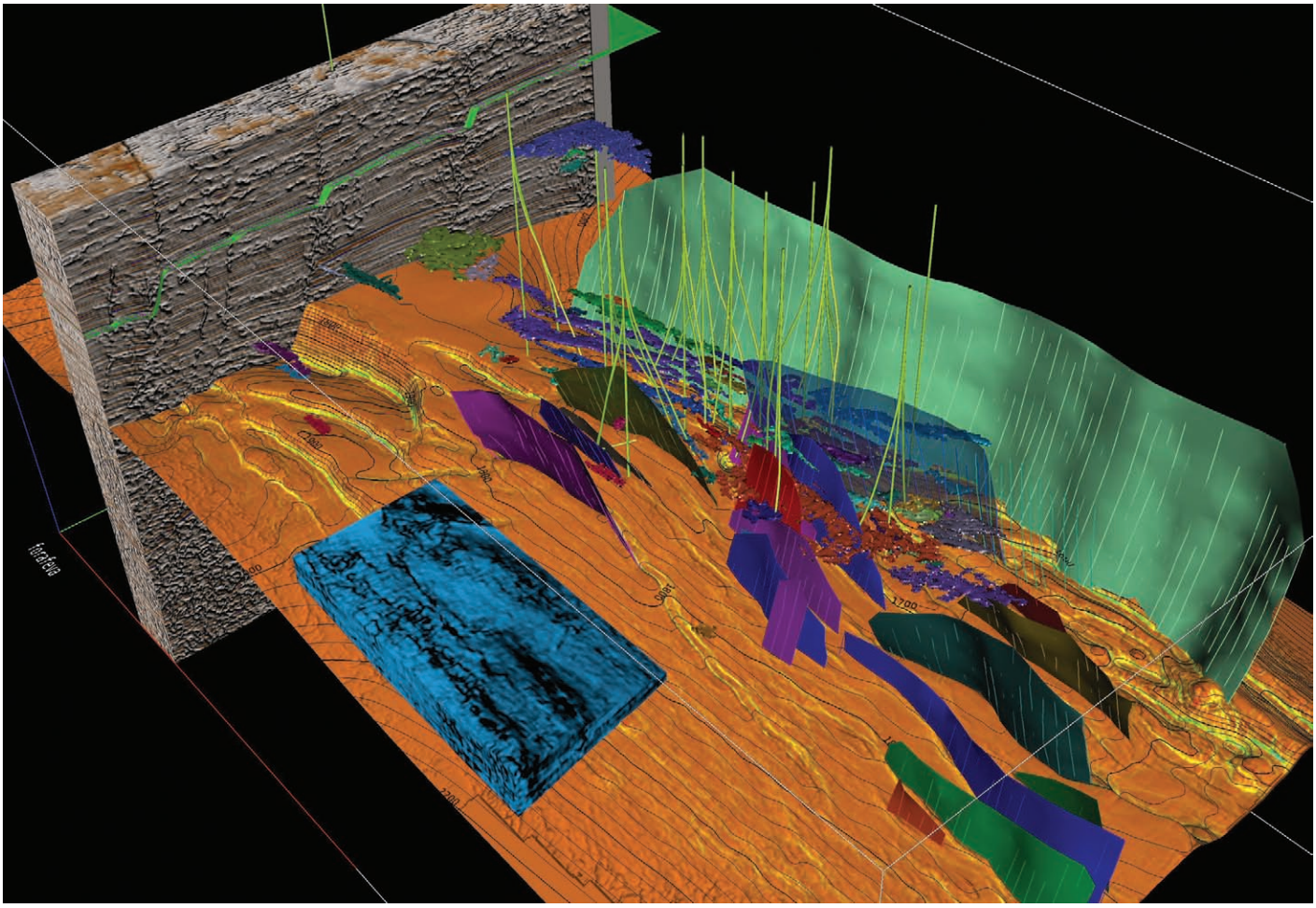

Fig. 12-16. Fault interpretation of the Triassic Sherwood sands of Wytch Farm, southern England. The 3-D seismic data comprise corendered amplitude and coherence volumes, and the blue time slice shows only coherence. On the surface, zones of maximum curvature, which indicate faulting, are highlighted in green and yellow. (Courtesy BP Exploration, the Wytch Farm partners, and Landmark.)

good example of this in an area where the faulting is very difficult to detect on vertical seismic data, due to its small vertical throw.

Advanced Attribute Visualization

Advanced attributes can be presented in a 3-D visualization environment such that rapid visual correlation with other data can be made. Figure 12-21 shows an RGB blend of three frequency-response volumes superimposed on a horizon in the North Sea. Variations in color represent changes in the dominant frequency response.

Figure 12-22 shows how multiattribute volumes have been displayed to show the regional setting of a meandering channel system. Opacity and different color tables are used to visualize these different attributes — which are amplitude, instantaneous frequency, coherence, and envelope — against a backdrop of conventional migrated data.

Interpretation Quality Control

Visualization offers a facility to rapidly check quality control for any interpretation, whether that interpretation has been conducted using 3-D visualization software or not. After using a conventional 3-D interpretation workstation approach, it is usually easy to load this interpretation into a 3-D visualization application and then "move

Text continues on page 432.

Downloaded 25 Jun 2012 to 95.28.162.50. Redistribution subject to SEG license or copyright; Terms of Use: http://segdl.org/

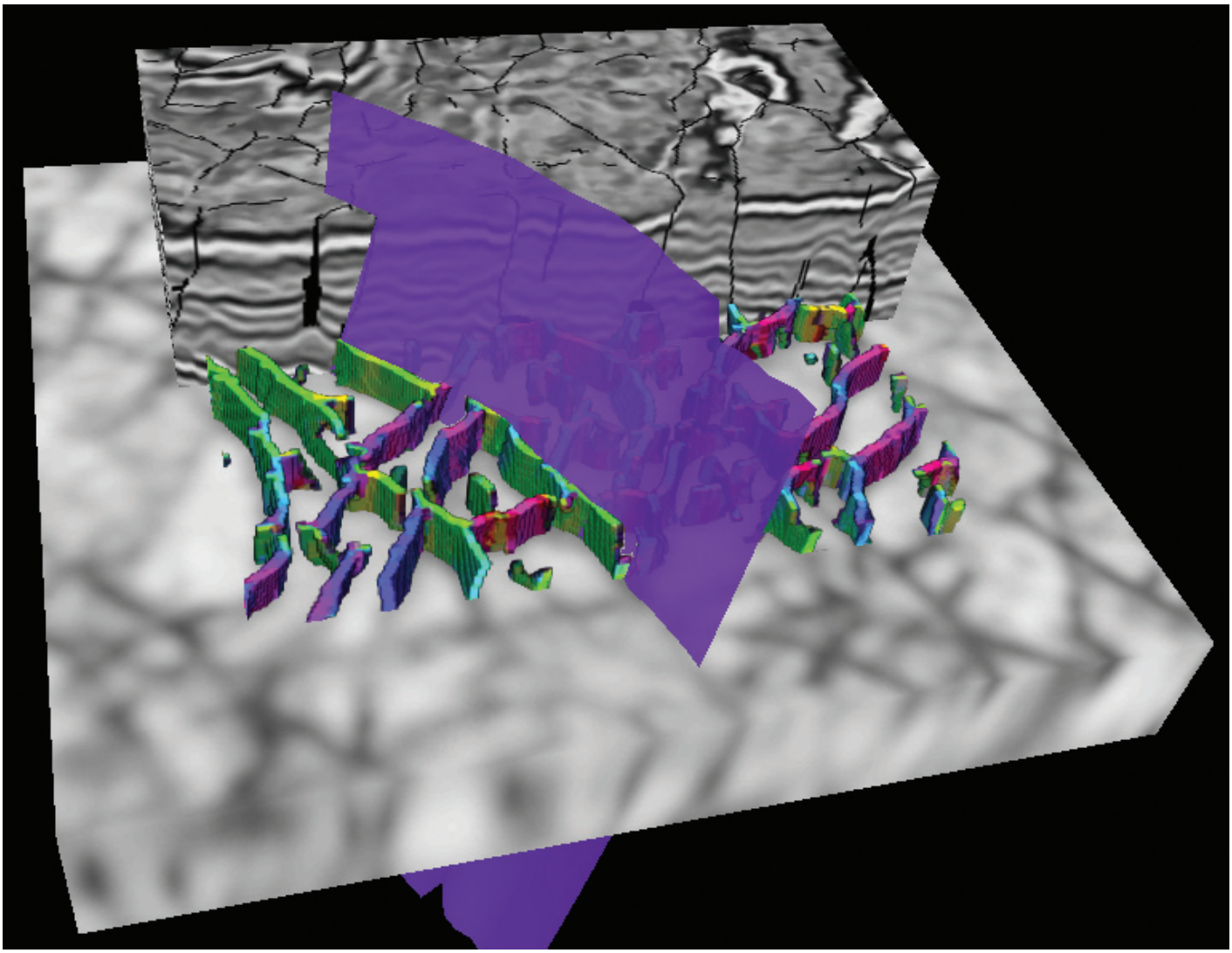

Fig. 12-17. Opacity-rendered fault volume with color variation representing orientation of the faults. The underlying fault attribute highlights discontinuities in the data. The volume at the back shows the faults embedded into the reflectivity data, providing a template for manual or automatic fault interpretation. (Courtesy ffA and StatoilHydro.)

Downloaded 25 Jun 2012 to 95.28.162.50. Redistribution subject to SEG license or copyright; Terms of Use: http://segdl.org/

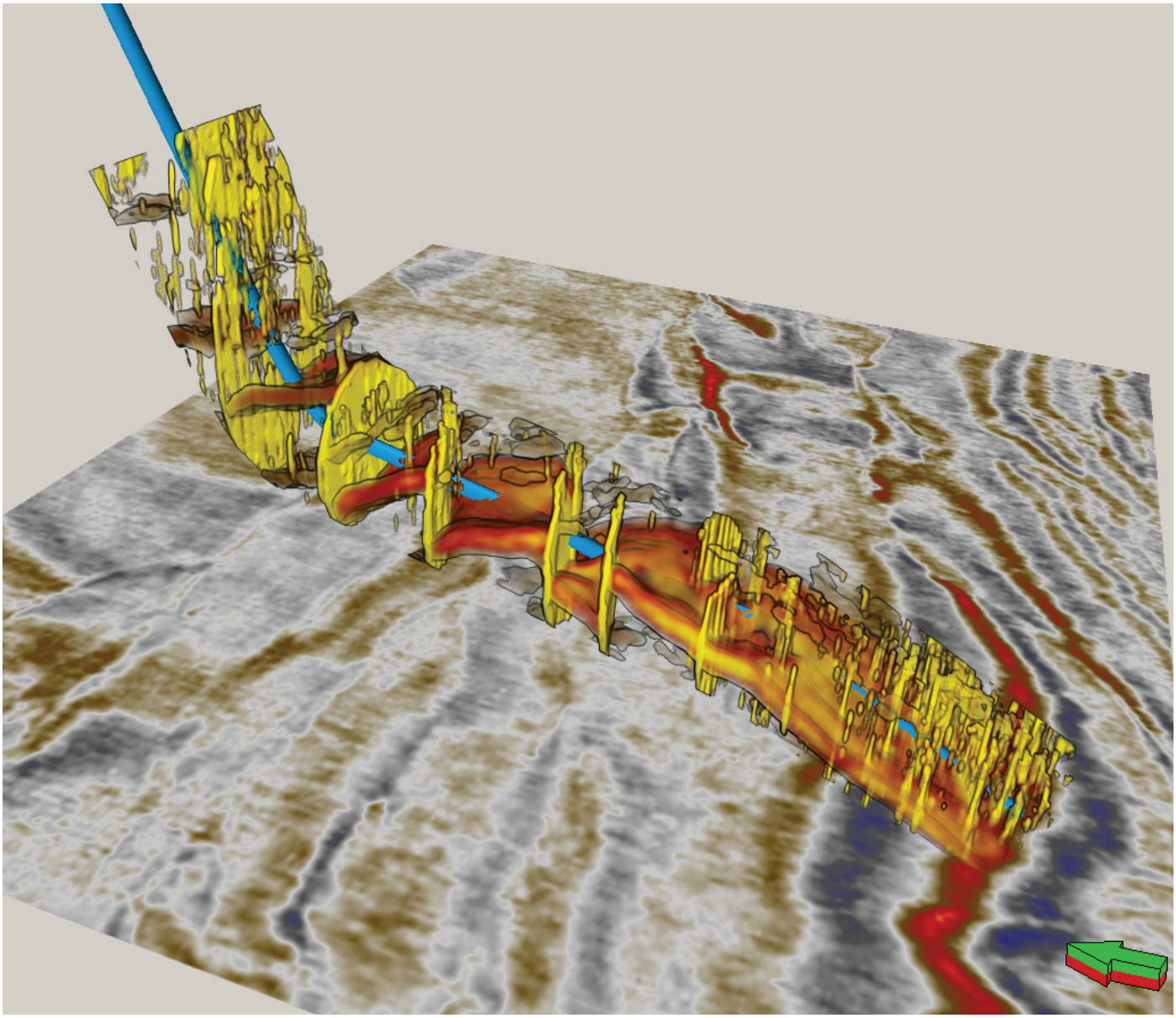

Fig. 12-18. Opacity applied to coherence data (yellow) blended with amplitude data (orange) to isolate structural and stratigraphic information around a wellbore. (Courtesy Schlumberger.)

Downloaded 25 Jun 2012 to 95.28.162.50. Redistribution subject to SEG license or copyright; Terms of Use: http://segdl.org/

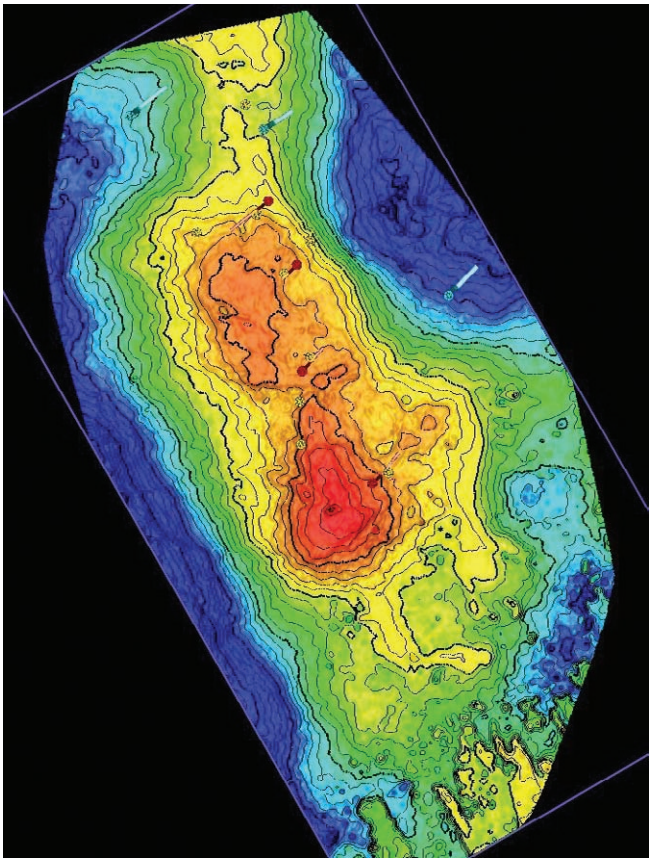

Fig. 12-19. Traditional top reservoir structural contour map, for comparison with Figure 12-20. (Courtesy BP Alternative Energy.)

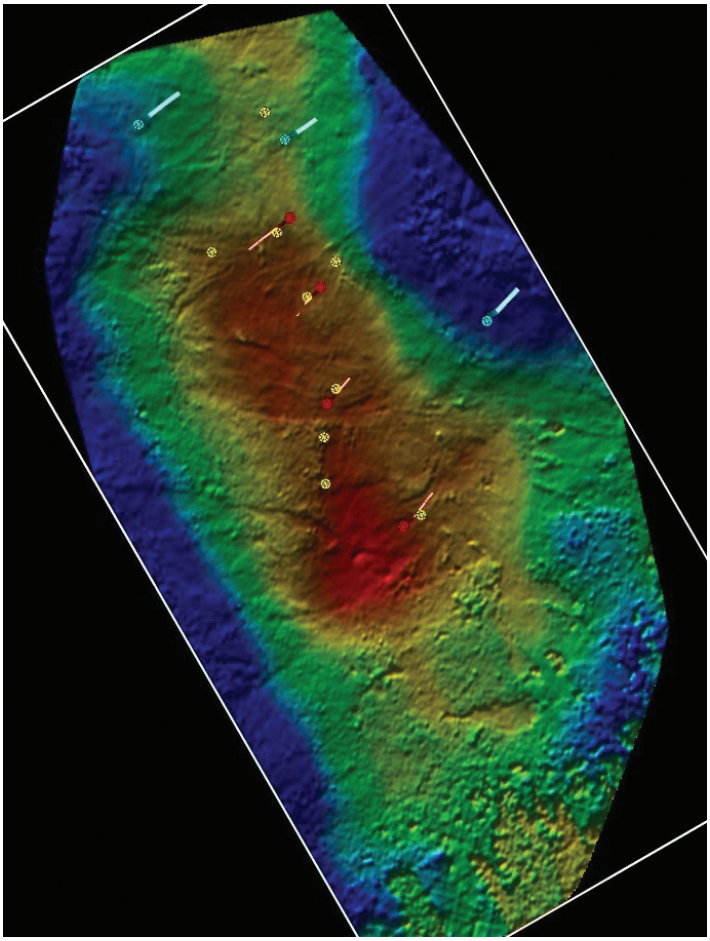

Fig. 12-20. Illuminated top reservoir structure, revealing subtle faults and acquisition footprint. (Courtesy BP Alternative Energy.)

Downloaded 25 Jun 2012 to 95.28.162.50. Redistribution subject to SEG license or copyright; Terms of Use: http://segdl.org/

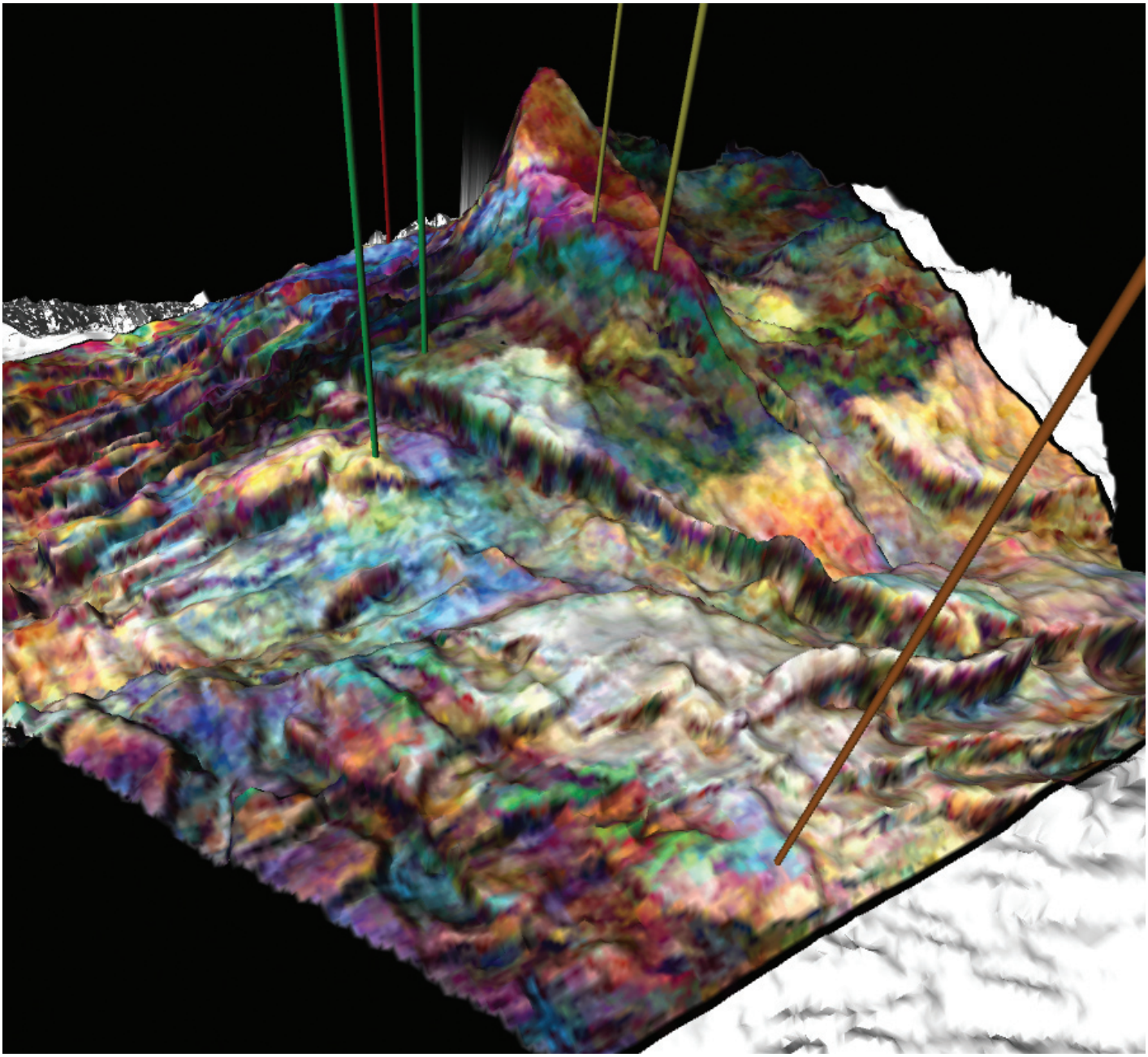

Fig. 12-21. RGB blend of three frequency-response volumes mapped onto the base Zechstein horizon of a North Sea data set. Variations in color represent changes in the dominant frequency. Red=low frequency, green=mid frequency, blue=high frequency. (Courtesy ffA and Quadrant Hydrocarbons.)

Downloaded 25 Jun 2012 to 95.28.162.50. Redistribution subject to SEG license or copyright; Terms of Use: http://segdl.org/

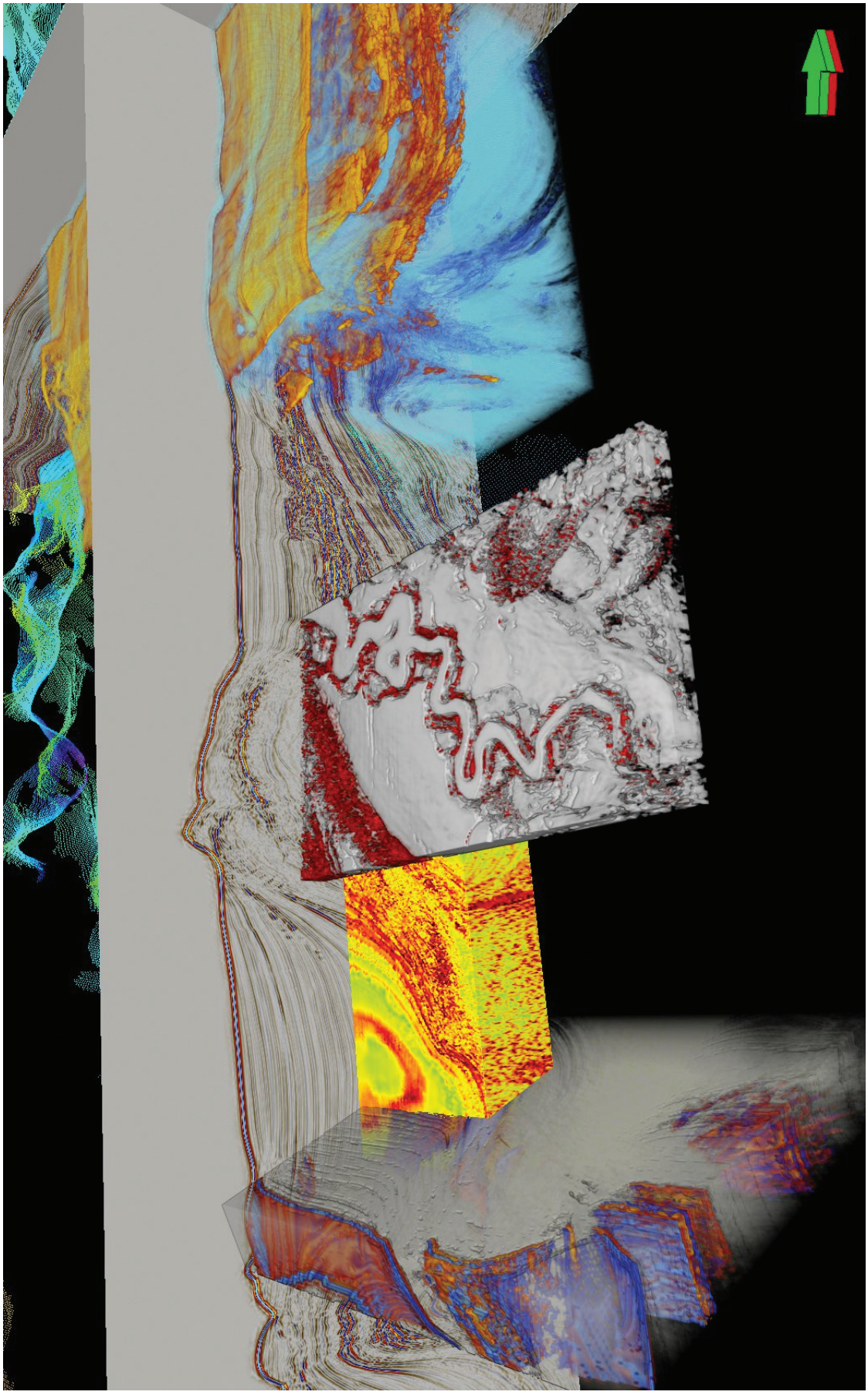

Fig. 12-22. Multiattribute volumes showing the regional setting of a meandering channel system. Opacity and different color tables are used to visualize the different attributes. The attributes from left to right are amplitude, instantaneous frequency, coherence, and envelope, against a backdrop of conventional migrated data. (Courtesy Schlumberger.)

Downloaded 25 Jun 2012 to 95.28.162.50. Redistribution subject to SEG license or copyright; Terms of Use: http://segdl.org/

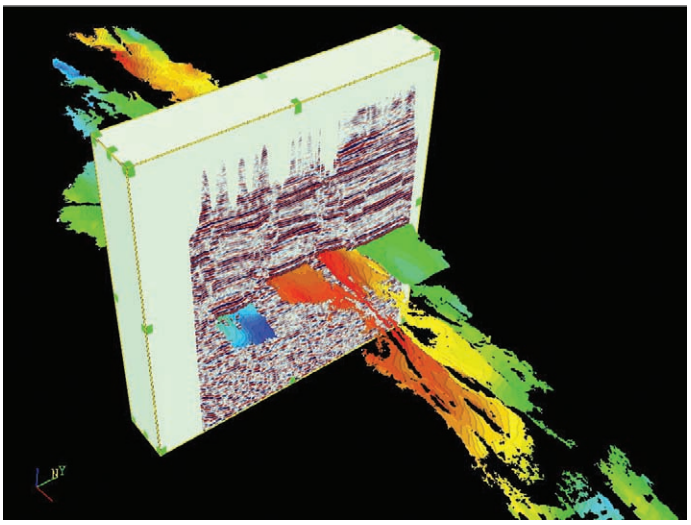

(a)

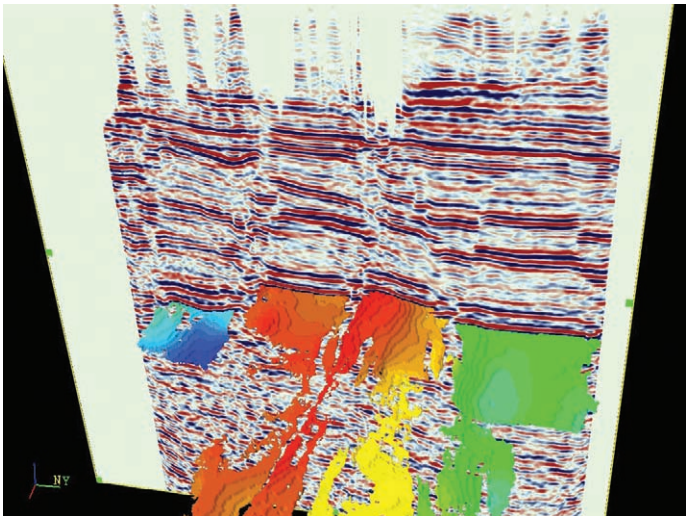

(b)

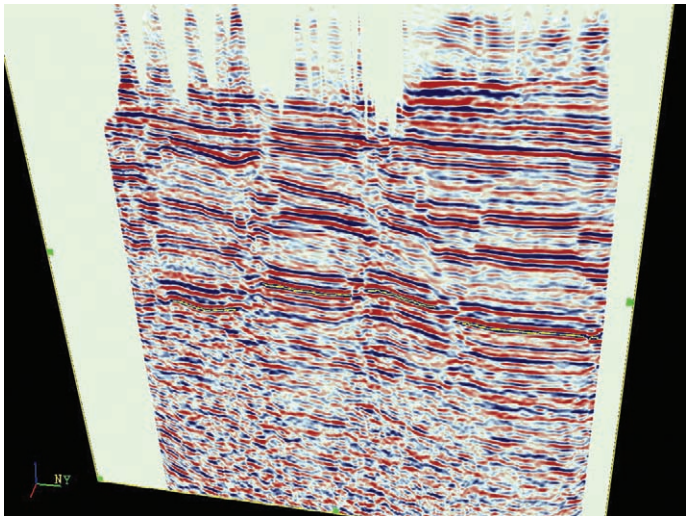

(c)

Fig. 12-23. Checking a structurally interpreted horizon surface against the 3-D seismic data: (a) the surface and a selected subvolume of data, (b) the same, from a different angle of view, and (c) the surface clipped back to the selected vertical section, thus appearing as a normal horizon track. (Courtesy BP Exploration and the Wytch Farm partners.)

Downloaded 25 Jun 2012 to 95.28.162.50. Redistribution subject to SEG license or copyright; Terms of Use: http://segdl.org/

the 3-D seismic data over the interpretation," or even just quickly scan through the inlines displaying the interpretation on each. The power here is in having all the 3-D seismic data in memory, such that the interpretation can be reviewed in real time and in 3-D. Figure 12-23 shows the way an interpretation can be checked by rotating and viewing the data from any angle and also by clipping the interpretation onto a chosen vertical section so that the exact pick can be examined (Figure 12-23c).

Visual Integration

Over the past few years, techniques have been developed which have allowed the integration of multiple data types into the visualization environment. This is known as visual integration or covisualization, and it allows geoscientists to integrate their 3-D seismic data and interpretations with other data that may have a significant impact on reducing risk. Figure 12-24 shows the Wytch Farm oilfield in the south of England. Conventional subsurface data have been integrated with surface topography draped with Landsat data. Along with helping nongeoscientists to get their bearings, covisualization of the Landsat data has several technical uses. Such uses include correlation of seismic quality with surface features, and also the use of both the surface and subsurface data to plan well surface locations, pipelines, and production facilities. Figure 12-25 shows a closer look at the Wytch Farm oilfield at Sherwood reservoir level and demonstrates the importance of visualizing the existing well paths in 3-D when planning new wells.

Still focusing on field development, Figure 12-26 shows 3-D and 4-D seismic data visually integrated with reservoir management data. In this example from the UK offshore, well data, structural models, reservoir simulation data, and production data are integrated with 3-D seismic volumes and time-lapse seismic attributes. Figure 12-27 shows an example of the covisualization of reservoir simulation data with 3-D seismic and well data around a UK salt dome. Figure 12-28 shows the covisualization of a geocellular model of a channel with 3-D seismic data. The geocellular model has been populated with porosity data extracted from the 3-D seismic data and calibrated by nearby wells.

Figure 12-29 shows the Krechba gas field in Algeria, which is the location of one of BP's first carbon dioxide storage projects. The visual integration illustrated here integrates all the diverse data types involved in the project and helps to communicate the result to the multidisciplinary technical and management teams. Figure 12-30 shows a similar arid surface environment and illustrates how projects can be extended away from fields to include any number of 3-D data sets and also 2-D seismic data. Figure 12-31 shows how three 3-D surveys and some 2-D regional lines have been integrated into one exploration data set. Conventional subsurface data are shown, as well as Landsat data.

Figure 12-32 develops this concept further by showing that "flat maps" can be georeferenced and integrated back into a 3-D seismic volume. This provides a way of correlating map data with the seismic data from which they originally were interpreted. This is very useful for communication and is also a powerful interpretation tool for quality control. Figure 12-33 shows how this technique has been extended to provide a base map for a multi-3-D/2-D seismic data set over a very large area offshore Norway. Also integrated and tied to the seismic data is a geologic cross section. Figure 12-34 shows an example of visual integration from the foothills of the Canadian Rockies. The image shows how topography draped with surface geology, geologic cross sections, 2-D seismic data, multiple 3-D seismic surveys, subsurface interpreted surfaces, well paths, well logs and picks, gravity data, and lease boundaries have been integrated to create a powerful environment within which 3-D seismic data can be interpreted.

Figure 12-35 shows a recent presentation made by BP and 3-DMR concerning the integration of 2-D seismic data with a georeferenced structural elements map offshore Brazil. Figure 12-36 shows the same 2-D seismic data, visually integrated with a grav-

Text continues on page 447.

Downloaded 25 Jun 2012 to 85.28.162.50. Redistribution subject to SEG license or copyright; Terms of Use: http://segdl.org/

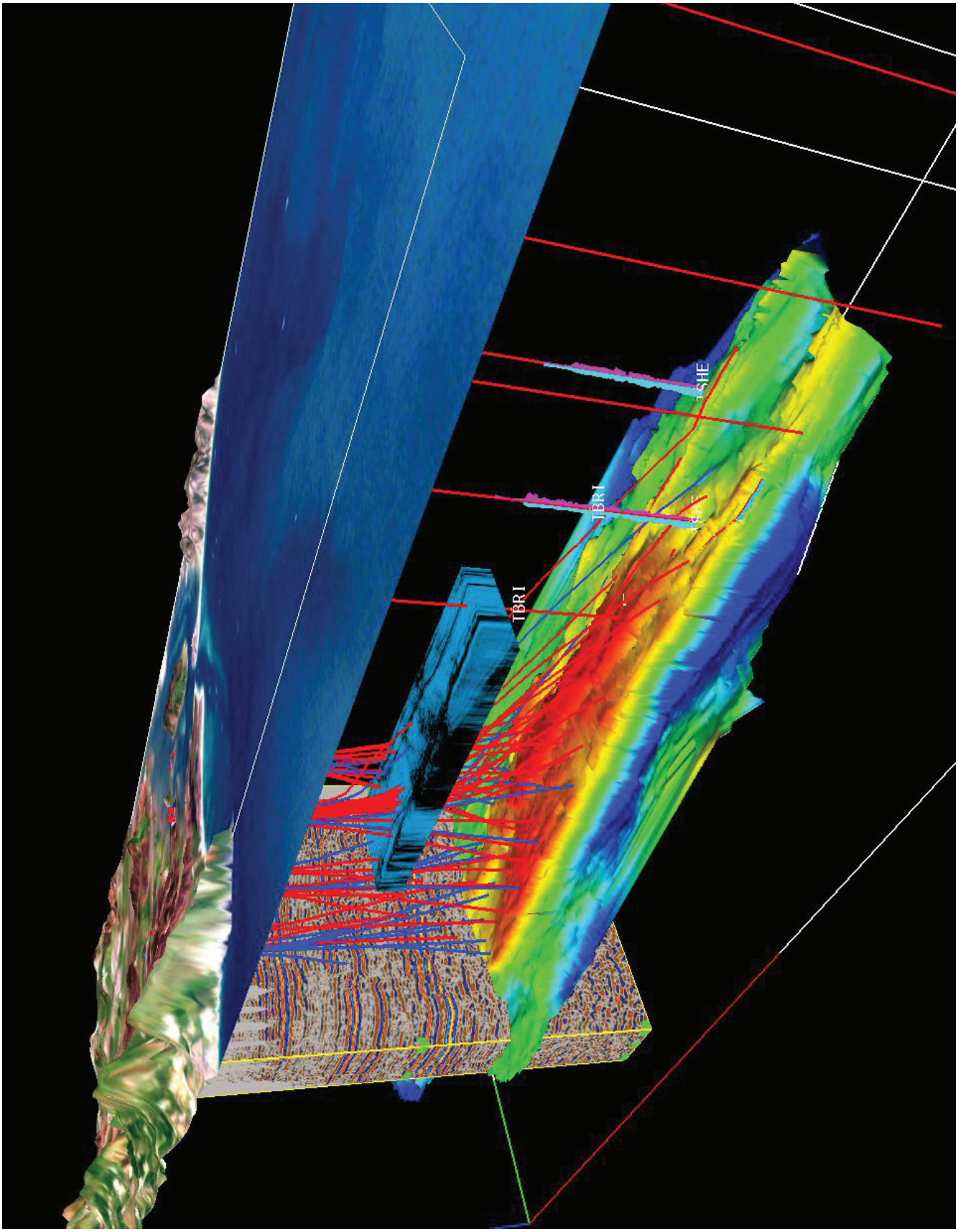

Fig. 12-24. Wytch Farm Field showing the visual integration of 3-D seismic data, coherence data, well paths, well logs, surface topography, and Landsat data. (Courtesy BP Exploration and the Wytch Farm partners.)

Downloaded 25 Jun 2012 to 95.28.162.50. Redistribution subject to SEG license or copyright; Terms of Use: http://segdl.org/

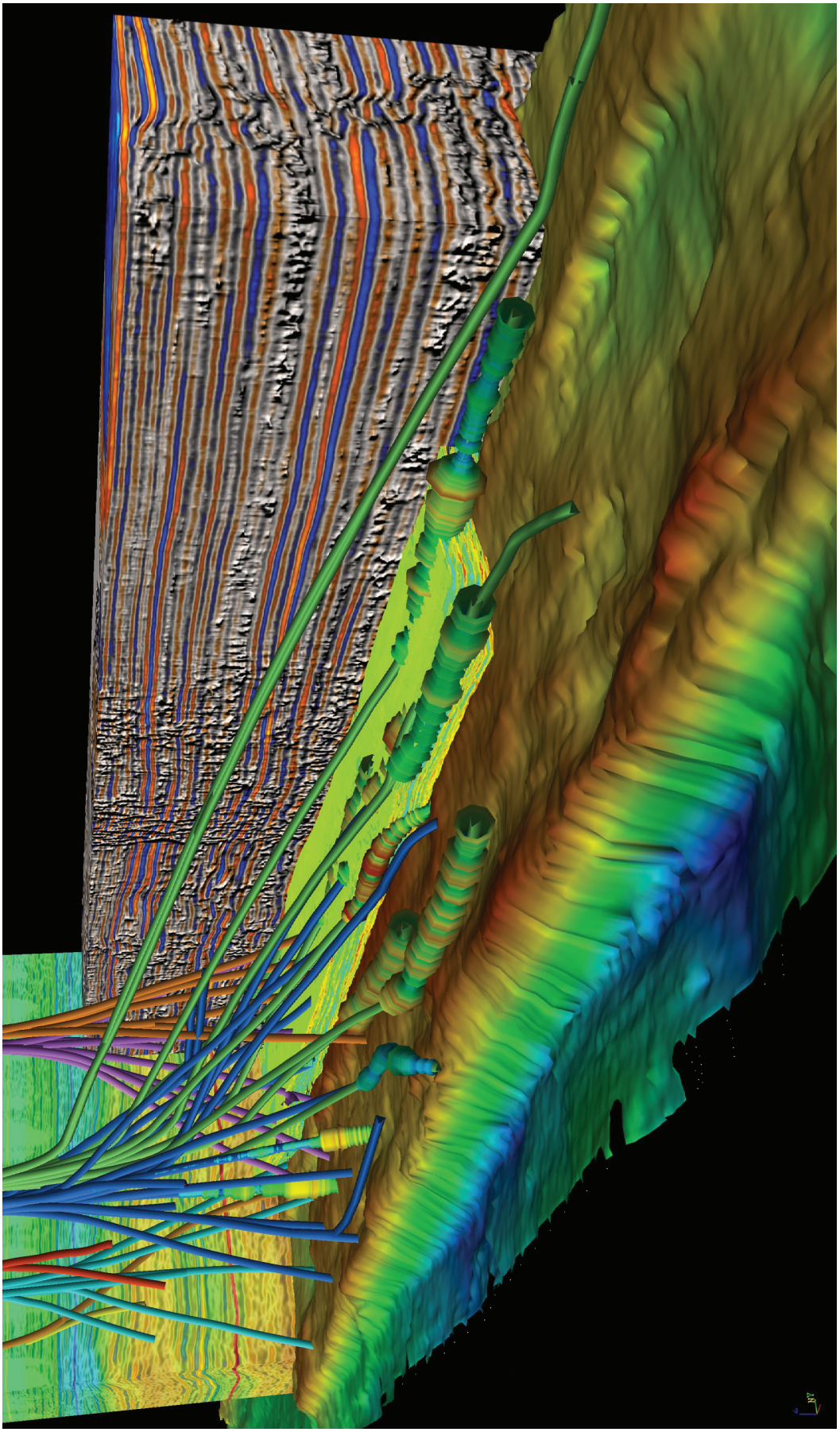

Fig. 12-25. Horizontal well planning in Triassic Sherwood sands of Wytch Farm. The well path is digitized on a porosity volume generated from a reservoir model. The other volume is a corendered amplitude and coherence volume. (Courtesy BP, the Wytch Farm partners, and Landmark.)

Downloaded 25 Jun 2012 to 95.28.162.50. Redistribution subject to SEG license or copyright; Terms of Use: http://segdl.org/

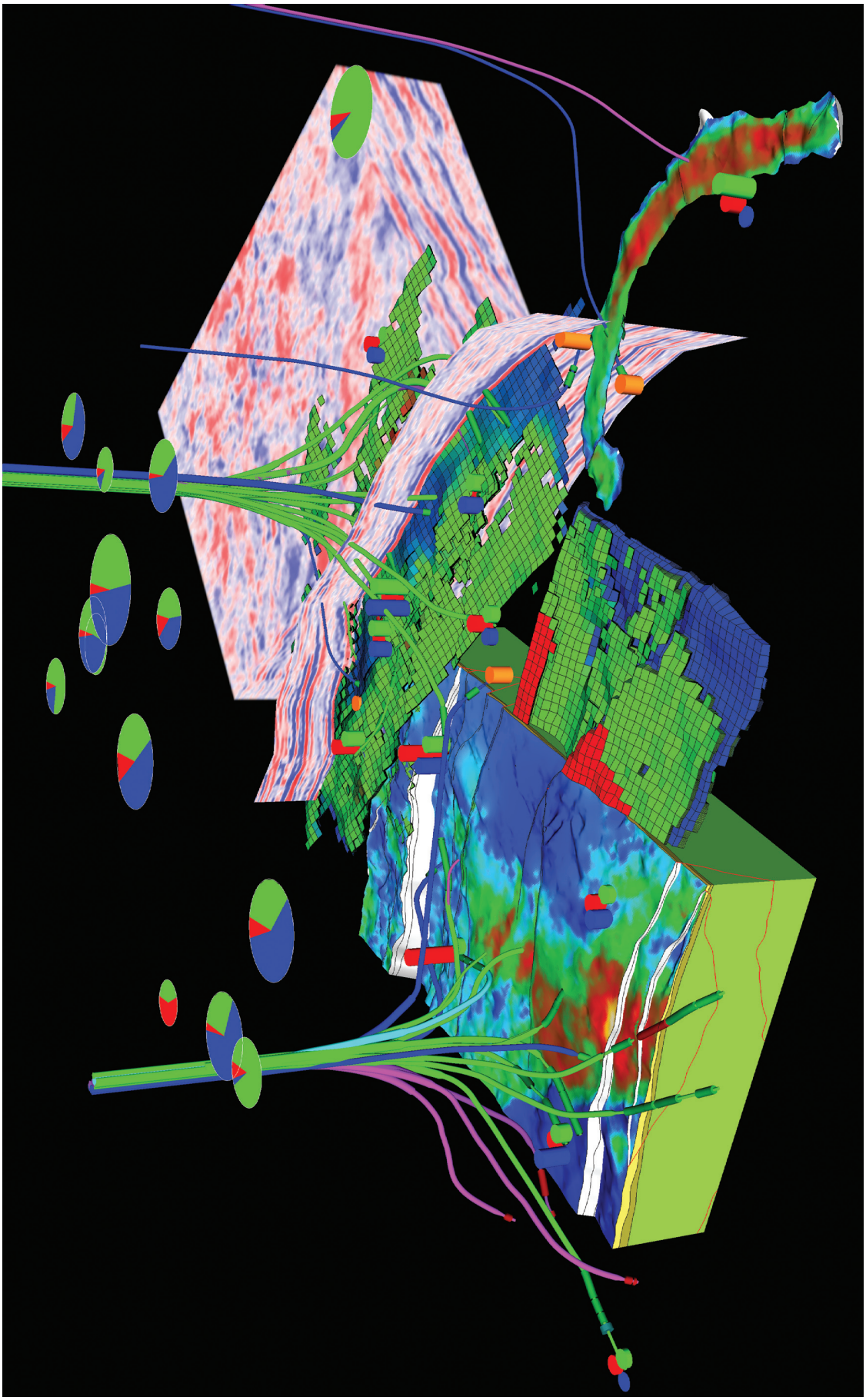

Fig. 12-26. 3-D and 4-D seismic visually integrated with reservoir management data. In this example from the UK offshore, well data, structural models, reservoir simulation data, and production data are integrated with 3-D seismic volumes and time-lapse seismic attributes. Temporal animation allows the user to analyze how the 4-D seismic response compares with the other time-dependent reservoir surveillance data. (Courtesy Dynamic Graphics.)

Downloaded 25 Jun 2012 to 95.28.162.50. Redistribution subject to SEG license or copyright; Terms of Use: http://segdl.org/

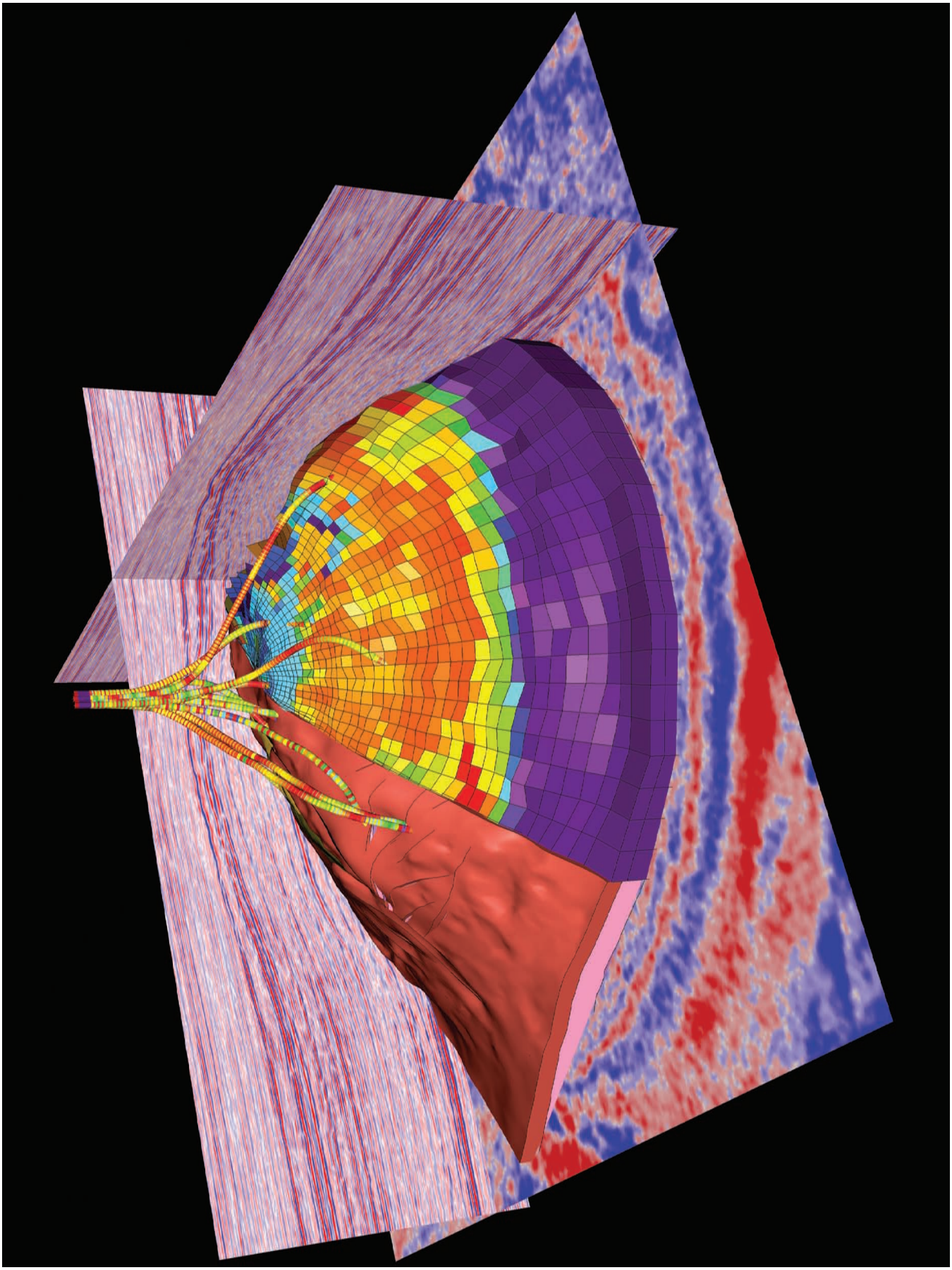

Fig. 12-27. Reservoir management data from the UK North Sea. This salt dome, clearly expressed on the 3-D seismic data, has been subjected to 3-D earth modeling and reservoir simulation. (Courtesy Dynamic Graphics.)

Downloaded 25 Jun 2012 to 95.28.162.50. Redistribution subject to SEG license or copyright; Terms of Use: http://segdl.org/

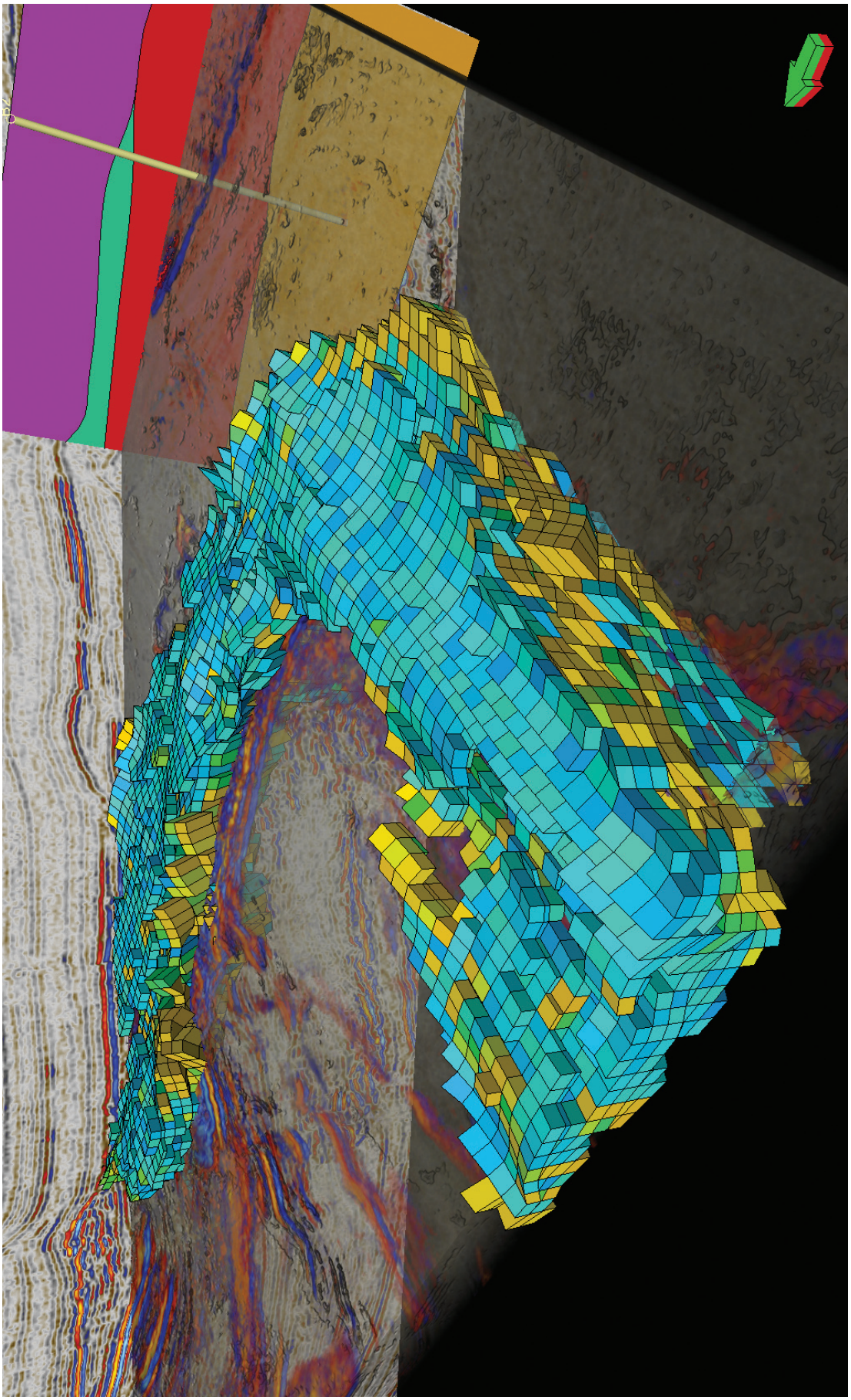

Fig. 12-28. A channel isolated from 3-D seismic and upscaled into a geocellular earth model. The model has then been populated with porosity computed from the seismic data and calibrated from nearby wells. (Courtesy Schlumberger.)

Downloaded 25 Jun 2012 to 95.28.162.50. Redistribution subject to SEG license or copyright; Terms of Use: http://segdl.org/

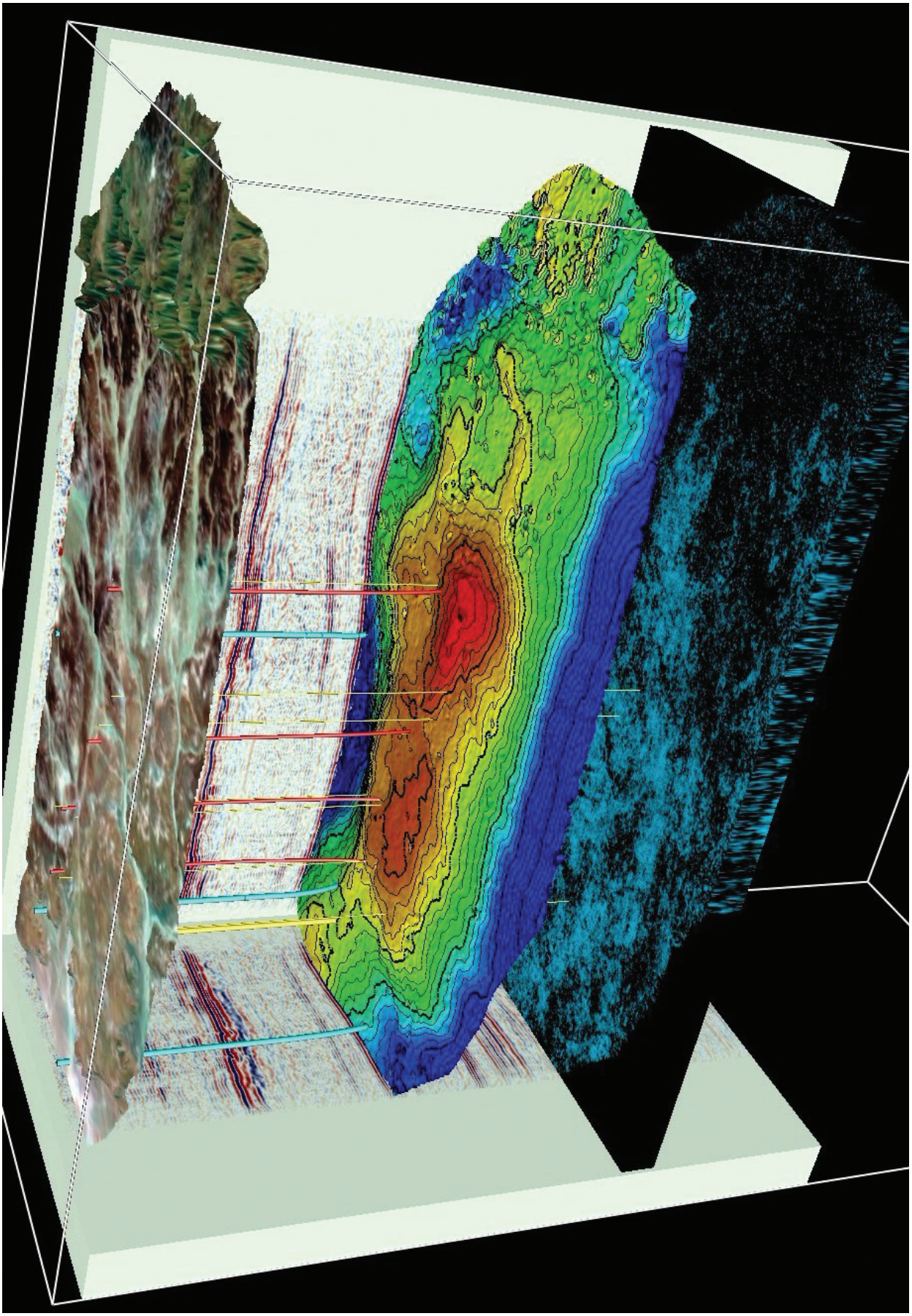

Fig. 12-29. Visual integration of 3-D seismic data, coherence data, structural surfaces, topography, Landsat, and well data at the Krechba field, Algeria, for the benefit of the multidisciplinary technical and management teams. (Courtesy BP Alternative Energy.)

Downloaded 25 Jun 2012 to 95.28.162.50. Redistribution subject to SEG license or copyright; Terms of Use: http://segdl.org/

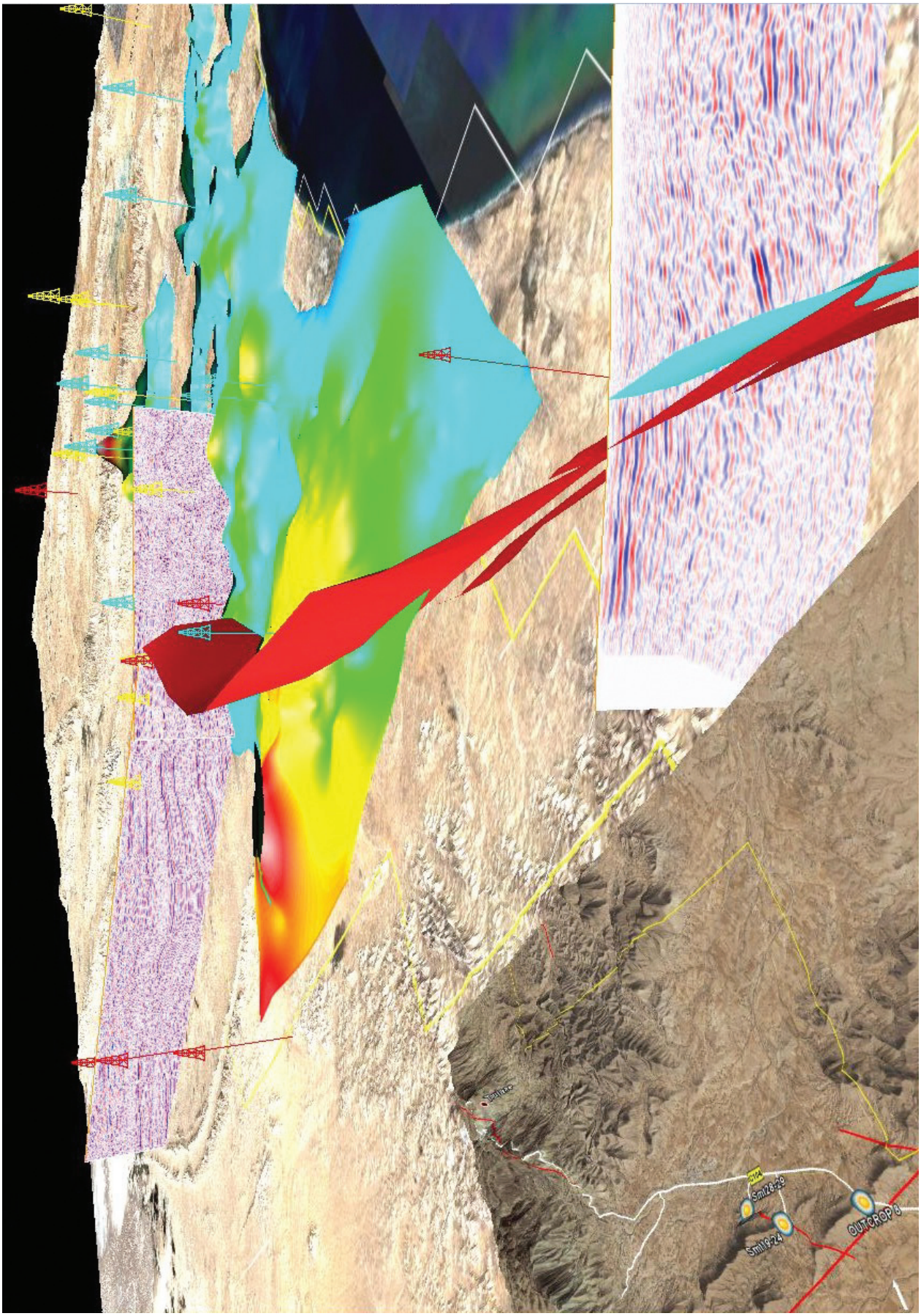

Fig. 12-30. Covisualization of surface outcrop information with surfaces from 3-D seismic data, with 2-D seismic lines, and with well data. (Courtesy Shell.)

Downloaded 25 Jun 2012 to 95.28.162.50. Redistribution subject to SEG license or copyright; Terms of Use: http://segdl.org/

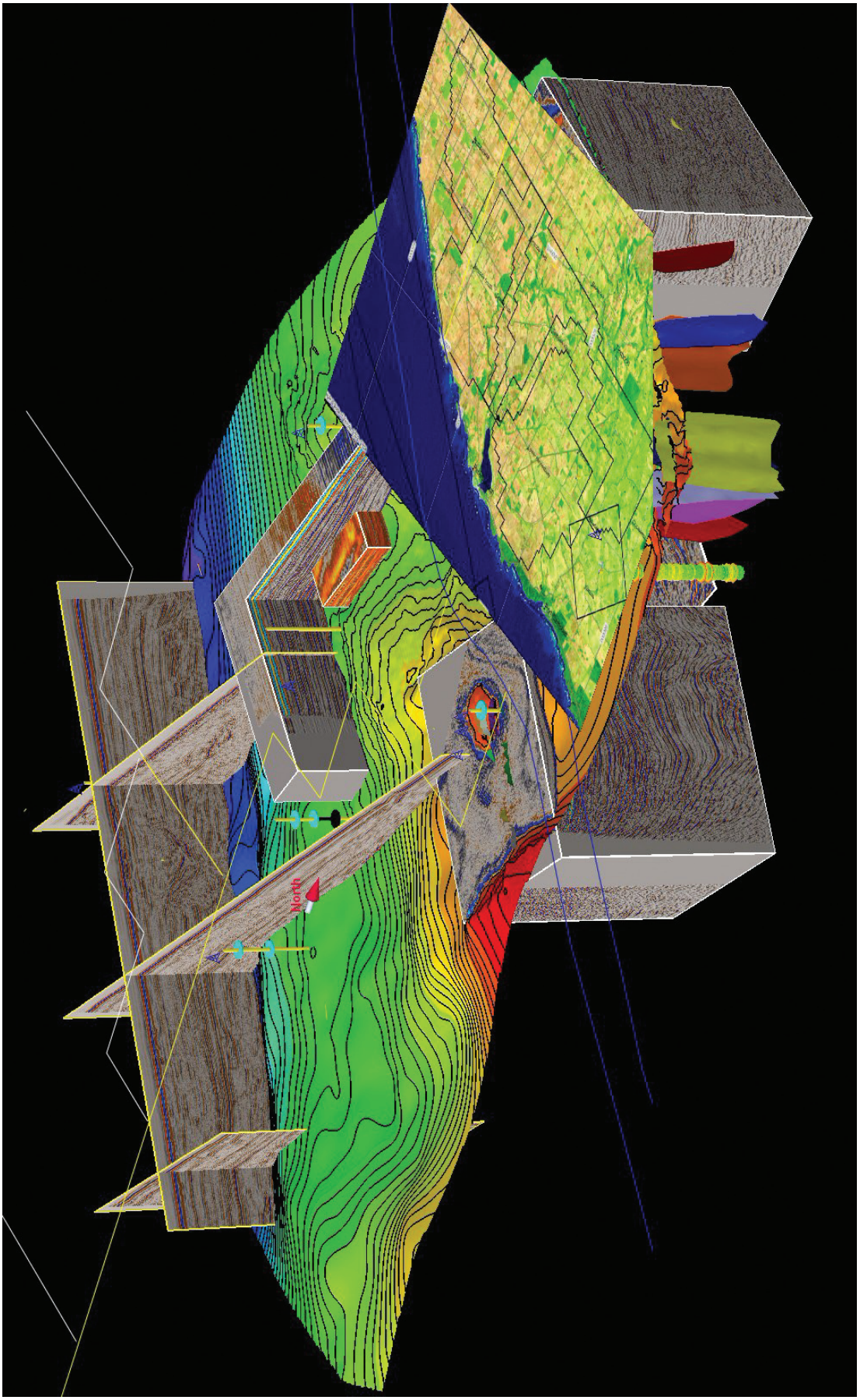

Fig. 12-31. Multiple 3-D data volumes integrated with 2-D regional lines and various surfaces. (Courtesy Paradigm).

Downloaded 25 Jun 2012 to 95.28.162.50. Redistribution subject to SEG license or copyright; Terms of Use: http://segdl.org/

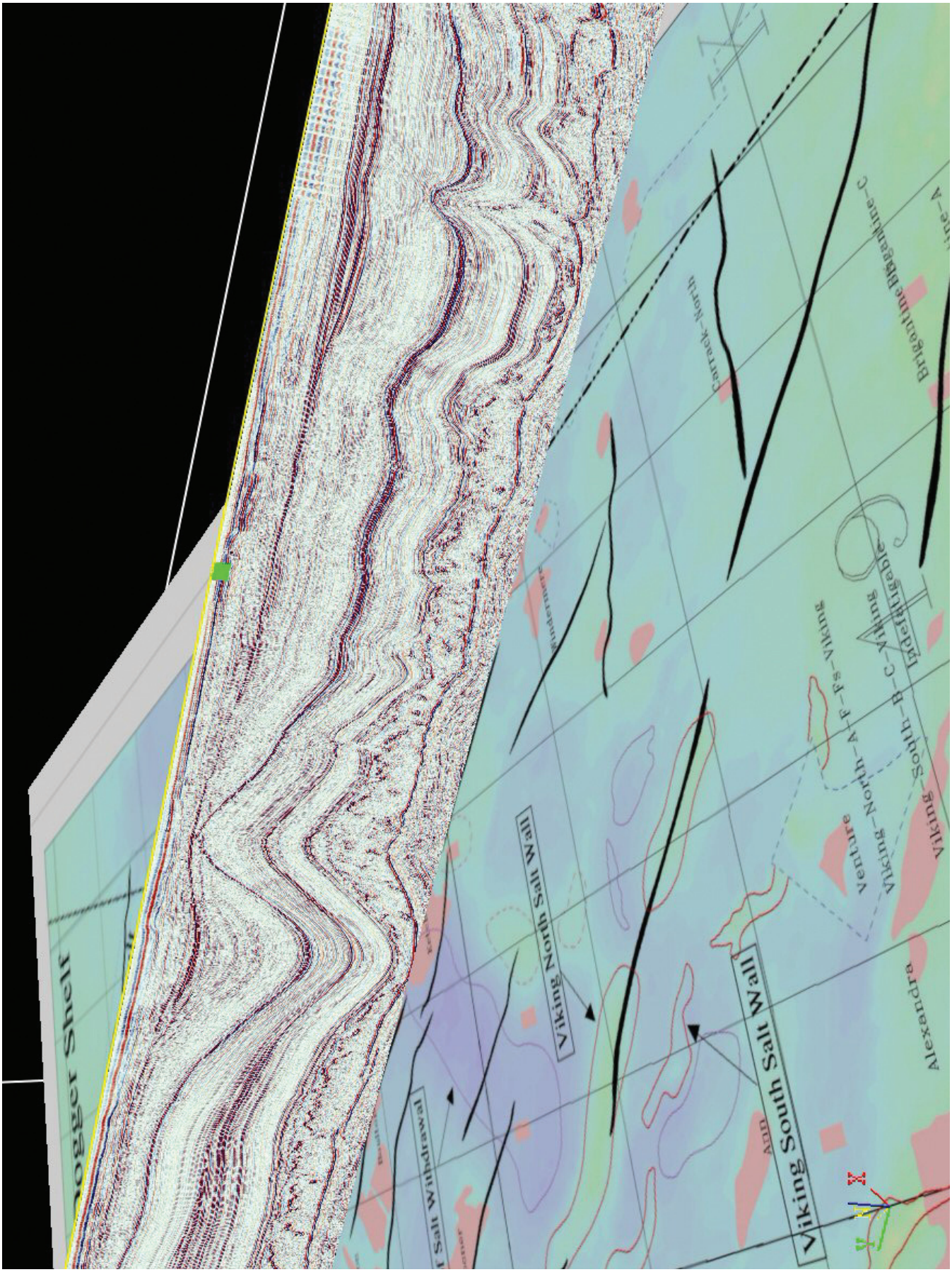

Fig. 12-32. An inline from the PGS Southern North Sea MegaSurvey integrated with a georeferenced structural elements base map. (Courtesy PGS and IHS Energy.)

Downloaded 25 Jun 2012 to 95.28.162.50. Redistribution subject to SEG license or copyright; Terms of Use: http://segdl.org/

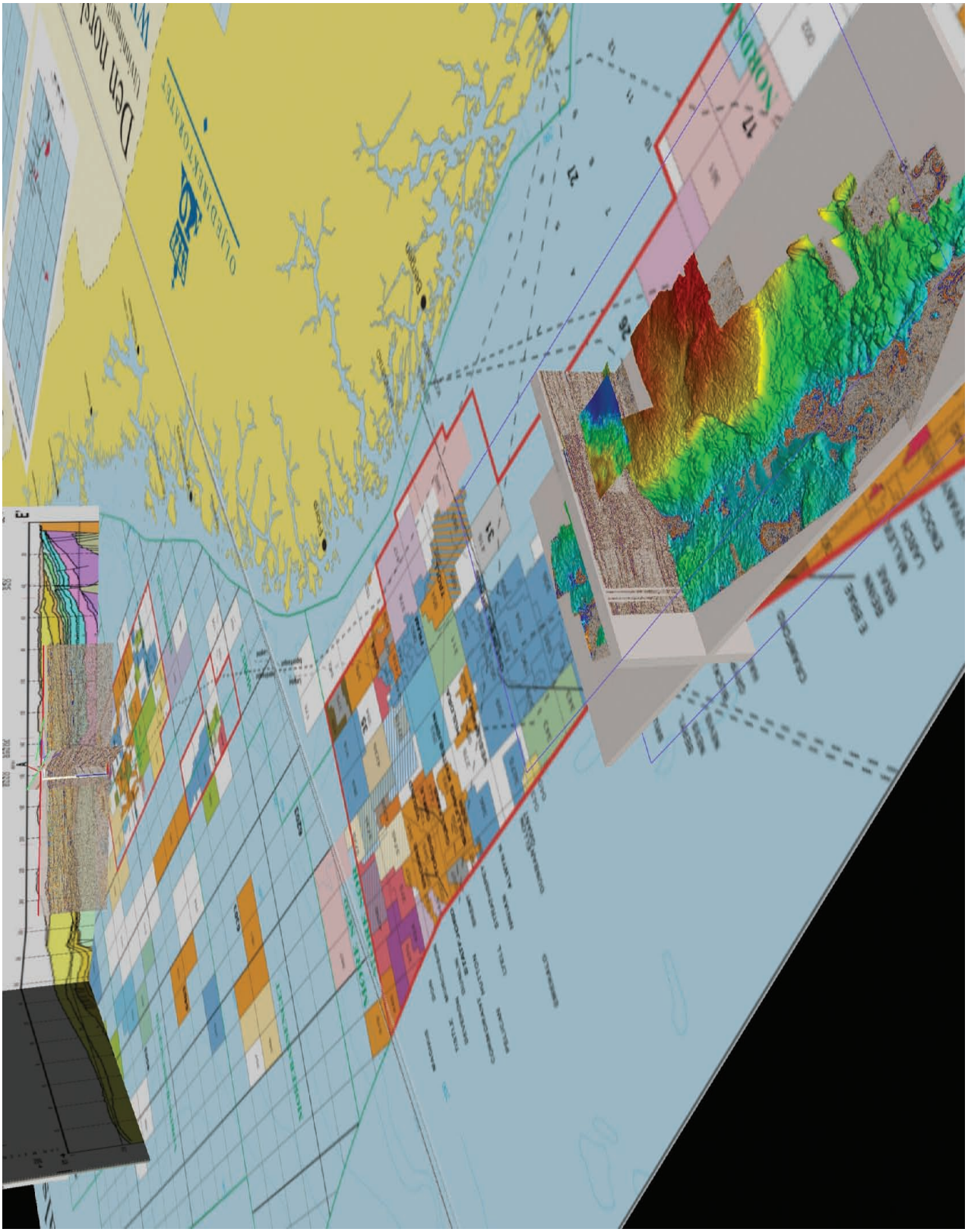

Fig. 12-33. An 18,000-sq-km 3-D seismic survey integrated into a project showing the basinwide trends off the coast of Norway. To the north is a smaller 3-D survey covering the Heidrun field and a 100-mile-long (161-km-long) 2-D seismic line in front of a regional geologic cross section. (Courtesy StatoilHydro, Norwegian Petroleum Directorate, and Landmark.)

Downloaded 25 Jun 2012 to 95.28.162.50. Redistribution subject to SEG license or copyright; Terms of Use: http://segdl.org/

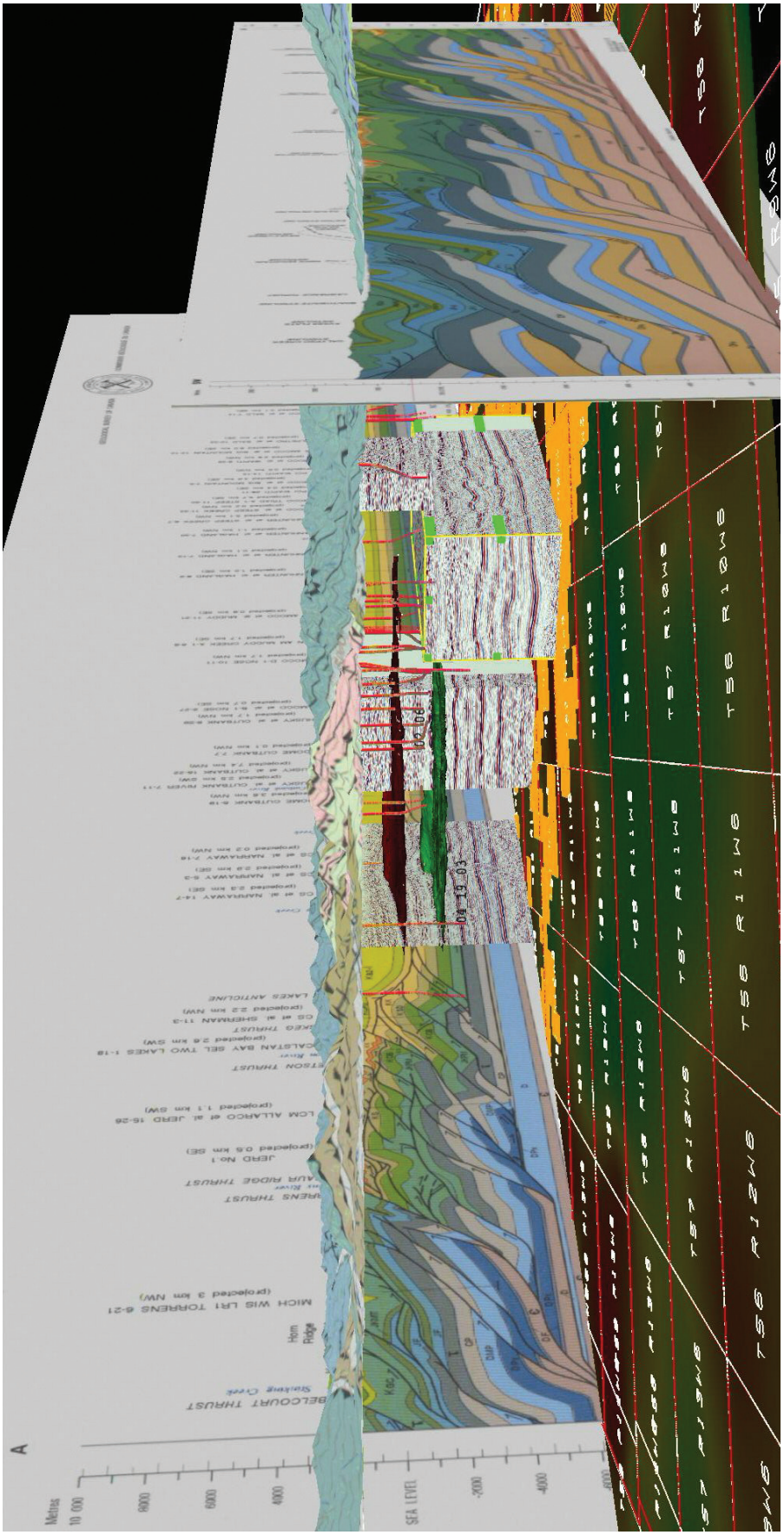

Fig. 12-34. Visual integration in the foothills of the Canadian Rockies. The image shows topography draped with surface geology, geologic cross sections, 2-D seismic data, multiple 3-D seismic surveys, subsurface interpreted surfaces, well paths, well logs and picks, gravity data, and lease boundaries integrated into an environment within which 3-D seismic data can be interpreted. (Courtesy ConocoPhillips, Natural Resources Canada 2008, Geological Survey of Canada, and CGG Veritas.)

Downloaded 25 Jun 2012 to 95.28.162.50. Redistribution subject to SEG license or copyright; Terms of Use: http://segdl.org/

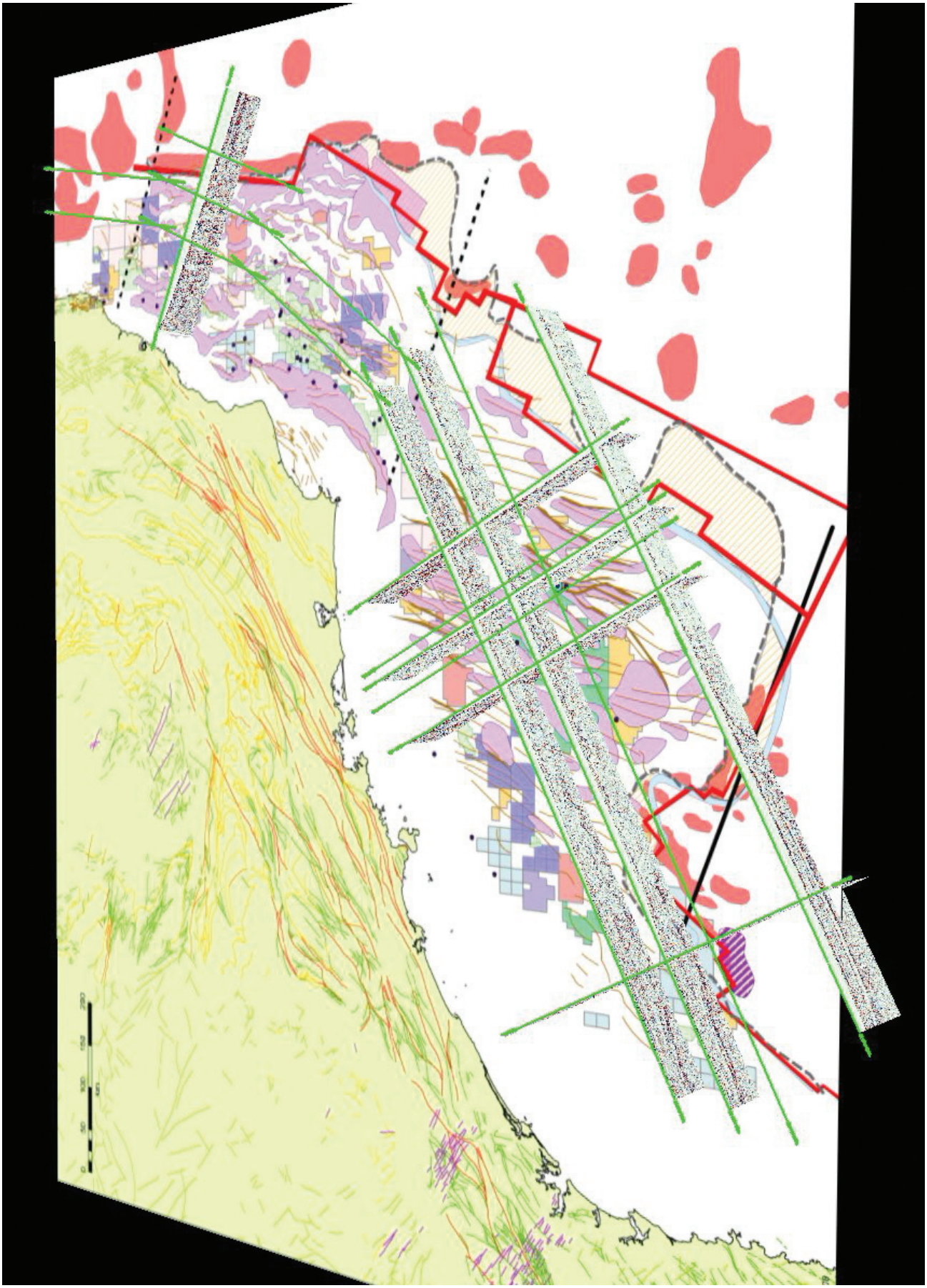

Fig. 12-35. Visual integration of regional 2-D seismic data with a tectonic elements map, offshore Brazil. (Courtesy BP Exploration, TGS, and WesternGeco.)

Downloaded 25 Jun 2012 to 95.28.162.50. Redistribution subject to SEG license or copyright; Terms of Use: http://segdl.org/

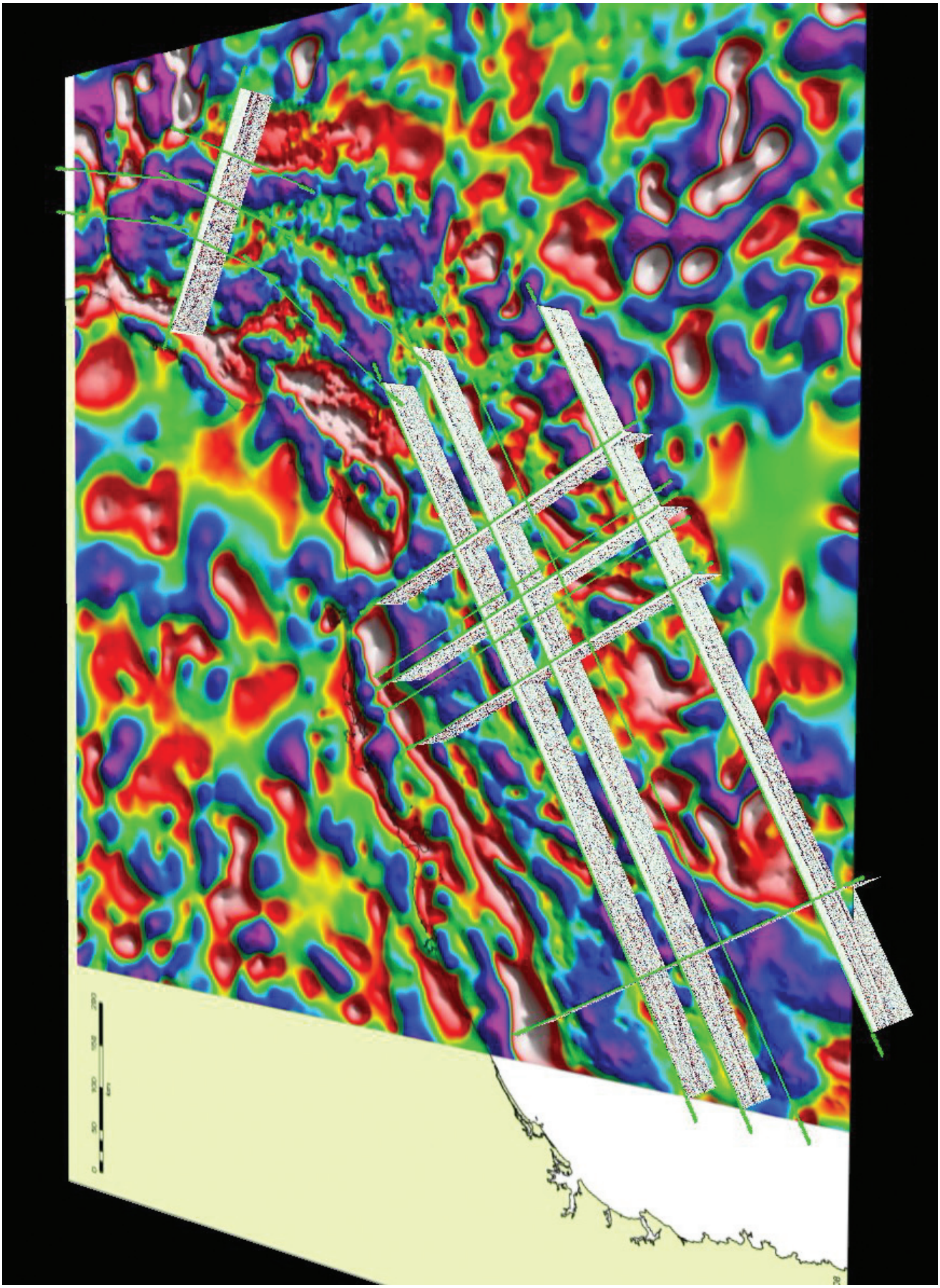

Fig. 12-36. Visual integration of the same regional 2-D seismic data shown in Figure 12-35 with a gravity map offshore Brazil. (Courtesy BP Exploration, TGS, and WesternGeco.)

Downloaded 25 Jun 2012 to 95.28.162.50. Redistribution subject to SEG license or copyright; Terms of Use: http://segdl.org/

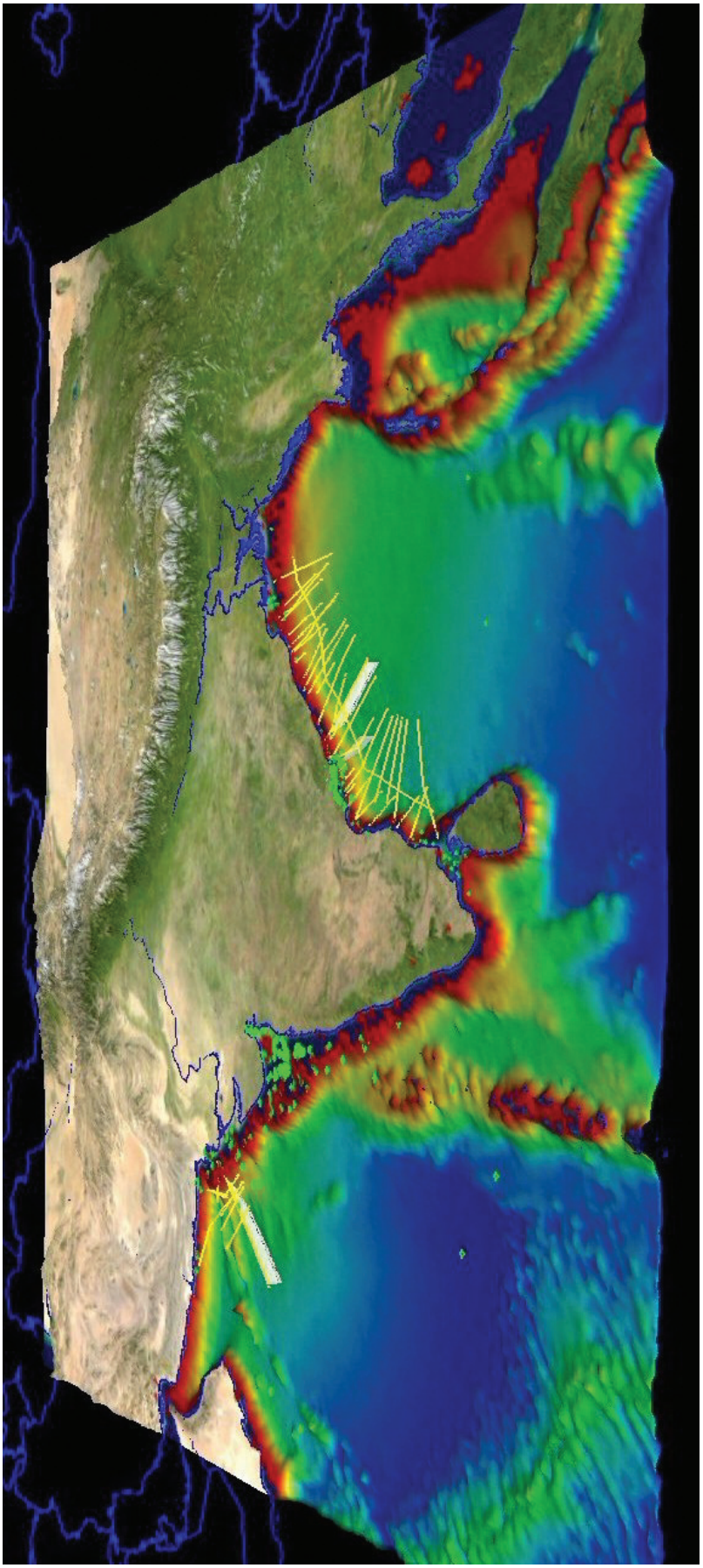

Fig. 12-37. Regional study of the Indian subcontinent. Note the 2-D seismic data loaded into this project in addition to topography, bathymetry, and Landsat data. (Courtesy BP Exploration.)

Downloaded 25 Jun 2012 to 95.28.162.50. Redistribution subject to SEG license or copyright; Terms of Use: http://segdl.org/

ity map. The full data set also includes 3-D seismic data, surface geology, topography, Landsat data, and magnetic and well data. Figure 12-37 shows a regional project featuring the whole of the Indian subcontinent. The full data set includes 3-D seismic data, Landsat data, gravity and magnetics data, and well data. The message here is that there is actually no geographic limit to the size of a visual integration project, provided one manages the size of the various data items very carefully. In this example it is possible to zoom in from the "bird's-eye" view depicted and to trace detail on a 2-D or 3-D seismic line, or the detail of a well log.

Concluding Comments

The intention of this chapter has not been to cover every known visualization or interpretation technique, but to highlight some of the more important visualization techniques in use in our industry today. Many examples of visualization have been provided, in order to emphasize the importance of this technology.

Acknowledgments

I would like to thank my friends and colleagues at BP, ConocoPhillips, Dynamic Graphics, Foster-Findlay Associates, Landmark, Paradigm, PGS, Schlumberger, and Shell for contributing to this chapter and for giving permission to publish their pictures.

Downloaded 25 Jun 2012 to 95.28.162.50. Redistribution subject to SEG license or copyright; Terms of Use: http://segdl.org/

Downloaded 25 Jun 2012 to 95.28.162.50. Redistribution subject to SEG license or copyright; Terms of Use: http://segdl.org/

4-D Reservoir Monitoring

Summary of Principles

Time-lapse seismic in reservoir management is an important technology to help understand petroleum reservoirs and thus to produce more oil and gas from them (Jack, 1997). Four-D reservoir monitoring, an important part of the above, involves the study of two or more 3-D seismic surveys over the same reservoir in the hope of observing changes with time caused by petroleum production. The expected changes in the seismic data are generally small, so good data coupled with careful processing and analysis are required.

Many projects to date have used legacy data, that is 3-D surveys which already exist, acquired at different times over the same area or overlapping areas. Differences in the positioning and acquisition of the seismic surveys are very problematical, so very careful reprocessing is required. Even then legacy data will suffice only where there is a fairly large acoustic change in the reservoir and where the data are very good (Figure 13-1). For lesser acoustic changes caused by production and for less good data areas, deliberately repeated surveys with conformable acquisition parameters will be needed. Some surveys have been and are being recorded by permanently-implanted receivers which greatly improves repeatability and which thus increases the detectability of subtle changes in the reservoir. Clearly this is easier to do on land than at sea. In this chapter you will find six case history examples of 4-D results; they are mentioned by name in Figure 13-1 in their appropriate category. There is a further example reported as Case History 2 in Chapter 14.

In fact 4-D seismic surveys to date have mostly studied secondary recovery. Figure 13-2 shows the effect on acoustic impedance of several common production processes. The effect of change in pressure within the reservoir is significant. In most cases there is a change in fluid saturation and a change in pressure, so the effect on acoustic impedance and thus amplitude is a combination of the two. We can reasonably expect to see a larger seismic change caused by production if the porosity of the reservoir rock is higher, if the rock is less consolidated, if it lies at a shallower depth, and if the exchanging fluids have a greater density contrast. Furthermore, because of seismic resolution a thicker reservoir will be a great benefit. Seismic traveltime is less affected by variations in positioning, acquisition or processing than seismic amplitude. So, if the reservoir changes affect traveltime, this may be a more robust indicator. Types of production that should be easier to monitor by 4-D seismic methods include steam injection for heavy oil and tar, water flood for light oil, gas injection, and oil production involving gas cap expansion.

Downloaded 25 Jun 2012 to 95.28.162.50. Redistribution subject to SEG license or copyright; Terms of Use: http://segdl.org/

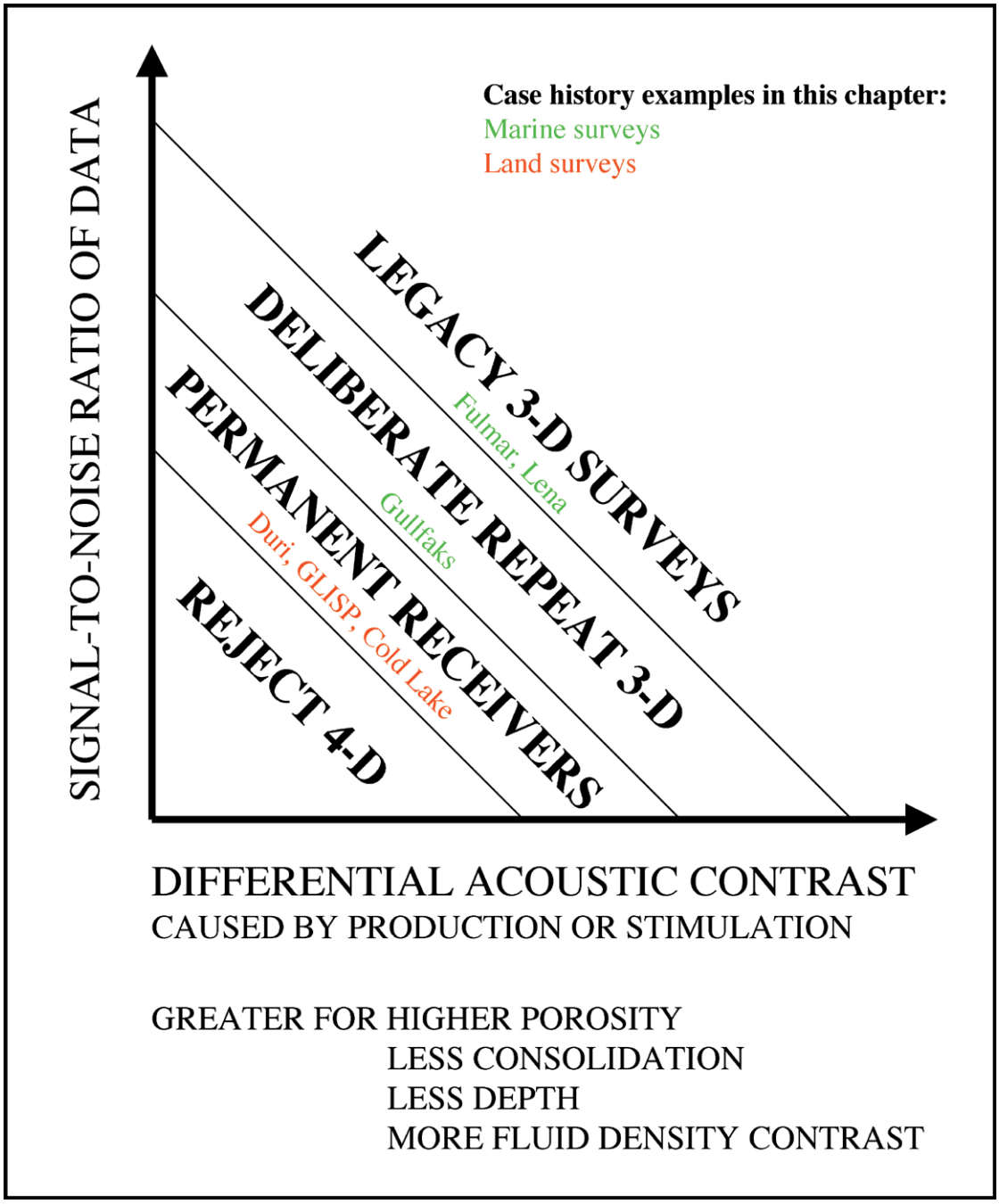

Fig. 13-1. For 4-D reservoir monitoring to be successful the production process must cause significant acoustic changes in the reservoir. The magnitude of the change and the quality of the seismic data determine what kind of 4-D seismic operation is required.

Four-D surveys are not a trivial extension of 3-D surveys. Different rocks respond to fluids and pressure in different ways, so it is important to understand well the reservoir being studied and the production process being used (Jack, 1997; Wang and Nur, 1989). A 4-D survey should be part of an overall reservoir management plan.

4-D Survey Results

The Duri Field in Indonesia produces oil from shallow deltaic sands of Miocene age. Because of high viscosity, primary recovery will produce only a small fraction of the original oil in place. Steam flooding reduces viscosity and drives oil towards production wells, and in this way is expected to improve recovery from 8% to nearly 60%. In order to monitor the steam flood a baseline survey was acquired in 1992 before any steam was injected, and then five monitor surveys were recorded after

Downloaded 25 Jun 2012 to 95.28.162.50. Redistribution subject to SEG license or copyright; Terms of Use: http://segdl.org/

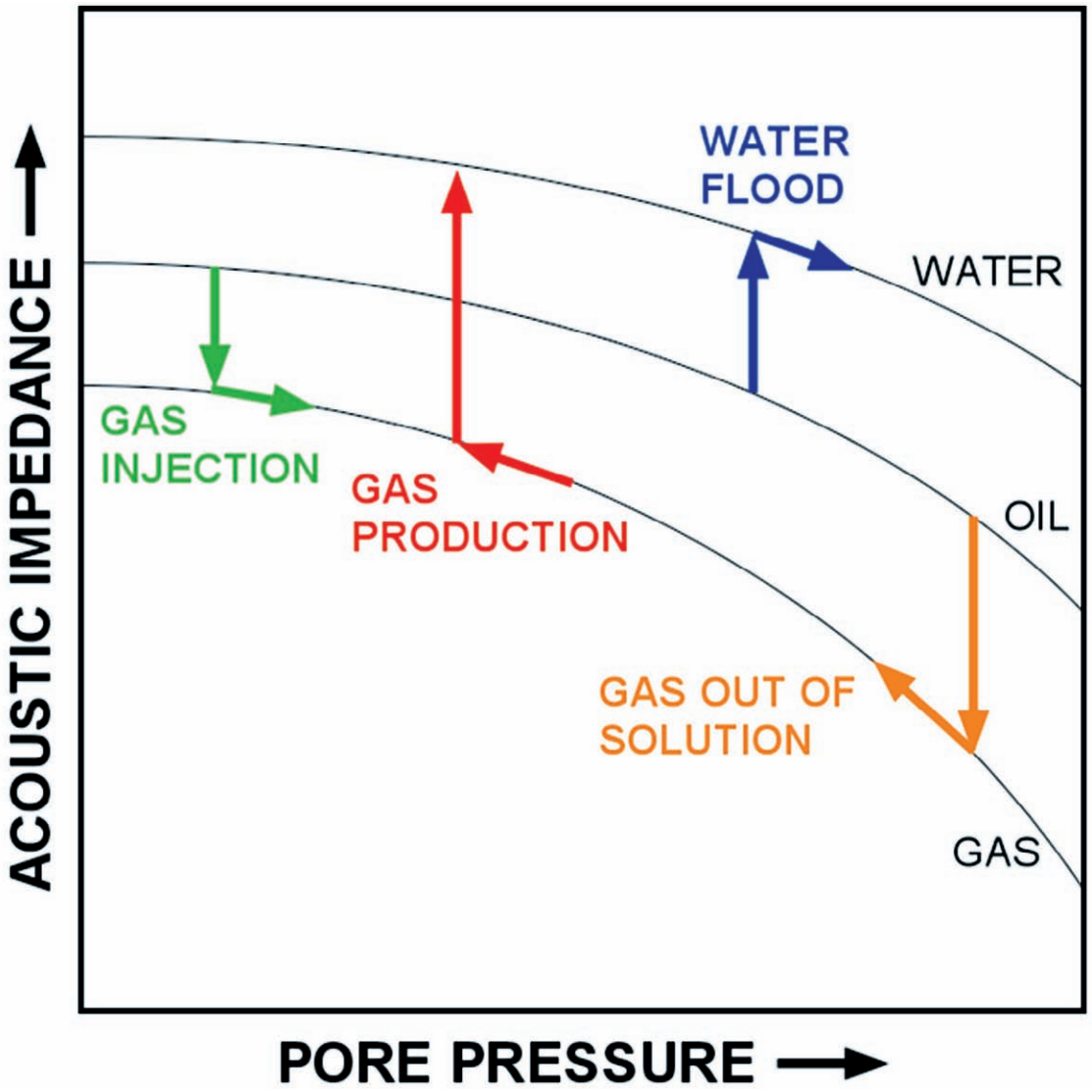

Fig. 13-2. Effect on acoustic impedance, and thus amplitude, of common production processes for a high porosity unconsolidated sandstone. Effects are smaller for more consolidated rocks and for less porous rocks. (After Wang and Nur, 1989. Used by permission.)

steaming the reservoir for 2, 5, 9, 13 and 19 months (Lumley, 1995; Jenkins, Waite, and Bee, 1997; Waite and Sigit, 1997). The pressure and heat of the steam causes progressive traveltime pull-ups and push-downs which can be seen on the sequence of vertical sections in Figure 13-3. The same progressive effects can be seen in Figure 13-4 where on the time slices the effect of the steam can be seen as expanding circles, like rings from a pebble dropped into a pool of still water. On the two time slices to the right, after 13 and 19 months, the steam can be seen moving preferentially to the northwest (up in Figure 13-4). Figures 13-5, 13-6 and 13-7 are individual larger displays after 0, 5 and 13 months.

In northern Alberta in Canada steam was injected into a heavy tar sand in order to make it producible. Four 3-D surveys were used to monitor the steam effects. An increase in the temperature of the tar of 100°C decreases its velocity by 50%. This was observed by push-down of a deeper reflector and by increased amplitude in the tar sand section (Pullin, Matthews and Hirsche, 1987). The individual data volumes were inverted into acoustic impedance and thence velocity. The velocity volumes were then differenced and these difference volumes sliced. One such velocity difference depth slice is shown in Figure 13-8, demonstrating in color the effect of the heat from injected steam.

Downloaded 25 Jun 2012 to 95.28.162.50. Redistribution subject to SEG license or copyright; Terms of Use: http://segdl.org/

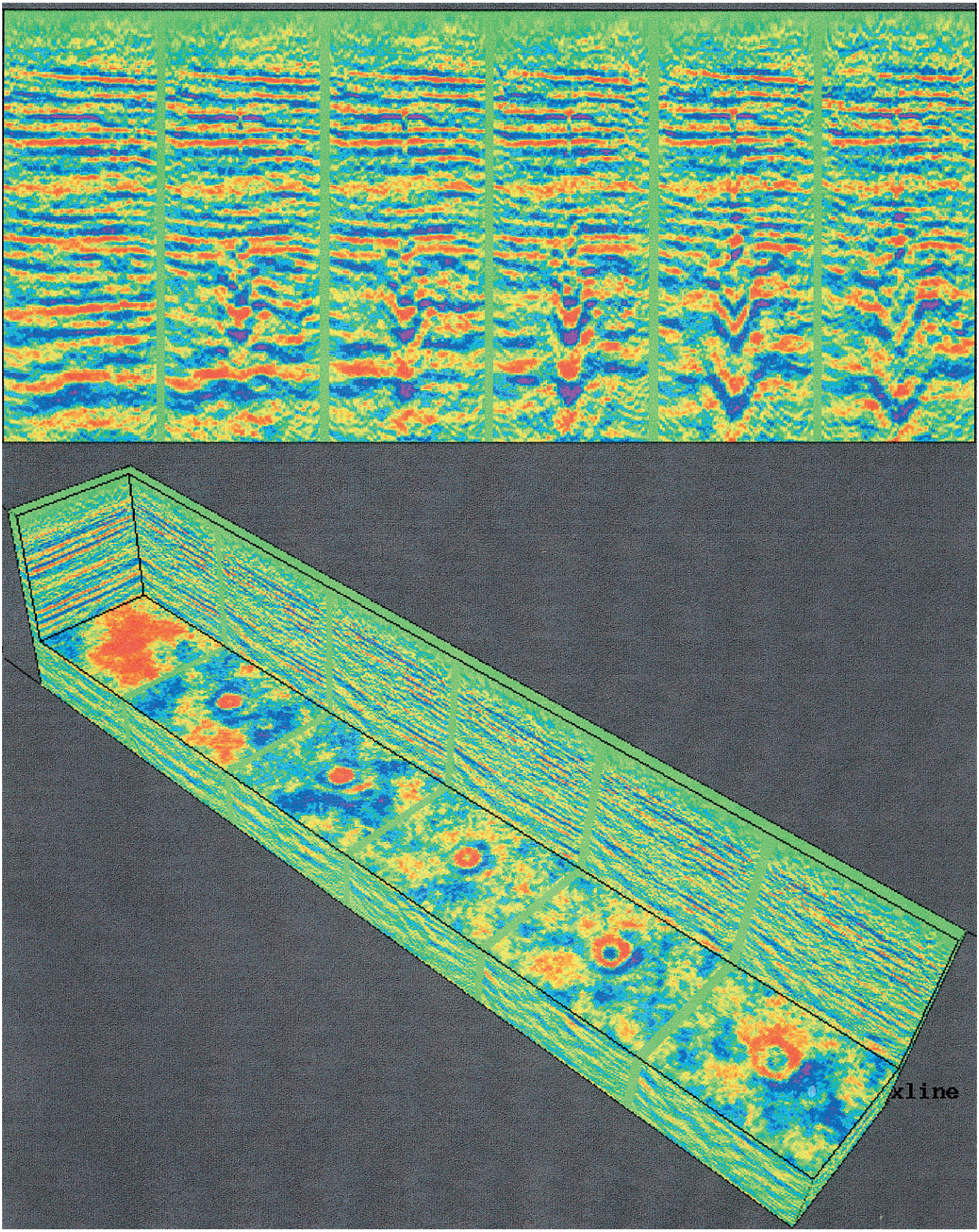

Downloaded 25 Jun 2012 to 95.28.162.50. Redistribution subject to SEG license or copyright; Terms of Use: http://segdl.org/

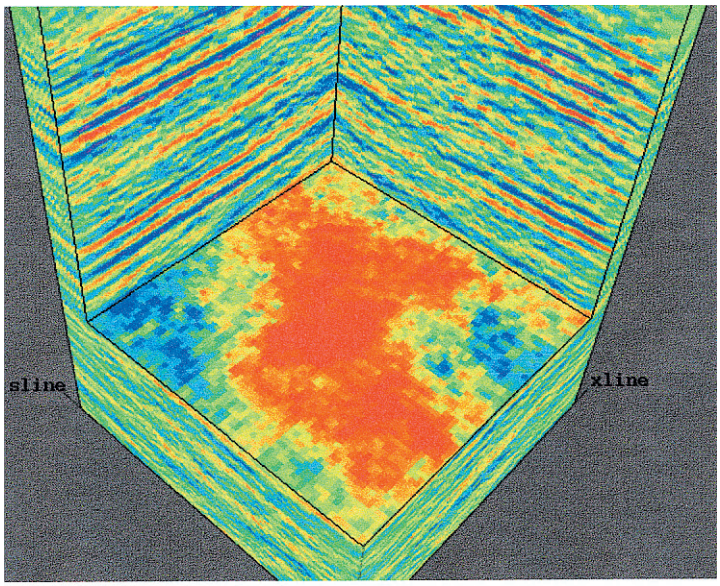

Fig. 13-5. Duri Field steam flood. Bench-cut display from baseline seismic survey before steam injection was started. (Courtesy David E. Lumley, Chevron/ Stanford, and Caltex Pacific Indonesia.)

Fig. 13-3. (Opposite Top) Duri Field, Indonesia, steam flood. Vertical sections from six repeated seismic surveys. The baseline survey before any steam was injected is on the left. The other surveys, from left to right, are after 2, 5, 9, 13 and 19 months of steam injection. Note the synclinal shape developing with time. (Courtesy David E. Lumley, Chevron/ Stanford, and Caltex Pacific Indonesia.)

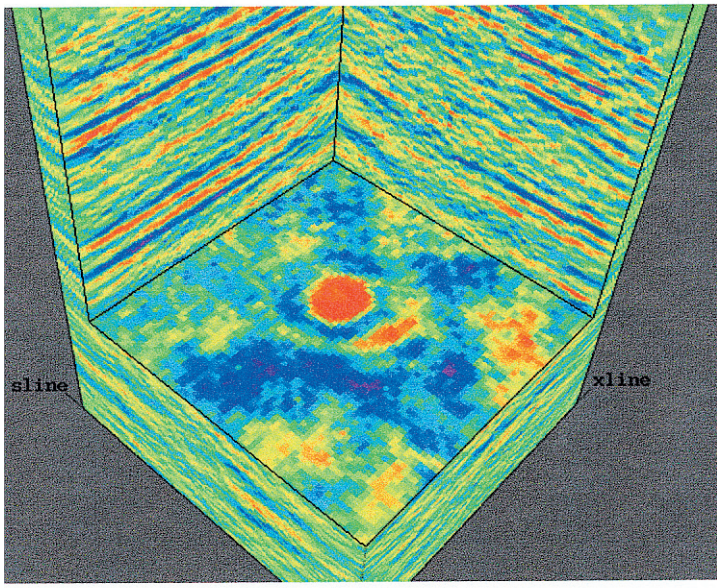

Fig. 13-6. Duri Field steam flood. Bench-cut display from seismic survey after steam injection for 5 months. (Courtesy David E. Lumley, Chevron/ Stanford, and Caltex Pacific Indonesia.)

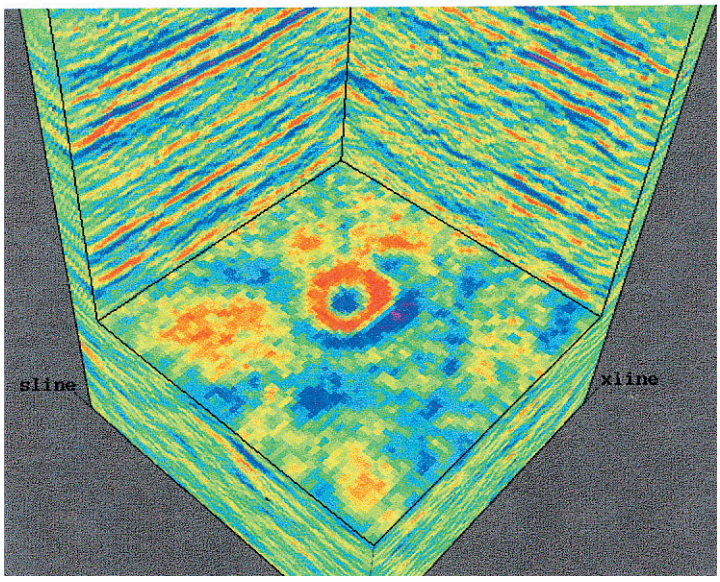

Fig. 13-7. Duri Field steam flood. Bench-cut display from seismic survey after steam injection for 13 months. (Courtesy David E. Lumley, Chevron/ Stanford, and Caltex Pacific Indonesia.)

Fig. 13-4. (Opposite Bottom) Duri Field steam flood. Concatenated bench-cut display from the six seismic surveys showing principally time slice views of the increasing steam effect after 0, 2, 5, 9, 13, and 19 months of steam injection. (Courtesy David E. Lumley, Chevron/ Stanford, and Caltex Pacific Indonesia.)

Downloaded 25 Jun 2012 to 95.28.162.50. Redistribution subject to SEG license or copyright; Terms of Use: http://segdl.org/

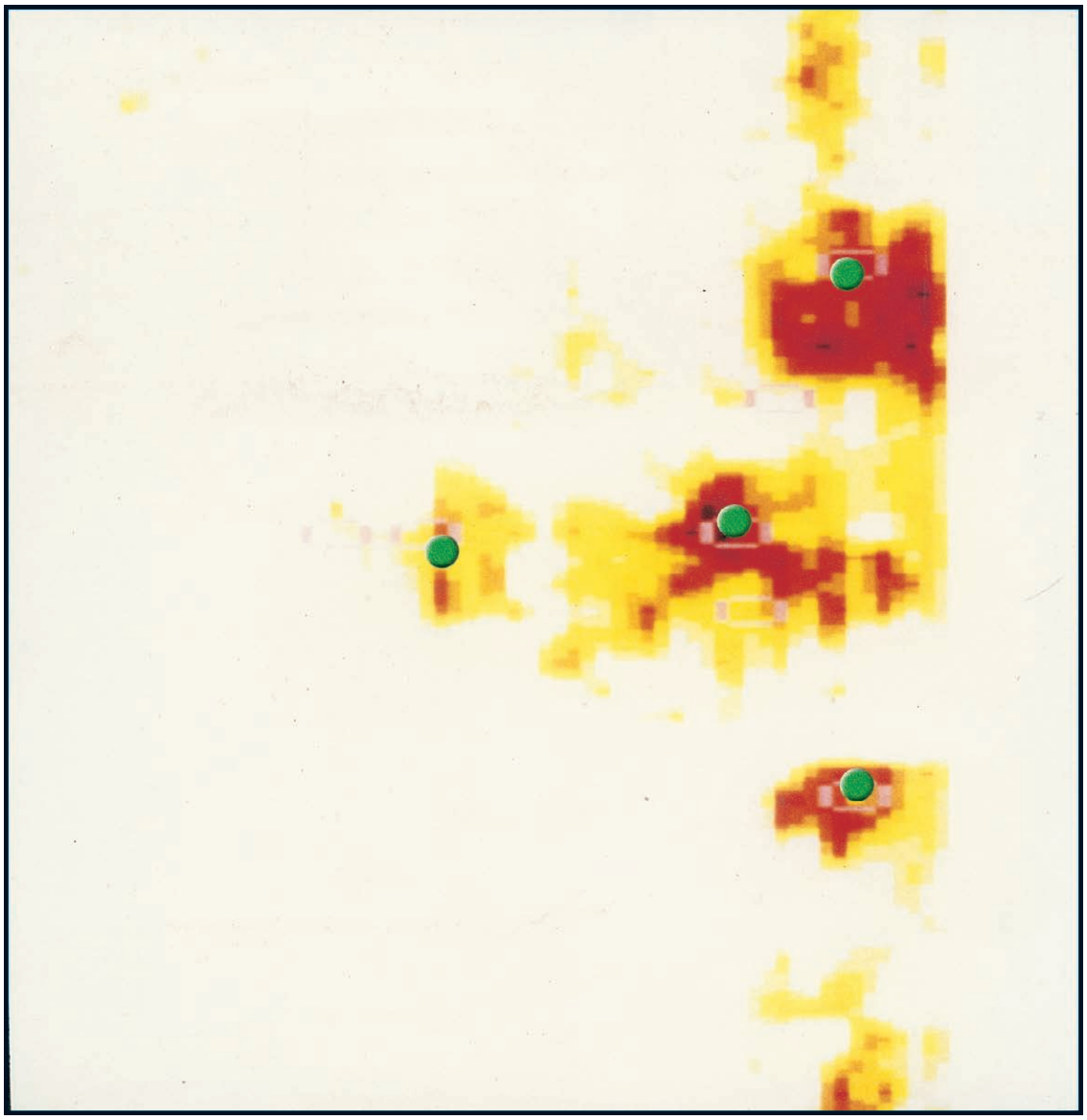

Fig. 13-8. GLISP tar sand, Alberta, Canada, steam flood. Velocity difference depth slice at a depth of 200 m between two surveys recorded several months apart. The colors indicate the sands affected by the heat of the injected steam. The green dots indicate injection and production wells. The velocity is derived by seismic inversion. (Courtesy Amoco Canada Petroleum Company and N. E. Pullin.)

Similarly in northern Alberta, Cold Lake has been under steam injection for the recovery of bitumen for more than 10 years. Seismic monitoring has definitively mapped steam-heated regions of the reservoir at several separate locations (Eastwood et al., 1994) allowing new wells to be drilled into the regions remaining cold. Figure 13-9 clearly shows an amplitude anomaly surrounding each steam-stimulated well. In fact the high amplitude is here caused by gas being driven out of the bitumen by the heat of the injected steam. Figure 13-10 shows a map of reservoir temperature based on seismic amplitude and other attributes. Temperatures measured in the wells confirm the seismic results.

The Gullfaks Field in the Norwegian North Sea was covered by a 3-D survey in 1985 before production started. In 1995 a second 3-D survey was acquired in the same direction over the same area. Unfortunately production platforms now caused obstruction to the seismic vessel and gaps in coverage resulted. In order to properly compare the results of the two surveys compensation for these effects was required (Sønneland et al., 1997). Figures 13-11 and 13-12 show horizon slices of Top Brent amplitude from the two surveys. The reservoir produces gassy oil. Clearly the high-amplitude area in Figure 13-11 shows the extent of the hydrocarbon before

Downloaded 25 Jun 2012 to 95.28.162.50. Redistribution subject to SEG license or copyright; Terms of Use: http://segdl.org/

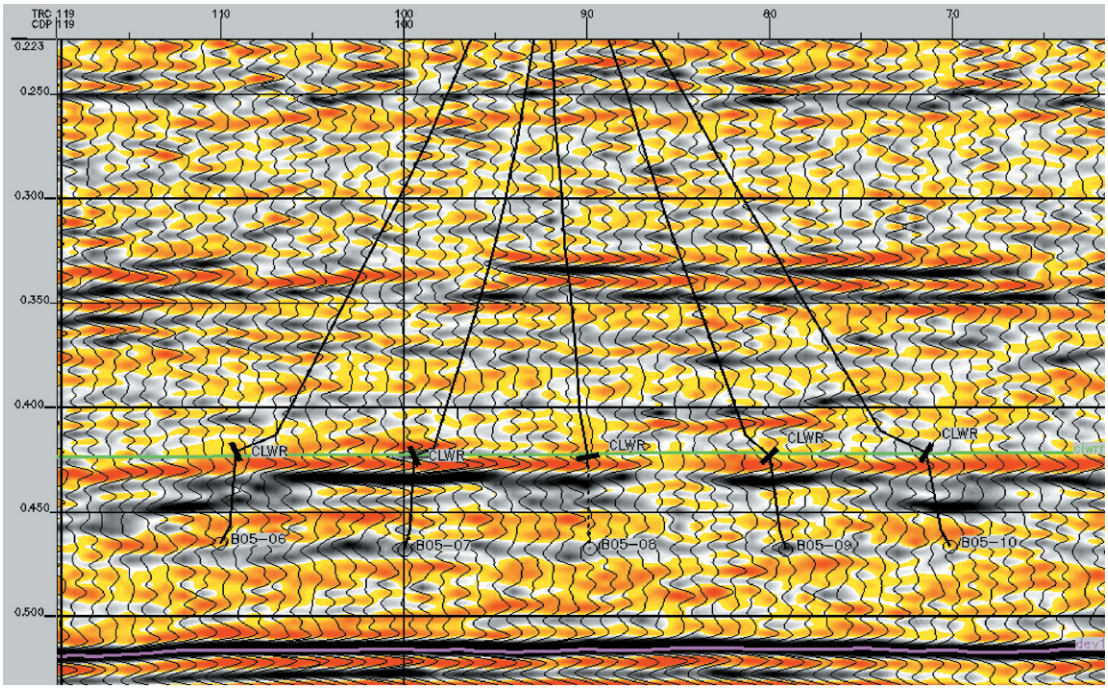

Fig. 13-9. Cold Lake, Alberta, Canada, steam flood. Seismic section through a row of steam-stimulated wells showing an amplitude anomaly associated with each. (Courtesy Exxon Production Research Company and Imperial Oil Limited.)

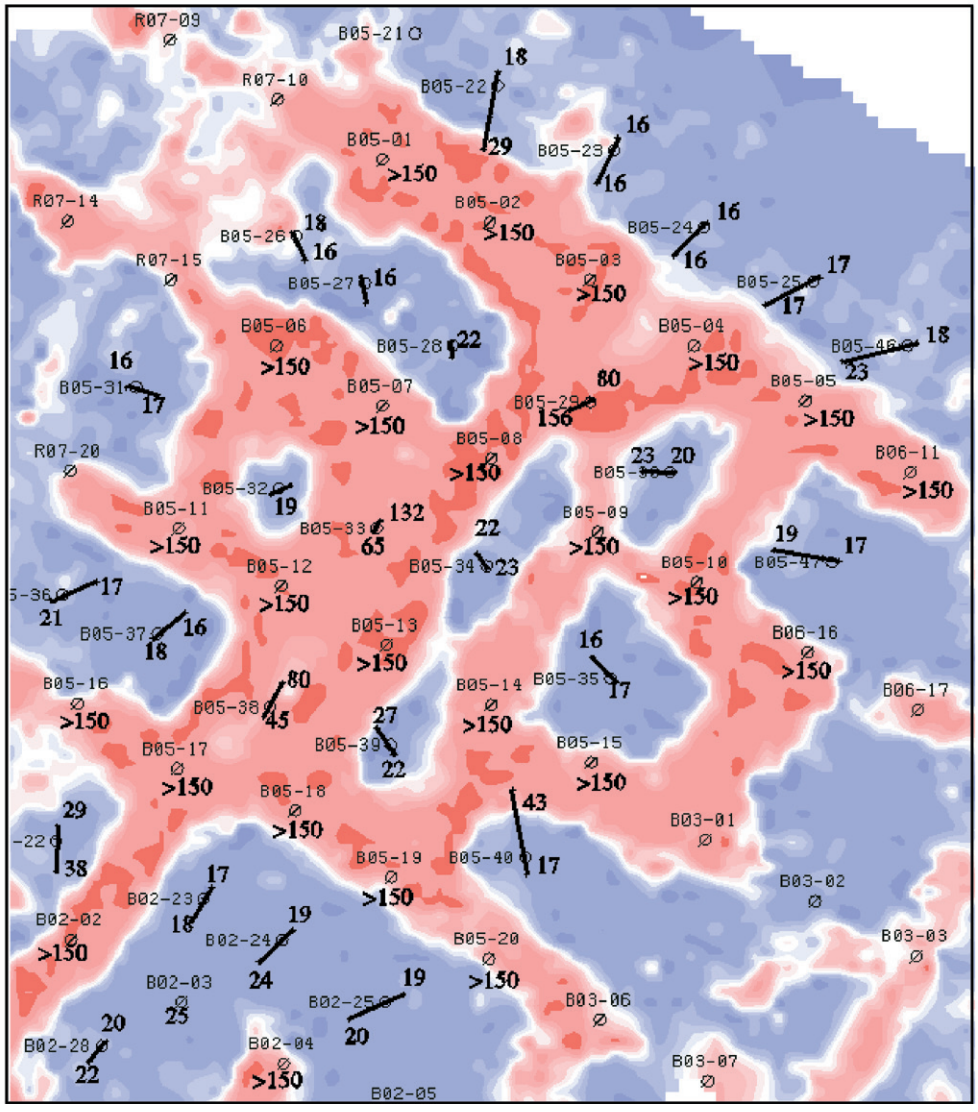

Fig. 13-10. Cold Lake, Alberta, Canada, steam flood. Seismically derived map of hot (red) and cold (blue) reservoir based on multiple seismic attributes including amplitude. Well-logged temperatures are annotated. (Courtesy Exxon Production Research Company and Imperial Oil Limited.)

Downloaded 25 Jun 2012 to 95.28.162.50. Redistribution subject to SEG license or copyright; Terms of Use: http://segdl.org/

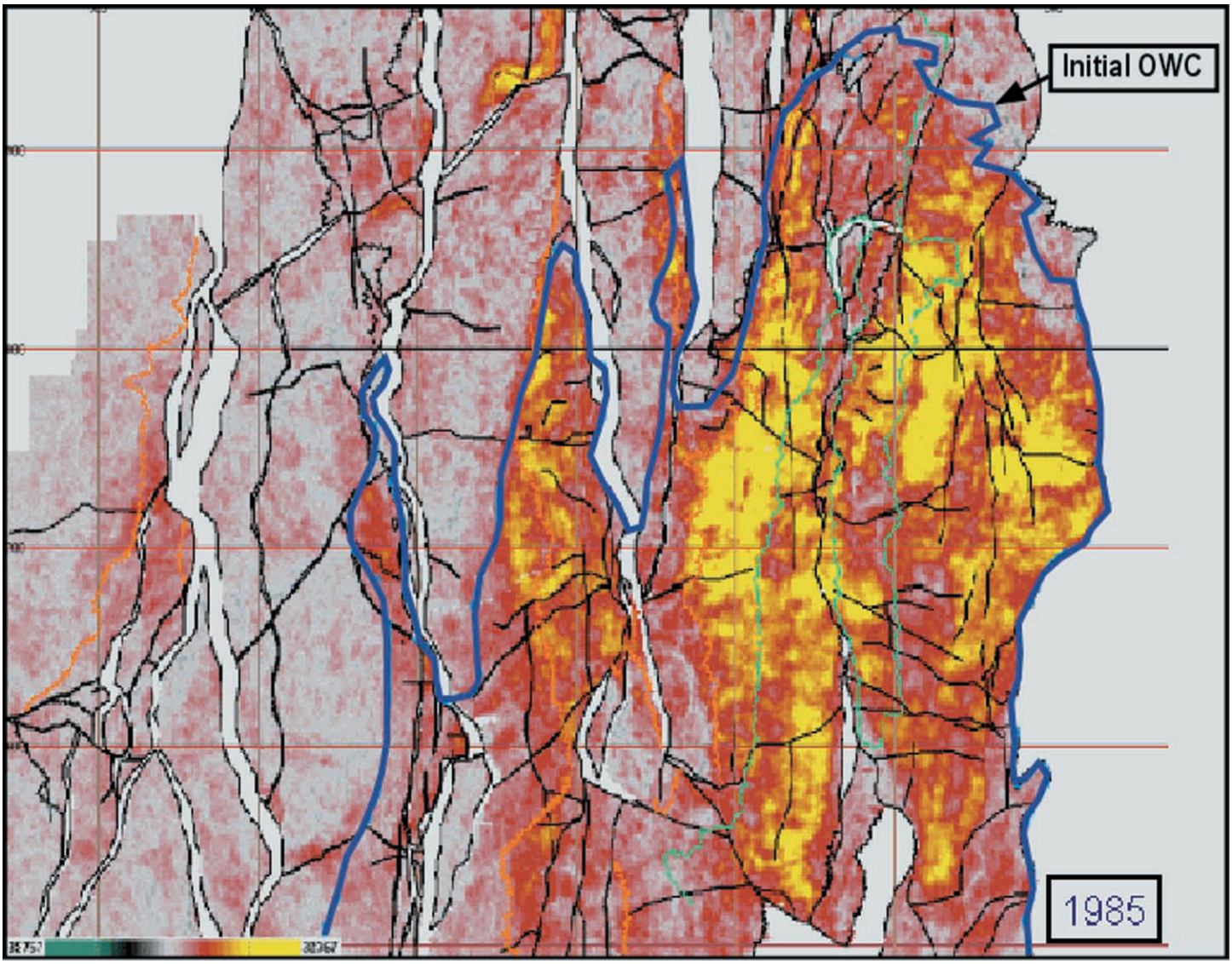

Fig. 13-11. Gullfaks Field, Norwegian North Sea, production of gassy oil. Horizon slice of Top Brent amplitude from 1985 3-D survey recorded before production started. High amplitudes tie with wells that found oil. OWC is at 1947 m. (Courtesy Statoil.)

production. The oil-water contact is rising by 13 m per year. Because of the residual saturation below the OWC the effect of production on the amplitude will be small. However, there are places in Figure 13-12 where the high amplitude seems to have moved back from the line of the initial OWC.

The Fulmar Field in the U.K. North Sea is covered by two legacy 3-D surveys recorded in 1977 and 1992. There should be good chance of observing seismic differences in this field because water is displacing light oil, the reservoir is a thick sand, and 10 years of production has taken place between the two surveys (Johnston et al., 1998). Bright spots and flat spots clearly indicate a seismic expression of hydrocarbons. Figure 13-13 shows horizon slices of Top Fulmar amplitude from the two surveys and they are different. At least some of the differences indicate the effects of production although there are also repeatability problems between the two legacy surveys. The two data sets were inverted into acoustic impedance; an average value was then calculated at each point from the top of the Fulmar Formation to the position of the original oil-water contact. Each of these was mapped and the difference between them produced Figure 13-14. Increases in impedance on the flanks of the structure are interpreted as indications of water influx and pressure decline. Decreases in impedance on the crest are probably caused by injected gas.

The Lena Field in the Mississippi Canyon area of the Gulf of Mexico produces from

Downloaded 25 Jun 2012 to 95.28.162.50. Redistribution subject to SEG license or copyright; Terms of Use: http://segdl.org/

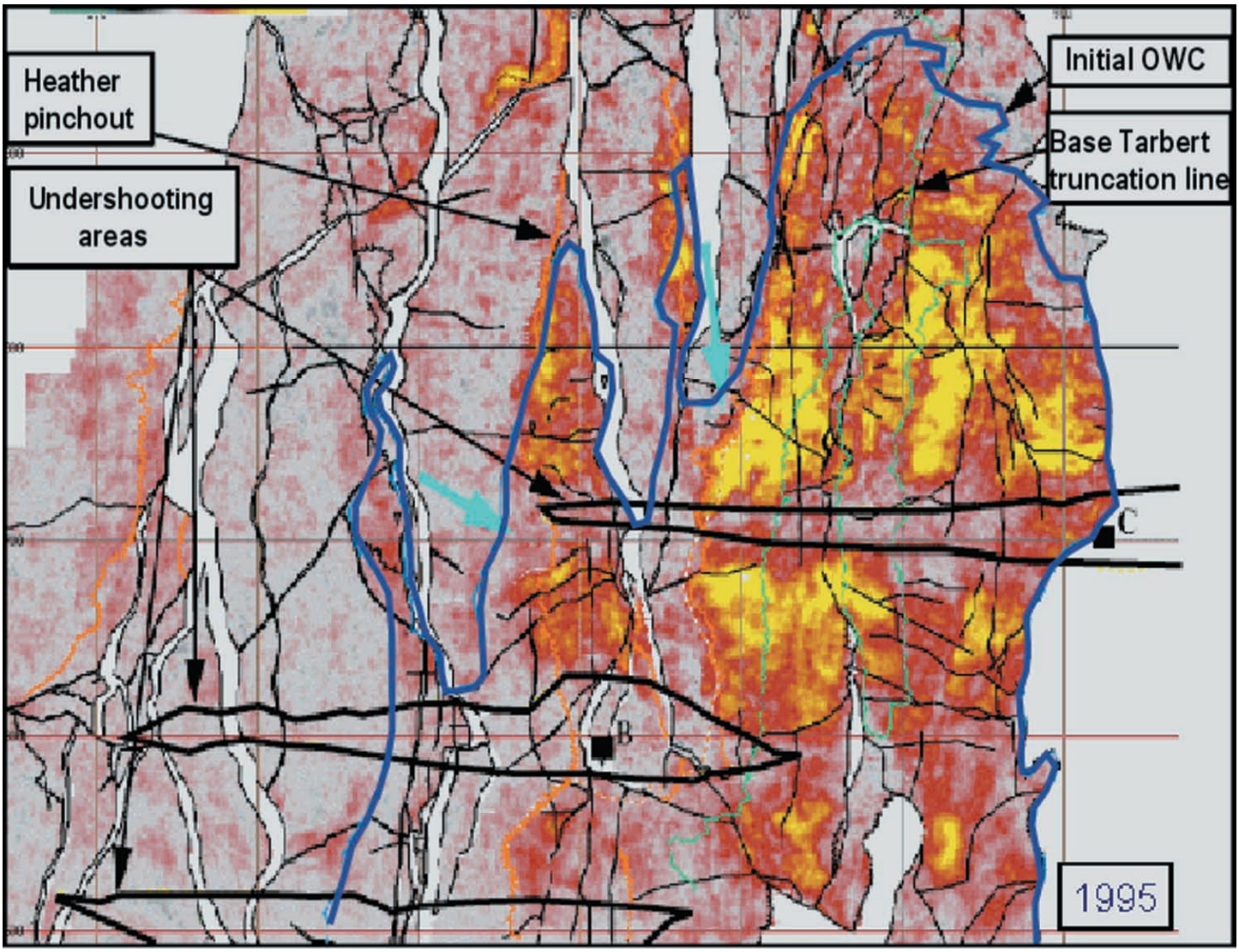

Fig. 13-12. Gullfaks Field, Norwegian North Sea, production of gassy oil. Horizon slice of Top Brent amplitude from 1995 3-D survey recorded during production. Movement of the high amplitude away from the dark blue line, the initial OWC, probably indicates production. The undershooting areas are where platforms blocked seismic operations. (Courtesy Statoil.)

Pliocene sands. Two legacy 3-D surveys acquired in 1983 and 1995 cover the field which in 1995 had been producing oil for 8 years. Very elaborate processing of the surveys was performed in order to minimize non-reservoir differences; these included matched filtering and residual migration (Eastwood et al., 1998). Figure 13-15 shows a striking amplitude anomaly on a seismic difference section between the two surveys. The extent of this anomaly is shown on the accompanying horizon slice difference display. Figure 13-16 shows the same horizon slice difference with a map overlay and accompanying annotated map, demonstrating that the amplitude anomaly is caused by gas cap expansion into the previous oil zone. Amplitude anomaly variations in the difference along strike are considered to be indications of variable amounts of gas expansion.

References

Eastwood, J. E., J. P. Lebel, A. Dilay, and S. Blakeslee, 1994, Seismic monitoring of steam-based recovery of bitumen: The Leading Edge, v. 13, p. 242–251.

Eastwood, J. E., D. H. Johnston, X. Huang, K. Craft, and R. Workman, 1998, Processing for robust time-lapse seismic analysis: Gulf of Mexico example, Lena Field: SEG 68th Annual Meeting expanded abstracts, p. 20–23.

Downloaded 25 Jun 2012 to 95.28.162.50. Redistribution subject to SEG license or copyright; Terms of Use: http://segdl.org/

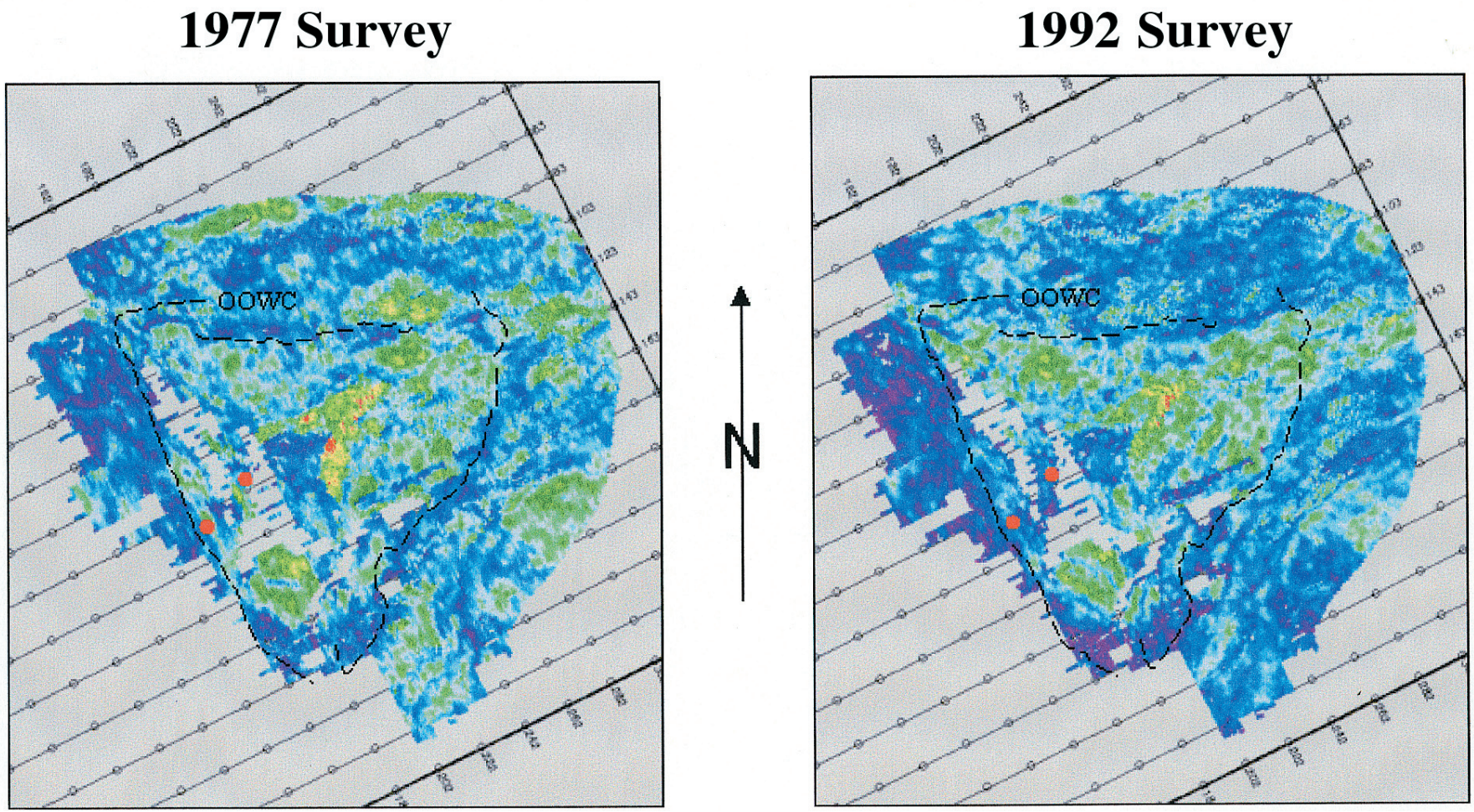

Fig. 13-13. Fulmar Field, U.K. North Sea, water flood. Horizon slices of Top Fulmar amplitude from 1977 survey before production of light oil started and from 1992 survey after 10 years of production. The differences partly indicate production. (Courtesy Exxon Production Research Company.)

Downloaded 25 Jun 2012 to 95.28.162.50. Redistribution subject to SEG license or copyright; Terms of Use: http://segdl.org/

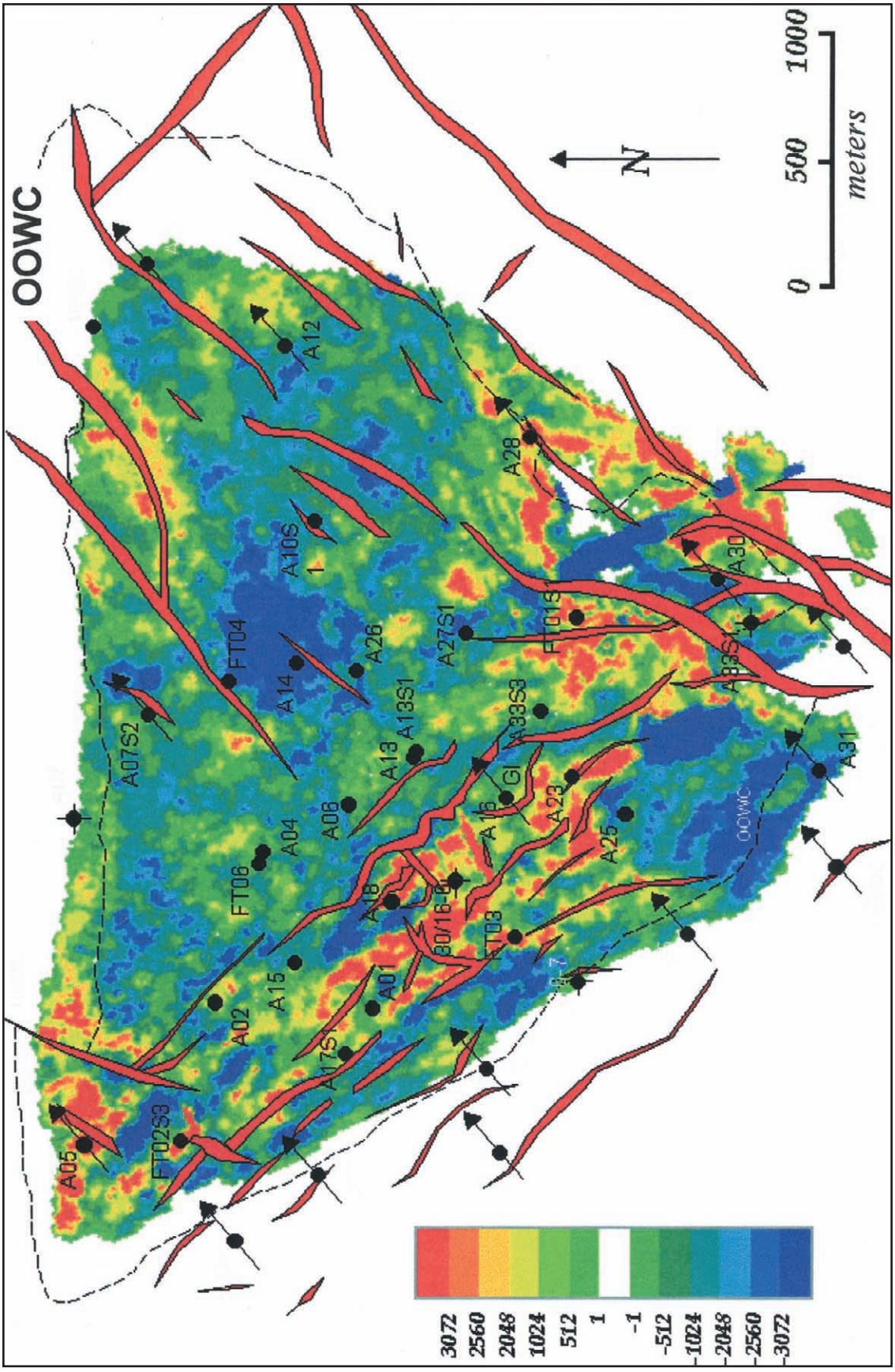

Fig. 13-14. Fulmar Field, U.K. North Sea, water flood. Change in Fulmar reservoir acoustic impedance between 1977 and 1992, calculated as the difference in average impedance from the top Fulmar Formation to the original OWC between the two surveys. Increases in impedance on the western and southern flanks are interpreted as indications of water influx and pressure decline. (Courtesy Exxon Production Research Company.)

Downloaded 25 Jun 2012 to 95.28.162.50. Redistribution subject to SEG license or copyright; Terms of Use: http://segdl.org/

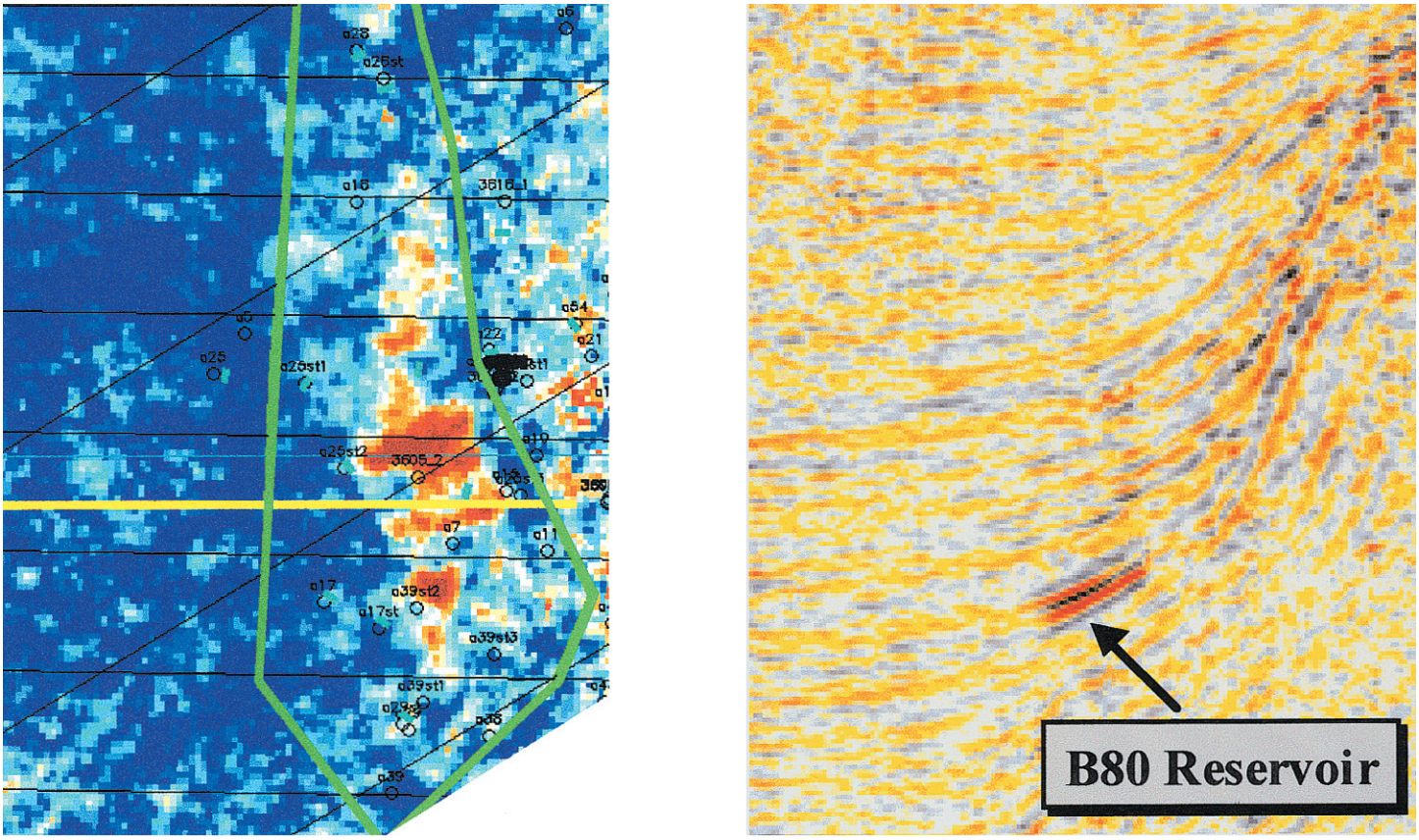

Fig. 13-15. Lena Field, Gulf of Mexico, oil production and gas cap expansion. Seismic difference section showing high amplitude caused by gas cap expansion in the B80 reservoir during 8 years of production. Equivalent horizon slice showing the aerial difference in amplitude between the 1983 and 1995 surveys. The yellow line shows the position of the section. (Courtesy Exxon Production Research Company and Western Geophysical.)

Jack, I. G., 1997, Time-lapse seismic in reservoir management: Distinguished Instructor Short Course notes, SEG.

Jenkins, S. D., M. W. Waite, and M. F. Bee, 1997, Time-lapse monitoring of the Duri steamflood: A pilot and case study: The Leading Edge, v. 16, p. 1267–1273.

Johnston, D. H., R. S. McKenny, J. Verbeek, and J. Almond, 1998, Time-lapse seismic analysis of Fulmar Field: The Leading Edge, v. 17, p. 1420–1428.

Lumley, D. E., 1995, Seismic time-lapse monitoring of subsurface fluid flow: Ph. D. thesis, Stanford University, California, U.S.A.

Pullin, N. E., L. Matthews, and K. W. Hirsche, 1987, Techniques applied to obtain very high resolution 3-D seismic imaging at an Athabasca tar sands thermal pilot: The Leading Edge, v. 6, no. 12, p. 10–15.

Sønneland, L., H. H. Veire, B. Raymond, C. Signer, L. Pedersen, S. Ryan, and C. Sayers, 1997, Seismic reservoir monitoring on Gullfaks: The Leading Edge, v. 16, p. 1247–1252.

Waite, M. W., and R. Sigit, 1997, Seismic monitoring of the Duri steamflood: Application to reservoir management: The Leading Edge, v. 16, p. 1275–1278.

Wang, Z., and A. Nur, 1989, Seismic and acoustic velocities in reservoir rocks, SEG.

Downloaded 25 Jun 2012 to 95.28.162.50. Redistribution subject to SEG license or copyright; Terms of Use: http://segdl.org/

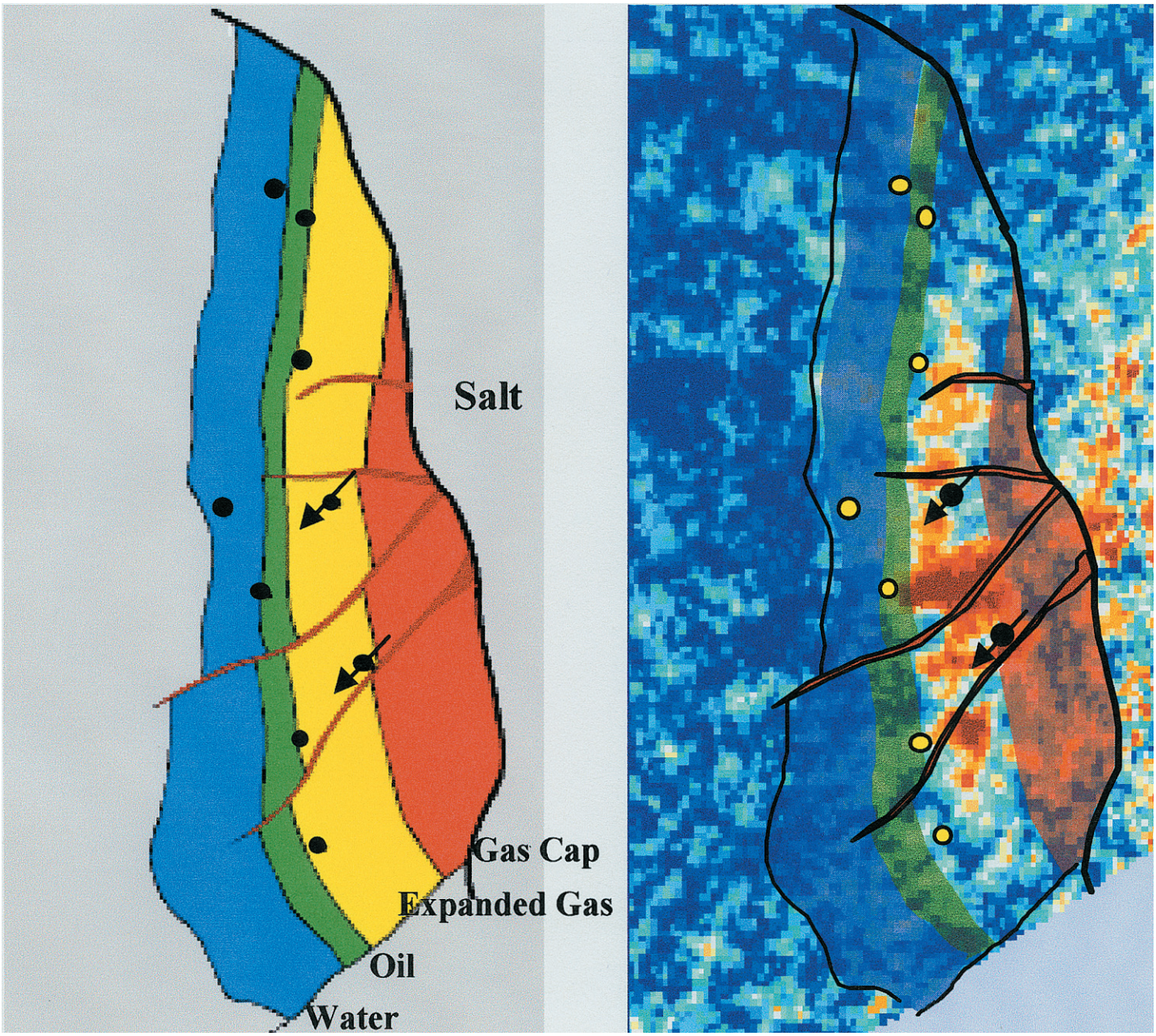

Fig. 13-16. Lena Field, Gulf of Mexico, oil production and gas cap expansion. Horizon slice difference between 1983 and 1995 surveys and corresponding map, demonstrating that the high amplitude coincides with the area of gas cap expansion. (Courtesy Exxon Production Research Company and Western Geophysical.)

Downloaded 25 Jun 2012 to 95.28.162.50. Redistribution subject to SEG license or copyright; Terms of Use: http://segdl.org/

Downloaded 25 Jun 2012 to 95.28.162.50. Redistribution subject to SEG license or copyright; Terms of Use: http://segdl.org/

Case Histories of Three-Dimensional Seismic Surveys

This chapter presents ten case histories contributed by various authors and demonstrating the solution of subsurface problems with 3-D seismic surveys. There are many other case histories now in the public domain, and below are four references to recommended anthologies.

Case History 10, new for the Seventh Edition, describes the unusually long history of a Gulf of Mexico field from 1938 up to the present. The story chronicles the use of gravity, seismic refraction, 2-D seismic reflection, 3-D seismic, 4-D seismic, and various special high-technology techniques in the discovery, delineation, development, production, and revitalization of this large oil field.

Allen, J. L., T. S. Brown, C. J. John, and C. F. Lobo, 1998, 3-D seismic case histories from the Gulf Coast Basin: Gulf Coast Association of Geological Societies.

Davies, R. J., J. A. Cartwright, S. A. Stewart, M. Lappin, and J. R. Underhill, 2004, 3D seismic technology—Application to the exploration of sedimentary basins: The Geological Society, London, Memoir No. 29.

Pacht, J. A., R. E. Sheriff, and B. F. Perkins, 1996, Stratigraphic analysis utilizing advanced geophysical and wireline technology for petroleum exploration and production: Gulf Coast Section, Society of Economic Paleontologists and Mineralogists Foundation.

Weimer, P., and T. L. Davis, 1996, Applications of 3-D seismic data to exploration and production: AAPG Studies in Geology, no. 42/SEG Geophysical Developments Series, no. 5.

Case History 1

Field Appraisal With Three-Dimensional Seismic Surveys Offshore Trinidad

Robert M. Galbraith, Texaco Inc., Latin America/West Africa Division
Alistair R. Brown, Geophysical Service Inc.

A consortium operated by Texaco Trinidad Inc. commenced exploration in the South East Coast Consortium block offshore Trinidad in 1973. After four years of intensive exploration, a gas/condensate discovery was announced in early 1977 on the Pelican

Downloaded 25 Jun 2012 to 95.28.162.50. Redistribution subject to SEG license or copyright; Terms of Use: http://segdl.org/

prospect. Later that year, in anticipation of the possible future need to site drilling/production platforms, a three-dimensional (3-D) seismic survey was recorded over the prospect. This survey resulted in improvements in seismic record quality, multiple attenuation, and fault resolution. A coordinated geologic-geophysical interpretation based on the 3-D seismic survey, a re-evaluation of log correlations, and the use of seismic logs differed significantly from earlier interpretations. Because of this, it is anticipated that the development of the field will need to be initiated in a different fault block from that previously envisioned.

A second 3-D survey contiguous to the Pelican survey was recorded in 1978 over the Ibis prospect. Results show significant data enhancement in the deeper part of the section and improved fault resolution relative to previous two-dimensional (2-D) control. The 3-D interpretation has revealed a much more complex fault pattern than originally mapped. Separate fault blocks will have to be individually evaluated, thus greatly increasing exploration risk.

Introduction

The Republic of Trinidad and Tobago lies approximately 8 mi (13 km) off the northeast coast of Venezuela on the continental shelf of South America. The South East Coast Consortium was formed in 1973 to evaluate an offshore license obtained from the government of Trinidad and Tobago in that year. The Consortium comprises Texaco Trinidad Inc. (operator), Trinidad and Tobago Oil Company Ltd., and Trinidad-Tesoro Petroleum Company Ltd.

The license area lies approximately 30 mi (48 km) off the southeast coast of Trinidad in the Galeota basin. This basin covers approximately 5,000 sq mi (13,000 sq km) in which thick Pleistocene to upper Miocene deltaic sandstones contain hydrocarbons in traps formed in gravity-induced structures. Closures consist of large diapiric anticlinal ridges and rollover features developed downthrown to major growth faults. To date, four major oil fields and four major gas fields have been discovered in the basin and recoverable reserves have been estimated at 1 billion bbls of oil and 13+ trillion cu ft of gas.

Exploratory drilling in the Consortium block was carried out between 1975 and 1977 with a total of nine wells drilled on four separate structures. Of this total, three were drilled on the Pelican prospect with a gas/condensate discovery declared in 1977. However, even after four years of intensive exploration, including the recording of 1,400 mi (2,250 km) of 2-D seismic data, the Consortium was still unable to determine a location for a development platform. In seeking a solution, the Consortium engaged GSI to conduct a 3-D seismic survey over the Pelican structure in 1977. Following this, the Ibis 3-D survey was recorded in 1978.

All data were recorded with 24-fold geometry along lines oriented southwest-northeast, the predominant dip direction over the block. The lines were 100 m (330 ft) apart, and the subsurface interval along each line was 33 m (108 ft). The currents in the area were commonly 6 to 8 knots at right angles to the shooting direction, so the cable drift was high. Continuously recorded streamer tracking data provided the location of each depth point for each shot. A common-depth-point (CDP) set was then defined as those traces whose source-receiver midpoints fell within a bin 67×100 m. This limited the lateral subsurface smear to an acceptable level with a consequent improvement in the stack response.

Results and Interpretation

One of the reservoirs in the Pelican area occurs at the top of the Miocene. The dip at this level between the Pelican-1 well and the northwestern boundary of the 3-D survey area was mapped to be 2,000 ft (610 m) on the pre-existing 2-D data. After the primary reflections had been correctly identified using the 3-D data, less than 1,000 ft (305 m) of dip were mapped on the north flank. This decrease in dip increased the interpreted hydrocarbon-bearing area under closure by approximately 20%, thus significantly affecting reserve estimates and development economics.

Downloaded 25 Jun 2012 to 95.28.162.50. Redistribution subject to SEG license or copyright; Terms of Use: http://segdl.org/

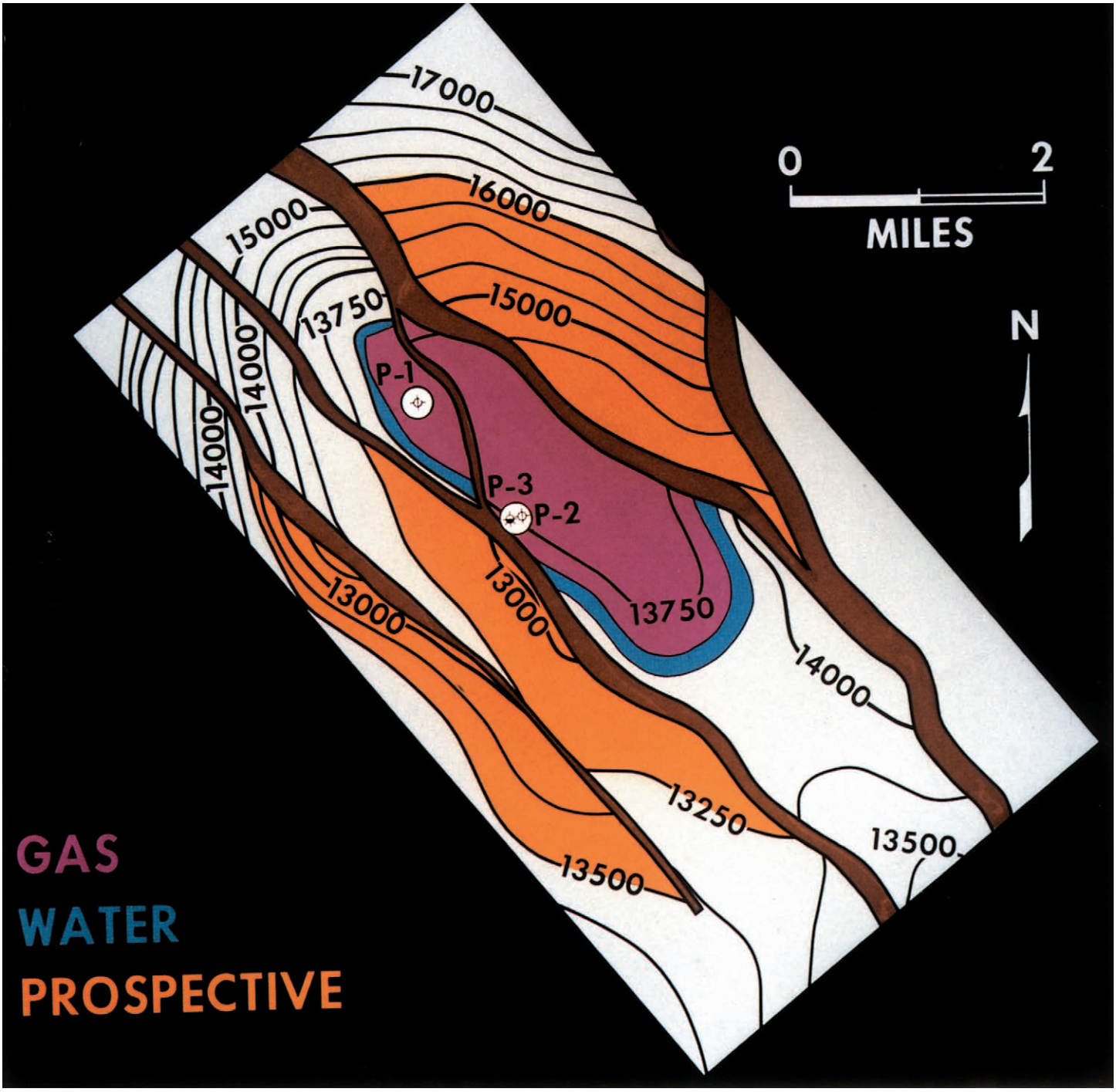

Fig. 14-1-1. Map of Pelican-3 sand, offshore Trinidad, interpreted from 2-D data. Contour interval 250 ft (76 m).

The prime reservoir in the area is the Pelican-3 sand. Figure 14-1-1 shows the interpreted map at this level before the 3-D survey. Figures 14-1-2 and 14-1-3 show two interpretations made from the 3-D survey data. While a similar difference in the northwest dip exists at this level as was mapped at top Miocene, the principal difference between pre- and post-3-D interpretations concerns the faulting.

Initial interpretation of the logs from Pelican-1 and Pelican-3 wells indicated different water levels in the Pelican-3 sand. This was explained by a cross-fault separating the two wells (Figure 14-1-1). The 3-D data precluded the possibility of this cross-fault. Instead, the growth fault has been interpreted farther northeast, thus separating the two wells at

Downloaded 25 Jun 2012 to 95.28.162.50. Redistribution subject to SEG license or copyright; Terms of Use: http://segdl.org/

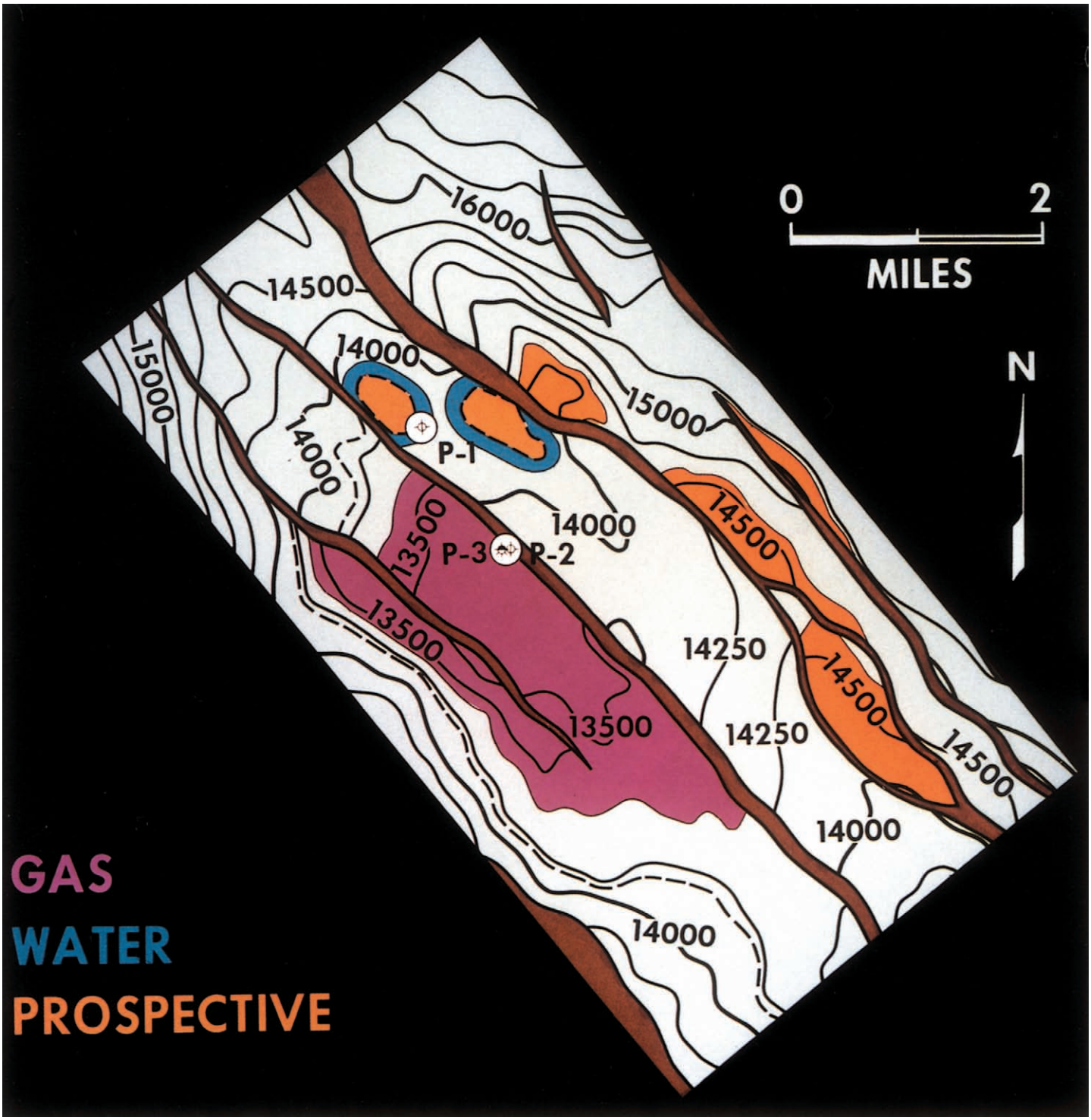

Fig. 14-1-2. Map of Pelican-3 sand interpreted from 3-D data, with southeastern structural closure but not honoring water level in well. Contour interval 250 ft (76 m).

the Pelican-3 sand. The impact of this on the interpreted position of the reserves is shown in Figure 14-1-2. The recommendation based on the 3-D interpretation was therefore to initiate development drilling in a different fault block from the one proposed prior to the acquisition of 3-D control. This change in interpretation has probably saved the South East Coast Consortium the expense of at least one dry hole and possibly the cost of mislocation of a development platform.

The water level in the Pelican-3 sand in the Pelican-3 well is near 13,800 ft (4,210 m). The contour at this level is shown by a dashed line in Figure 14-1-2. This is 200 ft (60 m) deeper than the structural spill point of 13,600 ft (4,150 m) which, on the basis of

Downloaded 25 Jun 2012 to 95.28.162.50. Redistribution subject to SEG license or copyright; Terms of Use: http://segdl.org/

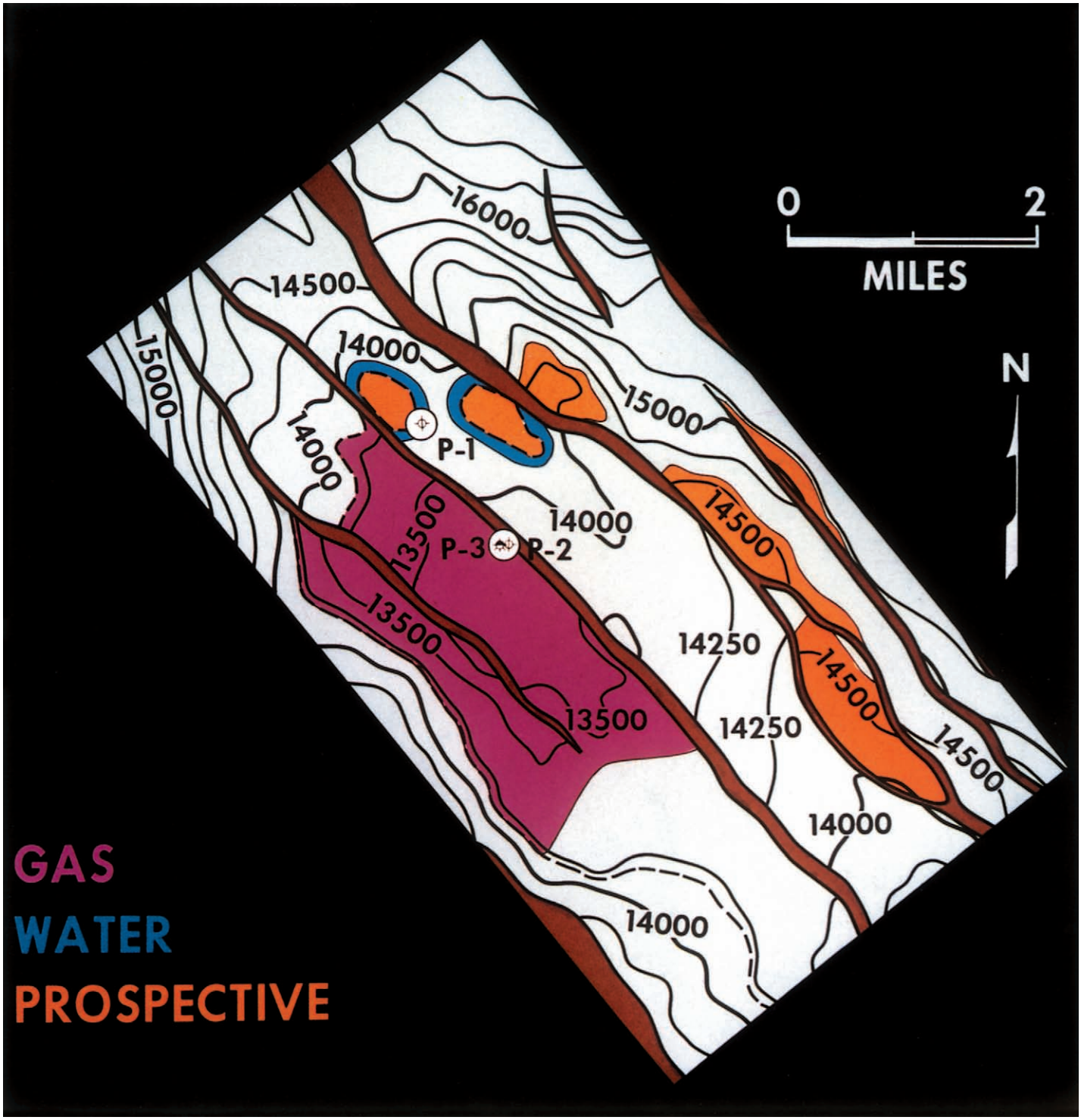

structural closure alone, would control the downdip extent of the gas. An alternative interpretation which honors the water level in the well is shown in Figure 14-1-3. This invokes a stratigraphic reservoir boundary on the southeast.

The seismic section along crossline 87, northwest-southeast through Pelican-3 well, shows a very marked character change at the Pelican-3 reservoir level southeast of the well. This probably indicates the position of the stratigraphic boundary. This character change is evident on seven crosslines which intersect the boundary, and also on several Seiscrop sections, from which its position was mapped (Figure 14-1-3).

The G-LOG* process of seismic inversion was applied to crossline 87 through Pelican-3 well

Fig. 14-1-3. Map of Pelican-3 sand interpreted from 3-D data, with southeastern stratigraphic boundary and honoring water level in well. Contour interval 250 ft (76 m).

Downloaded 25 Jun 2012 to 95.28.162.50. Redistribution subject to SEG license or copyright; Terms of Use: http://segdl.org/

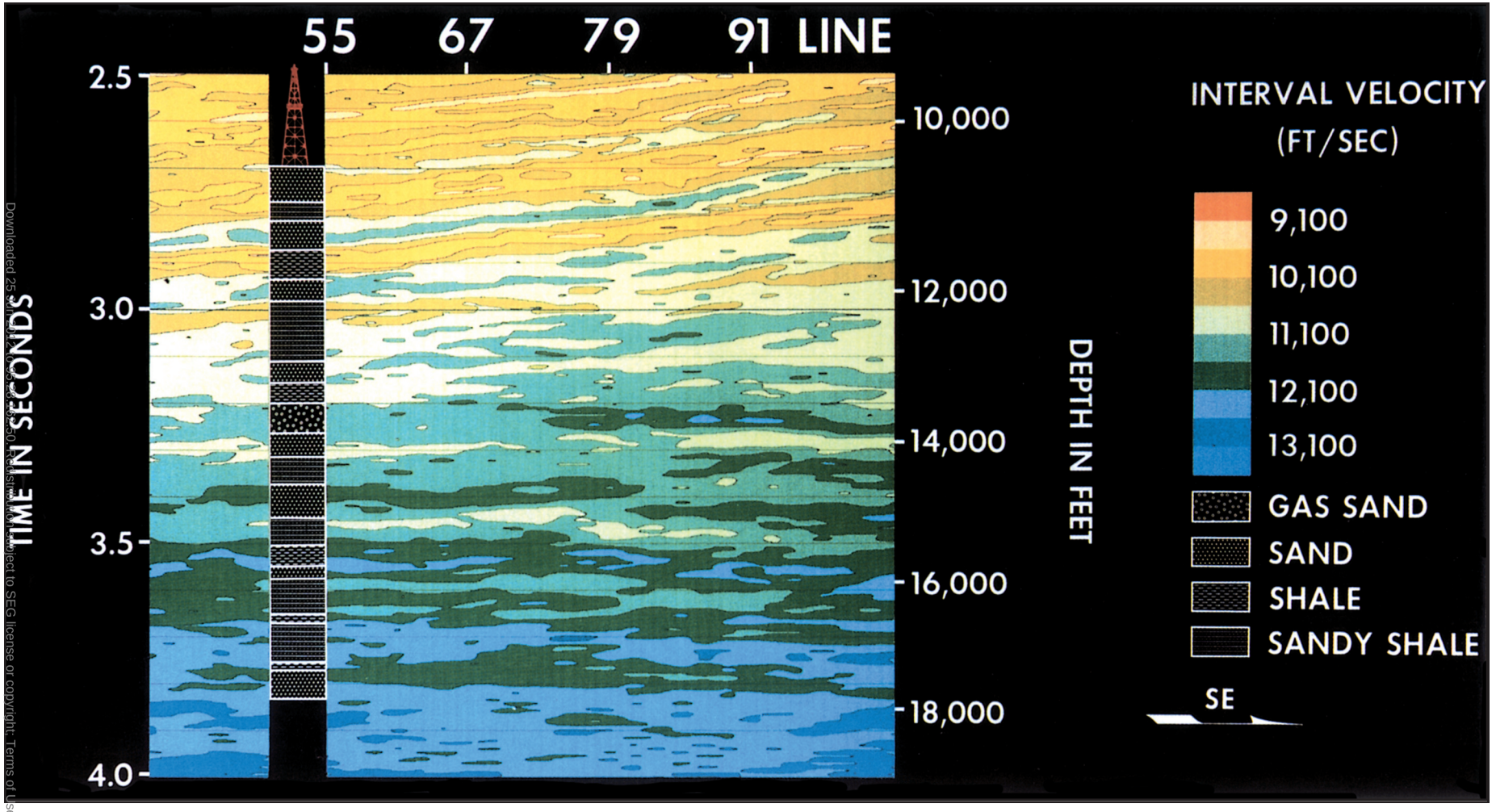

Fig. 14-1-4. G-LOG velocity section along crossline 87 through Pelican-3 well showing lateral velocity transition across inferred southeastern reservoir boundary.

Downloaded 25 Jan 2012 to 128.83.2.250. Redistribution subject to SEG license or copyright. Terms of Use: http://segdl.org/

in an attempt to study the nature and validity of the stratigraphic boundary. The resulting G-LOG section in color is shown in Figure 14-1-4. Generally, the higher velocities correspond to the sands and the lower velocities to the shales. Cyclical sand-shale deposition is evident above 3.0 seconds.

The simplified lithology in the well shows the Pelican-3 gas sand between 3.20 and 3.26 seconds (Figure 14-1-4). There is no low velocity expression of this interval on the G-LOG section. However, away from the well to the southeast, the correlative interval shows an abrupt lateral increase in velocity; this is interpreted as the stratigraphic reservoir boundary. Close examination of the transition suggests layering which is also observed in the well; in the upper portion of the reservoir the transition occurs at line 70, in the next layer at line 79, and in the lower half of the reservoir at line 73. The magnitude of the velocity contrast across the boundary is approximately 600 ft/sec (180 m/sec). It is concluded that this lateral change from low to high velocity indicates the change from a porous gas-filled sand to a tight sand, in which the pores are filled with cement which is probably clay.

Conclusions

Data quality has been improved. Processing took into account cable drift, a major problem offshore Trinidad, thus limiting subsurface smear during stack. Some deep primary events have been observed for the first time. Because of increased data density, fault definition is excellent. Structural interpretations are more reliable with removal of energy from outside the plane of the section. The flexibility which permits an interpreter to generate lines in any direction is a significant benefit. The probable containment of the principal Pelican reserves by a stratigraphic reservoir boundary to the southeast has been substantially validated after a detailed study of its nature.

The 3-D results have caused major changes in the Pelican field development plans. The interpreted area under closure has been increased. The possibilities of drilling an initial dry hole and mislocating a development platform have been reduced due to improved reliability of the coordinated geologic-geophysical interpretation based on the 3-D seismic survey and a re-evaluation of log correlations. This has had a positive effect on development economics.

The 3-D seismic method has proved to be a useful tool for field appraisal in this area offshore Trinidad and will be considered over other prospects prior to commitment to expensive offshore development programs.

*Trademark of Geophysical Service Inc.

Downloaded 25 Jun 2012 to 95.28.162.50. Redistribution subject to SEG license or copyright; Terms of Use: http://segdl.org/

Case History 2

Three-Dimensional Seismic Monitoring of an Enhanced Oil Recovery Process

Robert J. Greaves, Terrance J. Fulp, ARCO Oil and Gas Company

Seismic reflection data were used to monitor the progress of an in-situ combustion, enhanced oil recovery process. Three sets of three-dimensional (3-D) data were collected during a one-year period in order to map the extent and directions of propagation in time. Acquisition and processing parameters were identical for each survey so that direct one-to-one comparison of traces could be made. Seismic attributes were calculated for each common-depth-point data set, and in a unique application of seismic reflection data, the preburn attributes were subtracted from the midburn and postburn attributes. The resulting "difference volumes" of 3-D seismic data showed anomalies which were the basis for the interpretation shown in this case study.

Profiles and horizon slices from the data sets clearly show the initiation and development of a bright spot in the reflection from the top of the reservoir and a dim spot in the reflection from a limestone below it. Interpretation of these anomalies is supported by information from postburn coring. The bright spot was caused by increased gas saturation along the top-of-reservoir boundary. From postburn core data, a map of burn volume distribution was made. In comparison, the bright spot covered a greater area, and it was concluded that combustion and injection gases had propagated ahead of the actual combustion zone. The dim spot anomaly shows a good correlation with the burn volume in distribution and direction. Evidence from postburn logs supports the conclusion that the burn substantially decreased seismic velocity and increased seismic attenuation in the reservoir. Net burn thicknesses measured in the cores were used to calibrate the dim-spot amplitude. With this calibration, the dim-spot amplitude at each common depth point was inverted to net burn thickness and a map of estimated burn thickness was made from the seismic data.

Introduction

Improving the efficiency of reservoir production can increase proven reserves. The final stages in the production of a field are enhanced oil recovery (EOR) processes. Effective management of EOR processes requires detailed reservoir description and observations of the volume of the reservoir being swept by the process. High-resolution 3-D reflection seismic surveying can be an effective tool in obtaining reservoir description, and, as demonstrated by this case study, can in some cases actually map the EOR process as it proceeds.

In this case study, 3-D seismic reflection data were used to monitor the propagation of a pilot in-situ combustion (fire-flood) process. Three identical 3-D seismic surveys were recorded over the pilot site at preburn, midburn, and postburn times. In this way, the combustion propagation was monitored over (calendar) time.

Acquisition and computer processing of the data were identical for each set of survey data, so that a direct comparison of the individual data sets could be made. To facilitate interpretation, the attributes of the seismic traces were calculated using Hilbert transform techniques as described by Taner and Sheriff (1977). Reflection strength, in this paper referred to as "envelope amplitude," was then used in the analysis of the reflection seismic data. In a unique application of reflection seismic data, the envelope amplitude traces from the preburn data volume were subtracted from their counterpart traces in the midburn and postburn data volumes, generating "difference volumes."

The combustion process substantially increased in-situ temperature and gas saturation in those sections of the reservoir affected by the burn. Both seismic velocity and density of the reservoir were changed. Zones with altered properties were detected by anomalous amplitude responses in the reflection from the top of the reservoir and from a limestone formation directly below the reservoir. The direction of the combustion propagation and estimates of its volume were based on the interpretation of these anomalies as observed in the difference volumes. The interpretation was supported by data available from monitor wells and postburn coring.

Downloaded 25 Jun 2012 to 95.28.162.50. Redistribution subject to SEG license or copyright; Terms of Use: http://segdl.org/

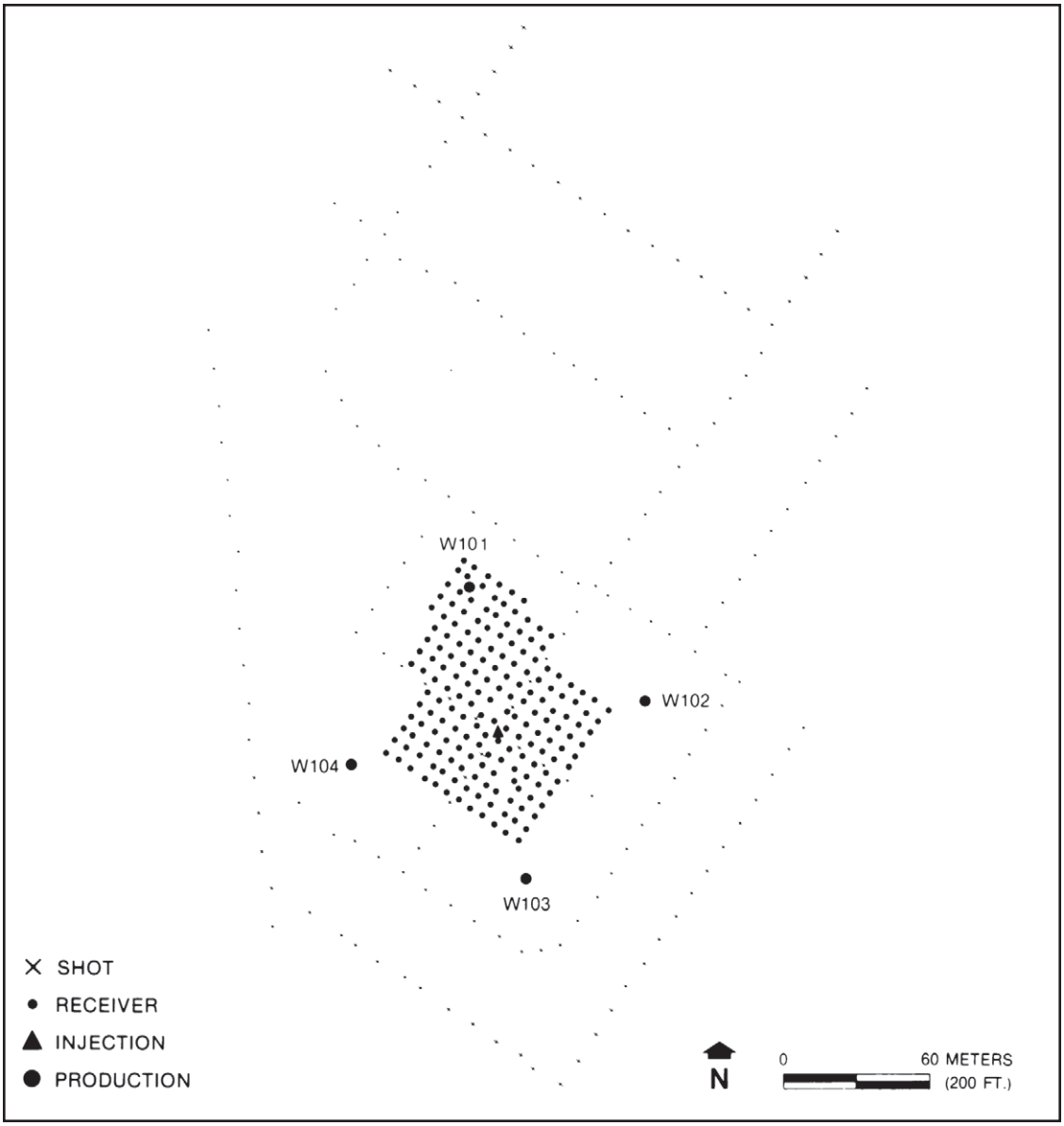

Fig. 14-2-1. 3-D seismic survey shot and receiver geometry with locations of production and injection wells.

Background

Three 3-D seismic surveys were shot over a period of 15 months. The first (preburn) survey was recorded several months previous to ignition of the combustion process. The second (midburn) survey was recorded four months after ignition, and the final (postburn) survey was shot ten months after ignition.

The objectives of the seismic program were to (1) detect a change in seismic reflection character attributable to the combustion process, (2) determine the direction of burnfront propagation, and (3) determine the volume of reservoir swept by the combustion process.

The basic premise was that an increase in gas saturation in the reservoir formation would produce measurable changes in reflection amplitude. Bright spots and dim spots, caused by anomalous gas concentrations, are well-known phenomena in exploration seismology. Increased gas saturation in the parts of the reservoir reached by the combustion process was expected to create bright spots and dim spots in the shadow zone (Sheriff, 1980). The 3-D data would be used to map that progression in time.

The EOR program consisted of a five-well pilot test covering a very small portion of the Holt Field in north-central Texas. The test consisted of four production wells separated by 90 m (300 ft) with a central injection well (Figure 14-2-1). The engineering objective was to propagate the combustion process from the injection well radially outward, creating and flushing an increased oil saturation zone, the oil bank, toward the production wells. Although the concept is simple,

Downloaded 25 Jun 2012 to 95.28.162.50. Redistribution subject to SEG license or copyright; Terms of Use: http://segdl.org/

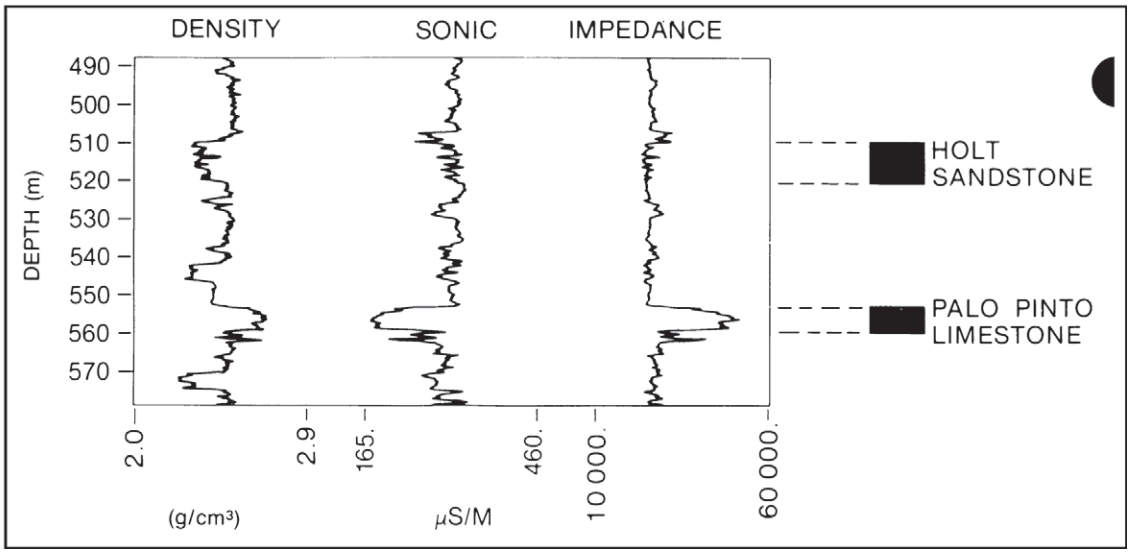

Fig. 14-2-2. Example of sonic and density logs with calculated impedance for the stratigraphic section including the Holt sandstone (reservoir) and the Palo Pinto limestone.

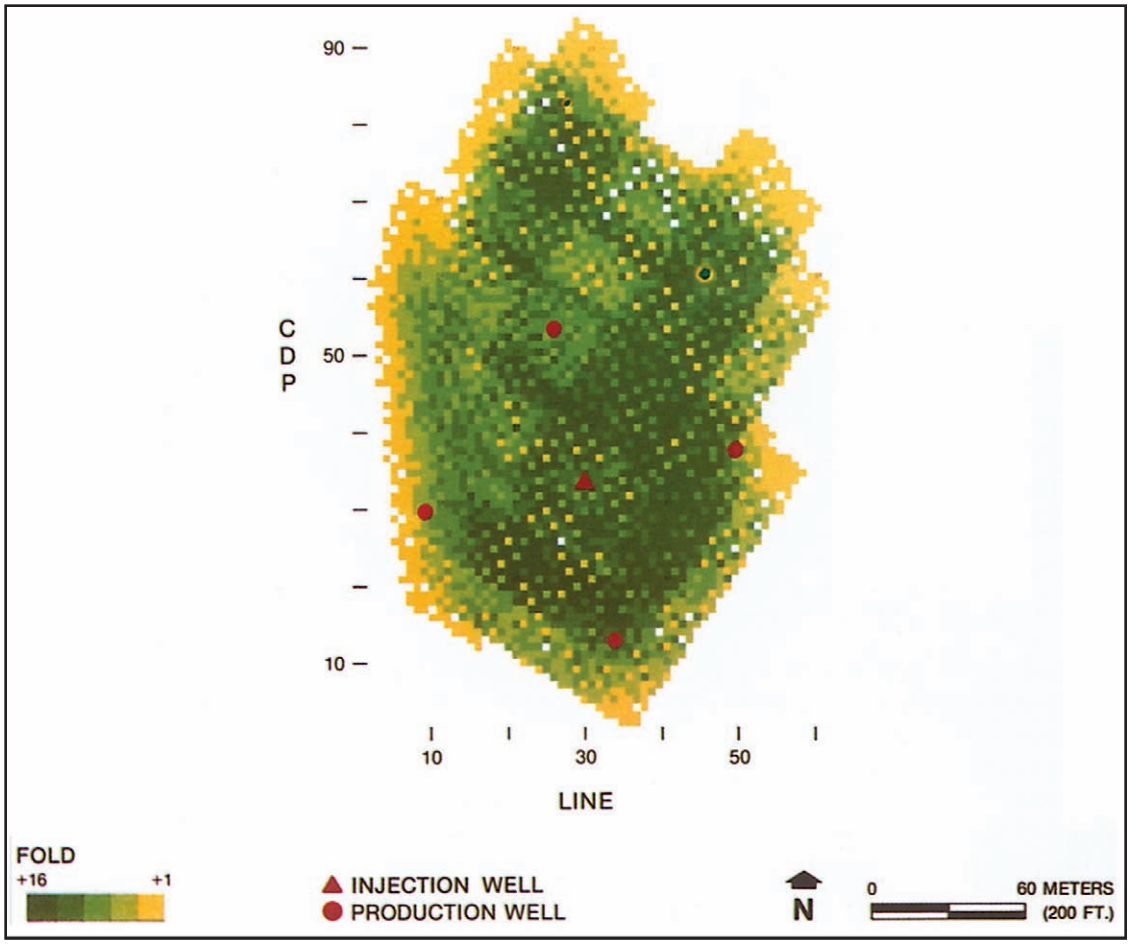

Fig. 14-2-3. CDP fold distribution of the seismic surveys. Each CDP bin covers a 3 × 3 m (10 × 10 ft) area.

the implementation is quite difficult and is very sensitive to the details of the reservoir geology.

The reservoir is the Holt sand, a 12 m (40 ft) thick sandstone capped by a 2.5 m (8 ft) thick limestone encased as a unit in thick shale (Figure 14-2-2). The sand is silty and laced with shale stringers and some calcite cementation zones. In this part of the field, the sand occurs at about 500 m (1650 ft) and dips to the north at 10°. A thin limestone occurs about 45 m (150 ft) below the reservoir and is identified as the Palo Pinto limestone. From extensive core analysis, the horizontal permeability of the sand was found to be several times greater than the vertical permeability. Numerous fractures were observed,

Downloaded 25 Jun 2012 to 95.28.162.50. Redistribution subject to SEG license or copyright; Terms of Use: http://segdl.org/

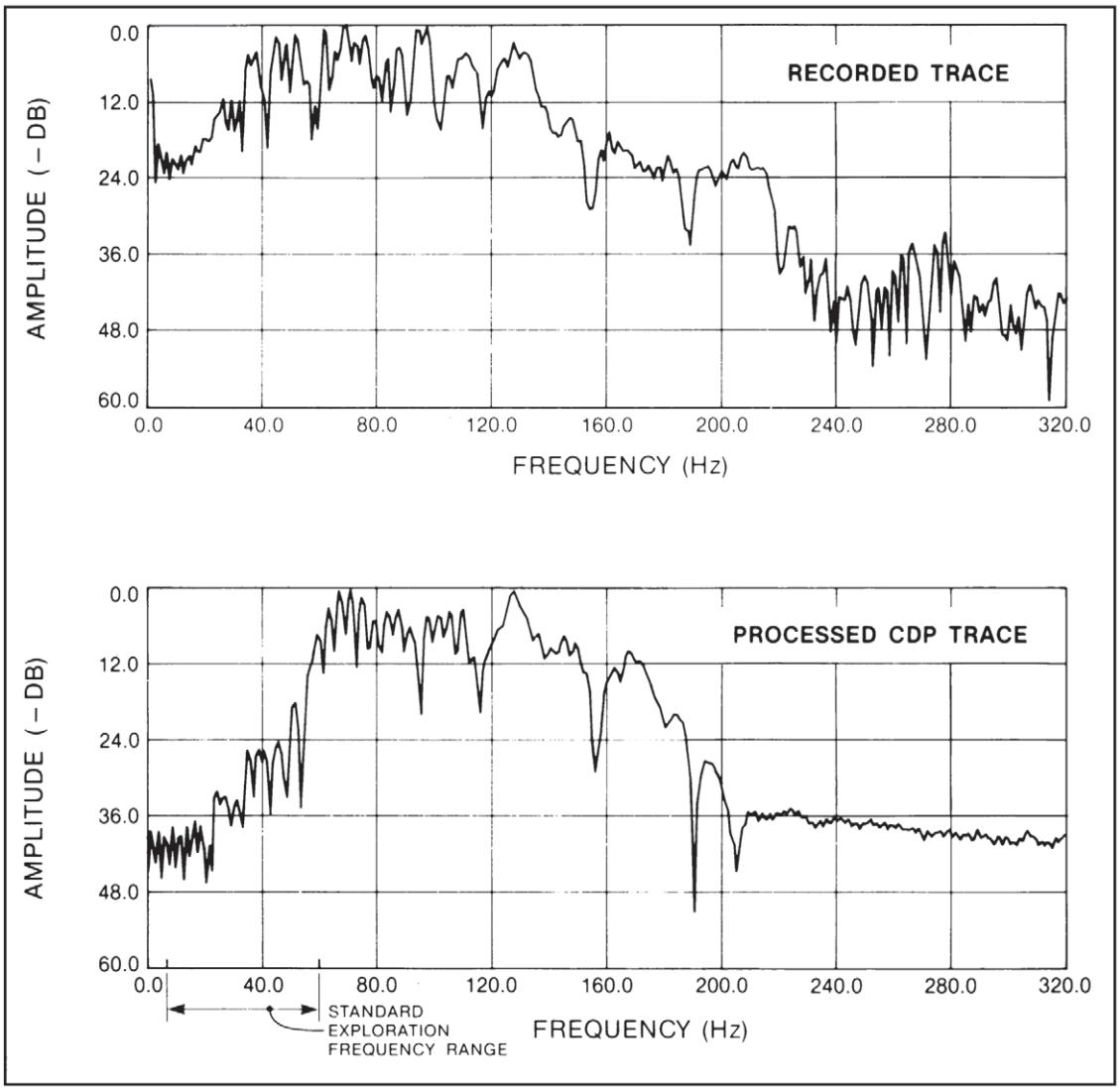

Fig. 14-2-4. An example of the power spectra of a trace before and after processing. The spectra are for the window from 0.350-0.750 s, which includes the reflection sequence from the Holt sandstone to and including the Palo Pinto limestone.

and an average orientation of N27E was measured. Although a detailed model of the reservoir and the burn process was not constructed, some effects of the process were anticipated. The combustion process would primarily propagate updip (to the south) due to the differing fluid densities. Propagation would primarily occur laterally within the reservoir from the initiation points. Vertical propagation would be limited to fractures or other natural permeability pathways. Finally, propagation might be further guided to the southwest along fracture-induced permeability pathways.

Acquisition and Processing

Several factors guided the choices of acquisition parameters:

(1) the target area was very small (90 × 90 m);
(2) the target was relatively shallow (500 m);
(3) the data collection was to be repeated as identically as possible; and
(4) the amplitudes and spatial extents of the seismic anomalies would probably be quite small.

Simple seismic modeling based on well logs and the anticipated effect of increased gas saturation indicated that *detection* of the burnfront would be straightforward. However, very high-resolution seismic data would be required to map the lateral extent of the process and determine the net burn volume. A calculation of the resolution limit was made based on Widess (1973), and the center frequency required to resolve 7.5 m (25 ft) vertically

Downloaded 25 Jun 2012 to 95.28.162.50. Redistribution subject to SEG license or copyright; Terms of Use: http://segdl.org/

was determined to be 100 Hz. The necessary resolution was felt to be achievable, given the shallow depth of the reservoir, if proper acquisition and processing techniques were applied.

The data collection array consisted of a modified 3-D patch geometry. Figure 14-2-1 shows the positions of shotpoints and receiver stations within the test area. This patch style of survey allowed the shot pattern to be arranged as necessary, such that the CDP data were collected with high fold over the area of primary interest (Figure 14-2-3) even though surface access was limited by buildings, wells, pipelines, etc. Furthermore, the geophones could be permanently installed at each receiver location to guarantee that the receiver array would be duplicated in each survey. A modification of the simple patch geometry was made to account for the migration of reflection points updip, by extending shot and receiver locations downdip (to the north).

The receiver group spacing was 6 m (20 ft) with a single high-frequency (40 Hz) marsh geophone comprising each group. Each of the 182 receivers was buried 6 m (20 ft) below the surface. The 165 shotpoints were distributed along crossed lines with a 12 m (40 ft) spacing between individual shots. Each shot consisted of a 2.5 kg (3 lb) dynamite charge buried at 23 m (75 ft). The recording system used was a 192-channel GUS-BUS with sampling interval of 1 ms and band-pass recording filters set a 50 Hz low-cut and 320 Hz antialias. The burial of both shots and receivers improved the signal-to-noise (S/N) ratio of the recorded data by eliminating air-wave noise and substantially reducing the amplitude of the surface-wave noise. The 50 Hz low-cut filter was chosen at this high level to eliminate surface-wave noise further and to preserve the dynamic range of the recording system for digitization of the desired high-frequency signal. For recording shallow reflection seismic data, it is especially important to eliminate surface-wave noise that can seriously degrade the quality of the shallow data window. The small, deeply buried shots, the high-frequency phones and the low-cut filter all combined to eliminate this problem. The resulting frequency range of the recorded data was substantially higher than the range of standard exploration seismic, as shown in Figure 14-2-4, and yet the range retained the minimum two-octave bandwidth considered necessary for high resolution.

The computer processing of the 3-D data sets used a standard sequence designed for 3-D CDP data. Throughout the processing, extra care was taken to retain true relative amplitude and the maximum usable frequency range. The traces were gathered into 3×3 m (10×10 ft) CDP bins. The statics and normal-movement (NMO) corrections were quite small due to the simple geologic structure and small area of the test. For more structurally complex geology, it would have been more difficult to make proper velocity adjustments because the patch geometry has the disadvantages of uneven fold and offset distribution. Three-dimensional surface-consistent statics were computed and were found to be on the order of 2 to 3 ms. Normal-moveout corrections were applied using a datumed root-mean-square (rms) velocity function derived from the well control. Standard spiking deconvolution was applied before stack. A phaseless deconvolution technique was applied to balance further the usable spectrum of each stacked trace. In the final processing step, the data were migrated using an *f-k* migration algorithm and the velocity function derived from the sonic logs. This approach to migration was deemed adequate, given the localized area of interest and the simple velocity structure. The frequency spectrum of a fully processed trace, windowed in the reflection zone of interest, indicates that the 40-180 Hz bandwidth of the recorded data was enhanced during processing and the center frequency of 100 Hz was obtained (Figure 14-2-4).

As postprocessing steps, the data were properly phase-corrected using well control, and the seismic attributes were calculated for each data set. To remove the geologic structure from the reflectors of interest, static adjustments were made, thereby allowing horizon views to be sliced from the 3-D data volume. Finally, in a unique step, the preburn horizon envelope amplitude at each level of interest was subtracted from the corresponding values in the midburn and postburn data volumes. The preburn data were used as the baseline seismic expression relative to which change was observed. Anomalies in the difference volumes were then interpreted directly.

Downloaded 25 Jun 2012 to 95.28.162.50. Redistribution subject to SEG license or copyright; Terms of Use: http://segdl.org/

Observed Anomalies—Bright Spots

Comparison of the envelope amplitudes of the reflection event at the top of the Holt sand reservoir revealed an increase in amplitude, a bright spot, which developed after the combustion process was initiated. In Figure 14-2-5, a north-south section, line 14, is shown as it appeared at preburn, midburn, and postburn times. The reflection from the top of the Holt sand is identified as a trough occurring at about 385 ms. At this horizon, the envelope amplitudes at preburn time compared to midburn time show a zone of increased amplitude near well W104, with maximum change between CDP 16 and CDP 30. By postburn time, the bright spot had increased in lateral extent from CDP 16 to CDP 36, but it had not increased in maximum amplitude relative to midburn time.

Horizon slices at the top of the Holt sand, from the envelope amplitude difference volumes, are displayed in Figure 14-2-6. The midburn difference shows a positive amplitude anomaly in the southwestern side of the data. This corresponds to the bright spot development observed in line 14 (Figure 14-2-5) at midburn time. Another, smaller bright spot is located to the southeast of the injection well at line 43, CDP 21. The difference amplitude at postburn time, Figure 14-2-6, shows that the bright spot has grown to cover most of the area within the production wells, the midburn peak to the southwest has shifted downdip toward well W104, and the maximum amplitude of the difference anomaly has increased by about 10 percent.

Observed Anomalies — Dim Spots

The strong reflection centered at 410 ms in line 14 (Figure 14-2-5) is identified as the Palo Pinto limestone. In line 14, a slight decrease in envelope amplitude occurs in the shadow of the bright spot centered around CDP 22. At midburn time, the decrease in amplitude is about 10 percent, but by postburn time, the decrease is nearly 25 percent, as marked by the change from deep orange and red shading to yellow.

A similar display of another north-south section, line 33, in Figure 14-2-7, shows a more substantial dim spot. This anomaly does not coincide with any bright spot at the Holt level at midburn time and only a modest Holt bright spot at postburn time. The dim-spot anomaly, pointed out by the arrows within the figure, is also stronger at midburn time than at postburn time. This lack of spatial coincidence (between bright and dim spots) is important in the interpretation of the results as described below.

The horizon slice difference section at the Palo Pinto reflection (Figure 14-2-8) clearly shows this anomaly. The dim spot at midburn time covers much of the pilot area with two negative-amplitude anomalies. One peak is located at the injection well, but the stronger peak lies about 30 m (100 ft) south-southwest of the injection well. The anomalies do not coincide with bright spots in the Holt reflection. A lower amplitude lobe of the dim spot extending to the southwest edge of the data does correlate with the maximum bright spot observed at midburn time. The dim spot observed at postburn time is lower in amplitude and extends over a significantly smaller portion of the pilot area. The two peaks of the midburn anomaly have merged into a ridge extending approximately southwest-northeast across the injection well with the larger area and peak of the anomaly to the southwest of the injection well.

Interpretation — Combustion Model

A simple model of the in-situ combustion process, based on combustion tube experiments, was described by Tadema (1959). The combustion process within the reservoir can be divided into various zones, with each zone defined by its relative temperature and fluid saturations. The "combustion zone" propagates through the reservoir and is defined by maximum oxidation of the heaviest, or immobile, hydrocarbons. In its wake is left the "clean-burnt sand," a hot reservoir matrix with high gas saturation. Ahead of the combustion zone are several zones at lower temperatures and with distinctive percentages of oil, water, and gases until at some distance the original reservoir temperature and fluid mixture are encountered. Of particular interest are (1) that the clean-burnt sand zone has been subjected to very high temperatures, and (2) that combustion gas, as well as some injection gas, are forced ahead of the combustion zone. If this model were expanded into three dimensions, it would consist of a series of concentric rings which propagate radially from the injection well. The model is quite simple and does not at all account for geologic complexities, but it is useful as a starting point for the interpretation of the seismic anomalies in terms of the physical process of in-situ combustion.

Generalizing this model to the Holt sand reservoir, it is important to point out that the Holt sand reservoir, at the initiation of the burn, had little to no gas saturation.

Downloaded 25 Jun 2012 to 95.28.162.50. Redistribution subject to SEG license or copyright; Terms of Use: http://segdl.org/

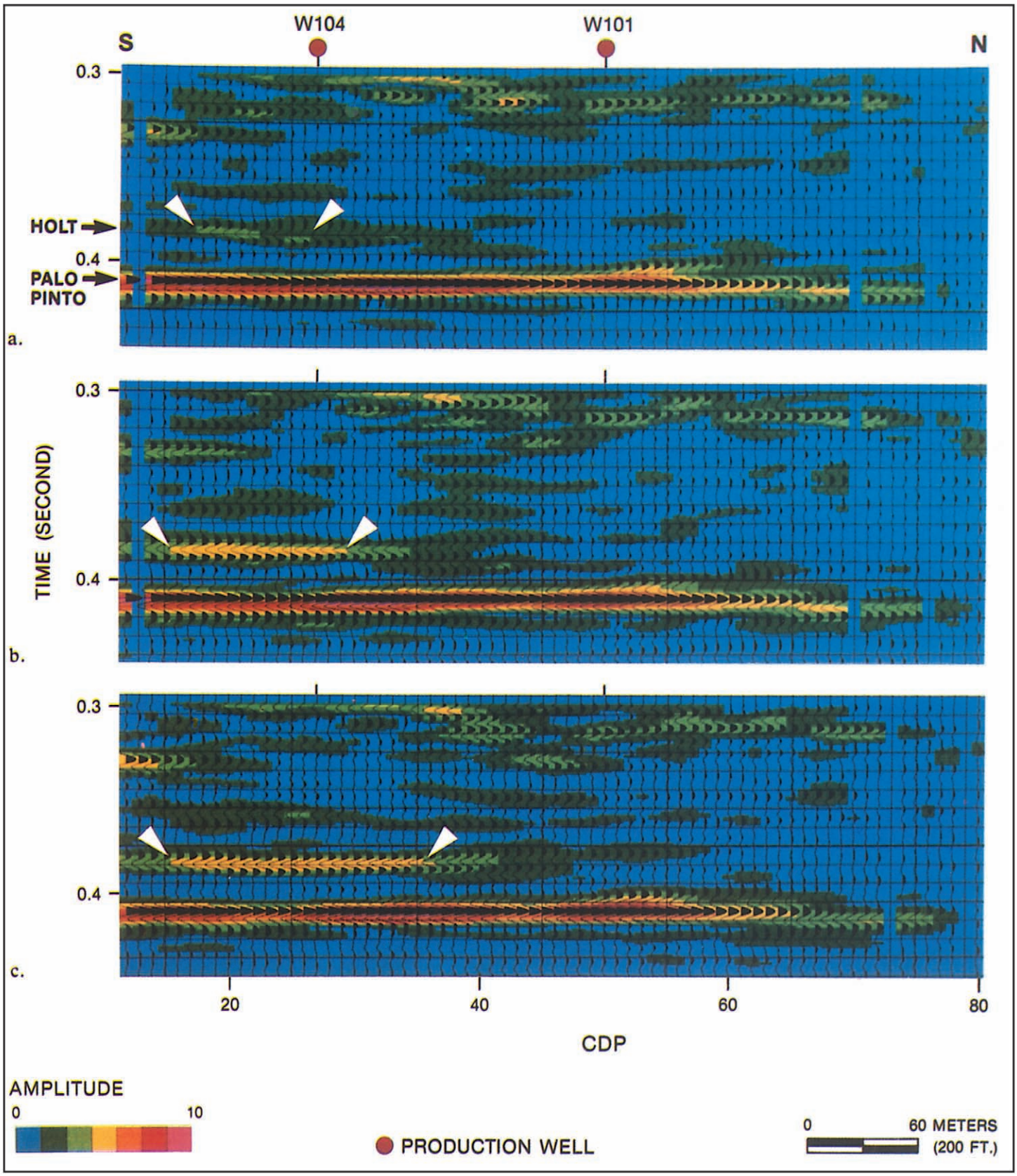

Fig. 14-2-5. Line 14, from (a) preburn, (b) midburn, and (c) postburn 3-D seismic data volumes. The reflection wiggle traces are overlain by a color scale of the calculated envelope amplitude. Dip was removed by static shifts before display. A bright spot was created (see arrows) at the top of the Holt sandstone by midburn time (b), and it increases in extent by postburn time (c). A dim spot in the reflection from the Palo Pinto limestone formed just below the peak of the bright spot.

Downloaded 25 Jun 2012 to 95.28.162.50. Redistribution subject to SEG license or copyright; Terms of Use: http://segdl.org/

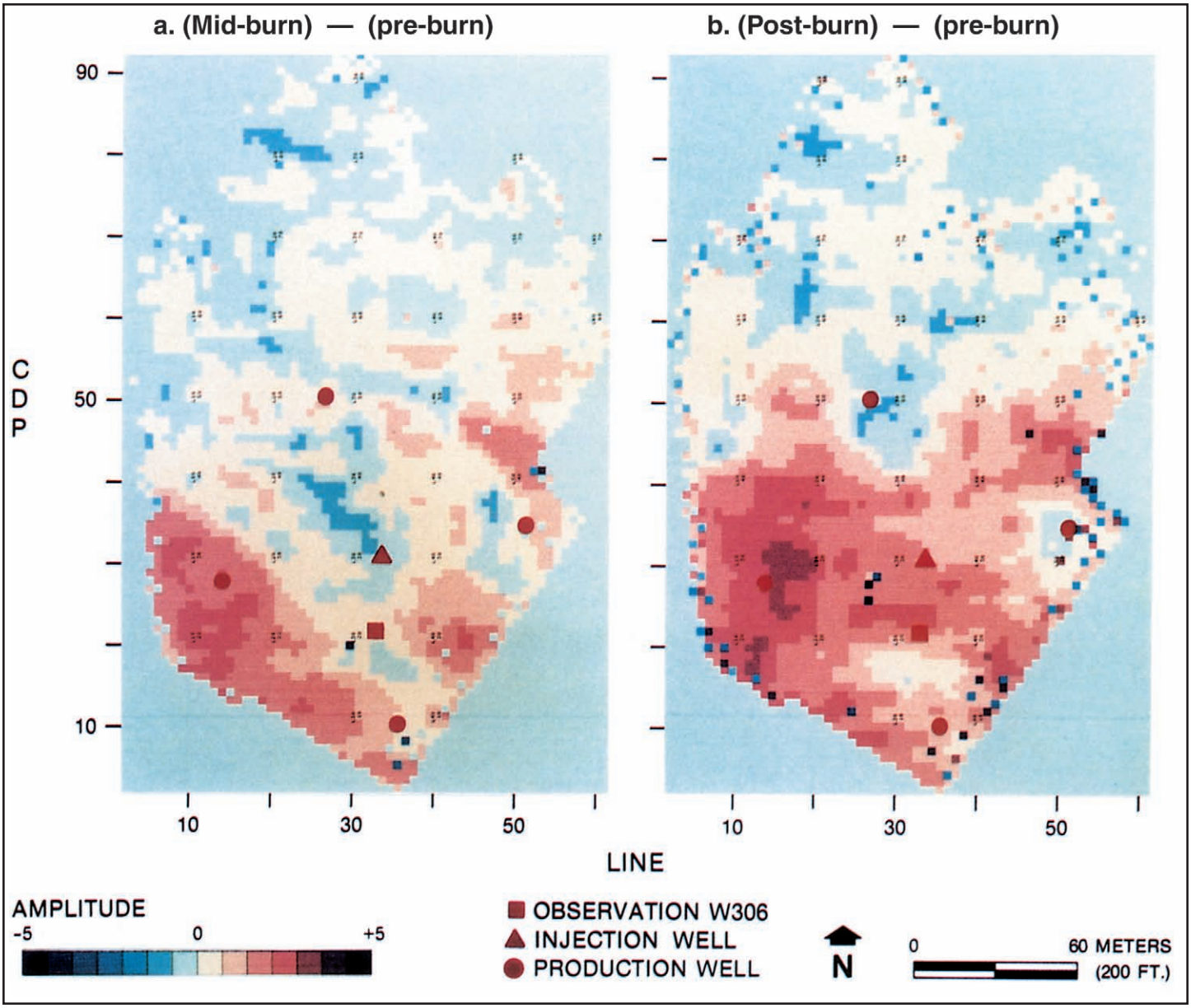

Fig. 14-2-6. The difference in envelope amplitude at the top of the Holt sandstone (0.385 s) displayed in horizon slice form. Bright spots occur as positive anomalies. Well locations are marked for position in the subsurface at the top of the Holt sandstone.

Interpretation — Detection

As stated, the first objective of the seismic program was to detect a change in reflection character attributable to the combustion process. The bright spots and dim spots are considered true combustion-caused anomalies for the following reasons. First, the changes do occur in the reflection from the reservoir and the reflection just below it, as expected. Searches through the difference data volumes substantially above and below the reservoir reflection showed no extended coherent anomalies. Second, the background noise level of the difference data volumes is substantially lower than the observed anomalies. Figures 14-2-6 and 14-2-8 show this by the amplitudes to the north of the injection well. Most importantly, the seismic anomalies were confirmed by well-log and core data. At the time postburn seismic data were collected, several cores and logs through the burned zone were collected.

In Figure 14-2-9, density and sonic traveltime logs showing the reservoir sand from a preburn observation well, W306, are compared to similar logs collected in two postburn boreholes. Within the zones of clean-burnt sand, the logs show substantial decreases in both density and velocity.

Downloaded 25 Jun 2012 to 95.28.162.50. Redistribution subject to SEG license or copyright; Terms of Use: http://segdl.org/

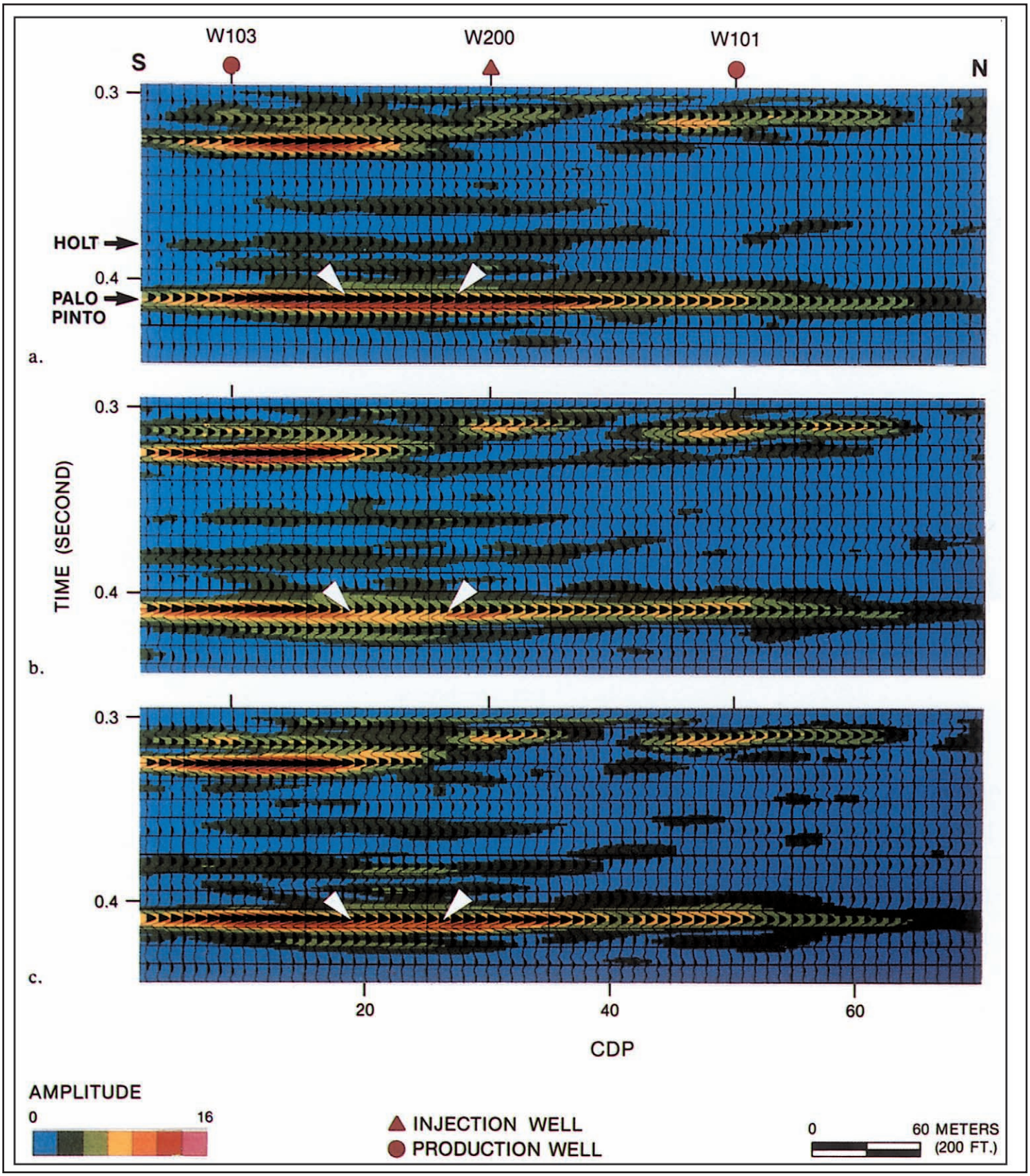

Fig. 14-2-7. Line 33, from (a) preburn, (b) midburn, and (c) postburn 3-D seismic data volumes. The reflection wiggle traces are overlain by a color scale of the calculated envelope amplitude. Dip was removed by static shifts before display. A dim spot was created (see arrows) in the Palo Pinto reflection (0.410 s) by midburn (b), but it decreases somewhat by postburn (c).

Downloaded 25 Jun 2012 to 95.28.162.50. Redistribution subject to SEG license or copyright; Terms of Use: http://segdl.org/

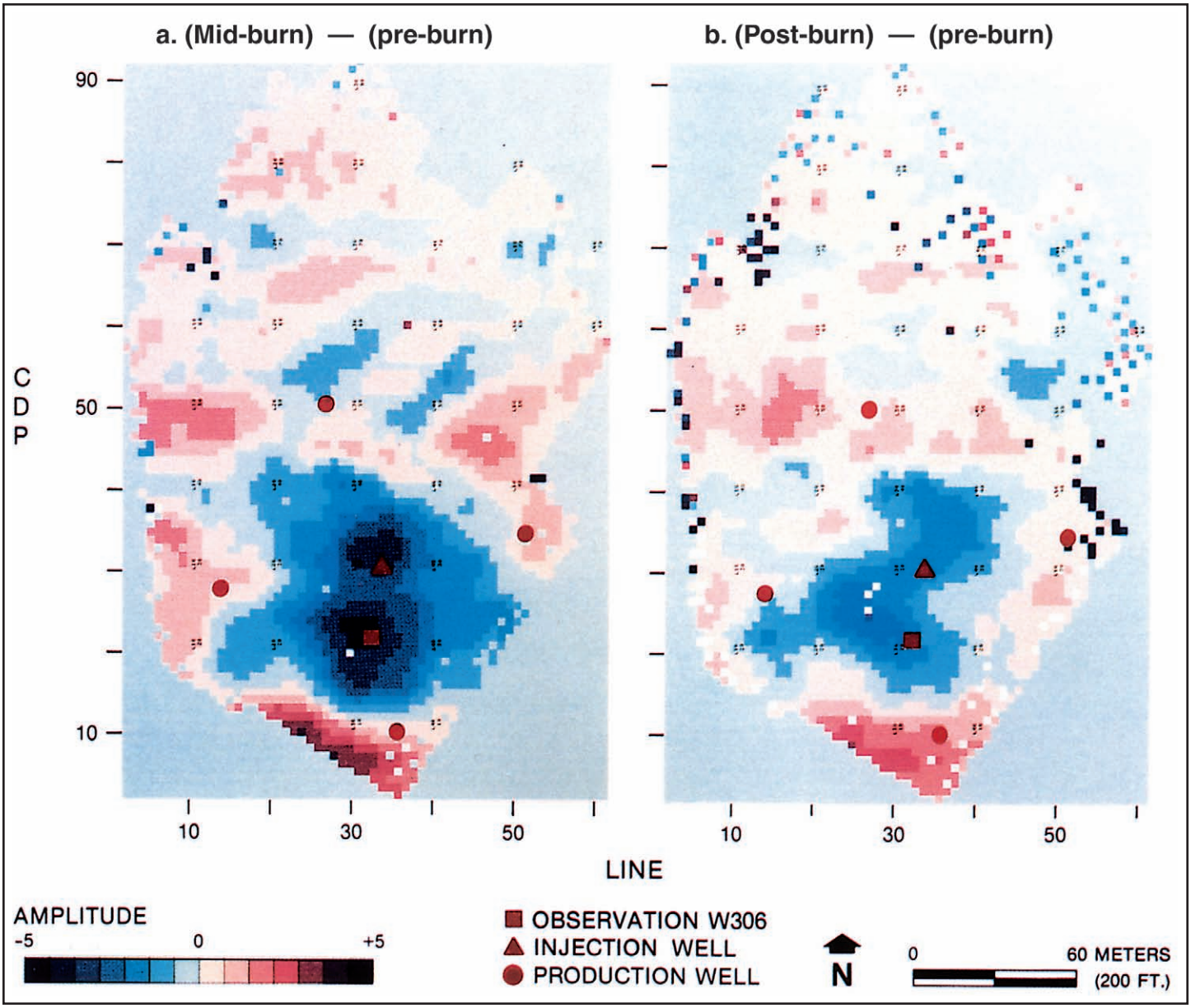

Fig. 14-2-8. The difference in envelope amplitude at the Palo Pinto reflection (0.410 s) displayed in horizon slice form. Dim spots occur as negative anomalies. Well locations are marked for position in the subsurface at the top of the Holt sandstone.

The combustion process was expected to increase the gas saturation with consequent changes in density and velocity. Comparison of log density values showed decreased density in burned zones averaging about 5 percent. This density decrease can be fully accounted for by a change from 100 percent fluid-filled pores to partial gas saturation. The sonic-log velocities measured in burned zones decreased 15 percent to 35 percent, averaging 25 percent. This decrease in velocity is much greater than can be accounted for by increased gas saturation in the original pore space.

Ultrasonic measurements made on preburn core showed a 3 to 4 percent decrease in velocity, going from 100 percent water saturation to 100 percent gas saturation. Although this is a smaller decrease than that reported by Domenico (1976), a similar result was reported by Frisillo and Stewart (1980). In our case, the larger effect on velocity was due to permanent alteration of the rock matrix by the very high formation temperatures. Ultrasonic measurements showed a 25 percent decrease in velocity for cores heated to 700°F. The velocity decrease may be due to weakening of the rock by oxidation of organics and an alteration of clays. Therefore, the observed velocity decrease is the combined effect of changes in fluid saturation and of damage to the rock matrix.

Downloaded 25 Jun 2012 to 95.28.162.50. Redistribution subject to SEG license or copyright; Terms of Use: http://segdl.org/

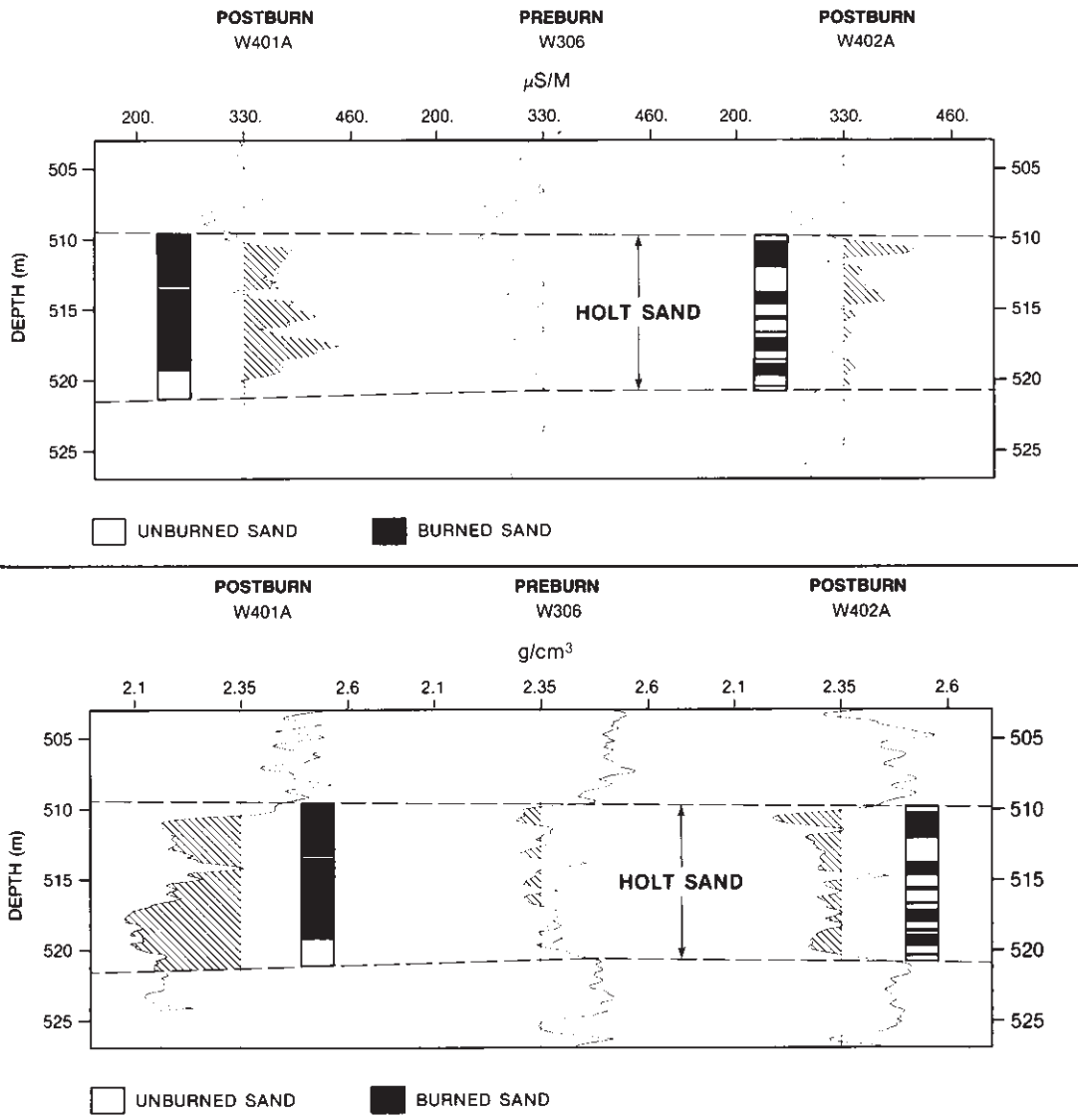

Fig. 14-2-9. Comparison of sonic traveltime logs (above) and density logs (below) from preburn well W306 and postburn core wells W401A and W402A.

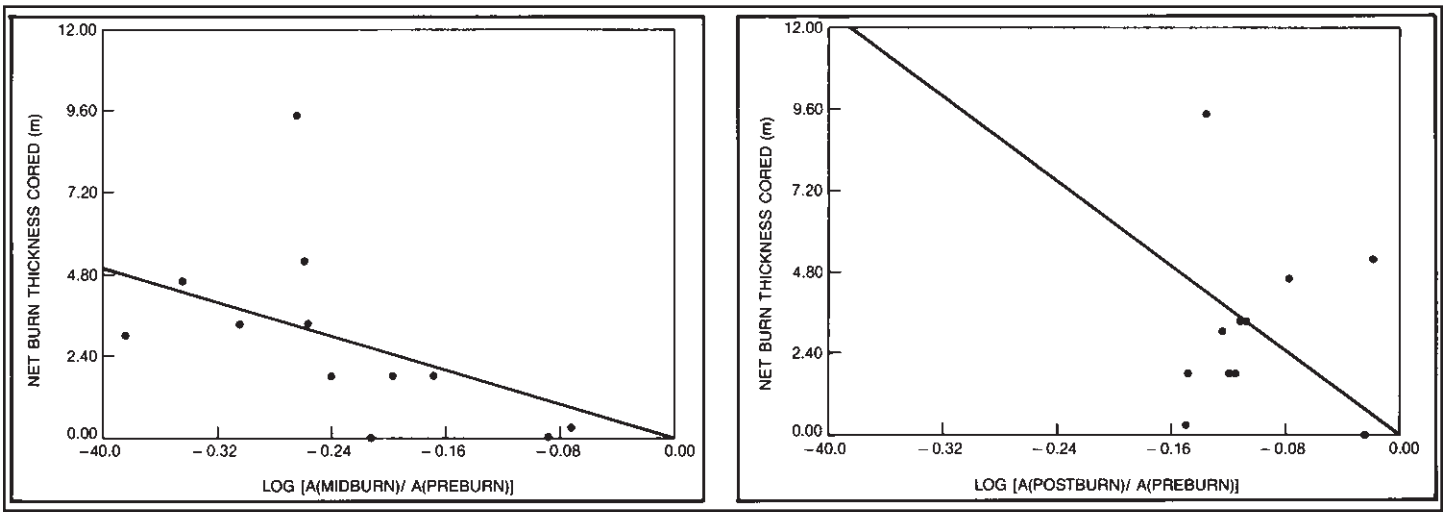

Fig. 14-2-10. Net burn thickness from postburn cores versus natural logarithm of the ratio of midburn (left) and postburn (right) to preburn dim-spot (Palo Pinto) amplitude. The line is a least-squares fit to the data points.

Downloaded 25 Jun 2012 to 95.28.162.50. Redistribution subject to SEG license or copyright; Terms of Use: http://segdl.org/

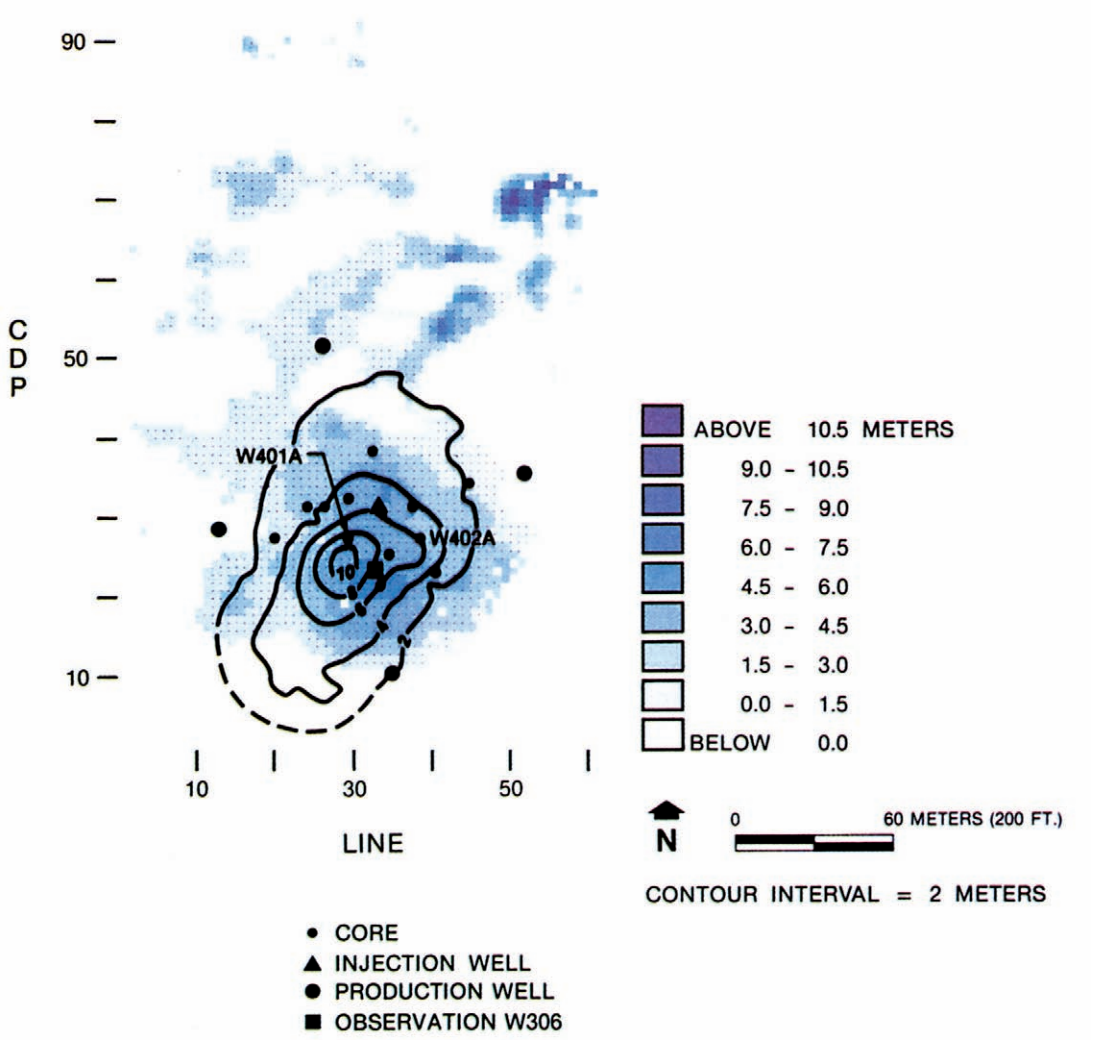

Fig. 14-2-11. Burn thickness calculated from midburn dim-spot amplitudes using equation (2) and the slope of the line in Figure 14-2-10 (left) for the calibration constant. Overlain is a line contour map of net burn thickness observed in cores.

The effect of increasing gas saturation on the seismic response is a nonlinear relation. As shown by Domenico (1974), it is the first few percentage increases in gas saturation (up to about 10 percent) that affect the seismic impedance the most. Further increases in gas saturation change the impedance very little. Therefore, if combustion gas is forced ahead of the burn zone in sufficient volume to increase gas saturation even a few percent, what is observed as a bright spot is both the clean-burnt zone and the zones ahead of the combustion point reached by steam and combustion gas.

Certainly the phenomenon of attenuation is even more complex. Similar to seismic impedance, it is the initial change from 100 percent water saturation that increases the attenuation substantially. However, unlike impedance, attenuation decreases as the rock reaches 100 percent gas saturation (Frisillo and Stewart, 1980). Therefore, in the initial stages of the process, the dim spot will reflect both the clean-burnt zone and the zone reached by combustion gases. However, as 100 percent gas saturation is reached, the dim spot will more likely be an indication of just the clean-burnt zone.

Interpretation — Propagation

Interpretation of the positions of the bright-spot and dim-spot anomalies over calendar time provides a reasonable description of the combustion propagation. First, it is quite clear from Figure 14-2-8 that the area around well W101 (to the north of the injection well) was not affected by the combustion process. This well was the only production well in which large quantities of gases were not observed. Therefore, this well was either too far downdip to be reached by the combustion process or was isolated by permeability barriers. One can

Downloaded 25 Jun 2012 to 95.28.162.50. Redistribution subject to SEG license or copyright; Terms of Use: http://segdl.org/

also see from Figure 14-2-8 that the process did propagate to the southwest of the injection well, probably guided by the fracture system. The location of the strongest dim spot at midburn time shown in Figure 14-2-8 was verified by an observation well W306, which recorded the highest formation temperature at the time of the midburn survey.

The postburn dim spot decreased in amplitude and lateral extent compared to midburn time. It appears that the combustion process reached its maximum lateral propagation within the production area by midburn time or soon after. In a full-scale EOR project, this knowledge would be crucial in adjusting the program to sweep the reservoir more efficiently.

Although the midburn bright spot (Figure 14-2-6) also shows that the process moved to the southwest, it does not extend back to the injection well. Therefore, the combustion gas most likely propagated laterally within the reservoir until it encountered a vertical permeability pathway which allowed the gas to stream to the top of the reservoir. Once established, this pathway also allowed the burn to move to the top of the reservoir. Up to that point, the successful part of the burn was contained in the middle of the reservoir.

The postburn bright spot (Figure 14-2-6) increased in area from midburn time. A major fault (providing the southern closure to the field) is located approximately 300 m (1000 ft) to the south of the test. This fault probably blocked further southward propagation of the combustion gases, forcing them back along the top of the reservoir toward the injection well. If sustained injection of gas from midburn to postburn time had continued to fuel the combustion process, that process would have moved out beyond the production area and the area of seismic coverage.

Burn Volume

The final objective of this study was to estimate the volume of reservoir swept by the combustion process. Although the data do not have the spatial resolution to map the detailed distribution of the process, we have attempted to interpret the decreased amplitudes in the Palo Pinto reflection as estimates of burn thickness. The mechanisms of the attenuation are not separable, but several factors are certainly important: pore fluid state and interaction with the rock matrix, formation temperature, matrix velocity and density, and the increased reflectivity due to gas saturation in the reservoir.

A simple mathematical approach was chosen (after Waters, 1978) in which amplitude is expressed as

$$A = A_o e^{-\alpha z}, \tag{1}$$

where A_o is the initial amplitude of the propagating wavelet, α is the attenuation parameter, and z is the propagation distance. If two seismic waves are considered identical except that one has passed through a zone Δz where the attenuation is different, then the reflection amplitude from a level past the zone of attenuation can be compared directly to find Δz. For this study, observed seismic waves are the before-burn and after-burn data traces, and Δz is the estimate of burn thickness. After taking the natural logarithms and accounting for two-way propagation, the equation becomes the linear relation

$$\Delta z = \frac{1}{2(\alpha_B - \alpha_A)} \ln\left(\frac{A_A}{A_B}\right). \tag{2}$$

The reservoir was cored in twelve locations within the test pattern at postburn time. The cores confirmed that the burn had occurred in somewhat vertically isolated zones within the reservoir. The net burn thickness observed in each core was compared to the logarithm of the ratio for appropriate seismic amplitudes at the CDPs corresponding to the bottom-hole location of each core. Figure 14-2-10 shows the comparison of net burn thickness to the logarithm of midburn amplitude over preburn amplitude, and also the same relationship for postburn data. Using least-squares estimation, lines were fitted through the data points and forced through the origin. The slope of either of these lines could be used in equation (2) to estimate burn thickness at all other CDPs. Since the midburn data appeared to fit

Downloaded 25 Jun 2012 to 95.28.162.50. Redistribution subject to SEG license or copyright; Terms of Use: http://segdl.org/

the simple model better, the midburn data were used to estimate burn thickness. This reemphasizes the belief that burn propagation, at least within the production area, had ceased by midburn time. The postburn dim spot is more likely a map of formation damage only, suggesting that a more complicated model is needed to explain the attenuation due to alteration of the rock fabric.

Using the slope of the midburn line in Figure 14-2-10 and equation (2), the midburn data were converted to an estimate of net burn thickness (Figure 14-2-11). Overlain on that estimate is a computer-generated contour map based on core data. A good correlation is observed, and the correlation could have been even better if there had been core data to the southwest. This also implies that even without the core data for calibration, a good estimate of relative burn thickness could have been made using only the seismic data. The observation of seismic attenuation is a useful approach in mapping certain recovery processes. Resolution could be improved utilizing borehole-to-borehole techniques.

Conclusions

Reflection seismic surveying can be used to monitor the progress of some EOR processes. In this case study, a fireflood process was detected, its propagation direction and extent were determined, and an estimate of net burn volume was made.

The 3-D seismic data detected the burn zone and showed that the gas propagated predominately updip to the southwest. A dim spot observed in a reflector just below the reservoir level was interpreted as a map of areal extent of the burned zone. A region of maximum net burn thickness was located about 30 m (100 ft) from the initiation point of the burn. Comparison of the midburn and postburn dim spots led to the conclusion that the majority of the reservoir swept by the combustion process occurred in the first few months after ignition. The shape, orientation, and volume of the burn interpreted from the seismic data were confirmed by temperature monitor wells and postburn coring.

It was concluded that the attenuation increase, due to high-temperature alterations of the reservoir rock and pore fluid changes, was the best seismic indicator of the combustion process.

The subtraction of the baseline (preburn) data from the midburn and postburn data for interpretation of dynamic anomalies proved to be a very powerful technique. The subtraction has great potential for detecting anomalous seismic response related to active reservoir processes.

Acknowledgments

The authors would like to thank ARCO Oil and Gas Company for allowing us to publish these results. Production Engineering Research provided the financial support for this project. In Geophysical Support, L. F. Konty and D. R. Paschal were instrumental in survey planning. L. J. Hix and P. W. Wise added their expertise in data acquisition. Data processing was designed by R. Chen and S. A. Svatek. M. L. Batzle made the petrophysical measurements on core samples and provided core descriptions. J. D. Robertson contributed support and ideas during the interpretation of the data sets.

References

Domenico, S. N., 1974, Effect of water saturation on seismic reflectivity of sand reservoir encased in shale: Geophysics, v. 39, p. 759-769.

Domenico, S. N., 1976, Effect of brine-gas mixture on velocity in an unconsolidated sand reservoir: Geophysics, v. 41, p. 882-894.

Frisillo, A. L., and T. J. Stewart, 1980, Effect of partial gas/brine saturation on ultrasonic absorption in sandstone: Journal of Geophysical Research, v. 85, p. 5209-5211.

Sheriff, R. E., 1980, Seismic stratigraphy: Boston, Massachusetts, International Human Resources Development Corporation, p. 185-198.

Tadema, H. J., 1959, Mechanism of oil production by underground combustion: Proceedings, 5th World Petroleum Congress, Section 11, p. 279-287.

Taner, M. T., and R. E. Sheriff, 1977, Applications of amplitude frequency, and other attributes to stratigraphic and hydrocarbon determination: AAPG Memoir 26, p. 301-302.

Waters, K. H., 1978, Reflection seismology: John Wiley and Sons, p. 203-207.

Widess, M. B., 1973, How thin is a thin bed?: Geophysics, v. 38, p. 1176-1180.

Downloaded 25 Jun 2012 to 95.28.162.50. Redistribution subject to SEG license or copyright; Terms of Use: http://segdl.org/

Case History 3

Impact of 3-D Seismic on Structural Interpretation at Prospect Cougar

C. J. McCarthy, P. W. Bilinski, Shell Offshore, Inc.

Introduction

Prospect Cougar (South Timbalier 300 Field) is an oil and gas field located in 104 m (340 ft) of water, 105 km (65 mi) south of the Louisiana shore (Figure 14-3-1). Blocks S.T. 299, 300, and 301 were acquired by Shell in 1981, 1979, and 1977, respectively.

Cougar was one of Shell's first fields to be covered by a 3-D seismic survey. Its position near the beginning of our 3-D learning curve, combined with the complex structure of the field, provides an interesting illustration of the impact 3-D seismic interpretation can have on the understanding of a field's geology. The evolution of our understanding of Cougar's structure, and the impact of seismic interpretation techniques on that understanding are reviewed here.

Geology

Prospect Cougar is situated in a salt-controlled basin, downthrown to a major down-to-the-south growth fault. Hydrocarbons are trapped in an anticline formed above a salt wing.

Two sands, the B and C, account for nearly all field reserves. We will concentrate exclusively on the B Sand. The B Sand is a thinly-bedded, cyclic stack of graded sand, silt, and mudstone, deposited by dilute turbidity currents. The sand package blankets the field. Gross thickness of the package averages 50 m (160 ft). Rock properties are such that there is little or no reflection where the B Sand is wet; the presence of hydrocarbons produces a strong bright spot.

3-D Seismic

A 3-D seismic survey was acquired by Shell in 1980 (Figure 14-3-1). An area of 78 sq km (30 sq mi) was covered with an inline subsurface point spacing of 15 m (50 ft) and a line spacing of 45 m (150 ft). The total migrated area at objective depths was 26 sq km (10 sq mi).

Structural Interpretation

The structural interpretation developed for lease sale is shown in Figure 14-3-2. The map is based on a coarse, irregular grid of 2-D seismic of various vintages. The play was for turbidite sands trapped in a mildly faulted anticline. Based on this interpretation, Shell made a successful bid of $6 million for S.T. 301.

Additional 2-D seismic was acquired in support of subsequent lease sales involving blocks S.T. 299 and 300. At the time (1980), we recognized that the bright spot did not fit structure. A model of a blanket turbidite sand cut by shale-filled channels was developed to explain the amplitude pattern. The essentially unfaulted interpretation is shown in Figure 14-3-3.

After successful bids for blocks S.T. 299 ($10.8 million) and 300 ($54.8 million), the 3-D seismic survey described above was acquired to assist in developing this complex stratigraphic field. New amplitude measurements provided a detailed picture of hydrocarbon distribution. A new structural interpretation was made using paper sections on a relatively coarse (230 m or 750 ft) grid. This interpretation, combined with early development drilling, indicated that faulting was more important than previously supposed. However, the bright spots still did not fit structure (Figure 14-3-4), so stratigraphy was assumed to play a major role in controlling hydrocarbon distribution.

At that point (1983), Shell had completed development of a photographic film-based 3-D interpretation system. Although primitive by today's standards, the system allowed digitized picking from enlarged profile displays and had "movie" capabilities in both vertical section and time slice orientations. Bookkeeping features of the system finally

Downloaded 25 Jun 2012 to 95.28.162.50. Redistribution subject to SEG license or copyright; Terms of Use: http://segdl.org/

made it feasible to interpret every line and crossline in the survey. The tight spatial grid provided by the 3-D survey enabled us to map small offsets and amplitude "glitches" which had been ignored on coarser interpretation grids.

The resulting structure map (Figure 14-3-5) shows a much more complex fault pattern. Faults were recognized as controlling hydrocarbon distribution in all but one instance. The cyclic nature of the B Sand and its high shale content make even 3-m (10-ft) faults potential seals. Because the gross thickness of the hydrocarbon column in the B Sand is generally at or below tuning thickness (35 m or 120 ft), local thinning of the hydrocarbon column associated with normal faulting produces observable amplitude decreases. These amplitude anomalies form linear patterns that often connect with actual event time offsets; in other words, they act like faults.

The fault density shown in Figure 14-3-5 was so high that it met with some disbelief. It certainly had a major impact on development strategy. Development drilling is now complete and as many as 4 years of production data are available for some wells. Production data suggested that some reservoirs were draining areas less than shown on Figure 14-3-5, prompting reexamination of the 3-D data. The 3-D seismic data have now been reprocessed and reinterpreted using a modern workstation and results from over 60 wells (including sidetracks). Our current structure map (Figure 14-3-6) shows even more faults than Figure 14-3-5. Drilling has confirmed faults picked on seismic with throws as small as 10 m (30 ft). Faults with throws of 15 m (50 ft) can be picked very reliably on seismic.

Conclusions

Three-dimensional seismic surveying has played a central role in shaping our understanding of Prospect Cougar. The field has gone from a simple, purely structural trap, to a complex stratigraphic trap, to an even more complex structural trap. The tight spatial sampling and proper imaging provided by 3-D have been the keys to unraveling the story. The tools and time available to the seismic interpreter have also had a major impact on our understanding of the field.

As a result of the detailed structural picture provided by the 3-D survey, a costly waterflood program was determined to have little chance of success and consequently was dropped. Reexamination of the seismic data after development drilling has clarified why some wells produced as expected while others declined more rapidly than anticipated, and has provided support for new drilling and workover proposals.

Acknowledgments

The authors wish to thank Shell Offshore, Inc. and Shell Oil Company for permission to publish this material. Obviously, the interpretations described here are the work of many individuals in both exploration and production, too numerous to mention here. Our passage up the learning curve with 3-D came largely as the result of a synergistic effort among geologists, geophysicists, and programmers, all trying to get a job done under both time and technology constraints.

Figures begin on page 486.

Downloaded 25 Jun 2012 to 95.28.162.50. Redistribution subject to SEG license or copyright; Terms of Use: http://segdl.org/

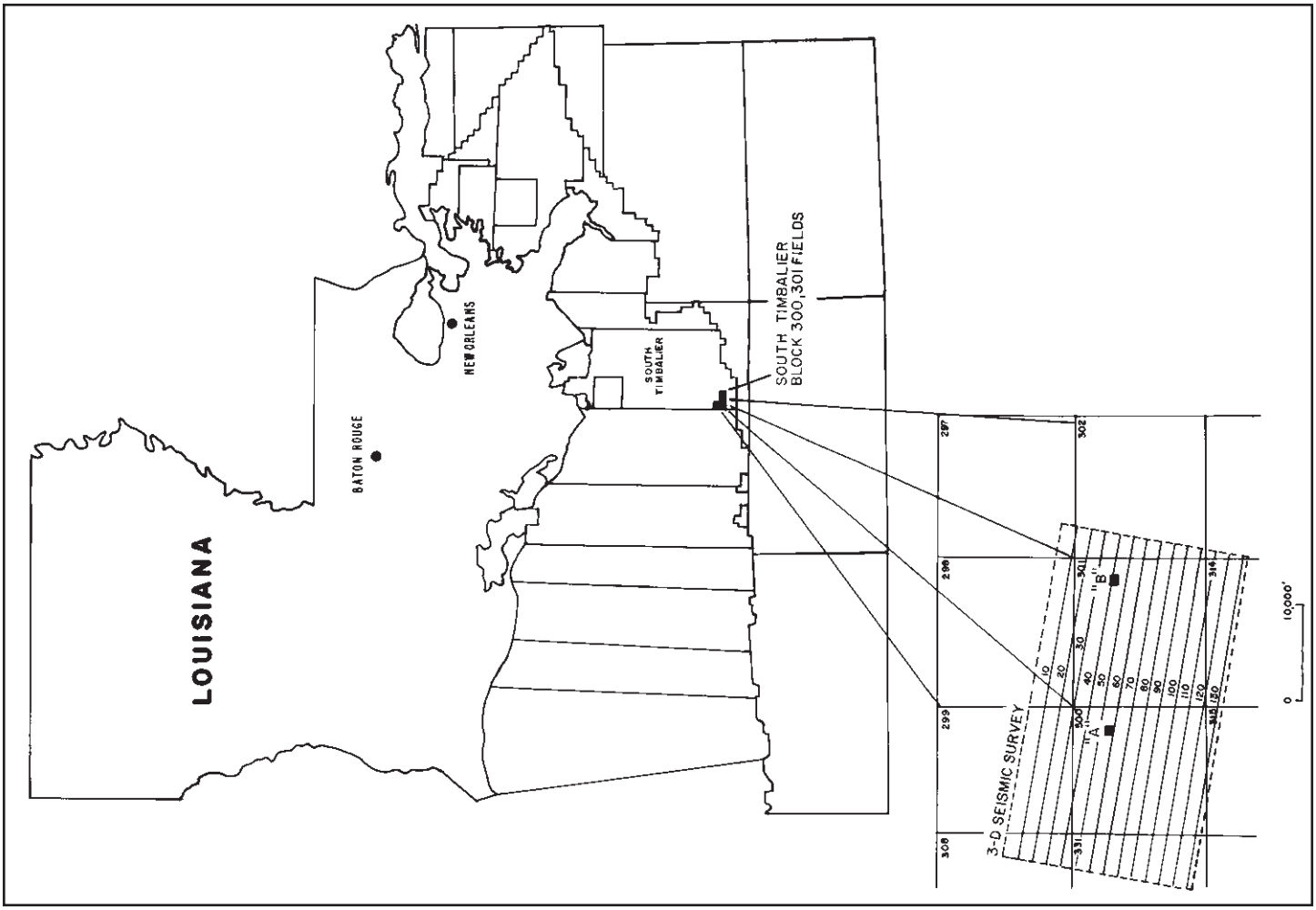

Fig. 14-3-1. Location map for Prospect Cougar (South Timbalier 300 Field). Area of 3-D seismic survey is shown.

Downloaded 25 Jun 2012 to 95.28.162.50. Redistribution subject to SEG license or copyright; Terms of Use: http://segdl.org/

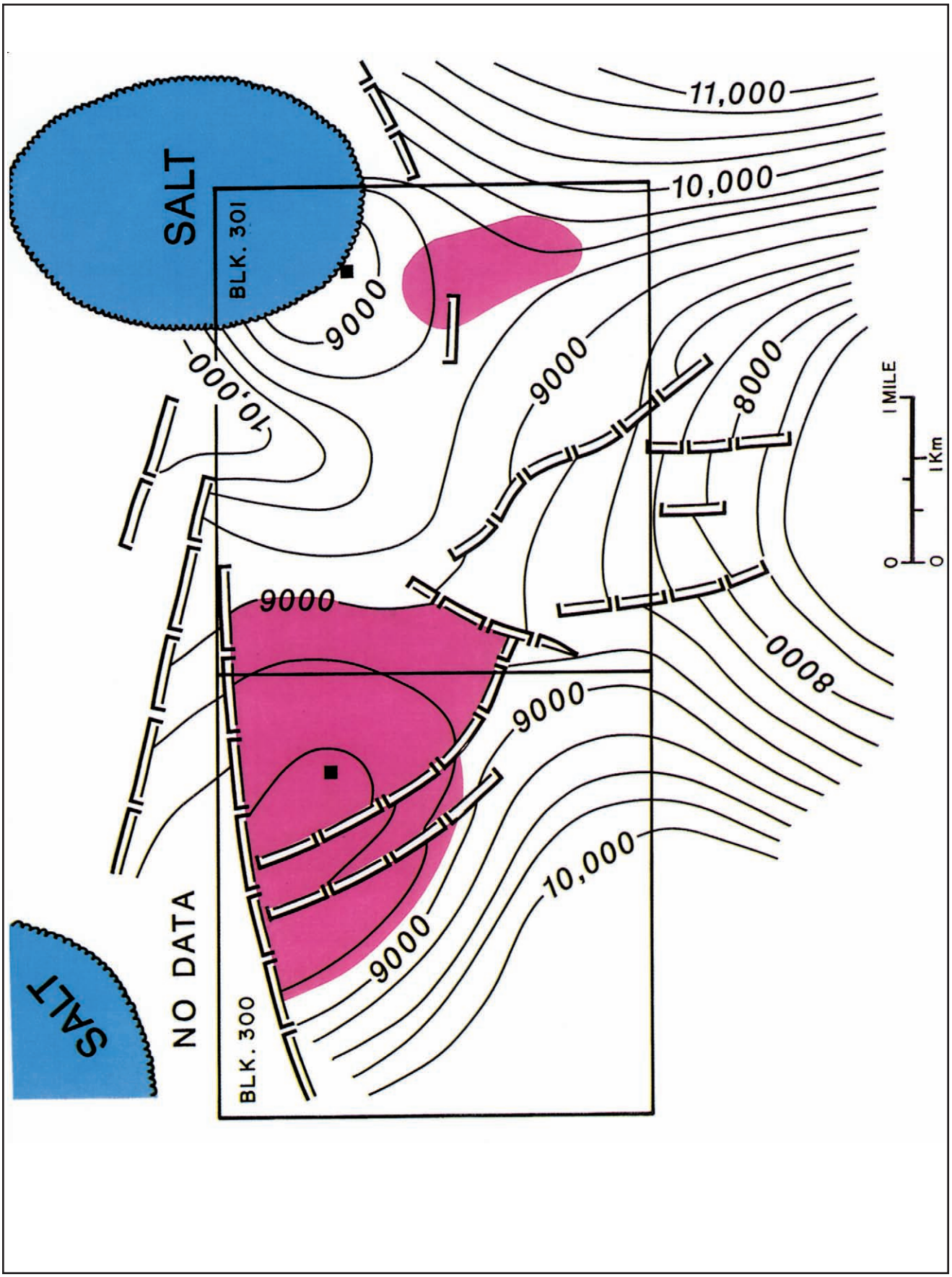

Fig. 14-3-2. Initial structure map prepared for first lease sale (1977) from 2-D seismic grid. Color indicates interpreted hydrocarbon distribution, red for gas and green for oil. Solid black squares show present location of platforms.

Downloaded 25 Jun 2012 to 95.28.162.50. Redistribution subject to SEG license or copyright; Terms of Use: http://segdl.org/

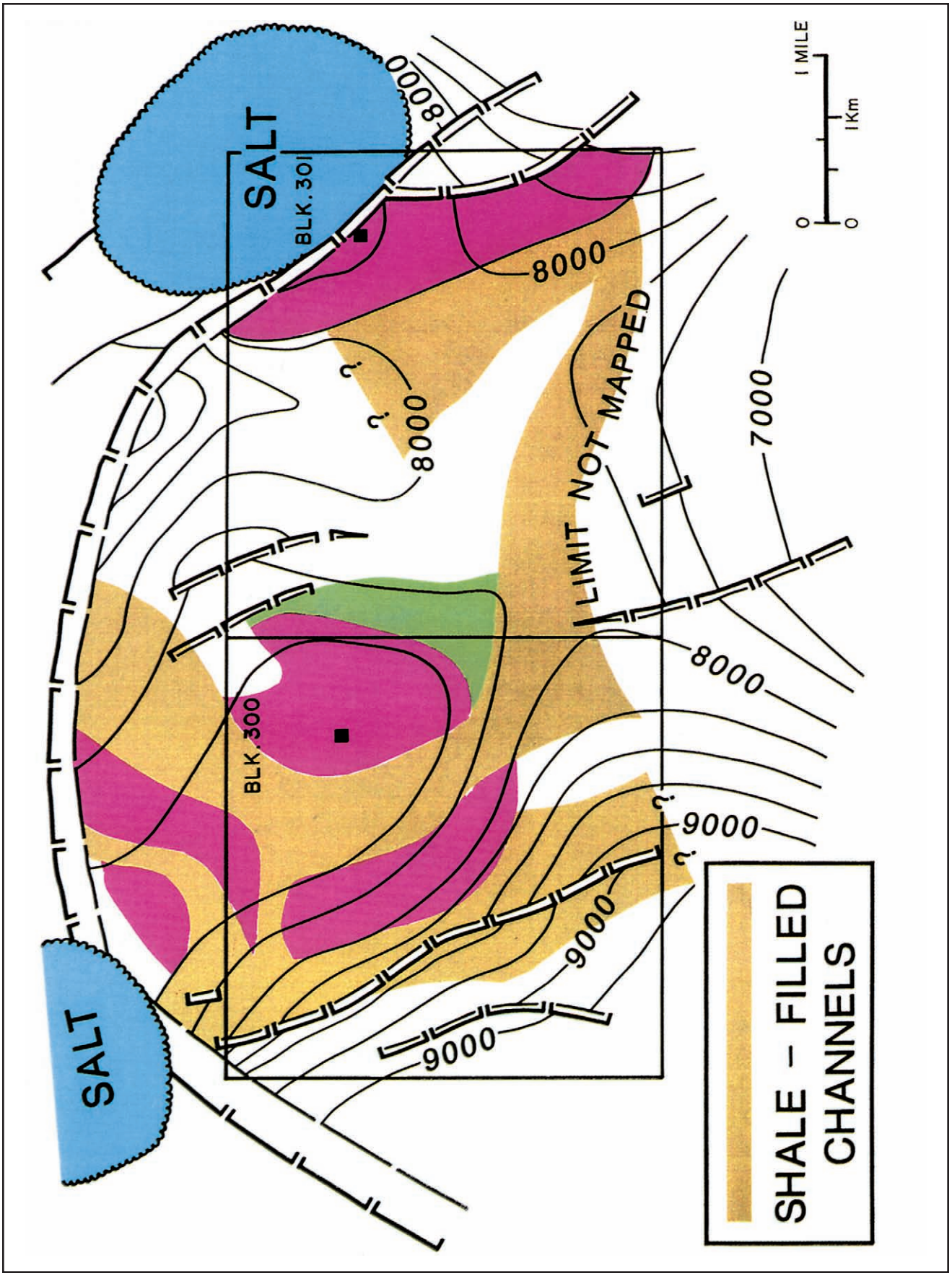

Fig. 14-3-3. Structure map from denser 2-D seismic grid after drilling three exploratory wells in S.T. 301 (1979).

Downloaded 25 Jun 2012 to 95.28.162.50. Redistribution subject to SEG license or copyright; Terms of Use: http://segdl.org/

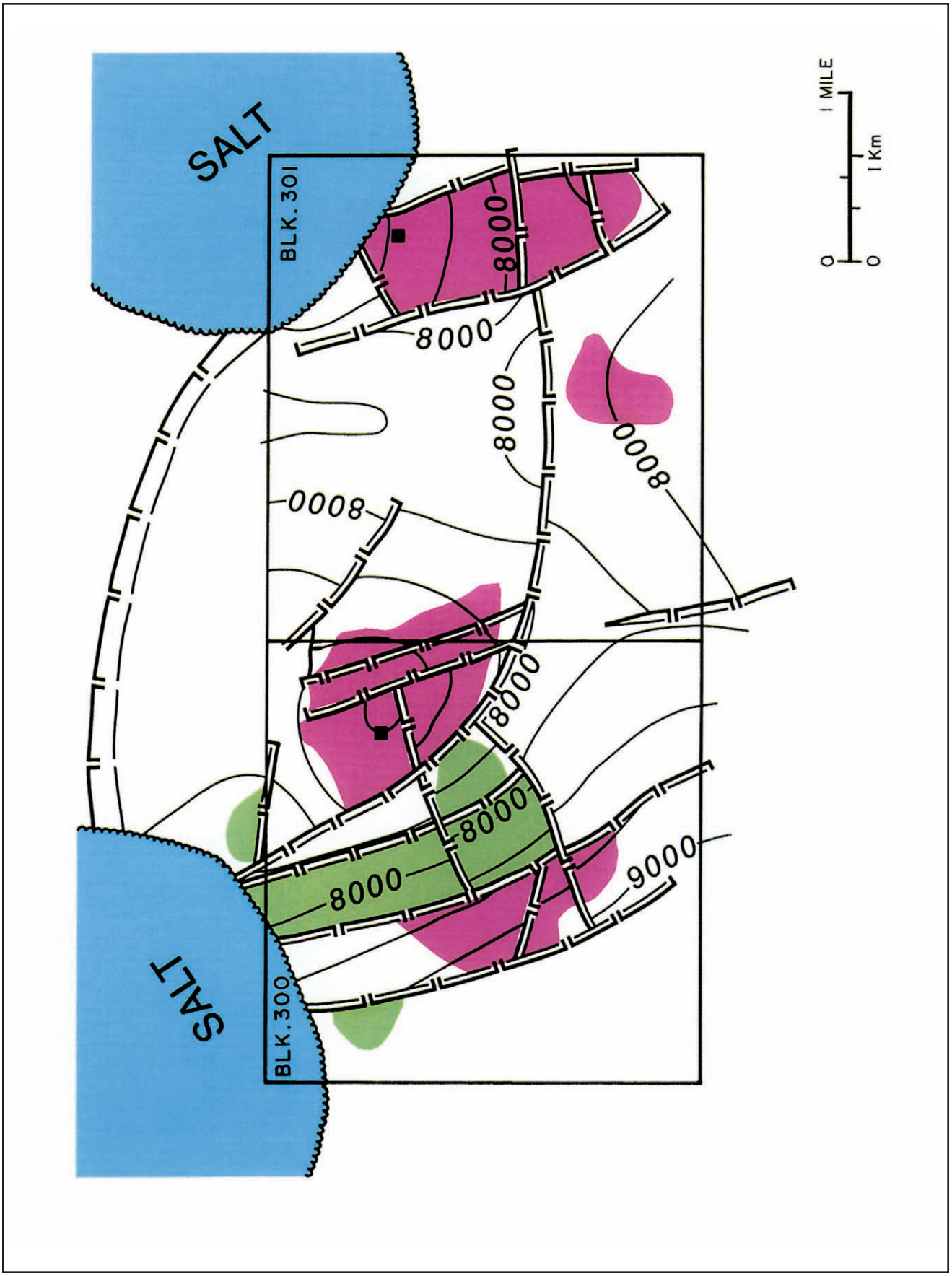

Fig. 14-3-4. Structure map based on coarse-grid interpretation of 3-D data after drilling six development wells from the S.T. 300 platform (1982).

Downloaded 25 Jun 2012 to 95.28.162.50. Redistribution subject to SEG license or copyright; Terms of Use: http://segdl.org/

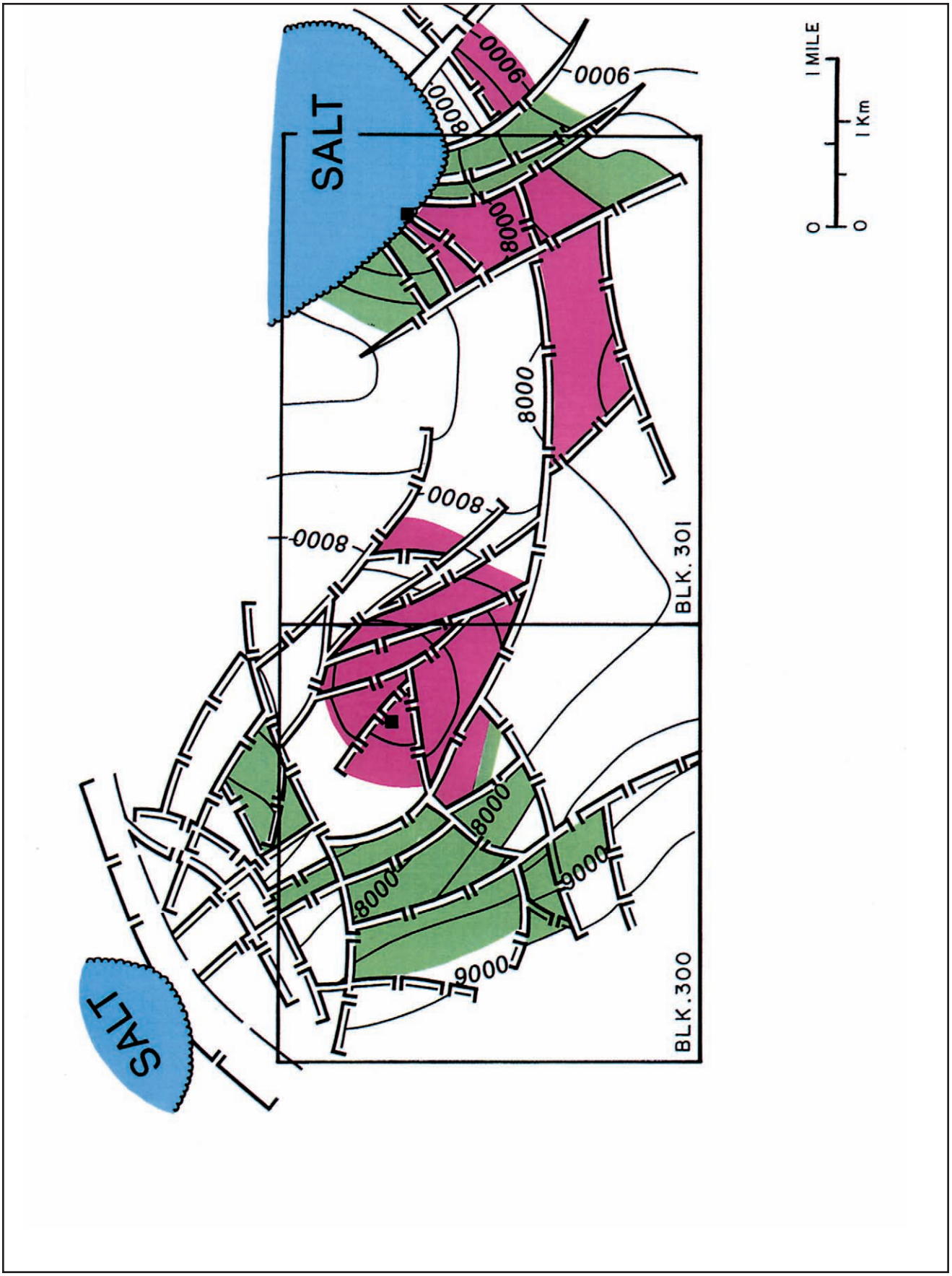

Fig. 14-3-5. Structure map based on complete line-by-line and time slice interpretation of 3-D data after 11 development wells (1983).

Downloaded 25 Jun 2012 to 95.28.162.50. Redistribution subject to SEG license or copyright; Terms of Use: http://segdl.org/

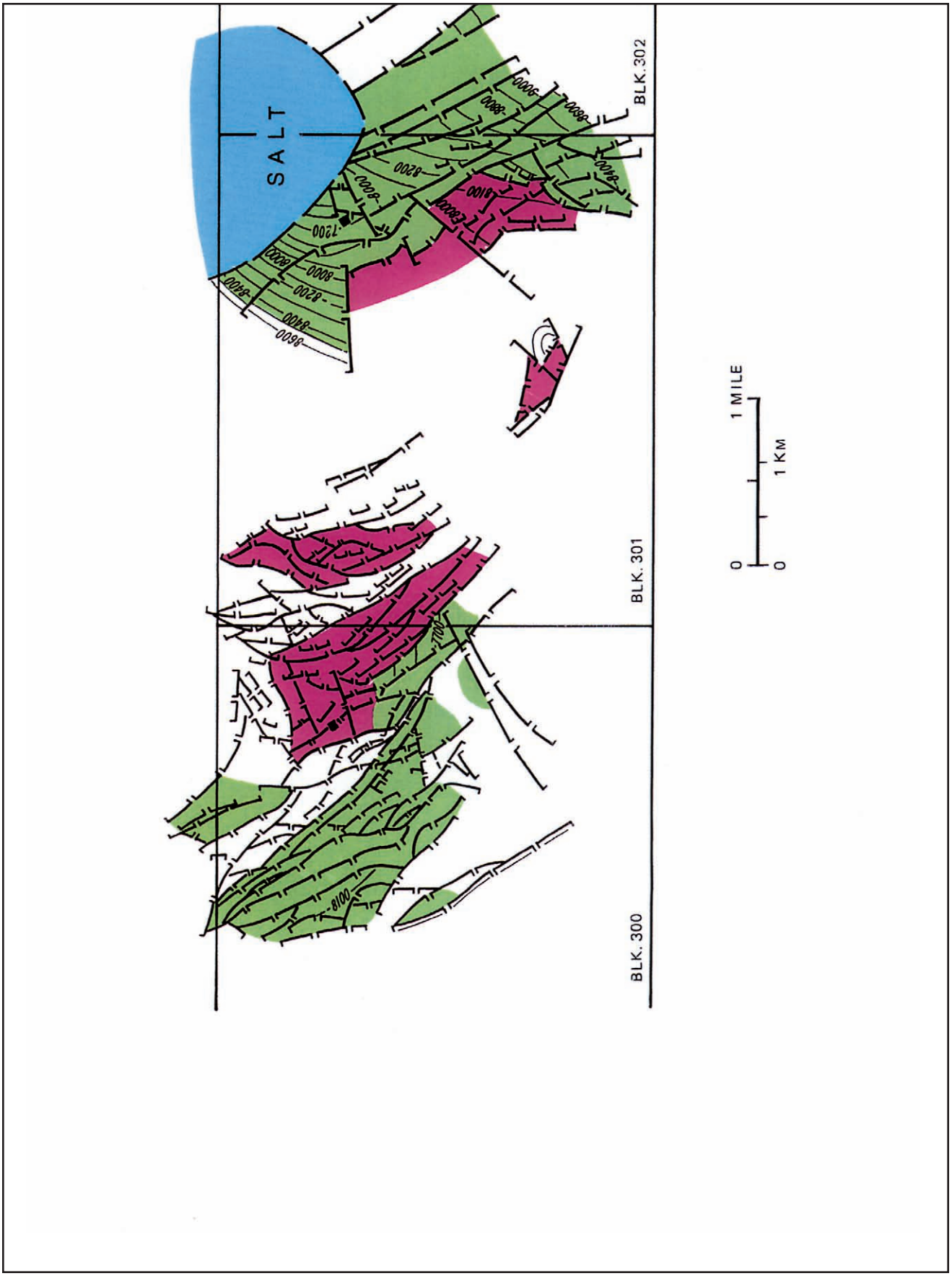

Fig. 14-3-6. Structure map based on interactive interpretation of reprocessed 3-D data and results of over 60 development wells (1988).

Downloaded 25 Jun 2012 to 95.28.162.50. Redistribution subject to SEG license or copyright; Terms of Use: http://segdl.org/

Case History 4

3-D Seismic Interpretation of an Upper Permian Gas Field in Northwest Germany

H. E. C. Swanenberg, F. X. Fuehrer, BEB Erdgas und Erdoel GmbH

Introduction

In northwest Germany, sour gas is produced from Zechstein (Upper Permian) carbonates in a number of mainly medium-sized fields. A 3-D survey was acquired in 1985 to optimize drilling in the Goldenstedt field and some smaller adjacent fields (Figure 14-4-1). Recent appraisal drilling has proved significantly more potential than originally assumed in this area of complex structure and facies. Total reserves are currently estimated at 0.5 tcf of sour gas with an H_2S content varying between 7 and 26%.

Structural definition and resolution of the target horizon at 3500 to 4000 m depth (corresponding to 2.2 to 2.4 sec two-way traveltime) is severely influenced by lateral velocity variations in the overburden, which complicated processing and interpretation of the survey. Despite nominally lower coverage than regular 2-D, the superiority of 3-D data significantly enhanced structural control. Some information on the reservoir was also obtained from reflection amplitudes. The 3-D data set thus revealed details of the tectono-depositional framework not observed on previous 2-D data.

Depositional Model, Diagenesis, Reservoir Quality

Core data and modern lithologic log interpretation techniques in conjunction with dipmeter data indicate that the Zechstein carbonates in the Goldenstedt area were deposited during a transgressional cycle of the Zechstein sea in a tidal flat environment with tidal channels influenced by syndepositional faulting. In the shallow, low-energy environment, mainly mudstones together with anhydrite were deposited with hardly any porosity and permeability. In the higher-energy environment, grainstones were produced that are now found mainly within the middle and upper parts of the sequence, intercalated within mudstones. In the tidal channels, the best reservoir facies (with up to 100 m of pure grainstones) accumulated due to continuous subsidence resulting from the syndepositional faulting. Early diagenesis has altered the originally deposited limestones into dolomites. Because of the variations in primary facies and diagenetic overprinting, net thicknesses in Goldenstedt now vary between 5 and 100 m, porosities range from very low to 16%, and permeabilities reach 320 md. Fortunately, in the tight reservoir parts, fractures usually enhance permeability. The Zechstein carbonates are directly overlain by 30 to 80 m of anhydrite and several hundred meters of Zechstein salt. During the Mesozoic and Cenozoic, sedimentation in the area continued, locally governed by various tectonic events.

Structural Setting

The Goldenstedt area straddles the boundary between a relatively stable block in the north and the inverted Lower Saxony Basin (LSB), a large intracratonic inversion structure in northwest Europe (Betz et al., 1987). In this part of the LSB (the edge of which is visible at the southern end of the north-south seismic line in Figure 14-4-2), and in the similarly inverted "Goldenstedt graben," a smaller satellite structure just north of it, Lower Cretaceous sediments accumulated during an extensional phase. During a subsequent compressional phase in the Late Cretaceous, these structures were inverted. Concomitantly, thick Upper Cretaceous sequences were deposited in the adjacent rim synclines. During these tectonic phases the Zechstein salt decoupled the Mesozoic from the Paleozoic so that their respective structural styles are quite different.

Downloaded 25 Jun 2012 to 95.28.162.50. Redistribution subject to SEG license or copyright; Terms of Use: http://segdl.org/

Structural Interpretation and Time-to-Depth Conversion

Interpretation of the 3-D survey was carried out using a SIDIS* workstation on a one-pass 3-D time-migrated data set.

The seismic horizon nearest to the Zechstein carbonates is the reflection originating from the interphase between the salt and the anhydrite covering the carbonates. This "Z-reflector" is the black peak on Figure 14-4-2 immediately above the reservoir level (colored in blue). In the areas not affected by Mesozoic inversion tectonics, interpretation of this Z-reflector is straightforward. Care has to be taken only to avoid confusing the Z-reflector with strong reflections originating from anhydrites floating in the salt. Within the zones of faulted overburden (shown stippled in Figure 14-4-1) interpretability of the Zechstein is markedly reduced. The problem becomes even more serious along the margins of these areas because of the lateral velocity contrast in the overburden. Here, faults in the Zechstein can only be inferred after careful time-to-depth conversion, but mispositioning due to ray bending remains. Detailed ray tracing, on the other hand, would be highly impractical for the total 3-D area. Therefore, we followed a different scheme, based on the concept of "pseudo-average velocities," which was accurate enough and practical.

Initially, depth-dependent velocities were calculated directly from reflection-seismic traveltimes of eight prominent, identifiable reflectors and their corresponding vertical depths as encountered in the well. Subsequently, these pseudo-velocities were mapped and used as input for a time-to-depth conversion down to the Z-level. A Top Zechstein carbonate map was constructed by adding isopach values of the anhydrite cover to the depth map of the Z-horizon.

Because of complex overburden and associated velocity pull-down effects, the result needed to be thoroughly screened. This problem was solved by careful editing of the average velocity field, calculated from Z-traveltimes and top carbonate depth values at every CMP. In this way, it has proved possible to restore an uninterrupted horizon in depth, otherwise distorted in time by velocity effects.

Basically, the top carbonate map (Figure 14-4-1) describes the dissected antiform of the Goldenstedt field in the west, presumably a Late Cretaceous "trapdoor," separated from the adjacent structural highs of Woestendoellen and Quaadmoor by a fault-controlled graben.

The north-south- and east-west-oriented, apparently normal faults are interpreted to be en echelon elements of a dextral oblique slip system, active during at least the final stages of carbonate deposition in this area.

Reservoir Facies from Reflection Amplitudes

Because of highly variable reservoir quality, the production rates of wells are also quite variable. A number of positive and negative surprises were experienced in wells where reservoir quality was predicted based on geologic mapping only. Attempts therefore were made to use 3-D seismic for reservoir facies prediction. Obviously, in areas where faulting has affected the overburden this is rather ambitious.

Within the 3-D area it was possible to identify three facies types with different seismic expressions. One type (top left of Figure 14-4-3) has the most porous zone at the top of the reservoir, immediately below the overlying anhydrite. This is expressed on a black-and-white, variable area seismic section as a strong "soft kick" (trough) immediately following the "hard kick" (peak) from the top of the overlying anhydrite, the Z-reflector. This facies type has been observed in the Woestendoellen area to the northeast of the main Goldenstedt field. Comparison of a well synthetic and a seismic section shows good agreement (lower left of Figure 14-4-3). In a second facies type the most porous streaks are found in the middle part of the reservoir (top center of Figure 14-4-3). This is expressed on a seismic section as a delay of a few milliseconds of the soft kick as compared with the previous facies type. Overall, this type also appears as a lower frequency event than does the first type and is mainly found in the northern part of the Goldenstedt field. Again, the well-to-seismic match gives good correspondence. The third facies type (top

*Trademark of Geophysical Service Inc.

Downloaded 25 Jun 2012 to 95.28.162.50. Redistribution subject to SEG license or copyright; Terms of Use: http://segdl.org/

right of Figure 14-4-3) is characterized by a very thin reservoir section with low porosity mudstones only. A strong soft kick following the Z-reflector cannot be found. This facies type is encountered in the southern part of the Goldenstedt field.

In order to visualize these observations over the whole 3-D area, horizon slices were produced at successive intervals below and parallel to the Z-reflector. Those for 8- and 20-ms delay are shown color coded in Figures 14-4-4 and 14-4-5, respectively. The 8-ms horizon slice (Figure 14-4-4) shows the strong soft kick characteristic of the first type as a distinct deep-blue event. By comparing Figures 14-4-4 and 14-4-1, it is apparent that this deep-blue event occurs in Woestendoellen, as well as in a number of other areas. In the Goldenstedt-N and Goldenstedt-S subareas, the reservoir reflection has not yet been reached at this particular time delay. Part of the amplitude variation over this horizon slice, however, is to be ascribed to signal deterioration and interference/absorption effects that are not related to reservoir development.

At 20 ms below the Z-reflector (Figure 14-4-5) the second facies type is clearly displayed in the Goldenstedt-N subarea, again by a distinct deep-blue event. Part of the time delay, however, is due to increased thickness of the overlying anhydrite. In the southern part of Goldenstedt a strong soft kick that would appear in dark blue colors cannot generally be found, either on the 20-ms horizon slice or on any other.

Conclusion

Using seismic data for reservoir prediction in areas of complex facies development requires detailed analysis of composite wavelet characteristics, because changes in the reflection shape cannot usually be attributed to variations of a single parameter of the reservoir only. Nevertheless, this example shows that even in rather complex cases, horizon slices can facilitate the study of the spatial distribution of wavelet characteristics. These studies can then be used to optimize well positioning in order to maximize production rates and minimize the number of wells required in field development.

Acknowledgment

Goldenstedt and surrounding fields are operated by BEB Erdgas und Erdoel, Hannover, an affiliate of Shell and Exxon, holding two-thirds of the interest in the fields. One-third is held by Mobil Oil. The authors are indebted to the managements of BEB and Mobil Oil for permission to publish this case history.

References

Betz, D., F. Fuehrer, G. Greiner, and E. Plein, 1987, Evolution of the Lower Saxony Basin: Tectonophysics, v. 137, p. 127-170.

Figures begin on page 495.

Downloaded 25 Jun 2012 to 95.28.162.50. Redistribution subject to SEG license or copyright; Terms of Use: http://segdl.org/

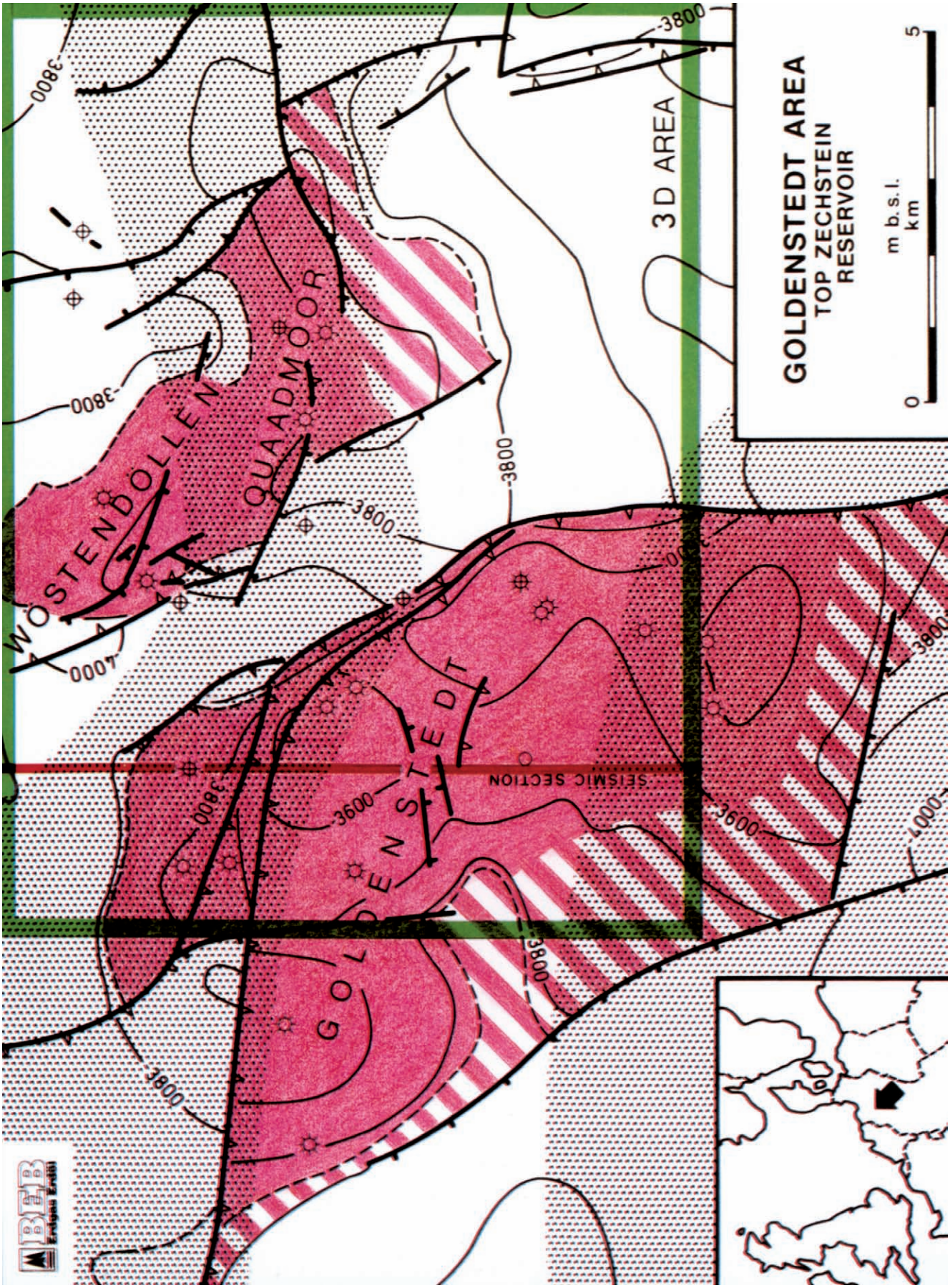

Fig. 14-4-1. Structural map of the Goldenstedt area. Contours in meters below sea level. Stippled zones indicate areas where resolution and time-to-depth conversion are affected by strongly tectonized overburden.

Downloaded 25 Jun 2012 to 95.28.162.50. Redistribution subject to SEG license or copyright; Terms of Use: http://segdl.org/

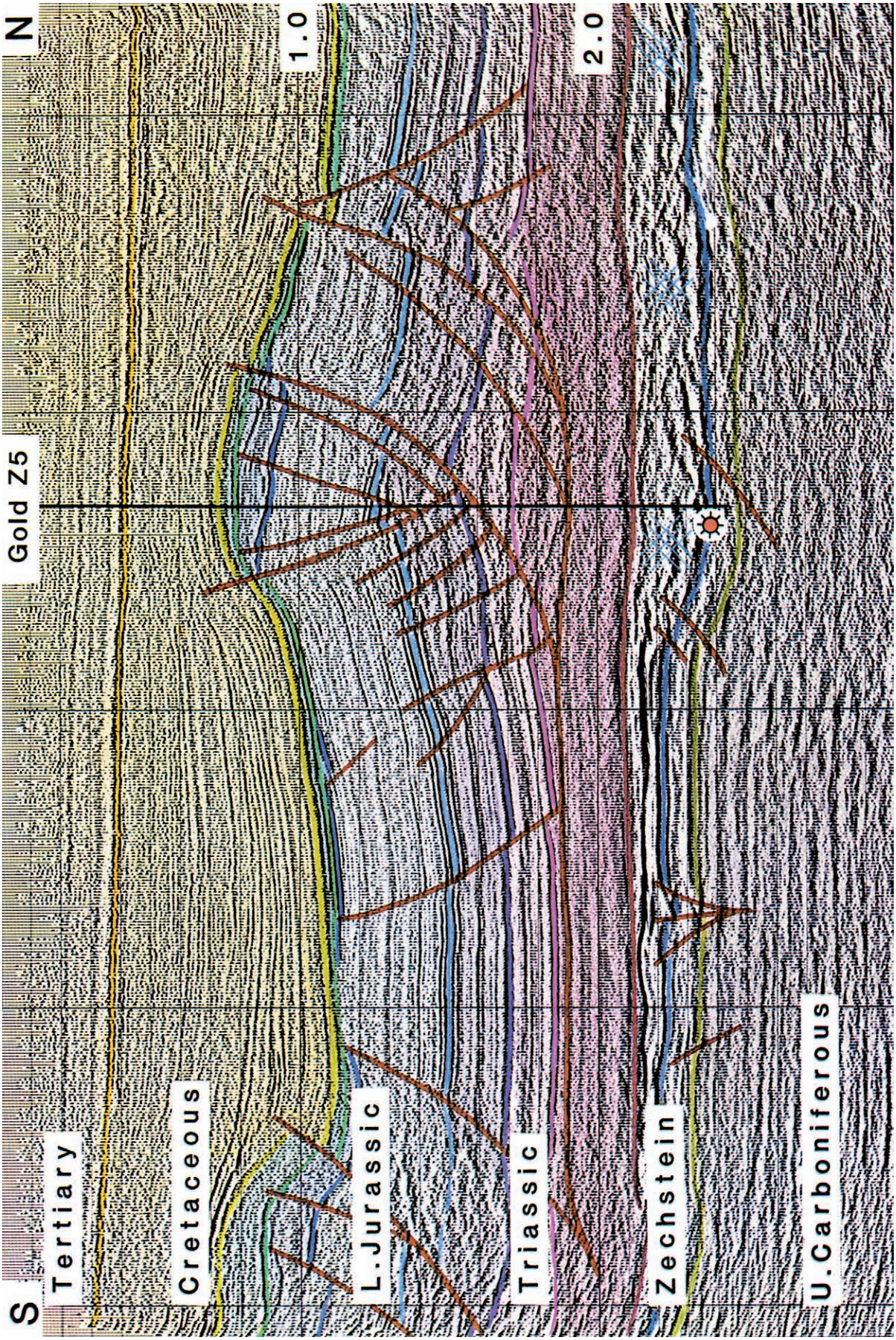

Fig.14-4-2. North–south-trending seismic section showing inversion tectonics in the overburden. Reservoir carbonates, at 2.2 to 2.4 s reflection time, are indicated in blue.

Downloaded 25 Jun 2012 to 95.28.162.50. Redistribution subject to SEG license or copyright; Terms of Use: http://segdl.org/

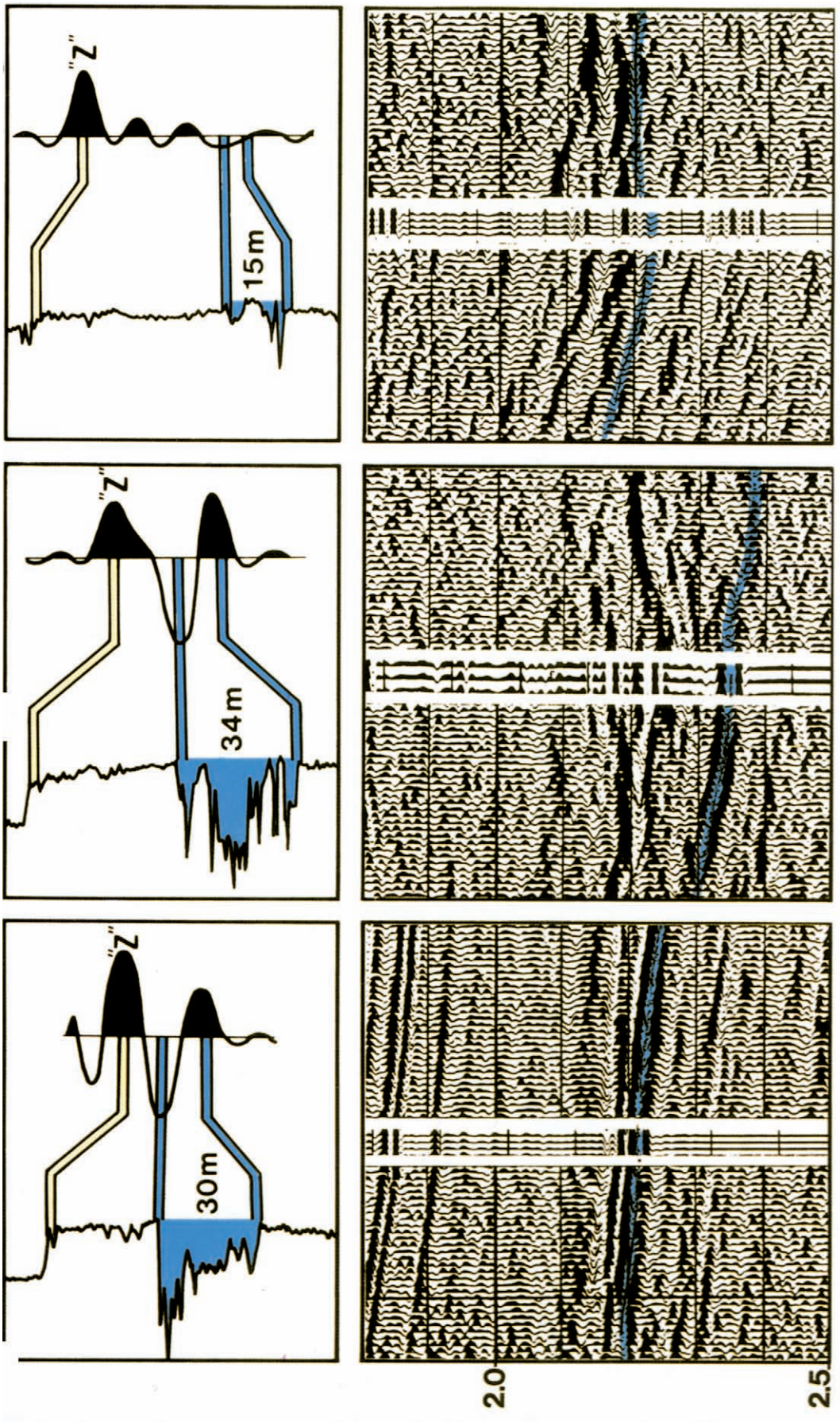

Fig. 14-4-3. Seismic facies types. Top of figure shows sonic log with the reservoir section in blue and the corresponding zero-phase synthetic. The Z-reflector originates from the top of the anhydrites overlying the reservoir. The lower part of the figure gives comparisons of synthetic seismograms and seismic section.

Downloaded 25 Jun 2012 to 95.28.162.50. Redistribution subject to SEG license or copyright; Terms of Use: http://segdl.org/

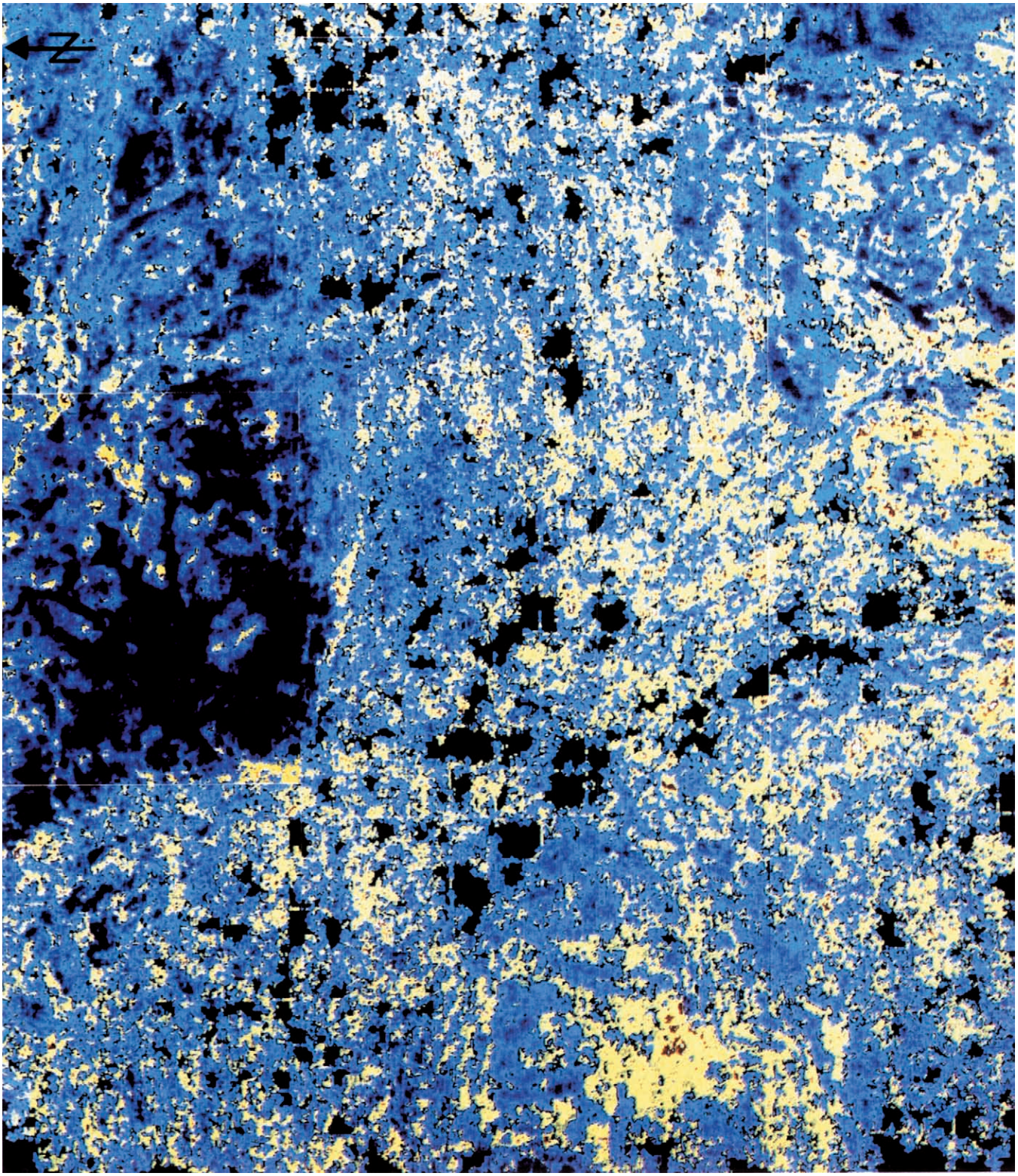

Fig. 14-4-4. Horizon slice with color-coded amplitudes at 8 ms below the Z-reflector. Deep blue represents reflection amplitudes of a strong "soft kick" (trough) indicating porosity in the upper part of the reservoir.

Downloaded 25 Jun 2012 to 95.28.162.50. Redistribution subject to SEG license or copyright; Terms of Use: http://segdl.org/

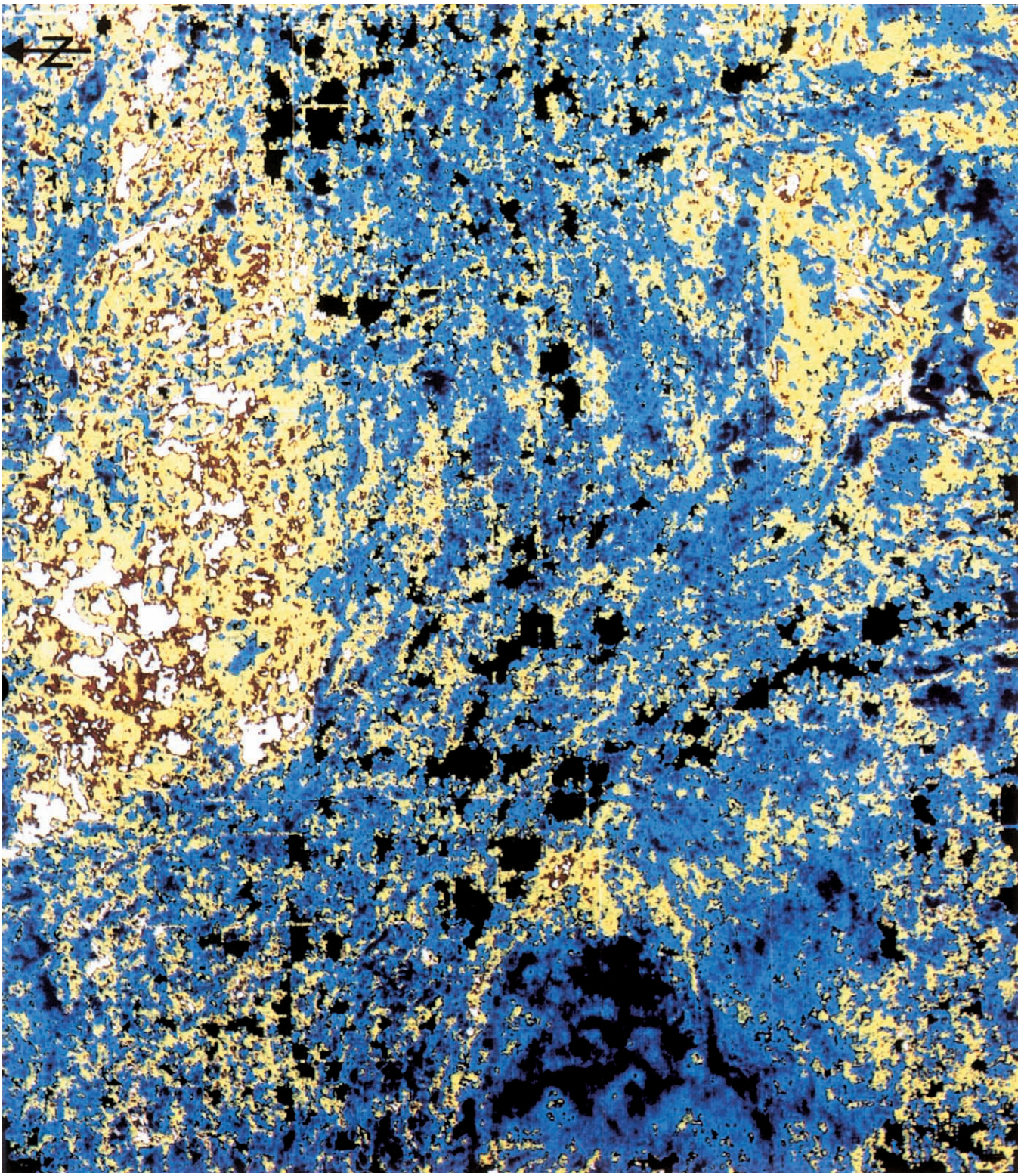

Fig. 14-4-5. Horizon slice at 20 ms below the Z-reflector. Deep blue represents reflection amplitudes of a strong "soft kick" (trough) indicating porosity in the central part of the reservoir.

Downloaded 25 Jun 2012 to 95.28.162.50. Redistribution subject to SEG license or copyright; Terms of Use: http://segdl.org/

Case History 5

Seismic Data Interpretation for Reservoir Boundaries, Parameters, and Characterization

William L. Abriel, Roger M. Wright, Chevron U.S.A. Inc.

Three-dimensional mapping of seismic data revealed a prospect not existing on the 1000′ 2-D grid. A bright spot was reviewed downdip of an abandoned competitor well that had apparently been faulted out. Normal 3-D mapping resulted in a new well proposal, but results from interactive workstation analysis moved the location downdip. Detailed structural and amplitude analyses revealed the presence of complex stratigraphic changes within the prospective reservoir, which were then avoided in a successful discovery well. Predictions of net pay and reservoir connectivity were confirmed. Future management of this reservoir will also be better served with combined geological, engineering, and geophysical analyses.

Introduction

An offshore area in the Gulf of Mexico was reviewed for prospects, based on a 305-m (1000-ft) 2-D seismic grid and available well data (Figure 14-5-1). No clear bright spots were observed on seismic data, and the abandoned competitor well was not encouraging (Figure 14-5-2) because of the shaly sands encountered. The area was later covered by 3-D seismic data as part of a larger survey, and the subsequent structural evaluation was quite different (Figure 14-5-3).

The 3-D survey was conducted in 1983 with an airgun source and a 3000-m streamer of 120 groups at 25-m spacing. Lines were shot at 70-m and interpolated to 35-m. 3-D processing consisted of relative amplitude scaling, zero-phase deconvolution, dip selective moveout, and finite difference 2-pass migration. Subsurface 3-D bins covered an area 12.5-m by 35-m.

Initial 3-D Mapping

A map was constructed from the 3-D data using wiggle trace variable area plots (Figure 14-5-4) and a Seiscrop table. Each line was reviewed, the faults tied, and the horizons of interest mapped. Although the area has fairly low dip, the 3-D data changed the fault pattern significantly from the 2-D map and also revealed large, undetected bright spot zones. As a result, a well proposal was considered on the 3-D line east–west through the abandoned #1 well to test the large bright spot downdip (Figure 14-5-4). The interpretation of the data suggested that the #1 well was faulted in the stratigraphic interval, and that the shaly gas sands of questionable productivity found in that well did not represent the overall stratigraphy of the downdip reservoir. Geologists and engineers reviewed the prospect with geophysicists and determined a location about 305 m (1000 ft) west of the #1 well. Gas was anticipated in a strong water-drive reservoir.

Interactive Workstation Review

Drilling could have proceeded at this point, but more time was allocated to review the 3-D data on an interactive workstation. The review showed some very important details that had bearing on the well proposal. Careful attention to color density representation of the lines (Figure 14-5-5) was possible with the workstation. The amplitudes of the troughs (negative acoustic impedance contrast) of the zero-phase data were displayed as increasing white-yellow-red, whereas the peaks (positive acoustic impedance contrast) were increasing black-green-blue. Variations in the amplitude of the bright spot could then be seen that were not visible in the amplitude-clipped black-and-white sections.

A simple review of the line containing the proposed #2 well showed it to be targeted at a slightly weaker amplitude spot (Figure 14-5-5). Past drilling experience in other areas had shown this to be a less than optimum site for development wells. The position of the #2 well on the 3-D structure map was at the north tip of a north-south fault, the throw of which could not be resolved by the 3-D data. A comprehensive review of the seismic data was in order.

Downloaded 25 Jun 2012 to 95.28.162.50. Redistribution subject to SEG license or copyright; Terms of Use: http://segdl.org/

Detailed Digital Structure and Amplitude

All of the lines in the bright spot area were reviewed in lines, crosslines, time slices, and in cubes (Figure 14-5-6). By picking the maximum amplitude of the first trough, a structure map was made on the top of the potential reservoir (Figure 14-5-7). The map of the bright spot reflects an updip termination against a fault, and several potential faults, within the anomaly. Structural variations along strike on the order of 15 m (50 ft) appeared to reflect potential compaction features, suggesting variations in sand distribution. After reviewing the lines in detail, it was determined that the potential reservoir was probably composed of overlapping sand units on a common water contact. Line 123 (Figure 14-5-8) showed a particularly good example of possible multiple sand lobes as opposed to a faulted uniform sand. The small faults mapped on black-and-white sections are thus more likely to be stratigraphic changes.

To better understand the distribution of the quality of the sands, the amplitudes of the reflecting interfaces were tracked, corrected for tuning effects, and represented in map form (Figure 14-5-9). In addition, a net pay map was generated (Figure 14-5-10). The procedures used were an extension of more established methods (see Chapter 7, and Brown et al., 1984). It is reasonable in this geologic area to expect the higher, detuned amplitude zones to represent thicker effective sands, and this is generally represented in the net pay map.

Revised Well Proposal

The resulting maps showed that the proposed #2 well lay in a very weak amplitude area relative to the rest of the major fault block. Net pay estimates here were not very favorable. A real danger existed that the well would be drilled in a shaly zone and would not effectively drain the potential reservoir. The connectivity of the sands appeared to be much better downdip, although considerable variation existed there as well. It was not simple to accept the movement of this potential gas well downdip. If the sands were to be uniform in distribution, the net recoverable would be less. Even so, after the seismic interpretation was considered along with other factors affecting the proposal, a new target was considered west (downdip) of the original proposed #2 (see Figure 14-5-10).

The #2 well was finally drilled after this extensive review, and the resulting well was a success (Figure 14-5-11). The #2 well was predicted to have much better sand characteristics than the #1 well and 17.7 m (58 ft) of effective pay. The #2 well actually logged 18.3 m (60 ft) of effective pay, and showed that the #1 well was in fact significantly faulted in its upper section of sands. Production tests confirm that the well is in a reasonably large and well-connected reservoir.

Future Reservoir Management

Additional wells may be considered in the future for this reservoir. The production characteristics of the #2 well may require more wells to drain all of the reserves effectively. Simple reservoir simulations are now possible using some of the data already generated from the geophysical workstation, especially the reservoir boundaries and net pay. Porosity values scaled to the #1 and #2 wells can also be generated from the amplitude data. To date, the reservoir is considered to be on a common water contact, but the apparent stratigraphic changes within the unit may potentially be permeability barriers (Figure 14-5-12).

Acknowledgments

The authors thank Chevron management for their support and permission to publish these data. Special recognition is intended for David Smith of Chevron, Eastern Region, who worked with the geologists, geophysicists, and engineers to help get the successful well drilled.

References

Brown, A. R., R. M. Wright, K. D. Burkart, and W. L. Abriel, 1984, Interactive seismic mapping of net producible gas sand in the Gulf of Mexico: Geophysics, v. 49, p. 686-714.

Figures begin on page 502.

Downloaded 25 Jun 2012 to 95.28.162.50. Redistribution subject to SEG license or copyright; Terms of Use: http://segdl.org/

Fig. 14-5-1. Depth map of the prospect area based on 1000-ft 2-D seismic grid. Competitor well #1 was abandoned.

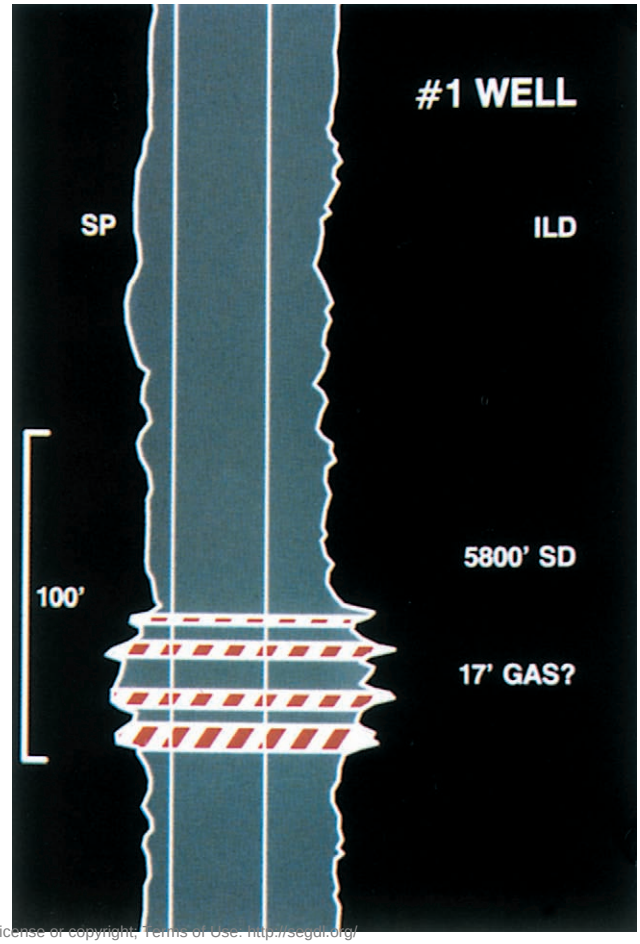

Fig. 14-5-2. E-log of abandoned competitor well #1. Sands contain gas in a few shaly stringers and are not considered economic.

Downloaded 25 Jun 2012 to 95.28.162.50. Redistribution subject to SEG license or copyright; Terms of Use: http://segdl.org/

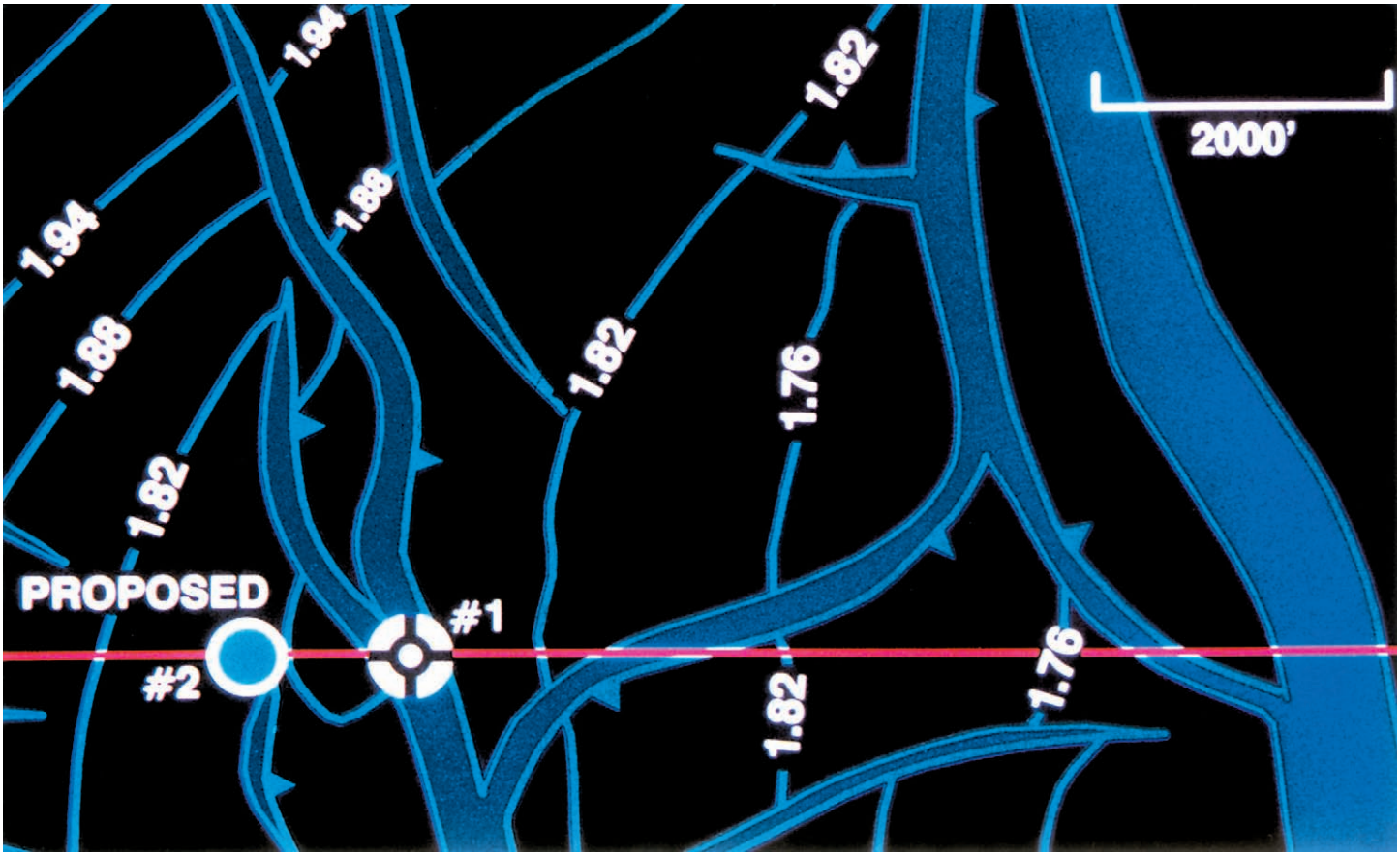

Fig. 14-5-3. Time map of the prospect area using 3-D sections and Seiscrop table. Note the significant change in fault positions, orientations, and throws compared with the 2-D map. Red line shows location of 3-D line 118 (Figure 14-5-4).

Downloaded 25 Jun 2012 to 95.28.162.50. Redistribution subject to SEG license or copyright; Terms of Use: http://segdl.org/

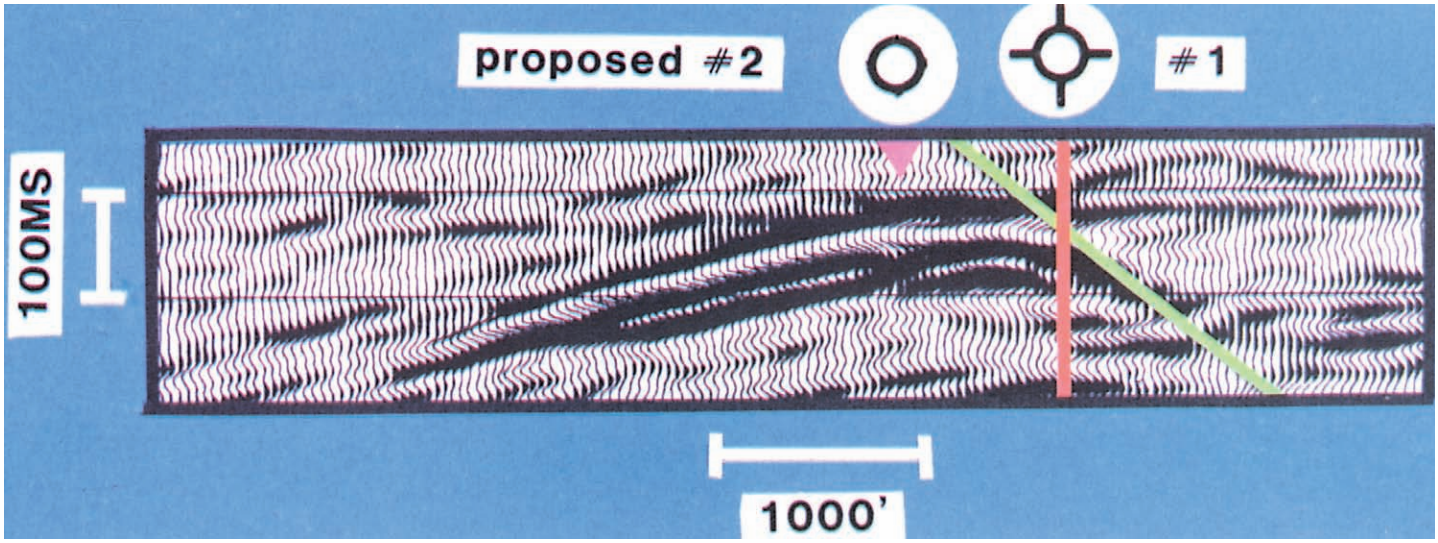

Fig. 14-5-4. 3-D seismic line 118, east-west through the #1 well. Data are zero phase with trough = negative acoustic impedance contrast. The bright spot can be drilled 1000 ft west of the faulted #1 well.

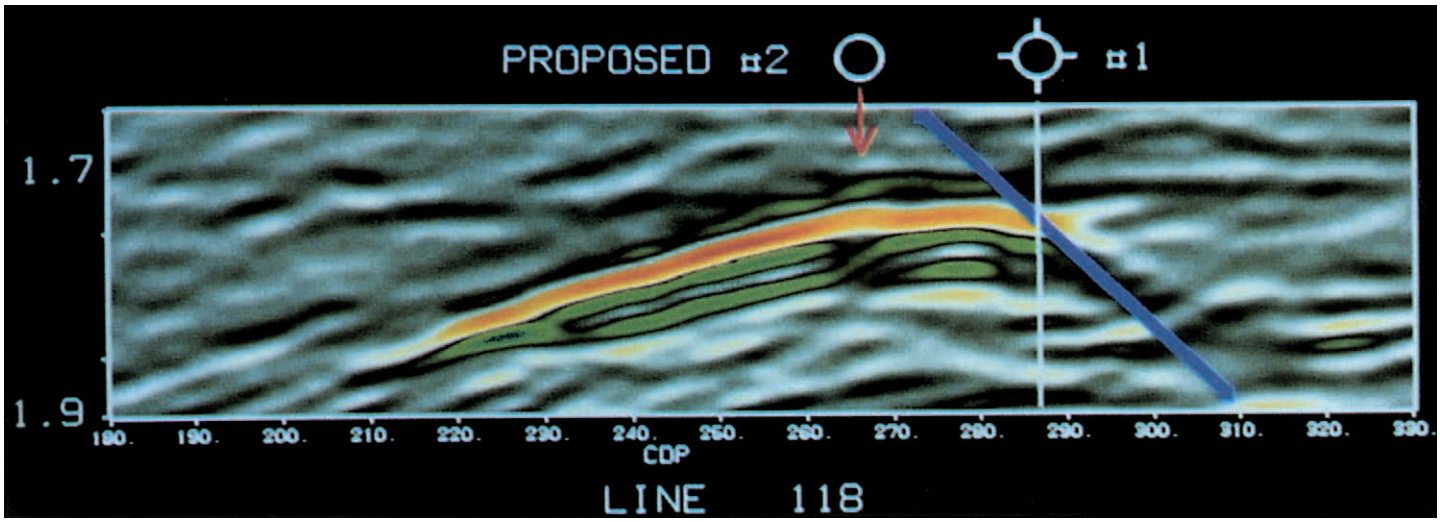

Fig. 14-5-5. Color display of line 118. Troughs are increasing amplitude white-yellow-red; peaks, black-green-blue. Note the detail not seen in clipped black-and-white data of Figure 14-5-4. Proposed #2 well is in a slightly weaker amplitude zone of the anomaly. This may not be an optimum drilling location.

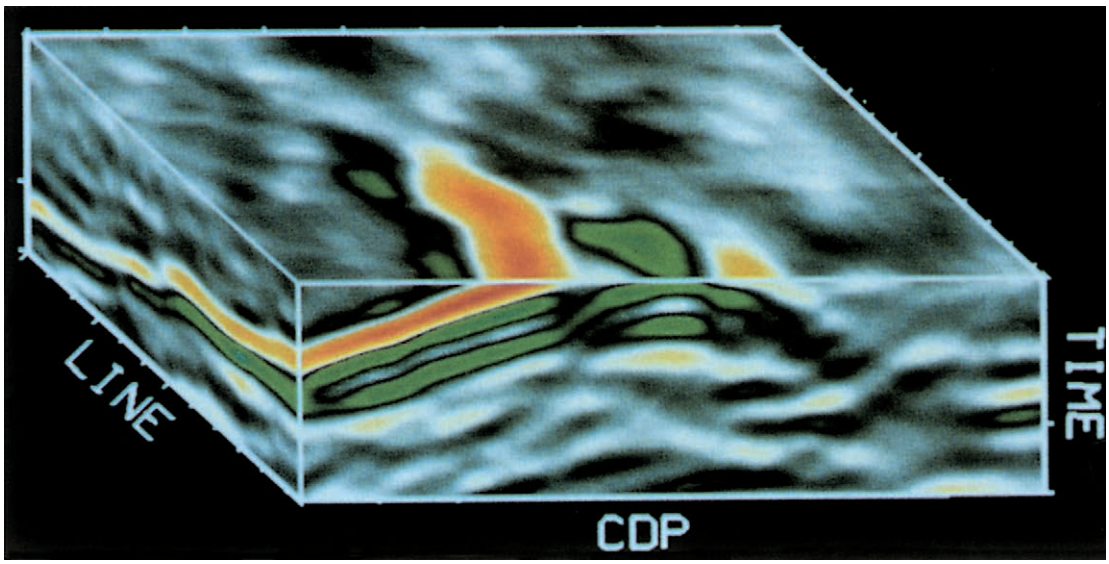

Fig. 14-5-6. Cube view of 3-D data. Front face is line 118.

Downloaded 25 Jun 2012 to 95.28.162.50. Redistribution subject to SEG license or copyright; Terms of Use: http://segdl.org/

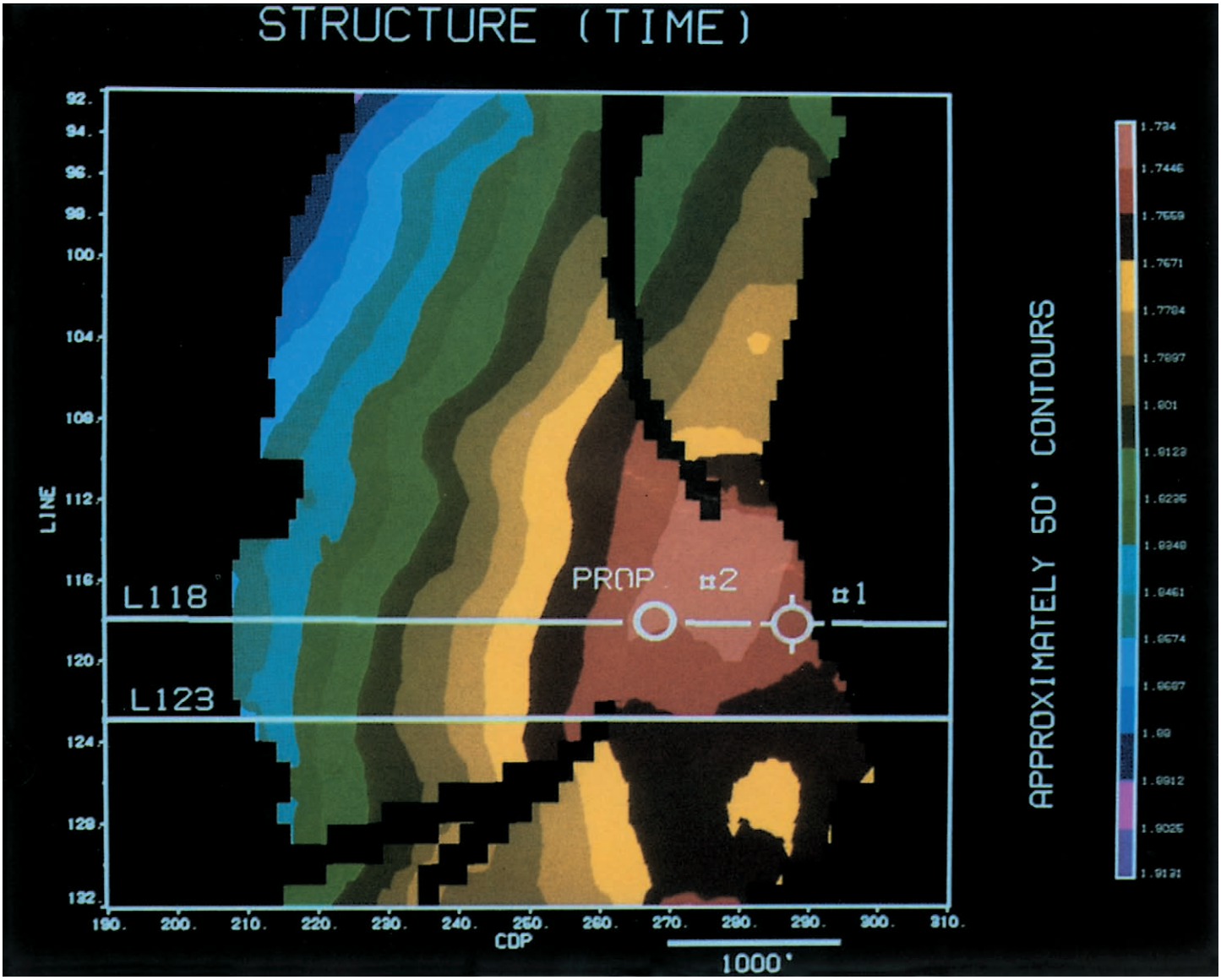

Fig. 14-5-7. Time-structure map of top of bright spot based on interactive analysis, picking maximum amplitude. Color bands represent approximately 50-ft contours. Lines 118 and 123 are referenced (Figures 14-5-5 and 14-5-8). Structural breaks in the prospect map may be stratigraphic changes instead of faults. Subtle changes in the contours of up to 50 ft may be a response to differential compaction (see also Figure 14-5-12).

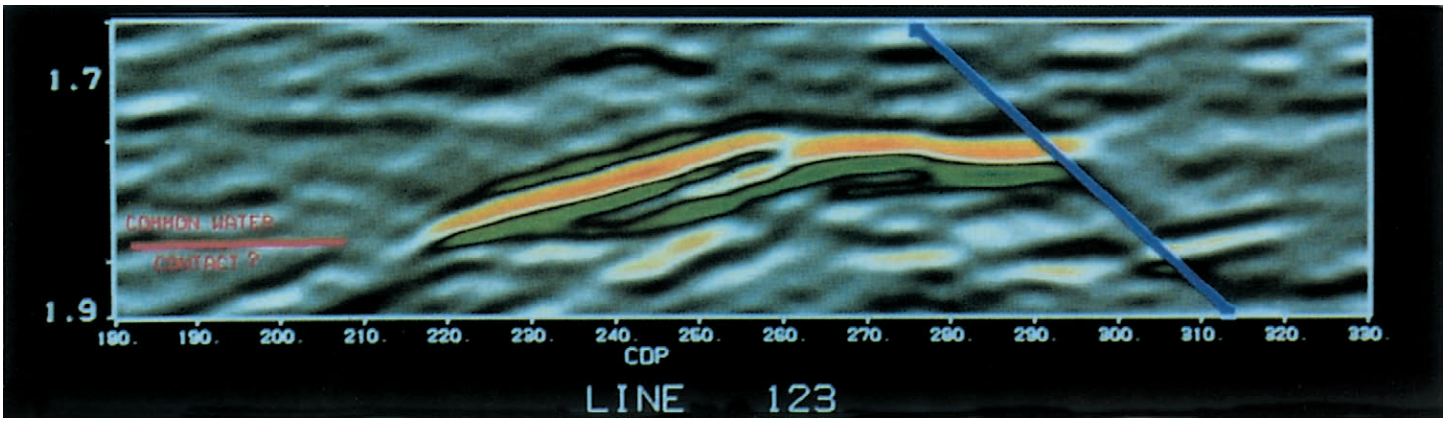

Fig. 14-5-8. Line 123 suggests overlapping sand bodies on a common water contact.

Downloaded 25 Jun 2012 to 95.28.162.50. Redistribution subject to SEG license or copyright; Terms of Use: http://segdl.org/

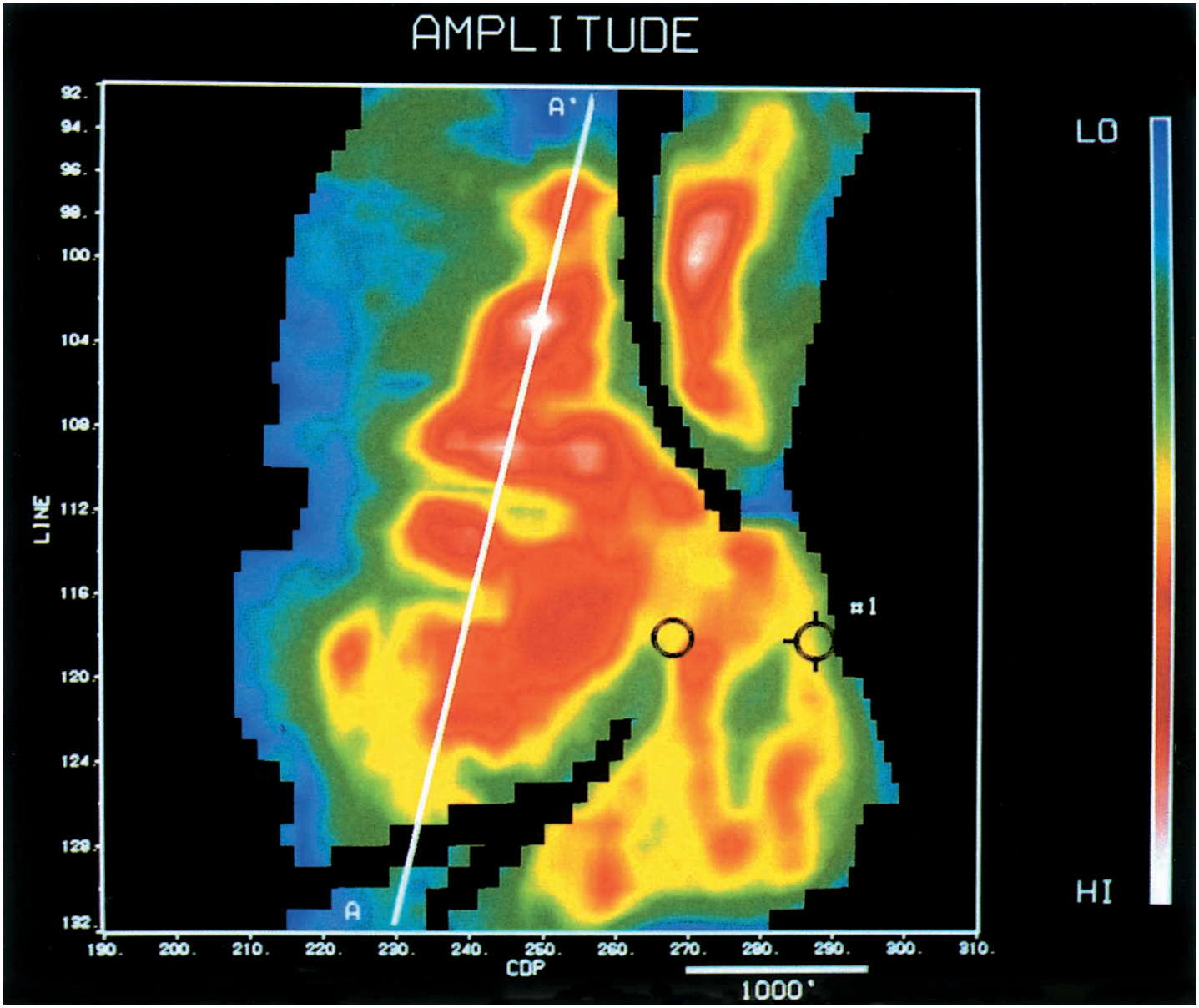

Fig. 14-5-9. Horizon slice showing detuned amplitude. Higher amplitude zones probably represent better sand development with higher porosity. Large variations suggest fast lateral stratigraphic changes. Note the #2 well proposed location is in a weak amplitude area. A well drilled farther downdip could be in a better position to produce. Cross section A-A′ is referenced to Figure 14-5-12.

Downloaded 25 Jun 2012 to 95.28.162.50. Redistribution subject to SEG license or copyright; Terms of Use: http://segdl.org/

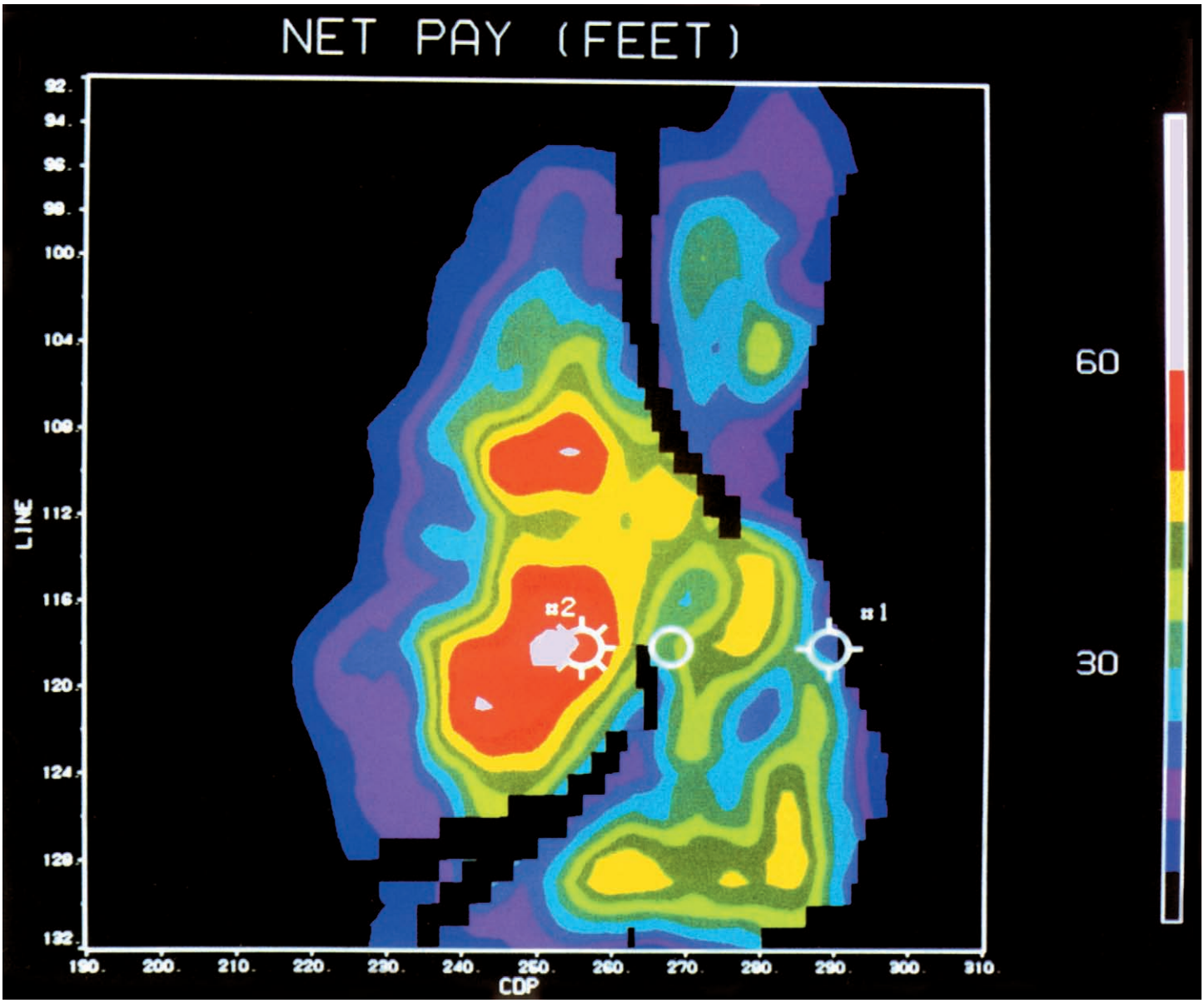

Fig. 14-5-10. Net pay map based on seismic data. Note the #2 well was drilled downdip of the original proposal. A prediction of 58 ft of net pay was confirmed in the #2 well (Figure 14-5-11), which drilled 60 ft of gas.

Downloaded 25 Jun 2012 to 95.28.162.50. Redistribution subject to SEG license or copyright; Terms of Use: http://segdl.org/

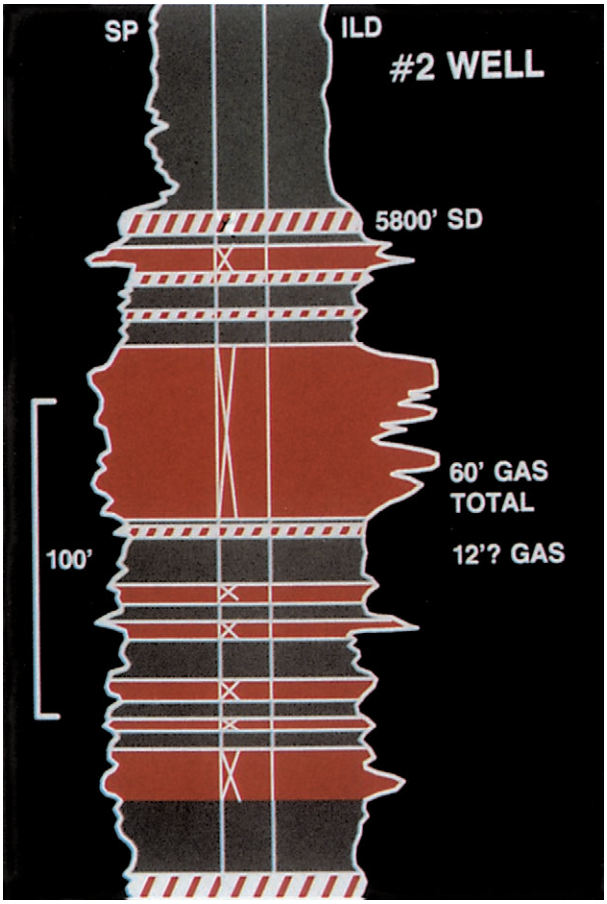

Fig. 14-5-11. E-log of the #2 well with 60 ft of pay. The stratigraphic interval can be correlated to the #1 well, but was mostly faulted there. Production tests show the well to be in a sizeable reservoir.

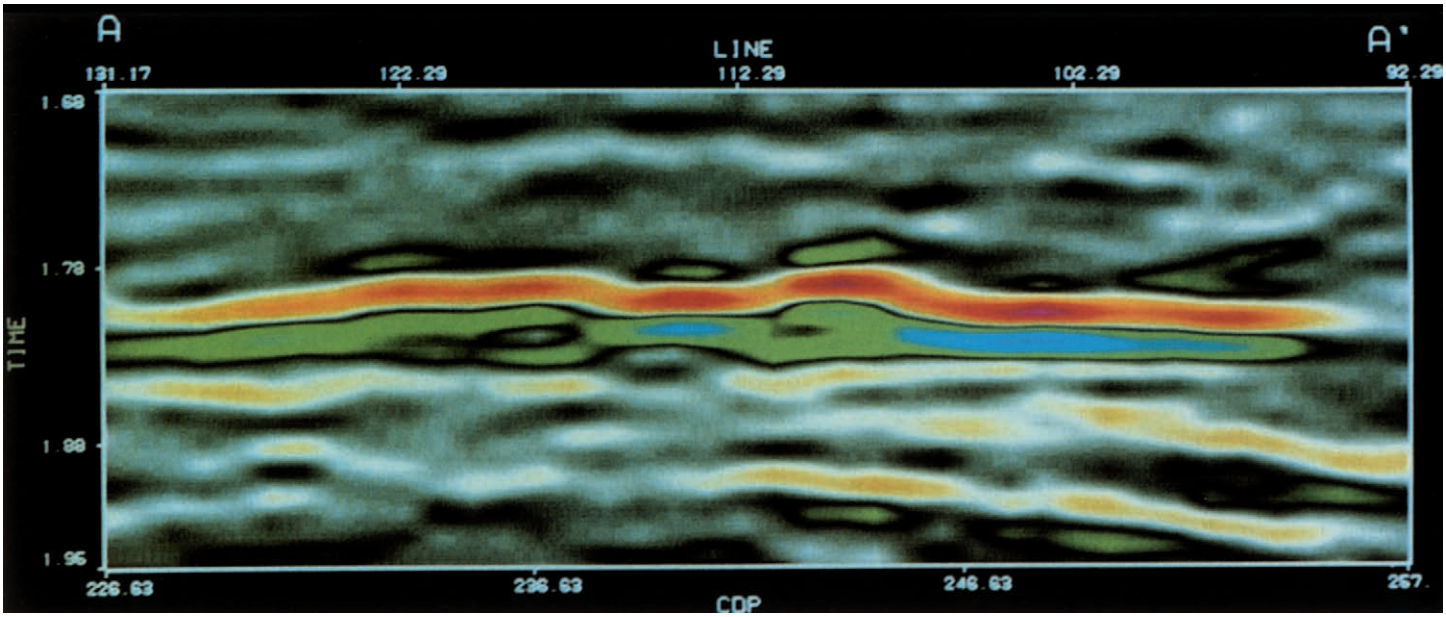

Fig. 14-5-12. Section A-A′ referenced to Figure 14-5-9. The amplitude and structure of the reservoir show rapid areal changes, but appear to be on a common water contact (note consistent flat spot). Apparent stratigraphic changes are potential production barriers.

Downloaded 25 Jun 2012 to 95.28.162.50. Redistribution subject to SEG license or copyright; Terms of Use: http://segdl.org/

Case History 6

A 3-D Reflection Seismic Survey Over the Dollarhide Field, Andrews County, Texas

Michael T. Reblin, Gregory G. Chapel, Unocal North American Oil & Gas Division; Steven L. Roche, Chuck Keller, Halliburton Geophysical Services

Introduction and Survey Planning

Because onshore 3-D surveys can be expensive, the results may not be considered cost-effective. This case history presents an onshore 3-D survey that was cost-effective and that shows the power of 3-D seismic versus well control and 2-D data.

Discovered in 1945, the Dollarhide field is a large faulted anticline in Andrews County which is located on the Central Basin Platform of west Texas. Production in this field is from the Permian *Clearfork, Devonian* Thirty-one, *Silurian* Wristen, and Ordovician *Ellenburger* formations. (The commonly used names for the reservoirs are in italics.) Well spacing is approximately 40 acres (16 ha) and the Devonian formation is currently undergoing CO_2 flooding.

In August and September 1988, a 3-D survey was acquired over a 24 mi^2 (62 km^2) area covering the Dollarhide field. The survey's primary purpose was to accurately image the location of faulting within and bounding the Devonian. This would aid in planning the CO_2 flood and possibly locate previously untested fault blocks.

Geophysicists from Unocal and Halliburton Geophysical Services (HGS) worked together to design the 3-D survey. Information (including depth of the main objective, velocity, maximum dip desired to be recorded, and reflection data quality) was compiled from previous 2-D seismic data and geologic data from well logs. Migration aperture, Vibroseis sweep bandwidth, source and receiver arrays, CMP fold, and offset geometry were all modeled and examined for optimum recording parameters. We determined that a subsurface bin size of 110 ft inline × 110 ft crossline would adequately sample the subsurface for processing through 3-D migration.

The high cost of land 3-D seismic surveys has been a deterrent to their use in both exploration and production geophysics. HGS suggested two innovations to reduce costs:

- Reduce the amount of data collected and replace it with trace interpolation prior to 3-D migration. Well control in the area reveals the general dip of the target horizon. Because the dip in the north-south direction is less steep than in the east-west direction, we could reduce the sampling in the former. We were able to use a subsurface sample interval of 110 ft (34 m) in the east-west (inline) direction and 330 ft in the north-south (crossline) direction, thus reducing by 66% the amount of data to be acquired. This also generated a further cost relief because the lessened number of receiver and vibrator lines meant fewer surface access permits to be obtained. And, economies were realized also in data processing because the number of records that had to go through CMP stack was reduced by 66%.
- Use two vibrators simultaneously to sweep two separate lines. This technique improved the productivity of the recording crews by approximately 70%. The separation of the two source signals is accomplished by upsweep-downsweep and phase rotation summing. Source separation is performed in the field during the correlation and sum processes. The isolation of the two sources using this method is on the order of 40 dB.

Data Collection and Processing

The data were acquired using a 384-channel DFS VII recording system deployed as a four-line swath. The receiver lines were spaced 1320 ft (400 m) apart with two source lines per swath (Figure 14-6-1). Each swath generated eight subsurface profiles, separated by 330 ft. After each swath, the spread was moved 2640 ft or 800 m (two cable lines) in the crossline direction. This geometry results in the subsurface swaths being adjacent as opposed to overlapping. This can be described also as "one fold crossline." With 12 swaths being recorded, the subsurface area is sampled 110 ft in the line and 330 ft in the crossline directions. The source interval averaged 440 ft (130 m). The resulting effective fold is 18-24 when source-to-receiver offsets are considered relative to the depth of interest.

Data processing techniques included: geometry description; field record quality control; surface-consistent deconvolution; preliminary stack; velocity analysis; residual static estimation; 3-D *f-k* DMO; stack; trace interpolation; and 3-D migration.

Downloaded 25 Jun 2012 to 95.28.162.50. Redistribution subject to SEG license or copyright; Terms of Use: http://segdl.org/

At several steps during the processing of this survey, different parameters were tested and reviewed — including the deconvolution method, benefit of DMO, migration velocity analysis, and poststack migration algorithm. A benefit was realized by including DMO in the processing sequence in that the diffracted image of the subsurface was improved. This enabled the trace interpolation algorithm to perform better in the conversion of 110 ft × 330 ft subsurface bins to 110 ft × 110 ft bins. After 3-D migration, the data volume was moved to a workstation for interactive interpretation.

Interpretation and Results

The results of this 3-D survey are impressive. Figure 14-6-2 shows the structure map of the Devonian at Dollarhide field as determined by the 40-acre-spaced well control. This map has gone through many evolutions in the 46 years since the field was discovered. Notice that the contours are relatively smooth, the anticline is cut by four simple cross-faults and bounded on the east by a fault.

The structure map from the 3-D seismic survey (Figure 14-6-3) is more complex. The contouring is more detailed and the cross-faults are not simple. The structure map shows the detail of the Devonian that the 3-D seismic has allowed us to see. This shouldn't be a surprise, as our seismic data points are equivalent to a spacing of approximately four wells per acre. Considering that a seismic trace is an approximation to a synthetic seismogram from a sonic log, we indeed have a very powerful means of detailed mapping of subsurface structure.

There are two principal ways to look at the 3-D seismic data volume. One is the conventional seismic line display (Figure 14-6-4). On the crest of the structure, the top of the Clearfork Formation is the strong event at approximately 780 ms. The Devonian, at approximately 1000 ms on the upthrown block and 1350 ms on the downthrown block, is colored purple. The top of the Ellenburger is a high-amplitude event at approximately 1250 ms. At about 960 ms, an unconformity can be seen that helps highlight one of the more remarkable features of the data — a fault zone showing over 2000 ft (610 m) of displacement on the Devonian marker. The imaging of this fault zone demonstrates one of the shortcomings of some 3-D surveys. Due to economics, lines may not be long enough to properly image all the features (such as large faults or extremely steep dip) within the survey limits. This survey was designed to image the upthrown block so that the incomplete image east of the major fault was as expected.

The other view of the 3-D data volume, and one not available with 2-D data, is the time slice. This view allows the interpreter to see subtle features which may not be apparent or as readily interpretable on conventional seismic sections. A time slice (Figure 14-6-5) through the 3-D data volume at 1008 ms (about 4600 ft subsea or 7800 ft below surface) demonstrates this. The cross-faults are seen as northeast-southwest lineations. The previously undetected grabens not seen on Figure 14-6-2 are seen as easterly pullouts on the time-sliced peaks (blue)

Fig. 14-6-1. Swath design of the 3-D dual-source survey.

Downloaded 25 Jun 2012 to 95.28.162.50. Redistribution subject to SEG license or copyright; Terms of Use: http://segdl.org/

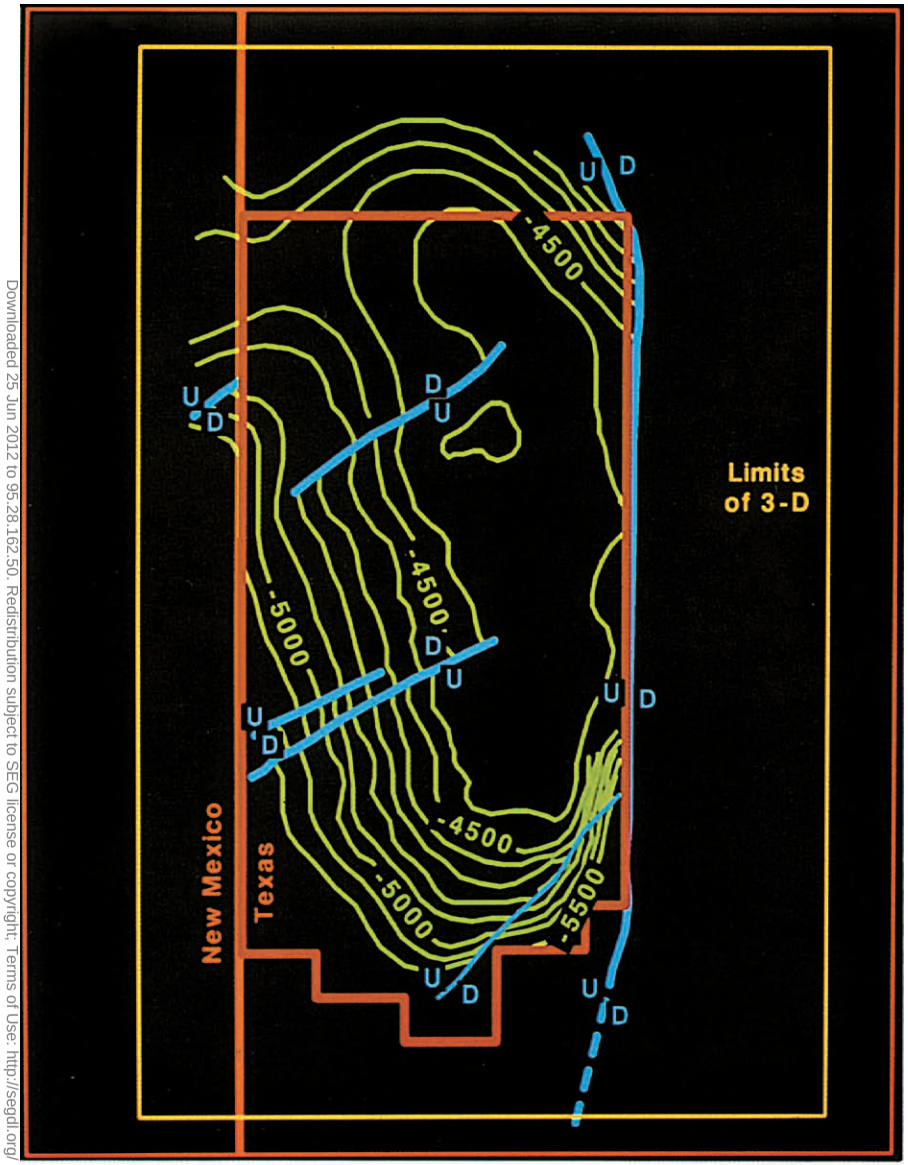

Fig. 14-6-2. Simplified Devonian structure map from 40-acre (16-ha) well control. The unit outline is red.

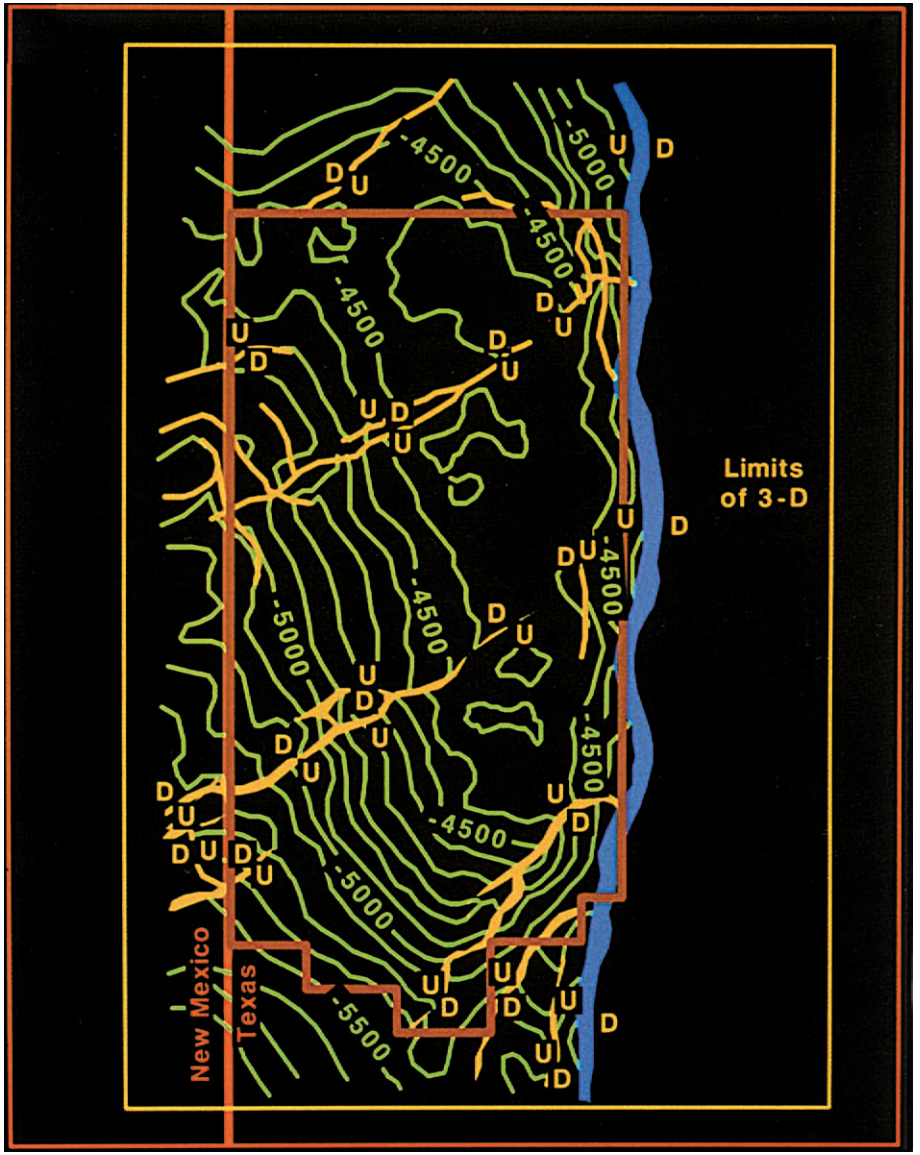

Fig. 14-6-3. Simplified Devonian structure map from 3-D seismic interpretation.

Downloaded 25 Jun 2012 to 95.28.162.50. Redistribution subject to SEG license or copyright; Terms of Use: http://segdl.org/

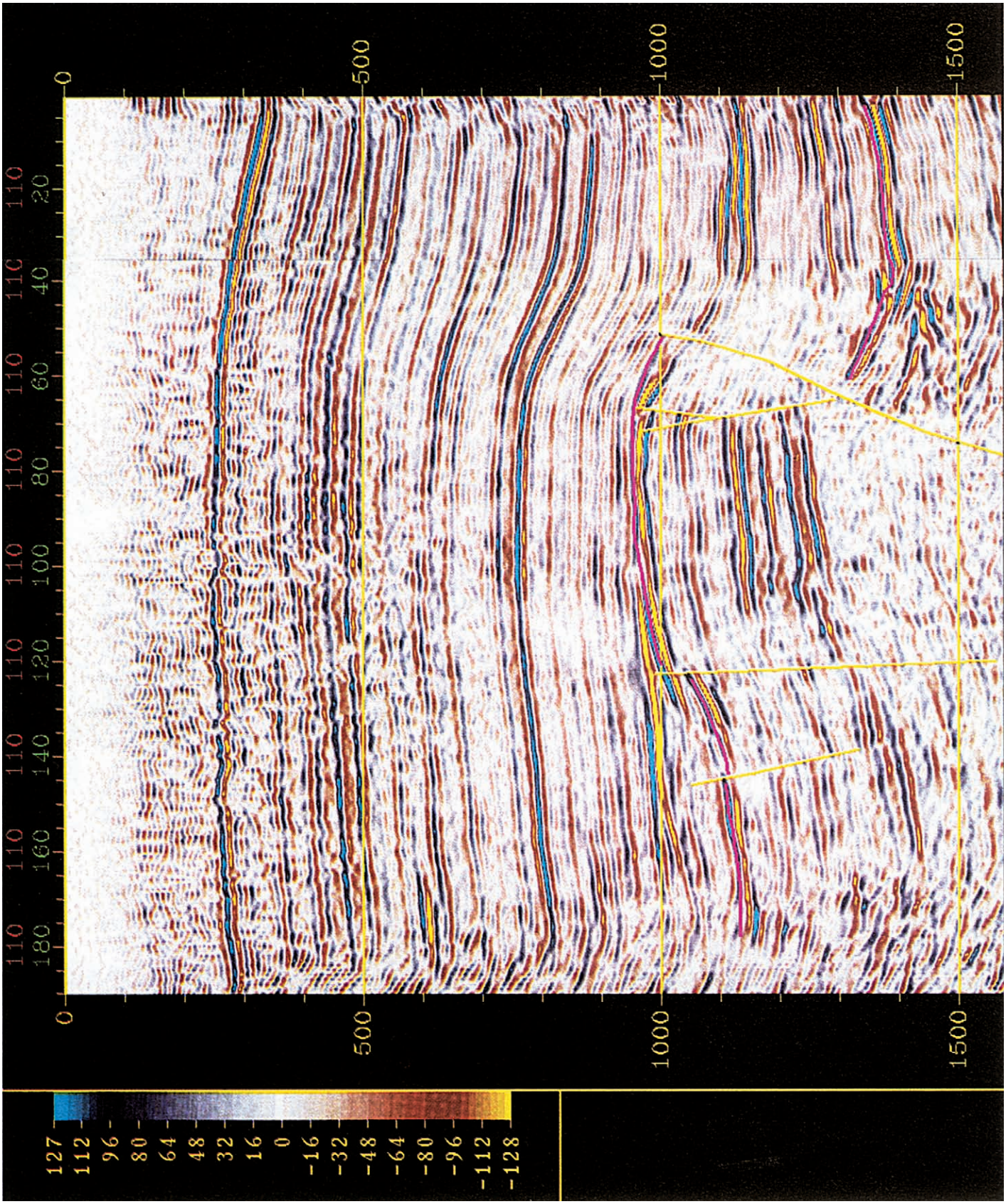

Fig. 14-6-4. East-west seismic line 110. Devonian horizon is annotated in purple; the interpreted faults are yellow.

Downloaded 25 Jun 2012 to 95.28.162.50. Redistribution subject to SEG license or copyright; Terms of Use: http://segdl.org/

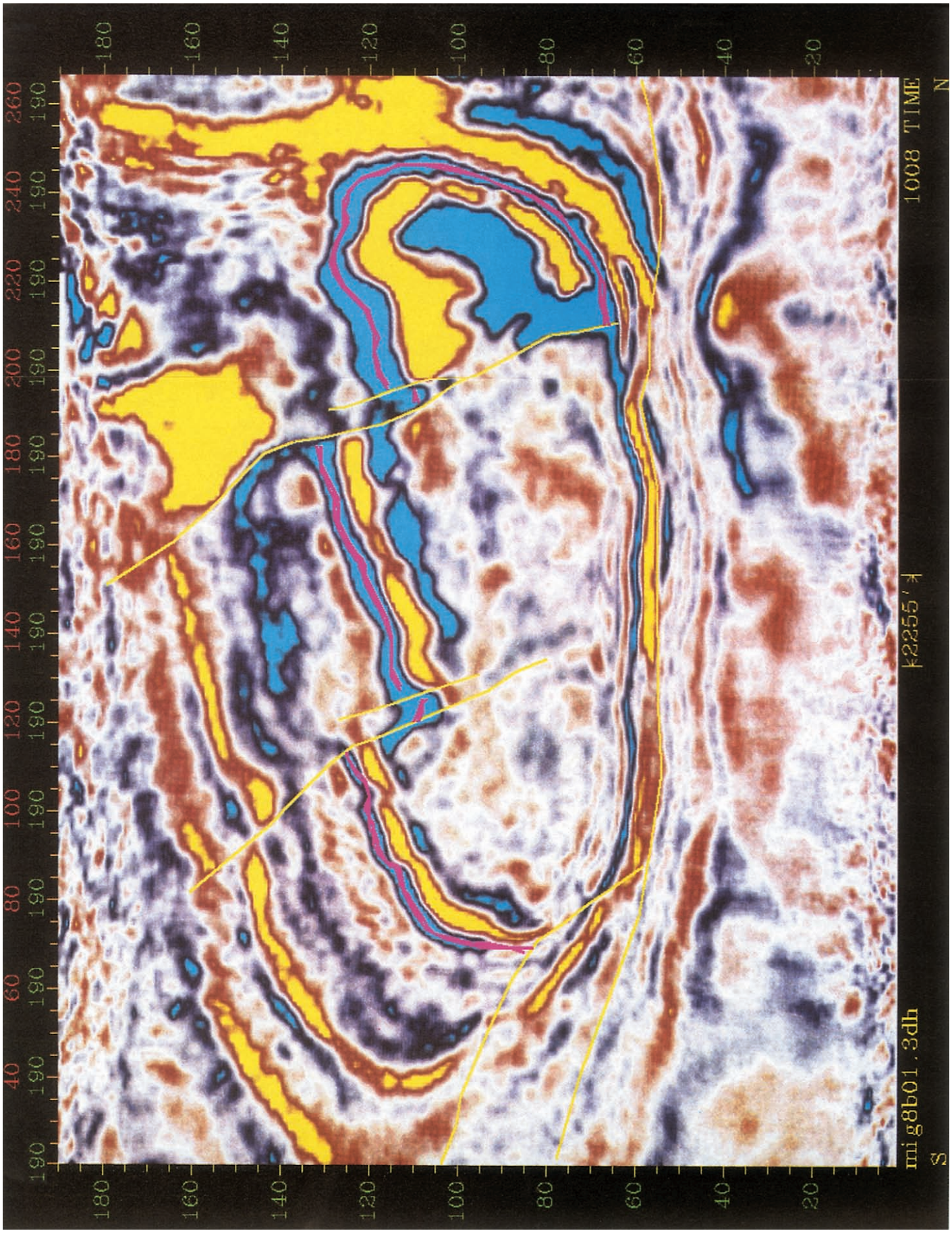

Fig. 14-6-5. Time slice at 1008 ms (about 4600 ft [1400 m] subsea or 7800 ft [2380 m] below surface). Devonian horizon is annotated in purple; the interpreted faults are yellow.

Downloaded 25 Jun 2012 to 95.28.162.50. Redistribution subject to SEG license or copyright; Terms of Use: http://segdl.org/

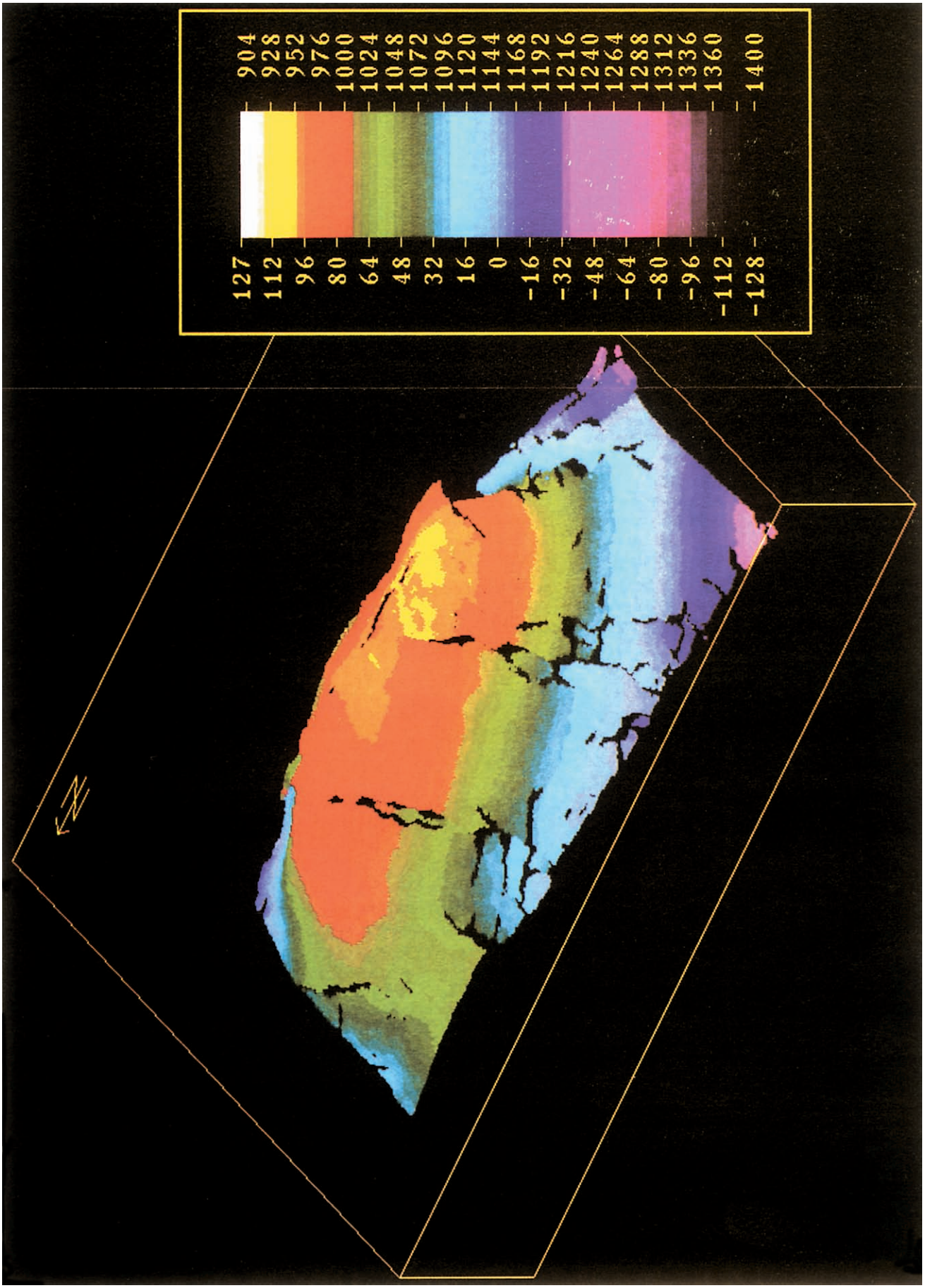

Fig. 14-6-6. Northeast perspective view of the Devonian time-structure map. The color change from red to green is at the same time as the time slice in Figure 14-6-5. Note the cross-fault definition.

Downloaded 25 Jun 2012 to 95.28.162.50. Redistribution subject to SEG license or copyright; Terms of Use: http://segdl.org/

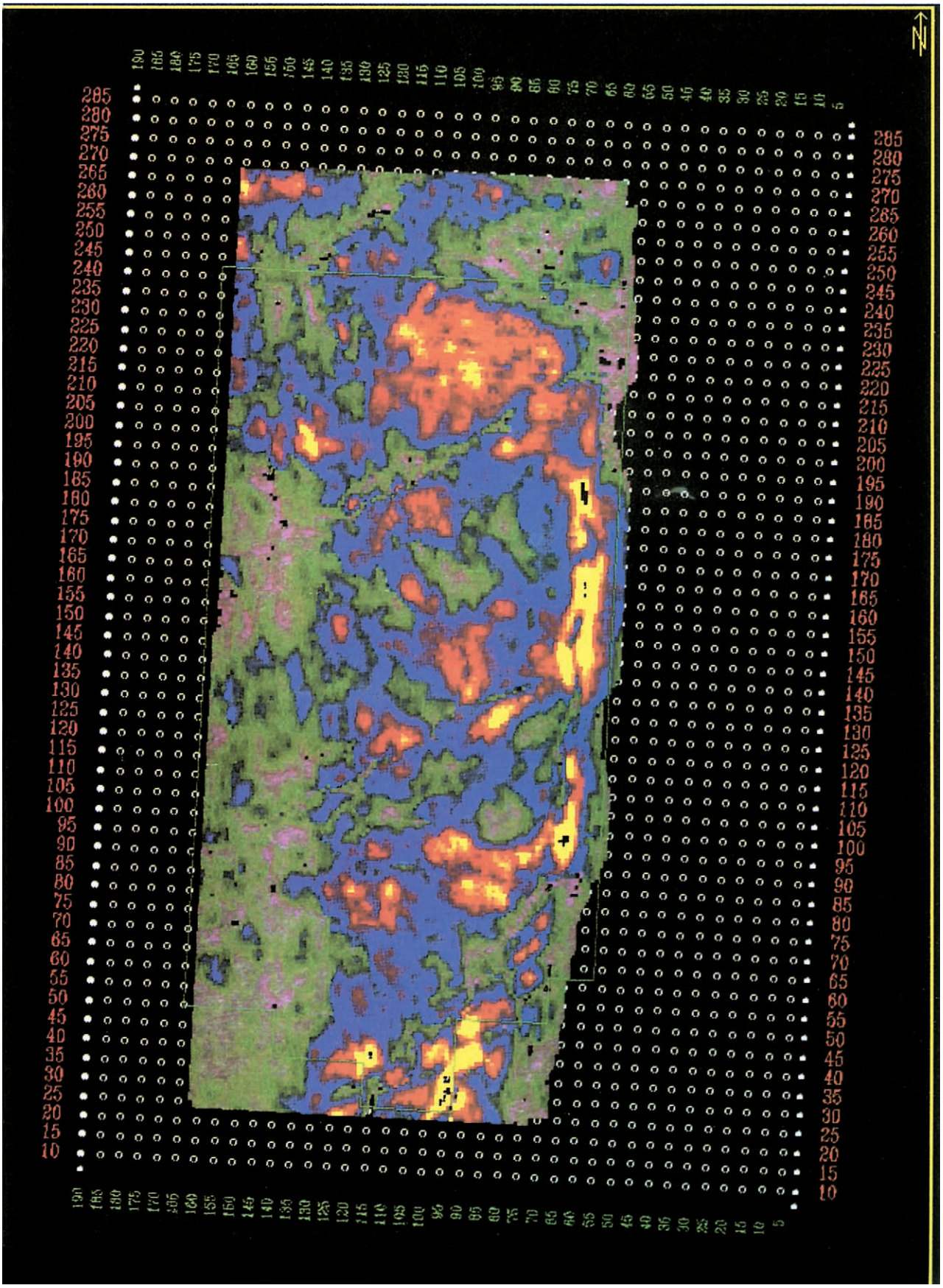

Fig. 14-6-7. Composite horizon slice (seismic-amplitude map) of the producing Devonian horizon. Largest amplitudes are yellow and red and smallest amplitudes are blue and green.

Downloaded 25 Jun 2012 to 95.28.162.50. Redistribution subject to SEG license or copyright; Terms of Use: http://segdl.org/

and troughs (red) in the areas of the cross-faulting. Mapping of the data is now possible in both the vertical and horizontal sense. Both offer unique perspectives of the data volume.

Because the 3-D survey gives an evenly sampled volume of data, another display of the data is possible after a horizon is interpreted. In Figure 14-6-6, a perspective view of the Devonian horizon time map as viewed from the southwest is presented. It shows the northerly plunge of the anticline, which isn't readily apparent on the Devonian horizon structure map (Figure 14-6-3). The cross-faults, with their associated grabens, are quite distinct and give a real feel for the relative throw of faults. This display has helped the geologists and engineers develop a better understanding of the field shape and how the faults impact the ongoing CO_2 flood project.

Having the 3-D data volume loaded on an interactive workstation allowed the interpreters to generate various attribute displays that took us beyond the traditional time interpretation. Using the seismic peak and trough associated with the producing Devonian horizon, a composite horizon slice (amplitude map) was made (Figure 14-6-7). The hot colors, yellow and red, represent larger amplitudes and, in most cases, correspond with the better wells in the field. The cool colors, blue and green, represent lower seismic trace amplitudes along the producing Devonian. The amplitudes are interpreted to be related to the thickness of the producing zone — high amplitudes to a thick zone, low amplitudes to a thin zone. The possible exception is the linear pattern next to the north-south bounding fault where we believe the larger amplitudes are possibly related to poorly imaged steep dips. The major cross-faults are seen as northeast-southwest lineations, which divide the structure into four major fault blocks. The CO_2 flood is expected to have better results in the northern block, which is denoted by the higher amplitudes. The flood was initiated in the northern block last year. The next block south has had the poorest flood results to date, which seem related to the dominance of the lower amplitudes on the composite amplitude map. The third fault block was the first one flooded and has the best results to date, as could be predicted from the abundance of high amplitudes. The smallest fault block, located to the southeast, is faulted below the producing limits of the field to the north. However, a well drilled to the productive Devonian horizon in 1948 recently has been reentered and reevaluated, and could open up an extension to the field. The higher amplitudes indicate it could be a very productive block with good CO_2 flood potential.

Conclusions

Earlier in this case history, we alluded to the cost-effectiveness of this 3-D survey. One of the features that helped us sell the concept to management was the comparison of the cost to shoot this 3-D survey to a 1/2-mi grid of 2-D data and the dryhole cost of a Devonian test. The 2-D survey cost (including acquisition, surface permits, and processing) was estimated at $750,000 for 150 line-mi. The dryhole cost of a Devonian test is approximately $300,000. To date, two Devonian locations have not been drilled as the 3-D results indicated they were uneconomic. Shooting conventional swath 3-D to record 110 ft × 110 ft bins was estimated at about $1,300,000 (generating 1140 mi (1820 km) of 3-D data over the 24 mi^2). Using the 3-1 interpolation technique and simultaneous source recording, the survey actually cost $400,000. This cost is approximately half that for a 2-D survey, a third of a conventional 3-D survey, and only slightly more than a dry hole. The after-tax profit of a primary Devonian development well in the Dollarhide field is about $1,000,000. By adding one well to the field, we easily recover the cost of the survey plus give the geologists and engineers a more detailed look at a reservoir that is still being developed during the tertiary recovery stage.

The results to date are multifold. The cross-faulting of the Devonian producing horizon is much more extensive than previously mapped. This knowledge has influenced the location of several wells for the CO_2 flood, and the engineers continue to use the results for future programs. Some of the newly discovered faults have generated fault traps within the field that have not been drilled and are now being evaluated to determine their potential. Evidence suggests that the fault block to the southeast may be productive, although it was drilled and abandoned over 40 years ago. Lastly, preliminary studies of the Clearfork Formation indicate the 3-D data will help in the development of the plan for the secondary recovery from that producing unit.

Land 3-D surveys can be economical and may produce results well beyond the initial goals. The two acquisition techniques discussed here are just two examples of how to shoot cost-effective land 3-D surveys. The 3-D seismic is a necessary tool to use in developing new discoveries and extending the life of old fields.

Downloaded 25 Jun 2012 to 95.28.162.50. Redistribution subject to SEG license or copyright; Terms of Use: http://segdl.org/

Case History 7

Shallow 3-D Seismic and a 3-D Borehole Profile at Ekofisk Field

John A. Dangerfield, Phillips Petroleum Company Norway

Ekofisk field in the Norwegian North Sea was discovered in 1969 but after more than 20 years of production much remains to be understood (Sulak, 1990). This case history describes some of the 3-D seismic work carried out at Ekofisk field by the Phillips Licence 018 Group of Companies: a short offset 3-D to image the very shallow layers, a normal surface seismic 3-D especially processed for shallow data, and a 3-D borehole profile, shot to image the crest of the field beneath a gas cloud.

Figure 14-7-1 shows the areas covered by the various 3-D surveys. It also shows the reservoir area that is obscured from normal seismic view by gas in the overlying sediments.

Acquisition and Processing of the Short Offset 3-D

This survey was acquired in 1987 to delineate faults close to the Ekofisk Complex that might be reactivated by the (now) 5 m subsidence of the field (Wiborg and Jewhurst, 1986). The 4 × 2 km survey was collected with flip-flop acquisition, using single water guns as the sources, and recording 1.5 s of data. The twin hydrophone cables each contained 48 five m groups. Reflection lines were 10 m apart. The processing was standard except for the extremely careful checking of recording geometry and effective time zero. One velocity function was used for the entire survey. A complete description is presented by Dangerfield (1992).

Acquisition and Processing of the Normal Surface Seismic

The acquisition in 1989 was aimed at all possible levels from sea bottom to 7 s. The 9 × 17 km area was shot using flip-flop, twin sources of 3680 $in.^3$ air guns, and twin hydrophone cables, collecting reflection lines that were 25 m apart.

The data from the uppermost 2 s were processed separately in order to obtain the highest possible resolution. They were processed with particular care in muting and velocity analysis. Surprisingly, one velocity function was optimal for almost the complete area.

Acquisition and Processing of the 3-D Borehole Profile

Imaging the crestal area below the gas never has been found possible with normal seismic methods but borehole profiles generally have worked extremely well by undershooting the gas. The borehole profiles, however, have revealed many faults that can be linked in many different patterns. The advantages of 3-D data sets for fault interpretation are so strong that we took the first opportunity to acquire a 3-D borehole profile in the gas-obscured area.

In July 1989, a series of 41 walkaway lines was shot into an eight-geophone array in the deviated well 2/4 K17. Each single walkaway line thus recorded a swath of eight roughly parallel reflection lines. The geophones in the array each were separated by 15 m. The hole deviation was about 45° so the geophone array spanned about 80 m horizontally. The 41 walkaway lines were shot in a regular grid (Figure 14-7-2) with the geophone array pulled up the hole such that each walkaway line passed over the middle of the geophone array. The walkaway lines were 5 km long and perpendicular to the well. Successive lines were 40 m apart. The acquisition area was limited by the presence of the Ekofisk Complex.

The acquisition resulted in a total of 328 reflection lines. Each line was processed separately to the velocity filter stage using standard walkaway techniques; then a one-pass migration of the whole data set was run, accomplishing both NMO and 3-D migration. Unfortunately, the deepest 15 levels were so severely distorted by the gas that it was not useful to migrate these data. The input to the migration was restricted to data from geophones 3 to 6 in each array, overlapping geophones not being used. Crossline migration was performed using a sliding window of five geophone levels. The results were output as a regular 10 × 10 m grid.

Interpretation of the Short Offset Data

The excellent resolution of the data, from the sea bottom at 100 ms down to 1 km depth, showed that there were no faults with throws of more than 2 m in the region examined.

Downloaded 25 Jun 2012 to 95.28.162.50. Redistribution subject to SEG license or copyright; Terms of Use: http://segdl.org/

Figures 14-7-3 and 14-7-4 show two of the time slices indicating clear subglacier river deposits (Dangerfield, 1992). Figure 14-7-3 shows the presence of a break of slope, running roughly north-northeast–south-southwest where the rivers abruptly change character as shown in the following figures.

Interpretation of the Normal 3-D Data

We had expected that the results of the shallow data would be compromised severely by the areal size of the source, 17 × 20 m, and by the flip-flop acquisition, necessitating 50 m between shots in each reflection line. In practice, the results turned out extremely well. The water bottom showed little detail but 40 ms deeper, and down to 2 s, sedimentary and structural features showed clearly, setting the data from the earlier survey into a more interesting context.

Figure 14-7-5 is a time slice from almost the same time as Figure 14-7-4 but encompassing a much larger area. It shows several rivers and streams carrying glacial meltwater. At this period the ice above is believed to have been about 3 km thick. The area southwest of the Complex was fairly flat, as evidenced by the complicated channeling there. The regular steps every 900 m or so in the major river north of the Complex may be due to the water channel flowing along the edges of blocks that were slightly tilted, like giant, uneven paving slabs.

The presence of two sets of nearly vertical fractures set at 90° to each other in the overburden is portrayed dramatically in the "arrowhead" appearance in Figure 14-7-6. This pattern repeats many times throughout the data, on different scales but with similar orientations, and indicates a pervasive fracture system. The orientation of one set is subparallel to that of the break of slope which controlled the river in Figure 14-7-3. Reactivation of the fracture system appears to control surface features during deposition and probably also produced the blocks suggested in Figure 14-7-5. The presence of faults displacing the "arrowhead" feature are very clearly displayed in Figure 14-7-7. The fault displacements are of the order of 3 m.

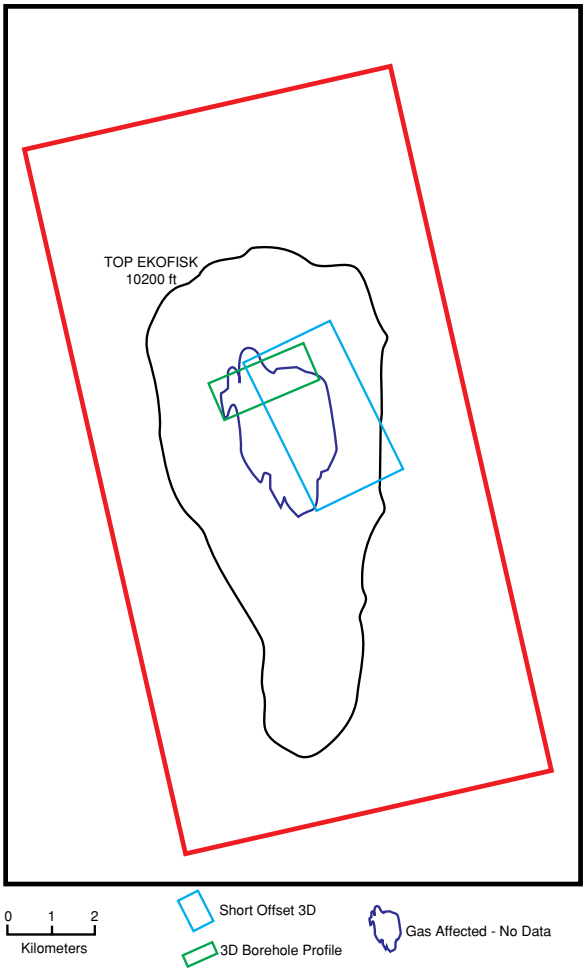

Fig. 14-7-1. 3-D seismic areas in relation to the field outline and the gas-affected area. The field is outlined in black and the full scale 3-D area in red.

Downloaded 25 Jun 2012 to 95.28.162.50. Redistribution subject to SEG license or copyright; Terms of Use: http://segdl.org/

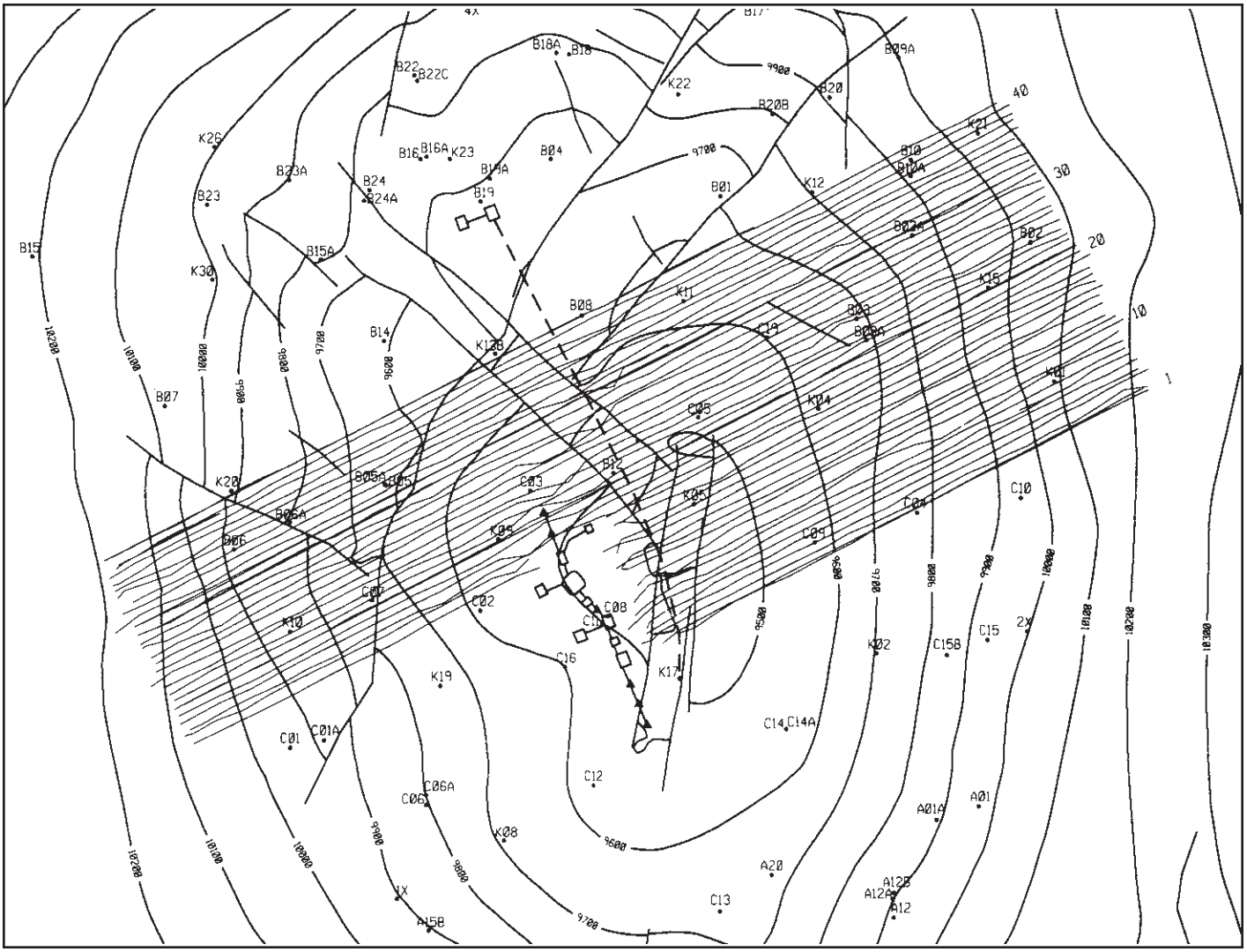

Fig. 14-7-2. 3-D borehole profile acquisition lines superimposed on the 1989 top reservoir depth map.

Although only a brief selection of time slices from the shallower layers have been shown, the complete 3-D data sets form continuous series, with slight but distinct differences in successive slices, so that the evolution of the sedimentary features can be followed on a meter by meter basis.

Interpretation of the 3-D Borehole Profile

The resulting borehole profile in the northern half of the data set showed a clear image in an area where our 3-D surface seismic failed completely. Figures 14-7-8, 14-7-9, and 14-7-10 locate and compare line 40 from the 3-D borehole profile with a 3-D surface seismic line from the same place. Figure 14-7-11 shows line 16 (east-west) and crossline 150 (north-south) with the top Ekofisk Formation interpreted. The data showed the presence of many faults too small to map but with similar orientations to those of the overburden fracture system. It also showed the continuation of a crestal graben originally found in the gas-affected area by walkaway profiling (Christie and Dangerfield, 1987) and subsequently penetrated by drilling. Figure 14-7-12 shows a time slice through the reservoir with the top Ekofisk marked in green. The graben clearly displaces the Ekofisk horizon.

Conclusions

1) The normal 3-D shallow data set showed the fracture system that pervades the Tertiary and controlled some surface features during deposition.

2) High-quality data close to the water bottom is readily available in the shallow section in normal 3-D data sets. This suggests that an important part of the work currently carried out by site survey vessels is accomplished in the course of a normal 3-D survey.

3) The 3-D borehole profile showed the extent of the crestal grabens inside an area opaque to normal seismic methods.

Downloaded 25 Jun 2012 to 95.28.162.50. Redistribution subject to SEG license or copyright; Terms of Use: http://segdl.org/

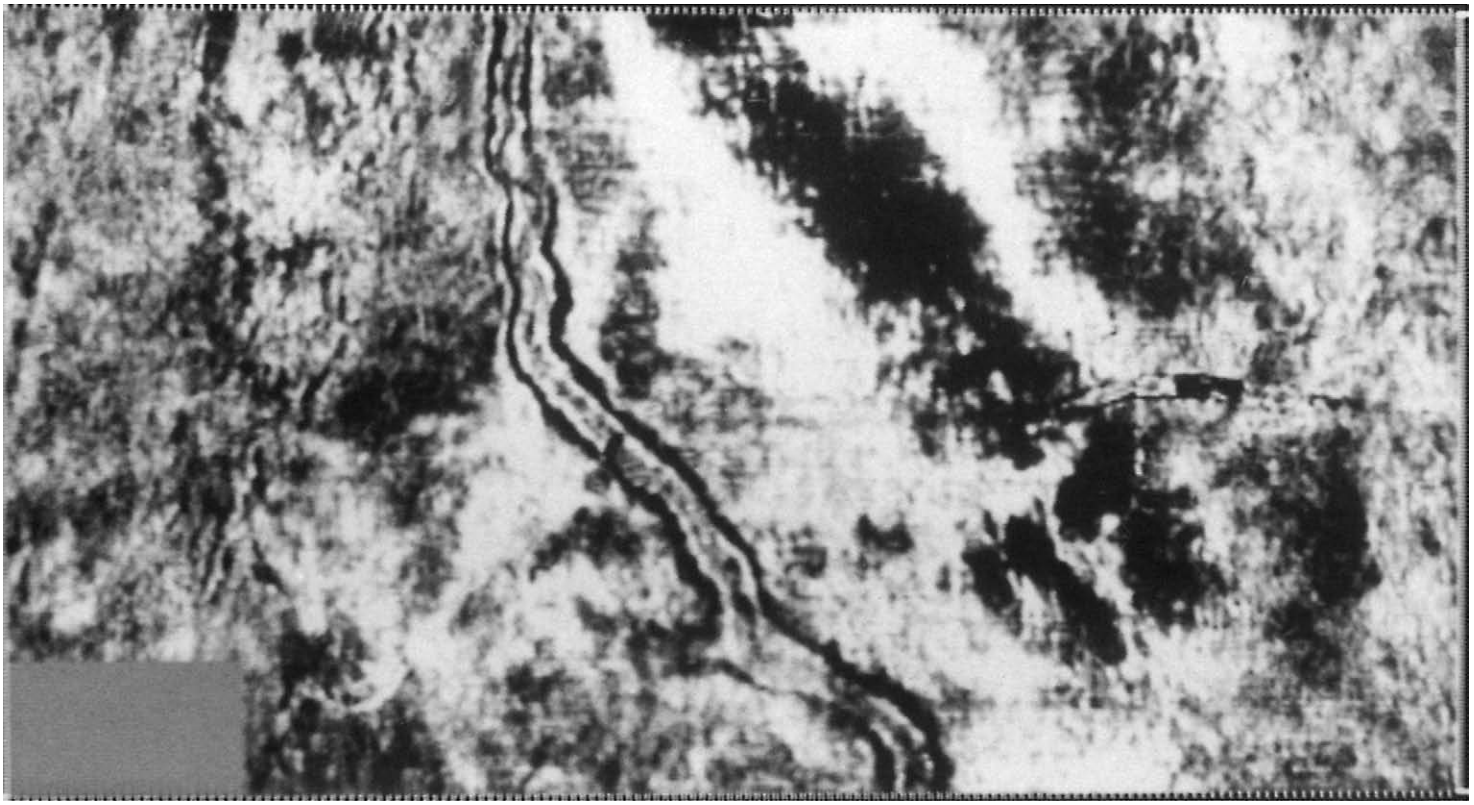

Fig. 14-7-3. Short offset survey time slice from 191 ms.

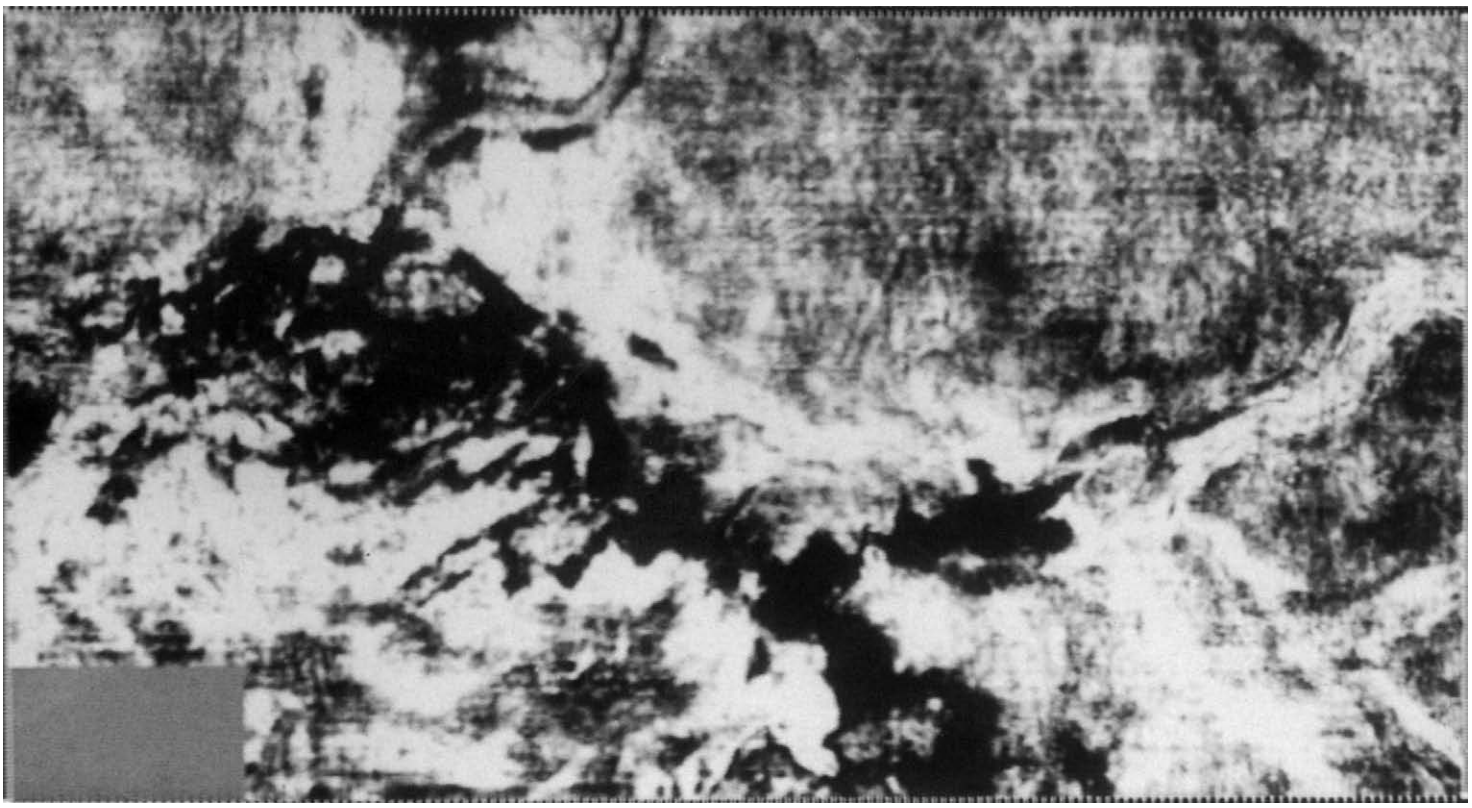

Fig. 14-7-4. Short offset survey time slice from 242 ms.

Downloaded 25 Jun 2012 to 95.28.162.50. Redistribution subject to SEG license or copyright; Terms of Use: http://segdl.org/

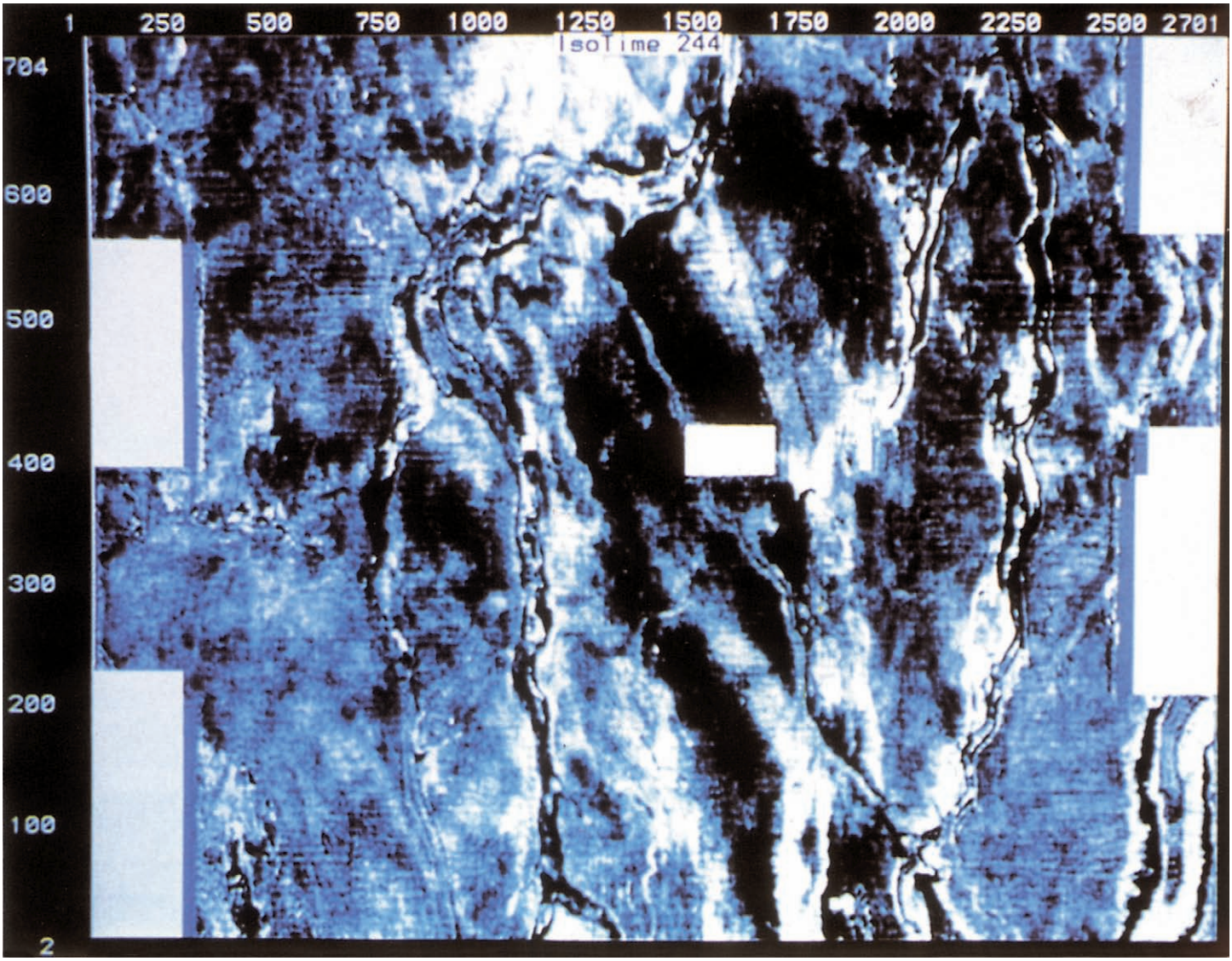

Fig. 14-7-5. Full-scale survey time slice from 244 ms.

4) 3-D borehole profiles should be considered as a working alternative to 2-D borehole profiles since the extra rig time and cost are surprisingly small and the benefits of 3-D are substantial. The method should be particularly suitable for time-lapse reservoir monitoring.

The statements in this case history reflect those of the author and not necessarily those of any of the Phillips Licence 018 Group of Companies. The author thanks the Group for permission to publish the data.

References

Brewster, J., J. Dangerfield, and H. Farrell, 1986, The geology and geophysics of the Ekofisk field waterflood: J. Marine and Petroleum Geology, v. 3, p. 139-170.

Christie, P. A. F., and J. A. Dangerfield, 1987, Borehole seismic profiles in the Ekofisk field: Geophysics, v. 152, p. 1328-1345.

Dangerfield, J. A., 1992, Ekofisk field — Subsidence fault analysis using 3-D seismic, *in* Reservoir Geophysics, R. E. Sheriff, ed., SEG Investigations in Geophysics No. 7, p. 110–121.

Sulak, R. M., 1990, Ekofisk field — The first twenty years: SPE Annual Conference, New Orleans, September 1990.

Wiborg, R., and J. Jewhurst, 1986, Ekofisk subsidence detailed and solutions assessed: Oil and Gas Journal, v. 84, no. 7, p. 47-55.

Downloaded 25 Jun 2012 to 95.28.162.50. Redistribution subject to SEG license or copyright; Terms of Use: http://segdl.org/

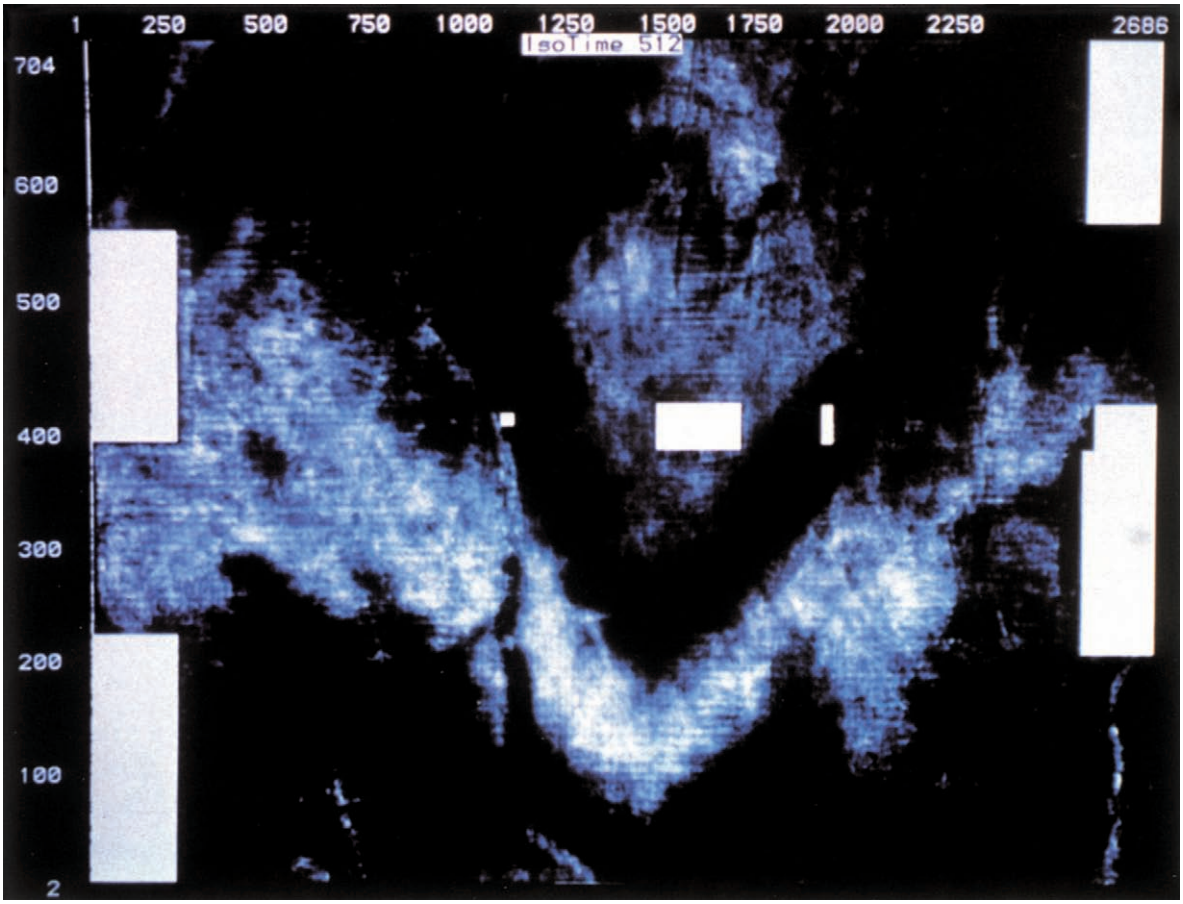

Fig. 14-7-6. Full-scale survey time slice from 512 ms.

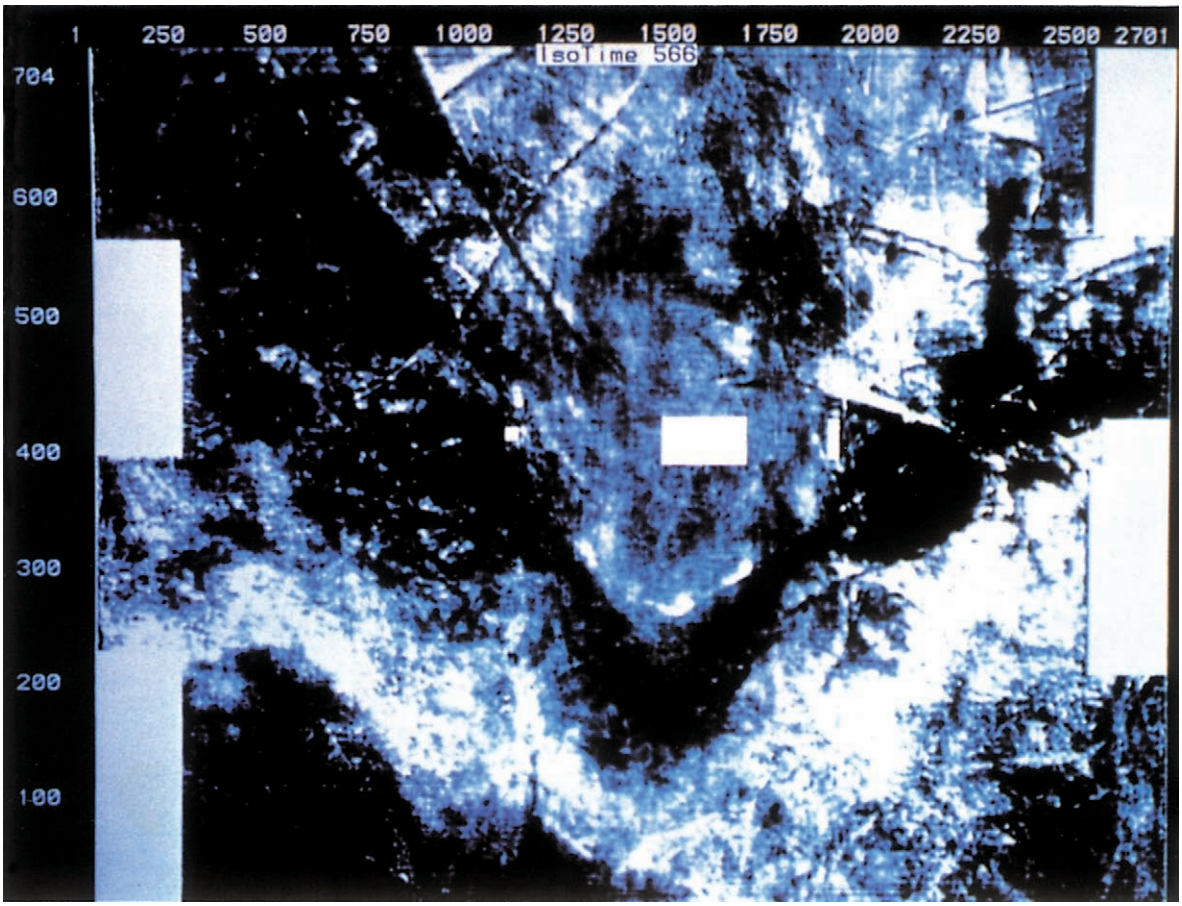

Fig. 14-7-7. Full-scale survey time slice from 566 ms.

Downloaded 25 Jun 2012 to 95.28.162.50. Redistribution subject to SEG license or copyright; Terms of Use: http://segdl.org/

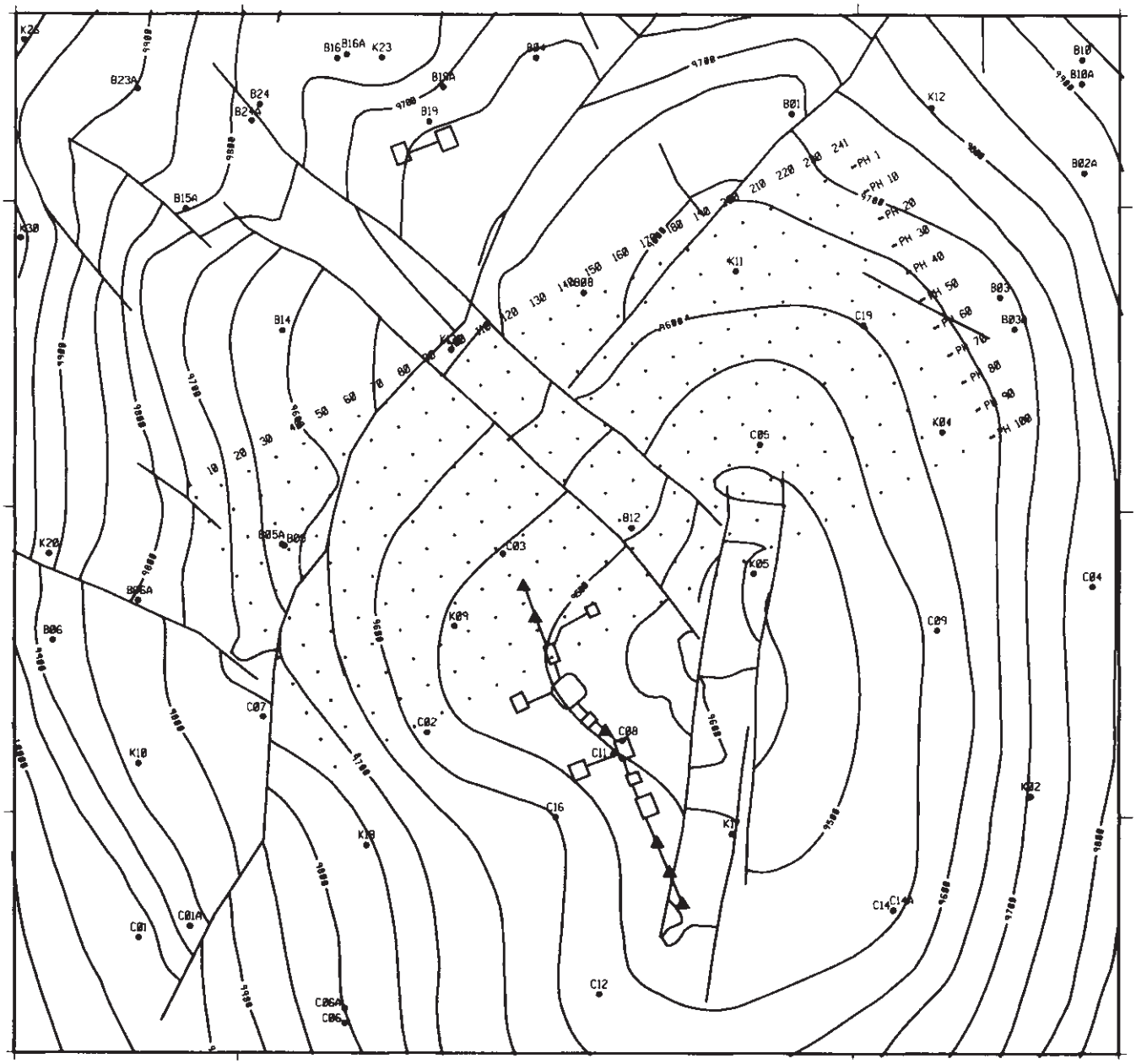

Fig. 14-7-8. Location of the 3-D borehole profile migrated data output grid superimposed on the 1991 reservoir map.

Downloaded 25 Jun 2012 to 95.28.162.50. Redistribution subject to SEG license or copyright; Terms of Use: http://segdl.org/

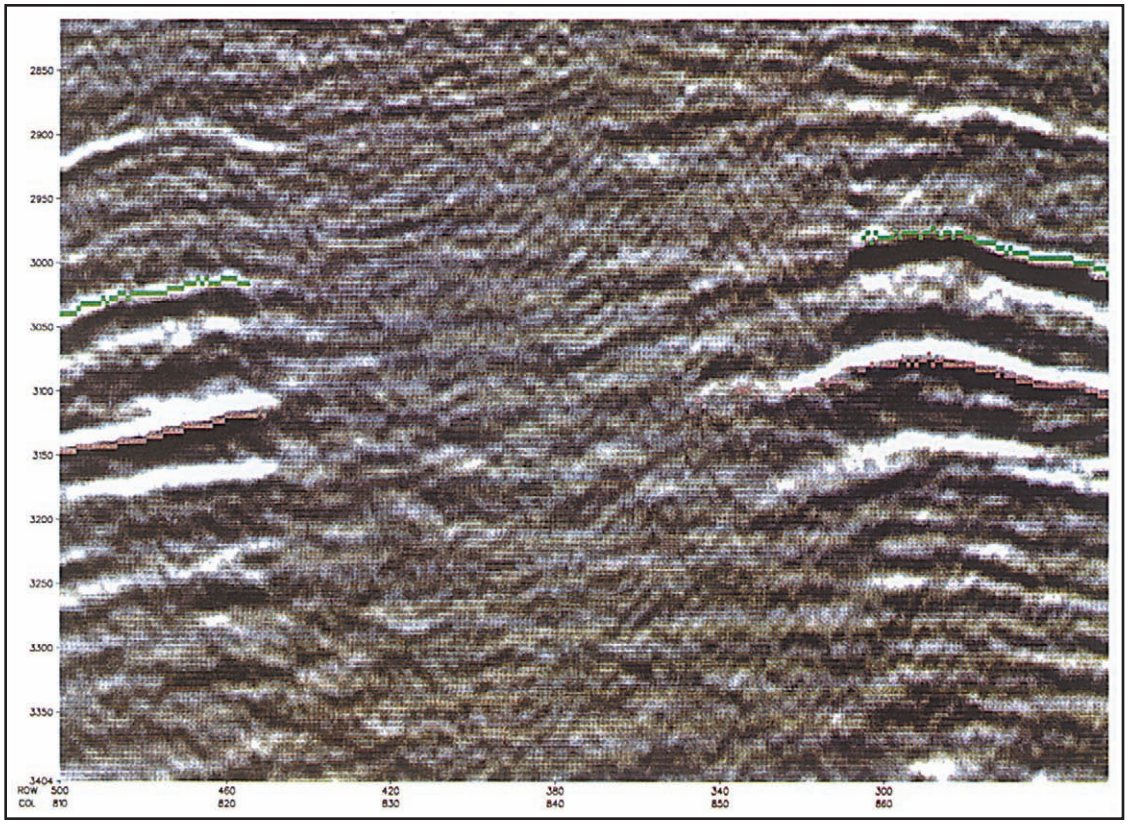

Fig. 14-7-9. Gas-affected seismic line in the borehole profile area.

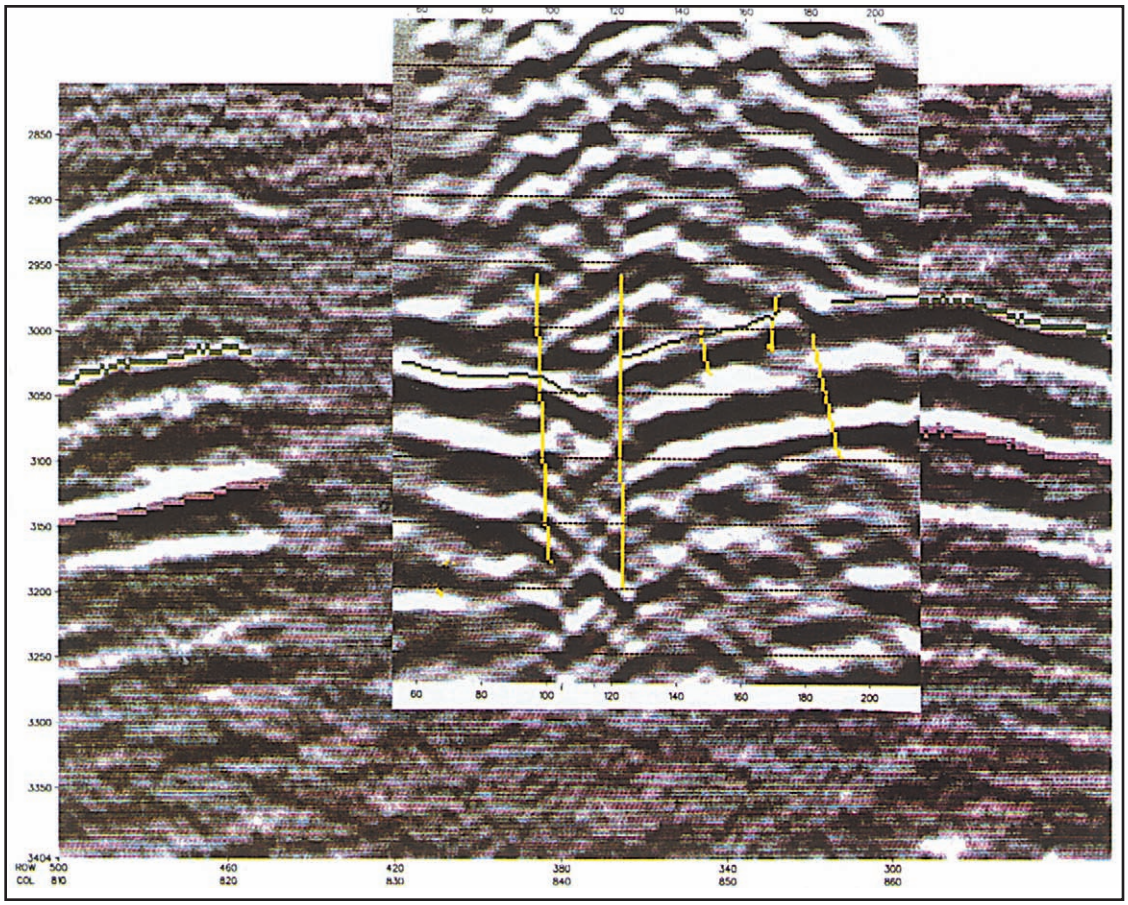

Fig. 14-7-10. Seismic line with the corresponding borehole profile line inserted.

Downloaded 25 Jun 2012 to 95.28.162.50. Redistribution subject to SEG license or copyright; Terms of Use: http://segdl.org/

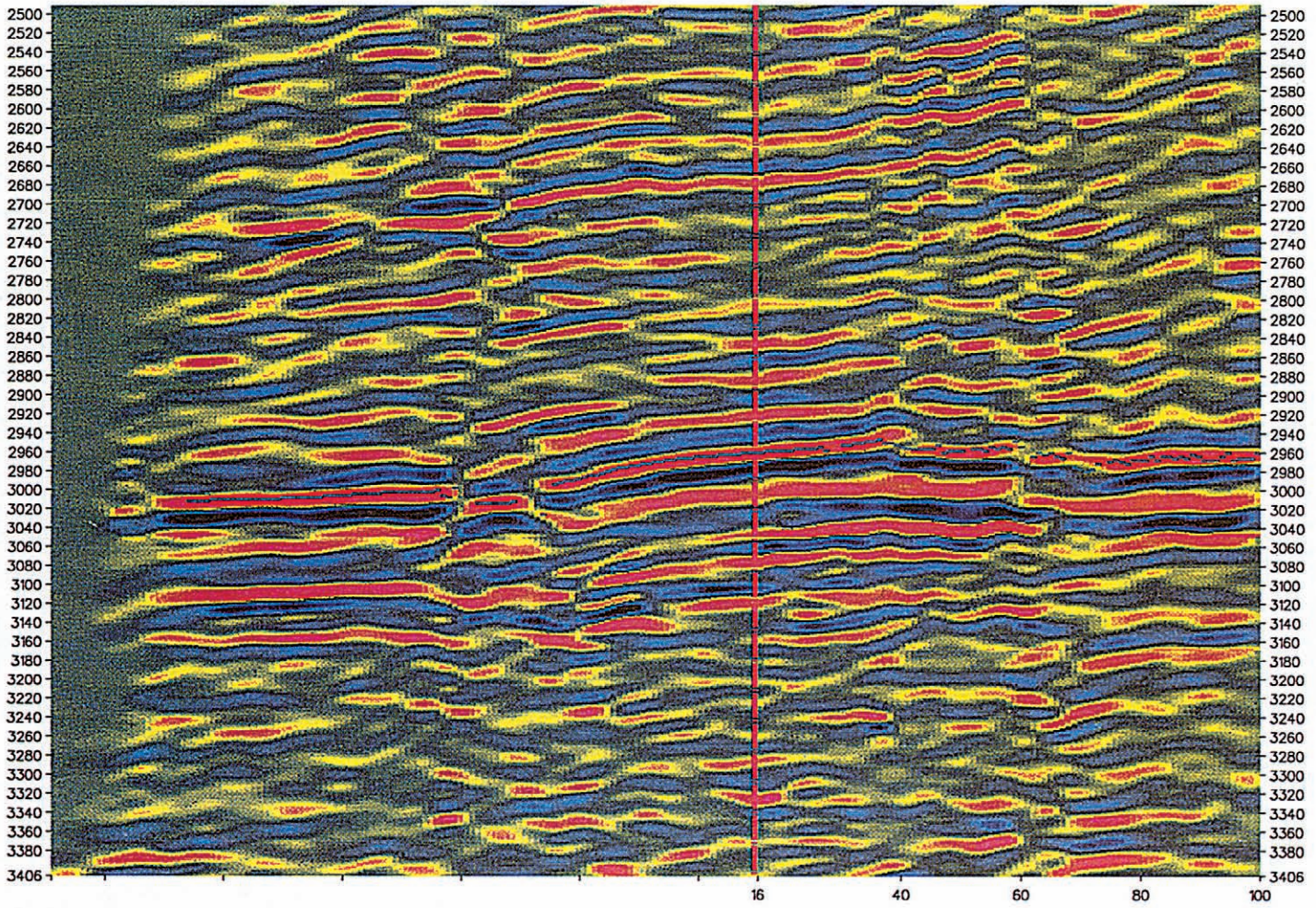

Fig. 14-7-11. Intersecting lines in the 3-D borehole profile.

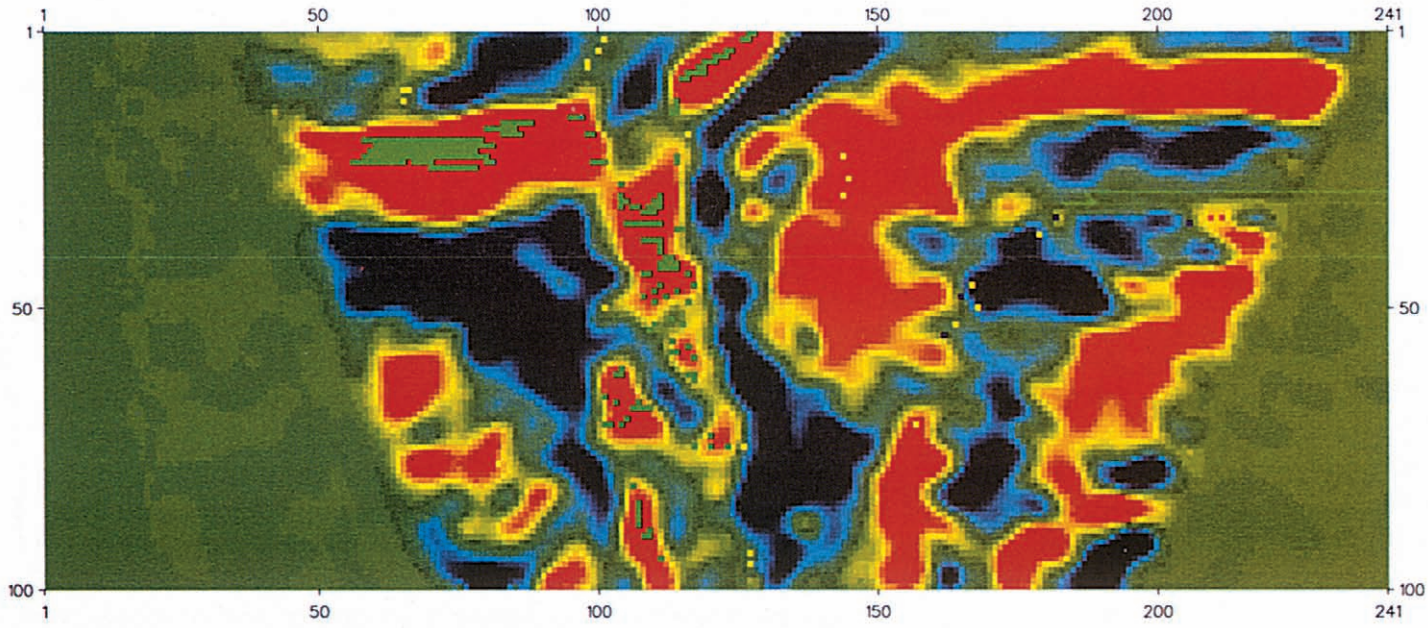

Fig. 14-7-12. Time slice at 3002 ms from the 3-D borehole profile.

Downloaded 05 Jun 2012 to 65.24.202.60. Redistribution subject to SEG license or copyright; Terms of Use: http://segdl.org/

Case History 8

Extending Field Life in Offshore Gulf of Mexico Using a 3-D Seismic Survey

Thomas P. Bulling, Rebecca S. Olsen, ARCO Oil and Gas Company

The High Island 24L field (ARCO), located in the Texas state waters of the Gulf of Mexico, was discovered in 1967. It had produced 320 billion cubic feet (bcf) of gas and 3.0 million bbl of oil by 1986. An engineering field study completed in 1986 projected the field declining to the point of unprofitability within three years. The study found the reservoir maps had three basic problems: volumetric reserve calculations did not equal reserves produced; hydrocarbon-water contacts were inconsistent between wells thought to be in communication; and maps did not define extension opportunities. Attempts to remap the field with the existing 2-D seismic data base and well logs proved unsuccessful.

In 1986, ARCO acquired a 3-D seismic survey and, in 1987, remapped the field starting with the key producing horizons. Integration of detailed well log correlations with the dense grid of 3-D seismic allowed construction of accurate reservoir maps. These new maps helped solve the engineering problems by more accurately defining the configuration of the reservoirs, closely matching volumetrics and fluid contacts as well as defining new extension opportunities. The 3-D seismic survey and its products, along with engineering modifications and operations cost containment, resulted in the extension of the field's economic life by at least eight years. As more wells are drilled and new information integrated, additional reserves are found.

Introduction

Many fields in the Gulf of Mexico discovered with the seismic data available in the 1960s and early 1970s are facing declining production and reaching the end of their economic life. After discovery and initial development drilling, many of these fields were simply put on production and maintained. High Island 24L field is an example of such a field; only two wells were drilled between 1972 (the end of development drilling) and 1986. 3-D seismic is often needed to extend the life of these mature oil and gas fields. High Island 24L field is an excellent example of using 3-D seismic for this extension.

Background and Geology

The High Island 24L field is ten miles offshore in the Texas state waters of the Gulf of Mexico. Discovered by ARCO in 1967, the field has produced 320 bcf of gas and 3 million bbl of oil from 30 lower Miocene sands ranging from the normally pressured CM-12 *(Robulus 43)* sand to the geopressured "IK" sand (Figure 14-8-1). The field produces from anticlinal and fault traps both upthrown and downthrown to a lower Miocene growth-fault system (Figure 14-8-2).

In 1986, a reservoir engineering study indicated the field would become unprofitable in two years (Figure 14-8-3, blue line). The study also identified some key problems with the reservoir maps including: reservoir volumetrics did not equal production (i.e., several fault blocks produced more than maps indicated); structure maps and fluid level contacts were inconsistent (wells within the same fault block had different gas/water contacts); engineers could not reasonably forecast ultimate reserves; and maps did not define extension opportunities.

Prompted by the engineering study, ARCO attempted to remap the field to better evaluate its potential. The endeavor represented the first integration of geology, geophysics, and engineering data since development drilling ended in 1972. However, the available 2-D seismic data were inadequate and could not resolve the mapping problems. The question arose whether to abandon/sell the field or acquire more high-quality seismic data. Because the 2-D mapping proved unsuccessful, we could not place a reliable value on the property on which to base abandonment or selling criteria. Geoscientists felt chances were good that untested reservoirs would be found if accurate maps could be generated. Therefore, ARCO decided to obtain better seismic data to determine the value and potential of the field.

After considering several options, we decided not to acquire more 2-D data since 14 vintages already existed (shot between 1967 and 1985). A dense, consistent 3-D survey would greatly benefit the project in five ways: improved mapping of subtle structures; identification and evaluation of amplitude anomalies related to hydrocarbon-bearing sands; resolution of deep, complicated structures; integration with data from numerous wells; and the ability to manipulate the seismic

Downloaded 25 Jun 2012 to 95.28.162.50. Redistribution subject to SEG license or copyright; Terms of Use: http://segdl.org/

data in a variety of ways using a 3-D interactive workstation. Cost of the survey was less per mile than 2-D and less than the cost of a shallow well in this field. Geoscientists began mapping the field in June 1987 using the 3-D seismic data. Initial work focused on the most prolific reservoir sands.

Results and Examples

Significant mapping changes appeared between old 2-D and new 3-D maps. This section illustrates three examples of these changes in the "HC," "KC," and CM-12 horizon interpretations.

The "HC" *(Siphonina davisi* in age) sand at about 8000 ft (2400 m) is the most prolific reservoir. The 3-D seismic data clearly identifies subtle structures not seen on 2-D seismic lines and not found on the old maps (Figures 14-8-4a and 14-8-4b). Three wells, B-2, 9, and B-4, drilled on subtle structural highs, found the "HC" sand productive. Figure 14-8-5 is a seismic example of a subtle "HC" high tested by the successful (post-3-D) #9 well. This example shows how 3-D helped to identify untested subtle structures and allowed us to generate seismic traverses to see relationships between drilled and proposed wells.

The second example shows mapping improvements in one of the deepest producing horizons, the "KC" (*Lower Planulina* in age), at about 11,000 ft. Figures 14-8-6a and 14-8-6b illustrate the drastic differences between the pre-3-D and the post-3-D maps. These maps are similar in area and orientation. Understanding fluid contacts and reservoir juxtaposition across faults always had been a problem in the *Lower Planulina* sands. The new, post-3-D map is based on new well log interpretation integrated with the 3-D seismic. This recent interpretation explains areas where volumetrics and fluid contacts previously did not make sense.

Mapping success at "KC" is largely due to the improvement in deep seismic resolution integrated with a new well log interpretation. Figures 14-8-7a and 14-8-7b are portions of seismic lines from the 2-D and 3-D data sets. Improvement in deep resolution on 3-D line 112 (Figure 14-8-7b) is demonstrated by clearer fault trace delineation and reflection continuity.

The final example of mapping changes is from the shallowest producing horizon, CM-12 (*Robulus* 43 in age), at about 5500 ft (1680 m). Old 2-D mapping (Figure 14-8-8a) is different from the newer post-3-D map (Figure 14-8-8b). Significant to the post-3-D map is a four-way dip structure on block 90S not adequately tested by the two wells on this block. Prior to interpreting the 3-D data, we did not recognize the 90S structure and the amplitude anomaly that conforms to it (Figure 14-8-9). This anomaly is very similar to a CM-12 anomaly known to produce in wells #4 and #5. An arbitrary line known as seismic traverse 11 (Figure 14-8-10) shows the relationship between the prospective 90S block amplitude and that of the producing #4 and #5 wells. Drilled in early 1988, the ARCO 90S #1 well found hydrocarbon-bearing sands causing the CM-12 amplitude anomaly. Also, CM-12 came in very close to target depth and expected reserve size. This example illustrates the ability of the interpreter to identify amplitude anomalies in a small area. Utilizing the 3-D workstation, we can relate the untested anomalies to similar productive anomalies in the field, resulting in reduced risk and better reservoir delineation.

The post-3-D maps resulted in drilling and completing eight wells to date that will recover 40 bcf equivalent (net to ARCO). The 3-D seismic survey was an excellent investment, costing less than a shallow well in the field. The new wells, based on 3-D mapping, resulted in a reversal of the field's declining Before Federal Income Tax cash flow curve (Figure 14-8-3, red line). Other wells currently are under consideration. In total, the post-3-D maps identified 50 bcf equivalent of potential reserves (40 bcf from new wells and 10 bcf from existing wells and recompletions).

Conclusions

The 3-D seismic survey aided our interpretation of the field by providing:

- a continuous and dense grid of data across the field;
- the capability to generate traverses at any orientation;
- excellent detection of subtle structures;
- horizon slices to help define accumulations on the basis of amplitude;
- better deep resolution to help add extension opportunities.

Overall, the use of 3-D seismic data allowed for a better understanding of the stratigraphic and structural complexities of the High Island 24L field. In addition, post-3-D maps helped solve the engineering problems by more accurately defining the configuration of the reservoirs. Reservoir maps now closely match volumetrics; fluid contacts within fault blocks are consistent; and we have a better definition of the extension opportunities available. The 3-D seismic survey and its products, along with engineering modifications and operations cost containment, resulted in the extension of the economic life of the field to at least 1996.

Downloaded 25 Jun 2012 to 95.28.162.50. Redistribution subject to SEG license or copyright; Terms of Use: http://segdl.org/

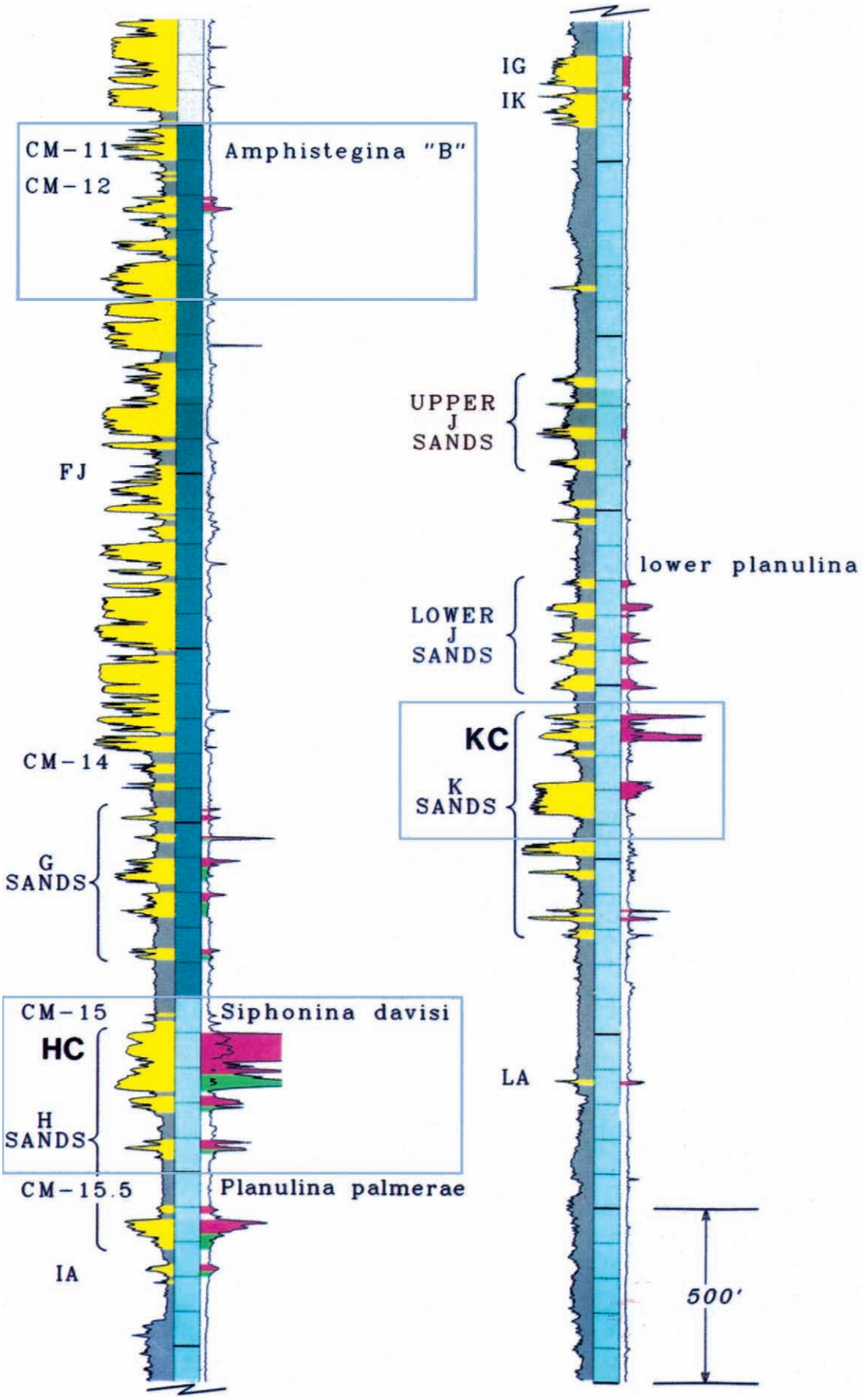

Fig. 14-8-1. The type log for the High Island 24L field, illustrating the 30 pay sands. The "HC" sand is the most productive reservoir.

Downloaded 25 Jun 2012 to 95.28.162.50. Redistribution subject to SEG license or copyright; Terms of Use: http://segdl.org/

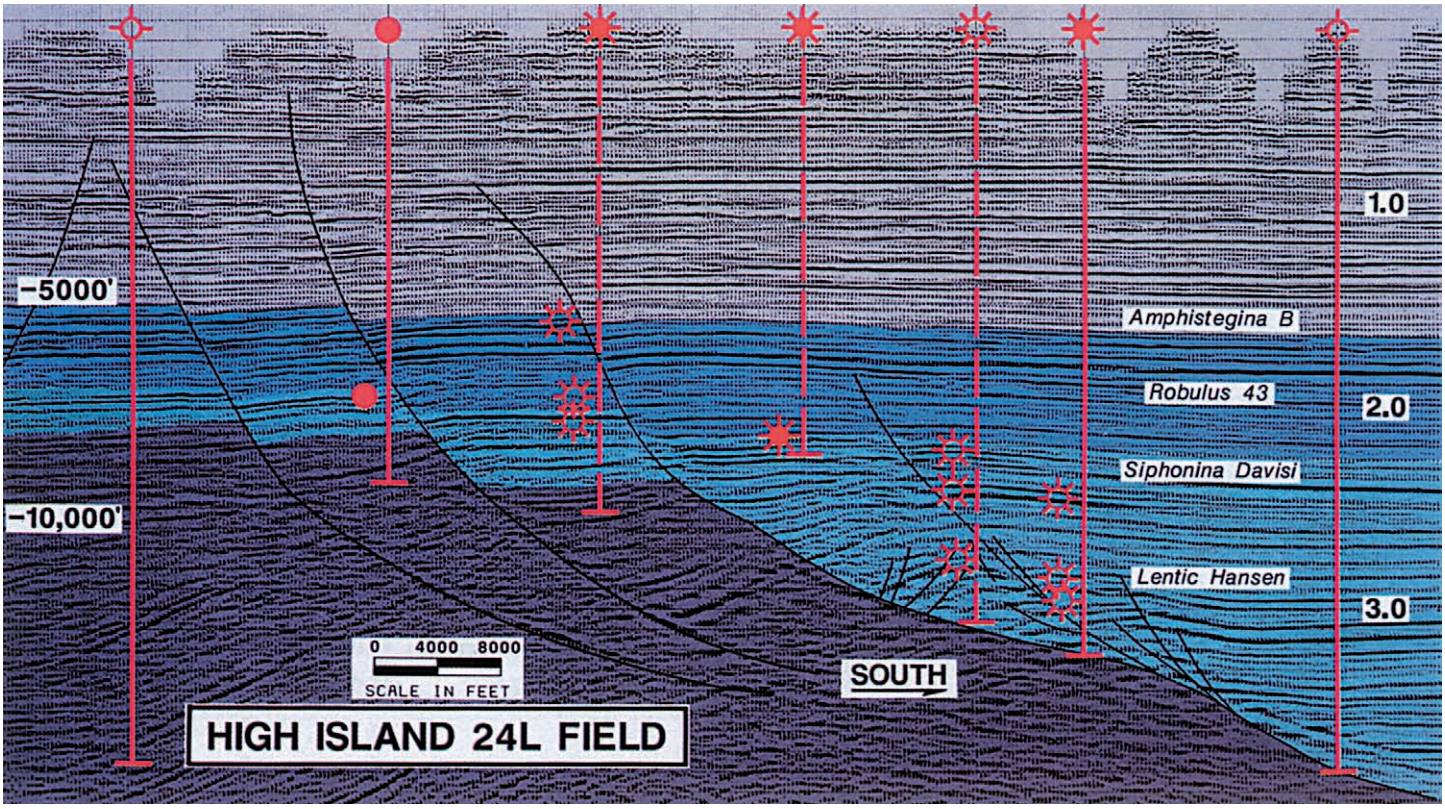

Fig. 14-8-2. Semiregional seismic traverse through the High Island 24L field, illustrating typical anticlinal and fault-related traps. Major producing intervals and lower Miocene growth-fault system also are shown.

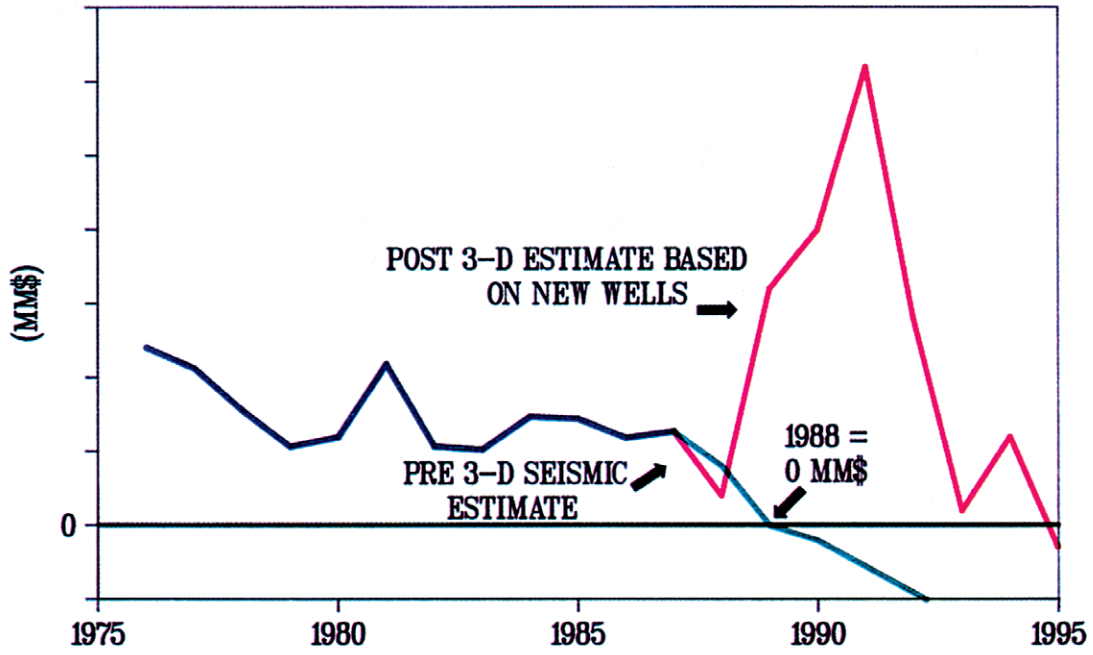

Fig. 14-8-3. Before Federal Income Tax cash flow versus time, for the High Island 24L field. The blue line (decline curve) represents pre-3-D seismic predictions and the red line represents the post-3-D estimate.

Acknowledgments

We extend a special thank-you to the numerous individuals who were involved in the success of this project and compilation of this case history. Thanks go to Garret Chong. Without his recommendations and support, this project may have taken a totally different tack. Also, the ARCO management team was very encouraging and supportive when budgets were tight. We appreciate ARCO's Houston drafting and reproduction for its professional and patient support. Joyce Settle typed and helped edit this manuscript and related versions. Gary Mitch helped edit this paper and advised us on its presentation. Critical to the success of extending the life of this field was the open communication and teamwork between the project geologists, geophysicists, and engineers (reservoir and drilling). Janet Miertschin, our engineering counterpart, sparked the reevaluation of this field with her 1986 field depletion study.

Downloaded 25 Jun 2012 to 95.28.162.50. Redistribution subject to SEG license or copyright; Terms of Use: http://segdl.org/

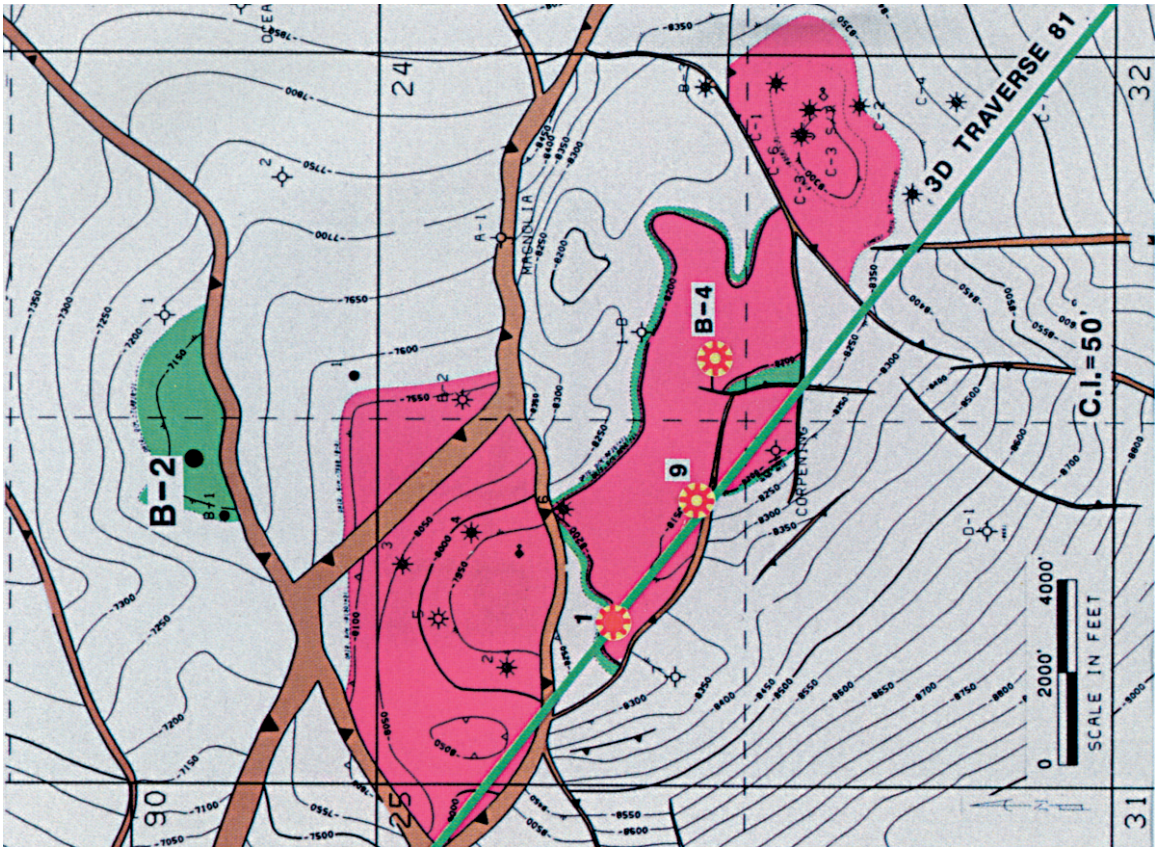

Fig.14-8-4b. Post-3-D seismic "HC" sand structure map. Note that the subtle highs on which wells 9, B-2, and B-4 were drilled do not exist on the pre-3-D structure map (Figure 14-8-4a).

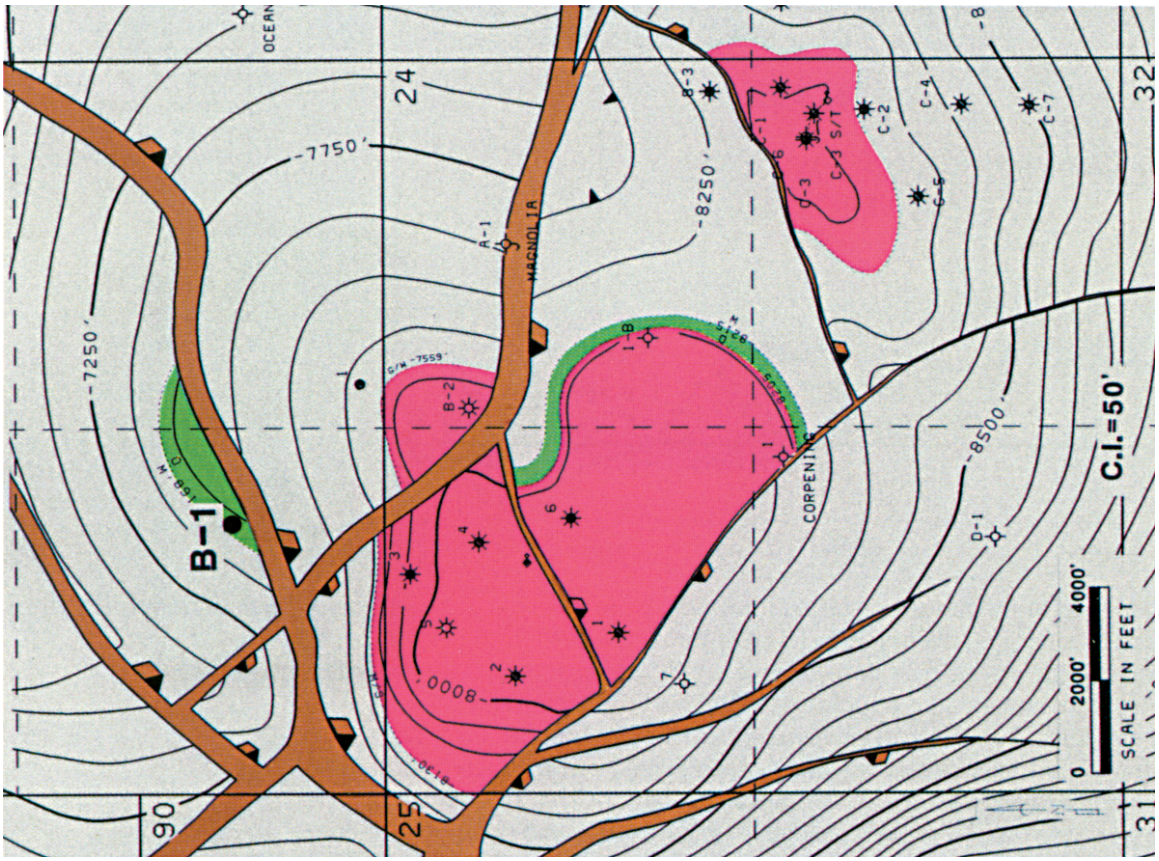

Fig. 14-8-4a. Pre-3-D seismic "HC" sand structure map.

Downloaded 25 Jun 2012 to 95.28.162.50. Redistribution subject to SEG license or copyright; Terms of Use: http://segdl.org/

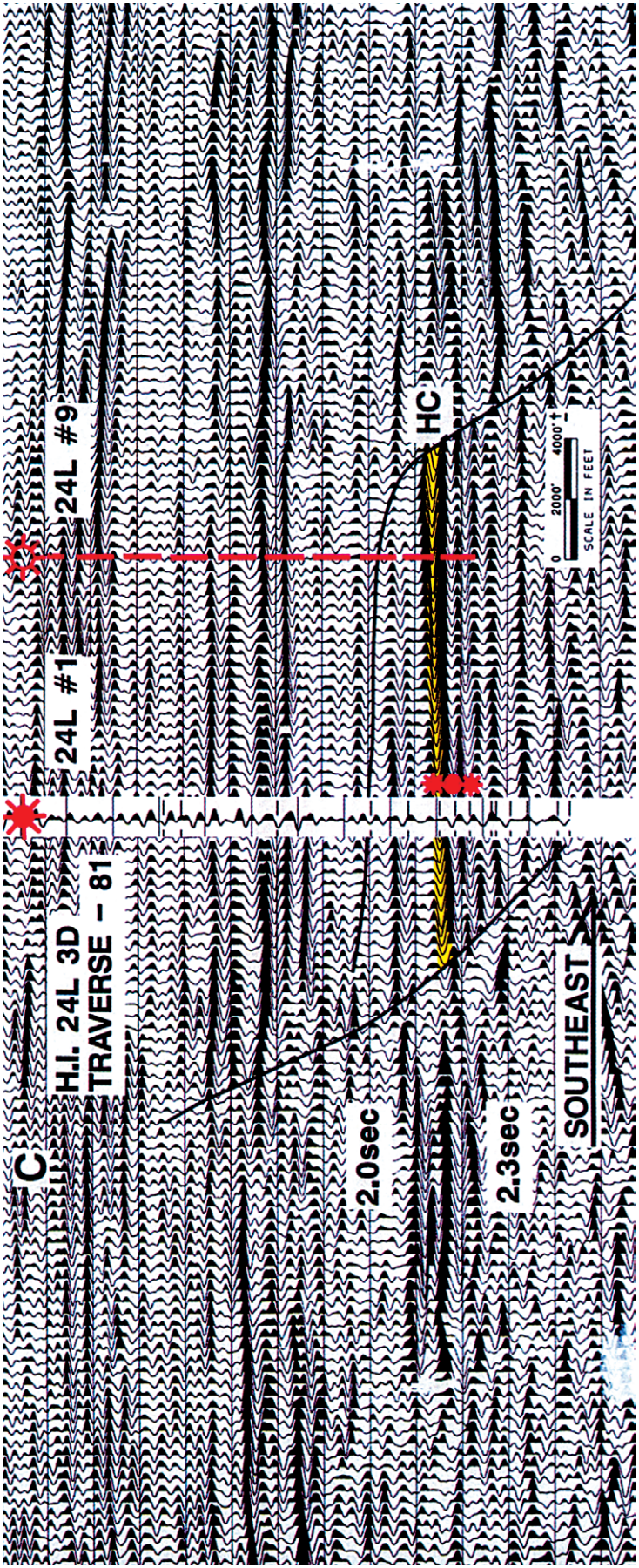

Fig. 14-8-5. Traverse 81 (arbitrary line) through a subtle "HC" high and the location of well #9. Note structural elevation and trough amplitude increase updip from 24L #1 to the proposed #9 well location. Well 24L #9 proved to be successful, close to target depth, and close to pre-drill reserve estimates.

Downloaded 25 Jun 2012 to 95.28.162.50. Redistribution subject to SEG license or copyright; Terms of Use: http://segdl.org/

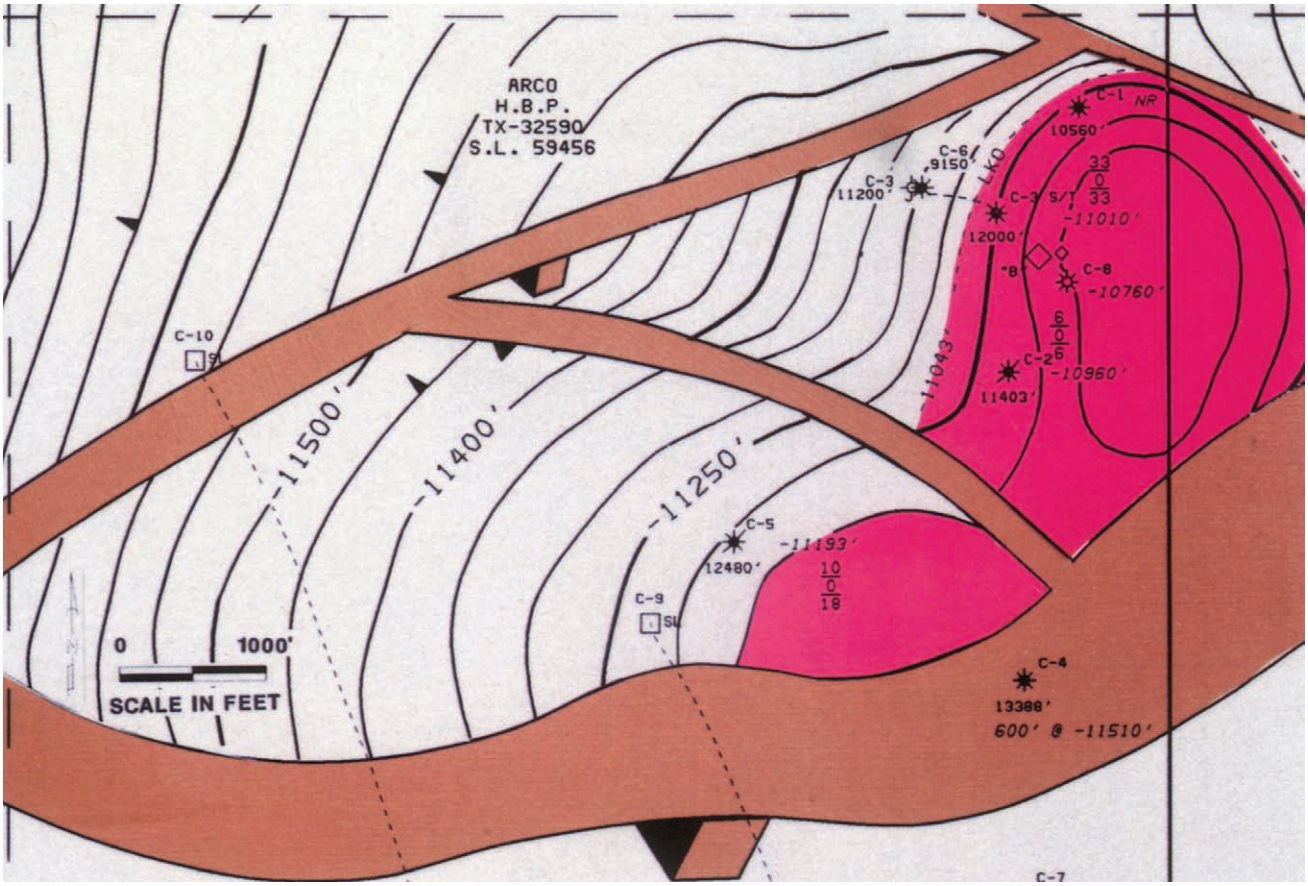

Fig. 14-8-6a. Pre-3-D seismic "KC" sand structure map.

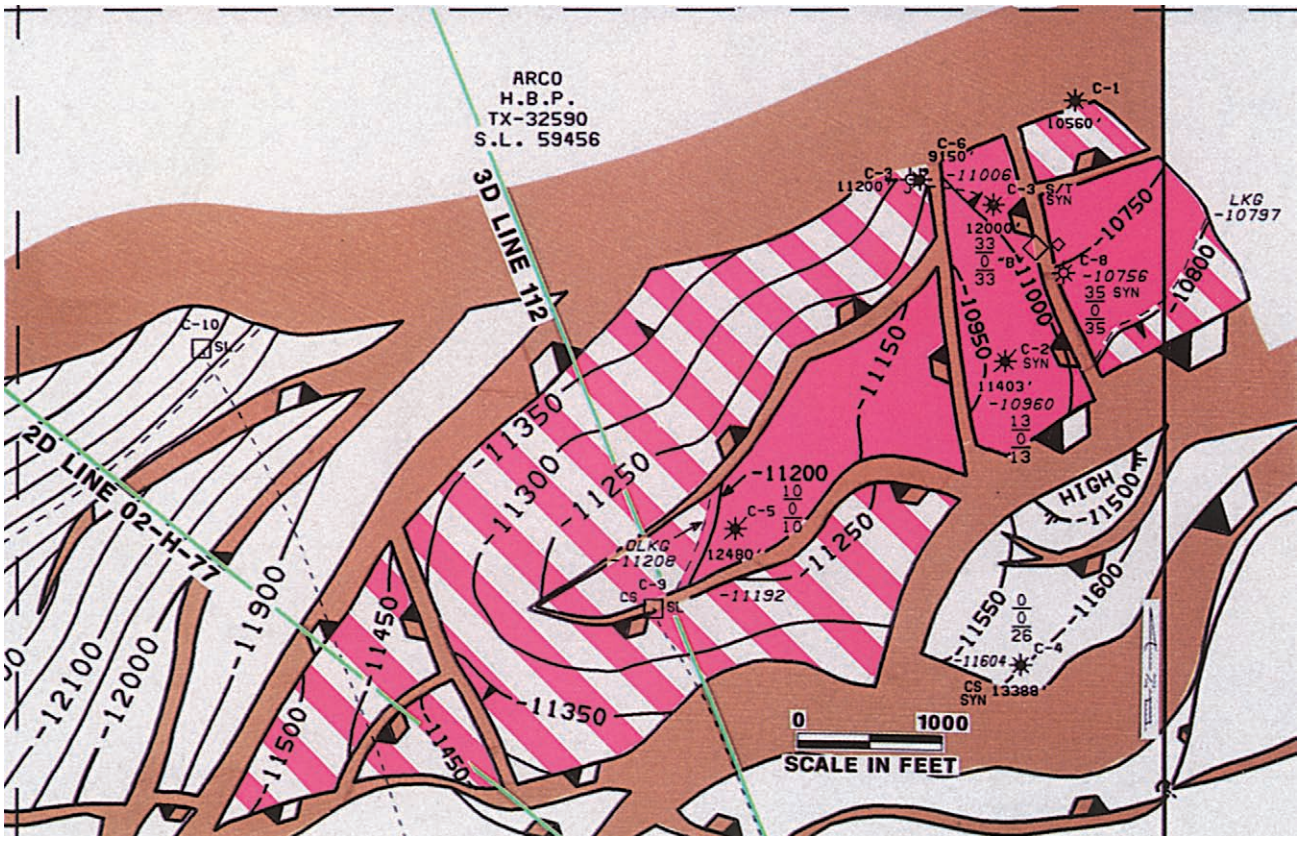

Fig. 14-8-6b. Post-3-D seismic "KC" sand structure map.

Downloaded 25 Jun 2012 to 95.28.162.50. Redistribution subject to SEG license or copyright; Terms of Use: http://segdl.org/

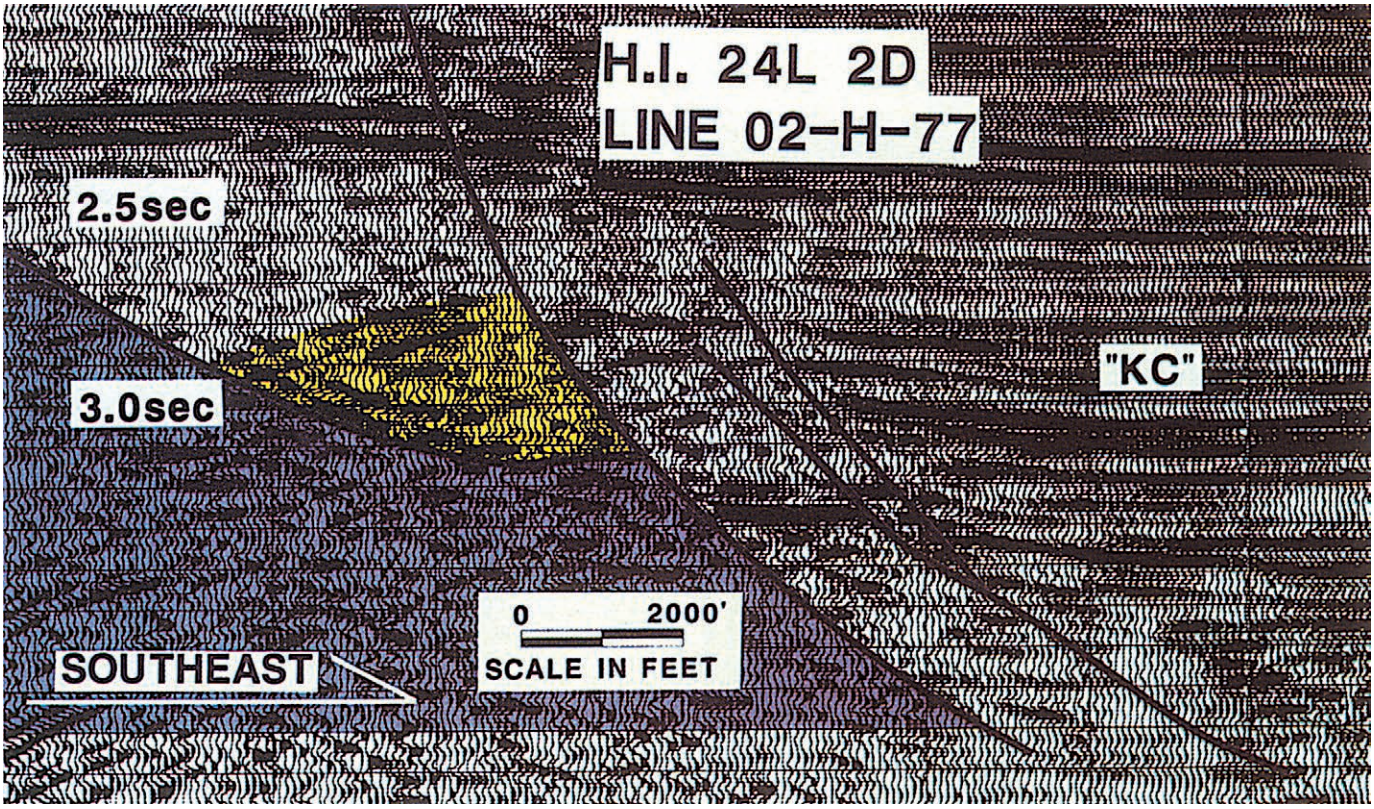

Fig. 14-8-7a. 2-D seismic line 02-H-77. Location of this line is shown on Figure 14-8-6b.

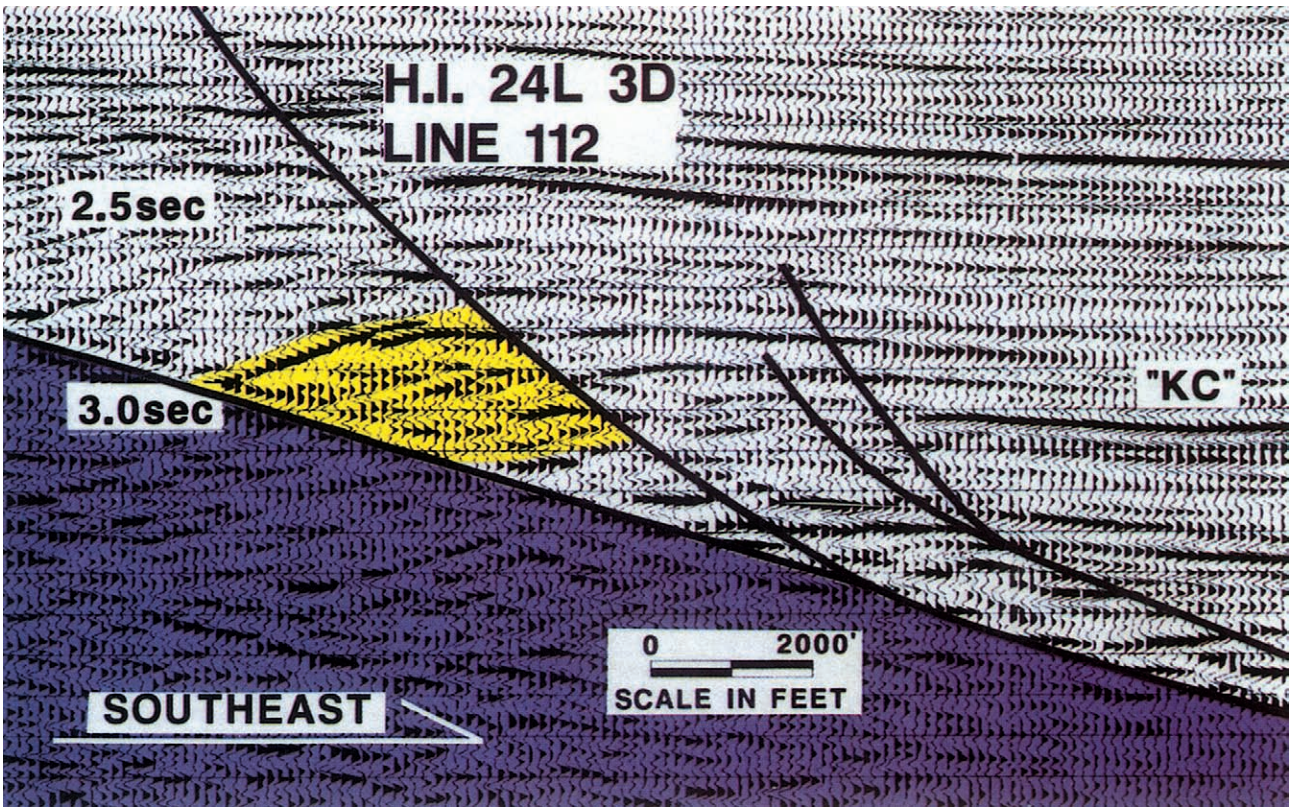

Fig. 14-8-7b. 3-D seismic line 112. Location of this line is shown on Figure 14-8-6b. Areas highlighted on Figures 14-8-7a and b are comparable. Line 112 is superior in deep resolution.

Downloaded 25 Jun 2012 to 95.28.162.50. Redistribution subject to SEG license or copyright; Terms of Use: http://segdl.org/

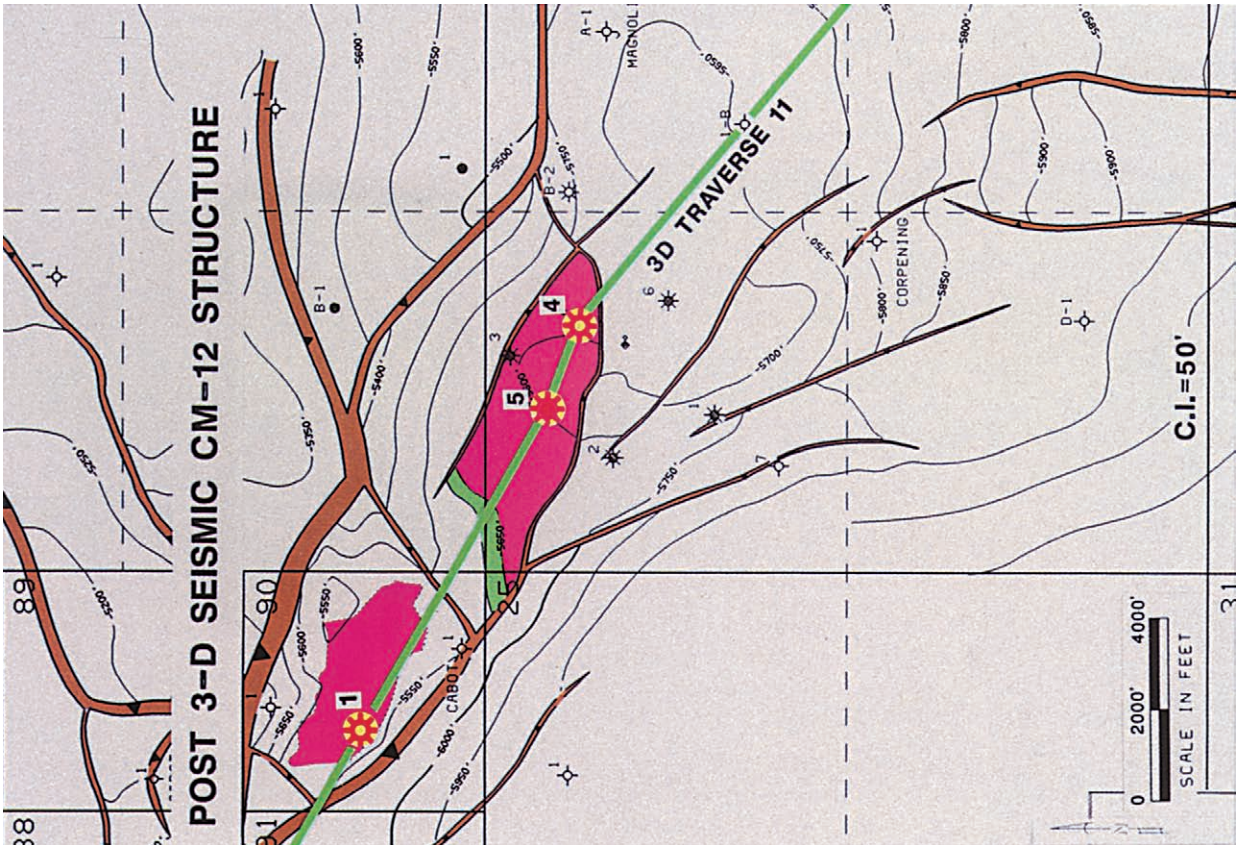

Figure 14-8-8b. Post-3-D seismic CM-12 structure map. Structural closure in block 90S was not tested by the two wells in this block. An amplitude anomaly conforms to this structure.

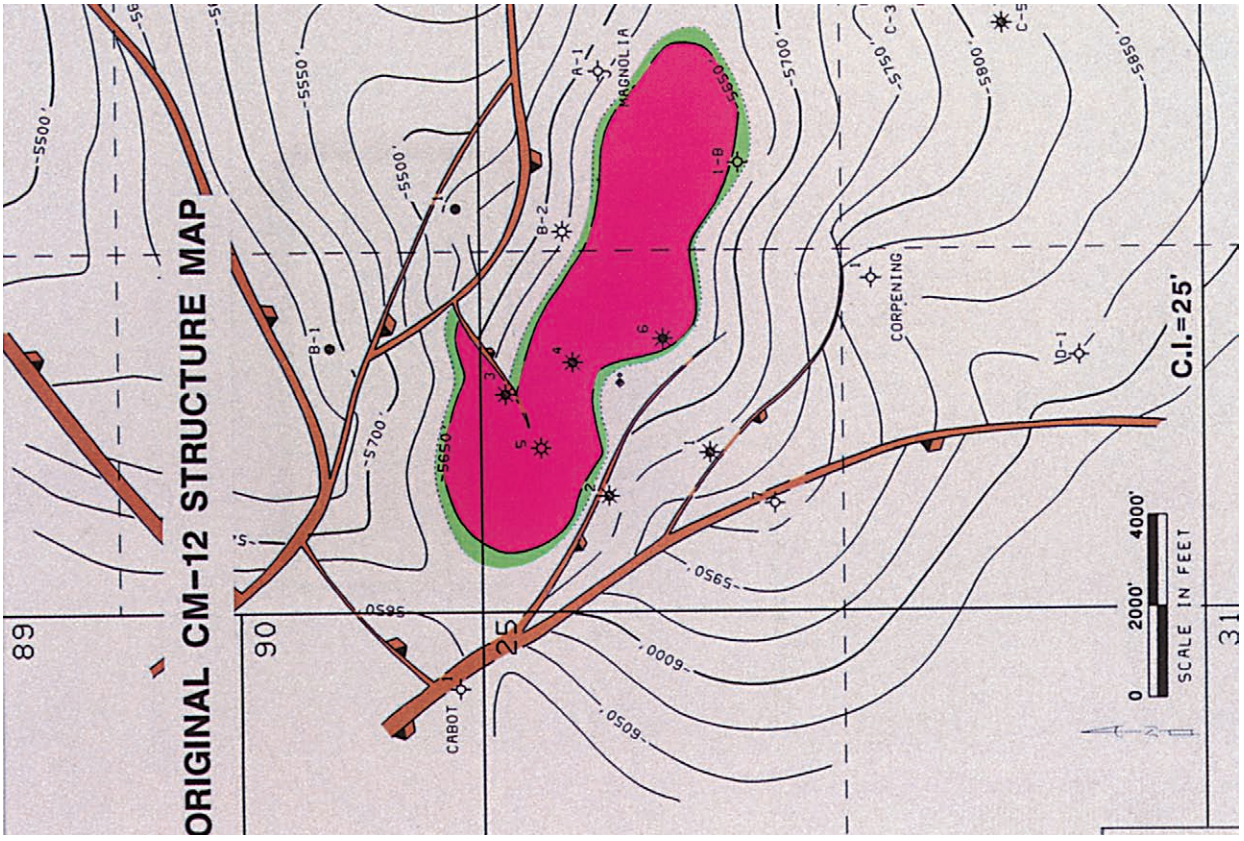

Fig. 14-8-8a. Pre-3-D seismic CM-12 structure map. No structure or amplitude anomaly in block 90S was noted when this map was made.

Downloaded 25 Jun 2012 to 95.28.162.50. Redistribution subject to SEG license or copyright; Terms of Use: http://segdl.org/

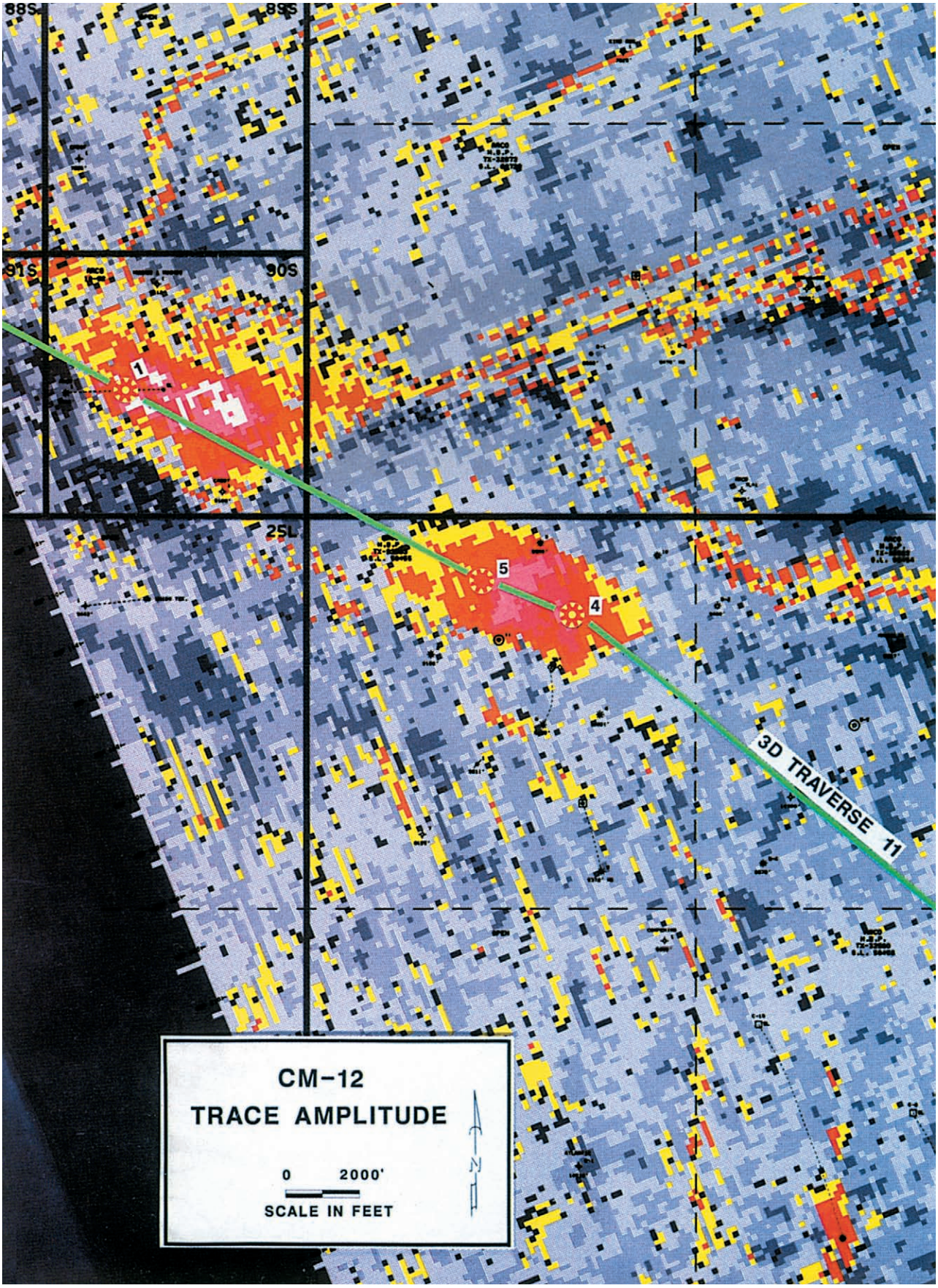

Fig. 14-8-9. CM-12 horizon slice (also termed amplitude map) illustrates strong trough amplitudes (pinks and reds) conforming to the 90S block structure (in the northwest corner of the figure). The 90S anomaly is stronger than the #4 and #5 producing anomaly to the southeast.

Downloaded 25 Jun 2012 to 95.28.162.50. Redistribution subject to SEG license or copyright; Terms of Use: http://segdl.org/

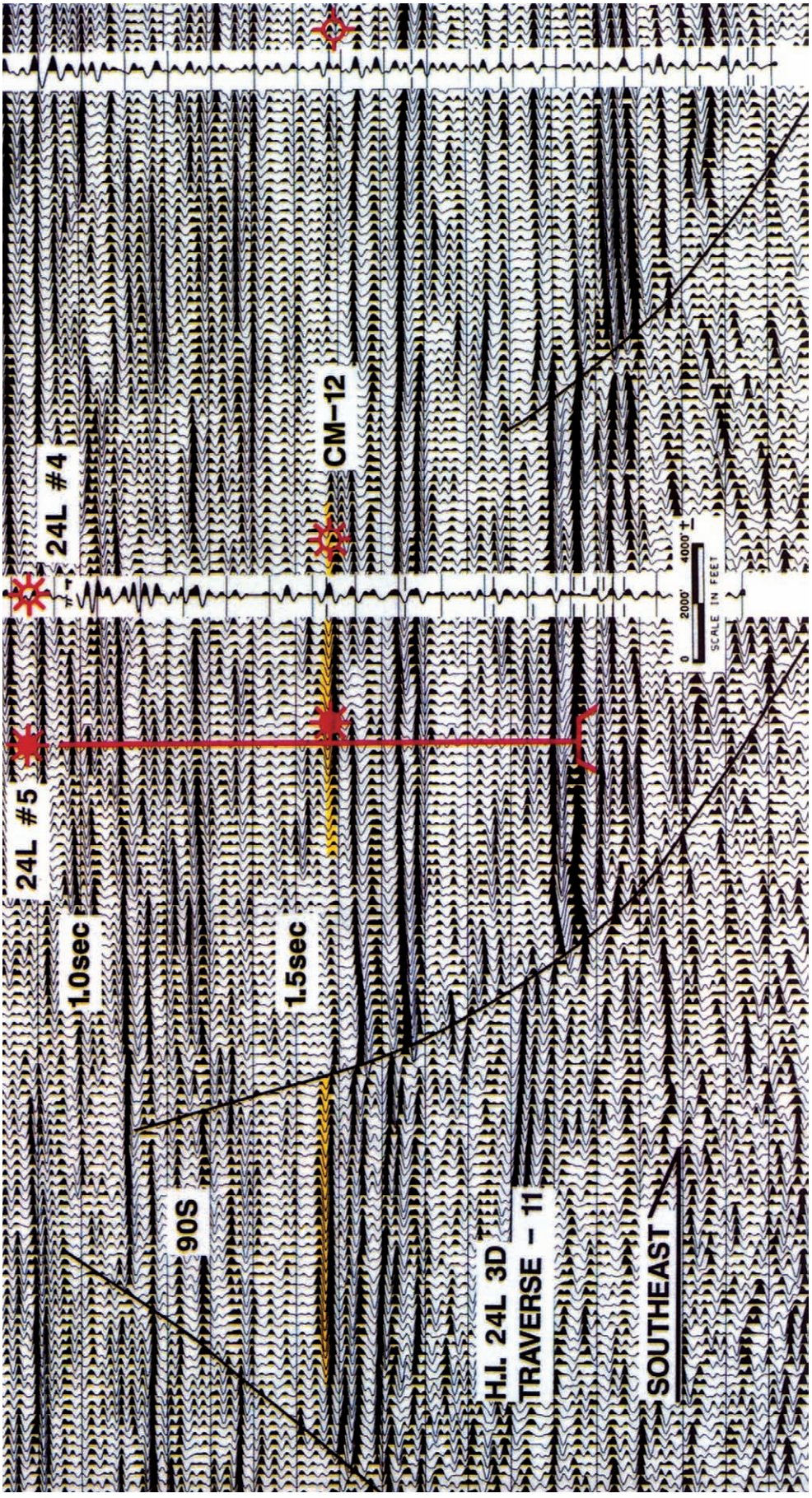

Fig. 14-8-10. Seismic traverse 11 (arbitrary line) showing the CM-12 trough amplitude anomalies marked in yellow for the 90S block and for the production in wells #4 and #5. Location of the traverse is shown on Figures 14-8-8b and 14-8-9.

Downloaded 25 Jun 2012 to 95.28.162.50. Redistribution subject to SEG license or copyright; Terms of Use: http://segdl.org/

Lisburne Porosity — Thickness Determination and Reservoir Management from 3-D Seismic Data

S. F. Stanulonis, H. V. Tran, ARCO Alaska, Inc.

Background

ARCO Alaska has developed a procedure to calculate total pore foot values directly from seismic amplitude, where pore foot is defined as reservoir thickness times average porosity. This was accomplished without an intermediate net pay map or average porosity map. The procedure was applied to the Lisburne Pool, a carbonate field located on the North Slope of Alaska. The upper Lisburne is Pennsylvanian in age, and stratigraphically separated from the overlying Permian-Triassic Sadlerochit formation. Structurally it lies on the crest and the southern flank of the Barrow arch. The field is bounded on the north by the major North Prudhoe Bay fault, truncated to the east by a major Cretaceous unconformity, and limited to the south and west by a variable oil-water contact. A porosity cross section through the area (Figure 14-9-1) shows the porosity is highly stratified and highly variable laterally. This makes porosity prediction difficult from wells alone.

The study was initiated in 1986 with 35 wells in the field. The area is covered by a 3-D seismic survey that was acquired in the late '70s. The survey consists of 45,000 bins with a trace every 220 ft (64 m), over an approximate 75 mi^2 (190 km^2) area. Production in 1990 was around 42,000 bbl/day from 65 wells. Production is mainly from the upper four zones (zones 7 to 4) of the reservoir, which consist of limestone and dolomite, each separated by a thin shale. The Lisburne is overlain stratigraphically by the Kavik shale, with a P-wave average velocity of 12,000 ft/s. Since this is much slower than the average Lisburne velocity of 17,000 ft/s, the horizon can be recognized as a peak on a positive polarity section. The seismic peak-to-trough amplitude of this horizon at the top of the Lisburne is plotted in Figure 14-9-2 where larger amplitudes are indicated by red, and smaller amplitudes by blue. The red, high seismic amplitude band occurring in the east, is where the Lower Cretaceous Unconformity (LCU) truncates to the top of Lisburne and replaces the overlying Kavik shale with slower Cretaceous shales. To avoid wavelet interferences and other complications in this region, the first part of this case history will be confined to the interpretation west of this truncation region.

Method West of LCU Truncation

Since there is no seismic lithology break in the upper zone of the Lisburne, the variations observed in seismic amplitude should be a function of variations in reservoir quality. One factor of reservoir quality is porosity. For a typical well in the area, the core porosity has been plotted against the sonic log velocity in Figure 14-9-3. As the core porosity increases, the sonic velocity decreases. Therefore, as the average interval porosity within the Lisburne increases, its average internal velocity will decrease, so that its contrast with the average velocity of the overlying Kavik formation will be smaller (Figure 14-9-4). Therefore, as the total pore footage increases within the Lisburne, the seismic amplitude will decrease, where 1 pore foot is defined as 1 foot of 100% porosity. Theoretically these are the results we expect to see by analyzing the surface seismic data. By plotting the total pore feet measured at each well against the seismic amplitude at that well location, that relation between seismic amplitude and total pore footage is observed in the reservoir, but within four separate regions.

Figure 14-9-5 shows that seismic amplitude decreases as the pore foot increases for each of four regions, marked R1 through R4. Not only are the regions statistically separate, they are also geographically separate (Figure 14-9-6). Therefore, the seismic amplitude at any proposed well location can be directly converted to a total pore foot value using Figure 14-9-5, since the region containing the proposed well location is known. The only problem with this method is that it will produce quantum leaps in the total pore foot map at these imaginary regional boundaries. To avoid this problem a different approach was taken.

For each well, an equation can be defined such that the seismic amplitude at that well location is equal to the slope of the regression line for that region, times the total pore foot values calculated at that well from logs, plus a constant value, "C." This C has interesting properties. Note that as the pore footage decreases, the seismic amplitude increases. At the

Downloaded 25 Jun 2012 to 95.28.162.50. Redistribution subject to SEG license or copyright; Terms of Use: http://segdl.org/

point where the total pore foot value equals zero, the seismic amplitude equals C. Stated another way, C is the seismic amplitude at zero porosity. It is the seismic amplitude due to the impedance contrast of the Kavik/Lisburne contact, where the average velocity within the Lisburne is equal to the matrix velocity. This C value will be referred to as the seismic amplitude of the rock matrix. Just as the matrix velocity changes locally due to type of cementation, fracturing, grain-to-grain contact, etc., so will the seismic matrix amplitude (C) change locally. The parameters that cause these variations are due to the geological and geophysical imprints of the rock. This would include amplitude effects superimposed on the lithologic signature that are inadequately corrected in processing.

Four major geological imprints are responsible for the regional pattern shown in Figure 14-9-5, and are shown in Figure 14-9-7. One of these is fractures. The detailed fault patterns in Region R1 are different from those in the other three regions. It is a heavily faulted area with a different fault pattern and an assumed higher density of fractures. A smaller seismic amplitude would be expected for the same pore foot value. Region R1 is the region with the lowest seismic amplitude. The difference in seismic amplitudes between R1 and R2, for the same pore footage, may be related directly to the fracture density. Another geological imprint is the variation in thickness of the Kavik shale. Eastward, the Kavik shale is truncated by the LCU. The average velocity above the Lisburne is reduced from 12,000 ft/s to approximately 9000 ft/s where Kavik is replaced by Lower Cretaceous shales. Therefore, going from Regions R1, to R2, to R3, to R4, the amplitudes should be expected to increase for the same pore footage. Additionally, zone 7 thickens from the southern Region R2 to R4, and eastward from R1 to R4. Both of these geological imprints have a combined effect of making the pore footage appear to increase as seismic amplitude increases, if the four regions are considered as one in Figure 14-9-5. Another geologic imprint is gas. A gas cap exists in the north part of the field, above approximately –8650 ft (–2640 m) subsea (ss), and gas has a very marked effect of decreasing seismic amplitude for the same porosity. Thus, going northward, the seismic amplitude will decrease for the same pore footage. In Figure 14-9-7, this affect is most markedly demonstrated by the rapid transition from Regions R4 to R3 to R2 northward, in the central area of the field. Additionally, note the eastward transition of Region R1 into R2 starting at the gas cap boundary. The combination of all these factors produces the four regions that are statistically represented in Figure 14-9-5. The Lisburne is a complicated reservoir. We believe that in a simpler stratigraphic and structural setting, only one region would exist. But in spite of these complexities, the procedure gives a fairly accurate pore foot map. The procedure is as follows.

For each well the seismic amplitude, the total pore footage and the regression line for that location are known, so that C can be calculated from Figure 14-9-8. The C values are mapped in Figure 14-9-9, which defines the regression line to be used to convert seismic amplitude to total pore footage at any location. The seismic amplitude of the rock matrix (C) can be thought of as an operator. It converts seismic information to well log information. In principle, it is analogous to deriving average velocity at a well from seismic and log information. The average velocity is used to convert the recorded seismic time of a particular seismic horizon to depth, as recorded by logs in the well. Similarly, C is used to convert the recorded seismic amplitude of a particular seismic horizon to total pore footage, as recorded in the well. The procedure is different in that it only uses the second measured value recorded in the field, seismic amplitude, instead of seismic time. Thus, using the C map in Figure 14-9-9, and the recorded seismic amplitude at each trace location, a total pore foot map can be calculated.

Results West of LCU Truncation

Figure 14-9-10 is the resulting pore foot map calculated directly from seismic amplitude. Around 40,000 points have been independently calculated at a in-line spacing of 220 ft. This figure contains 20 color levels with a contour interval of 3 pore ft, equivalent to 3 ft of 100% porosity. This map can be compared to the pore foot values derived just from well control in Figure 14-9-11. Here the pore foot values are plotted on top of a color-coded structure map. The increase in horizontal resolution that seismic 3-D allows can be clearly seen by comparing Figures 14-9-10 and 14-9-11 in the seismically derived pore foot map. By summing the pore foot values over the area of concern, the total maximum geological reserves can be calculated, assuming zero water saturation.

For the last three years we have predicted pore foot values from seismic amplitude and

Downloaded 25 Jun 2012 to 95.28.162.50. Redistribution subject to SEG license or copyright; Terms of Use: http://segdl.org/

compared them with drilled values. Results have been surprisingly accurate in spite of the complexities within the Lisburne. Seismically predicted pore foot values (from Figure 14-9-10) at these 16 new well locations were plotted against the log-measured pore foot values. The results are shown in Figure 14-9-12, and were achieved without updating Figure 14-9-10 after each of the 16 wells were logged.

Method East of LCU Truncation

The previous analysis concentrated on the area west of the truncation where a remnant of the Kavik shale still remains. The area east of the truncation is a transitional region where seismic amplitude would markedly change as a result of the loss of zones 7 through 4, and not as a result of loss of porosity. The thickness factor in the definition of pore footage is changing more rapidly than the average porosity factor. To examine the relation of seismic amplitude and pore foot in this area, a geological model was created (Figure 14-9-13). The resulting seismic amplitude of this synthetic seismic section is shown in Figure 14-9-14. The resulting peak-to-trough analysis shows that a cyclic pattern develops in the seismic amplitude as a result of the relative positioning of the shales and carbonates in the upper zones as they are being truncated. This cyclic pattern of the synthetic peak-to-trough analysis will take the shape of a banded structure in map view. The 3-D seismic amplitudes are mapped in Figure 14-9-15 and do appear banded. Again, the red regions are higher amplitudes. Also plotted are the synthetic times between this peak-to-trough event in the lower half of Figure 14-9-14. It, too, has a cyclic pattern, and the 3-D seismic peak-to-trough time differences also appear as a banded pattern in map view (Figure 14-9-16). Thus, by identifying the bands on synthetic analysis from wells with known truncated upper zones, a spatial correlation between the synthetic peak-to-trough analysis and the recorded 3-D seismic peak-to-trough amplitude and times will locate where the zones subcrop against the LCU. These interpreted subcrops are plotted in Figure 14-9-17. Additionally, for areas along these subcrops, the total zone thickness is approximately constant so that porosity thickness values could be derived as in the method west of the LCU truncation, in the first part of this case history.

Use of Porosity–Thickness Maps

Several applications are possible with a detailed seismic pore foot map. One is the construction of a truer geologic cross section. For any two wells in the area, only the porosity distribution of those wells is known. The seismically derived pore footage allows boundary conditions to be set every 220 ft laterally on the interpreted total pore foot distribution between these wells. Figure 14-9-18 shows such a porosity distribution between wells L3-08 and L3-02. The top of the Lisburne is indicated by the arrow and the red line. Notice that the peak-to-trough amplitude changes considerably between these two wells, suggesting that the total pore footage in zones 7 through 4 is changing at a faster horizontal rate than the geological cross section would indicate. The seismic cross section seems to indicate that the total pore footage is fairly constant for about 4400 ft (1340 m) from L3-08 and then decreases considerably for the next 3300 ft (1000 m). The cycle is repeated several times before L3-02 is reached. This is in contrast to the linear decrease laterally, derived from well values alone, between L3-08 to L3-02. Additionally, by studying the change in the wavelet shape through perturbing the porosity distribution within each zone separately, the zone of changing porosity can be inferred. For example, a decrease in seismic amplitude with an increase of peak-to-trough times is indicative of a zone 6 porosity enhancement. A lower zone 5 porosity enhancement has the same effect with an additional slight side lobe development. Thus, by studying the amplitude, character, and shape of this wavelet at the top of the Lisburne, a more detailed geologic porosity cross section can be constructed.

Another possible application using a detailed seismic pore foot map is the examination of the relation between faults and local pore foot anomalies. Figure 14-9-19 shows the seismically derived pore foot map with a detail fault overlay. Numerous regions are observed where the fault pattern appears to be directly related to the pore foot anomalies: in particular, locations X, O, and the area around E, A, and R. The change in pore footage around these minor faults (less than 20 ft) may be the result of preservation (or loss) of section due to this faulting, or it may be the result of porosity changes due to introduction of fluids along related fractures. Thus, local irregularities in the pore foot map can be used to study faults and their effects on porosity distribution. Conversely, examining the 3-D seismic at

Downloaded 25 Jun 2012 to 95.28.162.50. Redistribution subject to SEG license or copyright; Terms of Use: http://segdl.org/

the boundaries of these anomalous pore foot patterns may help locate minor faults near the limits of seismic resolution, such as location F (Figure 14-9-19). Only one small lateral fault was interpreted on the east side of this pore foot anomaly. But after careful examination, numerous discontinuous fault segments were linearly mapped on the west side with throws near resolution. Additional fault cuts were found on the east side, and the lower bounding northwest-extending fault line was projected farther northward. A horst block was therefore interpreted to be at location F bounding the anomalous pore foot pattern in Figure 14-9-19.

It is well known that gas has an effect on seismic P-wave velocity, which in this environment decreases amplitude considerably for the same porosity. Figure 14-9-20 is the peak seismic amplitude map at the Lisburne horizon, where blue is the low amplitude and red the high amplitude. The large blue region corresponds well to the original oil-gas contact (–8600 ft) and is within the –8650-ft contour interval. Additionally, other gas caps can be found to the south more than 150 ft deeper within the Lisburne section. If it were possible to reshoot the seismic survey with identically the same acquisition and recording parameters and ground conditions, large amplitude differences between the new and original processed amplitudes should correlate well to unswept, producible oil. Areas therefore may be mapped locating additional trapped oil.

The final application attempts to relate productivity to total pore foot values for the drainage area around a well bore, rather than just to the logged pore foot values at the well bore. Clearly, wells drain areas where the pore footage is not logged but is assumed to have a value proportional to the linearly weighed distance of the total pore foot difference between two wells. Figure 14-9-21 shows there is a relation between total pore foot and effective pore foot, where the latter term is defined as pore footage with enough permeability to contribute to production (Durfee, 1988). It is a permeability-weighted pore foot value. Those wells along the upper trend have more effective porosity for the same total pore footage and are all located in the truncation areas, or within the gas cap. Figure 14-9-10 then could be multiplied by this ratio and a total effective pore foot map produced. The lower well in Figure 14-9-22 shows that production should decrease faster over time than for the more eastern well, even though both wells have the same pore footage measured along the well bore. This is due to the more porous rocks around the eastern well. Production over time at any well then can be equated to the integrated effective seismic pore footage over selected radii from the well, and a set of simultaneous equations generated with factors for fault/fracture enhancements, as well as rock type.

Conclusions

ARCO Alaska has developed a procedure to calculate porosity-thickness directly from 3-D seismic amplitude. The procedure uses observed local trends between seismic amplitude and total porosity-thickness from wells to project the seismic amplitude that should occur at that location at zero porosity, i.e., for the rock matrix. The geologic and geophysical imprints that affect this value are complicated and numerous for the Lisburne formation, and yet it was still possible to derive an accurate, detailed pore foot map. The procedure is partly an empirical technique which, although it may have wide application, must be locally calibrated to available well control. The resulting detailed pore foot map serves to enhance reservoir description and assist engineers in developing a more accurate reservoir model.

The techniques and/or conclusions are those of the authoring company and may not be shared by other Working Interest Owners.

Reference

Durfee, B. A., 1988, Matrix characterization of the Upper Wahoo Formation, North Slope, Alaska: ARCO internal report, December.

Downloaded 25 Jun 2012 to 95.28.162.50. Redistribution subject to SEG license or copyright; Terms of Use: http://segdl.org/

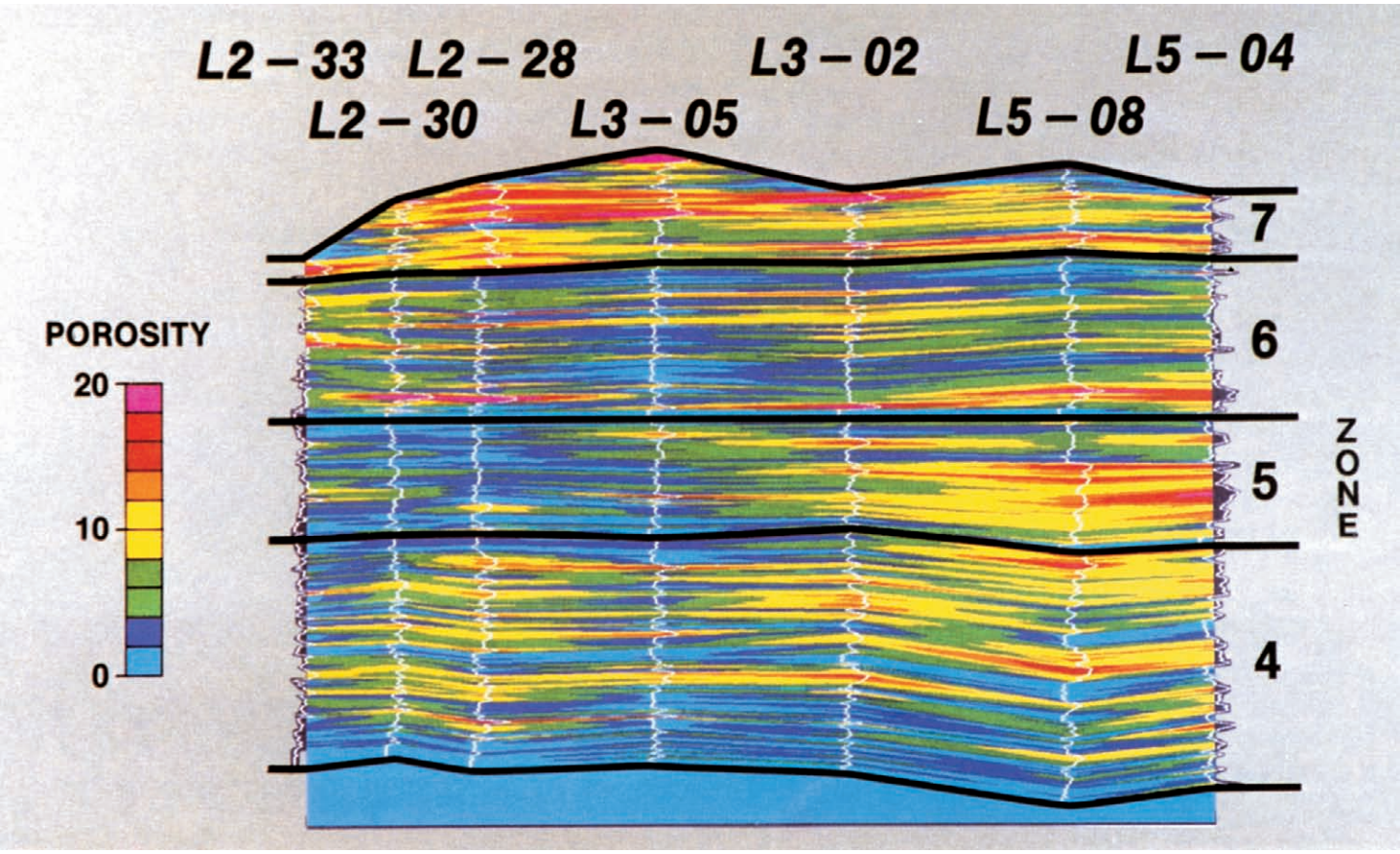

Fig. 14-9-1. Well-derived porosity cross section through Lisburne field.

Downloaded 25 Jun 2012 to 95.28.162.50. Redistribution subject to SEG license or copyright; Terms of Use: http://segdl.org/

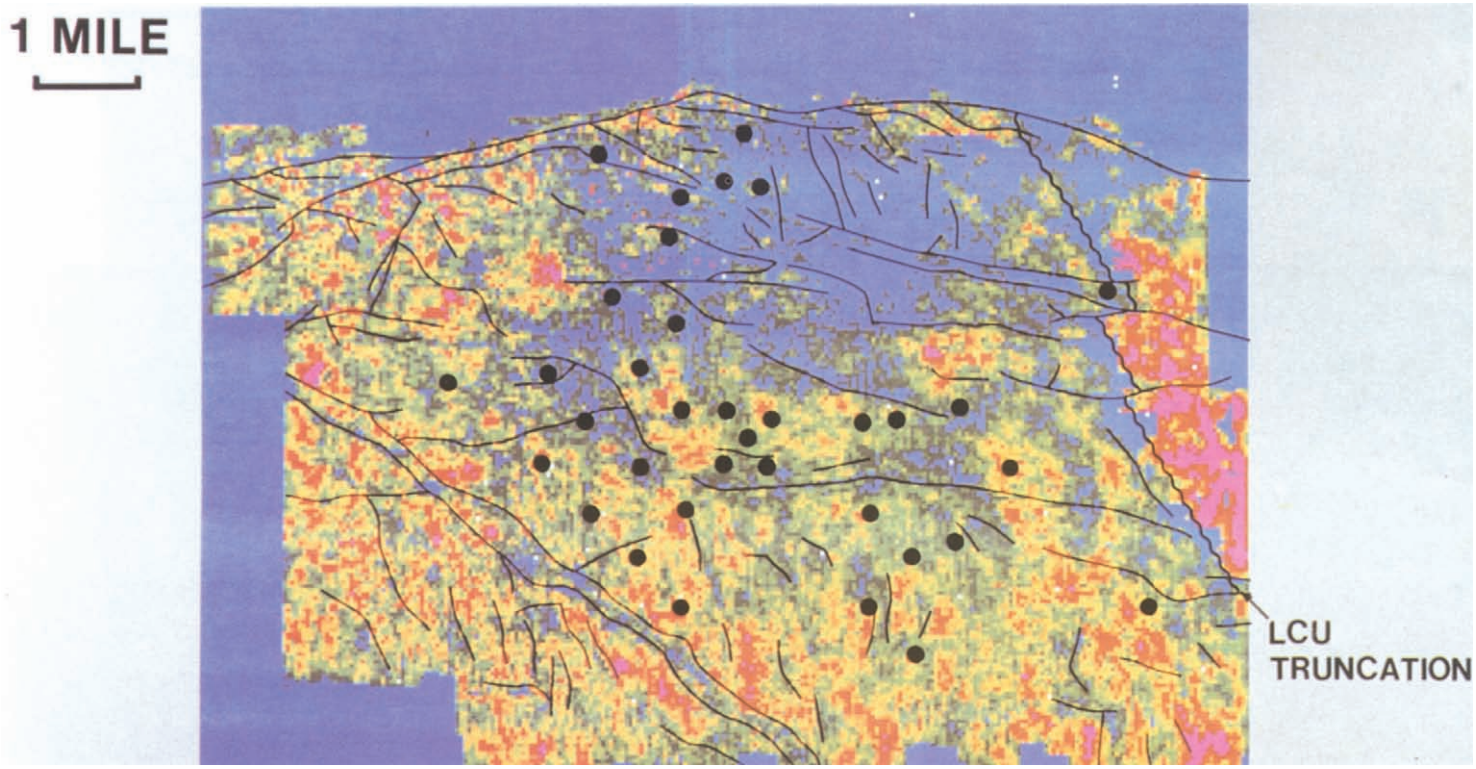

Fig. 14-9-2. Horizon slice for top Lisburne reflection displaying peak-to-trough amplitude. High amplitudes are red; low amplitudes are blue.

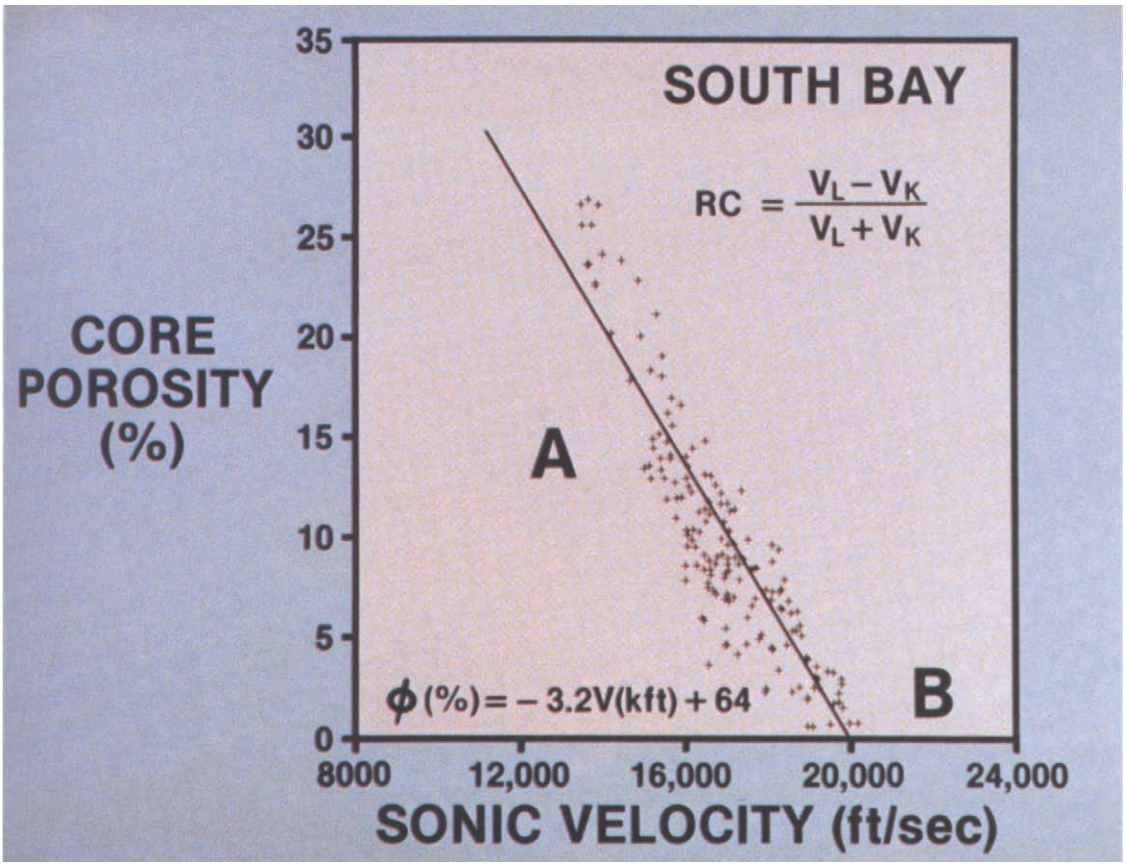

Fig. 14-9-3. Core porosity versus sonic velocity for a typical well. V_L is velocity of the Lisburne, and V_K is velocity of the Kavik; RC is reflection coefficient.

Downloaded 25 Jun 2012 to 95.28.162.50. Redistribution subject to SEG license or copyright; Terms of Use: http://segdl.org/

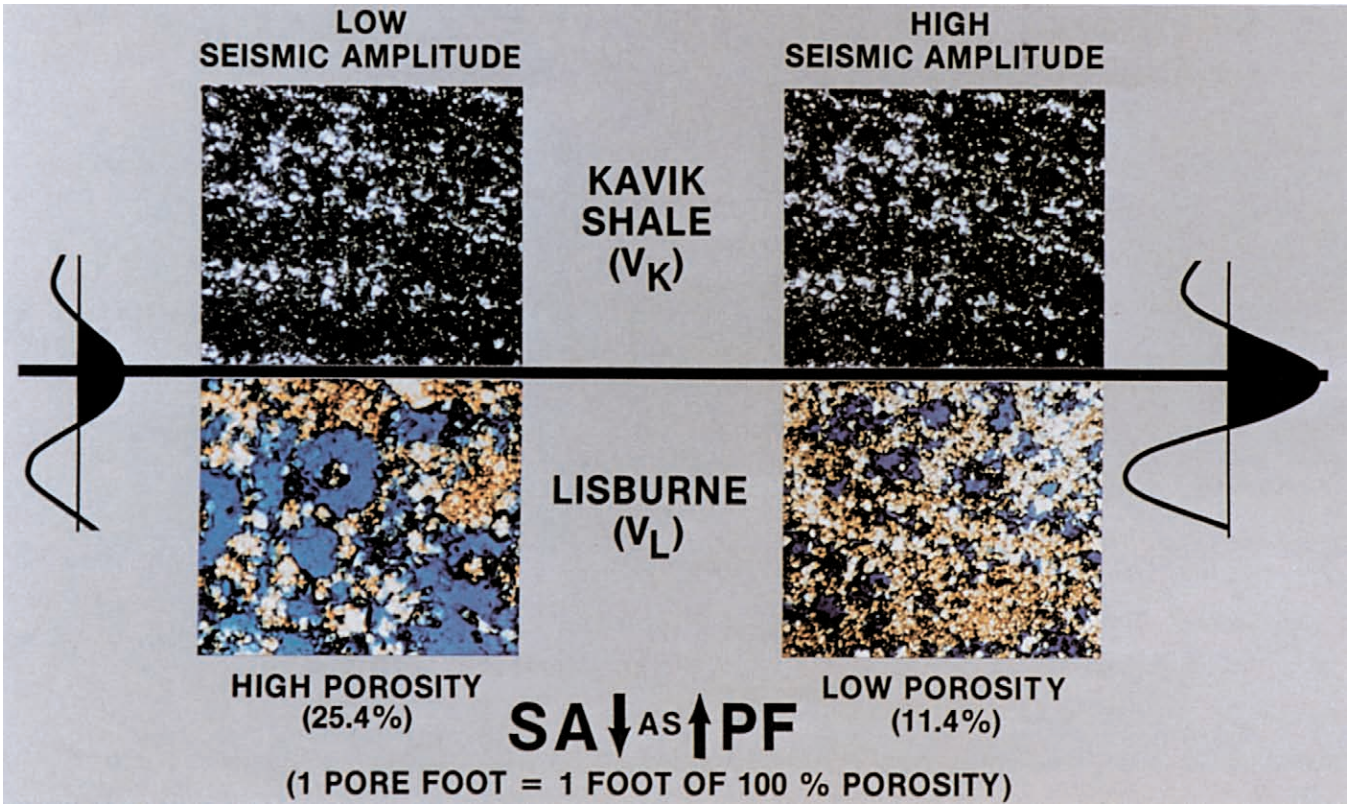

Fig. 14-9-4. Amplitude decreases as porosity increases.

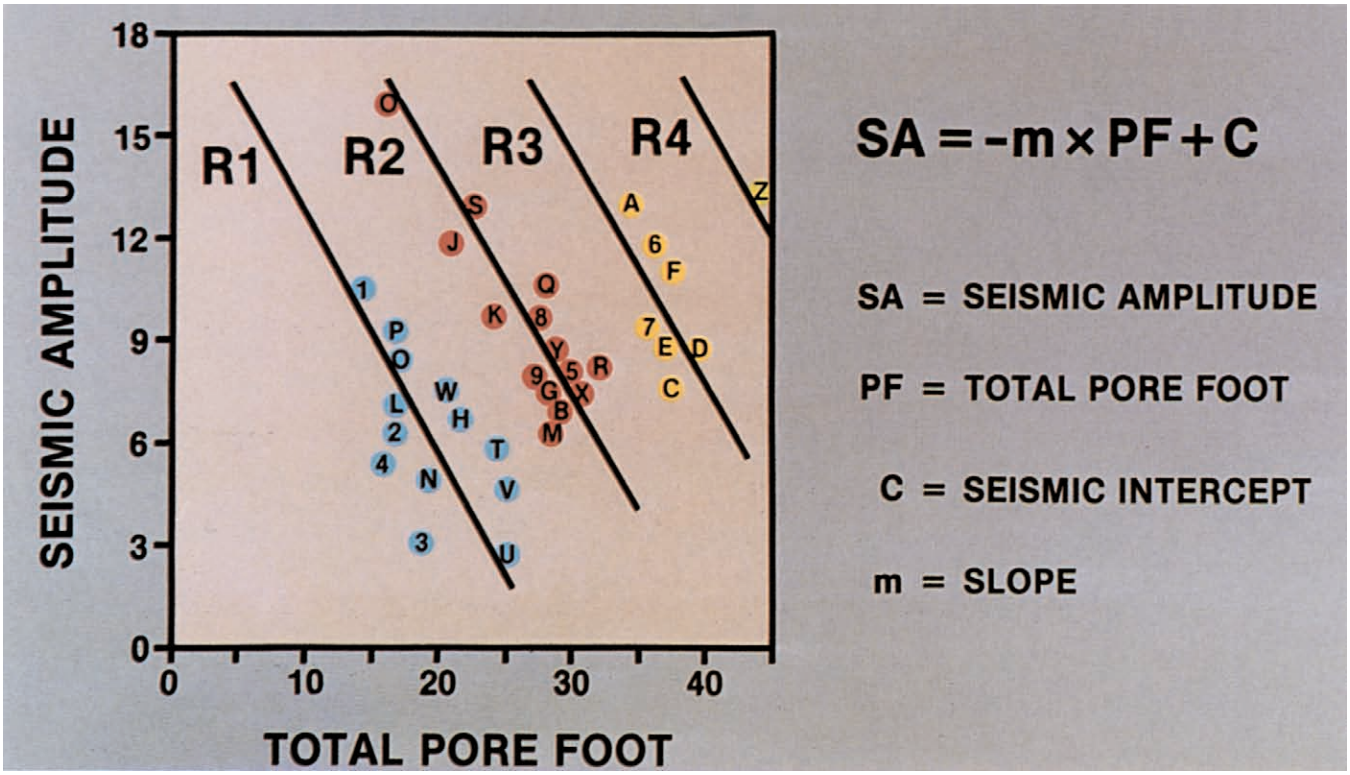

Fig. 14-9-5. Dependence of amplitude on porosity in four regions.

Downloaded 25 Jun 2012 to 95.28.162.50. Redistribution subject to SEG license or copyright; Terms of Use: http://segdl.org/

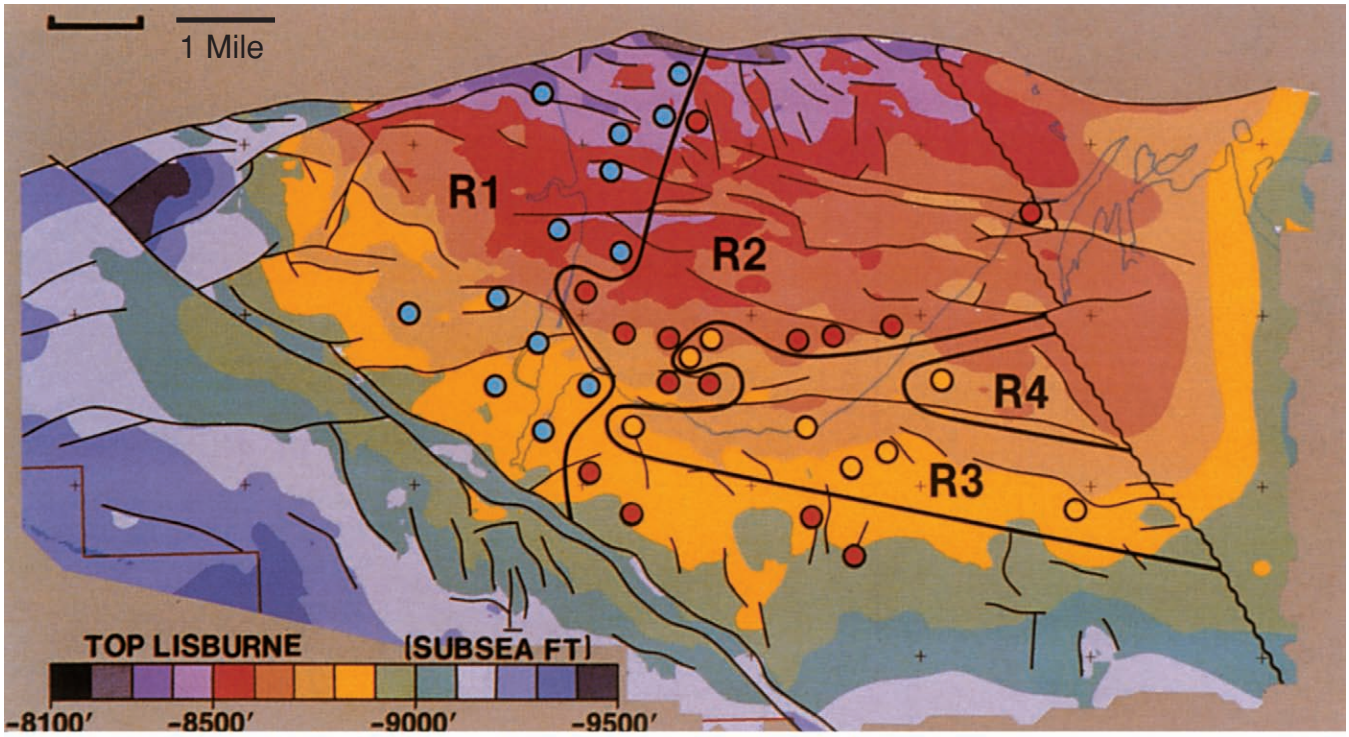

Fig. 14-9-6. Locations of seismic intercept regions.

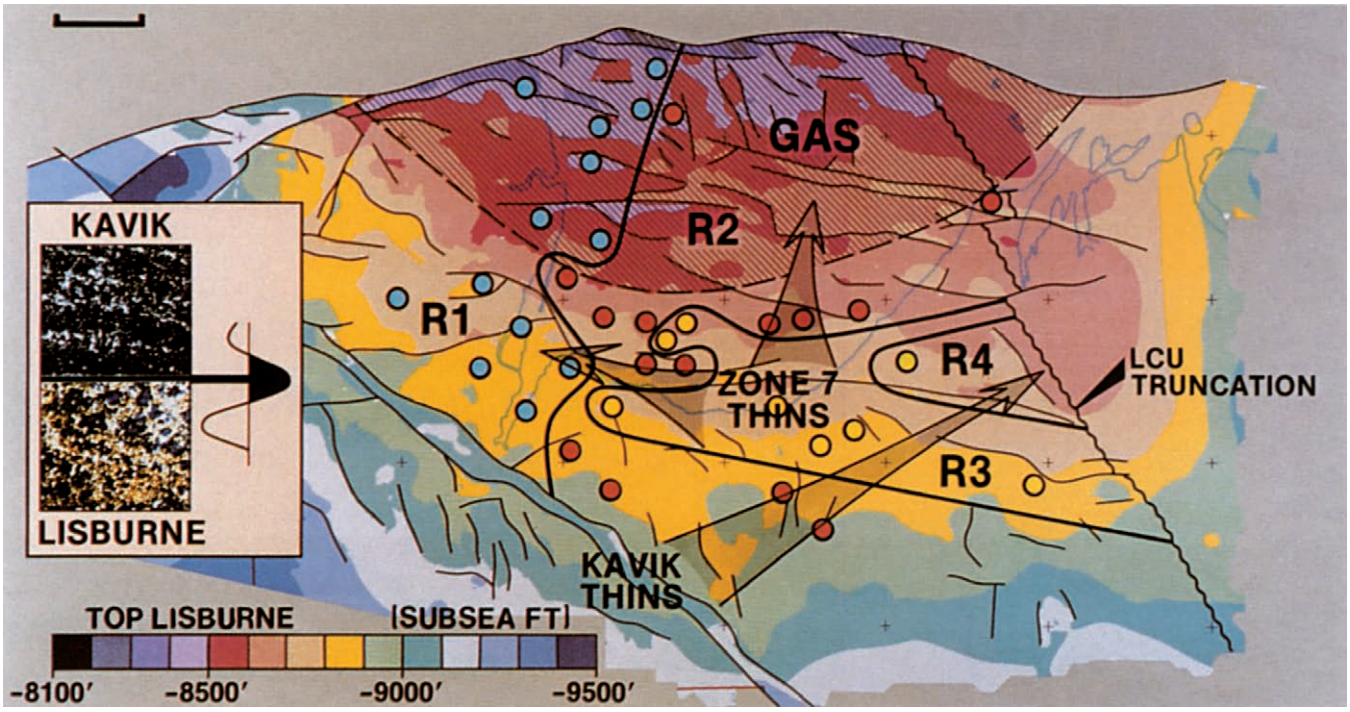

Fig. 14-9-7. Factors affecting seismic intercept regions.

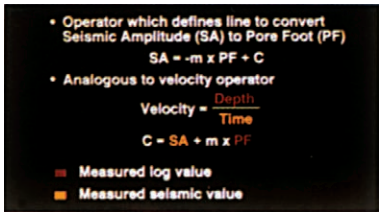
• Operator which defines line to convert Seismic Amplitude (SA) to Pore Foot (PF)
SA = -m x PF + C
• Analogous to velocity operator
Velocity = Depth / Time
C = SA + m x PF
Measured log value
Measured seismic value

Fig. 14-9-8. Calculation of seismic intercept at each well.

Downloaded 25 Jun 2012 to 95.28.162.50. Redistribution subject to SEG license or copyright; Terms of Use: http://segdl.org/

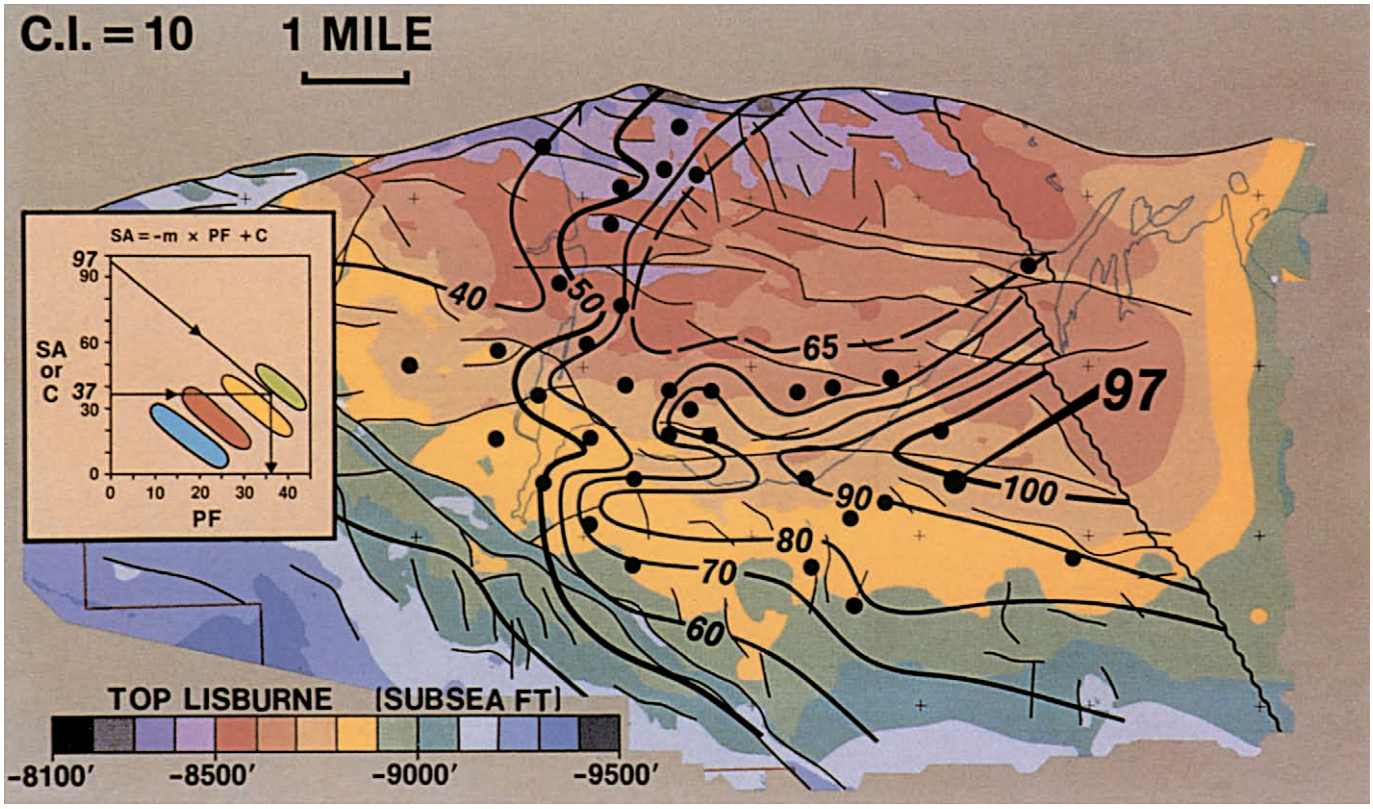

Fig. 14-9-9. Seismic intercept contour map superimposed on top Lisburne structure.

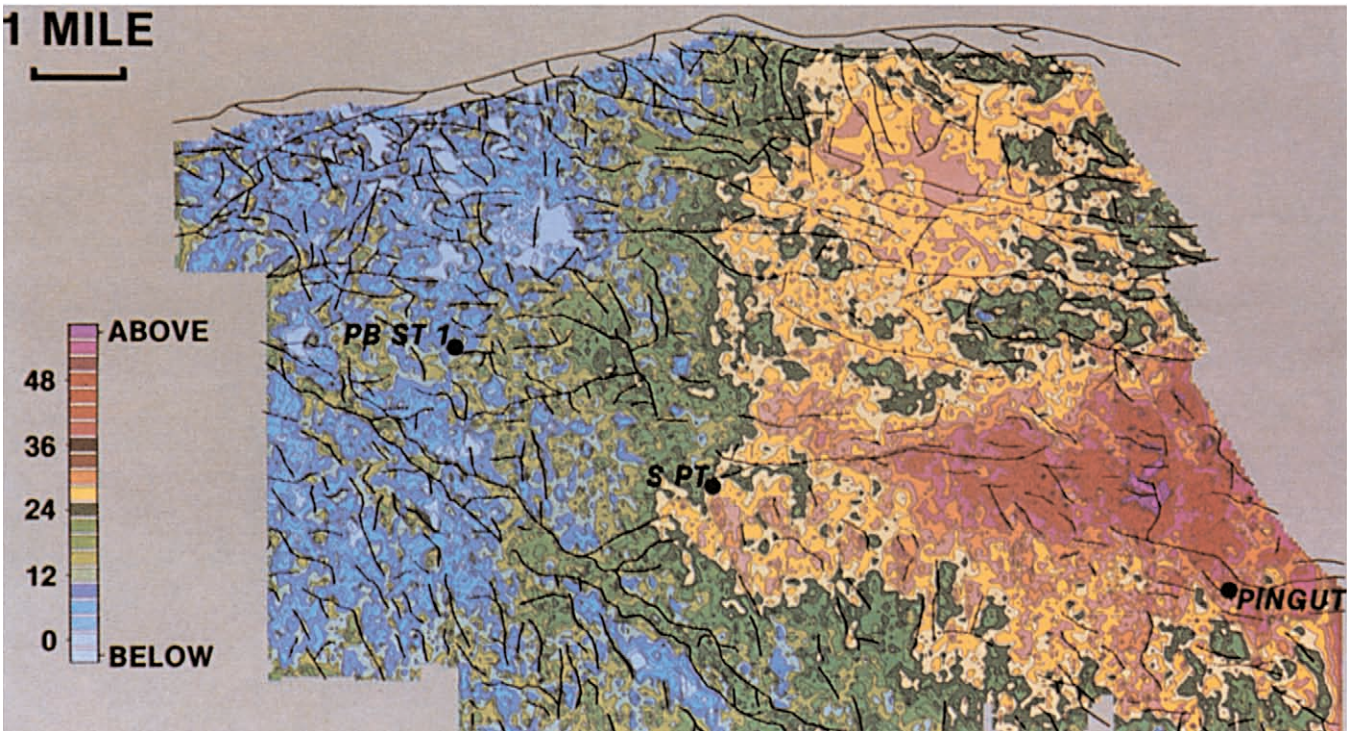

Fig. 14-9-10. Map of porosity-feet for Lisburne formation zones 7 to 4, derived from seismic amplitude.

Downloaded 25 Jun 2012 to 95.28.162.50. Redistribution subject to SEG license or copyright; Terms of Use: http://segdl.org/

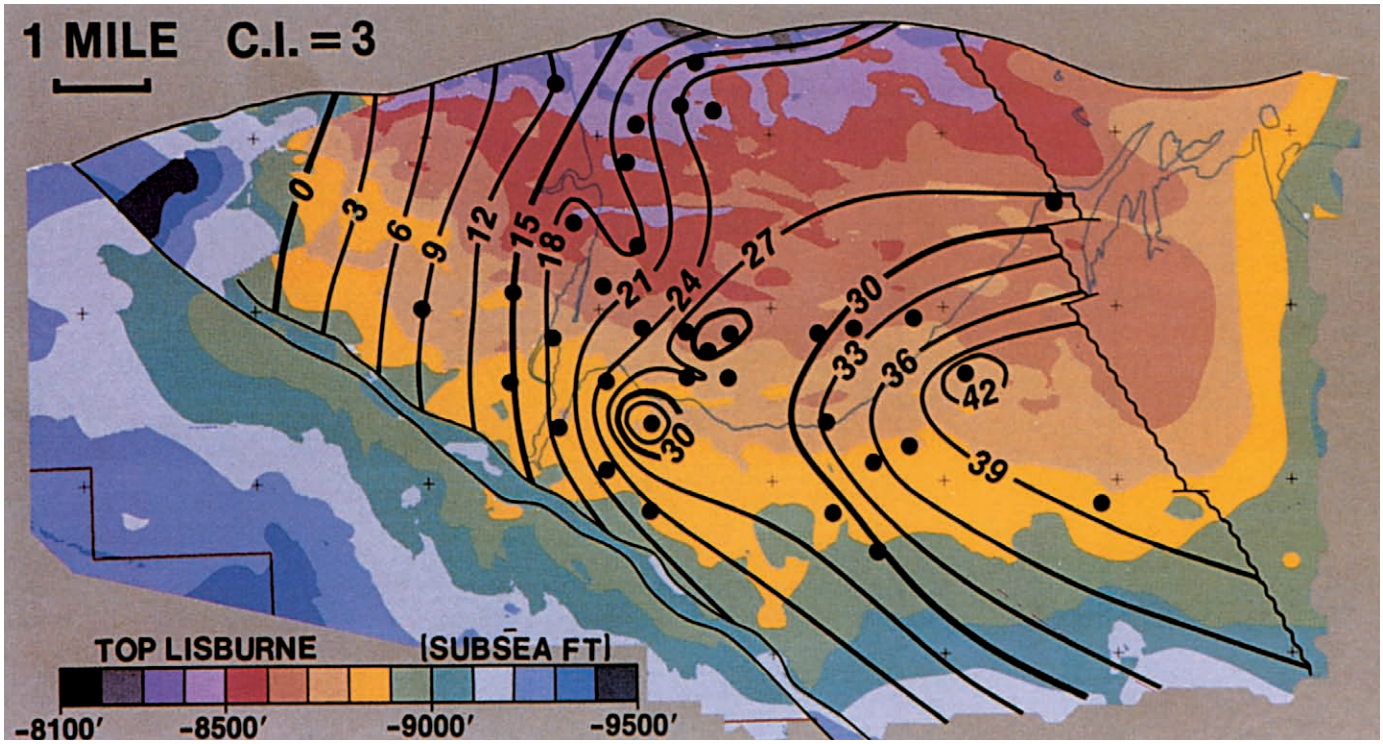

Fig. 14-9-11. Map of porosity-feet contoured from well values superimposed on top Lisburne structure.

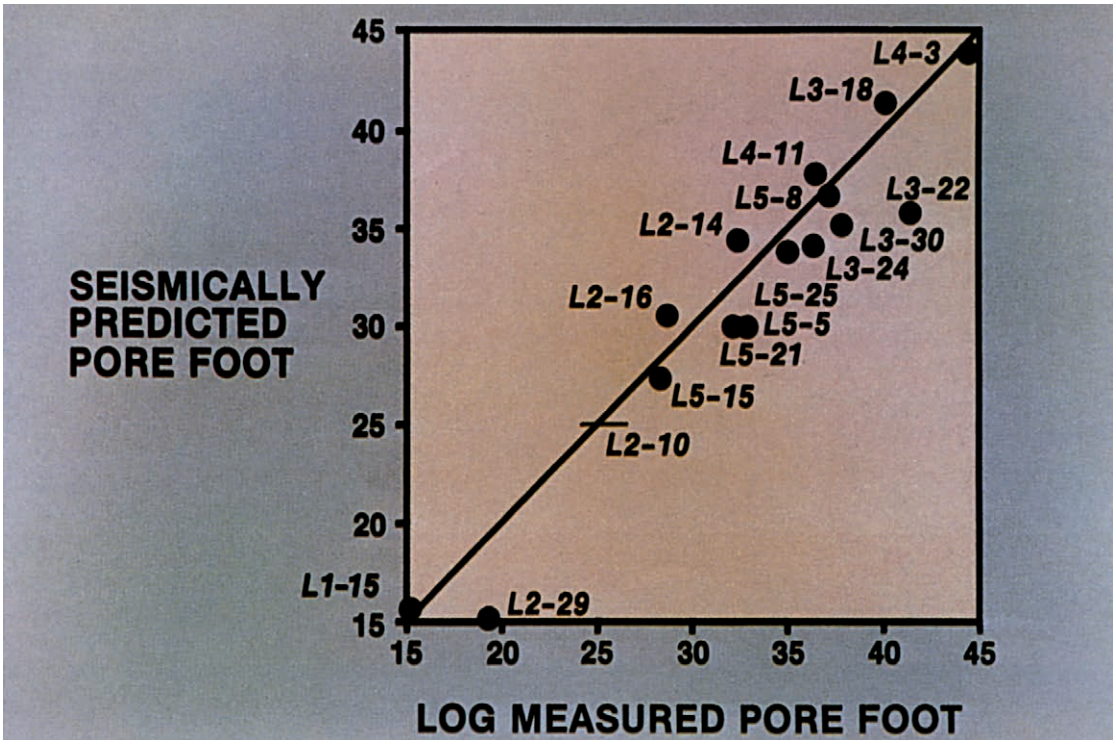

Fig. 14-9-12. Porosity-feet prediction results for 16 new wells.

Downloaded 25 Jun 2012 to 95.28.162.50. Redistribution subject to SEG license or copyright; Terms of Use: http://segdl.org/

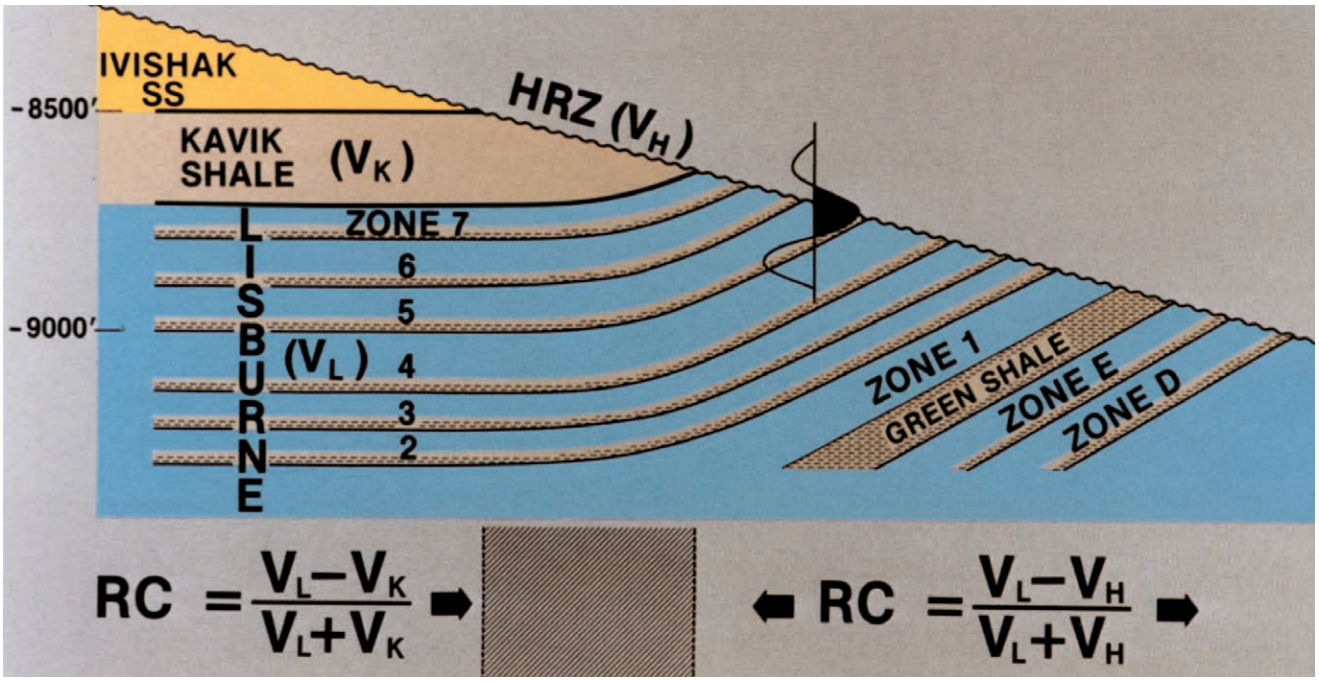

Fig. 14-9-13. Geologic cross section of Lisburne truncation. RC represents reflection coefficient; HRZ represents high-risk zone; V_H represents velocity in layer H.

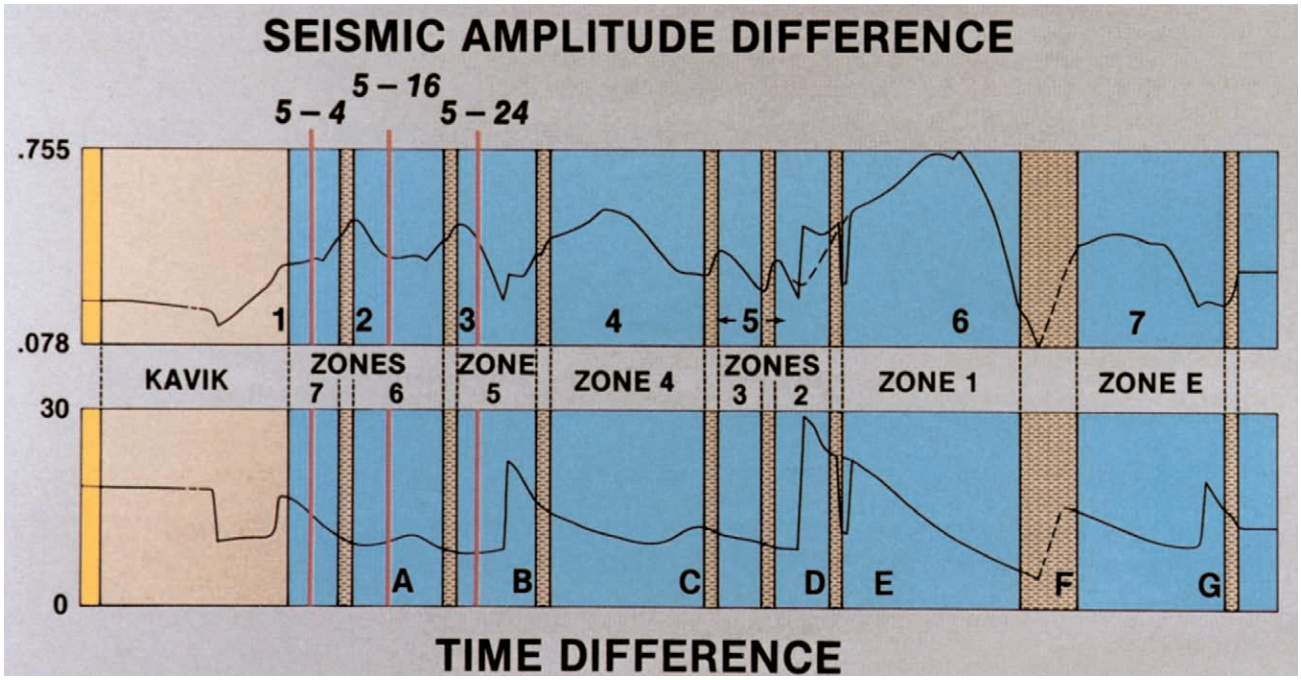

Fig. 14-9-14. Synthetic seismic amplitude and time difference along unconformity for cross section of Figure 14-9-13.

Downloaded 25 Jun 2012 to 95.28.162.50. Redistribution subject to SEG license or copyright; Terms of Use: http://segdl.org/

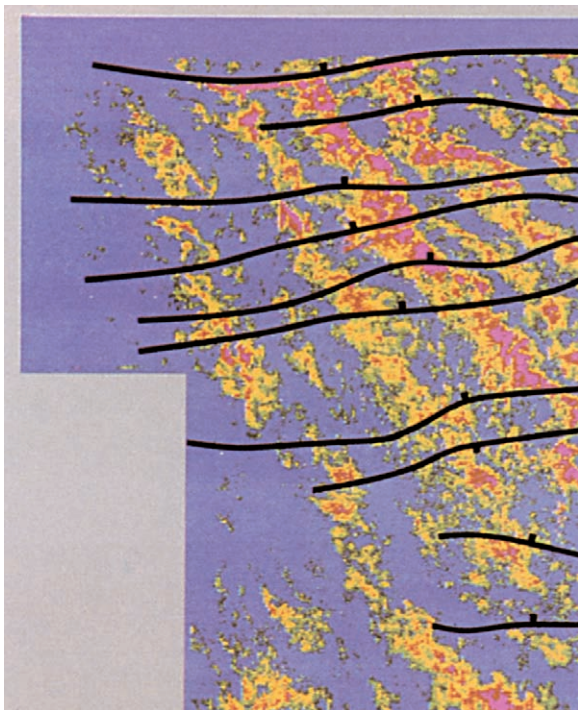

Fig. 14-9-15. Horizon slice along Lower Cretaceous Unconformity, showing banded patterns in seismic amplitude.

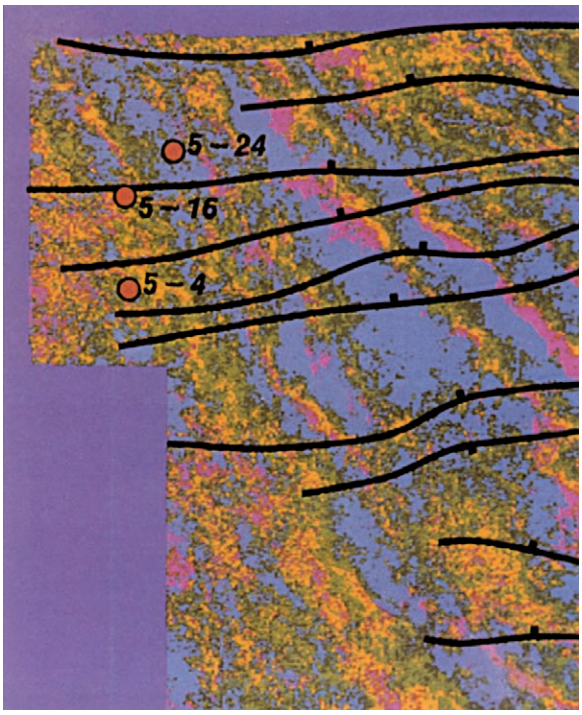

Fig. 14-9-16. Observed seismic time differences along Lower Cretaceous Unconformity, showing banded patterns.

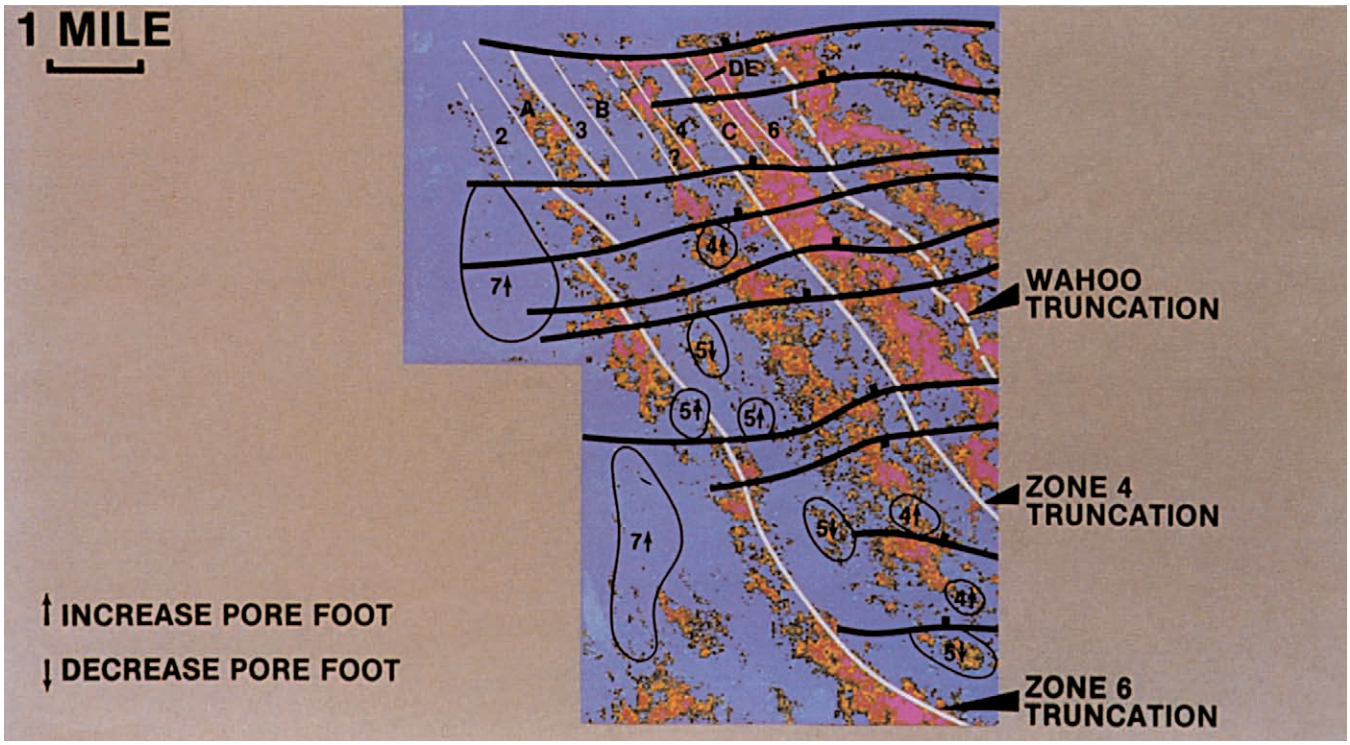

Fig. 14-9-17. Interpreted truncations superimposed on horizon slice of Figure 14-9-15.

Downloaded 25 Jun 2012 to 95.28.162.50. Redistribution subject to SEG license or copyright; Terms of Use: http://segdl.org/

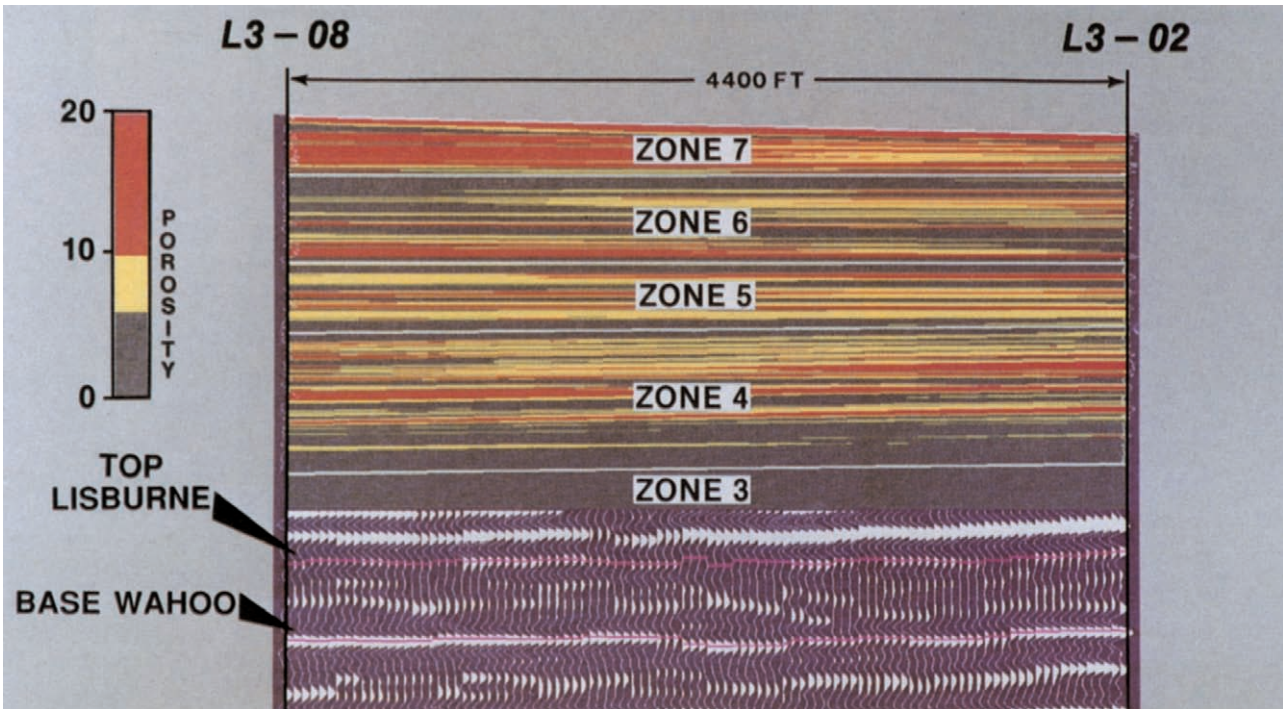

Fig. 14-9-18. Porosity cross section between wells L3-08 and L3-02.

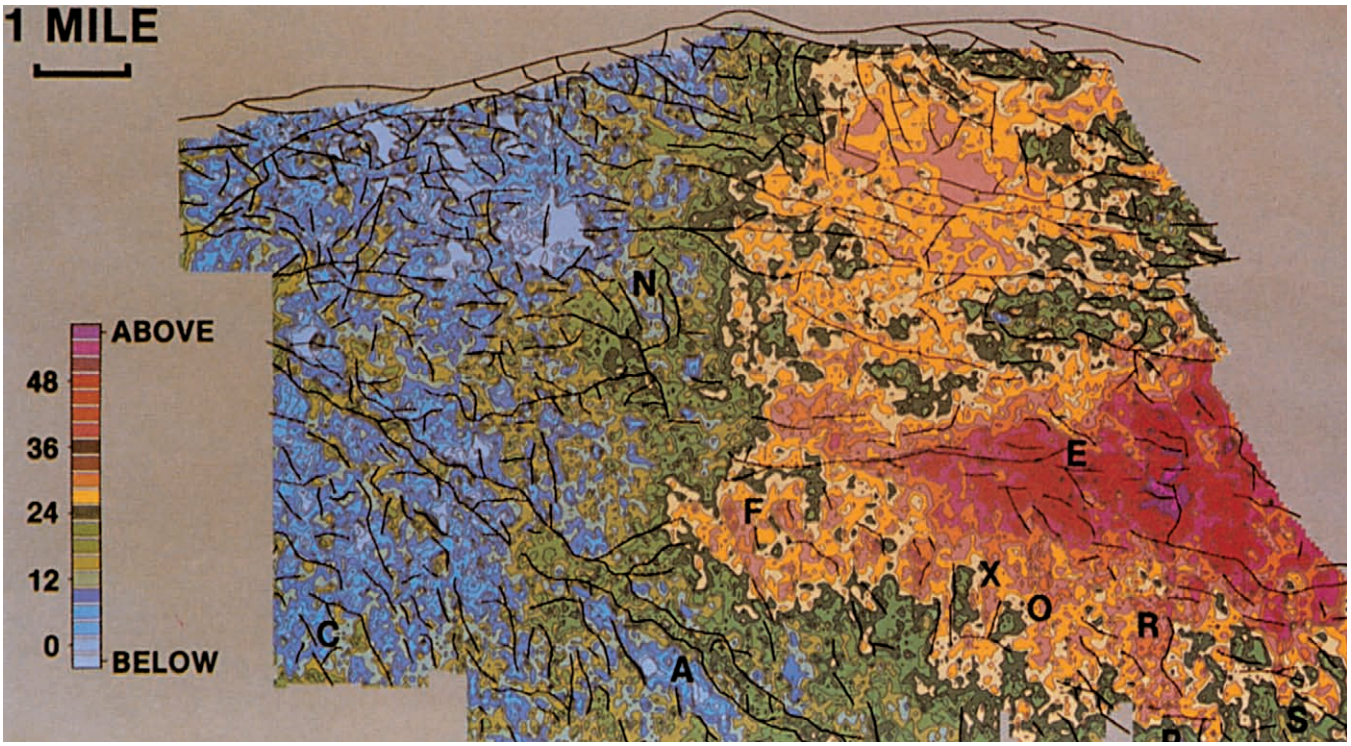

Fig. 14-9-19. Lisburne porosity foot map and its relation to faults and fractures.

Downloaded 25 Jun 2012 to 95.28.162.50. Redistribution subject to SEG license or copyright; Terms of Use: http://segdl.org/

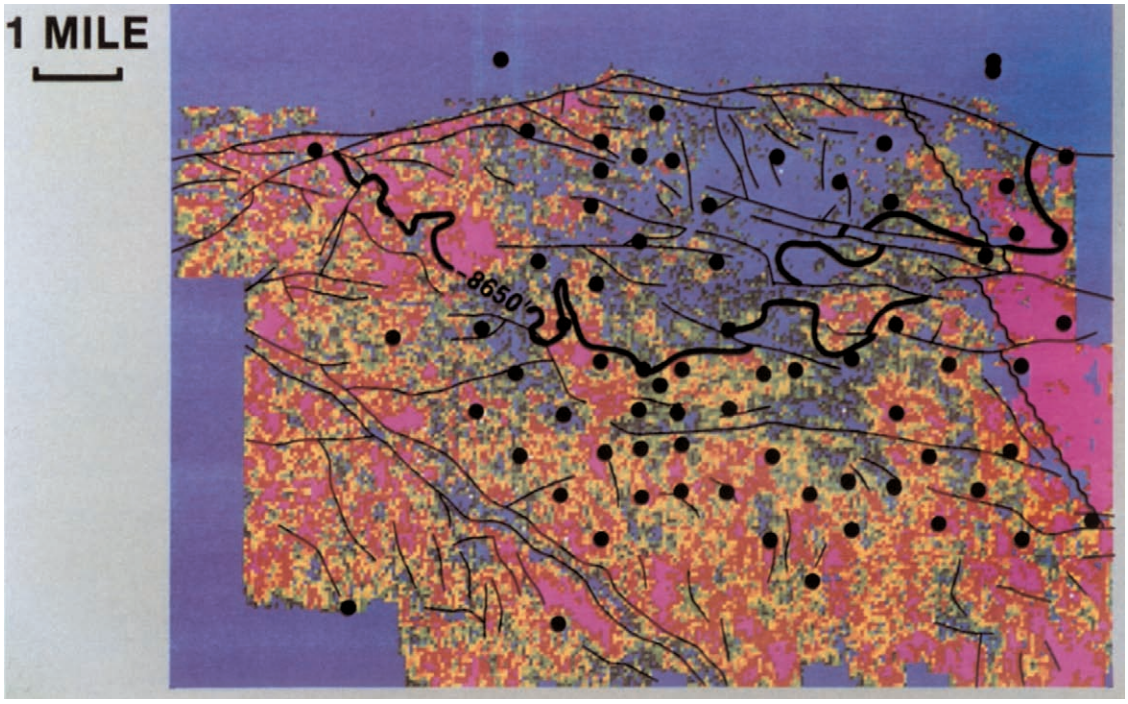

Fig. 14-9-20. Horizon slice for top Lisburne reflection showing low amplitudes (blue) corresponding to gas zones.

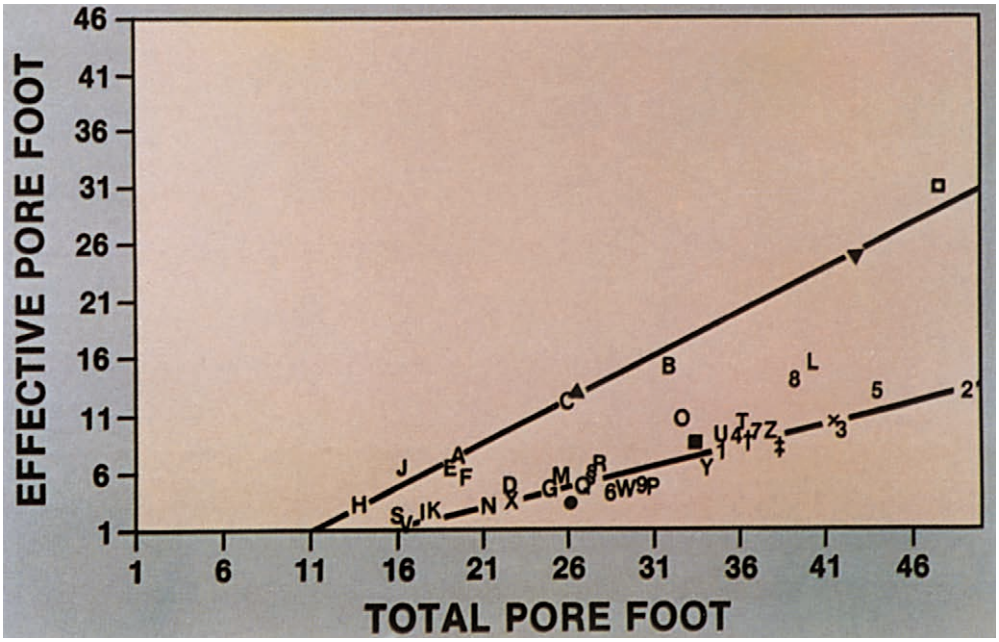

Fig. 14-9-21. Effective porosity foot versus total porosity-feet.

Downloaded 25 Jun 2012 to 95.28.162.50. Redistribution subject to SEG license or copyright; Terms of Use: http://segdl.org/

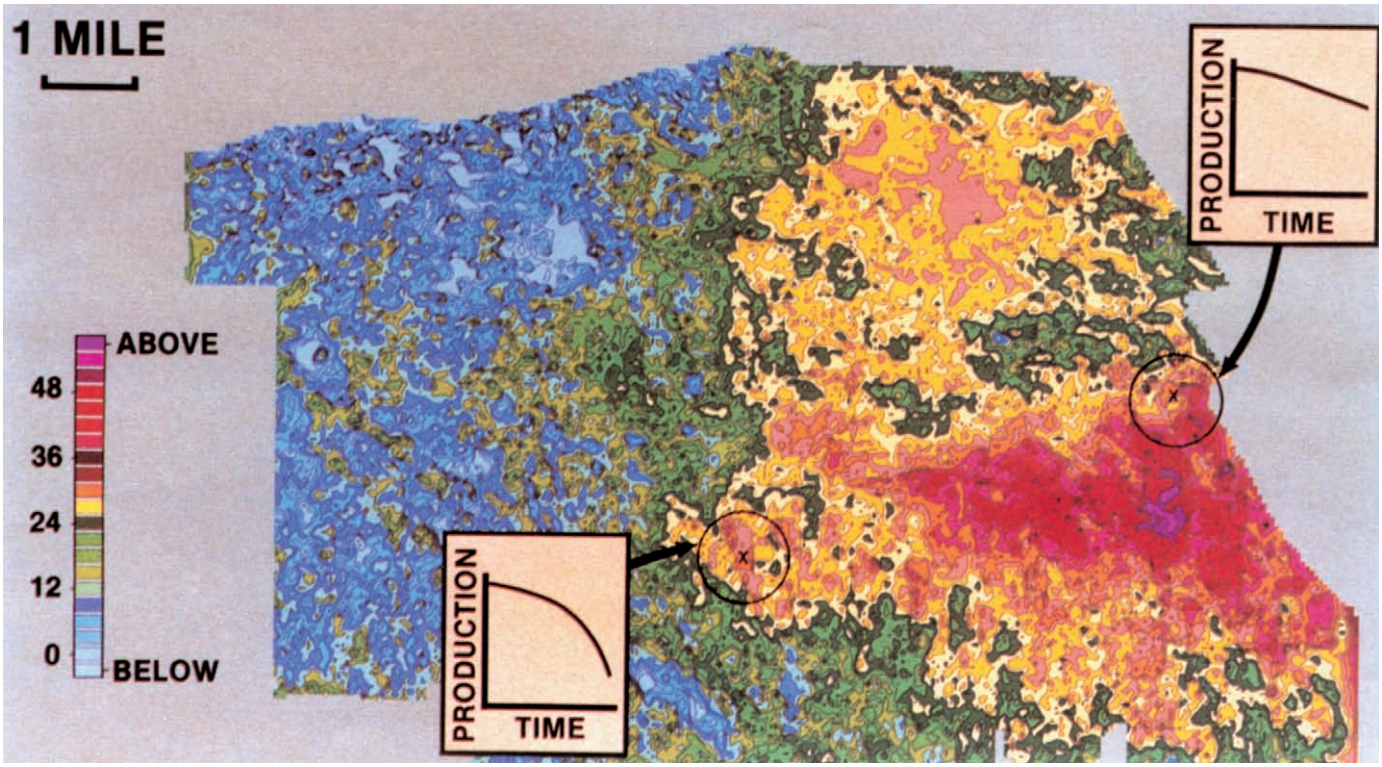

Fig. 14-9-22. Lisburne porosity-foot map and prediction of production over time.

Downloaded 25 Jun 2012 to 95.28.162.50. Redistribution subject to SEG license or copyright; Terms of Use: http://segdl.org/

Case History 10

Value of Geophysics in the Production of Bay Marchand Field

William L. Abriel, Chevron Energy Technology Company; William Haworth, Chevron North America Exploration and Production Company

Introduction

This is the story of how geophysics has helped Chevron produce more oil and gas from Bay Marchand than from any other field in the Gulf of Mexico. From 1938 until today, geophysics has had a measurable impact during discovery, delineation, development, production, and revitalization of the geologically complex field. During this time, as geophysical technology has become available it has been applied with largely successful results.

High-impact geophysical techniques applied to date and described in this paper include gravity, refraction seismic, 2-D reflection seismic, 3-D production seismic, high-resolution 3-D seismic, and time-lapse seismic (4-D). Additional applications of high-end geophysical techniques include inversion, AVO, shear-wave seismic, prestack time imaging, and depth imaging. The interest in and ability to use so many of the geophysical tools of the industry are due to both the geologic complexity of the field and the fortunate conditions of being in a generally good seismic-data area.

The role of these geophysical techniques is documented, and their impact is measured throughout the life of the field. Not only were the initial discovery and development supported by geophysics, but after production maturity and decline, geophysics had a primary role in the revitalization of the field and substantially extended the production life, which continues today.

A much shorter case history of Bay Marchand field was included in earlier editions of this book and also published as Abriel et al. (1991). This case history is a considerable expansion, starting earlier and finishing later in the field's history.

Geologic Setting

Bay Marchand field is a complexly faulted salt dome (Frey and Grimes, 1970) along the northern edge of the Gulf of Mexico shelf (Figure 14-10-1). The field is characterized by a number of structural and stratigraphic traps (Figure 14-10-2). As the dome was emplaced and altered during geologic history, major and minor faults both provided pathways for hydrocarbon migration and also provided traps for accumulation. Proximity to the salt and its history of movement also have had a substantial impact on the sedimentation of marine regressive sand reservoirs and associated sealing shales.

The field has produced from more than 50 sands, ranging in age from Pleistocene to middle Miocene, and from depths of 1000 ft to over 15,000 ft (300–4600 m) subsea. The complexity of faulting, along with stratigraphic variation and the large number of productive sands, resulted in more than 500 individual combination traps with varying fluids, pressures, and production characteristics. This situation has resulted in the drilling of more than 1200 production wells from 1950 to today — each targeted to a specific development or enhanced-recovery concept.

As with geophysical technology, reservoir management and drilling engineering technologies have addressed the geologically complex field, and have consistently been improved and applied to maximize production value. Production advances from waterflooding to horizontal drilling were applied as they developed in the industry. The application of geophysics to the field has directly supported these production-engineering activities by addressing answers to the issues of geologic complexity.

Discovery

In the initial exploration phase of the United States Gulf Coast, gravity data were an important tool in oil exploration, as they provided a primary method of locating large salt

Downloaded 25 Jun 2012 to 95.28.162.50. Redistribution subject to SEG license or copyright; Terms of Use: http://segdl.org/

domes expected to act as collecting areas for oil and gas. Bay Marchand salt dome was initially recognized by this method in the late 1920s, as were many other large domes along the south Louisiana coast (Figure 14-10-3). At that time drilling onshore was the only option, and Gulf Oil Company attempted this on the northern salt flank in 1930. Unfortunately, they were not successful in discovering hydrocarbons.

But not being discouraged by this, other companies drilled an additional nine dry holes onshore over the next ten years in search of oil. And one additional well had even been attempted with new technology — offshore drilling. Gulf was there first at the very top of the salt dome and in 1941 found an uneconomic accumulation with 25 feet of gas in the PP-1 well (Figure 14-10-4). Chevron (then Calco) conducted a reflection seismic survey and acquired more than 25,000 leased acres in 1947 and 1948. Utilizing the new reflection seismic and an existing refraction survey, they proposed three wells in September 1948. The first well (A-1) encountered salt near the crest of the dome and was a dry hole.

The B-1 and C-1 follow-up wells were designed to test opposite flanks of the dome and were drilled simultaneously. Both were successful. The B-1 well, the 13th exploratory well in the area, was credited as the discovery well and was completed as an oil producer from a depth of 2,873–2,892 ft in March 1949 (Figure 14-10-4). After 19 years of exploration, the giant Bay Marchand field came into existence.

Delineation

Immediately after the field's discovery, exploitation proceeded with the installation of three development platforms that had a total of 12 directional wells (Figure 14-10-5). The first platform installed was made of wood and remained in production for decades. The other platforms employed a new facilities concept — iron legs and an iron deck. All of this was accomplished by 1951, when production was initiated and further delineation was planned.

To support this additional delineation program, a more extensive refraction program was acquired to map the position of the salt-sediment interface, as proximity to salt was considered to be the key to oil accumulation. The A-1 well, which had penetrated salt, was used for a refraction survey in 1950. The well site was used as a position for dynamite shotpoints, and receivers were deployed extensively over the ocean bottom and above the dome (Figure 14-10-6). Seismic traveltimes from the shots were carefully measured, and the seismic waves that traveled through salt and along the salt-sediment interface were plotted in depth. The interpretation of the refraction data produced a detailed salt contour map in 1951 (Figure 14-10-7). This map is the first complete representation of the dome and rather closely resembles what we know today. Of special note is the identification of a salt overhang on the east flank — a concept that was lost in the 1960s only to reemerge again in the late 1980s.

Development

During the aggressive development of the field in the 1950s, early delineation focused on the reserves located near the crest of the dome. Over time, delineation proceeded down the flank of salt and resulted in finding additional reserves in both the north and east flanks (Figure 14-10-8). Production geology was the foundation of this development effort, with correlation of well logs as the critical subsurface data. What existed between wells was estimated on the basis of geologic models and imagination.

Delineation and development proceeded even farther down the flanks in the 1960s, extending production to the east and south (Figure 14-10-9). At that time, more expensive drilling of deeper reservoirs was supported by limited 2-D seismic reflection data. Those seismic data were good at predicting large faults and general dip rates but lacked the appropriate resolution to handle stratigraphic information. By the late 1960s the field reached its greatest development activity, having more than 800 wells, and was at its historical peak (Figure 14-10-10). The majority of development effort was done with geologic imagination and widespread drilling in just about every corner imaginable. There didn't seem to be much space left for finding new significant reserves.

Downloaded 25 Jun 2012 to 95.28.162.50. Redistribution subject to SEG license or copyright; Terms of Use: http://segdl.org/

Field Maturity

Peak production for the field (80,000 BOPD & 84 MMCFG/D) occurred in 1967. By the 1970s, production went into decline (Figure 14-10-10). That decline occurred despite the initiation of waterflooding and pressure maintenance in a number of the larger reservoirs on the east flank of the field. It was at that time that 2-D seismic reflection data began to significantly influence the geologic thinking about the field. With the advent of digital processing, seismic sections improved enough that they were used more commonly for structural analysis. In addition, the ability to preserve amplitude information was beneficial in the recognition of some stratigraphic attributes of the subsurface (Figure 14-10-11). With proper amplitude analysis, the direct detection of some hydrocarbons (especially gas) was also possible.

Two-D seismic data became a good tool for providing new subsurface information. With the geologic complexity of the field, valuable information was needed between the already close well interval, and seismic data provided the tool to show the inter-well geology. An extensive grid of 2-D seismic data was acquired (1) to support structural and stratigraphic models for the enhanced recovery, (2) to help locate production and injection wells, and (3) perhaps to find hidden reserves (Figure 14-10-12). Drilling during this period was less frequent than in prior decades and was targeted at potential new accumulations or specific wells needed to fine-tune production (Figure 14-10-13).

For Sale — The Largest Oil Field in the Gulf of Mexico

By 1984, production was in significant decline to the extent that Chevron reluctantly began the process of putting the field up for sale. Two-D seismic data had been acquired over most of the field, and apparently there weren't many places left to develop. After all, what more could be learned about such an extensively drilled asset? It was clear that the field was rapidly becoming uneconomic despite the use of enhanced oil recovery techniques and the best geology and geophysics available. It was time to get out.

But wait. A new technology was emerging that showed significant promise in subsurface geology — 3-D seismic data. Exploration in the Gulf of Mexico was undergoing an exciting new era in the early 1980s as structure and stratigraphy were being revealed in 3-D cubes with reflections accurately placed in their correct position. Old maps were being revised, and new plays were coming to light. Some geologic rules of thumb were being abandoned as the 3-D observations were coming in. What were the odds that this could impact an asset like Bay Marchand? Would new geology be revealed? Geophysicists certainly thought so, and the field management approved a project to acquire the first full field-scale 3-D seismic data specifically designed to support production.

If the 3-D survey was to be cost effective, it would have to have very significant impact. The price of acquisition and processing was the equivalent of ten new production wells, or approximately the entire year's drilling program. The seismic acquisition might not interfere with present production practices, but it would significantly delay much-needed production additions. A planned drilling program of 12 wells was put on hold pending the outcome of the survey, and the cash marked for those wells was moved to the seismic budget for acquisition of 3-D, which commenced in 1986.

The 1986 3-D Seismic Project

The decision to acquire 3-D seismic data was based on anticipated success from three primary objectives:

- Increase reserves by delineating new reservoirs in structural and stratigraphic traps.
- Increase production by identifying additional production-well locations in existing reservoirs.
- Enhance reservoir management through the unification of geology, geophysics, and reservoir engineering, thus obtaining better models for reservoir simulation and optimizing the location of water-injection wells for enhanced oil recovery.

In order to obtain a data set with exceptional quality, acquisition design objectives were set to cover the entire survey area with 60-fold data on a 55-ft-square bin. This was

Downloaded 25 Jun 2012 to 95.28.162.50. Redistribution subject to SEG license or copyright; Terms of Use: http://segdl.org/

accomplished with Western's Digiseis telemetry receivers and a recording ship equipped with a marine air-gun source. The geometry pattern was set with rows of hydrophone receivers placed at the seafloor every 220 ft (67 m) (Figure 14-10-14). Two rows were placed 880 ft apart. Air-gun sources were fired in a grid 110 ft inline and 220 ft crossline, resulting in subsurface bins of nearly identical offset and azimuth.

Although this design was attractive from a geophysical standpoint, it required significant effort to obtain because the field contained 114 production platforms, two major consortium pipelines, plus countless subsea production flow lines, power cables, and support systems (Figure 14-10-15). Western's outstanding acquisition team provided perfect coverage of the field by placing receivers under platforms or swapping shots and receivers. Every bin in the survey had exactly the same fold offset and azimuth distribution to cover the 60-sq-mi (155 sq km) survey.

Impact of 3-D Seismic Data

Three-D seismic data for the Bay Marchand field had a major impact. With the ability to image the reservoirs between wells, the original objectives of the survey were met, and production increased significantly.

Most of the salt dome was covered in the acquisition. An example seismic line over the top illustrated the very sharp and even angular nature of the salt-sediment interface (Figure 14-10-16). For the first time, both large- and small-scale faults could be accurately located and subtle details of stratigraphy inferred from amplitude changes on reflections. And because the data are represented in a cube, time and horizon slices could be analyzed. Surprising structural relations were revealed, such as the complex faulting of the salt dome and the horizontal sharp corners of the salt where faults intersected (Figure 14-10-17).

Recognition of the potential of this new information made it clear that the prior proposed drilling program was not well positioned, and that program was recycled so that new drilling opportunities could go forward. Over the next two years, twenty-three new production wells were located and drilled on the basis of the concepts revealed by the 3-D seismic data. All twenty-three wells were a success, and the new reserves were put into the production stream.

Some new reserves revealed by the 3-D seismic data were related to the identification of new fault blocks. Even in a densely drilled field with more than 800 wells, there was room to find untapped oil and gas. An example of this was the drilling of infill well #40. The producing interval was penetrated by numerous wells (Figure 14-10-18), and yet there was room for one more. A time slice showing the salt-sediment interface revealed an unknown embayment holding potential reserves (Figure 14-10-19). A new well was planned to drill into the embayment where high-amplitude reflectors suggested the presence of oil and gas that were not being produced (Figure 14-10-20). The well found both oil and gas in this structural embayment (Figure 14-10-21).

New structural information began to come to light in many places over the field. An example on the east flank is a case in point. A map of the producing reservoir (Figure 14-10-22) had been constructed from 40 well correlations and 2-D seismic data shot on a grid of 2000 ft. The fault intersections, log correlations, fluids, and pressure were all employed to map out areas of gas, oil, water, reservoir shale-outs, and new potential. However, when the 3-D seismic data were employed using the same well and engineering information, a new map of the reservoir showed a significantly different picture (Figure 14-10-23). Fault locations and sense of motion were changed. This opened opportunities to find undrilled reserves, and three new successful wells were immediately drilled on this new interpretation.

Additional reserves were uncovered by the recognition of stratigraphy from seismic data. For the first time, seismic amplitude measurements were found to be trustworthy enough to directly map reservoirs. Seismic sections such as Figure 14-10-24 revealed both subtle and dramatic changes in amplitude. But when the seismic horizons were picked and then represented in map view, the geology became apparent from the horizon slice (Figure 14-10-25). With this powerful tool, it was possible to search for bypassed stratigraphic traps.

Downloaded 25 Jun 2012 to 95.28.162.50. Redistribution subject to SEG license or copyright; Terms of Use: http://segdl.org/

An example of using seismic amplitude for understanding the impact of stratigraphy on field production is provided by a sandstone reservoir on the west flank. Several wells had penetrated the reservoir, which was producing oil. Some stratigraphic complications were recognized, such as a local shale-out and several permeability barriers, on the basis of production history and pressure measurements (Figure 14-10-26). The horizon slice from the seismic data (Figure 14-10-27) clearly revealed the location of quality reservoir sands that were not being produced, and subsequent drilling brought these areas under production. Later, the smaller amplitudes to the south were successfully drilled as well, and those reservoirs were developed.

As illustrated in the previous examples, the 3-D seismic data directly detected new fault blocks and bypassed reserves. In addition, the seismic data also played a role in reservoir management through reservoir characterization. The key parameters that seismic data provided were reservoir and aquifer structure, gross interval thickness, porosity, net pay, and the location of original fluid contacts. An example of this is shown in the characterization study of the FX reservoir as a potential waterflood candidate. Although the reservoir was never waterflooded, the characterization study is an excellent example of the impact that seismic data can have on reservoir modeling.

The FX reservoir had two oil-producing wells, numbers 24 and 25 (Figure 14-10-28). In addition, the reservoir was penetrated by a downdip well in the aquifer and an updip well that was shaled out (Figure 14-10-29). Production and pressure decline suggested that the oil system would be closed. A reservoir characterization was performed using seismic data support and compared with a characterization using only the well data. The characterization using the seismic data showed the potential for an additional 26% cumulative production over that of the model using only well data.

Three-D seismic data amplitudes of the 8200 sand show strong reservoir heterogeneity (Figure 14-10-30). The high-amplitude reflections of the top (red) and base (blue) of the unit extend well below the oil-water contact and thus are not a function of oil saturation but instead of reservoir porosity. The horizon slice of the reservoir reflectors (compensated for tuning) (Figure 14-10-31) shows that wells G-3, 24, and 25 lie approximately within the "yellow" reflection response. The porosity-thickness of the three wells is also similar. Using only the well data, the reservoir would appear to be of constant thickness and homogeneous in porosity, with local updip shale-out at well 27. However, when we view the seismic response on the horizon slice, we can see some very high-amplitude areas between the wells, which indicates thick and porous reservoir not seen in the well control. A net-sand map generated from the horizon amplitudes and time thickness shows the inter-well thicks and thins (Figure 14-10-32).

The net-sand map is a fundamental element of the volumetric calculations of the reservoir. The total oil volume can now be calculated and the amount produced subtracted to calculate the remaining oil potential. If the pressure history is then taken into account, it can be estimated that only about one-third of the total oil recovery is possible without pressure support. Thus, two reservoir simulations were run to estimate and predict the effect of injecting water into well G-3. One simulation was done from a characterization using only well parameters, and a separate and more heterogeneous one using parameters from seismic attributes (Figure 14-10-33). The resulting predictions of oil production at well 25 (Figure 14-10-34) show more than 28% greater oil recovery anticipated from the reservoir, if the seismic characterization is correct.

From the examples shown above, it can be seen that the 3-D seismic data were successful in meeting the primary objectives of finding new reserves, optimizing new producer and injector locations, and supporting reservoir characterization and reservoir management. An additional benefit of the 3-D seismic data was the ability to support the new drilling concept of horizontal wells, which were able to increase production rates per well. As a result of the new geologic information provided from the 3-D seismic data, an aggressive program was initiated to increase production. The successful production increase has significantly added to the value of the Bay Marchand field and has revitalized production (Figure 14-10-35).

Downloaded 25 Jun 2012 to 95.28.162.50. Redistribution subject to SEG license or copyright; Terms of Use: http://segdl.org/

Further 3-D Acquisition

The 1986 3-D survey covered a great deal of the Bay Marchand field, but additional areas needed more complete coverage. With the impact of 3-D seismic data well proven, additional 3-D seismic data acquisition continued in order to extend the coverage to the entire field. A west-flank survey was acquired to identify bypassed oil and provide resolution of thin-bed stratigraphy. A north-flank extension was acquired in 1998. This survey included data acquired in the onshore area merged with the offshore data. Again, those data provided indication of new fault blocks and bypassed reserves. As time progressed, service companies had acquired several speculative 3-D surveys that covered different portions of the field (Figure 14-10-36), and a decision was made to attempt to merge these into one consistent data set.

Merging was not a simple task, given the number of differences in the surveys. Sources were different, receivers used were both marine-streamer and ocean-bottom hydrophone receivers, and different recording systems were used as well. Stacks of the seismic data did not match (Figure 14-10-37), and significant cross-equalization in processing was required. Unmigrated gathers were used as input, requiring time, phase, and amplitude matching. The result of merging surveys (Figure 14-10-38) provided a much better regional picture of the geology. Fine-scale faulting was revealed, and further prospecting was enabled at the field edges. An additional benefit of survey merging was preparation of the data for 3-D prestack time and depth migration. And because there is overlap in space and time, the data could be used for time-lapse seismic analysis.

Time-lapse Seismic (4-D)

The 1986 3-D seismic survey prompted a review of most reservoirs that showed seismic response. Amplitude data from horizon slices were prime attributes for analysis, and many new stratigraphic views of the reservoirs were revealed, resulting in the location of bypassed fault blocks and stratigraphic traps. But at times, the seismic data did not fit the known stratigraphic model and suggested the detection of oil movement (Figure 14-10-39).

Oil bright-spot analysis was not common in 1986, and the suggestion that producing water fronts could be seen with seismic data was received with great skepticism. And yet, the data were of excellent quality and no other good explanation fitted all the observations. Gradually the concept was accepted, and engineering models began to take into account the seismic response. This led to identification of bypassed oil and recognition of significant geologic heterogeneity.

Mapping oil movement with seismic acquired at time intervals (4-D) was considered to be possible for some reservoirs in Bay Marchand, and a project was initiated. Key elements in the work included (1) petrophysical studies to determine strength of seismic signal from water movement, (2) reservoir characterization sufficient to support a 4-D seismic response, (3) forward seismic modeling for acquisition and processing parameters, and (4) selection of an acquisition technique to provide time-lapse data.

Petrophysical modeling showed favorable characteristics for 4-D seismic reservoir monitoring. Data from wells logged before and after production are appropriate data from which to make predictions and show that at times, the seismic response from oil production in Bay Marchand can be very dramatic. Because some reservoir sands are much lower in density than the encasing shales, they generate good reflection characteristics even when they are water wet (Figure 14-10-40). With the introduction of oil containing dissolved gas, velocity decreases significantly, creating an even higher impedance contrast (reflection coefficient), and an oil "bright spot" is formed. Then when that oil is depleted because of oil production and the voids are replaced with water, as is the case in strong water-drive reservoirs, the reservoir velocity decreases significantly and produces a large "dimming" of the amplitude in the water-swept areas.

In order to support reservoir monitoring from seismic data, a reservoir characterization was initiated in 1995. Its purpose was to compute the oil flow from reservoir simulation, forward model the seismic response to generate synthetic 4-D data, and then compare those data with 4-D seismic data actually acquired. To build the reservoir

Downloaded 25 Jun 2012 to 95.28.162.50. Redistribution subject to SEG license or copyright; Terms of Use: http://segdl.org/

characterizations, a team of geologists, geophysicists, and reservoir engineers from the Gulf of Mexico Business Unit and the Chevron Energy Technology Company (ETC) was assembled to build appropriately complex geologic models using well data, seismic data, and geostatistics. This team leveraged the detailed knowledge of the field possessed by the Gulf of Mexico personnel with the understanding of the new technology by ETC representatives. The procedures developed by the team have carried over into Chevron's reservoir-characterization work flows today. Within the reservoir characterizations, earth properties for seismic modeling were assigned and forward geophysical modeling was performed.

Forward modeling showed that a suitable seismic signature should be seen in 1996, ten years after acquisition of the first 3-D seismic survey. Acquisition of a monitoring 3-D survey began, with the intent to bury hydrophones in a semipermanent installation for repeat surveys over several years. The mechanics of this proved to be more difficult than anticipated, due to the highly mobile and unstable nature of the ocean bottom. Like many similar projects of that time, permanent sensor installation was not a success. Two years later, in 1998, a marine streamer 3-D was acquired by Geco over part of the field, and then 4-D seismic observations could be made.

The initial Bay Marchand 3-D seismic survey was not designed to be a base for later 4-D observations, and that created difficulties in making interpretations of time-lapse seismic effects. In some areas the data required time shifts, amplitude balancing, and phase corrections. But in many areas, a direct comparison of horizon slices from the different surveys provided insight into current reservoir conditions, water movement, and remaining hydrocarbon potential. Two examples are shown of water movement in the reservoirs during oil production. Both show heterogeneous sweep and bypassed oil potential. New drilling and completions then added to both the reserves and the production, as is shown in the following two examples.

The first example considers a fault block under oil production. The horizon slice of the reservoir from the 1986 3-D survey showed high amplitude remaining where wells A, B, and C are producing oil (Figure 14-10-41, top panel). An additional observation well (D) was full of oil in 1986. However, repeat cased-hole logging showed that by 1999, the reservoir was swept significantly, and the water level in the well had risen. By 1999, the three producing wells also were making significant water and not enough oil (Behrens et al., 2001). A second 3-D seismic survey, in 1998, showed the seismic response to be consistent with water encroachment in the wells (Figure 14-10-41, bottom panel). The high-amplitude area revealing unproduced oil indicated that producers were drawing up the water front in this relatively low-gravity oil. However, the new survey also showed a high-amplitude area directly between wells, suggesting uneven reservoir sweep and bypassed reserves. Follow-up drilling by Chevron proved that to be a correct interpretation and led to completion of an additional horizontal development well, which added good production rates to the field.

A similar but more complex result was observed in clastics at the deeper 7600-ft level. The repeat survey showed the oil sweep to be very uneven because of low-gravity oil plus the vertical and horizontal variability of reservoir facies (Figure 14-10-42). From 1986 through 1998, wells G, H, and I produced significant volumes of oil. Wells G and H were making significant water cuts by 1998, and well I had watered out completely. Again, the second seismic survey revealed bypassed oil reserves. Infill wells were drilled by Chevron and Energy Partners Ltd. in all three high-amplitude zones of the 1998 survey, proving bypassed reserves. Two were then put on stream, adding to production.

Stratigraphic Geophysics

Advances in seismic technology have opened the door to new opportunities in the understanding of geologic complexity for Bay Marchand. As an example, the legacy 1986 3-D data and the later 3-D seismic surveys were subjected to advanced inversion technology. The objective of such technology is to remove the wavelet from the seismic to reduce interference effects. With increased resolution from wavelet removal, the seismic data revealed previously unrecognized boundaries caused by horizontal stratigraphic

Downloaded 25 Jun 2012 to 95.28.162.50. Redistribution subject to SEG license or copyright; Terms of Use: http://segdl.org/

changes, especially in the predominantly deltaic environment of the majority of the field's reservoirs (Figure 14-10-43). This resulted in recognition of additional reserves in the field as stratigraphic traps and pinchouts, and in revelation of additional shallow reserves at the top of the field, known as "attic plays."

Following the success of higher resolution from inversion, more attention was directed to specialty acquisition for stratigraphic information. In 2004 and 2005, Bay Marchand was the site of the first commercial-production use of the VectorSeis Ocean Bottom Cable (OBC) acquisition using MEMS technology. MEMS (microelectromechanical systems) is the integration of mechanical elements, sensors, actuators, and electronics on a common silicon substrate through microfabrication technology (Figure 14-10-44). A positive indication was obtained from a value-of-information study (VOI) for ultra-sensitive recording at very high frequency, and from the recording of traditional acoustic waves plus additional recording of shear waves. New seismic data were acquired by GXT (ION) targeted solely at shallow reserves which had been obscured by imaging problems at the top of the salt dome.

The top of the Bay Marchand field is the site of historical and present-day expulsion of hydrocarbon fluids. The "chimney" of mobile hydrocarbon fluids invades lower-pressure geologic formations, and near the surface this includes silty and shaly lithologies as well as sands, resulting in a mélange of unstratified reflectors as seen by compressional (P)-waves (Figure 14-10-45a). Worldwide cases of shear (S)-wave recordings show that they can result in successfully imaging the subsurface where P-waves have failed, because S-waves respond more to the rock matrix than to the fluids or gas.

A limited acquisition trial was conducted to image through the chimney at the top of the salt dome and also to obtain higher frequency on the adjacent flanks. Spatial acquisition sampling was approximately three times denser (12.5 x 6.3-m bins) than in the legacy survey. The result was excellent P-wave data (Figure 14-10-45b). Far better fault definition and a consistent structural interpretation were now possible over portions of the area, and a valid top-salt reflection was revealed. Valid amplitude information showed the character of stratigraphic changes horizontally, and it was possible to detect the presence of gas migrating up specific faults. Unfortunately, the S-wave imaging has not been successful, due to difficulties in near-surface sampling density and the uncertainty in V_p/V_s ratios.

What Else Can One Possibly Do Here With Geophysics?

There are geophysical technologies that have not yet been applied to the field. Examples of these include seabed electromagnetic surveying, cross-borehole seismic and/or electromagnetics, and multi-azimuth seismic, among others. Bay Marchand geoscientists and reservoir engineers continually stay abreast of the potential for technology application and have the interest and support of the greater Chevron technology network. As good geophysical proposals are considered, they are subjected to review from value-of-information (VOI) analysis. This is appropriate, as geophysics is an expense and provides subsurface information — it does not produce oil!

New geophysical initiatives moving forward today include technologies that have succeeded elsewhere and appear to have application in Bay Marchand. Measuring amplitude variation at different angles of reflection (amplitude variation with offset, or AVO) provides another measure of earth properties that can reveal additional changes in stratigraphy and/or fluids. In 2006, a combined 3-D prestack data set was processed for advanced AVO analysis and is just now being evaluated. Initial results are promising, as yet further delineation and development prospects are emerging.

Finally, Bay Marchand holds at least one more deep secret. The field has been delineated, developed, and produced from sands on the top of the dome and on the flanks of the salt body, but there is also untested potential below the salt (Figure 14-10-46). As is the case with many salt bodies in the Gulf of Mexico, the Bay Marchand dome may hold reserves in traps that can only be visualized after depth migration, because imaging becomes confused below complex salt bodies. As of this writing, a merged 3-D prestack depth migration has been performed and the results are being evaluated (Figure 14-10-47).

Downloaded 25 Jun 2012 to 95.28.162.50. Redistribution subject to SEG license or copyright; Terms of Use: http://segdl.org/

Summary

Part of the reason why seismic data clearly add high value in the Bay Marchand field is a combination of geologic complexity, a large number of producing reservoirs, and the usually favorable rock physics. With hundreds of reservoirs and more than 1200 wells drilled, the chances of seeing good conditions for seismic response are high. It should not be expected that all reservoirs in the field or similar reservoirs worldwide will respond quite so well. Many of the reservoirs in Bay Marchand are difficult to image or do not have favorable acoustic characteristics. What is true, however, is that the majority of significant seismic technologies of the past 80 years have been successfully applied to the field. In every case the geophysical investment has been found to be worthwhile, and the impact on production and value creation have been directly measurable.

Bay Marchand is the field that has produced the most oil in the Gulf of Mexico for Chevron. It is also the field that has produced a great number of geophysical-technology advances. Geophysics supported the field discovery, delineation, and production. Perhaps more importantly, geophysics was directly involved in the revitalization of an extensively drilled and seemingly exhausted resource. Production decline was reversed and then sustained with seismic-technology advances in support of geologic interpretation and high-quality reservoir management. Bay Marchand stands out as an example of wise application of advanced technology to manage the hard-won subsurface assets of the petroleum industry. Every field deserves to be well operated, and seismic data can clearly play a role in that effort.

Acknowledgments

The authors wish to thank the management of Chevron North America Exploration and Production, and of Chevron Energy Technology Company, for permission to publish this work, and the management of WesternGeco and GX Technology for permission to show the seismic data. The authors also wish to thank the current and former members of the Bay Marchand Asset Team for their contributions to the development of this extraordinary field. Special thanks go to Abby Hymel, Torin Edwards, and Philip Richardson for their assistance in reviewing the paper and providing examples.

References

Abriel, W. L., P. S. Neale, J. S. Tissue, and R. M. Wright, 1991, Modern technology in an old area — Bay Marchand revisited: The Leading Edge, v. 10, no. 6, p. 21–35.

Behrens, R., P. Condon, W. Haworth, M. Bergeron, Z. Wang, and C. Ecker, 2001, 4-D seismic monitoring of water influx at Bay Marchand: The practical use of 4-D seismic in an imperfect world: SPE paper 71329.

Frey, M. G., and W. H. Grimes, 1970, Bay Marchand-Timbalier Bay-Caillou Island salt complex, Louisiana, *in* M. T. Halbouty, ed., Geology of giant petroleum fields: AAPG Memoir 14, p. 277–291.

Downloaded 25 Jun 2012 to 95.28.162.50. Redistribution subject to SEG license or copyright; Terms of Use: http://segdl.org/

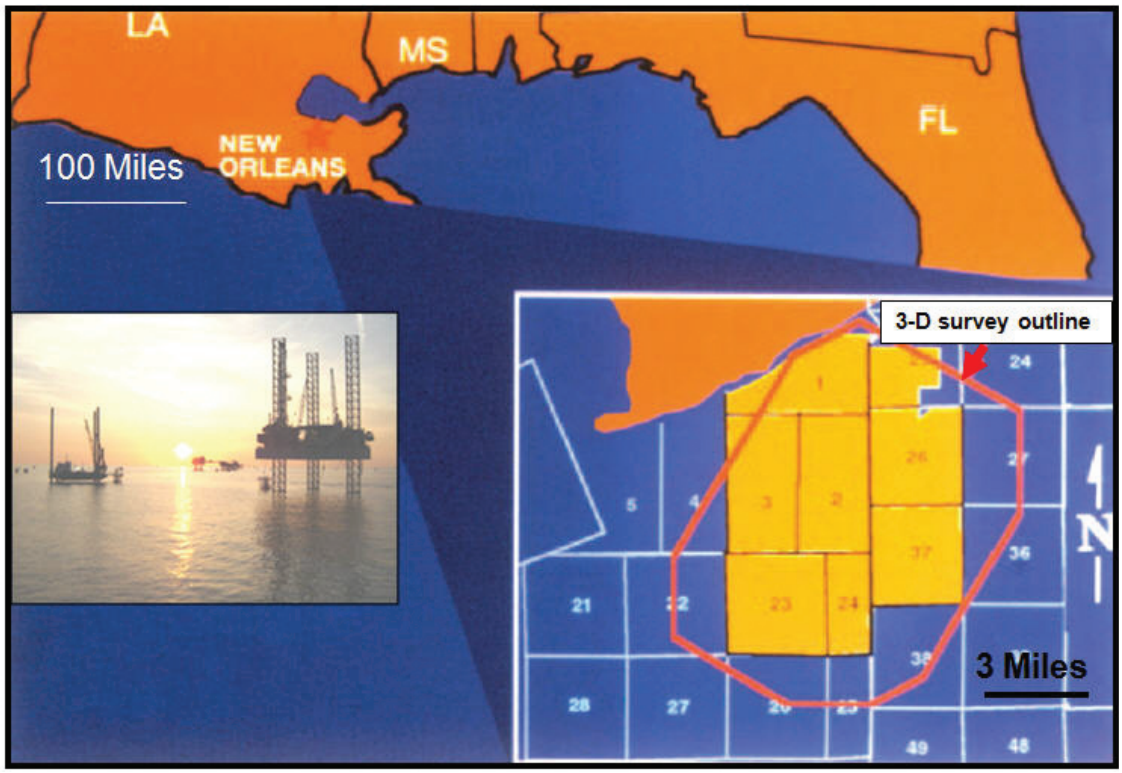

Fig. 14-10-1. The Bay Marchand field is located a few kilometers south of the Louisiana coast in the Gulf of Mexico.

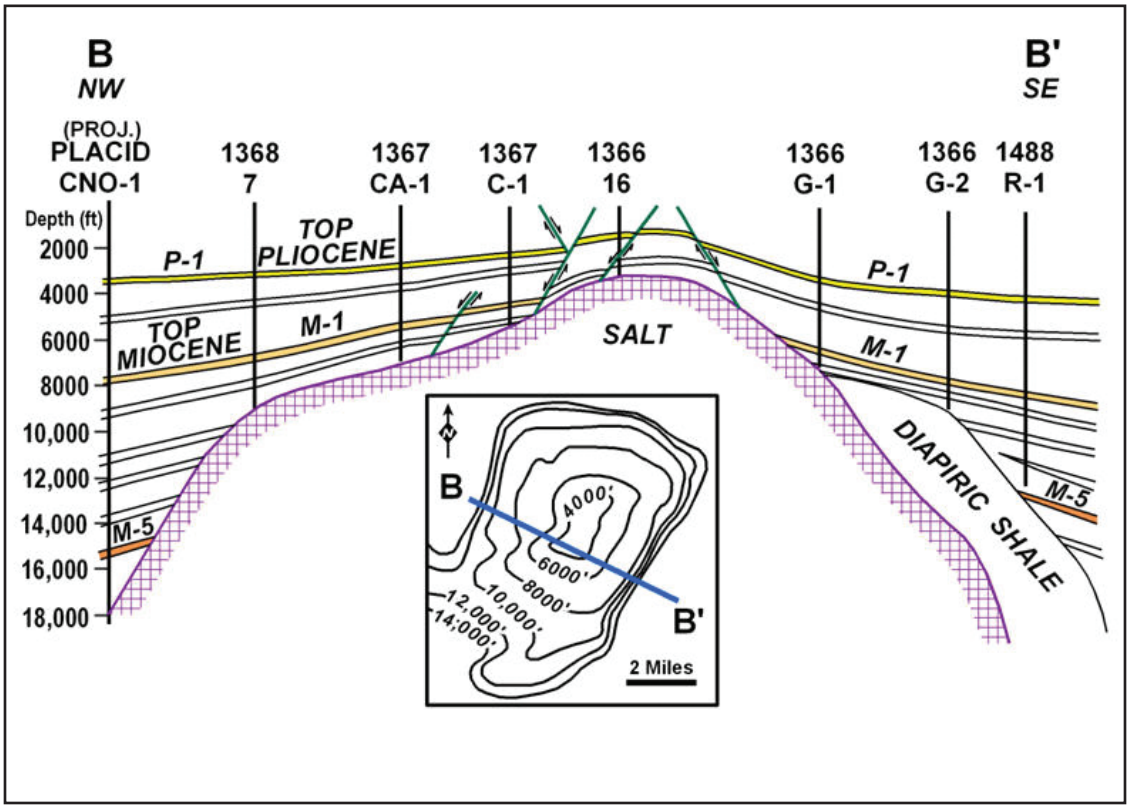

Fig. 14-10-2. A cross section of the Bay Marchand field. The field comprises many different accumulations of oil and gas in different types of traps. Most traps are combinations of structure and stratigraphy.

Downloaded 25 Jun 2012 to 95.28.162.50. Redistribution subject to SEG license or copyright; Terms of Use: http://segdl.org/

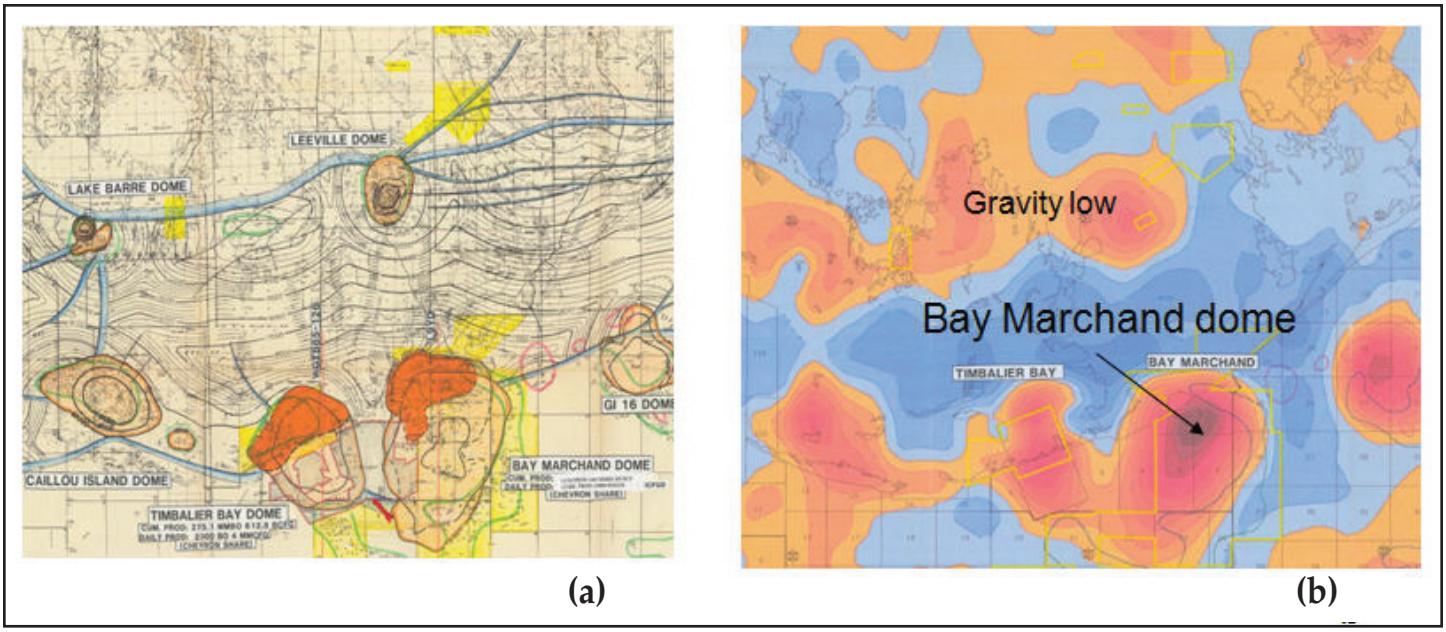

Fig. 14-10-3. The field lies in a structural trend characterized by deep- seated salt piercement domes (a). Early in the exploration phase, this structural trend was recognized from gravity data (b).

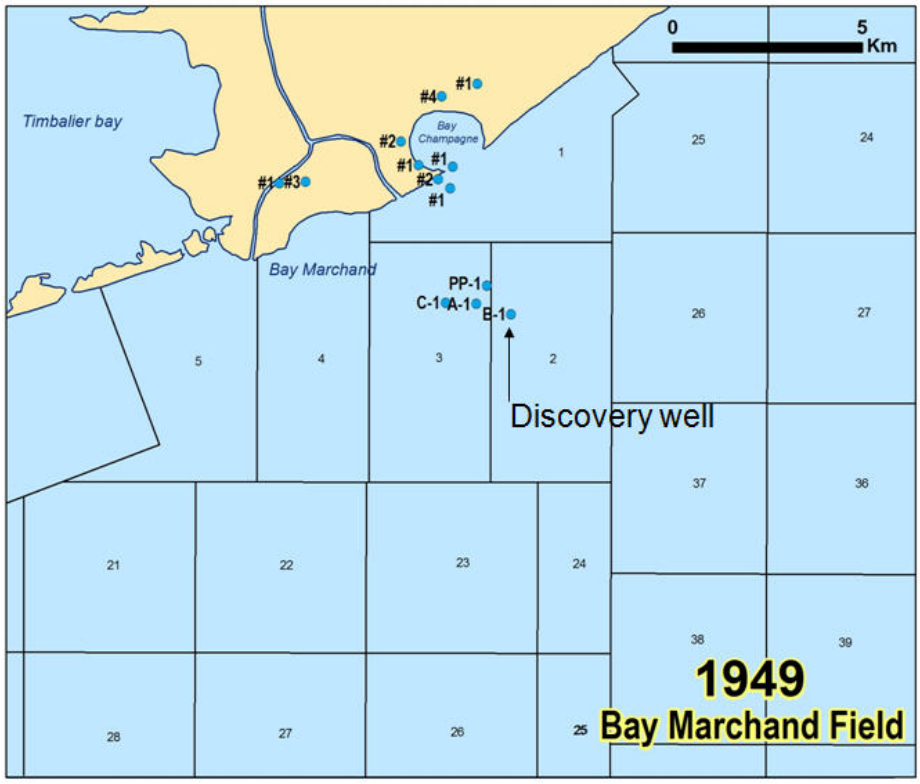

Fig. 14-10-4. The discovery in 1949 was preceded by twelve unsuccessful exploratory wells.

Downloaded 25 Jun 2012 to 95.28.162.50. Redistribution subject to SEG license or copyright; Terms of Use: http://segdl.org/

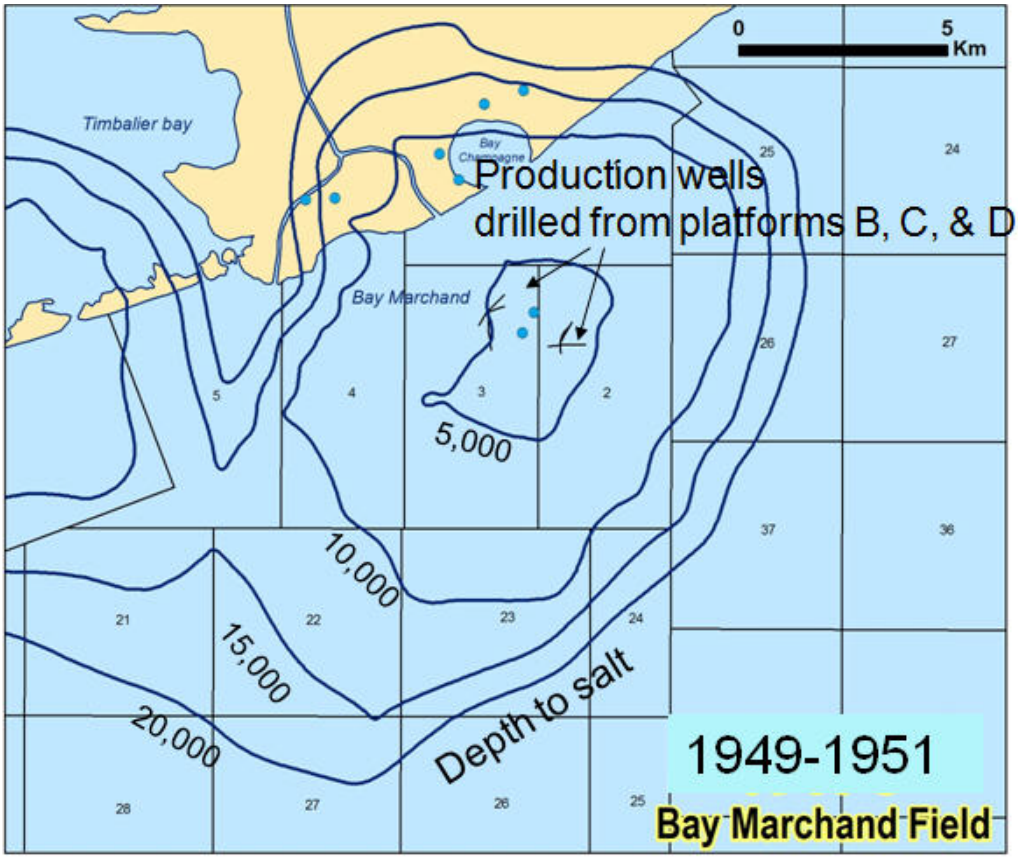

Fig. 14-10-5. Immediately after the discovery, three platforms were installed over the center of the salt dome. Directional wells were drilled from the platforms to develop and produce the discovered oil and gas.

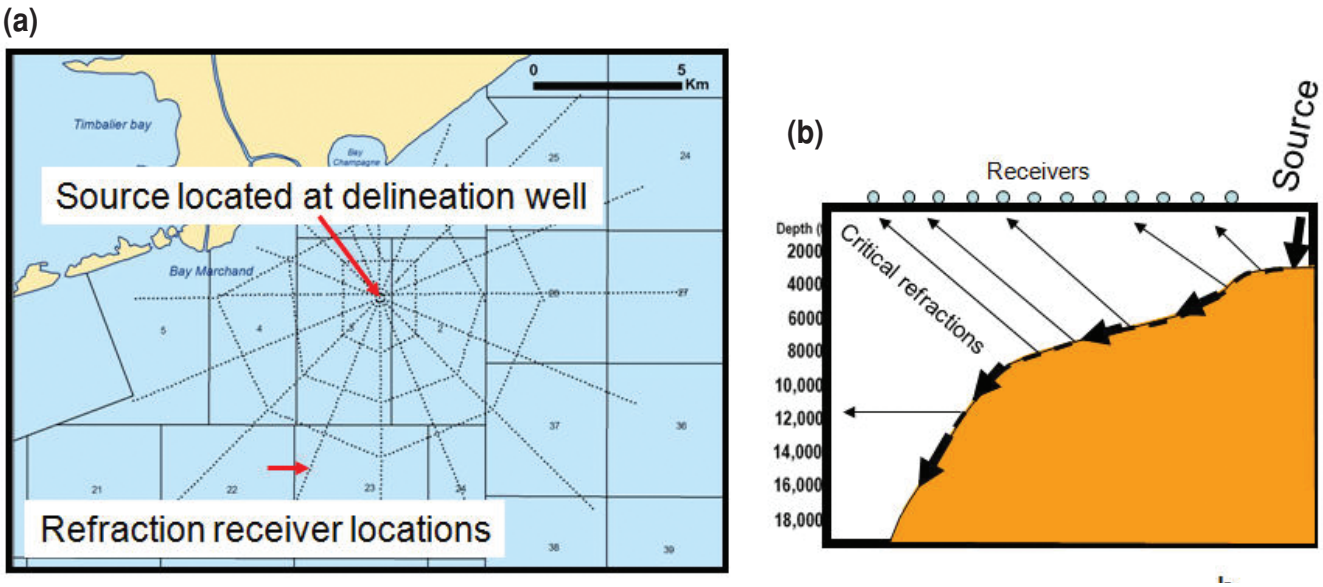

Fig. 14-10-6. Immediately after discovery, the depth and extent of the salt dome were confirmed by refraction seismic data. An exploration well was used as a source location at the center, and receivers were placed on the ocean floor in a spoke and wheel pattern (a). The time recordings of the refracted waves from the salt surface were used to map the location of the dome (b).

Downloaded 25 Jun 2012 to 95.28.162.50. Redistribution subject to SEG license or copyright; Terms of Use: http://segdl.org/

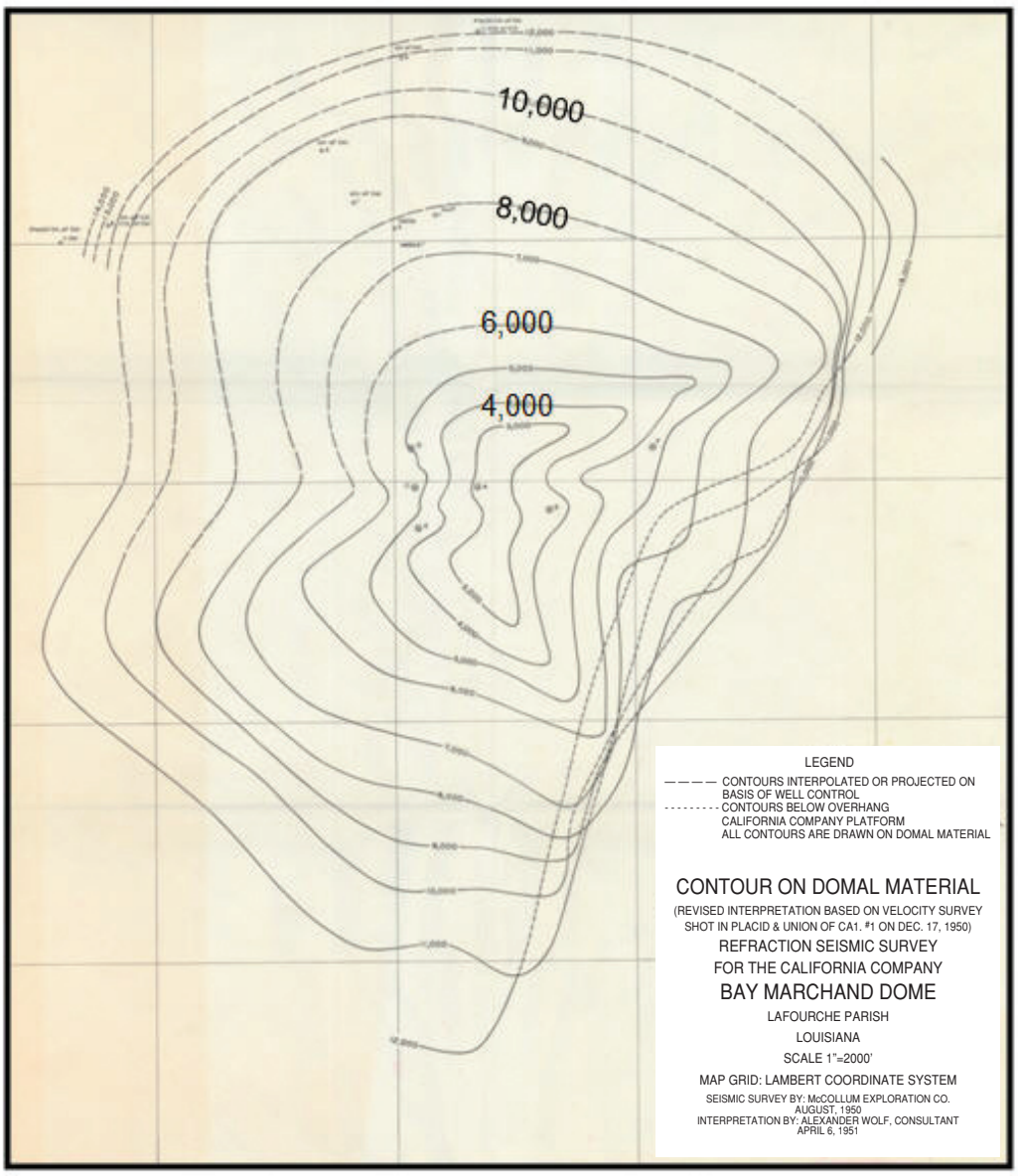

Fig. 14-10-7. Structure of top salt from the detailed refraction survey of 1950. The accuracy of this map has been confirmed after more than fifty years of drilling and hundreds of well penetrations. A salt overhang on the east flank was correctly recognized and was confirmed in later years with reflection seismic data.

Downloaded 25 Jun 2012 to 95.28.162.50. Redistribution subject to SEG license or copyright; Terms of Use: http://segdl.org/

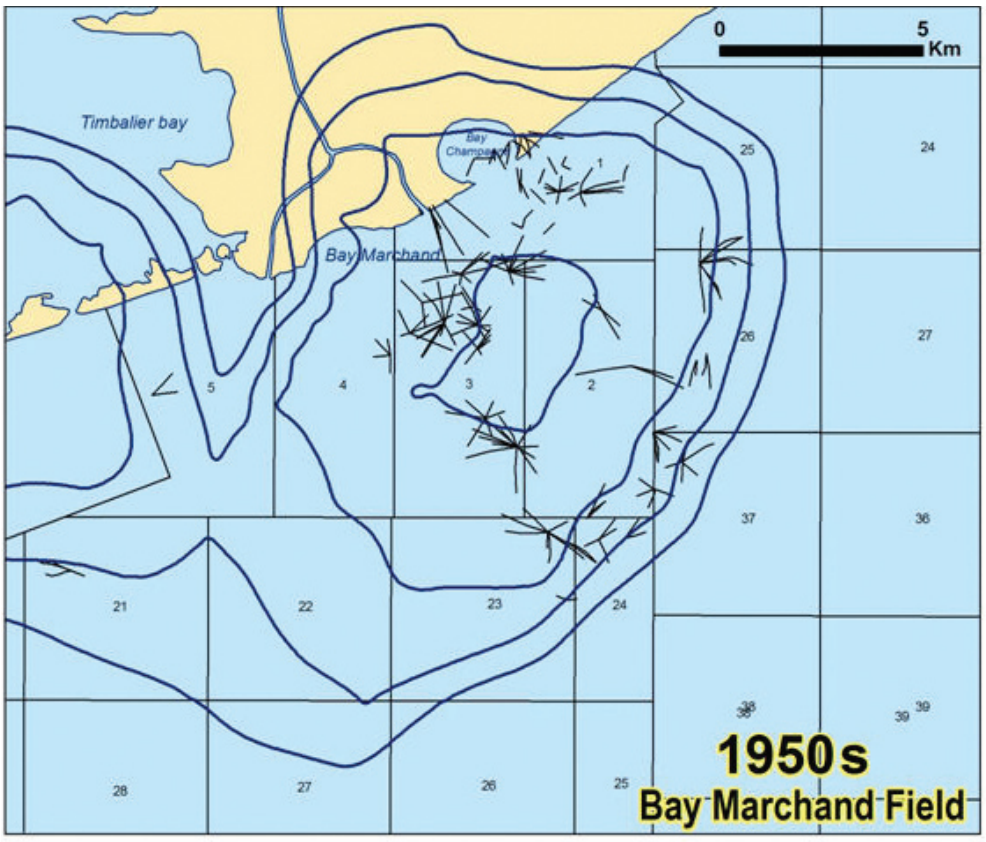

Fig. 14-10-8. During the 1950s, many platforms were installed northwest and southeast of the center of the dome. A large number of structural and stratigraphic accumulations were developed.

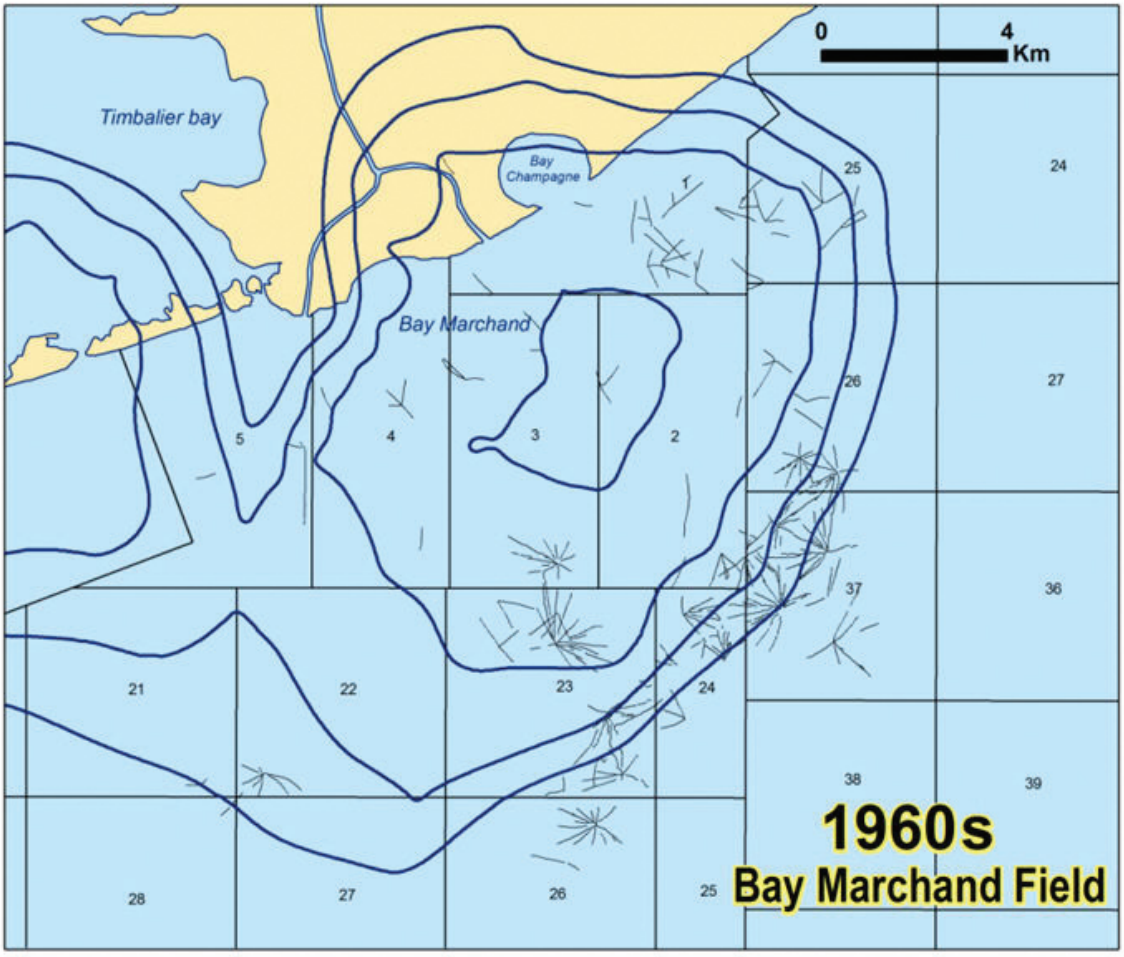

Fig. 14-10-9. During the 1960s, further development proceeded down the flank of the dome.

Downloaded 25 Jun 2012 to 95.28.162.50. Redistribution subject to SEG license or copyright; Terms of Use: http://segdl.org/

Fig. 14-10-10. The daily production of the field reached more than 80,000 barrels of oil per day in the 1960s. During the next decade, in the 1970s, daily production went into significant decline.

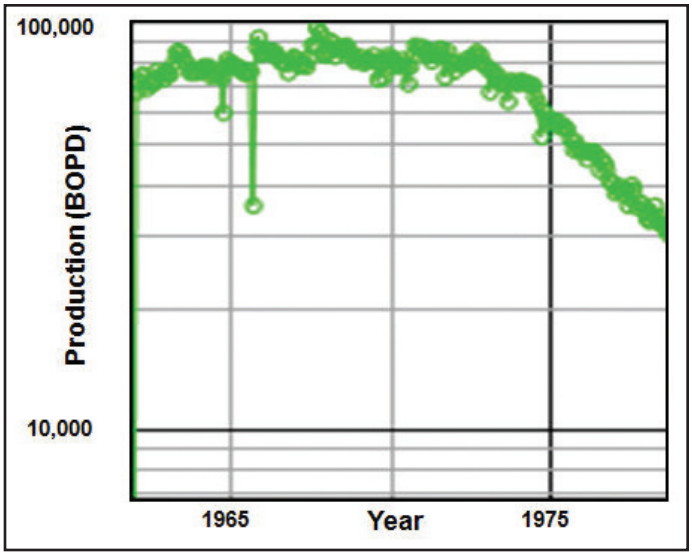

Fig. 14-10-11. Reflection seismic data and digital processing in the 1970s offered a substantial technological breakthrough. Using this type of data, it was possible to accurately interpolate structure between wells on the seismic profiles. In addition, reflection patterns and amplitudes were used to predict stratigraphic trends.

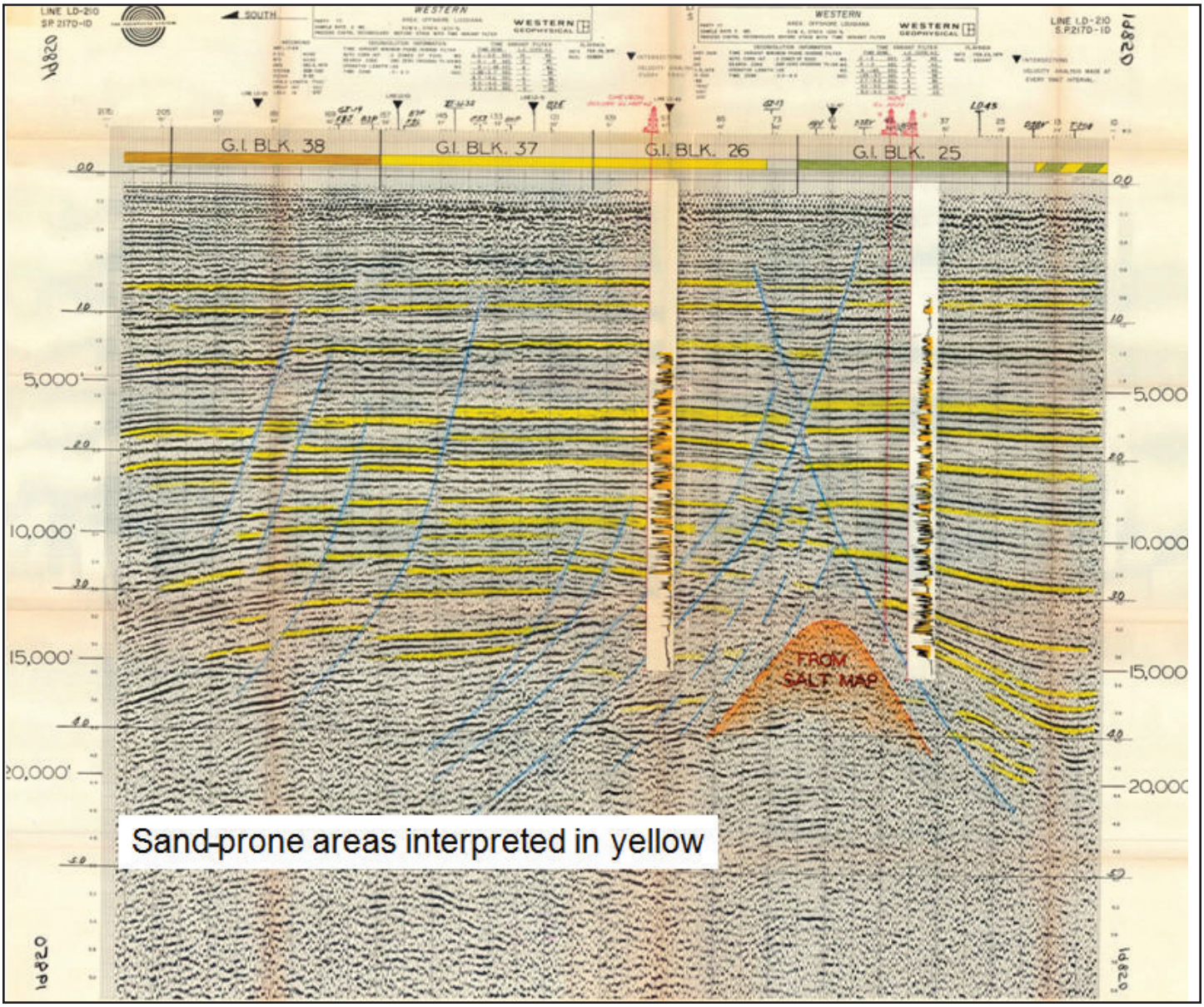

Downloaded 25 Jun 2012 to 95.28.162.50. Redistribution subject to SEG license or copyright; Terms of Use: http://segdl.org/

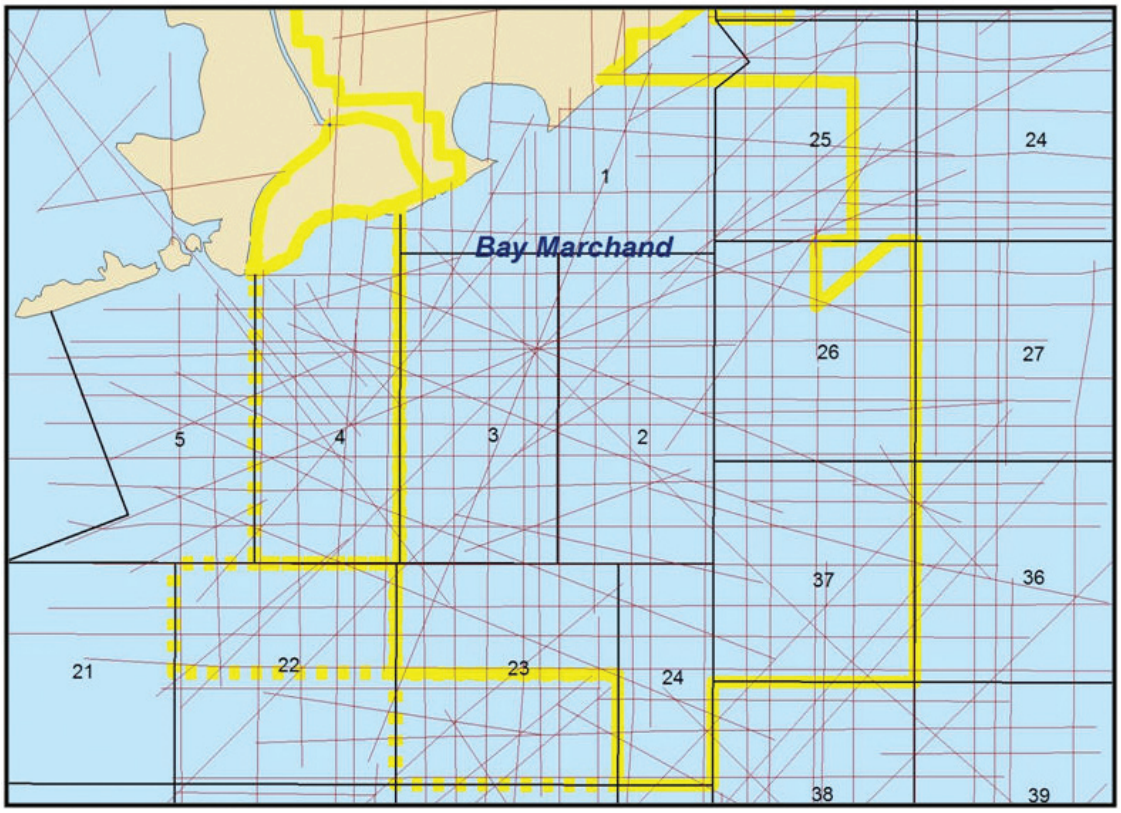

Fig. 14-10-12. In the 1970s, 2-D seismic reflection data were acquired on an approximately 500-m spacing, to support development and production of the field.

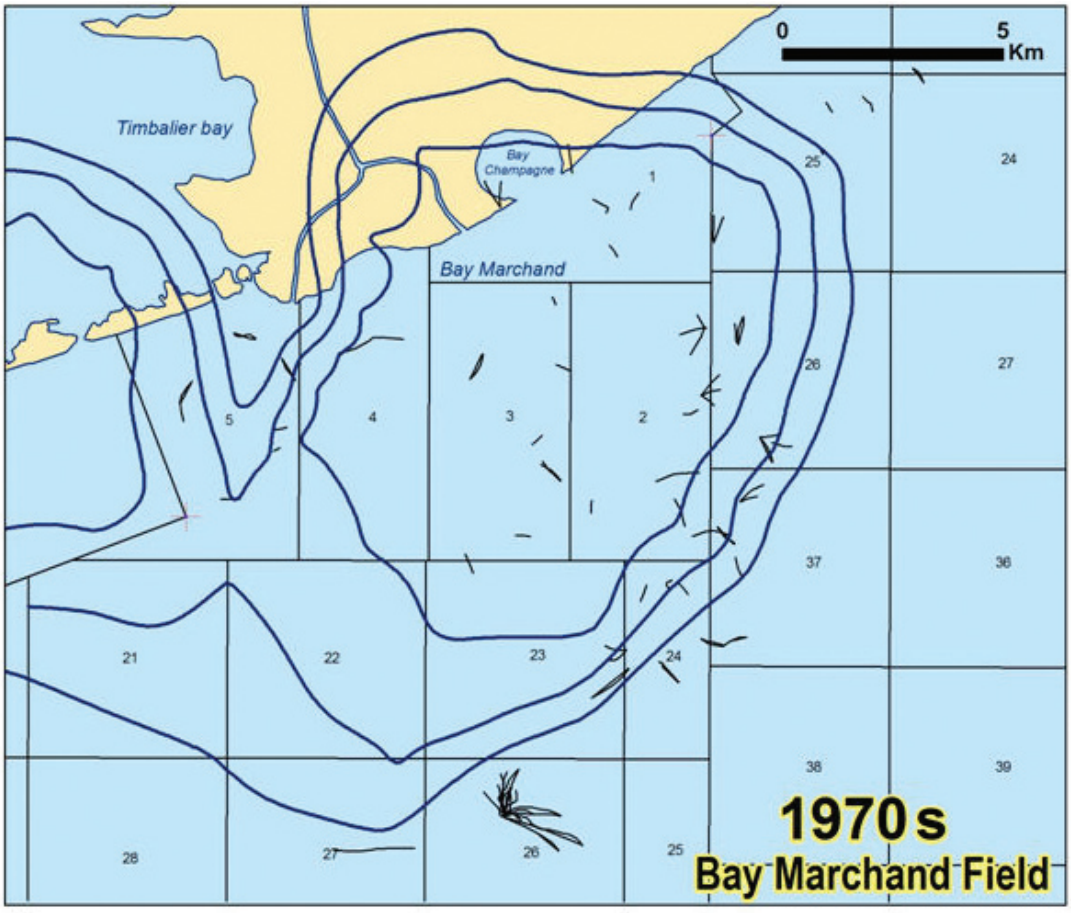

Fig. 14-10-13. 2-D seismic reflection data were used to support specific infill development wells and waterflood projects.

Downloaded 25 Jun 2012 to 95.28.162.50. Redistribution subject to SEG license or copyright; Terms of Use: http://segdl.org/

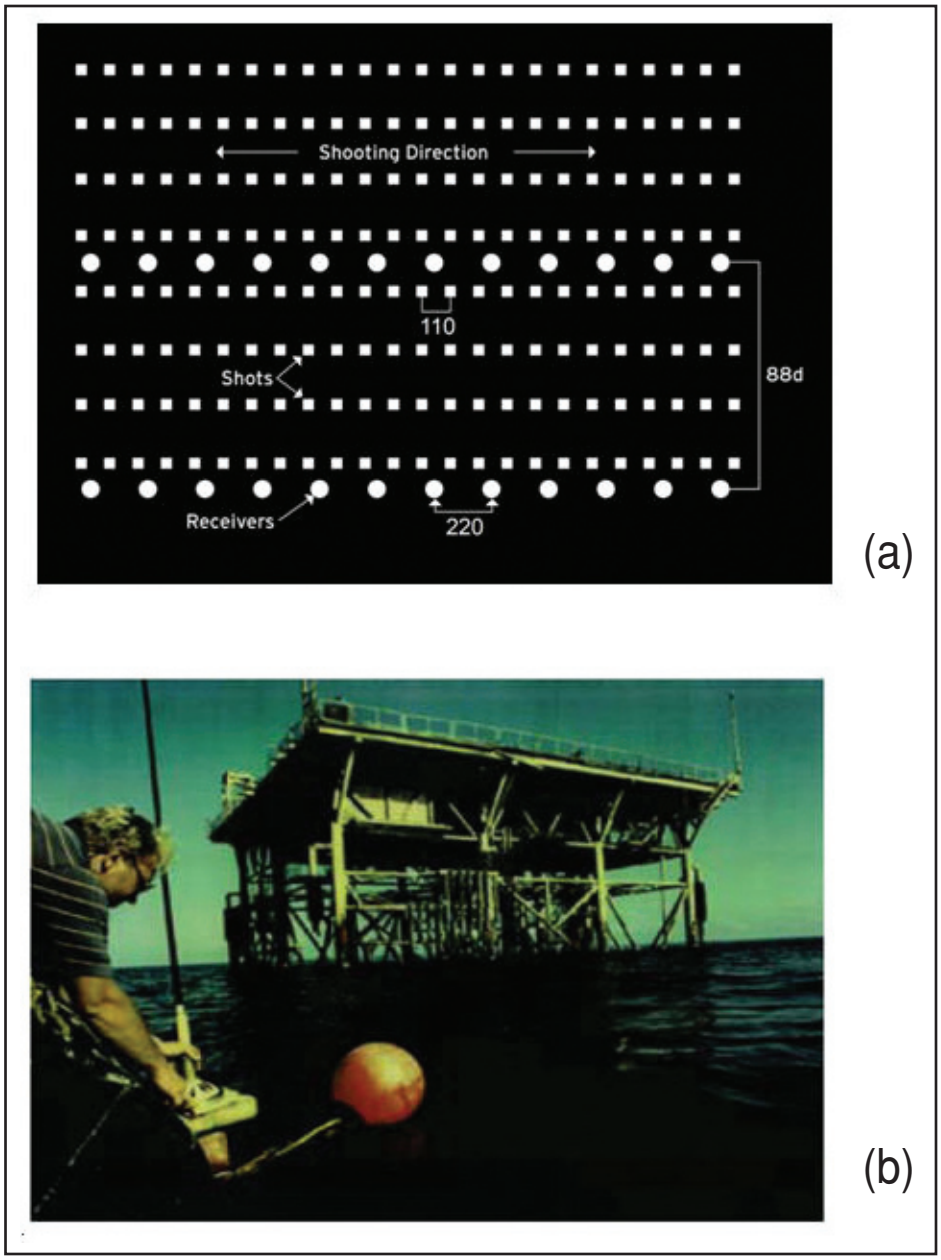

Fig. 14-10-14. In 1986, a 3-D seismic survey was conducted to cover the field for development and production support. Individual receivers were placed on the ocean floor at 220-foot intervals in two lines spaced 880 feet apart (a). Airgun sources were fired at 110-foot intervals along line. When it was not possible to position the source boat at the planned surface location, due to production facilities, placement of sources and receivers was switched (b). The acquisition of the data provided perfect coverage for every subsurface point in the field.

Downloaded 25 Jun 2012 to 95.28.162.50. Redistribution subject to SEG license or copyright; Terms of Use: http://segdl.org/

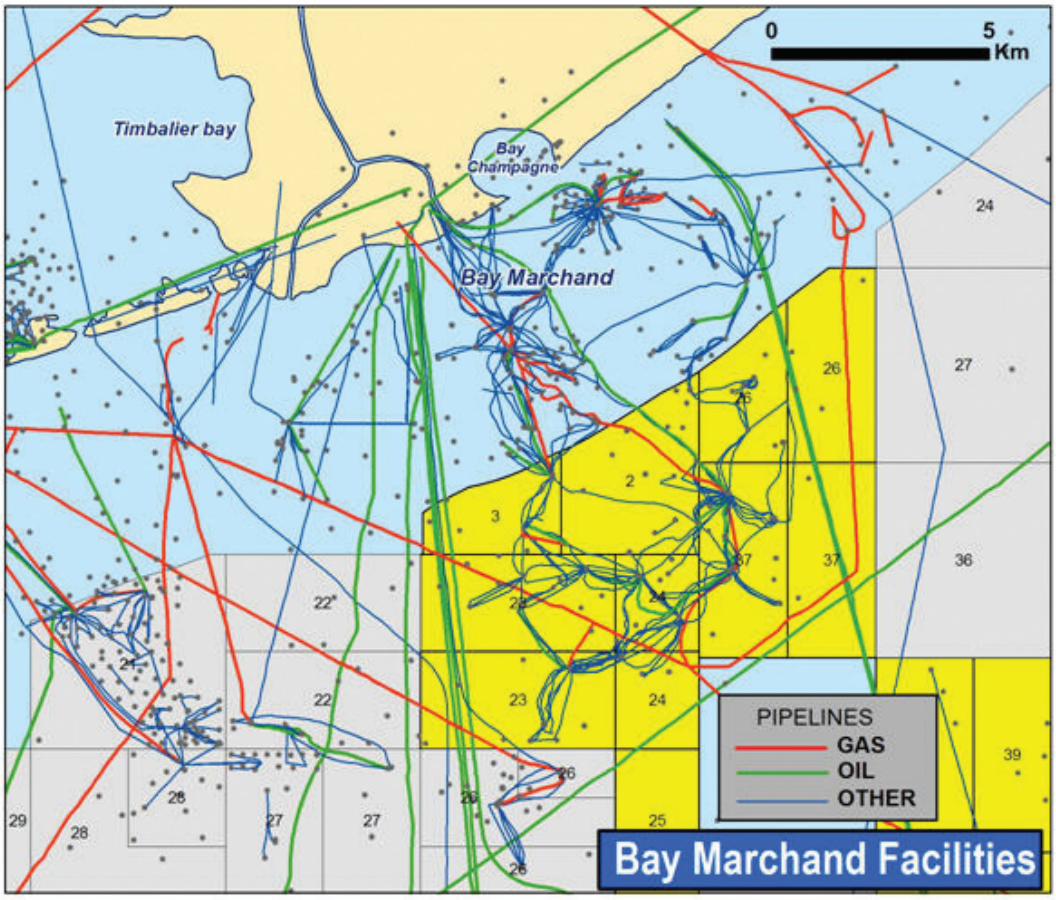

Fig. 14-10-15. Acquisition of the 3-D data was complicated by numerous surface obstacles, which included over 100 platforms, two major transport pipeline systems, collection and distribution pipelines, and high-voltage power systems. Operation of the oil field was not interrupted and no damage was sustained.

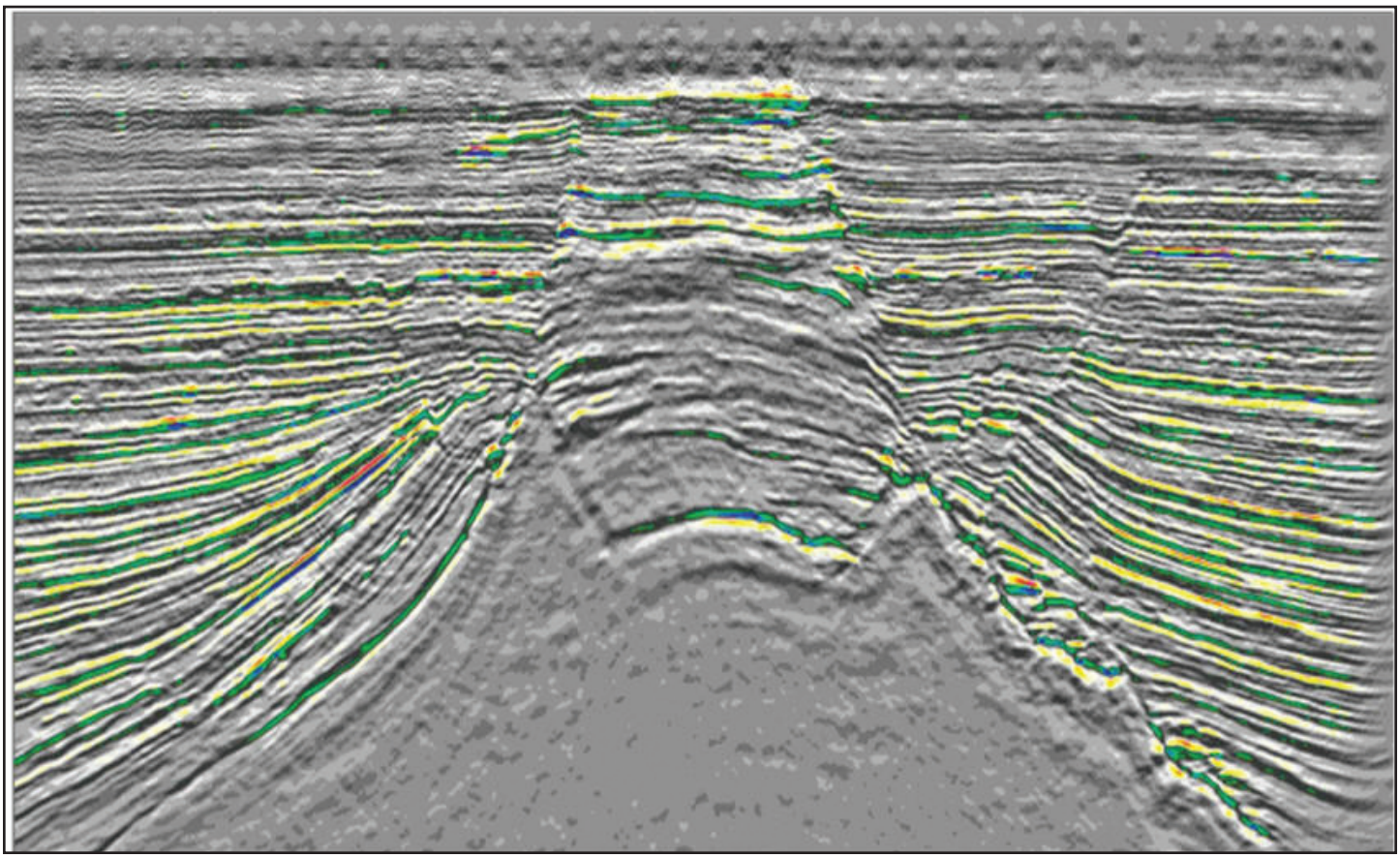

Fig. 14-10-16. East-west seismic cross section from the 3-D data. Faults interact with the salt dome to produce sharp interfaces. Oil and gas are located in numerous structural traps against faults. Numerous stratigraphic traps are also located on the flanks of the dome.

Downloaded 25 Jun 2012 to 95.28.162.50. Redistribution subject to SEG license or copyright; Terms of Use: http://segdl.org/

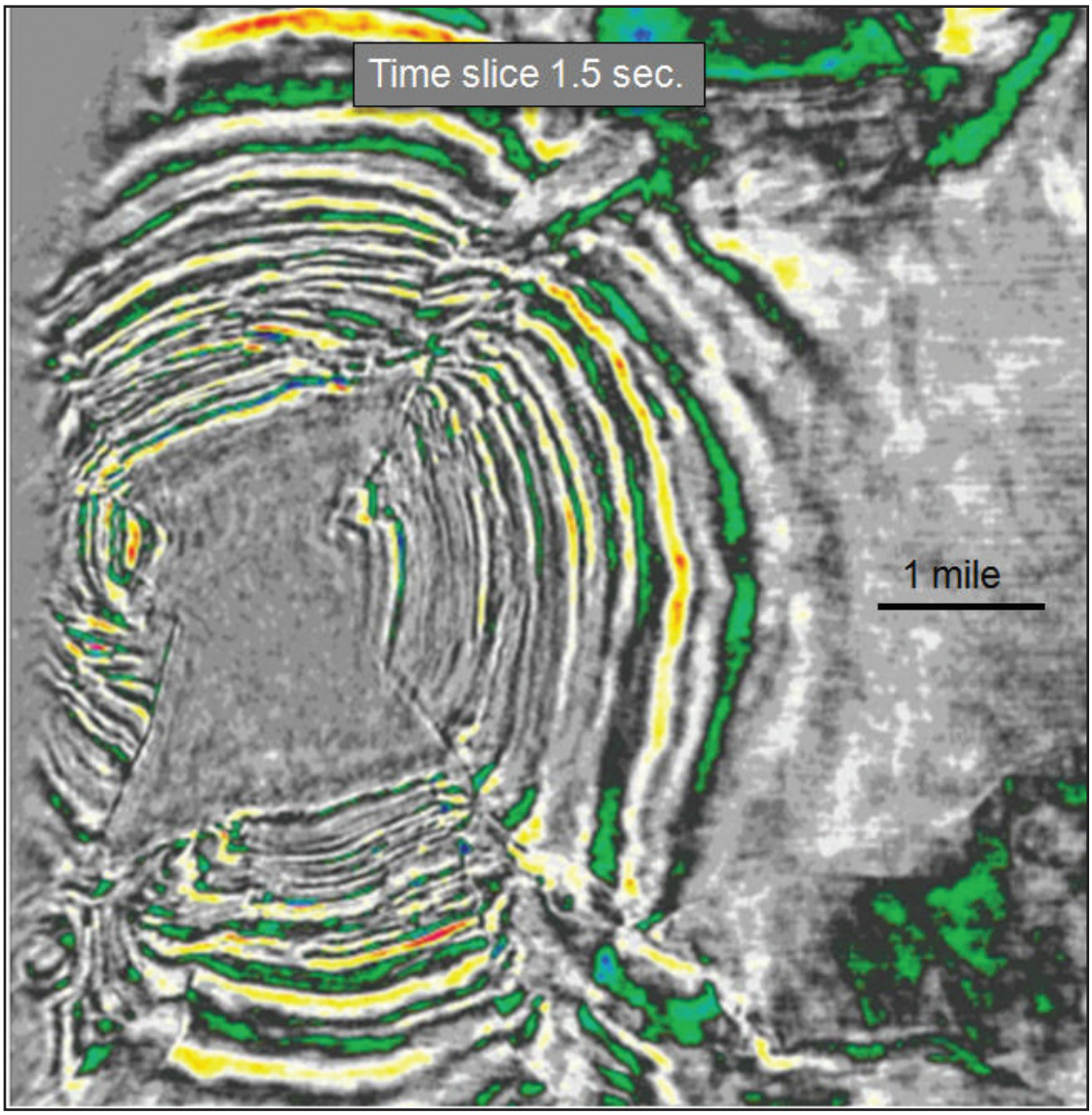

Fig. 14-10-17. A time slice of the 3-D seismic data shows the angular nature of the faults interacting with the salt-producing sharp corners.

Downloaded 25 Jun 2012 to 95.28.162.50. Redistribution subject to SEG license or copyright; Terms of Use: http://segdl.org/

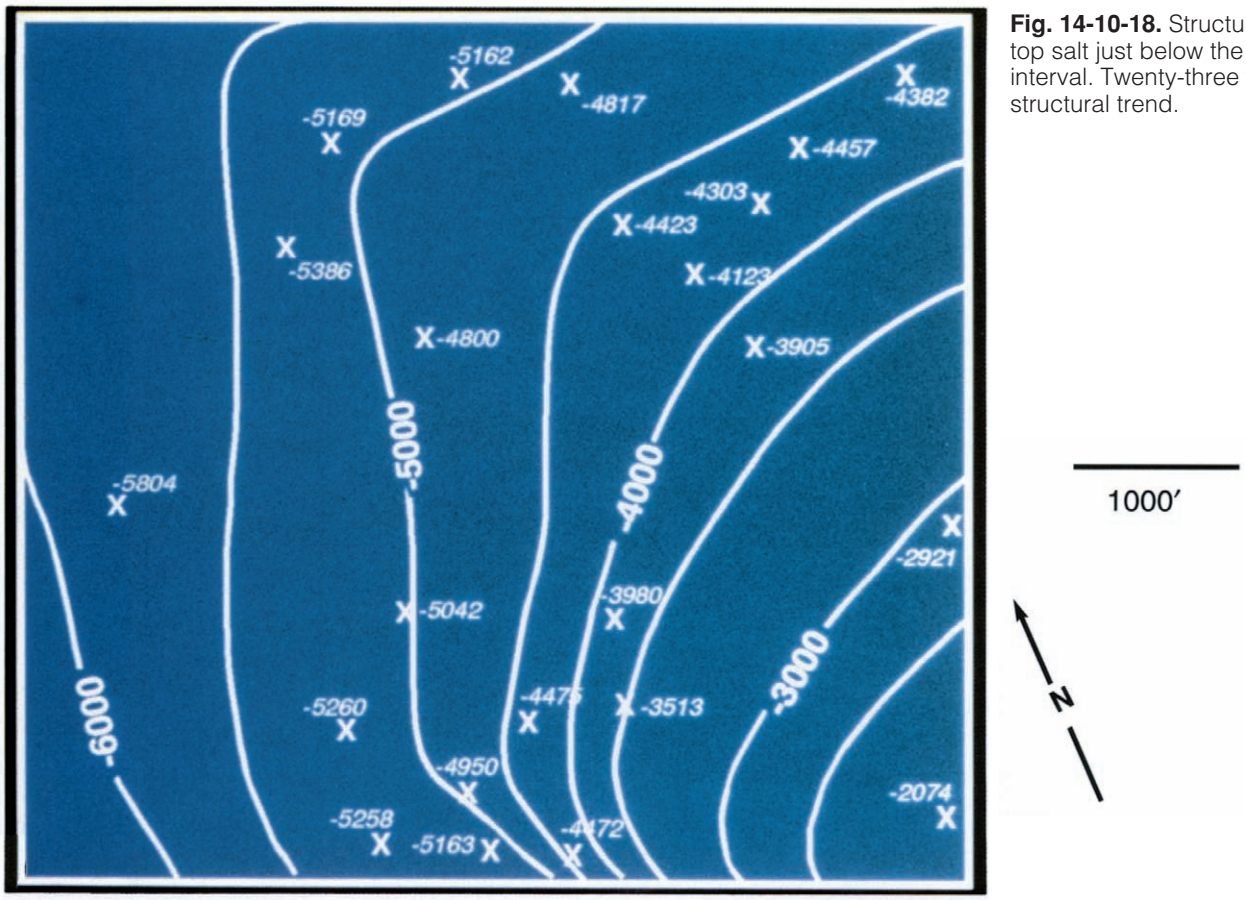

Fig. 14-10-18. Structure map of the top salt just below the major producing interval. Twenty-three wells establish the structural trend.

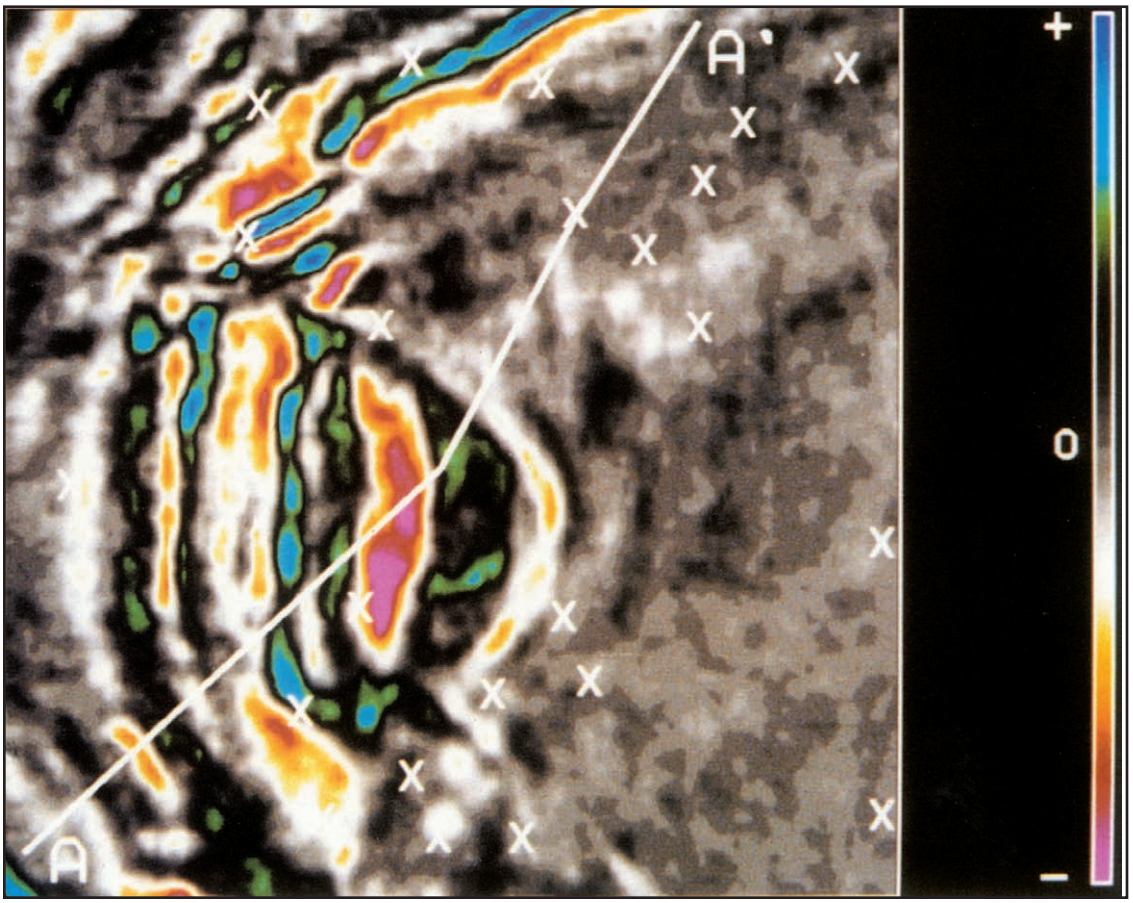

Fig. 14-10-19. Time slice of the 3-D survey at 1.5 seconds over area of Figure 14-10-18. Note the embayment in the center of the figure. This was not recognized from the structural analysis using well data.

Downloaded 25 Jun 2012 to 95.28.162.50. Redistribution subject to SEG license or copyright; Terms of Use: http://segdl.org/

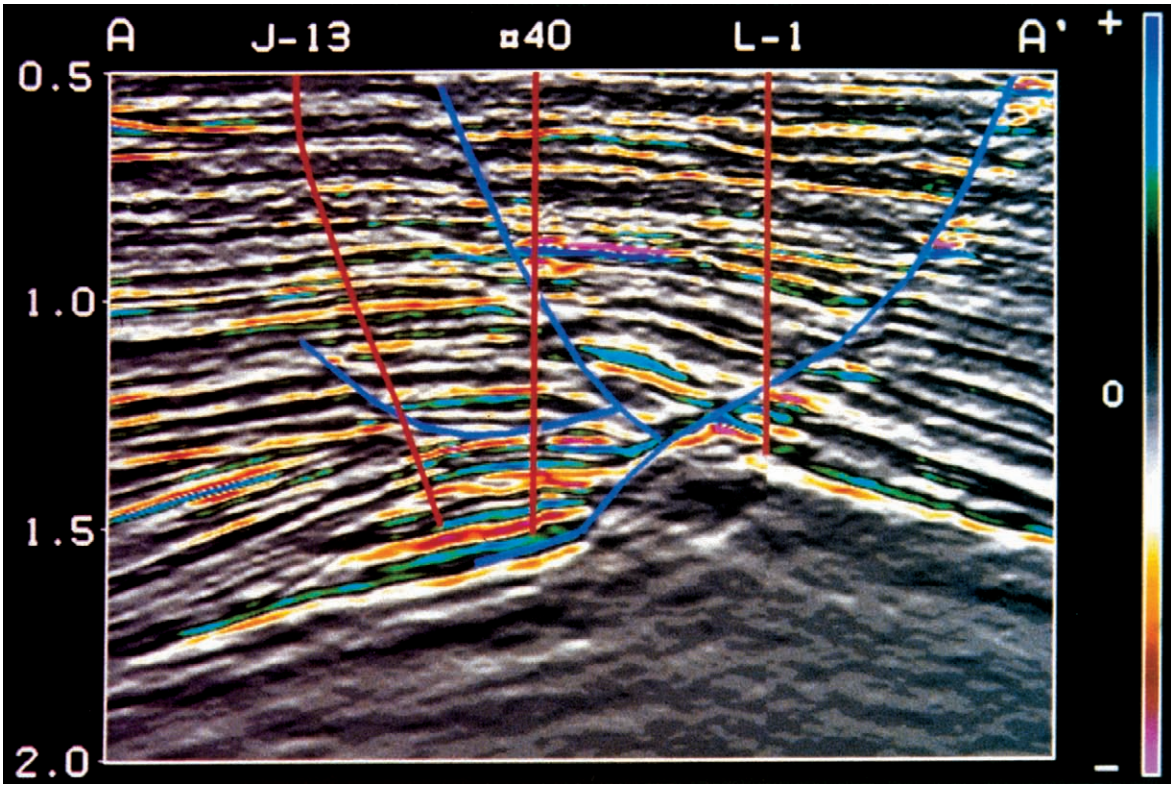

Fig. 14-10-20. Seismic arbitrary line A-A' as indicated on Figure 14-10-19. Structural analysis from well correlation of J-13 and L-1 was not sufficient to identify the potential of reservoirs between them. Well 40 was proposed as an infill opportunity.

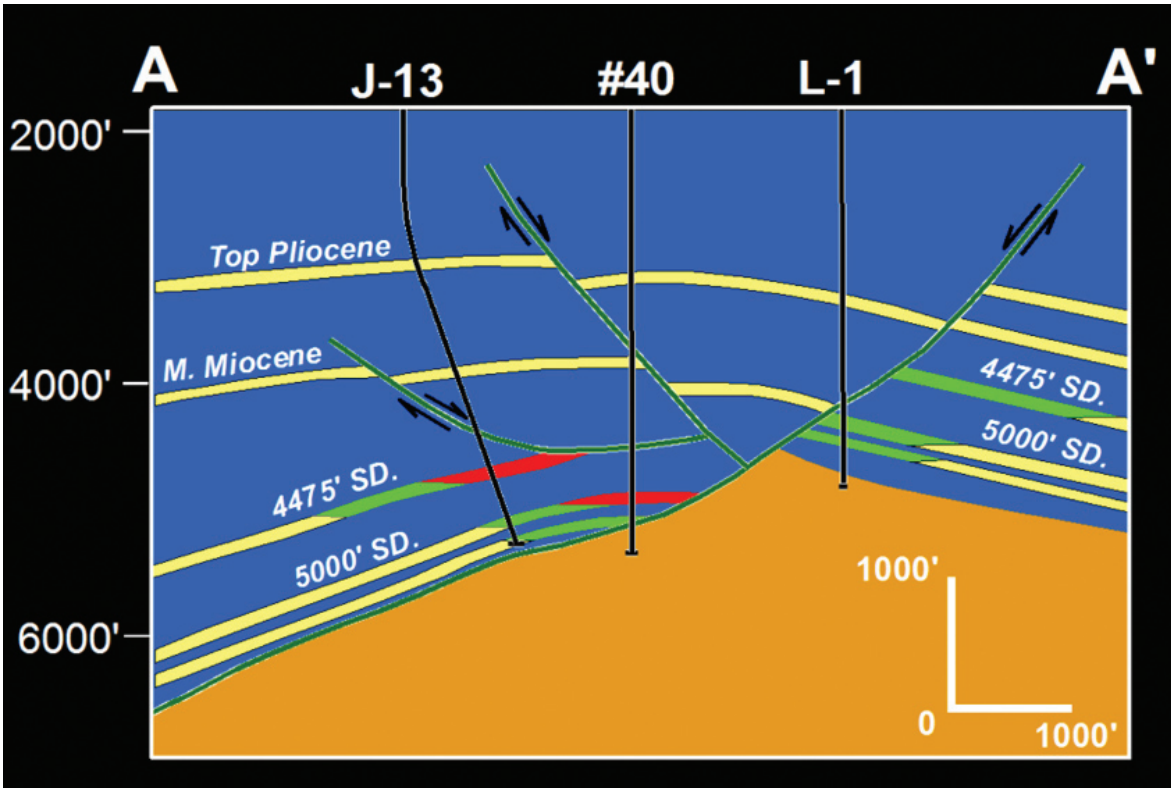

Fig. 14-10-21. The structural cross section of A-A' shows the results of the drilling of infill well 40 and the discovery of new reserves.

Downloaded 25 Jun 2012 to 95.28.162.50. Redistribution subject to SEG license or copyright; Terms of Use: http://segdl.org/

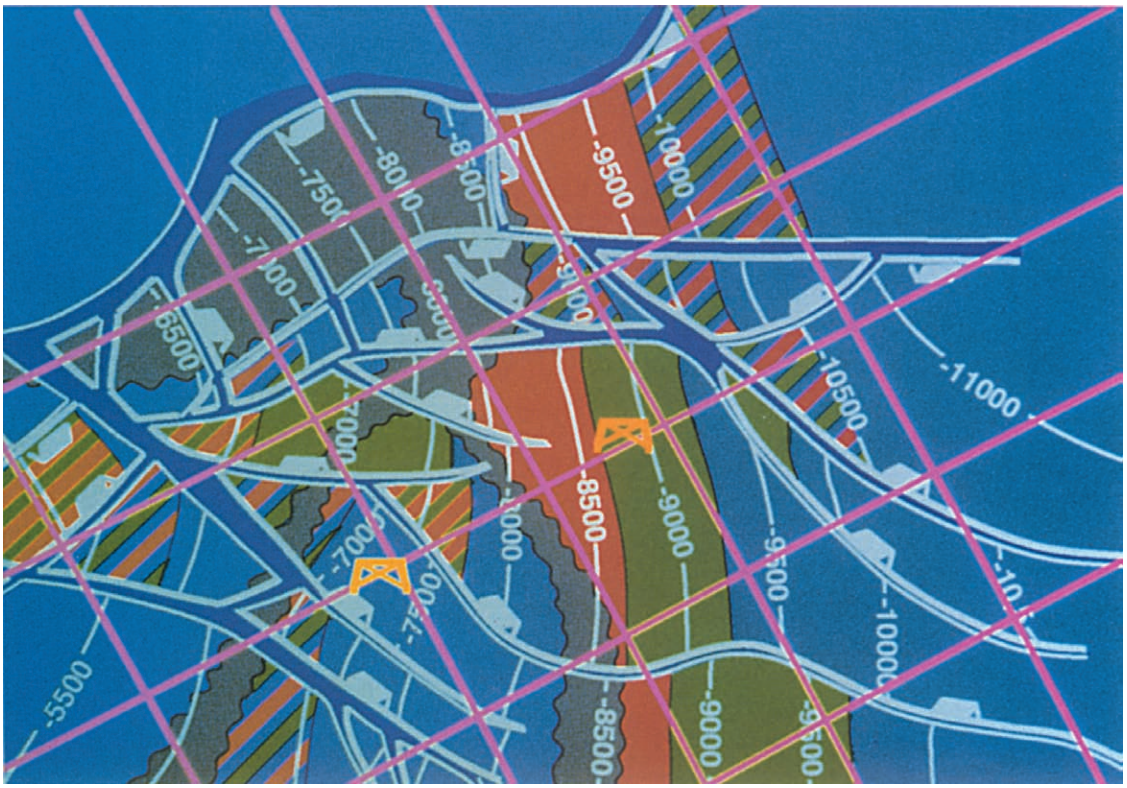

Fig. 14-10-22. Oil and gas map of the 8200 sand. The structural and fluid interpretation is controlled by a 2-D seismic grid, 40 well penetrations, production samples, and pressure measurements.

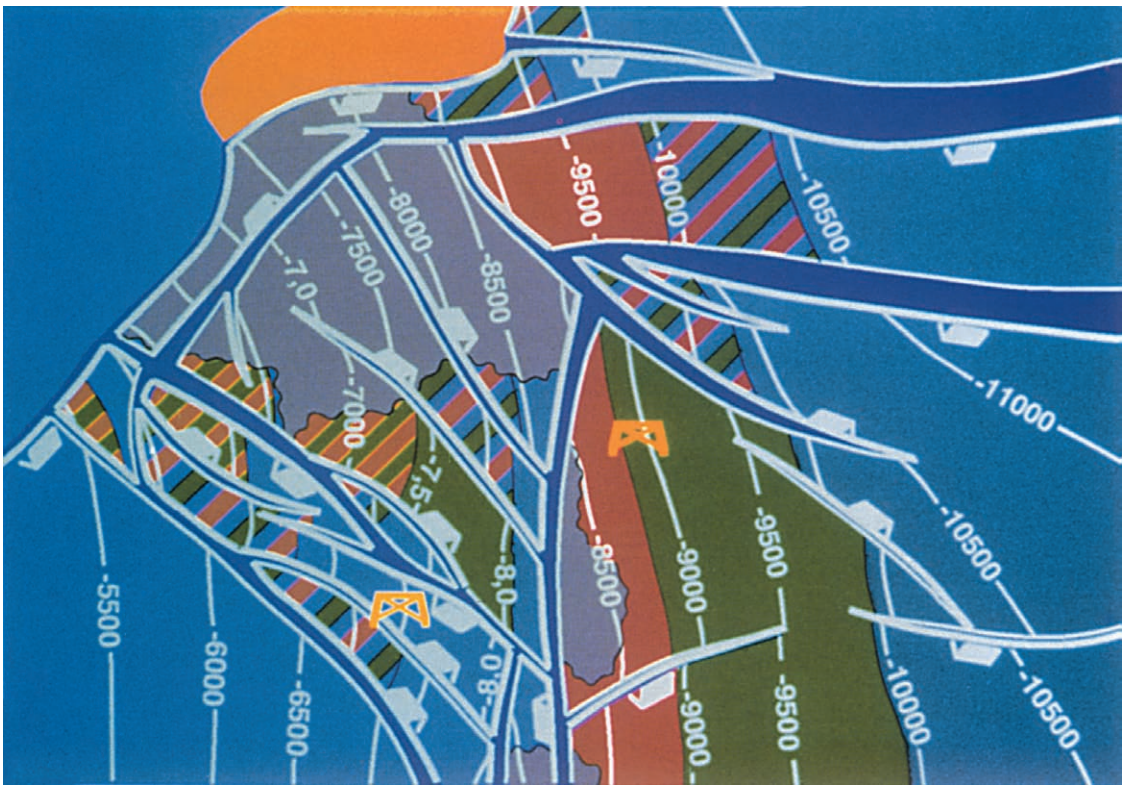

Fig. 14-10-23. Reinterpretation of the same area using the same well information but also using 3-D seismic data. Note the change in the faults and location of fluid compartments.

Downloaded 25 Jun 2012 to 95.28.162.50. Redistribution subject to SEG license or copyright; Terms of Use: http://segdl.org/

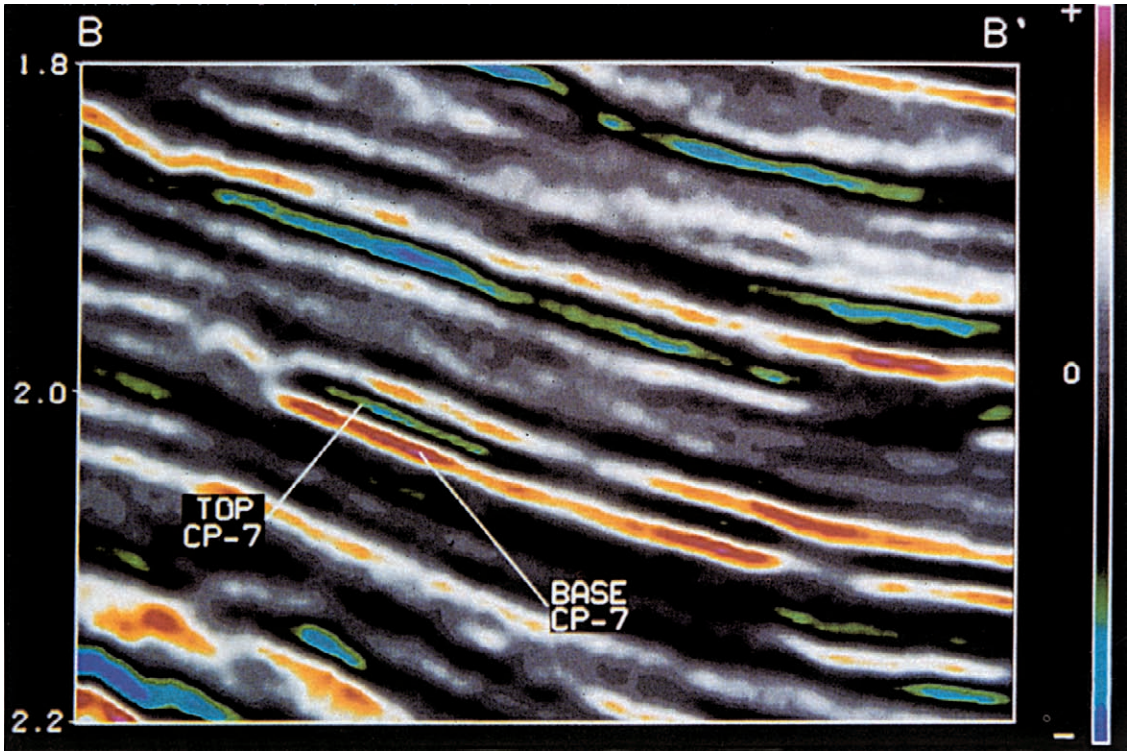

Fig. 14-10-24. Seismic cross section from the 3-D data, showing the location of the top and bottom of the CP-7 sandstone reservoir.

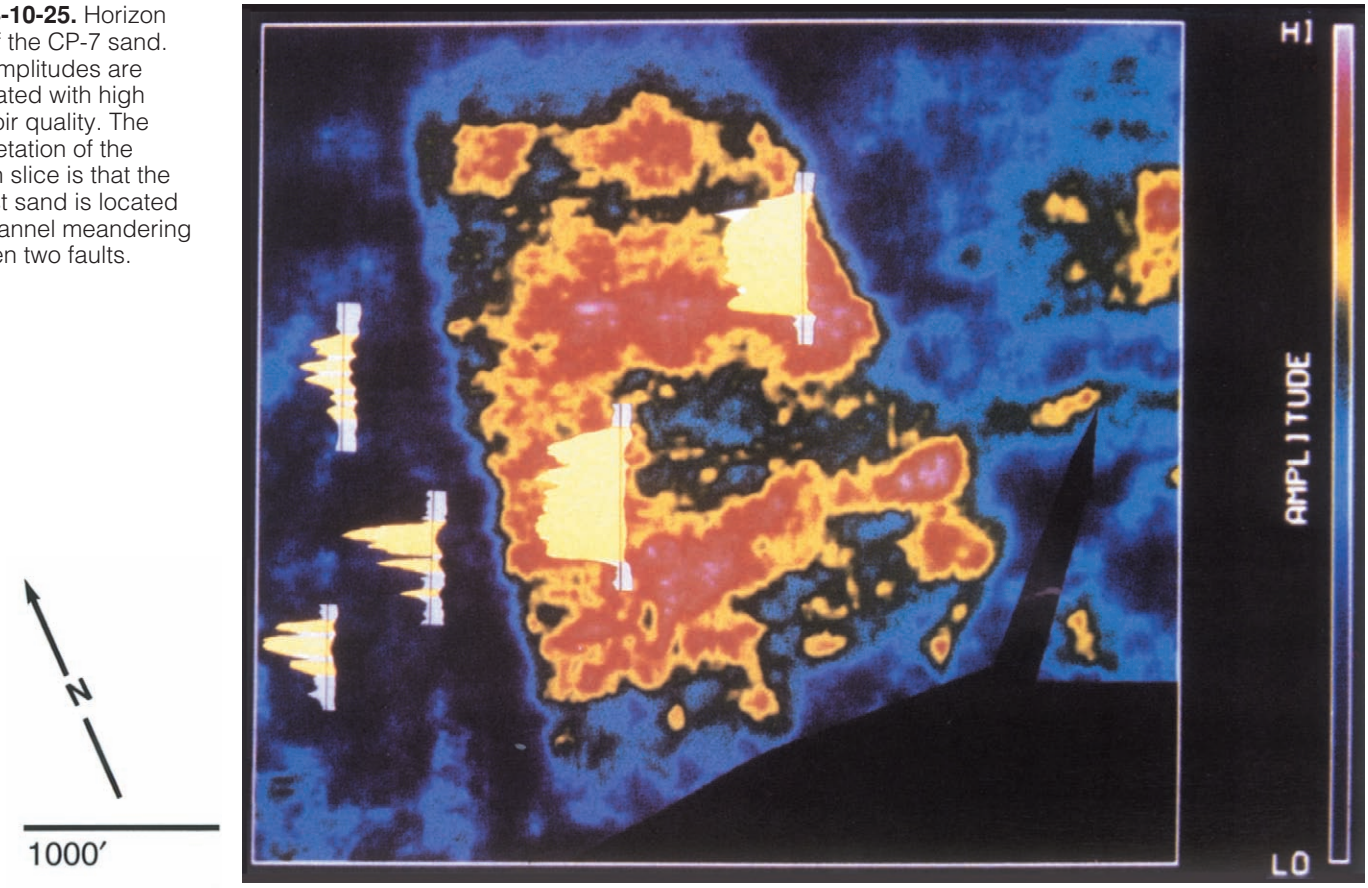

Fig. 14-10-25. Horizon slice of the CP-7 sand. High amplitudes are associated with high reservoir quality. The interpretation of the horizon slice is that the thickest sand is located in a channel meandering between two faults.

Downloaded 25 Jun 2012 to 95.28.162.50. Redistribution subject to SEG license or copyright; Terms of Use: http://segdl.org/

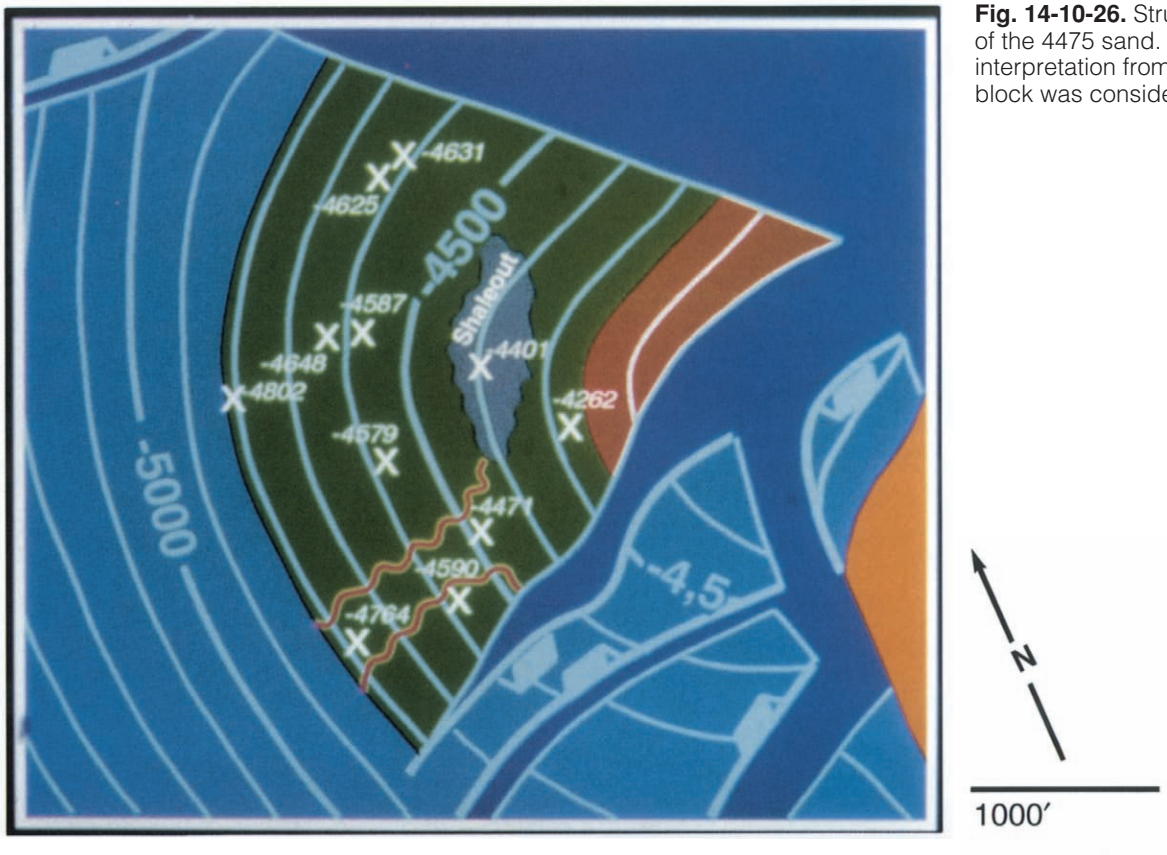

Fig. 14-10-26. Structure and fluid map of the 4475 sand. Prior to the new interpretation from the 3-D survey, the fault block was considered depleted.

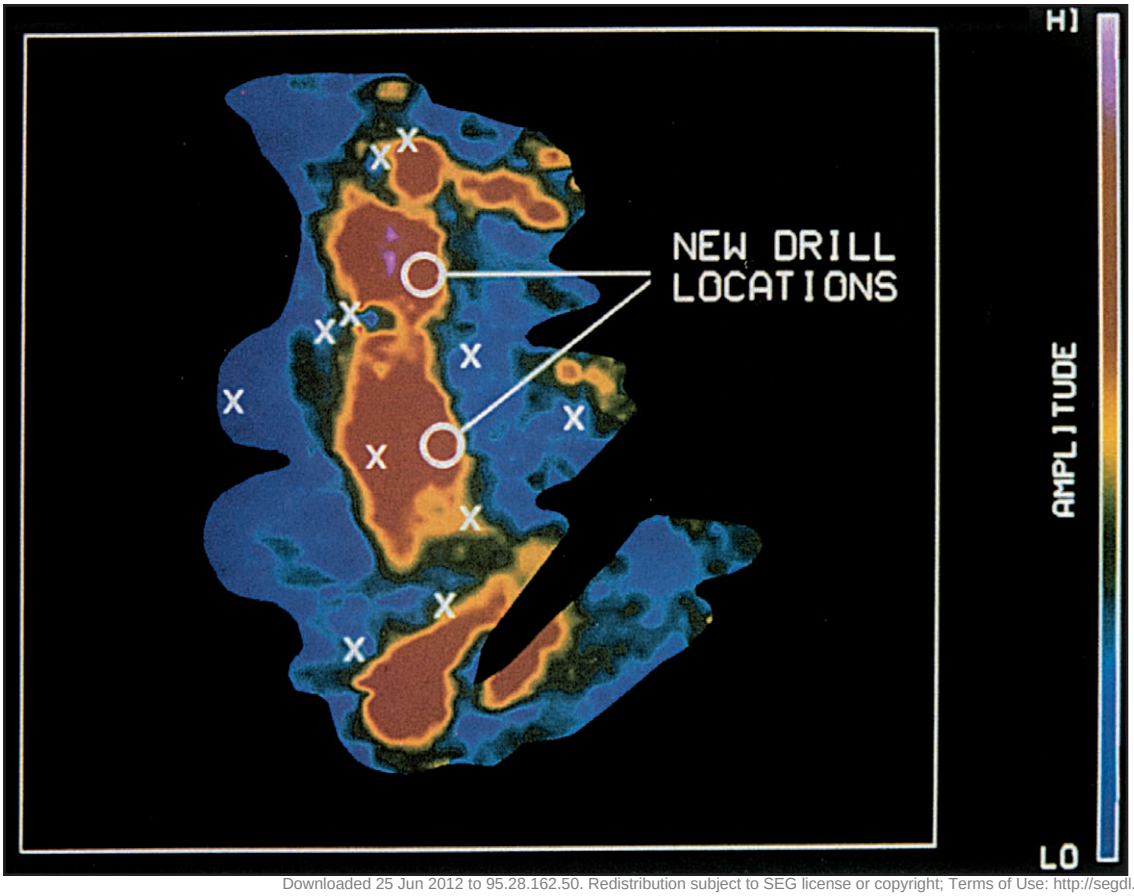

Fig. 14-10-27. Horizon slice of the producing 4475 sand. High-amplitude (red) seismic response was interpreted to be bypassed oil. New infill wells were drilled and successfully put into production.

Downloaded 25 Jun 2012 to 95.28.162.50. Redistribution subject to SEG license or copyright; Terms of Use: http://segdl.org/

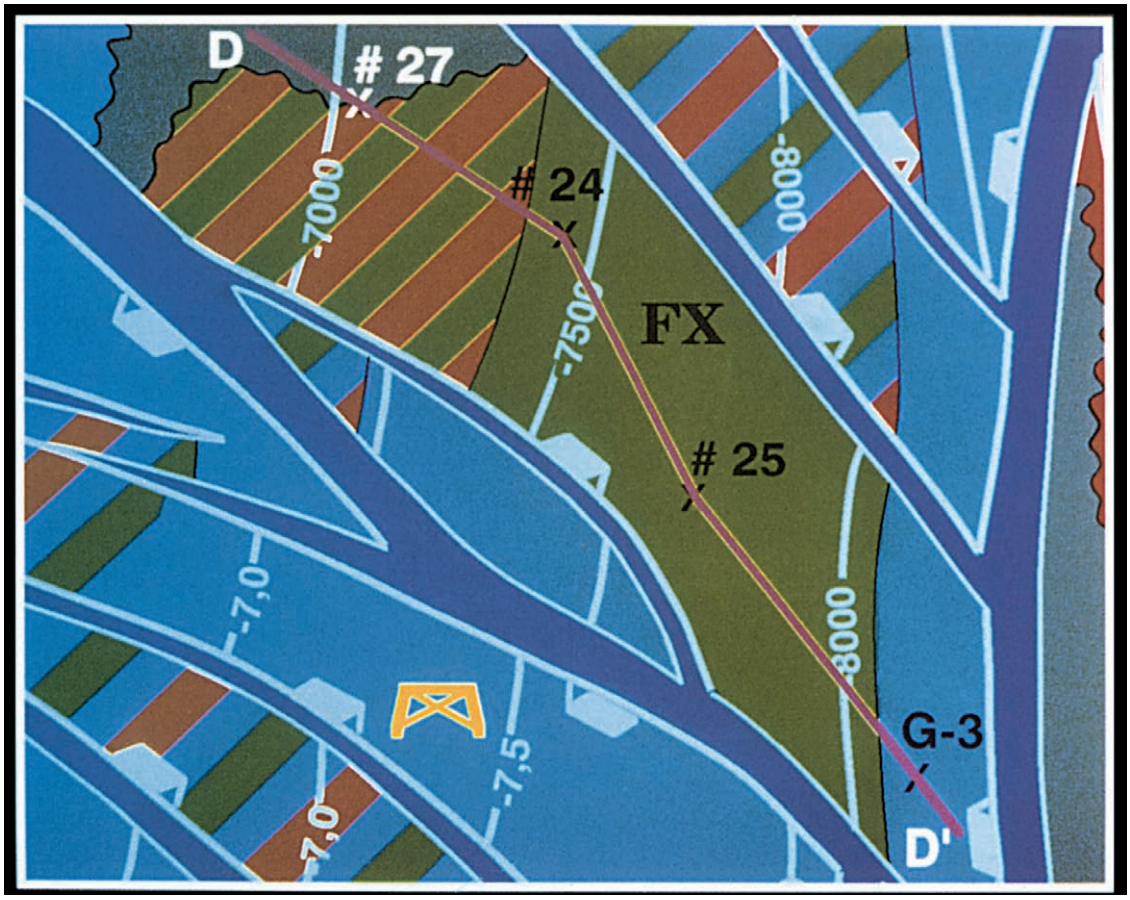

Fig. 14-10-28. Fluid and structure map of the producing FX reservoir. Water injection was proposed for well G-3, to move more oil into the producing wells 24 and 25.

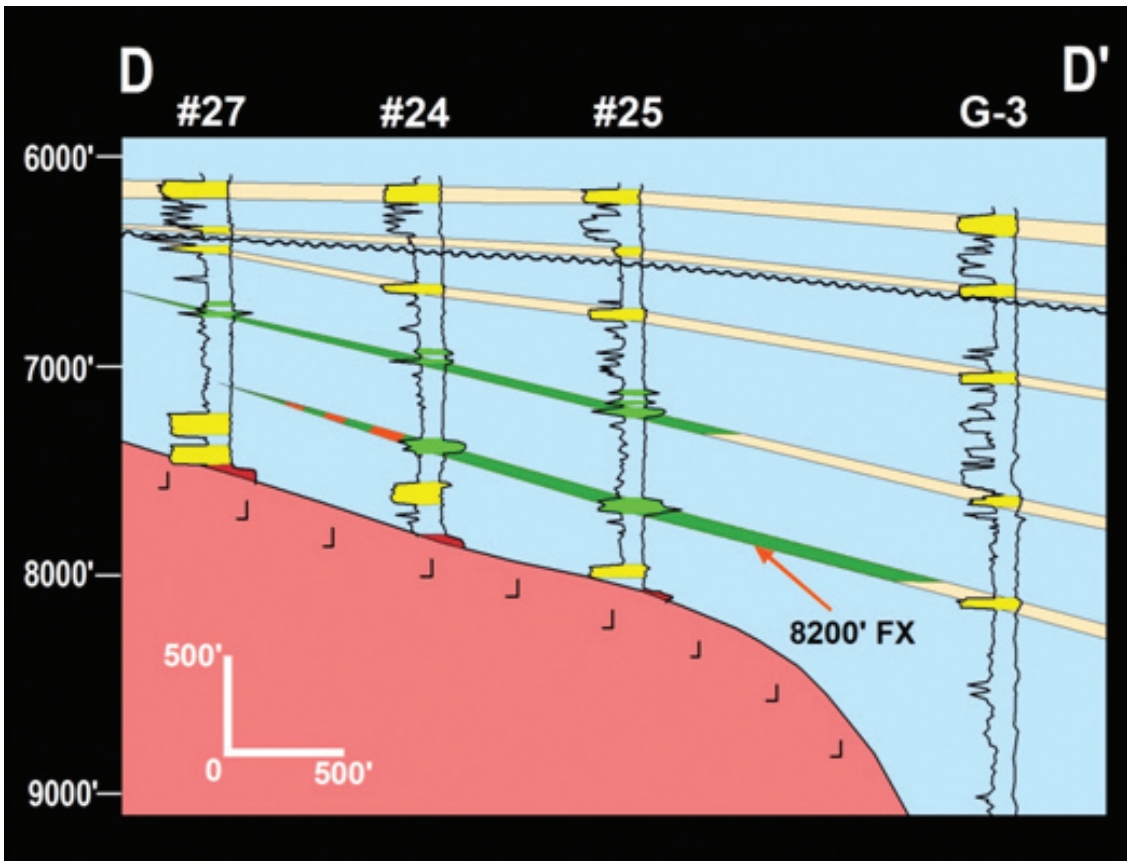

Fig. 14-10-29. A geologic cross section showing the well logs of the FX reservoir.

Downloaded 25 Jun 2012 to 95.28.162.50. Redistribution subject to SEG license or copyright; Terms of Use: http://segdl.org/

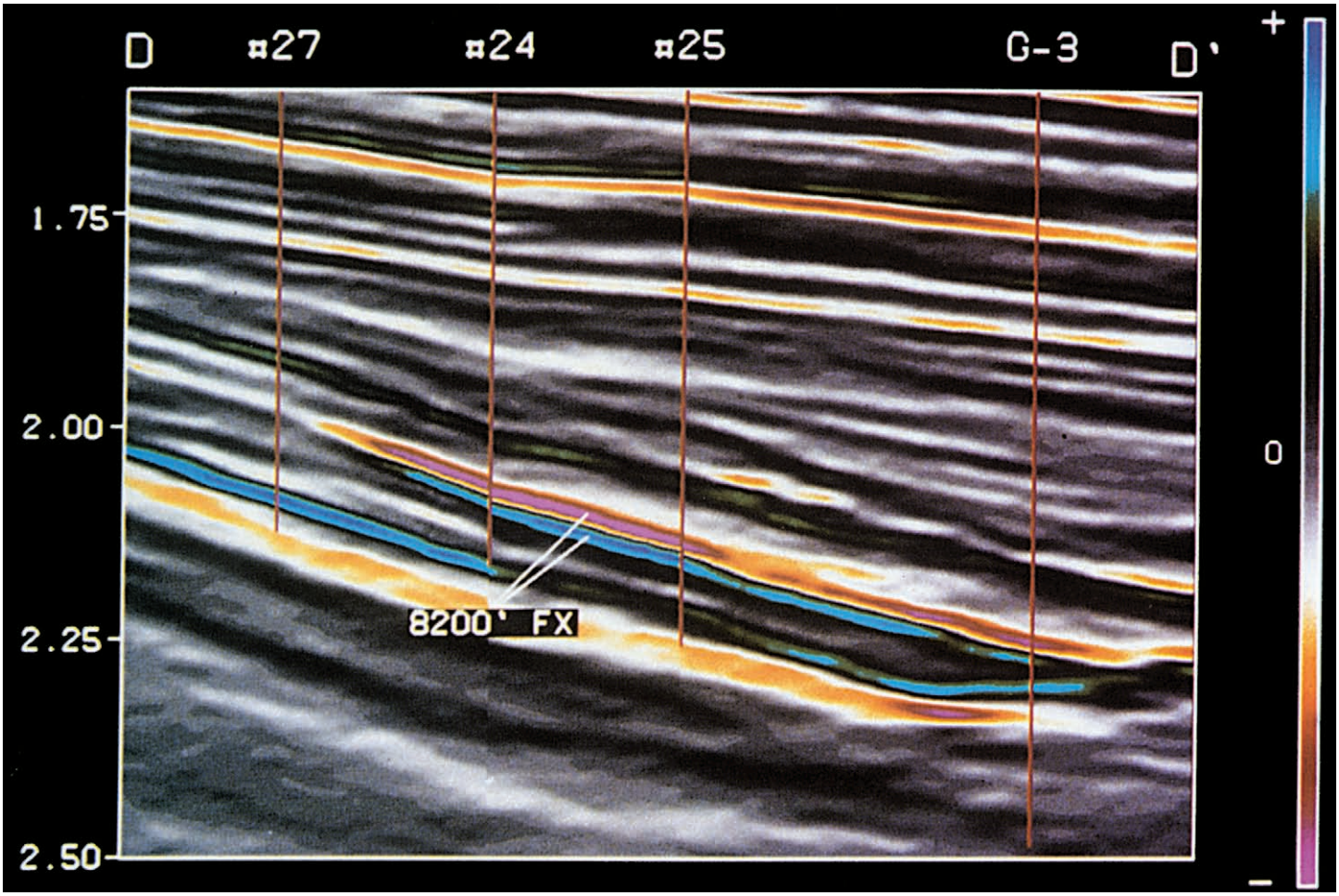

Fig. 14-10-30. The arbitrary seismic line associated with the cross section in Figure 14-10-29. The high-amplitude reflections in the center of the line are the FX reservoir.

Downloaded 25 Jun 2012 to 95.28.162.50. Redistribution subject to SEG license or copyright; Terms of Use: http://segdl.org/

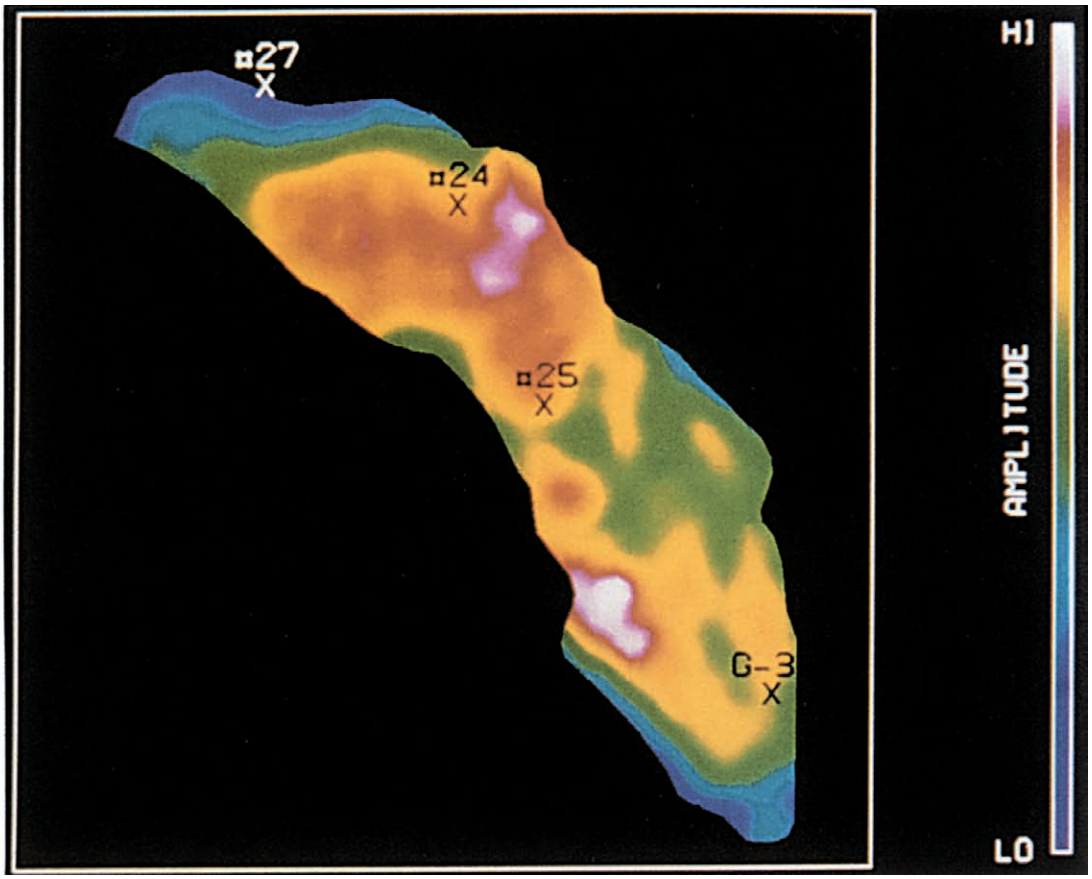

Fig. 14-10-31. Horizon slice of the FX reservoir. Note that all 3 wells in the reservoir are in the moderate (yellow) amplitude. Notice that the amplitude of the horizon slice between the wells is highly variable.

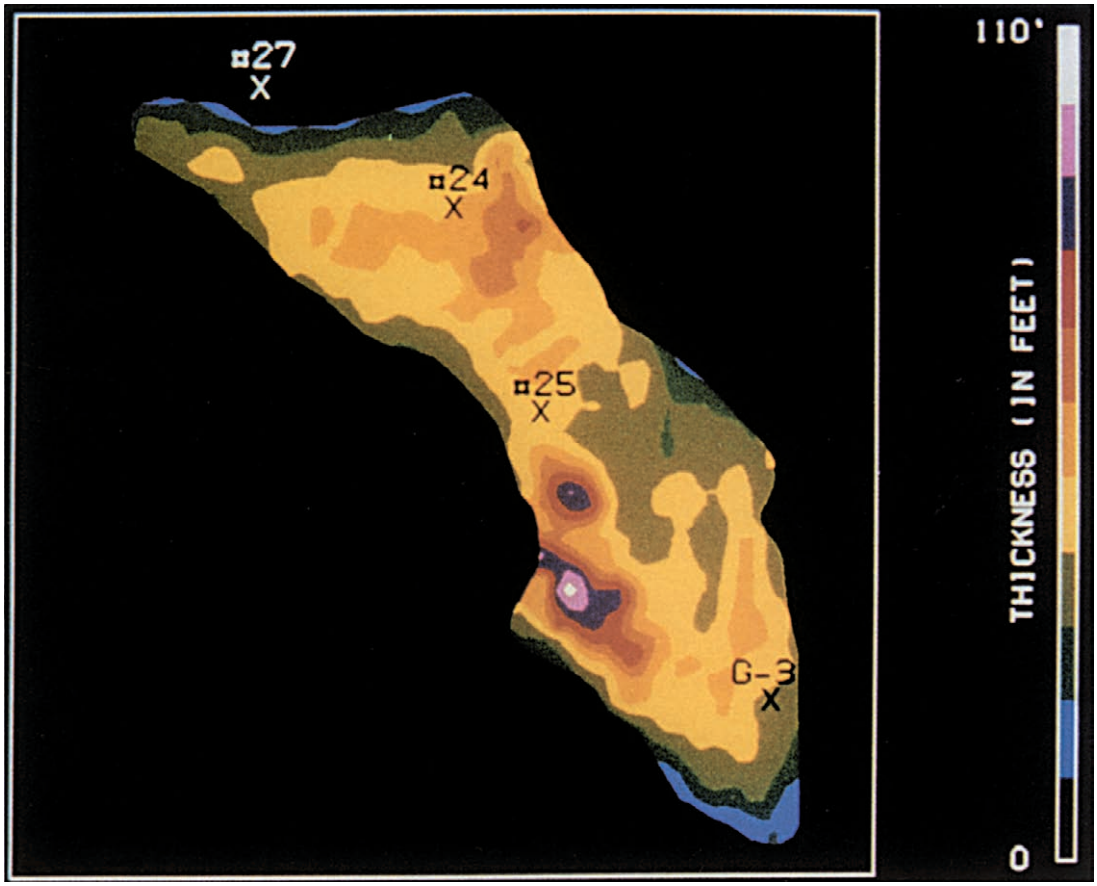

Fig. 14-10-32. Net-sand map of the FX reservoir. This is generated from well control plus the time thickness and amplitude of the seismic data.

Downloaded 25 Jun 2012 to 95.28.162.50. Redistribution subject to SEG license or copyright; Terms of Use: http://segdl.org/

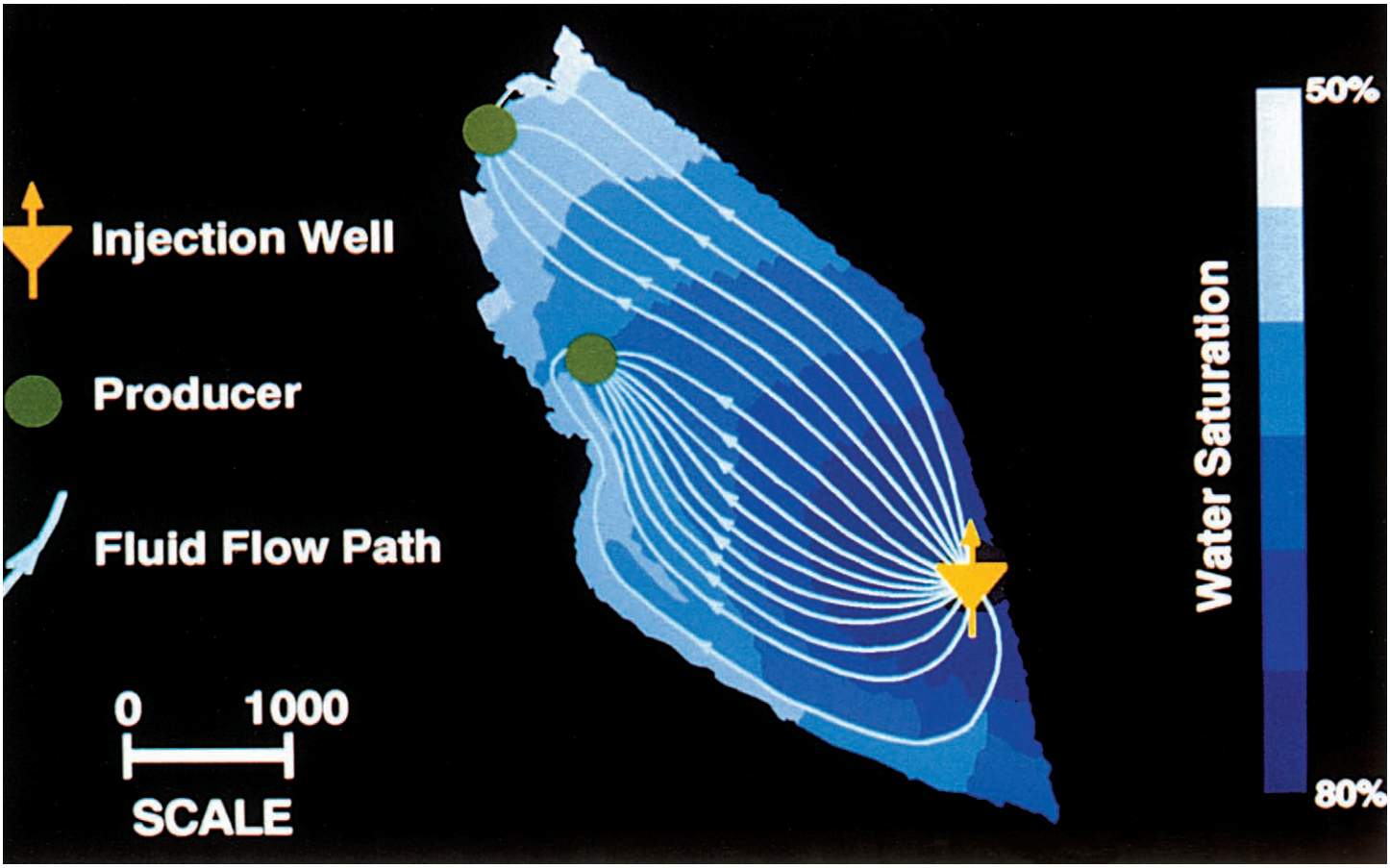

Fig. 14-10-33. Flow-line reservoir simulation of water injected into well G-3 and oil produced in wells 24 and 25. The thicker portion of the reservoir between wells G-3 and 25 shows a larger flow of water to move the oil, as indicated by the higher density of the flow lines.

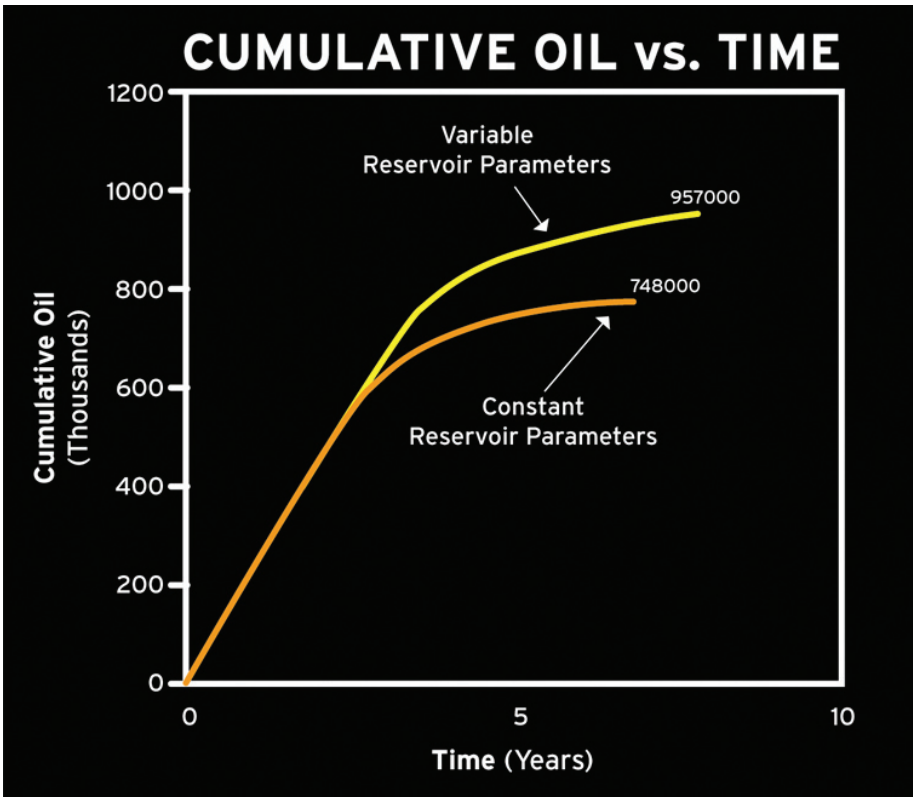

Fig. 14-10-34. Forecast production comparing reservoir models of constant thickness, derived from well data, and the variable-thickness model, derived from both well and seismic data. In this case, the variable reservoir model has a 28% higher recoverable.

Downloaded 25 Jun 2012 to 95.28.162.50. Redistribution subject to SEG license or copyright; Terms of Use: http://segdl.org/

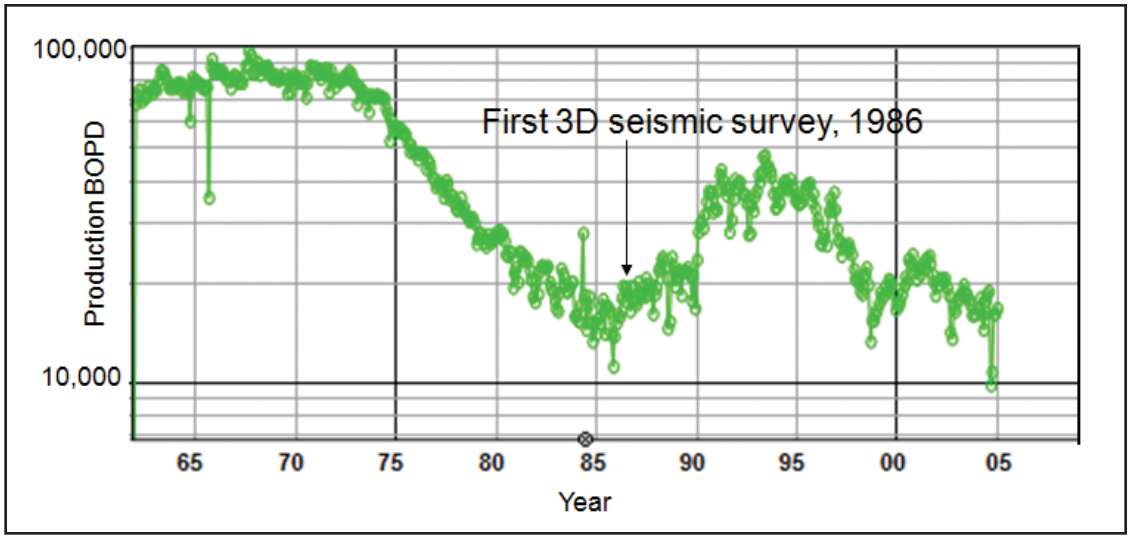

Fig. 14-10-35. Production of oil from the Bay Marchand field for a 50-year interval from startup. The production decline in the 1970s was reversed by field rejuvenation from infill wells, horizontal wells, and improved waterflood. This was accomplished with the subsurface knowledge provided from 3-D seismic data.

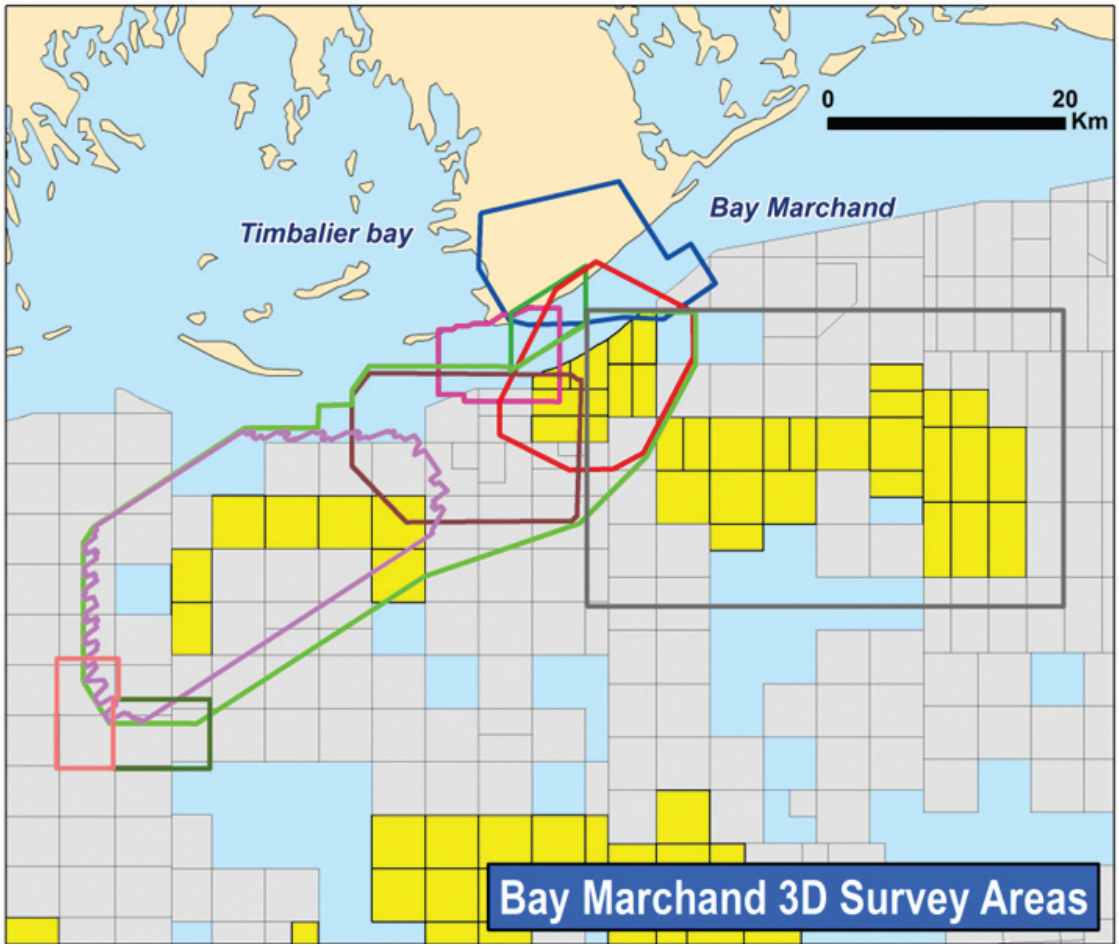

Fig. 14-10-36. Map of the outlines of several 3-D surveys that now cover the Bay Marchand field.

Downloaded 25 Jun 2012 to 95.28.162.50. Redistribution subject to SEG license or copyright; Terms of Use: http://segdl.org/

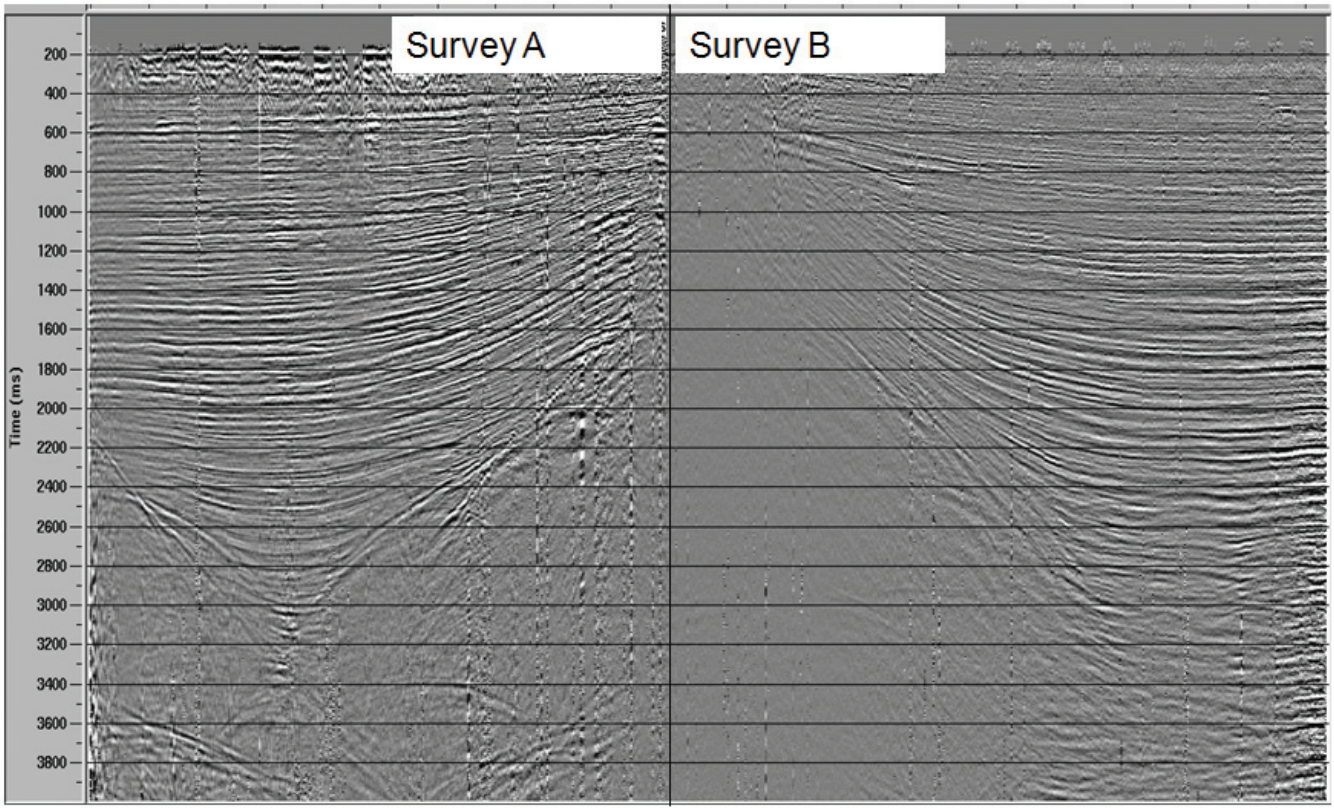

Fig. 14-10-37. Unmigrated seismic cross section composed of two of the 3-D surveys. Different acquisition and processing parameters cause the data to be poorly matched where they intersect.

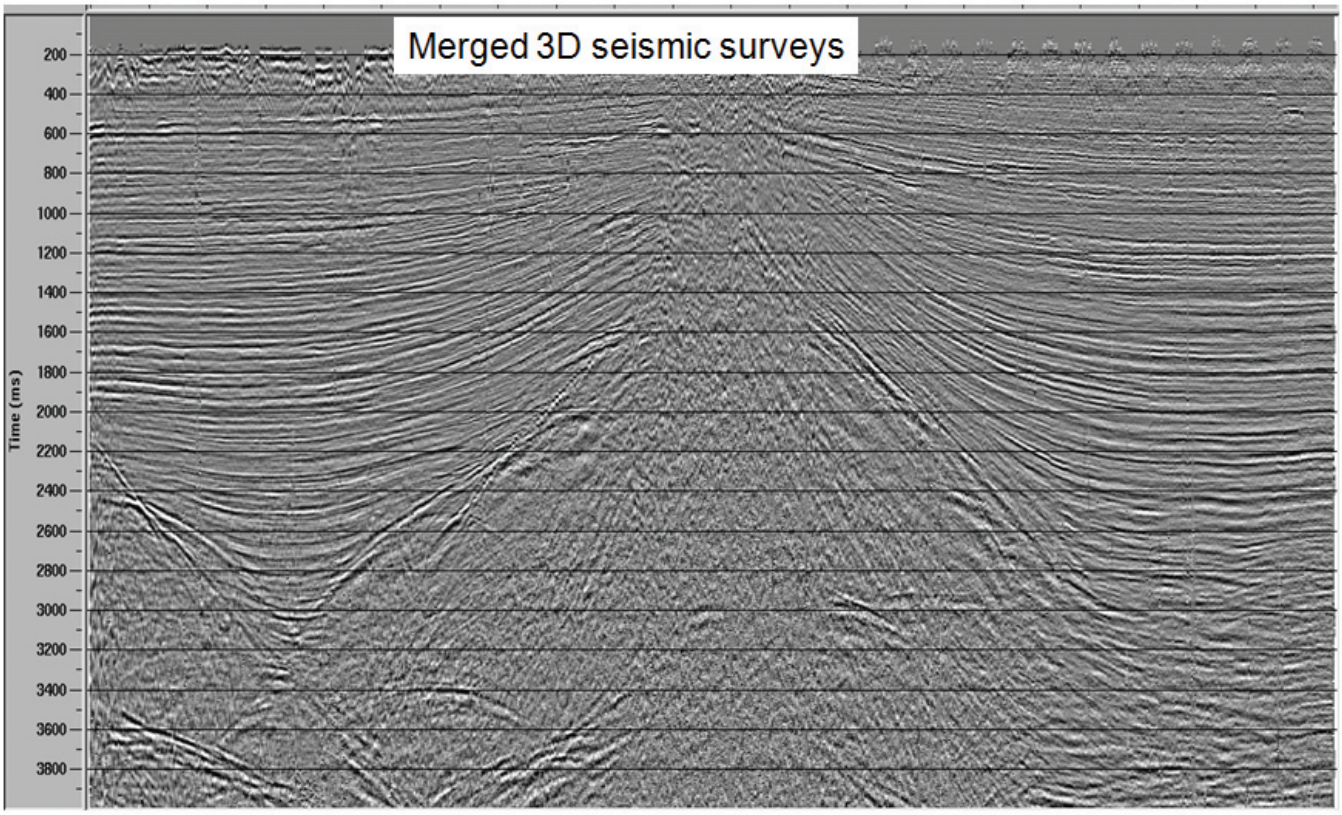

Fig. 14-10-38. Seismic cross section from Figure 14-10-37, reprocessed. The two surveys were processed together to match signal to noise, time position, amplitude, and phase.

Downloaded 25 Jun 2012 to 95.28.162.50. Redistribution subject to SEG license or copyright; Terms of Use: http://segdl.org/

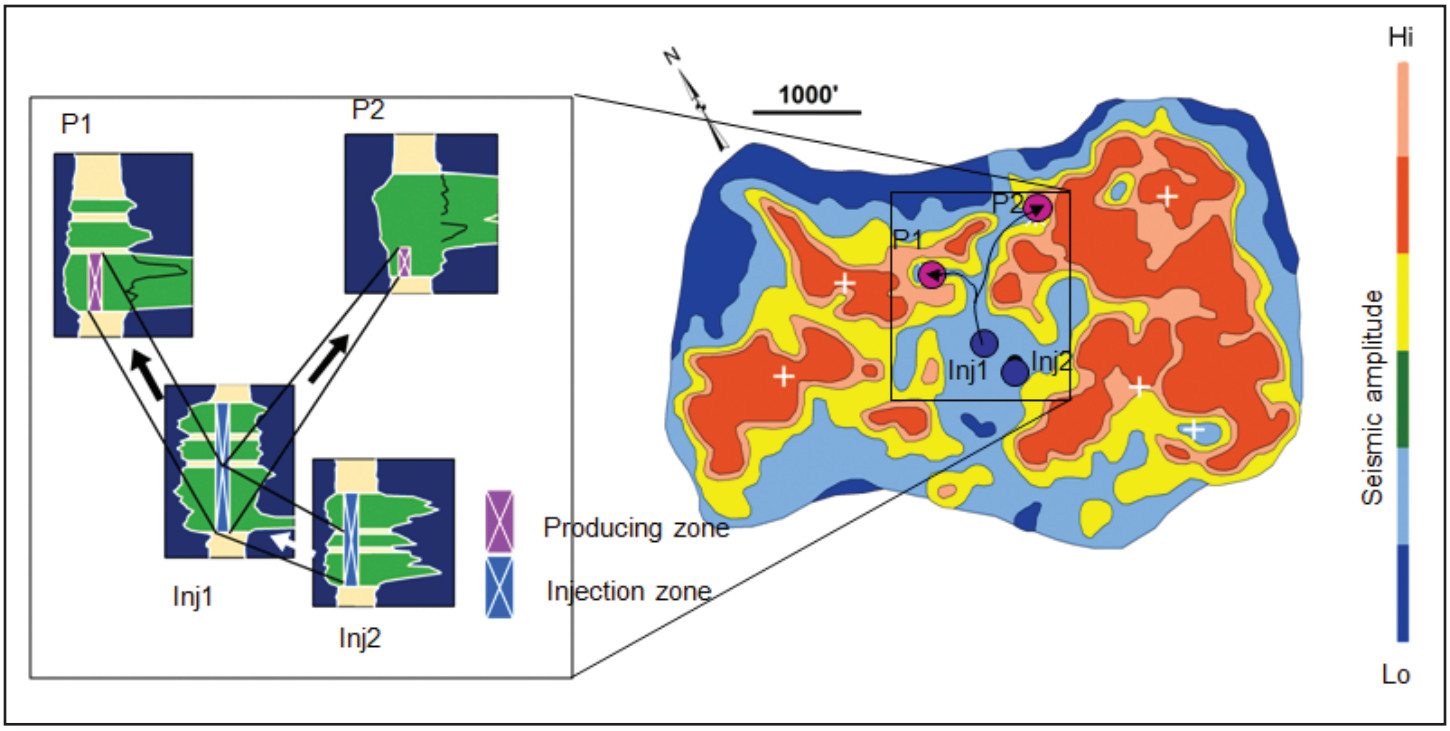

Fig. 14-10-39. Horizon slice of a produced oil reservoir. This reservoir compartment was on production for many years prior to acquisition of the 3-D survey. Amplitude did not correlate to the total reservoir thickness at the wells. Low amplitudes in the reservoir center did represent depletion of the oil in the reservoir. A flow pathway can be observed between water injectors 1 and 2 to the producing wells P1 and P2.

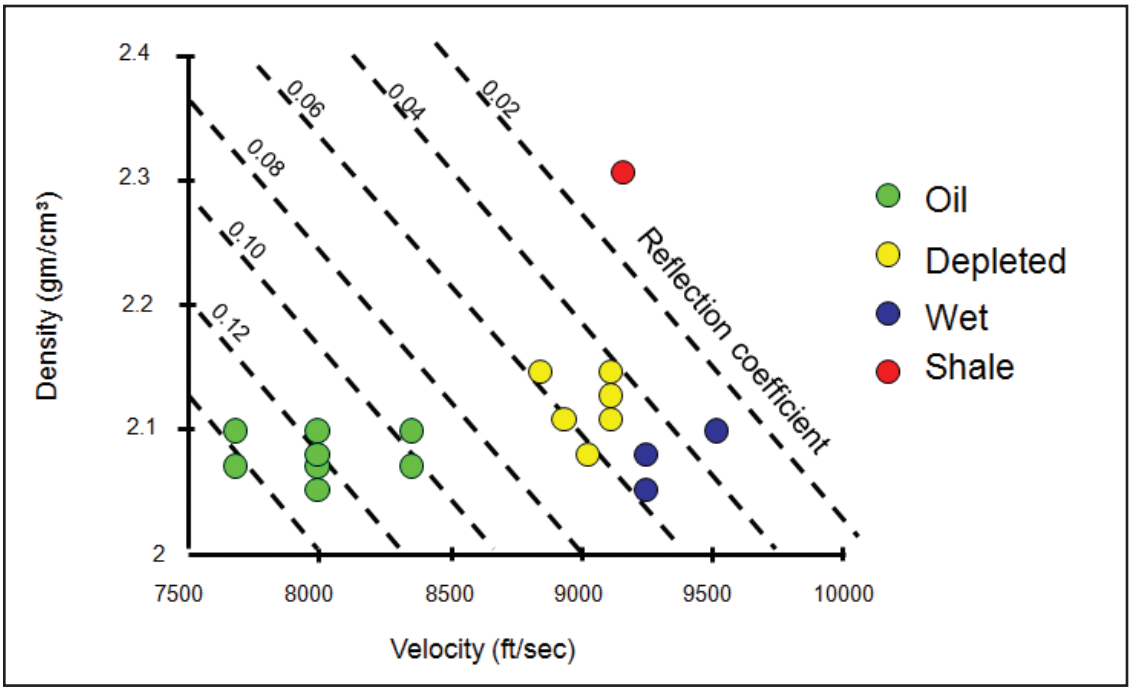

Fig. 14-10-40. Acoustic response of different fluids in reservoir sandstones at approximately 8000-ft depth. High-saturation oil sands respond with strong negative acoustic impedance. Production increases the water saturation and significantly reduces the reflection amplitude.

Downloaded 25 Jun 2012 to 95.28.162.50. Redistribution subject to SEG license or copyright; Terms of Use: http://segdl.org/

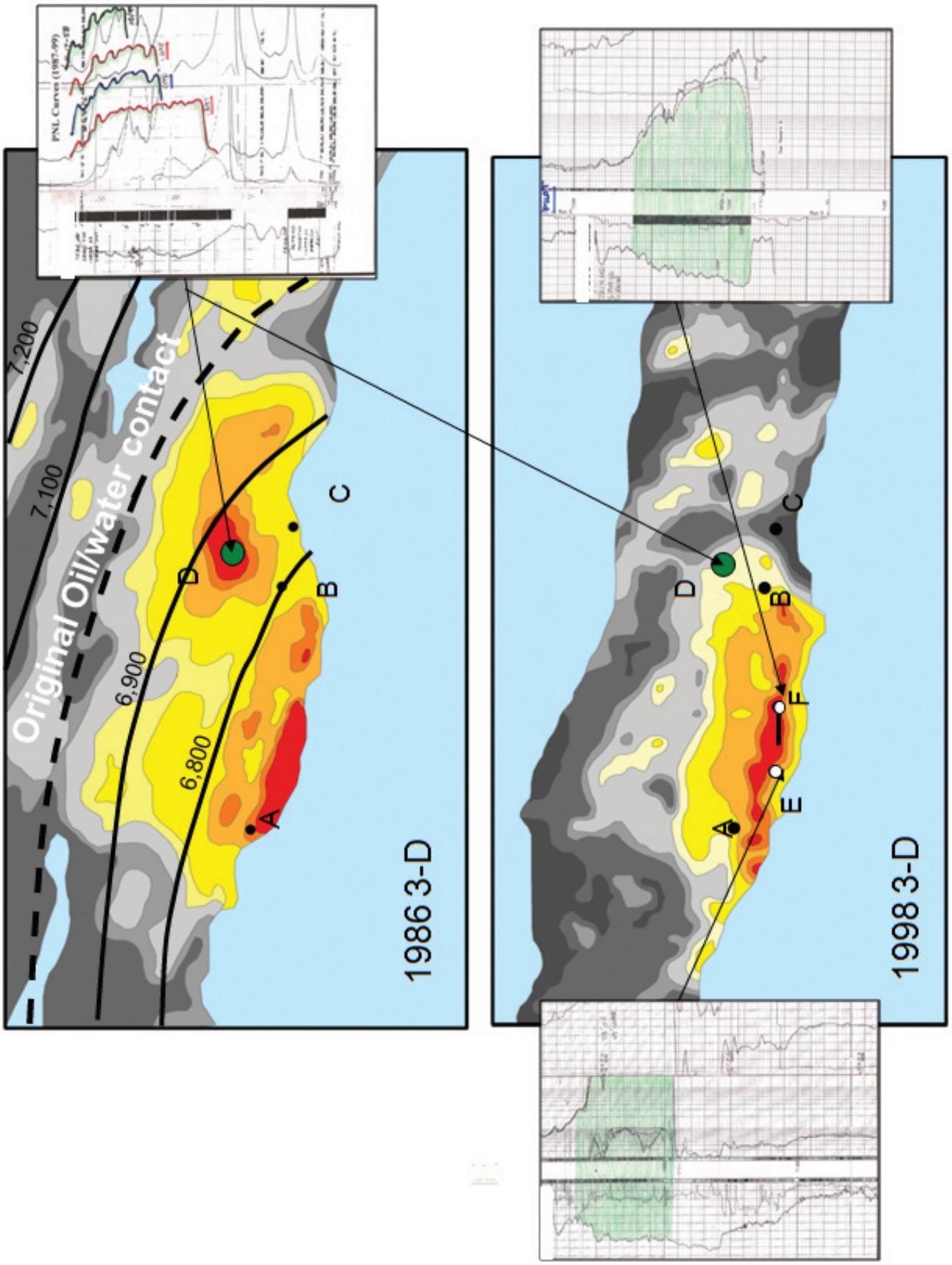

Fig. 14-10-41. Horizon slices from an oil-producing horizon in 1986 survey (top) and 1998 survey (bottom). The reduced amplitude area in the lower panel near well D is consistent with the repeat case-hole production logs showing water influx. Bypassed oil between wells A and B was drilled by wells E and F. Well F was completed at high production rates.

Downloaded 25 Jun 2012 to 95.28.162.50. Redistribution subject to SEG license or copyright; Terms of Use: http://segdl.org/

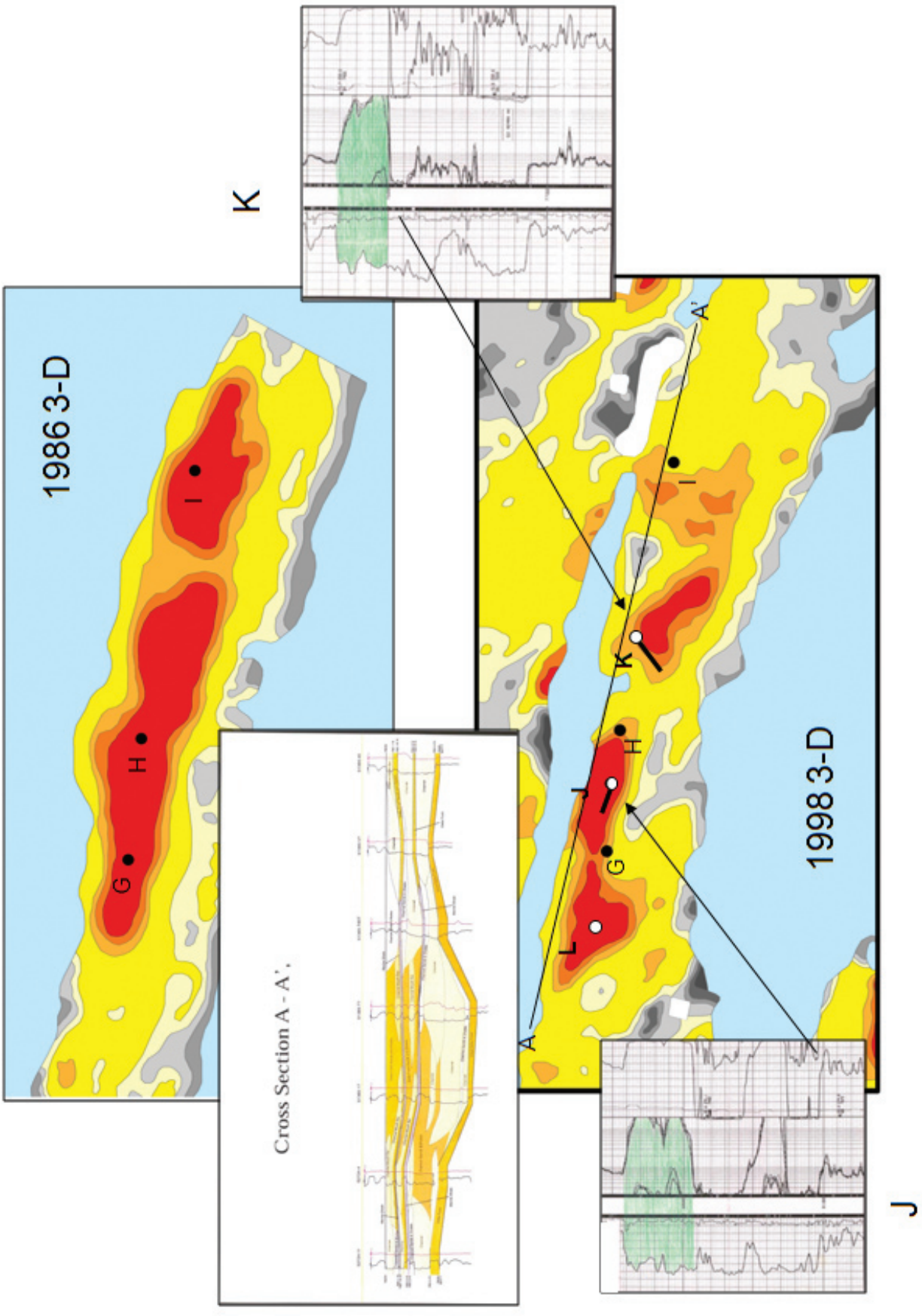

Fig. 14-10-42. Horizon slices similar to those of Figure 14-10-41 but for a deeper reservoir, showing detection of lowered seismic amplitude due to oil production and water inflow. Bypassed oil was drilled in wells J, K, and L and then put into production.

Downloaded 25 Jun 2012 to 95.28.162.50. Redistribution subject to SEG license or copyright; Terms of Use: http://segdl.org/

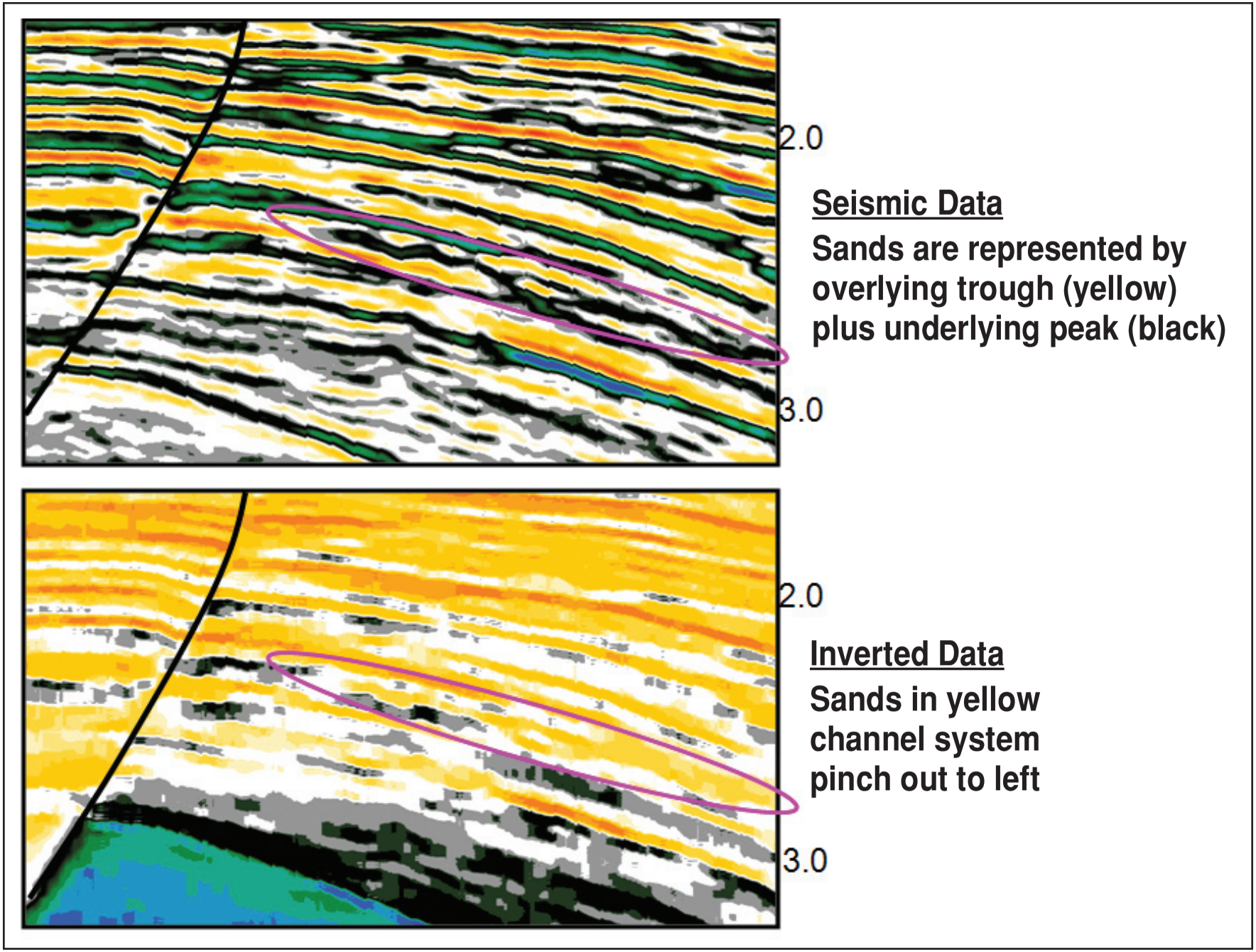

Fig. 14-10-43. Comparison of seismic data and inverted data. Low impedances (yellow) in the inverted data are sandstones embedded in shales. The inverted data are easier to interpret, because individual sands can be recognized.

Downloaded 25 Jun 2012 to 95.28.162.50. Redistribution subject to SEG license or copyright; Terms of Use: http://segdl.org/

Bay Marchand: 2004 VectorSeis 4C-OBC

- Rec. Lines per Swath: 2
- Rec. Line Orientation: NE-SW
- Rec. Length: 5975m
- 240 stations
- Receiver Group Interval: 25 meters
- Inline swath
- Source Lines per Swath: 18
  {12 lines every 16.67 meters between cables plus 6 lines outside of the cables, 3 on each side}
- Source Line Length: 6100m
- Source Line Orientation: NE-SW
- Source Interval: 25 meters
- PP Bin Size: 12.5 x 8.33 meters
- PS Bin Size: 25 x 50 meters
- Record Length: 7 seconds

RXT vessel
M/V Bourbon

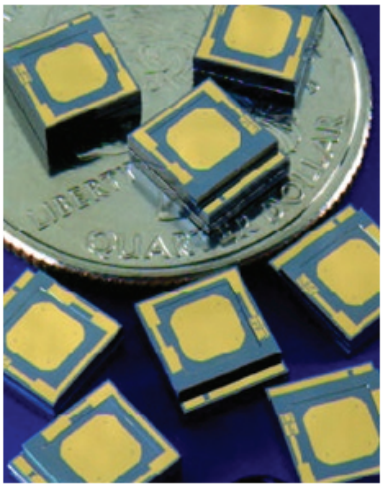

ION Geophysical
VectorSeis
MEMS sensors

Fig. 14-10-44. Survey parameters and photos of hardware used in a high-resolution acquisition program for detection of shallow reserves. Compressional (P)- and shear (S)-waves were recorded at very high and very low frequencies using microelectromechanical systems (MEMS).

Downloaded 25 Jun 2012 to 95.28.162.50. Redistribution subject to SEG license or copyright; Terms of Use: http://segdl.org/

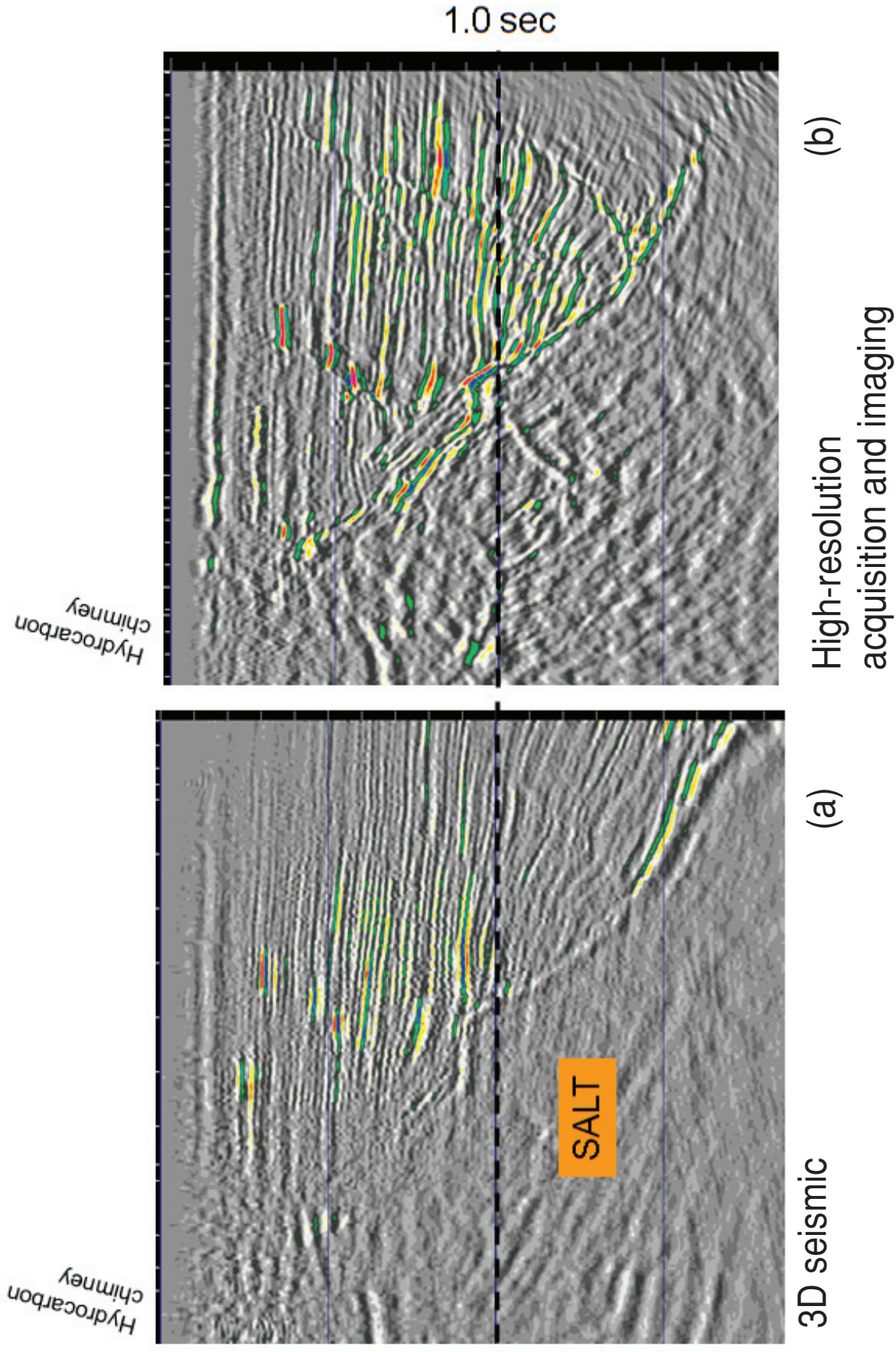

Fig. 14-10-45. Comparison of P-wave seismic cross sections from the 1986 3-D seismic survey (a) and the 2004 MEMS high-resolution 3-D survey (b). Improvements are seen in location of the salt interface, shallow faulting, definition of unconformities, and direct detection of hydrocarbons.

Downloaded 25 Jun 2012 to 95.28.162.50. Redistribution subject to SEG license or copyright; Terms of Use: http://segdl.org/

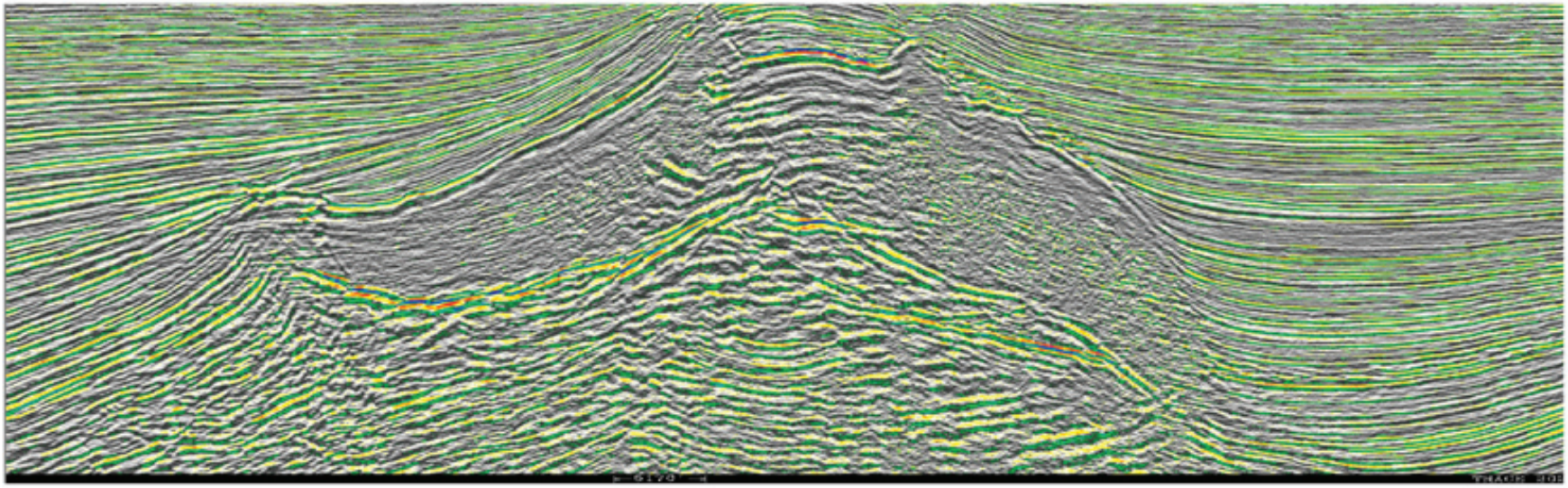

Fig. 14-10-46. 3-D time-migrated seismic cross section of the entire Bay Marchand salt dome. The data are thought to show high potential for subsalt oil and gas reservoirs.

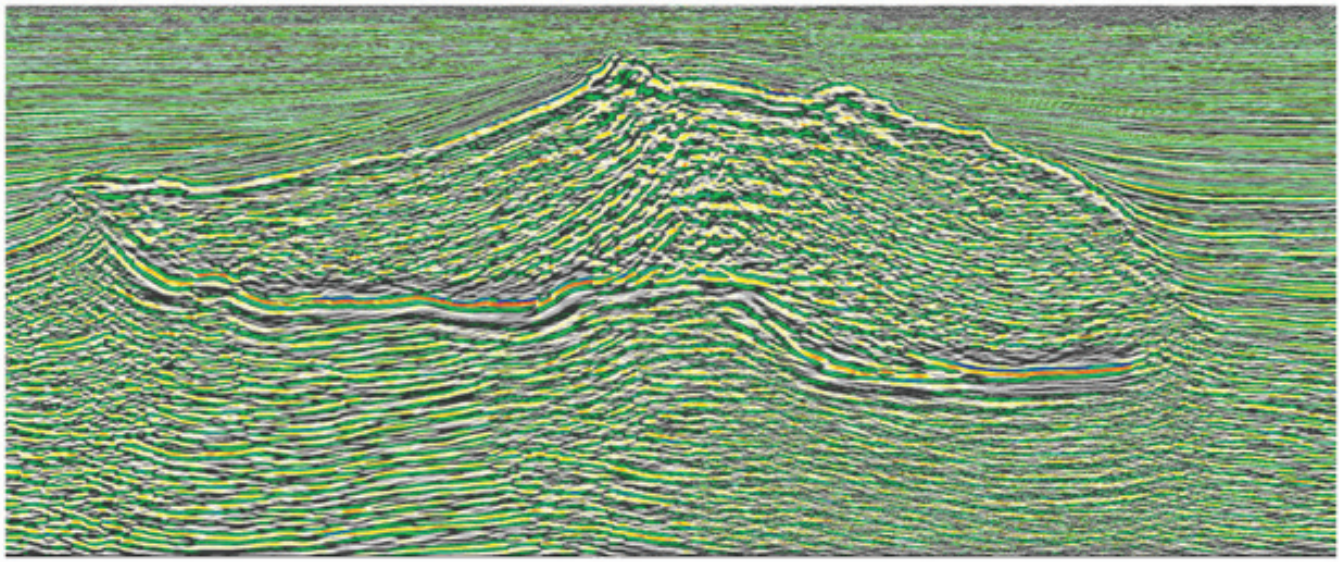

Fig. 14-10-47. 3-D prestack depth migrated cross section showing clear base salt. Subsalt reflectors may come from reservoirs that hold additional reserves.

Downloaded 25 Jun 2012 to 95.28.162.50. Redistribution subject to SEG license or copyright; Terms of Use: http://segdl.org/

Index

A
Abandoned lake, 130
Abasing, 16, 591
Above/below unconformity, 315
Above value summation of horizon slices, 223
Absolute impedance values, 317
Absolute positioning, 591
Absolute summation of reservoir amplitudes, 209, 215, 275
Absolute value to yield composite amplitude response of sand, 224
Acoustic-impedance, 330
  inversion, 343–344
Acoustic contrast, 203, 216
  of the gas sand, 167
Acoustic contrasts, 7, 58
Acoustic-impedance,
  data, 313, 322
  domain, 327
  inversion products, 309
  model, 311–312
Acoustic impedance, 141, 158, 161, 167, 171, 182–184, 196, 239, 275, 309, 312, 314, 328–329
  contrast, 590
  of gas, sand, water sand, and embedding
  shale, 157
  inversion, 309
  profiles, 196
  of a rock layer, 1
  and rock properties, 312
  of the sand, 158
  trend, 142
  values and traveltimes, 330
Acoustic properties, 157, 161
  of embedding media, 209
  of the medium, 203
  of the rocks, 1
Acoustic and shear impedances, 333
Accuracy of an AI inversion cube, 312
Acquisition, 26
  footprint, 25–27, 128, 589, 594
  geometry, 21, 589, 594
Actual downdip reservoir limit, 221
Additional/subtractive primaries, 37
Additive primary colors, 31
(ADI) angle-dependent inversion, 331
(ADI) approach, 331
Adjacent,
  advancing colors, 58
  advancing reds and yellows, 59
  colors, 33
  reflections, 157
Advantages of impedance data, 312
Affect amplitude, 233
Affect impedance, 220
Affects amplitude in opposite directions, 220
(AGC) Automatic Gain Control, 91
AI,
  characteristic of, 312
  concept, 312
  inversion, 327
  as a layer property, 312
  values (in color), 311
  volume, 312
Air gun arrays, 590
Air guns, 590
Aki-Richards,
  approximation, 331
  linearized reflectivity function, 330
Algorithm, 309, 312, 328, 330, 332–333
Algorithms, 327–329
Alternative noise attenuation, 594
  to be applied, 595
  field vibroseis correlation, 593
  noise-attenuation, 594
Algorithms' problems, 328
Alignment of event terminations, 73–75
Already-tuned reflections, 211
Ambiguities in geology, 216
American polarity, 45, 53, 56–57, 162–163, 176, 178, 181–182
  zero-phase data, 184
American and European polarity, 181
Amoco, 309
Amplitude, 44, 50, 211, 219, 298, 325, 597
Amplitude,
  anomalies of interest, 34
  anomaly, 188
  attribute, 275
  changes, 214
  channel is dominant, 145
  character anomaly, 103
  colors, 45
  compensation, 593
  of composite wavelet, 203
  not a consistent measure, 232
  to corrections, 127
  derived attributes, 142, 247
  dilute effect of objective, 145
  disease, 203
  displaying it spatially, 178
  errors, 591
  extracted,
  in a reservoir study, 215
  fit to structure, 178
  and frequency, 217
  from 3-D and 2-D data, 130
  as function of gross reservoir thickness, 228
  from the gas, 162–163
  grid-like pattern, 26
  information, 247
  lateral variations, 128
  with offset, 88
  recovery, 593
  of a seismic bright spot, 219
  by seismic inversion, 275
  trend, 142
  tuning, 204
  type, 275
  value, 24
  is visible, 171
Amplitudes, 17, 24, 167, 589

Downloaded 25 Jun 2012 to 95.28.162.50. Redistribution subject to SEG license or copyright; Terms of Use: http://segdl.org/

in blue, 131
changes in, 593
disease, 208
effects are squared, 593
enhanced section, 275
extracted without snapping, 127
extraction, 124
generated, 219
gradient, 203, 221
in a horizons, 24, 127
increase, 214
increases, 203
levels, 34, 90
lineations, 131
of the lower reservoir, 184
management of, 593
mapping, 126
measurements, 224
more accurate, 8
numbers, 24
objective, 26
of oil and gas, 184
one-sided range of, 41
output, 594
over angular unconformity, 131
P and T, 216
patches, 127
patterns, 222
peak and trough, 50
phase, 52
are positive, 126
preservation, 89
preserved, 157
processing, 593
ratio, 128
(of top and base reflections), 281
reconstruction resulting from 3-D migrations, 221
is reduced, 38
for all reflections, 26
of the reflections, 171, 206, 275
of reservoir, 215, 219
for sand, 216
sections, 52
smeared , 593
and spatial extent, 157
spectra, 299, 592
spectrum, 208, 299, 590, 592
of the seismic, 329
strength, 59
strong changes in, 594
terminations, 26
of the top, 222
unrelated to channels, 145
of the upper reservoir, 184
value, 24
variations, 37, 91, 593
with offset, 290
wider range of, 59
Analysis window, 275, 299
Ancient vs. modern stratigraphy, 103
Angle,
data, 331
impedances, 331
-impedance inversion, 331
impedances, 331
range or converted mode, 327
stacks, 313
stacks inverted, 331
between strikes, 73
Angles,
greater than zero, 331
seismic acquisition, 327
Anhydrate layer, 166
Anomalies, 257
Anomalous reservoir pressure, 219
Anomaly, 59, 157
Anticline, 11–12
Application of AVO to 3-D data, 188
Appropriate,
reflection-co-efficient series, 327
thickness of the layer, 317
Appropriateness of the inversion, 327
Arbitrary,
lines, 22, 87
vertical scales, 211
Accurate,
faults, 257
features, 256
Areal coverage, 18
Areas of highest porosity and permeability within reservoir, 290
Array orientations, 594
Arrays, 592
linear or receiver, 592
specifications, 590
Artifacts, 329, 334, 591
Assessment,
is ambiguous, 53
of relative amplitudes, 51
Associated,
tuning frequency, 304
unique wavelet, 330–331
Attenuation, 247, 299
Attitude,
coherence, 75
of a reflection, 61
Attribute,
arrays, 257
classification, 247
dip, 256
display, 257
and physical properties, 294
with many applications, 290
Attributes, 247, 274, 283, 287, 290, 294
and compares those with azimuth, 257
from relevant level in data, 290
how they are formed, 247–256
properties of an horizon, 290
in reservoir studies, 233
and uses, 290
using a window, 290
Australia line, 11
Automatic,
gain control, 157
spatial tracking, 224
or snapping, 256
Autotracked,
high-precision time map, 256
time surface, 257
Autotracker input, 87
Autotrackers, 88
Autotracking, 88

Downloaded 25 Jun 2012 to 95.28.162.50. Redistribution subject to SEG license or copyright; Terms of Use: http://segdl.org/

of faults, 274
(AVA) amplitude variation with angle geostatistical inversion, 333
Average absolute amplitude, 142, 145, 156
Average instantaneous frequency, 287
Average porosity of thirty percent, 163
AVO, 188, 247, 290, 331
attribute: far-near amplitude difference, 290
gradient, 188
information, 312
performed in 3-D, 290
Azimuth, 257, 290
is coded to hue, 257
dependence, 592
/dip azimuth, 256–257
distribution, 26
map, 257
of the maximum correlation, 274
ranges, 591
of splinter fault and its parent, 239
velocity, 594

B
"Band-limited" inversion, 328
"Band-limited impedance," 316
Band-limited data, 326
Band-limited earth reflectivity function, 328
Band-limited,
impedance, 326
data, 316
inversion, 324, 328
results, 323–324
near-and-far angle clastic impedances, 331
or relative data are pitfalls, 334
results, 323, 329
seismic data, 329
Band-pass filter, 207
Band limitation, 311, 317, 326
impedances, 315–316
issues, 315
band's lowest frequency, 211–212
bandpass filter, 49
Bands, 329
Bandwidth, 313, 590
detected, 304
of the inversion, 317
Bandwidths, 211
Barr and Sanders, 590
Basalt bed to P- and S-wave energy, 188
Base,
and amplitudes for a reservoir, 209
Bow Island, 129
of the event, 312
gas is flat, 204
horizon slice, 223
reflections, 222
reservoir reflection, 189
sand time, 235
Base as monitor surveys pre-stack and azimuth attributes, 592
Baseline, 210
Basement reflection, 53, 56
Basin, 333
Beasley, 591
Bed, 203, 206
geometry, 203
signature, 203
thickness, 203, 206
Bedding, 57
plane, 22, 61, 103, 127
planes, 112
surfaces, 127
Beds, 103, 224
in the Gulf of Thailand, 112
Below resolution of seismic data, 316
Better production from sands, 287
Bids to structural solution, 176
Bifurcating channel, 103
Bimodal, 326
Bin, 26
too wide, 593
Binning technique, 593
Bins,
use of over lapping, 593
Bit interpretation, 24
Bits, 22–25
Black,
areas, 90
arrows, 126, 188
features, 256
horizontal lines, 127
(top reservoir) reflection, 166
Blind-to-the-wells, 330
Blocks, 81
Blocky model, 329
Blue,
asterisks, 211–212
contact, 184
event, 50
intensities of, 126
for lineations, 290
lines, 145
"meaning" of, 256
-over-red, 50, 57, 158, 161, 176, 182
peak, 157
-red for amplitude, 45
/red data, 326
and red gradational scheme, 171
to a red, 178
reflection, 56, 176–177
reflections, 184
-white-red, 37
water-bottom reflection, 53
Boat, the, 591
Bodies of calcified sandstone, 256
Bold black lines, 311
Borehole effects, 313
Bottom-referenced systems, 590
Boundaries, 158
Bright,
events, within the reservoir, 181
and flat spots, 165
red events, 203
reflection,
at top and bottom of reservoir interval, 224

Downloaded 25 Jun 2012 to 95.28.162.50. Redistribution subject to SEG license or copyright; Terms of Use: http://segdl.org/

reflections, 161, 171–172, 224
response of oil, 184
spot,
or dim spot regime, 219
(without phase change), 161
reflection, 178
regime, 219–220, 230
validation, 157, 185, 188
spots, 38, 127, 145, 161, 163, 165, 176, 181–182, 194, 196, 203, 219
caused by oil, 184
character of, 209
/flat spots, 163
flat spots, hydrocarbon indicators, 157
and flat spots, 166
in Pliocene rocks, 196
strides, 24
suppressing, 196
as they were before, 157
Brightening, 158
Brine, 299
oil, and gas, 331
Brittle reservoir, 290
Broadband, 329
results, 317, 328, 330
Broadening of gas reservoir reflections, 185
Broad-closed anticline, 61
Brown, 239
(BSR) bottom simulating reflection, 57
Bulking an impedance model, 312
Business impact of 3-D seismic data, xv
Bypassed reserves, 287

C
Cable,
lay-out, 21
techniques, 591
Cables,
water depths of, 591
Calcite, 256
Calculation, 281
Calibrated to seismic-derived stacking velocities, 328
Calibrating the seismic-derived velocities
to well data, 326
Calibration, 312
factor, 229
to give relative pore volume, 231
Calibrations,
offshore locations, 194
Caliper data, 313
Campos Basin, 3
Canada, 129–130
Capability statistical analysis, 209
Carbonate,
buildup, 103
encased in shale, 290
Case histories of 3-D seismic surveys, 463–483
Causes of footprints, 26
CDP,
gathers/angle stacks, 331
positioning, 188
CDPs into constant angle groups, 331
Cells, 326
Cementation, 167
Center,
lobe for one octave wavelet, 214
of a zero-phase wavelet, 219
Central,
frequency, 324
lobe, 44
peak of the wavelet, 206–207
Chair, the, 81
displays, 87
Chalk, 318–320
Change,
in absolute AI units, 312
in amplitude, 166
in color, 323
in rock properties, 323
in velocity, 323
Changes,
in acoustic impedance, 312
in phase dots to liquids, 331
Channel, 16, 121, 127, 178, 299, 324
amplitudes, 145
bright spot, dim part, 178
center is blue, 299
changes direction, 275
continuity, 128
deeper, 112
edges, 275
fill, 126
how to recognize and delineate, 124
levees, 290
reflection, 127
represented in amplitude, 178
system for one frequency, 299
system, 41, 112
at two levels, 299
thalwegs, 290
visibility, 103, 275
in yellow, red, and green, 290
Channels, 121, 142, 145, 299
and their levees, 130
Character. See also individual colors and color combinations.
changes, 75, 112
of the display, 325
of geologic feature, 52
match, 188
symmetrical, 53
Characterization project, 189
Check-shot data, 313
Clastic,
basins, 24
-carbonate interface, 53, 56
interface, 141
section, 141
Circular arrays, 592
reservoirs, 181
Clastics, 161
Classification of attributes, 247–256
Clay smear potential, 239
Clipping, 24
of amplitudes, 24
is not necessary, 24
test, 163

Downloaded 25 Jun 2012 to 95.28.162.50. Redistribution subject to SEG license or copyright; Terms of Use: http://segdl.org/

(CMP) common mid-point stack, 594–595
gather, 593
gathers, 595
Coarsening-upward sequence, 312
Coherence, 274–275, 290
calculation, 275
horizon slice, 275
time slice, 274–275
Coherent house, 257
Cokriging, 294
Color, 189
bar, 163
bars, 324
boundaries, 38, 91
boundary, 91
chart, 32
contrasts, 37
cube, 32, 37
cubes, 31
density, 59
for detection, 38
display, 24, 33, 45
is expressed, 31
indicates amplitude, 287
intensity, 176
monitor, 23–24, 31–52
plotter, 31
principles, 31–60
scheme, 24, 214, 256
compression/expression, 37
a confusing, 38
a double-gradational, 36
higher phase dynamic, 184
inverted, 41
for peaks and troughs, 41
schemes, 1, 32–33, 36, 59, 121
balanced double-gradational, 37
single gradational, 38
superimposed on the top of the reservoir, 230
usage, 45
uses of, 59
Colored,
inversion algorithm, 329
sections, 45
Colors. See also hues, individual colors.
and gains, 171
Common,
and adjacent affects, 188
-depth-point gathers, 185–186, 188
gas/water contact, 235
Comparable gross and net isochron maps, 229
Complete inversion result, 317
Completed inversion process, 313
Complex,
geology, 595
trace, 90–91, 275
Complexity and gross thickness of target, 304
Composite amplitude, 209, 222–223, 229, 232, 275, 287
axis, 211
-isochron product, 231
for this reservoir, 223
response was easier, 228
composite,
displays, 81–87
of sections, 81
wavelength, 203, 325
Comprehensive processing report, 312
Compression wave amplitudes, 188
Compressional,
-and-shear-wave velocities, 333
waves, 188
Computation time, 329
Computer-driven workstation, 2
Confidence, 89
map, 89
qualitative assessment of, 89
Connolly (1999), 330
Constant,
flat time interval, 247
time shift, 88, 127
V/V ratio, 330
Constructive interference, 206
Constraints, 332
Contamination, 145
by sand, 216
Continuity, 274–275
of the channel, 128
of time slice, 274–275
Continuous red areas, 90
Contour, 91, 124
displacement, 131
disturbances, 256
on the fault line, 75
interval, 33
lines, 131
map, 62
Contrast, 158
Contrasting colors, 24, 41, 163
schemes, 37
Contrasts, 304
Contribution of the net gas/gross sand ratio, 229
Control,
on the geologic model, 330
points, 330
walk, 211
Conventional ocean-bottom systems,
water depths of, 591
Conventional,
seismic displays, 89
streamer acquisition, 591
Convergence,
of many lineations, 235
of reservoir reflections, 203
Conversion to AI, 34
Converted net gas isochron map, to net gas isochron map, 229
Convolution of a wavelet, 312, 325
Convolutional model, 329
Coordinates for turbidite reflection, 597
Correction map, 89
Correlation, 274, 325–326
among attributes and property, 294
coefficient, 294, 325–326
map, 89
is marginal, 325
Correlations, 326

Downloaded 25 Jun 2012 to 95.28.162.50. Redistribution subject to SEG license or copyright; Terms of Use: http://segdl.org/

Correlative P-wave, 188
Corresponding time/depth positions, 216
Cost,
structure, 589
of the survey, 589
Covariance, 274–275
Creation of a synthetic seismic, 312
Crest, 90
of an identified reflection, 275
of a reflection, 257
Crestal,
amplitudes, 194
points, 216
time, 257
Crested amplitudes, 127
Crevasse splays, 121
Cross-correlation, 44
calculation, 274
techniques, 208
Crossline, 21
Crossplot, 210–211, 224, 314, 325
attributes, 208–209
envelope, 211
log data, 326
points, 211, 235
of top sand amplitude, 209
of upper and lower sections, 314
using many wells, 232
view of elastic impedances, 331
Crossplots, 320, 331
establish relationships, 233
Crossplotted, 287, 290
Crossplotting, 75, 208–209, 325
Crossplots' data points, 235
(CSSI) constrained sparse-spike inversion algorithm, 323
CSSI inversion process, 323
Cube, 21
acoustic impedance, 322
culminations, 75
curvature, 290
and roughness, 257
volume, 290
curvilinear feature, 38–41, 124, 126
displays, 81
Cyan and yellow, 36–37

D
Danian (Basal Tertiary) chalk, 130
Dark blue linear features, 256
Darker blues, 126, 204
Data, 21, 23. See also color usage; polarity; processed.
acquisition, 26
geometry, 26, 589, 595
on land, 592
and processing, 1, 590
technology, 591
are prestack, 185
broad bandwidth, 592
clipping, 25, 37. See also clipping; feasible clipping
collection, 3, 81
direction, 256
content of high frequency, 591
-dependent amplitude sealing, 594
evaluation irregularities, 256
experimental phase rotation of, 50
images, 24
initialization, 593
locations, 274
loading, 24
management, 23–24
with non-zero source to receiver offsets, 594
not zero phase, 214
ocean bottom, 592
panel, 51
phase, 1, 156, 182
and polarity, 610
undetermined, 52
polarity, 1
poor and uninterpretable, 127
processing, 593–594
flow, 589
difficulties, 592
the objective of, 593
to optimize, 592
quality, 89
research, 44
solution, 592
set, 589
sets,
intersect and tie, 53
are opposite polarity, 176
and their subtraction, 591
zero phase, 56
systematic noise on the, 5
types, 313
visualization, 21
volume, 21, 24, 61,81, 112, 589
phase, 58
well-sampled, 594
into workstation, 163
zero-phase, 52
Deconvolution, 328
process, 593
Decrease (increase in acoustic competence), 157
Decreasing thickness below tuning, 228
Deep major gas field, 162
Deeper horizons, 256
Deferred bar, 126
Delta,
front channel, 113
prograding, 112–113
Definition of reflections,
terminating at the salt, 81
Degree of distortion, 49
Dendritic patterns of canyons, 113
Densities, 38
Density, 313, 333
of color, 31–32
and compressional velocity, 331
cube, 320, 322
conversion, 326
of maximum burial, 196
migration, 81
and other observations, 196
and shear effects, 333
slice, 21

Downloaded 25 Jun 2012 to 95.28.162.50. Redistribution subject to SEG license or copyright; Terms of Use: http://segdl.org/

-to-time conversion of well data, 326
or time match, 326
and velocity, 312
Depleted gas field, 163
Deployments, 590
Depositional,
clinoforms, 275
features, 103, 112–113, 121
models, 103
surface, 128
reconstruction of, 126
trend of higher porosity, 75, 221
Depressions in the vertical sections, 103
Deviated well, 22
Depth,
and age, 194
conversion, 326
-conversion velocities, 256
conversion and imaging, 351–395
horizons, 313
of maximum burial, 196
slices, 81
and velocity model, 595
Depths, 185, 590
points, 188
Derivation,
of accurate stacking velocities, 329
of a reservoir property map, 290
Derived amplitude spectrum, 329
Design process, 589
Detect gas, 283
Detecting faults, 290
Detection of hydrocarbons, 283
Determination,
of tuning effects, 210
of net sand in one water zone, 229
Deterministic,
points, 211
or stochastic process, 329
tuning curve, 204–208, 211
Development drilling, 219
Deviation from zero-phaseness, 208
Diagonal,
line, 22
of unit gradient, 235
yellow line, 209
Diagnostic, 165–166
benefits of flat spots, 157
Diagrammatic legend, 275
Difference-of-scale problem, 325. See also scale differences.
Differences of signal, 591
Different,
amplitude patterns, 221
Displays, 89–94
Diffraction patterns, 7
Digital database, 23, 224, 233
Diminished amplitude, 165
Dimming, 158
Dim spot, 167, 194
regime, 219–220, 231–232
reservoir, 220
Dim spots, 161, 167, 196
Dip, 7, 52, 62, 75, 203–204, 257, 274, 290
anomalies, 256
attitude, 203–204
and azimuth, 257
combination map, 257
of channel, 112
coded to color density, 257
components of the plane, 61
of the composite wavelength, 204
/dip magnitude, 256
displays from Nigeria, 257
is gentle, 121
of the local plane, 256
map, 256
of an horizon, 257
to the northeast, 257
perpendicular, 13
sections, 323
and strike, 61–62
directions in complex geology, 591
Dipping event, 62
reflection, 61
spatial sampling, 16
Dips,
on reflection strength, 275
to the southwest, 257
vs. sand direction, 597
Direct contouring, 61–72
Directing boat movement, 21
Direction strike,
to the salt/sediment interface, 81
Discontinuous black areas, 90
Discontinuities given continuity, 274
Discovery well, 167
Disk, 313
Displaced horizon, 127
map, 89
Display, 51
aspect ratio, 194
colors, 91
gain, 34
products, 22
is thick time slice, 247
Displays, 89
inversion velocity, 130
seismic amplitude, 130
Distortion, 81
in composite amplitude, 224
of seismic relativities, 233
Distributary channels, 113
Distribution, 24, 247
of amplitudes, 24, 219
attributes, 281
Distributions, 589
DMO, 593
algorithms, 594
dip movement, 594
made worse with, 594
Dominant frequencies, 287, 298
of a lower value, 299
seismic energy, 204
wavelength, 325
of the wavelet, 298
Double-gradational,
color display, 192
schemes, 35
Double-lobed red-blue, 53, 56
Downdip, 129

Downloaded 25 Jun 2012 to 95.28.162.50. Redistribution subject to SEG license or copyright; Terms of Use: http://segdl.org/

continuity, 176
limit, 203
of bright events, 162
of brightness, 162, 203
limits, 203
penchant, 204
reservoir limit, 203
Draping of reflections, 103
Drill, 333
Drilling,
hazard, 275
potential, 59
Dry well, 163
Dual polarity variable area, 51, 90
sections, 36
"Dual Sensor," 590–591
bottom-referenced, 590
Dual sensors, 591
Dynamic range, 21, 24, 36
color display, 49
problem, 24
of variable area, 51

E
Early Cretaceous horizon, 256
Earth-Scope facility experiment, 370
Earth, the, 3
Earth's reflectivity, 328
East-west yellow line, 256
Eastern and western lobes, 290
Edge/edge detection, 257
Edge map, 257
from southern Alberta in Canada—a reef, 257
on the top Tosca reflection in the Neuquen
Basin of Argentina, 257
Edges, 299
of colored areas, 87
defined, 257
Edited,
amplitude to hot gas/gross sand ratios, 229
phase, 91
Editing of response of yellow to orange, 224–228
Effect,
of bed thickness, 203
on acoustic properties, 157
of gas and oil, diminishes with depth, 157
of the overburden, 223
of overpressure, 196
in seismic amplitude, 161
of tuning on stratigraphic interpretation, 203–205
of the underburden, 223
Effects,
of gas and oil, 157
of depth and age, 196
Efficiency, 87
of the strike view, 87
Elastic,
attributes of lambda-rho and mu-rho, 333
inversion, 330
models, 331
parameters, 312, 330
wavelet, embedded, 325, 327
(EI) elastic-impedance, 312, 330
inversion, 330
Embedding,
material, 5, 216, 223
medium, 158, 167, 203, 219
shale, 158, 161
Encoded in the amplitude, 229
Encyclopedia Dictionary of Applied Geophysics, 325
En echelon faults in shallow, 257
Energy, 8, 184
absorption, 592
defined, 275
focusing of, 13, 16
half-time, 275, 281
incoherent or diffraction, 395
removing, 11
Engineers, 312
Enhancement, 112
Envelope,
amplitude, 52, 275
of the plotted points, 210
Envelope's variable shape, 210
Environment. See also local environment.
Equal increments of gross isochron, 235
Erosion, 113
channel, 126
Erosional,
truncation, of a sand, 131
unconformity, 314
Estimated wavelet, 329
Estimates of reservoir parameters, 330
European polarity, 45, 50, 52, 158, 163, 176, 224
Event terminations, 239
showed faults, 73
Events,
of different widths, 75
of interest, 89
moved with depth, 61
parallel the faults, 75
Examples of bright and flat spots, 163
dim spots, and phase changes, 161–181
Exercise, 62
Expanded vertical scale, 195
Experiment X95-02-1 at the University of Minnesota, 312
Exploration wells, 3
Explosive data, 593
Explosives,
data recorded with, 592
as a land source, 592
Extracted,
a reservoir reflection, 232
from volume, 290
wavelet, 208, 224, 329
Extracting of amplitude, 142
Extraction,
of multiple reservoir property maps, 233
of P- and S-wave velocity, 327
Extrapolating to zero, 203

Downloaded 25 Jun 2012 to 95.28.162.50. Redistribution subject to SEG license or copyright; Terms of Use: http://segdl.org/

Extreme,
clipping, 163
sag, 235

F
(f-k) frequency-noise, 594
False,
internal geometry, 311
stratigraphic-like effects, 312
structures, 589
Fan morphology, 121
Far-field source signature, 590
Far-right panel results, 323
Far traces (elastic impedances), 331
Faroe basin on U.K. Atlantic margin, 145
Fault, 62, 81, 257
blocks, 75, 128, 239
face, 22
and horizon pricks, 87
interpretation, 75, 275
patterns, 257
phase of interest, 239
plane, 239
mapping, 75
recognition, 38
and mapping, 73–80
scarp, 10
sealing and leaking, 239
slice, 239
slices, 22
slicing, 239–245
strike, 75
and structure, 274
unrolled, 239
visibility, 274
Faulting, 59, 80, 131, 221, 257
lineations due to, 59
Faults, 38, 73, 126, 128, 131, 142, 256–257, 299, 597
azimuth of, 81
conical in shape, 257
are curved, 274
from deviating of overpressure shale, 275
features of significance, 103
horizontal extension of, 81
increased, 73
on sections, 80
/highlighted/in shadow, 274
and other boundaries, 574
and salt movement, 257
throw, 239
trending NNE-SSW, 156
validated, 256
Features are structurally low, 256
File name, 313
Film-strip, 23
Filtering, 313, 325–326
effects of the earth, 44
the log data, 315–316
processes, 312
Final,
curve's shape, 211
data volume, 589
image, 595
interpreted curve, 211
inversion, 312, 316
merged volume, 324
structure image, 594
tuning curve, 211
Fine flat spot, 165
First,
negative side lobe, 204
notch in orange, 299
Flanking red side lobes, 176–177
Flat,
in depth, 181
lying beds, 103
spot, 52, 157–158, 163, 165–166, 178, 182, 220
and associated bright spot in Peruvian rocks in The Netherlands, 166
and bright spot, 166
broken, 182
dip, 181
of ninety-degree phase, 163
reflection, 52, 158, 161–162, 181, 235
reflections, 162, 235, 239
on 2-D data, 165
spots, 184
as black, 162
-time window, 142
Flatness, 165, 590
Flexing minimized, 233
Floating point scalar, 24
Flow,
analysis, 312
rates effective over geologic time, 235
Fluid contact, 52, 157–158, 166, 182–183, 220–221
contacts, 203, 595
/base hydrocarbon sand reflection, 167
coreflection, 157
fill, 313
properties from seismic data, 331
leak across the fault, 339
visible in red and green, 239
reflection, 11, 52, 158, 165, 178, 182, 203
(flat spot), 220
is red, 161
reflections, 611–614
Fold, 589
variations in, 594
Footprint,
now visible, 593
Footprints,
of marine data, 26
Formation attribute, 247
Formulas,
spacing per wavelengths, 16
"40% rule," 214
"4-component" or "4-C," 590
Front side lobe, 214
4-D acquisition,
azimuth preservation in, 592
4-D reservoir monitoring,
summary of principles, 449–451
survey results, 451–457

Downloaded 25 Jun 2012 to 95.28.162.50. Redistribution subject to SEG license or copyright; Terms of Use: http://segdl.org/

Four corner frequencies, 207–208
Four-shaped features, 130
Four octaves, 214
Forward model, 311
Fraction, 127–128
Fracturing, 290
  in carbonate reservoirs, 290
Frequencies, 299, 325, 329, 591
  attenuation of high, 593
  full spectrum of, 315
  of the inversion, 313
  loss of high, 592
  of the volumes, 331
Frequency, 304
  bond, 295, 298–299
  characteristics of wavelets, 287
  content, 44, 203
  dependence, 87
  -derived attributes, 247, 283–289
  differences, 324
  domain interference profile, 299
  is noisy, 219
  predominant, 4
  range, 312, 316
  ranges, 315, 326
  samples per highest, 16
  slice, 298–299
  slices, 298–299
    of amplitude, 298
  sub-bond, 295
  tuning, 204
  velocity, amplitude/offset, 157
Frequent anomaly, 299
Fresnel zone, 7, 16
  radius, 17–18
Fringe width, 17
Frio Formation of south Texas, 145
Full-band data, 326, 334
Full-bandwidth attribute, 299
Full-stack trace-inverted seismic data, 316
Full,
  fold, 313
  cube, 299
  variable intensity area, 80
Function of angle of impedance, 247

G
Gain to date, 176
Gamma-ray, 313
Gaps in the interpreted horizon, 256
Garden Banks area of the Gulf of Mexico, 162
Gas, 157–158, 162, 176, 185
  accumulation, 178
  chimney, 165
  column, 167
  content, 127, 178, 188
  extent, 221
  -filled and its amplitude, 158
  hydrate stability zone, 57
  indicator of, 185
  at low impedance, 176
  migrating toward the trap, 221
  -oil contact, 184
  -oil and oil-water, 182
  in the pore space, 157
  production, 128
  reservoir, 50, 161, 185, 290
  reservoirs are red, 162
  sand, 50–51, 157, 161, 188
  in sand bodies, 129
  sand interval velocity, 229
  sand reflections, 229
  sand thicknesses, 229
  sand well, 188
  sand,
    wedge-shaped, 181
  sands, 171, 185, 203
  saturation, 158
  trapped against salt, 221
  velocity sag, 181, 235
  vs. oil, 219
  /water contact, 129, 188
  and water sand, 158
Geographic position, 287
Geologic,
  continuity, 178
  dip is zero, 594
  environment, 275
  frequency, 283, 287
  heterogeneity, 298
  insight, 299, 331
  interface, 189
  interpretation (the model), 330–331
  -layer thickness, 330
  model, 330
  objectives, 592
  seismic data, 1
Geological,
  model, 330
  reasonableness, 276
  validity, 80
Geologists, 312
Geology, 57, 257, 290, 314–315, 317, 326, 330, 595,
  out of 3-D seismic data, 615
  sampling of, 591
  and seismic modeling, 171
Geometric effects, 210
  modern land recording, 594–595
Geometry,
  assignment, 593
    and data initialization, 593
  undershoot, 591
  used to acquire the data (or footprint), 592
Geophysical,
  and petrophysical reasoning, 290
  Service, Inc., 2–3
Geoplanes, 590
  below the surface, 592
  are burred, 592
Geophysics, 290, 309
Geoscientists, 324
Geostatistical,
  approaches, 233
  inversion, 309, 330
  modeling, 330
  reservoir, 294
Geostatisticians, 326
Geostatistics, 290–294

Downloaded 25 Jun 2012 to 95.28.162.50. Redistribution subject to SEG license or copyright; Terms of Use: http://segdl.org/

Ghost,
effects, 591
reflections, 590
removal, 592
Gippsland basin offshore Australia, 103
Glauconite zone, 129
Global/local minimum, 330
Global optimization, 330
Good,
reservoir response, 214
statistical correlations, 233
"Good will tie," a, 325
Good-quality impedance inversion, 312
Graben, 257
Grabens, 256, 412
Gradational,
color, 38–41, 51
display, 51
scheme, 34
colors, 59
contact, 52
degrees, 312
interface, 312
vs. variable area/wiggle trace, 35
Gradations, 37
Graph, 204
Gray,
-green, 256
plane, 61
scale, 121
Green, 80
arrow, 163, 182
blob, 124
and blue, 257
correlates with yellow, 176
data, 326
gradations scheme, 59
set of plots, 326
Greens and blue, 59
Grid,
cell, 20
loop, 20
points, 330
system based on cells, 326
Gridding, 326
Gross,
amplitude, 142
attribute measurement, 247
effects and trends, 185
isochron, 224, 229
map, 228–229
(measured thickness), 209
lithology, 219
of a reservoir rock, 219
sand intervals, 223
Ground force signal,
controlled to be flat, 592
of the vibrator, 592
Growth fault, 81, 239
Gulf of Mexico, 24, 53, 56, 81, 121, 127, 131, 161–162, 165, 176, 188, 274
bright spots on and flat spots, 162
deepwater, 290
field, 221
gas reservoir, 204
gas sand, 185
reservoir, 59
salt dome, 103
sediments, 53, 56
Gulf of Thailand, 112, 121, 128
Gun,
operation and timing, 590

H
Ha'py Field offshore Egypt, 163
Half-period of the seismic trace, 283
Hard-bed, 182
Hard water bottom, 178, 591
Hardware, 25
Heavy line of acoustic impedance equality, 161
Heterogeneity, 299
of interest, 295
Hierarchy of approved terms, 22
High-acoustic impedance background, 311
High amplitude, 41, 182, 157, 211, 219–220
anomaly, 124, 127
area, 59
bright spots, 145
featuring, 126
gas area, 221
reflection, 50, 52, 188
reflections, 158, 214, 221, 610–611
tasks, 24
trend, 221
triangular shape, 221
High amplitudes, 129
in red, 221
Higher amplitudes to the north and east, 229
High-density, high velocity shale section, 316
High-energy area, 281
High,
frequencies, 185, 324
attenuation of, 593
lack of, 315
frequency, 287
differences, 312
porosity streaks, 318
signal, 592
impedance,
layer, 182, 610–611
tight sand or salt, 317
reservoir, 220
High-impedance chalk, 318
High/low-cut filtering of data, 317
High-maintenance and frequency, 287
High-spatial-frequency drape, 256
High,
precision automatically-tracked time map, 256
side lobes, 49
surface redundancies, 573
value of curvature, 290
velocity material, 126
Higher,
acoustic contrast, 203
amplitude of the background, 126, 299

Downloaded 25 Jun 2012 to 95.28.162.50. Redistribution subject to SEG license or copyright; Terms of Use: http://segdl.org/

frequencies, 299, 329
frequency, 323
slices, 298
give increased resolution, 304
hydrocarbon saturation, 220
impedance material, 299
net-to-gross reservoir, 220
porosity, 220
Highest amplitude locally, 178
Highlighted/in shadow, 257
Histograms, 326
Horizon, 87, 124, 128, 142, 156, 188, 247, 257, 275, 290
amplitude, 156, 161, 275
amplitudes, 224
or travel time, 87
attribute, 274
displays, 22
extraction, 257
and/or window attributes, 290
corrections, 127
data, 209, 233
(deeper) map, 256
identification, 156
of interest, 80, 188
interpretation, 87, 330
mispicks, 275
offset arrow, 188
segments, 87
slice, 22, 26, 41, 58–59, 121, 126–129, 131, 178, 188, 219–221, 275
defined, 127
in curvature, 290
display, 275
displaying conventional stacked amplitude, 290
examples, 128
interpretation, 221
slices, 38, 103, 126, 130, 140, 167, 182, 184, 204, 221, 224, 290
AVO slices in AVO gradient, 188
methods of making, 126–128
over reservoir interfaces, 220–222
top and base, 222
slicing techniques, 216
surface, 178, 257, 290
time values, 256
track, 44
tracks (picks), 62, 239
tracking, 1, 126–127, 204, 224
under study, 124
and window amplitude, 156
Horizons, 126, 257
Horizontal,
blue line, 210
phase sections, 91
resolution of the data, 8
section, 21, 61, 75, 80, 103, 162
alignment, 73
contribution of, 61
are depth slices, 81
sections, 20, 38, 61–62, 75, 89, 124
horizontal and vertical, 22, 61, 81
"How thin is a thin bed" (Widess, 1973), 203
Hues, 32. 59
of green and blue, 58
of yellow, orange, and red, 58
Hybrid attributes, 247, 281–283
Hydrocarbon, 287
accumulations, 156
amplitude, 26
bright spot, 182
bright spots, 156
character, 181, 219
Hydrocarbon-charged silt, 315
Hydrocarbon,
diagnostic, 178, 181
effect, 370
fluids, 157, 165–166, 239
illuminated, 220
indicators, 157, 194–198
in Permian rocks, 196
indication, 194–198
migration pathway into zone 3, 145, 156
observations, 196
phenomena, 196
polarity reverses, 178
pore volume, 231
reflections, 158–161, 182
reserves, 2, 217
reservoirs, 52, 194
sand, 161, 194, 196
saturation, 219
is higher, 219
target, 327
transmission effect, 184
traps, 80
water contact, 157
Hydrocarbons, 24, 157, 163, 165, 182
Hydroplanes, 590

I
Idea flow, 24
Identification,
of fluid contact reflections, 165
of gas, 290
Identify reservoir reflections, 222
Igneous intrusion, 53, 56, 257
Illumination,
directions, 257–274
of internal layering, 181
lighting/shaded relief/sun shading, 257
Image,
area, 589
composition, 24
Images of the subsurface, 299
Imaging,
in data processing stages, 591
process, 595
DMD step, 594
techniques, 311
under salt, 81
Impact on the eye, 59
Impedance, 327
decrease, 178, 610–611
of the embedding rocks, 220
of the gas sand, 158
Increase, 52, 178, 610–611
Interpretation when the relationship is unclear, 337–343
and lithographic boundaries, 2

Downloaded 25 Jun 2012 to 95.28.162.50. Redistribution subject to SEG license or copyright; Terms of Use: http://segdl.org/

log data, 314, 325
and reflectivity, 328
of the reservoir, 220
rock age and depth, 194
scared to rock values, 329
values, 329
volume, 312
Improved,
fault visibility, 274
volume, 323
Improvements to seismic processing, 157
Increase of amplitude with offset, 185
Interval velocities, 185
Input,
data on the far left, 323
seismic,
trace, 328
is zero phase, 329
Inaccuracies, 326
Inadequate imaging, 589
Incasing material, 209
Incident angle, 188, 333
Incorrectly interpolated well data, 329
Increase,
in impedance with depth, 311
in resolution, 333
Increases in amplitude, 214
Increasing amplitude with offset, 290
Independent thickness measurement, 232
Inelastic attenuation compensation, 593
Inferred channel, 38, 41, 126
Inferred gas, 156
Information extraction, 87
Initial,
discovery, 287
model, 329–330
wavelet, 330
Individual lobes of producible gas sand, 224
Inline, 21
Input data after inversion, 323
Instantaneous frequency, 283
sections, 204
Instrument recording filters, 593
Integrating over chosen sub-areas, 230
Intelligent parameterization, 330
Interactive,
approach, 23
capabilities for procedure, 87
crossplot of gross isocheim, 293
interpretation, 209
systems, 24, 32, 126, 224
workstations, 24, 75, 87, 124
and color schemes, 32
Intercept and slope of a shale fit-line, 331
Interface,
property (seismic reflector data), 309
shape, 317
Interfaces, 50, 312
Interference, 299
between wavelets, 203
constructive or destructive, 325
Interfering wavelets, 203
Interlocking patterns, 221
Internal,
distribution, 281
layering is unreform, 224
layers, 189
reflections, 182, 220
Intermediate phase conditions, 58, 610–611
Interpolated from well data, 328
Interpolating, 326
Interpretation, 20, 24–25, 127–128, 142, 157, 290, 299–301, 323–324, 326, 331, 333. See also structural interpretation.
of amplitude, 37
consistency, 24
difficulties, 89
example, 315
full-scale structural, 124
of impedance data, 337
quality, 24
quantitative, 317
of reflection terminations, 80
of sands and shales, 239
of small rock types, 318
technology, 87
in vicinity of sands, 80–81
Interpretative power, 312
workstation, 589
Interpreted,
horizon, 22, 145
maps, 87
surfaces, 21
Interpreter, 20–21 24, 31, 34, 38, 45, 50–51, 58, 61, 73, 91, 157, 162, 176, 188–189, 203, 208, 214, 256, 312–314, 316, 329, 335, 593
of 3-D data, 81, 87
Interpreters, 44, 58, 211, 290, 209, 278, 314, 324–325
Intersecting horizontal section, 75
Interpretive,
approach to reservoir evaluations, 219
bias, 274–275
horizon, 274
phase assessment, 52
sequence, 228
time, 24
value, 61
Intersected, 80
Interval,
AB, 215
between horizons, 156
from top, 276, 281
treatment, 230
velocity, 185
Inverse,
filter, 590, 593
tangent of the slope of the slate-line, 332
Inversion, 311, 313
of angle or offset stack data, 312
of data, 326
data layer-based, 325
-induced change, 325
method, 313, 317, 333
methods, 327–328

Downloaded 25 Jun 2012 to 95.28.162.50. Redistribution subject to SEG license or copyright; Terms of Use: http://segdl.org/

methods—based on 3-D stratigraphic models, 330
methods—post-stack, 328–330
of the nears and fars, 331
operator, 329
prior to, 313
process, 312–313, 325
results, 313–314, 333
to rock properties, 311
is scaled to impedances, 328
strategies, 329
success, 343–344
Inversions, 329–330
algorithm, 313, 324, 328
defined, 309
Inverted,
AI traces are red, 317
data, 309, 312, 317, 326
for frequency ranges, 317
set, 312, 315
trace d, 312
traces in panel c, 312
wedge, 311
Inverting the seismic 328
data, 311–312
Investigation, 156
Irregular,
footprint, 26
yellow patterns downdip, 221
Irregularities, 589
Isochron, 210
defined, 232
gates, 211
Isofrequency running window, 295
Issues,
of sparsity (simplicity), 328
of structural detail, 256
Inconformity surface, 141

J
Jurassic rocks offshore Norway, 165
Jurassic Tank
data, 320
set, 323
experiment, 323, 326
impedance data, 322
Juxtaposed fault block, 339

K
Known geology, 590

L
L-7 well, 142
Lack,
of compaction in the shallow tank, 320
of gas, 167
of surface coverage, 26
Lake Mara Cabo, Venezuela, 257
Land data static corrections, 594
Land survey of 3-D survey in south Australia, 256
Land surveys, 593
static correction of, 594
Large velocity, 81
Larger,
acoustic control, 216
distortions, 49
Lateral,
amplitude increase, 214
changes,
in amplitude, 209
within the reservoir, 209
discontinuities, 299
distribution on log weights, 330
variations, 140
in amplitude, 209
variability in the reservoir, 222
velocity gradients, 595
Layer-based or blocky inversion, 329
Layer,
below the sand, 316
is bent, 290
boundaries, 312
boundary, 299
interference, 298
properties, 331
property, 312
stack, 299
stacking patterns, 304
velocity, 7
Layering, 275, 283, 287, 299
produces sand, 287
Leading Edge, The, 309, 318
Layers,
beneath the surface unconsolidated weathering, 592
of rock, 1
and seismic revolution, 329
with sharp boundaries, 329
Lease blocks, 230
Least-squares,
error, 329
inversion, 329
legend, 33
Lena Field in the Mississippi Canyon of the Gulf of Mexico, 456
Less than tuning, 229
Light-colored streaks, 126
Lighting, 257
Lignite, 188
Limestone, 127
/dolomite/shale sequence, 140
encased,
in anhydrite, 220
in shale, 220
reflection, 127
Limit of separability, 5, 7
(one quarter wavelength), 232
Limit of visibility, 5, 7, 203–204
Limitations of the data,
seismic frequency ranges, 315
Limited,
lateral extent, 287
optical dynamic range, 89
Limits of resolution, 316
Line, 21
-crossline, 41, 87
of a well, 38
of intersection, 81

Downloaded 25 Jun 2012 to 95.28.162.50. Redistribution subject to SEG license or copyright; Terms of Use: http://segdl.org/

segments, 145
structure perpendicular to, 8
-and trace spacing, 326
Linear,
compaction trend, 320–321
patterns on this residual, 256
Linearized AVO inversion, 332
Linearly decaying to zero, 228
Lineation, 131
with the correct slope, 239
of locally higher amplitudes, 204
Lineations, 59, 589
of event terminations, 75
of NNW-SSE, 256
Link to the seismic, 329
Lisburne,
carbonate section, 140
carbonates, 141
field, 140
reservoir, 140
section, 141
3-D survey, 131
Lithologic,
changes in reservoir, 209
detail, 219
and fluids, 333
vs. fluid properties, 333
vs. geometric, 209
Lithographic,
information, 185
Lithology, 7, 194, 312, 315–316, 323
and fluids, 310
vs. fluids, 327
type, 326
Lobes, 49, 611
within sands, 223
Local,
amplitude maxima, 203
of peak or trough, 90
environment, 194–196
plane, 256
Localized intrusive rock, 53, 56
Location data, 87
Locations,
offset source and receiver, 593
Log,
analysis, 327
editing, and rock properties, 313
crossplots, 315
curve, 324
data, 314–317, 331
filter, 326
high-cut filtered to the frequency of
seismic data, 326
interpretation software packages, 314
are preconditioned (filtered and resampled), 323
depth of, 214
processing, 313
vs. seismic data, 325
suite, 314
Logarithm of impedance, 330
Logs, 313
Longitudinal waves, 590
Loop area, 283
Loss of resolution (high frequencies), 323–324
Louisiana and Texas, 395
Low,
acoustic impedance,
contrast, 141
reservoir, 220
-density/high velocity, 314
end of the seismic band, 329
frequencies, 311, 317, 323, 327, 335
in absolute impedance logs, 320
are removed, 318
instantaneous frequencies anomalies, 185
to high frequency, 299
-pass filter, 329
side lobes, 49
surface redundancy, 594
values of density, 314
Low-amplitude, 156
events, 37
lineament, 142
seismic reflection, 141
surrounding area, 221
zones, 59
Low-frequency,
components, 299
data, 318
differences, 322
from log data, 312
and high frequencies, 326
information, 312, 317
model, 328, 330–331
replacement, 328
response, 591
test, 323
“trend,” 326
version, 311
Low,
impedance, 182
areas, 219
gas sand, 50
interval, 51
layer, 182, 610–611
reservoir, 219
sand or salt, 316
velocities, 322
velocity gas sand, 185
travel through, 181
instantaneous frequency, 185, 318
Lower,
acoustic impedance, 315
-amplitude equivalents downdip, 171–172, 176
amplitude feature, 141
anomaly, 182
-frequency seismic wiggle, 324
green horizon, 156
and higher frequencies, 330
-impedance hydrocarbon, 299
left point bars, 275
sand, 162, 317
signal to noise ratio, 185
Lower Cretaceous unconformity, 140–141
Lowering of frequency, 185
Lowest,
/highest frequencies, 328
amplitudes, 90
frequencies, 323

Downloaded 25 Jun 2012 to 95.28.162.50. Redistribution subject to SEG license or copyright; Terms of Use: http://segdl.org/

point, 81
values of P-impedance, 326

M
Mahakam delta in Indonesia, 113
Magenta and blue, 257
Magnitude,
of acoustic impedance, 161
and polarity, 206
of tuning effects, 211–214
Mahogany salt sill, 81
Mainstream interpretation systems, 21
Major,
growth fault, 239
faults, 87. See also faults.
Malaysian carbonate buildup, 53, 56
Manual,
approach, 89
to project, 89
amplitude mapping, 124
Map, 21
for the anticlinal structure, 61
of color, 32–33
extent and structure of the turbidite, 597
manipulation, 87
raw contour of the horizon, 61
of throw, 239
virtual distribution of sand, 275
Mappable reservoir interval, 230
Mapping, 23, 257, 323
of fault series, 239
of growth structure, 239
net pay, 230
process, 256
structure, 239
of times, 126
Maps, 140
Marginally inferior color contrast, 37
Marine,
acquisition, 591
data, 274
data acquisition, 590
shale, 142
streamers, 591
surveys, 591, 593–594
3-D surveys, 590–591
Marker surfaces, 313
Mathematical,
impedance, 330
limitation, 328
Maxima, 208, 211
Maximum,
acoustic response of the interval, 210
amplitude, 24, 62, 224
of the top reflection, 121
in the waveform, 224
amplitudes,
of peaks and troughs, 91
composite amplitude, 209
density, 33
pore volume, 232
thickness, 163
Mean of the reflectivity spectra, 329
Meander loops, 121
Meandering channel, 121
stream channel, 18, 128
system, 112
Meaningful patterns, 257
Measured,
impedance logs, 313
thickness, 204
Median amplitude, 298
Merged inversion, 324
on the right, 324
Merging of the low frequencies, 323
Merits of horizon amplitude, 275
Method and benefit of fault slicing, 239
Methodology for quality control, 309
Methods,
of interpolation, 320
of inverting seismic data-general considerations, 327–328
Mexican marine area, 145
Mid-Miocene, 112
to Pleistocene, 112
Midpoint of the interval, 281
Migrated,
is reliable, 18
data set, 140
data volume, 587
data volumes, 290
example, 593
Migration, 81, 593, 595
algorithm, 312
algorithms, 595
aperture, 589, 595
distance, 17, 595
effect on 2 and 3 dimensions, 8
and horizontal resolution, 7
operation, 595
post-stack as pre-stack, 595
process, 595
functions of, 7
visibility of a channel after, 13
volume often, 13
vs. two-pass approach, 81
Minimum phase, 590
assumption, 590
Miocene,
deltaic fans, 121
gas reservoir, 53, 56
karst topography, 103
Miscorrelation, 128
Mispositioning of reflections, 214
Missing,
frequencies outside seismic bandwidth, 317
low frequencies, 317, 320
Mississippi River, 112
Mistie map, 87, 89
Mobile shale, offshore Sabah, 178
"Model-based inversion," 329
Model, 50, 311–312, 317
-based inversion,
algorithms, 328
methodologies, 320
-based system, 326
based on input logs, 330
data, 49

Downloaded 25 Jun 2012 to 95.28.162.50. Redistribution subject to SEG license or copyright; Terms of Use: http://segdl.org/

to define layers, 330
to describe the subsurface, 309
the earth, 329
low-acoustic-impedance wedge, 311
quality control of, 594
or rock property values, 317
of the subsurface, 329
for testing, 322
3-D migration, 10
Modeled AI layer (wall AI in black), 317
Modeling, 50, 233, 330–331
Models, 49
Modes of display, 185
Monitor vs. base survey
and streamer featuring, 592
Most-positive curvatures, 290
Movement,
application, 595
to subsample accuracy, 333
Movie projector, 23
Mud volcano, 178
Multichannel processing, 16
Multi-trace processes,
DMO, 593
Multicomponent recording, 591
Multiple,
angle-stack seismic data, 331
attributes, 290
color bars, 37
contacts and transmission effects, 181–185
maxima or tuning curve, 208
regression analysis, 294
wavelet side lobes, 207–208
wells, 290, 330

N
Narrow frequency bands, 298
Narrower band wavelet, 49
Natural pairing, 1, 36, 158, 222
Nature,
of fluid, 219
of impedance data, 309
of the wavelet, 203
Near-field pressure measurements, 590
Near-affect traces, 290
Near-stack amplitude information, 331
Near-surface,
absorptive losses in, 592
effects, 592
model, 594
Near traces, 331
Near-zero angle, 330
Negative curvature, 290
Net-to-gross 219–220
Net,
gas/gross sand ratio, 228–229
gas isopach stage, 230
gas and maps, 229
gas sand information, 229
pay, 7
pay thickness, 228–230
is greater, 219
or net-to-gross ratio, 219
thickness, 232
Neutral grays, 59
New geological model, 2
Nigeria's fault slice, 239
Ninety-degree phase, 56–57, 182
condition, 52
data, 53
Ninety-degree phaseness, 182
No,
stacking, 188
tuning effects, 211
Noise, 2, 24, 50, 256–257, 298, 311, 591
coherent and source generated, 592
level, 203
model and remove, 594
or multiples, 211
random and coherent, 594
robustness in the presence of, 329
on the streamer, 591
Noisy, 283
data, 257
Nomogram, 33
No-permit zones, 26
Non-hyperbolic normal moveout, 594–595
Non-reservoir reflections, 158
Nonlinear,
frequency vs. time functions, 592
sweeps, 592, 593
Nonproductive segments, 223
Nonuniform thickness, 127
Nonuniqueness, 329
Normal-incidence seismic rays, 330
Nonzero incident angle, 330
Normal,
amplitude display, 290
moveout, 185
movement, 188, 591
Norms, 329
North Dakota's Williston basis, 103
North Sea, 166, 274
Danish sector, 318
prospect, 275
North slope of Alaska, 140
North–south faults, 257
Northeasterly lineations, 221
Northern,
dip-controlled boundary, 221
part of Vienna Basin in Austria, 163, 165
reservoir boundary, 221
Northwest shelf of Australia, 163, 167, 176
Norwegian North Sea, 130
Notching, 299
Number,
of iterations, 330
of seismic samples, 329
of zero crossings, 275, 287
Numeral color contrast, 33

O
(OBC) ocean-bottom cable, 590

Downloaded 25 Jun 2012 to 95.28.162.50. Redistribution subject to SEG license or copyright; Terms of Use: http://segdl.org/

OBC/OBS acquisition and processing techniques, 591
(OBS) ocean bottom seismic, 590
Obstacle avoidance, 591
Octave wavelet, 49
Offset-near offset amplitude, 188
Offset,
and azimuth,
distributions are more uniform, 593
dependence, 592
distribution, 26, 594
range,
Offshore lateral velocity variation, 594
source and receiver locations, 593
Louisiana, 244
Norway, 53, 56
reservoir,
fluid movement in, 591
Oil-bearing interval, 287
Oil-water contact, 184, 184
Oil, 157
reservoirs, 157
Old rocks, 196
Older rocks, 161, 196
One active wavelet, 214
Operator, 329
Opposite polarity, 188
Orange,
line, 235
lines, 124
reflection, 178
straight line, 235
Original modeled date, 323
Orthogonal,
array, 21
faces of the solid. 61
slices, 81orthogonal velocity sensors, 590
Outcrop, 324
Output amplitudes, 594
"Overprint," 335
Overall interference pattern, 299
Overlay for the reservoir reflections, 194
Overlain structural contours, 128
Overlaying formation, 142

P
Paired high-amplitude reflections, 181
Paleocene deep-water play, 145
Parallel to bedding, 57
Parent growth fault
Partial stacking, 188
Parametric approach, 330
Patches of porosity, 127
Patterns in amplitude, 145, 167
Peak-over-trough, 158
Peak, 41, 61, 87, 275
and lake, 49
and side lake, 49
and trough. See also amplitude peak and trough.
or trough, 49, 50, 216
to trough, 157
Peaks, 34, 35, 36, 90, 91, 126
and troughs, 45, 158
Pederson-Tatalovic paper, 318–320
Perfect velocity relationship, 214
Performance of an autotracker, 257
Perimeter areas, 589
Periphery of reservoirs, 203
Permeability, 247
Petroleum areas, 3–4
Petroleum Development Oman, 412
Petrophysical,
lithotype discrimination, 331
relationships between sands and shales, 332
Petrophysicists, 312
Petrophysics, 233
Phantom horizons, 88
Phase, 90, 587
centered on zero degrees, 91
and amplitude displays, 91
amplitude spectra, 593
assessment, 53, 56
change, 158, 171, 176, 188, 194
change polarity reversal, 161
changes, 196
change/bright spot combination, 161
circles, 58
component, 299
distortion, 50, 51, 91
effects, 325
errors, 593
P-impedance,
charged by hydrocarbons, 315
cutoff, 315
data, 314, 325
log, 316
instability, 299
of the inverted data, 323
locked,
to the pilot sweep, 592
matching filters, 592
P- and S-impedance, 331, 332
P and S reflections, 188
P-wave,
bright spot, 188
dim spot, 188
impedance, 331
response, 188
velocity, 309
Phase,
ninety-degrees, 33, 56
and polarity, 53, 56–58
and polarity circles, 51, 64
and polarity errors, 189
and polarity indicator, 57
rotated, 311
rotation, 309
section, 91
of the seismic wavelet, 5
spectrum,
minimum phase, 592
of wavelet, 189
Phases,
different, 52
Philosophy of seismic interpretation, 1–2
Picking of defaults, 75
Pilot sweep,

Downloaded 25 Jun 2012 to 95.28.162.50. Redistribution subject to SEG license or copyright; Terms of Use: http://segdl.org/

used for correlation, 593
Pink,
arrows, 90, 216
line in the crossplot, 235
Pleistocene,
gas reservoir, 220
sediments offshore Louisiana, 223
Pliocene turbidite sands, Ha'py field, offshore Egypt, 163
Plot, 325
with data points, 317
is narrower, 326
Plotting model response, 211
Plots of the frequency spectrum, 326
Point bars, 121
Points,
along the triangular pattern, 230
on one waveform flank, 215
A and B, 215
P and T, 215
plotted for isochrones, 211
Polarities of reflections, 158
Polarity, 4, 45, 203
convention, 45, 157
convertor, 126
of the data, 181
and phase, 157, 192
and phase errors, 188–189
and phase problems, 181–185
reversal, 157–158, 171, 176, 178
and sea floor, 176–177
unknown, 214
Poor,
connectivity between reservoir compartments, 220
data, 88
volume, 232
Pore,
fill, 312
flood within rocks, 188
volume, 230–232
formulas/methods for, 231–232
Porosity, 194, 219–220, 230, 312–313
and depth, 165
development, 142
is higher, 219
map, 283
multiples, 230
trend, 142
vs. impedance, 326
Porous,
dolomite, 326
vs. tight data, 326
Positioning technology, 591
Positive,
curvature, 290
numbers, 323
seismic trace amplitude data, 328
Possibility of hydrocarbons for exploration processes, 331
Post-data surveys, 312
Post-interpretation computation, 25
Post-stack,
amplitude attributes, 275–281
attributes, 247
inversion, 330
or pre-stack data, 329
and pre-stack inversions, 328
inverted data set, 309
seismic inversion, 333
seismic trace inversion, 309, 311, 328
Positive,
identification of hydrocarbon indicators, 157
reflection coefficient, 328
Post-stack,
seismic data, 313
seismic inversion, 333
Potential,
artifacts, 589
real fault, 256
PP and PS reflectivity, 333
Pre-and post processing,
schemes, 313
sequences, 313
Predominant frequencies, 7
Pre-existing 2-D data, 80
Pre-inversion analysis, 313, 314, 316
Preliminary time, 313
Preprocessing of seismic data, 333
Presence/absence of color, 31
Presence of hydrocarbons, 194
Pressure and temperatures, 219
Pre-stack,
algorithms, 331
attributes, 247
data, 309, 327
data analysis, 595
depth, 317
inversion, 330
methods, 331, 333
migration, 594
model-based simultaneous inversion algorithm, 332
random noise attenuation, 595
seismic data, 188
Principle reservoir properties, 217
Principles,
of spectral decomposition, 295
in 3-D procedures, 88
Probabilistic assumption, 326
Probability density function (pdf), 331
Problems in log, wavelength, or seismic data, 313
Probable shallow gas, 53
Procedure for 3-D interpretation, 87
Processed,
data, 49
data volume, 592
seismic data, 45
seismic trace, 208
Processing, 314, 326, 327
algorithms, 589, 591
cost, 594
developments, 81
parameters, 313
report/flow, 312
sequence, 312
Producing interval, 156
Product of velocity and density, 315
Production data,
first-arrivals, 594
Production platform, 22
Productive lobes, 324
Prograding, 324

Downloaded 25 Jun 2012 to 95.28.162.50. Redistribution subject to SEG license or copyright; Terms of Use: http://segdl.org/

Prominent faults, 75
Propagation, 473
Proper imaging, 17
Properties of the reservoir, 209
Proportion of sand within a sand/shale interval, 224
Proportional slices, 127
Proportionality, 209
  of fault slices. 239
Proximity of fault slices, 239
Prudhoe Bay,
  Field, 140
  gas cap, 140
Pseudo-acoustic-impedance logs, 309
Pseudo-checkshot data, 326
Pseudo-volume of shale (VSH), 331
Pseudo-well, 323
Psychological impact of color, 58–59
Purple color, 162
"Push-button" inversion, 311

Q
Quality control, 313
  of input data, 335–337
  measures, 590
  of seismic-derived inverted data, 312
Quality,
  of the initial model, 330
  of the input data, 312
  of the well tops, 313
Quantitative,
  numbers, 231
  study of the reservoirs, 209
Quarter,
  of a wavelength, 121
  wavelength, 232

R
Radical faults, 274
Radon, 594
(RAI) relative acoustic impedance, 328
Ranges,
  of impedances, 314
  of P-impedance, 314
Rapid,
  delineation of target bodies, 312
  lateral velocity variations, 595
Ratio of amplitude of tuning maximum to baseline value, 210
Raw,
  crossplot, 211
  data, 326
  tuning cube, 298
Raypath, 591
Real,
  data, 50
    in a carbonate environment, 326
  subtle faults vs. noise, 257
  trace, 188–189
Receivers on water bottom, 188
Reasoning variance explained, 294
Receiver axis, 591
Receiver,
  lines, 26
  ghost, 591
  notches, 591
  offset, 247
  problem, 590
  response, 44
Recommended workflow, 295–298
Recognition of depositional features, 38
Reconnaissance tuning cube, 295
Recorded,
  data, 590
  traces, 26
Recording, 590
  channel,
    a single geophone per, 592
  parameters, 26
  scales, 594
Recursive,
  algorithms, 328
  inversion (trace integration), 328
  or trace-integration algorithms (RTI methods), 327
Red-over-blue, 26
Red/yellow in the center, 56
Red,
  event, 50, 61–62
  trough, 52
Recording,
  sensors, 590
  system, 590
  vessel, 590
Recursive, 329
  inversion, 311, 329
Red, 158
  arrow, 204, 320
  arrows, 257, 274, 287
  red blob, 127
  or blue data ranges, 326
  and blues, 281
  and blue extremities, 36
  and blue structure reflective, 275
  contact, 184
  correlates with blue, 176
  for gas on salt, 221
  to green to blue, 299
  for limitations, 290
  polygon, 256
  reflection, 220
  trough, 157
  and yellow, 257
  and yellow patches, 256
Reducing impedance reduces contrast amplitude, 219
Reduced coverage, 593
Reduction in cost, 591
Reds and oranges, 129
Red-green-blue blending,
  of amplitude, 299
Red-over-blue, 50, 176, 181–182
Red-over-blue to blue over-red, 158
Red-over-blue and blue-over-red, 181
Red/yellow center, 53
Red-over-blue character, 57

Downloaded 25 Jun 2012 to 95.28.162.50. Redistribution subject to SEG license or copyright; Terms of Use: http://segdl.org/

Reciprocal of the octave bandwidth, 214
Recognition of characteristic shape, 103–121
Reconstruction of a depositional surface, 121–126
Reducing in visibility, 196
Reference surface parallel, 239
Reflected energy, 206
Reflecting,
  horizon, 188
  surface, 61
Reflection-coefficient series, 156, 312. See also isochron.
Reflection-amplitude, 58–59, 141, 275, 283
Reflection, 44, 53, 189
  from the base, 189
  coefficient, 206, 590
  (seismic trace), 328–329
  energy, 275, 299, 595
  events, 325
  heterogeneity, 299
  identification, 188–193
  Lower Cretaceous unconformity, 140
  red flat spot, 34
  segments
  spatial continuity, 112
  tracking of a, 127
  strives RC, 311
  strength, 275
  strength, 52
  terminations, 52
  within a data volume, 62
  from the top of the reservoir, 157
Reflections, 1, 34, 36, 49, 56, 103, 145, 203, 216, 610
  below the black arrow, 188
  closely-spaced, 203
  continuous, 61
  equal, 203
  from a gas sand, 188
    have moved around, 13
    normal, 274
  from hydrocarbons, 166
  multiples, or noise, 161
  in neighborhood of objective, 192
  occur, 216
  points of depth of normal, 8
  from shallow gas, 53
  top and base, 203
  top and bottom separate, 232
Reflective,
  energy, 278
  material, 299
  subsurface amplitude heterogeneity and noise, 298
Reflectivity, 10, 329, 333
  to acoustic impedance, 328
Reflectors, 325
Reflected energy, 304
Regional,
  gradient, 317
  project, 331
Regridding, 326
Regular,
  pattern basis, 287
  time slice, 274
Relationships with low-impedance data, 317
Relative,
  acoustic impedance, 194,
    data at the wells, 329
  amplitudes, of peaks, troughs, and side
    lobes, 51
  clastic values, 334
  fluid discrimination, 331
  inversions, 328
  strike of fault, 274
Reservoir, 142, 188, 194, 203, 214, 215. See also base sand impedance for a reservoir.
  fluids, 140
  identification, 189
  interfaces, 203
  layer, 214
  limitations, 216
  on the log, 214
  models, 194, 196
  periphery, 203
  reflections, 194
  thickness, 189, 204
  thins, 203
  thinner ports, 203
  tuning effects, 211
Responses: water sand, gas sand, lignite bed, basalt bed, 188
Reworked bar, 113
Richer wavelet, 207
Right polarity, 189
Rim syncline, 80

S
Salt, 221
  narrow events around, 80
Salt diaper, 11, 80, 81
Salt dome, 21, 103, 162, 274, 275
Salt/sediment interface, 81
Sample values used, 257
Sampling, 16, 18
  improved offset and azimuth, 595
  inadequacies in, 593
Sand, 275, 287
Sand above the unconformity, 317
Sand bar, 126
Sand base, 206, 207
Sand bed, 206. See also bed.
Sand dipping, 13
Sand-filled channel, 38
Sand-filled channel or bay
Sand if thick, 159
Sand (in red arrow), 316
Sand, may be hydrocarbon charged, 316
Sand reservoir, 36
Sand is invisible, 316
Sands, 156, 281, 314, 315, 316
Sand/shale, 1
Sand/shale interface, 36, 127
Sands and shales, 161
Sands are tight and shaly, 223
Sand's horizon times, 224
Sand signature, 158
Sands isolated in massive shale
Sand thickened, 316

Downloaded 25 Jun 2012 to 95.28.162.50. Redistribution subject to SEG license or copyright; Terms of Use: http://segdl.org/

Sand, thickness of, 235
Sands/shales, 332
Sand vs. shale, 316
Sands vs. silts, 315
Sands,
  wells with more, 267
Sand-filled channel faces of a slap fan, 290
Sand thickness, 216
Sand top, 204
Sands (yellow and red dots), 314
Saturation, 32, 219
Scale,
  between narrow lines, 161
  differences, 324–327, 343–344
Scaled with a single factor, 228
Screening tool, 309
Sea state, 591
Seamount, 53, 56
Search-and-gather operation, 124
Second,
  derivatives of structure, 257
  dominant frequency, 287
  interface, 312
  maximum is evident, 210
  wavelet, 207
Secondary,
  factors affecting amplitude, 233
  or splinter faults, 239
Sections,
  spliced, 81
  and well data, 87
Sedimentary,
  pod, 203
  reflections, 57
Sedimentary thickness, 299
Seed points, 87
SEG,
  Distinguished Lecture video, 323
Segmentation of the reservoir, 239
  recommendations,
  re: vibrator, 592
Seiscrop Interpretation Table, 23
Seismic,
  amplitude, 87, 124, 219, 224, 233, 312
  and attributes, 216
  analysis,
  attributes, 87, 217, 231
    as information source, 233
  attribute analysis, 257
  attribute and rock property, 294
  band, 328
  bandwidth, 327–328, 329–330
  character,
    of the water bottom, 53, 56
  cube, 326
data, 61, 157, 189, 216–217, 299, 309, 311–312, 316–317, 322–324, 326, 329–330. See also color schemes.
  contrasting color schemes
    band-limited nature of, 315
  display, 23
  frequency measurement, 287
  horizons, 126, 329
  interface properties, 331
  interpretation, 2
  interpreter, 19, 178
  inversion, 330
  inverted, 317
    inverted back to AI, 317
  line,
    information on a, 31
  logs, 12
  movement, 24
  period, 204
  phases,
    at one unique time, 87
  processing, 157, 326
    information, 313
  properties, 326
  quietly improves, 166
  range, 317
  rays, 330
  reflection, 1
    identification, 189–192
  reflections, 203, 223
    at P and T 214
    sources of, 52
  of a reservoir, 219
  resolution, 1
  response, 214, 216, 312
  resourcing power, 4
  revolution, 314
  (separation and visibility), 304
  sections, 325
  signature, 203
  signal, 4, 112
  source, 590
  survey, 489
  surveys, 333
  theory, 324
  trace, 214, 328
  traces, 325, 329
  travel time, 214
    addresses structure, 217
  and the use of color schemes, 36
  value, 233
  velocity, 4
  visibility, 7, 203
    of the beds, 7
  volume, 323
  waveform, 87, 90–91
  wavefronts, 7
  wavelength, 20
  wavelengths, 203
  and well data, 326
    scale differences, 325
  workstation, 320
Selection,
  attribute, 247
  chart, 32
Semicircular block event, 61
Semi-transparent data, 21
Sensible clipping, 24
Separation of effects, 221
Sequence,
  boundaries, 323
  of faults, 128
  stratigraphic impedance, 312
Series of frequency slices, 295
Set of well logs, 313
Shades of blue, 204
Shadow zones, 591
Shadowing effect, 127
Shale, 36, 81, 194, 196
  acoustic impedance, 196
  (in the arrow), 316

Downloaded 25 Jun 2012 to 95.28.162.50. Redistribution subject to SEG license or copyright; Terms of Use: http://segdl.org/

data, 332
interpreted from a fault slice, 239
limestone interface, 127
line, 332
Shale-dominated, 275
Shale-sand interface, 1
Shales,
(blue dots), 314
(in blue), 315
and sands, 314
Shale-to-sand ratio, 239
Shale,
to seal leaks, 239
wobble in, 316
Shallow,
deployment, 591
gas, 52, 56
horizon, 157
Shallow horizon,
in blue, 124
Shallow,
profile at Ekofisk Field, 517–519
reference, 128
water prospect, 128
Shape,
of sections, 61
of the tuning curve in detail, 224
of the wavelet, 203
Sharp,
amplitude terminations, 129
interface, 312
Shattering of a limestone layer, 81
Shear,
sonic data, 314
wave data, 188
wave information, 157
wave components, 590
waves, 188
wave velocity (clastic properties), 331
Sheet sand, 126
Shifts on data,
reduction in states, 592
Shooting configuration,
overlapped, 592
Short distances, 219
Shot lines, 26
Side lobe effects, 311
Side-lobe interference, 311
Side,
lobe levels of interfering wavelets, 210
lobes, 50
of the wavelet, 206
Signal,
attenuation, 592
bandwidth, 304
content,
continuity, 595
energy, 594
high-frequency, 592
Signal-to-noise, 281, 304
at each frequency, 304
decreases, 298
ratio, 7, 45, 52, 188, 299, 592
yields better imaging, 304
Signals true amplitude of, 594
Signature of red-over-blue, 158
Significance of spectral balancing, 298
Silts, 315
Similarity in shape, 208
Simple,
impedance layer model, 317
linear background, 320, 323
seismic cube, 312
Simulation algorithm, 330
Simulations, 330
Simultaneous,
AVO inversion, 332
inversion, 331, 333
Single,
blue-over-red signature, 224
gradient factor, 188
impedance decrease, 57
interface, 52
Single-polarity, 103
Single space-invariant scale factor, 233
Sinkholes, 103
SI (shear impedance), 327
Size,
of first side lobe, 214
of wavelet side lobe, 214
Slice, 21, 129
displays, 81
per frequency sub-band, 298
Slices, 22, 24
Slope fan, 290
Slump zones, 145
Small density increase, 178
Small-term reflectivity approximate, 330
Smearing of the seismic, 326
Smooth picked horizon, 275
Smoothed horizon, 256
Snapped horizon, 256
Snapped and smoothed version of horizon, 256
Snapping, 127
Society of Exploration Geophysicists, 309
Soft marine shale, 171
Sonic, 313
and density logs, 329
log, 329
values (low velocity), 314
San Jorge Basin of Argentina, 156
Source,
amplitude spectrum, 592
is flat, 592
arrays, 591
designation, 590
Source-generated noise, 593–594
Source,
ghost, 591
locations,
repeating, 592
and receive coupling variations, 593
and receiver,
geometry, 592
receiver lines, 593
Source signature, 590
Source-streamer axis, 593
Source,
wavelet, 44, 590

Downloaded 25 Jun 2012 to 95.28.162.50. Redistribution subject to SEG license or copyright; Terms of Use: http://segdl.org/

effects. See also source designative.
removal, 590
Southern Argentina, 287
South Texas, 287
Space,
the sampling theorem, 16
Space-variant scale factor, 233
Spacing,
and dips and velocities, 16
Sparse-spike algorithm, 311, 329
Sparsity criterion, 329
Spatial, 589
continuity, 87, 220
demonstrations of natural pairing, 222
distribution of net producible gas sand from seismic data, 224
extent of an anomaly, 103
interpolation, 233
irregularities, 26
patterns, 275
representation, 311
sampling, 591
simplicity, 591
smoothing, 127
smoothing filter, 257
statistics, 330
tracking, 20
variations, 593
in interference, 298
wavelength, 62
Spatially invariant time function, 593
Spectral,
balancing, 295
process, 298–299
step, 304
content, 590
decomposition, 304
effects, 591
notches, 590–591
response, 591
sequence of colors, 33
Spectrum, 208
Spherical divergence, 593
Splinter faults, 239
Spurious low frequency data, 328
S-section, 188
(SSI) sparse-spike inversion, 329
Stabilization, 329
Stacked,
amplitude, 188
gas reservoirs, 194
and migrated data volume, 247
Standard Alaska Production Company (BP Exploration-Alaska), 140
Standard color density, 311
Standard Oil, 140
Stack, 593
and lower fold, 593
traces included, 594
to be valid, 594
Stacking velocities,
dip dependence of, 594
Stacks, 333
Start/endtime, 142
Stated relief, 257
Static algorithms,
refraction and residual reflection, 593
Statistical,
analysis,
of the points, 211
of tuning phenomena, 233
identification of fluid contact, 239
program, 326
tuning curve, 210
tuning curves, 208–211
use of tracked horizon data, 233–239
Statistics of data, 325–326
Stat (statistical) slice, 247
Steam injection process, 13
Steep dips, 239, 595
around the intrusion, 80
Steerable streamers, 592
Steps look like faults, 257
Stippled,
areas, 24
regions, 24
Stochastic algorithm, 330
Stored one time and amplitude, 224
Straight high-dip pseudo faults, 257
Stratigraphic,
boundaries, 26
features, 18
Stochastically derived model, 333
Stratigraphic,
descriptions, 129
detail,
from 3-D data, 130
features, 103, 121, 275
information, 247
interpretation, 22, 26, 31, 243, 275
map, 597
objective, 44
patterns, 121, 127, 129
Stratigraphic/reservoir patterns, 128–129
Stratigraphic,
and reservoir striders, 283
Stratigraphy, 17
and structures' confusion, 121
Struck width, 126
Streamer,
acquisition, 591
depth, 591
feathering, 592
Streamers, 590–591
Streamer,
marine systems, 591
outer, 592
Streamers,
shallow deployment of, 591
Strength of the impedance, 304
Strike,
contours follow, 61
and dip, 8
direction, 593
east of the faults, 61
of a fault, 75
perspective, 61–72, 87, 121
and stratigraphic patterns, 121
Striking phase changes (polarity reverses), 176

Downloaded 25 Jun 2012 to 95.28.162.50. Redistribution subject to SEG license or copyright; Terms of Use: http://segdl.org/

Strike,
of the plane, 61
to the salt/sediment interface, 81
Strong,
amplitude effects, 299
fluid-contact reflection, 220
velocity decrease, 178
Structural,
boundaries, 217
continuity, 91, 171
contour map, 33, 61, 124
contours, 87
of 3-D and 2-D maps, 73
from horizontal sections, 62
overlaying, 178
detail, 73, 257
dip, 158, 181
is gentle, 121
errors, 589, 591
features, 75
horizons, 52
image, 593
information, 595
interpretation, 24, 37–38, 62
mapping, 62
position, 235
range, 221–222
reflections, 165
relationships, 87
/stratigraphic conflicts, 176
and stratigraphic information, 178
strike, 274
strike and fault strike, 73
Structurally,
dipping reflection, 184
interpreted horizon, 142, 247, 275, 290
Structure,
interpreted of a prospect, 75
map, 58, 126, 221
of the base of the gas, 162
maps, 224
of time and depths, 87
Structures, 145
Studies, 592
structure, stratigraphy, and reservoir properties, 247
time, amplitude, frequency, and attenuation, 247
Study, 229
Studying tuning, 210
Study of a reservoir, 223
Sub-area,
B, 235
C, 235
Subsurface,
coverage, 591
features, 299
information, 24
interface, 44, 53
position, 208–209
reflectivity, 593
rock,
and seismic data, 61
slab, 121
Subtidal to supratidal environment, 140
Subtle,
curvilinear features on dip, 257
discontinuities, 299
fault, 290
faults, 37, 75
structural features, 94
Successive surveys, 591
Surface,
acquisition grid, 589
area, 589
Signal bandwidth, 593
Surface-consistent amplitude compensation, 593
Surface,
abstractions, 593
areas around, 593
coverage, 26
and environmental constraints,
to geometry for a survey, 592
infrastructures, 589
of salt dome, 112
slices, 87
and subsurfaces area, 589
Subsurface, 590
interface, 56
objective, 21
regular points belong in, 8
structure and stratigraphy, 20
Subtle features, 87
Subtractive primary colors, 31
Sun shading, 257
Surface,
color, 32
normalization, 128
Surface-consistent processes, 593
Surface-consistent wavelength processing, 593
Surface,
noises, 592
obstructions, 593
Surrounding horizon surface, 257
Survey,
access, 26
area, 17, 112
acoustic impedance, 142
Survey,
cost, 591
data, 24
design, 16–19, 589
objectives, 18
orientation, 591, 593
Surveys,
energy sources, 593
ocean bottom, 592
recorded on land vs. streamer marina, 592
surface extent of, 589
with uniform fold, 594
Survival in the net isochron map, 229
S-wave,
data, 188
event, 188
impedance, 331
response, 188
velocity and density, 327
Sweet spots at low amplitude, 220
Symmetrical trough, 162
Syncline, 62, 81
Synthetic,

Downloaded 25 Jun 2012 to 95.28.162.50. Redistribution subject to SEG license or copyright; Terms of Use: http://segdl.org/

log data, 326
match, 329
seismogram, 44
seismic,
cubes, 322
data, 323
defined, 312
response, 329
set, 317
showing the prograding section, 324
Synthetic seismogram, 192, 20
Synthetic traces, 325

T
Tank data, 312
Target,
amplitude valve, 298
depths, 7
zone, 316
Targeted,
parameters, 298
tuning cube, 298
Tectonic movements, 121
Temporal thickness, 299
of the layer, 299
Tertiary,
clastic basins, 165, 221
clastics, 161
clastic environment, 93
clastic reservoirs, 203
sands and shales, 161
Test,
of a band-limited inversion, 326
of results of low frequencies, 323
of the trace impedance results, 325
Testing, 327
Thick,
uniform shale, 141
clastic reservoir, 220
Thickening sediments, 53
Thicker,
beds, 224
sands, 235
and thinner reservoirs, 232
Thickness,
of sand, 158
limitations, 275
of rock, 283
of the sand, 316
Thin,
beds, 203
black lines, 239
gas, 216
porous sandstone lenses, 204
productive lobes, 223
reservoir, 182
sands, 156, 216, 287, 316
stringers, 316
Thinner beds, 203, 216, 317
Thinning,
toward the edges, 324
wedges, 203
Third wavelet, 208
3-D,
analysis of post-stack amplitudes, 290
AVO projects, 2903-D data improvement, 8–15
data and 2-D data, 73
data volume, 87
data volumes, 21
data, zero phaseness, or a flat spot color, 165
depth point spacing, 18
display, 21, 188
forces models, 312
geologic models, 329
geometrics, 593
4-C survey, 188
or 4-D development or delineation, 334
history of, 2–3
imaging, 188
interpretation, 21–23
interpretation consultation, 87
interpreter, 21
issues, 7
map,
increased fault detail, 73
migration, 13
migration imaged reflections, 11–13
petrophysical property models, 312
seismic coverage, 395–412
benefit of, 2
data, 22, 216
experiments, 3
interpreter, 18
method, 3
survey, 140
the fundamental objective of a, 4
proper design of, 18
safety margin, 17
surveys, 3, 130, 145, 312, 595
volume, 16, 239
before migration, 13
of density, 320
Target for reserves in data set, 326
Thin events, 327
Three-D surveys, 593
Three dimensionality, 81
Throws, 142
Tie,
is reliable, 233
in reservoir property, 233
well data, 229
Tight limestones, 326
Time, 329
and amplitude of zero-phase reflections, 233
conversion, 313
delays, 325
Time-to-depth data, 313
or depth,
levels, 61
range analysis, 314
Time lapse,
surveys, 592
Time-lapse 3-D or 4-D, 591
Time-to-depth conversion, 326
Time-derived attributes, 247

Downloaded 25 Jun 2012 to 95.28.162.50. Redistribution subject to SEG license or copyright; Terms of Use: http://segdl.org/

Time-derived horizon attribute, 256–274
Time,
to frequency domain, 299
function,
spatially invariant, 593
horizon, 44, 50
interval, 87
map, 256
from Australia, 256
mapping, 141
maps, 224
misties, 192
separation, 206
shift, 127
slice, 21–22, 75, 81, 165
slices, 22, 87
(horizontal sections), 87
structures, 131
surface, 257
thickness and amplitude, 299
map, 224
measurement, 224
value, 256
Time-migration algorithm, 595
Time-migration velocities, 317
Time-structure maps, 128, 330, 597
Time-variant phase, 58
Time window, 274–275
Timing, posting, and contouring, 62
Top Balder reflection, 145
Top,
and base interval, 204
and base reflections, 162, 187, 203, 222, 224
of a bed, 57
reservoir, 182, 233, 275
Top and bottom,
base of sand, 216
of the correlative aquifer, 194
Top,
and fluid contact reflections, 203
gas reflection is clear, 178
gas sand, 178
horizon slice, 223
reservoir reflection, 165, 167, 184, 189, 203
from Oman, 256
of salt, 52
sand time, 233–235
axis, 239
water sand reflections, 178
Topographic mapping, 257
Total,
area crossplot, 235
drilling potential, 59
energy, 275
net producible gas sand, 230
quantity of sand, 275
Trace,
amplitudes, 589, 594
density, 51
increases, 593
deflection, 89
header, 24
high and low-cut filtered, 316
inversion algorithm, 326
spatial angles, 589
at well location, 45
Trace Field, 165
Traces, 326
Tracked,
horizon, 127
data, time, amplitude, 208–209
surfaces, 127
Tracker, 224
Tracking, 156, 257, 290
busts, 257
and editing, 87
of key horizons, 140
of sections, 87
Transform,
mathematics, 287
window, 295
Transforming data from seismic-reflection domain, 327
Transmission effect, 127
Three octaves, 214
Tidal and salinity effects, 594
Transparency, 21
Traps, 13
of the salt fare, 13
Trending lineaments, 142
Triplets and two pairs, 57
Trough, 61, 188, 275
distribution of, 41
(red), 158
(red event),
dipping west, 181
Troughs, 34–36, 90–91
Trough-over-peak, 126
True amplitude stack, 594
Truncate at an unconformity, 167–172
Truncating gas reservoirs, 171
Truncation, 141
of the Green Shale, 142
zone, 140
Tuning, 1, 203, 219, 221, 235, 311, 316, 325
in amplitude and time, 203–204, 209
in amplitude, 203
amplitudes, 204
maximum, 206
correction, 231
cube, 299
animations, 299
curve, 206–208, 211, 324–325
maximum, 207
effect, 165, 204, 209, 211, 214, 224, 311, 325, 328
in, 299
maxima, 210–211
mispositioning, 214
out, 299
phenomena, 203, 216
phenomenon, 34, 229
with reflections from fluid contact, 220
and resolution, 215
thickness, 203, 206, 210, 224, 228–229, 232, 304, 324
trend, 204
and unraveling the side-lobe effects, 327
Turbidite sand, 597
Twisting channels, 113

Downloaded 25 Jun 2012 to 95.28.162.50. Redistribution subject to SEG license or copyright; Terms of Use: http://segdl.org/

2-D,
interpretations, 23
lines, 8, 16
migration,
collapsed diffraction patterns, 11
survey depth points, 18
survey,
and sampling, 16
2-D and 3-D survey,
subsurface sampling, 18
2-D vertical section, 8
Two,
high-amplitude blue reflections, 182
strip/fringe widths, 17
Tying the reservoir, 215
Type,
of acquisition, 312
of amplitude, 290
extracted, 156
Tying reservoir on the log, 215

U
Uncertainties in the position of each well, 233
Uncertainty of well position, 233
Unconformability, 52, 53, 165
Unconformity, 131, 314, 316–317
horizon slices, 131–140
reflection,
improved continuity of, 11
surface, 142
sparse-like inversion, 329
Uniform,
acoustic properties, 224
embedding medium, 161
Universality, 208
Unobstructed shallow waters, 591
Unporous limestone, 127
Untuned baseline, 211
Upper,
amplitude anomaly, 181
green horizon, 156
Upthrown,
block, 239
side of fault A, 221
Usable frequency range, 299
Use,
of color, 87
of frequency, amplitude variations with offset and shear waves, 185
of machine provision, 257
of multiple attributes, 290–294
of net gas sand mapping, 230
User-specified subsurface area, 208
Uses,
of attributes, 247
of different types of attributes, 247
Using color, 90

V
V log data, 314
Valley fill, 299
Value,
of dip, 17
of impedance, 316
of interactive plotting, 233
of 3-D migration, 8
Values,
of geophysics in the production of Bay March and Field, 552–558
of shales, 316
used to determine the scale factor, 229
Variable,
area displays, 62
area/wiggle, 194
area sections, 89
area techniques, 89
area/wiggle trace, 51
clastic reservoir, 226
porosity, 221
shortcomings in, 35
thickness reservoirs, 232
Variance,
in the realizations, 333
reduction, 294
Variation,
of amplitude with recording offset, 185
with amplitudes, 188
of the attribute with in the window, 247
in reflection character, 131
Variations,
in fold, offsets, and azimuths, 593
of the near-bottom, 594
in surface geometry, 589
Variograms, 233
Velocities, 326
along different azimuths, 595
Velocity, 188
analysis, 595
corrections, 330
data volumes, 326
Velocity-dependent algorithms,
differences, 331
effects, 165
field, 594
fields, 591
model, 595
unchanged, 320
volume, 126
Velocity,
depth-to-time tie, 1
Vertical,
distribution within interval, 283
and horizontal section control, 257
and horizontal sections, 256
Vertical/horizontal views of data, 275
Vertical,
resolution, 4
section, 62, 141
on three horizons, 124
sections, 75, 87
seismic section,
intersects, 103
seismic sections, 103
stretching, 329

Downloaded 25 Jun 2012 to 95.28.162.50. Redistribution subject to SEG license or copyright; Terms of Use: http://segdl.org/

thickness (in time), 235
time as an axis, 239
Very-low-frequency check-slot data, 326
Vessel, 590
Vibrators, 592
Vibroseis, 592
data, 593
Visible channel, 121. See also channel.
faulting, 75
irregularities, 26
lineations, 235
Visibility,
amplitude/offset effects, 188
of thin beds, 204
Visual,
color contrast, 33–34
contrast, 33
increase in resolution, 325
Visualization, 2
and autotracking, 95–101
and visual integration, 413–447
Volcanic intrusions, 52
Volume,
concept, 19–28
of discontinuity, 274
content, 20–21
of continuity, 274–275
elements, 21
Volumetric,
attributes, 290
and curvature, 290
curvature, 290
display, 21
interpretation, 20
Voxels, 21
(VSH), 314
low-volume shale, 314

W
Water-bottom reflection, 53, 56
Water,
bottom, 52, 590
depth, 591
depths, 590
in pores of sand, 168
sand, 157–158, 161, 194, 196
with higher acoustic impedance, 161
sand to gas sand, 161
saturation, 313
values, 320
surface, 590
table,
variations in, 592
Wave,
amplitude, 188
equation consistent processes, 593
Waveform, 16, 44, 53, 56
Wavelength, 203. See also dominant wavelength.
calculate, the, 7
defined, 4
size of, 5
spacing per shortest, 16, 214
Wavelength-length slabs, 216
Wavelength fractions, 7
Wavelength thickness, 216
Wavelet interaction, 45, 210, 232, 304, 311, 329
central frequency, 323
frequency is increased, 317
Wavelet of known (zero) phase, 593
Wavelet in the model, 317
Wavelet to the next, 214
Wavelet overprint, 295
Wavelet in panel, 1, 312
Wavelet phase, 45, 592
Wavelet processing, 44, 593
Wavelet in the seismic, 328
Wavelet shape, 44, 211, 304
Wavelet side lobes, 312
Wavelet symmetry, 49
Wavelet is zero phase broadband, 328
Wavelet,
used to create synthetic seismic, 323
Wavelets, 5
Wavelets, 207, 312
of opposite polarity, 203
from top and base, 206
Waves modes-converted, 188
Wedge, the, 34
Wedge model, 309–311
Wedge thins, 311
Well, 38, 59, 208, 287
from a, 228
Wellbore, 330
Well calibration, 232–233
Well control, 327, 590
Well data, 312–313, 326, 330
correlation, 326
from L-7, 142
synthetic and seismic, 325
Well and geologic control, 330
Well 5X, 126
Well with highest amplitude, 233
Well intersection, 129
Well inserted, 194
Well location, at the, 73, 325, 329
Well log, 312, 325, 611
Well-log data, 313
Well logs, 239, 313, 330
Well logging, 312
Well response in character, 214
Well speed details, 313
Well ties, 233
Well tying and tuning effects, 214–216
Well value, 233
Well's measured property need, 233
Wells, 13, 22, 81, 129, 182, 233, 287, 294, 329
Wells used in the calibrations, 294
Well sand, 221
White areas, 90
White dots, 287
White points, 287
Whole interval, 156
Wide-tow geometrics, 591
Wide azimuth surveys, 594
Width of control peak, 207
Width of an event, 62
Width of the reflection,

Downloaded 25 Jun 2012 to 95.28.162.50. Redistribution subject to SEG license or copyright; Terms of Use: http://segdl.org/

seismic frequency, 103
Wiggle traces overlain, 311
Window, 145, 156, 247, 287
amplitude, 142
that calculated attributes, 283
of date, 287
definition, 156
mapped, 145
/time interval, 142
values, 247
Windowed amplitude, 142–156, 156, 275
attributes, 275
extracted over AB, 215
Windowed attributes, 257, 281
Workflow, 313
Workstation capabilities, 256, 335
Workstation sequence, 224
Workstations, 21–23
character, 182
data, 44, 52, 163, 203, 208, 224
two versions of, 58
Zero-phase equivalent wavelet, 208
Zero-phase European polarity, 57
Zero-phase expressions of single interfaces, 158
Zero-phase response, 50, 161
Zero-phase seismic representations, 311
Zero-phase wavelets, 44, 49, 58, 207, 211, 324
Zero-phaseness, 45, 49–50, 52, 224
of data, 281
Zoeppritz-Knott, 331
equations, 330–331
Zone of interest, 295
Zone 5, 142, 208, 313
of the Lisburne reservoir, 141–142

Y
Y=c-x form, 235
Yellow, 80, 211
Yellow-over-red, 182
Yellow curve, 211
Yellow and cyan, 163
Yellow sand, 216
Yellow tuning curve, 224
Yellow, green, and gray color scheme, 171
Yellow, red, and green, 290
Young rocks, 196
Younger to older sediments, 299

Z
Zero amplitude, 35
Zero crossing, 50
Zero crossings, 91
Zero density, 33–34
Zero phase, 44, 53, 56, 157, 162, 182, 208, 589, 593
bright spot, 158

Downloaded 25 Jun 2012 to 95.28.162.50. Redistribution subject to SEG license or copyright; Terms of Use: http://segdl.org/

Considerations for Optimum 3-D Survey Design, Acquisition and Processing

Contributed by R. Malcolm Lansley
Sercel, Inc.

General Issues

The ideal 3-D seismic survey would have offset and azimuth distributions which were spatially very consistent. This means that the fold would have to be high. Cost considerations, environmental concerns, topography, and the effects of surface infrastructure and other obstructions, usually result in the surface acquisition grid being quite coarsely sampled and the offset and azimuth distributions being less than uniform. These irregularities can cause difficulties in data processing and frequently result in significant spatial variations in the amplitudes and phase of the final data volume used for interpretation. Structural errors may also result. Because the variations in trace attributes follow the variations in the surface geometry used for the data acquisition, these effects cause an **acquisition footprint** or pattern of data acquisition lineations. Special processing algorithms may be required to minimize these effects, but they are almost always present at some level on every data set. Prior to the interpretation of any data volume the interpreter should become familiar with the acquisition geometry, the data processing flow, and potential artifacts that may have been produced. A careful balance between the spatial changes in trace attributes and the cost of the survey needs to be achieved during the design process.

There is also an important relationship between the spatial extent of the survey on the surface and the subsurface area that must be correctly imaged. In the early stages of survey design the necessary migration aperture is normally calculated and added to the image area (Figure 1-15). Once the data acquisition geometry has been designed, the appropriate fold tapers are added to the outside of the migration aperture, and this then defines the surface extent of the survey. Cost pressures frequently cause compromises to be made that result in the overall surface area being reduced. This leads to inadequate imaging of the target area that may result in the appearance of false structures, particularly near the edges of the survey. Furthermore, after data acquisition is completed, all of the data are sent to the data processing center and are used to create a migrated data volume. Upon completion of the data processing, the entire data volume normally is delivered to the interpreter and loaded onto the interpretation workstation. Only the central portion of this volume is correctly imaged, yet frequently the entire data volume is used for interpretation, including the perimeter areas which have less than adequate fold, incomplete offset and azimuth distributions, and are within the migration aperture.

Phase is one of the primary considerations for interpretation of the data volume (Chapter 2). In order to achieve a **zero-phase** interpretation wavelet, some fundamental

Downloaded 25 Jun 2012 to 95.28.162.50. Redistribution subject to SEG license or copyright; Terms of Use: http://segdl.org/

assumptions about the characteristics of the recorded data are frequently made in data processing. The most common of these are that the source wavelet and the response of the recording system and sensors are minimum phase, and that the amplitude spectrum of the source wavelet that was introduced into the subsurface was flat. If these assumptions are not satisfied, then additional processing steps may be required in order to phase match the seismic data to the well control and known geology.

Resolution is another important aspect of any survey. Both vertical and horizontal resolution are related to the wavelengths of the seismic energy being imaged (Chapter 1). Since wavelength is inversely proportional to frequency, higher-frequency data should result in better resolution. However, it should not be forgotten that low frequencies are also extremely important. Low frequencies provide much of the character for interpretation, critical bandwidth at depth, (where much of the high-frequency energy may have been attenuated by transmission effects) and are essential for good ties to borehole seismic. There are several places in the subsequent discussion where references are made to the spectral content of the data, and these considerations are very important in achieving the desired resolution for the survey.

Marine Data Acquisition

There are two fundamentally different methods used for data acquisition in marine environments. One of these uses hydrophones deployed in a streamer or streamers towed behind a vessel at a depth of a few meters, while the vessel moves at a speed of four or five knots. The seismic source may be attached to the same vessel or may be towed behind a separate vessel. In some deployments, several vessels may be synchronized to work together, each with one or more seismic sources and/or streamers. In the other technique, the recording sensors are allowed to sink to the ocean floor and are connected to a stationary recording vessel. These bottom-referenced systems are called ocean bottom cable (OBC) or ocean bottom seismic (OBS). The recording sensors used may be hydrophones, geophones, or both, and the latter technique, using both types of sensors, is called Dual Sensor[SM] (Barr and Sanders, 1989). In recent years this type of recording has been extended by the use of three orthogonal velocity sensors and a hydrophone (hence 4-component or 4-C) at each location. This permits the recording of shear wave components in addition to longitudinal waves.

Air guns are the traditional, and still the most widely used, energy source for the majority of marine 3-D surveys. There are two methods in common use for estimating and removing the source wavelet effects (source designature). The air gun arrays used are carefully tuned to optimize the amplitude spectrum and, in the first of these methods, are considered to be minimum phase. They are also configured with some redundancy of the air guns, so that if an individual gun or some small number of guns fails to operate, spare guns can be turned on to replace them and to maintain a consistent source signature. Quality control measures used to verify gun operation and timing are very comprehensive and, as long as the array specifications are not violated, the minimum phase assumption in data processing is reasonably correct. In the second method, the far-field source signature may be estimated deterministically from near-field pressure measurements in the vicinity of each of the individual air guns within the array (Ziolkowski et al., 1982). The source signature may then be used to design an inverse filter for source wavelet removal without invoking the minimum phase assumption.

In conventional marine data acquisition using streamers, there are several ways in which the amplitude spectrum of the recorded data can be compromised, both in overall bandwidth and in flatness. The water surface represents a strong acoustic impedance contrast which can result in significant ghost reflections and corresponding spectral notches. These are present both for the air gun arrays used at the source and also at the hydrophones within the streamer. The effect on the spectral content of the data will depend upon the source and streamer depths, the water depth, and the reflection coefficient of the water bottom. The receiver ghost problem can be solved by the use of bottom-referenced Dual Sensor data acquisition and processing. In

Downloaded 25 Jun 2012 to 85.28.162.50. Redistribution subject to SEG license or copyright; Terms of Use: http://segdl.org/

[SM] Dual Sensor is a service mark of WesternGeco

water depths up to approximately 130 meters (a physical limit of conventional ocean bottom systems) the conventional OBC/OBS acquisition and processing techniques work quite well. New data-acquisition technology now permits multicomponent recording with cables in water depths in excess of 2000 m, and for these water depths special processing techniques have been developed for managing the ghost effects. The source ghost theoretically should exist even on data acquired with dual sensors, although the spectral effects normally are not visible to the same extent as the receiver ghost notches, except in areas with hard water bottoms. For data recorded in these areas there are new processing algorithms that give good attenuation of the source ghost as well as the receiver ghost.

In unobstructed shallow waters or in deeper water there may be an operational preference for conventional streamer acquisition, but this will certainly result in significant spectral notches. Shallow deployment of streamers is frequently used to try to improve the high-frequency content of the data, but when the sea state worsens the noise evident on the streamer also worsens and may become the limiting factor. In order to reduce the noise, the streamer depth may have to be increased, which results in a very different spectral response, at both the high and low frequencies. It should be noted that the low-frequency response is increased and the high frequencies decreased with the deeper streamer deployment. Changes in either the source and/or the streamer depth within one survey should be avoided wherever possible. For reservoir monitoring using time-lapse 3-D (or 4-D as it is often called, Chapter 13), any changes in streamer and source depth between the recording of successive surveys must be avoided, because of both the noise differences and the spectral differences of the signal (Johnstad et al., 1993, 1995).

Another consideration for marine acquisition is the use of multi-boat, multi-source and multi-streamer surveys for obstacle avoidance and for reducing cost. Egan et al. (1991) showed that the differences in azimuth ranges when changing from an undershoot geometry back to a more conventional source-streamer geometry can cause artifacts in the processed data volume which result from the imaging processes. The current trend towards very large numbers of marine streamers with one or two source arrays towed behind a single vessel may also create problems. Beasley (1995) showed that some of these geometries can result in shadow zones with inadequate subsurface coverage which cannot be adequately resolved by the imaging processes in data processing, leaving both structural and amplitude errors in the interpretation data volume. Any of these wide-tow geometries may create problems for reservoir characterization and reservoir monitoring. If the water depth is not too great, Dual Sensor ocean-bottom cable techniques can resolve these problems, although this will almost certainly result in an increase in the cost of the survey.

The absolute positioning of marine surveys should not be a problem, with the accuracy of today's positioning systems, assuming that all of the appropriate corrections are made, and that current state-of-the-art streamer and source positioning technology is utilized. Because most marine surveys are recorded with the boat traveling in straight lines, survey orientation is still problematic. In areas with rapidly varying velocity fields, conventional wisdom now recommends the longest source to receiver axis being aligned in the strike direction (O'Connell et al., 1993, Manin and Hun, 1992, and Mougenot et al., 1992) in order to minimize the raypath complexity and thus make the normal moveout more hyperbolic (Figure 3-21). However, because the natural spatial sampling of streamer marine systems is typically finer in the inline direction than in the crossline direction, this results in coarser spatial sampling in the dip direction. This must be adequate to sample the geology or aliasing will occur. Another problem is that in complex geology there are not necessarily dip and strike directions, and therefore any survey orientation may result in imaging difficulties in the data processing stages.

For time-lapse 3-D surveys, Johnstad et al. (1993) showed that absolute positioning was not a critical factor and that marine 3-D surveys could be adequately repositioned to permit subtraction of the data sets to show fluid movements in an offshore reservoir.

Downloaded 25 Jun 2012 to 95.28.162.50. Redistribution subject to SEG license or copyright; Terms of Use: http://segdl.org/

However, it has been shown that minimizing the differences in the pre-stack offset and azimuth attributes between the base and monitor surveys is very important in reducing the seismic differences caused by the data acquisition. One method developed to achieve this is the use of steerable streamers to better match the streamer feathering of the monitor survey to that of the base survey. Another method described by Widmaier et al. (2003) showed that repeating source locations, together with an overlapped shooting configuration using additional outer streamers, improves azimuth preservation in 4-D acquisition. Also, by using a more closely spaced streamer configuration, source-receiver azimuths can be repeated very accurately.

An additional note is in order for ocean bottom surveys. Once the ghost removal has been accomplished, ocean bottom data are much closer in character to surveys recorded on land than to streamer marine surveys. Thus an interpreter who is familiar with marine surveys may experience some difficulty with the character of ocean bottom surveys.

Land Data Acquisition

In data acquisition on land, there are many factors which affect our ability to record broad bandwidth data with a good signal-to-noise ratio. One of the more significant of these is the use of arrays. We reduce the amount of noise recorded by increasing the size of the source or receiver arrays, but by doing so we may also attenuate the high-frequency signal. Significant energy absorption and loss of high frequencies also occurs in the unconsolidated weathering layers near the surface. If the geophones are buried, the effects of surface noises and the absorptive losses in the near-surface can be reduced. Pullin et al. (1986) showed a dramatic improvement in signal-to-noise ratio, high-frequency signal content, and reduction of static shifts on data recorded with a single geophone per recording channel buried 10 meters below the surface. Although the improvement was significant, geophones are rarely buried more than a few centimeters, except for reservoir monitoring studies. Here geophones or hydrophones are frequently deeply buried and left in place permanently so that they are available for subsequent monitoring surveys. This gives the added advantage that variations in the water table and other near-surface effects are minimized on subsequent time-lapse surveys.

When amplitude-versus-offset or amplitude-versus-offset-and-azimuth studies are planned, the use of linear source and receiver arrays to attenuate both coherent source-generated noise and random noise can be really problematical. This is because the arrays also attenuate the signal differently with offset and azimuth. Even if circular arrays are used to eliminate the dependence on azimuth, there is still an offset dependence. This signal attenuation is also frequency dependent, which makes a data processing solution very difficult to achieve.

When explosives are used as a land source, we can normally make the data processing assumption that the source amplitude spectrum is flat and that the phase spectrum is minimum phase. With vibroseis, however, the amplitude and phase spectra of the recorded data are frequently misunderstood. In order to optimize the data quality and minimize data processing difficulties, it is recommended that vibrators be set up such that the ground force signal of the vibrator is phase locked to the pilot sweep according to SEG recommendations (Geophysics, v. 59, p. 315-322) and that the amplitude spectrum of the fundamental of the ground force signal is controlled to be flat. When this is done and the data are processed correctly, the resultant vibrator data will be reverse polarity to data recorded with explosives. No additional phase matching filters should be required. The use of nonlinear sweeps (i.e., nonlinear frequency versus time functions) will require special treatment in data processing in order to handle the wavelet phase correctly.

The source and receiver geometry used for a survey is normally a compromise between competing factors: geologic objectives, environmental and other surface constraints, and cost. Quite often it is possible to see effects on the finally processed data volume which relate to the geometry used to acquire the data (footprint). These

Downloaded 25 Jun 2012 to 95.28.162.50. Redistribution subject to SEG license or copyright; Terms of Use: http://segdl.org/

effects will be reduced as trace density increases and offset and azimuth distributions become more uniform. The footprint is usually more visible in the shallow section than the deeper section because of the restricted offsets contributing to the stack and hence the lower fold. This problem can be reduced by acquisition of a survey with more closely spaced source and receiver lines. Great care should be taken in the areas around surface obstructions to minimize the variations in fold, offsets and azimuths. Reduced coverage often occurs because of rivers, lakes, villages, production facilities or unpermitted areas.

Data Processing

In data processing the objective is to maximize the useful signal bandwidth, to provide the interpreter with a correct structural image, and to generate a wavelet of known, usually zero, phase and amplitudes that represent, as closely as possible, the spatial variations in the subsurface reflectivity. Because amplitudes are fundamental in seismic analysis, correct management of amplitudes is very important in reservoir characterization studies. Also, as changes in amplitudes are of critical importance in reservoir monitoring studies, correct amplitude processing is essential. When wave equation consistent processes are being considered, inadequacies in the sampling will result in amplitude variations and phase errors, which are much more difficult to detect and correct.

An interpreter may be called upon to judge or suggest the applicability or effectiveness of an intermediate process prior to migration. This may be a dangerous step, even for the very experienced. It can be very difficult to evaluate the final result of some process on a shot or CMP gather before it has gone through the complete processing sequence including migration. It is always a good idea to request to see a migrated example both with and without the proposed process.

Great care should be taken in the initial steps of **geometry assignment and data initialization,** because most subsequent processes depend upon the geometry assigned at this stage. On land surveys, special attention should be paid to areas around surface obstructions to ensure that offset source and receiver locations are correctly assigned. In marine surveys, particular attention should be paid to the binning technique used, especially in areas where the source-streamer axis is in the strike direction. In this case, if the bin is made too wide in the crossline (and hence dip) direction, attenuation of high frequencies may result. Also, the use of overlapping bins should be used with care, because even though the fold of the resultant stack may be more even, amplitudes will be smeared and will require special management in multi-trace processes such as DMO.

A spatially invariant time function should be used for **spherical divergence and inelastic attenuation compensation**, and velocity-dependent algorithms should be avoided. Care should be taken to ensure that the amplitude recovery is based on the primary reflectors and not on the energy of multiples and coherent source-generated noises.

Three-D surveys typically have high surface redundancies that make **surface-consistent processes** very powerful. Surface-consistent wavelet processing, amplitude compensation, and static algorithms (both refraction and residual reflection) normally provide very stable solutions for most 3-D geometries.

In **wavelet processing,** it is important to ensure that the phase and amplitude spectra of the recorded data match the assumptions that are made in the deconvolution process. Particular attention should be paid to the phase and amplitude spectra of vibroseis data, especially when nonlinear sweeps are used or when surveys use more than one energy source. Because the pilot sweep used for correlation is normally filtered with the same instrument recording filters as the data channels, the phase effects of the recording filters are removed and the amplitude effects are squared. Thus the observed filter effects are very different between the vibroseis and explosive data. Also the field vibroseis correlation algorithms are normally zero-phase, and either a model-based or analytically derived inverse filter may be necessary to convert the phase and amplitude spectra.

Downloaded 25 Jun 2012 to 95.28.162.50. Redistribution subject to SEG license or copyright; Terms of Use: http://segdl.org/

Surface-consistent amplitude compensation will correct for source and receiver coupling variations and any further data-dependent amplitude scaling or balancing should be avoided.

The near-surface model used for long- to medium-wavelength **static correction** of land surveys is frequently derived from refraction analysis of the first arrivals of the production data. In some cases, the acquisition geometry may lead to some instability of the solution, particularly in areas with low surface redundancy around obstructions or near the edges of the survey. Rigorous quality control of the model is essential to ensure the integrity of the final structural image. Static corrections, although traditionally regarded as only being a problem for land data, are frequently necessary on marine surveys also. Compensation is required for tidal and salinity effects and residual statics may also be necessary to compensate for short spatial wavelength variations in the velocities and thicknesses of the near-water bottom layers.

Frequency-wavenumber (*f-k*) noise-attenuation algorithms work well for **attenuating coherent source-generated noise** (including multiples) as long as the data are well sampled spatially. They are not very good, however, at preserving true amplitudes, and should therefore be avoided wherever possible. With wide azimuth surveys, the characteristics of the noises may vary considerably along different azimuths because of different source and receiver array orientations. Alternative noise attenuation algorithms such as radon or *f-x* methods may be required to model and remove the noise. There are a wide variety of noise-attenuation algorithms available in the industry, and the ability of any particular algorithm to correctly retain true amplitude of the signal should be verified before its use.

Dip moveout (DMO) is used to compensate for the difference between the midpoint and the zero-offset point of data recorded with non-zero source to receiver offsets. In accomplishing this, DMO produces true common reflection point gathers and eliminates the dip dependence of the stacking velocities. It is, however, very sensitive to changes in both the azimuth and offset distributions of the data being processed. Even with perfectly regular geometry, the acquisition footprint caused by the normal spatial variations in offset distribution is frequently made worse with the application of DMO. Variations in fold and azimuths may also lead to strong amplitude changes and artifacts that are not truly representative of changes in the subsurface. Modifications to the DMO algorithms to compensate for these variations (e.g., Beasley et al., 1992) are available and should be used to minimize these effects. Unless prestack migration is going to be performed, DMO is a necessary step in the imaging process, even when the geologic dip is zero. However, it is frequently omitted from the processing sequence both as a cost-saving measure and also to eliminate any problems associated with its application on data that are inadequately sampled.

The amplitudes output from a conventional **common mid-point (CMP) stack** are normally corrected for variations in fold by a recovery scalar which divides the summed input trace amplitudes by the number of traces contributing to the stack. If the energy being stacked is pure signal, then the output amplitudes should be correct. When the input traces are subject to varying amounts of random and coherent noise, this recovery scalar will not result in a true amplitude stack. Although alternative schemes do exist to try to compensate for varying degrees of signal and random noise, the most consistent amplitudes will result from a survey that is recorded with as uniform fold as possible.

Another consideration for CMP stacking is the range of lateral velocity variation within the offset range being included in the stack. For the stack to be valid, any lateral velocity variations need to be sufficiently gradual such that the normal moveout for the traces to be included in the stack is hyperbolic. Where the velocity field changes too rapidly, and non-hyperbolic normal moveout is apparent, prestack depth migration should be performed. An additional issue that has become more evident in recent years is azimuthal velocity anisotropy. Modern land recording geometries

Downloaded 25 Jun 2012 to 95.28.162.50. Redistribution subject to SEG license or copyright; Terms of Use: http://segdl.org/

have become much wider in azimuth and much better sampled in offset. With the improved offset and azimuth sampling, it is often possible to observe different velocities along different azimuths. Unless the velocity analysis and moveout application comprehend these azimuthal variations, the CMP stack will be degraded.

Although significant improvement of signal continuity is frequently apparent after the application of **post-stack random noise attenuation,** some of the energy that appears to be incoherent may, in fact, be diffraction energy that should be preserved for the migration process. It is recommended that these algorithms be applied *after* migration.

In order to complete the imaging process and accurately focus the reflection energy at its correct spatial location and time (or depth), the process of **migration** is required. There are a number of different migration algorithms and methodologies that vary in their ability to handle steep dips and also in their inherent positioning accuracy. There is a considerable amount of literature discussing the strengths and weaknesses of different migration algorithms that is available elsewhere, so no discussion of algorithm differences will be made here. The accuracy of structural information from 3-D surveys is related not only to the accuracy of the migration algorithms, but also to the accuracy of the velocity field that is used for the imaging. It should be emphasized, therefore, that great care must be exercised in building an accurate velocity model for migration, particularly in areas of complex geology. Deregowksi et al. (1997) showed how small errors in the velocity field used for migration can dramatically reduce the lateral resolution in the final image.

The main decisions to be made with respect to migration are whether the migration will be performed prestack or post-stack, and whether a time or depth migration algorithm should be used. This selection is necessarily based on the complexity of the geology, the data acquisition geometry and, in particular, the severity of the lateral velocity gradients within the survey area (Figure 10-2). In a time-migration algorithm, the migration operator is spatially symmetric and therefore cannot correctly handle significant lateral velocity variations within the migration aperture. A depth-migration operator is spatially variable and is designed to accurately position data according to the travel paths defined by the depth and velocity model provided to the algorithm. The importance of the correctness of this model cannot be overemphasized, and close involvement of the interpreter in the development of the model is essential.

The processing expert should consider whether a post-stack migration will provide an accurate image, or whether a prestack migration will be necessary. As long as the normal moveout within the CMP gathers is hyperbolic, a post-stack migration should prove satisfactory from a structural-interpretation point of view. If the lateral velocity gradients are significant within the range of prestack source to receiver offsets and azimuths, then non-hyperbolic normal moveout will be apparent on the prestack CMP gathers and pre-stack depth migration will be necessary to correctly migrate the data. Survey orientation is sometimes carefully selected to minimize the effects of rapid lateral velocity variations (e.g., streamer marine acquisition in the strike direction), in order to permit the use of more economical post-stack migration algorithms. It should be noted, however, that because of an increasing requirement for prestack data analysis, the increase in computing power, and the development of more accurate and faster migration algorithms, prestack migration is becoming more and more common. Frequently, a post-stack migration may be just an intermediate product.

If it is determined that a post-stack migration will be adequate, and if the lateral velocity gradients are small compared with the required migration aperture, then a post-stack time migration should be satisfactory. If, however, the lateral velocity changes are significant within the spatial extent of the migration aperture, then a post-stack depth migration is required.

For reservoir monitoring studies, the velocity model used for the imaging of successive surveys should be the same, or small differences in migration distance might well be interpreted as changes in the fluid content.

Downloaded 25 Jun 2012 to 95.28.162.50. Redistribution subject to SEG license or copyright; Terms of Use: http://segdl.org/

References

Barr, F.J., and J.I. Sanders, 1989, Attenuation of water-column reverberations using pressure and velocity detectors in a water-bottom cable: 59th Annual International Meeting, SEG, Expanded Abstracts, p. 653-656 .

Beasley, C. J., and R. Klotz, 1992, Equalization of DMO for irregular spatial sampling: 54th Annual EAEG Conference & Exhibition, Extended Abstracts, p. 232-233.

Beasley, C. J., and E. Mobley,1995, Spatial sampling characteristics of wide-tow marine acquisition: 57th Annual EAGE Conference & Exhibition, Extended Abstracts.

Deregowski, S., R. Bloor, and C. Koeninger, 1997, Increasing lateral resolution: 59th Annual EAGE Conference & Exhibition, Extended Abstracts.

Egan, M. S., K. Dingwall, and J. Kapoor, 1991, Shooting direction — a 3-D marine survey design issue: The Leading Edge, v. 10, no. 11, p. 37-41.

Johnstad, S.E., R.C. Uden, and K.N.B. Dunlop, 1993, Seismic reservoir monitoring over the Oseberg Field: First Break, v. 11, no. 5, p.177-185.

Johnstad, S.E., R.H. Seymour, and P.J. Smith, 1995, Seismic reservoir monitoring over the Oseberg Field during the period 1989-1992: First Break, v. 13, no. 5, p.169-183.

O'Connell, J.K., M. Kohli, and S. Amos, 1993, Bullwinkle — A unique 3-D experiment: Geophysics, v. 58, p. 167-176 .

Manin, M., and F. Hun, 1992, Comparison of seismic results after dip and strike acquisition: 54th Annual EAEG Conference and Exhibition, Extended Abstracts, p. 4-5.

Mougenot, J.M., E. Robein, I. Ravat, and A. Morash, 1992, Design of 3-D land acquisition in a structurally complex environment: 54th Meeting, European Association of Exploration Geophysicists, Extended Abstracts, p. 8-9.

Pullin, N. E., L. W. Matthews, and W. K. Hirsche, 1986, Techniques applled to obtain very high-resolution 3-D seismic imaging at an Athabasca tar sands thermal pilot: 56th Annual International Meeting, SEG, Expanded Abstracts, p. 494-497.

Widmaier, M., S. Hegna, F. Smit, and E. Tijdens, 2003, Azimuth preservation in marine 4-D acquisition: 65th Annual EAGE Conference & Exhibition, Extended Abstracts.

Ziolkowski, A., G. Parkes, L. Hatton, T. Haugland, 1982, The signature of an air gun array: Computation from near-field measurements including interactions: Geophysics, v. 47, p. 1413-1421.

Downloaded 25 Jun 2012 to 95.28.162.50. Redistribution subject to SEG license or copyright; Terms of Use: http://segdl.org/

Interpretation Exercise

Background Information

The object of this exercise is to map the structure and extent of a turbidite sand, known from well control to be visible on the 3-D seismic data as a high amplitude peak. You are provided with two vertical sections (Figures B-1 and B-2) and eight horizontal sections (Figures B-3 through B-10). The coordinates of a point at which you can identify the turbidite reflection are:

Line 539
Crossline 600
Time 1,600 ms

Structural Component of Exercise

Follow the crest of the identified blue event on each horizontal section to yield a time structure map on this horizon with a contour interval of 20 ms. Be careful to follow structural continuity regardless of lateral changes in amplitude. Faults will be seen as lateral displacements, not simply as amplitude changes. As a guide, continuity without amplitude superimposed is visible directly along the adjacent zero crossings.

Stratigraphic Component of Exercise

Using the structure map to identify the high amplitudes associated with the turbidite, outline the dark blue areas for this horizon on each horizontal section supplied. Connect these outlined areas interpretively to yield a stratigraphic map of the extent and possible flow direction of the turbidite. Because you are supplied with horizontal sections at only 20-ms intervals, there will be some gaps in coverage in the direction of dip. More interpolation and smoothing will thus be needed in the dip direction than in the strike direction.

Procedure

Take a piece of transparent paper and register it on the annotation frame of the horizontal sections. Use the vertical sections as a guide to structural continuity only. Complete the structural component before attempting the stratigraphic component.

Solution

One interpreter's map of the extent and structure of the turbidite is shown in Figure B-11. This map is based only on the data supplied for the exercise. The horizon slice and superimposed structure that were generated interactively and based on all the data are shown in Figure B-12.

Downloaded 25 Jun 2012 to 95.28.162.50. Redistribution subject to SEG license or copyright; Terms of Use: http://segdl.org/

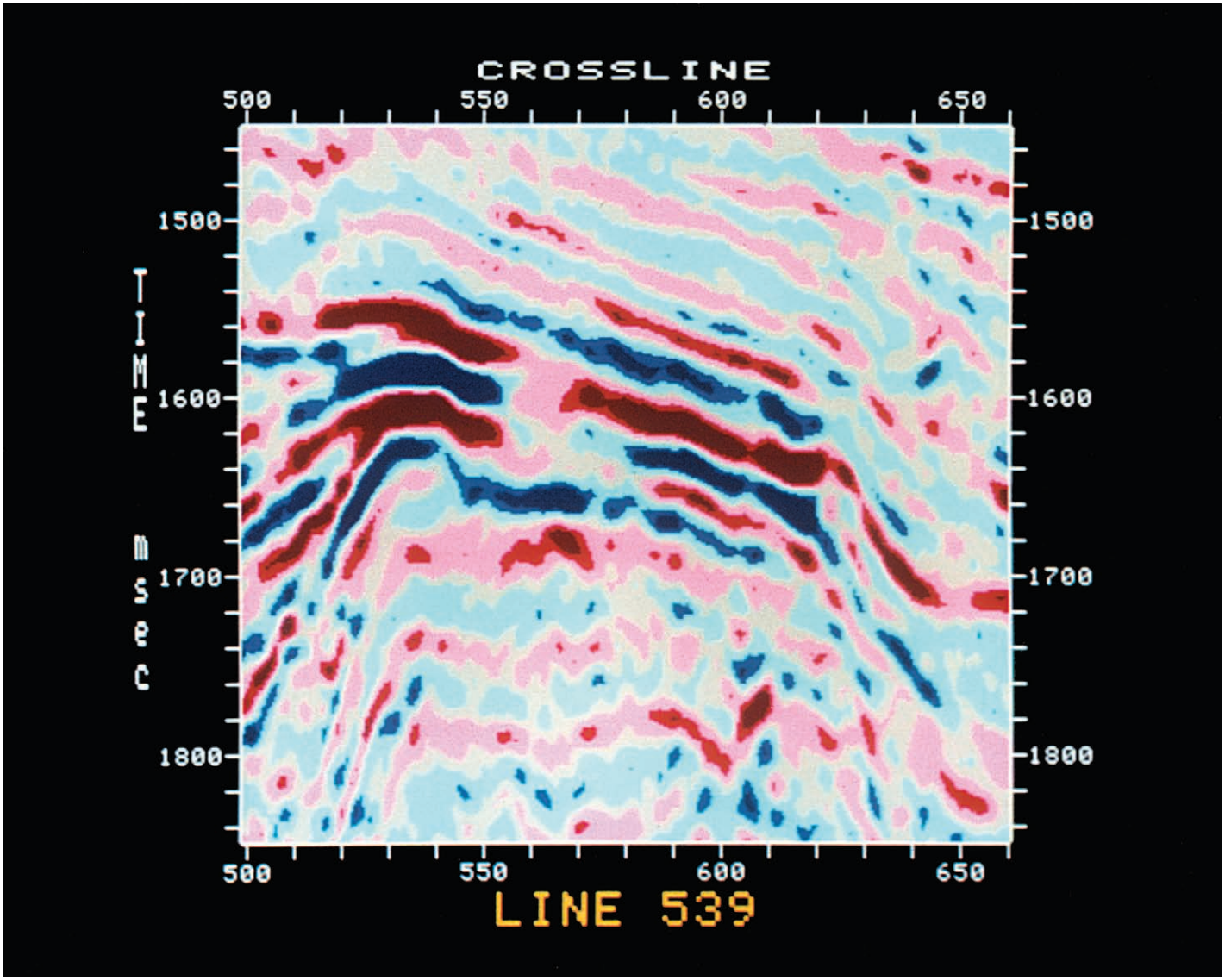

Fig. B-1.

Downloaded 25 Jun 2012 to 95.28.162.50. Redistribution subject to SEG license or copyright; Terms of Use: http://segdl.org/

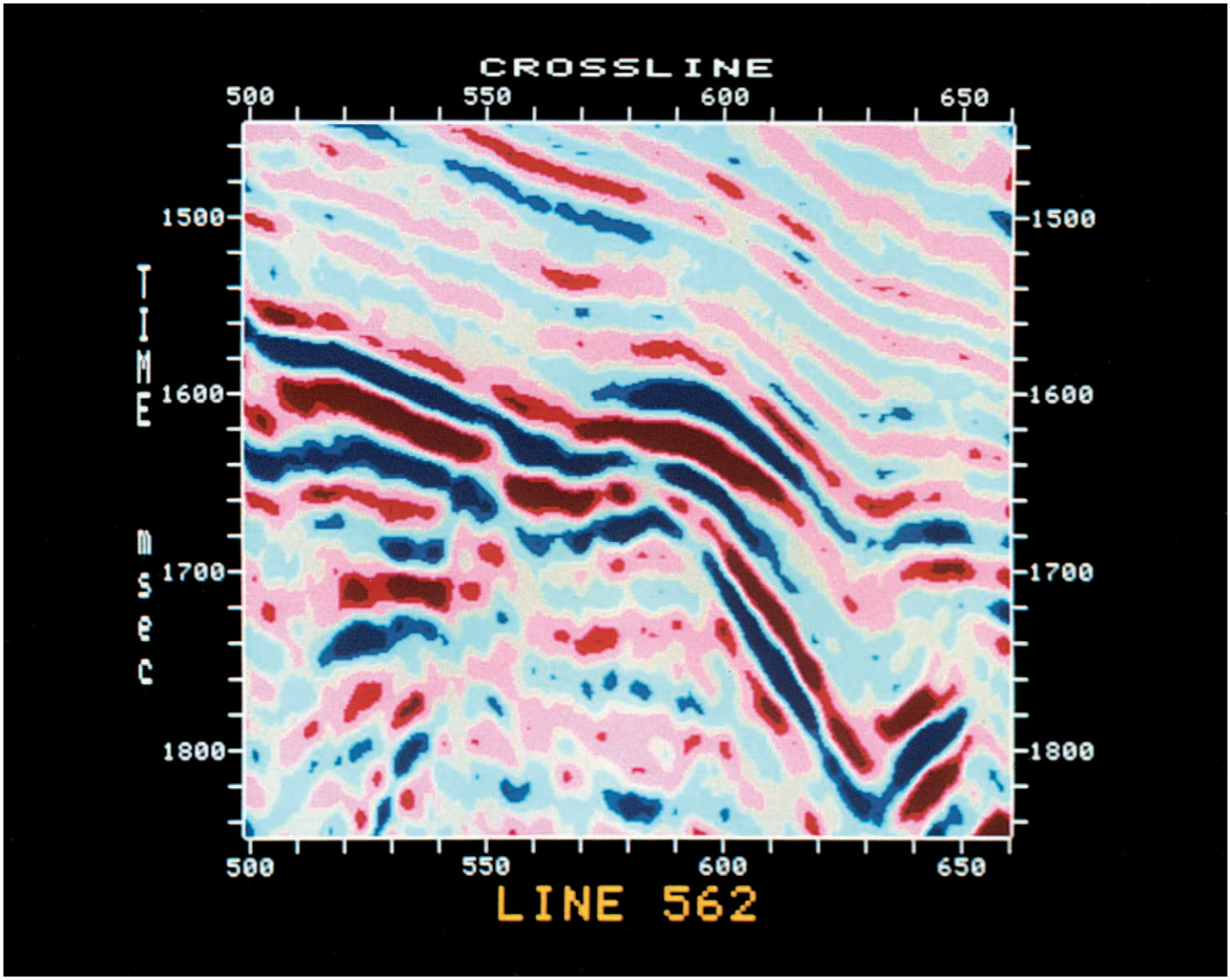

Fig. B-2.

Downloaded 25 Jun 2012 to 95.28.162.50. Redistribution subject to SEG license or copyright; Terms of Use: http://segdl.org/

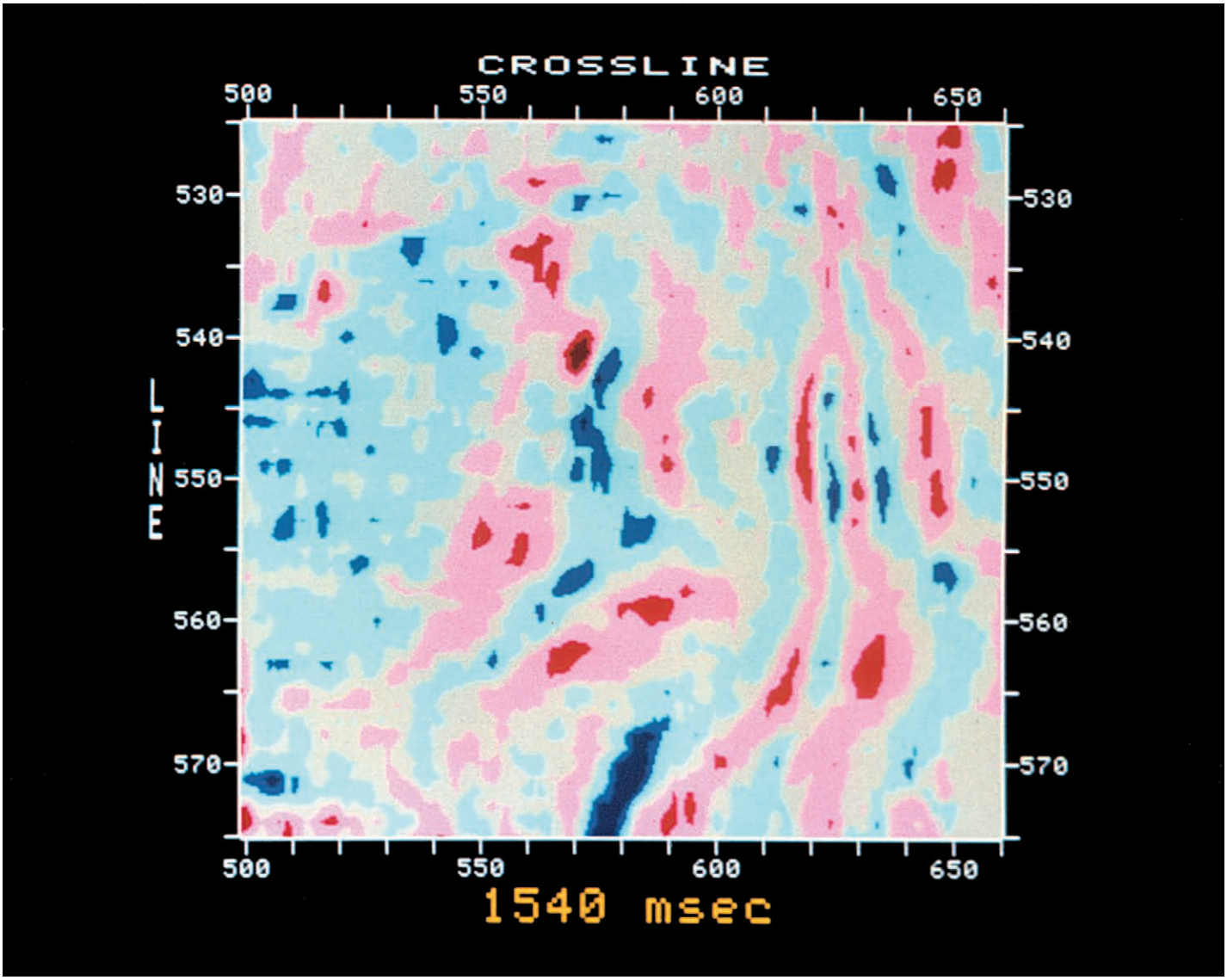

Fig. B-3.

Downloaded 25 Jun 2012 to 95.28.162.50. Redistribution subject to SEG license or copyright; Terms of Use: http://segdl.org/

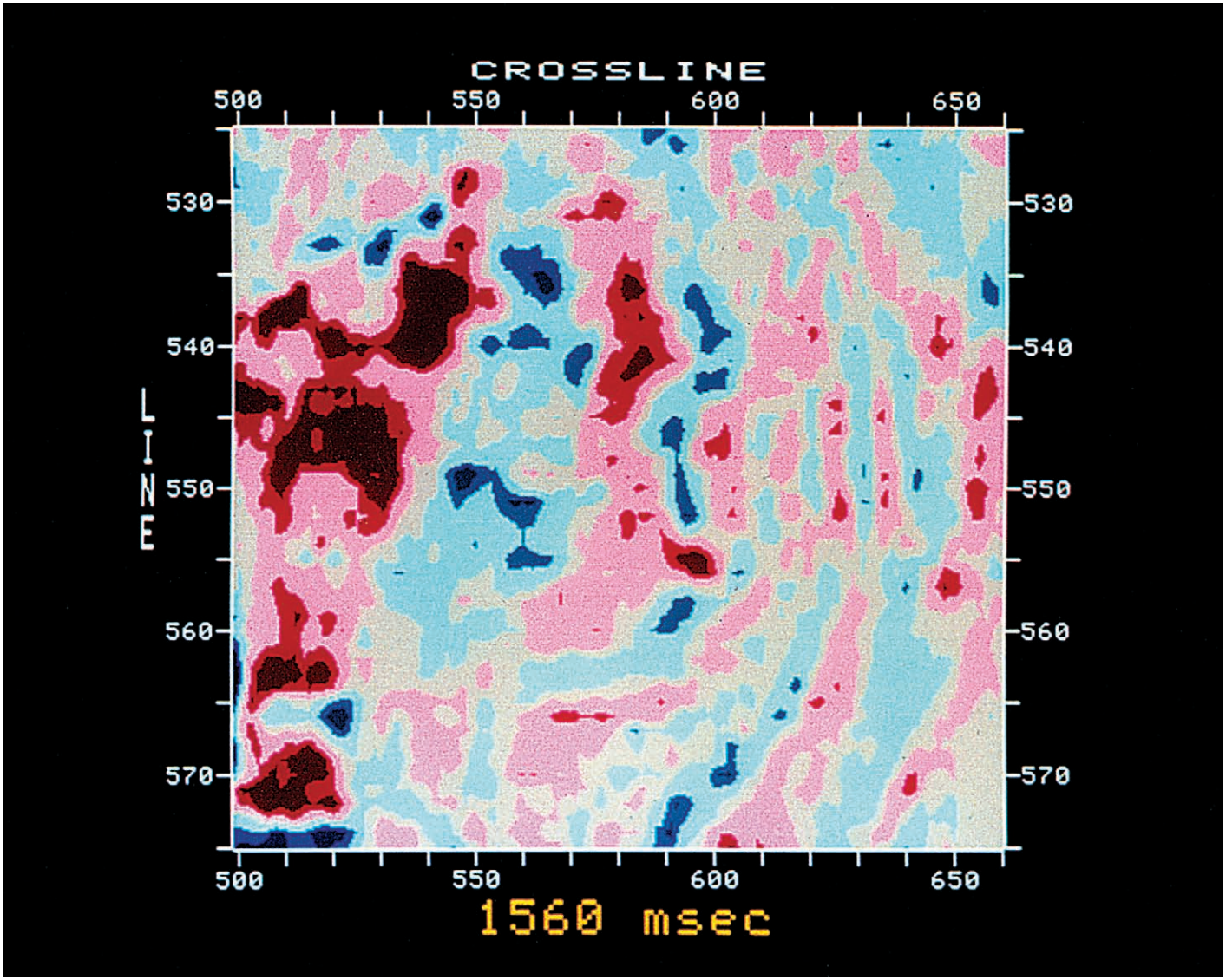

Fig. B-4.

Downloaded 25 Jun 2012 to 95.28.162.50. Redistribution subject to SEG license or copyright; Terms of Use: http://segdl.org/

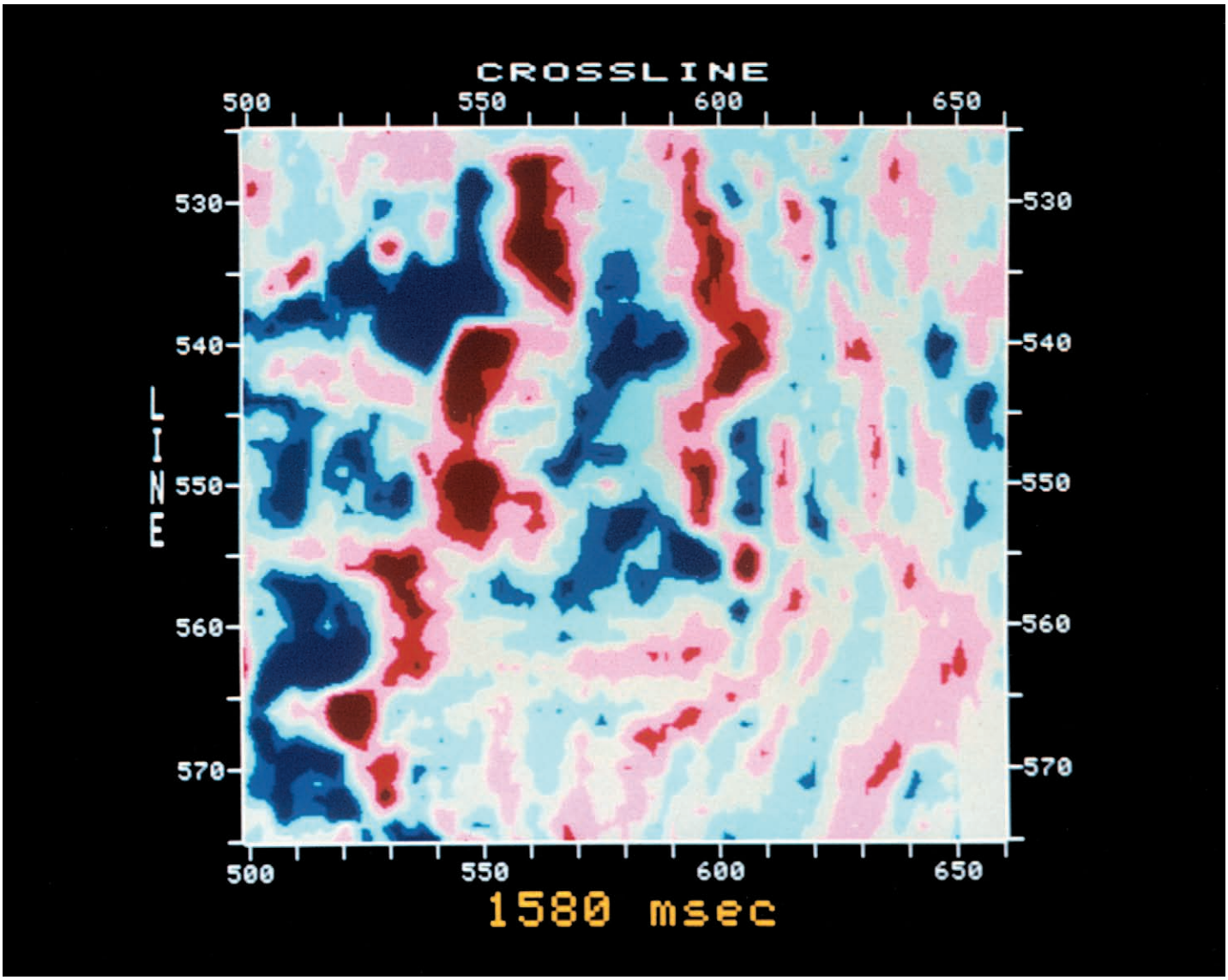

Fig. B-5.

Downloaded 25 Jun 2012 to 95.28.162.50. Redistribution subject to SEG license or copyright; Terms of Use: http://segdl.org/

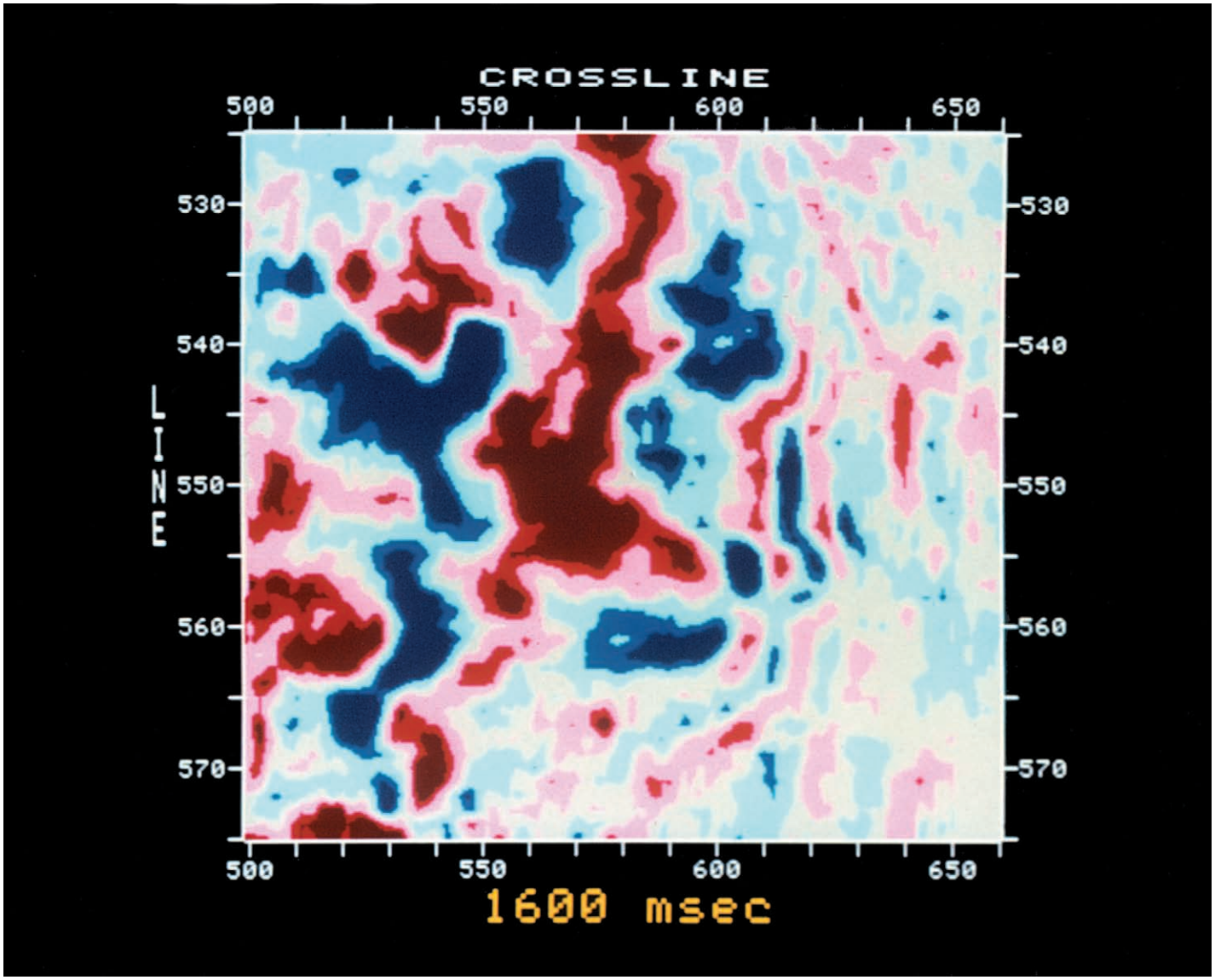

Fig. B-6.

Downloaded 25 Jun 2012 to 95.28.162.50. Redistribution subject to SEG license or copyright; Terms of Use: http://segdl.org/

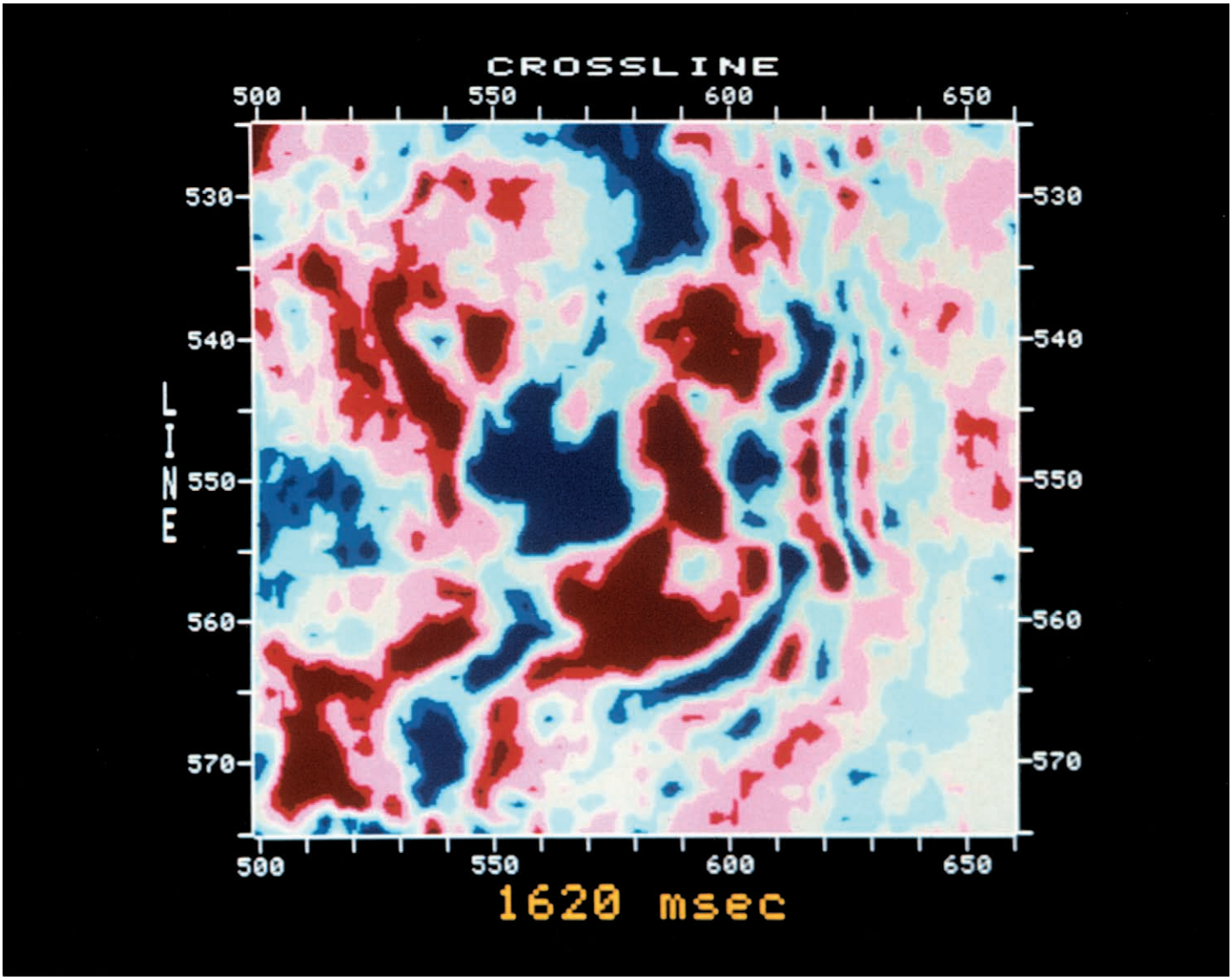

Fig. B-7.

Downloaded 25 Jun 2012 to 95.28.162.50. Redistribution subject to SEG license or copyright; Terms of Use: http://segdl.org/

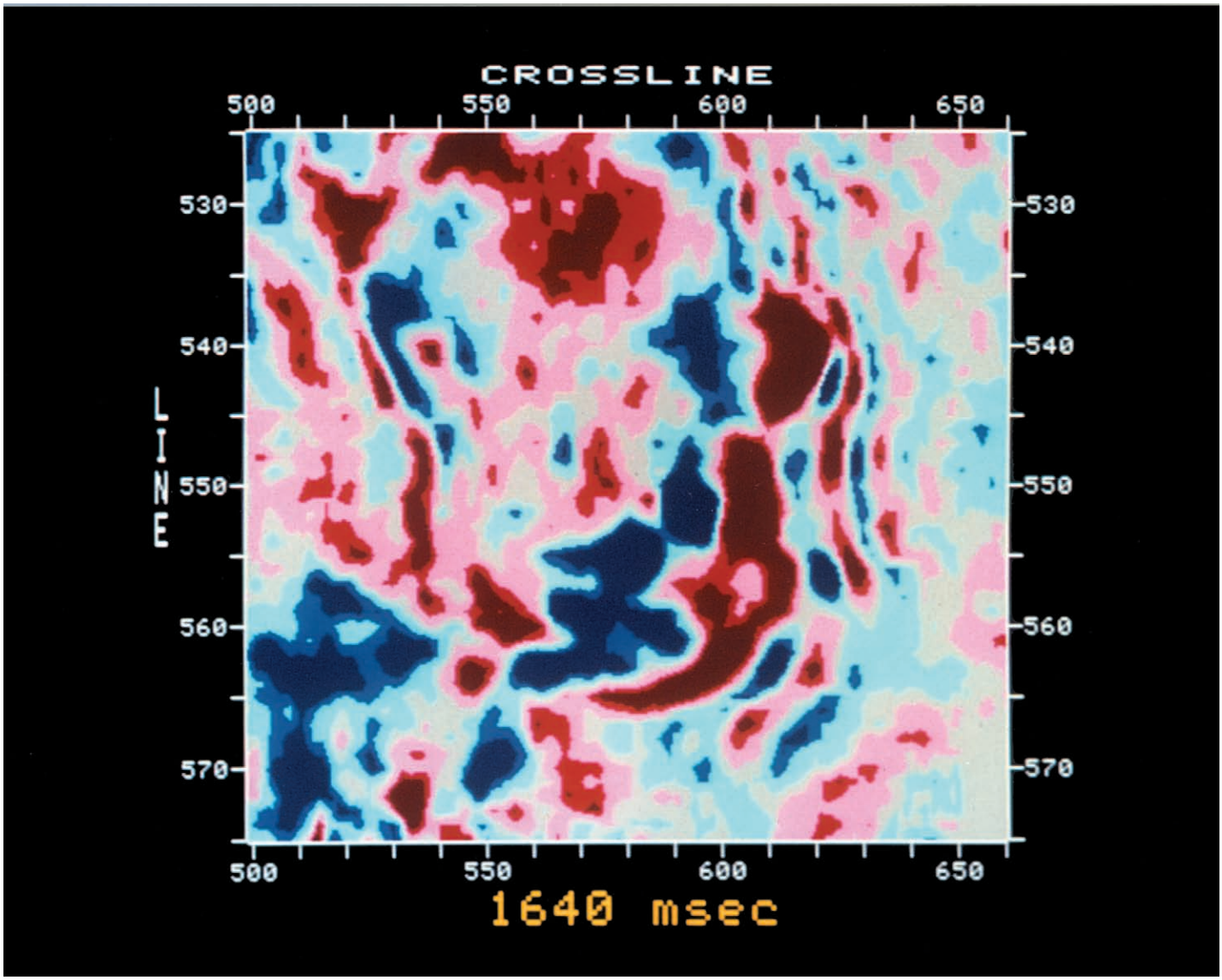

Fig. B-8.

Downloaded 25 Jun 2012 to 95.28.162.50. Redistribution subject to SEG license or copyright; Terms of Use: http://segdl.org/

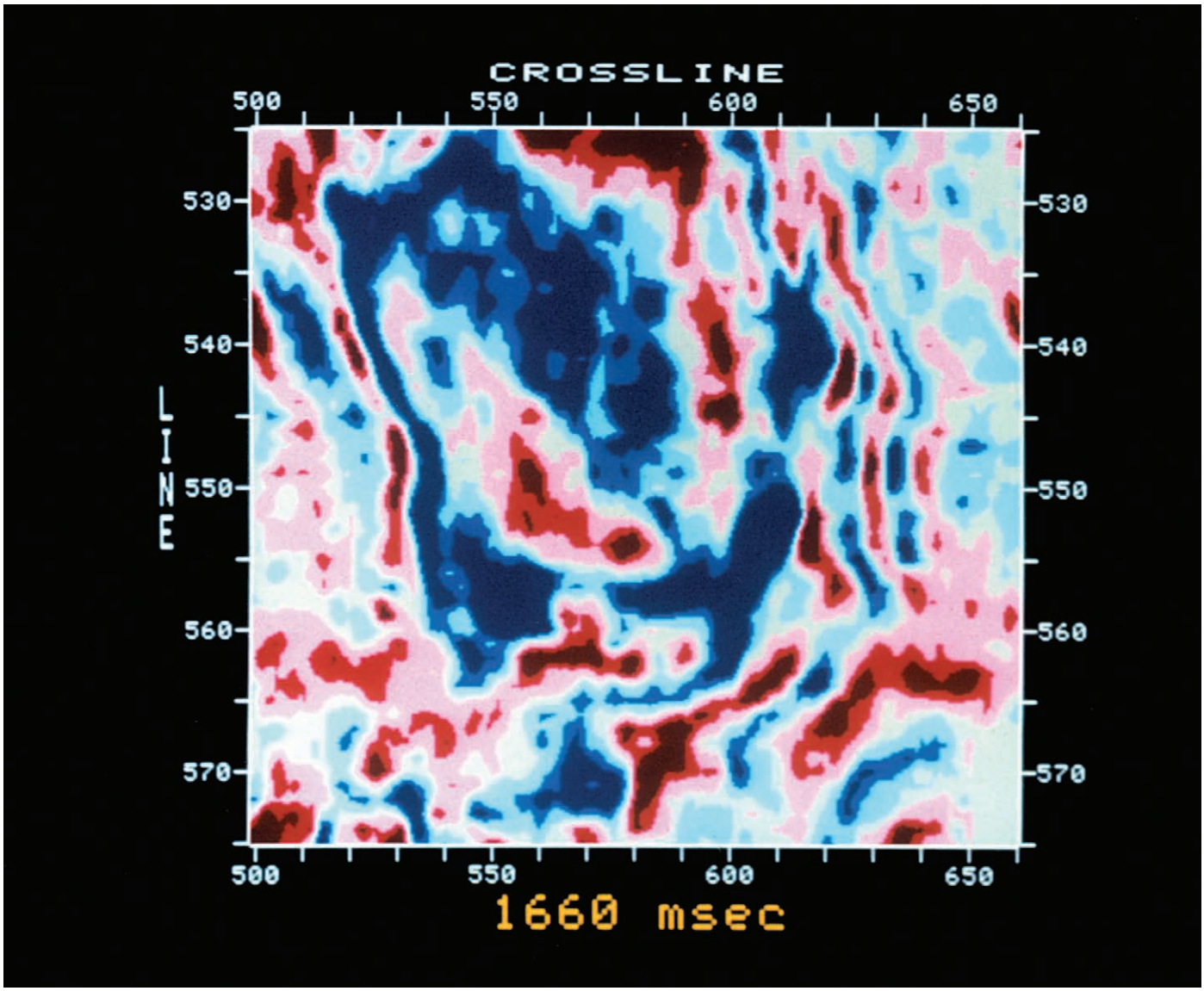

Fig. B-9.

Downloaded 25 Jun 2012 to 95.28.162.50. Redistribution subject to SEG license or copyright; Terms of Use: http://segdl.org/

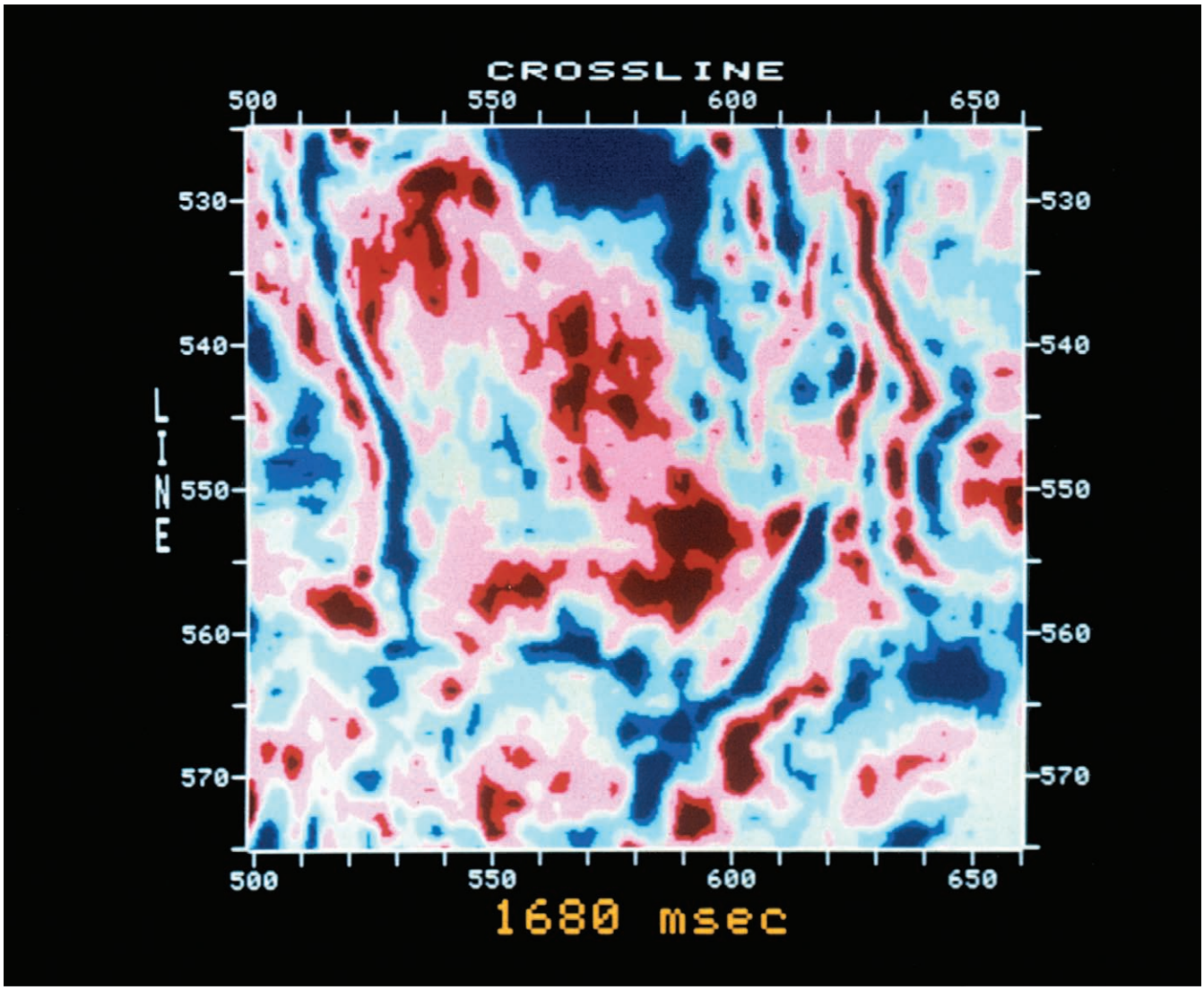

Fig. B-10.

Downloaded 25 Jun 2012 to 95.28.162.50. Redistribution subject to SEG license or copyright; Terms of Use: http://segdl.org/

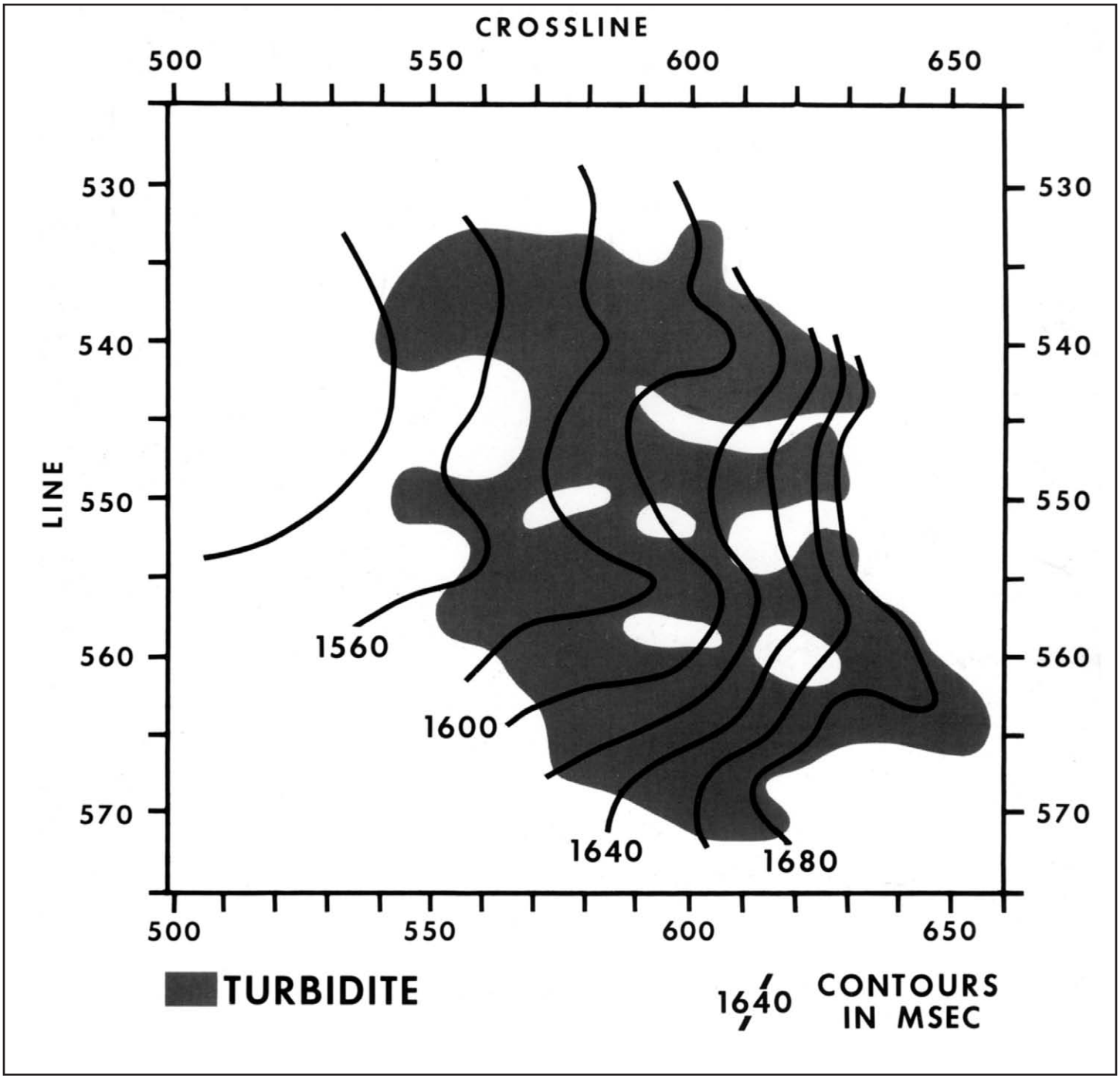

Fig. B-11.

Downloaded 25 Jun 2012 to 95.28.162.50. Redistribution subject to SEG license or copyright; Terms of Use: http://segdl.org/

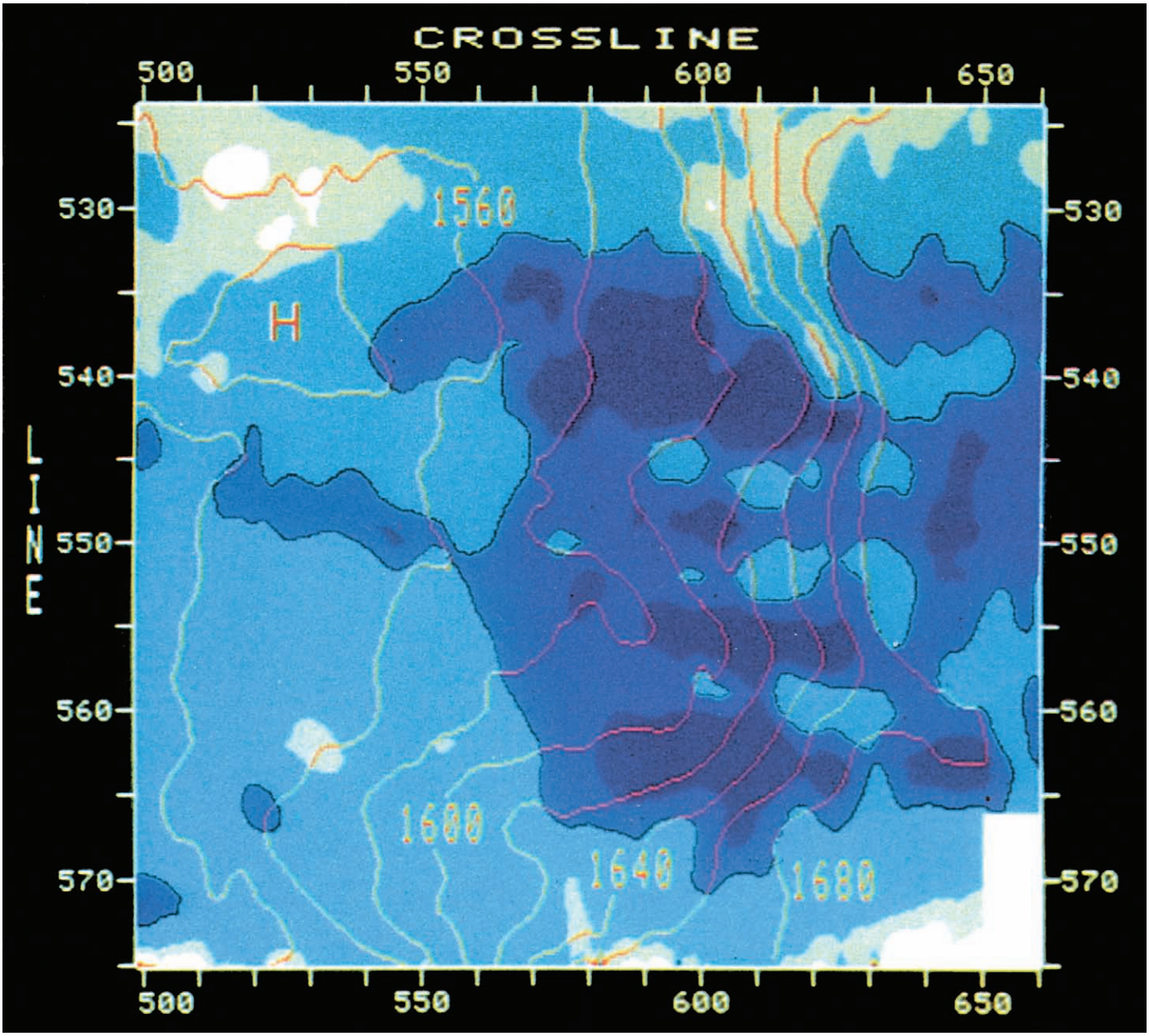

Fig. B-12.

Downloaded 25 Jun 2012 to 95.28.162.50. Redistribution subject to SEG license or copyright; Terms of Use: http://segdl.org/

APPENDIX C

Instructions for Assessing Phase and Polarity

The key to the interpretive assessment of data phase and polarity is to identify high-amplitude reflections and to understand their geologic cause. Reflections are generated by acoustic-impedance contrasts, and thus high-amplitude reflections result from large contrasts. It is important to understand whether the reflection package studied is caused by a single interface or by a layer with interfaces top and base.

The probable cause of a package of high-amplitude reflections should be one of the following:

Impedance Increase

e.g. fluid contact
top of massive carbonate
top of basement
water bottom
top of salt

Impedance Decrease

e.g. top of thick hydrocarbon sand
base of massive carbonate
base of hydrate stability zone
base of salt

Low-impedance Layer

e.g. hydrocarbon sand
shallow gas sand
clean porous sand

High-impedance Layer

e.g. igneous intrusion
thin carbonate
thin salt layer

Downloaded 25 Jun 2012 to 95.28.162.50. Redistribution subject to SEG license or copyright; Terms of Use: http://segdl.org/

Using general geologic knowledge of the area or using a well log, you should first decide which of these profiles is applicable. Then you should refer to the relevant diagram, and compare the actual character of the high-amplitude reflections with the four principal phase and polarity conditions. The data should be displayed with a balanced double-gradational color scheme using blue for positive amplitude and red for negative amplitude. Select the diagrammatic character that best fits the data. Remember that only primary lobes are shown in the diagrams; there will often be flanking side lobes visible.

Phase and polarity circles are presented diagrammatically for a low-impedance layer (Figure C-1), for a high-impedance layer (Figure C-2), and for an impedance increase (Figure C-3). An impedance decrease is not often used and is not shown. The feature that is generally the most useful is the low-impedance layer. A second phase and polarity circle using real data examples is presented for this feature (Figure C-4). An additional phase circle for a low-impedance layer is presented in Figure C-5. This shows some different data examples and examples of intermediate phase conditions. Figure C-6 shows a phase circle for fluid-contact reflections.

Downloaded 25 Jun 2012 to 95.28.162.50. Redistribution subject to SEG license or copyright; Terms of Use: http://segdl.org/

Fig. C-1.

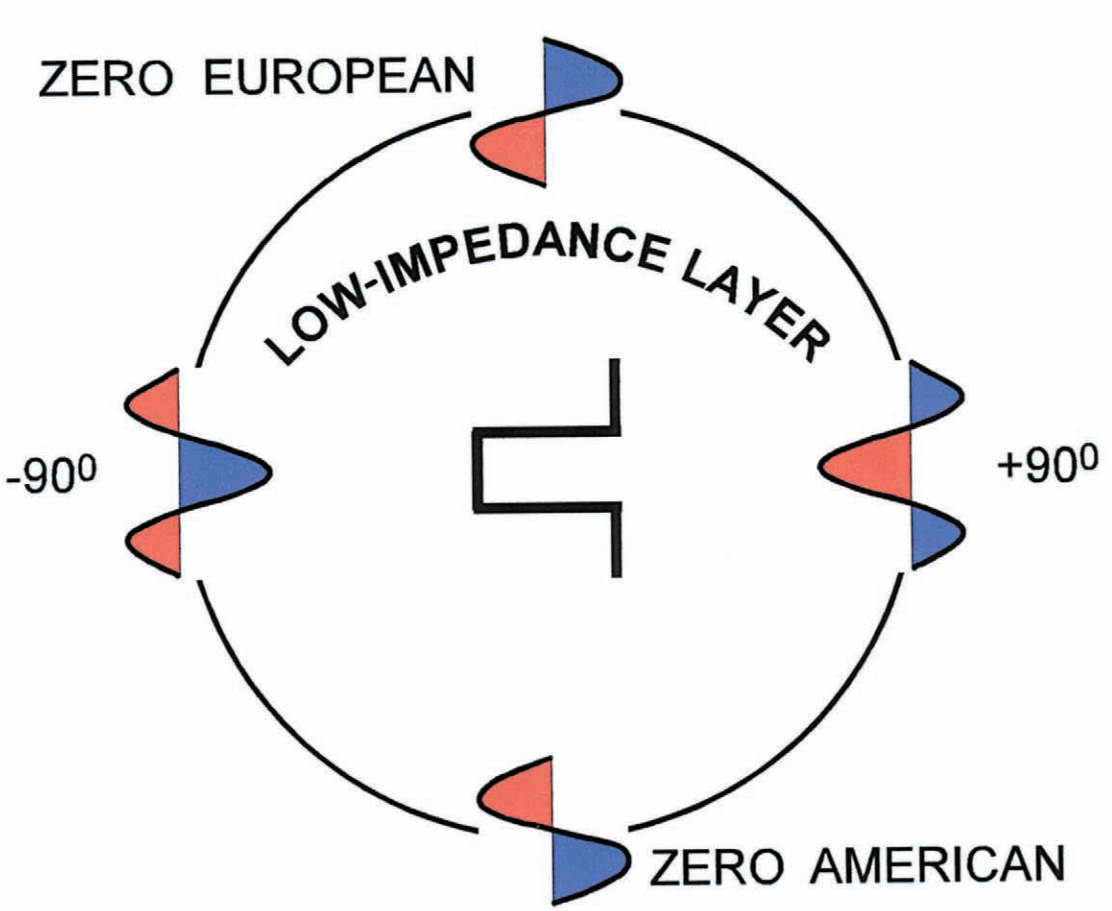

Fig. C-4.

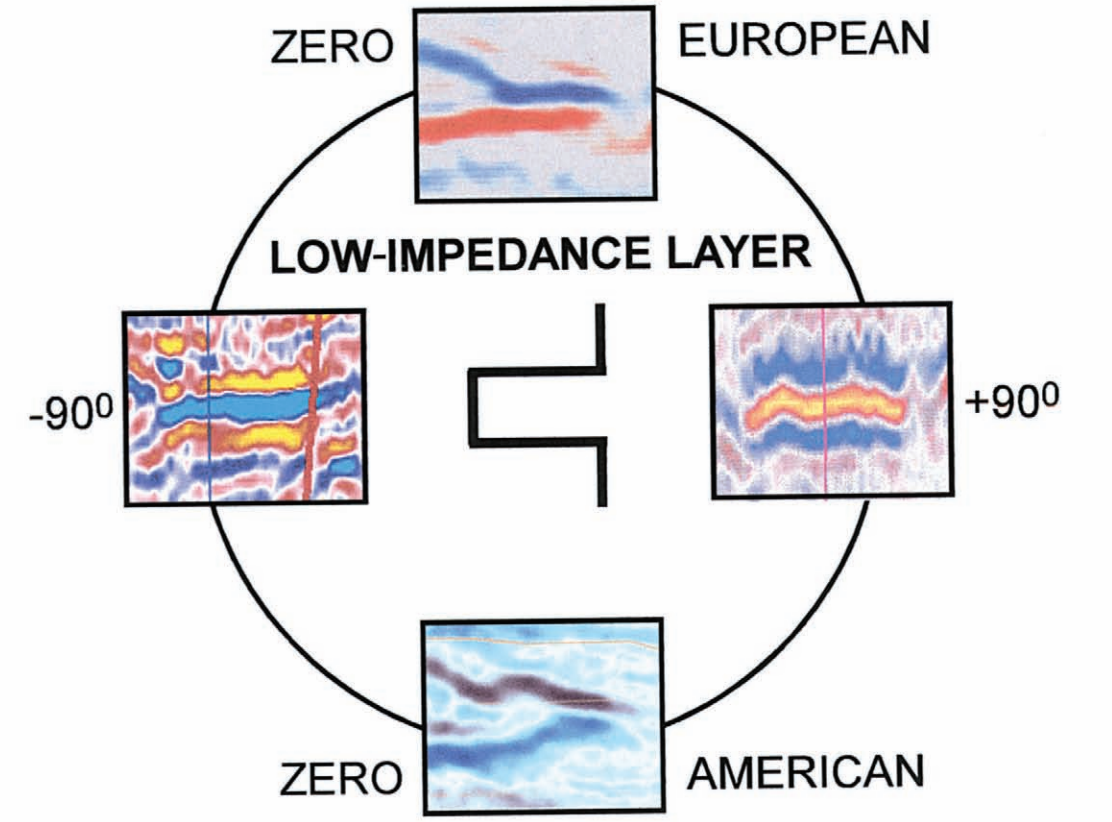

Downloaded 25 Jun 2012 to 95.28.162.50. Redistribution subject to SEG license or copyright; Terms of Use: http://segdl.org/

Fig. C-2.

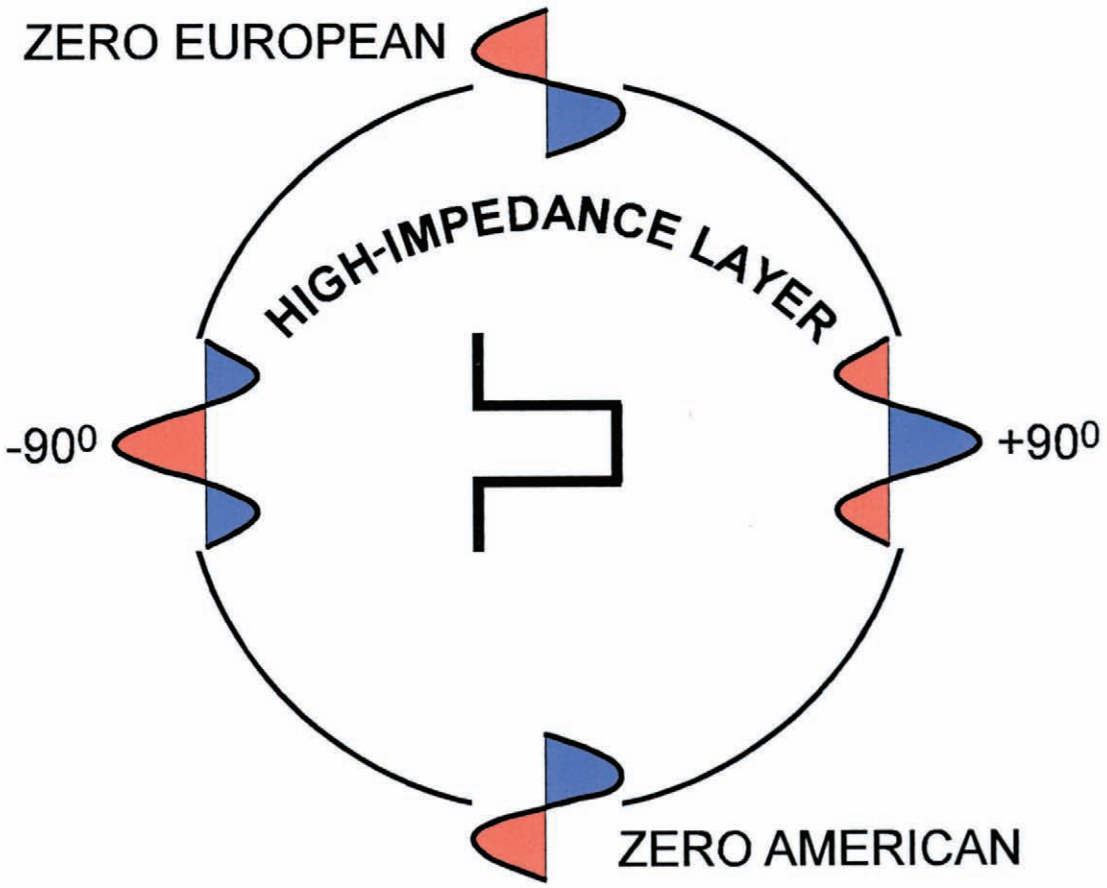

Fig. C-3.

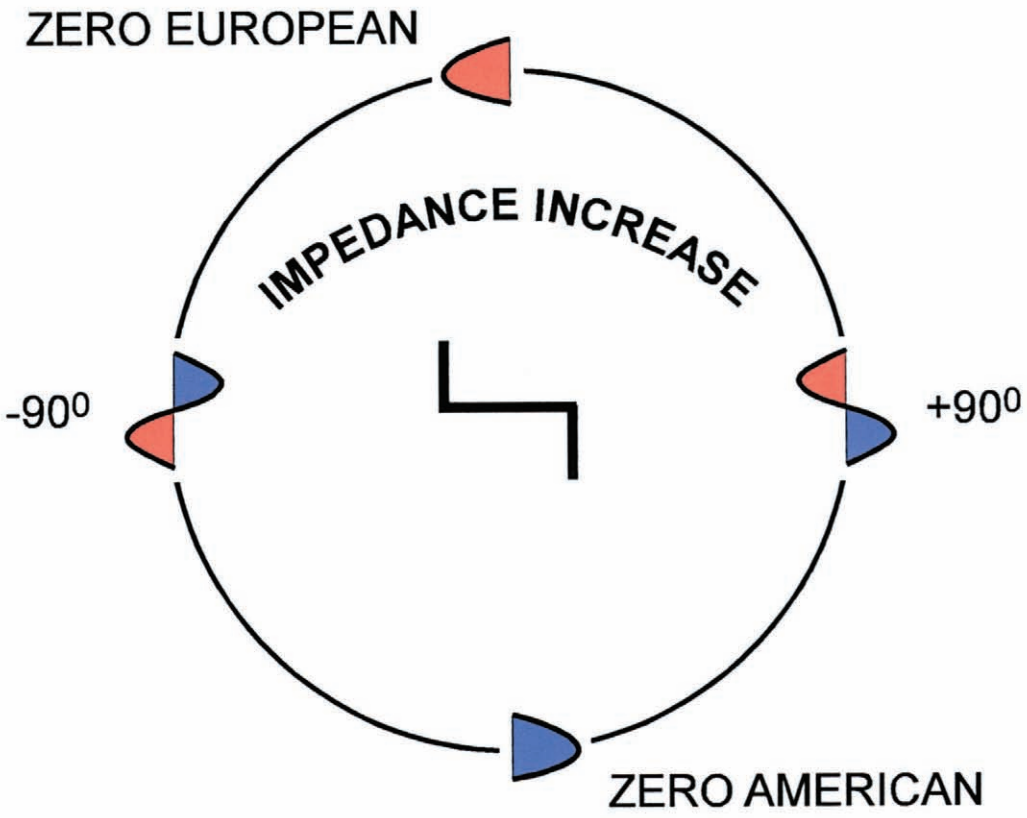

Downloaded 25 Jun 2012 to 95.28.162.50. Redistribution subject to SEG license or copyright; Terms of Use: http://segdl.org/

Fig. C-5.

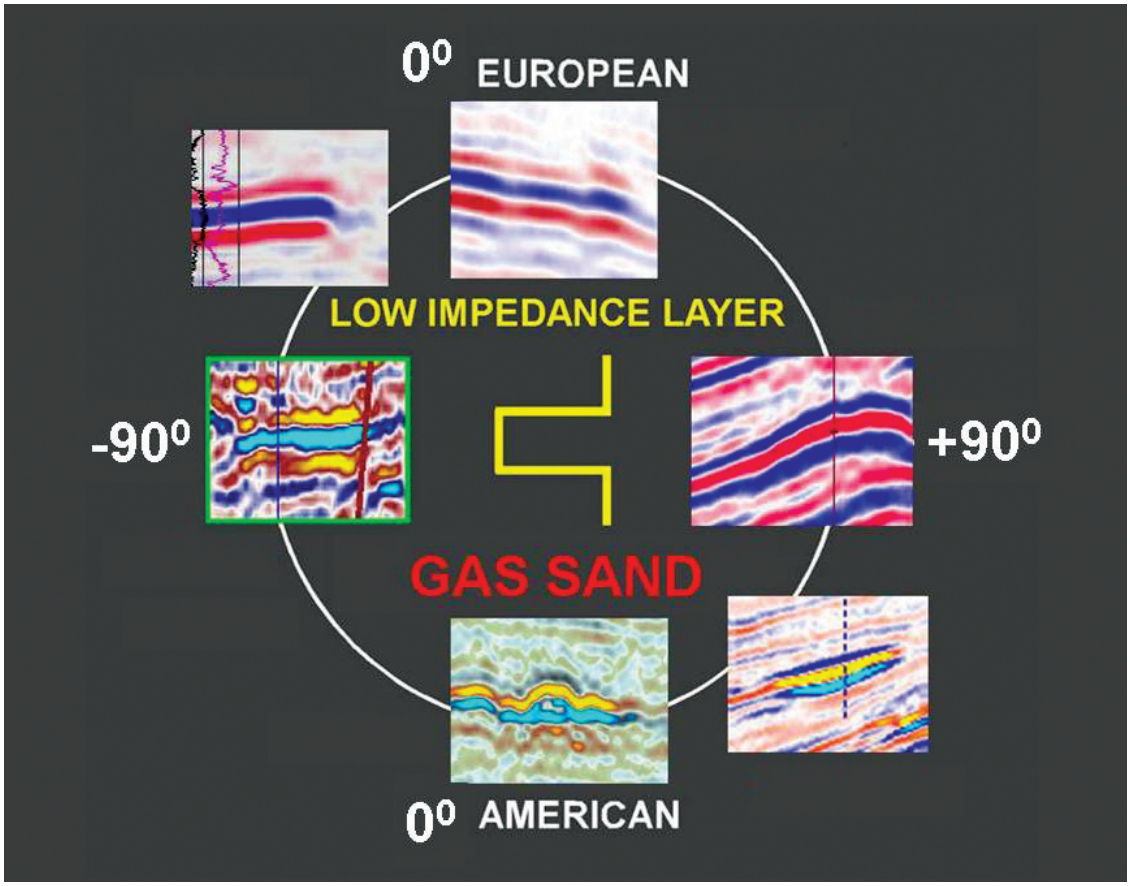

Fig. C-6.

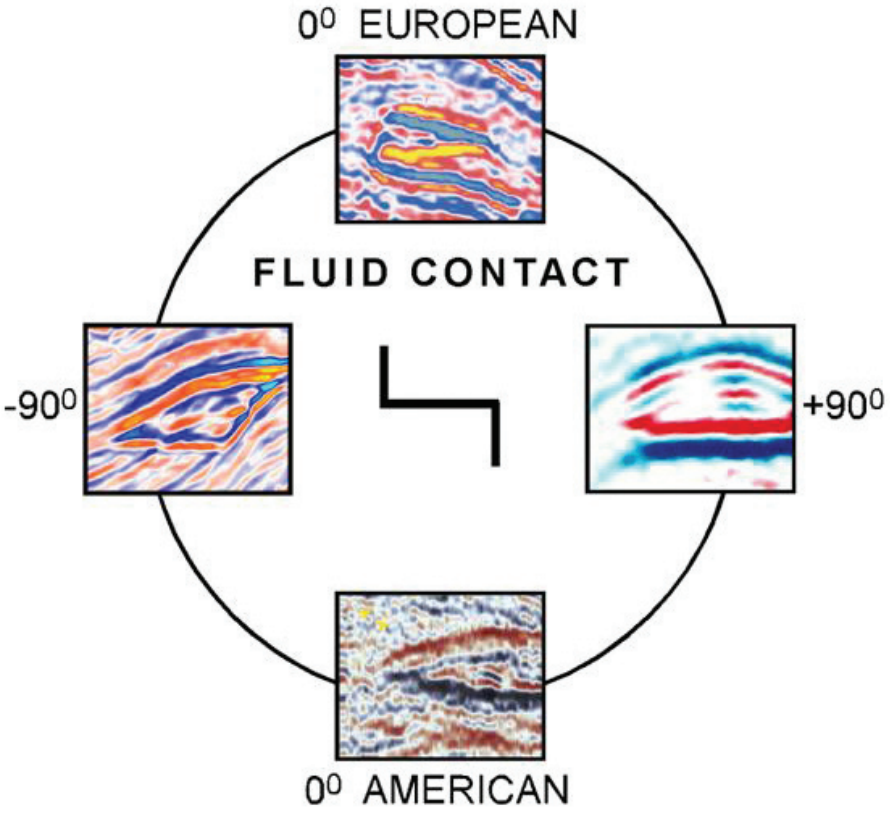

Downloaded 25 Jun 2012 to 95.28.162.50. Redistribution subject to SEG license or copyright; Terms of Use: http://segdl.org/

Summary of Recommendations to Help Today's Interpreter Get More Geology Out of 3-D Seismic Data in a Reasonable Period of Time

- Expect detailed subsurface information
- Don't rely on the workstation to find the solution
- Use all the data
- Understand the data and appreciate their defects
- Use time (or depth) slices/horizontal sections
- Visualize subsurface structure
- Use machine autotracking and snapping
- Select the color scheme with care
- Question data phase and polarity
- Tie seismic data to well data on character
- Try to believe seismic amplitude
- Understand the seismic attributes you use
- Prefer horizon attributes to windowed attributes
- Use techniques that maximize signal-to-noise ratio

Downloaded 25 Jun 2012 to 95.28.162.50. Redistribution subject to SEG license or copyright; Terms of Use: http://segdl.org/